Transactions of the ASME

Technical Editor, LEON M. KEER (1993)

The Technological Institute
Northwestern University
Evanston, IL 60201

APPLIED MECHANICS DIVISION

Chairman, WILLIAM S. SARIC
Secretary, THOMAS A. CRUSE
Associate Technical Editors,
R. ABEYARATNE (1995)
T. R. AKYLAS (1995)
S. A. BERGER (1995)
R. M. BOWEN (1994)
S. K. DATTA (1993)
G. J. DVORAK (1993)
M. E. FOURNEY (1994)
R. L. HUSTON (1994)
D. J. INMAN (1995)
J. T. C. LIU (1993)
X. MARKENSCOFF (1995)
R. M. McMEEKING (1994)
A. K. NOOR (1994)
J. W. RUDNICKI (1995)
W. N. SHARPE, JR. (1994)
C. F. SHIH (1993)
P. D. SPANOS (1995)
F. Y. M. WAN (1995)

BOARD ON COMMUNICATIONS
Chairman and Vice-President
M. E. FRANKE
Members-at-Large
W. BEGELL, T. F. CONRY, T. DEAR, R. L. KASTOR, J. KITTO, R. MATES, W. MORGAN, E. M. PATTON, R. E. REDER, A. VAN DER SLUYS, F. M. WHITE, B. ZIELS

President, N. H. HURT, JR.
Exec. Dir.
D. L. BELDEN
Treasurer, ROBERT A. BENNETT

PUBLISHING STAFF
Mng. Dir., Publ.,
CHARLES W. BEARDSLEY
Managing Editor,
CORNELIA MONAHAN
Production Editor, JUDY SIERANT
Prod. Asst., MARISOL ANDINO

Transactions of the ASME, Journal of Applied Mechanics (ISSN 0021-8936) is published quarterly (Mar., June, Sept., Dec.) for $160.00 per year by The American Society of Mechanical Engineers, 345 East 47th Street, New York, NY 10017. Second class postage paid at New York, NY and additional mailing offices. POSTMASTER: Send address changes to Transactions of the ASME, Journal of Applied Mechanics, c/o THE AMERICAN SOCIETY OF MECHANICAL ENGINEERS, 22 Law Drive, Box 2300, Fairfield, NJ 07007-2300.

CHANGES OF ADDRESS must be received at Society headquarters seven weeks before they are to be effective. Please send old label and new address.

PRICES: To members, $29.00, annually: to nonmembers, $160.00. Add $20.00 for postage to countries outside the United States and Canada.

STATEMENT from By-Laws. The Society shall not be responsible for statements or opinions advanced in papers or . . . printed in its publications (B7.1, Par. 3).

COPYRIGHT © **1992** by The American Society of Mechanical Engineers. Reprints from this publication may be made on condition that full credit be given the TRANSACTIONS OF THE ASME, JOURNAL OF APPLIED MECHANICS, and the author, and date of publication be stated.

INDEXED by Applied Mechanics Reviews and Engineering Information, Inc. Canadian Goods & Services Tax Registration #126148048.

Journal of Applied Mechanics

Published Quarterly by The American Society of Mechanical Engineers

VOLUME 59 • NUMBER 2 • PART 2 • JUNE 1992

TECHNICAL PAPERS

S1 **Differential Hardening in Sheet Metal Under Biaxial Loading: A Theoretical Framework** (92-APM-17)
R. Hill and J. W. Hutchinson

S10 **Transient Hygrothermal Stresses Induced in General Plane Problems by Theory of Coupled Heat and Moisture** (92-APM-8)
Tei-Chen Chen, Cheng-I Weng, and Win-Jin Chang

S17 **Grain Size Reduction in Granular Flows of Spheres: The Effects of Critical Impact Energy** (91-WA/APM-20)
M. W. Richman and A. A. Oyediran

S23 **Elementary Solutions and Process Sensitivities for Plane-Strain Sheet-Metal Forming** (92-APM-15)
M. L. Wenner

S29 **Viscoelastic Behavior of Elastomeric Membranes** (92-APM-1)
William W. Feng

S35 **Stochastic Modeling of Crack Initiation and Short-Crack Growth Under Creep and Creep Fatigue Conditions** (92-APM-5)
Takayuki Kitamura, Louis J. Ghosn, and Ryuichi Ohtani

S43 **Thermal Stresses in Nonlinearly Viscoelastic Solids** (91-WA/APM-37)
Giancarlo U. Losi and Wolfgang G. Knauss

S50 **An Evaluation of the Neuber and Glinka Relations for Monotonic Loading** (91-WA/APM-43)
W. N. Sharpe, Jr., C. H. Yang, and R. L. Tregoning

S57 **The Sliding Circular Inclusion in an Elastic Half-Plane** (91-WA/APM-35)
Mikyoung Lee, I. Jasiuk, and E. Tsuichida

S65 **Stress Concentration at a Nearly Circular Hole With Uncertain Irregularities** (91-WA/APM-22)
Dan Givoli and Isaac Elishakoff

S72 **The Elastic Potentials for Coplanar Interaction Between an Infinitesimal Prismatic Dislocation Loop and a Circular Crack for Transverse Isotropy** (91-WA/APM-27)
M. T. Hanson

S79 **Crack Deflection at an Interface Between Two Orthotropic Media** (91-WA/APM-42)
V. Gupta, A. S. Argon, and Z. Suo

S88 **Creep of Power-Law Material Containing Spherical Voids** (91-WA/APM-25)
P. Sofronis and R. M. McMeeking

S96 **A Method to Evaluate Three-Dimensional Time-Harmonic Elastodynamic Green's Functions in Transversely Isotropic Media** (92-APM-12)
H. Zhu

S102 **The Influence of Thermal Deformation on the Contact Temperature of Sliding Asperities** (92-APM-16)
C.-J. Lu and D. B. Bogy

S107 **The Stress Fields Caused by a Circular Cylindrical Inclusion** (91-WA/APM-32)
Hisao Hasegawa, Ven-Gen Lee, and Toshio Mura

S115 **Multiply Loaded Rigid Punch on a Stressed Orthotropic Half-Plane Via a Thin Elastic Layer** (91-WA/APM-30)
Hans L. Bjarnehed

S123 **The Elastic Field for Conical Indentation Including Sliding Friction for Transverse Isotropy** (91-WA/APM-39)
M. T. Hanson

S131 **A General Treatment of the Elastic Field of an Elliptical Inhomogeneity Under Antiplane Shear** (92-APM-23)
S. X. Gong and S. A. Meguid

S136 **Analysis of Acoustic Pulses Reflected From Fiber-Reinforced Composite Laminates** (91-WA/APM-18)
A. K. Mal, C.-C. Yin, and Y. Bar-Cohen

S145 **Transient Wave Propagation in a Harmonically Heterogeneous Elastic Solid** (91-WA/APM-34)
Hyun-Sil Kim and Jerry H. Ginsberg

S152 **Impact Response of a Single Edge Crack in an Orthotropic Strip** (92-APM-22)
Yasuhide Shindo, Hiroaki Higaki, and Hideaki Nozaki

S158 **Dynamic Crack Propagation Analysis by Moving Singular Boundary Elements** (92-APM-3)
Rafael Gallego and Jose Dominguez

S163 **A Study of the Fiber-Matrix Interface in Composite Materials** (92-WA/APM-33)
Jin O. Kim and Haim H. Bau

S166 **A Variational Approach to Three-Dimensional Elasticity Solutions of Laminated Composite Plates** (92-WA/APM-31)
M. Savoia and J. N. Reddy

S176 **Modification of the Shear Lag Analysis for Determination of Elastic Modulus of Short-Fiber (or Whisker) Reinforced Metal Matrix Composites** (91-WA/APM-44)
S. V. Nair and H. G. Kim

S183 **Effect of Interphase on Compressive Strength of Unidirectional Composites** (92-APM-4)
A. M. Waas

(Contents continued on Inside Back Cover)

Downloaded 04 May 2010 to 171.66.16.49. Redistribution subject to ASME license or copyright; see http://www.asme.org/terms/Terms_Use.cfm

S189 Flexural Wave Propagation in an Elastic Beam With Periodic Structure (91-WA/APM-40)
Sen Yung Lee and Huei Yaw Ke

S197 Natural Frequencies and Normal Modes of A Spinning Timoshenko Beam With General Boundary Conditions (92-APM-6)
Jean Wu-Zheng Zu and Ray P. S. Han

S205 Exact Solutions for the Analysis of General Elastically Restrained Nonuniform Beams (91-WA/APM-26)
Sen Yung Lee and Yee Hsiung Kuo

S213 Compression of a Cord (91-WA/APM-36)
Amit Prakash, Ted A. Conway, and George A. Costello

S217 Effect of Accuracy Loss in Classical Shell Theory (91-WA/APM-38)
V. Berdichevsky and V. Misyura

S224 The Equations of Motion for the Torsional and Bending Vibrations of a Stranded Cable (91-WA/APM-19)
Warren N. White, Srinivasan Venkatasubramanian, P. Michael Lynch, and Chi-Lung D. Huang

S230 Effects of Load Parameters on the Natural Frequencies and Stability of a Flexible Spinning Disk With a Stationary Load System (92-APM-2)
Jen-San Chen and D. B. Bogy

S236 Frequency Window Method for Strongly Coupled and Multiply Connected Structural Systems: One-Mode Windows (91-WA/APM-23)
Kyung-Win Min, Takeru Igusa, and Jan D. Achenbach

S244 Frequency Window Method for Strongly Coupled and Multiply Connected Structural Systems: Multiple-Mode Windows (91-WA/APM-24)
Kyung-Win Min, Takeru Igusa, and Jan D. Achenbach

S253 Response of a Flexible Printed Circuit Board to Periodic Shock Loads Applied to its Support Contour (92-APM-9)
E. Suhir

S260 Simulation of Homogeneous Two-Dimensional Random Fields: Part I—AR and ARMA Models (91-WA/APM-28)
Marc P. Mignolet and Pol D. Spanos

S270 Simulation of Homogeneous Two-Dimensional Random Fields: Part II—MA and ARMA Models (91-WA/APM-29)
Pol D. Spanos and Marc P. Mignolet

S278 Eigenvalue Inclusion Principles for Discrete Gyroscopic Systems (91-WA/APM-14)
B. Yang

S284 Vibration of Harmonically Excited Oscillators With Asymmetric Constraints (91-WA/APM-21)
S. Natsiavas and H. Gonzalez

S291 Weakly Nonlinear Instability of a Liquid Jet in a Viscous Gas (91-WA/APM-15)
E. A. Ibrahim and S. P. Lin

ANNOUNCEMENTS AND SPECIAL NOTES

S42 Symposium on High Performance Computing for Flight Vehicles

S122 10th Biennial Conference on Reliability, Stress Analysis, and Failure Prevention—Call for Papers

S144 SES-ASME-ASCE Joint Meeting—Call for Papers

S188 Second International Conference on Vibration Problems of Mathematical Elasticity and Physics—Call for Papers

Downloaded 04 May 2010 to 171.66.16.49. Redistribution subject to ASME license or copyright; see http://www.asme.org/terms/Terms_Use.cfm

Differential Hardening in Sheet Metal Under Biaxial Loading: A Theoretical Framework

R. Hill
Department of Applied Mathematics and Theoretical Physics, University of Cambridge, Cambridge CB3 9EW, England

J. W. Hutchinson
Division of Applied Sciences, Harvard University, Cambridge, MA 02138
Fellow ASME

A simple constitutive framework is proposed to take account of progressive changes in a stress-based criterion of yielding as plastic deformation accumulates. The analysis is relevant to a sheet of isotropic or orthotropic material which is subsequently loaded in its plane by biaxial tensions (σ_1, σ_2) *in arbitrary fixed ratio. Under these circumstances there is evidence that texture development causes significant changes in the shapes of successive yield loci in* (σ_1, σ_2) *space. Here such departures from geometric similarity are explicitly linked to a presumed dependence on* σ_1/σ_2 *of the exponent* m *in a standard power-law representation of the stress-strain characteristic under each constant value of* σ_1/σ_2. *The linkage is formulated in detail for several types of representation, and it is shown how a family of yield loci associated with any conjectural dependence* $\mathrm{m}(\sigma_1/\sigma_2)$ *can be generated readily by computer graphics. Some typical examples are given, in particular when* $\mathrm{m}(\sigma_1/\sigma_2)$ *reflects the distinctive trends reported for certain kinds of brass and aluminum sheet (e.g., Wagoner, 1980; Stout and Hecker 1983).*

1 Objectives

The context is elastoplastic response of a textured sheet of polycrystalline material under in-plane biaxial loads. In its as-received condition the material is assumed to be orthotropic at a macroscopic level. Uniform tensions in arbitrary fixed ratios are applied parallel to the orthotropic axes, which hence remain embedded in the material as it deforms. The aim of the analysis is a constitutive framework that accommodates differential hardening due to textural changes accompanying plastic deformation. The approach is macroscopic and phenomenological only: we attempt no correlation with statistics at the level of crystal geometries, orientations, slip systems, or Schmid stresses (e.g., Lequeu and Jonas, 1988; Chan and Lee, 1990).

2 General Framework

A typical yield locus in the cartesian space of the principal Cauchy stresses (σ_1, σ_2) will be expressed in polar coordinates:

$$\phi(\tau,\theta) = \sigma \tag{1}$$

where $(\sigma_1,\sigma_2) = \tau(\cos\theta, \sin\theta)$ as shown in Fig. 1 and $0 \le \theta \le 2\pi$. The function ϕ is here normalized by the current yield stress σ in equibiaxial tension, which means that $\phi(\sqrt{2}\sigma, 1/4\pi) \equiv \sigma$. Regarding the conceptual status of yield loci, it is recalled that any particular one is the product of a *specific* loading path. Moreover, its geometry and scale necessarily reflect the terminal texture generated by the associated strain history, which is likewise specific for that locus.

In principle, then, if the same terminus in stress space were to be approached by some other route, the strain history and final texture would both differ. So therefore would the resulting locus, in greater or lesser degree according to the circumstances. Since the nature of this latter type of path dependence has been little explored, we ignore it. In so doing, we follow custom and idealize the totality of yield loci attainable from a given initial state as a *non-intersecting* and *singly infinite* family. Its members are not required to be self-similar, however, as in classical formulations where function $\phi(\tau,\theta)$ reduces to $\tau\phi(\theta)$ simply. On the contrary, progressive changes

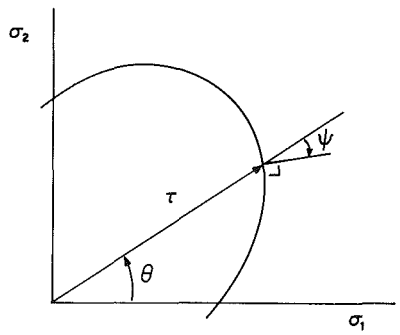


Fig. 1 Typical yield locus in (σ_1,σ_2) space, showing polar coordinates (τ,θ) and the clockwise angle ψ between a radius and the local outward normal

Contributed by the Applied Mechanics Division of THE AMERICAN SOCIETY OF MECHANICAL ENGINEERS for presentation at the 1992 ASME Summer Mechanics and Materials Meeting, Tempe, AZ, Apr. 28-May 1, 1992.

Discussion on this paper should be addressed to the Technical Editor, Prof. Leon M. Keer, The Technological Institute, Northwestern University, Evanston, IL 60208, and will be accepted until four months after final publication of the paper itself in the JOURNAL OF APPLIED MECHANICS. Manuscript received by the ASME Applied Mechanics Division, Apr. 12, 1991; final revision, Sept. 25, 1991.

Paper No. 92-APM-17.

Copyright © 1992 by ASME
Downloaded 03 May 2010 to 171.66.16.247. Redistribution subject to ASME license or copyright; see http://www.asme.org/terms/Terms_Use.cfm

in shape within a family are of paramount concern: we see them as inevitable concomitants of textural development during deformation.

Henceforward we focus on radial paths since these predominate in experiments on in-plane plastic response. Let γ be conjugate to τ in that

$$dw = \tau d\gamma \quad \text{at fixed } \theta \tag{2}$$

where w is the total work expended per unit volume and γ is reckoned from the origin. Generally,

$$dw = \sigma_1 d\epsilon_1 + \sigma_2 d\epsilon_2 \tag{3}$$

in terms of the logarithmic strains (ϵ_1, ϵ_2) parallel to the orthotropic axes, so the work conjugate is identifiable as

$$\gamma = \epsilon_1 \cos\theta + \epsilon_2 \sin\theta. \tag{4}$$

It is noted in passing that

$$\tau\gamma = \sigma_1\epsilon_1 + \sigma_2\epsilon_2. \tag{5}$$

Elasticity being neglected, the relation between τ and γ can be regarded as the stress versus plastic strain characteristic in a test at fixed θ. More suited to our purpose, however, is the corresponding relation between τ and w, say

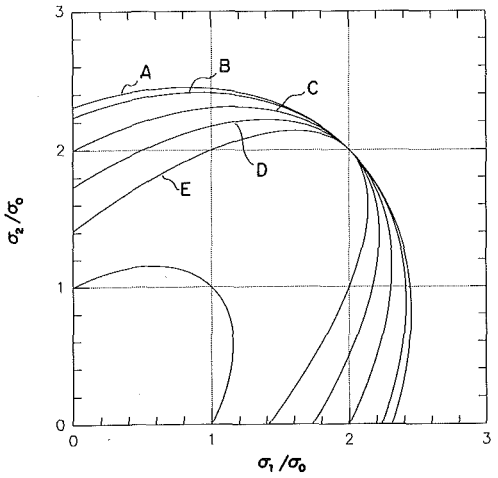


Fig. 2(*a*)

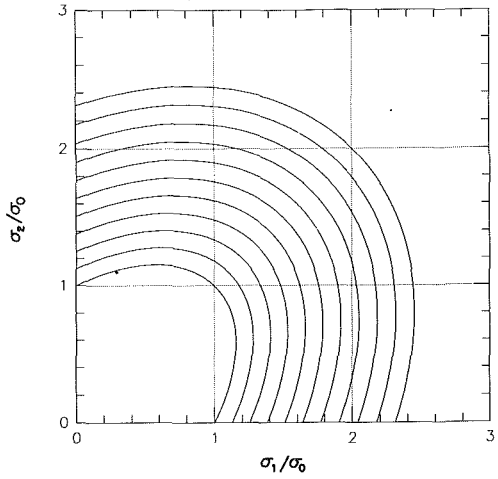


Fig. 3(*a*)

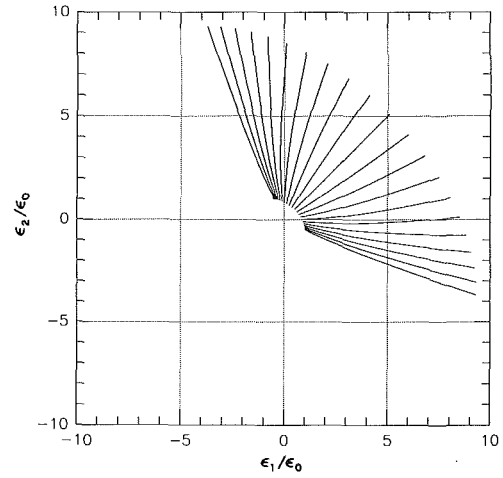


Fig. 3(*b*)

Fig. 3(*a*) Family of loci between $\tau_0(\theta)$ and $\tau_\infty(\theta)$ for case A of Fig. 2; (*b*) strain trajectories for radial stress loading with θ in the range $(0,\pi/2)$

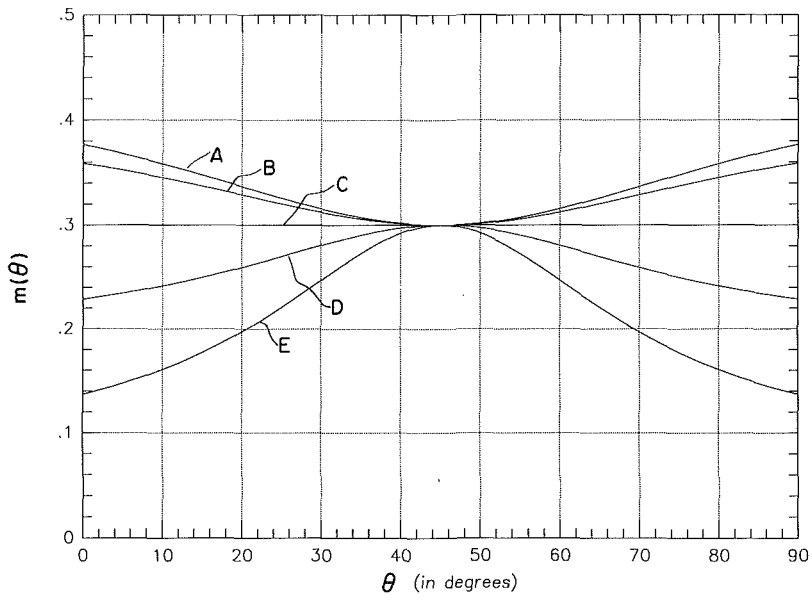


Fig. 2(*b*)

Fig. 2 The relationship between $m(\theta)$ and the outer prescribed locus $\tau_\infty(\theta)$ for $n = 0.3$ and $\sigma_\infty/\sigma_0 = 2$. The five outer loci are ellipses specified in the text. The inner locus is the Mises ellipse.

Downloaded 03 May 2010 to 171.66.16.247. Redistribution subject to ASME license or copyright; see http://www.asme.org/terms/Terms_Use.cfm

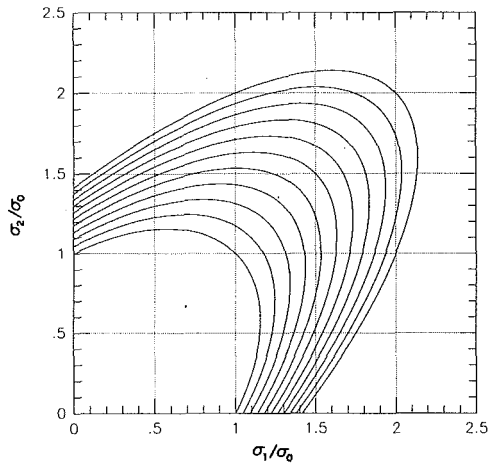


Fig. 4(*a*)

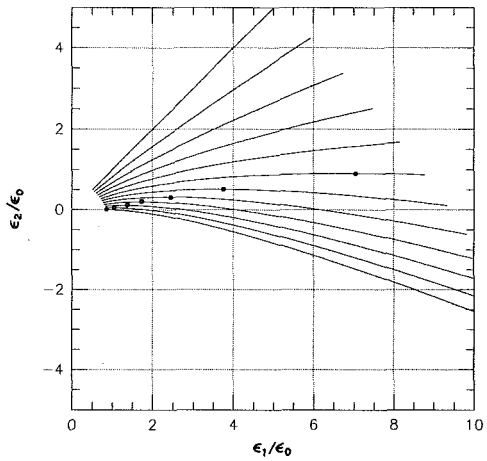


Fig. 4(*b*)

Fig. 4(*a*) Family of loci between $\tau_0(\theta)$ and $\tau_\infty(\theta)$ for case E of Fig. 2; (*b*) strain trajectories for radial stress loading with θ in the range $(\theta^*, \pi/4)$ where $\theta^* = \tan^{-1}(1/2)$

$$f(\tau,\theta) = w. \tag{6}$$

In particular this is

$$f\left(\sqrt{2}\sigma, \frac{1}{4}\pi\right) = w \tag{7}$$

in equibiaxial tension. Let ϵ be conjugate to σ in that

$$dw = \sigma d\epsilon \quad \text{when} \quad \theta = \frac{1}{4}\pi. \tag{8}$$

Then

$$\epsilon = \sqrt{2}\gamma = \epsilon_1 + \epsilon_2 = -\epsilon_3 \tag{9}$$

where ϵ_3 is the through-thickness logarithmic strain (the material being incompressible).

We wish to construct a family of yield loci from the radial test data. For that purpose it is hypothesized that the same amount of work per unit volume is expended on every ray to a given locus. Then the family can be parameterized by w just as well as by σ. From this standpoint the assemblage (6) of radial test data (namely $\tau(w)$ at any fixed θ) also generates the individual loci (namely $\tau(\theta)$ at any fixed w). The equivalent parameterization by σ is obtained by combining (6) and (7) as

$$f(\tau,\theta) = f\left(\sqrt{2}\sigma, \frac{1}{4}\pi\right) \tag{10}$$

which can be reduced to (1). Conversely, when a family of loci in stress space is given, it is automatically parameterized by values of σ known from intersections with the equibiaxial ray $\theta = \pi/4$. If, in addition, we assign the $\sigma(w)$ characteristic on $\theta = \pi/4$, the parameterization (6) is induced from (1), and hence the test data $\tau(w)$ at any fixed θ. Equivalently, $\sigma(\epsilon)$ for $\theta = \pi/4$ generates $\tau(\gamma)$ for any θ when the loci are given.

The proposed framework and its complementary aspects are now explained further by means of particular examples.

3 Particular Frameworks

Analytical representations of experimental stress-strain data on radial paths are often sought within a class of so-called power laws. In the present variables these laws are of type

$$\tau(\gamma,\theta) = \kappa(\theta)\gamma^{m(\theta)} \tag{11}$$

where $0 < m < 1$. There is evidence indicating that the scale factor κ and the exponent m depend on the path direction θ in at least some materials (e.g., Ghosh and Backofen, 1973; Ghosh, 1978; Wagoner, 1980, 1982; Stout and Hecker, 1983; Stout and Staudhammer, 1984). In the expectation that these dependences will be found more widely, both are allowed for in the formula. The associated increment in work along a radial path is given variously by

$$dw = \tau d\gamma = \gamma d\tau/m = d(\tau\gamma)/(1+m) \tag{12}$$

per unit volume, where for brevity the possible dependence on θ is not shown explicitly.

Empirical representations by power laws, however, are usually sufficiently accurate only above a certain threshold of strain. In order to take account of this limitation we replace (11) by

$$\tau(\gamma,\theta) = \kappa(\theta)\gamma^{m(\theta)} \quad \text{if and only if} \quad \kappa(\theta)\gamma^{m(\theta)} \geq \tau_0(\theta). \tag{13}$$

Here, $\tau_0(\theta)$ is an inner reference locus and is presumed to be attained by the expenditure of work w_0 on a radial path from the as-received state. The intervening stress-strain behavior is not represented by this formula, nor is there need of any other. Instead it is supposed merely that $\tau_0(\theta)$ and w_0 are chosen empirically in the course of fitting (13) to data over a range of strain such that $\gamma \geq \gamma_0(\theta)$, say. Then a formula corresponding to (6) for the work w on radial paths from the origin is

$$(1+m)(w-w_0)/\kappa = (\tau/\kappa)^{(1+m)/m} - (\tau_0/\kappa)^{(1+m)/m}. \tag{14}$$

Subsequent loci parameterized by values of $w > w_0$ are thus given by

$$(\tau/\tau_0)^{(1+m)/m} - 1 = (1+m)(w-w_0)/\tau_0\gamma_0. \tag{15}$$

Here

$$\tau_0 = \kappa\gamma_0^m \quad \text{but} \quad w_0 \neq \tau_0\gamma_0/(1+m) \tag{16}$$

in general, since (12) does not apply when $\gamma < \gamma_0(\theta)$. As an illustration the computations will be simplified by taking $\tau_0(\theta)\gamma_0(\theta)$ to be constant (which would be the case if, for instance, the loci within $\tau_0(\theta)$ were geometrically similar to it). Then the exterior family is generated parametrically by

$$\{(\tau/\tau_0)^{(1+m)/m} - 1\}/(1+m) = \text{constant} \tag{17}$$

on each locus. Another possibility worth considering is uniform $\tau_0(\theta)\gamma_0(\theta)/\{1+m(\theta)\}$. The exterior family is now generated by

$$(\tau/\tau_0)^{(1+m)/m} = \text{constant} \tag{18}$$

on each locus.

An alternative representation of radial stress-strain data, more suitable for certain materials, is

$$\tau = \kappa(\gamma+\eta)^m \tag{19}$$

for any range of strain. Here the material constants m, κ, and $\eta(>0)$ may all depend on θ. In the as-received state the yield locus is $\tau = \xi(\theta)$ where

$$\xi = \kappa\eta^m. \tag{20}$$

The initial rate of hardening is $d\tau/d\gamma = m\xi/\eta$, which suggests that η will usually be less than m in practice. The work on radial paths from the origin is now such that

Downloaded 03 May 2010 to 171.66.16.247. Redistribution subject to ASME license or copyright; see http://www.asme.org/terms/Terms_Use.cfm

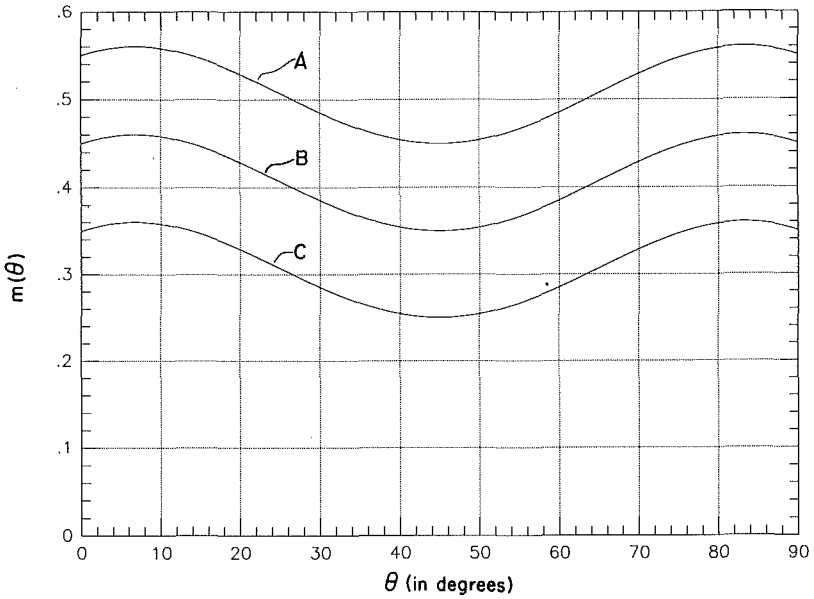


Fig. 5(*a*)

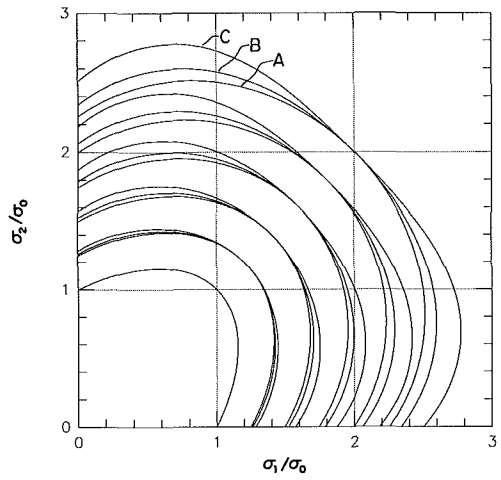


Fig. 5(*b*)

Fig. 5 Yield loci associated with inner Mises ellipse, $\tau_0(\theta)$, and variations of $m(\theta)$ prescribed by Eqs. (39) and (40)

$$(1+m)w/\kappa = (\tau/\kappa)^{(1+m)/m} - (\xi/\kappa)^{(1+m)/m} \tag{21}$$

where $\tau > \xi$. Subsequent loci parameterized by positive values of w are given by

$$(\tau/\xi)^{(1+m)/m} - 1 = (1+m)\,w/\xi\eta \tag{22}$$

in terms of assigned functions $m(\theta)$, $\xi(\theta)$, and $\eta(\theta)$. If $\xi(\theta)\eta(\theta)$ were constant, for example, then

$$\{(\tau/\xi)^{(1+m)/m} - 1\}/(1+m) = \text{constant} \tag{23}$$

on each locus, which is formally analogous to (17).

In these examples the differential hardening relative to $\tau_0(\theta)$ or $\xi_0(\theta)$ is governed solely by the dependence of exponent m on direction θ. It is this alone that determines how the ratios $\tau(\theta)/\tau_0(\theta)$ and $\tau(\theta)/\xi(\theta)$ vary over each yield locus for any given value of σ/σ_0 (the family being now regarded as parameterized by the equibiaxial tension σ). From that standpoint, explicit formulae for the relative hardening associated with (17) and (18) are

$$\{\tau(\theta)/\tau_0(\theta)\}^{[1+m(\theta)]/m(\theta)} = 1 + \left[\frac{1+m(\theta)}{1+n}\right]\{(\sigma/\sigma_0)^{(1+n)/n} - 1\}, \tag{24}$$

$$\{\tau(\theta)/\tau_0(\theta)\}^{n/(1+n)} = (\sigma/\sigma_0)^{m(\theta)/[1+m(\theta)]} \tag{25}$$

respectively, where $n = m(1/4\pi)$ and $\sqrt{2}\,\sigma_0 = \tau_0(1/4\pi)$. Similarly a replacement of (23) is available in terms of n and $\xi(\pi/4)$.

If loci generated in this fashion are always to be convex, regardless of the nature and degree of the textural changes, then admissible variations of m with θ must be constrained rather narrowly. The needed restrictions are not easily formulated, however, and so the overall outcome of any a priori selection of $m(\theta)$ tends to be unpredictable, even over quite modest ranges of σ/σ_0. At an early stage in the investigation this caused us to adopt an alternative strategy. Instead of $m(\theta)$ an outer locus, $\tau_\infty(\theta)$ say, was chosen together with the inner one, $\tau_0(\theta)$. When both are convex, so are all loci in the annulus between them (but not necessarily elsewhere). The function $m(\theta)$ is then determined by solving an equation such as (24) or (25) with n given and $\tau(\theta)$ equal to $\tau_\infty(\theta)$ (correspondingly σ equal to σ_∞). As to the status of an outer curve, it could be an empirical limit to representation by a power law; or it could be a conjectural cut-off associated with saturation hardening; or it could merely be an unexceptional locus marking an arbitrary limit to the computations.

4 Strain Paths Under Prescribed Loadings

The classical normality rule is adopted as the basis for calculating cumulative strains (ϵ_1,ϵ_2) along any path in (σ_1,σ_2) space. The direction of an outward normal to any yield locus is specified by its clockwise orientation ψ to the local radius vector, as in Fig. 1. This angle is obtainable conveniently from

$$\tan\psi = d\tau/\tau d\theta \tag{26}$$

evaluated at fixed σ in (1) or at fixed w in (6), whichever is the preferred parameterization. The anticlockwise orientation of a normal to the σ_1 coordinate axis is calculable as $\theta - \psi$, and then the incremental components of strain as

$$\frac{d\epsilon_1}{\cos(\theta-\psi)} = \frac{d\epsilon_2}{\sin(\theta-\psi)} = \frac{\sigma d\epsilon}{\sigma_1\cos(\theta-\psi) + \sigma_2\sin(\theta-\psi)} \tag{27}$$

having regard to (3) and (8). This pair of relations can be integrated straightforwardly along any path segment traversing a considered family. The only test data involved directly is that for equibiaxial tension, namely $\epsilon(\sigma)$ or $w(\sigma)$; the rest is accounted for already in the particular geometry.

Various aspects of the general correspondence between paths

Downloaded 03 May 2010 to 171.66.16.247. Redistribution subject to ASME license or copyright; see http://www.asme.org/terms/Terms_Use.cfm

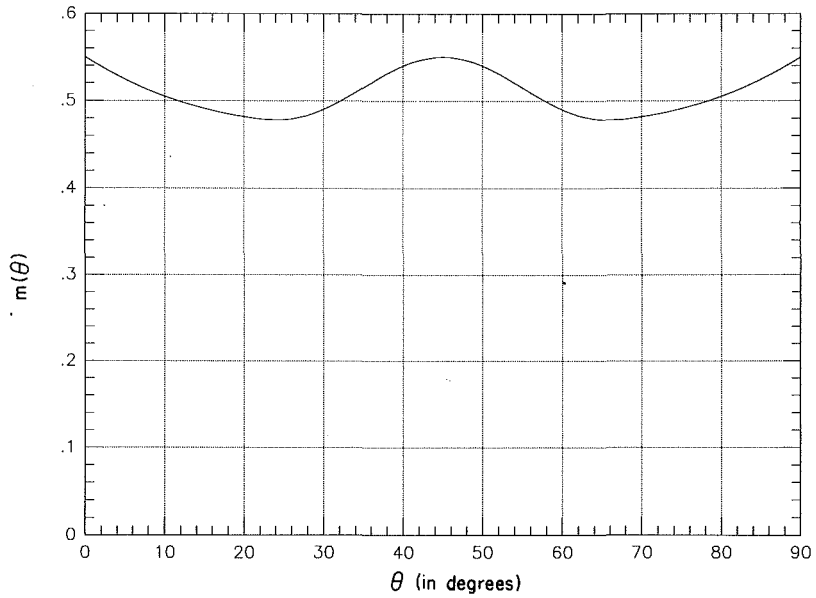


Fig. 6(*a*)

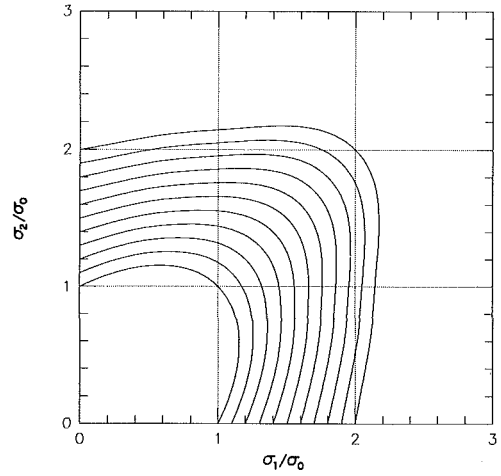


Fig. 6(*b*)

Fig. 6 Yield loci associated with inner Mises ellipse, $\tau_0(\theta)$, and a $m(\theta)$ satisfying (41) and reflecting trends reported by Stout and Hecker for brass

of stress and strain with arbitrary differential hardening have been treated by Hill (1991). Here we are concerned solely with the deformations that accompany stress paths at constant θ. Then (27) simplifies to

$$d\epsilon_1/\cos(\theta-\psi)=d\epsilon_2/\sin(\theta-\psi)=d\gamma/\cos\psi \tag{28}$$

after the substitutions $(\sigma_1,\sigma_2) = \tau(\cos\theta,\sin\theta)$ and $d\gamma = (\sigma/\tau)d\epsilon$. In a case such as (13), the integration starts from a reference locus where $\gamma_0(\theta)$ is known empirically as part of the global representation of radial test data.

The angle ψ varies along a ray in stress space unless successive loci happen to be self-similar. Consequently the associated path in strain space is generally curved. The precise dependence of its curvature on the local geometry and current stress can be seen in Hill (1991, Eq. (4.17)). Typical paths will be exhibited later for values of θ in $(0, \pi/2)$. At this stage we make only a qualitative observation. It is that a strain path may eventually bend so far as to become parallel, momentarily, to one or other orthotropic axis. That is,

$$d\epsilon_1=0 \quad \text{when} \quad \psi=\theta-\frac{1}{2}\pi; \text{ or } d\epsilon_2=0 \quad \text{when} \quad \psi=\theta. \tag{29}$$

In the presence of differential hardening, therefore, an increment of strain can be plane even when both components of the accumulated strain are positive. As remarked by Hill (1991, pp. 295 and 303), this offers a natural way to account for at least some of the failures by localized necking which often terminate strain paths in the positive quadrants of forming limit diagrams.

Finally we record an elementary formula for future reference. The total differential of τ is expressible as

$$d\tau/\tau=\tan\psi d\theta+\rho d\sigma/\sigma \tag{30}$$

when a family of loci is parameterized by σ. The coefficient ρ here was introduced by Hill (1991) as a convenient measure of the local departure from geometric similarity. It is defined by

$$\rho=(\sigma d\tau)/(\tau d\sigma) \tag{31}$$

where $d\tau$ and $\sqrt{2}\,d\sigma$ here are specifically the radial distance between a pair of neighboring loci in the directions θ and $\pi/4$, respectively; correspondingly $d\tau/\tau$ and $d\sigma/\sigma$ are the proportionate increases in the radii. As an example

$$\rho=\frac{m}{n}\left(\frac{\sigma}{\sigma_0}\right)^{(1+n)/n}\Bigg/\left(\frac{\tau}{\tau_0}\right)^{(1+m)/m} \tag{32}$$

for the family (24). Along a reference locus, in particular, ρ is equal to m/n simply; this can be compared with $(1 + n)m/(1 + m)n$ for the family (25).

5 Implementation and Examples

Two procedures for generating families of nonsimilar yield loci were proposed in Section 3. Their implementation is now illustrated in detail by examples for the power law (13). The method would be similar for the alternative law (19) and is readily extended to any other type of hardening.

Procedure (i). Inner and outer loci, $\tau_0(\theta)$ and $\tau_\infty(\theta)$, are specified together with a value of the exponent n for equibiaxial tension. The exponents $m(\theta)$ for loading along any other ray are then calculated by substituting $\tau_\infty(\theta)$ for τ in (24). It is reiterated that this equation is dependent on the hypothesis that converts (15) to (17). Intermediate loci can now be generated at will from (24) as it stands. Precisely the same steps could be followed in relation to (25) when the hypothesis leading to (18) is more appropriate.

Downloaded 03 May 2010 to 171.66.16.247. Redistribution subject to ASME license or copyright; see http://www.asme.org/terms/Terms_Use.cfm

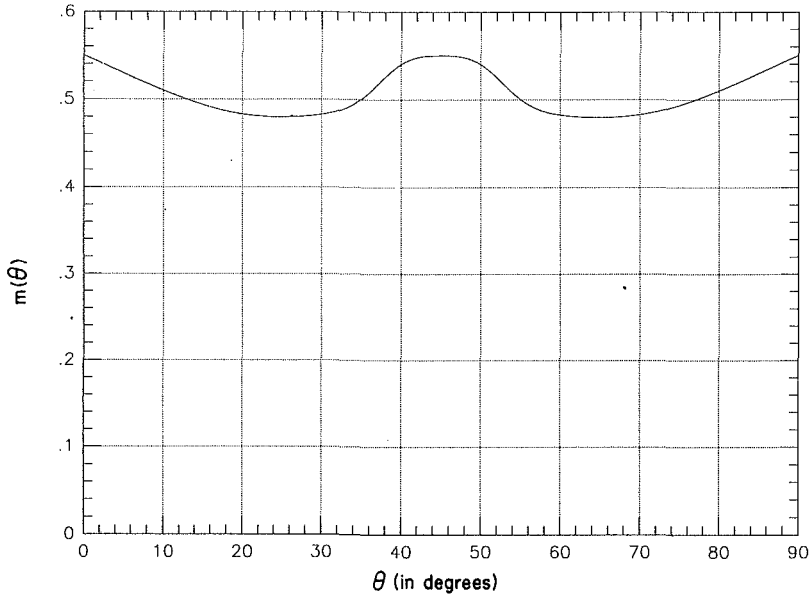


Fig. 7(*a*)

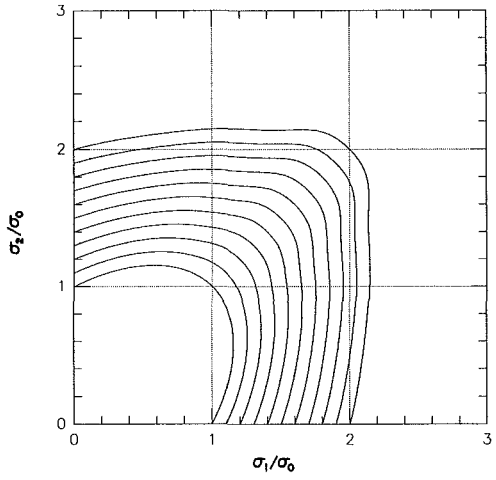


Fig. 7(*b*)

Fig. 7 An example of $m(\theta)$ which results in non-convex loci. This was one of the iterative variations used in arriving at Fig. 6.

Procedure (ii). An inner locus $\tau_0(\theta)$ is specified together with a predetermined function $m(\theta)$ in $(0, \pi/2)$. This includes the value of n at $\theta = \pi/4$. Exterior loci $\tau(\theta)$ through any designated values of σ/σ_0 can be generated directly from (24) or (25) according to choice.

Procedure (i) will be illustrated by taking the inner and outer loci to be ellipses in (σ_1,σ_2) space. In terms of the standard parameters F, G, H (e.g., Hill, 1990) their equations are

$$(G+H)\sigma_1^2 - 2H\sigma_1\sigma_2 + (F+H)\sigma_2^2 = 1, \tag{33}$$

where the values of F, G, and H are subject to $F + G = 1/\sigma^2 > 0$ and $FG + GH + HF > 0$. Correspondingly

$$\tau(\theta) = [(G+H)\cos^2\theta - 2H \sin\theta \cos\theta + (F+H)\sin^2\theta]^{-1/2}. \tag{34}$$

Suppose, for instance, that the as-received state is characterized by in-plane isotropy (alternatively called normal anisotropy). This necessarily also characterizes the idealized single infinity of loci associated with radial loadings. Therefore $F = G$ for both ellipses; for simplicity we further set $F = H$ on the inner one. The outer ellipse is arbitrarily required to pass through the point $\sigma_1 = \sigma_2 = \sigma_\infty = 2\sigma_0$, and five representative aspect ratios are considered. These are such that

$$H/F = 1/2, 3/5, 1, 5/3, 3.$$

In Fig. 2(*a*) the corresponding loci are labeled A, B, C, D, E in the same order. C is just another Mises ellipse, so in that case the intermediate loci are geometrically similar and $m(\theta) \equiv n$. With the value of n set at 0.3 in all cases, the respective functions $m(\theta)$ resulting from (24) are shown in Fig. 2(*b*). Intermediate members of the corresponding families are shown in Fig. 3(*a*) for case A and in Fig. 4(*a*) for case E. The associated strain paths under various radial loadings are shown in Fig. 3(*b*) and Fig. 4(*b*), respectively. They were computed with (13) rewritten as

$$\tau(\theta) = \tau_0(\theta)\{\gamma(\theta)/\gamma_0(\theta)\}^{m(\theta)}, \quad \gamma(\theta) \geq \gamma_0(\theta). \tag{35}$$

Here $\gamma_0(\theta)$ is defined in relation to $\tau_0(\theta)$ by

$$\tau_0(\theta)\gamma_0(\theta) = \sigma_0\epsilon_0 \tag{36}$$

as explained before, where

$$\sigma = \sigma_0(\epsilon/\epsilon_0)^n \tag{37}$$

under equibiaxial tension. The strain components are computed incrementally by means of (26) and (28). Starting values at the inner locus are assumed to have developed proportionally and are hence given by (28) with ϵ_1, ϵ_2 and $\gamma_0(\theta)$ in place of $d\epsilon_1$, $d\epsilon_2$, and $d\gamma$. On the inner Mises ellipse the values of τ and ψ are given by

$$\tau_0(\theta) = \sigma_0(1 - \sin\theta\cos\theta)^{-1/2},$$

$$\tan\psi_0 = \frac{1}{2}\cos 2\theta/(1 - \sin\theta\cos\theta). \tag{38}$$

The strain paths for case A in Fig. 3(*b*) correspond to loadings along radial rays in $(0, \pi/2)$ at equal intervals, whereas those for case E in Fig. 4(*b*) correspond to rays in $(\theta^*, \pi/4)$ at equal intervals where $\tan\theta^* = 1/2$ (i.e., $d\epsilon_2 = 0$ initially). Note that all paths are curved except under equibiaxial tension. Moreover they bend to an extent such that the criterion (29) for incremental plane strain is eventually met (namely at stages indicated by the solid dots).

To illustrate procedure (ii) we again assume in-plane isotropy and take a Mises ellipse as the inner locus $\tau_0(\theta)$. Consistent with symmetry about $\theta = \pi/4$ and with periodicity π in θ, we chose

Downloaded 03 May 2010 to 171.66.16.247. Redistribution subject to ASME license or copyright; see http://www.asme.org/terms/Terms_Use.cfm

$$m(\theta) = m_0 + m_1 \cos\left\{2\left(\theta - \frac{1}{4}\pi\right)\right\} + m_2 \cos\left\{4\left(\theta - \frac{1}{4}\pi\right)\right\} \quad (39)$$

and consider three cases A, B, C (Fig. 5(a)) in which the constants m_0, m_1, m_2 are disposed so that

$$\left.\begin{aligned} &\text{A: } m(0)=0.55, \quad m(\theta^*)=0.50, \quad m\left(\frac{1}{4}\pi\right)=0.45;\\ &\text{B: } m(0)=0.45, \quad m(\theta^*)=0.40, \quad m\left(\frac{1}{4}\pi\right)=0.35;\\ &\text{C: } m(0)=0.35, \quad m(\theta^*)=0.30, \quad m\left(\frac{1}{4}\pi\right)=0.25. \end{aligned}\right\} \quad (40)$$

Here, $\tan\theta^* = 1/2$ as before. These choices reflect qualitative trends in the hardening exponents for an aluminum alloy investigated by Wagoner (1980, p. 170); this material was confirmed to retain in-plane isotropy up to strains of order 0.2.

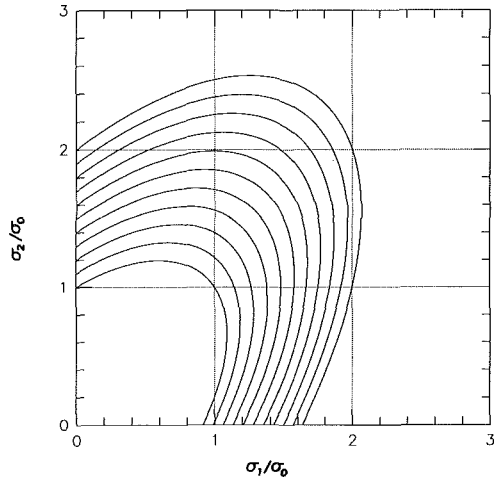


Fig. 8(a)

The subsequent loci computed by (24) are shown in Fig. 5(b). Probably by chance, some of these are broadly similar in shape to ones constructed by Wagoner (1980, Fig. 8) from an entirely different standpoint. In particular, he predetermined their geometry to conform with the simplest version of Hill's (1979) general yield function. Further, a parameter in this version was varied with strain so that each curve passed through two points determined by experiment: namely a uniaxial yield stress and another inferred from a test in quasi-plane strain (the pair being associated by equal expenditure of work). The respective approaches thus have little or nothing in common, so we have not troubled to simulate another characteristic of this particular aluminum.[1] We are in fact primarily concerned here (and to understand in general terms) how the change in shape of successive loci depends on the magnitude and type of fluctuations in the function $m(\theta)$.

The next example of procedure (ii) was motivated by nonuniformity of the hardening exponent in 70/30 brass as reported by Stout and Hecker (1983). Because of various uncertainties we aim only at qualitative simulation and accordingly impose the constraints

$$m(0)=0.55, \quad m(\theta^*)=0.48, \quad m\left(\frac{1}{4}\pi\right)=0.55. \quad (41)$$

With a Mises inner locus and the representation (39) we found that the resulting yield loci began to develop concavities when σ/σ_0 exceeded 1.5 or so (plots not shown). This phenomenon was still encountered when two more terms with disposable coefficients were added to (39). A different type of representation was therefore tried: values of m were specified at seven points within the interval $(0, \pi/4)$, including those in (41) enforcing symmetry about $\theta = \pi/4$. Interpolation was by cubic splines. By iterating the disposable values we eventually achieved convexity with $m(\theta)$ in Fig. 6(a). Some members of the associated family are depicted in Fig. 6(b). For comparison, a typical $m(\theta)$ at an intermediate stage of the iteration is given in Fig. 7(a). It is seen from Fig. 7(b) that a slight concavity has developed in some associated loci. A relatively small variation in $m(\theta)$ was enough to produce this effect. We are inclined to believe that the a priori values stipulated in (41) are

[1]The strain ratio under uniaxial tension did not vary; here this would entail constant ψ and $m'(\theta) = 0$ when $\theta = 0$ and $\pi/2$.

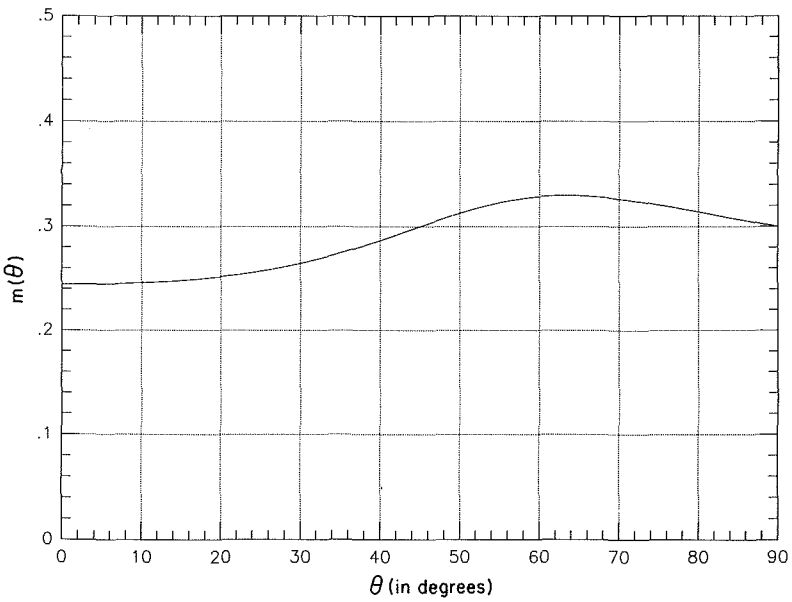


Fig. 8(b)

Fig. 8 An example with in-plane orthotropy. The inner locus in an ellipse with $G = H$ and $F/G = 2/3$ and the outer locus is an ellipse with $G = H$ and $F/G = 1/3$; $n = 0.3$ and $\sigma_\infty/\sigma_0 = 2$.

Downloaded 03 May 2010 to 171.66.16.247. Redistribution subject to ASME license or copyright; see http://www.asme.org/terms/Terms_Use.cfm

on the edge of possibilities consistent with convexity over the range $1 \leq \sigma/\sigma_0 \leq 2$. For instance we could not achieve this with any function $m(\theta)$ whatsoever when its value at θ^* was set at 0.45 without changing the others in (41).

In the preceding examples the material was considered to be isotropic in the plane of symmetry; correspondingly its yield function was written as $\phi(\tau,\theta)$, a symmetric function of σ_1 and σ_2 alone. Isotropy was not invoked in full, however, as the biaxial stresses were not oriented arbitrarily within the material but always in the same two directions. In that context the material could alternatively be considered to be one with a special kind of orthotropy. To express this formally, let the yield function be written as $\Phi(\tau,\theta,\alpha)$ where α is the arbitrary angle which σ_1 and σ_2 make with the respective axes of orthotropy. For our purpose the precise dependence on α can be left open; some possibilities have been formulated by Hill (1990). Here we require the function Φ to be special only in that $\Phi(\tau,\theta,0)$ is identified with $\phi(\tau,\theta)$ and is hence likewise symmetric with respect to interchange of σ_1 and σ_2 (equivalent to replacement of θ by $\pi/2 - \theta$). Even though the loci change shape with deformation, this symmetry persists because they are generated as an idealized single infinity from the data in tests where σ_1 and σ_2 are maintained in fixed ratio.

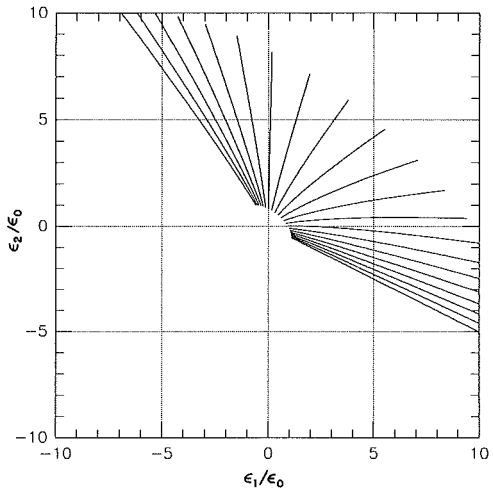


Fig. 9(*a*)

In our next example there is no symmetry of that kind and $\phi(\tau,\theta) \neq \phi(\tau, \pi/2 - \theta)$ in the as-received state. Such a function is incompatible with isotropy and can only be associated with orthotropy in the general sense. Procedure (i) will be adopted in connection with inner and outer ellipses in the family (33) with $F \neq G$. Correspondingly an outward normal is inclined to the local radius at a clockwise angle ψ given by

$$\tan\psi = \{H + (G-F)\tan\theta - H\tan^2\theta\}/\{(G+H) - 2H\tan\theta + (F+H)\tan^2\theta\} \quad (42)$$

from (26). We choose $G = H$ on both ellipses, which has the effect that $\sigma_2 = \sigma$ when $\sigma_1 = 0$ (σ denotes the yield stress in equibiaxial tension). Moreover $\tan\psi = 1/2$ on both when $\theta = 0$, regardless of the value of F/H. There are further consequences under the assumptions (17) and (24). Thus $m(\theta) = n$ on any ray where $\tau_\infty(\theta)/\tau_0(\theta) = \sigma_\infty/\sigma_0$; this happens when $\theta = \pi/2$ if $G = H$. Also $m'(\theta) = 0$ on any ray that meets both ellipses at the same angle; it is easy to verify from (17) and (26) that the ray necessarily meets all intervening loci at a constant angle. By (42) there are two such rays (conjugate with respect to each ellipse), namely $\theta = 0$ deg where $\sigma_2 = 0$ and $\psi = \tan^{-1} 1/2 = 26.565$ deg, and $\theta = \tan^{-1} 2 = 63.435$ deg where $\sigma_2 = 2\sigma_1$ and $\psi = -\tan^{-1} 1/2$. Both values of ψ are unaffected by the ratio F/G when $G = H$. Furthermore the incremental strain is plane ($d\epsilon_1 = 0$) on the latter ray, and so the associated strain path is linear ($\epsilon_1 = 0$). All these features are seen in Fig. 8(*a*), (*b*) which show $m(\theta)$ and the family of loci when $n = 0.3$ and F/G is chosen to be 2/3 on the inner ellipse and 1/3 on the outer one through $\sigma_\infty/\sigma_0 = 1$ and 2, respectively. Their major axes are inclined to the σ_1 axis at angles 49.7 deg and 54.2 deg, respectively. Representative strain paths are shown in Fig. 9(*a*) for rays equally spaced between $\theta = 0$ and $\pi/2$, and in Fig. 9(*b*) for rays equally spaced between $\theta = \theta^*$ and $\pi/4$, where now $\theta^* = 30.7$ deg at the point where $d\epsilon_2 = 0$ on the inner ellipse. Points where the incremental strain is plane are indicated by solid dots.

We conclude with some practical observations regarding the computing technique. With procedure (i) any convex curves could be considered for $\tau_0(\theta)$ and $\tau_\infty(\theta)$ (and not just ellipses). Values of these functions can be prescribed on selected rays and then interpolated by splines or an appropriate alternative. The values of m can likewise be computed on arbitrarily selected rays; we chose to space these equally but as closely as

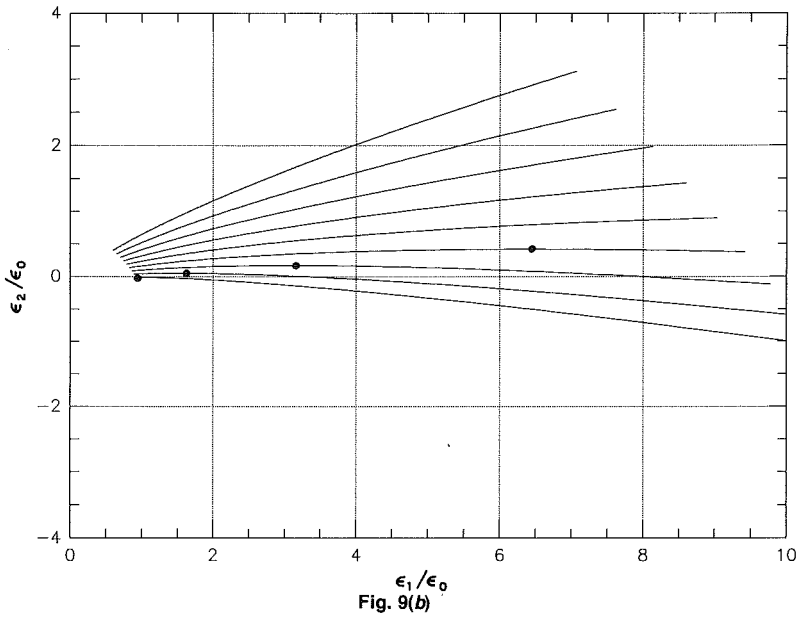


Fig. 9(*b*)

Fig. 9 Strain trajectories under radial stress loading for the family of loci shown in Fig. 8

Downloaded 03 May 2010 to 171.66.16.247. Redistribution subject to ASME license or copyright; see http://www.asme.org/terms/Terms_Use.cfm

required. In procedure (ii), $m(\theta)$ has to be prescribed in advance; we used either cubic splines or formula (39) to represent this function. The former was found very effective when checking convexity, as interpolation could be based on relatively few values of m. In both procedures the angle ψ has to be determined by computing $m'(\theta)$. Several methods could be adopted, depending on how $m(\theta)$ is represented; for convenience we always used the simplest approximation: namely $\{m(\theta + \delta) - m(\theta - \delta)\}/2\delta$.

6 Closing Remarks

The preceding analysis is concerned with the plastic response of isotropic or orthotropic sheet under biaxial loading, more especially when the shape of successive yield loci varies. This is an expected consequence of changes in crystalline texture during continued deformation. As often remarked in regard to the normality flow rule, relatively small variations in shape can significantly affect the cumulative strains associated with a given stress path. On that account among others, experimental determinations of successive loci over a finite range of strain are a prerequisite for any useful theory. Such tests are technically demanding, and the area to be explored is extensive. With this in mind, we have devised a simple analytical framework in the hope that it may contribute to the design of future tests and sharpen the perceived objectives.

Aside from admitting families of nonsimilar yield loci, the constitutive basis is broadly classical. For the present we see no advantage in relaxing any other element in that description. We have, in particular, retained the customary fiction that the totality of potential loci is singly infinite, nonintersecting, and parameterized by the work expended. The idealization is plainly unrealistic in detail, for instance by virtue of the path dependence mentioned at the outset.

It must be regarded, therefore, as a pragmatic expedient until such time as it can be confronted by quantifiable data. Meantime some minor improvements are feasible and should be considered. Representation of radial tests by the power law (13) is not obligatory, and it is conceivable that (19) would be more apt for some materials in their as-received states. More generally, contours $\tau(\theta,w_1)$, $\tau(\theta,w_2)$, ... of equal work at discrete values of w could just as easily be constructed from any kind of representation $\tau(w,\theta_1)$, $\tau(w,\theta_2)$, ... of the radial test characteristics at discrete values of θ. A basic question remains: to what extent, and in what circumstances, is it realistic for contours of equal work to act as yield loci in the limited sense of determining normals for the classical flow rule?

Acknowledgment

The work of JWH was supported in part by the National Science Foundation under Grant MSM-88-12779, and in part by the Division of Applied Sciences, Harvard University.

References

Chan, K. C., and Lee, W. B., 1990, "A Theoretical Prediction of the Strain Path of Anisotropic Sheet Metal Deformed under Uniaxial and Biaxial Stress State," *Int. J. Mech. Sci.*, Vol. 32, pp. 497–511.

Ghosh, A. K., and Backofen, W. A., 1973, "Strain Hardening and Instability in Biaxially Stretched Sheets," *Metall. Trans.*, Vol. 4, pp. 1113–1123.

Ghosh, A. K., 1978, "Plastic Flow Properties in Relation to Localized Necking in Sheets," *Mechanics of Sheet Metal Forming, Material Behavior and Deformation Analysis*, D. P. Koistinen and N.-M. Wang, eds., Plenum Press, New York.

Hill, R., 1979, "Theoretical Plasticity of Textured Aggregates," *Proc. Cambridge Philos. Soc.*, Vol. 85, pp. 179–191.

Hill, R., 1990, "Constitutive Modelling of Orthotropic Plasticity in Sheet Metals," *J. Mech. Phys. Solids*, Vol. 38, pp. 405–417.

Hill, R., 1991, "A Theoretical Perspective on In-plane Forming of Sheet Metal," *J. Mech. Phys. Solids*, Vol. 39, pp. 295–307.

Lequeu, P. H., and Jonas, J. J., 1988, "Modelling of the Plastic Anisotropy of Textured Sheet," *Metall. Trans.*, Vol. 19A, pp. 105–120.

Stout, M. G., Hecker, S. S., and Bourcier, R., 1983, "An Evaluation of Anisotropic Effective Stress-Strain Criteria for the Biaxial Yield and Flow of 2024 Aluminum Tubes," ASME *Journal of Engineering and Materials Technology*, Vol. 105, pp. 242–249.

Stout, M. G., and Hecker, S. S., 1983, "Role of Geometry in Plastic Instability and Fracture of Tubes and Sheet," *Mech. Mat.*, Vol. 2, pp. 23–31.

Stout, M. G., and Staudhammer, K. P., 1984, "Biaxial Deformation of 70-30 Brass: Flow Behaviors, Texture, Microstructures," *Metall. Trans.*, Vol. 15A, pp. 1607–1612.

Wagoner, R. H., 1980, "Measurement and Analysis of Plane-Strain Work Hardening," *Metall. Trans.*, Vol. 11A, pp. 165–175.

Wagoner, R. H., 1982, "Plastic Behavior of 70/30 Brass Sheet," *Metall. Trans.*, Vol. 13A, pp. 1481–1500.

Downloaded 03 May 2010 to 171.66.16.247. Redistribution subject to ASME license or copyright; see http://www.asme.org/terms/Terms_Use.cfm

Transient Hygrothermal Stresses Induced in General Plane Problems by Theory of Coupled Heat and Moisture

Tei-Chen Chen

Cheng-I Weng

Win-Jin Chang

Department of Mechanical Engineering,
National Cheng Kung University
Tainan, Taiwan, R.O.C.

A general finite element model is proposed to deal with the transient, hygrothermal stress problems by the linear theory of coupled heat and moisture that is required in the analysis of some porous and composite materials. The method consists of formulating and solving the problem in the Laplace transform domain by the finite element method and then numerically inverting the transformed solution to obtain the time domain response. Therefore, the transient solutions at any time could be evaluated directly. A number of examples are presented which demonstrate the accuracy, efficiency, and versatility of the proposed method. It can be found from the numerical results that the coupling effect between thermal and moisture is significant for composite material T300/5208. The maximum discrepancy between coupled and uncoupled solutions might be as high as 50 percent.

Introduction

Physically, there exists a coupling effect between temperature and moisture in most materials. It has been verified that the influence of the coupling effect becomes significant as the ratio of thermal conductivity and moisture diffusivity approaches unity. For instance, the coupling effect has little influence for most metals whose values of thermal conductivity is much higher than that of moisture diffusivity. However, it becomes significant for some porous and composite materials whose thermal conductivity and moisture diffusivity have a close value. G. S. Springer (1984) investigated the effects of environment (that includes temperature and moisture) on composite materials and obtained some basic data by experiment. C. D. Shirrell (1978) experimentally studied the interactive effect between thermal and moisture for some composite materials and obtained the data of some coefficients that are relevent to the coupling effect. Some investigators (Hartranft and Sih, 1980; Sih et al., 1980; Sih and Ogawa, 1982) utilized the previous experimental data to analyze the hygrothermal stresses of plate by the theory of coupled heat and moisture. Due to the mathematical difficulties encountered in these coupled terms, this kind of problem that admits to a closed-form solution was evidently scarce and was confined to one-dimensional problems only (Chang et al., 1990). However, if more complex geometries, multiple substances, and time-dependent boundary conditions are involved additionally in the analysis of the problems, numerical techniques, instead of analytical methods, have to be adopted. Due to the versatility of the finite element technique, considerable attention has been focused on this methods in many engineering fields. Generally, the treatment of time gradient in the finite element equations has been discretized by time integration method (Prevost and Tao, 1983). Therefore, the solutions, at any time, shall be evaluated step-by-step from initial values, and an optimum algorithm for time increment is required to achieve both numerical stability and rapid convergence (Hughes and Liu, 1978a, 1978b). Due to this severe limitation on the interval of the time step, an excessive amount of computer time may be required to obtain the long-term transient solutions.

A general and efficient numerical procedure, by combining the finite element method, Laplace and inverse Laplace transform techniques, is proposed in this work to analyze the linear problems of coupled heat and moisture. Recently, a similar numerical technique has also been successfully developed to solve some transient heat conduction (Chen et al., 1987) and coupled thermoelastic (Chen and Weng, 1988) problems. The solid under consideration may be composed of composite materials with irregular geometry and subjected to arbitrary time-dependent hygrothermal loading conditions. The governing equations are first formulated by the finite element technique in the Laplace transform domain. Then the solutions in the transformed domain are evaluated. From these transformed solution the response in the real-time domain, at any time, could be evaluated directly. Since the problems of coupled heat and moisture have a relatively long transient period, it is believed that this kind of problem is appropriate to be approached by the present numerical method. A number of examples are

Contributed by the Applied Mechanics Division of THE AMERICAN SOCIETY OF MECHANICAL ENGINEERS for presentation at the 1992 ASME Summer Mechanics and Materials Meeting, Tempe, AZ, Apr. 28-May 1, 1992.

Discussion on this paper should be addressed to the Technical Editor, Prof. Leon M. Keer, The Technological Institute, Northwestern University, Evanston, IL 60208, and will be accepted until two months after final publication of the paper itself in the JOURNAL OF APPLIED MECHANICS. Manuscript received by the ASME Applied Mechanics Division, Dec. 18, 1990; final revision, Apr. 10, 1991.

Paper No. 92-APM-8.

Copyright © 1992 by ASME

Downloaded 03 May 2010 to 171.66.16.247. Redistribution subject to ASME license or copyright; see http://www.asme.org/terms/Terms_Use.cfm

presented which demonstrates the accuracy and efficiency of the proposed method. It can be found from the numerical results that the coupling effect between thermal and moisture is significant for composite material T300/5208. The maximum discrepancy between coupled and uncoupled solutions might be as high as 50 percent.

Temperature and Moisture Distributions

Basic Equations. The derivation of the basic equations with coupled heat and moisture content in a solid has already been made and discussed (Hartranft and Sih, 1980). The associated equations of the second model described in previous work can be expressed as follows:

$$\nabla \cdot (L \nabla T) - \frac{\partial}{\partial t}(T - \nu C) = 0 \tag{1}$$

$$\nabla \cdot (D \nabla C) - \frac{\partial}{\partial t}(C - \lambda T) = 0 \tag{2}$$

where T is the temperature; C is the mass of moisture per unit volume of void space in the solid; λ is the coupling coefficient having the unit of mass per unit volume per unit temperature; ν is another coupling coefficient having the reciprocal unit of λ; L and D are the equivalent diffusion coefficients of heat and moisture, respectively. When ν and λ vanish Eqs. (1) and (2) reduce to the uncoupled theory.

Suppose the material properties L and D are constant. By introducing the dimensionless variables defined as

$$T^* = (T - T_i)/(T_f - T_i), \quad C^* = (C - C_i)/\lambda(T_f - T_i),$$

Eqs. (1) and (2) can then be converted to the following forms:

$$L \nabla^2 T^* = \frac{\partial}{\partial t}(T^* - \nu \lambda C^*) \tag{3}$$

$$D \nabla^2 C^* = \frac{\partial}{\partial t}(C^* - T^*) \tag{4}$$

where T_i and C_i are the reference temperature and moisture, respectively; T_f is the final equilibrium temperature.

The associated hygrothermal boundary conditions may be of the following types:

$$T^* = T_s^* \quad \text{on } S_{h1} \tag{5}$$

$$-K \frac{\partial T^*}{\partial n} = q_h \quad \text{on } S_{h2} \tag{6}$$

$$-K \frac{\partial T^*}{\partial n} = h_h (T^* - T_\infty^*) \quad \text{on } S_{h3} \tag{7}$$

$$C^* = C_s^* \quad \text{on } S_{m1} \tag{8}$$

$$-D_m \frac{\partial C^*}{\partial n} = q_m \quad \text{on } S_{m2} \tag{9}$$

$$-D_m \frac{\partial C^*}{\partial n} = h_m (C^* - C_\infty) \quad \text{on } S_{m3} \tag{10}$$

where the first three equations belong to the thermal boundary conditions while the last three denote the moisture boundary conditions. $S_{h1}(S_{m1})$ is the part of the boundary on which the temperature T^* (moisture C^*) is prescribed; $S_{h2}(S_{m2})$ is the part of the boundary on which the heat flux q_h (moisture flux q_m) is prescribed; $S_{h3}(S_{m3})$ is the part of the boundary on which the convective heat (moisture) transfer is prescribed. Each set of subsurfaces S_{h1}, S_{h2}, S_{h3} (S_{m1}, S_{m2}, S_{h3}) forms the complete boundary surface S of the solid. K and D_m are the thermal conductivity and moisture diffusion coefficients, respectively.

The initial conditions are

$$T^*(x, y, 0) = T_o^*(x, y), \quad C^*(x, y, 0) = C_o^*(x, y). \tag{11}$$

Finite Element Formulation. The formulation associated with this initial boundary value problem of coupled theory is obstained in a standard way. The intro-differential equations of variational forms, derived from Eqs. (3) and (4), can be expressed as

$$\int_V L T_{,i}^* \delta T_{,i}^* dV + \int_V \dot{T}_{,i}^* \delta T^* dV - \nu\lambda \int_V \dot{C}^* \delta T^* dV = \int_S q_h \delta T^* dS \tag{12}$$

$$\int_V D C_{,i}^* \delta C_{,i}^* dV + \int_V \dot{C}_{,i}^* \delta C^* dV - \int_V \dot{T}^* \delta C^* dV = \int_S q_m \delta C^* dS. \tag{13}$$

The solid, under consideration, is divided into nonoverlapping finite element and nodal points. Two sets of shape functions are introduced to approximate both the temperature and moisture fields on the element level.

$$T^* = \sum_{i=1}^{n} N_i T_i^* = [N]\{T^{*e}\} \tag{14}$$

$$C^* = \sum_{i=1}^{n} N_i' C_i^* = [N']\{C^{*e}\} \tag{15}$$

where $\{T^{*e}\}$ and $\{C^{*e}\}$ are the vectors of nodal point temperature and moisture, respectively; $[N]$ and $[N']$ are the shape functions for temperature and moisture, respectively; i the node number; n the number of nodes per element. In the following analysis, $[N]$ and $[N']$ are made identical to each other.

Substituting Eqs. (14) and (15) into (12) and (13), the following equations expressed by matrices could be obtained:

$$\sum_{e=1}^{N} \begin{bmatrix} [H] & \cdot & -\nu\lambda[H] \\ \cdot & \cdot & \cdot \\ -[H] & \cdot & [H] \end{bmatrix} \begin{Bmatrix} \{\dot{T}^{*e}\} \\ \cdots \\ \{\dot{C}^{*e}\} \end{Bmatrix} + \begin{bmatrix} L[K] & \cdot & 0 \\ \cdot & \cdot & \cdot \\ 0 & \cdot & D[K] \end{bmatrix} \begin{Bmatrix} \{T^{*e}\} \\ \cdots \\ \{C^{*e}\} \end{Bmatrix} = \begin{Bmatrix} \{F_1^e\} \\ \cdots \\ \{F_2^e\} \end{Bmatrix}. \tag{16}$$

In Eq. (16), some matrices involving integrals are defined as

$$[H] = \int_V [N]^t [N] dV$$

$$[F_1] = \int_{S_{h2}} q_h [N] dS + \int_{S_{h3}} h_h T_\infty^* [N] dS$$

$$[K] = \int_V [M]^t [M] dV$$

$$[F_2] = \int_{S_{m2}} q_m [N] dS + \int_{S_{m3}} h_m C_\infty^* [N] dS \tag{17}$$

where $q_h(q_m)$ is the heat (moisture) flow along the boundary surface S_{h2} (S_{m2}); $h_h(h_m)$ the heat (moisture) transfer coefficient; $S_{h3}(S_{m3})$ the boundary surface wherein heat (moisture) convection is specified; $T_\infty^*(C_\infty^*)$ the environment temperature (moisture).

Laplace Transform. Making application of the Laplace transform defined by

$$\bar{f}(s) = \int_o^\infty e^{-st} f(t)\, dt, \tag{18}$$

Eq. (16) yields

Downloaded 03 May 2010 to 171.66.16.247. Redistribution subject to ASME license or copyright; see http://www.asme.org/terms/Terms_Use.cfm

$$\sum_{e=1}^{N}\begin{bmatrix} s[H]+L[K] & \cdot & -s\nu\lambda[H] \\ \cdots\cdots & \cdot & \cdots\cdots \\ -s[H] & \cdot & s[H]+D[K] \end{bmatrix}\begin{Bmatrix} \{\bar{T}^{*e}\} \\ \cdots\cdots \\ \{\bar{C}^{*e}\} \end{Bmatrix}$$

$$=\begin{Bmatrix} \{\bar{F}_1{}^e\}+[H]\{T_o{}^*\}-\nu\lambda[H]\{C_o{}^*\} \\ \cdots\cdots\cdots\cdots\cdots\cdots \\ \{\bar{F}_2{}^e\}+[H]\{C_o{}^*\}-[H]\{T_o{}^*\} \end{Bmatrix}, \quad (19)$$

where $\{\bar{T}^{*e}\}$ and $\{\bar{C}^{*e}\}$ are the vectors of nodal point temperature and displacement in the transformed domain, respectively; s the Laplace transform parameter ($s = v + iw$).

Method of Inversion. The inversion of the Laplace transform is defined as

$$f(t)=\mathcal{L}^{-1}[\bar{f}(s)]=\frac{1}{2\pi i}\int_{v-i\infty}^{v+i\infty} e^{st}\bar{f}(s)ds. \quad (20)$$

In accordance with the method of Durbin (1973), the following relation can be derived by performing the Fourier series expansion of $H(t) = e^{-vt}f(t)$ in the interval $[0, 2\tau]$.

$$f(t)=\frac{e^{vt}}{\tau}\left\{-\frac{1}{2}\,\mathrm{Re}[\bar{f}(v)]+\sum_{k=1}^{\infty}\mathrm{Re}\left[\bar{f}\left(v+\frac{ik\pi}{\tau}\right)\right]\cos\frac{k\pi t}{\tau}\right.$$

$$\left.-\sum_{k=0}^{\infty}\mathrm{Im}\left[\bar{f}\left(v+\frac{ik\pi}{\tau}\right)\right]\sin\frac{k\pi t}{\tau}\right\}-Fl(v,\,t,\,\tau)+FA(n,\,v,\,t,\,\tau) \quad (21)$$

for $0<t<2\tau$,

in which $Fl(v, t, \tau)$ is the discretization error given by

$$Fl(v,\,t,\,\tau)=\sum_{k=1}^{\infty}e^{-2v k\tau}f(2k\tau+t), \quad (22)$$

$FA(N, v, t, \tau)$ is the truncation error given by

$$FA(N,\,v,\,t,\,\tau)=\frac{e^{vt}}{\tau}\left[\sum_{k=N+1}^{\infty}\left\{\mathrm{Re}\left\{\bar{f}\left(v+\frac{ik\pi}{\tau}\right)\cos\frac{k\pi t}{\tau}\right\}\right.\right.$$

$$\left.\left.-\mathrm{Im}\left\{\bar{f}\left(v+\frac{ik\pi}{\tau}\right)\sin\frac{k\pi t}{\tau}\right\}\right]\right], \quad (23)$$

where τ is the half period of $f(t)$.

The solution of Eq. (19) for the transformed temperature and moisture vectors are evaluated numerically by the "front method," for a sequence of "s" that is required by the scheme of numerical inversion of the transformed solutions shown as Eq. (21).

It is obvious from Eq. (22) that the discretization error can be made arbitrarily small if the product $v\tau$ is sufficiently large. However, the truncation error shown as Eq. (23) may diverge for large values of $v\tau$ if τ is selected to be equal to t. In this paper, an accurate and efficient numerical method known as Korrektur, proposed by Honig and Hirdes (1984), is used to obtain the inversion of the Laplace transform. This inversion method allows a remarkable reduction of the discretization error without increasing the truncation error by the simultaneous application of a method to accelerate the convergence of the Fourier series and a procedure to calculate approximately the optimal value of the free parameter v, which is the real part of the Laplace transform parameter s. Therefore, for a wide range of applications, good accuracy can be achieved with fewer terms of the Fourier series. The detail procedures to obtain the solutions at a specific time can be found in the work by (Chen and Weng (1988)).

Hygrothermal Stress Distributions

The equations of motion can be expressed as

$$\sigma_{ij,j}+\rho b_i=\rho\ddot{u}_i \quad (24)$$

where σ_{ij} are the components of stress tensor; ρ the density; b_i the body force vector; u_i the components of displacement vector.

The integro-differential equations of variational forms, derived from Eq. (24), can be expressed as

$$\int_V\rho\ddot{u}_i\delta u_i dV-\int_V\sigma_{ij}\delta\epsilon_{ij}dV-\int_S\delta u_i f_i dS=\int_V\rho b_i\delta u_i dV. \quad (25)$$

A shape function is introduced to approximate the displacement field on the element level.

$$\{u\}=[N'']\{u^e\} \quad (26)$$

where $\{u^e\}$ is the vector of nodal point displacement; $[N'']$ is the shape function for displacement. In the following analysis, $[N'']$ is identical to the shape function for temperature and moisture.

The strain and stress tensors can be expressed in terms of displacement, temperature, and moisture as follows:

$$\{\epsilon\}=[B_1]\{u^e\}$$

$$\{\sigma\}=[D]\{\epsilon\}+[E'][N]\{T^e\}+[A'][N]\{m^e\} \quad (27)$$

$$=[D][B_1]\{u^e\}+[E][N]\{T^{*e}\}+[A][N]\{C^{*e}\}. \quad (28)$$

Substituting Eqs. (26), (27), and (28) into (25), the following equations expressed by matrices could be obtained:

$$[M]\{\ddot{u}^e\}+[K_1]\{u^e\}+[K_2]\{T^{*e}\}+[K_3]\{C^{*e}\}=\{F^e\}. \quad (29)$$

In Eq. (29), some matrices are defined as

$$[M]=\int_V[N]^t\rho[N]dV$$

$$[K_1]=\int_V[B]^t[D][B]dV$$

$$[K_2]=\int_V[B]^t[E][N]dV$$

$$[K_3]=\int_V[B]^t[A][N]dV$$

$$[F]=\int_V[N]^t\rho[b]dV+\int_S[N]^t[f]dS \quad (30)$$

in which

$$[B]=\begin{bmatrix} \frac{\partial N_1}{\partial x} & 0 & \cdot & \frac{\partial N_2}{\partial x} & 0 & \cdot & & \cdot & \frac{\partial N_n}{\partial x} & 0 \\ 0 & \frac{\partial N_1}{\partial y} & \cdot & 0 & \frac{\partial N_2}{\partial y} & \cdot & \cdots & \cdot & 0 & \frac{\partial N_n}{\partial y} \\ \frac{\partial \mathrm{N}_1}{\partial \mathrm{y}} & \frac{\partial N_1}{\partial x} & \cdot & \frac{\partial N_2}{\partial y} & \frac{\partial N_2}{\partial x} & \cdot & & \cdot & \frac{\partial N_n}{\partial y} & \frac{\partial N_n}{\partial x} \end{bmatrix}$$

$$[D_1]=\frac{E(1-\nu)}{(1+\nu)(1-2\nu)}\begin{bmatrix} 1 & \frac{\nu}{1-\nu} & 0 \\ \frac{\nu}{1-\nu} & 1 & 0 \\ 0 & 0 & \frac{1-2\nu}{2(1-\nu)} \end{bmatrix}$$

$$[E]=-\frac{\alpha' E}{1-2\nu}\begin{Bmatrix}1\\1\\0\end{Bmatrix}$$

$$[A]=-\frac{\beta' E}{1-2\nu}\begin{Bmatrix}1\\1\\0\end{Bmatrix} \quad (31)$$

where $\alpha' = (\alpha-\beta\omega)(T_f-T_i)$; $\beta' = \beta\omega(T_f-T_i)$.

Making Laplace transform of (29), it yields

$$([M]s^2+[K_1])\{\bar{u}^e\}=\{\bar{F}^e\}-[K_2]\{\bar{T}^{*e}\}-[K_3]\{\bar{C}^{*e}\}. \quad (32)$$

Downloaded 03 May 2010 to 171.66.16.247. Redistribution subject to ASME license or copyright; see http://www.asme.org/terms/Terms_Use.cfm

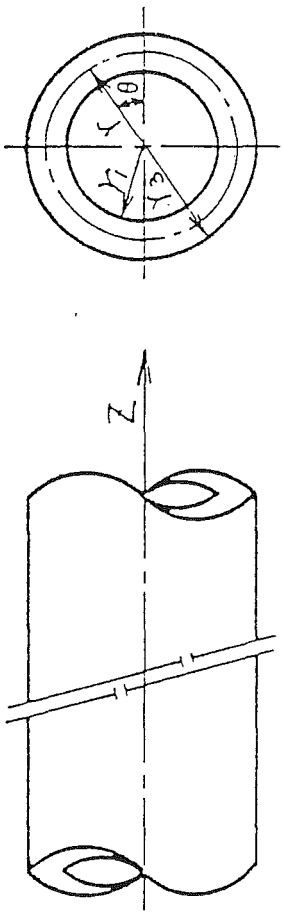


Fig. 1 Infinitely long annular cylinder subjected to hygrothermal loadings

Therefore, the displacement field in the real-time domain can also be evaluated through the application of Eq. (32) and the scheme of numerical inversion in the same manner as in the previous description. However, if the inertia term is disregarded, the displacement field can be directly evaluated by Eq. (29).

Numerical Applications

In the following examples, an eight-node isoparametric quadrilateral element is used for both temperature and displacement calculations. And the material is assumed to be homogeneous and isotropic. The evaluated values of an optimal free parameter for each nodal variable, in each example, are approximately ranged from 5.4 to 7.2. In order to accelerate the convergence of the Fourier series evenly in the domain considered, an assigned value of optimal parameter 6.4, by averaging the maximum and the minimum data, is selected as the basis of the optimal parameter for the whole domain. It could be found in the following examples that the solutions converge very well even if only a 15-terms approximation of a Fourier series is used by adopting this assigned optimal parameter. Furthermore, in these examples, the effect of an inertia term is insignificant and could be satisfactorily disregarded.

Example 1. Consider an infinitely long annular cylinder, as shown in Fig. 1, having inner and outer radii r_1 and r_3, respectively, subjected to symmetrical hygrothermal loadings as follows:

$$T^*(r_1, t)=1, \quad T^*(r_3, t)=1, \quad t>0$$
$$C^*(r_1, t)=0, \quad C^*(r_3, t)=0, \quad t>0.$$

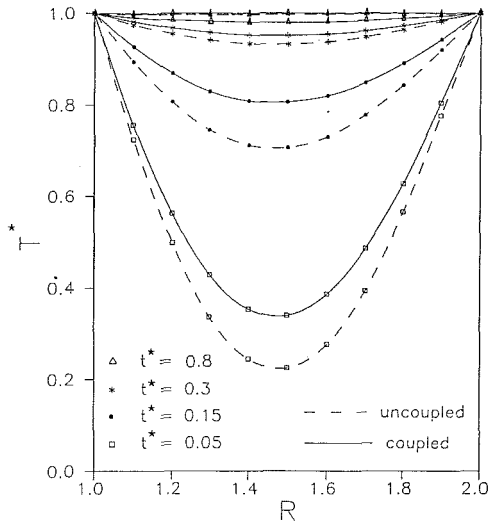


Fig. 2 Temperature T^* distributions for various time (t^* = 0.05, 0.15, 0.30, 0.80)

The initial conditions are

$$T^*(r, 0)=0, \quad C^*(r, 0)=0, \quad r_1<r<r_3.$$

The solutions are conveniently interpreted in terms of following dimensionless variables:

$$R=\frac{r}{r_1}, \; R_1=\frac{r_1}{r_1}=1, \; R_3=\frac{r_3}{r_1}, \; \sigma_{ij}^*=\frac{\sigma_{ij}(1-2\mu)}{\alpha E(T_f-T_i)},$$
$$u^*=\frac{u}{\alpha(1+\mu)r_3(T_f-T_i)}, \; t^*=\frac{Lt}{r_1^2}.$$

The numerical results are determined for a T300/5208 composite circular cylinder whose material properties (Sih et al., 1986) and radius are listed as follows:

$\alpha=31.3\times10^{-6}$ cm/cm − °C,

$\beta=2.68\times10^{-3}$ cm/cm − percent H_2O,

$\mu=0.33$, $E=64.3$ GPa,

$\lambda=0.5$ g/cm^3 − °C, $\nu=0.5$ cm^3 − °C/g, $L=7.78\times10^{-6}$ cm^2/hr,

$D=7.78\times10^{-7}$ cm^2/hr, $R_3=2.0$.

The analytical closed-form solutions for T^*, C^*, u^*, and σ_{ij}^* have been obtained by Chang et al. (1990) and are given in the Appendix. The numerical nodal temperature, moisture, displacement, and stress for various times are compared with the corresponding analytical solutions and listed in Tables 1 and 2. A good agreement can be found between them which demonstrates the accuracy and reliability of the proposed numerical method. The temperature distributions along a radial direction for various time are plotted in Fig. 2. The distributions of circumferential stress for various time are plotted in Fig. 3. It is seen from the previous results that the coupling effect between thermal and moisture is significant for composite material T300/5208. The maximum discrepancy of temperature and hygrothermal stress between coupled and uncoupled solutions might be as high as 50 percent. Furthermore, the maximum value of transient stress for the coupled case is lower than that for the uncoupled case.

If the classical time-integration method is adopted to deal with this example, it reveals that more than one thousand time steps are required to evaluate the solutions at time instant t^* = 0.8, due to the constraint on the interval of the time step (Hughes and Liu, 1978a). However, this solution could be directly evaluated with much less computer time by the method proposed in this article. Generally, it is only equivalent to take

Downloaded 03 May 2010 to 171.66.16.247. Redistribution subject to ASME license or copyright; see http://www.asme.org/terms/Terms_Use.cfm

15 times in solving Eq. (19) if an optimal free parameter is given. Therefore, the present method is more economical and better than the classical time-integration techniques in case a long-time solution is required.

Example 2. Consider an infinitely long two-layer annular cylinder, show in Fig. 4, having inner, intermediate, and outer radii r_1, r_2, and r_3, respectively, subjected to symmetrical hygrothermal loadings as follows:

Table 1 Comparison of the present solutions T^* and C^* with the analytical solutions (Chang et al., 1990) at $t^* = 1.0$ for various R

R	T^*	T^* (Exact sol.)	Error (percent)
1.2	0.991	0.991	0.0
1.4	0.986	0.986	0.0
1.6	0.987	0.987	0.0
1.8	0.992	0.992	0.0
R	C^*	C^* (Exact sol.)	Error (percent)
1.2	0.336	0.337	0.3
1.4	0.506	0.506	0.0
1.6	0.476	0.475	0.2
1.8	0.278	0.278	0.0

Table 2 Comparison of the present solutions σ_{ij}^* and u^* with the analytical solutions (Chang et al., 1990) at $t^* = 1.0$ for various R

R	σ_{rr}^*	σ_{rr}^* (Exact sol.)	Error (percent)
1.2	0.0028	0.0027	3.70
1.4	0.0001	0.0001	0.00
1.6	−0.0026	−0.0025	4.00
1.8	−0.0028	−0.0027	3.70
R	$\sigma_{\theta\theta}^*$	$\sigma_{\theta\theta}^*$ (Exact sol.)	Error (percent)
1.0	0.0385	0.0407	5.41
1.4	−0.0235	−0.0224	4.91
1.6	−0.0168	−0.0159	5.67
1.8	0.0082	0.0088	6.82
R	σ_{zz}^*	σ_{zz}^* (Exact sol.)	Error (percent)
1.0	−0.2378	−0.2363	0.63
1.2	−0.2798	−0.2782	0.58
1.6	−0.2981	−0.2955	0.88
R	u^*	u^* (Exact sol.)	Error (percent)
1.0	0.407	0.407	0.0
1.2	0.484	0.484	0.0
1.6	0.657	0.657	0.0

$$T_1^*(r_1, t) = 1, \qquad T_2^*(r_3, t) = 1, \qquad t > 0$$

$$C_1^*(r_1, t) = 0 \qquad C_2^*(r_3, t) = 0 \qquad t > 0$$

$$T_1^*(r_2, t) = T_2^*(r_2, t), \quad C_1^*(r_2, t) = C_2^*(r_2, t), \quad t > 0$$

$$K_1 \frac{\partial T_1^*(r_2, t)}{\partial n} = K_2 \frac{\partial T_2^*(r_2, t)}{\partial n},$$

$$D_{m1} \frac{\partial C_1^*(r_2, t)}{\partial n} = D_{m2} \frac{\partial C_2^*(r_2, t)}{\partial n}, \quad t > 0$$

The initial conditions are

$$T_1^*(r, 0) = T_2^*(r, 0) = 0, \; C_1^*(r, 0) = C_2^*(r, 0) = 0, \; r_1 < r < r_3.$$

The solutions are conveniently interpreted in terms of following dimensionless variables:

$$R = \frac{r}{r_1}, \; R_1 = \frac{r_1}{r_1} = 1, \; R_3 = \frac{r_3}{r_1}, \; \sigma_{ij}^* = \frac{\sigma_{ij}(1-2\mu)}{\alpha E(T_f - T_i)},$$

$$u^* = \frac{u}{\alpha(1+\mu) r_3 (T_f - T_i)}, \; t^* = \frac{Lt}{r_1^2}.$$

The material properties and radius of this two-layer cylindrical structure are listed as follows:

$\alpha_1 = \alpha_2 31.3 \times 10^{-6}$ cm/cm − °C,

$\beta_1 = \beta_2 = 2.68 \times 10^{-3}$ cm/cm − percent H_2O,

$\mu_1 = \mu_2 = 0.33$, $\nu_1 = \nu_2 = 0.5$ cm^3 − °C/g,

$\lambda_1 = \lambda_2 = 0.5$ g/cm^3 − °C,

$L_1 = 5L_2 = 7.78 \times 10^{-6}$ cm^2/hr, $D_1 = D_2 = 7.78 \times 10^{-7}$ cm^2/hr,

$E_1 = 64.3$ GPa, $E_2 = 79.7$ Gpa, $R_1 = 1.0$, $R_2 = 1.6$, $R_3 = 2.0$,

where the properties of the inner and outer layers are denoted by the subscript 1 and 2, respectively.

The temperature distributions along the radial direction for various time are plotted in Fig. 5. The distributions of circumferential stress for various time are plotted in Fig. 6. It is seen from the results that, in this example, the coupling effect between thermal and moisture is still significant and shall be considered.

Example 3. A $d \times d$ square cylinder with elliptical hole, shown in Fig. 7, with semi-major and semi-minor axes a and b, respectively, is subjected to surface heating on its traction-free inner surface by sudden exposure to a temperature $T^* = 1.0$ at $t > 0$, and remains its original temperature on its traction-free outer surface. These boundary conditions could be expressed as follows:

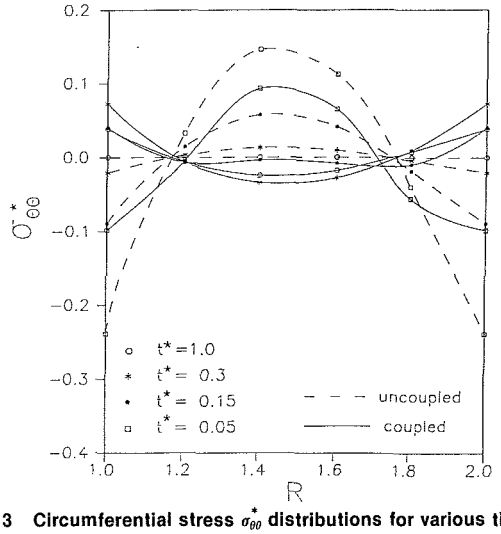


Fig. 3 Circumferential stress $\sigma_{\theta\theta}^*$ distributions for various time

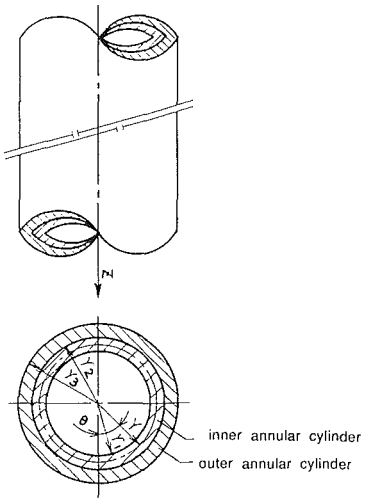


Fig. 4 Infinitely long two-layer annular cylinder subjected to hygrothermal loadings

Downloaded 03 May 2010 to 171.66.16.247. Redistribution subject to ASME license or copyright; see http://www.asme.org/terms/Terms_Use.cfm

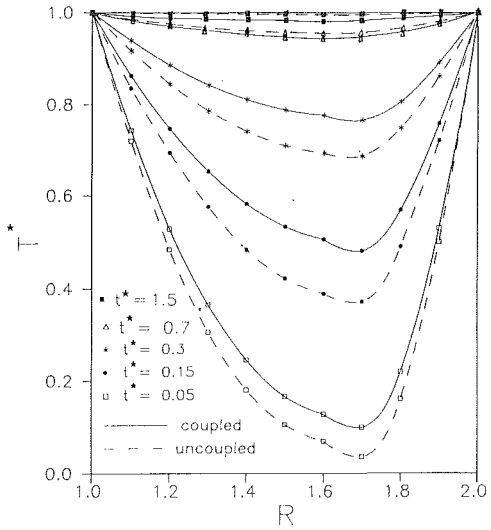


Fig. 5 Temperature T^* distributions for various time ($t^* = 0.05, 0.15, 0.30, 0.70, 1.50$)

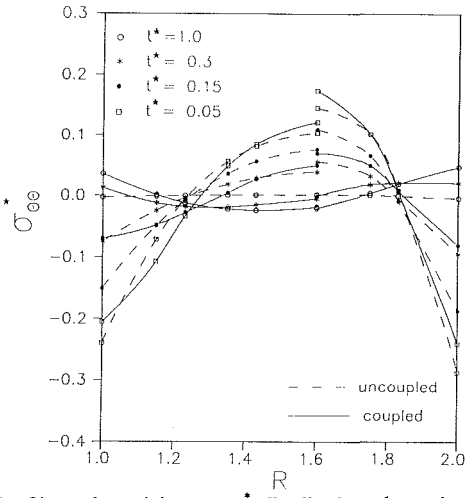
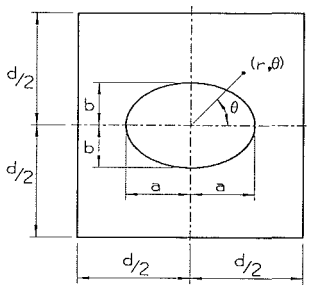


Fig. 6 Circumferential stress $\sigma^*_{\theta\theta}$ distributions for various time



24 elements and 93 nodes

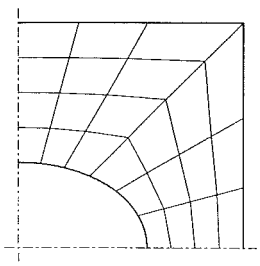


Fig. 7 Geometry of square cylinder with elliptical hole

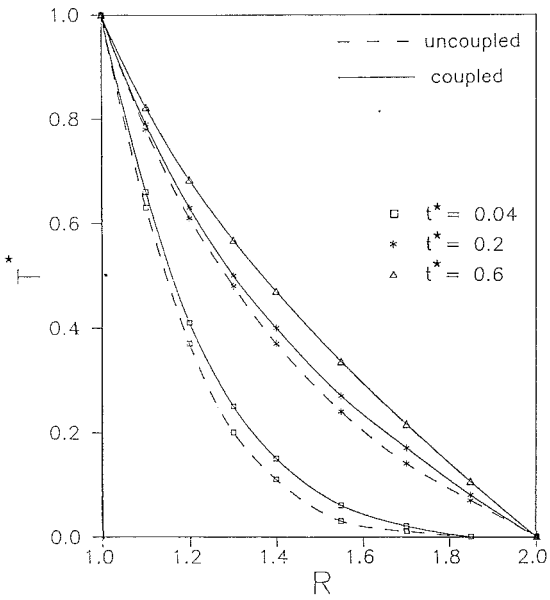


Fig. 8 Temperature T^* distributions along the direction $\theta = 0$ deg for various time

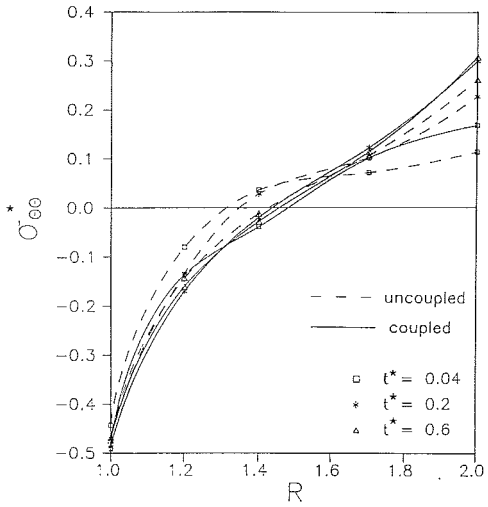


Fig. 9 Circumferential stress $\sigma^*_{\theta\theta}$ distributions along the direction $\theta = 0$ deg for various time

$$T^* = H(t), \quad C^* = 0, \quad \text{at the inner surface when } t > 0$$

$$T^* = 0, \quad C^* = 0, \quad \text{at the outer surface when } t > 0.$$

The initial conditions are

$$T^* = 0, \quad C^* = 0, \quad \text{when } t = 0.$$

The solutions are conveniently interpreted in terms of following dimensionless variables.

$$R = \frac{r}{a}, \quad t^* = \frac{Lt}{a^2}, \quad \sigma^*_{ij} = \frac{\alpha_{ij}(1-2\nu)}{\alpha E(T_f - T_i)}$$

Suppose the selected material is the same as the first example and the geometry of the cylinder is

$$\frac{a}{b} = 2, \quad \frac{d}{a} = 4.$$

The problem is symmetric about both the x and y axes. Thus, only a quarter of the cylinder need be considered. The temperature distributions for various times along the directions $\theta = 0$ deg are shown in Fig. 8. The circumferential stress distributions for various times along the directions $\theta = 0$ deg are plotted in Fig. 9. It is seen, in this example, that there still

Downloaded 03 May 2010 to 171.66.16.247. Redistribution subject to ASME license or copyright; see http://www.asme.org/terms/Terms_Use.cfm

exists a significant discrepancy between coupled and uncoupled solutions. The maximum hygrothermal stress is taken place at the inner surface of the semi-major axis.

Discussion and Conclusion

In this study, a general finite element method/Laplace transform model is proposed to deal with the plane problems of coupled temperature and moisture. To illustrate the numerical accuracy and efficiency of the present method, three different examples are analyzed. Since the present model takes off the time dimension by the Laplace transform, the solution of a specific location at a specific time, that is either long or short, can be evaluated directly. This kind of approach is quite different from the conventional procedure that treats the time domain by the time integration method. The latter process will thus lead to a step-by-step or recurrence calculation and is appropriate to evaluate a short-time solution. The only shortcoming of the present method is concerned with the treatment of the numerical Laplace inversion, which required more computer time (generally, it is equivalent to take 15 times in solving equation (19) if an optimal free parameter is given) than step-by-step integration schemes. However, it is believed that the present methods is still more economical and better than the classical time-integration techniques in case a long-time solution is required, since several hundred or more time steps may be required to achieve this long-time solution by time-integration techniques. Furthermore, it can be seen in all the examples that the coupling effect between thermal and moisture is significant for the studied composite material T300/5208. The maximum discrepancy of temperature and hygrothermal stress between coupled and uncoupled solutions might be as high as 50 percent.

References

Belystchko, T., and Mullen, R., 1978, "Stability of Explicit-Implicit Mesh Partitions in Time Integration," *Int. J. Num. Meths. Eng.*, Vol. 12, pp. 1575–1586.

Chang, W. J., Chen, T. C., and Weng, C. I., 1990, "Transient Hygrothermal Stresses in an Infinitely Long Annular Cylinder: Coupling of Heat and Moisture," submitted to *J. Therm. Stresses*.

Chen, H. T., Chen, T. M,. and Chen, C. K., 1987, "Hybrid Laplace Transform/Finite Element Method for Two-Dimensional Transient Heat Conduction Problems," *Comput. Meths. Appl. Mech. Eng.*, Vol. 63, pp. 83–95.

Chen, T. C., and Weng, C. I., 1988, "Generalized Coupled Transient Thermoelastic Plane Problems by Laplace Transform/Finite Element Method," ASME JOURNAL OF APPLIED MECHANICS, Vol. 55, No. 2, pp. 377–382.

Dubin, F., 1973, "Numerical Inversion of Laplace Transform: An Effective Improvement of Dubner and Abate's Method," *Comput. J.*, Vol. 17, pp. 371–376.

Hartranft, R. J., and Sih, G. C., 1980, "The Influence of the Soret and Dufour Effects on the Diffusion of Heat and Moisture in Solids," *Int. J. Engng. Sci.*, Vol. 18, pp. 1375–1383.

Honig, G,. and Hirdes, U., 1984, "A Method for the Numerical Inversion of Laplace Transform," *J. Comput. Appl. Maths.*, Vol. 10, pp. 113–132.

Hughes, T. J. R., and Liu, W. K., 1978, "Implicit-Explicit Finite Elements in Transient Analysis: Stability Theory," ASME JOURNAL OF APPLIED MECHANICS, Vol. 45, pp. 371–374.

Hughes, T. J. R., and Liu, W. K., 1978, "Implicit-Explicit Finite Elements in Transient Analysis: Implementation and Numerical Examples," ASME JOURNAL OF APPLIED MECHANICS, Vol. 45, pp. 375–378.

Shirrell, C. D., 1978, "Diffusion of Water Vapor in Graphite/Epoxy Composites. n: Advanced Composite Materals-Environmental Effects," J. R. Vinson, ed., ASTM, STP658, pp. 21–42.

Sih, G. C., Shih, M. T., and Chou, S. C., 1980, "Transient Hygrothermal Stresses in Composites: Coupling of Moisture and Heat with Temperature Varying Diffusivity," *Int. J. Engng. Sci.*, Vol. 18, pp. 19–42.

Sih, G. C., and Ogawa, A., 1982, "Transient Thermal Change on a Solid Surface: Coupled Diffusion of Heat and Moisture," *J. Thermal Stresses*, Vol. 5, pp. 265–282.

Sih, G. C., Michopoulos, J. G., and Chou, S. C., 1986, *Hygrothermoelasticity*, Kluwer Academic Publishers, USA.

Springer, G. S., 1984, *Environmental Effects on Composite Materials*, Vol. 2, Technomic Publishing Company.

APPENDIX

The dimensionless closed-form solutions of temperature T^*, moisture C^*, displacement u^*, and various components of stress σ_{ij}^* are given as follows:

$$T^* = 1 - \frac{\pi}{(S_1+S_2)} \sum_{n=1}^{\infty} \frac{[J_o(\lambda_n r_1) - J_o(\lambda_n r_3)] J_o(\lambda_n r_1) U_o(\lambda_n r)}{J_o^2(\lambda_n r_1) - J_o^2(\lambda_n r_3)} \times (S_1 e^{-\lambda_n^2 t/d_1^2} + e^{-\lambda_n^2 t/d_n^2}) \quad \text{(A1)}$$

$$C^* = \frac{\pi L S_1 S_2}{D(S_1+S_2)} \sum_{n=1}^{\infty} \frac{[J_o(\lambda_n r_1) - J_o(\lambda_n r_3)] J_o(\lambda_n r_1) U_o(\lambda_n r)}{J_o^2(\lambda_n r_1) - J_o^2(\lambda_n r_3)} \times (-e^{-\lambda_n^2 t/d_1^2} + e^{-\lambda_n^2 t/d_2^2}) \quad \text{(A2)}$$

$$u^* = \frac{1}{\alpha(1-\mu^2)(T_f - T_i) r r_3} \left\{ \sum_{n=1}^{\infty} (V_n + W_n) \left\{ (1+\mu) \times \left[-J_o(\lambda_n r_3) Y_1(\lambda_n r) \frac{r}{\lambda_n} + J_1(\lambda_n r) Y_o(\lambda_n r_3) \frac{r}{\lambda_n} - \frac{2 J_o(\lambda_n r_3)}{\pi \lambda_n^2 J_o(\lambda_n r_1)} \right] + \frac{(1+\mu)(1-2\mu) r^2 + r_1^2 (1+\mu)}{r_3^2 - r_1^2} \times \left(\frac{2[J_o(\lambda_n r_1) - J_o(\lambda_n r_3)]}{\pi \lambda_n^2 J_o(\lambda_n r_1)} \right) \right\} \right\} + \frac{\alpha' r}{\alpha r_3 (T_f - T_i)} \quad \text{(A3)}$$

$$\sigma_{rr}^* = \frac{(1-2\mu)}{\alpha(1-\mu)(T_f - T_i) r^2} \sum_{n=1}^{\infty} (V_n + W_n) \left\{ \frac{r^2 - r_1^2}{r_3^2 - r_1^2} \times \left(\frac{2[J_o(\lambda_n r_1) - J_o(\lambda_n r_3)]}{\pi \lambda_n^2 J_o(\lambda_n r_1)} \right) + J_o(\lambda_n r_3) Y_1(\lambda_n r) \frac{r}{\lambda_n} - J_1(\lambda_n r) Y_o(\lambda_n r_3) \frac{r}{\lambda_n} + \frac{2 J_o(\lambda_n r_3)}{\pi \lambda_n^2 J_o(\lambda_n r_1)} \right\} \quad \text{(A4)}$$

$$\sigma_{\theta\theta}^* = \frac{(1-2\mu)}{\alpha(1-\mu)(T_f - T_i) r^2} \sum_{n=1}^{\infty} (V_n + W_n) \left\{ \frac{r^2 + r_1^2}{r_3^2 - r_1^2} \times \left(\frac{2[J_o(\lambda_n r_1) - J_o(\lambda_n r_3)]}{\pi \lambda_n^2 J_o(\lambda_n r_1)} \right) - J_o(\lambda_n r_3) Y_1(\lambda_n r) \frac{r}{\lambda_n} + J_1(\lambda_n r) Y_o(\lambda_n r_3) \frac{r}{\lambda_n} - \frac{2 J_o(\lambda_n r_3)}{\pi \lambda_n^2 J_o(\lambda_n r_1)} - r^2 U_o(\lambda_n r) \right\} \quad \text{(A5)}$$

$$\sigma_{zz}^* = \frac{(1-2\mu)}{\alpha(1-\mu)(T_f - T_i)} \left\{ \frac{2\mu}{r_3^2 - r_1^2} \left[\sum_{n=1}^{\infty} (V_n + W_n) \times \left(\frac{2[J_o(\lambda_n r_1) - J_o(\lambda_n r_3)]}{\pi \lambda_n^2 J_o(\lambda_n r_1)} \right) + \frac{\alpha'(r_3^2 - r_1^2)}{2} \right] - \sum_{n=1}^{\infty} (V_n + W_n) U_o(\lambda_n r) - \alpha' \right\} \quad \text{(A6)}$$

where

$$S_1 = \{(L-D) \pm [(L-D)^2 + 4\nu\lambda LD]^{1/2}\}/2\nu\lambda L$$

$$S_2 = \{(D-L) \pm [(L-D)^2 + 4\nu\lambda LD]^{1/2}\}/2\nu\lambda L$$

$$V_n = \frac{-\alpha'\pi}{S_1+S_2} \frac{[J_o(\lambda_n r_1) - J_o(\lambda_n r_3)] J_o(\lambda_n r_1)}{J_o^2(\lambda_n r_1) - J_o^2(\lambda_n r_3)} \times (S_1 e^{-\lambda_n^2 t/d_1^2} + S_2 e^{\lambda_n^2 t/d_2^2})$$

$$W_n = \frac{\beta'\pi L S_1 S_2}{D(S_1+S_2)} \frac{[J_o(\lambda_n r_1) - J_o(\lambda_n r_3)] J_o(\lambda_n r_1)}{J_o^2(\lambda_n r_1) - J_o^2(\lambda_n r_3)} \times (e^{-\lambda_n^2 t/d_1^2} + e^{-\lambda_n^2 t/d_2^2})$$

And $d_1^2 = (S_1 - 1)/LS_1 = (1 - S_1\nu\lambda)/D$; $d_2^2 = (S_2 + 1)/LS_2 = (1 + S_2\nu\lambda)/D$; $U_o(\lambda_n r) = J_o(\lambda_n r) Y_o(\lambda_n r_3) - J_o(\lambda_n r_3) \times Y_o(\lambda_n r)$; J_o and Y_o are the Bessel functions of the first and second kind of order zero, respectively, in which the eigenvalue λ_n satisfies the relation $J_o(\lambda_n r_1) Y_o(\lambda_n r_3) - J_o \times (\lambda_n r_3) Y_o(\lambda_n r_1) = 0$, $n = 1, 2, 3, \ldots$; $\alpha' = (\alpha - \beta\omega)(T_f - T_i)$; $\beta' = \beta\omega(T_f - T_i)$.

Downloaded 03 May 2010 to 171.66.16.247. Redistribution subject to ASME license or copyright; see http://www.asme.org/terms/Terms_Use.cfm

Grain Size Reduction in Granular Flows of Spheres: The Effects of Critical Impact Energy

M. W. Richman
Associate Professor,
Mechanical Engineering Department,
Higgins Laboratories,
Worcester Polytechnic Institute,
Worcester, MA 01609
Assoc. Mem. ASME

A. A. Oyediran
Research Associate,
National Research Council,
Fluid Dynamics Branch,
Space Science Laboratory,
NASA Marshall Space Flight Center,
Huntsville, AL 35812

We extend methods employed to derive recent kinetic theories for rapid noncomminuting granular flows, to homogeneous flows in which a fraction of the repeated collisions produce tiny fractures on the particles' peripheries and gradually reduce their effective diameters. The theory consists of balance equations for mass, momentum, and energy, as well as constitutive relations for the pressure tensor and collisional rates of mass and energy lost. We improve upon the work of Richman and Chou (1989) by incorporating into the constitutive theory the critical impact energy below which no mass loss occurs in a binary collision. The theory is applied to granular shear flows and, for fixed shear rates, predicts the time variations of the solid fraction, granular temperature, and induced stresses, as well as their extreme sensitivities to small changes in the critical impact energy.

Introduction

Comminution is the process by which the discrete solid particles that comprise a granular material are reduced in size. Typically, when the unrefined particles are relatively large they are treated in any of an assortment of crushers, and when they are smaller they are treated in any of a variety of mills. The methods currently employed to control the comminution process have been concisely outlined by Austin (1984) and reviewed in detail by Prasher (1987). There are also circumstances, such as those that occur in the handling of pharmaceuticals and crystalline polymers, under which size reduction results from the repeated interactions between particles during the natural course of their transport. In these cases, the size reduction is undesirable and may be quite costly. Interestingly, the occurrence of such a size reduction mechanism has been observed by Savage and Sayed (1984), who found after shearing samples of initially smooth glass beads in an enclosed annular trough, that the surfaces of the beads became pitted with many small fractures and that as a consequence a fine powder collected at the bottom of the trough.

In this paper, we extend the methods employed in deriving recent kinetic theories for noncomminuting granular flows, such as those reviewed by Richman (1986), Jenkins (1987), and Campbell (1990), to flows in which repeated collisions between particles produce tiny fractures on their peripheries and over time reduce their average size. We improve upon the work of Richman and Chou (1989) by accounting in a simple manner for the dependence of the mass lost from each particle in a binary collision on the relative impact energy and the location of the point of impact. We do so by incorporating the critical impact energy, below which no mass loss occurs in a binary collision, into the statistical averaging required to derive the appropriate constitutive relations.

The theory applies to homogeneous flows and consists of balance equations for mass, momentum, and energy as well as constitutive relations for the pressure tensor and the collisional rates of mass and energy lost. As an example, the theory is applied to shear flows and predicts for fixed shear rates and particle number densities, the time variations of the solid fraction, granular temperature, and the induced stresses. In presenting the results, we pay special attention to the effects of the critical impact energy on these time variations.

Mean Fields and Balance Equations

Of interest here are flows of identical spheres of diameter σ, mass m, and mass density ρ_p. The statistics of the spheres' velocities and positions are governed by the single particle distribution function f, defined such that $f(\mathbf{c}, \mathbf{r}, t)d\mathbf{c}d\mathbf{r}$ gives the number of particles at time t whose centers travel with velocity $\mathbf{c}$ within the velocity range $d\mathbf{c}$ and are located at position $\mathbf{r}$ within the volume element $d\mathbf{r}$. The number $n(\mathbf{r}, t)$ of particles per unit volume is then given by,

$$n(\mathbf{r},t) = \int f(\mathbf{c},\mathbf{r},t)\,d\mathbf{c}, \tag{1}$$

where the integration is taken over all velocities. With f and n defined in this manner, the mean value $<\psi>$ of any particle property $\psi(\mathbf{c}, \mathbf{r}, t)$ may be calculated as the weighted average,

$$<\psi> = \frac{1}{n}\int \psi(\mathbf{c},\mathbf{r},t)f(\mathbf{c},\mathbf{r},t)\,d\mathbf{c}, \tag{2}$$

where the integration is taken over all velocities.

Contributed by the ASME Applied Mechanics Division of THE AMERICAN SOCIETY OF MECHANICAL ENGINEERS for presentation at the Winter Annual Meeting, Atlanta, Ga., Dec. 1-6, 1991.

Discussion on this paper should be addressed to the Technical Editor, Prof. Leon M. Keer, The Technological Institute, Northwestern University, Evanston, IL 60208, and will be accepted until two months after final publication of the paper itself in the JOURNAL OF APPLIED MECHANICS. Manuscript received by the ASME Applied Mechanics Division, Dec. 28, 1989; final revision, Mar. 7, 1991.
Paper No. 91-WA/APM-20.

Copyright © 1992 by ASME
Downloaded 03 May 2010 to 171.66.16.247. Redistribution subject to ASME license or copyright; see http://www.asme.org/terms/Terms_Use.cfm

Three mean fields that are necessary to describe granular flows are the solid volume fraction $\nu(\mathbf{r}, t) = n\pi\sigma^3/6$ or the mass density $\rho(\mathbf{r}, t) = \rho_p\nu$; the mean velocity $\mathbf{u}(\mathbf{r}, t) \equiv <\mathbf{c}>$; and the granular temperature $T(\mathbf{r}, t)$, defined in terms of the fluctuation velocity $\mathbf{C} = \mathbf{c} - \mathbf{u}$ as the average $<C^2>/3$.

In the homogeneous flows of interest, the velocity gradient $\nabla\mathbf{u}$, the density ρ, the solid fraction ν, and the granular temperature T vary with time only. For these flows, the balance of mass is simply,

$$\frac{d\rho}{dt} + \rho\nabla\cdot\mathbf{u} = -M, \tag{3}$$

where M is the rate per unit volume at which mass is lost by the flow particles due to binary collisions. We assume that the mass lost by the particles is removed from and has no effect on the remaining flow.

In terms of the total pressure tensor $\boldsymbol{P}$, the balance of momentum reduces to

$$\nabla\cdot\boldsymbol{P} = 0, \tag{4}$$

where $\boldsymbol{P}$ is the sum of the transport contribution $<\rho\mathbf{CC}>$ and the collisional contribution $\boldsymbol{\phi}$ to the rate per unit area at which momentum is transferred throughout the flow. Finally, the balance of energy has the simple form,

$$\frac{3\rho}{2}\frac{dT}{dt} = -tr(\boldsymbol{P}\cdot\nabla\mathbf{u}) - \gamma + \frac{3T}{2}M, \tag{5}$$

where γ is the rate per unit volume at which fluctuation energy is removed from the flow due to binary collisions. The net sink γ appears in Eq. (5) because in each collision energy is lost to plastic deformation, and, in those collisions that result in mass loss, energy is dissipated during the fracture process and removed as mass with nonzero velocity. The occurrence of mass loss influences the balance of energy explicitly through the appearance of M and implicitly through its effect on γ.

Constitutive Theory

In this section we derive the constitutive relations for the rate of mass removed M, the rate of fluctuation energy lost γ, and the total pressure tensor $\boldsymbol{P}$. Both M and γ, which are due entirely to particle collisions, as well as $\boldsymbol{\phi}$, which is the collisional contribution to the total pressure tensor, are statistical averages of the changes per collision in the appropriate particle property weighted by the frequency of each collision.

In order to carry out the averaging process, it is necessary to know, in terms of the precollisional velocities and the location of the point of contact, the changes in mass, momentum, and energy experienced by any two particles when they collide. To calculate these changes, we employ the collision model of Richman and Chou (1989), in which the effects of mass loss are accounted for by assuming that identical spheres depart from each binary collision as two possibly smaller but always identical spheres. If m is the mass of each sphere just prior to a collision, and μ is the ratio of the mass just after a collision to the mass just prior, then the total change in mass per collision is

$$2(m' - m) = -2(1-\mu)m, \tag{6}$$

where here and in what follows primes denote post-collisional quantities. Furthermore, if $\mathbf{c}_1$ and $\mathbf{c}_2$ are the particles' velocities just prior to impact and $\mathbf{k}$ is the unit vector directed from the center of the first to the center of the second at impact, then the changes in momenta of each particle are given in terms of $\mathbf{k}$, $\mathbf{c}_1$, $\mathbf{c}_2$, and the difference $\mathbf{g} \equiv \mathbf{c}_1 - \mathbf{c}_2$ by

$$m'\mathbf{c}_1' - m\mathbf{c}_1 = m[(\mu-1)\mathbf{c}_1 - \mu(1+e)(\mathbf{g}\cdot\mathbf{k})/2], \tag{7}$$

and

$$m'\mathbf{c}_2' - m\mathbf{c}_2 = m[(\mu-1)\mathbf{c}_2 + \mu(1+e)(\mathbf{g}\cdot\mathbf{k})/2], \tag{8}$$

where e is the ratio $-(\mathbf{g}'\cdot\mathbf{k})/(\mathbf{g}\cdot\mathbf{k})$ that is analogous to the coefficient of restitution in collisions that involve no mass loss. Finally, Eqs. (7) and (8) may be combined to yield the total change in momentum per collision,

$$m'\mathbf{c}_1' + m'\mathbf{c}_2' - m\mathbf{c}_1 - m\mathbf{c}_2 = m(\mu-1)[\mathbf{c}_1 + \mathbf{c}_2], \tag{9}$$

and the total change in energy per collision,

$$(m'c_1'^2 + m'c_2'^2 - mc_1^2 - mc_2^2)/2 = -(m/2)[(1-\mu)(c_1^2 + c_2^2) + \mu(1-e^2)(\mathbf{g}\cdot\mathbf{k})^2/2]. \tag{10}$$

The general value of μ will depend on the material properties of the grains, their impact velocities, and the location of their point of contact. We anticipate, for example, that for prescribed grain properties there are relative impact velocities below which no mass is lost in the collision. For these velocities, μ is equal to one, the change in momentum (9) vanishes, and the change in energy (10) reduces to the change experienced by inelastic spheres that collide without fracture.

The sinks M and γ are, each to within an algebraic sign, the collisional sources of mass and fluctuation energy throughout the flow. Jenkins and Savage (1983) have derived a general integral expression for the collisional source $\chi(\psi)$ of any particle property $\psi(\mathbf{c}, \mathbf{r}, t)$ in a flowing assembly of identical inelastic spheres. The integral is the average of the total change $\Delta\psi$ in ψ per collision experienced by any two colliding particles, which, when linearized with respect to first-order spatial gradients, reduces to

$$\chi(\psi) = \frac{\sigma^2 g_0}{2}\int\Delta\psi\left[1 + \frac{\sigma}{2}\mathbf{k}\cdot\nabla\ln\left(\frac{f_2}{f_1}\right)\right]f_1 f_2(\mathbf{g}\cdot\mathbf{k})d\mathbf{k}d\mathbf{c}_1 d\mathbf{c}_2, \tag{11}$$

where $g_0(\nu)$ is the function $(2-\nu)/2(1-\nu)^3$ of solid fraction, f_α is shorthand for $f(\mathbf{c}_\alpha, \mathbf{r}, t)$, and $d\mathbf{k}$ is an element of solid angle centered about $\mathbf{k}$. In order to ensure that a collision is impending, the integration is carried out only over those velocities and points of contact for which $\mathbf{g}\cdot\mathbf{k} > 0$.

The contribution $\boldsymbol{\phi}$ to the total pressure tensor is the collisional flux of momentum measured relative to the mean motion. If the difference $\psi_1' - \psi_1$ is the change in any property ψ experienced by particle 1 in a collision with particle 2, then the appropriate integral expression for the collisional flux of ψ that is linear in first-order spatial gradients is given by the sum $\boldsymbol{\theta}(\psi) + \mathbf{E}(\psi)$, where

$$\boldsymbol{\theta}(\psi) = \frac{-\sigma^3 g_0}{2}\int(\psi_1' - \psi_1)\mathbf{k} \times\left[1 + \frac{\sigma}{2}\mathbf{k}\cdot\nabla\ln\left(\frac{f_2}{f_1}\right)\right]f_1 f_2(\mathbf{g}\cdot\mathbf{k})d\mathbf{k}d\mathbf{c}_1 d\mathbf{c}_2 \tag{12}$$

is the flux integral derived by Jenkins and Savage (1983), and

$$\mathbf{E}(\psi) = \frac{-\sigma^4 g_0}{2}\int\Delta\psi\mathbf{k}[\mathbf{k}\cdot\nabla(f_1 f_2)](\mathbf{g}\cdot\mathbf{k})d\mathbf{k}d\mathbf{c}_1 d\mathbf{c}_2 \tag{13}$$

is the extra term derived by Richman and Chou (1989) that must be included when ψ is not a summational invariant. Integrations (12) and (13) are carried out for $\mathbf{g}\cdot\mathbf{k} > 0$.

In terms of the general source integral χ, the collisional rates M and γ are equal to $-\chi(m)$ and $-\chi(mC^2/2)$, respectively. The collisional pressure tensor $\boldsymbol{\phi}$ is equal to the sum of flux integrals $\boldsymbol{\theta}(m\mathbf{C}) + \mathbf{E}(m\mathbf{C})$. For $\chi(m)$, the total change $\Delta\psi$ is given by Eq. (6), and for $\chi(mC^2/2)$, $\Delta\psi$ is given by Eq. (10) with $\mathbf{c}_1$ and $\mathbf{c}_2$ replaced by their fluctuating counterparts $\mathbf{C}_1$ and $\mathbf{C}_2$. For $\boldsymbol{\theta}(m\mathbf{C})$ and $\mathbf{E}(m\mathbf{C})$, the changes $\psi_1' - \psi_1$ and $\Delta\psi$ are given by Eqs. (7) and (9) with $\mathbf{c}_1$ and $\mathbf{c}_2$ replaced by $\mathbf{C}_1$ and $\mathbf{C}_2$ in each.

We improve upon the work of Richman and Chou (1989) by accounting for the dependence of the fraction of mass loss per collision on the particles' incoming masses and velocities as well as on their instantaneous point of contact. We do so

Downloaded 03 May 2010 to 171.66.16.247. Redistribution subject to ASME license or copyright; see http://www.asme.org/terms/Terms_Use.cfm

by incorporating into the constitutive theory the critical value $\mathcal{E}$ of relative normal impact energy below which no fracture occurs in a collision. In the integrations, the mass loss parameter μ is therefore equal to unity when $m(\mathbf{g} \cdot \mathbf{k})^2/2$ is less than $\mathcal{E}$ and, for simplicity, is equal to a constant value $1 - \epsilon$ when $m(\mathbf{g} \cdot \mathbf{k})^2/2$ is greater than $\mathcal{E}$. The value of $1 - \epsilon$ may be interpreted as the average value of μ in those collisions that involve mass loss.

In order to illustrate, we take the single particle distribution function to be the Maxwellian,

$$f(\mathbf{c}, \mathbf{r}, t) = \frac{n}{(2\pi T)^{3/2}} \exp\left(\frac{-C^2}{2T}\right), \tag{14}$$

and carry out the required integrations. In terms of the dimensionless quantity $\xi \equiv \mathcal{E}/2mT$, the source integrations yield the constitutive relations for both the collisional rate of mass removed,

$$M = \frac{24\epsilon\rho_p\nu^2 g_0 T^{1/2}}{\pi^{1/2}\sigma}\left\{\exp(-\xi^2) - [\sqrt{\pi}\,erfc\,\xi + 2\xi\exp(-\xi^2)]\,\frac{\sigma tr\boldsymbol{D}}{6T^{1/2}}\right\}, \tag{15}$$

where $\boldsymbol{D}$ is the symmetric part of $\nabla\mathbf{u}$; and the collisional rate of energy lost,

$$\gamma = \frac{6\rho_p\nu^2 g_0 T^{3/2}}{\pi^{1/2}\sigma}\left(\alpha - \beta\,\frac{\sigma tr\boldsymbol{D}}{6T^{1/2}}\right), \tag{16}$$

where the variations of the coefficients α and β with e, ϵ, and ξ are given by

$$\alpha = 2(1-e^2) + \epsilon[7 - 2(1-e^2)(1+\xi^2)]\exp(-\xi^2), \tag{17}$$

and

$$\beta = \frac{\sqrt{\pi}}{2}(1-e^2) + \frac{\epsilon}{6}\{(5+3e^2)[\sqrt{\pi}\,erfc\,\xi + 2\xi\exp(-\xi^2)] + 4e^2\xi^3\exp(-\xi^2)\}. \tag{18}$$

The sum $\boldsymbol{\phi} = \boldsymbol{\theta}(m\mathbf{C}) + \mathbf{E}(m\mathbf{C})$ of momentum-flux integrations yields the collisional contribution to the pressure tensor,

$$\boldsymbol{\phi} = 2\rho_p\nu^2 g_0 T\left\{\left[\delta - \zeta\,\frac{\sigma tr\boldsymbol{D}}{3\sqrt{\pi T}}\right]\boldsymbol{I} - 2\zeta\,\frac{\sigma\hat{\boldsymbol{D}}}{5\sqrt{\pi T}}\right\}, \tag{19}$$

where $\hat{\boldsymbol{D}}$ is the deviatoric part of $\boldsymbol{D}$ and the variations of δ and ζ with e, ϵ, and ξ are given by

$$\delta = (1+e) - \epsilon e\left[erfc\,\xi + \frac{2\xi}{\sqrt{\pi}}\exp(-\xi^2)\right], \tag{20}$$

and

$$\zeta = 2(1+e) - \epsilon[1 + 2e(1+\xi^2)]\exp(-\xi^2). \tag{21}$$

Although each of the contributions $\boldsymbol{\theta}(m\mathbf{C})$ and $\mathbf{E}(m\mathbf{C})$ to $\boldsymbol{\phi}$ involves the antisymmetric part of the mean velocity gradients, their sum does not. The total pressure tensor $\boldsymbol{P}$ is equal to the sum of the transport pressure $<\rho\mathbf{CC}>$ given by $\rho_p\nu T$, and collisional pressure $\boldsymbol{\phi}$ given by Eq. (19). The resulting constitutive relation for $\boldsymbol{P}$ may be written in the familiar form,

$$\boldsymbol{P} = (p - \omega tr\boldsymbol{D})\boldsymbol{I} - 2\eta\hat{\boldsymbol{D}}, \tag{22}$$

where the normal pressure p is

$$p = \rho_p\nu T(1 + 2\nu g_0\delta), \tag{23}$$

the bulk viscosity ω is

$$\omega = \frac{2\sigma\rho_p\nu^2 g_0 T^{1/2}}{3\pi^{1/2}}\,\zeta, \tag{24}$$

and the shear viscosity η is

$$\eta = \frac{2\sigma\rho_p\nu^2 g_0 T^{1/2}}{5\pi^{1/2}}\,\zeta. \tag{25}$$

If the deformation rate is purely deviatoric and the fraction of mass lost in each collision is independent of impact energy, then the trace of $\boldsymbol{D}$ and the dimensionless measure ξ of the critical energy $\mathcal{E}$ both vanish. Under these circumstances, constitutive relations (15) and (16) for the rates of mass removed M and energy lost γ, and constitutive relation (23) for the pressure tensor $\boldsymbol{P}$ reduce to those obtained by Richman and Chou (1989). On the other hand, if there is no fracture due to collisions, then either ϵ vanishes or $\mathcal{E}$ and therefore ξ become unbounded. In this limit, M vanishes and the expressions for γ and $\boldsymbol{P}$ reduce to those for noncomminuting granular flows obtained by Jenkins and Savage (1983) when their ad hoc collisional anisotropy parameter is zero.

Shear Flow

Balance Eqs. (3), (4), and (5) and constitutive relations (15), (16), and (22) may be applied to homogeneous shear flows in which the shear rate $\lambda/2$ and the particle number density n are fixed, while the particle diameter σ, and therefore the solid fraction ν, as well as the granular temperature T, vary with time only. In terms of the dimensionless time $\tau \equiv \lambda t$ and the dimensionless measure $w^2 \equiv 6n\sigma\nu T/\lambda^2$ of fluctuation energy, the balance of mass (3) becomes

$$\frac{d\nu}{d\tau} = -(4\epsilon\nu g_0 w)\exp(-\xi^2), \tag{26}$$

in which constitutive relation (15) has been employed to eliminate M. If $\mathcal{E}^* \equiv 3(6n^5/\pi)^{1/3}\mathcal{E}/\rho_p\lambda^2$ is the dimensionless value of the critical impact energy for fracture, then the dependence of the parameter ξ^2 on ν, w, and $\mathcal{E}^*$ is given by $\mathcal{E}^*\nu^{1/3}/w^2$.

The energy Eq. (5) may be written in terms of ν, w, and the time derivative of w by employing constitutive relation (16) to eliminate γ and Eq. (26) to eliminate the time derivative of ν. In this manner we find that

$$\frac{dw}{d\tau} = \frac{4g_0}{5\pi}\{2(1+e) - \epsilon[1 + 2e(1+\xi^2)]\exp(-\xi^2)\}\nu^2 - \frac{g_0}{3}\{2(1-e^2) + \epsilon[9 - 2(1-e^2)(1+\xi^2)]\exp(-\xi^2)\}w^2. \tag{27}$$

For fixed parameter values ϵ and e are prescribed initial values ν_i and w_i of ν and w, Eqs. (26) and (27) determine the temporal variations $\nu(\tau)$ and $w(\tau)$. Equation (22) then determines the corresponding variations in the induced shear and normal stresses within the flow. For nonzero values of ϵ, the only steady state admitted by Eqs. (26) and (27) is $\nu = w = 0$.

Here we take ϵ to be a small parameter and employ the method of matched asymptotic expansions (Van Dyke, 1975) to obtain simple approximate expressions for $\nu(\tau)$ and $w(\tau)$. In the inner interval, the short time variable is τ, and the lowest-order terms in the asymptotic series for ν and w are $\nu_0(\tau)$ and $w_0(\tau)$, respectively. In this interval, the lowest-order balance of mass,

$$\frac{d\nu_0}{d\tau} = 0, \tag{28}$$

demonstrates that ν_0 is equal to the initial solid fraction ν_i, and the lowest-order balance of energy,

$$\frac{dw_0}{d\tau} = g_i(a^2\nu_i^2 - b^2 w_0^2), \tag{29}$$

in which $g_i \equiv g_0(\nu_i)$, $a^2 \equiv 8(1+e)/5\pi$, and $b^2 \equiv 2(1-e^2)/3$, has the solution,

$$w_0 = \frac{a\nu_i}{b}\tanh\left[ab\nu_i g_i\tau + \tanh^{-1}\left(\frac{bw_i}{a\nu_i}\right)\right]. \tag{30}$$

In the outer interval, the compressed time variable s is equal to $\epsilon\tau$, and ν and w are expanded in asymptotic series whose first terms are $V_0(s)$ and $W_0(s)$, respectively. In this interval, the lowest-order energy balance reduces to the algebraic relation,

Downloaded 03 May 2010 to 171.66.16.247. Redistribution subject to ASME license or copyright; see http://www.asme.org/terms/Terms_Use.cfm

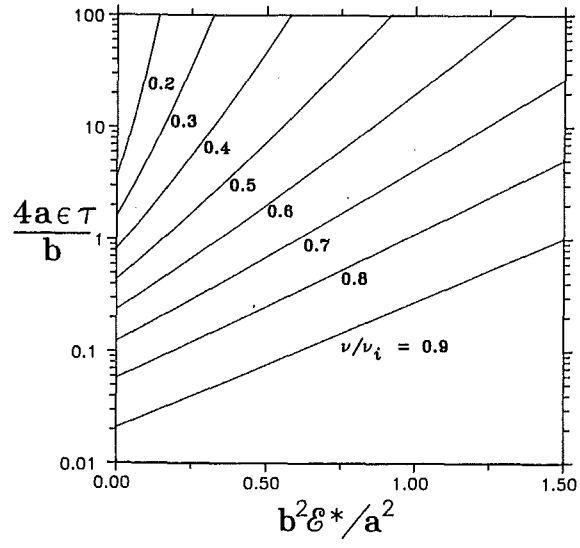


Fig. 1 Variations with critical impact energy $b^2\mathcal{E}^*/a^2$ of the times $4a\epsilon\tau/b$ at which ν/ν_i = .9, .8, .7, .6, .5, .4, .3, and .2 for ν_i = .6

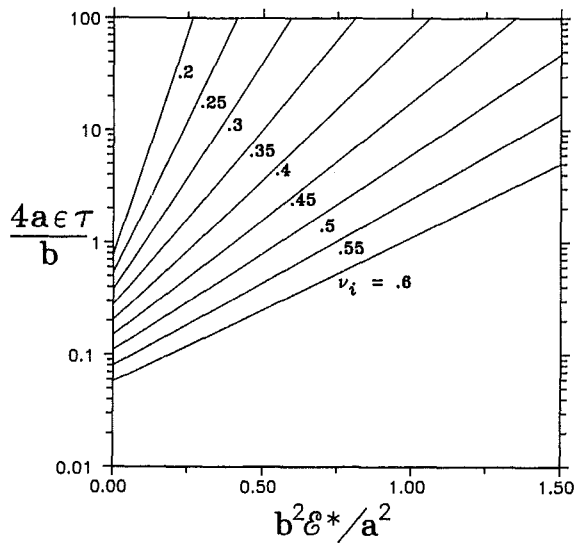


Fig. 2 Variations with critical impact energy $b^2\mathcal{E}^*/a^2$ of the times $4a\epsilon\tau/b$ at which ν/ν_i = .8 for ν_i = .6, .55, .5, .45, .4, .35, .3, .25, and .2

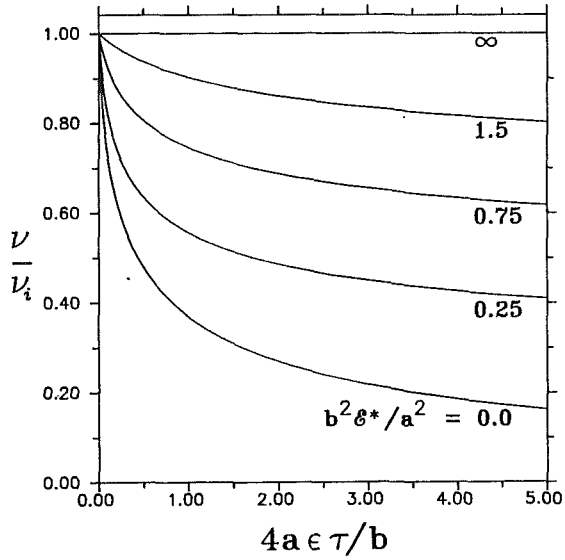


Fig. 3 Time variations of normalized solid fraction ν/ν_i for $b^2\mathcal{E}^*/a^2$ = 0, .25, .75, 1.5, and ∞, and ν_i = .6

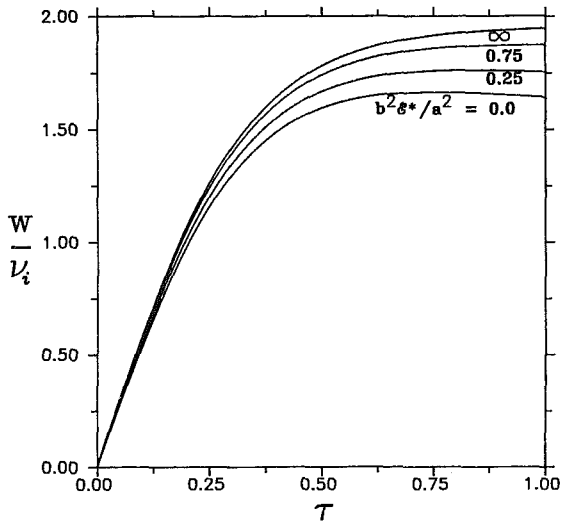


Fig. 4 Short-time variations of the measure w/ν_i for $b^2\mathcal{E}^*/a^2$ = 0, .25, .75, and ∞, w_i = 0, ν_i = .6, ϵ = .005, and e = .8

$$W_0 = \frac{a}{b} V_0, \tag{31}$$

between W_0 and V_0. When this relation is employed to eliminate W_0, the lowest-order mass balance becomes,

$$\frac{dV_0}{ds} = \frac{-4a}{b} G_0 V_0^2 \exp\left(\frac{-b^2\mathcal{E}^*}{a^2 V_0^{5/3}}\right), \tag{32}$$

where G_0 is equal to $g_0(V_0)$. By integrating Eq. (32) with respect to s, and ensuring that $V_0(s \to 0)$ matches $\nu_0(\tau \to \infty)$, we find that the composite expansion for $\nu(\tau)$ is given implicitly by the integral,

$$\frac{4a\epsilon\tau}{b} = \int_{\nu}^{\nu_i} \frac{\exp(b^2\mathcal{E}^*/a^2\nu^{5/3})}{\nu^2 g_0}\, d\nu. \tag{33}$$

In a similar manner, by matching $W_0(s \to 0)$ to $w_0(\tau \to \infty)$ we find that the composite expansion for $w(\tau)$ is,

$$w = \frac{a}{b}\left\{\nu_i \tanh\left[ab\nu_i g_i \tau + \tanh^{-1}\left(\frac{bw_i}{a\nu_i}\right)\right] - \nu_i + \nu\right\}, \tag{34}$$

in which $\nu(\tau)$ is determined by integral (33). For short times, $\nu(\tau)$ is close to ν_i, the last two terms on the right-hand side of Eq. (34) nearly cancel, and the first term on the right-hand side dominates the behavior of $w(\tau)$. For long times, the first two terms on the right-hand side of Eq. (34) nearly cancel, $w(\tau)$ approaches zero linearly with $\nu(\tau)$, and the actual granular temperature $T(t)$ approaches zero with $\nu^{2/3}(t)$.

In Fig. 1, we show the variations with critical impact energy $b^2\mathcal{E}^*/a^2$ of the scaled times $4a\epsilon\tau/b$ at which the solid fraction ν is equal to prescribed fractions ν/ν_i of the initial solid fraction ν_i = .6. For fixed values of e and ϵ, increases in the impact energy required for fracture on collision can cause dramatic decreases in the rates at which the solid fraction and average particle diameter diminish due to the shearing. In Fig. 2, we show the variations with critical impact energy $b^2\mathcal{E}^*/a^2$ of the scaled times $4a\epsilon\tau/b$ at which the solid fraction ν is reduced to 80 percent (ν/ν_i = .8) of its initial value ν_i for several values of ν_i between .2 and .6. For fixed values of e, ϵ, and $\mathcal{E}^*$, increases in the initial solid fraction result in increases in the frequency at which collisions occur and subsequent increases in the rate at which mass is lost due to the shearing.

The variations of normalized solid fraction ν/ν_i with scaled

Downloaded 03 May 2010 to 171.66.16.247. Redistribution subject to ASME license or copyright; see http://www.asme.org/terms/Terms_Use.cfm

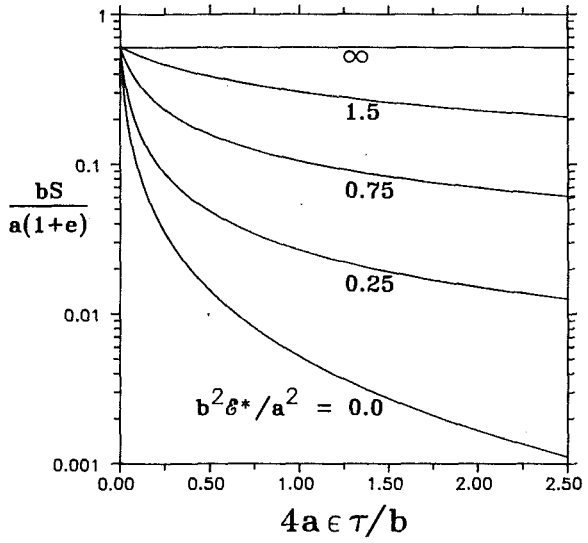


Fig. 5 Long-time variations of the shear stress $bS/a(1 + e)$ for $b^2\mathcal{E}^*/a^2 = 0, .25, .75, 1.5$, and ∞, and $\nu_i = .6$

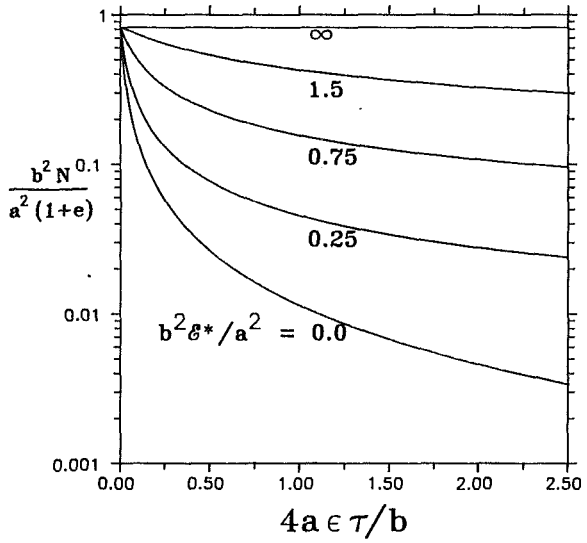


Fig. 6 Long-time variations of the normal pressure $b^2N/a^2(1 + e)$ for $b^2\mathcal{E}^*/a^2 = 0, .25, .75, 1.5$, and ∞, $\nu_i = .6$, and $e = .8$

time $4a\epsilon\tau/b$ are shown in Fig. 3 for critical impact energies $b^2\mathcal{E}^*/a^2 = 0, .25, .75, 1.5$, and ∞, and initial solid fraction $\nu_i = .6$. These are detailed time variations of solid fraction that may be inferred only approximately from several discrete times in Fig. 1. Comments made regarding the influence of the critical impact energy on the rate at which the solid fraction diminishes are illustrated here as well. In Fig. 4, the corresponding short-time variations of the measure w/ν_i of granular temperature are shown for $w_i = 0$, $\epsilon = .005$, and $e = .8$. As $\mathcal{E}^*$ increases from zero, the short-time behavior of w approaches the transient behavior of w in noncomminuting shear flows. The long-time behavior of $w(\tau)/\nu_i$ is linear in $\nu(\tau)$ and is shown in Fig. 3 to within a factor of a/b.

Of interest also are the time variations of the normal pressure p and, with x in the direction of the velocity and y in the direction of the velocity gradient, the shear stress $-P_{xy}$. These are the components of the traction that must be applied to parallel plates in order to sustain the constant shear rate $\lambda/2$. To lowest order, the dimensionless shear stress $S \equiv -\sigma n P_{xy}/\rho_p\lambda^2$ determined by the deviatoric piece of $\boldsymbol{P}$ is,

$$S = \frac{4}{5\pi}(1+e)w\nu^2 g_0, \tag{35}$$

and the dimensionless normal pressure $N \equiv \sigma np/\rho_p\lambda^2$ determined by the isotropic piece (23) of $\boldsymbol{P}$ is,

$$N = \frac{1}{6}[1+2(1+e)\nu g_0]w^2, \tag{36}$$

where $\nu(\tau)$ is given implicitly by integral (33) and $w(\tau)$ is given in terms of τ and ν by Eq. (34). For short times, S and N are given by Eqs. (35) and (36) with ν replaced by ν_i and w replaced by its inner interval approximation (30). During these times, the variations of S and N with τ are to within numerical factors given by $w(\tau)$ and $w^2(\tau)$, respectively. For any initial granular temperature, both the shear stress and normal pressure rapidly approach values that are nearly equal to their steady-state values in the absence of mass loss. If, for example, $w_i = 0$, $\nu_i = .6$, $\epsilon = .005$, and $e = .8$, then the short-time behaviors of S and N rise rapidly from zero and may be inferred from Fig. 4 for $b^2\mathcal{E}^*/a^2 = 0, .25, .75$, and ∞. For long times, S and N are determined by Eqs. (35) and (36) with w replaced by $a\nu/b$ and ν determined by integral (33). During these times, both the shear stress and normal pressure diminish to zero. Because S and N vary with ν^3 and ν^2 when ν is small, their dimensional counterparts $-P_{xy}$ and p vanish with $\nu^{5/3}$ and $\nu^{8/3}$. The long-time variations of the scaled shear stress $bS/a(1+e)$ are shown in Fig. 5 for $\nu_i = .6$ and $b^2\mathcal{E}^*/a^2 = 0, .25, .75, 1.5$, and ∞. The corresponding variations of scaled normal pressure $b^2N/a^2(1 + e)$ are shown in Fig. 6 for $e = .8$.

Conclusions

We have derived a constitutive theory for dry rapid flows of spheres that experience gradual grain-size reduction. The size reduction results from repeated binary collisions, some of which cause tiny fractures on and mass loss from the peripheries of the colliding spheres, and over time reduce their effective diameters. The theory consists of constitutive relations for the pressure tensor, which includes the effects of particle transport and particle collisions, and the rates of mass and energy lost, which are due entirely to particle collisions. The theory is relatively simple because it applies only to homogeneous flows of identical spheres and because it is based on simple rules that govern the amounts of mass, momentum, and energy lost in each binary collision. However, it is more elaborate than the theory derived by Richman and Chou (1989) because it accounts for the critical impact energy between grains, below which no fracture and mass loss occur in a binary collision.

When applied to granular shear flows, the theory predicts, for fixed shear rates and particle number densities, the evolutions of the solid fraction, granular temperature, normal pressure, and shear stress with time. For short times the granular temperature, normal pressure, and shear stress vary as though no mass is lost in any collision, and for longer times the granular temperature, and therefore the normal pressure and shear stress, diminish to zero with different powers of the solid fraction.

As an example, we consider assemblies of identical spherical glass beads with initial diameter equal to 1 mm, Young's modulus equal to 80×10^9 N/m^2, Poisson's ratio equal to .25, maximum stress before fracture equal to 2000×10^6 N/m^2, and coefficient of restitution equal to .9 that are sheared at shear rates equal to 200 sec^{-1}. The Hertz contact solution predicts that for these beads the dimensionless measure $b^2\mathcal{E}^*/a^2$ of critical impact energy is approximately equal to 1.25. Furthermore, in a collision with exactly the critical impact energy the ratio of the compressed volume of each sphere to the corresponding undeformed volume is roughly equal to 7×10^{-7} and is at least an order of magnitude greater than ϵ.

Downloaded 03 May 2010 to 171.66.16.247. Redistribution subject to ASME license or copyright; see http://www.asme.org/terms/Terms_Use.cfm

For this reason, we estimate that for these beads ϵ is at most of order 10^{-8}. Then, according to Fig. 1, when ν_i is equal to .6, it would take at least 75 minutes of shearing to reduce the solid fraction by ten percent and the corresponding particle diameter by 3.5 percent of their initial values.

The theory also predicts the influence of varying critical impact energies on these time evolutions. For all values of critical impact energy, both the solid fraction and its long-time derivative are decreasing functions of time. When, for example, the critical impact energy is equal to zero, all collisions result in mass loss, the solid fraction is a relatively rapidly decreasing function of time, and the time derivative of the solid fraction decreases only because the frequency of collisions diminishes with decreasing solid fraction. However, for nonzero values of critical impact energy, not all collisions result in mass loss, the solid fraction diminishes more slowly with time, and the time derivative of the solid fraction decreases both because the frequency of collisions and, as the particles become less massive, the percentage of the collisions that result in mass loss, diminish with decreasing solid fraction. Consequently, even modest changes in the critical impact energy may cause rather dramatic changes in the rates at which the solid fraction, and therefore the granular temperature, normal pressure, and shear stress vary with time.

Acknowledgments

M. W. Richman is grateful to the National Science Foundation for its support of this work through Grant MSM-8707911. A. A. Oyediran acknowledges the support of the National Research Council and the NASA Marshall Space Flight Center. The authors are also grateful to Dr. Nicholas C. Costes of the NASA Space Flight Center for many fruitful discussions and comments, to Prof. Tony Rosato of the New Jersey Institute of Technology for his encouragement and technical advice, and to C. S. Chou of Worcester Polytechnic Institute for his help in preparing the figures. M. W. R. is especially indebted to M. E. P. R. for countless enlightening late night sessions.

References

Austin, L. G., 1984, "Size Reduction of Solids: Crushing and Grinding Equipment," *Handbook of Powder Sci. and Tech.*, M. E. Fayed and L. Otten, eds., Van Nostrand Reinhold Co., New York, pp. 562–606.

Campbell, C. S., 1990, "Rapid Granular Flows," *Ann. Rev. Fluid Mech.*, Vol. 20, pp. 57–92.

Jenkins, J. T., 1987, "Balance Laws and Constitutive Relations for Rapid Flows of Granular Materials," *Constitutive Models of Deformation*, J. Chandra and R. P. Srivastav, eds., SIAM, pp. 109–119.

Jenkins, J. T., and Savage, S. B., 1983, "A Theory for the Rapid Flows of Identical, Smooth, Nearly Elastic, Spherical Particles," *J. Fluid Mech.*, Vol. 130, pp. 313–328.

Prasher, C. L., 1987, *Crushing and Grinding Handbook*, John Wiley and Sons, New York.

Richman, M. W., 1986, "Kinetic Theories for Rate-Dependent Granular Flows," *Proc. Tenth U.S. Nat'l. Cong. Appl. Mech.*, J. P. Lamb, ed., Austin, Tex., pp. 339–346.

Richman, M. W., and Chou, C. S., 1989, "A Theory for Grain-Size Reduction in Granular Flows of Spheres," *J. Appl. Math. Phys.* (*ZAMP*), Vol. 40, pp. 883–898.

Savage, S. B., and Sayed, M., 1984, "Stresses Developed by Dry Cohesionless Granular Materials Sheared in an Annular Shear Cell," *J. Fluid Mech.*, Vol. 142, pp. 391–430.

Van Dyke, M., 1975, *Perturbation Methods in Fluid Mechanics*, Parabolic Press, Stanford, Calif.

Downloaded 03 May 2010 to 171.66.16.247. Redistribution subject to ASME license or copyright; see http://www.asme.org/terms/Terms_Use.cfm

Elementary Solutions and Process Sensitivities for Plane-Strain Sheet-Metal Forming

M. L. Wenner
Mathematics Department,
General Motors Research Laboratories,
Warren, MI 48090-9055
Mem. ASME

Solutions to simple, plane-strain sheet-metal forming problems are developed using an exact solution to the membrane equilibrium equations and a pre-integrated version of the plasticity equations. This approach allows the numerical errors to be driven to very low levels in an economical manner. Both stretch and draw conditions are considered, and solutions are presented for several problems which have been proposed as benchmarks for sheet-metal forming computer programs. The simplicity of this approach allows us to calculate formulas for the sensitivity of the solutions to process parameters. It is demonstrated that draw problems can exhibit very strong dependencies on parameters, especially drawbead restraint force.

1 Introduction

There has recently been a substantial increase in interest in computational analysis of sheet-metal forming problems. At one recent conference (Thompson et al., 1989), an informal session was devoted to a comparison of the solutions to several simple plane-strain and axisymmetric sheet-forming benchmark problems (proposed by Wagoner et al., 1988) by over 20 participants, most of whom used finite element codes. Although for each of the problems several of the codes gave results which seemed to be consistent with each other and with physical intuition, there was in general an unacceptably large variation in predicted strain distributions. One of the purposes of this paper is to provide simple solutions to the plane-strain benchmark problems, by applying an elementary method which uses exact geometry and which allows us economically to drive the spatial and time discretization errors to very low levels. Although this approach is not easily generalizable beyond the plane-strain membrane theory used here, or to more complex geometries, it does yield an easily generated solution, formulas for process sensitivities, and an intuitive understanding of the problem.

Consider the symmetric forming operation shown in Fig. 1. The sheet, originally flat, is forced into the die cavity by a smooth, convex punch. We assume here that a gap exists between the punch and die so that the sheet material never becomes vertical. In the binder area, beads control the boundary conditions. They can be lockbeads, which prevent any motion of the sheet at that point (a stretch problem) or drawbeads, which allow the sheet to flow into the die cavity under a constant force restraint (a draw problem). These boundary conditions are applied at location R_0 in Fig. 1. The binder is flat and horizontal, and the die shoulder is cylindrical with radius R_d.

The sheet is assumed to be a membrane deforming under plane-strain conditions. Interaction between the tools and sheet is described by Coulomb friction. These assumptions allow us to apply a simple foil-friction formula whenever the sheet is sliding on the tools. If the material is assumed to be rate insensitive, then as long as no unloading takes place, the force per unit length in the sheet can be assumed to be a (nonunique) function of strain. This allows reduction of the problem to a numerical integration and solution of a single nonlinear equation.

Use of the friction formula to develop results in sheet forming problems is not new. See, e.g., Swift (1948), Duncan and Bird (1978) or Wenner (1983). In this paper, however, it is

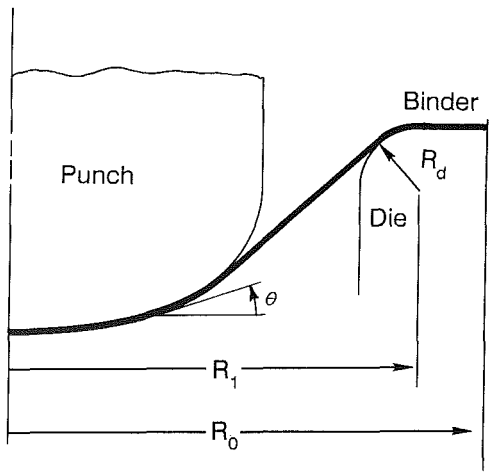


Fig. 1 Sketch of the symmetric plane-strain problem

Contributed by the Applied Mechanics Division of THE AMERICAN SOCIETY OF MECHANICAL ENGINEERS for presentation at the 1992 ASME Summer Mechanics and Materials Meeting, Tempe, AZ, Apr. 28–May 1, 1992.

Discussion on this paper should be addressed to the Technical Editor, Prof. Leon M. Keer, The Technological Institute, Northwestern University, Evanston, IL 60208, and will be accepted until four months after final publication of the paper itself in the JOURNAL OF APPLIED MECHANICS. Manuscript received by the ASME Applied Mechanics Division, July 3, 1990; final revision, Sept. 25, 1991.
Paper No. 92-APM-15.

Copyright © 1992 by ASME
Downloaded 03 May 2010 to 171.66.16.247. Redistribution subject to ASME license or copyright; see http://www.asme.org/terms/Terms_Use.cfm

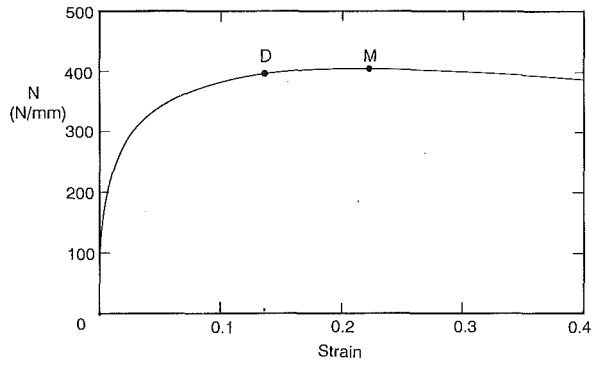


Fig. 2 Results of integrating the constitutive equations: force per unit length as a function of logarithmic strain

used to generate full solutions and to evaluate sensitivities of solutions. The methodology is outlined in the next section. Section 3 contains the main results, while some surprising conclusions on the sensitivity of solutions are given in Section 4. The last section contains a discussion of the results and some speculation on the effects of relaxing some of the assumptions used here.

2 Problem Formulation and Solution

2.1 Constitutive Equations. Let τ_α be the principal Kirchhoff stresses and ϵ_α the corresponding natural strains, where α takes values 1 and 2. We use a standard approach in which the total strain rate is assumed to be the sum of the elastic and plastic strain rates and the yield function $\tau(\tau_\alpha)$ is the flow potential. Plane stress is assumed. Then by defining

$$L=\frac{E}{1-\nu^2}\begin{bmatrix}1 & \nu\\ \nu & 1\end{bmatrix},$$

$$P_\alpha=\partial\tau/\partial\tau_\alpha,$$

$$Q_\alpha=L_{\alpha\beta}P_\beta, \tag{1}$$

the flow equations can be derived in the conventional manner:

$$\dot{\tau}_\alpha=\left[L_{\alpha\beta}-\frac{Q_\alpha Q_\beta}{\psi}\right]\dot{\epsilon}_\beta, \tag{2}$$

where a dot is the material time derivative and

$$\psi=P_\gamma Q_\gamma+\frac{EE_t}{E-E_t}. \tag{3}$$

E is Young's modulus, ν is Poisson's ratio, and E_t is the tangent modulus. Repeated indices are summed, but these equations hold only in the principal coordinate system (assumed fixed in the material).

Let subscript 2 denote the direction normal to the paper in Fig. 1, while 1 denotes the direction tangent to the sheet. Then, under the plane-strain conditions $\epsilon_2=0$, the ordinary differential Eq. (2) can be numerically integrated to give τ_α as functions of ϵ_1 (for continued plastic loading). The tangential force per unit length is given by $N=h\,\tau_1$, where h is the current metal thickness, calculated from plastic incompressibility. For this integration, we use Hill's yield criterion,

$$\tau=\left[\tau_1^2+\tau_2^2-\frac{2R}{1+R}\,\tau_1\tau_2\right]^{1/2}, \tag{4}$$

where R is the coefficient of anisotropy. The uniaxial hardening law is

$$\tau=K\,(\epsilon_0+\epsilon^p)^n, \tag{5}$$

where K, ϵ_0, and n are material parameters and ϵ^p is the plastic strain. A Runge-Kutta method was used for the integration, and the results stored as about 500 pairs of N and strain. For a given N, the corresponding strain is evaluated by linear interpolation on the appropriate side of the load maximum. Figure 2 shows a typical result of this exercise.

An explicit approximation of the N versus ϵ_1 curve is easily derived by using rigid plasticity. As shown in Wenner (1983), this result is

$$N=Kh_0\exp(-\epsilon_1)(\epsilon_1+d\epsilon_0)^n/d^{1+n}, \tag{6}$$

where

$$d=(1+2R)^{1/2}/(1+R), \tag{7}$$

and h_0 is the initial metal thickness. This formula will be useful later for a sensitivity analysis. Equation (6) shows that the maximum load occurs at a strain of approximately n (if ϵ_0 is assumed small). This is the point M on Fig. 2.

2.2 Basic Solution. We let s be the arc length along the deforming sheet, r the radius of curvature, and q and p the tangential and normal applied loads per unit area, respectively. The membrane equations of equilibrium are

$$dN/ds=q, \tag{8}$$

$$N/r=p. \tag{9}$$

In the unsupported region (called the wall), both p and q vanish, so that (8) and (9) imply that N is constant and the sheet is straight. In regions of sliding contact, we use Coulomb's friction law[1]

$$q=-\text{sign}(v)\mu|p|, \tag{10}$$

where μ is the coefficient of friction and v is the velocity of the sheet relative to the tool. Using Eqs. (9) and (10), with $ds=rd\theta$, where θ is the angle of inclination of the sheet (see Fig. 1), Eq. (8) is

$$\frac{dN}{d\theta}=\pm\mu N, \tag{11}$$

which has the solution

$$N=k\exp(\pm\mu\theta), \tag{12}$$

where k is a constant of integration, and the sign is chosen according to the direction of motion. Equation (12) is often referred to as the foil friction formula.

Referring to Fig. 1, assume that the sheet is moving to the left with respect to the die and to the right with respect to the punch. Then the formula

$$N(\theta)=N_B\exp(\mu\theta), \tag{13}$$

where N_B is the force per unit length in the binder and at the centerline, is valid from the centerline to the right-hand end point. N_B is unknown and generally varies with the punch depth. Equation (13) holds only for sliding conditions, and any solution generated by it must be checked to insure that the assumptions are correct. Anticipating some later results, it is found that (13) holds at the beginning of forming, but that sticking of the sheet to the tools occurs somewhat before the instability load of the material is reached, at least for the types of material properties, friction and geometry studied here.

The solution is completed by determining N_B from the boundary conditions. To this end, assume that ϵ_1 is uniquely related to N, i.e., that the maximum load of the material has not been reached anywhere in the sheet and no unloading has occurred. Natural strain is defined by

$$\epsilon_1=\ln(ds/dS), \tag{14}$$

where S is the arc length in the original configuration. Both S and s are measured from the centerline. By symmetry, this

[1]We assume the static and dynamic coefficients of friction are identical.

Downloaded 03 May 2010 to 171.66.16.247. Redistribution subject to ASME license or copyright; see http://www.asme.org/terms/Terms_Use.cfm

material point does not move horizontally. Consider first a stretch problem. For a given punch depth the sheet geometry is known, so θ can be calculated at any point. Thus, for an estimated value of N_B, Eq. (13) yields N, from which we can get ϵ_1. Then the calculated original length of the sheet, $L(N_B)$ is

$$L(N_B) = \int \exp(-\epsilon_1) ds. \tag{15}$$

The integration is carried out numerically over the deformed sheet; N_B is iterated until $L(N_B) = R_0$, the arc length in the original configuration.

For draw problems, displacement at the bead is zero until the force per unit length in the sheet in the binder area reaches some specified level, N_{DB} (called the drawbead restraint force); subsequently, the force remains at the level N_{DB} and motion through the bead is allowed. Initially, the draw problem is identical to the stretch case, and the above analysis holds. When the sheet force at the bead reaches N_{DB}, Eq. (13) applies with N_B replaced by the (constant) N_{DB}. (We iterate on the punch depth to insure that N in the binder area just reaches N_{DB}.) It thus yields a full solution for N and therefore for strain as long as flow through the bead and sliding over the die radius continue. Equation (15), when integrated to the bead location, yields the original length of the sheet currently inside the bead. Subtracting R_0 from it gives the amount of material drawn in.

2.3 Sticking Conditions. The above holds only while the sheet slides over the tools, but for nonzero friction, sticking may occur at some point in the forming process. Consider a stretching problem and assume for now that the load maximum has not been reached anywhere in the part. As long as solutions are obtained using (13) and N_B is increasing with punch depth, it is straightforward to prove that material points are moving toward the unsupported area and experience increasing strains. Hence, the assumptions are satisfied and the solutions are correct. If a solution is obtained with a decreased value of N_B, it is clearly invalid, because it would imply decreasing strains and metal motion in the wrong direction near $\theta = 0$. The solution is rejected, locking is assumed over the entire contact region, and all material which subsequently contacts a tool is assumed to stick. Hence, all further deformation occurs in the unsupported region. When the load in the unsupported area exceeds the maximum of the load-strain curve, solutions are obtained using the right-hand side of that curve. We ignore for now the fact that the load maximum generally represents an instability point of a rate-insensitive material.

To justify the above approach, assume that metal sticks to the punch (for example) as soon as it contacts it, and consider two configurations, one with a wall angle ϕ, one with wall angle $\phi + \Delta\phi$. Let the values of N in the walls be N_{WP} and N_W, respectively. Since sticking is assumed, $q < \mu p$ in the material adjacent to the wall. But Eqs. (8) and (9) give, approximately,

$$q = dN/ds = (N_W - N_{WP})/(r\Delta\phi),$$

$$p = N/r = (N_W + N_{WP})/(2r). \tag{16}$$

Taking the limit as $\Delta\phi$ goes to zero and using the inequality, we find that

$$dN_W/d\phi < \mu N_W, \tag{17}$$

is a necessary condition for sticking at the wall. Since the point on the axis of symmetry is also fixed, it is reasonable to assume (at least for rate insensitive material) that all the material in punch contact sticks. Equation (17) is also sufficient for sticking. Assume that it holds and that material slides where $\theta > \theta_1$. Then in the region $\theta > \theta_1$,

$$N(\theta,\phi) = N_W(\phi)\exp[-\mu(\phi - \theta)], \tag{18}$$

which implies that

$$\partial N/\partial\phi = (dN_W/d\phi - \mu N_W)\exp[-\mu(\phi - \theta)]. \tag{19}$$

If (17) holds, then (19) shows that the load is falling everywhere, in particular, at the locked point $\theta = \theta_1$. But at this point, the strain and therefore the load must be constant, so sliding cannot occur anywhere. Evaluated at $\theta = 0$ when $\theta_1 = 0$, (19) also justifies the sticking criterion of a falling N_B used above. By use of the chain rule, (17) becomes

$$dN_W/d\epsilon_W < \mu N_W/(d\epsilon_W/d\phi), \tag{20}$$

where ϵ_W is the strain in the wall. Since the right-hand side is positive, this shows that sticking occurs before the maximum load in the metal is reached.

Sticking conditions on the die shoulder radius are treated similarly. In the present problem, sticking occurs simultaneously on punch and die. The possibility that material slides in the direction away from the wall has been ignored. This might occur when the wall material has been deformed well past maximum load and the wall load is falling. But these would be elastic strains, and would scarcely change the results given here.

Draw problems can be similarly analyzed, but only the main results are described. Initially, the drawbead prevents displacement, and sticking can be detected as above. If sticking occurs, then the bead does not release, and the problem is exactly like the stretching case. If the bead releases before sticking occurs, then the solution is obtained as described in Section 2.2. If the load maximum is approached, the metal may cease to flow through the bead. This is detected computationally by a decrease in the amount of draw. The boundary condition is changed to zero displacement and calculations continue as for the stretching case, but with $L(N_B)$ in Eq. (15) required to be equal to the total amount of original material which has passed through the bead.

3 Results

The foregoing analysis was applied to the case in which the punch was a circular cylinder of radius 50.8 mm, the die radius was 6.35 mm, and R_1 was 59.18 mm. Stretch boundary conditions were enforced at $R_0 = R_1$. Draw conditions were applied at $R_0 = 66$ mm, with a restraint force of 300 N/mm. The material parameters were $K = 589$ MPa, $n = 0.216$, $\epsilon_0 = 0.0001$, $E = 69004$ MPa, $\nu = 0.3$, $R = 1.0$, and $h_0 = 1$ mm. Figure 2 is plotted for this material. Values of 0, 0.15, and 0.30 were used for the coefficients of friction. These are the problems previously proposed by Wagoner et al. (1988) as benchmarks for plane-strain sheet-metal forming.

Figures 3 and 4 show strain distributions at several punch depths for $\mu = 0.15$ and 0.30, respectively. Strains are plotted as functions of current distance from the axis of symmetry. Dashed lines are used to indicate that sticking has occurred, and the intermediate plots are at depths just before sticking

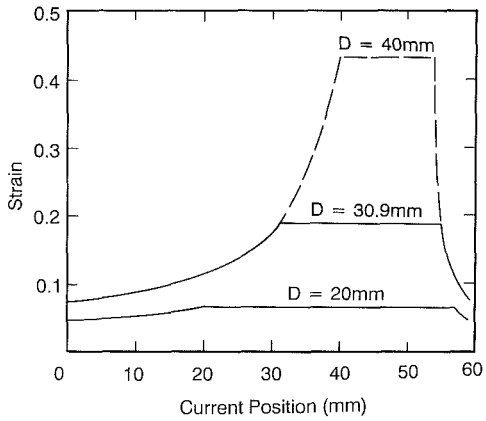


Fig. 3 Strain distribution for $\mu = 0.15$ for stretching problem

Downloaded 03 May 2010 to 171.66.16.247. Redistribution subject to ASME license or copyright; see http://www.asme.org/terms/Terms_Use.cfm

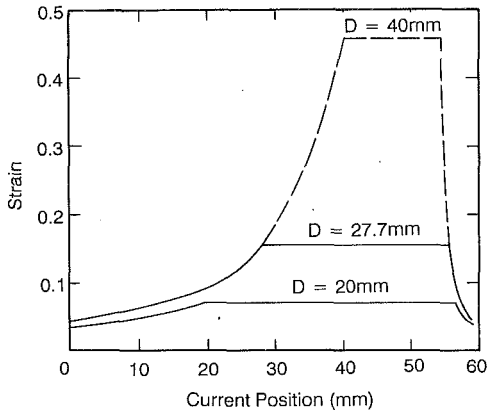


Fig. 4 Strain distribution for $\mu = 0.30$ for stretching problem

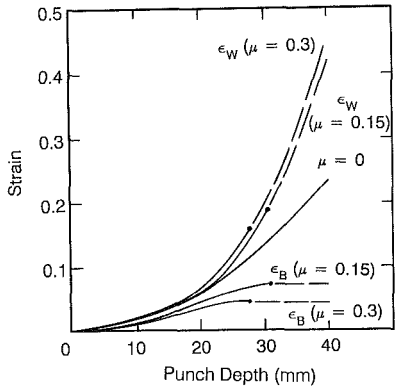


Fig. 5 Wall strains and binder strains as functions of punch depth for the stretching problem

takes place. As expected, strains are largest in the wall regions, taper off rapidly over the die radius and less rapidly over the punch. The strains for these two values of friction show little difference, as can be seen from Fig. 5, which shows wall and boundary strains as functions of punch depth. Also indicated are the strains for no friction. In this latter case, the strains are uniform at any depth.

Solutions for the draw problem are given in Figs. 6 and 7. The shapes of the strain distributions are similar to the stretch cases, but the levels are much lower because of the additional metal flow into the die cavity. Note that the strains in the contact areas do not change for the depths plotted, because the drawbead has already released. Wall strains are plotted as functions of punch depth in Fig. 8. The sudden change in slope in each of these curves indicates bead release. In contrast to the stretch case, a high sensitivity to friction is shown. Numerical calculations indicate that the ratio of the increase in strain to that of the coefficient of friction at a punch depth of 40 mm for $\mu = 0.3$ is about 0.1 for stretch and 1.4 for draw, even though the strain levels for stretch are much higher. The sensitivity of the draw problem to variations in parameters is discussed in the next section.

4 Sensitivity to Parameters

This section contains formulas for sensitivity of the wall strain to the process parameters μ, ϕ, and N_{DB}. Sensitivity is defined here by

$$S(z) = \frac{z}{\epsilon_W} \frac{\partial \epsilon_W}{\partial z}, \tag{21}$$

where z stands for any of the above parameters. Consider first

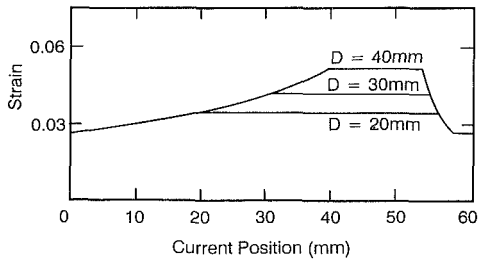


Fig. 6 Strain distribution for $\mu = 0.15$ for the draw problem

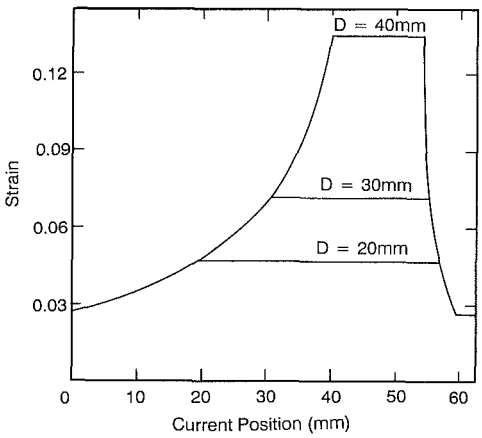


Fig. 7 Strain distribution for $\mu = 0.30$ for the draw problem

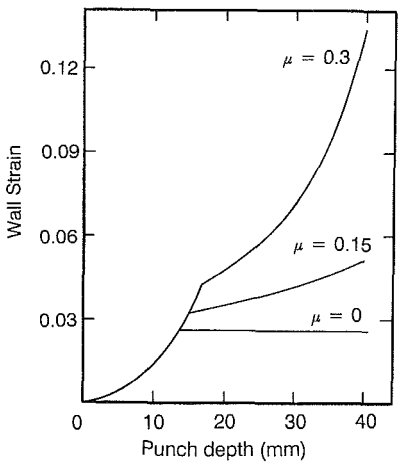


Fig. 8 Wall strain as a function of punch depth for the draw problem

the stretching problem. Equation (13) evaluated for the wall load gives

$$N_W = N_B \exp(\mu\phi). \tag{22}$$

Differentiating this with respect to μ and ϕ and using the chain rule yields

$$S(\mu) = \frac{1}{G}\left(\mu\phi + \frac{\mu}{N_B}\frac{\partial N_B}{\partial \mu}\right),$$

$$S(\phi) = \frac{1}{G}\left(\mu\phi + \frac{\phi}{N_B}\frac{\partial N_B}{\partial \phi}\right), \tag{23}$$

where

$$G = \left(\frac{\epsilon}{N}\frac{dN}{d\epsilon}\right)_{\epsilon=\epsilon_W}. \tag{24}$$

Downloaded 03 May 2010 to 171.66.16.247. Redistribution subject to ASME license or copyright; see http://www.asme.org/terms/Terms_Use.cfm

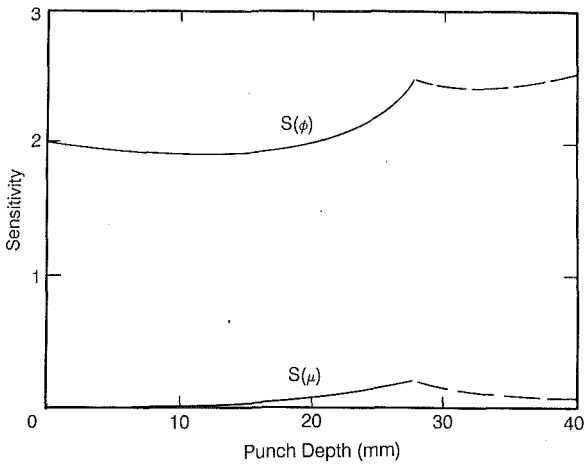


Fig. 9 Sensitivity of wall strain to coefficient of friction and wall angle for the stretching problem

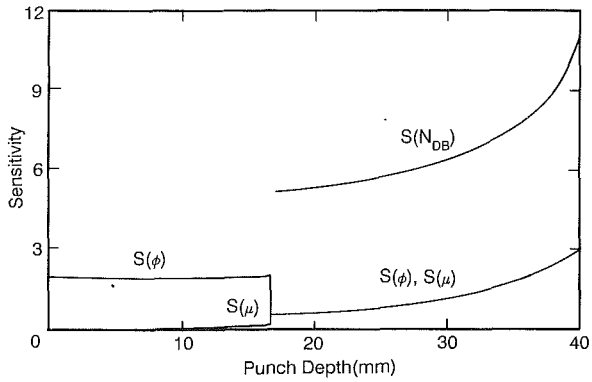


Fig. 10 Sensitivity of wall strain to coefficient of friction, wall angle, and drawbead restraint force for the drawing problem

Recall that the strain distribution satisfies

$$R_0 = \int \exp(-\epsilon_1) ds,$$

where R_0 is a constant. By breaking the integral into four regions of punch contact, unsupported region, die shoulder contact and binder region, and differentiating using Leibniz's formula, the following are found:

$$\frac{\mu}{N_B}\frac{\partial N_B}{\partial \mu} = \frac{-\mu v}{u},$$

$$\frac{\phi}{N_B}\frac{\partial N_B}{\partial \phi} = \frac{\phi \dfrac{ds_t}{d\phi} e^{-\epsilon_W} - \mu \phi s_u e^{-\epsilon_W} \dfrac{d\epsilon_W}{dN} N_W}{u}, \qquad (25)$$

where s_t is the total arc length of the part, s_u is the unsupported length, and u and v are integrals over the entire deformed sheet:

$$u = \int N \exp(-\epsilon_1)(d\epsilon_1/dN) ds,$$

$$v = \int N \exp(-\epsilon_1)(d\epsilon_1/dN)\theta ds. \qquad (26)$$

Using (25) and (26) in (23) gives the sensitivities. In addition to the basic solution, they require evaluation of the integrals in (26) and the function G, which depends only upon the plasticity law.

As noted previously, drawing problems are the same as stretching until the beads release, at which point N_B in Eq. (22) is replaced by N_{DB}:

$$N_W = N_{DB} \exp(\mu\phi), \qquad (27)$$

where N_{DB} is the bead restraint force. Differentiating as before, we find simply

$$S(\mu) = S(\phi) = \mu\phi/G,\ S(N_{DB}) = 1/G. \qquad (28)$$

Using the rigid-plastic relations (6) and assuming ϵ_0 is negligible, these can be approximated as

$$S(\mu) = S(\phi) = \mu\phi/(n - \epsilon_W),\ S(N_{DB}) = 1/(n - \epsilon_W), \qquad (29)$$

which clearly show that sensitivities become large as the wall strain approaches n. (Since these results do not hold for locked conditions, and since locking occurs before the strain reaches n, the sensitivities do not become unbounded.)

Results of these calculations are shown in Fig. 9 for the stretching case with $\mu = 0.3$. The solid lines represent Eqs. (23), which hold until locking. After this point, finite differencing was used to generate the data (the dashed lines). The two methods gave virtually identical results from initial contact until locking. Clearly, the wall strain is far more sensitive to the wall angle, which is really a surrogate for punch depth, than to the coefficient of friction. This is not unexpected, since the stretching problem is displacement controlled. Increasing the punch depth increases the average strain. Increasing the friction does not change the average strain, it redistributes it. This is not to say that incorporating friction is unimportant in these problems (it is crucial). But for the parameters used here, strain is more sensitive to changes in wall angle than to coefficient of friction.

Figure 10 contains the drawing results for $\mu = 0.3$. Until the bead releases at a punch depth of 16.7 mm, the solution is much like the stretching problem. After bead release, sensitivity to friction becomes much larger while wall angle sensitivity declines, then increases. By far the largest sensitivity, however, is to the drawbead restraint force, reflecting the fact that drawing is a force-dominated problem. The large sensitivity to bead force can be easily understood physically. The wall load at a punch depth of 40 mm and $\mu = 0.3$ is 394 N/mm, which has been plotted as point D on the force-strain curve of Fig. 2. Clearly, a very small addition to the wall load will produce large strain increases because of the flatness of the curve, and (27) shows that bead restraint force appears directly in the wall load, amplified by the factor $\exp(\mu\phi)$. Real rate-insensitive metals will experience localized deformation and failure at a strain corresponding to the load maximum (point M on Fig. 2). An important conclusion here is that the peak strain can be relatively far from the failure strain, but the workpiece is nevertheless in danger of fracture.

5 Discussion

The sensitivity of the draw solution in a plane-strain regime which is apparently not close to failure implies that control of process parameters on the shop floor and control of numerical errors in computation are crucially important for reliable results. Computational errors can accrue from approximations in geometrical descriptions, spatial discretizations in the equilibrium conditions, and time integration of the plasticity equations. Two finite element approximations of such a problem could give widely divergent strain predictions, even if they both were accurate to within two percent, say, in stresses. Even so, the calculations might be useful, but only if the analyst recognized the sensitivities of these solutions to process parameters. Automatic error analysis (Zienkiewicz and Huang, 1989) and calculation of design sensitivities (Mukherjee and Chandra, 1989) for plasticity problems are active areas of research, and it is hoped that the results given here will be useful as benchmarks for such studies.

Downloaded 03 May 2010 to 171.66.16.247. Redistribution subject to ASME license or copyright; see http://www.asme.org/terms/Terms_Use.cfm

In order to derive results as simply and explicitly as possible, the problems treated here have been stripped of all but the most relevant detail. This is reasonable for our main purpose of providing benchmark solutions and developing intuition, but two physical phenomena which can be important in sheet-metal forming have been neglected: strain-rate sensitivity and bending/unbending effects. Strain-rate sensitivity is known to have some effect on strain distributions (Wang and Wenner, 1978). It helps to distribute strain more uniformly and it greatly increases the failure strain (Ghosh, 1977), so that strains well in excess of n are available. These will ameliorate somewhat the sensitivities calculated here for rate-independent materials, but one would still expect rather strong dependencies on process parameters under some conditions.

Bending effects can also have an effect on in-plane strains. See, e.g., Stoughton (1985), Ni (1988), or Wang and Tang (1988). Consider again the drawing problem. The work done to bend and straighten the metal which passes over the die radius must manifest itself as a higher wall load. The paper by Swift (1948) is devoted to this effect, and using either this paper or the drawbead formula of Stoughton (1988), this additional force is estimated to be about 12 to 20 N/mm, enough to cause the wall load to exceed the maximum for $\mu = 0.3$. Hence, one expects that a three-dimensional or shell formulation would give much larger wall strains for this problem.

There are many forming parameters whose sensitivities have not been addressed here, e.g., material properties and geometrical shape. Sa (1989) has used multiple runs of a finite element program to study some of these additional parameters. Analyses similar to that given here could also be constructed for these terms.

References

Duncan, J. L., and Bird, J. E., 1978, "Die Forming Approximations for Aluminum Sheet," *Sheet Metal Industries*, Vol. 55, pp. 1015–1025.

Ghosh, A. K., 1977, "The Influence of Strain Hardening and Strain-Rate Sensitivity on Sheet Metal Forming," ASME *Journal of Engineering Materials and Technology*, Vol. 99, pp. 264–274.

Mukherjee, S., and Chandra, A., 1989, "A Boundary Element Formulation for Design Sensitivities in Materially Nonlinear Problems," *Acta Mech.*, in press.

Ni, C. M., 1988, "Bending and Draw-in Effects on Sheet Metal Formability in Plane Strain and Axisymmetric Metal Forming," *Materials in Manufacturing Processes*, B. V. Kiefer, J. J. Gavigan, and C. M. Ni, eds., ASME MD-Vol. 8.

Sa, C. Y., 1989, "Sensitivity of Sheet Metal Forming Parameters," SAE Paper 890346, *Steel Stamping Technology*, SP-779, SAE, Warrendale, Penn., pp. 37–45.

Stoughton, T. B., 1985, "Finite Element Modeling of 1008 AK Sheet Steel Stretched over a Rectangular Punch with Bending Effects," Computer Modeling of Sheet Metal Forming Processes, N. M. Wang and S. C. Tang, eds., The Metallurgical Society, Warrendale, Penn., pp. 143–159.

Stoughton, T. B., 1988, "Model of Drawbead Forces in Sheet Metal Forming," *Proc. 15th Biennial Congress*, International Deep Drawing Research Group ASM International, pp. 205–215.

Swift, H. W., 1948, "Plastic Bending under Tension," *Engineering*, Vol. 166, pp. 333–335; 357–359.

Thompson, E. G., et al. eds., 1989, *NUMIFORM 89, Numerical Methods in Industrial Forming Processes*, A. A. Balkema, Rotterdam.

Wagoner, R. H., Nakamachi, E., and Lee, J. K., 1988, private communication.

Wang, N. M., and Tang, S. C., 1988, "Analysis of Bending Effects in Sheet Forming Operations," *Int. J. Numer. Methods Eng.*, Vol. 25, pp. 253–267.

Wang, N. M., and Wenner, M. L., 1978, "Elastic-Viscoplastic Analyses of Simple Stretch Forming Problems," *Mechanics of Sheet Metal Forming*, D. P. Koistinen and N. M. Wang, eds., Plenum, New York, pp. 367–398.

Wenner, M. L., 1983, "On Work Hardening and Springback in Plane Strain Metal Forming," *J. Applied Metalworking*, Vol. 2, pp. 277–287.

Zienkiewicz, O. C., and Huang, G. C., 1989, "Adaptive Modelling of Transient Coupled Metal Forming Processes," *NUMIFORM 89, Numerical Methods in Industrial Forming Processes*, E. G. Thompson et al., eds., Balkema, Rotterdam, pp. 3–10.

Downloaded 03 May 2010 to 171.66.16.247. Redistribution subject to ASME license or copyright; see http://www.asme.org/terms/Terms_Use.cfm

Viscoelastic Behavior of Elastomeric Membranes

William W. Feng
Lawrence Livermore National Laboratory,
University of California,
Livermore, CA 94550
Mem. ASME

The formulation for large deformations of an axisymmetric nonlinear plane viscoelastic membrane is developed. The solutions from the formulation for both creep and relaxation of a circular membrane are presented. An experiment that demonstrates the relaxation phenomenon was performed, and the experimental data are used to determine the constitutive equation of an elastomer.

Introduction

The inflation of a plane circular membrane was first studied experimentally by Treloar (1944) and analytically by Adkins and Rivlin (1952), who employed the Taylor's series approach to calculate the deformation of a neo-Hookean membrane. The same problem with different constitutive equations was solved by Klingbeil and Shield (1964). Later, Yang and Feng (1970) further extended the formulation to a class of axisymmetric membranes of Mooney material under large deformations. A very efficient formulation for the numerical integration, by which all axisymmetric nonlinear elastic membranes problems can be solved numerically, was developed.

The membranes studied usually have been elastomeric materials, which often exhibit viscoelastic behavior. To date, very few problems pertaining to nonlinear viscoelastic membranes have been investigated because of the inherent complexities associated with nonlinearity, both in geometry and in material.

In this paper, we demonstrate that viscoelastic solutions can be obtained. The nonlinear viscoelastic constitutive equation used here was developed by Christensen (1980). For sufficiently slow processes, the integral terms in the constitutive equation become negligibly small, and the remaining terms constitute the theory of rubber elasticity. Therefore, the constitutive equation can be used for studying both elastic and viscoelastic effects.

The formulation centers on determining the deformed configuration of a plane circular membrane under an inflating pressure. Two sets of polar cylindrical coordinates are used, one to describe the undeformed configuration and one to describe the deformed configuration. Although the coordinate values that describe the deformed configuration are unknown functions both of the undeformed coordinates and of the inflating pressure, they can be determined from the force-equilibrium equations in the tangential and normal directions. The equilibrium equations are reduced to a set of nonlinear differential-integral equations.

In order to simplify the numerical procedures for solving these equations, two steps are taken. First, we introduce three new variables: the stretch ratios in both meridional and circumferential directions, and the angle between the axis of symmetry and the vector normal to the midsurface of a deformed membrane. The governing equations are written in terms of these variables. Second, a recurrence formula developed recently (Feng, 1991) is used. With the recurrence formula, it is not necessary to recalculate the hereditary integrals in the convolution operation at each new value of time. As a result, the governing equations are reduced to three first-order differential equations for each time step.

Geometric Formulation

The coordinate systems for describing an axisymmetric membrane clamped at the edge, in both its undeformed and deformed state, are shown in Fig. 1. Two sets of polar cylindrical coordinates are used in the analysis. The coordinates $(R,\phi,0)$ are used to describe the undeformed midsurface of the membrane. The coordinates $[r(R),\phi,z(R)]$ are used to describe the deformed midsurface. The thickness of the undeformed plane circular membrane is H and the radius is R_0. Since the membrane is assumed to be relatively thin compared with other dimensions ($H \ll R_0$), all variations of physical quantities across the thickness can be neglected. Furthermore, the deformation is axisymmetric, and a point $A(R,\phi,0)$ on the

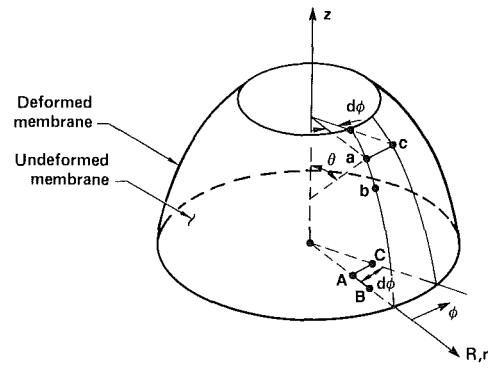


Fig. 1 Coordinate systems for describing undeformed and deformed axisymmetric membranes

Contributed by the Applied Mechanics Division of THE AMERICAN SOCIETY OF MECHANICAL ENGINEERS for presentation at the 1992 ASME Summer Mechanics and Materials Meeting, Tempe, AZ, Apr. 28–May 1, 1992.

Discussion on this paper should be addressed to the Technical Editor, Prof. Leon M. Keer, The Technological Institute, Northwestern University, Evanston, IL 60208, and will be accepted until two months after final publication of the paper itself in the JOURNAL OF APPLIED MECHANICS. Manuscript received by the ASME Applied Mechanics Division, June 20, 1990; final revision, Mar. 19, 1991.

Paper No. 92-APM-1.

Copyright © 1992 by ASME
Downloaded 03 May 2010 to 171.66.16.247. Redistribution subject to ASME license or copyright; see http://www.asme.org/terms/Terms_Use.cfm

undeformed midsurface is deformed to $a(r,\phi,z)$. A neighboring point in the meridional direction $B(R+dR,\phi,0)$ is deformed to $b(r+dr,\phi,z+dz)$, and another neighboring point in the circumferential direction $C(R,\phi+d\phi,0)$ is deformed to $c(r,\phi+d\phi,z)$. Hence, the arc length between A and B in the undeformed meridional direction is dR, and the arc length between a and b in the deformed meridional direction is $[(dr)^2+(dz)^2]^{1/2}$. The arc length between A and C in the undeformed circumferential direction is $Rd\phi$, and the arc length between a and c in the deformed circumferential direction is $rd\phi$.

The stretch ratios λ_1 and λ_2 in the meridional and circumferential directions, respectively, are

$$\lambda_1=\frac{[(dr)^2+(dz)^2]^{1/2}}{dR}, \tag{1a}$$

$$\lambda_2=\frac{r}{R}. \tag{1b}$$

The principal curvatures κ_1 and κ_2 of the deformed membrane in the normal and circumferential directions, respectively, are

$$\kappa_1=\frac{d\theta}{[(dr)^2+(dz)^2]^{1/2}}, \tag{2a}$$

$$\kappa_2=\frac{\sin\theta}{r}, \tag{2b}$$

where θ is the angle between a vector normal to the midsurface at point a and the axis of symmetry. In terms of the stretch ratios defined in Eqs. (1), Eqs. (2) can be written as

$$\kappa_1=\frac{\theta'}{\lambda_1}, \tag{3a}$$

$$\kappa_2=\frac{\sin\theta}{R\lambda_2}, \tag{3b}$$

where the prime denotes differentiation with respect to R.

Another geometric relation can also be obtained from Fig. 1:

$$\cos\theta=\frac{dr}{[(dr)^2+(dz)^2]^{1/2}}, \tag{4}$$

or

$$\cos\theta=\frac{(R\lambda_2'+\lambda_2)}{\lambda_1}. \tag{5}$$

Equations (1) through (5) complete the geometric formulations of the deformation of a circular membrane under axisymmetric deformations.

Constitutive Equation

Before we proceed with the governing equations that determine the unknown functions r and z, we need to define a constitutive equation for the material. The constitutive equation, obtained by Christensen (1980) and based on the viscoelastic generalization of the kinetic theory of rubber elasticity, is used in this paper to model the time-dependent viscoelastic effects. The constitutive equation is rewritten here:

$$\sigma_{ij}(t)=-p\delta_{ij}+x_{i,K}(t)x_{j,L}(t)\left[g_0\delta_{KL}+\int_0^t g_1(t-T)\frac{\partial E_{KL}(T)}{\partial T}\,dT\right], \tag{6}$$

where σ_{ij} is the Cauchy stress, p is the pressure, $x_{i,K}$ denotes the displacement gradient, δ_{KL} is the Kronecker delta, and E_{KL} are the components of the Green strain tensor. There are two material property functions, g_0 and g_1. The g_0 term is the long-term elastic material constant and is the contribution of the kinetic theory of rubber elasticity; it is closely related to the material constant used in neo-Hookean constitutive equations. The $g_1(t)$ is a viscoelastic relaxation function.

For the special case of a uniform orthogonal deformation field, the deformation tensor has only diagonal components $(\lambda_1,\lambda_2,\lambda_3)$, where λ_1 and λ_2 are defined in Eqs. (1) and λ_3 is the stretch ratio in the normal direction of the membrane; that is,

$$\lambda_3=\frac{h}{H}. \tag{7}$$

In Eq. (7), h is the thickness of the deformed membrane at point a. Hence, the general constitutive equation, Eq. (6), is reduced to

$$\sigma_i=-p+\lambda_i^2\left[g_0+\frac{1}{2}\int_0^t g_1(t-T)\frac{\partial\lambda_i^2(T)}{\partial T}\,dT\right],\quad i=1,2,3. \tag{8}$$

For incompressible materials and the assumption that for a thin membrane the stress in the normal direction is small, we obtain two more conditions:

$$\lambda_1\lambda_2\lambda_3=1, \tag{9}$$

and

$$\sigma_3=0. \tag{10}$$

These two conditions enable us to eliminate two unknown functions, p and λ_3. Equation (8) then becomes

$$\sigma_1=g_0\left(\lambda_1^2-\frac{1}{\lambda_1^2\lambda_2^2}\right)+\frac{\lambda_1^2}{2}\int_0^t g_1(t-T)\frac{\partial\lambda_1^2(T)}{\partial T}\,dT-\frac{1}{2\lambda_1^2\lambda_2^2}\int_0^t g_1(t-T)\frac{\partial}{\partial T}\left(\frac{1}{\lambda_1^2(T)\lambda_2^2(T)}\right)dT. \tag{11}$$

Equation (11) and a similar equation for σ_2 describe the constitutive relationships of a thin membrane under axisymmetric deformation; both involve three convolution integrals with kernels. Theoretically, these integrals can be solved easily; however, since the kernels are functions of time t, they must be evaluated from $t=0$ to $t=t$ (current time) for each increment of time, Δt. In general, the solution becomes slower and slower to obtain as the creep or relaxation proceeds. The recurrence formula obtained by Feng (1991) is used in this paper for a special case when the relaxation function g_1 is written in terms of the exponential law,

$$g_1(t)=C\exp(-t/\tau), \tag{12}$$

where C is a material constant and τ is a relaxation time constant. With this relaxation function and the mean-value theorem, the convolution integral,

$$A_{KL}(t_{n+1})=C\int_0^{t_{n+1}}\exp\left(\frac{t_{n+1}-T}{\tau}\right)\frac{\partial E_{KL}(T)}{\partial T}\,dT, \tag{13}$$

can be written in recurrence form

$$A_{KL}(t_{n+1})=\exp(-\Delta t/\tau)A_{KL}(t_n)+C\exp(-\Delta t/2\tau)[E_{KL}(t_{n+1})-E_{KL}(t_n)], \tag{14}$$

and $\Delta t=t_i-t_{i-1}$.

Now, with the geometric formulation and the constitutive equation obtained, the governing equations can be considered, and the unknown function, $r(R)$ and $z(R)$, can be determined.

Governing Equations

The force-equilibrium equation must be satisfied in both the tangential and normal directions; respectively,

$$\frac{dT_1}{dr}+\frac{1}{r}(T_1-T_2)=0, \tag{15a}$$

and

$$\kappa_1T_1+\kappa_2T_2=P, \tag{15b}$$

Downloaded 03 May 2010 to 171.66.16.247. Redistribution subject to ASME license or copyright; see http://www.asme.org/terms/Terms_Use.cfm

where T_1 and T_2 are the tangential stress resultants in the meridional and circumferential directions, respectively, and P is the inflating pressure. The stress resultants are related to the stresses σ_1 and σ_2 by

$$T_1 = \frac{H\sigma_1}{\lambda_1\lambda_2}, \tag{16a}$$

and

$$T_2 = \frac{H\sigma_2}{\lambda_1\lambda_2}. \tag{16b}$$

In terms of the undeformed coordinates, Eq. (15a) reduces to

$$\frac{dT_1}{dR} + \frac{r'}{r}(T_1 - T_2) = 0. \tag{17}$$

With Eqs. (1), Eq. (17) is further reduced to

$$\frac{dT_1}{dR} + \frac{(R\lambda_2' + \lambda_2)}{R\lambda_2}(T_1 - T_2) = 0. \tag{18}$$

For the numerical analysis in this paper, the following dimensionless quantities are introduced:

$$\tilde{T}_i = \frac{T_i}{g_0 H}\ (i = 1,2), \tag{19a}$$

$$\tilde{g}_1 = \frac{g_1}{g_0},\ \tilde{C} = \frac{C}{g_0},\ \tilde{P} = \frac{PR_0}{g_0 H},\ \tilde{t} = \frac{t}{\tau}, \tag{19b}$$

$$\tilde{z} = \frac{z}{R_0},\ \tilde{R} = \frac{R}{R_0},\ \tilde{r} = \frac{r}{R_0},\ \tilde{?}' = R_0\frac{d?}{dR}, \tag{19c}$$

where ? is any symbol.

With Eqs. (3), (5), (16), and (19) and after proper differentiation, Eqs. (15) can be cast in a standard form for numerical integration:

$$\lambda_1' = \frac{-1}{F_1}(F_2\lambda_2' + F_3 + F_4), \tag{20a}$$

$$\lambda_2' = \frac{1}{R}(\lambda_1\cos\theta - \lambda_2), \tag{20b}$$

$$\theta' = \frac{\lambda_1}{T_1}\left(P - \frac{\sin\theta T_2}{R\lambda_2}\right). \tag{20c}$$

Equation (20b) is not derived from the equilibrium equations; it is a compatibility equation derived from Eq. (5). The primes denote the differentiation with respect to the dimensionless quantity $\tilde{R}$, and the tildes have been dropped for simplicity. The functions F_1, F_2, F_3, and F_4 are given in the Appendix.

Note, in Eqs. (20), that the variables λ_1, λ_2, and θ are used instead of r and z; λ_1, λ_2, and θ simplify the formulation and, hence, the numerical integration. After the solutions for λ_1, λ_2, and θ are obtained, the functions r and z can be obtained. These relations are rewritten in the integration forms:

$$r = R\lambda_2, \tag{21a}$$

$$z = \int_0^r \lambda_1\sin\theta dr. \tag{21b}$$

The governing equations (Eqs. (20)) are cast in standard form; they are a system of three first-order ordinary differential-integral equations. In order to integrate these equations more efficiently, the recurrence formula (14) is used whenever a convolution integral is involved. With the recurrence formula, the governing equations are reduced to three first-order ordinary differential equations with explicit derivatives for each time step. In solving these equations, the symmetry and boundary conditions and initial conditions are specified. For the inflation of a plane circular membrane clamped at the edge, the symmetry and boundary conditions are

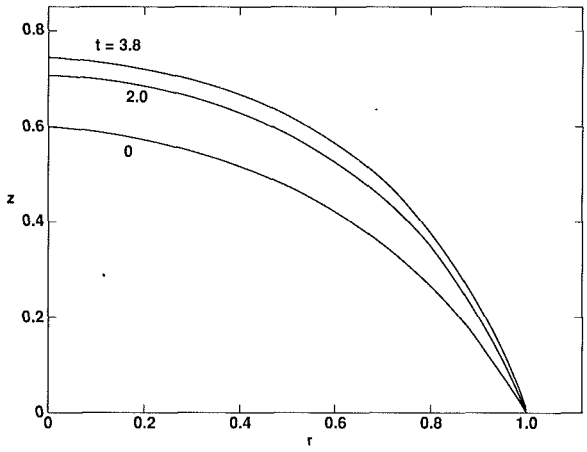


Fig. 2(*a*)

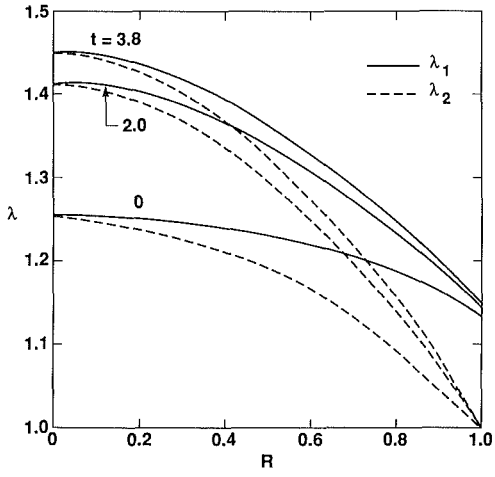


Fig. 2(*b*)

Fig. 2 Numerical results for the deformation of a flat circular membrane under an inflating pressure; (*a*) meridional-section creep profiles and (*b*) principal stretch ratios along a meridional section

$$R = 0;\ \lambda_1 = \lambda_2 = \lambda_0, \tag{22a}$$

$$R = 1;\ \lambda_2 = 1, \tag{22b}$$

and the initial conditions are

$$P = 0;\ t < 0, \tag{23a}$$

$$P = P;\ t \geq 0. \tag{23b}$$

The value λ_0 (the stretch ratios λ_1 and λ_2 at the pole) is an initial guess; it should be iterated so that all symmetry and boundary conditions are satisfied for a given inflating pressure P.

Numerical Results

The creep response of a membrane is obtained by determining the deformation change when the inflating pressure is kept constant. The relaxation response of a membrane is obtained by determining the inflating pressure change when the deformation of the membrane is kept constant.

Figure 2(*a*) shows meridional-section creep profiles of a membrane at various times. The inflating pressure P is 1.75, and the material constant C is 1.0. The quantities z, R, r, P, and t in Figs. 2–5 are dimensionless, as defined in Eqs. (19); the tildes have been dropped for simplicity.

In Fig. 2(*b*), the stretch ratios along a meridional section are shown. The maximum values for both λ_1 and λ_2 occur at the pole.

Figure 3(*a*) shows the inflated membrane configuration used in the relaxation study. The height of the membrane at the

Downloaded 03 May 2010 to 171.66.16.247. Redistribution subject to ASME license or copyright; see http://www.asme.org/terms/Terms_Use.cfm

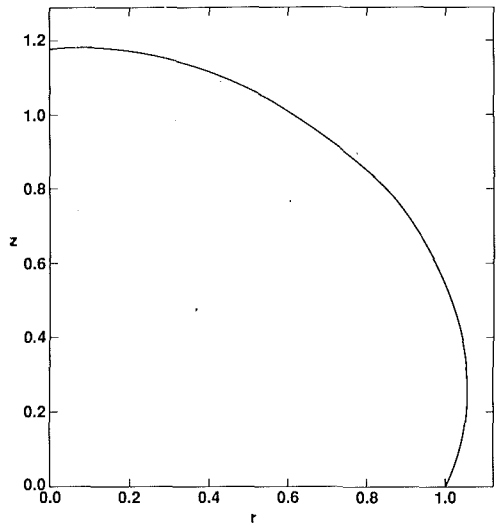


Fig. 3(*a*)

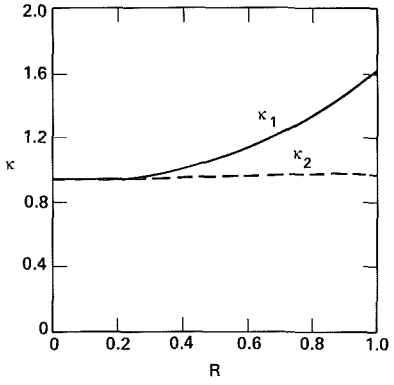


Fig. 3(*b*)

Fig. 3 Numerical results for (*a*) relaxation profile of the inflated membrane and (*b*) variation of principal curvatures

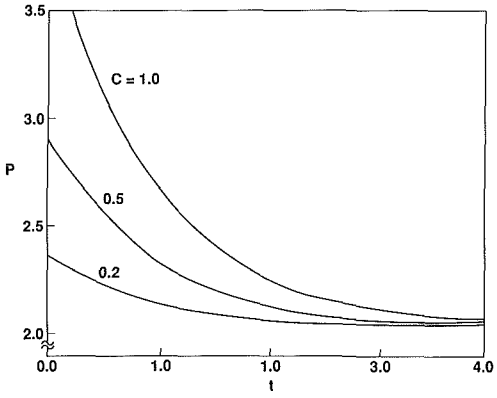


Fig. 4 Relaxation-pressure history of an inflated membrane

pole is kept constant at 1.18, which corresponds to the stretch ratio at the pole of 2.0. Figure 3(*b*) shows the variation of the principal curvatures as a function of R. For the configuration shown in Fig. 3(*a*), the values for both principal curvatures at the pole are 0.96.

Figure 4 shows the relaxation of the inflating pressure of a membrane for the deformed configuration shown in Fig. 3(*a*). Three values of C are given. All numerical results in this section are based on the relaxation function given in Eq. (12).

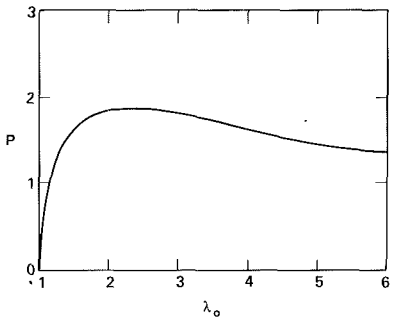


Fig. 5 Inflating pressure versus stretch ratio for an inflated neo-Hookean membrane

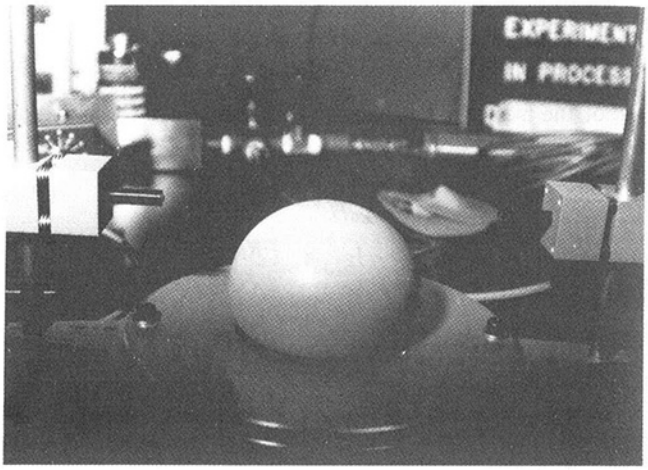


Fig. 6 Experimental set-up used to measure the deformation of an inflated plane circular membrane.

Experimental Results

In order to show the viscoelastic deformation of an elastomeric membrane, we performed an experiment. Before designing the apparatus for the test, however, we had to decide whether to do a creep test or a relaxation test. From the theoretical study, one can obtain the inflating pressure P versus the deformation λ_0 at time $t = \infty$. This curve, plotted in Fig. 5, shows clearly that there is an instability point at which the initial rise of the inflating pressure is followed by a fall as the deformation increases. Therefore, in a creep test, two or more membrane configurations exist for each inflating pressure. Furthermore, the pressure-deformation curve is relatively flat beyond the instability point; this will produce very inaccurate results. For these reasons, we decided to do a relaxation test.

The experimental apparatus is shown in Fig. 6. The membrane is made of latex rubber and clamped between two plates. The thickness of the membrane is 0.0762 cm, and its radius is 2.54 cm. The membrane is inflated by air from a reservoir. The height of the deformed membrane at the pole is fixed at 3.0 cm.

An infrared photosensor controls the maximum height of the deformed membrane at the pole. In order to decrease the pressure during the relaxation test, a "leaky" valve is provided. The photosensor is connected to a solenoid valve that closes the air-intake valve when the membrane blocks the photosensor's light path and opens the air-intake valve when the membrane deflates. The infrared photosensor keeps the height of the deformed membrane at the pole constant to within 0.002 cm, and the pressure transducer is sensitive to within 10 Pa.

A pressure transducer, coupled with a digital voltage converter, is used for data acquisition. Data are automatically recorded by a microcomputer.

Downloaded 03 May 2010 to 171.66.16.247. Redistribution subject to ASME license or copyright; see http://www.asme.org/terms/Terms_Use.cfm

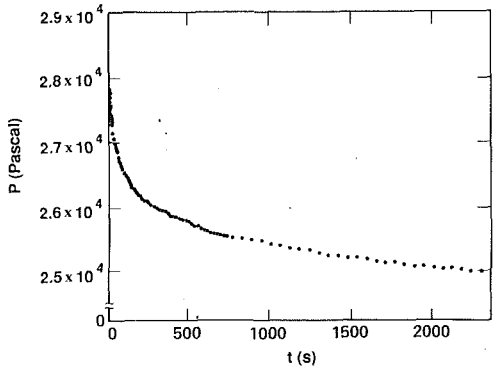


Fig. 7 Experimental pressure-relaxation history

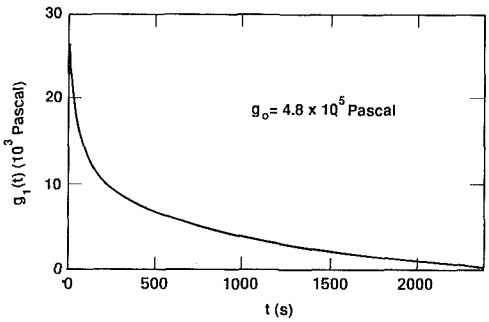


Fig. 8 Viscoelastic material-property functions g_0 and $g_1(t)$ for the experimental results

Figure 7 shows the experimental results as a graph of inflation pressure versus time. The results demonstrate the viscoelastic effect of latex rubber.

Determining Viscoelastic Material Properties

Another purpose of the experiment discussed in the previous section is to determine the material property functions g_0 and $g_1(t)$. Two methods are described here.

At the pole of the deformed membrane, $\lambda_1=\lambda_2=\lambda_0$, $T_1=T_2=T_0$, $\kappa_1=\kappa_2=\kappa_0$, and the derivative of the stress resultant, T_1, with respect to R is zero due to symmetry. Therefore, the equilibrium equation in the meridional direction is automatically satisfied. The only equilibrium equation that needs to be satisfied is in the normal direction:

$$2\kappa_0 T_0 = P. \tag{24}$$

In the data analyses, the value for P is considered to be a unit step function; i.e.,

$$P = Pu(t). \tag{25}$$

Then the response, λ_0, is also a unit step function. The convolution operations reduce to algebric operations; e.g.,

$$\int_0^t g_1(t-\tau)\frac{\partial \lambda_0^2(T)}{\partial T}\,dT = g_1(t)\lambda_0^2, \tag{26}$$

and Eq. (24) reduces to

$$g_1(t) = \frac{2}{\lambda_0^2-\lambda_0^{-10}}\left[\frac{P(t)}{2H\kappa_0} - g_0\left(1-\frac{1}{\lambda_0^6}\right)\right]. \tag{27}$$

Since $g_1(\infty)=0$, from Eq. (12), g_0 is determined by

$$g_0 = \frac{P(\infty)}{2H\kappa_0(1-\lambda_0^{-6})}. \tag{28}$$

With g_0 determined, $g_1(t)$ can be determined by Eq. (27). Hence, all viscoelastic properties are determined. For the experimental results given in the previous section, these viscoelastic properties are shown in Fig. 8.

The material properties determined with Eqs. (27) and (28) are valid only if an asymptotic value for the relaxation pressure has been obtained. Sometimes, the asymptotic value may not be reached in a reasonable test duration. The following analysis provides another method to determine the viscoelastic properties. Instead of a long test, one needs only to perform two brief tests at two different degrees of inflation. The stretch ratios at the pole for these two tests are denoted by λ_a and λ_b, and the corresponding curvatures at the pole are κ_a and κ_b. The measured pressure history for these two inflations are $P_a(t)$ and $P_b(t)$, respectively. Equation (27) then becomes

$$g_1(t) = \frac{2}{\lambda_a^2-\lambda_a^{-10}}\left[\frac{p_a(t)}{2H\kappa_a} - g_0\left(1-\frac{1}{\lambda_a^6}\right)\right], \tag{29a}$$

and

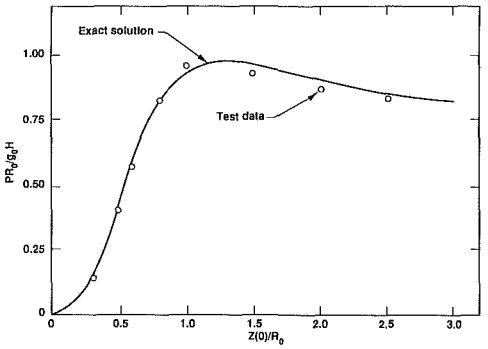


Fig. 9 Test data and the exact numerical solution for inflating a thin circular membrane ($t=0$)

$$g_1(t) = \frac{2}{\lambda_b^2-\lambda_b^{-10}}\left[\frac{p_b(t)}{2H\kappa_b} - g_0\left(1-\frac{1}{\lambda_b^6}\right)\right]. \tag{29b}$$

In fact, g_0 can be determined at any time (say, $t=t_1$). Eliminating $g_1(t_1)$ from Eqs. (29), one obtains g_0. With g_0 determined, either Eq. (29*a*) or (29*b*) yields the material properties for the viscoelastic relaxation function $g_1(t)$.

Comparison Between Theoretical and Experimental Results

The dimensionless pressure versus the dimensionless displacement at the pole for an elastic membrane are shown in Fig. 9. The solid line is the predicted analytical solution, and the open dots are the experimental data. Only one constant $g_1(0)/g_0$ is used to adjust the shape of the analytical curve. For this material, the value is 0.03. It can be seen that the deformations predicted by the analytical formulation agree with the experimental data.

The viscoelastic material properties presented in this paper are determined from the experimental data. As in the elastic case, when these material properties are used to make analytical predictions at different degrees of inflation, the results agree with experimental data. The values for the dimensionless pressure are a function of time due to relaxation.

Conclusions and Discussion

The nonlinear viscoelastic membrane mechanics have been formulated, solved, and experimentally verified for the inflation of an initially flat, circular, thin membrane. With some minor modifications of these formulations, the whole class of axisymmetric viscoelastic membrane problems can be studied. In the formulation, both geometric nonlinearity and material nonlinearity are included. The theoretical value for the strains can be as large as needed; for practical applications, however,

Downloaded 03 May 2010 to 171.66.16.247. Redistribution subject to ASME license or copyright; see http://www.asme.org/terms/Terms_Use.cfm

these values are limited by the fracture strength and are usually less than a few hundred percent.

The constitutive equation admits neck propagation; therefore, a bulge will develop as the membrane is inflated if there is an initial imperfection. However, the initial imperfection was not considered in the theoretical formulation and the bulge was not observed during experimental tests.

In the formulation, a single exponential term that does not represent the material properties in reality is considered. However, the formulation presented here can be extended to a more realistic relaxation function, which is represented by a series of exponential functions:

$$g_1(t) = \sum_{i=1}^{n} C_i \exp(-t/\tau_i). \tag{30}$$

The viscoelastic effect for elastomers is about ten percent of the total elastic effect; therefore, the experimental apparatus must be very precise. It has been demonstrated that the apparatus used in this project is adequate for studying the viscoelastic effect.

Acknowledgment

This work was performed under the auspices of the U. S. Department of Energy by the Lawrence Livermore National Laboratory under Contract No. W-7405-ENG-48. The work was completed while the author was a visiting professor at the National Cheng Kung University in Taiwan, Republic of China and at The Pennsylvania State University, University Park, PA.

References

Adkins, J. E., and Rivlin, R. S., 1952, "Large Elastic Deformations of Isotropic Materials. IX. The Deformation of Thin Shells," *Phil. Trans. Royal Soc., London*, Vol. A244, p. 505.

Christensen, R. M., 1980, "A Nonlinear Theory of Viscoelasticity for Application to Elastometers," ASME JOURNAL OF APPLIED MECHANICS, Vol. 47, (Vol. 102, Series E) p. 762.

Feng, W. W., 1991, "A Recurrence Formula for Viscoelastic Constitutive Equations," to be published in the *International Journal of Nonlinear Mechanics*.

Klingbeil, W. W., and Shield, R. T., 1964, "Some Numerical Investigations on Empirical Strain Energy Functions in the Large Axisymmetric Extension of Rubber Membranes," *ZAMP*, Vol. 15, p. 608.

Treloar, L. R. G., 1944, "Stress in an Inflated Rubber Sheet and the Mechanism of Bursting," *Inst. Rubber Ind. Trans.*, Vol. 19, p. 201.

Yang, W. H., and Feng, W. W., 1970, "On Axisymmetrical Deformation of Nonlinear Membranes," ASME JOURNAL OF APPLIED MECHANICS, Vol. 37, (Vol. 92, Series E), p. 1002.

APPENDIX

Explicit forms for F_1, F_2, F_3, and F_4 of Eq. (20*a*) are

$$F_1 = \frac{1}{\lambda_2}\left(1+\frac{1}{2}g_1{}^*\lambda_1^2\right) + \frac{3}{\lambda_1^4\lambda_2^3}\left(1+\frac{1}{2}g_1{}^*\frac{1}{\lambda_1^2\lambda_2^2}\right) + C\exp\left(\frac{\Delta t}{2}\right)\left(\lambda_1+\frac{1}{\lambda_1^3\lambda_2^2}\right),$$

$$F_2 = \frac{3}{\lambda_1^3\lambda_2^4}\left(1+\frac{1}{2}g_1{}^*\frac{1}{\lambda_1^2\lambda_2^2}\right) - \frac{\lambda_1}{\lambda_2}\left(1+\frac{1}{2}g_1{}^*\lambda_1^2\right),$$

$$F_3 = \frac{1}{\lambda_1^3\lambda_2^3}\left(g_1{}^*\frac{\lambda_2'}{\lambda_1^2\lambda_2^3}\right) + \frac{\lambda_1}{\lambda_2}\left[\exp(-\Delta t)(g_1{}^*\lambda_1\lambda_1') - C\exp\left(\frac{\Delta t}{2}\right)\lambda_1\lambda_1'\right]_{t=t_{i-1}} + \frac{1}{\lambda_1^3\lambda_2^3}\left[\exp(\Delta t)\left(g_1{}^*\frac{\lambda_1'}{\lambda_1^3\lambda_2^2}\right) - \frac{C\exp(\Delta t/2)\lambda_1'}{\lambda_1^3\lambda_2^2}\right]_{t=t_{i-1}},$$

$$F_4 = \left(\frac{\lambda_2'}{\lambda_2}+\frac{1}{R}\right)\left[\frac{\lambda_1}{\lambda_2}\left(1+\frac{1}{2}g_1{}^*\lambda_1^2\right) - \frac{\lambda_2}{\lambda_1}\left(1+\frac{1}{2}g_1{}^*\lambda_2^2\right)\right].$$

The convolution integral are denoted by the asterisks ($*$), and all quantities are evaluated at time t_i unless otherwise specified, as in F_3. The last few terms in F_3 are evaluated at the previous time step t_{i-1}.

Downloaded 03 May 2010 to 171.66.16.247. Redistribution subject to ASME license or copyright; see http://www.asme.org/terms/Terms_Use.cfm

Stochastic Modeling of Crack Initiation and Short-Crack Growth Under Creep and Creep-Fatigue Conditions

Takayuki Kitamura[1]
Lewis Research Center,
Cleveland, OH 44135

Louis J. Ghosn
Sverdrup Technology, Inc.,
Lewis Research Center Group,
Brook Park, OH 44142
Assoc. Fellow, ASME

Ryuichi Ohtani
Kyoto University,
Kyoto, Japan

A simplified stochastic model is proposed for crack initiation and short-crack growth under creep and creep-fatigue conditions. Material inhomogeneity provides the random nature of crack initiation and early growth. In the model, the influence of microstructure is introduced by the variability of (1) damage accumulation along grain boundaries, (2) critical damage required for crack initiation or growth, and (3) the grain-boundary length. The probabilities of crack initiation and growth are derived by using convolution integrals. The model is calibrated and used to predict the crack density and crack-growth rate of short cracks of 304 stainless steel under creep and creep-fatigue conditions. The mean crack initiation lives are predicted to be within an average deviation of about ten percent from the experimental results. The predicted cumulative distributions of crack-growth rate follow the experimental data closely. The applicability of the simplified stochastic model is discussed and the future research direction is outlined.

Introduction

Life prediction is an important parameter in evaluating the safety and reliability of structural components for high-temperature applications such as rocket engines, gas turbines, and nuclear powerplants. Crack initiation and early growth constitute most of the life of components, especially under creep and creep-fatigue conditions. Experimental observations (Ohtani et al., 1983, 1986, 1987) have shown large fluctuations in the crack initiation and growth rates of short cracks. These fluctuations are caused by the randomness in the grain size, the local stress, and the resistance to local failure. Few analyses have been conducted of the stochastic nature of the growth of microstructurally short cracks. However, a considerably larger number of investigations (Kozin and Bogdanoff, 1981; Virkler et al., 1979; Lin and Yang, 1983; Ishikawa et al., 1987; Spencer and Tang, 1988) have been carried out for long-crack problems. Long cracks usually show smaller fluctuations in the crack-growth rates than short cracks. The two approaches taken for short cracks thus far are based either on Monte Carlo simulations (Kitamura and Ohtani, 1987, 1988, Cox and Morris, 1988) or on the randomization of empirical crack-growth equations (Cox and Morris, 1987). The approach taken here is based on the damage accumulation along grain boundaries and the critical damage required for failure under creep and creep-fatigue conditions.[2] The fluctuation of the crack-growth rate is formulated with the fundamental reliability analysis (Thoft-Christensen and Baker, 1982), which is based on the variability of the damage accumulation and the critical damage of the grain boundaries. The model is calibrated and is then used to predict the crack initiation and early growth rate of short cracks under creep and creep-fatigue conditions. The determination of the distribution of the critical time to failure is beyond the scope of this paper.

Stochastic Model for Crack Initiation and Growth

For many polycrystalline alloys under creep or creep-fatigue conditions, cracks initiate and grow along preferential grain boundaries. This localization of the cracking sites is due to the operative high-temperature failure mechanisms. Growth and coalescence of cavities and grain-boundary sliding are examples of local failure mechanisms leading to grain-boundary cracking (Garofalo, 1965). The time required for the initiation of a crack differs between seemingly identical grain boundaries because of creep resistance and geometric differences. The crack-growth rate is also dependent on such things as the grain-

[1]National Research Council—NASA Research Associate. Present address: Department of Engineering Science, Kyoto University, Kyoto, Japan.

Contributed by the Applied Mechanics Division of THE AMERICAN SOCIETY OF MECHANICAL ENGINEERS for presentation at the 1992 ASME Summer Mechanics and Materials Meeting, Tempe, AZ Apr. 28–May 1, 1992.

Discussion on this paper should be addressed to the Technical Editor, Prof. Leon M. Keer, The Technological Institute, Northwestern University, Evanston, IL 60208, and will be accepted until four months after final publication of the paper itself in the JOURNAL OF APPLIED MECHANICS. Manuscript received by the ASME Applied Mechanics Division, Mar. 20, 1989; final revision, May 30, 1990.

Paper No. 92-APM-5.

[2]The term "creep fatigue", as used here, implies a reversed cyclic creep deformation at high temperature under which creep dominates the failure process. A discussion of synergistic creep-fatigue interaction is beyond the scope of this report.

Copyright © 1992 by ASME
Downloaded 03 May 2010 to 171.66.16.247. Redistribution subject to ASME license or copyright; see http://www.asme.org/terms/Terms_Use.cfm

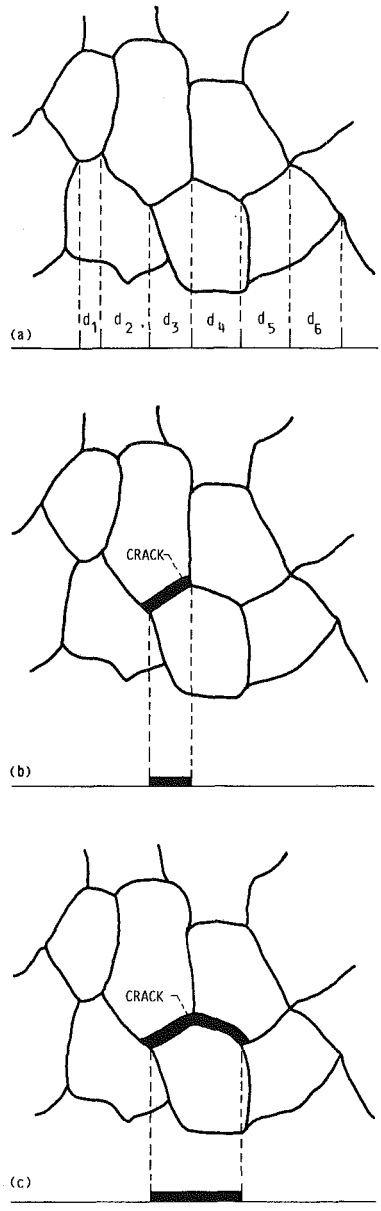


Fig. 1 Schematic views of crack initiation and growth; (*a*) projected grain-boundary length, d_i, (*b*) crack initiation, and (*c*) crack growth

boundary orientation with respect to the loading axis, the distance between triple points, and the distribution of the precipitates and ledges on the boundaries. The highly random crack initiation and growth processes are created by the presence of microstructural inhomogeneities. The local loading conditions along grain boundaries are also random because of creep deformation anisotropy, grain shape, and constraints. A simplified stochastic model is proposed for predicting the probability of crack initiation and growth under creep and creep-fatigue conditions. This model takes into consideration material inhomogeneities, microstructure geometric variations, and local loading randomness.

The assumptions included in the model are that (1) cracks grow only along grain boundaries, (2) crack length is measured as the projected length on a plane perpendicular to the loading axis, (3) projected grain-boundary length between adjacent triple points d is a random variable with density function $f(d)$, and (4) the width of the crack is ignored. The two-dimensional model can be modified, if necessary, to a three-dimensional model by converting the crack length into crack area. It is also

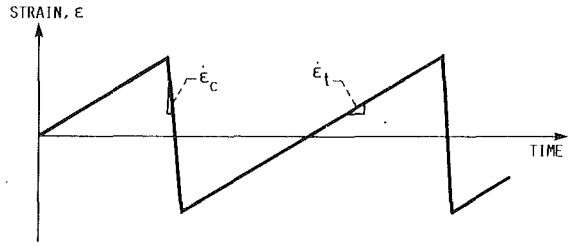


Fig. 2 Strain variation for slow-fast creep fatigue of 304 stainless steel. $\dot{\epsilon}_c$ = strain rate in compression, $\dot{\epsilon}_t$ = strain rate in tension, $\dot{\epsilon}_t \ll \dot{\epsilon}_c$.

assumed that crack initiation and growth occur in a discrete manner, increasing in segments that are equal to the distance d between two triple points after a certain time t (Fig. 1). It has been observed experimentally that grain-boundary triple points act as crack arresters (Ohtani et al., 1984). Therefore, crack growth is usually halted at triple points or grain-boundary kinks (sharp bends) until enough damage is accumulated in the adjacent grain boundary for the crack to extend again. It is postulated that crack initiation and growth occur when the accumulated damage ϕ equals a critical value ϕ_c. The critical damage ϕ_c can be interpreted as the resistance of a particular grain boundary to cracking, which is a random variable. The density function of the critical damage ϕ_c is given by $g(\phi_c)$. The damage accumulation ϕ is the local driving failure parameter for a particular grain boundary. The critical damage ϕ_c is independent of the applied stress but ϕ is strongly related to it. The damage accumulation ϕ is the integral of the damage accumulation rate $\dot{\phi}$:

$$\phi = \int_0^t \dot{\phi} dt \tag{1}$$

The damage rate $\dot{\phi}$ is a random variable that is a function of the local stress σ_l. The local stress state σ_l is a function of the constant global applied stress σ_g and the crack length l. Assuming a steady-state failure process, the damage accumulation rate is taken to be independent of time.

$$\phi = \dot{\phi} t \tag{2}$$

The density function k of ϕ is related to the density function of $\dot{\phi}$, $h(\dot{\phi} | \sigma_g, l)$ by

$$k(\phi | \sigma_g, l) = 1/t \cdot h(\dot{\phi} | \sigma_g, l). \tag{3}$$

If the grain boundary under consideration is adjacent to a crack, the failure is called crack growth. If the grain boundary is isolated from other cracked regions, the failure is called crack initiation.

This model is applicable, but not limited, to monotonic creep conditions. It can also be applied to time-dependent fatigue (i.e., creep-dominant fatigue). As an example, under a slow-fast fatigue loading (Fig. 2) of 304 stainless steel at 973 K in vacuum, irreversible grain-boundary sliding was observed. This was due to the creep deformation in the tensile half of the cycle (Taira et al., 1978). Under those conditions, the intergranular crack initiation is associated with creep damage accumulation in the tensile half of the cycle. Thus, the time should be converted into the number of cycles and the local stress σ_l should be interpreted as an equivalent stress of the tensile half of the loading cycle.

This damage accumulation formulation is expressed in mathematical terms only. Physical explanation of the damage equation is discussed next. If one considers that the damage is associated with cavity growth, the damage function ϕ can be written in terms of the number and the radii of the cavities observed on a particular grain boundary. The damage function ϕ can be formulated as the ratio of the summation of cavity length over the grain-boundary length. Experimental observations have shown that the summation of the length of grain-

Downloaded 03 May 2010 to 171.66.16.247. Redistribution subject to ASME license or copyright; see http://www.asme.org/terms/Terms_Use.cfm

boundary cavities is proportional to time (Yang, 1984). Hence, a physical meaning is given to the steady-state damage accumulation of Eq. (2). More sophisticated damage equations can, of course, replace Eq. (2), which can be written in terms of cavity initiation and growth laws.

Probability of Crack Initiation and Growth

Crack Initiation. As seen previously, failure on a specific grain boundary occurs when the damage accumulation exceeds a critical damage level. Let us now define a new variable ϕ_m, known as the failure function, as the difference between ϕ_c and ϕ:

$$\phi_m = \phi_c - \phi. \tag{4}$$

The failure criterion is simply reduced to $\phi_m = 0$. Consequently, the probability of a crack initiating at a particular grain boundary $P_f(t)$ is the probability that ϕ_m is less than or equal to zero:

$$P_f(t) = P(\phi_m \le 0). \tag{5}$$

The density function of the new random variable ϕ_m is given by $m_o(\phi_m | t, \sigma_g)$ for a given time t and global stress σ_g. The density function m_o is related to the density functions of the two independent random variables ϕ_c and ϕ, by the following convolution integral:

$$m_o(\phi_m | t, \sigma_g) = \int_0^\infty g(\phi_m + \phi) k(\phi | t, \sigma_g, l=0) d\phi. \tag{6}$$

Knowing that $\phi = \dot{\phi} t$, then

$$m_o(\phi_m | t, \sigma_g) = \int_0^\infty g(\phi_m + \dot{\phi} t) h(\dot{\phi} | \sigma_g, l=0) d\dot{\phi}. \tag{7}$$

If the density functions of ϕ_c and $\dot{\phi}$ are known, then the probability $P_f(t)$ for crack initiation at one particular grain boundary before time t for a given global stress σ_g is given by

$$P_f(t) = P(\phi_m \le 0) = \int_{-\infty}^0 m_o(\phi_m | t, \sigma_g) d\phi_m. \tag{8}$$

A polycrystalline material has many grain boundaries, which are potential crack initiation sites. The probability that n number of cracks initiated in time t for a total number of potential crack initiation sites N is given by the following binomial distribution:

$$(P_f)_n = \frac{N![P_f(t)]^n [1 - P_f(t)]^{N-n}}{(N-n)!n!}. \tag{9}$$

The expected value or mean number of crack initiations in a given time t and its variance are given, respectively, by

$$E(n) = NP_f(t) \tag{10}$$

and

$$VAR = E([n - E(n)]^2) = NP_f(t)[1 - P_f(t)]. \tag{11}$$

Crack Growth. The criterion for crack growth in terms of accumulated damage is similar to that for crack initiation. The crack-growth criterion still corresponds to the damage accumulation ϕ reaching a critical value, ϕ_c; however, the damage accumulation rate is accelerated by the presence of a crack. The failure function ϕ_m of Eq. (4) for the grain boundary i immediately adjacent to the crack tip is redefined for crack growth as

$$\phi_m = \phi_c - \dot{\phi}_i(l, \sigma_g) t \tag{12}$$

where $\dot{\phi}_i(l, \sigma_g)$ is the damage accumulation rate at grain boundary i and t is the time elapsed after the crack reaches the particular grain boundary i. Since crack growth occurs when $\phi_m = 0$, the time interval t_i required for the crack to travel the entire grain boundary i is given by

$$t_i = \phi_c / \dot{\phi}_i. \tag{13}$$

The density function of the time t_i in terms of the density functions $g(\phi_c)$ and $h(\dot{\phi}_i)$ can be shown to be

$$s(t_i | \sigma_g, l) = \int_0^\infty \dot{\phi}_i g(\dot{\phi}_i t_i) h(\dot{\phi}_i | \sigma_g, l) d\dot{\phi}_i. \tag{14}$$

The crack-growth rate of a short crack is then given by

$$dl/dt = d_i / t_i \tag{15}$$

where d_i is the projected distance between two triple points of grain boundary i. The density function of the crack-growth rate in terms of the density functions $s(t_i)$ and $f(d_i)$ of t_i and d_i, respectively, is given by

$$P_g(dl/dt | \sigma_g, l) = \int_0^\infty t_i f(dl/dt \cdot t_i) s(t_i | \sigma_g, l) dt_i. \tag{16}$$

The damage accumulated before the grain boundary i becomes adjacent to the crack tip is assumed negligible because it was shown experimentally that predamage of stainless steel specimens has little effect on crack growth under creep and creep-fatigue conditions (Ohtani and Kitamura, 1986). A formulation that takes into consideration the predamage effect is described in the Appendix.

Normalization

As seen previously, the damage accumulation rate $\dot{\phi}$ is a function of the local stress σ_1, which depends on the applied global stress σ_g and crack length l. For simplicity, the following relation can be assumed:

$$\sigma_1 = K(u | l) \sigma_g \tag{17}$$

where $K(u | l)$ is a random stress concentration factor function of the crack length l and microstructural randomness u. Under creep conditions, the damage accumulation rate can be taken to be a power function of the local stress

$$\dot{\phi} = A \sigma_1^\alpha \tag{18}$$

where A and α are assumed to be material constants. Assuming a steady-state damage rate, the damage accumulation is then given as a function of the global stress and $K(u | l)$ by substituting Eqs. (17) and (18) in Eq. (2):

$$\phi = \dot{\phi} t = A(K(u | l) \sigma_g)^\alpha t \tag{19}$$

$$\phi = \bar{\dot{\phi}} \bar{t} \tag{20}$$

where

$$\bar{\dot{\phi}} = AK(u | l)^\alpha$$
$$\bar{t} = \sigma_g^\alpha t. \tag{21}$$

Here, $\bar{\dot{\phi}}$ is a random variable because $K(u | l)$ is a random variable, but $\bar{t}$ is a deterministic variable. The density function $\bar{h}$ of the normalized damage accumulation rate is related to h of $\dot{\phi}$ by

$$\bar{h}(\bar{\dot{\phi}}) = \sigma_g^\alpha h(\dot{\phi}). \tag{22}$$

The probability of the crack initiation can be rewritten in terms of the normalized variables as

$$\bar{P}_f(\bar{t}) = \int_{-\infty}^0 \bar{m}_o(\phi_m | \bar{t}) d\phi_m = \sigma_g^\alpha P_f \tag{23}$$

where

$$\bar{m}_o(\phi_m | \bar{t}) = \int_0^\infty g(\phi_m + \bar{\dot{\phi}} \bar{t}) \bar{h}(\bar{\dot{\phi}} | l=0) d\bar{\dot{\phi}}. \tag{24}$$

The density function of the crack-growth rate, in terms of the normalized time interval $\bar{t}_i = \sigma_g^\alpha t_i$, can be shown to be equal to

Downloaded 03 May 2010 to 171.66.16.247. Redistribution subject to ASME license or copyright; see http://www.asme.org/terms/Terms_Use.cfm

$$\bar{P}_g(dl/d\bar{t}\,|\,l) = \int_0^\infty \bar{t}_i f(dl/d\bar{t}\cdot\bar{t}_i)\bar{s}(\bar{t}_i|l)d\bar{t}_i. \tag{25}$$

$$\bar{s}(\bar{t}_i|l) = \sigma_g^\alpha s(t_i|\sigma_g,\ l). \tag{26}$$

Therefore, the actual density function is related to the normalized density function by

$$P_g(dl/dt\,|\,\sigma_g,\ l) = (1/\sigma_g)^\alpha \bar{P}_g(dl/d\bar{t}\,|\,l). \tag{27}$$

It should be noted that $\bar{P}_f$ and $\bar{P}_g$ are independent of σ_g. The terms P_f and P_g are easily calculated for any arbitrarily applied global stress σ_g by Eqs. (23) and (27), respectively.

Applicability of Stochastic Model

Few experiments have been carried out to determine crack initiation and growth of short cracks at high temperature. Because of the small data base available, only the applicability of the stochastic model is discussed. This model is applied to two different data sets for which experimental data are available. Both experiments were carried out on smooth specimens of 304 stainless steel with an average grain diameter of 40 μm. The cracks initiated and grew on the specimen surface. In the first experiment (Ohtani et al., 1983), the number of crack initiations was monitored under monotonic creep at 923 K in air at applied stress levels of 98.1 MPa and 147.1 MPa. In the second experiment, crack initiation and growth were measured under slow-fast fatigue (Ohtani et al., 1986). The total strain range was equal to one percent and the strain rates in tension and compression were 10^{-3} percent/s and one percent/s, respectively, at 923 K in vacuum.

For the model calibration, the density functions of the damage rate $h(\dot{\phi}\,|\,\sigma_g,\ l)$ and of the critical damage $g(\phi_c)$ should be determined from actual experimental data. However, standard density functions are assumed in this study because of the limited data available. Since ϕ_c and $\dot{\phi}$ are positive variables, the two-parameter Weibull and logarithmic normal distributions are adopted here for ϕ_c and $\dot{\phi}$, respectively, and are given below for completeness:

$$g(\phi_c) = \frac{\beta}{b}\left(\frac{\phi_c}{b}\right)^{\beta-1} e^{-\left(\frac{\phi_c}{b}\right)^\beta} \tag{28}$$

$$h(\dot{\phi}\,|\,\sigma_g,\ l) = \frac{1}{\sqrt{2\pi}\ \sigma_{\ln\dot{\phi}}\dot{\phi}}\ e^{-\frac{1}{2}\left[\frac{\ln\left(\frac{\dot{\phi}}{m_{\dot{\phi}}}\right)}{\sigma_{\ln\dot{\phi}}}\right]^2} \tag{29}$$

where β and b are material constants, $m_{\dot{\phi}}$ is the mean value of $\dot{\phi}$, and $\sigma_{\ln\dot{\phi}}$ is standard deviation of $\ln\dot{\phi}$. The normalized function of the damage accumulation rate $\bar{h}(\bar{\dot{\phi}}\,|\,l)$ and the density function of the damage accumulation $k(\phi\,|\,\sigma_g,\ t,\ l)$, which are derived from Eq. (29), are given by

$$\bar{h}(\bar{\dot{\phi}}\,|\,l) = \frac{1}{\sqrt{2\pi}\ \sigma_{\ln\bar{\dot{\phi}}}\bar{\dot{\phi}}}\ e^{-\frac{1}{2}\left[\frac{\ln\left(\frac{\bar{\dot{\phi}}}{m_{\bar{\dot{\phi}}}}\right)}{\sigma_{\ln\bar{\dot{\phi}}}}\right]^2} \tag{30}$$

$$k(\phi\,|\,\sigma_g,\ t,\ l) = \frac{1}{\sqrt{2\pi}\ \sigma_{\ln\dot{\phi}}\phi}\ e^{-\frac{1}{2}\left[\frac{\ln\left(\frac{\phi}{m_{\bar{\dot{\phi}}}t}\right)}{\sigma_{\ln\dot{\phi}}}\right]^2} \tag{31}$$

where $m_{\bar{\dot{\phi}}}$ is the mean value of $\bar{\dot{\phi}}$.

The exponent α, in Eq. (23), is given by $(\gamma + 1)$ where γ is the creep exponent of the material. The choice of α to be equal to $(\gamma + 1)$ is based on the assumption that the damage accumulation is proportional to the local strain energy density rate $U\alpha\dot{\varepsilon}\sigma_1$, which is proportional to $\sigma_1^{(\gamma+1)}$ for a power-law creep material. The creep exponent γ of 304 stainless steel is equal to 7 under monotonic creep conditions at 923 K in air (Kitamura and Ohtani, 1988).

Crack Initiation. The constants in the density functions of the critical damage and the damage rate are calibrated with actual experimental data under monotonic creep at 98.1 MPa and 923 K in air. Under these conditions, the damage accumulation observed was associated with grain boundary cavitation which was shown to be a steady-state process (Yang, 1984). The constants are adjusted for the theoretical expected value of the number of crack initiation sites $E(n)$ to fit the actual data (Ohtani et al., 1983). The total number of potential crack initiation sites N is approximately equal to 900 sites/mm^2 for this material. The constants obtained from the calibration are listed in Table 1. The expected value of the crack initiation sites is plotted versus time and compared with the experimental results (Fig. 3(*a*)). The rate of change of the expected value $E(n)$ increases with increasing time. Also shown is the scatter band of the mean value, plus and minus one standard deviation. The calibration fits the data well in view of the restriction of the assumed density functions for $\dot{\phi}$ and ϕ_c.

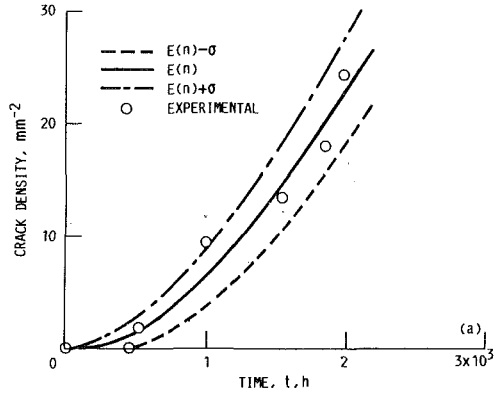
As a check to the validity of the calibration, the expected value of the number of cracks initiated is calculated for a different stress level and then compared with experimental data. Figure 3(*b*) shows the predicted results under creep conditions at an applied stress level of 147.1 MPa and 923 K. The experimental results are shown to be within one standard deviation and are always lower than the predicted mean value $E(n)$.

Short-Crack Growth. The stochastic model for early crack growth is applied to 304 stainless steel under creep-fatigue condition at 923 K (Ohtani et al., 1986). The constants β and b of $g(\phi_c)$ are assumed to have the same values as in the previous crack initiation study under creep condition because the variability of the critical damage is only material dependent. The acceleration of the damage accumulation rate $h(\phi)$, caused by the presence of a crack, is taken to be a simple linear variation of the mean with crack length l as given by

Table 1 Calibrated Constants for Distributions of ϕ_c, $\dot{\phi}$, and $\bar{\dot{\phi}}$ for Crack Initiation Analysis for Monotonic Creep of 304 Stainless Steel

Constants for density function of critical damage (Eq. (28)), $g(\phi_c)$	Constants for density function of damage accumulated (Eq. (29)), $h(\phi)$	Constants for normalized density function of damage accumulated (Eq. (30)), $\bar{h}(\bar{\dot{\phi}})$
$\beta = 2$ $b = 10$	$\sigma_{\ln\dot{\phi}} = 1.0$ $m_{\dot{\phi}} = 3.4\times10^{-4}$ ($\sigma_g = 98.1$ MPa)	$\sigma_{\ln\bar{\dot{\phi}}} = 1.0$ $m_{\bar{\dot{\phi}}} = 3.9\times10^{-20}$

Downloaded 03 May 2010 to 171.66.16.247. Redistribution subject to ASME license or copyright; see http://www.asme.org/terms/Terms_Use.cfm



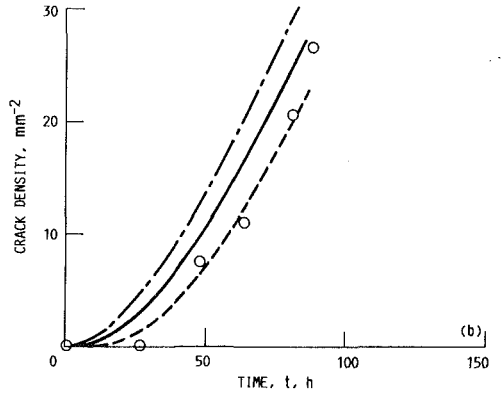


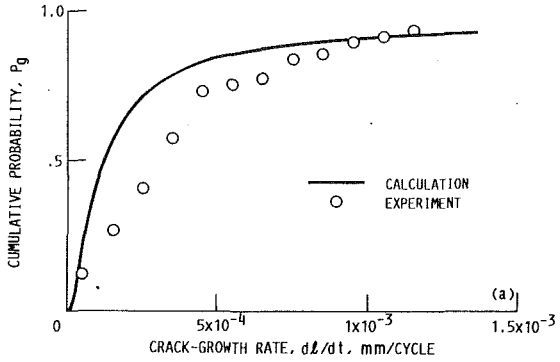
Fig. 3 Crack-initiated density in monotonic creep of 304 stainless steel. At 923 K in Air. *E(n)* = mean number of initiated crack density, σ = standard deviation of the cracking density; (*a*) calibrated—global stress level, 98.1 MPa and (*b*) predicted—global stress level, 147.1 MPa.

Table 2 Calibrated Constants for Distributions of ϕ_c and $\dot{\phi}$ for Crack-Growth Analysis Under Creep-Fatigue Conditions of 304 Stainless Steel

Constants for density function of critical damage (Eq. (28)), $g(\sigma_c)$	Constants for density function of damage accumulated for crack growth as a function of crack length l (Eq. (29)), $h(\dot{\phi} \mid \sigma_g, l)$
$\beta = 2$ $b = 10$	$m_{\ln\dot{\phi}} = C_0 + C_1 l$ $C_0 = 0.008$ $C_1 = 1.08$ $\sigma_{\ln\dot{\phi}} = 1.0$

$$m_{\dot{\phi}} = C_0 + C_1 l. \tag{32}$$

The standard deviation $\sigma_{\ln\dot{\phi}}$ is assumed to be independent of l for simplicity. The constant C_0 corresponds to the mean value of $\dot{\phi}$ for $l = 0$, which can be determined easily from crack initiation data as described in the preceding section. The constant C_1 is calibrated by using long crack-growth rate data of notched specimens with crack length greater than 1 mm. Note that C_1 is calibrated by using long-crack notched specimens that are different from the smooth, short-crack specimens. The calibrated constants C_0 and C_1 are listed in Table 2. The distribution of the grain-boundary length $f(d)$ is calculated by assuming a normal distribution with an average grain length of 0.02 mm and a standard deviation of 0.005 mm.



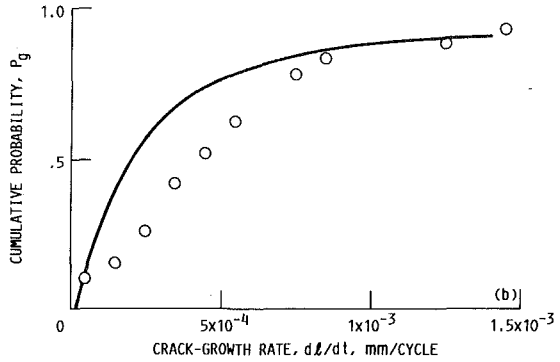


Fig. 4 Cumulative density functions of crack-growth rate of 304 stainless steel for two crack lengths under creep-fatigue condition. At 923 K in vacuum; slow-fast fatigue; strain range, $\Delta\epsilon$, one percent; (*a*) crack length, l = 0.03 mm and (*b*) crack length, l = 0.06 mm.

The sensitivity of the damage accumulation prior to the dominant crack's reaching a particular grain boundary is investigated first with the formulation given in the Appendix. The values of the constants C_1 and C_0 used in this study are listed in Table 2. The analysis reveals the probability that the crack-growth rate dl/dt is insensitive to the predamage time t_o for $l \geq 0.03$ mm. When the crack reaches the grain boundary under consideration, the damage accumulation due to stress concentration is accelerated to a much faster rate than the predamage rate. This is due to the large difference between the values of C_1 and C_0. These calculations are consistent with experimental observations (Ohtani and Kitamura, 1986) indicating that, once a crack appears, the overwhelming damage is localized in the grain boundary immediately adjacent to the crack tip. The predicted cumulative probability distributions of short crack-growth rates for two different crack lengths of 0.03 mm and 0.06 mm are given in Fig. 4. The experimental results are shown for purposes of comparison. For the given density distributions of ϕ_c and $\dot{\phi}$, the stochastic model gives the same range of crack-growth rates as the experimental data. The predicted distributions show good correlation with the experimental results for higher crack-growth rates. For lower crack-growth rates, the disagreement may be due in part to the difficulty of monitoring extremely slow crack-growth rates. The dependence of the crack-growth rate on crack lengths is plotted in Fig. 5. The mean crack-growth rates with the 10 percent and 90 percent confidence lines are shown for crack lengths ranging from 0.03 mm to 0.2 mm. Also shown are the experimental upper and lower crack-growth rates of approximately 50 initially monitored cracks. The predicted mean value falls between the upper and lower values of the experimental crack-growth rates. The predicted 90 percent and 10 percent confidence lines follow closely the experimental upper and lower limits, respectively.

Downloaded 03 May 2010 to 171.66.16.247. Redistribution subject to ASME license or copyright; see http://www.asme.org/terms/Terms_Use.cfm

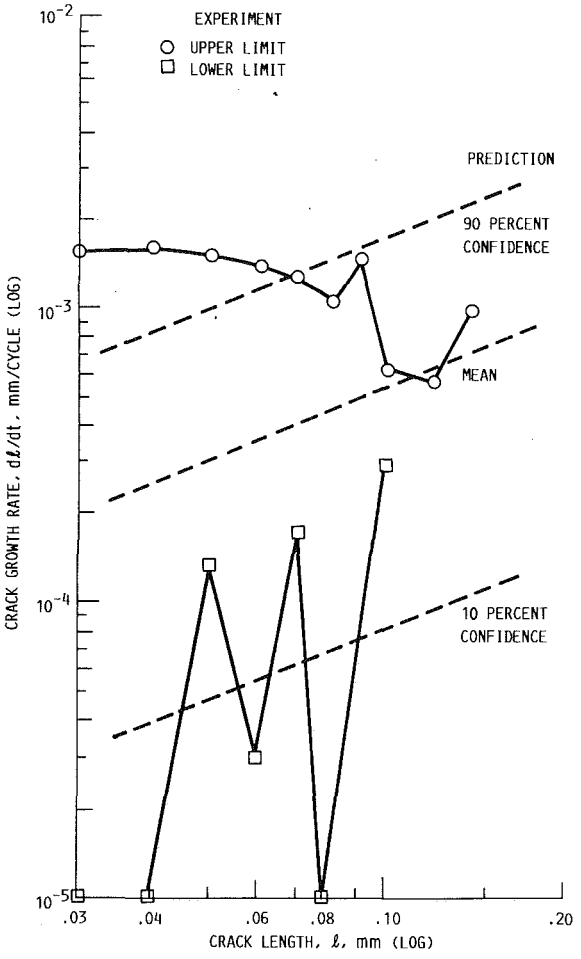


Fig. 5 Comparison of predicted and experimental variation of crack-growth rate of 304 stainless steel as a function of crack length under creep-fatigue condition. At 923 K in vacuum; slow-fast fatigue; strain range, $\Delta\epsilon$, one percent.

Summary of Results

A simplified stochastic model was proposed to predict the distribution of the initiation of cracks and their early growth under creep and creep-fatigue conditions. The model was formulated by using concepts of damage accumulation and critical damage required for grain-boundary failure. The density functions of the damage rate and the critical damage were assumed to have standard forms (log-normal and Weibull distributions, respectively). The mean and the variance were calibrated by comparing the predicted results with experimental data. Damage history and the presence of a dominant crack were introduced in a simple form that influenced the mean of the damage accumulation rate. The standard deviation of the damage rate was assumed constant in this study. The model predicted mean-crack initiation lives at different stress levels within an average deviation of about ten percent. The cumulative distributions of the crack-growth rates under creep-fatigue conditions for different crack lengths followed closely the variability of the experimental data.

Although the proposed model gave good predictions, there is a need for model improvements and sensitivity studies of the damage distributions and their dependence on crack length and predamage. The damage accumulation should be formulated from a micromechanics, or cavity growth law. The crack-growth behavior was oversimplified by allowing for only one dominant propagating crack. Multiple cracks and crack coalescence, based on the formulation in the Appendix, should be considered. Damage recovery must be accounted for in the formulation for more complex loading conditions with compressive segments. The effect of predamage formulation in the appendix must be verified with additional experiments.

References

Brent-Hall, W., 1988, "Reliability of Service-Proven Structures," *ASCE Journal of Structural Engineering*, Vol. 114, pp. 608–624.

Cox, B. N., and Morris, W. L., 1985, "Monte Carlo Simulations of the Growth of Small Fatigue Cracks," *Engineering Fracture Mechanics*, Vol. 31, pp. 591–610.

Cox, B. N., and Morris, W. L., 1987, "A Probabilistic Model of Short Fatigue Crack Growth," *Fatigue and Fracture of Engineering Materials and Structures*, Vol. 10, pp. 419–428.

Garofalo, F., 1965, *Fundamentals of Creep and Creep-rupture in Materials*, MacMillan, New York.

Ishikawa, H., Tsurui, A., and Kimura, H., 1987, "Stochastic Fatigue Crack Growth Model and Its Wide Applicability in Reliability-Based Design," *Statistical Research on Fatigue and Fracture* (Current Japanese Materials Research, Vol. 2) T. Tanaka, and M. Ichikawa, eds., Elsevier Applied Science, pp. 45–58.

Kitamura, T., and Ohtani, R., 1987, "Numerical Simulation of Microstructurally Short Crack Propagation in Creep," *Nippon Kikai Gakkai Ronbunshu A Hen* (*Trans. JSME*), Vol. 53, pp. 1064–1070, (in Japanese).

Kitamura, T., and Ohtani, R., 1989, "Creep Life Prediction Based on Stochastic Model of Microstructurally Short Crack Growth," *ASME Journal of Engineering Materials and Technology*, Vol. 111, pp. 169–175.

Kozin, F., and Bogdanoff, J. L., 1981, "A Critical Analysis of Some Probabilistic Models of Fatigue Crack Growth," *Engineering Fracture Mechanics*, Vol. 14, pp. 59–89.

Lin, Y. K., and Yang, J. N., 1983, "On Statistical Moments of Fatigue Crack Propagation," *Engineering Fracture Mechancis*, Vol. 18, pp. 243–256.

Ohtani, R., and Nakayama, S., 1983, "Growth and Distribution of Microcracks at the Surface of Smooth Specimen of 304 Stainless Steel in Creep and Effect of High Temperature Oxidation," *Zairyo* (*Journal for the Society of Material Science, Japan*), Vol. 32, pp. 635–639, (in Japanese).

Ohtani, R., and Nakayama, S., and Taira, T., 1984, "Applicability of Creep J-Integral to Microcrack Propagation of Creep in 304 Stainless Steel," *Zairyo* (*Journal for the Society of Material Science, Japan*), Vol. 33, pp. 590–595, (in Japanese).

Ohtani, R., and Kinami, T., and Sakamoto, H., 1986, "Small Crack Propagation in High Temperature Creep-Fatigue of 304 Stainless Steel," *Nippon Kikai Gakkai Ronbunshu A Hen* (*Trans. JSME*), Vol. 52, pp. 1824–1830, (in Japanese).

Ohtani, R., and Kitamura, T., 1987, "Crack Propagation Behavior and Fatigue Life Under Creep-fatigue Interaction Condition," *Role of Fracture Mechanics in Modern Technology*, G. C. Sih, G. C. and T. Ishihara, T., eds., North Holland, pp. 353–367.

Spencer, B. F., Jr., and Tang, J., 1988, "Stochastic Modeling of Fatigue Crack Growth," *Probabilistic Methods in Civil Engineering*, P. D. Spanos, ed., American Society of Civil Engineers, New York, pp. 25–28.

Taira, S., Fujino, M., and Yoshida, M., 1978, "Grain Boundary Sliding in Isothermal and Thermal Fatigue of 304 Stainless Steel," *Zairyo* (*Journal of the Society of Materials Science, Japan*), Vol. 27, pp. 447–453, (in Japanese).

Thoft-Christensen, P., and Baker, M. J., 1982, *Structural Reliability Theory and its Application*, Springer-Verlag, New York.

Virkler, D. A., Hillberry, B. M., and Goel, P. K., 1979, "The Statistical Nature of Fatigue Crack Propagation," *ASME Journal of Engineering Materials and Technology*, Vol. 101, pp. 148–152.

Yang, M. S., 1984, "Study of Grain Boundary Cavitation of High Purity Copper in High Temperature Fatigue and Creep," D. Phil. Thesis, Northwestern University, Chicago, IL.

APPENDIX

Predamage Effect on Crack Growth

The failure function ϕ_m of Eq. (4) with predamage is now expressed as

$$\phi_m = \phi_c - \phi_{oi} - \dot{\phi}_i(l,\sigma_g)t \tag{A1}$$

where $\dot{\phi}_i(l,\sigma_g)$ is the damage accumulation rate at boundary i when the crack is immediately adjacent to that particular boundary, t is the time elapsed after the crack reaches the particular grain boundary i, and ϕ_c is the critical damage needed for the grain-boundary failure. The function ϕ_{oi} is the damage accumulated at that grain boundary prior to becoming adjacent to the crack tip. In other words, ϕ_{oi} represents the damage

Downloaded 03 May 2010 to 171.66.16.247. Redistribution subject to ASME license or copyright; see http://www.asme.org/terms/Terms_Use.cfm

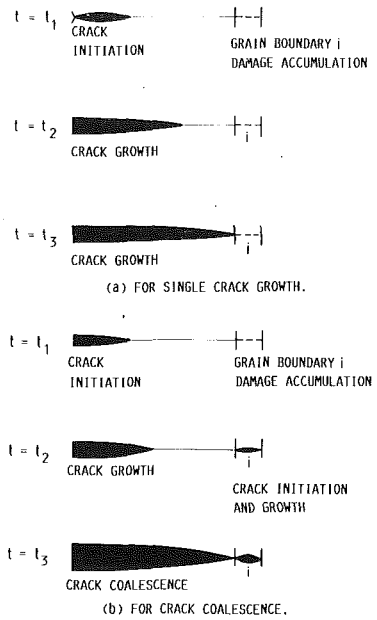


Fig. A1 Schematic views of crack-growth process, $t_1 < t_2 < t_3$; (*a*) for single crack growth and (*b*) for crack coalescence

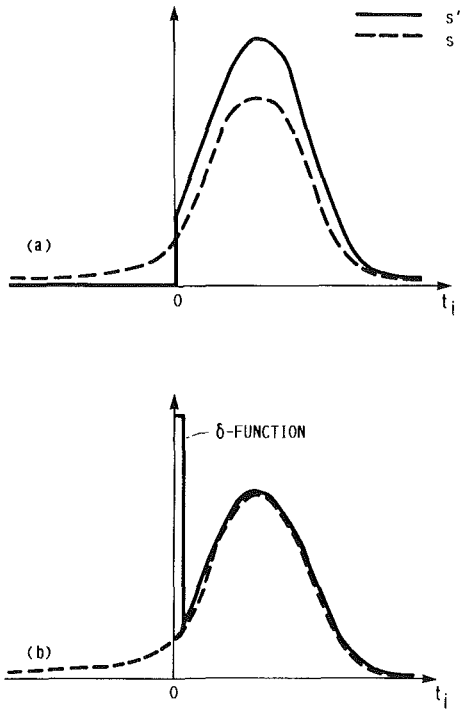
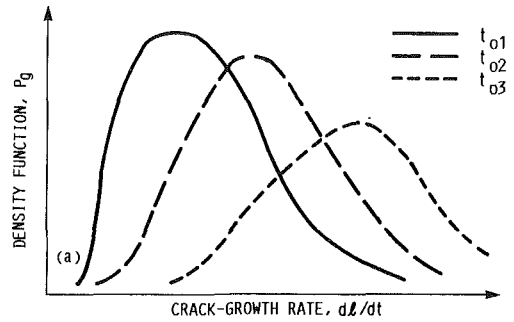


Fig. A2 Diagrams of $s(t_i)$ and $s'(t_i)$ density functions of the time interval t_i. The corrected density function, s', represents the impossibility of crack growth before $t_i = 0$; (*a*) for single crack growth and (*b*) for crack coalescence.

state of the grain boundary prior to its being located adjacent to the main crack. Assuming that the dominant crack affects only the adjacent grain boundary, the damage ϕ_{oi} can be expressed as a function of the damage accumulation rate:

$$\phi_{oi} = \dot{\phi}_i(\sigma_g, l=0) \sum_{j=0}^{j-1} t_j = \dot{\phi}_i(\sigma_g, l=0)\, t_o \tag{A2}$$

where t_j is the time interval for the crack to travel the entire length of grain boundary j. Summation of t_j is equal to the



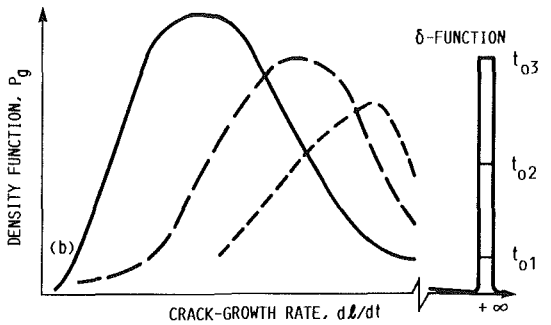


Fig. A3 Diagram of the density functions of the crack growth rate. Global stress, σ_g, constant; crack length, l, constant; predamage time, t_o; $t_{o1} < t_{o2} < t_{o3}$; (*a*) for single crack growth and (*b*) for crack coalescence.

total time t_o elapsed before the crack reaches the grain boundary i. The density $q(\phi_t)$ of $(\phi_{oi} + \dot{\phi}_i t)$ is given by:

$$q(\phi_t|\sigma_g,l,t,t_o) = \int_0^\infty h_{oi}\left(\frac{\phi_t - \dot{\phi}_i t}{t_o}, \dot{\phi}_i\right) \frac{1}{t_o}\, d\dot{\phi}_i \tag{A3}$$

where $h_{oi}(\dot{\phi}_i(\sigma_g, l=0), \dot{\phi}_i(\sigma_g, l))$ is the joint probability density of $\dot{\phi}_i(\sigma_g, l=0)$ and $\dot{\phi}_i(\sigma_g, l)$. The density function $m(\phi_m)$ of the failure function is therefore given by

$$m(\phi_m|\sigma_g,l,t,t_o) = \int_0^\infty g(\phi_m+\phi_t)\, q(\phi_t|\sigma_g,l,t,t_o)\, d\phi_t \tag{A4}$$

The cumulative probability function $S(t_i|\sigma_g,l,t_o)$ of the time interval required for the crack to travel the entire length of grain boundary i is given by

$$S(t_i|\sigma_g,l,t_o) = \int_{-\infty}^0 m(\phi_m,l,t_i,t_o)\, d\phi_m. \tag{A5}$$

The density function of the crack-growth rate dl/dt is given by Eq. (16) with $s(t_i|\sigma_g,l,t_o)$ being the derivative of Eq. (A5). However, a special constraint must be placed on the function $s(t_i)$. It is assumed that no crack growth occurs on a particular grain boundary unless that boundary is immediately adjacent to the main crack. Therefore, $s(t_i)$ for $t_i \le 0$ must be zero. The following two requirements are needed to satisfy the positive constraint on $s(t_i)$ for $t_i = 0$:

(1) The function ϕ_{oi} does not exceed ϕ_c at grain boundary i before the crack reaches that grain boundary.

(2) If ϕ_{oi} is greater than ϕ_c at grain boundary i, the boundary acts as a potential crack. The main crack instantaneously jumps to the next boundary, $i + 1$, when it reaches grain boundary i.

Case (1) is consistent with the assumption shown in Fig. A1(*a*) for a single crack growth. Case (2) gives future directions for handling crack coalescence for multiple crack growth (Fig.

Downloaded 03 May 2010 to 171.66.16.247. Redistribution subject to ASME license or copyright; see http://www.asme.org/terms/Terms_Use.cfm

A1(*b*)). The procedure for adjusting $s(t_i)$ to be always positive for case (1) is similar to the adjustment of the density function of strength after proof testing (Brent-Hall, 1988). The adjusted function, shown schematically in Fig. A2(*a*), is given by

$$s'(t_i|\sigma_g,l,t_o)=\begin{cases}0 & t_i\le 0\\ \dfrac{s(t_i)}{1-S(t_i=0)} & t_i>0\end{cases}. \tag{A6}$$

For case (2), the negative part of t_i is lumped in a delta function at 0^+ with a magnitude equal to $S(t_i)$. The adjusted density function is then given by

$$s'(t_i|\sigma_g,l,t_o)=\begin{cases}0 & t_i\le 0\\ s(t_i)+\delta(0^+)\,S(t_i=0) & t_i>0\end{cases} \tag{A7}$$

This relation is illustrated in Fig. A2(*b*). The density functions P_g, for cases (1) and (2), are schematically drawn in Fig. A3. For both cases, the crack growth accelerates as the historical time t_o increases. The infinite crack-growth rate, $dl/dt = \infty$ (Fig. A3(*b*)), corresponds to the coalescence of the main crack with a potential crack. Crack coalescence is an important phenomenon that can shorten creep life drastically. However, the exact solution is beyond the scope of this report because a multiple crack-growth model is required.

Downloaded 03 May 2010 to 171.66.16.247. Redistribution subject to ASME license or copyright; see http://www.asme.org/terms/Terms_Use.cfm

Thermal Stresses in Nonlinearly Viscoelastic Solids

Giancarlo U. Losi

Wolfgang G. Knauss
Fellow ASME.

Graduate Aeronautical Laboratories,
California Institute of Technology,
Pasadena, CA 91125

Three different rheological models are applied to the study of transient and residual thermal stresses in amorphous polymers cooled across the glass transition. The models differ mainly in their treatments of the nonequilibrium (time-dependent) portion of the morphological changes in the polymer and their influence on the relaxation process. The interstitial volume between polymer chains (free volume) is found to play an important role in the residual stresses; they are affected by the relative time scale of thermal diffusion and thermoviscoelastic relaxation/creep. This result has implications for injection molded parts of different section dimensions and for extrusion products. This fact must also be accounted for in determining the thermomechanical properties in the glass transition range. The step cooling of PVAc spheres (1 and 20 mm dia.) and a cylinder (20 mm dia.) have been considered; most of the results presented apply to the sphere(s). Residual stresses can vary by as much as 100 percent depending on whether the interstitial molecular (free) volume is counted or not. It is also demonstrated that residual stresses can be higher than an elastic analysis based on the glassy properties would suggest; thus the "stress-free temperature" is found to be significantly above the glass transition.

Introduction

The widespread application of polymers in engineering designs demands almost universally that structural parts be formed at elevated temperatures, and then be cooled below the glass transition temperature. Because of the associated heat flow and inhomogeneous temperature fields, these components develop residual stresses which can seriously affect their long term strength. These observations apply, for example, in the manufacture of bonded joints and composite materials with polymeric matrices, as well as in extruded and injection molded parts employed widely in many engineered projects. In this paper we address the problem of residual stress formation in polymers in terms of a newly developed constitutive law (Losi and Knauss, 1990) which incorporates specifically the polymer response in transit through the glass transition.

Previous investigations related to this topic (Morland and Lee, 1959; Muki and Sternberg, 1961) consider two fundamental issues only marginally, namely those of the time dependence of the coefficient of thermal expansion/contraction and the nature of the discontinuity in material properties across the glass transition. At the time of those initial investigations neither the background for these issues nor the requisite (super) computational power were available.

In order to relate the recent developments in thermoviscoelastic behavior to the residual stress problem we investigate the transient and residual thermal stress fields in an infinite cylinder and in a sphere for three constitutive models possessing different degrees of approximation, the relevant features of which we summarize here briefly:

- The "elementary" model, used in the literature mentioned above, accounts for the effects of temperature by allowing the thermal strains to be merely a function of temperature (and by explicitly subtracting them from the dilatational history). The coefficient of thermal expansion, α, is assumed to take on two different (time-independent) values on either side of the glass transition, and the standard time-temperature shifting governs the relaxation behavior for the whole temperature range in terms of the WLF equation, which is strictly applicable only above the glass transition.
- The "thermorheological" model considers α to be a time-dependent operator inverse to the time-dependent bulk modulus. The relaxation/creep behavior is governed by the scaling of internal time on the basis of free volume consideration, where the latter is affected additively by temperature and by the isotropic stress component. This model also accounts for the change of material properties in passing through the glass transition. This model is believed to represent the polymer behavior best on physical grounds.
- The "semi-elementary" model retains the notion of a rate-dependent operator for α, but replaces the scaling of the internal relaxation/retardation times by a shift factor, which is now a function of temperature only and which is derived from isothermal test data encompassing the glass transition. The shift factor differs thus from that rendered by the WLF equation below the glass transition (elementary model) because the latter is in disagreement with the experimental data in that

Contributed by the Applied Mechanics Division of THE AMERICAN SOCIETY OF MECHANICAL ENGINEERS for presentation at the Winter Annual Meeting, Atlanta, Ga., Dec. 1-6, 1991.

Discussion on this paper should be addressed to the Technical Editor, Prof. Leon M. Keer, The Technological Institute, Northwestern University, Evanston, IL 60208, and will be accepted until two months after final publication of the paper itself in the JOURNAL OF APPLIED MECHANICS. Manuscript received by the ASME Applied Mechanics Division, Oct. 16, 1990; final revision, May 24, 1991.
Paper No. 91-WA/APM-37.

Copyright © 1992 by ASME
Downloaded 03 May 2010 to 171.66.16.247. Redistribution subject to ASME license or copyright; see http://www.asme.org/terms/Terms_Use.cfm

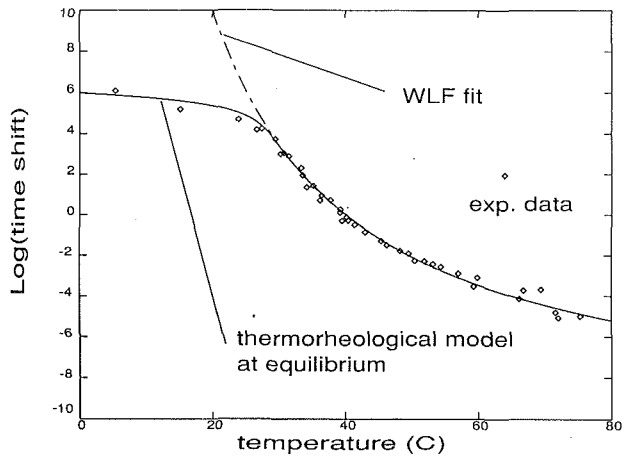


Fig. 1 Logarithm (base 10) of the experimental time shift for PVAc, referenced to 40°C (squares). The WLF fit to the experimental data is shown by the dashed line, while the representation of the thermorheological model at equilibrium is shown by the continuous curve.

temperature range. This model should thus represent an improvement over the elementary model.

The differences in the three constitutive models are apparent primarily when the material is far from its equilibrium state, as, for example, when the material still experiences viscoelastic relaxation and physical aging after thermal transients have settled. That situation occurs typically when a polymer is cooled rapidly across the glass transition. In the two cases of the sphere and the infinite cylinder, the differences in predictions of the three models are found to grow as the time scale of the thermal transients approaches, or becomes smaller than the time scale of viscoelastic relaxation. In that situation, mechanical relaxation is forced to follow and compete with thermal diffusion.

The Elementary Model

In order to examine the effect of different material models, and to compare their predictions with those based on the presumably "best" (thermorheological) model, two simpler material characterizations are also considered. The first of these models is similar to that employed by Muki and Sternberg (1961)[1] in which temperature effects reduce to the explicit subtraction of the thermal strains from the mechanical strain history, to give the stress-strain relation as

$$\sigma_{ij}=\int_{-\infty}^{t} 2G(\xi(t)-\xi(\tau))\frac{\partial\epsilon'_{ij}(\tau)}{\partial\tau}\,d\tau+\delta_{ij}\int_{-\infty}^{t} K(\xi(t)-\xi(\tau))\frac{\partial(\epsilon_{kk}-\epsilon_\theta)}{\partial\tau}\,d\tau. \quad (1)$$

Denoted, respectively, by α_l and α_g, the rubbery and glassy coefficients of thermal expansion, one uses

$$\frac{d\epsilon_\theta}{dT}=\alpha_l \text{ for } T>T_g$$
$$=\alpha_g \text{ for } T<T_g \quad (2)$$

with T_g denoting the glass transition temperature. Also,

$$\epsilon'_{ij}=\epsilon_{ij}-\frac{1}{3}\delta_{ij}\epsilon_{kk} \quad (3)$$

represents the deviatoric part of the strain tensor and $K(t)$ and $G(t)$ are the time-dependent bulk and shear moduli, approximated through Prony-Dirichlet series

$$K(t)=K_\infty+\sum_i K_i e^{-t/\tau_i} \text{ and } G(t)=G_\infty+\sum_j G_j e^{-t/\tau_j}.$$

[1]The original model used by Sternberg and Muki did not take into account a discontinuity in the heat capacity across the glass transition.

The quantity $\xi(t)$, defined by

$$\xi(t)=\int_0^t \frac{d\tau}{a_t[T(\tau)]}, \quad (4)$$

is the so-called internal time scale, related to the experimental time t through the (time-temperature) shift factor $a_t(T)$. In this elementary model we adopt, for $a_t(T)$, an empirical representation known as the WLF equation (Williams, Landel and Ferry, 1955) which well captures the change in the time scale of relaxation for amorphous polymers above their glass transition

$$\log(a_t)=\frac{c_1(T-T_0)}{c_2+T-T_0}, \quad (5)$$

where c_1, c_2, and T_0 are experimentally determined parameters. As shown in Fig. 1, the WLF representation diverges from the experimental results below the glass transition which occurs around 29°C for polyvinylacetate (PVAc), the material used in this study.

In this "elementary" model the glass transition temperature is considered to be constant (T_g = 29°C), and the coefficient of thermal expansion, as well as the heat capacity, are characterized by a discontinuity across T_g. The thermal strains are thus computed from

$$\frac{d\epsilon_\theta}{dT}=\alpha_l=6.0\times10^{-4}K^{-1} \quad \text{for } T>T_g=29°\text{C}$$
$$=\alpha_g=2.5\times10^{-4}K^{-1} \quad \text{for } T<T_g. \quad (6)$$

The Fourier law of heat conduction is written in the form[2]

$$\kappa\nabla^2T=\rho C_p\frac{dT}{dt}, \quad (7)$$

where the heat conductivity and the heat capacity are given by (Sandberg and Bäckström, 1980)

$$\kappa=.19\,\frac{\text{Watt}}{mK}, \quad (8)$$

$$\rho C_p=\rho C_{pl}=2.09\times10^6\frac{J}{m^3K} \text{ for } T>T_g,$$
$$=\rho C_{pg}=1.29\times10^6\frac{J}{m^3K} \text{ for } T<T_g. \quad (9)$$

In this and in the following models we consider the heat conductivity κ to be constant.

The Thermorheological Model

Before delineating the second of the simpler models we consider the thermorheological formulation, more extensively exposed in the reference by Losi and Knauss (1990a). We believe this model to be the physically most descriptive and realistic one, and thus treat the other two as approximations with the objective of evaluating the degree by which the simpler constitutive assumptions can approximate the thermorheological one.

Following thermodynamic arguments (e.g., Coleman, 1964), an expression for the stress tensor in terms of the deformation and temperature history derives in the form

$$\sigma_{ij}(t)=\int_{-\infty}^{t} 2G(\xi(t)-\xi(\tau))\frac{\partial\epsilon'_{ij}(\tau)}{\partial\tau}\,d\tau+\delta_{ij}\int_{-\infty}^{t} K(\xi(t)-\xi(\tau))\frac{\partial\epsilon_{kk}}{\partial\tau}\,d\tau-\delta_{ij}\int_{-\infty}^{t}\Theta(\xi(t)-\xi(\tau))\frac{\partial T}{\partial\tau}\,d\tau, \quad (10)$$

[2]The effect of material energy dissipation resulting from viscoelastic behavior is not taken into account in the energy equation of which the Fourier law of heat conduction is a simple form. The justification for this neglect derives from the fact that the model is restricted to small deformations; the dissipated energy, which is a quadratic function of the strains, is considered therefore to be very small compared to the other terms of the energy equation such as the change in the internal energy of the material.

Downloaded 03 May 2010 to 171.66.16.247. Redistribution subject to ASME license or copyright; see http://www.asme.org/terms/Terms_Use.cfm

where $\Theta(t)$ is a (possibly) time-dependent material function which accounts for the effects of temperature on the stress state. Upon postulating a time-dependent coefficient of (isobaric) thermal expansion, through which the thermal strains are computed as

$$\epsilon_\theta(t) = \int_{-\infty}^{t} \alpha(\xi(t) - \xi(\tau)) \frac{\partial T}{\partial \tau}\, d\tau, \tag{11}$$

it follows that

$$\Theta(t) = \int_{-\infty}^{t} K(\xi(t) - \xi(\tau)) \frac{\partial \alpha}{\partial \tau}\, d\tau. \tag{12}$$

Because there exists no experimental information regarding $\Theta(t)$, we choose it to be a constant on the basis of the following reasoning (for more detail see Losi, 1989): The time-dependent response of a polymer is the result of short and long-range rearrangements of molecular chains associated with the global deformation. If all global volume deformation vanishes, one might expect that the local segmental molecular motions do not occur either. Thus, if all volumetric deformation vanishes, only the thermal agitation of the molecules is excited to produce pressure changes. By contrast, if the pressure were kept constant, say zero, while the polymer is heated suddenly and homogeneously, one would expect long-range molecular motion and a consequential time-dependent thermal expansion. While the argumentation to set $\Theta(t)$ to be a constant is not unequivocal, it appears reasonable in view of the total absence of experimental data.

If follows then that the effect of temperature on the stress and strain fields is determined through an equivalent, time-independent "thermal pressure" $\hat{p}(T)$, which is that pressure which would occur following a temperature change under isochoric deformation. This "thermal pressure" is considered to be linearly dependent on temperature across the glass transition and is therefore computed as the isotropic stress which can be evaluated in the rubbery regime as

$$\hat{p}(T)_{\text{equil}} = \hat{p}(T) = K_\infty \alpha_l \Delta T. \tag{13}$$

The constitutive equations are thus summarized as

$$\sigma_{ij} = -\delta_{ij}\hat{p}(T) + \int_{-\infty}^{t} 2G(\xi(t) - \xi(\tau)) \frac{\partial \epsilon'_{ij}(\tau)}{\partial \tau}\, d\tau + \delta_{ij} \int_{-\infty}^{t} K(\xi(t) - \xi(\tau)) \frac{\partial \epsilon_{kk}}{\partial \tau}\, d\tau \tag{14}$$

where, for reason of clarity, we emphasize that ϵ_{kk} is the total dilatation, inclusive of the thermal expansion/contraction. The inversion of the isotropic component of Eq. (14) yields an explicit expression for the volume change, namely

$$\epsilon_{kk}(t) = \frac{1}{3} \int_{-\infty}^{t} M(\xi(t) - \xi(\tau)) \frac{\partial [\hat{p}(\tau) + \sigma_{kk}(\tau)]}{\partial \tau}\, d\tau, \tag{15}$$

$M(t)$ being the viscoelastic bulk compliance, related to the bulk modulus through

$$\int_{-\infty}^{t} K(t-\tau) M(\tau)\, d\tau = t. \tag{16}$$

In the absence of external pressurization ($\sigma_{kk} = 0$) accompanying a sudden temperature jump ΔT, the constitutive model thus predicts $\epsilon_{kk} = [K_\infty \alpha_l \Delta T] M(t)$, and therefore a time-dependent thermal expansion.

We now focus attention on the effect of temperature on the time scale of the relaxation process. In the elementary model, the internal time was governed by a time shift factor $a_t(T)$ which depends on temperature only. We generalize this concept by considering the shift factor a_t not to be a direct function of temperature, but rather to depend on the amount of vacancies (disorder, voids) present in the polymer, which can be quantified trough the fractional free volume content f. Such dependence is written phenomenologically in the form (Doolittle, 1951)

$$\log(a_t) = B\left(\frac{1}{f} - \frac{1}{f_0}\right) \tag{17}$$

where B is a material parameter and f_0 is the fractional free volume (reference free volume) corresponding to the state of the polymer in which the time-dependent viscoelastic moduli were measured. We assert specifically that the validity of Eq. (17) spans across the glass transition, with the fractional free volume f allowed to change under the influence of an isotropic stress and temperature variation. The fractional free volume increments are taken to be some fraction of the total dilatation so that

$$f(t) = f_{\text{init}} + \int_0^t \delta(f(\tau))\, d\epsilon_{kk}(\tau), \tag{18}$$

where f_{init} is the free volume content in the initial, unperturbed state and ϵ_{kk} is given by Eq. (15). Thus, the stress state affects the free volume changes, inducing a coupling between the local pressure and the local relaxation process (in shear and in bulk), which coupling is absent in linearly viscoelastic behavior.

The factor δ in Eq. (18) has been determined to depend on the fractional free volume in the form (Losi and Knauss, 1990a)

$$\delta(f) = \frac{\beta_{f_0}\phi(f)}{1 + \beta_{f_0}\phi(f)} \tag{19}$$

where β_{f_0} is the ratio between free and occupied volume changes (relative compliances) above the glass transition. That ratio is obtainable from experimental data as (Losi and Knauss, 1990)

$$\beta_{f_0} = \frac{\Delta V_{\text{free}}}{\Delta V_{\text{occupied}}} = \left[\frac{\alpha_l}{\alpha_g} - 1 - \sum_i \frac{K_i}{K_\infty}\right]$$

and has the value of about .63 for polyvinylacetate. The function $\phi(f)$, which appears in the definition of $\delta(f)$, is obtained from a stochastic analysis of the viscoelastic process and is defined as

$$\phi(f) = \frac{1}{1 - \frac{A}{2}\exp\left(\frac{B}{f} - \frac{B}{f_0}\right)\left[1 - \frac{B}{f}\right]}, \tag{20}$$

where the only "free" parameter is the variable A, which is proportional to the amplitude of the stochastic variations of the volume of the vacancies (Losi and Knauss, 1990a) the value of A can be inferred from time-temperature shift data, as those shown in Fig. 1, which data, given the values of the reference fractional free volume at 40°C, $f_0 = 0.0095$, and of the parameter $B = 0.10$, lead to $A \sim 2 \times 10^{-6}$ for PVAc.

The function $\phi(f)$ is very close to unity well above the glass transition ("large" values of f) and approximately zero well below it ("small" values of f). An additional difference, with respect to the elementary model, is the change in the time-independent part of the volumeteric response resulting from the freezing-in of the free volume sites, so that the effective time-independent component of the bulk modulus, below the glass transition, is given by

$$\hat{K}_\infty = K_\infty \frac{1 + \beta_{f_0}}{1 + \beta_{f_0}\phi(f)} \tag{21}$$

with K_∞ the long-time or rubbery component of the bulk modulus above the transition. The time-temperature shift factor for the thermorheological model at equilibrium (infinitesimally small cooling rate) is shown in Fig. 1 by the continuous line.

The coefficient of heat capacity possesses a discontinuity at the glass transition, but the glass transition itself is considered to occur at a critical value of fractional free volume (rather than at a prescribed temperature), resulting in a pressure and rate-dependent transition temperature. That critical value of fractional free volume is set to be 0.65 percent (Losi and Knauss,

Downloaded 03 May 2010 to 171.66.16.247. Redistribution subject to ASME license or copyright; see http://www.asme.org/terms/Terms_Use.cfm

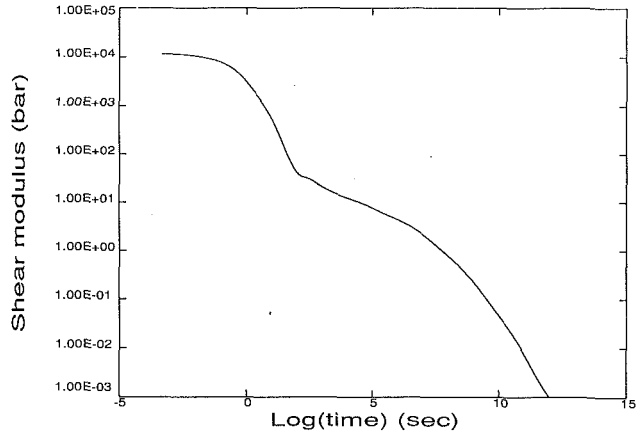


Fig. 2 Shear modulus of PVAc, referenced to 40°C

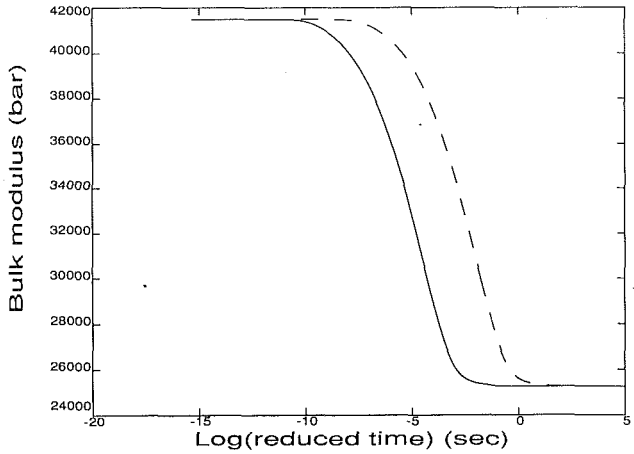


Fig. 3 Bulk modulus of PVAc, referenced to T_{ref} = 40°C. The "modified" modulus is shown by the dashed curve.

1990a), corresponding to a glass transition temperature of 29°C for an infinitesimally small rate of cooling at atmospheric pressure. The transition is assumed to be of second order, i.e., there is no finite jump in the equilibrium entropy, and the coefficient of heat conduction is kept constant.

The Semi-Elementary Model

Recall that the thermorheological model allows for a time and temperature-dependent response of the material which accounts for the coupling between time-dependent volume and shear creep/relaxation as well as temperature. Thus, different rates of cooling will result in different thermomechanical responses. Figure 1 illustrates the special case for very slow thermal changes (nearly "equilibrium" response). For different thermal and pressure changes different "shift factors" could result.[3] However, it is of interest to investigate the possible approximations for which one assumes that the experimental data (or solid curve) in Fig. 1 determines the time-temperature shifting. In that case the stress state (in particular the dilatational component) has no influence on the internal time scale of the material. We call the material model semi-elementary when it retains all the features of the thermorheological one, such as the discontinuity in the heat capacities and the dependence of the glass transition on pressure, except that the time shift is governed by the (experimental) equilibrium shift factor under exclusion of free volume changes resulting from the local state of stress.

Two Thermal Stress Problems

We consider the two example geometries of an infinite circular cylinder in plane strain (all axial gradients vanish) and that of a sphere. Both are subjected on their surfaces to a sudden temperature drop from above to below the glass transition. The properties of polyvinylacetate (PVAc) are used in the analysis. The shear modulus, shown in Fig. 2, was obtained from the creep compliance as measured by Heymans (1983), while the time-dependent bulk modulus was extracted from data by McKinney and Belcher (1963) and is shown in Fig. 3. The bulk modulus is found to possess an unexplained short time scale and an unusually low glass transition temperature of 17°C is also reported for these measurements. We shall use McKinney and Belcher's data for the studies of residual stresses; however, when we turn later to the examination of time-dependent volume shrinkage, for demonstration purposes we shall employ the same bulk function but in keeping with a significantly higher transition temperature, we shift the time response two and half decades towards longer relaxation times.[4] This latter function is then designated the "modified" bulk modulus.

The constitutive models were implemented in a finite element code, FEAP,[5] which was modified to accommodate materials with nonlinearly viscoelastic properties (cf. Taylor et al., 1981). Since the thermal diffusion problem had to be addressed concurrently, the numerical code was structured so that it solved the two problems separately and then iterated the solution until convergence was obtained for each time step. This method is numerically more convenient than addressing the two problems simultaneously. The thermal problem was solved using a three-step method, known as Gear's method with an averaged Crank-Nicolson start, which is well suited to address integration of parabolic equations with discontinuous initial boundary conditions (cf. Wood and Lewis, 1975).

In the two example cases, the circular cylinder and the sphere both with 2-cm radius, experience a sudden temperature drop at the surface from +60 to −5°C ($T_g \sim +29$°C). However, for brevity of presentation we report here, with one graphical exception, only the results for the sphere. The full comparisons are given in the reference by Losi and Knauss (1990b). The following presentation pursues a double purpose: On the one hand, we delineate the evolution of the stress field for a given cooling history; on the other hand, we compare the predictions of the thermorheological model and its approximations. For the first purpose we show the stress distribution at various times, while for the second one, we present the stress history at different locations; these are demonstrated in Figs. 4 through 9. Results for the cylinder that are not shown here are also similar.

With regard to the features of the transient and residual stress fields, these figures show that initially tensile stresses build up near the surface of the sphere (and of the cylinder) later evolving into compressive stresses as the temperature field abates. The evolution of the long-term residual stresses is the result of early solidification of the "outer shell" of material, inside of which the then still soft core contracts as the temperature drops to the final uniform distribution. The stress distributions differ remarkably from those in the same elastic geometries. An elastic rod in plane strain develops an axial stress $\sigma_{zz} = (1/3)E\alpha\Delta T$, E and α being Young's modulus and the volumetric coefficient of thermal expansion, respectively, and all other stress components vanish, an elastic sphere would be uniformly stress-free. We note that in the viscoelastic cyl-

[3]Due to the inherent dependence on thermal and mechanical histories, there is no uniquely defined shift factor below T_g.

[4]All the relaxation times were thus multiplied by $10^{2.5} = 3.13$.

[5]This code was originally devised by R. J. Taylor of U. C. Berkeley and made available to our research group through the courtesy of Dr. Ravichandran of Brown University.

Downloaded 03 May 2010 to 171.66.16.247. Redistribution subject to ASME license or copyright; see http://www.asme.org/terms/Terms_Use.cfm

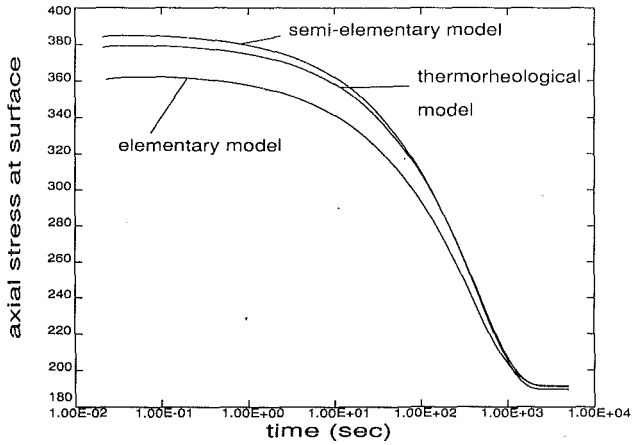


Fig. 4 Axial stress in the infinite cylinder of a 2-cm radius, cooled from +60 to −5°C (thermorheological model)

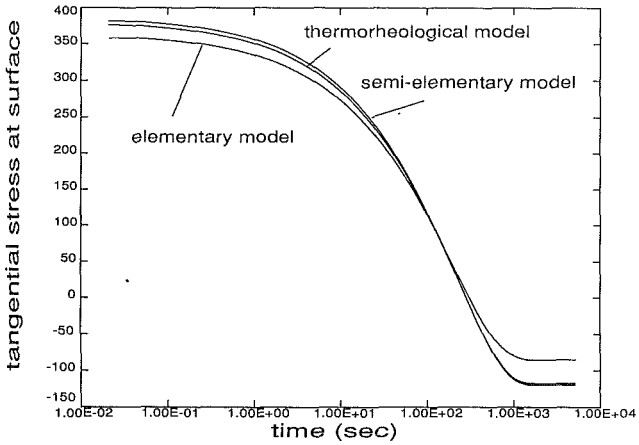


Fig. 7 Comparison of the three model predictions for the tangential stress at the surface of the sphere of 2-cm radius

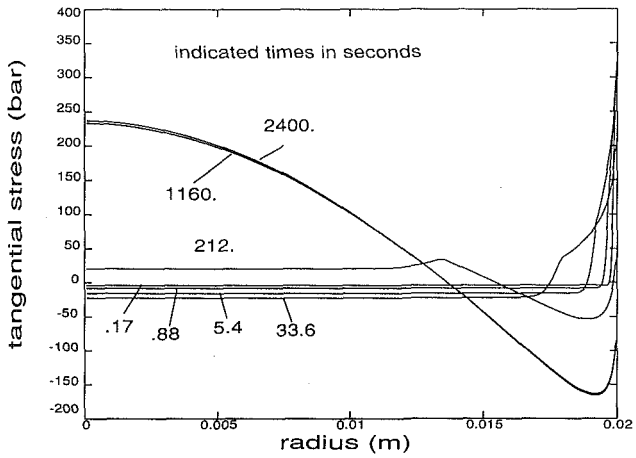


Fig. 5 Tangential stress in the sphere of 2-cm radius, cooled from +60 to −5°C (elementary model)

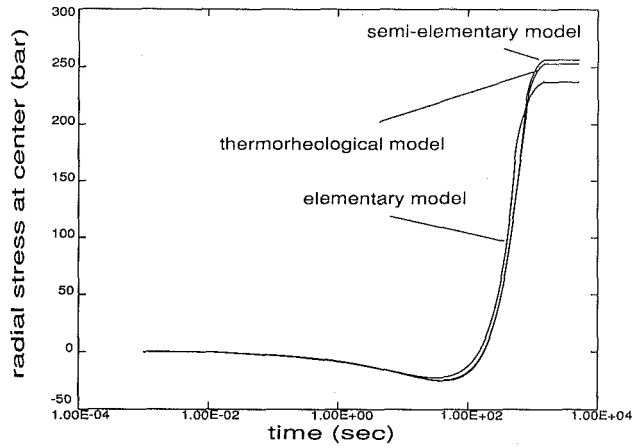


Fig. 8 Comparison of the three model predictions for the radial stress at the center of the sphere of 2-cm radius

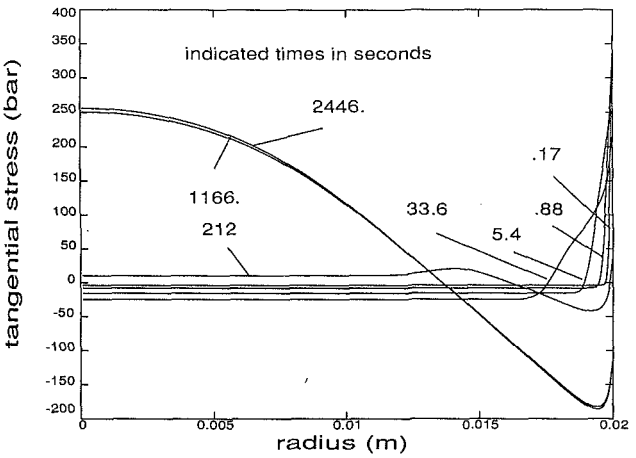


Fig. 6 Tangential stress in the sphere of 2-cm radius, cooled from +60 to −5°C (thermorheological model)

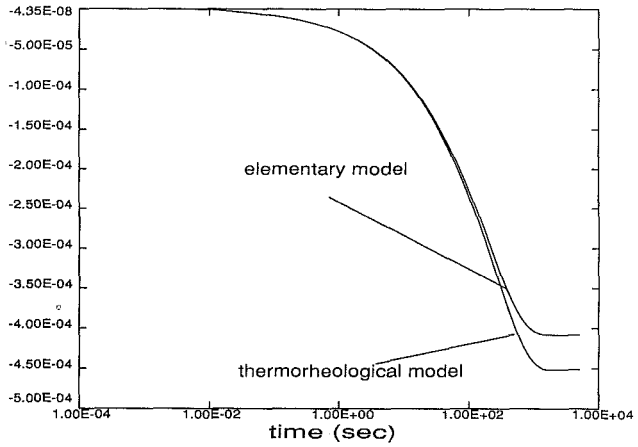


Fig. 9 Reduced volume contraction ($\Delta V/[V\,|T_{initial} - T_{final}|]$) of the PVAc sphere of 2-cm radius, cooled from +60 to −5°C (the semi-elementary model renders the same results as the thermorheological model)

inder (thermorheological description) the maximum axial stress achieves 260 bars, while the average residual stress is approximately 160 bars. This average stress translates, with $E = E(0) \sim 32000$ bars and $\alpha = \alpha_g$, into a stress-free temperature of 55°C, not far from the initial one and well above T_g. Thus, the often-practiced assumption that the stress-free temperature is the glass transition temperature is definitely nonconservative.

We now turn our attention to the differences in the predictions of the three material models. As is evident from Fig. 5, the elementary model produces a moving discontinuity in the gradient of the stress distribution, which discontinuity occurs where the material is passing through the glass transition. This "cusp" derives from the jump in the coefficient of thermal expansion across the glass transition and is particularly noticeable in the tangential stress field; it is noticeably smoothed by the thermorheological model (cf. Fig. 6). This qualitative difference is less evident in the radial and axial (for the cylinder case) stresses not shown for the elementary and semi-elementary models.

Downloaded 03 May 2010 to 171.66.16.247. Redistribution subject to ASME license or copyright; see http://www.asme.org/terms/Terms_Use.cfm

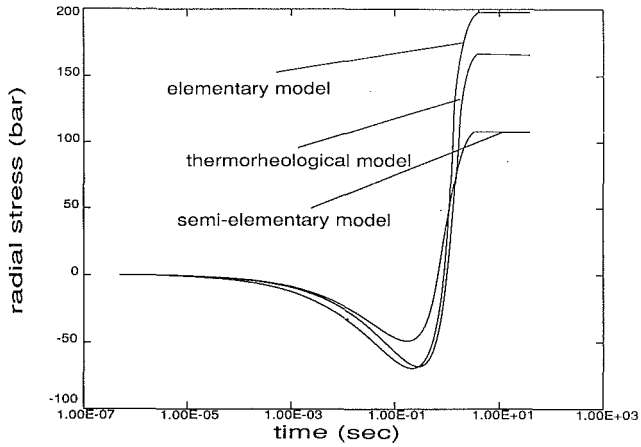


Fig. 10 Predictions for the radial stress at the center of the sphere of 1-mm radius, cooled from +60 to −5°C ("modified" bulk modulus)

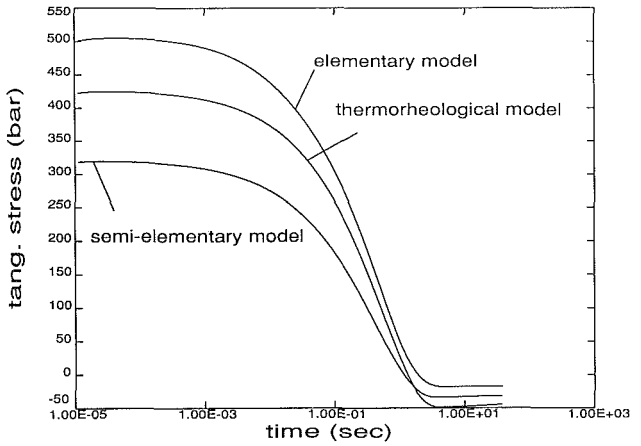


Fig. 11 Predictions for the tangential stress at the surface of the sphere of 1-mm radius, cooled from +60 to −5°C ("modified" bulk modulus)

Considering more quantitative differences, one notes that the three material descriptions particularly differ where the time scale of the local thermal transients is shortest. As shown by Fig. 8, the differences in the radial stress at the center of the sphere, where the temperature drop is slowest, are initially negligible, and result in less than seven or six percent variations in the residual stress. In contrast, differences are larger at the surface (cf. Fig. 7) where the thermal transients in the outer material shell closely follow the initial, instantaneous drop in surface temperature. The residual stress differences result to be around 30 to 35 percent, with the elementary model significantly underestimating the residual compressive stress while the semi-elementary model is in closer agreement with the thermorheological one.

In comparing the effects of the three material models, it may seem surprising that the final differences are not larger. The primary reason for this result is that, in most of the temperature range considered, the time scale of thermal transients in geometries of these particular sizes is large in comparison to the bulk relaxation times of the polymer, which makes the relaxation/creep phenomenon to occur in a quasi-equilibrium situation.

In order to illustrate this point we also considered the case of the sphere of only 1-mm radius and, in addition to thus shortening the thermal transients, we used the "modified" (cf. Fig. 3) bulk modulus. The time histories for the two stress components are illustrated in Figs. 10 and 11, and it is clear that now the final stresses differ considerably more for the three models than for the earlier case. Moreover, even though the change in surface temperature is the same as for the larger

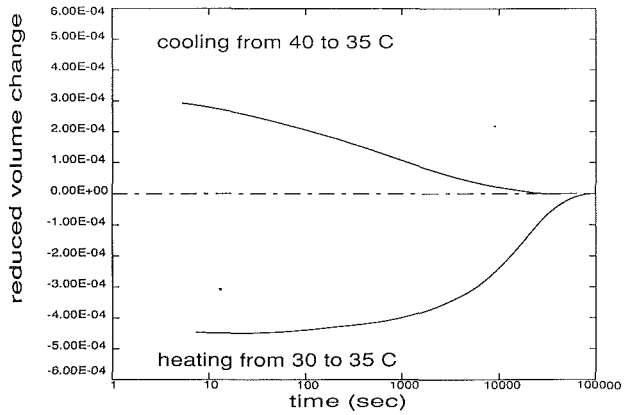


Fig. 12 Reduced volume change $V - V_\infty/V_\infty|\Delta T|$ of PVAc, plotted versus time; data obtained by Kovacs (1963)

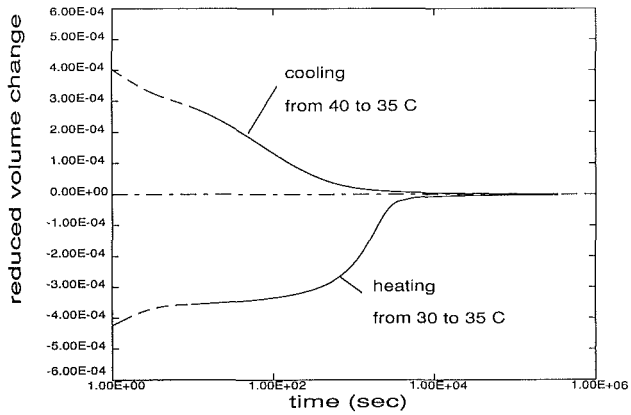


Fig. 13 Reduced volume change $V - V_\infty/V_\infty|\Delta T|$ for the sphere of 1-mm radius, cooled from 40 to 35°C and heated from 30 to 35°C (thermorheological model, "modified" bulk modulus)

sphere, the final stress state is different: Both the radial stress at the center and the tangential stress at the surface are significantly lower for the smaller sphere.

Time-Dependent Volume Change

More than 30 years ago Kovacs measured the volume contraction and expansion of PVAc across the glass transition. Figure 12 illustrates some of Kovacs's (1958) results for which a specimen (of unspecified dimensions) was either cooled or heated by 5°C through immersion at a final temperature just above the glass transition. A typical asymmetric response resulted for the heating and cooling experiments. In conjunction with examining that data in light of the free volume theory (thermorheological model), the question arose whether the rate of volume contraction is a functional of the dilatational stress. We have simulated Kovacs's experiment, assuming sudden heating and cooling, for the sphere of 1-mm radius, employing the "modified" bulk properties. Figure 13 shows the result of that computation, where those portions of the response that could not reasonably be expected to be experimentally observable have been drawn dashed. The similarity[6] of the asymptotic response is obvious. In order to illustrate the influence of the nonequilibrium behavior of the thermorheological model, we have also computed the same response for the sphere of 1-mm radius with the unchanged bulk modulus as in Fig. 3. Because of the fast bulk relaxation and comparatively slow cooling in that case, the volume change of the sphere, shown in Fig. 14, exhibits nearly symmetric response for the heating

[6]The PVAc used by Kovacs was Mowilit, manufactured by Höchst. The precise properties of that compound are not available, so that closer comparison of Kovacs's data and the computation is not reasonable.

Downloaded 03 May 2010 to 171.66.16.247. Redistribution subject to ASME license or copyright; see http://www.asme.org/terms/Terms_Use.cfm

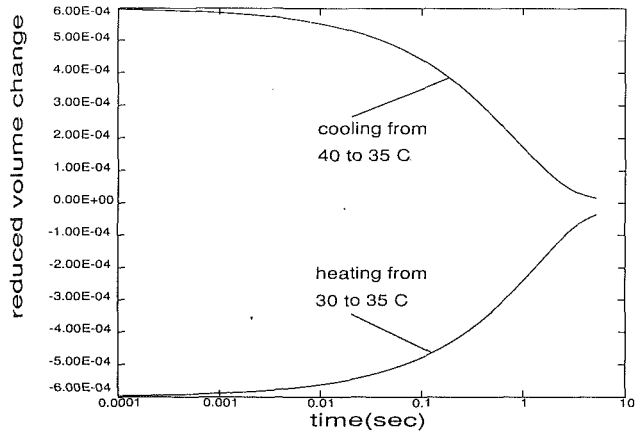


Fig. 14 Reduced volume change $V - V_\infty/V_\infty|\Delta T|$ for the sphere of 1-mm radius, cooled from 40°C and heated from 30°C to a final temperature of 35°C (thermorheological model, McKinney's and Belcher's bulk modulus)

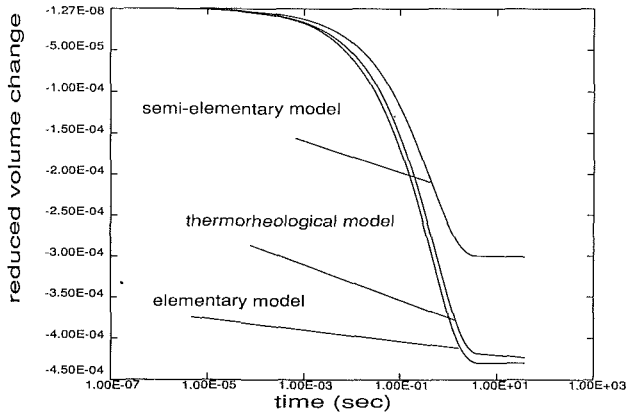


Fig. 15 Reduced volume change $V - V_\infty/V_\infty|\Delta T|$ of the sphere of 1-mm radius, cooled from +60 to −5°C ("modified" bulk modulus)

and cooling processes. Finally, it is of interest to emphasize that the models can produce measurably different volume responses because the effect of the transient dilatational stress on the shear relaxation cannot necessarily be neglected. Figure 15 shows that in a 65°C jump across the glass transition, sizable differences may result in the time-dependent volume of the shrinking sphere. These latter observations impact the interpretation of dilatometric measurements near and across the glass transition range.

Conclusions

The problem of transient and residual thermal stresses in a nonlinearly viscoelastic material has been considered in the context of a thermorheological (free-volume) model and two approximations. The thermorheological model explicitly addresses the effect of time-dependent dilatational changes on the relaxation behavior across the glass transition, and is thus sensitive to how far the material is from thermomechanical equilibrium. In passing through the glass transition, the size of the geometry is inseparably linked with the transient and residual stresses since the time scale of the thermal transients competes with the (dilatation/stress-dependent) relaxation process. Moreover, it has been shown that residual stresses can take on magnitudes which are possibly on the order of those which can cause long-term failure. Under such a scenario it is important to recognize that deviation on the order of 100 percent rendered by the three models is an important difference, and that long-term failure analysis requires more careful modeling tools than have been available to date. In the same vein it is important to recognize that assuming the glass temperature to be the temperature from which residual stresses should be reckoned may not be correct, nor conservative. Differences arising out of the uncertainty in the relaxation behavior of the bulk modulus point to the need for a concerted effort of measuring this quantity if a better understanding of the residual stresses in polymeric structures is to emerge.

Acknowledgments

This study was supported in part by the Office of Naval Research, under grant N00014-84-K-0424, and in part by Caltech's Program on Advanced Technologies, sponsored by Aerojet General, General Motors and TRW. We also want to thank the San Diego Supercomputer Center for providing access to the computational facilities.

References

Cohen, M. H., and Turnbull, D., 1959, "Molecular Transport in Liquids and Glasses," *Journal of Chemical Physics*, Vol. 31, pp. 1164–1169.

Coleman, B. D., 1964, "Thermodynamics of Materials with Memory," *Archive for Rational Mechanics and Analysis*, Vol. 17, pp. 1–46.

Doolittle, A. K., 1951, "Studies in Newtonian Flow. I. The Dependence of the Viscosity of Liquids on Temperature," *Journal of Applied Physics*, Vol. 22, No. 8, pp. 1031–1035.

Doolittle, A. K., 1951, "Studies in Newtonian Flow. II. The Dependence of the Viscosity of Liquids on Free-Space," *Journal of Applied Physics*, Vol. 22, No. 12, pp. 1471–1475.

Heymans, L., 1983, "An Engineering Analysis of Polymer Film Adhesion to Rigid Substrates," Ph.D. Thesis, California Institute of Technology.

Kovacs, A. J., 1958, "La Contraction Isotherme du Volume des Polymères Amorphes," *Journal of Polymer Science*, Vol. 30, pp. 131–147.

Kovacs, A. J., 1963, "Transition Vitrense dans les Polymères Amorphes," *Fortschr. Hochpolym.-Forsch*, Vol. 3, pp. 394–507.

Losi, G. U., 1989, "Nonlinear Thermoviscoelastic Behavior of Polymers," Ph.D. Thesis, GALCIT Report SM89-7, California Institute of Technology, Pasadena, Calif., Sept.

Losi, G. U., and Knauss, W. G., 1990, "Thermal Stresses in Nonlinearly Viscoelastic Solids: Cylinder and Sphere Results," GALCIT Report SM90-16, California Institute of Technology, Pasadena, Calif., Oct.

Losi, G. U., and Knauss, W. G., 1992, "Free Volume Theory and Nonlinear Thermoviscoelasticity" *Polymer Engineering and Science*, in press.

McKinney, J. E., and Belcher, H. V., 1963, "Dynamic Compressibility of Poly(vinyl acetate) and Its Relation to Free Volume," *Journal of Research of the National Bureau of Standards*, Vol. 67A, pp. 43–53.

Morland, L. W., and Lee, E. H., 1960, "Stress Analysis for Linearly Viscoelastic Materials with Temperature Variations," *Transactions of the Society of Rheology*, Vol. 4, pp. 233–263.

Muki, R., and Sternberg, E., 1961, "On Transient Thermal Stresses in Viscoelastic Materials with Temperature Dependent Properties," ASME JOURNAL OF APPLIED MECHANICS, Vol. 28, pp. 193–207.

Sandberg, O., and Bäckström, G., 1980, "Thermal Conductivity and Heat Capacity of Liquid and Glassy Poly(vinyl acetate) under pressure," *Journal of Polymer Science*, Polymer Physics Edition, Vol. 18, pp. 2123–2133.

Taylor, R. L., Pister, K. L., and Goudreau, G. L., 1970, "Thermomechanical Analysis of Viscoelastic Solids," *International Journal for Numerical Methods in Engineering*, Vol. 2, pp. 45–59.

Williams, M. L., Landel, R. F., and Ferry, J. D., 1955, "The Temperature Dependence of Relaxation Mechanisms in Amorphous Polymers and Other Glass-forming Liquids," *Journal of the American Chemical Society*, Vol. 77, pp. 3701–3706.

Wood, L. W., and Lewis, R. W., 1975, "A Comparison of Time Marching Schemes for the Transient Heat Conduction Equation," *International Journal for Numerical Methods in Engineering*, Vol. 9, pp. 679–689.

Downloaded 03 May 2010 to 171.66.16.247. Redistribution subject to ASME license or copyright; see http://www.asme.org/terms/Terms_Use.cfm

An Evaluation of the Neuber and Glinka Relations for Monotonic Loading

W. N. Sharpe, Jr.
Fellow ASME.

C. H. Yang

R. L. Tregoning

Department of Mechanical Engineering,
The Johns Hopkins University,
Baltimore, MD 21218

The Neuber relation is widely used to compute elastoplastic stresses and strains at stress concentrations, but a newer relation has been developed by Glinka. Prediction of local strain response is important because low cycle, fatigue life models are based on the strain range. The effects of notch root constraint on the response have been difficult to predict or measure. This paper evaluates the abilities of six models of notch root behavior by comparing them with experimental results over a range of constraints. The models are: the Neuber model, the Neuber model as modified by Walker, the Glinka models for plane stress and for plane strain, and two modifications of the Glinka models that are presented in this paper. Comparisons are made with strains measured at the roots of notches by resistance gages or by laser-based interferometry; data come from previous works as well as some new results of the authors. The constraints vary from plane stress to plane strain with several intermediate cases. Conclusions must take into account the fact that elastoplastic strain measurements have scatter arising from the gage length relative to the grain size. But, in general, one can say that the Neuber model is best for plane stress and the Glinka plane-strain model is best for very large constraint. Response for intermediate amounts of constraint are predicted better by one of the other models.

1 Introduction

Failures of components and structures usually start at stress concentrations, and therefore it is important to be able to compute the local stresses and strains. This is straightforward if the local response is elastic, and the predictions can be compared with experimental results obtained by photoelasticity or resistance strain gages. The classic handbook by Peterson (1974) is a starting point for the designer in this case. But if the local response is elastoplastic, both the computations and the experimental verifications are much more difficult.

This paper evaluates simple models for predicting elastoplastic stresses and strains at notch roots subjected to monotonic loading by comparing the predicted strains with measured ones. For both the models and the measurements, previous works are used as well as recent work by the authors. Simple models of notch root behavior are needed to enable the designer to make a quick evaluation which may then be studied more carefully by finite element methods and/or experimentation if warranted.

Although monotonic response is the subject of this paper, a major use of the results would be for the prediction of fatigue life. Fatigue failures initiate at stress concentrations, and the life models are based on the stress range if the life is long and the strain range if the life is short. Long life generally requires elastic local behavior, and elastoplastic local behavior leads to short lives, i.e., low-cycle fatigue. The results of this paper are more useful in the latter case.

The most widely used model is the Neuber relation (Neuber, 1961) which is included in textbooks and incorporated into codes (ASME, 1980). A more recent model has been developed (Molski and Glinka, 1981; Glinka et al., 1988) for both plane stress and plane strain loading. These models are reviewed in the background section. The authors have extended the Glinka model to both constant strain-ratio and constant stress-ratio to accommodate situations intermediate between plane stress and plane strain; these are presented in the modified Glinka relation section.

The emphasis in this paper is not on experimental techniques but on the comparisons of results with predictions; those are presented in the comparison with experimental results section. The experimental techniques fall into two classes—those using resistance strain gages and those using a laser-based technique with a very short gage length. Experimental results in the first class are taken from other researchers, while those using the laser-based system were obtained by the authors and their colleagues. These direct comparisons are the best test of a model, and conclusions are drawn from them.

Contributed by the ASME Applied Mechanics Division of THE AMERICAN SOCIETY OF MECHANICAL ENGINEERS for presentation at the Winter Annual Meeting, Atlanta, Ga., Dec. 1-6, 1991.

Discussion on this paper should be addressed to the Technical Editor, Prof. Leon M. Keer, The Technological Institute, Northwestern University, Evanston, IL 60208, and will be accepted until two months after final publication of the paper itself in the JOURNAL OF APPLIED MECHANICS. Manuscript received by the ASME Applied Mechanics Division, Oct. 16, 1990; final revision, May 24, 1991.
Paper No. 91-WA/APM-43.

Copyright © 1992 by ASME
Downloaded 03 May 2010 to 171.66.16.247. Redistribution subject to ASME license or copyright; see http://www.asme.org/terms/Terms_Use.cfm

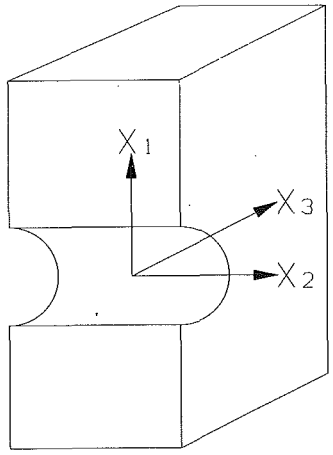


Fig. 1 Coordinate system. The origin is at the center of the notch root.

2 Background

In this paper, the coordinate system of Fig. 1 is used at the notch root. x_1 is in the direction of largest principal stress, x_2 lies on the surface, and x_3 is into the specimen. Considering only principal stresses and coincident strains, there are five unknowns at the notch root—σ_1, σ_2, ϵ_1, ϵ_2, ϵ_3. There are three elastoplastic constitutive equations available, and the other two equations must come from some assumption about constraint and from a simple model relating the remote loads to the local stresses.

The Neuber relation is the most widely used one for predicting local elastoplastic response; however, the more recent Glinka relation shows considerable promise. There are other approximate approaches (e.g., James et al., 1989), but only these two are considered here.

2.1 The Neuber Relation. Neuber's paper of 1961 (Neuber, 1961) analyzed notches with various flank angles subjected to shear; the nonlinear material response was represented by a simple equation. He found the local response to be independent of the flank angle and concluded that

$$K_\sigma \times K_\epsilon = K_t^2. \tag{1}$$

K_t is the elastic stress concentration factor which may be determined from analysis, experimental studies, or finite element techniques. K_σ is the stress concentration factor defined as the local stress, σ_1, divided by an average stress, S, and K_ϵ is the strain concentration factor defined as the local strain, ϵ_1, divided by an average strain, e. Rice (1968) has pointed out that this rule applies only in the case of small-scale yielding. Neuber's comment at the conclusion of his paper, "This rule may become really important for further stress-concentration research work." has turned out to be a classic understatement.

Although derived for shear, Neuber suggests that the rule may be valid for other stress states if effective stresses are used. Walker (1977) has indeed done just that and presents a scheme for accounting for constraint at the notch root. He assumes that the ratio of stresses at the surface of the notch root remains constant and uses this ratio to construct an effective stress versus plastic strain curve from the material's uniaxial-stress response. This stress-strain relation, along with a modulus of elasticity that is modified to account for the constraint, is then used in the Neuber relation.

The solution for σ and ϵ at a notch is found from the Neuber relation in combination with a constitutive equation, $\sigma = f(\epsilon)$. A very useful and widely applicable constitutive representation is that of Ramberg and Osgood, which is

$$\epsilon = \sigma/E + (\sigma/K)^{1/n} \tag{2}$$

where E, K, and n are material properties obtained from curve fits to the uniaxial stress-strain curve.

Combining Eqs. (1) and (2) gives the equation

$$S^2 K_t^2/E = \sigma_1^2/E + \sigma_1 (\sigma_1/K)^{1/n}. \tag{3}$$

Given the geometry, material properties, and the applied average stress, S, one solves, for the local stress, σ_1.

2.2 The Glinka Relation. Glinka developed a similar relation (Molski and Glinka, 1981) based on the assumption that the energy density at the notch root does not change significantly if the localized plasticity is surrounded by predominantly elastic material. In other words, computation of the local strain energy

$$W = \int_0^\epsilon \sigma(\epsilon) d\epsilon \tag{4}$$

will yield the same result for either the linear elastic or the elastoplastic constitutive law. Glinka (1985a) points out that this assumption is similar to the result of Hutchinson (1968) who found the strain energy density at a crack tip in a bilinear material to be exactly the same as that computed from the purely elastic solution. Later, Glinka (1988) verified the assumption with an elastoplastic finite element analysis.

For plane stress, Glinka computes the elastic energy density to be $\frac{1}{2E} S^2 K_t^2$ and equates it to the plastic energy density computed using the Ramberg-Osgood equation. The result is

$$S^2 K_t^2/E = \sigma_1^2/E + [2/(1+n)]\sigma_1(\sigma_1/K)^{1/n}. \tag{5}$$

The only difference from the Neuber relation of Eq. (3) is the factor $[2/(1+n)]$ in front of the last term. Since n in the Ramberg-Osgood equation is less than one, a smaller σ (and smaller ϵ) will be obtained for a given S than from the Neuber relation.

Glinka (1988) also developed a plane-strain version which assumes that ϵ_2/ϵ_1 remains zero throughout the deformation. The stress ratio σ_2/σ_1 does change, and this is computed from the plasticity equations (following a procedure by Dowling (1977)) by setting ϵ_2 equal zero and solving for the stress ratio. This is a curious approach in that it uses the deformation theory of plasticity (which assumes proportional stresses) to compute a changing stress ratio.

Another paper (Glinka, 1985b) corrects the strain energy density by a factor C_p which accounts for the increase in plastic zone size because of local yielding. This correction factor is analogous to the one introduced by Irwin (1968) into fracture mechanics in which the plastic zone size is increased to account for the fact that the stresses at the notch root cannot exceed the material's elastoplastic response. This factor must be incorporated into the calculations, but is important only at larger local deformations (e.g., strains greater than one percent).

In most of Glinka's papers, comparisons are made between his predicted notch strains and experimental results from other researchers. Based on those papers, one would conclude that the Glinka relation is more accurate than the Neuber relation.

3 Modified Glinka Relation

The Glinka relations have been developed for either plane stress or plane strain, but in practice there are many geometries and loadings with stress/strain states that are intermediate. With the widespread usage of elastic finite element programs, a designer can know the initial state at the notch root. The goal of this section is to present two approaches that enable calculations for intermediate stress/strain states. Recall that there are five unknowns at the notch root. However, only three constitutive equations plus one relation (to be developed) between remote load and the local state will be available. One

Downloaded 03 May 2010 to 171.66.16.247. Redistribution subject to ASME license or copyright; see http://www.asme.org/terms/Terms_Use.cfm

must therefore make one more assumption about the local stress/strain state. The choices are obvious—either assume that the ratio of stresses, σ_2/σ_1, or the ratio of strains, ϵ_2/ϵ_1, remain constant throughout the elastoplastic response.

3.1 Elastic Strain Energy Density. We make the following two definitions:

$$\beta = \sigma_2/\sigma_1;\ \alpha = \epsilon_2/\epsilon_1. \tag{6}$$

For an elastic state,

$$\alpha = \frac{\beta - \nu}{1 - \nu\beta};\ \beta = \frac{\alpha + \nu}{1 + \alpha\nu} \tag{7}$$

where ν is Poisson's ratio. Note that ν is taken as a positive value; α is negative and β is positive. The elastic strain energy density is

$$SED^e = \frac{K_t^2 S^2}{2E}\,(1 - 2\nu\beta + \beta^2) \tag{8}$$

where S is the remote stress and E is the elastic modulus of the material.

3.2 Constant Stress Ratio. The plane stress Glinka relation (Molski and Glinka, 1981) is quite straightforward; there is only one stress component, σ_1, and the stress ratio remains constant at zero throughout the deformation.

If we assume that β remains constant and use the J_2-deformation theory of plasticity, the plastic strain energy density is

$$SED^p = \int_0^{\sigma_1} \left(\frac{\sigma_1}{E} - \frac{\nu\beta\sigma_1}{E}\right) d\sigma_1 + \int_0^{\epsilon_p} \frac{\sigma_1}{\sigma_e}\,(\sigma_1 - 1/2\beta\sigma_1)\,d\epsilon_p$$

$$+ \int_0^{\sigma_1} \left(\frac{\beta^2\sigma_1}{E} - \frac{\nu\beta\sigma_1}{E}\right) d\sigma_1 + \int_0^{\epsilon_p} \frac{\sigma_1}{\sigma_e}\,(\beta\sigma_1 - 1/2\sigma_1)\,d\epsilon_p \tag{9}$$

where

$$\epsilon_p = f(\sigma_e);\ \sigma_e = \sigma_1(1 - \beta + \beta^2). \tag{10}$$

The equation $\epsilon_p = f(\sigma_e)$ is the relation between the plastic strain and the applied uniaxial stress in a tensile test. Completing the algebra and equating the strain energy densities yields

$$\frac{K_t^2 S^2}{2E} = \frac{\sigma_1^2}{2E} + \left(\frac{1 - \beta + \beta^2}{1 - 2\nu\beta + \beta^2}\right) \int_0^{\sigma_1} \frac{df}{d\sigma_e}\,\sigma_1 d\sigma_1. \tag{11}$$

If the material response is known through E, ν, and $f(\sigma_e)$ and the geometry is known through K_t and β, then Eq. (11) predicts the local σ_1 for a given applied stress S. The rest of the stress/strain state follows from the elastoplasticity equations.

3.3 Constant Strain Ratio. A constant strain ratio implies that the stress ratio changes as the component is loaded; the incremental theory of plasticity must then be used. The approach here is to compute the stress ratio required to hold the strain ratio constant for a small increment of load. The stresses and strains for each small increment are therefore known and can be used to compute the elastoplastic strain energy density. When the sum of the elastoplastic strain energy density matches the elastic strain energy density for an applied load (calculated from Eq. (8)), then a solution has been found.

The incremental equations of the J_2-theory of plasticity are

$$\Delta\epsilon_1 = \frac{\Delta\sigma_1}{E} - \frac{\nu\Delta\sigma_2}{E} + \frac{\Delta\epsilon_p}{\sigma_e}\,(\sigma_1 - 1/2\sigma_2)$$

$$\Delta\epsilon_2 = \frac{\Delta\sigma_2}{E} - \frac{\nu\Delta\sigma_1}{E} + \frac{\Delta\epsilon_p}{\sigma_e}\,(\sigma_2 - 1/2\sigma_1). \tag{12}$$

The increment in effective plastic strain, $\Delta\epsilon_p$, is for small increments

$$\Delta\epsilon_p = \frac{df}{d\sigma_e}\left[\left(\frac{\sigma_1 - 1/2\sigma_2}{\sigma_e}\right)\Delta\sigma_1 + \left(\frac{\sigma_2 - 1/2\sigma_1}{\sigma_e}\right)\Delta\sigma_2\right]. \tag{13}$$

We define the stress ratio for the kth increment as

$$\mu^k = \frac{\Delta\sigma_2^k}{\Delta\sigma_1^k}. \tag{14}$$

Using Eqs. (6), (12), (13), and (14), the stress ratio for a given increment is given by (the k superscripts have been omitted for clarity)

$$\mu = \frac{(\alpha + \nu)\sigma_e^2 + E df/d\sigma_e[\alpha(\sigma_1 - 1/2\sigma_2)^2 - (\sigma_1 - 1/2\sigma_2)(\sigma_2 - 1/2\sigma_1)]}{(1 + \alpha\nu)\sigma_e^2 - E df/d\sigma_e[(\sigma_2 - 1/2\sigma_1)^2 - \alpha(\sigma_1 - 1/2\sigma_2)(\sigma_2 - 1/2\sigma_1)]}. \tag{15}$$

The elastoplastic strain energy density is computed from

$$SED^p = \sum_{k=1}^{N} \sigma_1^k \Delta\epsilon_1^k + \mu^k \sigma_1^k \alpha \Delta\epsilon_1^k, \tag{16}$$

and when this matches the elastic strain energy density, the local stresses and strains produced by an applied remote stress have been found.

The short FORTRAN program that does these calculations actually increments σ_1 and solves for S to produce a plot of applied remote stress versus local stresses or strains. The approach is to start with the elastic stress ratio, $\mu^k = \beta$, taken from an elastic finite element analysis. At the k_{th} step, one has σ_1^k, σ_2^k, μ^k, S^k, etc., along with the value of SED^p to that point. σ_1 is then incremented by a fixed amount, $\Delta\sigma_1$, and σ_2^{k+1} is computed as $\sigma_2^k + \mu^k\Delta\sigma_1$. This enables the computation of σ_e^{k+1}, $\Delta\epsilon_p^{k+1}$, μ^{k+1} etc., and a new value of SED^p. This value of the plastic strain energy density at the $(k + 1)_{\text{th}}$ is equated to the elastic strain energy density of Eq. (8) so that the remote stress S^{k+1} can be found.

3.4 The Elastoplastic Stress-Strain Relation. To determine $df/d\sigma_e$, one needs a mathematical representation of the uniaxial stress versus plastic strain curve. One may use the Ramberg-Osgood formula, Eq. (2), but it often does not fit the stress-strain curve with sufficient fidelity. The approach taken here is to use a cubic spline fit to points selected from the raw data of the uniaxial-stress test. These points, a dozen or so, are selected over the range of data and are chosen so that the fitted spline curve not only gives a good visual fit to the data, but also guarantees that the second derivatives are always negative.

3.5 Comparison of the Models. It is interesting to examine the predictions of the various ways of predicting the stresses and strains at notch roots. Six have been discussed or presented here: Neuber, Neuber-Walker, Glinka plane stress, Glinka plane strain, Glinka constant stress, and Glinka constant strain.

Take, as an example, a geometry with $K_t = 2.0$ (notch radius 4.76 mm) and a specimen-thickness to notch-radius ratio such that $\alpha = -0.13$ and $\beta = 0.20$ when $\nu = .32$. Use the Ramberg-Osgood relation (for simplicity) with $E = 72.6 \times 10^3$ MPa, $K = 706$ MPa, and $n = 0.083$. The predicted net-stress versus strain (ϵ_1) responses for the six models are plotted in Fig. 2 which also includes the material's stress-strain curve. The results are plotted out to a strain of two percent, which is higher

Downloaded 03 May 2010 to 171.66.16.247. Redistribution subject to ASME license or copyright; see http://www.asme.org/terms/Terms_Use.cfm

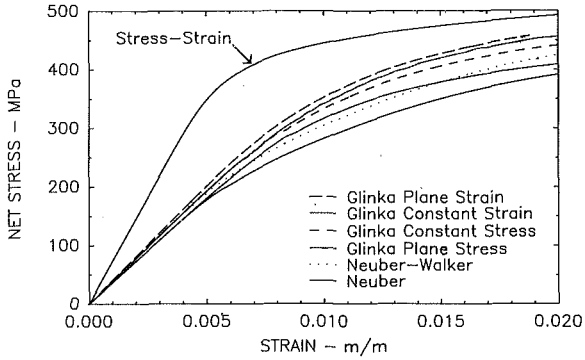


Fig. 2 Predicted notch stress, σ_1, from the six models for a typical case. The example had $K_t = 2.0$ and a constraint, α, of -0.13; the stress-strain curve used is also shown.

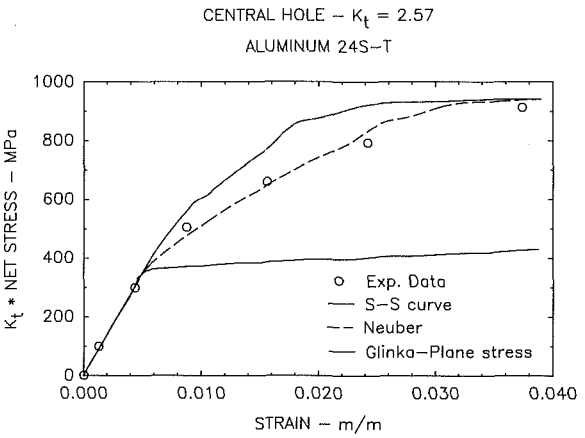


Fig. 3 Comparison of two plane-stress models with the strain data of Griffith (1948)

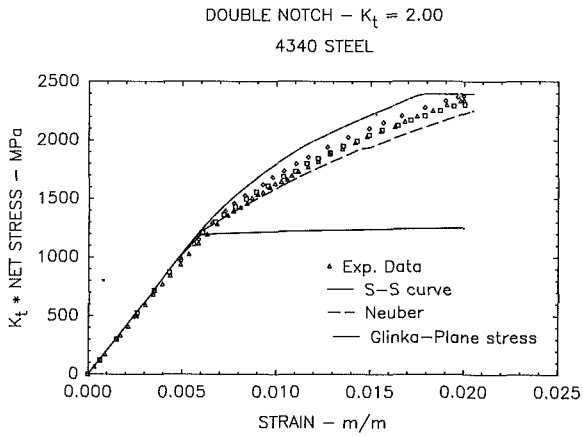


Fig. 4 Comparison of two plane-stress models with the strain data of Papirno (1971)

than considered in the rest of this paper in order to illustrate the differences. Glinka's correction factor, C_p, has been incorporated into all four models based on his approach; it is included in all subsequent computations using them.

Figure 2 shows the large differences between the Glinka models and the Neuber models. These differences become greater when there is significant constraint, although the Neuber model and the Glinka plane stress model assume no constraint. A useful measure of constraint is the quantity $\alpha = \epsilon_2/\epsilon_1$. Plane stress implies $\alpha = -\nu$, whereas $\alpha = 0$ implies plane strain. The value chosen for this example, $\alpha = -0.13$, represents an intermediate level of constraint.

Among the Glinka models, there is, for example, a 22 percent spread among the predicted strains at a net stress of 350 MPa. This is quite significant when one considers the effect that a small change in strain has on fatigue life. Presumably, the models introduced in this paper, which assume either constant stress-ratio or constant strain-ratio, should be more accurate.

4 Comparison With Experimental Results

There have been numerous experimental studies of strains in notched specimens, beginning in 1948 with the works of Griffith (1948) and Box (1951). Most of the later ones have involved measurements on the sides of flat, notched specimens, and a variety of experimental techniques have been used. Theocaris (1962) and Crews (1969) used photoelastic coatings, and Durelli and Sciammarella (1963) used moire grids to study monotonic response with whole-field methods. However, it is difficult to extrapolate these surface measurements to the critical notch root on the edge of a specimen, so this paper discusses only measurements taken at the notch root. The presentation is broken into two parts: measurements made with resistance strain gages and measurements made with laser-based interferometry.

The results are presented in plots with the product $K_t \times$ net stress as the ordinate (so that the material's stress-strain curve can be included); the abscissa is the axial strain at the root of the notch. In the cases where an elastic finite element analysis has been conducted, the measures of the constraint, α, is given. Some of the plotted curves have a wavy appearance arising from the digitization of the data from the original papers.

4.1 Resistance Strain Gage Results. The data in Fig. 3 are taken from the classical experiments of Griffith (1948)—before any model of the phenomenon was available. He tested 24S-T aluminum specimens that were 2-ft (0.61-m) wide by 0.091 in. (2.31-mm) thick with a 4-in. (102-mm) hole in the center. Strains were measured on the edge of the hole with a clip gage having a 1/2-in. (12.7-mm) gage length. The specimens were tested not only under monotonic loading to large strains, but also for 100 cycles. The notch root data and the stress-strain curve are taken from Griffith's report (his Figs. 3 and 4). The Neuber relation and the plane stress version of the Glinka relation are the two models ($K_t = 2.57$) used to predict the notch root behavior. Figure 3 shows that the Neuber relation predicts the data quite well—even to large strains of four percent.

Papirno (1971) used, in 1971, foil resistance strain gages, 0.04 in. long by 0.05 in. wide (1.02 mm by 1.27 mm), at the roots of notches having radiuses as small as 0.159 in. (4.04 mm). His double-notched specimens were 0.1-in. (2.54-mm) thick and 1.0 in. (25.4-mm) wide at the gross section. The material was 4340 steel to which he fitted a monotonic stress-strain curve in three parts. One of Papirno's results (from his Fig. 8) with $K_t = 2.00$ is shown in Fig. 4. He did compare his results with the Neuber relation; the plane stress version of Glinka is added. Note the scatter among the three tests; this is typical of elastoplastic measurements at notches as will be observed in subsequent figures. The elastoplastic response at the notch is bounded by the Neuber and the Glinka plane stress predictions.

Seeger (1985) has studied round specimens with different circumferential notches subjected to monotonic axial, torsional, and bending loads. The specimens were quite large—the gross-section diameter was 140 mm (5.5 inches)—and the material was a very low strength mild steel. Biaxial strains at the notch roots were measured with foil strain gages having gage lengths as short as 2 mm. One of Seeger's cases—axial loading of a circumferentially grooved rod with $K_t = 3.32$ (his Fig. 1.10)—is shown in Fig. 5. This geometry produces a case of plane strain at the notch root; i.e., $\alpha = 0$. Although he

Downloaded 03 May 2010 to 171.66.16.247. Redistribution subject to ASME license or copyright; see http://www.asme.org/terms/Terms_Use.cfm

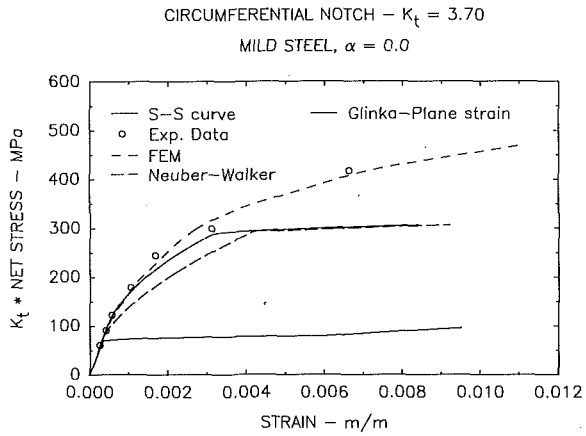


Fig. 5 Comparison of two plane-strain models with the strain data and finite element results of Seeger (1985)

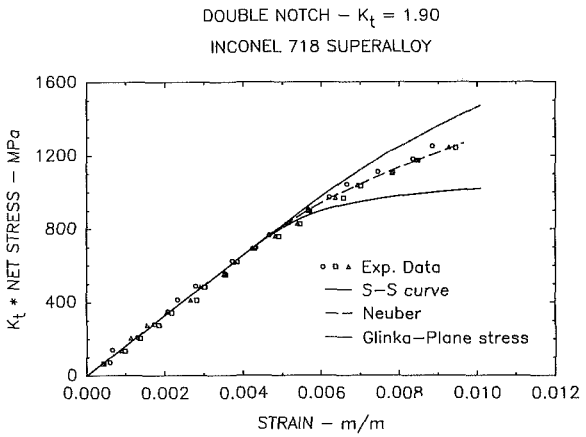


Fig. 6 Comparison of two plane-stress models with the strain data of 650C of Ward and Sharpe (1983)

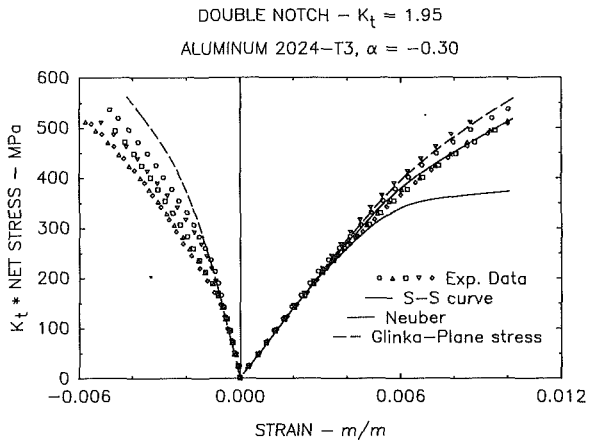


Fig. 7 Comparison of two plane-stress models with the biaxial strain data of Sharpe and Wang (1991)

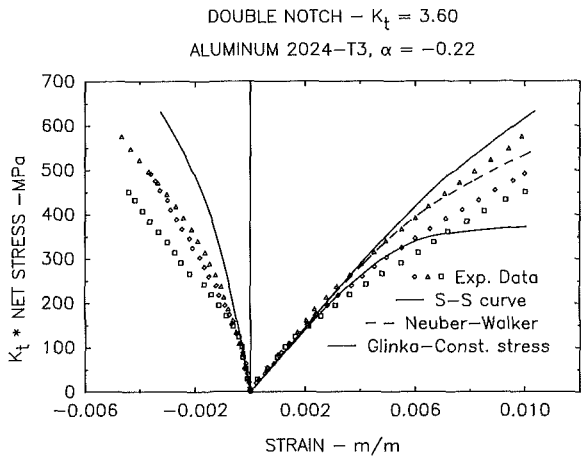


Fig. 8 Comparison of two models for moderate constraint with the biaxial strain data of Sharpe and Wang (1991)

tested to eight percent strain, general yielding began around 0.3 percent strain, so only the initial portion of his results are shown. The data points in Fig. 5 are his axial strain measurements for the one specimen tested. He also ran an elastoplastic finite element analysis which is plotted and predicts the results quite well even for larger strains.

The Neuber-Walker prediction misses the experimental results quite badly—and of course it stops when it reaches the material's elastoplastic stress. Seeger has a modification of the Neuber relation which permits one to continue the calculations to larger strains and stresses (higher stresses can be sustained because of the triaxiality of the stress state). The Glinka plane strain model gives fairly good (as good as the FEM computations) agreement—as far as it goes.

4.2 Interferometric Strain Gage Results. The difficult aspect of strain measurement at notch roots is, of course, the need for a short gage length—unless very large specimens are tested (as did Griffith and Seeger). A suitable technique is the laser-based interferometric strain/displacement gage (or ISDG) (Guillot and Sharpe, 1983) which has a gage length that can be as short as 25 μm but is usually 150 or 200 μm. It has been used to measure uniaxial monotonic and cyclic strains at notch roots at 650C in superalloy specimens (Ward and Sharpe, 1983). A more recent version permits biaxial strain measurements at notch roots (Sharpe and Wang, 1991; and Sharpe, 1991).

The principle of the ISDG is simple: Two tiny indentations are pressed into the notch root with a Vickers microhardness tester. These two indentations form the gage, and when they are illuminated with a laser, interference fringe patterns form in space. These fringes move as the distance between the gage points change, and a computer-controlled measuring system translates that motion into strain. The biaxial version uses three indentations in an orthogonal pattern. The effect of the indentations on the local elastoplastic strain field has been examined by comparing ISDG measurements on smooth specimens with simultaneous measurements by foil and clip gages; the conclusion is that the ISDG does give a valid measure. Details of the ISDG may be found in (Sharpe, 1989).

Data from uniaxial notch-root strain measurements with the ISDG on three double-notched (K_t = 1.9) superalloy specimens at 650C (Ward and Sharpe, 1983) are presented in Fig. 6. These experiments were stopped at one percent strain because the emphasis was on low-cycle fatigue; there is little yielding at the notch root. The specimens were 2.5-mm thick and 18-mm wide at the net section, so the Neuber relation and the plane-stress version of Glinka were used. Again, the Neuber relation gives a good prediction of the results as it did in the Griffith case.

The first biaxial strain measurements at notch roots are shown in Fig. 7 for a specimen with $\alpha = -0.30$ (nearly plane stress). The material is 2024-T3 aluminum in sheet form, and it has elongated grains (when viewed from the edge) that are approximately 100 μm long and 25 μm wide. The ISDG gage length was 200 μm; nevertheless, the reproducibility among 5 tests was reasonably good. The double-notched specimens are 2.54-mm thick and have a notch radius of 4.76 mm with a net-section width of 18.16 mm (Sharpe and Wang, 1991). K_t is 1.95 so the geometry is similar to the superalloy specimens

Downloaded 03 May 2010 to 171.66.16.247. Redistribution subject to ASME license or copyright; see http://www.asme.org/terms/Terms_Use.cfm

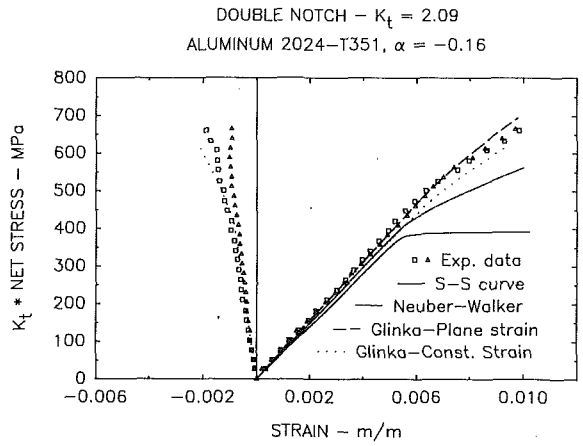


Fig. 9 Comparison of two models for more severe constraint with the biaxial strain data of Sharpe and Wang (1991)

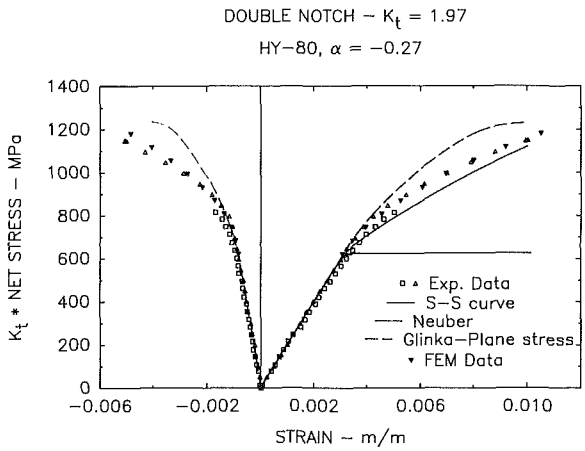


Fig. 10 Comparison of two plane-stress models with biaxial strain data and elastoplastic finite element results

used for Fig. 5. Predictions from the Neuber relation and the plane-stress Glinka relation show that the data are more or less bounded by the two predictions—a result similar to the one with Papirno's data in Fig. 4. The lateral strain is predicted from Glinka's plane stress relation and is considerably smaller than measured.

Figure 8 presents the measurements and predictions for a specimen with more constraint, $\alpha = -0.22$. The specimen geometry had double VEE notches with a root radius of 1 mm. The gage length was shorter (150 μm as opposed to 200 μm for the specimens of Fig. 7) which generates more scatter among the three experiments. The Neuber relation uses the modification of Walker with a stress ratio, β, of 0.11 determined from an elastic finite element analysis. The Glinka constant stress relations are from Eqs. (7), (11), and (12); they predict the biaxial strains. There is a lot of scatter among the three tests because the gage length was only 150 μm and the root radius is so small. All predictions miss the mark, so the notch root behavior may not be amenable to a continuum mechanics analysis in this case.

Results from the double-notch geometry with the most constraint, $\alpha = -0.16$; $\beta = 0.19$, are given in Fig. 9. This was achieved with specimens of the same shape as the ones of Fig. 7, but with a thickness of 25.4 mm. The material is also different; it is 2024-T351 aluminum. The Glinka predictions are made from the constant stress and plane stress versions. The plane strain results are actually closest to the data overall.

Results from HY-80 steel specimens with the same geometry, and with predictions made in the same manner, as those in Fig. 7 are shown in Fig. 10. The shape of the stress strain curve

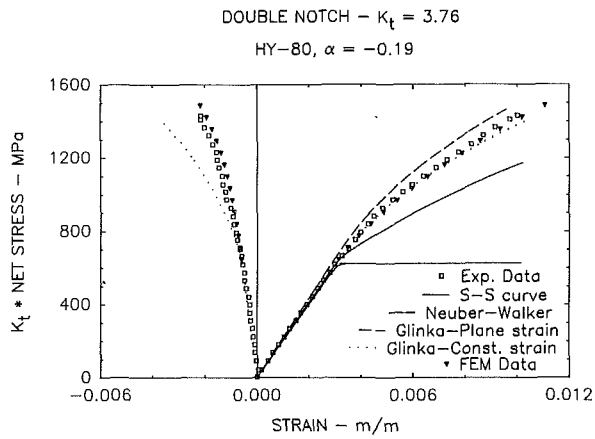


Fig. 11 Comparison of two models for moderate constraint with biaxial strain data and elastoplastic finite element results

is different than in Fig.7; it is bilinear with little hardening. But the main difference is in the grain size and isotropy of the material. The steel has grains on the order of 20 μm in size and is almost perfectly isotropic. The 2024-T3 aluminum has elongated, pancake-shaped grains that can be 100 μm long, and it is very anisotropic. The steel is a much better material with which to test a continuum theory. However, the two models still bound the experimental results as they did in Fig. 7.

The effect of constraint is Fig. 11 via an HY80 specimen with the same geometry as Fig. 8. The Glinka constant strain model gives the best prediction for the axial strain; the lateral strain is still not modeled correctly.

4.3 Elastoplastic Finite Element Analysis. A finite element analysis of the two HY80 geometries has been conducted using a three-dimensional code written at NASA-Langley (Chermahini et al., 1988). The code solves the elastoplastic problem by employing the initial stress method proposed initially by Zienkiewitz et al. (1969). The physical problem is first broken down by ignoring the effect of the notch at a distance of 25.4 mm in the axial direction. The stress at this point in the specimen is assumed to be uniform as a result of the tensile loading on the specimen ends. Then, by applying typical symmetry conditions, only one-eighth of the physical three-dimensional specimen is actually modeled in the finite element calculations.

Two-dimensional four-node quadrilateral meshes are first developed for the plane normal to the notch axis. These meshes are then optimized, replicated, and placed every 0.254 mm in the thickness direction to form five rows of eight-node three-dimensional brick elements. The meshes consist of 3006 nodes and 3534 nodes for the U and V-notched specimens, respectively. The meshes are highly graded so that the smallest elements at the notch root have volumes on the order of 1 cubic micrometer for the U-notch and 0.1 cubic micrometer for the V-notch. The axial and lateral strains shown in Figs. 10 and 11 are taken at the centroid of the elements closest to the notch root in the center of the specimen. This point should correspond most closely with the ISDG measurement.

The agreement between the finite element predictions and the ISDG measurements of axial and lateral strains is excellent—as seen in Figs. 10 and 11. The HY80 was chosen as a material which is a good model of a continuum, and the close agreement verifies that choice. These results also indicate that the ISDG measurements at the notch roots are accurate.

5 Conclusions

This research is an attempt to answer the question: "Which simple model is the best one to use to predict notch-root stresses and strains?" Predictions from six models have been compared

Downloaded 03 May 2010 to 171.66.16.247. Redistribution subject to ASME license or copyright; see http://www.asme.org/terms/Terms_Use.cfm

with results from various studies. Elastoplastic behavior of metals is more complicated than elastic behavior and there is more scatter in the measurements. Nevertheless, the results presented here permit one to draw some general conclusions:

- It is useful to quantify the amount of constraint, and that has been done by defining it as $\alpha = \epsilon_2/\epsilon_1$. α = the negative of Poisson's Ratio implies plane stress, and $\alpha = 0$ implies plane strain. Results here show that a value of α of -0.2 is a useful divider between "nearly plane stress" and "nearly plane strain."
- If the state at the notch root is nearly plane stress, the Neuber relation is the best single model for predicting the response. However, the Glinka plane stress model gives an upper bound and enables one to assign an uncertainty to the prediction. If the strains are most important, as in low-cycle fatigue, the Neuber relation is conservative.
- If the state at the notch root is nearly plane strain, the Glinka plane strain model or the modified version that assumes either constant strain ratio or constant stress ratio gives a better prediction. The Neuber relation is clearly inadequate for this case.
- If the gage length of the measurement or the local dimension of the notch is near the grain size of the material, these continuum models are inadequate. They cannot account for the extreme variation in local response.
- One can study, experimentally and with finite element techniques, cases where the assumptions of continuum elastoplasticity are fully met. Figures 10 and 11 show such cases, and the agreement between measurements and computations is excellent. The appropriate simple model enables the designer to predict the axial strains with an acceptable margin of error in such a case. However, many, if not most, engineering materials do not meet those assumptions, and predictions will have a larger error.

The answer to the question posed is not clear—as is often the case. Certainly the models enable one to make a useful first estimate of the local stress and strains, but more accurate predictions require further computational and experimental study of the particular case at hand.

Acknowledgments

The authors appreciate the support of this research by the National Science Foundation through Grant MSM-8702110. The first author acknowledges the support of the Humboldt Foundation of the Federal Republic of Germany for the period Jan.–June 1990. Mr. Tregoning was supported by a NASA Research Fellowship.

References

ASME, 1980, "ASME Boiler and Pressure Vessel Code Case N47-17," ASME, New York.

Box, W. A., 1951, "The Effect of Plastic Strains on the Stress Concentrations," *Proceedings of the Society for Experimental Stress Analysis*, Vol. 8, pp. 99–110.

Chermahini, R. G., Shivakumar, K. N., and Newman, J. C., Jr., 1988, "Three-Dimensional Finite-Element Simulation of Fatigue Crack Growth and Closure," *Mechanics of Fatigue Crack Closure*, ASTM-STP-982, pp. 398–413.

Crews, Jr., J. H., 1969, "Elastoplastic Stress-Strain Behavior at Notch Roots in Sheet Specimens Under Constant-Amplitude Loading," NASA TN D-5253.

Dowling, N. E., 1977, "Performance of Metal-foil Strain Gages During Large Cyclic Strains," *Experimental Mechanics*, Vol. 17, pp. 193–197.

Durelli, A. J., and Sciammarella, C. A., 1963, "Elastoplastic Stress and Strain Distribution in a Finite Plate with a Circular Hole Subjected to Unidimensional Load," ASME JOURNAL OF APPLIED MECHANICS, Vol. 30, pp. 115–121.

Glinka, G., 1985a, "Energy Density Approach to Calculation of Inelastic Strain-Stress near Notches and Cracks," *Engineering Fracture Mechanics*, Vol. 22, pp. 485–508.

Glinka, G., 1985b, "Calculation of Inelastic Notch-Tip Strain-Stress Histories under Cyclic Loading," *Engineering Fracture Mechanics*, Vol. 22, pp. 839–854.

Glinka, G., 1988, "Relations between the Strain Energy Density Distribution and Elastic-Plastic Stress-Strain Fields near Cracks and Notches and Fatigue Life Calculation," Low Cycle Fatigue, ASTM-STP-942, pp. 1022–1047.

Glinka, G., Ott, W., and Nowack, H., 1988, "Elastoplastic Plane Strain Analysis of Stresses and Strains at the Notch Root," *Journal of Engineering Materials and Technology*, Vol. 110, pp. 195–204.

Griffith, G. E., 1948, "Experimental Investigation of the Effects of Plastic Flow in a Tension Panel with a Circular Hole," NACA TN 1705.

Guillot, M. W., and Sharpe, W. N., Jr., 1983, "A Technique for Cyclic-plastic Notch-strain Measurement," *Experimental Mechanics*, Vol. 23, pp. 354–360.

Hutchinson, J. H., 1968, "Singular Behavior at the End of a Tensile Crack in a Hardening Material," *Journal of the Mechanics and Physics of Solids*, Vol. 16, pp. 13–34.

Irwin, G. R., 1968, "Linear Fracture Mechanics, Fracture Transition and Fracture Control," *Engineering Fracture Mechanics*, Vol. 1, pp. 241–257.

James, M. N., Dimitriou, C., and Chandler, H. D., 1989, "Low Cycle Fatigue Lives of Notched Components," *Fatigue and Fracture of Engineering Materials and Structures*, Vol. 12, pp. 213–225.

Molski, K., and Glinka, G., 1981, "A Method of Elastic-Plastic Stress and Strain Calculation at a Notch Root," *Materials Science and Engineering*, Vol. 50, pp. 93–100.

Neuber, H., 1961, "Theory of Stress Concentration for Shear-Strained Prismatical Bodies With Arbitrary Nonlinear Stress-Strain Law," ASME JOURNAL OF APPLIED MECHANICS, Vol. 28, pp. 544–550.

Papirno, R., 1971, "Plastic Stress-Strain History at Notch Roots in Tensile Strips under Monotonic Loading," *Experimental Mechanics*, Vol. 11, pp. 446–452.

Peterson, R. E., 1974, *Stress Concentration Factors*, John Wiley and Sons, New York.

Rice, J. R., 1968, *Mathematical Analysis in the Mechanics of Fracture* (Fracture, Volume III), H. Liebowitz, ed., Academic Press, New York.

Seeger, T., 1985, *Ermittlung und Beschriebung mehrachsiger Kerppeanspruchungen im nichtlinearen Berich*, Heft 115, Forschungskuratorium Machinenbau e. V. Frankfurt.

Sharpe, W. N., Jr., 1989, "An Interferometric Strain/Displacement Measurement System," NASA Technical Memorandum 101638.

Sharpe, W. N., Jr., 1991, "Measurement of Monotonic Biaxial Elastoplastic Stresses at Notch Roots," ASME JOURNAL OF APPLIED MECHANICS, in press.

Sharpe, W. N., Jr., and Wang, K. C., 1991, "Evaluation of a Modified Neuber Relation," *ASME Journal of Engineering Materials and Technology*, in press.

Theocaris, P. S., 1962, "Experimental Solution of Elastic-Plastic Plane-Stress Problems," ASME JOURNAL OF APPLIED MECHANICS, Vol. 29, pp. 735–743.

Walker, E. K., 1977, "Multiaxial Stress-Strain Approximations for Notch Fatigue Behavior," *Journal of Testing and Evaluation*, Vol. 5, pp. 106–113.

Ward, M., and Sharpe, W. N., Jr., 1983, "Benchmark Cyclic Plastic Notch Strain Measurements," *ASME Journal of Engineering Materials and Technology*, Vol. 105, pp. 235–241.

Zienkiewitz, O. C., Valliappen, S., and King, J. P., 1969, "Elasto-Plastic Solutions of Engineering Problems, 'Initial Stress,' Finite Element Approach," *International Journal for Numerical Methods in Engineering*, Vol. 1, pp. 75–100.

Downloaded 03 May 2010 to 171.66.16.247. Redistribution subject to ASME license or copyright; see http://www.asme.org/terms/Terms_Use.cfm

Mikyoung Lee
Mem. ASME.

I. Jasiuk
Mem. ASME.

Department of Metallurgy, Mechanics, and Materials Science, Michigan State University, East Lansing, MI 48824

E. Tsuchida
Faculty of Engineering, Department of Mechanical Engineering, Saitama University, 255 Shimo-Okubo, Urawa 338, Japan

The Sliding Circular Inclusion in an Elastic Half-Plane

The elastic fields due to a circular inclusion embedded in an elastic half-plane, subjected either to a uniform uniaxial stress at infinity parallel to the edge boundary, or a uniform nonshear type eigenstrain loading, are investigated. The interface between the inclusion and the remaining material is perfectly bonded, or allows pure sliding (shear tractions are specified to vanish).

Introduction

The presence of inhomogeneities (inclusions) in an elastic material has been the subject of extensive investigations due to the importance of stress concentrations in design. When inclusions exist in a material, the stress is intensified in their vicinity. The degree of this stress disturbance depends on the mismatch of the elastic constants, the shape, size, location of the inclusions, the boundary conditions at the inclusion-matrix interface, the loading, and other factors.

Most of the papers dealing with inclusions (see Mura, 1987), along with Eshelby's celebrated paper (Eshelby, 1957), involve the cases when the inclusion is embedded in an infinitely extended material and is perfectly bonded.

In this paper, the problem of a sliding circular inclusion in a half-plane under either a uniaxial loading at infinity parallel to the edge boundary, or a uniform nonshear type eigenstrain (transformation strain) is considered. The inclusion may represent, for example, the cross-section of a fiber located near the free surface of a composite material. Both the inclusion and the surrounding matrix are assumed to be linear elastic and isotropic. The interface between the inclusion and the matrix allows sliding: The shear tractions are specified to vanish and no separation takes place in the normal direction. The perfect bonding case is included for comparison. In this study, the joint effect of a traction-free edge boundary and sliding is investigated.

The problem of a semi-infinite plate with a hole subjected to a uniaxial loading was solved by Jeffery (1920). Jeffery's paper, however, contains an error, and the solution does not satisfy the traction-free boundary conditions at the straight edge. The above solution was corrected by Mindlin (1948). This problem has been reexamined recently by Callias and Markenskoff (1989), who analyzed the singularity of the hoop stress at a hole, as the hole approaches the free boundary. The problem of a circular inclusion in a half-plane undergoing an expansion was solved by Richardson (1969). The inclusion was assumed to be of the same material as the matrix. The problem of semi-infinitely extended material with a perfectly bonded circular inclusion was addressed by Saleme (1958). Coincidentally, Saleme's solution also contains an error, since it does not include the rigid body displacement of the inclusion, as pointed out by Shioya (1967). Most of the aforementioned authors used bipolar coordinates and Airy stress functions in a form of infinite series in their analysis. In this paper, Papkovich-Neuber displacement potentials in an infinite integral form and infinite series in polar coordinates are used. One of the advantages of using displacement potentials for this problem is that the formulation is similar in both two and three dimensions (Ishiwata, 1986; Tsuchida and Mura, 1983). The other one is that we can get displacements directly, while Airy's stress function method demands integration of strain or stress to determine the displacements.

The corresponding problem in three dimensions for eigenstrain loading was solved by Mindlin and Cheng (1950) and Aderogba (1976) for a spherical inclusion, and by Seo and Mura (1979) for an ellipsoidal inclusion. The problem of an inhomogeneity near the free surface subjected to all-around tension at infinity was solved by Tsutsui and Saito (1973) for a spherical inclusion and Tsuchida and Mura (1983) for a spheroidal inclusion.

The problem of a sliding inclusion in an infinite material was addressed in two dimensions by Tsuchida et al. (1986) and Kouris et al. (1988), and in three dimensions by Mura and

Contributed by the ASME Applied Mechanics Division of THE AMERICAN SOCIETY OF MECHANICAL ENGINEERS for presentation at the Winter Annual Meeting, Atlanta, Ga., Dec. 1-6, 1991.

Discussion on this paper should be addressed to the Technical Editor, Prof. Leon M. Keer, The Technological Institute, Northwestern University, Evanston, IL 60208, and will be accepted until two months after final publication of the paper itself in the JOURNAL OF APPLIED MECHANICS. Manuscript received by the ASME Applied Mechanics Division, Aug. 15, 1990; final revision, Mar. 20, 1991.

Paper No. 91-WA/APM-35.

Copyright © 1992 by ASME
Downloaded 03 May 2010 to 171.66.16.247. Redistribution subject to ASME license or copyright; see http://www.asme.org/terms/Terms_Use.cfm

Furuhashi (1984), Mura et al. (1985), and Jasiuk et al. (1987). The problem of a sliding hemispherical or hemispheroidal inclusion at a free surface was solved by Kouris and Mura (1989), Kouris et al. (1989), and Tsuchida et al. (1990). The problem of a sliding inhomogeneity in a half-space was considered by Jasiuk et al. (1991).

Method of Solution

Consider the plane elasticity problem of a circular elastic inclusion embedded in an elastic half-plane. The inclusion has different elastic moduli from those of the matrix. The purpose of this study is to find the stresses and displacements, when either a uniaxial loading parallel to the edge boundary is applied at infinity, or the inclusion is subjected to uniform eigenstrains. The eigenstrains, given by ϵ^*_{ij}, are nonshear type such that $i=j$, where $i, j=x, y, z$. The solution will apply to two physical cases of a disk-like inclusion embedded in a semi-infinite plate (plane stress), or a cylindrical inclusion embedded in a half-space (plane strain).

Let the origin of coordinates be at the center of the circular inclusion and the x-axis be directed down into the interior of the semi-infinite body. It is convenient to use a polar coordinate system, which is related to the Cartesian system by $x=r\cos\theta$ and $y=r\sin\theta$. Without the loss of generality, the distance between the center of inclusion and the point on the free boundary closest to the inclusion is taken as unity. Therefore, the free surface (the straight edge of the plate or the plane surface of the semi-infinite body) is given by $x=-1$. The radius of inclusion is taken as $r=a$.

The following boundary conditions are used:

(i) the traction-free condition on the surface $x=-1$:

$$(\sigma_{xx})_{x=-1}=(\sigma_{xy})_{x=-1}=0 \tag{1}$$

(ii) either the pure sliding conditions at the interface of the inclusion:

$$(\sigma_{rr})_{r=a}=(\bar{\sigma}_{rr})_{r=a},$$
$$(\sigma_{r\theta})_{r=a}=(\bar{\sigma}_{r\theta})_{r=a}=0$$
$$(u_r)_{r=a}=(\bar{u}_r)_{r=a} \tag{2}$$

or the perfect bonding conditions at the interface of the inclusion:

$$(\sigma_{rr})_{r=a}=(\bar{\sigma}_{rr})_{r=a}$$
$$(\sigma_{r\theta})_{r=a}=(\bar{\sigma}_{r\theta})_{r=a}$$
$$(u_r)_{r=a}=(\bar{u}_r)_{r=a}$$
$$(u_\theta)_{r=a}=(\bar{u}_\theta)_{r=a} \tag{3}$$

(iii) either a uniaxial stress applied at infinity:

$$\sigma_{xx}=0, \quad \sigma_{xy}=0, \quad \sigma_{yy}=p_o \tag{4}$$

or the vanishing tractions for eigenstrain case:

$$\sigma_{ij}=0, \quad i,j=x,y. \tag{5}$$

In the preceding expressions the quantities defined in the inclusion are denoted by a superior bar.

The Papkovich-Neuber displacement potentials are used to solve the above boundary value problems. The displacement potentials, ϕ_0 and ϕ_1, that account for the disturbance due to the inhomogeneity and the effect of free surface, are given as follows:

(i) for the matrix ($r>a$), ϕ_0 and ϕ_1 are

$$\text{(I)} \quad \begin{cases} \phi_0 = C_0\left(-A_0 \log r + \sum_{m=1}^{\infty} A_m \dfrac{\cos m\theta}{r^m}\right) \\ \phi_1 = C_0 \sum_{m=1}^{\infty} B_m \dfrac{\cos m\theta}{r^m} \end{cases} \tag{6}$$

$$\text{(II)} \quad \begin{cases} \phi_0 = C_0 \int_0^{\infty} \psi_1(\lambda)\, e^{-\lambda x} \cos \lambda y \, d\lambda \\ \phi_1 = C_0 \int_0^{\infty} \lambda\, \psi_2(\lambda)\, e^{-\lambda x} \cos \lambda y \, d\lambda \end{cases} \tag{7}$$

(ii) and for the inclusion ($r<a$), ϕ_0 and ϕ_1 are

$$\text{(III)} \quad \begin{cases} \phi_0 = C_0 \sum_{n=1}^{\infty} \bar{A}_n\, r^n \cos n\theta \\ \phi_1 = C_0 \sum_{n=0}^{\infty} \bar{B}_n\, r^n \cos n\theta \end{cases} \tag{8}$$

where

$$C_0 = \begin{cases} p_o & \text{for uniaxial loading} \\ 2G\epsilon^* & \text{for eigenstrain loading} \quad (\epsilon^* = \epsilon^*_{xx},\ \epsilon^*_{yy} \text{ or } \epsilon^*_{zz}) \end{cases}$$

where G is the shear modulus of the matrix and ϵ^*_{xx}, ϵ^*_{yy}, and ϵ^*_{zz} are the eigenstrains. A_m, B_m, $\bar{A}_n$, and $\bar{B}_n$ are the unknown constants and $\psi_1(\lambda)$ and $\psi_2(\lambda)$ are the unknown functions of λ, which are determined from the boundary conditions (1)–(5). Note that (I) is expressed by suffix m and (III) by suffix n. For reference, the relations between the displacement potentials ϕ_0 and ϕ_1 and the stresses and displacements are given in the Appendix.

When a uniaxial loading is applied, the displacement potentials are given as

$$\text{(IV)} \quad \begin{cases} \phi_0 = \dfrac{p_o}{8}(\kappa+1)(y^2-x^2) \\ \phi_1 = -\dfrac{p_o}{2}\, x. \end{cases} \tag{9}$$

The stresses and displacements obtained from (IV) are given as

$$\sigma_{xx}=0$$
$$\sigma_{xy}=0$$
$$\sigma_{yy}=p_o$$
$$2G\, u_x = -\frac{3-\kappa}{4}\, p_o\, x$$
$$2G\, u_y = \frac{\kappa+1}{4}\, p_o\, y \tag{10}$$

where

$$\kappa = \begin{cases} 3-4\nu & \text{for plane strain} \\ \dfrac{3-\nu}{1+\nu} & \text{for plane stress} \end{cases}$$

where ν is Poisson's ratio. The stresses and displacements, given in Eq. (10), are expressed in polar coordinates as

$$\sigma_{rr}=p_o\frac{1}{2}(1-\cos 2\theta)$$
$$\sigma_{r\theta}=p_o\frac{1}{2}\sin 2\theta$$
$$\sigma_{\theta\theta}=p_o\frac{1}{2}(1+\cos 2\theta)$$

Downloaded 03 May 2010 to 171.66.16.247. Redistribution subject to ASME license or copyright; see http://www.asme.org/terms/Terms_Use.cfm

$$2G\,u_r = p_o \frac{r}{4}\{(\kappa-1)-2\cos 2\theta\}$$

$$2G\,u_\theta = p_o \frac{r}{2}\sin 2\theta. \tag{11}$$

When the inclusion is subjected to an eigenstrain loading, the displacements inside the inhomogeneity are the sum of displacements of the inclusion if there would be no constraint from the matrix

$$u_x^* = (\epsilon_{xx}^* + \eta\,\epsilon_{zz}^*)x$$
$$u_y^* = (\epsilon_{yy}^* + \eta\,\epsilon_{zz}^*)y \tag{12}$$

where

$$\eta = \begin{cases} \nu & \text{for plane strain} \\ 0 & \text{for plane stress} \end{cases}$$

and the elastic displacements obtained from (III). The displacements, given in (12), are expressed in polar coordinates as

$$u_r^* = \frac{r}{2}\{2\eta\,\epsilon_{zz}^* + (\epsilon_{xx}^* + \epsilon_{yy}^*) + (\epsilon_{xx}^* - \epsilon_{yy}^*)\cos 2\theta\}$$

$$u_\theta^* = \frac{r}{2}(\epsilon_{yy}^* - \epsilon_{xx}^*)\sin 2\theta. \tag{13}$$

The corresponding stresses are zero.

Note that the stress components derived from (I) and (II) vanish at infinity. Therefore, for the eigenstrain loading, the boundary condition (5) is automatically satisfied. For the case of uniaxial loading, ϕ_0 and ϕ_1, given by (IV), yield uniaxial tension p_o. Therefore, the boundary condition (4) is also automatically satisfied. To satisfy the traction-free boundary condition (1) at the free surface, (I) is considered as follows:

(I)-1 $$\phi_0 = -C_0 A_0 \log r$$

(I)-2 $$\begin{cases} \phi_0 = C_0 \sum_{m=1}^{\infty} A_m \dfrac{\cos m\theta}{r^m} \\ \phi_1 = C_0 \sum_{m=1}^{\infty} B_m \dfrac{\cos m\theta}{r^m}. \end{cases} \tag{14}$$

Using one of the following mathematical relations

$$\frac{\cos m\theta}{r^m} = \frac{(-1)^m}{(m-1)!}\int_0^\infty \lambda^{m-1} e^{\lambda x}\cos \lambda y\, d\lambda \qquad (x<0) \tag{15}$$
$$\frac{\sin m\theta}{r^m} = \frac{(-1)^{m-1}}{(m-1)!}\int_0^\infty \lambda^{m-1} e^{\lambda x}\sin \lambda y\, d\lambda,$$

(I)-2 is expressed in Cartesian coordinates as

(I)-2* $$\begin{cases} \phi_0 = C_0 \sum_{m=1}^{\infty} \dfrac{(-1)^m}{(m-1)!} A_m \int_0^\infty \lambda^{m-1} e^{\lambda x}\cos \lambda y\, d\lambda \\ \qquad\qquad (x<0) \\ \phi_1 = C_0 \sum_{m=1}^{\infty} \dfrac{(-1)^m}{(m-1)!} B_m \int_0^\infty \lambda^{m-1} e^{\lambda x}\cos \lambda y\, d\lambda. \end{cases} \tag{16}$$

As for (I)-1,

$$\phi_0 = -C_0 A_0 \log r = -C_0 A_0 \frac{1}{2}\log (x^2+y^2), \tag{17}$$

and the stresses are obtained directly from Eq. (17) as

$$\sigma_{xx} = C_0 A_0 \frac{\cos 2\theta}{r^2}$$
$$\sigma_{xy} = C_0 A_0 \frac{\sin 2\theta}{r^2}, \tag{18}$$

and using (15) they are expressed as

$$\sigma_{xx} = C_0 A_0 \int_0^\infty \lambda\, e^{\lambda x}\cos \lambda y\, d\lambda$$
$$(x<0) \tag{19}$$
$$\sigma_{xy} = -C_0 A_0 \int_0^\infty \lambda\, e^{\lambda x}\sin \lambda y\, d\lambda.$$

Using Eqs. (7), (16), and (19), the boundary conditions (1) are written as

$$\frac{(\sigma_{xx})}{C_0}_{x=-1} = \int_0^\infty \lambda^2 \left[\psi_1(\lambda)\, e^{\lambda} + \left(\frac{\kappa+1}{2}-\lambda\right)\psi_2(\lambda)\, e^{\lambda} + \sum_{m=1}^{\infty} A_m \frac{(-1)^m}{(m-1)!}\lambda^{m-1} e^{-\lambda} - \sum_{m=1}^{\infty}\left(\frac{\kappa+1}{2}+\lambda\right)\lambda^{m-2} e^{-\lambda} B_m \frac{(-1)^m}{(m-1)!} + A_0 \lambda^{-1} e^{-\lambda}\right]\cos \lambda y\, d\lambda = 0 \tag{20}$$

$$\frac{(\sigma_{xy})}{C_0}_{x=-1} = \int_0^\infty \lambda^2 \left[\psi_1(\lambda)\, e^{\lambda} + \left(\frac{\kappa-1}{2}-\lambda\right)\psi_2(\lambda)\, e^{\lambda} - \sum_{m=1}^{\infty} A_m \frac{(-1)^m}{(m-1)!}\lambda^{m-1} e^{-\lambda} + \sum_{m=1}^{\infty}\left(\frac{\kappa-1}{2}+\lambda\right)\lambda^{m-2} e^{-\lambda}\frac{B_m(-1)^m}{(m-1)!} - A_0 \lambda^{-1} e^{-\lambda}\right]\sin \lambda y\, d\lambda = 0 \tag{21}$$

Setting the quantities in the brackets in Eqs. (20)-(21) to zero, two equations for the two unknowns $\psi_1(\lambda)$ and $\psi_2(\lambda)$ are obtained. Solving these equations, $\psi_1(\lambda)$ and $\psi_2(\lambda)$ are found as

$$\psi_1(\lambda) = A_0 \lambda^{-1} e^{-2\lambda}(\kappa-2\lambda) + \sum_{m=1}^{\infty}\left[\frac{A_m(-1)^m}{(m-1)!}\lambda^{m-1} e^{-2\lambda}(\kappa-2\lambda) - B_m \frac{(-1)^m}{(m-1)!}\lambda^{m-2} e^{-2\lambda}\frac{(\kappa^2-1-4\lambda^2)}{2}\right] \tag{22}$$

$$\psi_2(\lambda) = -2A_0 \lambda^{-1} e^{-2\lambda} - \sum_{m=1}^{\infty}\left[2\frac{A_m(-1)^m}{(m-1)!}\lambda^{m-1} e^{-2\lambda} - \frac{B_m(-1)^m}{(m-1)!}(\kappa+2\lambda)\lambda^{m-2} e^{-2\lambda}\right]. \tag{23}$$

In order to satisfy the boundary conditions (2) or (3) at the inclusion's interface, the following relation is used:

Downloaded 03 May 2010 to 171.66.16.247. Redistribution subject to ASME license or copyright; see http://www.asme.org/terms/Terms_Use.cfm

$$e^{-\lambda x}\cos\lambda y=\sum_{n=0}^{\infty}(-1)^n\frac{(\lambda r)^n}{n!}\cos n\theta. \tag{24}$$

(II) is rewritten by using Eq. (24) as follows:

$$\text{(II)}^*\quad\begin{cases}\phi_0=C_0\sum_{n=0}^{\infty}\alpha_n r^n\cos n\theta\\ \phi_1=C_0\sum_{n=0}^{\infty}\beta_n r^n\cos n\theta\end{cases} \tag{25}$$

where

$$\alpha_n=\int_0^{\infty}\psi_1(\lambda)\frac{(-1)^n\lambda^n}{n!}d\lambda$$

$$\beta_n=\int_0^{\infty}\lambda\,\psi_2(\lambda)\frac{(-1)^n\lambda^n}{n!}d\lambda \tag{26}$$

and

$$\alpha_n=A_0\,\alpha_{n1}+\sum_{m=1}^{\infty}\alpha_{n2}^m A_m+\sum_{m=1}^{\infty}\alpha_{n3}^m B_m$$

$$\beta_n=A_0\,\beta_{n1}+\sum_{m=1}^{\infty}\beta_{n2}^m A_m+\sum_{m=1}^{\infty}\beta_{n3}^m B_m \tag{27}$$

where

$$\alpha_{n1}=\int_0^{\infty}(\kappa-2\lambda)(-1)^n\frac{\lambda^{n-1}}{n!}e^{-2\lambda}d\lambda$$

$$\alpha_{n2}^m=\int_0^{\infty}(\kappa-2\lambda)(-1)^{m+n}\frac{\lambda^{m+n-1}}{(m-1)!\,n!}e^{-2\lambda}d\lambda$$

$$\alpha_{n3}^m=\int_0^{\infty}\frac{(\kappa^2-1-4\lambda^2)}{2}(-1)^{m+n+1}\frac{\lambda^{m+n-2}}{(m-1)!\,n!}e^{-2\lambda}d\lambda$$

$$\beta_{n1}=\int_0^{\infty}(-2)(-1)^n\frac{\lambda^n}{n!}e^{-2\lambda}d\lambda$$

$$\beta_{n2}^m=\int_0^{\infty}(-2)(-1)^{m+n}\frac{\lambda^{m+n}}{(m-1)!\,n!}e^{-2\lambda}d\lambda$$

$$\beta_{n3}^m=\int_0^{\infty}(\kappa+2\lambda)(-1)^{n+m}\frac{\lambda^{m+n-1}}{(m-1)!\,n!}e^{-2\lambda}d\lambda. \tag{28}$$

Using Euler's Integral of second kind

$$\int_0^{\infty}e^{-ax}x^b\,dx=\frac{\Gamma(b+1)}{a^{b+1}}\quad(a,\,b>0) \tag{29}$$

and the relation

$$\int_0^{\infty}\frac{1}{\xi}e^{-\xi z}\cos\xi a\,d\xi=-\frac{1}{2}\log(a^2+z^2), \tag{30}$$

Eqs. (28) can be simplified as

$$\alpha_{n1}=-\kappa\,\epsilon_n-2\,\gamma_n^0$$

$$\alpha_{n2}^m=-\kappa\,\gamma_n^{m-1}-2m\,\gamma_n^m$$

$$\alpha_{n3}^m=\frac{\kappa^2-1}{2}\gamma_n^{m-1}-2m(m+1)\,\gamma_n^m$$

$$\beta_{n1}=-2\,\gamma_n^0$$

$$\beta_{n2}^m=-2m\,\gamma_n^m$$

$$\beta_{n3}^m=m\,\kappa\,\gamma_n^m-2m(m+1)\,\gamma_n^m \tag{31}$$

where

$$\gamma_n^m=\frac{(-1)^{m+n}}{m!\,n!}\int_0^{\infty}e^{-2\lambda}\lambda^{m+n}d\lambda=\frac{(-1)^{m+n}}{m!\,n!}\frac{(m+n)!}{2^{m+n+1}} \tag{32}$$

and

$$\epsilon_n=\begin{cases}\log 2 & n=0\\ \dfrac{\gamma_{n-1}^0}{n} & n\geq 1.\end{cases} \tag{33}$$

Next, the stresses and the displacements are derived from the displacement potentials given by (I), (II)*, and (III), and the Eqs. (11) are used for uniaxial loading and Eqs. (13) for eigenstrain loading cases. Substituting these results in the sliding boundary conditions (2), the following four equations are obtained:

(i) the continuity of normal tractions $(\sigma_{rr})_{r=a}=(\bar{\sigma}_{rr})_{r=a}$:

$$\sum_{n=0}^{\infty}[s_{A1}A_n+s_{B1}B_{n-1}+s_{B2}B_{n+1}+s_{\alpha 1}\alpha_n+s_{\beta 1}\beta_{n-1}+s_{\beta 2}\beta_{n+1}-\bar{s}_{A1}\bar{A}_n-\bar{s}_{B1}\bar{B}_{n-1}-\bar{s}_{B2}\bar{B}_{n+1}]\cos n\theta=\frac{A_0}{a^2}-\frac{p_o}{C_0}\frac{(1-\cos 2\theta)}{2}, \tag{34}$$

(ii) the condition of continuity of normal displacements $(u_r)_{r=a}=(\bar{u}_r)_{r=a}$:

$$\sum_{n=0}^{\infty}[\{k_{A1}A_n+k_{B1}B_{n-1}+k_{B2}B_{n+1}+k_{\alpha 1}\alpha_n+k_{\beta 1}\beta_{n-1}+k_{\beta 2}\beta_{n+1}\}-\frac{1}{\Gamma}\{\bar{k}_{A1}\bar{A}_n+\bar{k}_{B1}\bar{B}_{n-1}+\bar{k}_{B2}\bar{B}_{n+1}\}]\cos n\theta=\frac{A_0}{a}-\frac{p_o}{C_0}\frac{a}{4}\{(1-\kappa)-2\cos 2\theta\}+\frac{2G}{C_0}\frac{a}{2}\{2\eta\,\epsilon_{zz}^*+(\epsilon_{xx}^*+\epsilon_{yy}^*)+(\epsilon_{xx}^*-\epsilon_{yy}^*)\cos 2\theta\}, \tag{35}$$

(iii) the continuity of tangential tractions $(\sigma_{r\theta})_{r=a}=(\bar{\sigma}_{r\theta})_{r=a}$:

$$\sum_{n=1}^{\infty}[t_{A1}A_n+t_{B1}B_{n-1}+t_{B2}B_{n+1}+t_{\alpha 1}\alpha_n+t_{\beta 1}\beta_{n-1}+t_{\beta 2}\beta_{n+1}-\bar{t}_{A1}\bar{A}_n-\bar{t}_{B1}\bar{B}_{n-1}-\bar{t}_{B2}\bar{B}_{n+1}]\sin n\theta=-\frac{p_o}{C_0}\frac{1}{2}\sin 2\theta, \tag{36}$$

(iv) and the condition of vanishing shear tractions given by either $(\bar{\sigma}_{r\theta})_{r=a}=0$:

$$\sum_{n=1}^{\infty}[\bar{t}_{A1}\bar{A}_n+\bar{t}_{B1}\bar{B}_{n-1}+\bar{t}_{B2}\bar{B}_{n+1}]\sin n\theta=0 \tag{37}$$

or $(\sigma_{r\theta})_{r=a}=0$.

The problem of perfectly bonded inclusion can be solved by using the first three Eqs. (34)–(36), and the last one, (37), is replaced by the condition of continuity of tangential displacements $(u_\theta)_{r=a}=(\bar{u}_\theta)_{r=a}$:

$$\sum_{n=1}^{\infty}[\{l_{A1}A_n+l_{B1}B_{n-1}+l_{B2}B_{n+1}+l_{\alpha 1}\alpha_n+l_{\beta 1}\beta_{n-1}+l_{\beta 2}\beta_{n+1}\}-\frac{1}{\Gamma}\{\bar{l}_{A1}\bar{A}_n+\bar{l}_{B1}\bar{B}_{n-1}+\bar{l}_{B2}\bar{B}_{n+1}\}]\sin n\theta=-\frac{p_o}{C_0}\frac{a}{2}\sin 2\theta+\frac{2G}{C_0}\frac{a}{2}(\epsilon_{yy}^*-\epsilon_{xx}^*)\sin 2\theta \tag{38}$$

Downloaded 03 May 2010 to 171.66.16.247. Redistribution subject to ASME license or copyright; see http://www.asme.org/terms/Terms_Use.cfm

where $\Gamma=\overline{G}/G$, and G and $\overline{G}$ are the shear moduli of the matrix and inclusion, respectively, and

$$k_{A1}=\frac{-n}{a^{n+1}},\quad k_{B1}=\frac{-(n-1+\kappa)}{2a^{n-1}},\quad k_{B2}=\frac{-(n+1+\kappa)}{2a^{n+1}},$$

$$k_{\alpha 1}=na^{n-1},\quad k_{\beta 1}=\frac{(n-1-\kappa)a^{n-1}}{2},\quad k_{\beta 2}=\frac{(n+1-\kappa)a^{n+1}}{2} \tag{39}$$

$$l_{A1}=\frac{-n}{a^{n+1}},\quad l_{B1}=\frac{-(n-1-\kappa)}{2a^{n-1}},\quad l_{B2}=\frac{-(n+1+\kappa)}{2a^{n+1}},$$

$$l_{\alpha 1}=(-n)a^{n-1},\quad l_{\beta 1}=\frac{(\kappa-n+1)a^{n-1}}{2},\quad l_{\beta 2}=\frac{-(\kappa+n+1)a^{n+1}}{2} \tag{40}$$

$$s_{A1}=\frac{n(n+1)}{a^{n+2}},\qquad s_{B1}=\frac{(n-1)(n+2)}{2a^{n}},$$

$$s_{B2}=\frac{(n+1)(n+1+\kappa)}{2a^{n+2}},\qquad s_{\alpha 1}=n(n-1)a^{n-2},$$

$$s_{\beta 1}=\frac{(n-1)(n-1-\kappa)a^{n-2}}{2},\quad s_{\beta 2}=\frac{(n+1)(n-2)a^{n}}{2} \tag{41}$$

$$t_{A1}=\frac{n(n+1)}{a^{n+2}},\qquad t_{B1}=\frac{n(n-1)}{2a^{n}},$$

$$t_{B2}=\frac{(n+1)(n+1+\kappa)}{2a^{n+2}},\qquad t_{\alpha 1}=(-n)(n-1)a^{n-2},$$

$$t_{\beta 1}=\frac{(1-n)(n-1-\kappa)a^{n-2}}{2},\quad t_{\beta 2}=\frac{-(1+n)n\,a^{n}}{2} \tag{42}$$

Note that the terms involving barred quantities $\bar{k}_{A1}$, $\bar{k}_{B1}$, $\bar{l}_{A1}$, . . . can be obtained directly from $k_{\alpha 1}$, $k_{\beta 1}$, $l_{\alpha 1}$, . . . by replacing κ with $\bar{\kappa}$.

The displacement containing the coefficients α_1 and β_0 corresponds to the rigid body motion of the matrix. Therefore, α_1 and β_0 are taken as zero. The displacements containing $\overline{A}_1$ and $\overline{B}_0$ represent the rigid body motion of the inclusion in the x-direction. Since the terms containing $\overline{A}_1$ and $\overline{B}_0$ give the same rigid body displacement of the inclusion, one of the two constants can be chosen to be zero. In this paper, $\overline{B}_0=0$ and $\overline{A}_1\neq 0$ ($\overline{B}_0\neq 0$, $\overline{A}_1=0$ will give the same result).

Equating the coefficients of $\sin n\theta$ and $\cos n\theta$ in the left and right sides of either Eqs. (34)–(37) for the sliding case, or (34)–(36) and (38) for the perfect bonding case, an infinite set of algebraic equations for the unknown constants A_n, B_n, $\overline{A}_n$, and $\overline{B}_n$ is obtained. Each of these four sets of unknowns is associated with an integer n, which varies from zero or one to infinity. In the numerical calculations, the infinite series are truncated at $n=N$. For the examples included in this paper, N ranges from 2 to 33. N is chosen in such a way that the boundary conditions are satisfied to 3 or more significant figures, which means that the error involved is 1.0×10^{-3} percent or less. The accuracy is improved by increasing a number of terms in the series. The solution holds for the whole range of a, $0<a<1$. As $a\to 1$, only the number of terms needs to be increased. When a perfectly bonded or sliding inclusion is embedded in the infinite matrix, i.e., the inclusion is far away from the free surface, the solution is given by finite series involving constants A_0, A_2, B_1, A_2, and $\overline{B}_1$. After A_n, B_n, $\overline{A}_n$, and $\overline{B}_n$ are evaluated, the stresses and displacements are known everywhere in the inclusion and the matrix.

Results and Discussion

In the numerical examples considered in this paper, the plane-strain case is assumed. This case is of interest in the light of applications to composite materials reinforced with unidirectional fibers. For simplicity, $\nu=\overline{\nu}=0.3$ is taken.

Figures 2-3 illustrate the stress σ_{yy} at points M, N, N', P, and P' (see Fig. 1) for perfect bonding (dashed lines) and pure sliding (solid lines) cases for different positions of the inclusion relative to the free surface. The radius "a" is varied from 0.2 to 0.99, while the center of the inclusion remains at a unit distance from the free surface (Fig. 1). The loading conditions include the remote uniaxial stress $\sigma_{yy}=p_o$ (Fig. 2) and the eigenstrain loading $\epsilon^*_{xx}=\epsilon^*_{yy}=\epsilon^*_{zz}$ (Fig. 3). The inclusion is assumed to be stiffer than the matrix such that the ratio $\Gamma=\overline{G}/G=100$ (note that the higher the Γ, the more pronounced is the effect of interface). It can be observed that the effect of free surface contributes significantly to the stress disturbance when the inclusion is embedded less than one diameter away from the free surface (which corresponds to $1/a<3$).

When the uniaxial loading is applied (Fig. 2) and the inhomogeneity is perfectly bonded, the maximum stress σ_{yy} occurs in the inclusion at the point N', which is closest to the free surface. The stress in the matrix near the inclusion is almost zero since the inclusion, which is stiffer than the matrix, carries the load. It is also observed that the stress σ_{yy} at the free surface is less than the applied load when the inclusion is close to the free surface. Quite a different behavior is observed when the sliding takes place at the interface. The highest stress occurs in the matrix near the free surface when the inclusion is close to the free boundary. It is interesting to observe that the hoop stress in the sliding inclusion at points N' and P' and the vicinity is compressive, while the perfect bonding solution yields tensile stresses in these regions. This compressive stress in the sliding inclusion is due to the fact that the sliding interface does not transfer shear tractions and due to the curvature of the inclusion. Therefore, the matrix, which is allowed to flow more freely around the inclusion, causes the local compressive stress in the inclusion.

When the inclusion is soft ($\Gamma\ll 1$), the presence of free surface gives rise to very high stress concentration in the matrix at point N. For this case the contribution of interface is negligible. This is expected, because in a limiting case when the inclusion becomes a hole ($\Gamma=0$), both perfect bonding and sliding cases reduce to the same result. In this limit case the present solution (for plane stress case) coincides with Mindlin's solution (Mindlin, 1948). When inclusion is away from the free surface, the solution agrees with the result for the inclusion embedded in the infinitely extended material (Muskhelishvili, 1953; Eshelby, 1957), as expected.

When discussing a solution of a sliding inclusion, which is subjected to either a uniaxial remote loading or an eigenstrain loading (nondilatational), a comment needs to be made about the tensile normal tractions that may arise at the inclusion-matrix interface. These tensile tractions imply a tendency to debond in the normal direction, but the debonding is not allowed by the sliding boundary conditions. In order to avoid the possibility of debonding, the case of remote loading may be considered in conjunction with the eigenstrain loading, when the eigenstrains are chosen in a way that the total radial stress is compressive all along the interface as suggested by Muskhelishvili (1953). This case can be obtained by a superposition of these two solutions. However, it is more informative to separate these two cases when giving the numerical results.

The more realistic boundary conditions for this problem would allow for a local debonding. This would give rise to a mixed boundary value problem. The analytical solutions to a problem, when a sliding inclusion is subjected to a uniaxial tensile loading at infinity and debonding is allowed are given by Stippes et al. (1962), Noble and Hussain (1969), Margetson

Downloaded 03 May 2010 to 171.66.16.247. Redistribution subject to ASME license or copyright; see http://www.asme.org/terms/Terms_Use.cfm

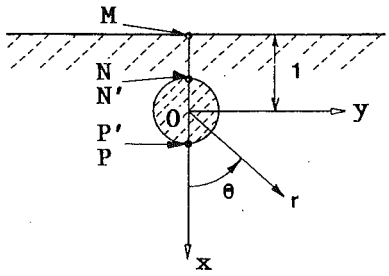


Fig. 1 Circular inclusion in a half-plane

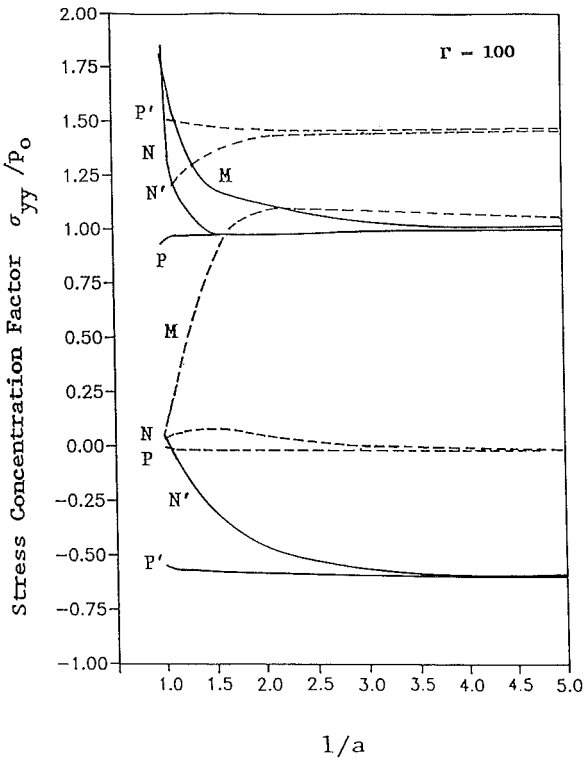


Fig. 2 σ_{yy} versus $1/a$ for a uniaxial loading $\sigma_{yy}=p_o$ when $\Gamma=100$ for perfect bonding case (dashed lines) and pure sliding case (solid lines)

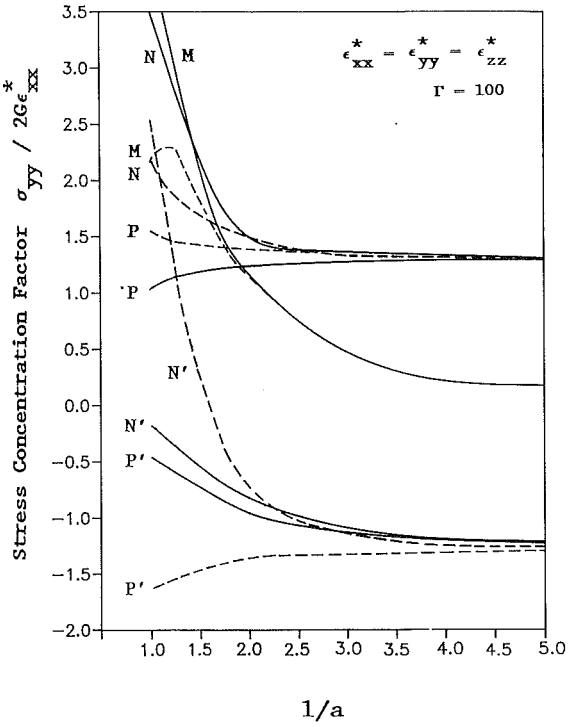


Fig. 3 σ_{yy} versus $1/a$ for an eigenstrain loading $\epsilon^*_{xx}=\epsilon^*_{yy}=\epsilon^*_{zz}$ when $\Gamma=100$ for perfect bonding (dashed lines) and pure sliding (solid lines)

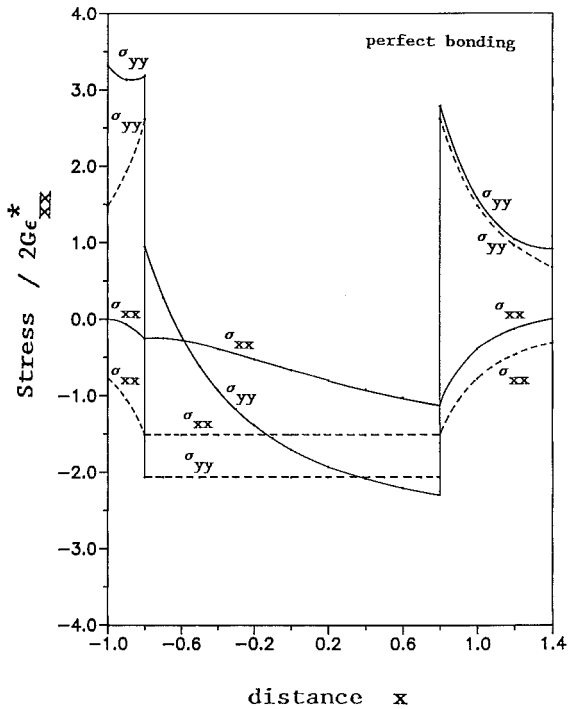


Fig. 4 σ_{xx} and σ_{yy} along the x-axis for eigenstrain loading $\epsilon^*_{xx}=\epsilon^*_{yy}/2=\epsilon^*_{zz}$ when $\Gamma=100$. Solid lines represent the case when an inclusion is located near the free surface ($a=0.8$), while dashed lines correspond to the case when the inclusion is embedded in the infinite medium.

and Morland (1970), and Keer et al. (1973), among others. In the present paper, the debonding in the normal direction is not allowed, for simplicity.

Figure 3 illustrates σ_{yy} at chosen points along the x-axis for eigenstrain loading $\epsilon^*_{xx}=\epsilon^*_{yy}=\epsilon^*_{zz}$ for both perfect bonding and pure sliding. The highest stress occurs in the matrix at the free surface for the sliding case. Also, the free surface gives rise to higher stresses in the matrix and in the inclusion near the free surface for both interfacial conditions.

Figure 4 gives stress σ_{xx} and σ_{yy} along the x-axis when the eigenstrain loading $\epsilon^*_{xx}=\epsilon^*_{yy}/2=\epsilon^*_{zz}$ is applied and $\Gamma=100$ for the perfect bonding case. The effect of free surface is illustrated by comparing the stress field of the inclusion located near the free surface (solid lines) and of the inclusion embedded in the infinite matrix (dashed lines). Note that the stresses are uniform when a perfectly bonded inclusion is embedded in the infinite medium as expected from Eshelby's solution (Eshelby, 1957), but they cease to be uniform when the inclusion is located near the free surface.

Figure 5 illustrates the jump in the tangential displacement $[u_\theta]$ along the interface of the sliding inclusion for different eigenstrain loadings $\epsilon^*_{yy}=\epsilon^*_{xx}$, $\epsilon^*_{yy}=2\epsilon^*_{xx}$ and $\epsilon^*_{yy}=\epsilon^*_{xx}/2$, while $\epsilon^*_{zz}=\epsilon^*_{xx}$, and $\Gamma=100$, when the inclusion is located a distance of one radius away from the free surface ($a=0.5$). Note that the free surface influences the degree of sliding. It is interesting to observe that the sliding occurs for the dilatational eigenstrain loading for the half-space problem, while in the infinite space, the sliding cylindrical inclusion would experience no sliding due to this symmetric eigenstrain loading. Figure 6 shows the shear stress along the interface of the perfectly bonded inclusion for the above eigenstrain loadings.

Downloaded 03 May 2010 to 171.66.16.247. Redistribution subject to ASME license or copyright; see http://www.asme.org/terms/Terms_Use.cfm

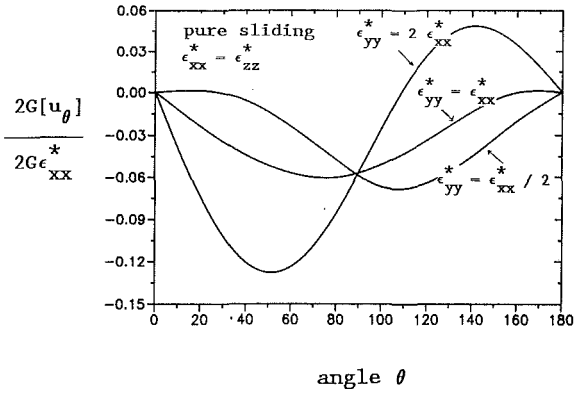


Fig. 5 Jump in the tangential displacement $[u_\theta]$ along the inclusion-matrix interface for eigenstrain loading when $\Gamma = 100$ and $a = 0.5$ (pure sliding case)

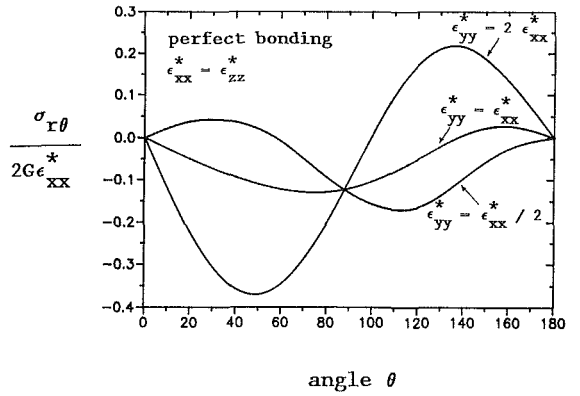


Fig. 6 Shear stress $\sigma_{r\theta}$ versus θ for eigenstrain loading when $\Gamma = 100$ (perfect bonding case)

Figure 7 gives the displacement u_x along the free surface for $0 \le y \le 1$, for both perfect bonding (dashed lines) and sliding (solid lines) cases, when a remote uniaxial loading is applied. The inclusion is embedded a distance of one radius away from the free boundary, which implies $a = 0.5$. Note that the displacement is significantly affected by Γ. The influence of interface can also be observed. The determination of the displacements at the free surface can be of interest to experimentalists since the differential strains can be measured by the experimental techniques such as stereoscopy and interference microscopy (Cox et al., 1988). These experimental and theoretical results can be used as a nondestructive technique to predict the nature of the defects inside a material (Mura, 1985).

Conclusions

In this paper, an exact elasticity solution (given in a series form) is presented for a circular sliding inclusion embedded in a half-plane in order to investigate the joint effect of a traction-free boundary and an interface. The inclusion is subjected to either a uniform remote tension or nonshear-type eigenstrain loading. It is observed that the free surface has a significant effect on the stress and displacement fields in the matrix and in the inclusion, when the inclusion is located less than one diameter from the free boundary. The effect of sliding is more pronounced when the inclusion is stiffer than the matrix. Both the free boundary and sliding give rise to the higher stress concentrations. The magnitude of these stresses depends on several factors: the mismatch of the elastic constants, the size and location of the inclusion, the boundary conditions, and other items.

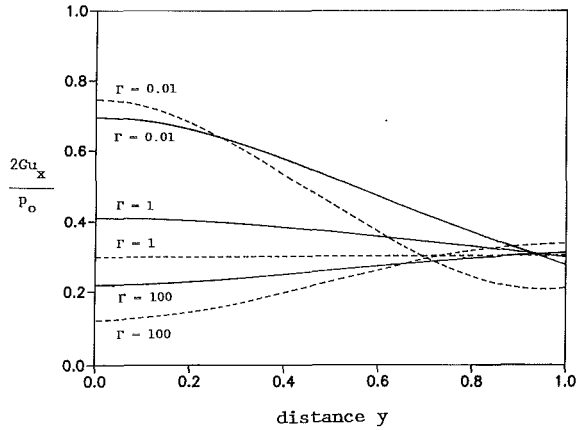


Fig. 7 Displacement u_x along the free surface for a uniaxial loading $\sigma_{yy} = p_o$ for perfect bonding (dashed lines) and pure sliding (solid lines) cases when $a = 0.5$

Acknowledgments

This research has been supported by the National Science Foundation Grant No. MSM-8810920 and the 1989/90 Research Excellence Fund from State of Michigan. The authors would also like to thank Prof. John Dundurs for some valuable comments.

References

Aderogba, K., 1976, "On Eigenstresses in a Semi-Infinite Solid," *Mathematical Proceedings of the Cambridge Philosophical Society*, Vol. 80, pp. 555–562.

Callias, C. J., and Markenscoff, X., 1989, "Singular Asymptotics Analysis for the Singularity at a Hole Near a Boundary," *Quarterly of Applied Mathematics*, Vol. 47, pp. 233–245.

Cox, B. N., Marshall, D. B., Kouris, D., and Mura, T., 1988, "Surface Displacement Analysis of the Transformed Zone in Magnesia Partially Stabilized Zirconia," *ASME Journal of Engineering Materials and Technology*, Vol. 110, pp. 105–109.

Eshelby, J. D., 1957, "The Determination of the Elastic Fields of an Ellipsoidal Inclusion, and Related Problems," *Proceedings of Royal Society, London*, Vol. A241, pp. 376–396.

Hussain, M. A., and Pu, S. L., 1971, "Slip Phenomenon for a Circular Inclusion," ASME Journal of Applied Mechanics, Vol. 38, pp. 627–633.

Ishiwata, K., 1986, "Stress Concentration Due to an Elliptic Hole or a Griffith Crack in a Semi-Infinite Elastic Plate Under Tension," Master's Dissertation, Saitama University, Japan.

Jasiuk, I., Tsuchida, E., and Mura, T., 1987, "The Sliding Inclusion Under Shear," *International Journal of Solids and Structures*, Vol. 23, pp. 1373–1385.

Jasiuk, I., Tsuchida, E., and Mura, T., 1991, "Spheroidal Sliding Inclusion in an Elastic Half Space," *Applied Mechanics Reviews*, Vol. 44, No. 11, Pt. 2, to be published.

Jeffery, G. B., 1920, "Plane Stress and Plane Strain in Bipolar Coordinates," *Transactions of Royal Society, London*, Series A, Vol. 221, pp. 265–293.

Keer, L. M., Dundurs, J., and Kiattikomol, K., 1973, "Separation of a Smooth Circular Inclusion From a Matrix," *International Journal of Engineering Science*, Vol. 11, pp. 1221–1233.

Kouris, D., and Mura, T., 1989, "The Elastic Field of a Hemispherical Inhomogeneity at the Free Surface of an Elastic Half Space," *Journal of the Mechanics and Physics of Solids*, Vol. 37, pp. 365–379.

Kouris, D., Tsuchida, E., and Mura, T., 1988, "An Anomaly of Sliding Inclusions," ASME Journal of Applied Mechanics, Vol. 53, pp. 724–726.

Kouris, D., Tsuchida, E., and Mura, T., 1989, "The Hemispheroidal Inhomogeneity at the Free Surface of an Elastic Half Space," ASME Journal of Applied Mechanics, Vol. 56, pp. 70–76.

Margetson, J., and Morland, L. W., 1970, "Separation of Smooth Circular Inclusions From Elastic and Viscoelastic Plates Subjected to Uniaxial Tension," *Journal of the Mechanics and Physics of Solids*, Vol. 18, pp. 295–309.

Mindlin, R. D., 1948, "Stress Distribution Around a Hole Near the Edge of a Plate Under Tension," *Proceedings of the Society for Experimental Stress Analysis*, Vol. 5, pp. 56–68.

Mindlin, R. D., and Cheng, D. H., 1950, "Thermoelastic Stress in the Semi-Infinite Solid," *Journal of Applied Physics*, Vol. 21, pp. 931–933.

Mura, T., 1985, "A New NDT: Evaluation of Plastic Strains in Bulk From Displacements on Surfaces," *Mechanics Research Communications*, Vol. 12, pp. 243–248.

Mura, T., 1987, *Micromechanics of Defects in Solids*, 2nd ed., Martinus Nijhoff, Dordrecht.

Mura, T., and Furuhashi, R., 1984, "The Elastic Inclusion With a Sliding Interface," ASME Journal of Applied Mechanics, Vol. 51, pp. 308–310.

Downloaded 03 May 2010 to 171.66.16.247. Redistribution subject to ASME license or copyright; see http://www.asme.org/terms/Terms_Use.cfm

Mura, T., Jasiuk, I., and Tsuchida, E., 1985, "The Stress Field of a Sliding Inclusion," *International Journal of Solids and Structures*, Vol. 21, pp. 1165–1179.

Muskhelishvili, N. I., 1953, *Some Basic Problems of the Mathematical Theory of Elasticity*, P. Noordhoff Ltd., Groningen, Holland, pp. 214–217.

Noble, B., and Hussain, M. A., 1969, "Exact Solution of Certain Dual Series for Indentation and Inclusion Problems," *International Journal of Engineering Science*, Vol. 7, pp. 1149–1161.

Richardson, M. K., 1969, "Interference Stresses in a Half Plane Containing an Elastic Disk of the Same Material," ASME JOURNAL OF APPLIED MECHANICS, Vol. 36, pp. 128–130.

Saleme, E. M., 1958, "Stress Distribution Around a Circular Inclusion in a Semi-Infinite Elastic Plate," ASME JOURNAL OF APPLIED MECHANICS, Vol. 25, pp. 129–135.

Seo, K., and Mura, T., 1979, "The Elastic Field in a Half-Space Due to Ellipsoidal Inclusions With Uniform Dilatational Eigenstrains," ASME JOURNAL OF APPLIED MECHANICS, Vol. 46, pp. 568–572.

Shioya, S., 1967, "On a Semi-Infinite Thin Plate With a Circular Inclusion Under Uniform Tension," *Bulletin of JSME*, Vol. 10, pp. 1–9.

Stippes, M., Wilson, H. B., and Krull, F. N., 1962, "A Contact Stress Problem for a Smooth Disk in an Infinite Plate," *Proceedings of the 4th U.S. National Congress of Applied Mechanics*, ASME, New York, pp. 799–806.

Tsuchida, E., Kouris, D., and Jasiuk, I., 1990, "The Hemispherical Inhomogeneity Subjected to a Concentrated Force," *Micromechanics and Inhomogeneity—The Toshio Mura 65th Anniversary Volume*, G. J. Weng, M. Taya, and H. Abe, eds., Springer-Verlag, New York, pp. 497–509.

Tsuchida, E., and Mura, T., 1983, "The Stress Field in an Elastic Half-Space Having a Spheroidal Inhomogeneity Under All-Around Tension Parallel to the Plane Boundary," ASME JOURNAL OF APPLIED MECHANICS, Vol. 50, pp. 807–816.

Tsuchida, E., Mura, T., and Dundurs, J., 1986, "The Elastic Field of an Elliptic Inclusion With a Slipping Interface," ASME JOURNAL OF APPLIED MECHANICS, Vol. 53, pp. 103–107.

Tsutsui, S., and Saito, K., 1973, "On the Effect of a Free Surface and a Spherical Inhomogeneity on Stress Fields of a Semi-Infinite Medium Under Axisymmetric Tension," *Proceedings of the 23rd Japan National Congress for Applied Mechanics*, Vol. 23, pp. 547–560.

APPENDIX

The displacements and stresses are related to the Papkovich-Neuber displacement potentials ϕ_0 and ϕ_1 as follows:

(a) in Cartesian coordinates:

$$2Gu_x=\frac{\partial\phi_0}{\partial x}+x\frac{\partial\phi_1}{\partial x}-\kappa\,\phi_1$$

$$2Gu_y=\frac{\partial\phi_0}{\partial y}+x\frac{\partial\phi_1}{\partial y}$$

$$\sigma_{xx}=\frac{\partial^2\phi_0}{\partial x^2}+x\frac{\partial^2\phi_1}{\partial x^2}-\frac{1}{2}(\kappa+1)\frac{\partial\phi_1}{\partial x}$$

$$\sigma_{yy}=\frac{\partial^2\phi_0}{\partial y^2}+x\frac{\partial^2\phi_1}{\partial y^2}-\frac{1}{2}(3-\kappa)\frac{\partial\phi_1}{\partial x}$$

$$\sigma_{xy}=\frac{\partial^2\phi_0}{\partial x\partial y}+x\frac{\partial^2\phi_1}{\partial x\partial y}-\frac{1}{2}(\kappa-1)\frac{\partial\phi_1}{\partial y} \tag{A1}$$

and (b) in polar coordinates:

$$2Gu_r=\frac{\partial\phi_0}{\partial r}+r\cos\theta\frac{\partial\phi_1}{\partial r}-\kappa\cos\theta\,\phi_1$$

$$2Gu_\theta=\frac{1}{r}\frac{\partial\phi_0}{\partial\theta}+\cos\theta\frac{\partial\phi_1}{\partial\theta}+\kappa\sin\theta\,\phi_1$$

$$\sigma_{rr}=\frac{\partial^2\phi_0}{\partial r^2}+r\cos\theta\frac{\partial^2\phi_1}{\partial r^2}-\frac{1}{2}(\kappa+1)\cos\theta\frac{\partial\phi_1}{\partial r}+\frac{1}{2}(3-\kappa)\frac{\sin\theta}{r}\frac{\partial\phi_1}{\partial\theta}$$

$$\sigma_{\theta\theta}=\frac{1}{r}\frac{\partial\phi_0}{\partial r}+\frac{1}{r^2}\frac{\partial^2\phi_0}{\partial\theta^2}+\frac{\cos\theta}{r}\frac{\partial^2\phi_1}{\partial\theta^2}+\frac{1}{2}(\kappa-1)\cos\theta\frac{\partial\phi_1}{\partial r}+\frac{1}{2}(\kappa+1)\frac{\sin\theta}{r}\frac{\partial\phi_1}{\partial\theta}$$

$$\sigma_{r\theta}=\frac{1}{r}\frac{\partial^2\phi_0}{\partial r\partial\theta}-\frac{1}{r^2}\frac{\partial\phi_0}{\partial\theta}+\cos\theta\frac{\partial^2\phi_1}{\partial r\partial\theta}+\frac{1}{2}(\kappa-1)\sin\theta\frac{\partial\phi_1}{\partial r}-\frac{1}{2}(\kappa+1)\frac{\cos\theta}{r}\frac{\partial\phi_1}{\partial\theta} \tag{A2}$$

where

$$\nabla^2\phi_1=\nabla^2\phi_2=0$$

and

$$\nabla^2=\frac{\partial^2}{\partial x^2}+\frac{\partial^2}{\partial y^2}=\frac{\partial^2}{\partial r^2}+\frac{1}{r}\frac{\partial}{\partial r}+\frac{1}{r^2}\frac{\partial^2}{\partial\theta^2}\,.$$

Downloaded 03 May 2010 to 171.66.16.247. Redistribution subject to ASME license or copyright; see http://www.asme.org/terms/Terms_Use.cfm

Stress Concentration at a Nearly Circular Hole With Uncertain Irregularities[1]

Dan Givoli
Senior Lecturer,
Faculty of Aerospace Engineering,
Technion-Israel Institute of Technology,
Haifa 32000, Israel

Isaac Elishakoff
Professor,
Department of Mechanical Engineering and
Associate Director,
Center for Applied Stochastics Research,
Florida Atlanta University,
Boca Raton, FL 33431-0991

We study the stress concentration on the boundary of an uncertain nearly circular hole in an infinite elastic plane under uniform radial tension at infinity. The uncertainty in the deviation of the hole profile from an ideal circle is modeled deterministically. The shape of the hole boundary in polar coordinates is assumed to have the form $r = R + \epsilon h(\theta)$, where R is the radius of the unperturbed circle and ϵ is a small parameter. First, we find an asymptotic solution for the stress concentration factor around the hole for any profile $h(\theta)$. Then we consider a certain set of bounded profiles, and we find the specific profile that yields the maximum stress concentration factor. This may provide the designer with a useful "worst case" information regarding the influence of the uncertainty of the hole shape on the uncertainty of the resulting stress concentration factor.

1 Introduction

Stress concentrations in the vicinity of holes of various profiles have been treated in a number of publications. For the pertinent bibliography one may consult Neuber (1958), Savin (1961), and Peterson (1974). Traditionally, the stress concentration factors (SCF) around holes of ideal shapes have been considered. However, in practice the manufacturing process of structural parts inevitably produces imperfections which may affect the actual value of the SCF. Irregularities of ideally shaped holes have been modeled using a probabilistic description by Pal'mov (1964). The profile of the hole as a random function was also treated by Sayles (1982).

Lomakin (1968) has developed a double perturbation scheme for a hole with a rapidly oscillating boundary. The boundary was characterized as a random stationary Gaussian function with zero mean and with a specified autocorrelation function. The stress concentration factor κ was determined, as suggested by Pal'mov (1964), from the condition that $\sigma_{\theta\theta} < \kappa E(\sigma_{\theta\theta})$ holds in the region $0 \leq \theta \leq 2\pi$ with specified probability P. Here $\sigma_{\theta\theta}$ is the circumferential stress at the boundary (which turns out to be a random function too), and $E(\sigma_{\theta\theta})$ is its mathematical expectation. If one has a complete probabilistic description of the irregularity of the hole boundary, Lomakin's approach is an attractive method to examine its effect on the stress concentration. Yet, in many cases, only a limited amount of information on the irregularities may be available.

In the present paper we investigate the stress concentration at the boundary of a nearly circular hole in an infinite elastic plane under uniform radial tension at infinity. We consider the apparently more realistic situation, where we do not possess the full probabilistic information, but only have a partial knowledge with regard to the shape of the imperfection around the hole boundary. We define an admissible imperfection profile as one which is bounded in some sense, and which may be required to have (depending on the boundedness restriction of the profile) a finite number of harmonics in its Fourier expansion. Then we find the worst case possible, namely the imperfection profile that gives, among all admissible profiles, the maximal SCF.

The technique used here to obtain the SCF for a circular hole with arbitrary irregularities is the boundary perturbation method. Early works employed other methods to treat holes of arbitrary shapes (Isida and Tagami, 1959; Averin, 1964).

In Section 2 we find a first-order asymptotic approximation of the SCF at the boundary of a nearly circular hole. We compare our results with the exact solution of Tunguskova (1970) for the specific geometry of a hypotrochoid, and make some conclusions regarding the quality of our approximate solution. In Section 3 we solve the "optimization" problem and find the worst admissible imperfection profile and the corresponding SCF. We present some results for typical numerical data.

2 An Asymptotic Solution for the Stress Concentration Problem

We consider an infinite isotropic elastic plane with a nearly circular hole. We denote the boundary of the hole $\mathcal{B}^\epsilon$, to indicate that it is an ϵ-perturbation from an ideal circle denoted

[1]Dedicated to the 100 Anniversary of the birth of the Academician, N. I. Muskhelishvili.

Contributed by the ASME Applied Mechanics Division of The American Society of Mechanical Engineers for presentation at the Winter Annual Meeting, Atlanta, GA., Dec. 1-6, 1991.

Discussion on this paper should be addressed to the Technical Editor, Prof. Leon M. Keer, The Technological Institute, Northwestern University, Evanston, IL 60208, and will be accepted until two months after final publication of the paper itself in the JOURNAL OF APPLIED MECHANICS. Manuscript received by the ASME Applied Mechanics Division, Jan. 24, 1990; final revision, May 14, 1991.
Paper No. 91-WA/APM-22.

Copyright © 1992 by ASME
Downloaded 03 May 2010 to 171.66.16.247. Redistribution subject to ASME license or copyright; see http://www.asme.org/terms/Terms_Use.cfm

$\mathcal{B}$. The domains outside $\mathcal{B}$ and $\mathcal{B}^\epsilon$ are denoted Ω and Ω^ϵ, respectively. The boundary of the hole $\mathcal{B}^\epsilon$ is assumed to be traction-free. We describe this boundary in polar coordinates by

$$r^\epsilon(\theta) = R + \epsilon h(\theta) \tag{1}$$

where r^ϵ is the value of the radial distance r on $\mathcal{B}^\epsilon$, R is the radius of the circle $\mathcal{B}$, ϵ is a small parameter, and $h(\theta)$ is a 2π-periodic function. It is assumed that $h(\theta)$ possess a sufficient number of continuous derivatives, according to the requirements of the asymptotic expansion below, and that ϵ is small with respect to h/R, h'/R, etc.

At infinity, a uniform radial tensile stress σ_∞ is prescribed. Radially nonuniform loading (e.g., uniaxial tension) may also be treated by exactly the same technique, but the algebraic manipulations become considerably more complicated in this case. We shall treat nonuniform loading as well as the anisotropic case in future work.

The statement of the problem whose solution is the stress distribution in Ω^ϵ is:

$$\sigma_{ij,j} = 0 \quad \text{in} \quad \Omega^\epsilon \tag{2}$$

$$\sigma_{rr} = \sigma_\infty, \quad \sigma_{r\theta} = 0 \quad \text{at} \quad r \to \infty \tag{3}$$

$$T_i = \sigma_{ij} n_j = 0 \quad \text{on} \quad \mathcal{B}^\epsilon, \tag{4}$$

with a standard notation. In (4), n_j is the j-component of the unit vector $\mathbf{n}$ normal to $\mathcal{B}^\epsilon$ and pointing outside Ω^ϵ.

We shall solve the problem (2)–(4) using a perturbation method. A general treatment of perturbation methods for eigenvalue problems with distorted boundaries has been given by Morse and Feshbach (1953). Van Dyke (1975) used the method to solve Laplace's equation outside a slightly distorted circle with $h(\theta) = -R\sin^2\theta$ in (1). Recently, Parnes and Beltzer (1986) used it to solve elasticity problems in circular domains with eccentric loading and in elliptic domains. We shall use a similar method, but with no restriction on the function $h(\theta)$ in (1), namely we shall find an asymptotic solution valid for any small perturbation from the perfect circular hole.

We write the stress σ_{ij} as a perturbation series:

$$\sigma_{ij} = \sigma_{ij}^{(0)} + \epsilon\sigma_{ij}^{(1)} + \epsilon^2\sigma_{ij}^{(2)} + \dots . \tag{5}$$

Substituting (5) into (2) and into (3), and setting the coefficients of different powers of ϵ equal to zero, we conclude

$$\sigma_{ij,j}^{(k)} = 0 \quad \text{in} \quad \Omega; \quad k = 0, 1, 2 \dots \tag{6}$$

$$\sigma_{rr}^{(0)} = \sigma_\infty, \quad \sigma_{r\theta}^{(0)} = 0, \quad \text{at} \quad r \to \infty, \tag{7}$$

$$\sigma_{rr}^{(k)} = \sigma_{r\theta}^{(k)} = 0, \quad k \geq 1, \quad \text{at} \quad r \to \infty. \tag{8}$$

The derivation of asymptotic boundary conditions on $\mathcal{B}$ from (4) is more complicated. First, the tractions in (4) are defined with respect to the normal $\mathbf{n}$ to $\mathcal{B}^\epsilon$ whereas the asymptotic expressions for the tractions on $\mathcal{B}$ have to be given with respect to the normal $\mathbf{e}_r$ (see Fig. 1). We derive an expression for the vector $\mathbf{n}$ in Appendix A. Its components in the directions $\mathbf{e}_r$ and $\mathbf{e}_\theta$ are found to be

$$-n_r = 1 - \epsilon^2\frac{(h')^2}{2R^2} + O(\epsilon^3) \tag{9}$$

$$-n_\theta = -\epsilon\frac{h'}{R} + \epsilon^2\frac{h'h}{R^2} + O(\epsilon^3). \tag{10}$$

This agrees with Lomakin's result (Lomakin, 1968). Here a prime indicates differentiation with respect to θ. Now (4) in polar coordinates reads

$$T_r = \sigma_{rr}n_r + \sigma_{r\theta}n_\theta = 0$$
$$\text{on} \quad \mathcal{B}^\epsilon. \tag{11}$$
$$T_\theta = \sigma_{\theta r}n_r + \sigma_{\theta\theta}n_\theta = 0$$

Using (5), (9), and (10) in (11), we obtain two equations involving $\sigma_{rr}^{(k)}(r^\epsilon, \theta)$ and $\sigma_{r\theta}^{(k)}(r^\epsilon, \theta)$. However, we still cannot

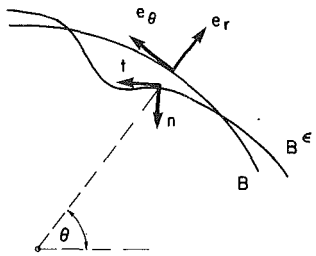


Fig. 1 Unit vectors on the ideal circular boundary $\mathcal{B}$ and on the imperfect boundary $\mathcal{B}^\epsilon$

equate like powers of ϵ to zero since r^ϵ is also a function of ϵ. Therefore, we first expand $\sigma_{ij}^{(k)}(r^\epsilon, \theta)$ in a Taylor series around $\sigma_{ij}^{(k)}(R, \theta)$:

$$\sigma_{ij}^{(k)}(r^\epsilon,\theta) = \sigma_{ij}^{(k)}(R,\theta) + \epsilon h\sigma_{ij,r}^{(k)}(R,\theta) + \frac{1}{2}\epsilon^2h^2\sigma_{ij,rr}^{(k)}(R,\theta) + \dots . \tag{12}$$

After substituting (12) in the two equations obtained by (11) we can equate like powers of ϵ to zero and obtain the desired boundary conditions on the circle $\mathcal{B}$. We write the resulting boundary conditions up to the second order:

$$\sigma_{rr}^{(0)}(R,\theta) = 0 \tag{13}$$

$$\sigma_{rr}^{(1)}(R,\theta) = \frac{h'}{R}\sigma_{r\theta}^{(0)} - h\sigma_{rr,r}^{(0)} \tag{14}$$

$$\sigma_{rr}^{(2)}(R,\theta) = \frac{h'}{R}\sigma_{r\theta}^{(1)} - h\sigma_{rr,r}^{(1)} - \frac{1}{2}h^2\sigma_{rr,rr}^{(0)} + \frac{(h')^2}{2R^2}\sigma_{rr}^{(0)} + \frac{hh'}{R}\sigma_{r\theta,r}^{(0)} - \frac{hh'}{R^2}\sigma_{r\theta}^{(0)} \tag{15}$$

$$\sigma_{r\theta}^{(0)}(R,\theta) = 0 \tag{16}$$

$$\sigma_{r\theta}^{(1)}(R,\theta) = \frac{h'}{R}\sigma_{\theta\theta}^{(0)} - h\sigma_{r\theta,r}^{(0)} \tag{17}$$

$$\sigma_{r\theta}^{(2)}(R,\theta) = \frac{h'}{R}\sigma_{\theta\theta}^{(1)} - h\sigma_{r\theta,r}^{(1)} - \frac{1}{2}h^2\sigma_{r\theta,rr}^{(0)} + \frac{(h')^2}{2R^2}\sigma_{r\theta}^{(0)} + \frac{hh'}{R}\sigma_{\theta\theta,r}^{(0)} - \frac{hh'}{R^2}\sigma_{\theta\theta}^{(0)}. \tag{18}$$

In (13)–(18), all the functions on the right side are evaluated at $r = R$.

We note that Eqs. (13), (16), and (17) can be used to simplify Eqs. (14), (15), and (18). Thus, Eqs. (14), (15), and (18) can be replaced by

$$\sigma_{rr}^{(1)}(R,\theta) = -h\sigma_{rr,r}^{(0)} \tag{14a}$$

$$\sigma_{rr}^{(2)}(R,\theta) = \left(\frac{h'}{R}\right)^2\sigma_{\theta\theta}^{(0)} - h\sigma_{rr,r}^{(1)} - \frac{1}{2}h^2\sigma_{rr,rr}^{(0)} \tag{15a}$$

$$\sigma_{r\theta}^{(2)}(R,\theta) = \frac{h'}{R}\sigma_{\theta\theta}^{(1)} - h\sigma_{r\theta,r}^{(1)} - \frac{1}{2}h^2\sigma_{r\theta,rr}^{(0)} + \frac{hh'}{R}\sigma_{\theta\theta,r}^{(0)} - \frac{hh'}{R^2}\sigma_{\theta\theta}^{(0)}. \tag{18a}$$

Equations (6), (7), (8), and (13)–(18) define a sequence of problems in the domain Ω. In what follows we solve the first two problems in this sequence, namely we find a first-order asymptotic approximation. The zeroth-order problem is axisymmetric and is easily solved. Its solution is

$$\sigma_{rr}^{(0)} = \sigma_\infty(1 - R^2/r^2)$$

$$\sigma_{\theta\theta}^{(0)} = \sigma_\infty(1 + R^2/r^2)$$

$$\sigma_{r\theta}^{(0)} = 0. \tag{19}$$

Downloaded 03 May 2010 to 171.66.16.247. Redistribution subject to ASME license or copyright; see http://www.asme.org/terms/Terms_Use.cfm

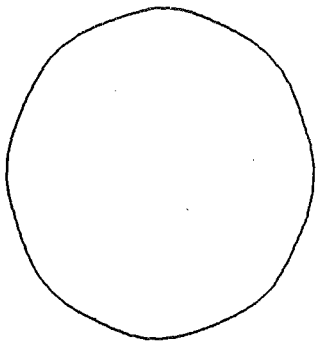


Fig. 2 A hypotrochoid with $k = 7$ and $\epsilon = 0.01$

Using this solution as well as (6), (8), (14), and (17), we conclude that $\sigma_{ij}^{(1)}$ must satisfy

$$\sigma_{ij,j}^{(1)} = 0 \quad \text{in} \quad \Omega \tag{20}$$

$$\sigma_{rr}^{(1)} = \sigma_{r\theta}^{(1)} = 0 \quad \text{at} \quad r \to \infty \tag{21}$$

$$\sigma_{rr}^{(1)}(R,\theta) = -\frac{2\sigma_\infty}{R} h(\theta) \tag{22}$$

$$\sigma_{r\theta}^{(1)}(R,\theta) = \frac{2\sigma_\infty}{R} h'(\theta). \tag{23}$$

This problem is solved in Appendix B. The solution for $\sigma_{\theta\theta}^{(1)}$ can be written in the form

$$\sigma_{\theta\theta}^{(1)} = \frac{2\sigma_\infty}{R} \sum_{n=0}^{\infty} \int_0^{2\pi} [-B_r^n(r,\theta,\theta')h(\theta') + B_\theta^n(r,\theta,\theta')h'(\theta')]d\theta' \tag{24}$$

where the kernels B_r^n and B_θ^n are given by Eqs. (B14)–(B15) of Appendix B.

Now, (19) and (24) provide us with an approximate solution on the circular boundary $\mathcal{B}$. To obtain a solution on the actual boundary $\mathcal{B}^\epsilon$ we use (12) and (5) again. This gives

$$\sigma_{ij}(r^\epsilon,\theta) = \sigma_{ij}^{(0)}(R,\theta) + \epsilon[h(\theta)\sigma_{ij,r}^{(0)}(R,\theta) + \sigma_{ij}^{(1)}(R,\theta)] + O(\epsilon^2) \tag{25}$$

which provides an expression for $\sigma_{\theta\theta}$ on $\mathcal{B}^\epsilon$. However, the SCF is defined via the circumferential stress σ_{tt} on $\mathcal{B}^\epsilon$ rather than via $\sigma_{\theta\theta}$. (See Fig. 1 for the difference between $\mathbf{t}$ and $\mathbf{e}_\theta$.) To find σ_{tt} we transform the stresses according to the formula

$$\sigma_{tt} = \sigma_{rr}\sin^2\phi + \sigma_{\theta\theta}\cos^2\phi - \sigma_{r\theta}\sin 2\phi, \tag{26}$$

where ϕ is the angle between $\mathbf{e}_r$ and $\mathbf{n}$. We readily find that $\cos\phi = n_r$ and $\sin\phi = -n_\theta$. Then from (26), (25), (9), (10), (19), and (24) we obtain the stress concentration factor κ along $\mathcal{B}^\epsilon$:

$$\frac{\kappa}{2} \doteq \frac{\sigma_{tt}(r^\epsilon,\theta)}{2\sigma_\infty} = 1 - \frac{\epsilon}{R}\left\{h(\theta) + \sum_{n=0}^{\infty} \int_0^{2\pi} [B_r^n(R,\theta,\theta')h(\theta') - B_\theta^n(R,\theta,\theta')h'(\theta')]d\theta'\right\} + O(\epsilon^2) \tag{27}$$

Now we substitute the expressions (B16)–(B21) of Appendix B for the kernels B_r^n and B_θ^n in (27) and integrate by parts the last term on the right side, to finally obtain

$$\kappa = 2\left[1 - g(\theta) + \frac{1}{\pi} \sum_{n=0}^{\infty} \alpha_n \int_0^{2\pi} \cos n(\theta - \theta')g(\theta')d\theta'\right] \tag{28}$$

$$g(\theta) = \epsilon h(\theta)/R \tag{29}$$

$$\alpha_0 = \frac{1}{2}, \quad \alpha_n = 2n - 1 \quad \text{for} \quad n \geq 1. \tag{30}$$

It is easy to verify that if $g(\theta)$ is constant, corresponding to an ideal circle, then $\kappa = 2$. Moreover, even when $g(\theta) = \cos\theta$ or $g(\theta) = \sin\theta$, then (28) yields the constant value $\kappa = 2$. This implies that, for these boundary profiles, the effect which the deviation from the ideal circle has on the SCF does not manifest itself in the first-order perturbation term.

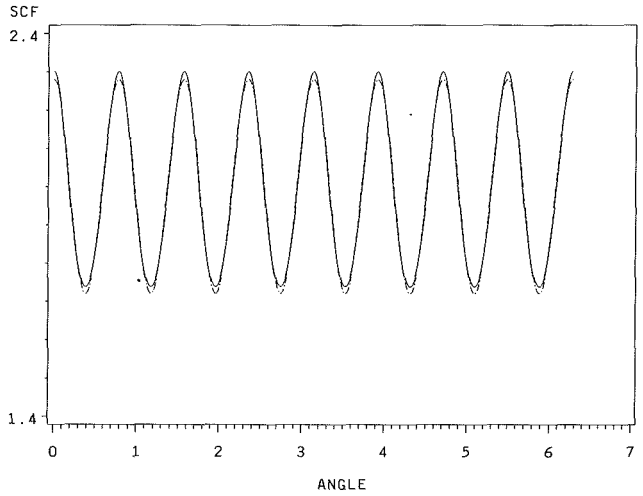


Fig. 3 A comparison between Tunguskova's exact SCF (the solid line) and the present asymptotic SCF (the dashed line) for the hypotrochoid of Fig. 2

We now compare our result to that of Tunguskova (1970), who presented an exact expression for the SCF around a hole in the shape of a hypotrochoid (Lockwood, 1961). In cartesian coordinates this curve is defined by the parametric equations

$$x = R(\cos t + \epsilon \cos kt), \quad y = R(\sin t - \epsilon \sin kt) \tag{31}$$

where k is a non-negative integer and $0 < \epsilon k < 1$. The polar coordinates on this curve can easily be written as a function of the parameter t and be expanded in powers of ϵ. This results in

$$\tan\theta = \tan t - \epsilon \frac{\sin(k+1)t}{\cos^2 t} + O(\epsilon^2) \tag{32}$$

$$r = R + \epsilon R\cos(k+1)t + O(\epsilon^2). \tag{33}$$

One also can see that $\cos(k+1)t = \cos(k+1)\theta + O(\epsilon)$. Comparing (33) with (1) and using (29) we obtain

$$g(\theta) = \epsilon \cos(k+1)\theta. \tag{34}$$

Figure 2 describes a hypotrochoid with $k = 7$ and $\epsilon = 0.01$.

Tunguskova's exact stress concentration factor κ^* around the hole is

$$\kappa^* = \frac{2(1-\epsilon^2k^2)}{1 - 2\epsilon k \cos(k+1)t + \epsilon^2k^2}, \tag{35}$$

with a maximum value of

$$\max \kappa^* = \frac{2(1+\epsilon k)}{1-\epsilon k}. \tag{36}$$

On the other hand, we obtain from our asymptotic solution (28) after substituting the function $g(\theta)$ given in (34) and using the orthogonality property of the trigonometric functions,

$$\kappa = 2[1 + 2\epsilon k\cos(k+1)\theta], \tag{37}$$

with a maximum value of

$$\max \kappa = 2(1 + 2\epsilon k). \tag{38}$$

Note that (37) and (38) can be obtained from (35) and (36), respectively, by using Taylor series up to first order in ϵ.

In Fig. 3 we compare between the exact solution (35) (the solid line) and the asymptotic solution (37) (the dashed line) for $k = 7$ and $\epsilon = 0.01$. The agreement between the two solutions is excellent. An easy calculation shows that the relative difference between the maximum values of κ^* and κ is

Downloaded 03 May 2010 to 171.66.16.247. Redistribution subject to ASME license or copyright; see http://www.asme.org/terms/Terms_Use.cfm

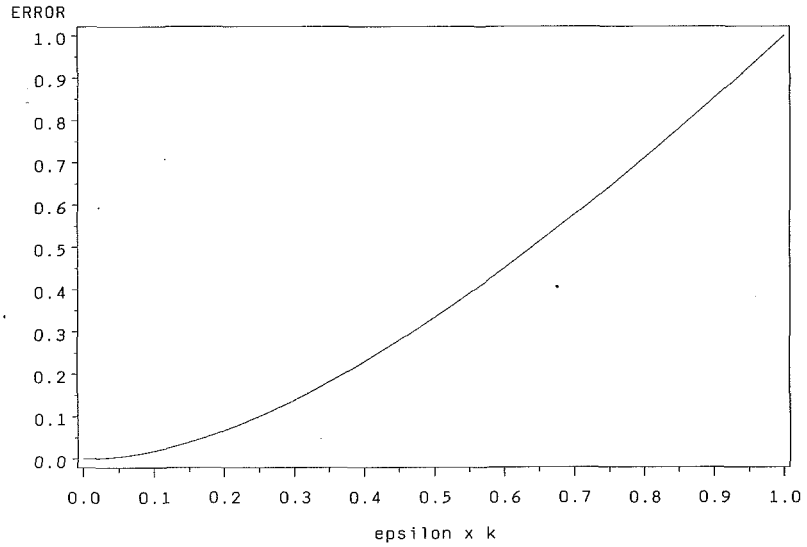


Fig. 4 The relative error in the maximal asymptotic SCF as a function of ϵk

$$\frac{\max \kappa^* - \max \kappa}{\max \kappa^*} = \frac{2(\epsilon k)^2}{1+\epsilon k}. \tag{39}$$

In Fig. 4 we plot this relative error as a function of ϵk. With the choice $k = 7$ and $\epsilon = 0.01$, the relative error amounts to 0.9 percent only. Enlarging ϵ to 0.035 we get an error of about 10 percent. This may raise the question whether our first-order asymptotic solution (28) is satisfactory. We claim that in many practical situations it is, since ϵk is very small. We are interested in *small* irregularities, and an irregularity characterized by $\kappa = 0.01$ is quite usual in practice. As to the value of k, we confine ourselves to the case where k is of order 10 at the most. If k is large, say 100, we may use Lomakin's asymptotic solution (Lomakin, 1968), which is valid only for this case of a rapidly oscillating boundary. In this sense, our solution and that of Lomakin are complementary.

3 A Worst-Case Investigation

Now we shall define a set of admissible functions $g(\theta)$, namely a set of admissible hole profiles. Then we shall find the admissible profile that gives the maximal SCF at a given point on the boundary of the hole.

We first assume that an admissible profile has only a *finite* number M of "important" Fourier components in the angle θ, and that all higher harmonics can be neglected. (Later we shall consider some other cases in which this requirement is eliminated.) Thus, we write

$$g(\theta) = \sum_{m=0}^{M} (A_m \cos m\theta + B_m \sin m\theta). \tag{40}$$

We also assume that the irregularities are bounded in the L_2 sense, namely

$$\int_0^{2\pi} g^2(\theta) d\theta \le \alpha, \tag{41}$$

where α is a given constant. The set of admissible profiles $g(\theta)$ consists of those functions which are of the form (40) and satisfy (41).

We wish to find $g(\theta)$ which maximizes κ in (28) at a given angle $\theta = \theta_0$. The angle θ_0 will turn out later to be arbitrary. Substituting (40) in (28) and setting $\theta = \theta_0$ results in

$$I \doteq \frac{\kappa(\theta_0)}{2} = 1 + \sum_{m=1}^{M} 2(m-1)(A_m \cos m\theta_0 + B_m \sin m\theta_0). \tag{42}$$

In addition, (40) and (41) give the inequality constraint

$$2\pi A_0^2 + \pi \sum_{m=1}^{M} (A_m^2 + B_m^2) \le \alpha. \tag{43}$$

We write (43) in the form of an equality constraint,

$$J \doteq 2A_0^2 + \sum_{m=1}^{M} (A_m^2 + B_m^2) + p^2 - \frac{\alpha}{\pi} = 0 \tag{44}$$

where p is considered as a new unknown. Now the problem is to find the coefficients A_m and B_m that will maximize I subject to the constraint $J = 0$.

This problem is easily solved by the Lagrange multiplier method. The unknowns are A_0, A_m, B_m ($m = 1, 2, \ldots, M$), p, and the Lagrange multiplier λ. The necessary conditions for extremum are

$$\frac{\partial(I+\lambda J)}{\partial A_m} = 2(m-1)\cos m\theta_0 + 2A_m\lambda = 0, \quad m \ge 1, \tag{45}$$

$$\frac{\partial(I+\lambda J)}{\partial B_m} = 2(m-1)\sin m\theta_0 + 2B_m\lambda = 0, \quad m \ge 1, \tag{46}$$

$$\frac{\partial(I+\lambda J)}{\partial p} = 2\lambda p = 0, \quad \frac{\partial(I+\lambda J)}{\partial A_0} = 4\lambda A_0 = 0. \tag{47}$$

From (45) and (46) we deduce that $\lambda \neq 0$, and therefore from (47) $p = 0$, namely the constraint is active, and $A_0 = 0$. Also,

$$A_m = -\lambda^{-1}(m-1)\cos m\theta_0, \quad m \ge 1, \tag{48}$$

$$B_m = -\lambda^{-1}(m-1)\sin m\theta_0, \quad m \ge 1. \tag{49}$$

Using these expressions in (44) with $p = 0$ we get

$$\lambda^2 = \frac{\beta_M \pi}{\alpha}, \tag{50}$$

where

$$\beta_M = \sum_{m=2}^{M} (m-1)^2 = \frac{M(M-1)(2M-1)}{6}. \tag{51}$$

Then, from (48) and (49) we finally have

$$A_m = \frac{(m-1)\cos m\theta_0}{(\beta_M \pi/\alpha)^{1/2}}, \quad m \ge 1, \tag{52}$$

Downloaded 03 May 2010 to 171.66.16.247. Redistribution subject to ASME license or copyright; see http://www.asme.org/terms/Terms_Use.cfm

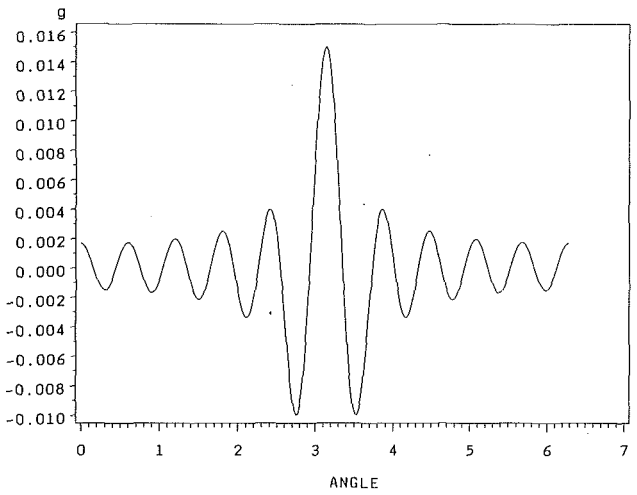


Fig. 5 The "worst-case" profile $g(\theta)$ for the parameters $M = 10$ and $\alpha = 10^{-4}$

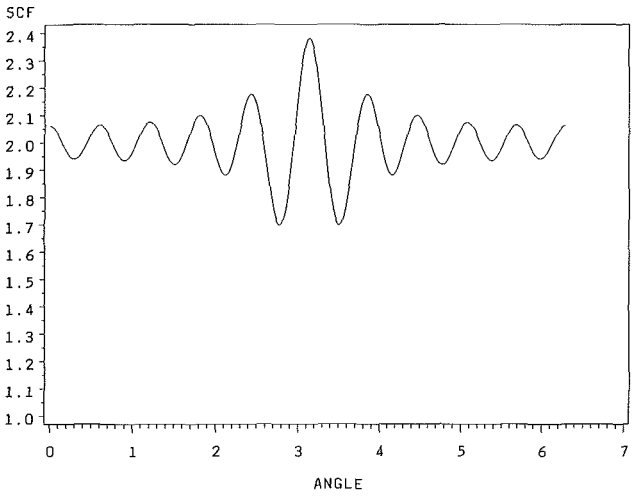


Fig. 6 The distribution of the SCF around the "worst-case" profile

$$B_m = \frac{(m-1)\sin m\theta_0}{(\beta_m \pi/\alpha)^{1/2}}, \quad m \geq 1. \tag{53}$$

Note that we chose the negative root of λ^2 in (50), because in order to obtain a maximum for I, A_m and B_m must have the same signs as $\cos m\theta_0$ and $\sin m\theta_0$, respectively.

Equations (40), (51), (52), and (53) define the admissible "worst case" profile. The corresponding maximal stress concentration factor κ is found from (42) to be

$$\kappa(\theta_0) = 2\left(1 + 2\sqrt{\frac{\beta_M \alpha}{\pi}}\right). \tag{54}$$

As expected, the maximal κ does not depend on the angle θ_0. The SCF around the hole boundary is given by (cf. (42))

$$\kappa(\theta) = 2\left[1 + \sum_{m=2}^{M} 2(m-1)(A_m \cos m\theta + B_m \sin m\theta)\right]. \tag{55}$$

It is interesting to note that the *average* of κ around the boundary of the hole, $(1/2\pi)\int_0^{2\pi} \kappa(\theta)d\theta$, is always 2, i.e., it is equal to the SCF for a circle.

Figure 5 is the graph of the profile function $g(\theta)$ for the parameters $M = 10$ and $\alpha = 10^{-4}$. The angle θ_0 was arbitrarily chosen to be π. Any other choice for θ_0 would just shift the plot horizontally. The maximal value of g, namely the maximal imperfection size divided by R, is 0.015 at θ_0. Figure 6 shows the corresponding distribution of κ around the hole boundary. The maximal SCF is 2.38, namely 19 percent higher than the SCF associated with the ideal boundary.

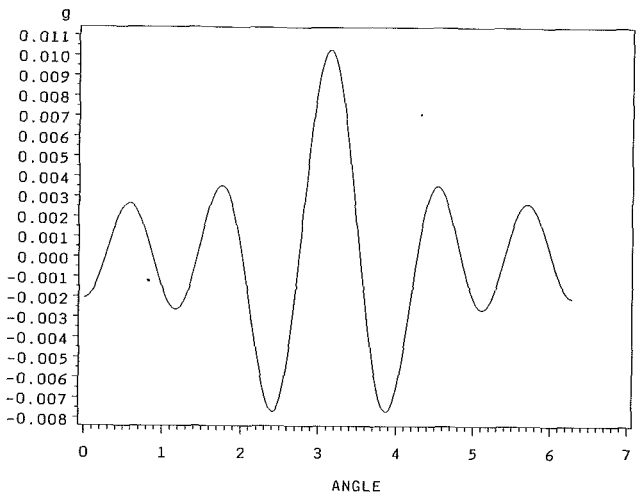


Fig. 7 The "worst-case" profile $g(\theta)$ for the parameters $M = 5$ and $\alpha = 10^{-4}$

Figure 7 is the graph of $g(\theta)$ for the parameters $M = 5$ and $\alpha = 10^{-4}$. Here, the maximal value of g is 0.010. The maximal corresponding SCF is now 2.12, or 6 percent above that for a circle.

It is instructive to compare the SCF obtained by the worst profile with the one obtained by a hypotrochoid, as found by Tunguskova (1970). The maximal stress concentration factor $(\kappa_h)_{\max}$ for a hypotrocoid is given in (38) as $(\kappa_h)_{\max} = 2 + 4\epsilon k$. To compare it with the worst-case stress concentration factor $(\kappa)_{\max}$, we set the maximal number of harmonics to $M = k + 1$ (cf. (34)). Also, the appropriate bound α in (41) is calculated from (34) to be

$$\alpha = \int_0^{2\pi} g^2(\theta)d\theta = \epsilon^2 \pi. \tag{56}$$

Then, from (54) and (51) we deduce that

$$(\kappa)_{\max} = 2 + 4\epsilon\left(\frac{(k+1)k(2k+1)}{6}\right)^{1/2}. \tag{57}$$

Comparing (38) with (57) it is easy to verify that always $(\kappa)_{\max} \geq (\kappa_h)_{\max}$, and that the equality holds only if $k = 1$, namely $M = 2$. This means that among all the holes whose profile is described by at most two harmonics, the hypotrochoid is the worst one. Substituting the numerical values $\epsilon = 0.01$ and $k = 7$, as in Fig. 2, we get $(\kappa_h)_{\max} = 2.30$ and $(\kappa)_{\max} = 2.47$. In other words, the hypotrochoid and the worst profile yield stress concentration factors which are greater by 15 percent and 23.5 percent, respectively, than that of a circle.

One may wonder whether it is also possible to find the "best-case" profile, for which the stress concentration factor κ would be minimal. Since the average of κ around the nearly circular boundary according to our asymptotic analysis is always 2, there is no profile within the set considered which gives a SCF smaller than 2 at all the points on the boundary. Therefore, the "optimal" profile in the general sense is a circle. However, an interesting (although maybe academic) question is: What is the lowest κ that one can achieve within the set of admissible profiles (as defined above)? The answer is obtained by repeating the analysis while choosing the positive root of λ^2 in (50) instead of the negative root. The minimal κ is found to be

Downloaded 03 May 2010 to 171.66.16.247. Redistribution subject to ASME license or copyright; see http://www.asme.org/terms/Terms_Use.cfm

$$\kappa(\theta_0) = 2\left(1 - 2\sqrt{\frac{\beta_M \alpha}{\pi}}\right). \tag{58}$$

For $M = 10$ and $\alpha = 10^{-4}$ the minimal SCF is 1.62. The corresponding profile is the same as the one in Fig. 5, but with an opposite sign. The maximal κ obtained for this profile is 2.30.

Up to this point the set of admissible imperfection profiles $g(\theta)$ was defined via the boundedness restriction (41) and the requirement that $g(\theta)$ has a *finite* number of harmonics. The latter requirement has several deficiencies. First, it is a very strong requirement which causes many otherwise reasonable profiles to be excluded. Second, it may be impractical for the designer to determine how many harmonics are needed in the analysis. Third, and perhaps most important, the SCF result obtained above (see Eqs. (54) and (51)) grows without limit as the number of harmonics M increases. This is expected since Eq. (41) does not pose any restriction on the *curvature* of the profile, and so the worst-case profile tends to a saw-type function as M tends to infinity.

To overcome these deficiencies, we now replace Eq. (41) by a constraint on the curvature of the profile, i.e.,

$$\int_0^{2\pi} (g''(\theta))^2 d\theta \le \gamma, \tag{59}$$

where γ is a given positive number. This enables us to go again through the derivation while totally eliminating the requirement that $g(\theta)$ has a finite number of harmonics. The end result of this derivation for the maximal SCF is found to be (cf. Eq. (54)),

$$\kappa = 2\left(1 + 2\sqrt{\frac{\mu\gamma}{\pi}}\right), \tag{60}$$

where

$$\mu = \sum_{m=2}^{\infty} \frac{(m-1)^2}{m^4} = 0.3230\ldots . \tag{61}$$

Thus, with the constraint of the form (59) we are able to sum the series in (60), whereas the series in (51), which is based on the constraint (41), does not converge as M tends to infinity.

Both restrictions (41) and (59) can be viewed as special cases of the general restriction,

$$\int_0^{2\pi} [\alpha_0 g^2 + \alpha_1 (g')^2 + \alpha_2 (g'')^2 + \ldots + \alpha_L (g^{(L)})^2] d\theta \le \gamma, \tag{62}$$

where the α_i are given real constants. The maximal SCF in this general case is again given by (60), where the expression (61) for μ is replaced by

$$\mu = \sum_{m=2}^{\infty} \frac{(m-1)^2}{\alpha_0 + \alpha_1 m^2 + \alpha_2 m^4 + \ldots + \alpha_L m^{2L}}. \tag{63}$$

The sum in (63) converges if and only if at least one of the coefficients α_i for $i \ge 2$ is nonzero. Thus, in order that no requirement on the number of harmonics of $g(\theta)$ would be needed, the second derivative and/or higher derivatives of g must be restricted.

Acknowledgments

The authors are grateful to Prof. V. Fabrikant of Concordia University for his very constructive criticism and to the two reviewers for their helpful remarks. Dan Givoli appreciates the support of the Technion's Postdoctoral Chicago Endowment Fund. Isaac Elishakoff appreciates the support by the National Science Foundation under grant number MSM-9015371. Any options, findings, and conclusions or recommendations expressed by this publication are those of the authors and do not necessarily reflect the views of the National Science Foundation.

References

Averin, A. M., 1964, "On the Bending of a Cantilever Plate Weakened by a Hole of a General Shape," *Proceedings of the 4th USSR Conference on Plates and Shells*, Armenian Academy of Sciences Press, Erevan, pp. 167–170 (in Russian).

Filonenko-Borodich, M., 1968, *Theory of Elasticity*, Mir Publishers, Moscow, p. 223.

Hearn, A. C., 1987, *REDUCE User's Manual*, The RAND Corporation, Santa Monica, Calif.

Isida, M., and Tagami, S., *1959*, "On the Tension of an Infinite Strip Containing a Hole of an Arbitrary Profile," *Proceedings of the 9th Japan National Congress for Applied Mechanics*, pp. 51–54.

Lockwood, E. H., 1961, *A Book of Curves*, Cambridge University Press, Cambridge, U.K., p. 148.

Lomakin, V. A., 1968, "Concentration of Stresses Near a Surface With Rapidly Oscillating Irregularities," *Prikladnaya Mekhanika*, Vol. 4, No. 2, pp. 1–8 (English translation: *Soviet Applied Mechanics*, No. 2, pp. 1–4).

Morse, P. M., and Feshbach, H., 1953, *Methods of Theoretical Physics*, McGraw-Hill, New York, pp. 1052–1060.

Muskhelishvili, N. I., 1953, *Some Basic Problems of the Mathematical Theory of Elasticity*, Noordhoff, Groningen.

Neuber, M., 1958, *Kerbspannungslehre: Grundlagen für genaue Festgkeitsberechnung mit Berücksichtigung von Konstruktioonsform und Werkstoff*, Springer, Berlin.

Pal'mov, V. A., 1964, "An Elastic Plane With Hole of Random Shape," *Trudy Leningradskogo Politekhnicheskogo Instituta*, No. 235 (in Russian).

Parnes, R., and Beltzer, A. I., 1986, "A Higher-Order Boundary Perturbation Method for Asymmetric Dynamic Problems in Solids—I. General Formulation," *International Journal of Solids and Structures*, Vol. 22, No. 11, pp. 1177–1187.

Peterson, R. E., 1974, *Stress Concentration Design Factors, Charts and Relations Useful on Making Strength Calculations for Machine Parts and Structural Elements*, John Wiley and Sons, New York.

Savin, G. N., 1961, *Stress Concentration Around Holes*, Pergamon, Oxford, U.K.

Sayles, R. S., 1982, "The Profile as a Random Process," *Rough Surfaces*, T. R. Thomas, ed., Longman, London, pp. 91–118.

Timoshenko, S., and Goodier, J. N., 1951, *Theory of Elasticity*, McGraw-Hill, New York, p. 116.

Tunguskova, Z. G., 1970, "Stress Concentration Around a Hole With Periodic Irregularities," *Vestnik Moskovskogo Universiteta*, No. 4, pp. 127–133 (in Russian).

Van Dyke, M., 1975, *Perturbation Methods in Fluid Mechanics*, Parabolic Press, Stanford, Calif., pp. 13–14.

APPENDIX A

The Normal to a Distorted Circle

We use the unit vectors $\mathbf{e}_r$ and $\mathbf{e}_\theta$ shown in Fig. 1. We define the radial vector

$$\mathbf{r}^\epsilon(\theta) = r^\epsilon(\theta)\mathbf{e}_r(\theta), \tag{A1}$$

where $r^\epsilon(\theta)$ is given in (1). Now a tangent vector $\hat{\mathbf{t}}$ to the curve $\mathcal{B}^\epsilon$ is given by

$$\hat{\mathbf{t}} = (\mathbf{r}^\epsilon)' \tag{A2}$$

where a prime indicates differentiation with respect to θ. The unit tangent vector $\mathbf{t}$ is then found by $\mathbf{t} = \hat{\mathbf{t}}/|\hat{\mathbf{t}}|$, where we need to use Taylor's formula to expand the denominator in powers of ϵ. We have used the symbolic manipulation software REDUCE (Hearn, 1987) to obtain the result

$$\mathbf{t} = \mathbf{e}_\theta + \left(\frac{h'}{R}\mathbf{e}_r\right)\epsilon - \left(\frac{h'(2h\mathbf{e}_r + h'\mathbf{e}_\theta)}{2R^2}\right)\epsilon^2 + O(\epsilon^3). \tag{A3}$$

The normal vector $\mathbf{n}$ can be found from $\mathbf{t}$ by using the first Serret-Frenet equation for a curve. However, it is easy to see that $n_r = -t_\theta$ and $n_\theta = t_r$. Therefore,

$$-\mathbf{n} = \mathbf{e}_r - \left(\frac{h'}{R}\mathbf{e}_\theta\right)\epsilon + \left(\frac{h'(2h\mathbf{e}_\theta - h'\mathbf{e}_r)}{2R^2}\right)\epsilon^2 + O(\epsilon^3). \tag{A4}$$

To account for the minus sign in front of $\mathbf{n}$, recall that $\mathbf{n}$ points out of the domain Ω^ϵ, namely into the hole.

APPENDIX B

Stresses in an Infinite Plane With a Circular Hole

The problem to be solved here is that of an infinite elastic

Downloaded 03 May 2010 to 171.66.16.247. Redistribution subject to ASME license or copyright; see http://www.asme.org/terms/Terms_Use.cfm

plane with a circular hole, with tractions in the form of general functions prescribed on the hole boundary. The statement of the problem is

$$\sigma_{ij,j}=0 \quad \text{in} \quad r>R, \tag{B1}$$

$$\sigma_{ij}=0 \quad \text{at} \quad \infty, \tag{B2}$$

$$\sigma_{rr}(R,\theta)=s_r(\theta), \tag{B3}$$

$$\sigma_{r\theta}(R,\theta)=s_\theta(\theta). \tag{B4}$$

We use the stress function due to Michell (Timoshenko and Goodier, 1951; Filonenko-Borodich, 1968)

$$\phi=a_0\log r+\sum_{n=1}^{\infty} r^{-n}(a_n\cos n\theta+c_n\sin n\theta) + \sum_{n=2}^{\infty} r^{-n+2}(b_n\cos n\theta+d_n\sin n\theta), \tag{B5}$$

which satisfies the biharmonic equation $\nabla^4\phi = 0$ in polar coordinates. Here, a_n and b_n are unknown coefficients. From ϕ we obtain the desired expression for the stress $\sigma_{\theta\theta} = \partial^2\phi/\partial r^2$, as well as expressions for σ_{rr} and $\sigma_{r\theta}$.

Now, we expand the functions s_r and s_θ in Fourier series:

$$s_r(\theta)=\frac{A_0}{2}+\sum_{n=1}^{\infty}(A_n\cos n\theta+B_n\sin n\theta),$$
$$s_\theta(\theta)=\frac{C_0}{2}+\sum_{n=1}^{\infty}(C_n\cos n\theta+D_n\sin n\theta). \tag{B6}$$

Here the constants A_n, B_n, C_n, and D_n are

$$A_n=\frac{1}{\pi}\int_0^{2\pi} s_r\cos n\theta\, d\theta, \qquad B_n=\frac{1}{\pi}\int_0^{2\pi} s_r\sin n\theta\, d\theta,$$
$$C_n=\frac{1}{\pi}\int_0^{2\pi} s_\theta\cos n\theta\, d\theta, \quad D_n=\frac{1}{\pi}\int_0^{2\pi} s_\theta\sin n\theta\, d\theta. \tag{B7}$$

We then compare (B6) with the formulas for σ_{rr} and $\sigma_{r\theta}$ at $r = R$. This comparison yields the conditions

$$C_0=0, \quad A_1=D_1, \quad B_1=-C_1, \tag{B8}$$

which correspond to the requirement that the given tractions s_r and s_θ be self-equilibrated. In addition, we get some relations between the constants a_n, b_n, c_n, and d_n on one hand, and A_n, B_n, C_n and D_n on the other. Using (B7) as well, we express a_n, b_n, c_n, and d_n in terms of the functions s_r and s_θ. Finally, we substitute these expressions back in the formula for $\sigma_{\theta\theta}$. The final result is

$$\sigma_{\theta\theta}=\sum_{n=0}^{\infty}\int_0^{2\pi}[B_r^n(r,\theta,\theta')s_r(\theta')+B_\theta^n(r,\theta,\theta')s_\theta(\theta')]d\theta' \tag{B9}$$

where

$$B_r^0(r,\theta,\theta')=-\frac{1}{2\pi}\left(\frac{R}{r}\right)^2 \tag{B10}$$

$$B_\theta^0(r,\theta,\theta')=0 \tag{B11}$$

$$B_r^1(r,\theta,\theta')=\frac{1}{2\pi}\left(\frac{R}{r}\right)^3\cos(\theta-\theta') \tag{B12}$$

$$B_\theta^1(r,\theta,\theta')=\frac{3}{2\pi}\left(\frac{R}{r}\right)^3\sin(\theta-\theta') \tag{B13}$$

$$B_r^n(r,\theta,\theta')=-\frac{1}{2\pi}\left[(n-2)\left(\frac{R}{r}\right)^n-n\left(\frac{R}{r}\right)^{n+2}\right]\cos n(\theta-\theta'), \quad n\geq 2 \tag{B14}$$

$$B_\theta^n(r,\theta,\theta')=\frac{1}{2\pi}\left[(n+2)\left(\frac{R}{r}\right)^{n+2}-(n-2)\left(\frac{R}{r}\right)^n\right]\sin n(\theta-\theta'), \quad n\geq 2. \tag{B15}$$

Note that Eqs. (B12)–(B13) were obtained using the relations (B8). Setting $r = R$ in Eqs. (B10)–(B15) we get

$$B_r^0(R,\theta,\theta')=-\frac{1}{2\pi} \tag{B16}$$

$$B_\theta^0(R,\theta,\theta')=0 \tag{B17}$$

$$B_r^1(R,\theta,\theta')=\frac{1}{2\pi}\cos(\theta-\theta') \tag{B18}$$

$$B_\theta^1(R,\theta,\theta')=\frac{3}{2\pi}\sin(\theta-\theta') \tag{B19}$$

$$B_r^n(R,\theta,\theta')=\frac{1}{\pi}\cos n(\theta-\theta'), \quad n\geq 2 \tag{B20}$$

$$B_\theta^n(R,\theta,\theta')=\frac{2}{\pi}\sin n(\theta-\theta'), \quad n\geq 2. \tag{21}$$

An alternative tool for the derivation of Eqs. (B9)–(B15) is the use of the Kolosov-Muskhelishvili complex potentials (Muskhelishvili, 1953).

Downloaded 03 May 2010 to 171.66.16.247. Redistribution subject to ASME license or copyright; see http://www.asme.org/terms/Terms_Use.cfm

The Elastic Potentials for Coplanar Interaction Between an Infinitesimal Prismatic Dislocation Loop and a Circular Crack for Transverse Isotropy

M. T. Hanson

Department of Engineering Mechanics,
University of Kentucky,
Lexington, KY 40506-0046

This paper gives a closed-form evaluation in terms of elementary functions for the title problem of coplanar dislocation—crack interaction. The two cases of an external and internal crack are considered and the potential for each is found for an isotropic material. The similarity between isotropy and transverse isotropy is discussed in the beginning sections and is used to write the corresponding potential for a transversely isotropic material from the isotropic result.

1 Introduction

In a previous paper, Hanson (1990) has considered the interaction between an infinitesimal prismatic dislocation loop coplanar with a circular internal or external crack. Interest in this Green's function stems from the development of appropriate integral equations over a reduced crack domain which can be used to analyze multiple coplanar cracks or cracks with noncircular contours under tensile loading. This integral formulation, which eliminates a portion of the crack area, allows a more accurate numerical solution to be obtained. This previous analysis evaluated the crack-opening displacement and normal stress on the crack plane in terms of closed-form expressions for an isotropic material.

In many instances, it is advantageous to have a knowledge of the entire elastic field throughout the body. Recent results in potential theory by Fabrikant (1989) have revealed that closed-form analytical expressions in terms of elementary functions can be obtained for many boundary value problems with transversely isotropic materials. This paper uses some of these new results to evaluate the potential function for the dislocation—crack interaction in an isotropic material. Previous analysis by Green and Zerna (1968) and Kassir and Sih (1975) has shown that the solution for transverse isotropy can be written in terms of a single harmonic potential which has boundary values similar to the isotropic case. This result is reviewed here first, and then it is used subsequently to write the transversely isotropic potential directly from the isotropic case.

The coplanar prismatic dislocation interaction with an external circular crack is equivalent to the Green's function for circular internal contact problems, and the results here agree with the solution previously given by Fabrikant (1990). The present analysis displays how this solution is obtained by integral transform methods. The prismatic dislocation interaction with a circular internal crack is equivalent to circular external contact, and the potential function evaluated here appears to be new.

2 Isotropic Potential Function for a Half Space

For a half space $z > 0$, a potential function representation for displacements and stresses has been given by Galin (1961). The cartesian displacements u, v, and w in the x, y, and z directions, respectively, are given in terms of a potential function ϕ as

$$u = (1-2\nu)\int_z^\infty \frac{\partial \phi}{\partial x}\,dz - z\frac{\partial \phi}{\partial x} \tag{1}$$

$$v = (1-2\nu)\int_z^\infty \frac{\partial \phi}{\partial y}\,dz - z\frac{\partial \phi}{\partial y} \tag{2}$$

$$w = 2(1-\nu)\phi - z\frac{\partial \phi}{2z} \tag{3}$$

where ν is Poisson's ratio and μ is the shear modulus. The stress field is given in Galin (1961) (or see Hanson, 1990). The potential function ϕ is harmonic and hence satisfies Laplace's equation

$$\left(\frac{\partial^2}{\partial x^2}+\frac{\partial^2}{\partial y^2}+\frac{\partial^2}{\partial z^2}\right)\phi(x,y,z) = 0. \tag{4}$$

Contributed by the ASME Applied Mechanics Division of THE AMERICAN SOCIETY OF MECHANICAL ENGINEERS for presentation at the Winter Annual Meeting, Atlanta, Ga., Dec. 1-6, 1991.

Discussion on this paper should be addressed to the Technical Editor, Prof. Leon M. Keer, The Technological Institute, Northwestern University, Evanston, IL 60208, and will be accepted until two months after final publication of the paper itself in the JOURNAL OF APPLIED MECHANICS. Manuscript received by the ASME Applied Mechanics Division, Sept. 27, 1990; final revision, Mar. 19, 1991.

Paper No. 91-WA/APM-27.

Copyright © 1992 by ASME
Downloaded 03 May 2010 to 171.66.16.247. Redistribution subject to ASME license or copyright; see http://www.asme.org/terms/Terms_Use.cfm

It is convenient to define a new potential function ψ by the relation

$$\phi(x,y,z)=\frac{1}{2\mu}\frac{d\psi(x,y,z)}{dz}, \tag{5}$$

and hence ψ is also harmonic. The elastic displacement field given by Galin (1961) can be written in terms of ψ as follows:

$$2\mu u=-(1-2\nu)\frac{\partial\psi}{\partial x}-z\frac{\partial^2\psi}{\partial x\partial z}, \tag{6}$$

$$2\mu v=-(1-2\nu)\frac{\partial\psi}{\partial y}-z\frac{\partial^2\psi}{\partial y\partial z}, \tag{7}$$

$$2\mu w=2(1-\nu)\frac{\partial\psi}{\partial z}-z\frac{\partial^2\psi}{\partial z^2}, \tag{8}$$

where the stresses follow suit. The stress on planes with a z-directed normal are

$$\sigma_{zz}=\frac{\partial^2\psi}{\partial z^2}-z\frac{\partial^3\psi}{\partial z^3}, \tag{9}$$

$$\tau_{xz}=-z\frac{\partial^3\psi}{\partial x\partial z^2}, \tag{10}$$

$$\tau_{yz}=-z\frac{\partial^3\psi}{\partial y\partial z^2}. \tag{11}$$

This form of the solution is more convenient since no integrations of z are included. The potential function ψ above is but a constant multiplier different from the potential function ψ of Green and Zerna (1968).

In writing the foregoing relations the order of differentiation with respect to x or y, and integration with respect to z, has been interchanged and it has been assumed that $\psi(x, y, z)$ vanishes for $z \to \infty$. This is not necessarily true, and in fact it will be shown in a later example that $\phi(x, y, z)$ and hence $d\psi(x, y, z)/dz$ are $0(1/z)$ and $\psi(x, y, z)$ is $0(\ln z)$ for $z \to \infty$ and therefore $\psi(x,y,z)$ is not bounded at $z = \infty$. This difficulty arises when the orders of differentiation and integration are interchanged and thus deserves special attention. It will be shown subsequently that if this difficulty arises, the above relations are valid provided that the function $\psi(x, y, z)$ is evaluated correctly.

From Eqs. (10), (11) it is evident that the shear stress vanishes on the surface $z = 0$, and the above potential function is appropriate for solving mixed boundary value problems between the normal stress and normal displacement on the surface. The surface values of w and σ_{zz} are given in terms of ψ as

$$w=\frac{(1-\nu)}{\mu}\frac{\partial\psi}{\partial z}\Big|_{z=0}, \tag{12}$$

$$\sigma_{zz}=\frac{\partial^2\psi}{\partial z^2}\Big|_{z=0}. \tag{13}$$

3 Transversely Isotropic Potential Function for a Half Space

A potential function formulation for a transversely isotropic half space $z > 0$ (where the half space surface $z = 0$ is parallel to the plane of isotropy) has been given by Elliot (1948). Here we adopt the notation used by Fabrikant (1989). The five elastic constants A_{11}, A_{13}, A_{33}, A_{44}, and A_{66} are defined there. The displacement field is written as

$$u=\frac{\partial}{\partial x}(F_1+F_2), \tag{14}$$

$$v=\frac{\partial}{\partial y}(F_1+F_2), \tag{15}$$

$$w=\frac{\partial}{\partial z}(m_1F_1+m_2F_2), \tag{16}$$

where $F_k = F_k(x, y, z)$, $k = 1, 2$ are two potential functions satisfying

$$\left(\frac{\partial^2}{\partial x^2}+\frac{\partial^2}{\partial y^2}\right)F_k+\gamma_k^2\frac{\partial^2}{\partial z^2}F_k=0, \quad k=1,2. \tag{17}$$

The constants m_k are related to the constants γ_k as

$$m_k=\frac{A_{11}\gamma_k^2-A_{44}}{A_{13}+A_{44}}=\frac{(A_{13}+A_{44})\gamma_k^2}{A_{33}-\gamma_k^2A_{44}}, \quad k=1,2. \tag{18}$$

The constants $\gamma_k^2 = n_k$, $k = 1, 2$ where n_k are the two (real or complex conjugate) roots of the quadratic equation

$$A_{11}A_{44}n^2+[A_{13}(A_{13}+2A_{44})-A_{11}A_{33}]n+A_{33}A_{44}=0. \tag{19}$$

The constant $\gamma_3^2 = A_{44}/A_{66}$ will also be used.

The stress components acting on planes with a normal vector in the z direction are

$$\sigma_{zz}=A_{44}\frac{\partial^2}{\partial z^2}[(1+m_1)\gamma_1^2F_1+(1+m_2)\gamma_2^2F_2], \tag{20}$$

$$\tau_z=A_{44}\left(\frac{\partial}{\partial x}+i\frac{\partial}{\partial y}\right)\frac{\partial}{\partial z}[(1+m_1)F_1+(1+m_2)F_2], \tag{21}$$

where $\tau_z = \tau_{xz} + i\tau_{yz}$ is the complex shear stress.

Following previous analysis, the functions F_1 and F_2 are defined in terms of a single function F as

$$F_k(x,y,z)=(-1)^{k+1}\frac{\gamma_k}{1+m_k}\frac{1}{A_{44}(\gamma_1-\gamma_2)}F(x,y,z_k), \quad k=1,2, \tag{22}$$

where $z_k = z/\gamma_k$. Substituting for F_1 and F_2 from Eq. (22) into Eq. (17) reveals that $F(x, y, z)$ is harmonic in the variables x, y, and z. Furthermore, substituting from Eq. (22) into Eq. (21) results in $\tau_z = 0$ on $z = 0$ for an arbitrary function F.

The surface values of w and σ_{zz} become

$$w=2\pi H\frac{\partial F(x,y,z)}{\partial z}\Big|_{z=0}, \tag{23}$$

$$\sigma_{zz}=\frac{\partial^2F(x,y,z)}{\partial z^2}\Big|_{z=0}. \tag{24}$$

Here the relation

$$\frac{m_1-m_2}{m_1+m_2+2}=\frac{m_1-1}{m_1+1}=2\pi A_{44}H(\gamma_1-\gamma_2), \tag{25}$$

along with $m_1m_2 = 1$ (Fabrikant, 1989), has been used. The constant H is also defined there.

Now compare the mixed boundary values in Eqs. (12), (13) for the isotropic harmonic function ψ with those in Eqs. (23), (24) for the transversely isotropic harmonic function F. It is evident that F and ψ are equal if the displacement boundary condition is homogeneous or they differ by a constant multiplier if the normal stress boundary condition is homogeneous. This relation between the isotropic and transversely isotropic potentials has been pointed out previously by Green and Zerna (1968) and Kassir and Sih (1975). It is obvious that the isotropic results can be obtained from the transversely isotropic solution by an appropriate limiting procedure. However, the equivalence of the potentials indicates that if the isotropic solution is known, than one can deduce the analogous solution for transverse isotropy directly.

4 Interaction Between an Infinitesimal Prismatic Dislocation Loop and a Circular External Crack

Consideration is first given to the full space problem of an infinitesimal prismatic dislocation loop coplanar with a circular external crack. Adopting cylindrical coordinates (r, θ, z), the crack occupies the domain $z = 0$, $r > a$ while the dislocation loop is at the point $(r_o, \theta_o, 0)$ with $r_o < a$. Symmetry requires

Downloaded 03 May 2010 to 171.66.16.247. Redistribution subject to ASME license or copyright; see http://www.asme.org/terms/Terms_Use.cfm

that the shear stress vanish on the plane $z = 0$ along with the conditions

$$\sigma_{zz}(r,\theta,0)=0, \quad r>a, \tag{26}$$

$$w(r,\theta,0)=\frac{b}{2r}\,\delta(r-r_o)\delta(\theta-\theta_o), \quad r<a, \quad r_o<a. \tag{27}$$

Here, b is the Burgers vector or displacement jump across the dislocation in the z direction.

The harmonic isotropic Galin potential function $\phi(x, y, z) = \phi(r, \theta, z)$ can be written in separated form as

$$\phi(r,\theta,z)=\sum_{-\infty}^{\infty}\int_0^{\infty}\xi C_n(\xi)e^{-\xi z}J_{|n|}(\xi r)d\xi e^{in\theta}, \tag{28}$$

where for this problem the function $C_n(\xi)$ is evaluated by Hanson (1990) to be

$$C_n(\xi)=\frac{b}{2\pi(\kappa+1)}\,e^{-in\theta_o}\left(J_{|n|}(\xi r_o)+\frac{\sqrt{2}}{\sqrt{\pi\xi}}\,r_o^{|n|}\int_a^{\infty}\frac{x^{-|n|+3/2}J_{|n|-1/2}(\xi x)}{(x^2-r_o^2)^{3/2}}\,dx\right), \tag{29}$$

where $\kappa = 3 - 4\nu$. It was also shown that the first term represents the dislocation in a full space while the second term represents the interaction with the crack which vanishes for $a \to \infty$.

To evaluate the potential function ϕ consider the full space term first. Performing the summation as (Watson, 1980)

$$\sum_{-\infty}^{\infty}J_{|n|}(\xi r)J_{|n|}(\xi r_o)e^{in(\theta-\theta_o)}=J_0(\xi\alpha), \tag{30}$$

where $\alpha^2 = r^2 + r_o^2 - 2rr_o\cos(\theta-\theta_o)$ and then using the integral

$$\int_0^{\infty}\xi J_0(\xi\alpha)e^{-\xi z}d\xi=\frac{z}{R^3}, \tag{31}$$

where $R^2 = r^2 + r_o^2 - 2rr_o\cos(\theta-\theta_o) + z^2$, the full space potential ϕ^f becomes

$$\phi^f(r,\theta,z)=\frac{b}{2\pi(\kappa+1)}\,\frac{z}{R^3}. \tag{32}$$

Now, consider the interaction potential ϕ^i. Substituting the interaction term from Eq. (29) into Eq. (28), the Bessel integral can be performed as (Appendix A)

$$\int_0^{\infty}\sqrt{\xi}J_{|n|-1/2}(\xi x)J_{|n|}(\xi r)e^{-\xi z}d\xi=\frac{\sqrt{2}}{\sqrt{\pi x}}\left(\frac{rx}{l_2^2(x)}\right)^{|n|}\frac{1}{\sqrt{l_2^2(x)-r^2}}\,\frac{zl_2(x)}{(l_2^2(x)-l_1^2(x))}, \tag{33}$$

where $l_1(x)$ and $l_2(x)$ are defined as

$$l_1(x)=\frac{1}{2}\{\sqrt{(x+r)^2+z^2}-\sqrt{(x-r)^2+z^2}\}, \tag{34}$$

$$l_2(x)=\frac{1}{2}\{\sqrt{(x+r)^2+z^2}+\sqrt{(x-r)^2+z^2}\}. \tag{35}$$

Next, evaluating the summation according to

$$\sum_{-\infty}^{\infty}t^{|n|}e^{in\beta}=\frac{1-t^2}{1+t^2-2t\cos(\beta)}=\lambda(t,\beta), \tag{36}$$

one obtains

$$\phi^i(r,\theta,z)=\frac{bz}{\pi^2(\kappa+1)}\int_a^{\infty}\frac{xl_2(x)}{(x^2-r_o^2)^{3/2}\sqrt{l_2^2(x)-r^2}\;(l_2^2(x)-l_1^2(x))}\,\lambda\left(\frac{rr_o}{l_2^2(x)},\theta-\theta_o\right)dx. \tag{37}$$

This integral, although appearing formidable, can be evaluated in terms of elementary functions. Introducing the new function $h(x)$ as

$$h(x)=\frac{\sqrt{x^2-r_o^2}\,\sqrt{x^2-l_1^2(x)}}{x}, \tag{38}$$

where (Fabrikant, 1989)

$$\lambda\left(\frac{rr_o}{l_2^2(x)},\theta-\theta_o\right)=\frac{(l_2^2(x)-l_1^2(x))\sqrt{x^2-r_o^2}}{\sqrt{x^2-l_1^2(x)}}\,\frac{1}{R^2+h^2(x)}\,\frac{dh(x)}{dx}, \tag{39}$$

and using the identity

$$\frac{l_2(x)}{\sqrt{l_2^2(x)-r^2}}=\frac{x}{\sqrt{x^2-l_1^2(x)}}, \tag{40}$$

one finally obtains

$$\phi^i(r,\theta,z)=\frac{bz}{\pi^2(\kappa+1)}\int_{h(a)}^{\infty}\frac{dh}{h^2(R^2+h^2)}. \tag{41}$$

This last integral is straightforward and the result may be written as

$$\phi^i(r,\theta,z)=-\frac{b}{2\pi(\kappa+1)}\,\frac{z}{R^3}+\frac{bz}{\pi^2(\kappa+1)}\left\{\frac{1}{R^2h(a)}+\frac{1}{R^3}\tan^{-1}\left(\frac{h(a)}{R}\right)\right\}. \tag{42}$$

Adding the full space potential from Eq. (32) to the interaction potential above, the total potential becomes

$$\phi(r,\theta,z)=\frac{b}{\pi^2(\kappa+1)}\,\frac{z}{R^2}\left\{\frac{1}{h(a)}+\frac{1}{R}\tan^{-1}\left(\frac{h(a)}{R}\right)\right\}. \tag{43}$$

The evaluation of the displacements in Eqs. (1)-(3) or Eqs. (6)-(8) require the integration of $\phi(r,\theta,z)$ with respect to z, or equivalently, the potential function ψ which can be written by integrating Eq. (5) according to Eqs. (1), (2) as

$$\psi(r,\theta,z)=-\frac{2\mu b}{\pi^2(\kappa+1)}\int_z^{\infty}\frac{z}{R^2}\left\{\frac{1}{h(a)}+\frac{1}{R}\tan^{-1}\left(\frac{h(a)}{R}\right)\right\}dz. \tag{44}$$

It is interesting to note that the integrand is $0(1/z)$ for $z \to \infty$ and is not integrable at $z = \infty$. Temporarily neglecting the limits of integration, this integral has been evaluated as indefinite by Fabrikant (1989) with the result

$$\int\frac{z}{R^2}\left(\frac{1}{h(a)}+\frac{1}{R}\tan^{-1}\left(\frac{h(a)}{R}\right)\right)dz=-\frac{1}{R}\tan^{-1}\left(\frac{h(a)}{R}\right)+\frac{1}{\sqrt{a^2-r_o^2}}\left\{\ln[l_2(a)+\sqrt{l_2^2(a)-r^2}]+\frac{1}{\sqrt{\zeta-1}}\tan^{-1}\left(\frac{\sqrt{a^2-l_1^2(a)}}{a\sqrt{\zeta-1}}\right)+\frac{1}{\sqrt{\bar{\zeta}-1}}\tan^{-1}\left(\frac{\sqrt{a^2-l_1^2(a)}}{a\sqrt{\bar{\zeta}-1}}\right)\right\}, \quad \zeta=\frac{r}{r_o}\,e^{i(\theta-\theta_o)}, \tag{45}$$

where an overbar denotes the complex conjugate value. Since $l_2(a)$ is $0(z)$ for $z \to \infty$, it is easy to see that the right-hand side of the above equation is $0(\ln z)$ for $z \to \infty$.

This problem was noted at the end of Section 2 where it was pointed out that the order of integration on z and differentiation with respect to x and y was interchanged in going from

Downloaded 03 May 2010 to 171.66.16.247. Redistribution subject to ASME license or copyright; see http://www.asme.org/terms/Terms_Use.cfm

Eqs. (1), (2) to Eqs. (6), (7) for displacements (and similarly for stresses) when the substitution in Eq. (5) was used. It is easy to see from Eq. (43) that $\partial\phi/\partial x$ and $\partial\phi/\partial y$ are $0(1/z^3)$ for $z \to \infty$ and are integrable at $z = \infty$. One way to proceed would be to differentiate Eq. (45) with respect to x or y first and then evaluate at the limits z and ∞ yielding the analytical expressions for $\partial\psi/\partial x$ and $\partial\psi/\partial y$ needed for the elastic field. However, it is more efficient to have a single expression for the potential ψ which can be inserted into the Eqs. (6)–(11) for the elastic field.

To obtain a correct single expression for the potential function ψ note that for the terms on the right-hand side of Eq. (45) which are bounded for $z \to \infty$, the order of differentiation with respect to x or y and integration on z may be interchanged. For the unbounded logarithmic term, it is easy to see that its x or y derivative vanishes for $z \to \infty$, and hence this divergent term may be discarded for the purpose of evaluating the elastic field. The final result for the potential function ψ takes the form

$$\psi(r,\theta,z) = -\frac{2\mu b}{\pi^2(\kappa+1)}\left[\frac{1}{R}\tan^{-1}\left(\frac{h(a)}{R}\right) - \frac{1}{\sqrt{a^2-r_o^2}}\left\{\ln[l_2(a)+\sqrt{l_2^2(a)-r^2}] + \frac{1}{\sqrt{\zeta-1}}\tan^{-1}\left(\frac{\sqrt{a^2-l_1^2(a)}}{a\sqrt{\zeta-1}}\right) + \frac{1}{\sqrt{\bar{\zeta}-1}}\tan^{-1}\left(\frac{\sqrt{a^2-l_1^2(a)}}{a\sqrt{\bar{\zeta}-1}}\right) - \frac{1}{\sqrt{\zeta-1}}\tan^{-1}\left(\frac{1}{\sqrt{\zeta-1}}\right) - \frac{1}{\sqrt{\bar{\zeta}-1}}\tan^{-1}\left(\frac{1}{\sqrt{\bar{\zeta}-1}}\right)\right\}\right]. \quad (46)$$

It is interesting to note an alternative method to evaluate ψ. The Eqs. (6)–(11) satisfy the elasticity equations as is well known. Using Eq. (5) and (43) one can write

$$\frac{\partial\psi}{\partial z} = \frac{2\mu b}{\pi^2(\kappa+1)}\frac{z}{R^2}\left\{\frac{1}{h(a)}+\frac{1}{R}\tan^{-1}\left(\frac{h(a)}{R}\right)\right\}. \quad (47)$$

The foregoing expression is a harmonic function satisfying the boundary conditions on the surface $z = 0$ appropriate to the dislocation-crack interaction. The function ψ can be evaluated as the indefinite integral of the above expression using Eq. (45); however, one must add an arbitrary function of x and y. This arbitrary function must be such that $\partial\psi/\partial x$ and $\partial\psi/\partial y$ vanish at $z = \infty$ as required by vanishing of displacements. This leads to Eq. (46) above for ψ. This reasoning does not require any consideration of the singular nature of ψ for $z \to \infty$.

Using the similarity between isotropy and transverse isotropy, the potential function F for transverse isotropy becomes

$$F(r,\theta,z) = -\frac{b}{4\pi^3 H}\left[\frac{1}{R}\tan^{-1}\left(\frac{h(a)}{R}\right) - \frac{1}{\sqrt{a^2-r_o^2}}\left\{\ln[l_2(a)+\sqrt{l_2^2(a)-r^2}] + \frac{1}{\sqrt{\zeta-1}}\tan^{-1}\left(\frac{\sqrt{a^2-l_1^2(a)}}{a\sqrt{\zeta-1}}\right) + \frac{1}{\sqrt{\bar{\zeta}-1}}\tan^{-1}\left(\frac{\sqrt{a^2-l_1^2(a)}}{a\sqrt{\bar{\zeta}-1}}\right) - \frac{1}{\sqrt{\zeta-1}}\tan^{-1}\left(\frac{1}{\sqrt{\zeta-1}}\right) - \frac{1}{\sqrt{\bar{\zeta}-1}}\tan^{-1}\left(\frac{1}{\sqrt{\bar{\zeta}-1}}\right)\right\}\right]. \quad (48)$$

5 Interaction Between an Infinitesimal Prismatic Dislocation Loop and a Circular Internal Crack

In this case the crack is located on the $z = 0$ plane inside the circle $r = a$ while the dislocation is at the point $(r_o, \theta_o, 0)$ with $r_o > a$. The boundary conditions become

$$\sigma_{zz}(r,\theta,0) = 0, \quad r < a, \quad (49)$$

$$w(r,\theta,0) = \frac{b}{2r}\delta(r-r_o)\delta(\theta-\theta_o), \quad r > a, \quad r_o > a. \quad (50)$$

The function $C_n(\xi)$ is now (Hanson, 1990)

$$C_n(\xi) = \frac{b}{2\pi(\kappa+1)}e^{-in\theta_o}\left(J_{|n|}(\xi r_o) + \frac{\sqrt{2}}{\sqrt{\pi\xi}}r_o^{-|n|}\int_0^a \frac{x^{|n|+3/2}J_{|n|+1/2}(\xi x)}{(r_o^2-x^2)^{3/2}}dx\right). \quad (51)$$

The first term is again the full space contribution, while the second term represents the interaction which now vanishes for $a \to 0$.

To evaluate the interaction potential ϕ^i, substitute the second term of Eq. (51) into Eq. (28). Evaluating the Bessel integral as (Appendix A)

$$\int_0^\infty \sqrt{\xi}J_{|n|+1/2}(\xi x)J_{|n|}(\xi r)e^{-\xi z}d\xi = \frac{\sqrt{2}}{\sqrt{\pi x}}\left(\frac{l_1^2(x)}{rx}\right)^{|n|}\frac{1}{\sqrt{r^2-l_1^2(x)}}\frac{zl_1(x)}{(l_2^2(x)-l_1^2(x))}, \quad (52)$$

and using the summation in Eq. (36) results in

$$\phi^i(r,\theta,z) = \frac{bz}{\pi^2(\kappa+1)}\int_0^a \frac{xl_1(x)}{(r_o^2-x^2)^{3/2}\sqrt{r^2-l_1^2(x)}\ (l_2^2(x)-l_1^2(x))}\lambda\left(\frac{l_1^2(x)}{rr_o}, \theta-\theta_o\right)dx. \quad (53)$$

This integral can be evaluated by introducing the function $j(x)$ as

$$j(x) = \frac{\sqrt{r_o^2-x^2}\sqrt{l_2^2(x)-x^2}}{x}, \quad (54)$$

with (Fabrikant, 1989)

$$\lambda\left(\frac{l_1^2(x)}{rr_o}, \theta-\theta_o\right) = -\frac{(l_2^2(x)-l_1^2(x))\sqrt{r_o^2-x^2}}{\sqrt{l_2^2(x)-x^2}}\frac{1}{R^2+j^2(x)}\frac{dj(x)}{dx}, \quad (55)$$

which allows the integral to be written as

$$\phi^i(r,\theta,z) = -\frac{bz}{\pi^2(\kappa+1)}\int_\infty^{j(a)}\frac{dj}{j^2(R^2+j^2)}. \quad (56)$$

Evaluating the integral and adding the full space potential from Eq. (32) gives the total potential ϕ as

$$\phi(r,\theta,z) = \frac{b}{\pi^2(\kappa+1)}\frac{z}{R^2}\left\{\frac{1}{j(a)}+\frac{1}{R}\tan^{-1}\left(\frac{j(a)}{R}\right)\right\}. \quad (57)$$

The function ψ can be evaluated similar to the previous case by integrating Eq. (5) as

$$\psi(r,\theta,z) = -\frac{2\mu b}{\pi^2(\kappa+1)}\int_z^\infty \frac{z}{R^2}\left\{\frac{1}{j(a)}+\frac{1}{R}\tan^{-1}\left(\frac{j(a)}{R}\right)\right\}dz. \quad (58)$$

The following indefinite integral may be used (Appendix B)

Downloaded 03 May 2010 to 171.66.16.247. Redistribution subject to ASME license or copyright; see http://www.asme.org/terms/Terms_Use.cfm

$$\int \frac{z}{R^2}\left(\frac{1}{j(a)}+\frac{1}{R}\tan^{-1}\left(\frac{j(a)}{R}\right)\right)dz=-\frac{1}{R}\tan^{-1}\left(\frac{j(a)}{R}\right)$$
$$+\frac{1}{\sqrt{r_o^2-a^2}}\left\{\sin^{-1}\left(\frac{l_1(a)}{r}\right)+\frac{1}{\sqrt{1-\zeta}}\tan^{-1}\left(\frac{\sqrt{l_2^2(a)-a^2}}{a\sqrt{1-\zeta}}\right)\right.$$
$$\left.+\frac{1}{\sqrt{1-\bar{\zeta}}}\tan^{-1}\left(\frac{\sqrt{l_2^2(a)-a^2}}{a\sqrt{1-\bar{\zeta}}}\right)\right\},\quad \zeta=\frac{r}{r_o}e^{i(\theta-\theta_o)}. \quad (59)$$

In this case the integrand is $0(1/z^2)$ for $z \to \infty$ and hence is integrable there. The result becomes

$$\psi(r,\theta,z)=-\frac{2\mu b}{\pi^2(\kappa+1)}\left\{\frac{1}{R}\tan^{-1}\left(\frac{j(a)}{R}\right)\right.$$
$$-\frac{1}{\sqrt{r_o^2-a^2}}\left[\sin^{-1}\left(\frac{l_1(a)}{r}\right)-\frac{1}{\sqrt{1-\zeta}}\tan^{-1}\left(\frac{a\sqrt{1-\zeta}}{\sqrt{l_2^2(a)-a^2}}\right)\right.$$
$$\left.\left.-\frac{1}{\sqrt{1-\bar{\zeta}}}\tan^{-1}\left(\frac{a\sqrt{1-\bar{\zeta}}}{\sqrt{l_2^2(a)-a^2}}\right)\right]\right\}. \quad (60)$$

Similarily, the potential function F for transverse isotropy is

$$F(r,\theta,z)=-\frac{b}{4\pi^3 H}\left\{\frac{1}{R}\tan^{-1}\left(\frac{j(a)}{R}\right)\right.$$
$$-\frac{1}{\sqrt{r_o^2-a^2}}\left[\sin^{-1}\left(\frac{l_1(a)}{r}\right)-\frac{1}{\sqrt{1-\zeta}}\tan^{-1}\left(\frac{a\sqrt{1-\zeta}}{\sqrt{l_2^2(a)-a^2}}\right)\right.$$
$$\left.\left.-\frac{1}{\sqrt{1-\bar{\zeta}}}\tan^{-1}\left(\frac{a\sqrt{1-\bar{\zeta}}}{\sqrt{l_2^2(a)-a^2}}\right)\right]\right\}. \quad (61)$$

6 Discussion

The above analysis has provided closed-form analytical expressions in terms of elementary functions for the potential function for an infinitesimal prismatic coplanar dislocation loop interacting with a circular crack. The closed-form analytical expressions for the elastic field can be found by differentiation. The main step in evaluating the potential in terms of elementary functions is the knowledge of the Bessel integrals in Eqs. (33) and (52). These integrals have been evaluated previously in Watson (1980) and elsewhere, but the result has always been given in terms of hypergeometric functions. As pointed out in Appendix A, the integral evaluations used here have been obtained by a comparison of a previous integral transform solution to a recent closed-form analytical solution given by Fabrikant (1989). Further work will provide a direct proof of these integral evaluations. It is also important to note that one of the above solutions has been previously obtained by Fabrikant (1990) in the context of a frictionless contact problem for a half space $z > 0$. Consider the surface contact region $r < a$ to have a specified normal displacement $\omega(\rho, \phi)$, while outside the contact area ($r > a$) the surface is stress-free. From the superposition property, the transversely isotropic potential F can be written as

$$F(r,\theta,z)=\int_0^{2\pi}\int_0^a K(r,\theta,z;\rho,\phi)\omega(\rho,\phi)\rho d\rho d\phi. \quad (62)$$

Here, $K(r, \theta, z; \rho, \phi)$ is the Green's function for a point displacement of unit magnitude. The Green's function is analogous to the solution for an infinitesimal prismatic dislocation loop coplanar with an external crack if one correctly identifies the dislocation strength b as twice the half space displacement ω.

The potential for the dislocation interacting with an internal crack is equivalent to the Green's function for the external contact problem (when the normal displacement ω is specified outside the circle $r = a$ and the normal stress is zero inside). The closed-form evaluation of this potential appears to be new.

As a final point of discussion, the net force and moment on the dislocation-crack plane is considered. The solution for a dislocation in a full space is associated with a zero net force and moment but the effects of the crack must now be accounted for. Considering the external crack, it has been pointed out by Stallybrass (1981a, b) that boundary conditions at infinity must also be included. This has been considered by Comninou and Barber (1982), Stallybrass (1982), Fabrikant et al. (1986), and Gao and Rice (1987) where the possibility of crack-face overlap has been discussed. For the external crack the normal stress in the bond ligament was given for isotropy by Hanson (1990) as

$$\sigma_{zz}(r,\theta,0)=\frac{2\mu b}{\pi^2(\kappa+1)}\left\{\frac{1}{R^3}\tan^{-1}\left(\frac{h(a)}{R}\right)+\frac{1}{R^2 h(a)}\right\}, \quad (63)$$

where $h(a)$ is given in Eq. (38) with $z = 0$ (hence, $l_1^2(a) = r^2$) and $R^2 = r^2 + r_o^2 - 2rr_o\cos(\theta - \theta_o)$.

Integrating this expression over the bond ligament gives the net force and moment. The integrals are formally divergent since the dislocation point has a nonintegrable singularity at $R = 0$. This can be separated as

$$\sigma_{zz}(r,\theta,0)=\frac{\mu b}{\pi(\kappa+1)}\frac{1}{R^3}$$
$$+\frac{2\mu b}{\pi^2(\kappa+1)}\left\{-\frac{1}{R^3}\tan^{-1}\left(\frac{R}{h(a)}\right)+\frac{1}{R^2 h(a)}\right\}. \quad (64)$$

The first term is singular and corresponds to the dislocation in the full space while the second term represents the interaction and is not singular for $R \to 0$. The divergent integrals must be interpreted as finite part integrals and this can be proven by analyzing the dislocation in a full space. The integrations are performed in Appendix C with the result

$$P=-\frac{4\mu b}{\pi(\kappa+1)}\frac{1}{\sqrt{a^2-r_o^2}}, \quad (65)$$

$$M_x+iM_y=-\frac{8\mu b}{\pi(\kappa+1)}ie^{i\theta_o}\frac{r_o}{\sqrt{a^2-r_o^2}}. \quad (66)$$

For calculating the net force the integrand is the normal stress given above which is everywhere positive, but the net force is negative. This results from the finite part nature of the integral. Thinking of this in terms of a Green's function for frictionless contact, the negative net force arising from identation is understandable. Multiplying the above expressions by the ratio $(\kappa+1)/(8\mu\pi H)$ gives the corresponding results for transverse isotropy. These results agree with those given by Fabrikant (1989) if one accounts for the negative sign difference in defining the normal stress. Knowing the net force and moment above allows the appropriate conditions at infinity to be included using the closed-form solutions for the flat and inclined punch derived previously by Fabrikant (1989).

The net force and moment for the internal crack case can be found as above. The net force is given in Fabrikant (1989).

References

Comninou, M., and Barber, J. R., 1982, "Letter to the Editor on the Plane External Crack," *Letters in Applied Engineering Science*, Vol. 20, pp. 695-696.

Elliot, H. A., 1948, "Three-Dimensional Stress Distributions in Hexagonal Aeolotropic Crystals," *Proceedings of the Cambridge Philosophical Society*, Vol. 44, pp. 522-533.

Fabrikant, V. I., Sankar, T. S., and Xistris, G. D., 1986, "On the Conditions at Infinity in External Crack Problems," *Engineering Fracture Mechanics*, Vol. 23, pp. 921-924.

Fabrikant, V. I., 1989, *Applications of Potential Theory in Mechanics; A Selection of New Results*, Kluwer Academic Publishers, The Netherlands, pp. 20, 22, 71-75, 83-84, 94, 329-330, 341-348.

Downloaded 03 May 2010 to 171.66.16.247. Redistribution subject to ASME license or copyright; see http://www.asme.org/terms/Terms_Use.cfm

Fabrikant, V. I., 1990, "Complete Solutions to Some Mixed Boundary Value Problems in Elasticity," *Advances in Applied Mechanics*, Vol. 27, pp. 217–218.

Galin, L. A., 1961, *Contact Problems in the Theory of Elasticity*, North Carolina State University Publications, pp. 133–135.

Gao, H., and Rice, J. R., 1987, "Nearly Circular Connections of Elastic Half Spaces," ASME JOURNAL OF APPLIED MECHANICS, Vol. 54, pp. 627–634.

Green, A. E., and Zerna, W., 1968, *Theoretical Elasticity*, Oxford University Press, London, pp. 167–169, 177–181.

Hanson, M. T., 1990, "A Dislocation Green's Function for the Analysis of Multiple Coplanar Cracks or Cracks with Non-Uniform Crack Fronts," ASME JOURNAL OF APPLIED MECHANICS, Vol. 57, pp. 589–595.

Kassir, M. K., and Sih, G. C., 1975, "Three-Dimensional Crack Problems," *Mechanics of Fracture*, Vol. 2, Noordhoff International Publishing, The Netherlands, pp. 336–349.

Stallybrass, M. P., 1981a, "Some Comments on External Crack Problems in 2-Dimensional Elastostatics," *International Journal of Engineering Science*, Vol. 19, pp. 57–61.

Stallybrass, M. P., 1981b, "On the Concentrated Loading of Certain Elastic Half-Space Problems and Related External Crack Problems. A New Approach," *International Journal of Engineering Science*, Vol. 19, pp. 1123–1144.

Stallybrass, M. P., 1982, "Some Comments on External Crack Problems in 2-Dimensional Elastostatics," *Letters in Applied Engineering Science*, Vol. 20, pp. 969–976.

Watson, G. N., 1980, *Theory of Bessel Functions*, Cambridge University Press, Cambridge, U. K., pp. 358–359.

APPENDIX A

The following integral is given in Fabrikant (1989):

$$\int_0^\infty \frac{1}{\sqrt{s}} J_{n+1/2}(as) J_n(\rho s) e^{-sz} ds = \frac{\sqrt{2}}{\sqrt{\pi a}} (a\rho)^{-n} \int_0^{l_1(a)} \frac{t^{2n} dt}{\sqrt{\rho^2 - t^2}}, \quad \text{(A1)}$$

where

$$l_1(a) = \frac{1}{2}\left\{\sqrt{(a+\rho)^2+z^2} - \sqrt{(a-\rho)^2+z^2}\right\}. \quad \text{(A2)}$$

The above integral was not formally proven but inferred by comparing a closed-form solution to a previous integral transform solution. Letting $a \to x$, $\rho \to r$ and differentiating with respect to z results in

$$\int_0^\infty \sqrt{\xi} J_{n+1/2}(\xi x) J_n(\xi r) e^{-\xi z} d\xi = \frac{\sqrt{2}}{\sqrt{\pi x}} \left(\frac{l_1^2(x)}{rx}\right)^n \frac{1}{\sqrt{r^2 - l_1^2(x)}} \frac{z l_1(x)}{(l_2^2(x) - l_1^2(x))}, \quad \text{(A3)}$$

where $l_1(x)$ and $l_2(x)$ are defined in Eqs. (34), (35). Here the following identity has been used:

$$\frac{dl_1(x)}{dz} = -\frac{z l_1(x)}{l_2^2(x) - l_1^2(x)}. \quad \text{(A4)}$$

Equation (A3) is Eq. (52) with n replaced by $|n|$. If in Eq. (A3) the substitutions $r \to x$, $x \to r$ and $n \to n - 1/2$ are made, there results

$$\int_0^\infty \sqrt{\xi} J_{n-1/2}(\xi x) J_n(\xi r) e^{-\xi z} d\xi = \frac{\sqrt{2}}{\sqrt{\pi x}} \left(\frac{rx}{l_2^2(x)}\right)^n \frac{1}{\sqrt{l_2^2(x) - r^2}} \frac{z l_2(x)}{(l_2^2(x) - l_1^2(x))}, \quad \text{(A5)}$$

where the following relations have been used:

$$l_1(x) = \frac{rx}{l_2(x)}, \quad \frac{1}{\sqrt{x^2 - l_1^2(x)}} = \frac{l_2(x)}{x} \frac{1}{\sqrt{l_2^2(x) - r^2}}. \quad \text{(A6)}$$

Equation (A5) above is Eq. (33) in the text with n replaced by $|n|$.

APPENDIX B

Here the integral

$$\int \frac{z}{R^2}\left(\frac{1}{j(a)} + \frac{1}{R}\tan^{-1}\left(\frac{j(a)}{R}\right)\right) dz, \quad \text{(B1)}$$

is evaluated where $R^2 = r^2 + r_o^2 - 2rr_o\cos(\theta - \theta_o) + z^2$ and $j(a)$ is given in Eq. (54). This integral can be rewritten as

$$\int \frac{z}{R^2 j(a)} dz - \int \tan^{-1}\left(\frac{j(a)}{R}\right) d\left(\frac{1}{R}\right) = -\frac{1}{R}\tan^{-1}\left(\frac{j(a)}{R}\right) + \int \frac{z}{R^2 j(a)} dz + \int \frac{1}{R} d\left(\tan^{-1}\left(\frac{j(a)}{R}\right)\right). \quad \text{(B2)}$$

Using the result

$$\frac{d}{dz}\tan^{-1}\left(\frac{j(a)}{R}\right) = -\frac{z}{R j(a)}$$

$$+ Rz \frac{(r^2 r_o^2 - l_1^4(a)) l_1(a)}{\sqrt{r_o^2 - a^2}\sqrt{r^2 - l_1^2(a)}\,[l_2^2(a) - l_1^2(a)][l_1^4(a) + r^2 r_o^2 - 2l_1^2(a) r r_o \cos(\theta - \theta_o)]}, \quad \text{(B3)}$$

the integral in Eq. (B1) becomes

$$-\frac{1}{R}\tan^{-1}\left(\frac{j(a)}{R}\right) + \int \frac{(l_1^4(a) - r^2 r_o^2) dl_1(a)}{\sqrt{r_o^2 - a^2}\sqrt{r^2 - l_1^2(a)}\,[l_1^4(a) + r^2 r_o^2 - 2l_1^2(a) r r_o \cos(\theta - \theta_o)]}. \quad \text{(B4)}$$

Here, the integration variable has been changed from z to $l_1(a)$ and Eq. (A4) has been used. The integrand can be factored as

$$\frac{l_1^4(a) - r^2 r_o^2}{l_1^4(a) + r^2 r_o^2 - 2l_1^2(a) r r_o \cos(\theta - \theta_o)} = \frac{l_1^4(a) - r^2 r_o^2}{[l_1^2(a) - r r_o e^{i(\theta - \theta_o)}][l_1^2(a) - r r_o e^{-i(\theta - \theta_o)}]} = 1 + \frac{r^2}{\zeta l_1^2(a) - r^2} + \frac{r^2}{\bar{\zeta} l_1^2(a) - r^2}, \quad \zeta = \frac{r}{r_o} e^{i(\theta - \theta_o)}. \quad \text{(B5)}$$

Using the integrals

$$\int \frac{dl_1(a)}{\sqrt{r^2 - l_1^2(a)}} = \sin^{-1}\left(\frac{l_1(a)}{r}\right), \quad \text{(B6)}$$

$$\int \frac{r^2 dl_1(a)}{\sqrt{r^2 - l_1^2(a)}\,(\zeta l_1^2(a) - r^2)} = \frac{1}{\sqrt{1-\zeta}}\tan^{-1}\left(\frac{\sqrt{l_2^2(a) - a^2}}{a\sqrt{1-\zeta}}\right), \quad \text{(B7)}$$

the result in Eq. (59) is obtained.

APPENDIX C

The net force can be written using Eq. (63) as

$$P = \frac{2\mu b}{\pi^2(\kappa+1)} \int_0^{2\pi} \int_0^a \left\{\frac{1}{R^3}\tan^{-1}\left(\frac{h(a)}{R}\right) + \frac{1}{R^2 h(a)}\right\} r dr d\theta. \quad \text{(C1)}$$

The above integral is divergent at $R = 0$ and must be interpreted

Downloaded 03 May 2010 to 171.66.16.247. Redistribution subject to ASME license or copyright; see http://www.asme.org/terms/Terms_Use.cfm

as a finite part. Considering the second term, one can perform the θ integration as

$$\int_0^{2\pi}\int_0^{a}\frac{1}{R^2h(a)}\,rdrd\theta=2\pi\int_0^{r_o}\frac{rdr}{h(a)(r_o^2-r^2)}+2\pi\int_{r_o}^{a}\frac{rdr}{h(a)(r^2-r_o^2)}. \quad \text{(C2)}$$

Denoting the first integral as

$$T(a)=\int_0^{2\pi}\int_0^{a}\frac{1}{R^3}\tan^{-1}\left(\frac{h(a)}{R}\right)rdrd\theta, \quad \text{(C3)}$$

one can differentiate with respect to a giving

$$T'(a)=\int_0^{2\pi}\int_0^{a}\frac{1}{R^2}\frac{1}{R^2+h^2(a)}\frac{dh(a)}{da}\,rdrd\theta. \quad \text{(C4)}$$

Here it is noted that

$$R^2+h^2(a)=\frac{1}{a^2}[a^4+r^2r_o^2-2a^2rr_o\cos(\theta-\theta_o)]. \quad \text{(C5)}$$

Performing the θ integration results in

$$T'(a)=2\pi\int_0^{r_o}\frac{r}{h^2(a)(r_o^2-r^2)}\frac{dh(a)}{da}\,dr+2\pi\int_{r_o}^{a}\frac{r}{h^2(a)(r^2-r_o^2)}\frac{dh(a)}{da}\,dr-2\pi\int_0^{a}\frac{r}{ah^3(a)}\,dr. \quad \text{(C6)}$$

It is noted that the second and third integrals above are divergent for $r \to a$; however, the divergencies cancel. Each may be evaluated separately and the divergencies discarded. This is not related to the divergent nature of the integrand at $R = 0$ in Eq. (C1). Performing the integration in the third term and discarding the divergency results in

$$T'(a)=2\pi\int_0^{r_o}\frac{r}{h^2(a)(r_o^2-r^2)}\frac{dh(a)}{da}\,dr+2\pi\int_{r_o}^{a}\frac{r}{h^2(a)(r^2-r_o^2)}\frac{dh(a)}{da}\,dr+2\pi\frac{a}{(a^2-r_o^2)^{3/2}}. \quad \text{(C7)}$$

The integral $T(a)$ can be written as

$$T(a)=-\int_a^{\infty}T'(t)dt, \quad \text{(C8)}$$

where we have taken $T(\infty) = 0$. This is because $a = \infty$ corresponds to the dislocation in the full space with no net force. This also gives the finite part evaluation. Substituting Eq. (C7) into (C8) and interchanging the orders of integration yields

$$T(a)=-2\pi\int_0^{r_o}\frac{rdr}{(r_o^2-r^2)}\int_a^{\infty}\frac{1}{h^2(t)}\frac{dh(t)}{dt}\,dt-2\pi\int_{r_o}^{a}\frac{rdr}{(r^2-r_o^2)}\int_a^{\infty}\frac{1}{h^2(t)}\frac{dh(t)}{dt}\,dt-2\pi\int_a^{\infty}\frac{rdr}{(r^2-r_o^2)}\int_r^{\infty}\frac{1}{h^2(t)}\frac{dh(t)}{dt}\,dt-2\pi\frac{1}{\sqrt{a^2-r_o^2}}. \quad \text{(C9)}$$

The integrals can be evaluated by changing the integration variable from t to $h(t)$. The third integral is divergent at $t = r$ which corresponds to the divergency discarded earlier. The final result for $T(a)$ becomes

$$T(a)=-2\pi\int_0^{r_o}\frac{rdr}{h(a)(r_o^2-r^2)}-2\pi\int_{r_o}^{a}\frac{rdr}{h(a)(r^2-r_o^2)}-2\pi\frac{1}{\sqrt{a^2-r_o^2}}. \quad \text{(C10)}$$

Adding Eqs. (C2) and (C10) gives P as

$$P=-\frac{4\mu b}{\pi(\kappa+1)}\frac{1}{\sqrt{a^2-r_o^2}}. \quad \text{(C11)}$$

The moment $M_x + iM_y$ is defined as

$$M_x+iM_y=\int_0^{2\pi}\int_0^{a}ire^{i\theta}\sigma_{zz}(r,\theta,0)rdrd\theta, \quad \text{(C12)}$$

where $\sigma_{zz}(r, \theta, 0)$ is given in Eq. (63). The integration can be performed in the same manner as above giving the result in Eq. (66).

Downloaded 03 May 2010 to 171.66.16.247. Redistribution subject to ASME license or copyright; see http://www.asme.org/terms/Terms_Use.cfm

Crack Deflection at an Interface Between Two Orthotropic Media

V. Gupta[1]
Assoc. Mem. ASME.

A. S. Argon
Massachusetts Institute of Technology, Cambridge, MA 02139

Z. Suo[2]
Harvard University, Cambridge, MA 02138

To achieve toughness in many brittle composites, crack deflection at interfaces is essential. For this, it is necessary to establish crack deflection criteria by employing the principles of interfacial fracture mechanics applicable to anisotropic pair of materials. Such an analysis, with two aligned orthotropic media, is considered here. The stress and deformation fields derived for such cases are shown to depend on material parameters λ and ρ for the two media and on the two so-called Dundur constants α and β. For $\beta = 0$, the dependence on λ_1 and λ_2 collapses to $\Lambda = (\lambda_1/\lambda_2)^{1/4}$. The delamination criterion is insensitive to λ, ρ, Λ, and β over practical ranges of these material parameters. Thus, generalized delamination charts become possible as a function of the bi-material constant α alone, which characterizes the elastic dissimilarity between the two media. Using these charts, it is possible to determine the desired level of the interface strength required in composite manufacturing in order to enhance the overall toughness of a composite. Furthermore, such charts can be used for the interfaces between fiber/coating, fiber/matrix, or matrix/coating, depending on which interface is of critical interest for the crack deflection. It is shown how these charts can be used to identify composite systems where it is possible to maximize both the transverse strength and the longitudinal toughness.

1 Introduction

It is now widely appreciated that the mechanical properties of interfaces play a key role in the overall performance of a composite material, and that the desirable levels of toughness in composites can be obtained through the tailoring of interface properties. Interfaces across which the physical and mechanical properties of component phases change abruptly can be either the sites of unwanted premature separation due to deformation-induced stress concentration or they can be made to act in a beneficial sense to arrest or deflect cracks. The various strategies on how damaged parts of a composite can be controllably decoupled from undamaged parts by promoting delamination across interfaces, have been discussed by many investigators (see, e.g., Cook and Gordon, 1964; Gupta et al., 1989). The two basic choices for a crack are shown in Fig. 1, where a brittle crack momentarily impinges on an interface between a matrix or a coating and a reinforcing fiber at right angles. The crack can either propagate ahead into the fiber or be deflected along the interface and continue to propagate along it in a benign manner. Strategies to achieve the second and desirable alternative rely on two complementary criteria based on either local crack-tip stresses or differences of work of fracture along possible alternative crack paths.

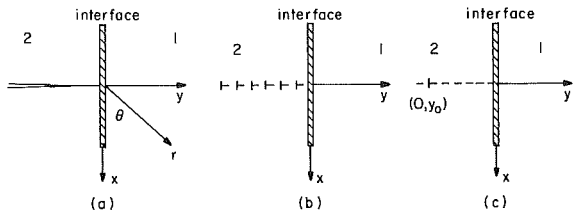


Fig. 1(*a*) Semi-infinite crack terminating perpendicular to the interface between two orthotropic materials with aligned principal axis, (*b*) semi-infinite crack represented as a continuous distribution of edge dislocations, and (*c*) a single edge dislocation in the vicinity of an interface

The local stress criterion for crack deflection demands that, under the probing of the crack-tip stress field, the decohesion stress for tensile or for shear separation along the interface be reached before the cohesive strength is reached in the fiber at the crack tip. The complementary fracture work criterion, on the other hand, demands that, when the crack is about to grow, for virtual extensions of a crack ahead in its plane or along the interface, the work of fracture should be less along the interface than ahead into the fiber. Here we will pursue only the local stress criterion, particularly in the context of highly anisotropic fibers (e.g., for the Pitch-55 carbon fiber which has an axial modulus of 380 GPa and a transverse modulus of only 20 GPa). The degree of anisotropy considered here is restricted to the orthotropic level, as most cases of current interest fall in this category.

[1]Presently at the Thayer School of Engineering, Dartmouth College, Hanover, NH 03755.

[2]Presently at the Department of Mechanical and Environmental Engineering, University of California at Santa Barbara, Santa Barbara, CA 93106.

Contributed by the Applied Mechanics Division of THE AMERICAN SOCIETY OF MECHANICAL ENGINEERS for presentation at the Winter Annual Meeting, Atlanta, Ga., Dec. 1-6, 1991.

Discussion on this paper should be addressed to the Technical Editor, Prof. Leon M. Keer, The Technological Institute, Northwestern University, Evanston, IL 60208, and will be accepted until two months after final publication of the paper itself in the JOURNAL OF APPLIED MECHANICS. Manuscript received by the ASME Applied Mechanics Division, Oct. 16, 1990; final revision, May 24, 1991.

Paper No. 91-WA/APM-42.

Copyright © 1992 by ASME
Downloaded 03 May 2010 to 171.66.16.247. Redistribution subject to ASME license or copyright; see http://www.asme.org/terms/Terms_Use.cfm

The problem of a crack terminating at right angles on an interface between two dissimilar, but isotropic media, has been solved in the past by several investigators (Zak and Williams, 1963; Swenson and Rau, 1970; Erdogan and Biricikoglu, 1973). Solutions to the corresponding problem for a pair of anisotropic materials also exist (Ting and Hoang, 1984; Erdogan, 1972). While they are equally useful for the statement of the crack deflection criterion by interface delamination, they are less adequate to the solution of the problem of the energy release upon crack extension than the approach using continuously distributed dislocations that we will develop here. In this communication, however, we will not pursue the question of energy release. Here we present new results for the problem of a crack impinging at normal incidence on an interface between two orthotropic media with principal material axes parallel and perpendicular to the interface for the purpose of developing the crack deflection criterion applicable to specific cases such as the pair of SiC coating and pitch-55 fiber.

Furthermore, we identify critical anisotropic elastic constants influencing the structure of the solution so as to give generalized results useful for most practical ranges of bi-material combinations of interest to the current composite systems. Clearly, our solutions will be a special case of a more general (but far more difficult) problem of a crack impinging on an interface at an arbitrary angle. Nevertheless, our solution should be widely applicable to aligned fiber composite materials.

2 Crack Normal to a Bi-Material Interface

2.1 Problem Statement and Solution Structure. The basic problem to be analysed is shown in Fig. 1(*a*). A semi-infinite crack terminates normal to the interface between two orthotropic materials with aligned principal axes. Both media are taken to be homogeneous, linear elastic solids. Both plane stress and plane strain deformation are considered. For generally anisotropic materials, Hooke's law can be written as

$$\epsilon_i = \sum_{j=1}^{6} s_{ij}\sigma_j, \quad (i = 1\text{–}6). \tag{1a}$$

Where the standard correspondence is adopted, i.e., $\{\epsilon_i\} = \{\epsilon_x, \epsilon_y, \epsilon_z, \gamma_{yz}, \gamma_{zx}, \gamma_{xy}\}$, $\{\sigma_i\} = \{\sigma_x, \sigma_y, \sigma_z, \tau_{yz}, \tau_{zx}, \tau_{xy}\}$, and s_{ij} are elements of a six-by-six symmetric matrix of compliances with 21 independent elements in the most general case. When the material has orthotropic symmetry, then the elastic stress-strain equations can be reduced to (see Lekhnitskii, 1963)

$$\epsilon_i = \sum_{j=1,2,6} b_{ij}\sigma_j, \quad (i = 1,2,6) \tag{1b}$$

$$b_{ij} = \begin{cases} s_{ij}, \text{ for plane stress} \\ s_{ij} - (s_{i3}s_{j3})/s_{33}, \text{ for plane strain} \end{cases} \quad i,j = 1,2,6 \tag{1c}$$

with only four remaining independent elastic compliances, b_{11}, $b_{12} = b_{21}$, b_{22}, and b_{66} ($b_{16} = b_{26} = 0$); in each of the two media. It was shown by Suo (1988) that for a singly connected domain of an orthotropic medium with prescribed traction on its boundary, the stress in each medium depends on two dimensionless elastic constants λ and ρ, defined as

$$\lambda = s_{11}/s_{22}, \tag{2a}$$

$$\rho = \frac{2s_{12} + s_{66}}{2\sqrt{s_{11}s_{22}}}. \tag{2b}$$

These constants measure the anisotropy in the sense that $\lambda = 1$ when the material has transverse cubic symmetry, and $\lambda = \rho = 1$ when the material becomes transversely isotropic. The positive definiteness of the strain energy density requires that

$$\lambda > 0, \quad -1 < \rho < \infty. \tag{3}$$

Following Lekhnitskii (1963), for plane deformation, the elastic field can be represented in terms of two complex potential functions $\Phi_1(z_1)$, $\Phi_2(z_2)$, each of which is holomorphic in its argument $z_j = x + \mu_j y$. Here, μ_j are two distinct complex numbers with positive imaginary parts, which are obtained as the roots of the following characteristic equation

$$\lambda\mu^4 + 2\rho(\lambda)^{1/2}\mu^2 + 1 = 0. \tag{4}$$

The foregoing equation is a special form of the sixth-order characteristic equation obtained by Lekhnitskii (1963), when the governing differential equation for the stress potential is expressed as six first-order equations. The roots with the positive imaginary parts of Eq. (4) are

$$\mu_1 = i\lambda^{-1/4}(n+m),$$

$$\mu_2 = i\lambda^{-1/4}(n-m), \quad (\text{for } 1 < \rho < \infty) \tag{5a}$$

$$\mu_1 = \lambda^{-1/4}(in+m),$$

$$\mu_2 = \lambda^{-1/4}(in-m), \quad (\text{for } -1 < \rho < 1) \tag{5b}$$

$$\mu_1 = \mu_2 = i\lambda^{-1/4}, \quad (\text{for } \rho = 1) \tag{5c}$$

$$n = \sqrt{\frac{1+\rho}{2}} \quad m = \sqrt{\left|\frac{1-\rho}{2}\right|} \tag{5d}$$

With these holomorphic functions, the representation for the displacements u_i, stresses σ_{ij}, and the resultant forces on an arc f_i (the medium is kept on the left-hand side as an observer travels in the positive direction of the arc) is

$$u_i = 2\,\mathrm{Re}\left[\sum_{j=1}^{2} A_{ij}\Phi_j(z_j)\right] \tag{6a}$$

$$\sigma_{2i} = 2\,\mathrm{Re}\left[\sum_{j=1}^{2} L_{ij}\Phi_j'(z_j)\right] \tag{6b}$$

$$\sigma_{1i} = -2\,\mathrm{Re}\left[\sum_{j=1}^{2} L_{ij}\mu_j\Phi_j'(z_j)\right] \tag{6c}$$

$$f_i = -2\,\mathrm{Re}\left[\sum_{j=1}^{2} L_{ij}\Phi_j(z_j)\right]. \tag{6d}$$

Here, $(\,)'$ designates the derivative with respect to the associated arguments, and **A** and **L** are two matrices whose elements depend upon the elastic constants as

$$\mathbf{A} = \begin{bmatrix} (s_{11}\mu_1^2 + s_{12}) & (s_{11}\mu_2^2 + s_{12}) \\ (s_{12}\mu_1 + s_{22}/\mu_1) & (s_{12}\mu_2 + s_{22}/\mu_2) \end{bmatrix} \tag{7a}$$

$$\mathbf{L} = \begin{bmatrix} -\mu_1 & -\mu_2 \\ 1 & 1 \end{bmatrix}. \tag{7b}$$

2.2 Solution of the Problem. For two aligned orthotropic media, it is possible to define two generalized Dundurs (1968) parameters α and β, which are the only bi-material constants that enter the solution for the problem involving dissimilar materials with prescribed tractions at the boundary. Thus, the solution for the problem under consideration should depend upon λ and ρ for each material and the two bi-material parameters α and β, defined as (Suo, 1988)

$$\alpha = \frac{[\sqrt{(s_{11}s_{22})_2}/\sqrt{(s_{11}s_{22})_1} - 1]}{[\sqrt{(s_{11}s_{22})_2}/\sqrt{(s_{11}s_{22})_1} + 1]} \tag{8a}$$

$$\beta = \frac{[\sqrt{s_{11}s_{22}} + s_{12}]_2 - [\sqrt{s_{11}s_{22}} + s_{12}]_1}{\sqrt{H_{11}H_{22}}} \tag{8b}$$

where

$$H_{11} = [2n\lambda^{1/4}\sqrt{s_{11}s_{22}}]_1 + [2n\lambda^{1/4}\sqrt{s_{11}s_{22}}]_2 \tag{8c}$$

$$H_{22} = [2n\lambda^{-1/4}\sqrt{s_{11}s_{22}}]_1 + [2n\lambda^{-1/4}\sqrt{s_{11}s_{22}}]_2. \tag{8d}$$

2.3 Engineering Approximations. Suo and Hutchinson

Downloaded 03 May 2010 to 171.66.16.247. Redistribution subject to ASME license or copyright; see http://www.asme.org/terms/Terms_Use.cfm

(1989) have pointed out that for the case of a crack lying along the interface, the Dundurs parameter β is responsible for the pathological oscillatory behavior of the stresses near the crack tip. Due to the weak dependence of stresses on β and the fact that β itself only takes on small values for most practical cases of interest, Suo and Hutchinson (1989) have suggested that β could be equated to zero to establish a useful engineering approach to such interface problems. However, in the present class of problems discussed here where the cracks terminate at right angles to the interface, there is no oscillatory behavior associated with the nonzero values of β. Therefore, the development of the entire stress field in terms of finite β, without equating it *a priori* to zero, is meaningful. In most of the practical cases the variation of β is between $-1/4$ and $1/4$. The variation of the normal stress at the interface as a function of α could then be up to 25 percent for the above range of β values, which could be relevant since this is the stress component that directly affects the interface delamination criterion. Fortunately, the greatest sensitivity of the normal stress at the interface is restricted to values of α in the range of $|\alpha| > 0.5$, where very few of the practical bi-material combinations fall. Hence, for operational purposes, we have taken $\beta = 0$ in discussing specific cases, because this simplifies the computations without much loss of accuracy. Specifically, neglecting β diagonalizes the bi-material matrix **H** presented in the Appendix, whose elements depend only on the bi-material constants.

With $\beta = 0$, it is possible to further re-scale the x-axis to collapse the dependence of the solution on λ_1 and λ_2 into a new parameter Λ ($[\lambda_1/\lambda_2]^{1/4}$), thereby reducing the number of independent parameters characterizing the solution to 4, i.e., ρ_1, ρ_2, Λ, and the Dundurs parameter α.

2.4 Method of Solution. The semi-infinite crack is simulated as an array of continuously distributed edge dislocations along the negative y-axis, with components $b_1(y_o)$ at $y = y_o$ as shown in Fig. 1(*b*). The traction-free condition on the plane of the crack with the dislocation distribution results in the integral equation

$$\sigma_{11} = 0 = \frac{1}{8\pi m_2 n_2 s_2}\,\mathrm{Re}\left[\int_{-\infty}^{0}\left[\frac{[-\mu_1^{II}C_{11}^*]}{y+y_o}+\frac{[\mu_2^{II}C_{22}^*]}{y+y_o}-\frac{[\mu_2^{II}C_{21}^*]}{y+(\mu_1^{II}/\mu_2^{II})y_o}+\frac{[\mu_1^{II}C_{12}^*]}{y+(\mu_2^{II}/\mu_1^{II})y_o}\right]b_1'(y_o)d(iy_o)\right]$$
$$+\frac{1}{8\pi m_2 n_2 s_2}\,\mathrm{Re}\left[\int_{-\infty}^{0}\left[\frac{[\mu_1^{II}-\mu_2^{II}]}{y-y_o}\right]b_1'(y_o)d(iy_o)\right] \quad (9)$$

where $s_2 = (\sqrt{s_{11}s_{22}})_2$, and m and n are the same as defined before in Eq. (5*d*), and $b_1'(y_o)d(iy_o)$ is the local Burgers vector density of the continuous distribution of dislocation between y_o and $y_o + dy_o$. The constants C_{ij}^* are coefficients of a matrix depending upon ρ_1, ρ_2, Λ, and α characterizing the corresponding kernel solution of an edge dislocation at $(0, y_o)$ near the bi-material interface as shown in Fig. 1(*c*). The superscript II on μ's and the subscript 2 on m, n, and s is chosen to refer to medium 2, which in turn hosts the crack. The constant β influences the solution only through the C_{ij}^*'s. The complete kernel solution along with the expressions for C_{ij}^*'s are given in the Appendix. In this class of problems the radial dependence of the stresses is of the form

$$\sigma\alpha(r)^{\gamma}, \quad (10)$$

where γ is the strength of the singularity. Therefore, each integral in Eq. (9) can be evaluated in a closed form leading to the following characteristic equation

$$[t_2^{II}C_{22} - t_1^{II}C_{11}] + t_1^{II}C_{12}\left(\frac{t_1^{II}}{t_2^{II}}\right)^{(\gamma+1)} - C_{21}t_2^{II}\left(\frac{t_2^{II}}{t_1^{II}}\right)^{(\gamma+1)} - \cos[\pi\gamma(t_1^{II}-t_2^{II})] = 0, \quad (11)$$

where $t_1 = n + m$, $t_2 = n - m$. Since the C_{ij}^*'s are known from the kernel solution, the strength of the singularity, γ, can be determined for a given material pair (thereby fixing μ_1 and μ_2) from Eq. (11).

2.5 Results for Stresses. Knowing γ, the stress obtained from the kernel solution can be integrated over the complex domain to determine the expressions for stresses in the two media. The resulting stresses in the vicinity of the interface crack are obtained in closed form

$$\tilde{\sigma}_{11}^{I}(0\text{ deg}) = \sin(\pi\gamma)\left\{\begin{matrix}[-C_{11}(t_1^I)^2(t_1^{II})^{-(\gamma+1)}]+[C_{12}(t_1^I)^2(t_2^{II})^{(\gamma+1)}]\\ -[C_{21}(t_2^I)^2(t_1^{II})^{-(\gamma+1)}]+[C_{22}(t_2^I)^2(t_2^{II})^{-(\gamma+1)}]\end{matrix}\right\} \quad (12a)$$

$$\tilde{\sigma}_{22}^{I}(0\text{ deg}) = \tilde{\sigma}_{22}^{II}(0\text{ deg}) = \sin(\pi\gamma)\left\{\begin{matrix}[C_{11}(t_1^{II})^{-(\gamma+1)}]-[C_{12}(t_2^{II})^{-(\gamma+1)}]\\ +[C_{21}(t_1^{II})^{-(\gamma+1)}]-[C_{22}(t_2^{II})^{-(\gamma+1)}]\end{matrix}\right\} \quad (12b)$$

$$\tilde{\sigma}_{12}^{I}(0\text{ deg}) = \tilde{\sigma}_{12}^{II}(0\text{ deg}) = -(\cos(\pi\gamma)-1)\left\{\begin{matrix}-[C_{11}t_1^I(t_1^{II})^{-(\gamma+1)}]+[C_{12}t_1^I(t_2^{II})^{-(\gamma+1)}]\\ -[C_{21}t_2^I(t_1^{II})^{-(\gamma+1)}]+[C_{22}t_2^I(t_2^{II})^{-(\gamma+1)}]\end{matrix}\right\} \quad (12c)$$

$$\tilde{\sigma}_{11}^{II}(0\text{ deg}) = -\sin(\pi\gamma)\left\{\begin{matrix}[C_{11}(t_1^{II})^2(t_1^{II})^{-(\gamma+1)}]-[C_{12}(t_1^{II})^2(t_2^{II})^{-(\gamma+1)}]\\ +[C_{21}(t_2^{II})^2(t_1^{II})^{-(\gamma+1)}]-[C_{22}(t_2^{II})^2(t_2^{II})^{-(\gamma+1)}]\end{matrix}\right\} + \sin(\pi\gamma)[-(t_1^{II})^{(1-\gamma)}+(t_2^{II})^{(1-\gamma)}] \quad (12d)$$

$$\tilde{\sigma}_{11}^{I}(90\text{ deg}) = 2\sin(\pi\gamma/2)\times\left\{\begin{matrix}[-C_{11}(t_1^I)^{(2+\gamma)}(t_1^{II})^{-(\gamma+1)}]+[C_{12}(t_1^I)^{(2+\gamma)}(t_2^{II})^{-(\gamma+1)}]\\ -[C_{21}(t_2^I)^{(2+\gamma)}(t_1^{II})^{-(\gamma+1)}]+[C_{22}(t_2^I)^{(2+\gamma)}(t_2^{II})^{-(\gamma+1)}]\end{matrix}\right\} \quad (12e)$$

$$\tilde{\sigma}_{22}^{I}(90\text{ deg}) = 2\sin(\pi\gamma/2)\left\{\begin{matrix}[C_{11}(t_1^I)^{\gamma}(t_1^{II})^{-(\gamma+1)}]-[C_{12}(t_1^I)^{\gamma}(t_2^{II})^{-(\gamma+1)}]\\ +[C_{21}(t_2^I)^{\gamma}(t_1^{II})^{-(\gamma+1)}]-[C_{22}(t_2^I)^{\gamma}(t_2^{II})^{-(\gamma+1)}]\end{matrix}\right\} \quad (12f)$$

in the Appendix. Finally, the actual stresses σ_{ij} are obtained from

$$\sigma_{ij} = \left[\frac{K(2\pi r)^{\gamma}}{8n_2s_2m_2}\right]\tilde{\sigma}_{ij} \quad (13)$$

where K is the generalized stress intensity factor having the dimensions (stress/(length)$^{\gamma}$) and is defined on the basis of

$$K(2\pi r)\gamma = \sigma_{xx}(\theta = 90\text{ deg}, r), \quad (14)$$

so as to recover the conventional stress intensity factor for cracks in an infinite homogeneous isotropic material. The expressions for stresses given via Eqs. (12) and (13) can be further normalized in terms of this stress intensity factor as defined above, as

$$\frac{\sigma_{ij}}{K(2\pi r)^{\gamma}} = \bar{\sigma}_{ij}. \quad (15)$$

Thus, for a given bi-material pair, the stress ratios can be

Downloaded 03 May 2010 to 171.66.16.247. Redistribution subject to ASME license or copyright; see http://www.asme.org/terms/Terms_Use.cfm

calculated using the above expressions. The explicit expressions for C_{ij}'s in terms of β and other elastic constants of the two media are given in the Appendix. In the next section we work out the stress ratios for the case of a crack in a SiC coating terminating perpendicularly on an interface between it and a Pitch-55 fiber.

2.6 Crack Deflection Criterion for the SiC Coating/Pitch-55 Fiber Interface. Since the present investigation was motivated by the specific goal to tailor the properties of an interface between a coating such as SiC and a fiber such as Pitch-55, in a composite with a matrix such as aluminum, we calculate here the crack deflection criterion specifically for a crack in a SiC coating terminating perpendicularly on a Pitch-55 fiber. The fiber is modelled as a homogeneous orthotropic material with the elastic constants given in Table 1, while the SiC coating is considered as isotropic with elastic constants also shown in Table 1. For a pair consisting of high modulus SiC coating and Pitch-55 fiber, the bi-material parameters are: $\alpha = -0.4$; $\beta = 0.04$, $\rho_1 = 2.43$, $\lambda_1 = 0.034$, $\rho_2 = 1$ and $\lambda_2 = 1$ (SiC coating is considered to be isotropic as stated above). For these material constants, the singularity exponent γ is equal to -0.46, as determined from Eq. (11), and the values of the various crack-tip stresses in the fiber and the coating are given in Table 2. The stresses are normalized as discussed above.

The stress acting across the interface, particularly the normal component of it, is of interest for the determination of the crack deflection criterion discussed in Section 1. Since the normal stress in Table 2 is normalized with respect to the axial stress in the fiber, therefore, the crack deflection criterion is satisfied if the ratio of σ_i^*/σ_f^* is less than 0.136 where σ_i^* and σ_f^* are the tensile cohesive strengths of the interface and the fiber, respectively. The average strength of the Pitch-55 fiber was determined from independent experiments to be 1.2 GPa (Zhang et al., 1990). Hence, in order to deflect the crack along the interface, the interface tensile strength should be less than 163 MPa. This calculation is specific to the above pair. Coatings of SiC deposited under different conditions can have different elastic properties and interface strength when deposited on Pitch-55 fibers. Therefore, to cope with a wide range of possibilities and with other general coating/fiber systems, we develop generalized interface delamination charts—albeit with operational simplifications.

Table 1 Elastic constants for the Pitch-55 fiber and SiC coating

material	E_{11}	E_{22}	μ_{12}	ν_{12}
Pitch-55 fiber	380	13	-	0.45
SiC Coating (Isotropic, high IBE)	300	300	115.4	0.3
SiC Coating (Isotropic, low IBE)	16	16	6.5	0.3

IBE: ion beam energy

Table 2 Normalized stress components at an interface between a anisotropic Pitch-55 fiber and SiC coating

Normalized Components	Calculated Stress Ratios
$\sigma_{xx}(\pi/2)^I/(K(2\pi r)^\gamma)$	1.000
$\sigma_{yy}(\pi/2)^I/(K(2\pi r)^\gamma)$	0.516
$\sigma_{xx}(0)^I/(K(2\pi r)^\gamma)$	1.157
$\sigma_{xx}(0)^{II}/(K(2\pi r)^\gamma)$	4.487
$\sigma_{yy}(0)^I/(K(2\pi r)^\gamma) = \sigma_{yy}(0)^{II}/(K(2\pi r)^\gamma)$	0.136
$\sigma_{xy}(0)^I/(K(2\pi r)^\gamma) = \sigma_{xy}(0)^{II}/(K(2\pi r)^\gamma)$	0.344

3 Generalized Delamination Charts

3.1 Factors Affecting Interface Delamination. The advantage of expressing the solution set in closed form is that the relations given in Section 2.5 can be used to determine the interface stress state for any material pair as demonstrated above for a special case of a SiC/Pitch-55 pair. However, through considerations of wider ranges of properties of bi-material pairs, it can be noted that the stress components are not very sensitive to all the anisotropic constants within certain engineering approximations. In this section, we identify the key anisotropic parameters having major influence on the delamination criterion, for the purpose of constructing generalized delamination charts. While the effect of the Dundurs parameter β has already been identified as being relatively weak for practical bi-material pairs, the effect of ρ and λ on the delamination condition must be assessed. Typical values of ρ and λ for some engineering materials are assembled in Table 3 (Suo, 1988). We note that while the values of λ change quite significantly, those for ρ change much less with increasing degree of anisotropy. For example, for the epoxy matrix/fiber composite with GY70 fibers, the homogenized orthotropic composite will have a value of $1/\lambda = 42$ relative to unity for a reference material with transverse cubic symmetry, while the value of ρ will only be 3.36 relative to unity for a reference material with transverse isotropy. Since the variation in the parameter ρ is relatively little and, as we will see below in Section 3.1.3, the dependence of the stresses on ρ are relatively weak, we will simplify the following discussion considerably by choosing ρ_1 and ρ_2 to be unity. For the case of the cracked component, the choice of $\rho_2 = 1$ is physically acceptable, since the cracked component is often an isotropic coating. For the case of the probed component, the choice of $\rho_1 = 0$ is merely an operational simplification for a usually anisotropic solid without serious sacrifice in accuracy.

3.1.1 Effect of β. Figure 2(*a*, *b*) shows the effect of the variation of β on various normalized (normalized with σ_{xx}^I(90 deg)) stress components for the special case of $\lambda_1 = \lambda_2 = \rho_1 = \rho_2 = 1.0$, i.e., for transverse isotropy in both the materials. Since the magnitude of the axial stress at the interface in medium 2 (i.e., σ_{xx}(0 deg)) is large as compared to the other components, it has been plotted separately in Fig. 2(*b*). The effect of β on most of the important stress components is negligible for practical ranges of β between 1/4 and $-1/4$. However, for certain values of α, the normal stress acting across the interface (σ_{yy}(0 deg) and the transverse stress in the

Table 3 λ and ρ values (Suo, 1989)

material	plane stress		plane strain	
	$1/\lambda$	ρ	$1/\lambda$	ρ
Al (fcc)	1	0.76	1	0.72
Cr (bcc)	1	1.51	1	1.52
Cu (fcc)	1	.02	1	-0.19
Nb (bcc)	1	2.28	1	2.47
ash (LR)	10.5	1.68	7.9	1.88
balsa (LR)	21.0	2.13	17.8	2.29
oak (LR)	2.7	1.16	2.3	1.21
pine (LR)	14.8	1.09	12.1	1.18
boron/epoxy	9.1	6.14	8.3	6.43
S-glass/epoxy	2.4	1.47	2.3	1.51
graphite/epoxy	14.0	2.73	12.8	2.85
aramid/epoxy	17.4	3.49	16.0	3.64
pitch-55 fiber	-	-	29.23	2.43

Downloaded 03 May 2010 to 171.66.16.247. Redistribution subject to ASME license or copyright; see http://www.asme.org/terms/Terms_Use.cfm

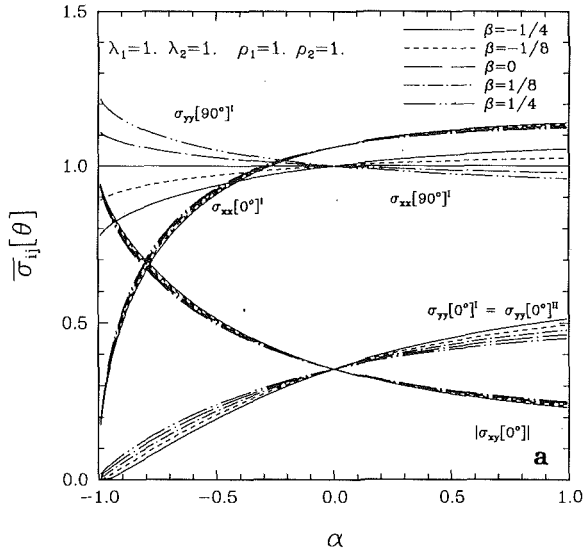


Fig. 2(*a*) Effect of β on normalized stress components

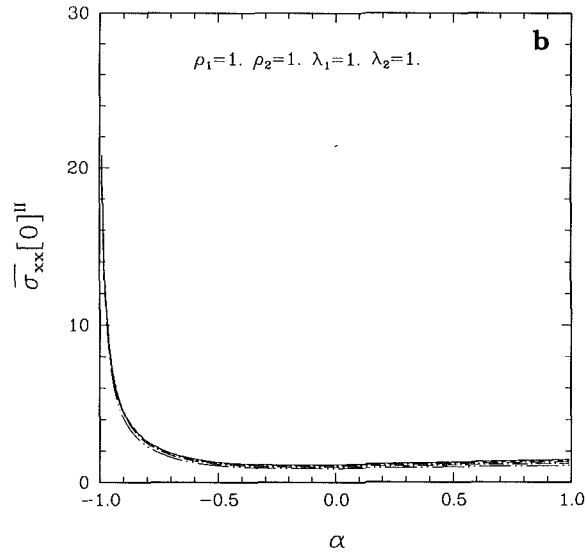


Fig. 2(*b*) σ_{xx} (0 deg) plot in medium II

fiber (σ_{yy}(90 deg)) shows significant dependence on β. The normal stress at the interface is most sensitive to the variation in β for $\alpha < -0.5$. It changes by almost 15 percent for $\alpha = -0.7$ with a corresponding variation in β from $-1/4$ to $1/4$. Thus, for bi-material combinations lying in this sector, the effect of β should be considered. Similarly, the transverse component of stress in the fiber, i.e., σ_{yy}(90 deg) shows a strong dependence on β for values of α in the ranges $\alpha < -0.5$ and $\alpha > 0.6$. Specifically, for $\alpha = -0.9$, σ_{yy}(90 deg) varies by almost 17 percent from that for the $\beta = 0$ case. Such effects may be critical in understanding the transverse behavior of the composite. Nevertheless, if the bi-material pair falls within the sensitive ranges of Dundurs parameters, the dependence on β directly can be calculated by using the expressions for stresses given in Section 2.5. Data for the interdependence of the Dundurs parameters has been explored by Suga et al. (1988) who have discovered that in all the cases considered β depends only weakly on α, and that the associated changes in β are only approximately one tenth of the change in α. Thus, a choice of $\beta = 0$ for arbitrary α provides little compromise in accuracy as Fig. 2(*a*) shows for most of the relevant components of stress. Hence, for the remainder of our discussion, $\beta = 0$ will be chosen. For $\beta = 0$, it is possible to further rescale the x-axis to collapse the dependence on λ_1 and λ_2 into one parameter Λ, thereby reducing the number of independent parameters

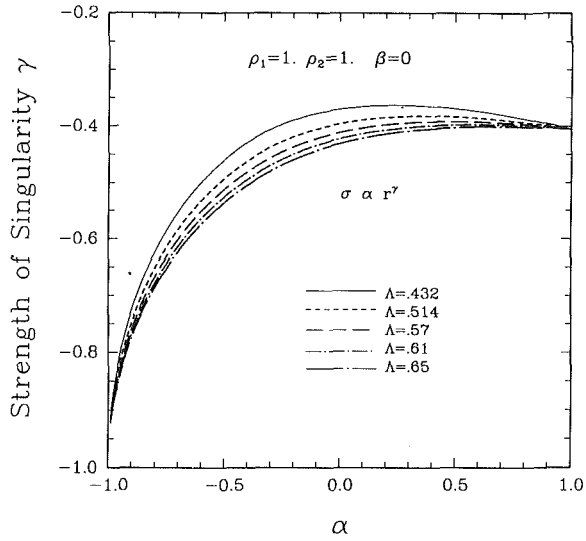


Fig. 3 Effect of Λ on the stress singularity

characterizing the solution to only 4 parameters, i.e., ρ_1, ρ_2, Λ, and α. It is interesting to note that the parameters used to determine solutions presented in Fig. 2(*a*) and (*b*) make both the materials isotropic, albeit still quite different from each other. Thus, these figures give another representation of the earlier solution of Swenson and Rau (1970) presented here in terms of the Dundurs parameters rather than the ratios of moduli and Poisson's ratios.

3.1.2 Effect of Λ. Figure 3 shows the effect of the variation of Λ on the dependence of the stress singularity exponent γ on α for $\rho_1 = \rho_2 = 1.0$ with the qualifications stated in Section 3.1.1. The strength of the singularity exponent is most sensitive to the variation in Λ in the range $-0.75 < \alpha < 0.35$. In this range, the maximum change in singularity exponent is 16 percent (for $\alpha = -0.375$) with an increase in the value of Λ from 0.43 to 0.65. Thus, for certain specific values of α between -0.75 and 0.5, it may become necessary to account for the effect of Λ while calculating the structure of the stress and displacement field if higher accuracy is required. However, for certain ranges of α, i.e., $-1 < \alpha < -0.75$ and $0.5 < \alpha < 1$, the effect of the variation of Λ on the strength of the singularity exponent can be practically ignored. Since all the stress components have the same radial dependence, the effect of Λ on most of the normalized stress components is almost negligible as depicted in Fig. 4, with the exception of σ_{yy}(90 deg)^I; i.e., the normalized stress probing the fiber in the transverse direction is most sensitive to Λ. As shown in Fig. 4, it changes by almost 27 percent for $\alpha = -0.75$. While this stress is of no importance in interface decohesion, it could be of importance in axial delamination of the fiber just ahead of the crack tip in a manner envisioned by Cook and Gordon (1964). The normalized stress components governing the interface delamination in tension (σ_{yy}(0 deg)) and shear (i.e., σ_{xy}(0 deg)) are insensitive to the variation in Λ. Thus, in presenting the interface delamination criteria, the effect of Λ can be largely ignored within engineering approximations. It is, however, important to understand the implications of high normal stresses generated across the fiber for certain values of α on the transverse strength of the composite. Qualitatively, it appears that these high stresses will further intensify the stresses at the interface when the composite is simultaneously loaded in the transverse direction. Results for such stress concentrations were given by Zywicz and Parks (1988) when the composite was loaded only in the transverse direction. Further analysis for the stress concentrations at the interface are required for the case of simultaneous loading of the composite in the axial and the transverse direction.

Downloaded 03 May 2010 to 171.66.16.247. Redistribution subject to ASME license or copyright; see http://www.asme.org/terms/Terms_Use.cfm

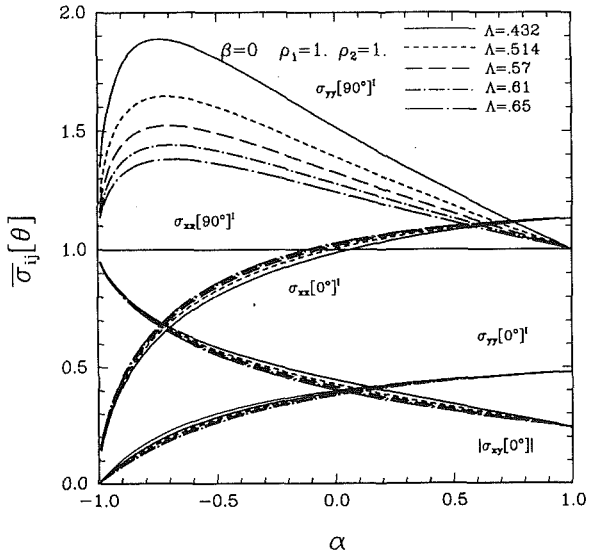


Fig. 4 Effect of Λ on normalized stress components

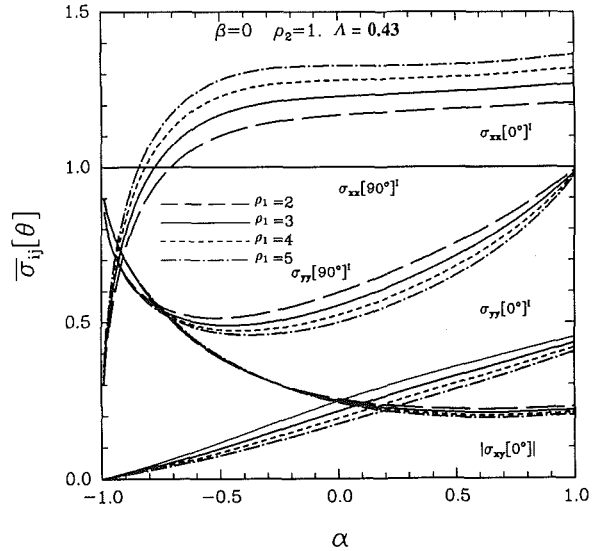


Fig. 5 Effect of ρ_1 on normalized stress components

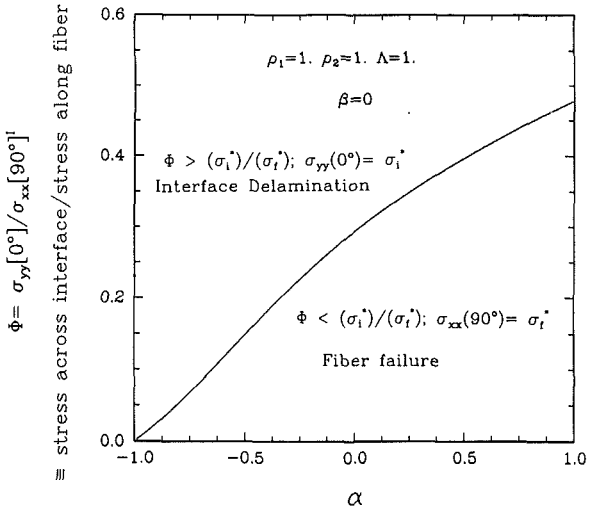


Fig. 6 Generalized interface chart for $\beta = 0$

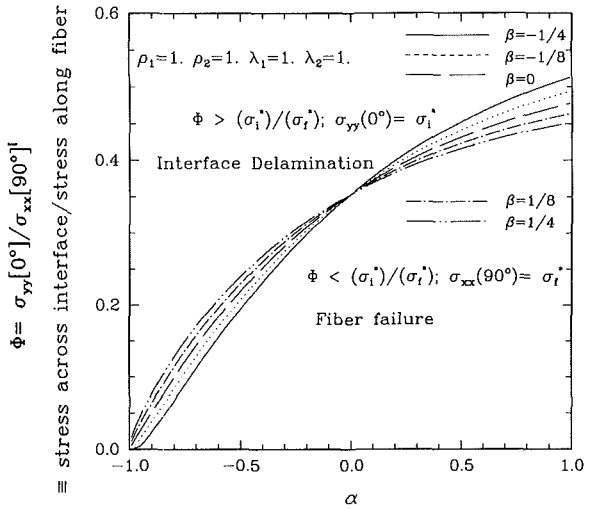


Fig. 7 Generalized interface chart for large values of β

3.1.3 Effect of ρ_1. Since the coatings are usually isotropic, only the effect of the variation of ρ_1 on the various components of normalized stress is studied in this section. Figure 5 shows such effects. Interestingly, all but the shear stress at the interface shows significant dependence on ρ_1.

In conclusion, except for certain ranges of α and β values, the normal stress at the interface is not very sensitive to the variation in ρ_1, Λ, and β from their corresponding isotropic values. Therefore, a generalized delamination chart can be constructed as shown in Fig. 6 for $\beta = 0$ and with ρ_1, ρ_2, and Λ assuming their isotropic values. For material pairs falling in the range where the effect of β is important, Fig. 7 can be used to determine the delamination criterion for a specific value of β. While reading the values from the delamination charts, it is reminded that the cracked component is to be designated as material 2. For exact results, the formulae given in Section 2.5 should be used.

Since the parameters used to determine the stresses that are plotted in Figs. 6 and 7 make each of the two media isotropic, it appears that a generalized crack deflection criterion for a pair of aligned orthotropic solids coincides with that for a pair of isotropic materials, albeit in an approximate manner. This is merely a coincidence. Since the results presented in Figs. 6 and 7 still contain the most important influence of anisotropy through the two Dundurs parameters α and β, it becomes possible to determine the crack deflection criterion for a pair of anisotropic materials by calculating α and β via Eqs. 8(*a*, *b*) in terms of the orthotropic elastic constants. In the absence of such considerations in the existing solution of Swenson and Rau (1970), it is only possible to estimate the crack deflection criterion by defining an effective modulus, which in turn can be taken as an arithmetical or geometrical mean of the orthotropic stiffnesses. In the absence of any formulae accounting for anisotropy, substantial errors can be introduced through such averaging techniques in cases with large differences between the axial and transverse direction elastic properties. In fact, the present developments were motivated because the Pitch-55 fiber has an axial modulus of 380 GPa and a transverse modulus of only 13 GPa.

Although knowledge of these normalized stresses for cracks terminating on the interface should be quite useful for purely elastic behavior, experimental observations on interface delamination (Gupta et al., 1989; Argon et al., 1989) indicate that additional considerations will be necessary when plastic deformation in the fiber accompanies the propagation of the delamination crack. Initial attempts to solve such problems have been made recently by Zywicz and Parks (1990) and Shih and Asaro (1989).

Downloaded 03 May 2010 to 171.66.16.247. Redistribution subject to ASME license or copyright; see http://www.asme.org/terms/Terms_Use.cfm

4 Optimizing Toughness and Transverse Strength in Composites With the Delamination Charts

In addition to high toughness by controlled interface delamination, the ability of the composite to sustain high transverse stresses in service is of considerable importance. Unfortunately, maximizing these two properties demand satisfying conflicting requirements on the interface strength. High interface strength is required for the composite to carry high transverse stresses. In contrast, low interface strength is desirable to enhance the toughness of the composite by crack deflection at interfaces. Interestingly, the level of the interface strength required to satisfy the longitudinal delamination criterion can be elevated by an appropriate choice for the elastic properties of the coating or the fiber and thereby permit the composite to support higher transverse operating stresses. Specifically, with respect to the delamination chart shown in Fig. 6 or 7, the bi-material properties can be chosen to push α towards extreme positive values. Since α depends on the relative elastic properties of the two media (see Eq. (8*a*)), this could be achieved in several ways. First, in composite systems where protective coatings are deposited on the fiber surface by using the plasma CVD technique, it is possible to control the coating modulus by controlling the deposition conditions (Landis, 1987). Second, it is also possible to use different types of carbon fibers with different elastic properties.

Table 4 shows the calculated values of the maximum permissible interface strength required for the operation of the crack deflection criterion for various coating/fiber interfaces. These interface values are calculated in the following way: Using the known elastic compliances for various materials, the value of α is calculated via Eq. (8*a*). For these values of α, the ratio σ_i^*/σ_f^* is determined from Fig. 6. Finally, taking the value of σ_f^* either from the manufacturer's handbooks or from the experiments of Zhang et al. (1990) in the case of Pitch-55 fiber, the permissible peak value for the interface strength is calculated. The transverse strength of the composite is then estimated by assuming a transverse interface stress concentration; e.g., 2.4 as determined by Zywicz and Parks (1988) for a hexagonal array of Pitch-55 carbon fibers surrounded by an aluminum matrix. Table 4 shows that for the case of low energy ion beam SiC coated Pitch-100 fiber the maximum level of the interface strength can be dramatically increased to 0.390 GPa. With the Al/Nicalon composite system, it appears that transverse strength values as high as 0.47 GPa can be achieved using the same transverse stress concentration factor of 2.4 determined for the Pitch-55/aluminum case.

Thus, it is possible to maximize both the transverse strength and the toughness in fiber composites with a judicious choice of the coating/fiber/matrix system based on the delamination charts given here.

5 Discussion

The strategy of deflecting cracks along interfaces to enhance the toughness of fiber composites is under active study (see, e.g., Argon et al., 1989; Evans, 1989). The first step in this attempt is to establish the crack deflection criterion. For composites with anisotropic high modulus carbon fibers, it becomes necessary to incorporate the elastic anisotropy of the fiber in these deflection analyses. Such analysis, with two aligned orthotropic media, has been considered here. The stress and deformation fields derived for such cases are shown to depend on the material parameters λ and ρ for the two media and the two bi-material constants α and β. The delamination criterion is insensitive to λ, ρ, Λ, and β over practical ranges of these material parameters. Thus, generalized delamination charts can be constructed as a function of the main bi-material constant α, which characterizes the elastic dissimilarity of the two media. Using these charts, it is possible to determine the desired level of interface strength required in composite manufacturing in order to enhance its overall toughness. Furthermore, these charts can be used for the fiber/coating or the fiber/matrix or the matrix/coating interface, depending upon which interface is of critical interest to achieve the crack deflection process.

Table 4 Maximum allowable interface strength for interface delamination.

Composite System (Matrix or Coating/Fiber)	α	Required Interface Strength (GPa)	Calculated Transverse Strength (GPa)
Al/P-55	0.001	0.475	0.197
Al/P-100	0.153	0.726	0.300
SiC (HBE**)/P-55	-0.605	0.209	0.086
SiC (LBE*)/P-55	0.574	0.836	0.350
SiC (HBE)/P-100	-0.499	0.330	0.136
SiC (LBE)/P-100	0.668	0.946	0.390
SiC (LBE)/Alumina	0.904	0.788	0.326
Al/Nicalon	0.468	1.148	0.470
TiC/Alumina	-0.085	0.508	0.210

** SiC deposited with high ion beam energy.

* SiC deposited with low ion beam energy

Acknowledgment

This research was supported by the Office of Naval Research under contract N00014-85-K-0645. For this support, we are grateful to Dr. S. Fishman of that agency. Useful discussions with Prof. J. W. Hutchinson are also acknowledged. We are also grateful to Dr. James Cornie for providing the information used in constructing Table 4.

References

Argon, A. S., Gupta, V., Landis, H. S., and Cornie, J. A., 1989, "Intrinsic Toughness of Interfaces Between SiC Coatings and Substrates of Si and C Fibers," *Journal of Materials Science*, Vol. 24, pp. 1207–1218.

Cook, J., and Gordon, J. E., 1964, "A Mechanism for the Control of Crack Propagation in all Brittle Systems," *Proceedings of the Royal Society, London*, Vol. A282, pp. 508–520.

Dundurs, J., 1968, "Elastic Interaction of Dislocations with Inhomogeneities," *Mathematical Theory of Dislocations*, ASME, New York, pp. 70–115.

Erdogan, F., 1972, "Fracture Problems in Composite Materials," *Engineering Fracture Mechanics*, Vol. 4, No. 4, pp. 811–840.

Erdogan, F., and Biricikoglu, V., 1973, "Two Bonded Half Planes with a Crack Going Through an Interface," *International Journal of Engineering Science*, Vol. 11, pp. 745–766.

Eshelby, J. D., Read, W. T., and Shockley, W., 1953, "Anisotropic Elasticity with Applications to Dislocation Theory," *Acta Metallurgica*, Vol. 1, pp. 251–259.

Evans, A. G., 1989, "The Mechanical Performance of Fiber-Reinforced Ceramic Matrix Composites," *Materials Science and Engineering*, Vol. A107, pp. 227–239.

Gupta, V., Argon, A. S., and Cornie, J. A., 1989, "Interfaces with Controlled Toughness as Mechanical Fuses to Isolate Fiber from Damage," *Journal of Materials Science*, Vol. 24, pp. 2031–2040.

Landis, H. S., 1987, "Amorphous Hydrogenated SiC by Plasma Enhanced Chemical Vapor Deposition for Metal Matrix Composite Applications," Ph.D. Thesis, Department of Materials Science and Engineering, M.I.T., Cambridge, Ma.

Lekhnitskii, S. G., 1963, *Theory of Elasticity of an Anisotropic Body*, Holden-Day, San Francisco.

Shih, C. F., and Asaro, R. J., 1989, "Elastic-Plastic Analysis of a Collinear Array of Cracks on a Bi-material Interface," *Materials Science and Engineering*, Vol. A107, pp. 227–239.

Stroh, A. N., 1958, "Dislocations and Cracks in Anisotropic Elasticity," *Philosophical Magazine*, Vol. 3, pp. 625–646.

Suga, T., Elssner, E., and Schmander, S., 1988, "Composite Parameters and Mechanical Compatibility of Mechanical Joints," *Journal of Composite Materials*, Vol. 22, pp. 917–934.

Suo, Z., 1989, "Singularities Interacting with Interfaces and Cracks," *International Journal of Solids and Structures*, Vol. 25, No. 10, pp. 1133–1142.

Suo, Z., 1990, "Delamination Specimens for Orthotropic Materials," ASME JOURNAL OF APPLIED MECHANICS, Vol. 57, pp. 627–634.

Suo, Z., and Hutchinson, J. W., 1989, "Sandwich Test Specimens for Meas-

Downloaded 03 May 2010 to 171.66.16.247. Redistribution subject to ASME license or copyright; see http://www.asme.org/terms/Terms_Use.cfm

uring Interface Crack Toughness," *Materials Science and Engineering*, Vol. A107, pp. 135–143.

Swenson, D. O., and Rau, C. A., Jr., 1970, "The Stress Distribution Around a Crack Perpendicular to an Interface Between Materials," *International Journal of Fracture Mechanics*, Vol. 6, pp. 357–360.

Ting, T. C. T., and Hoang, P. H., 1984, "Singularities at the Tip of a Crack Normal to the Interface of an Anisotropic Layered Composite," *International Journal of Solids and Structures*, Vol. 20, No. 5, pp. 439–454.

Zak, A. K., and Williams, M. L., 1963, "Crack Point Singularities at a Bi-material Interface," ASME JOURNAL OF APPLIED MECHANICS, Vol. 30, pp. 142–143.

Zhang, G-D., Feng, F. R., Li, Q., Blucher, J. T., and Cornie, J. A., 1990, "Control of Interface Reactions Between P-55 Fibers and Aluminum Alloy Matrices during Pressure Infiltration Processing," *Controlled Interfaces in Composite Materials, Proceedings of the International Conference on Composite Interfaces-III*, H. Ishida, ed., Elsevier, N.Y., pp. 343–357.

Zywicz, E., and Parks, D. M., 1988, "Thermo Viscous Plastic Residual Stresses in Metal Matrix Composites," *Composite Science and Technology*, Vol. 33, pp. 295–315.

Zywicz, E., and Parks, D. M., 1990, "Elastic-Plastic Analysis of Frictionless Contact at Interfacial Crack Tips," *International Journal of Fracture*, Vol. 42, pp. 129–143.

APPENDIX

In Section 2.4, the solution of an edge dislocation embedded at $(0, y_o)$ in a composite of two aligned orthotropic material (Fig. 1*c*) is used as the kernel of the integral equation. This solution is constructed in this Appendix using the fundamental solution of a dislocation in an infinite homogeneous orthotropic medium.

The potential function for an edge dislocation with Burger vector b_1 at the point $(0, y_o)$ in an infinite homogeneous orthotropic body with the principal axis along the x and y axes are given by (Eshelby et al., 1953)

$$\Phi_{jo}(Z) = W_j \ln(Z - S_j),\ S_j = \mu_j y_o. \tag{A1}$$

where the suffix "o" is attached to the potential to indicate that the solution is for the infinite body.

$$W_1 = \frac{1}{[\mu_1^{II} - \mu_2^{II}]}\,[-B_1]$$
$$W_2 = \frac{1}{[\mu_1^{II} - \mu_2^{II}]}\,[B_1] \tag{A2}$$

where

$$B_1 = \frac{b_1}{8\pi n_2 s_2 m_2} \tag{A3}$$

on the matrix are used to indicate the two materials. The matrix $\mathbf{B}$ is a positive definite Hermitian matrix (Stroh, 1958),

$$\mathbf{B} = i\mathbf{A}\mathbf{L}^{-1} \tag{A5}$$

where $\mathbf{A}$ and $\mathbf{L}$ are defined in Section 2.2. Here, $i = \sqrt{-1}$. $\mathbf{H}$ is a positive definite Hermitian matrix defined as

$$\mathbf{H} = \mathbf{B}_1 + \overline{\mathbf{B}}_2. \tag{A6a}$$

Physically, the $\mathbf{H}$ matrix includes the bi-material effects, and hence its element involves the Dundurs parameters α and β. This matrix can be written explicitly as

$$\mathbf{H} = \begin{bmatrix} H_{11} & -i\beta\sqrt{H_{11}H_{22}} \\ i\beta\sqrt{H_{11}H_{22}} & H_{22} \end{bmatrix} \tag{A6b}$$

$$H_{11} = [2n\lambda^{1/4}\sqrt{s_{11}s_{22}}]_1 + [2n\lambda^{1/4}\sqrt{s_{11}s_{22}}]_2 \tag{A6c}$$

$$H_{22} = [2n\lambda^{-1/4}\sqrt{s_{11}s_{22}}]_1 + [2n\lambda^{-1/4}\sqrt{s_{11}s_{22}}]_2 \tag{A6d}$$

$$\sqrt{H_{11}H_{22}}\beta = [\sqrt{s_{11}s_{22}} + s_{12}]_1 - [\sqrt{s_{11}s_{22}} + s_{12}]_2. \tag{A6e}$$

Here, β is a generalization of the Dundurs (1968) parameter. $\beta = 0$ will diagonalize the matrix $\mathbf{H}$ and reduces the extent of matrix algebra. Using Eq. (A4) and Φ_o from Eq. (A1), the potentials for the problem depicted in Fig. 1 can be derived. Once the potentials are known, stresses and displacements can be computed using Eqs. 6(*a–d*). The complete normalized stresses at the interface are given by:

$$\tilde{\sigma}_{11}^I = b_1\left\{\frac{[C_{11}(t_1^I)^2 t_1^{II} y_o]}{[x^2 + (y_o t_1^{II})^2]} - \frac{[C_{12}(t_1^{II})^2 t_2^{II} y_o]}{[x^2 + (y_o t_2^{II})^2]} + \frac{[C_{21}(t_2^I)^2 t_1^{II} y_o]}{[x^2 + (y_o t_1^{II})^2]} - \frac{[C_{22}(t_2^I)^2 t_2^{II} y_o]}{[x^2 + (y_o t_2^{II})^2]}\right\} \tag{A7a}$$

$$\tilde{\sigma}_{12}^I = b_1\left\{\frac{[C_{11} t_1^I x]}{[x^2 + (y_o t_1^{II})^2]} - \frac{[C_{12} t_1^I x]}{[x^2 + (y_o t_2^{II})^2]} + \frac{[C_{21} t_2^I x]}{[x^2 + (y_o t_1^{II})^2]} - \frac{[C_{22} t_2^I x]}{[x^2 + (y_o t_2^{II})^2]}\right\} \tag{A7b}$$

$$\tilde{\sigma}_{22}^I = -b_1\left\{\frac{[C_{11} t_1^{II} y_o]}{[x^2 + (y_o t_1^{II})^2]} + \frac{[C_{12} t_2^{II} y_o]}{[x^2 + (y_o t_2^{II})^2} - \frac{[C_{21} t_1^{II} y_o]}{[x^2 + (y_o t_1^{II})^2]} + \frac{[C_{22} t_2^{II} y_o]}{[x^2 + (y_o t_2^{II})^2]}\right\} \tag{A7c}$$

$$\tilde{\sigma}_{11}^{II} = b_1\left\{\frac{[C_{11}^*(t_1^{II})^2 t_1^{II} y_o]}{[x^2 + (y_o t_1^{II})^2]} - \frac{[C_{12}^*(t_1^{II})^2 t_2^{II} y_o]}{[x^2 + (y_o t_2^{II})^2]} + \frac{[C_{21}^*(t_2^{II})^2 t_1^{II} y_o]}{[x^2 + (y_o t_1^{II})^2]} - \frac{[C_{22}^*(t_2^{II})^2 t_2^{II} y_o]}{[x^2 + (y_o t_2^{II})^2]} - \frac{[(t_2^{II})^2 t_2^{II} y_o]}{[x^2 + (y_o t_2^{II})^2]} + \frac{[(t_1^{II})^2 t_1^{II} y_o]}{[x^2 + (y_o t_1^{II})^2]}\right\} \tag{A7d}$$

μ_1^{II} and μ_2^{II} are the roots of the characteristic Eq. (4) defined in Section 2.2 and m, n, and s are same as defined before in Eqs. (5*a–d*) and Section 2.4. Now, the potentials for the interaction of an edge dislocation with the interface (Fig. 1) can be obtained in terms of $\Phi_{jo}(z)$ by invoking the standard analytical continuation arguments, along with the continuity of tractions and displacements along the interface, as described by Suo (1989). The solution for the two media can be written as

$$\Phi(z) = \phi^1(z),\ z\epsilon 1 \tag{A4a}$$

$$\Phi(z) = \Phi^2(z) + \Phi_o(z),\ z\epsilon 2 \tag{A4b}$$

$$\Phi^1(z) = \mathbf{C}\Phi_o(z) \tag{A4c}$$

$$\mathbf{C} = \mathbf{L}_1^{-1}\mathbf{H}^{-1}(\overline{\mathbf{B}_2} + \mathbf{B}_2)\mathbf{L}_2,\ z\epsilon 1 \tag{A4d}$$

$$\Phi^2(z) = \mathbf{G}\overline{\Phi_o}(z) \tag{A4e}$$

$$\mathbf{G} = \mathbf{L}_2^{-1}\overline{\mathbf{H}}^{-1}(\overline{\mathbf{B}_2} - \mathbf{B}_1)\overline{\mathbf{L}}_2,\ z\epsilon 2 \tag{A4f}$$

where $(\bar{\ })$ denotes the complex conjugation and the subscripts

The component of normalized stresses in front of the crack tip in medium I can be written as:

$$\tilde{\sigma}_{11}^I = -b_1\left\{-\frac{[C_{11} t_1^I]}{[y - y_o(t_1^{II}/t_1^I)]} + \frac{[C_{12} t_1^I]}{[y - y_o(t_2^{II}/t_1^I)]} - \frac{[C_{21} t_2^I]}{[y - y_o(t_1^{II}/t_2^I)]} + \frac{[C_{22} t_2^I]}{[y - y_o(t_2^{II}/t_2^I)]}\right\} \tag{A7e}$$

$$\tilde{\sigma}_{22}^I = b_1\left\{\frac{[C_{11}]}{t_1^I[y - y_o(t_1^{II}/t_1^I)]} - \frac{[C_{12}]}{t_1^I[y - y_o(t_2^{II}/t_1^I)]} + \frac{[C_{21}]}{t_2^I[y - y_o(t_1^{II}/t_2^I)]} - \frac{[C_{22}]}{t_2^I[y - y_o(t_2^{II}/t_2^I)]}\right\} \tag{A7f}$$

where

$$\sigma_{ij} = \left[\frac{1}{8\pi n_2 s_2 m_2}\right]\tilde{\sigma}_{ij}. \tag{A7g}$$

Downloaded 03 May 2010 to 171.66.16.247. Redistribution subject to ASME license or copyright; see http://www.asme.org/terms/Terms_Use.cfm

Here, C_{ij} and C^*_{ij} are, respectively, the elements of the matrices **C** and **G** as defined in Eq. (A4). The expressions for C_{ij} and C^*_{ij} are given by

$$C_{11}=\frac{1}{(t_2^I-t_1^I)}\left[-Q_1t_1^{II}+Q_2+t_2^I(Q_3t_1^{II}+Q_4)\right] \quad \text{(A8}a\text{)}$$

$$C_{12}=\frac{1}{(t_2^I-t_1^I)}\left[-Q_1t_2^{II}+Q_2+t_2^I(Q_3t_2^{II}+Q_4)\right] \quad \text{(A8}b\text{)}$$

$$C_{21}=\frac{1}{(t_2^I-t_1^I)}\left[Q_1t_1^{II}-Q_2-t_1^I(Q_3t_1^{II}+Q_4)\right] \quad \text{(A8}c\text{)}$$

$$C_{22}=\frac{1}{(t_2^I-t_1^I)}\left[Q_1t_2^{II}-Q_2-t_1^I(Q_3t_2^{II}+Q_4)\right] \quad \text{(A8}d\text{)}$$

$$C^*_{11}=\frac{1}{(t_2^{II}-t_1^{II})}\left[Q_1^*t_1^{II}-Q_2^*+t_2^{II}(Q_3^*t_1^{II}+Q_4^*)\right] \quad \text{(A8}e\text{)}$$

$$C^*_{12}=\frac{1}{(t_2^{II}-t_1^{II})}\left[Q_1^*t_2^{II}-Q_2^*+t_2^{II}(Q_3^*t_2^{II}+Q_4^*)\right] \quad \text{(A8}f\text{)}$$

$$C^*_{21}=\frac{1}{(t_2^{II}-t_1^{II})}\left[-Q_1^*t_1^{II}+Q_2^*-t_1^{II}(Q_3^*t_1^{II}+Q_4^*)\right] \quad \text{(A8}g\text{)}$$

$$C^*_{22}=\frac{1}{(t_2^{II}-t_1^{II})}\left[-Q_1^*t_2^{II}+Q_2^*-t_1^{II}(Q_3^*t_2^{II}+Q_4^*)\right] \quad \text{(A8}h\text{)}$$

where Q_1 and Q_1^* are used to write the expressions for C_{ij} and C^*_{ij} in compact form. The expressions for Q_1 and Q_1^* depend only on the elastic constants of the two media and are given by

$$Q_1=\frac{2\Sigma}{\left[\left(\frac{n_1}{n_2}\right)\Lambda+\Sigma\right](1-\beta^2)} \quad \text{(A9}a\text{)}$$

$$Q_2=\frac{\beta}{(1-\beta^2)}\times\left[\frac{2}{\sqrt{\left[\frac{1}{\Sigma}\left(\frac{n_1}{n_2}\right)(\lambda_1\lambda_2)^{1/4}+\lambda_2^{1/2}\right]\left[\frac{n_1}{n_2}\left(\frac{1}{\Lambda\Sigma}\right)+1\right]}}\right] \quad \text{(A9}b\text{)}$$

$$Q_3=\frac{-\beta}{(1-\beta^2)}\times\left[\frac{2}{\sqrt{\left[\frac{1}{\Sigma}\left(\frac{n_1}{n_2}\right)(\lambda_1\lambda_2)^{-1/4}+\lambda_2^{-1/2}\right]\left[\frac{n_1}{n_2}\left(\frac{\Lambda}{\Sigma}\right)+1\right]}}\right] \quad \text{(A9}c\text{)}$$

$$Q_4=\frac{2\Sigma\Lambda}{\left[\left(\frac{n_1}{n_2}\right)+\Lambda\Sigma\right](1-\beta^2)} \quad \text{(A9}d\text{)}$$

$$Q_1^*=\frac{1}{(H_{11}(1-\beta^2))}\left[(2n_2s_2\lambda_2^{1/4})-(2n_1s_1\lambda_1^{1/4})\right]+\frac{\beta^2}{(1-\beta^2)} \quad \text{(A9}e\text{)}$$

$$Q_2^*=\frac{\beta}{(\sqrt{H_{11}H_{22}}(1-\beta^2))}\left[(2n_2s_2\lambda_2^{-1/4})-(2n_1s_1\lambda_1^{-1/4})\right]+\frac{\beta}{(1-\beta^2)}\left(\sqrt{\frac{H_{22}}{H_{11}}}\right) \quad \text{(A9}f\text{)}$$

$$Q_3^*=\frac{\beta}{(\sqrt{H_{11}H_{22}}(1-\beta^2))}\left[(2n_2s_2\lambda_2^{1/4})-(2n_1s_1\lambda_1^{1/4})\right]+\left[\frac{\beta}{(1-\beta^2)}\left(\sqrt{\frac{H_{11}}{H_{22}}}\right)\right] \quad \text{(A9}g\text{)}$$

$$Q_4^*=\frac{1}{(H_{22}(1-\beta^2))}\left[2n_2s_2\lambda_2^{-1/4})-(2n_1s_1\lambda_1^{-1/4})\right]+\frac{\beta^2}{(1-\beta^2)}. \quad \text{(A9}h\text{)}$$

Here

$$\Lambda=\left(\frac{\lambda_1}{\lambda^2}\right)^{1/4} \quad \text{(A9}i\text{)}$$

$$\Sigma=\frac{s_2}{s_1},\ s_1=(\sqrt{s_{11}s_{22}})_1 \text{ and } s_2=(\sqrt{s_{11}s_{22}})_2. \quad \text{(A9}j\text{)}$$

It is interesting to note that the effect of β in the overall solution is introduced only through the coefficients Qs and Q^*s. Since for most practical bi-material combinations the value of β is usually small, it is proposed to take $\beta = 0$. This simplifies the expressions for Qs considerably. For $\beta = 0$, the expressions for Qs and Q^*s reduces to

$$Q_1=\frac{[2\Sigma]}{\left[\Sigma+\left(\frac{n_1}{n_2}\right)\Lambda\right]} \quad \text{(A10}a\text{)}$$

$$Q_2=Q_3=0 \quad \text{(A10}b\text{)}$$

$$Q_4=\frac{[2\Sigma\Lambda]}{\left[\Lambda\Sigma+\left(\frac{n_1}{n_2}\right)\right]} \quad \text{(A10}c\text{)}$$

$$Q_1^*=\frac{\left[1-\left(\frac{n_1}{n_2}\right)\left(\frac{\Lambda}{\Sigma}\right)\right]}{\left[1+\left(\frac{n_1}{n_2}\right)\left(\frac{\Lambda}{\Sigma}\right)\right]} \quad \text{(A10}d\text{)}$$

$$Q_2^*=Q_3^*=0 \quad \text{(A10}e\text{)}$$

$$Q_4^*=\frac{\left[1-\left(\frac{n_1}{n_2}\right)\left(\frac{1}{\Sigma\Lambda}\right)\right]}{\left[1+\left(\frac{n_1}{n_2}\right)\left(\frac{1}{\Sigma\Lambda}\right)\right]} \quad \text{(A10}f\text{)}$$

Downloaded 03 May 2010 to 171.66.16.247. Redistribution subject to ASME license or copyright; see http://www.asme.org/terms/Terms_Use.cfm

P. Sofronis

R. M. McMeeking
Mem. ASME

Materials Department and Mechanical Engineering Department, College of Engineering, University of California, Santa Barbara, CA 93106

Creep of Power-Law Material Containing Spherical Voids

Finite element calculations have been carried out for spherical unit cells containing a concentric spherical hole to characterize the power law creep of a material containing voids. Axisymmetric states of macroscopic stress were applied to the unit cells ranging from purely hydrostatic loading to purely deviatoric stressing. The results of the unit cell calculations are approximated well by a creep potential for the macroscopic behavior of a porous material. This potential agrees with the unit cell results for purely hydrostatic stress and purely deviatoric stress and involves a simple elliptical interpolation in between. The model predicts quite well the ratio of transverse to axial strain rate in uniaxial compression tests.

Introduction

Power-law creep of a material containing voids is of interest in creep damage and rupture of metals and ceramics (Ashby and Dyson, 1984) and the consolidation of powder to form solids (Helle, Easterling, and Ashby, 1985). In the former case, the levels of macroscopic stress triaxiality are modest with the ratio of mean stress to effective stress typically no higher than 2. In contrast, in the pressing of powders the stress triaxiality is often high. Indeed, in hot isostatic pressing (HIPing) the ratio of mean stress to effective stress is infinite. Those models that exist are designed to cover limited porosity levels or a restricted range of stress space. For example, Duva and Hutchinson (1984) devised a constitutive law for power-law creep of dilutely voided material, and it is thought to be reliable for states of stress with modest triaxiality up to about ten percent by volume of voids. However, when the stress state is highly triaxial, the constitutive law is only useful for tiny levels of porosity, less than one percent. The proposal of McMeeking (1984) for power-law materials is of dubious validity in states of high triaxial stress, but Duva (1986) has improved the original model of Duva and Hutchinson (1984) so that it is accurate to a higher level of porosity for states of stress with low triaxiality. However, it is unsatisfactory for high triaxial stress states except when the void volume fraction is very low. Cocks (1989), on the other hand, has made use of Duva's (1986) calculations and additional ones of his own and developed a power-law creep model which is reliable for a larger range of stress states and levels of porosity. Opposite to the model of Duva and Hutchinson (1984) and Duva (1986), the Cocks (1989) constitutive law for the power-law case is not accurate for low levels of porosity when the stress is predominantly hydrostatic but is satisfactory for higher volume fractions of voids in that situation.

In contrast to the set of constitutive laws discussed in the previous paragraph where the problems occur when the triaxiality of stress is high, the model of Wilkinson and Ashby (1975), as used by Arzt, Ashby, and Easterling (1983) and Helle et al. (1985) is only valid for states of pure hydrostatic stress. However, it is probably accurate for substantial levels of porosity and has been compared successfully with experiments up to void volume fractions of ten percent (Helle et al., 1985). At this level of porosity, the predicted creep rate of the Wilkinson and Ashby (1975) constitutive law is similar to that of the Cocks (1989) model at the same macroscopic stress. However, at porosities of one percent, the predicted creep rates are very different.

In this paper a power-law creep potential is proposed for materials containing spherical voids. We claim that the creep constitutive law resulting from this potential is valid for all axisymmetric stress states and is probably reliable for arbitrary stress states as well. It should work well for higher porosities, too. In particular, it is accurate for void volume fractions up to at least ten percent, agrees with the Wilkinson and Ashby (1975) model for pure hydrostatic stress and is similar to the Cocks (1989) constitutive law for low triaxial stress states. The claim of accuracy is based on an extensive set of results from cell model calculations carried out by the finite element method.

Cell Model

The macroscopic behavior of a power-law material was modeled by the response of a sphere of the material containing a concentric spherical void. This approach has been taken by Gurson (1977) for rate-independent elastic-plastic materials and by Duva (1986) and Cocks (1989) for power-law materials. It is also the method used to develop the law for pure hydrostatic macroscopic stress developed by Wilkinson and Ashby (1975) and used by Helle et al. (1985).

The unit cell is shown in Fig. 1. The void radius is a and the outer cell radius is b. The ratio a/b is equal to $\rho^{1/3}$ so that

Contributed by the ASME Applied Mechanics Division of THE AMERICAN SOCIETY OF MECHANICAL ENGINEERS for presentation at the Winter Annual Meeting, Atlanta, Ga., Dec. 1-6, 1991.

Discussion on this paper should be addressed to the Technical Editor, Prof. Leon M. Keer, The Technological Institute, Northwestern University, Evanston, IL 60208, and will be accepted until two months after final publication of the paper itself in the JOURNAL OF APPLIED MECHANICS. Manuscript received by the ASME Applied Mechanics Division, Aug. 16, 1990; final revision, May 14, 1991.

Paper No. 91-WA/APM-25.

Copyright © 1992 by ASME

Downloaded 03 May 2010 to 171.66.16.247. Redistribution subject to ASME license or copyright; see http://www.asme.org/terms/Terms_Use.cfm

the void occupies the fraction ρ of the total volume of the cell. The solid material is incompressible and obeys the creep law

$$\dot{\epsilon}_{ij} = \frac{3}{2}\,\dot{\epsilon}_0 \left(\frac{\sigma_e}{\sigma_o}\right)^n \frac{\sigma'_{ij}}{\sigma_e} \tag{1}$$

where $\dot{\epsilon}$ is the strain rate, $\dot{\epsilon}_o$, σ_o and n are material parameters, σ_e is the effective stress such that

$$\sigma_e = \sqrt{\frac{3}{2}\,\sigma'_{ij}\,\sigma'_{ij}} \tag{2}$$

and σ' is the deviatoric stress.

A macroscopic element of the material contains many voids at a volume fraction ρ and is in an axisymmetric state of macroscopic stress Σ with principal values $\Sigma_{zz} = S$ and $\Sigma_{xx} = \Sigma_{yy} = T$. The unit cell represents this, so tractions in equilibrium with this stress state were applied to the outer surface A_o of the sphere as indicated in Fig. 1. The surface of the spherical void was traction-free. The solutions to the cell model problems were found by the finite element method. A standard velocity based finite element method was used and, for $n > 1$, Newton iteration was utilized. Iteration was performed until a strict convergence criterion was met. For a given stress exponent n, the process was initiated by using the solution at $n-1$. The linear case with $n = 1$ was solved directly.

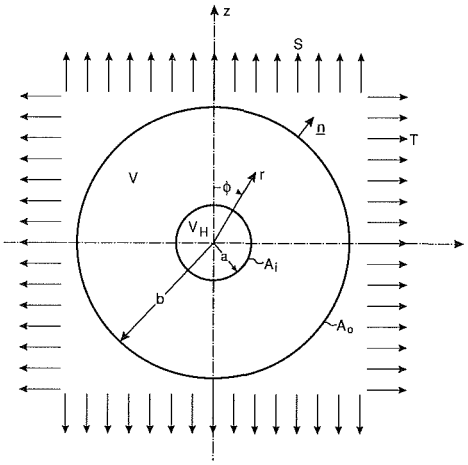


Fig. 1 The unit cell in an axisymmetric state of stress

The incompressibility constraint on the velocity field was enforced by the penalty method (Zienkiewicz, 1977). The mean stress $\sigma_{kk}/3$ was set equal to $\lambda\,\dot{\epsilon}_{kk}$ where the penalty λ has a very large value. This treatment combined with reduced integration of the stiffness matrices assured incompressibility. Eight-noded quadratic isoparametric axisymmetric elements were used with a 2×2 rule for integrating the stiffness.

By symmetry the solution in the first quadrant only was required (see Fig. 1). Surfaces $\phi = 0$ and $\phi = \pi/2$ were prescribed to have zero normal velocity and to be free of shear traction. A total of 400 elements with 1281 nodes were used. There were 20 concentric rings of elements. For two consecutive rings the ratio of element sides in the radial direction was 1.2. The penalty λ was chosen such that $\lambda/2\mu = 2499999.5$ where μ is the effective shear viscosity given by

$$\mu = \frac{1}{3}\,\frac{\sigma_o}{\dot{\epsilon}_o}\left(\frac{\dot{\epsilon}_0}{\dot{\epsilon}_e}\right)^{\frac{n-1}{n}} \tag{3}$$

where

$$\dot{\epsilon}_e = \sqrt{\frac{2}{3}\,\dot{\epsilon}'_{ij}\,\dot{\epsilon}'_{ij}}. \tag{4}$$

Computed dilatational strain rates were at least seven orders of magnitude less than the components of the deviatoric strain rate. The convergence parameter was chosen so that iteration continued until changes to $\dot{\epsilon}_e$ were less than 10^{-7} compared to $\dot{\epsilon}_e$. The rate of convergence was rapid, and usually eight iterations were sufficient if convergence was achieved.

Results

Finite element solutions were obtained for the purely isostatic case with $S = T$. In this case the solution for v_r, the radial velocity, is independent of ϕ.

The exact solution is

$$\frac{v_r}{v_o} = \left(\frac{b}{r}\right)^2 \tag{5}$$

where

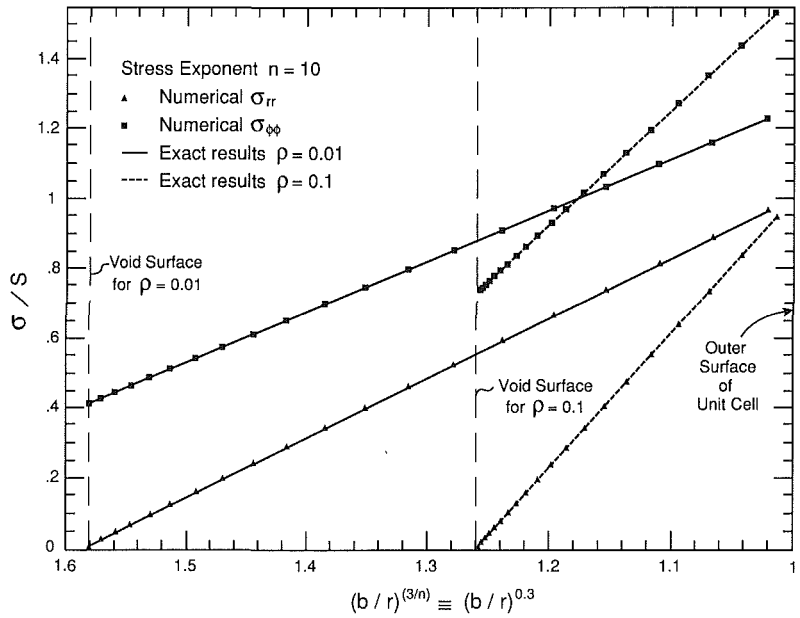


Fig. 2 Comparison of the stresses predicted by the finite element method with the exact stresses for the isostatic case

Downloaded 03 May 2010 to 171.66.16.247. Redistribution subject to ASME license or copyright; see http://www.asme.org/terms/Terms_Use.cfm

$$v_0 = \frac{\dot{\epsilon}_o}{2}\left\{\frac{\frac{3}{2}\frac{S}{\sigma_o}}{n\left[\left(\frac{1}{\rho}\right)^{\frac{1}{n}}-1\right]}\right\}^n b. \tag{6}$$

The finite element results for v_r were essentially in exact agreement with the exact formulae for $\rho = 1$ percent and 10 percent.

The results for stress for $S = T$ for $n = 10$ are shown in Fig. 2 where σ_{rr} and $\sigma_{\phi\phi}$ are the radial and the circumferential components, respectively. The exact results

$$\frac{\sigma_{rr}}{S} = \frac{\left[\left(\frac{1}{\rho}\right)^{\frac{1}{n}} - \left(\frac{b}{r}\right)^{\frac{3}{n}}\right]}{\left[\left(\frac{1}{\rho}\right)^{\frac{1}{n}}-1\right]} \tag{7}$$

and

$$\frac{\sigma_{\phi\phi}}{S} = \frac{\left[\left(\frac{1}{\rho}\right)^{\frac{1}{n}} + \left(\frac{3}{2n}-1\right)\left(\frac{b}{r}\right)^{\frac{3}{n}}\right]}{\left[\left(\frac{1}{\rho}\right)^{\frac{1}{n}}-1\right]} \tag{8}$$

are shown for comparison. Figure 2 shows that the finite element solutions are very accurate. This comment applies equally well to the hydrostatic stress, which is the term most difficult to compute accurately because of the incompressibility constraint and its effect on the numerical scheme.

Finite element results were obtained also for the nonisostatic case, i.e., $S \neq T$. Of interest is the macroscopic strain rate $\dot{\mathbf{E}}$, defined as the volume average of the microscopic strain rate so that

$$\dot{E}_{ij} = (V + V_H)^{-1}\int_{V+V_H} \dot{\epsilon}_{ij}\, dV, \tag{9}$$

where V_H is the volume of the spherical hole. Through the divergence theorem this becomes

$$\dot{E}_{ij} = \frac{1}{2}(V + V_H)^{-1}\int_{A_o} (v_i n_j + v_j n_i) dA_o \tag{10}$$

where $\mathbf{n}$ is the outward normal to the surface A_o. As in Duva's (1986) work, the results for macroscopic strain rate are computed from Eq. (10).

A convenient way to present the results is through use of a potential function $\Psi(\Sigma)$ as follows: Hill (1967), Duva and Hutchinson (1984), and Cocks (1989) used Eq. (9) to construct the potential for the macroscopic creep behavior. That is, by virtual work,

$$d\Sigma_{ij}\dot{E}_{ij} = (V + V_H)^{-1}\int_V d\sigma_{ij}\frac{\partial \psi}{\partial \sigma_{ij}} dV$$
$$= (V + V_H)^{-1}\int_V d\psi dV = d\Psi \tag{11}$$

and so

$$\dot{E}_{ij} = \frac{\partial \Psi}{\partial \Sigma_{ij}} \tag{12}$$

where

$$\Psi = (V + V_H)^{-1}\int_V \psi dV. \tag{13}$$

According to Cocks (1989), the potential Ψ can be written as

$$\Psi = \frac{\sigma_0 \dot{\epsilon}_0}{n+1}\left(\frac{\Phi}{\sigma_o}\right)^{n+1} \tag{14}$$

where Φ is homogeneous of degree one in Σ. Because of this, the macroscopic dissipation rate per unit volume $\Sigma_{ij}\dot{E}_{ij}$ is equal to $(n+1)\Psi$. It follows that

$$\Phi(\Sigma) = \sigma_o\left[\frac{\Sigma_{ij}\dot{E}_{ij}(\Sigma)}{\sigma_o \dot{\epsilon}_o}\right]^{\frac{1}{n+1}}. \tag{15}$$

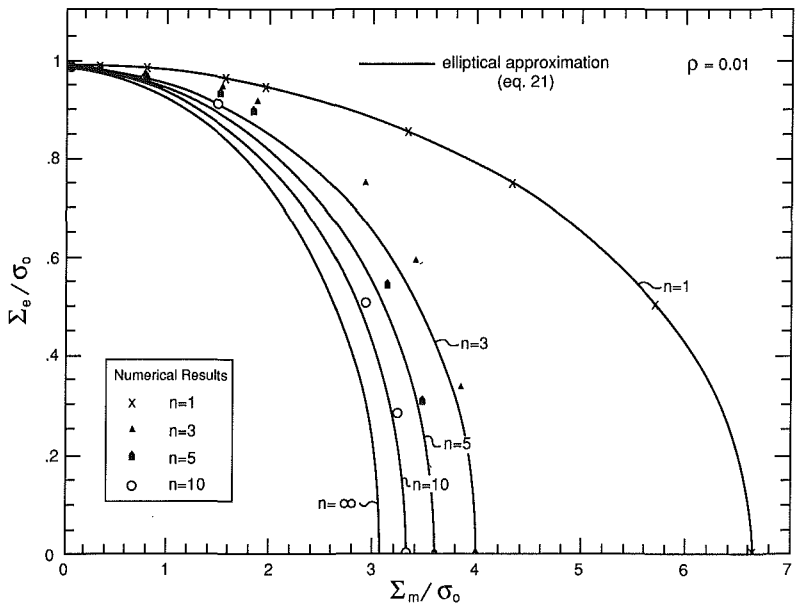


Fig. 3 Points in stress space for which $\Phi/\sigma_o = 1$ from the finite element method computations for $\rho = 1$ percent compared with the elliptical approximation from Eq. (21)

Downloaded 03 May 2010 to 171.66.16.247. Redistribution subject to ASME license or copyright; see http://www.asme.org/terms/Terms_Use.cfm

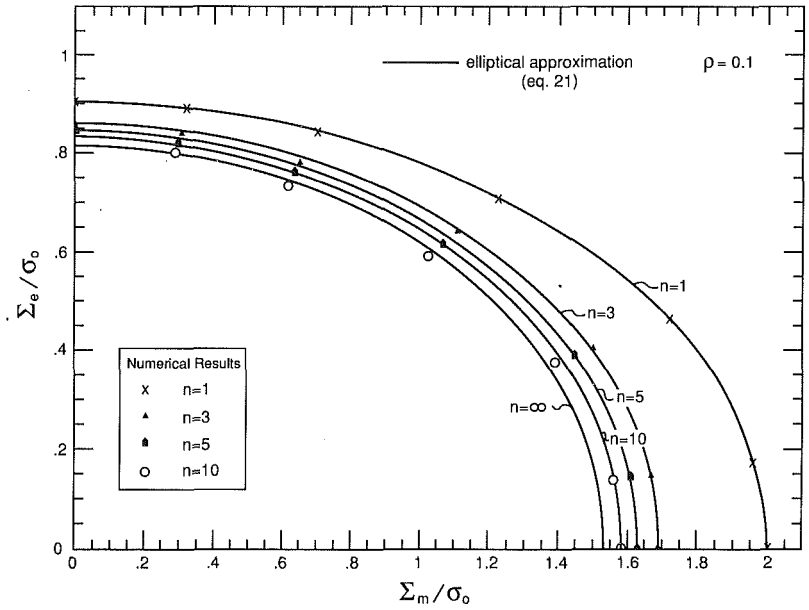


Fig. 4 Points in stress space for which $\Phi/\sigma_0 = 1$ from the finite element method computations for $\rho = 10$ percent compared with the elliptical approximation from Eq. (21)

As Cocks (1989) has shown, this function is useful for presenting the numerical results of cell calculations. They are conveniently presented as contours of constant Φ in stress space and these contours are thus also contours of constant macroscopic dissipation rate. Equations (12) and (14) show that the strain rate is coaxial with the normal to these contours.

The stress necessary to make $\Phi/\sigma_o = 1$ in the finite element solutions is plotted for various values of n in Fig. 3 for $\rho = 1$ percent and in Fig. 4 for $\rho = 10$ percent. The contours are plotted in axes of macroscopic tensile equivalent stress versus macroscopic mean stress. The macroscopic tensile equivalent stress is

$$\Sigma_e = \sqrt{\frac{3}{2}\,\Sigma'_{ij}\,\Sigma'_{ij}} \tag{16}$$

where Σ' is the macroscopic stress deviator and the macroscopic mean stress is

$$\Sigma_m = \frac{1}{3}\,\Sigma_{kk}. \tag{17}$$

It should be noted that some results are missing because the specified degree of convergence was not obtained. These missing results are for higher n values with intermediate levels of triaxiality.

Creep Law

To ease the application of the results, it is convenient to represent $\Phi(\Sigma)$ by an elementary form. Since the shape of the curves in Figs. 3 and 4 is suggestive of an ellipse, this seems to be an appropriate choice for the dependence of Φ on Σ_e and Σ_m. Indeed, Duva and Hutchinson (1984), Duva (1986), Ponte and Willis (1988), and Cocks (1989) all have used elliptical forms for the representation of Φ.

In the purely isostatic situation, the potential should be

$$\Phi(\Sigma_m) = \left[\frac{\rho n}{\left(1-\rho^{\frac{1}{n}}\right)^n}\right]^{\frac{1}{n+1}} \frac{3\Sigma_m}{2n}. \tag{18}$$

This ensures that the dilatation rate in the purely isostatic case computed from Eq. (12) is

$$\dot{E}_{kk} = \frac{3}{2}\,\dot{\epsilon}_o\,\frac{\rho}{\left(1-\rho^{\frac{1}{n}}\right)^n}\left(\frac{3\Sigma_m}{2n\sigma_o}\right)^n. \tag{19}$$

This is equal to $3\,v_o/b$ when $S = \Sigma_m$ which is the dilatation rate of the unit cell when the stress is purely hydrostatic. In the purely deviatoric situation, we find that Φ can be approximated well by

$$\Phi = \left(\frac{1+\rho}{1-\rho}\right)^{\frac{n}{n+1}}\Sigma_e \tag{20}$$

which exceeds a lower bound developed by Ponte and Willis (1988) for small ρ and approximates well results by Duva and Hutchinson (1984).

The elliptical form, which agrees with Eqs. (18) and (20), is

$$\Phi = \left\{\left(\frac{1+\rho}{1-\rho}\right)^{\frac{2n}{n+1}}\Sigma_e^2 + \left[\frac{\rho n}{\left(1-\rho^{\frac{1}{n}}\right)^n}\right]^{\frac{2}{(n+1)}}\left(\frac{3\Sigma_m}{2n}\right)^2\right\}^{\frac{1}{2}}. \tag{21}$$

Contours with $\Phi/\sigma_o = 1$ from Eq. (21) have been plotted in Figs. 3 and 4 for comparison with the finite element results. It can be seen that there is good agreement between the form of Eq. (21) and the numerical results. It should be noted that Cocks' (1989) form (his Eq. (35)) agrees quite well with the numerical results for $\rho = 10$ percent. For $\rho = 1$ percent, his form is accurate for stress states with $|\Sigma_m|/\Sigma_e < 2$. Cocks (1989) designed his form for just such stress states with limited triaxialities.

Additional contours have been plotted in Figs. 3 and 4 for completeness. In particular, the limiting contours for $n = \infty$ from Eq. (21) have been drawn. These essentially portray yield surfaces for perfectly plastic materials.

The agreement between the numerical results and the elliptical form in Figs. 3 and 4 can be misleading because the normal direction to the approximate and numerical contours can differ noticeably even if the contours are close together. Furthermore, the strain rates are computed by raising Φ to the nth power so that small errors in Φ can be magnified greatly

Downloaded 03 May 2010 to 171.66.16.247. Redistribution subject to ASME license or copyright; see http://www.asme.org/terms/Terms_Use.cfm

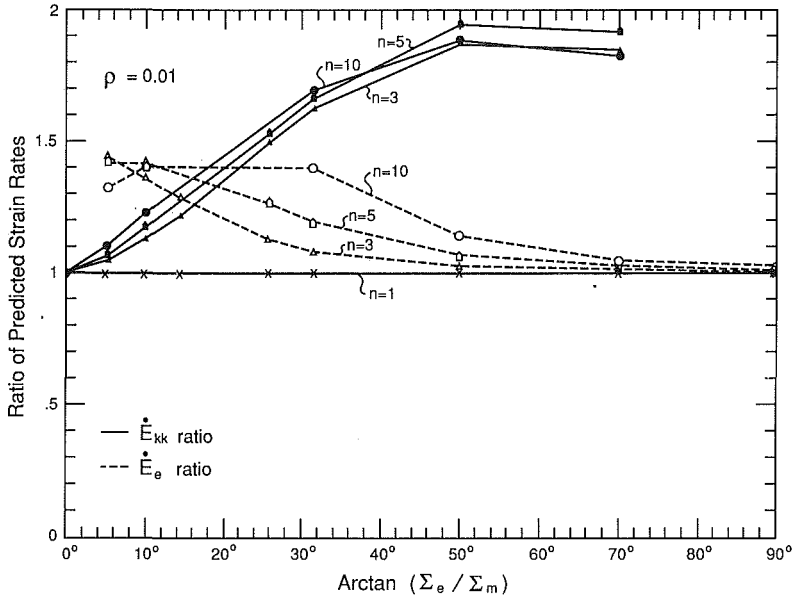


Fig. 5 Comparison of the strain rates $\dot{E}_{kk}$ and $\dot{E}_e$ predicted by the elliptical model with those numerically calculated for various combinations of applied stress and $\rho = 1$ percent

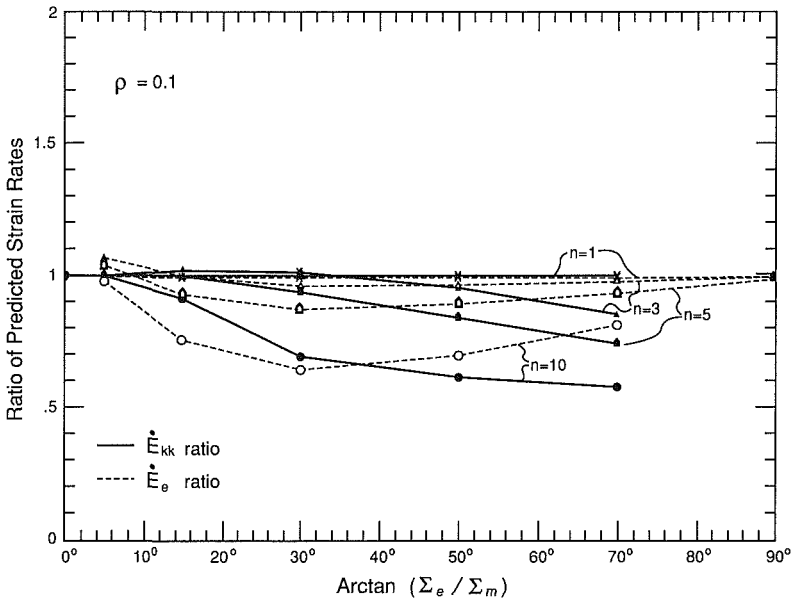


Fig. 6 Comparison of the strain rates $\dot{E}_{kk}$ and $\dot{E}_e$ predicted by the elliptical model with those numerically calculated for various combinations of applied stress and $\rho = 10$ percent

when n is large. This concern can be addressed by comparing the numerically calculated strain rates with those arising from Eqs. (12) and (14) with use of Eq. (21).

The strain rates computed from Eqs. (12), (14), and (21) are

$$\dot{E}_{ij} = \dot{\epsilon}_0 \left(\frac{\Phi}{\sigma_o}\right)^{n-1} \left\{ \left(\frac{1+\rho}{1-\rho}\right)^{\frac{2n}{(n+1)}} \frac{3\Sigma'_{ij}}{2\sigma_o} + \left(\frac{3}{2n}\right)^2 \left[\frac{\rho n}{\left(1-\rho^{\frac{1}{n}}\right)^n}\right]^{\frac{2}{(n+1)}} \frac{\Sigma_m}{\sigma_o} \frac{1}{3} \delta_{ij} \right\}. \quad (22)$$

As a consequence, the tensile equivalent strain rate

$$\dot{E}_e = \sqrt{\frac{2}{3} \dot{E}'_{ij} \dot{E}'_{ij}} \quad (23)$$

is

$$\dot{E}_e = \dot{\epsilon}_o \left(\frac{\Phi}{\sigma_o}\right)^{n-1} \left(\frac{1+\rho}{1-\rho}\right)^{\frac{2n}{(n+1)}} \frac{\Sigma_e}{\sigma_o} \quad (24)$$

where $\dot{\mathbf{E}}'$ is the macroscopic deviatoric strain rate. The dilatation rate is

$$\dot{E}_{kk} = \dot{\epsilon}_0 \left(\frac{\Phi}{\sigma_o}\right)^{n-1} \left(\frac{3}{2n}\right)^2 \left[\frac{\rho n}{\left(1-\rho^{\frac{1}{n}}\right)^n}\right]^{\frac{2}{(n+1)}} \frac{\Sigma_m}{\sigma_o}. \quad (25)$$

Downloaded 03 May 2010 to 171.66.16.247. Redistribution subject to ASME license or copyright; see http://www.asme.org/terms/Terms_Use.cfm

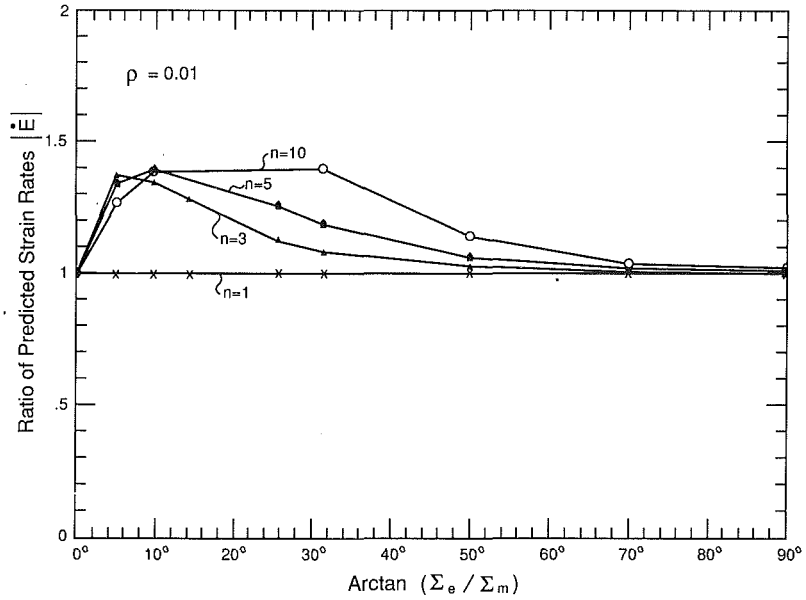


Fig. 7 Comparison of the strain rate $|\dot{E}|$ predicted by the elliptical model with that numerically calculated for various combinations of applied stress and $\rho = 1$ percent

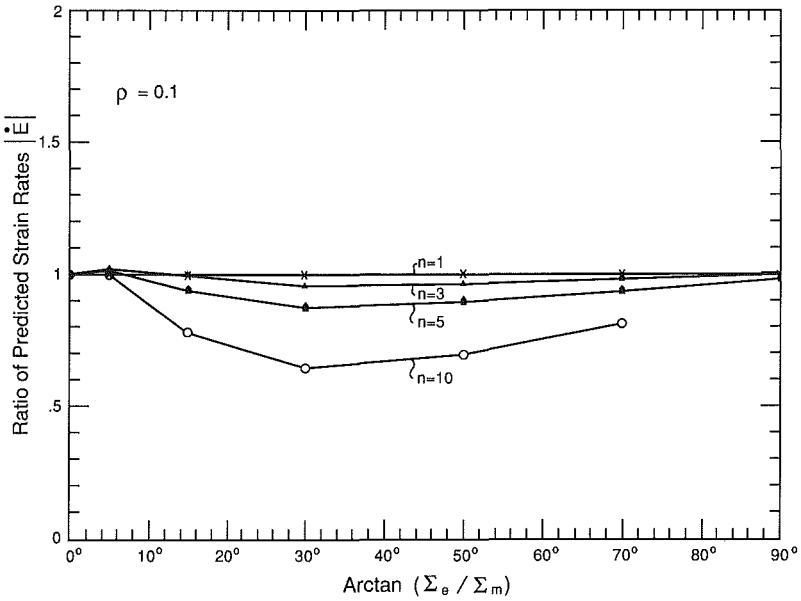


Fig. 8 Comparison of the strain rate $|\dot{E}|$ predicted by the elliptical model with that numerically calculated for various combinations of applied stress and $\rho = 1$ percent

The ratio of the strain rates given by Eqs. (24) and (25) to those obtained from the finite element calculations are plotted in Figs. 5 and 6. Since the macroscopic strain rates are homogeneous of degree n in the macroscopic stresses, the resulting quotient is a function of only ρ, n, and Σ_e/Σ_m. Thus, the strain rate ratios have been plotted against arctan (Σ_e/Σ_m) for various n in the case $\rho = 1$ percent in Fig. 5 and in Fig. 6 for $\rho = 10$ percent. There are differences, but it should be noted that the difference in $\dot{E}_e$ occurs when the tensile equivalent stress is small compared to the mean stress so that the strain rates are dominated by the dilatation rate $\dot{E}_{kk}$. Similarly, the differences in the dilatation rate occur when the mean stress is small compared to the tensile equivalent stress so that the dilatation rate is a relatively small component of the strain rate. This point is confirmed by the ratio of $|\dot{E}| = \sqrt{\dot{E}_{ij}\dot{E}_{ij}}$ from Eq. (22) to $|\dot{E}|$ from the finite element calculations plotted for various values of n in Fig. 7 for $\rho = 1$ percent and in Fig. 8 for $\rho = 10$ percent. In the worst case, the difference is 40 percent. Since

$$|\dot{E}| = \sqrt{\frac{3}{2}\dot{E}_e^2 + \frac{1}{3}\dot{E}_{kk}^2}, \tag{26}$$

this shows that the difference in both $\dot{E}_e$ and $\dot{E}_{kk}$ is always small compared to the strain rate magnitude $|\dot{E}|$. In summary, the formula Eq. (22) provides a strain rate whose magnitude is quite close to those of the finite element calculations. Furthermore, the dominant component, whether deviatoric or dilatational, is always quite accurately represented by Eq. (22).

Discussion

It is probable that the cell calculations carried out for this paper represent quite well the creep behavior of a power-law

Downloaded 03 May 2010 to 171.66.16.247. Redistribution subject to ASME license or copyright; see http://www.asme.org/terms/Terms_Use.cfm

Table 1

	Experiments				Model (eq. 30 & 31)			
	ρ	f	c	ν	n	f	c	ν
Astroloy (Abouaf et al., 1988)	0.05	0.14	3.6	0.44	2.136	0.020	1.15	0.47
	0.10	0.23	7.8	0.46	2.136	0.036	1.31	0.46
René 95 (Bouvard and Lafer, 1989)	0.01	0.009	1.06	0.49	3.34	0.007	1.03	0.49
	0.05	0.061	1.35	0.44	3.34	0.022	1.17	0.47
316L (Bouvard and Lafer, 1989)	0.01	0.003	1.07	0.496	4.07	0.008	1.03	0.488
	0.05	0.020	1.41	0.48	4.07	0.023	1.17	0.47

material containing spherical voids. The porosities in the cells are one percent and ten percent and at this level, the smallness of the voids suggests that the shape of the cell is not very important. That is, the spherical cell represents well, though not exactly, the strain rate field around an individual void embedded in a typical region of the porous material. In addition, the potential Φ according to Eq. (21), in conjunction with Eqs. (12) and (14), gives a good approximation to the finite element results. Given that the finite element results are themselves approximations to the actual creep behavior of the porous material, it seems appropriate to use Eq. (21) directly without any attempt to adjust for the differences between the strain rates due to Eq. (21) and the finite element results. Thus, the form of Eq. (21) is recommended for representing the creep behavior of a power-law material containing a dilute concentration of spherical voids up to at least ten percent.

Abouaf and Chenot (1986) have developed a creep constitutive law for porous material which can be specialized to the form resulting from Eqs. (13), (14), and (21). The general form of Abouaf and Chenot (1986) has been used successfully by Abouaf et al. (1988) for astroloy powder and by Besson and Abouaf (1989) for alumina powder. The general form is equivalent to

$$\Phi = [c\Sigma_e^2 + 9f\Sigma_m^2]^{\frac{1}{2}} \tag{27}$$

with

$$\Psi = \epsilon_o \int_o^{\Phi} \left[\sinh\left(\frac{\Phi}{\sigma_o}\right) \right]^n d\Phi, \tag{28}$$

instead of Eq. (14). The terms c and f are functions of ρ, n, σ_o and perhaps other material parameters. They are fitted by Abouaf and co-workers to experimental data so that for a given material c and f can be tabulated against the porosity level. This tabulation should be independent of temperature since it can be arranged that $\dot{\epsilon}_o$ is the only term depending on temperature. It should be noted that Abouaf and co-workers tabulate c and f for porosities both less and greater than ten percent, the latter being in the contact controlled regime. We will consider their results only for $\rho \leq 0.1$.

In the case of astroloy, Abouaf et al. (1988) determined that $n = 2.136$, and at five and ten percent porosity measured c and f to have the values shown in the experiments section in Table 1. Also shown is

$$\nu = -\dot{E}_t/\dot{E}_a \tag{29}$$

where $\dot{E}_t$ and $\dot{E}_a$ are the transverse and axial strain rates, respectively, in a uniaxial stress (compression) test which was used to determine f or c or both. The values for c and f have been read from graphs of Abouaf et al. (1988) and ν computed from $(c/2-f)/(c+f)$. For René 95 ($n = 3.34$) and 316L stainless steel ($n = 4.07$), Bouvard and Lafer (1989) have provided information from which f, c, and ν can be computed. In these cases a pure power-law creep behavior is evident. The values for f, c, and ν are shown in Table 1 also.

When Φ/σ_o is small compared to unity, the integral in Eq. (28) is approximately the same as Eq. (14). In that situation, the Abouaf and Chenot (1986) constitutive law can accommodate the purely power-law model developed in this paper and would agree with it when

$$c = \left[\frac{(1+\rho)}{(1-\rho)}\right]^{\frac{2n}{(n+1)}} \tag{30}$$

and

$$f = \frac{1}{4n^2}\left[\frac{\rho n}{\left(1-\rho^{\frac{1}{n}}\right)^n}\right]^{\frac{2}{(n+1)}}. \tag{31}$$

These formulae have been used to compute f, c, and ν for astroloy, René 95, and 316L stainless steel. The results are listed in Table 1 in the model section. It can be seen that the model does not predict the values of c and f at all well. This indicates that the rate of creep in uniaxial stress is well above the predictions of the model. However, the parameter ν is predicted fairly well. Thus, the ratio of transverse to axial strain rate in the uniaxial compression experiments is predicted by the model, but the absolute level of the magnitudes of those strain rates does not agree. It is possible that the differences in strain rate magnitude could be due to differences in microstructure between porous and dense material which would influence ϵ_o, σ_o, and possibly n. It is of interest that Ashby (1989) has found that the model Eq. (31) predicts a density which is slightly too high in the case of low-carbon steel powder in power-law creep subject to pure pressure. This implies that in that case the experimental value of f is lower than the model value of Eq. (31) in contrast to the situation portrayed in Table 1.

Downloaded 03 May 2010 to 171.66.16.247. Redistribution subject to ASME license or copyright; see http://www.asme.org/terms/Terms_Use.cfm

Closure

Finite element unit cell calculations have been used to characterize a constitutive law for the power-law creep of a material containing spherical voids. The recommended constitutive law has a relatively simple form but approximates well the results of the unit cell computations. In comparison with experiments for porous materials, the constitutive law does not predict well the absolute rate of creep, which is highly dependent on the material state including such features as grain size. The discrepancy can be attributed to uncertainties concerning the material state. However, the ratio of transverse to axial strain rate in uniaxial compression is predicted quite well by the recommended constitutive law.

Acknowledgment

This research was support by the National Science Foundation through Grant DMR 87-13919. The calculations on an FPS 500EA Computer were made possible by FPS Computing through the UCSB Industrial Liaison Program.

References

Abouaf, M., and Chenot, J. L., 1986, "Modelisation Numerique de la Déformation à Chaud de Poudres Metalliques," *Journal Mechanique Theoretique et Applique*, Vol. 5, p. 121.

Abouaf, M., Chenot, J. L., Raisson, G., and Bauduin, P., 1988, "Finite Element Simulation of Hot Isostatic Pressing of Metal Powders," *International Journal for Numerical Methods in Engineering*, Vol. 25, p. 191.

Arzt, E., Ashby, M. F., and Easterling, K. E., 1983, "Practical Applications of Hot Isostatic Pressing Diagrams: Four Case Studies," *Metallurgical Transactions A*, Vol. 14A, p. 211.

Ashby, M. F., 1989, *HIP 6.0 Background Reading*, University of Cambridge Engineering Department Report, Cambridge, U.K.

Ashby, M. F., and Dyson, B. F., 1984, *Creep Damage Mechanics and Mechanisms*, National Physical Laboratory Report DMA (A) 77, Teddington Lock, U.K.

Besson, J., and Abouaf, M., 1989, "Finite Element Simulation of Hot Isostatic Pressing of Ceramic Powders," *Proceedings of the 6th International Conference on HIP-Theory and Practice*, to be published.

Bouvard, D., and Lafer, M., 1989, "Rheological Characterization of Metal Powder at High Temperature," *Advances in Powder Metallurgy*, Vol. 1, MPIF (ed), Princetown.

Cocks, A. C. F., 1989, "Inelastic Deformation of Porous Materials," *Journal of the Mechanics and Physics of Solids*, Vol. 37, p. 693.

Duva, J. M., 1986, "A Constitutive Description of Nonlinear Materials Containing Voids," *Mechanics of Materials*, Vol. 5, p. 137.

Duva, J. M., and Hutchinson, J. W., 1984, "Constitutive Potentials for Dilutely Voided Nonlinear Materials," *Mechanics of Materials*, Vol. 3, p. 41.

Gurson, A. L., 1977, "Continuum Theory of Ductile Rupture by Void Nucleation and Growth: Part 1—Yield Criteria and Flow Rules for Porous Ductile Media," *ASME Journal of Engineering Materials and Technology*, Series H, Vol. 99, p. 2.

Helle, A. S., Easterling, K. E., and Ashby, M. F., 1985, "Hot Isostatic Pressing Diagrams: New Developments," *Acta Metallurgica*, Vol. 33, p. 2163.

Hill, R., 1967, "The Essential Structure of Constitutive Laws for Metal Composites and Polycrystals," *Journal of the Mechanics and Physics of Solids*, Vol. 15, p. 79.

McMeeking, R. M., 1984, "Estimates for the Constitutive Moduli of Ductile Materials Containing a Small Volume Fraction of Voids or Inclusions," *Mechanics of Material Behavior*, G. J. Dvorak and R. T. Shield, eds., Elsevier, Amsterdam, p. 275.

Ponte, P., and Willis, J. R., 1988, "On the Overall Properties of Nonlinearly Viscous Composites," *Proceedings of the Royal Society, London*, Vol. A416, p. 217.

Wilkinson, D. S., and Ashby, M. F., 1975, "Pressure Sintering by Power Law Creep," *Acta Metallurgica*, Vol. 23, p. 1277.

Zienkiewicz, O. C., 1977, *The Finite Element Method*, 2nd Ed., McGraw-Hill, U.K.

Downloaded 03 May 2010 to 171.66.16.247. Redistribution subject to ASME license or copyright; see http://www.asme.org/terms/Terms_Use.cfm

A Method to Evaluate Three-Dimensional Time-Harmonic Elastodynamic Green's Functions in Transversely Isotropic Media

H. Zhu

Department of Engineering Science and Mechanics,
The University of Tennessee,
Knoxville, TN 37996-2030
Assoc. Mem. ASME

The three-dimensional time-harmonic elastodynamic Green's functions in infinite transversely isotropic media have been derived explicitly. The Green's functions consist of the corresponding static Green's functions and double integral representations over a finite domain with the integrands being continuous. The Green's functions will reduce to those for the isotropic case when the isotropic elastic constants are substituted. The singular parts of the Green's functions have been shown to be the same as those of the static ones. The far-field approximations have been obtained by using the stationary phase method. In addition, a simpler method to construct wave front curves has been presented.

Introduction

With the development of modern technology and science which involves solid mechanics, dislocation theory, semismology, NDE technology, and composite materials, etc., the study of wave propagation in transversely isotropic media attracts more and more attention. These is no doubt that the isotropic Green's functions played a very important role in the development of wave propagation theory for isotropic media. The Green's functions in transversely isotropic media would be a useful tool in the study of wave phenomenon in transversely isotropic media. Since the late 1950's, numerous literature has been devoted to the study of the Green's functions in transversely isotropic media. Buchward (1959) gave an approximation of the harmonic Green's functions at far field by using local plane wave expansions. In Kraut's (1963) paper, the asymptotic expansions of harmonic Green's functions at far field were discussed. Lighthill (1960) suggested a special technique to an integral which was related to the Fourier transform of the Green's functions. The derivatives of the harmonic Green's functions were studied by Barnett (1972). The major achievements of this topic before 1983 can be found in the Payton's book (1983). Ha (1986) gave a numerical algorithm for far-field wave computations. Kazi-Aoual, Bonnet, and Jouanna (1988) derived the time-harmonic Green's functions in the Hankel space with the point force acting at the axis of symmetry. However, as to the author's knowledge, a complete solution to the time-harmonic Green's functions has not been published at this time. As such, this paper is part of the author's effort to discover the solution.

Contributed by the Applied Mechanics Division of THE AMERICAN SOCIETY OF MECHANICAL ENGINEERS for presentation at the 1992 ASME Summer Mechanics and Materials Meeting, Tempe, AZ, Apr. 28–May 1, 1992.

Discussion on this paper should be addressed to the Technical Editor, Prof. Leon M. Keer, The Technological Institute, Northwestern University, Evanston, IL 60208, and will be accepted until four months after final publication of the paper itself in the JOURNAL OF APPLIED MECHANICS. Manuscript received by the ASME Applied Mechanics Division, Feb. 20, 1991; final revision, Aug. 8, 1991.
Paper No. 92-APM-12.

1 Triple Integral Representations

A Cartesian coordinate system $\mathbf{x}(x_1, x_2, x_3)$ has been set up to a homogeneous, transversely isotropic, and linearly elastic solid whose axis of symmetry coincides with the x_3-axis. The components of the time-harmonic Green's functions $G_{mn}(\mathbf{x})$, $m, n = 1, 2, 3$ in this Cartesian coordinate system are the solutions to the following set of differential equations:

$$L_{mp}\left(\frac{\partial}{\partial \mathbf{x}}\right) G_{pn}(\mathbf{x}) + \rho\omega^2 G_{mn}(\mathbf{x}) = -\delta_{mn}\delta(\mathbf{x}),\ m, n = 1, 2, 3 \quad (1)$$

where

$$L_{11}\left(\frac{\partial}{\partial \mathbf{x}}\right) = C_{11}\frac{\partial^2}{\partial x_1^2} + 0.5\,(C_{11} - C_{12})\frac{\partial^2}{\partial x_2^2} + C_{44}\frac{\partial^2}{\partial x_3^2} \quad (2a)$$

$$L_{12}\left(\frac{\partial}{\partial \mathbf{x}}\right) = L_{21}\left(\frac{\partial}{\partial \mathbf{x}}\right) = 0.5\,(C_{11} + C_{12})\frac{\partial^2}{\partial x_1 \partial x_2} \quad (2b)$$

$$L_{13}\left(\frac{\partial}{\partial \mathbf{x}}\right) = L_{31}\left(\frac{\partial}{\partial \mathbf{x}}\right) = (C_{13} + C_{44})\frac{\partial^2}{\partial x_1 \partial x_3} \quad (2c)$$

$$L_{22} = \left(\frac{\partial}{\partial \mathbf{x}}\right) = 0.5\,(C_{11} - C_{12})\frac{\partial^2}{\partial x_1^2} + C_{11}\frac{\partial^2}{\partial x_2^2} + C_{44}\frac{\partial^2}{\partial x_3^2} \quad (2d)$$

Copyright © 1992 by ASME
Downloaded 03 May 2010 to 171.66.16.247. Redistribution subject to ASME license or copyright; see http://www.asme.org/terms/Terms_Use.cfm

$$L_{23}\left(\frac{\partial}{\partial \mathbf{x}}\right)=L_{32}\left(\frac{\partial}{\partial \mathbf{x}}\right)=(C_{13}+C_{44})\frac{\partial^2}{\partial x_2 \partial x_3} \tag{2e}$$

$$L_{33}\left(\frac{\partial}{\partial \mathbf{x}}\right)=C_{44}\frac{\partial^2}{\partial x_1^2}+C_{44}\frac{\partial^2}{\partial x_2^2}+C_{33}\frac{\partial^2}{\partial x_3^2} \tag{2f}$$

where C_{11}, C_{12}, C_{13}, C_{33}, and C_{44} are elastic constants, ρ is the mass density of the material, ω is the circular frequency, δ_{mn} is the Kronecker delta, $\delta(\mathbf{x}) = \delta(x_1)\,\delta(x_2)$, $\delta(x_3)$, and $\delta(\ )$ is the Dirac delta function.

The use of the Fourier transform technique to the differential equations in Eq. (1) yields

$$-L_{mp}(\mathbf{y})\,G^*_{pn}(\mathbf{y})+\rho\omega^2 G^*_{mn}(\mathbf{y})=-\delta_{mn},\ m,\ n=1,\ 2,\ 3 \tag{3}$$

and, $G_{mn}(\mathbf{x})$ and $G^*_{mn}(\mathbf{y})$ are related by:

$$G_{mn}(\mathbf{x})=\iiint_{-\infty}^{+\infty}\frac{G^*_{pn}(\mathbf{y})}{8\pi^3}e^{-i\mathbf{x}\mathbf{y}}\,d\mathbf{y} \tag{4}$$

where $i^2=-1$ and $\mathbf{y}=\mathbf{y}\ (y_1,\ y_2,\ y_3)$.

By a few algebraic manipulations, the first component of $G^*_{mn}(\mathbf{y})$ in Eq. (3), $G^*_{11}(\mathbf{y})$, can be further expressed by

$$G^*_{11}(\mathbf{y})=\frac{-Q(\mathbf{y},\mathbf{C})+y_1^2P(\mathbf{y},\mathbf{C})}{C_{44}L(\mathbf{y},\mathbf{C})Q(\mathbf{y},\mathbf{C})} \tag{5}$$

and then

$$G_{11}(\mathbf{x})=\iiint_{-\infty}^{+\infty}\frac{[-Q(\mathbf{y},\mathbf{C})+y_1^2P(\mathbf{y},\mathbf{C})]e^{-i\mathbf{x}\mathbf{y}}}{8C_{44}\pi^3L(\mathbf{y},\mathbf{C})Q(\mathbf{y},\mathbf{C})}\,d\mathbf{y} \tag{6}$$

where, upon introducing the change of variables $y_1=r\sin\alpha\cos\beta$, $y_2=r\sin\alpha\sin\beta$ and $y_3=r\cos\alpha$, $L(\mathbf{y},\mathbf{C})$, $P(\mathbf{y},\mathbf{C})$, and $Q(\mathbf{y},\mathbf{C})$ in Eqs. (5) and (6) may be expressed as

$$L(\mathbf{y},\mathbf{C})=-r^2\cos^2\alpha-a_5r^2\sin^2\alpha+k_0^2 \tag{7a}$$

$$P(\mathbf{y},\mathbf{C})=-r^2\cos^2\alpha(1+a_2a_5-a_4)+(k_0^2-y^2\sin^2\alpha)(a_5-a_3) \tag{7b}$$

$$Q(\mathbf{y},\mathbf{C})=A(\alpha)r^4-B(\alpha)k_0^2r^2+k_0^4 \tag{7c}$$

where

$$A(\alpha)=(a_2-a_4+a_3)\cos^4\alpha+(a_4-2a_3)\cos^2\alpha+a_3 \tag{8a}$$

$$B(\alpha)=(a_2-a_3)\cos^2\alpha+a_3+1 \tag{8b}$$

$$k_0^2=\rho\omega^2/C_{44},\ a_1=(1+a_2a_3-a_4)^{0.5},\ a_2=c_{33}/c_{44} \tag{8c-e}$$

$$a_3=c_{11}/c_{44},\ a_4=1+a_2a_3-(1+C_{13}/C_{44})^2 \tag{8f,g}$$

$$a_5=0.5\,(C_{11}-C_{12})/C_{44}. \tag{8h}$$

A partial fraction decomposition of $Q^{-1}(\mathbf{y},\mathbf{C})$ and $L^{-1}(\mathbf{y},\mathbf{C})$ also yields

$$\frac{1}{Q(\mathbf{y},\mathbf{C})}=\sum_{j=1}^{2}\frac{g_j(\alpha)}{r^2-k_j^2(\alpha)} \tag{9a}$$

$$\frac{1}{L(\mathbf{y},\mathbf{C})Q(\mathbf{y},\mathbf{C})}=-\sum_{j=1}^{3}\frac{k_j^2(\alpha)f_j(\alpha)}{r^4[r^2-k_j^2(\alpha)]} \tag{9b}$$

where

$$f_1(\alpha)=\frac{k_1^2(\alpha)}{A(\alpha)[(1-a_5)\cos^2\alpha+a_5][k_2^2(\alpha)-k_1^2(\alpha)][k_3^2(\alpha)-k_1^2(\alpha)]} \tag{10a}$$

$$f_2(\alpha)=\frac{k_2^2(\alpha)}{A(\alpha)[(1-a_5)\cos^2\alpha+a_5][k_3^2(\alpha)-k_2^2(\alpha)][k_1^2(\alpha)-k_2^2(\alpha)]} \tag{10b}$$

$$f_3(\alpha)=\frac{k_3^2(\alpha)}{A(\alpha)[(1-a_5)\cos^2\alpha+a_5][k_1^2(\alpha)-k_3^2(\alpha)][k_2^2(\alpha)-k_3^2(\alpha)]} \tag{10c}$$

$$g_1(\alpha)=-g_2(\alpha)=\frac{1}{A(\alpha)[k_1^2(\alpha)-k_2^2(\alpha)]} \tag{11a,b}$$

$$k_1^2(\alpha)=\frac{2k_0^2}{B(\alpha)-[B^2(\alpha)-4A(\alpha)]^{0.5}} \tag{12a}$$

$$k_2^2(\alpha)=\frac{2k_0^2}{B(\alpha)+[B^2(\alpha)-4A(\alpha)]^{0.5}} \tag{12b}$$

$$k_3^2(\alpha)=\frac{k_0^2}{(1-a_5)\cos^2\alpha+a_5}. \tag{12c}$$

Here and henceforth in this paper we assume that $k_j(\alpha)$, $j=1,\ 2,\ 3$ defined in Eqs. (12*a-c*) are of positive values. A discussion on the relation of the position definition of $k_j(\alpha)$, $j=1,\ 2,\ 3$ and the material constants will be given later in this paper.

After we replace the integrand in the integral in Eq. (6) with the relations in (7)–(12) and do some manipulation in the spherical coordinates $\mathbf{x}=\mathbf{x}\ (R,\ \theta,\ \phi)$, $G_{11}(\mathbf{x})$ can be rewritten as a summation of a simple function and an integral representation over an infinite integration domain

$$G_{11}(R,\theta,\phi)=\frac{e^{ik_0R_0}}{4\pi a_5R_0C_{44}}+\int_0^{\infty}\int_0^{\pi}\int_0^{2\pi}\frac{\sin^2\alpha\cos^2\beta}{8\pi^3C_{44}}\sum_{j=1}^{3}\frac{P_j(\alpha)e^{-iR\cos\psi}}{r^2-k_j^2(\alpha)}r^2\sin\alpha\,dr\,d\alpha\,d\beta \tag{13}$$

where

$$P_j(\alpha)=(1-\delta_{j3})(a_5-a_3)g_j(\alpha)k_j^2(\alpha)+(a_5-a_3)(1-a_5)f_j(\alpha)k_j^2(\alpha)+[1+a_2a_5-a_4-a_5+a_3-(a_5-a_3)(1-a_5)]\cos^2\alpha f_j(\alpha)k_j^2(\alpha),\ j=1,\ 2,\ 3 \tag{14a}$$

$$R_0=\left[\frac{x_1^2}{a_5}+\frac{x_2^2}{a_5}+x_3^2\right]^{0.5} \tag{14b}$$

$$\delta_{3j}=\begin{cases}0 & j\neq 3\\ 1 & j=3\end{cases} \tag{14c}$$

$$\cos\psi=\cos\alpha\cos\theta+\sin\theta\sin\alpha\cos(\beta-\phi) \tag{14d}$$

$$x_1=R\sin\theta\cos\phi,\ x_2=R\sin\theta\sin\phi,\ x_3=R\cos\theta. \tag{15a-c}$$

The integration domain for the integral representation in Eq. (13) is infinite. In what follows we try to reduce that infinite integration domain to the a finite one. For this purpose, we need to apply Cauchy's theorem to the integral with respect to the variable r. Therefore, we wish to extend the integration interval for the variable r from (0, ∞) to (−∞, ∞) by the method of change of variables. The first step is to replace ϕ by $2\pi-\phi$ in the integral in Eq. (13) which yields

$$G_{11}(R,\theta,2\pi-\phi)=\frac{e^{ik_0R_0}}{4\pi a_5R_0C_{44}}+\int_0^{\infty}\int_0^{\pi}\int_0^{2\pi}\frac{\sin^2\alpha\cos^2\beta}{8\pi^3C_{44}}\sum_{j=1}^{3}\times\frac{P_j(\alpha)e^{-iR\cos\psi'}}{r^2-k_j^2(\alpha)}r^2\sin\alpha\,dr\,d\alpha\,d\beta \tag{16a}$$

where

$$\cos\psi'=\cos\alpha\cos\theta+\sin\alpha\sin\theta\cos(\beta+\phi). \tag{16b}$$

By changing the variable β to $2\pi-\beta'$ in the integral at the right-hand side of Eq. (16*a*), it is easy to verify the following relation

$$G_{11}(R,\theta,\phi)=G_{11}(R,\theta,2\pi-\phi). \tag{17}$$

Downloaded 03 May 2010 to 171.66.16.247. Redistribution subject to ASME license or copyright; see http://www.asme.org/terms/Terms_Use.cfm

Next, by introducing new integration variables $\beta' = \beta - \phi$ in $G_{11}(R, \theta, \phi)$ in Eq. (13) and $\beta'' = \beta + \phi$ in $G_{11}(R, \theta, 2\pi - \phi)$ in Eq. (16*a*), we obtain

$$G_{11}(R,\theta,\phi) = \frac{e^{ik_0R_0}}{4\pi a_5 R_0 C_{44}} + \int_0^\infty \int_0^\pi \int_{-\phi}^{2\pi-\phi} \times \frac{\sin^2\alpha[\cos^2\beta'\cos^2\phi + \sin^2\beta'\sin^2\phi - 2\cos\beta'\cos\phi\sin\beta'\sin\phi]}{8\pi^3 C_{44}} \sum_{j=1}^{3} \frac{P_j(\alpha)e^{-iRr(\cos\alpha\cos\theta + \sin\alpha\sin\theta\cos\beta')}}{r^2 - k_j^2(\alpha)} r^2\sin\alpha dr d\alpha d\beta' \quad (18)$$

and

$$G_{11}(R,\theta,2\pi-\phi) = \frac{e^{ik_0R_0}}{4\pi a_5 R_0 C_{44}} + \int_0^\infty \int_0^\pi \int_{\phi}^{2\pi+\phi} \frac{\sin^2\alpha[\cos^2\beta''\cos^2\phi + \sin^2\beta''\sin^2\phi + 2\cos\beta''\cos\phi\sin\beta''\sin\phi]}{8\pi^3 C_{44}} \times \sum_{j=1}^{3} \frac{P_j(\alpha)e^{-iRr(\cos\alpha\cos\theta + \sin\alpha\sin\theta\cos\beta'')}}{r^2 - k_j^2(\alpha)} r^2\sin\alpha dr d\alpha d\beta''. \quad (19)$$

Since the integrands in Eqs. (18) and (19) are periodic functions of the variables β' and β'' with period 2π, the upper and lower limits for the integration over β' and β'' can be redefined by 2π and 0, respectively. Then, with the relation given by Eq. (17), $G_{11}(R, \theta, \phi)$ can be expressed as a mean value of $G_{11}(R, \theta, \phi)$ and $G_{11}(R, \theta, 2\pi - \phi)$

$$G_{11}(R,\theta,\phi) = 0.5G_{11}(R,\theta,\phi) + 0.5G_{11}(R,\theta,2\pi-\phi) = \frac{e^{ik_0R_0}}{4\pi a_5 R_0 C_{44}} + \int_0^\infty \int_0^\pi \int_0^{2\pi} \frac{\sin^2\alpha[\cos^2\beta\cos^2\phi + \sin^2\beta\sin^2\phi]}{8\pi^3 C_{44}} \times \sum_{j=1}^{3} \frac{P_j(\alpha)e^{-iRr(\cos\alpha\cos\theta + \sin\alpha\sin\theta\cos\beta)}}{r^2 - k_j^2(\alpha)} r^2\sin\alpha dr d\alpha d\beta. \quad (20)$$

Through these manipulations, it can be seen that the evaluation of Eq. (20) requires the computation to an integral of the form

$$I(R,\theta,\phi) = \int_0^\infty \int_0^\pi \int_0^{2\pi} \frac{F(\alpha,\beta,\phi)}{r^2 - k^2(\alpha)} \times e^{-iRr(\cos\alpha\cos\theta + \sin\alpha\sin\theta\cos\beta)} \sin\alpha dr d\alpha d\beta \quad (21)$$

with the following properties for $F(\alpha, \beta, \phi)$ and $k(\alpha)$:

$$F(\alpha,\beta,\phi) = F(\cos^2\alpha, (\sin\alpha\cos\beta)^2, (\sin\alpha\sin\beta)^2, \phi) \quad (22)$$

$$F(\alpha,\beta,\phi) = F(\alpha,\beta+2\pi,\phi) = F(\pi-\alpha,\beta+\pi,\phi) \quad (23a,b)$$

$$k(\alpha) = k(\cos^2\alpha),\ k(\alpha) > 0. \quad (24a,b)$$

By virtue of these properties, and by introducing the change of variables α to $\pi - \alpha$, β to $\pi + \beta$ and r to $-r$ in the integral in Eq. (21), we may also write

$$I(R,\phi,\phi) = \int_{-\infty}^0 \int_0^\pi \int_0^{2\pi} \frac{F(\alpha,\beta,\phi)\ r^2}{r^2 - k^2\ (\alpha)} \times e^{-iRr(\cos\alpha\cos\theta + \sin\alpha\sin\theta\cos\beta)} \sin\alpha dr d\beta. \quad (25)$$

Again, $I(R, \theta, \phi)$ can be expressed as a mean value of Eq. (21) and Eq. (25). This yields

$$I(R,\theta,\phi) = 0.5 \int_{-\infty}^\infty \int_0^\pi \int_0^{2\pi} \frac{F(\alpha,\beta,\phi)r^2}{r^2 - k^2(\alpha)} \times e^{-iRr(\cos\alpha\cos\theta + \sin\theta\cos\beta)} \sin\alpha dr d\alpha d\beta. \quad (26)$$

2 Double Integral Representations

To further simplify the integral $I(R,\theta,\phi)$, a rotation of the coordinate system is introduced

$$\mathbf{y} = \mathbf{T}\mathbf{y}^*,\ \mathbf{T} = \begin{pmatrix} \cos\theta & 0 & \sin\theta \\ 0 & 1 & 0 \\ -\sin\theta & 0 & \cos\theta \end{pmatrix} \quad (27a,b)$$

where

$$y_1^* = r\sin\psi\cos\gamma,\ y_2^* = r\sin\psi\sin\gamma,\ y_3^* = r\cos\psi. \quad (28a-c)$$

The relations among α, β, ψ, and γ are:

$$\sin\alpha\cos\beta = \cos\theta\sin\psi\cos\gamma + \sin\theta\cos\psi \quad (29a)$$

$$\sin\alpha\sin\beta = \sin\psi\sin\gamma \quad (29b)$$

$$\cos\alpha = -\sin\theta\sin\psi\cos\gamma + \cos\theta\cos\psi \quad (29c)$$

In the $\mathbf{y}^*$ coordinate system, $F(\alpha, \beta, \phi)$ should be written

$$F(\alpha,\beta,\phi) = F(\psi,\gamma,\theta,\phi) \quad (30a)$$

$$k_j(\alpha) = k_j(\psi,\gamma,\theta),\ j = 1, 2, 3. \quad (30b)$$

With Eqs. (22), (23*a–c*), and (29*a–c*), it is easy to verify

$$F(\psi,\gamma,\theta,\phi) = F(\psi,2\pi+\gamma,\theta,\phi) = F(\pi-\psi,\pi+\gamma,\theta,\phi) \quad (31a\text{-}c)$$

$$k_j(\psi,\gamma,\theta) = k_j(\psi,2\pi+\gamma,\theta) = k_j(\pi-\psi,\ \pi+\gamma,\ \theta),\ j = 1, 2, 3. \quad (32a\text{-}c)$$

Now, in the $\mathbf{y}^*$ coordinate system, $I(R, \theta, \phi)$ in Eq. (26) can be further decomposed into three parts with the help of Eqs. (29)–(32)

$$I(R,\theta,\phi) = I_1 + I_2 + I_3 \quad (33)$$

where

$$I_1 = 0.5\int_0^\pi \int_0^{2\pi} F(\psi,\gamma,\theta,\phi)\sin\psi d\psi d\gamma \int_{-\infty}^\infty e^{-iRr\cos\psi} dr = \int_0^\pi \int_0^{2\pi} F(\psi,\gamma,\theta,\phi)\pi\delta(R\cos y)\ \sin\psi d\psi d\gamma = \frac{\pi}{R}\int_0^{2\pi} F(\psi=0.5\pi,\gamma,\theta,\phi)\ d\gamma \quad (34)$$

$$I_2 = 0.5\int_0^{\pi/2} \int_0^{2\pi} F(\psi,\gamma,\theta,\theta)\ k^2(\psi,\gamma,\theta)\sin\psi d\psi d\gamma \times \int_{-\infty}^\infty \frac{e^{-iRr\cos\psi}}{r^2 - k^2\ (\psi,\gamma,\theta)} dr \quad (35)$$

$$I_3 = 0.5\int_{\pi/2}^{\pi} \int_0^{2\pi} F(\psi,\gamma,\theta,\phi)k^2\ (\psi,\gamma,\theta)\sin\psi d\psi d\gamma \times \int_{-\infty}^\infty \frac{e^{-iRr\cos\Psi}}{r^2 - k^2\ (\psi,\gamma,\theta)} dr = I_2. \quad (36)$$

The identity of I_2 and I_3 can be easily shown by making the change of variables ψ to $\pi - \psi$, γ to $\pi + \gamma$ and r to $-r$ with the use of eqs. ($31a-c$) and ($32a-c$).

The integral with respect to the variable r in Eq. (35),

$$I_4 = \int_{-\infty}^\infty \frac{e^{iRr\cos\psi}}{r^2 - k^2\ (\psi,\gamma,\theta)} dr, \quad (37)$$

can be evaluated analytically by the Cauchy integral theorem. The integrand in (37) has two simple poles at $r = -k\ (\psi, \gamma, \theta)$ and $r = k\ (\psi, \gamma, \theta)$, respectively. The contribution from the pole $r = -k\ (\psi, \gamma, \theta)$ gives a positive phase factor while the contribution from the pole $r = k\ (\psi, \gamma, \theta)$ gives a negative phase factor. We assume that the time factor for the Green's functions in this paper is of the form $e^{-i\omega t}$. Therefore, in order to let the I_2 represent an outgoing wave, considered only is the contribution which comes from the pole $r = -k\ (\psi, \gamma, \theta)$. Thus, the application of the Cauchy integral theorem to I_2 yields

Downloaded 03 May 2010 to 171.66.16.247. Redistribution subject to ASME license or copyright; see http://www.asme.org/terms/Terms_Use.cfm

$$I_2=\frac{i\pi}{2}\int_0^{\pi/2}\int_0^{2\pi}F(\psi,\gamma,\theta,\phi)k(\psi,\gamma,\theta)\times e^{iRk(\psi,\gamma,\theta)\cos\psi}\sin\psi d\psi d\gamma. \quad (38)$$

For the convenience of deriving the far-field asymptotic expansion later in this paper, one more change of variable $\psi'=\pi/2-\psi$ has also been made to I_2. The final I_2 becomes

$$I_2=\frac{i\pi}{2}\int_0^{\pi/2}\int_0^{2\pi}F(\psi',\gamma,\theta,\phi)k(\psi',\gamma,\theta)\times e^{iRk\ (\psi',\gamma,\theta)\ \sin\psi'}\cos\psi' d\psi' d\gamma. \quad (39)$$

With all these preparations, we are able to cast G_{11} (R, θ, ϕ) in the form of a double integral

$$G_{11}(R,\theta,\phi)=\frac{i}{8\pi^2 C_{44}}\int_0^{\pi/2}\int_0^{2\pi}\sum_{j=1}^{3}P_j(\eta)k_j(\eta)e^{ik_j(\eta)R\ \sin\psi}\times[(\cos\theta\cos\psi\cos\gamma+\sin\theta\sin\psi)^2\cos^2\phi+\cos^2\psi\sin^2\gamma\sin^2\phi]\times\cos\psi d\psi d\gamma+\frac{e^{ik_0R_0}-1}{4\pi a_5C_{44}R_0}+G_{11}^{\text{static}}\ (R,\theta,\phi) \quad (40a)$$

where

$$\eta=\cos\theta\sin\psi-\sin\theta\cos\psi\cos\gamma. \quad (40b)$$

The definitions of P_j and k_j, $j=1, 2, 3$, can be found in Eqs. (12) to (14*a*) but the argument of these functions now is η in place of $\cos\alpha$. R_0 is defined in Eq. (14*b*).

The evaluation of G_{11} (R, θ, ϕ) is the most difficult to compute among all the components of the Green's function. Following similar steps, the other components can also be obtained as the double integral representations. They are

$$G_{12}(R,\theta,\phi)=\frac{i}{8\pi^2C_{44}}\int_0^{\pi/2}\int_0^{2\pi}\sum_{j=1}^{3}P_j(\eta)k_j(\eta)\times e^{ik_j(\eta)R\sin\psi}[(\cos\theta\cos\psi\cos\gamma+\sin\theta\sin\psi)^2-\cos^2\psi\sin^2\gamma]\sin\phi\cos\phi\cos\psi d\psi d\gamma+G_{12}^{\text{static}}\ (R,\theta,\phi) \quad (41)$$

$$G_{13}(R,\theta,\phi)=\frac{-ia_1}{8\pi^2C_{44}}\int_0^{\pi/2}\int_0^{2\pi}\sum_{j=1}^{2}g_j(\eta)k_j^3(\eta)\times e^{ik_j(\eta)R\sin\psi}(\cos\theta\cos\psi\cos\gamma+\sin\theta\sin\psi)(\cos\theta\sin\psi-\sin\theta\cos\psi\cos\gamma)\cos\phi\cos\psi d\psi d\gamma+G_{13}^{\text{static}}\ (R,\theta,\phi) \quad (42)$$

$$G_{22}(R,\theta,\phi)=\frac{i}{8\pi^2C_{44}}\int_0^{2\pi}\int_0^{2\pi}\sum_{j=1}^{3}P_j(\eta)k_j(\eta)\times e^{ik_j(\eta)R\sin\psi}[(\cos\theta\cos\psi\cos\gamma+\sin\theta\sin\psi)^2\sin^2\phi+\cos^2\psi\sin^2\gamma\cos^2\phi]\cos\psi d\psi d\gamma+\frac{e^{ik_0R_0}-1}{4\pi a_5C_{44}R_0}+G_{22}^{\text{static}}\ (R,\theta,\phi) \quad (43)$$

$$G_{23}(R,\theta,\phi)=\frac{-ia_1}{8\pi^2C_{44}}\int_0^{\pi/2}\int_0^{2\pi}\sum_{j=1}^{2}g_j(\eta)k_j^3(\eta)\times e^{ik_j(\eta)R\sin\psi}(\cos\theta\cos\psi\cos\gamma+\sin\theta\sin\psi)(\cos\theta\sin\psi-\sin\theta\cos\psi\cos\gamma)\sin\phi\cos\psi d\psi d\gamma+G_{23}^{\text{static}}\ (R,\theta,\phi) \quad (44)$$

$$G_{33}(R,\theta,\phi)=\frac{i}{8\pi^2C_{44}}\int_0^{\pi/2}\int_0^{2\pi}\sum_{j=1}^{2}N_j(\eta)k_j(\eta)\times e^{ik_j(\eta)R\sin\psi}\cos\psi d\gamma d\psi+G_{33}^{\text{static}}\ (R,\theta,\phi) \quad (45)$$

where

$$N_j(\eta)=\{[a_3+(1-a_3)\eta^2]k_j^2(\eta)-k_0^2\}g_j(\eta),\ j=1,\ 2 \quad (46)$$

and η is defined in Eq. (40*b*). The definitions of R_0, P_j, k_j, f_j, and g_j, $j=1, 2, 3$, can be found in Eqs. (10) to (14), but the argument of these functions again is η in place of $\cos\alpha$. The static solutions G_{mn}^{static} (R, θ, ϕ), $m, n=1, 2, 3$ can be found in the Pan and Chou paper (1976).

3 Asymptotic Expansions for Green's Functions at Far Field

At the far field $R \gg 1$, the stationary phase method (Gamkrelidze, 1989) can be applied to the Green's functions in (40)–(45). The stationary phase points are the roots governed by the following equations in the region $0\le\psi\le\pi/2$ and $0\le\gamma\le2\pi$:

$$\frac{\partial k_j(\eta)}{\partial\gamma}\sin\psi=\frac{\partial k_j(\eta)}{\partial\eta}\sin\theta\sin\gamma\sin\psi\cos\psi=0,\ j=1,\ 2,\ 3 \quad (47)$$

$$\frac{\partial[k_j(\eta)\sin\psi]}{\partial\psi}=\frac{\partial k_j(\eta)}{\partial\eta}(\sin\theta\sin\psi\cos\gamma+\cos\theta\cos\psi)\sin\psi+k_j(\eta)\cos\psi=0\ j=1,\ 2,\ 3 \quad (48)$$

where $\eta = -\sin\theta\cos\psi\cos\gamma+\cos\theta\sin\psi$.

One of the roots for Eq. (47) is $\psi=\pi/2$. However, the integrands in Eqs. (40)–(45) all contain the term $\cos\psi$. Therefore, the contribution from this root is trivial. Another root of the equation in (47) is $\psi=0$. For this root, the equation in (48) will never hold true regardless of the value of γ, since k_j, $(j=1, 2, 3,)$ is always positive. Hence, $\psi=0$ is not a stationary phase point. The same conclusion can be drawn for these roots at which the quantity $\dfrac{\partial k_j(\eta)}{\partial\eta}$ becomes zero.

Therefore, the roots $\gamma=0$ and $\gamma=\pi$ are the only roots to be considered in Eq. (47). For the root $\gamma=0$, the corresponding equation in (48) becomes

$$\frac{\partial k_j[\sin(\psi-\theta)]}{\partial\psi}\sin\psi+k_j\ [\sin(\psi-\theta)]\ \cos\psi=0,\quad 0\le\psi\le\pi/2,\ j=1,\ 2,\ 3. \quad (49)$$

For the root $\gamma=\pi$, the corresponding equation in (48) becomes

$$\frac{\partial k_j[\sin(\psi+\theta)]}{\partial\psi}\sin\psi+k_j[\sin(\psi+\theta)]\ \cos\psi=0,\quad 0\le\psi\le\pi/2,\ j=1,\ 2,\ 3. \quad (50)$$

It is easily observed that a change of variable $\psi'=\pi-\psi$ in Eq. (50) will result in an equation of the same form as Eq. (49). But ψ' is defined in the interval $\pi/2\le\psi'\le\pi$. Consequently, we are able to write a single equation

$$\frac{\partial k_j[\sin(\psi-\theta)]}{\partial\psi}\sin\psi+k_j\ [\sin(\psi-\theta)]\ \cos\psi=0,\quad 0\le\psi\le\pi,\ j=1,\ 2,\ 3 \quad (51)$$

to determine all the roots ψ for both $\gamma=0$ $(0\le\psi\le\pi/2)$ and $\gamma=\pi(\pi/2\le\psi\le\pi)$.

Simultaneously, the same change of variable $\psi'=\pi-\psi$ made to the integrands in Eqs. (40)–(45) at the stationary phase point $\gamma=\pi$ will also make these integrands exactly the same in form as those at the stationary phase point $\gamma=0$.

Indeed, what is demonstrated at this point suggests the contributions from two sets of stationary phase points to the asymptotic expansions at far field can be expressed in the same manner. Hence, by the application of the stationary phase method, the approximations at far field for Green's functions have been obtained

$$G_{11}^{\infty}\ (R,\theta,\phi)=\frac{e^{ik_0R_0}}{4\pi a_5C_{44}R_0}+\frac{i\cos^2\phi}{4\pi RC_{44}}\times\sum_{j=1}^{3}\sum_{n=1}^{N}H_j(\psi_n,\theta)P_j(\eta_n)\cos^2(\psi_n-\theta) \quad (52)$$

Downloaded 03 May 2010 to 171.66.16.247. Redistribution subject to ASME license or copyright; see http://www.asme.org/terms/Terms_Use.cfm

$$G_{12}^{\infty}(R,\theta,\phi)=\frac{i\sin\phi\cos\phi}{4\pi RC_{44}} \times\sum_{j=1}^{3}\sum_{n=1}^{N} H_j(\psi_n,\theta)P_j(\eta_n)\cos^2(\psi_n-\theta) \quad (53)$$

$$G_{13}^{\infty}(R,\theta,\phi)=\frac{-ia_1\cos\phi}{8\pi RC_{44}} \times\sum_{j=1}^{2}\sum_{n=1}^{N} H_j(\psi_n,\theta)g_j(\eta_n)\,k_j^2(\eta_n)\sin 2(\psi_n-\theta) \quad (54)$$

$$G_{22}^{\infty}(R,\theta,\phi)=\frac{e^{ik_0R_0}}{4\pi a_5C_{44}R_0}+\frac{i\sin^2\phi}{4\pi RC_{44}} \times\sum_{j=1}^{3}\sum_{n=1}^{N} H_j(\psi_n,\theta)P_j(\eta_n)\cos^2(\psi_n-\theta) \quad (55)$$

$$G_{23}^{\infty}(R,\theta,\phi)=\frac{-ia_1\sin\phi}{8\pi RC_{44}} \times\sum_{j=1}^{2}\sum_{n=1}^{N} H_j(\psi_n,\theta)\,g_j(\eta_n)\,k_j^2(\eta_n)\sin 2(\psi_n-\theta) \quad (56)$$

$$G_{33}^{\infty}(R,\theta,\phi)=\frac{i}{4\pi RC_{44}}\sum_{j=1}^{2}\sum_{n=1}^{N} H_j(\psi_n,\theta)\,N_j(\eta_n) \quad (57)$$

$$H_j(\psi_n,\theta)=e^{ik_j(\eta_n)R\sin\psi_n+0.25\pi i\{\mathrm{sgn}(H_{22nj})-\mathrm{sgn}[\cos(\psi_n-\theta)]\}} \times\left|\frac{k_j(\eta_n)\cos(\psi_n-\theta)}{\sin\theta h_{22nj}}\right|^{0.5},\ j=1,2,3 \quad (58)$$

where $\eta_n=\sin(\psi_n-\theta)$, ψ_n is the ηth root of the equation in (49), $n=1,\ldots,N$. The definition of $P_j(\eta_n)$ and $N_j(\eta_n)$ can be found in Eqs. (15*a*) and (46), respectively. The second derivatives of the phase functions $k_j(\eta)\sin\psi$, $j=1, 2, 3$ at the stationary points are

$$\left.\frac{\partial^2[k_j(\eta)\sin\psi]}{\partial\gamma^2}\right|_{\gamma=0,\ \psi=\psi_n}=-\frac{k_j[\sin(\psi_n-\theta)]\cos^2\psi_n\sin\theta}{\cos(\psi_n-\theta)},\quad n=1,\ldots,N,\ j=1,2,3 \quad (59)$$

$$\left.\frac{\partial^2[k_j(\eta)\sin\psi]}{\partial\gamma\partial\psi}\right|_{\gamma=0,\ \psi=\psi_n}=0,\ n=1,\ldots,N,\ j=1,2,3 \quad (60)$$

$$\left.\frac{\partial^2[k_j(\eta)\sin\psi]}{\partial\psi^2}\right|_{\gamma=0,\ \psi=\psi_n}=h_{22nj},\quad n=1,\ldots,N,\ j=1,2,3 \quad (61)$$

and $\eta=-\sin\theta\cos\psi\cos\gamma+\cos\theta\sin\psi$.

4 Some Discussions

The results obtained so far suggest these observations:

(*a*) Obviously, at the points $k_1=k_2$, or $k_2=k_3$, P_j, N_j, g_j, and f_j in (40)–(45) have simple poles. However, the singularity of the following summation is removable

$$\sum_{j=1}^{3}P_jk_je^{ik_jR\sin\psi}=\frac{(k_1-k_2)(k_2-k_3)(k_3-k_1)}{(k_1^2-k_2^2)(k_2^2-k_3^2)(k_3^2-k_1^2)}H_1+\frac{k_1-k_2}{k_1^2k_2^2}\frac{e^{ik_1R\sin\psi}-e^{ik_3R\sin\psi}}{k_1^2-k_3^2}H_2+\frac{k_1-k_2}{k_1^2-k_2^2}\frac{e^{ik_2R\sin\psi}-e^{ik_3R\sin\psi}}{k_2^2-k_3^2}H_3. \quad (62)$$

Here, H_1, H_2, and H_3 are analytical functions of k_1, k_2, and k_3. The same conclusions hold true for $\sum_{j=1}^{2}g_jk_j^3e^{ik_jR\sin\psi}$ and $\sum_{j=1}^{2}N_jk_je^{ik_jR\sin\psi}$. Therefore, the integrands in (40)–(45) are continuous over the regions of integration and this should make the numerical evaluation of these integrals possible.

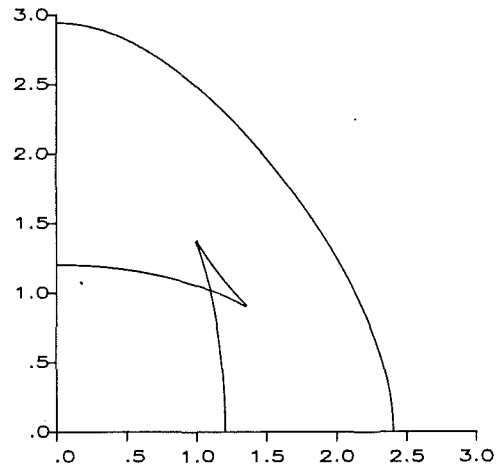


Fig. 1 The wave front for the case $a_2=4$, $a_3=6$, and $a_4=20$

(*b*) The singularity parts of the Green's functions are the same as those of the static solutions

$$G_{mn}(R,\theta,\phi)=G_{mn}^{\mathrm{static}}(R,\theta,\phi),\ R\to 0. \quad (63)$$

(*c*) The trace, $k_j(\eta_n)R\sin\psi_n=$ constant, is called the wave front. We have numerically obtained some wave front curves for the material constants that match the cases in Payton's book. One example of these curves is shown in Fig. 1. The present method to construct a wave front appears simpler than other methods known to the public.

(*d*) The far-field approximations in (52)–(57) are valid under the assumption that h_{22nj}, $j=1, 2, 3$ in (61) $\neq 0$ for any θ in $0\le\theta\le\pi$. Under this assumption, $H_j(\psi_n,\theta)$, $j=1, 2, 3$ in Eq. (58) will never become infinite. This is because when θ approaches zero or π, the root ψ_1, decided by Eq. (51), also approaches $\pi/2$. Consequently, it can be shown that the quantity $\cos(\psi_1-\theta)/\sin\theta$ remains finite and so does $H_j(\psi_n,\theta)$.

(*e*) For the isotropic case, $C_{44}=\rho\omega^2/k_T^2$, $a_1=k_T^2/k_L^2-1$, $a_2=a_3=0.5$, $a_4=k_T^2/k_L^2$, $a_5=1$, $k_1=k_L$ and $k_2=k_3=k_T$. Here, k_L and k_T are the longitudinal and transverse wave numbers, respectively. Then $G_{11}(R,\theta,\phi)$ becomes

$$G_{11}(R,\theta,\phi)=\frac{i}{8\pi^2\rho\omega^2}\int_0^{\pi/2}\int_0^{2\pi}(k_L^3e^{ik_LR\sin\psi}-k_T^3e^{ik_TR\sin\psi})[(\cos\theta\cos\psi\cos\gamma+\sin\theta\sin\psi)^2\cos^2\psi+\cos^2\psi\sin^2\gamma\sin^2\phi]\cos\psi d\psi d\gamma+\frac{k_T^2(e^{ik_TR}-1)}{4\pi\rho\omega^2R}+G_{11}^{\mathrm{static}}(R,\theta,\phi). \quad (64)$$

The analytical evaluation of $G_{11}(R,\theta,\phi)$ in (64) is available and the final result gives the following expression for $G_{11}(R,\theta,\phi)$

$$G_{11}(R,\theta,\phi)=\frac{k_L^2e^{ik_LR}}{4\pi\rho\omega^2R}\left[\sin^2\theta\cos^2\phi+\frac{1}{k_LR}\left(i-\frac{1}{k_LR}\right)(3\sin^2\theta\cos^2\phi-1)\right]+\frac{k_T^2e^{ik_TR}}{4\pi\rho\omega^2R}[1-\sin^2\theta\cos^2\phi-\frac{1}{k_TR}\left(i-\frac{1}{k_TR}\right)(3\sin^2\theta\cos^2\phi-1)]. \quad (65)$$

It is seen that $G_{11}(R,\theta,\phi)$ is the same as for the isotropic case. For the other components of $G_{mn}(R,\theta,\phi)$, the same conclusion can also be obtained in a similar manner.

Downloaded 03 May 2010 to 171.66.16.247. Redistribution subject to ASME license or copyright; see http://www.asme.org/terms/Terms_Use.cfm

For the far-field approximations, the equations in (51) has only one root, $\psi_1 = \pi/2$, and

$$H_1(\psi_1,\theta) = e^{ik_L R - 0.5\pi i} \tag{66a}$$

$$H_2(\psi_1,\theta) = H_3(\psi_1,\theta) = e^{ik_T R - 0.5\pi i}. \tag{66b,c}$$

It is not difficult to verify that the expressions in Eqs. (52)–(57) all converge to the far-field isotropic Green's functions.

(*f*) A basic assumption always employed in the wave propagation theory is that the material constants are positive definite. Under this assumption, the following inequalities can be derived (Payton, 1983),

$$C_{11} > \text{abs}(C_{12}),\ (C_{11}+C_{12})C_{33} > 2(C_{13})^2,\ C_{44} > 0, \tag{67a-c}$$

as well as some direct conclusions from above inequalities and the definitions of a_2, a_3 and a_5 in Eqs. (8*e*), (8*f*), and (8*h*), respectively.

$$C_{33} > 0,\ C_{11}C_{33} > (C_{13})^2,\ a_2 > 0,\ a_3 > 0,\ a_5 > 0 \tag{68a-e}$$

where the notation abs() means taking the absolute value.

In view of Eqs. (8*b*) and (12*c*), the positive definition of $B(\alpha)$ and $k_3(\alpha)$ is certainly obvious. By observation of Eqs. (12*a*−*b*), in order to have $k_1(\alpha) > 0$ and $k_2(\alpha) > 0$, $A(\alpha)$ in Eqs. (8*a*) must always be greater than zero, and similarly, so does $B^2(\alpha) - 4A(\alpha)$. By the change of variable $t = \cos^2\alpha$, $A(\alpha)$ can be arranged as

$$A(t) = a_2 t^2 + a_3 (1-t)^2 + a_4 t (1-t),\ 0 \le t \le 1. \tag{69}$$

It is easily seen that when $a_4 \ge 0$, $A(t)$ is positive. When $a_4 < 0$, with a few manipulation, $A(t)$ appears to have a minimum $[A(t)]_{\min}$ at $t = t_{\min}$

$$[A(t)]_{\min} = \frac{[2(a_2a_3)^{0.5} - a_4][2(a_2a_3)^{0.5} + a_4]}{4(a_2 + a_3 - a_4)} \tag{70a}$$

$$t_{\min} = \frac{a_3 - 0.5a_4}{a_2 + a_3 - a_4},\ 0 < t_{\min} < 1. \tag{70b}$$

The term $2(a_2a_3)^{0.5} + a_4$ in Eq. (70*a*) is equivalent to

$$2(a_2a_3)^{0.5} + a_4 = \left(1 + \frac{(C_{11}C_{33})^{0.5}}{C_{44}}\right)^2 - \left(1 + \frac{C_{13}}{C_{44}}\right)^2. \tag{71}$$

With the help of Eqs. (68*b*) and (71), we see immediately that the denominator and the numerator of the expression in Eq. (70*a*) are both positive when $a_4 < 0$. Therefore, $A(t)$ at $0 \le t \le 1$ is always greater than zero regardless of the value of a_4. In other words, $A(\alpha)$ is positive defined as long as the material constants are positive definite.

Similar to $A(t)$ in Eq. (69), $B^2(\alpha) - 4A(\alpha)$ can also be arranged as

$$B^2(t) - 4A(t) = b_2 t^2 + b_3 (1-t)^2 + b_4 t(1-t),\ 0 \le t \le 1 \tag{72}$$

$$b_2 = (1-a_2)^2,\ b_3 = (1-a_3)^2,$$

$$b_4 = 2[(1+a_2)(1+a_3) - 2a_4]. \tag{73a-c}$$

It is clear that when $b_4 \ge 0$, $B_2(t) - 4A(t) \ge 0$. When $b_4 < 0$, $B^2(t) - 4A(t)$ in the interval $0 \le t \le 1$ reaches its minimum at $t = t_{\min}$

$$[B^2(t) - 4A(t)]_{\min} = \frac{[2(b_2b_3)^{0.5} - b_4][2(b_2b_3)^{0.5} + b_4]}{4(b_2 + b_3 - b_4)} \tag{74a}$$

$$t_{\min} = \frac{b_3 - 0.5b_4}{b_2 + b_3 - b_4},\ 0 < t_{\min} < 1. \tag{74b}$$

The term $2(b_2b_3)^{0.5} + b_4$ in Eq. (74*a*) is equivalent to

$$2(b_2b_3)^{0.5} + b_4 = 2\{\text{abs}\,[(1-a_2)(1-a_3)] - (1-a_2)(1-a_3)\} + 2\left(1 + \frac{C_{13}}{C_{44}}\right)^2. \tag{75}$$

Since the quantity inside the { } in Eq. (75) is non-negative, we can again conclude that $B^2(\alpha) - 4A(\alpha)$ is always a positive value regardless of the value of b_4. In summary, the discussion conducted here states that the present analysis is valid provided the material constants are positive definite.

Acknowledgments

This paper was written during the period when the author was a graduate student at Northwestern University. The author gratefully acknowledges that the incentive to study this topic was provided by Dr. T. Mura who presented this topic in his class "Micromechanics," which the author attended in the winter quarter of 1985. The author wishes to sincerely thank his Ph.D. advisor, Dr. J. D. Achenbach, who reviewed part of the manuscript and provided many helpful comments. Dr. Achenbach also kindly held a group meeting to let the author address this topic in Feb. 1987. The encouragement from Drs. M. Kitahara and F. J. Rizzo during the preparation of this paper, a query on an inadequately proposed inequality in the original manuscript from two anonymous reviewers as well as the grammatical corrections from my colleague, D. Erdman, is also greatly appreciated.

References

Barnett, D. M., 1972, "The Precise Evaluation of Derivatives of the Anisotropic Elastic Green's Functions," *Phys. Status Solid, B*, Vol. 49, pp. 741–748.

Buchward V. T., 1959, "Elastic Wave in Anisotropic Media," *Proc. Roy Soc. London*, Vol. A253, pp. 563–580.

Gamkrrelidze, R. V., 1989, "Asymptotic Methods in Analysis," *Analysis I*, Springer-Verlag, New York, pp. 110–112.

Ha, J., 1986, "Wave Propagation in Transversely Isotropic and Periodically Layered Isotropic Media," *Geophys. J. R. Astr. Soc.*, Vol. 86, pp. 635–650.

Kazi-Aoual, M. N., Bonnett, G., and Jouanna, P., 1988, "Response of an Infinite Elastic Transversely Isotropic Medium a Point Force. An Analytical Solution in Hankel Space," *Geophys. J.*, Vol. 39, pp. 587–590.

Kraut, E. A., 1963, "Advances in the Theory of Anisotropic Elastic Wave Propagation," *Reviews of Geophysics*, Vol. 1, pp. 401–448.

Lighthill, M. J., 1960, "Anisotropic Wave Motions," *Phil. Trans. Roy. Soc. London*, Vol. A252, pp. 397–470.

Pan, Y. C., and Chow, T. W., 1976, "Point Force Solution for an Infinite Transversely Isotropic Solid," ASME JOURNAL OF APPLIED MECHANICS, Vol. 43, pp. 608–612.

Payton, R. G., 1983, *Elastic Wave Propagation in Transversely Isotropic Media*, Martinus Nijhoff, The Hague.

Downloaded 03 May 2010 to 171.66.16.247. Redistribution subject to ASME license or copyright; see http://www.asme.org/terms/Terms_Use.cfm

C.-J. Lu
Graduate Student.

D. B. Bogy
Professor,
Mem. ASME.

Computer Mechanics Laboratory,
Department of Mechanical Engineering,
University of California
Berkeley, CA 94720

The Influence of Thermal Deformation on the Contact Temperature of Sliding Asperities

The effect of thermal deformation on contact temperature is investigated by considering a spherical asperity sliding on the surface of a semi-infinite insulated solid. The usual assumption that thermal deformation does not change the contact conditions is examined. The problem is mathematically formulated using appropriate Green's functions to derive singular integral equations for the contact pressure. The relations between the radius of contact area, indentation, surface temperature, and moving velocity are calculated. A two asperities model is used to explain the load partition due to thermal deformation.

Introduction

Whenever two bodies slide relative to each other in contact there is a loss of mechanical energy associated with friction. This mechanical energy transfers into heat. It is this energy that is responsible for the increase in temperature of bodies sliding in contact. Temperature strongly affects various surface phenomena and material properties. For example, the elastic modulii of many polymeric magnetic media start to degrade just above the ambient temperature (Bhushan, 1987). The magnetic readback signal loss that results from sliding of the head in contact with the media might be the effects of temperature and stress on the magnetostatic equilibrium of the medium (Phipps, 1990). Since no physical surface is perfectly smooth, only a few small areas distributed on the nominal contact area are actually in contact. The heat generated at sliding contact points by friction dissipates into these small contact spots and produces high local temperatures. Experimental work by Bowden and Tabor (1950) showed that this "flash temperature" may approach the melting point of the solids.

Many investigators have presented theories for calculating surface temperature. Carslaw and Jaeger (1947) solved for the temperature distribution due to a given heat source moving on the surface of a semi-infinite body. By treating the contact asperities as independent heat sources, Archard (1959) calculated the interface temperature at a single asperity. He used the Hertz contact pressure and contact area in his calculation of the heat flux. Ting and Winer (1989) used integral transforms to solve for the stresses due to a moving asperity.

In order to apply these theories we must know the pressure distribution and number of contact areas in advance. The usual approach is to assume that the pressure distribution and contact area are independent of the thermal deformation and friction force. Then the Hertz contact solution can be used to determine the contact areas and pressure fields. However, owing to some uncertain factors in the real sliding process, there exists discrepancies between the calculated and measured values. Based on the Jaeger-Archard theory Lingard (1984) showed that the calculated values exceed the measured temperatures, but Griffioen (1985) presented contrary results.

One possible factor contributing to such inconsistent results is the uncertainty of the number of real contact spots. Also, the assumption that thermal deformation does not change the pressure distribution is questionable.

Barber (1969, 1971a, 1976, 1984), Burton and Nerlikar (1975), and Burton (1980) studied the thermoelastic instability and surface distortion due to frictional heating. They found that the asperity model must be supplemented by the concept of thermal deformation. Since frictional heat is proportional to pressure the originally highest asperity, which carries the greatest pressure, will expand more than the surroundings. Thus the thermal distortion tends to exaggerate the initial irregularity of the surface.

In this study, first a single asperity is isolated and the analysis is focused on the steady-state solution. The influence of thermal deformation on the interface temperature, contact area, and indentation is investigated. Then a pair of asperities, with different initial heights, is studied to determine the load partition as a function of sliding speed and total load.

Problem Formulation

Consider a spherical asperity moving on a rigid insulated semi-infinite solid ($z > 0$) with velocity V. The material is homogeneous and isotropic. We want to know the steady-state pressure and temperature distribution at the interface. The following assumptions are adopted.

Contributed by the Applied Mechanics Division of THE AMERICAN SOCIETY OF MECHANICAL ENGINEERS for presentation at the 1992 ASME Summer Mechanics and Materials Meeting, Tempe, AZ, Apr. 28–May 1, 1992.

Discussion on this paper should be addressed to the Technical Editor, Professor Leon M. Keer, The Technological Institute, Northwestern University, Evanston, IL 60208, and will be accepted until four months after final publication of the paper itself in the JOURNAL OF APPLIED MECHANICS. Manuscript received by the ASME Applied Mechanics Division, Feb. 14, 1991; final revision, July 22, 1991.

Paper No. 92-APM-16.

Copyright © 1992 by ASME
Downloaded 03 May 2010 to 171.66.16.247. Redistribution subject to ASME license or copyright; see http://www.asme.org/terms/Terms_Use.cfm

(1) The radius of the sphere is large compared to the radius of the contact area.

(2) Friction force does not change the contact area and pressure distribution except through thermal effects.

(3) All frictional power transfers into heat at the interface.

By making assumption (1) we can treat the sphere as a half space. From assumption (2) the contact area is still circular and the problem remains axisymmetric. From assumption (3) the total heat Q, generated by friction, is

$$Q = fVP \tag{1}$$

where P is the total load and f is the friction coefficient. We treat the problem within the context of linear thermoelastic, i.e., we do not consider plasticity or any wear phenomenon.

One way to solve this problem is to write the governing integral equation in terms of appropriate Green's functions (Barber, 1984).

For a point load P on a semi-infinite solid in the positive z-direction, the normal surface displacement is (Timoshenko and Goodier, 1970).

$$u(r) = \frac{1-\nu^2}{\pi E}\frac{P}{r}. \tag{2}$$

Having this result we can find the normal displacement produced by a circular axisymmetric distributed load $p(r)$ (Johnson, 1985).

$$u(r) = \frac{4(1-\nu^2)}{\pi E}\int_0^a K_p(r,s)p(s)ds$$

$$K_p(r,s) = \frac{s}{r+s}K\left(\frac{2\sqrt{rs}}{r+s}\right) \tag{3}$$

where $K(x)$ is the complete elliptic function of the first kind. E is Young's modulus and ν is Poisson's ratio.

The normal surface displacement due to a point heat source of strength Q on a semi-infinite insulated solid is (Parkus, 1968),

$$u(r) = \frac{(1+\nu)\alpha}{2\pi k}Q\log(r/L) \tag{4}$$

where α is the thermal expansion coefficient, k is the thermal conductivity, and L is the reference distance where the displacement is zero. Here, as in the two-dimensional elastic displacement problems, we can not choose the point at infinity as reference point. The effect of the choice of reference point on the solution will be made clear. The normal displacement produced by a circular axisymmetric distributed heat source with strength $q(r)$ is (Barber, 1971b)

$$u(r^*) = \frac{\alpha(1+\nu)L}{2\pi k}\int_0^{a^*} K_q(r^*,s^*)q(s^*)ds$$

$$K_q(r^*,s^*) = \begin{cases} -2\pi s^*\ln(r^*), 0<r^*<s^* \\ -2\pi s^*\ln(s^*), r^*<s^*<a^* \end{cases} \tag{5}$$

where $a^* = a/L$, $r^* = r/L$ and $s^* = s/L$.

The total surface normal displacement, which is the superposition of (3) and (5), satisfies the following equation:

$$u(r) = D - \frac{r^2}{2R},\ 0 \le r \le a \tag{6}$$

where D is the indentation and R is the radius of the sphere.

From (1), we have $q(s) = fVp(s)$. Combining this relation with Eqs. (4), (5), (6), we obtain the governing equation for the unknown contact pressure $p(s)$ in the dimensionless form as:

$$\int_0^{a^*} p^*(s^*)K_p(r^*,s^*)ds^* + \beta\int_0^{a^*} p^*(s^*)K_q(r^*,s^*)ds^* = D^* - \frac{r^{*2}}{2R^*} \tag{7}$$

where

$$\beta = \frac{E\alpha\mu LV}{8(1+\nu)k} \tag{8}$$

$$p^*(s^*) = \frac{p(s^*)}{\pi E/4(1-\nu^2)}$$

and $a^* = a/L$, $D^* = D/L$, $r^* = r/L$, $s^* = s/L$, $R^* = R/L$.

Given the total load P, the pressure must satisfy the equilibrium condition

$$P^* = \frac{P}{P_0} = 2\pi\int_0^{a^*} p^*(r^*)r^*ds^* \tag{9}$$

where P_0 is the reference load

$$P_0 = \frac{\pi EL^2}{4(1-\nu^2)}.$$

The surface temperature field due to a point heat source Q which satisfies the insulated boundary condition is

$$T(r) = \frac{Q}{2\pi k}\frac{1}{r} = \frac{P\mu V}{2\pi k}\frac{1}{r}.$$

For an axisymmetric distributed heat source $q(r)$

$$T(r) = \int_0^a \frac{q(s)sds}{2\pi k}\int_0^{2\pi}\frac{d\theta}{\sqrt{r^2+s^2-2rs\cos\theta}}$$

$$= \frac{4\mu V}{2\pi k}\int_0^a \frac{p(s)s}{r+s}K\left(\frac{2\sqrt{rs}}{r+s}\right)ds. \tag{10}$$

The maximum temperature occurs at the origin, and is given by

$$T_{\max} = T(0) = \frac{\mu V}{k}\int_0^a p(s)ds. \tag{11}$$

The average temperature is

$$T_{\text{ave}} = \frac{2\pi}{a^2}\int_0^a T(r)rdr. \tag{12}$$

Equations (11)–(12) can be put into the following dimensionless form:

$$T^*_{\max} = \frac{T_{\max}}{T_0} = \beta\int_0^{a^*} p^*(s^*)ds^* \tag{13}$$

$$T^*_{\text{ave}} = \frac{T_{\text{ave}}}{T_0} \tag{14}$$

where T_0 is the reference temperature

$$T_0 = \frac{2\pi}{(1-\nu)\alpha}.$$

Equation (7) is a nonlinear integral equation since a^* is a function of p^*. Given the total load P^* we must solve (7) subject to (9) to get the pressure field p^*, contact radius a^*, and indentation D^*. Then from (10) we can obtain the temperature field. From now on, for convenience, the asterisks will be deleted with the understanding that all quantities are dimensionless.

Numerical Method

The "traction element" method (Johnson, 1985) is used to solve equation (7) subject to (9). In this method, the pressure field is replaced by piecewise constant pressure elements.

$$p(r) = \sum_{k=1}^{n} a_k\Delta_k(r) \tag{15}$$

where

Downloaded 03 May 2010 to 171.66.16.247. Redistribution subject to ASME license or copyright; see http://www.asme.org/terms/Terms_Use.cfm

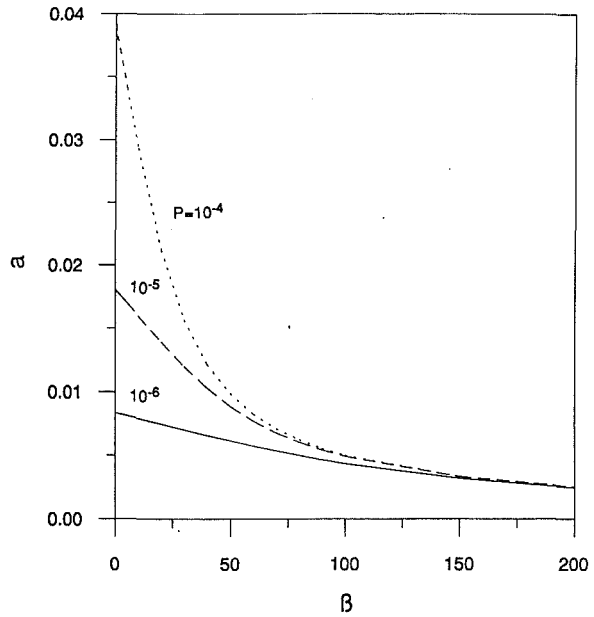


Fig. 1 Relation between contact radius a and velocity β for different loads P

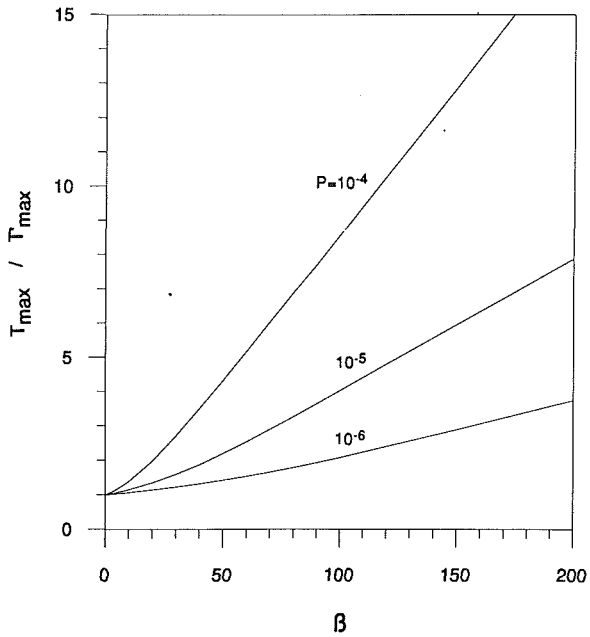


Fig. 2 T_{max}/T'_{max} versus β for different loads P

$$\Delta_k(r) = \begin{cases} 1, & r_{k-1} < r < r_k \\ 0, & \text{otherwise} \end{cases}$$

in which

$$r_k = \left(\frac{k}{n}\right) a$$

where a is the radius of contact area and n is the number of elements.

Define the influence coefficients C_{ij} as the displacement at r_i due to the pressure element $\Delta_j(r)$. Then the displacement u_i at point r_i is

$$u_i = \sum_{k=1}^{n} a_k C_{ik},$$

and Eq. (6) reduces to

$$\sum_{k=1}^{n} C_{ik} a_k = D - \frac{r_i^2}{2} \tag{16}$$

where

$$r_i = \left(\frac{i - \frac{1}{2}}{n}\right) a, \quad i = 1, 2, \ldots, n.$$

Now we have n equations for $n + 2$ unknowns, a, D, and a_k. The other two equations are from total load equilibrium and continuity of pressure, i.e.,

$$2\pi \int_0^a p(r) r dr = P,$$

and

$$p(a) = 0.$$

Substituting (15) into the above equations we obtain

$$\sum_{k=1}^{n} \frac{2\pi r_k}{n} a_k = P, \tag{17}$$

$$a_n = 0. \tag{18}$$

The pressure, $p(r)$, radius of contact area, a, and indentation, D, can be found by solving (16)–(18).

The formulae for the C_{ij}'s are given in the Appendix.

Results and Discussion

First, the relations between the radius of the contact area, the indentation, and the moving velocity for a given load are found. Then, the effects of the thermal deformation on the maximum and average surface temperatures are investigated.

Figure 1 is obtained from solving (7) subject to (9) and it shows the relation between the radius of contact area and velocity for different total loads. We see that the contact radius decreases rapidly as velocity (or β) increases. For a given load, $a\beta$ approaches a constant value as β increases to infinity.

$$a\beta \to 0. \text{ as } \beta \to \infty$$

or

$$a\left(\frac{E\alpha\mu V}{2(1+\nu)k}\right) \to 2.0.$$

This numerical result is in close agreement with that of Barber's (1976) limit value 2.0332. In fact, the curves in Fig. 1 can be put into a single curve by using different dimensionless forms as Barber (1976) does. We prefer to display the solution as shown in Fig. 1 because it is more convenient to obtain the contact area for a given load and velocity.

To check the influence of the thermal deformation on the surface temperature we compare the maximum surface temperature obtained, including the effect of thermal deformation, with that obtained without considering the thermal deformation effect. The maximum surface temperature occurs at the origin as seen in Eq. (11). Replacing the pressure field and contact radius in (11) by results from the Hertz contact solution, we can obtain an approximate maximum temperature T'_{max}. The ratio T_{max}/T'_{max} reveals the effect of the thermal deformation. Figure 2 shows T_{max}/T'_{max} versus velocity for fixed values of total load. This ratio is always greater than one as expected. As the velocity increases (increasing β), this ratio increases monotonically. Therefore, using the Hertz contact solution in the integral equation may cause large error in contact temperature.

Usually, what is measured in the laboratory is the average temperature over the contact area. If we check the relation between T_{ave}/T'_{ave} and velocity, we will find it is similar to that between T_{max}/T'_{max} and velocity. So, in conclusion, we cannot always neglect the effect of thermal deformation when calculating interface temperature.

Downloaded 03 May 2010 to 171.66.16.247. Redistribution subject to ASME license or copyright; see http://www.asme.org/terms/Terms_Use.cfm

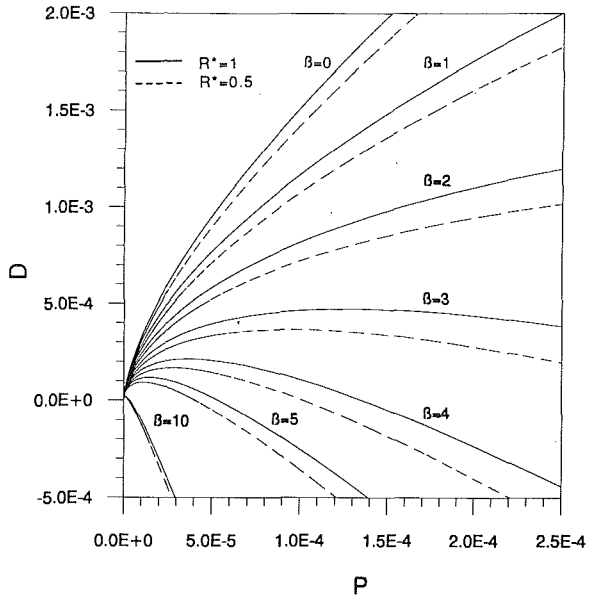


Fig. 3 Relation between indentation D and load P for different velocities β

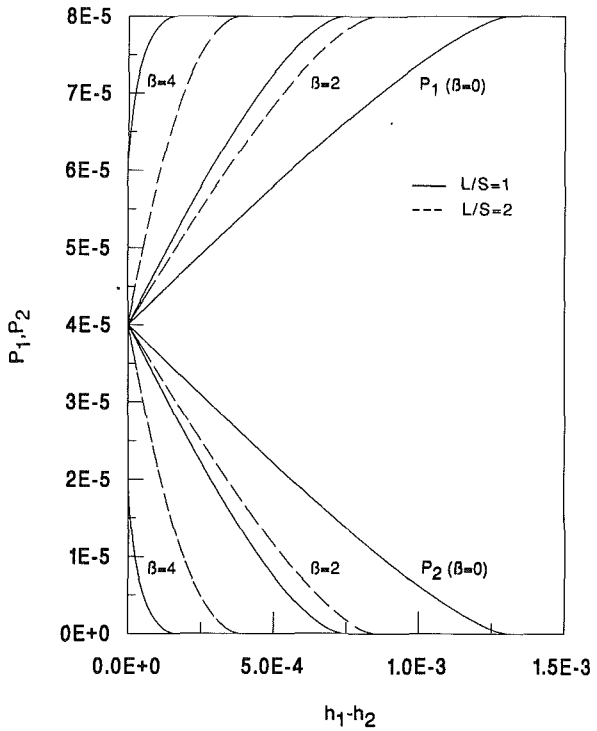


Fig. 4 Load distribution P_1, P_2 versus initial height difference $h_1 - h_2$, for different velocities β

The reduction of contact area is due to thermoelastic instability. Barber's (1969) explanation of thermoelastic instability is as follows. Any nonuniform loading over the surface causes a corresponding nonuniform heat generation and the temperature will reach its maximum value in the region of highest loading. These regions of high temperature will therefore expand more than their surroundings. So the load will transfer more to the originally higher parts.

To study the load partition between asperities, we must know the relation between load and indentation for a single asperity. As shown in Eq. (4), the displacement caused by a point heat source varies logarithmically with distance. Thus, we cannot take the point at infinity as reference point. That means the indentation depends on the choice of reference distance. However, the qualitative nature of the load-indentation curves do not change with reference length. Figure 3 shows the relation between indentation and total load for different values of β with $R^* = 1$ and 0.5. We see that, for a given load, the indentation decreases as velocity increases. That means the more heat flux an asperity takes, the more it will expand. Also we see that for fixed β there is a load above which increasing the load causes the surfaces to separate.

Now let us consider a two-asperity model. Two asperities with initial heights, h_1, h_2, support a total load P_0. The loads on the asperities are P_1 and P_2, respectively. The indentation of asperity 1 under load P_1 alone is D_1 and that of asperity 2 under load P_2 alone is D_2. What we are concerned with here is the difference between the displacements of the two asperities, so the choice of datum point is not important. However, the interaction between the two asperities cannot be neglected because the logarithm function is unbounded. Let the distance between the two asperities be S. The displacement at asperity 1 due to the heat at asperity 2 is $-\beta P_2 \log(L/S)$. Similarly, the displacement at asperity 2 due to the heat at asperity 1 is $-\beta P_1 \log(L/S)$. From equilibrium and compatibility conditions, we have

$$P_1 + P_2 = P_0$$

$$h_1 - h_2 = D_1 - D_2 + \beta(P_1 - P_2)\log(L/S).$$

The relation between P_i and D_i is given as (7), (8). The load partition P_1, P_2, can be found by solving the above equations. Figure 4 shows P_1, P_2 versus $h_1 - h_2$ for $P_0 = 8 \times 10^{-5}$ at different β's, where the solid lines are for $L/S = 1$ and the dashed lines are for $L/S = 2$. The load distribution at $\beta = 0$ does not depend on the reference length. Since the qualitative properties for the two reference lengths are the same, it is sufficient to consider the case $L/S = 1$. When $\beta = 0$, $P_2 = 0$, for $h_1 - h_2 > 1.27 \times 10^{-3}$. That is, when the initial height difference is larger than 1.27×10^{-3}, all the load will be carried by the higher asperity. On the other hand, when the initial height difference is less than 1.27×10^{-3}, the load will distribute between these two asperities. For $\beta = 4$, the corresponding value of $h_1 - h_2$ is 0.14×10^{-3}, which is less than that for $\beta = 0$.

Assume two asperities with initial height difference $h_1 - h_2 = 0.8 \times 10^{-3}$ are put in contact with a smooth slider with a load of 8×10^{-5}. Initially, both asperities are in contact with the slider. Then the slider starts to move with velocity $\beta = 4$ and reaches steady state. Since $0.8 \times 10^{-3} > 0.14 \times 10^{-3}$ according to Fig. 4, all the load will be carried by the higher asperity. Generalizing to multiple asperity contact, this means that frictional sliding transfers the load to the highest asperities, which accelerates their failure.

Conclusion

In this study, the effects of thermal deformation on contact area, surface temperature, and indentation are examined by considering a spherical asperity sliding on the surface of a semi-infinite solid. By using appropriate Green's functions we derive the integral equation for the contact pressure. The "traction element" method is used to solve the integral equation. The temperature field is obtained by treating the sliding asperity as a distributed heat source. The effects of thermal deformation are described as follows:

- The contact area decreases as sliding velocity increases. The product of contact radius and velocity approaches a limiting value as velocity increases.
- The contact temperature obtained by including the thermal deformation effect is much higher than that without considering it. So it is inappropriate to approximate the real contact area and pressure by those from the Hertz contact solution.

Downloaded 03 May 2010 to 171.66.16.247. Redistribution subject to ASME license or copyright; see http://www.asme.org/terms/Terms_Use.cfm

• The indentation for a given load decreases as velocity increase. By examining a two asperity model, we find that the load is transferred more to the higher asperity; and therefore for multiple asperity contact, the number of contact asperities decreases as velocity increases.

Acknowledgment

This work was supported by the Computer Mechanics Laboratory. C. J. Lu also gratefully acknowledges support by an IBM Predoctoral Fellowship. The authors would also like to acknowledge helpful comments and suggestions by one of the reviewers.

References

Archard, J. F., 1959, "The Temperature of Rubbing Surfaces," *Wear*, pp. 438–455.

Barber, J. R., 1969, "Thermoelastic Instabilities in the Sliding of Conforming Solids," *Proceedings of the Royal Society of London*, Vol. A312, pp. 381–394.

Barber, J. R., 1971a, "Distortion of the Semi-Infinite Solid Due to Transient Surface Heating," *International Journal of Mechanics and Science*, Vol. 14, pp. 377–393.

Barber, J. R., 1971b, "The Solution of Heated Punch Problems by Point Source Methods," *International Journal of Engineering Science*, Vol. 9, pp. 1165–1170.

Barber, J. R., 1976, "Some Thermoelastic Contact Problems Involving Frictional Heating," *Quarterly Journal of Mechanics and Applied Mathematics*, Vol. 29, pp. 1–13.

Barber, J. R., 1984, "Thermoelastic Displacements and Stresses Due to a Heat Source Moving Over the Surface of a Half-Plane," ASME JOURNAL OF APPLIED MECHANICS, Vol. 51, pp. 636–640.

Bhushan, B., 1987, "Magnetic Head-Media Interface Temperatures," ASME *Journal of Tribology*, Vol. 109, pp. 243–251.

Bowden, F. P., and Tabor, D., 1950, *Friction and Lubrication of Solids*, Oxford University Press, London, U.K.

Burton, R. A., 1980, "Thermal Deformation in Fractionally Heated Contact," *Wear*, Vol. 59, pp. 1–20.

Burton, R. A., and Nerlikar, V., 1975, "Large Disturbance Solution for Initially Flat Frictionally Heated Thermoelastically Deformed Surfaces," ASME *Journal of Lubrication Technology*, Vol. 97, pp. 546–551.

Carslaw, H. S., and Jaeger, J. C., 1980, *Conduction of Heat in Solids*, Oxford University Press, Oxford, U.K.

Griffioen, J. A., Bair, S., and Winer, W. O., 1985, "Infrared Surface Temperature Measurements in s Sliding Ceramic-Ceramic Contact," *Mechanism and Surface Distress*, D. Dowson, ed. Butterworths, Boston, pp. 238–245.

Johnson, K. L., 1985, *Contact Mechanics*, Cambridge University Press, Cambridge, U.K.

Lingard, S., 1984, "Estimation of Flash Temperature in Dry Sliding," *Proceedings, Institution of Mechanical Engineers*, Vol. 198C, pp. 91–97.

Parkus, H., 1968, *Thermoelasticity*, Springer-Verlag, New York.

Phipps, P. B. P., 1990, "Measurements of the Wear of a Thin Film Disk," *IEEE Transactions on Magnetics*, Vol. 26, No. 5, pp. 2496–2498.

Timoshenko, S. P., and Goodier, J. N., 1970, *Theory of Elasticity*, McGraw-Hill, New York.

Ting, B.-Y., and Winer, W. O., 1989, "Friction-Induced Thermal Influences in Elastic Contact Between Spherical Asperities," ASME *Journal of Tribology*, Vol. 111, pp. 315–322.

APPENDIX

Derivation of Influence Coefficients C_{ij}.

C_{ij} can be divided into two parts, C_{ij}^p and C_{ij}^q, where C_{ij}^p and C_{ij}^q are the displacements at r_i due to a pressure element Δ_j^p and heat source element Δ_j^q, respectively.

From Eq. (3), the displacement due to a pressure element Δ_j is

$$u(r)=\frac{4(1-\nu^2)}{\pi E}\int_{s_{j-1}}^{s_j} K_p(r,s)\,ds.$$

For convenience, $K_p(r,s)$ is written in the form

$$k_p(r,s)=\begin{cases}\dfrac{s}{r}\,k\left(\dfrac{s}{r}\right), & s<r<a\\[2ex] \mathrm{k}\left(\dfrac{r}{s}\right), & 0<r<s\end{cases}$$

and

$$S_j=\left(\frac{j}{n}\right)a.$$

Choosing

$$r_i=\left(i-\frac{1}{2}\right)\left(\frac{a}{n}\right),\quad i=1,\,2,\,\ldots,\,n$$

and using

$$\int\frac{K(k)}{k^2}\,dk=-\frac{E(k)}{k},$$

$$\int kK(k)dk=E(k)-k'^2K(k),$$

where $E(k)$ is the complete elliptic integral of the second kind, and

$$k'=\sqrt{1-k^2}.$$

We can get

$$C_{ij}^p=\begin{cases} S_jE\left(\dfrac{r_i}{S_j}\right)-S_{j-1}E\left(\dfrac{r_i}{S_{j-1}}\right), & i<j,\\[2ex] r_i\left[E\left(\dfrac{S_j}{r_i}\right)-\left(1-\dfrac{S_j^2}{r_i^2}\right)K\left(\dfrac{S_j}{r_i}\right)\right.\\ \left.-E\left(\dfrac{S_{j-1}}{R_r}\right)+\left(1-\dfrac{S_j^2}{r_i^2}\right)K\left(\dfrac{S_{j-1}}{r_i}\right)\right], & i>j,\\[2ex] S_jE\left(\dfrac{r_i}{S_j}\right)-r_iE\left(\dfrac{S_{j-1}}{r_i}\right)+r_i\left(1-\dfrac{S_{j-1}^2}{r_i^2}\right)K\left(\dfrac{S_{j-1}}{r_i}\right), & i=j.\end{cases}$$

Similarly,

$$C_{ij}^q=\begin{cases}\dfrac{S_j^2}{2}\log S_j-\dfrac{S_j^2}{4}-\dfrac{S_{j-1}^2}{2}\log S_{j-1}+\dfrac{S_{j-1}^2}{4}, & i<j,\\[2ex] \log r_i(S_j^2-S_{j-1}^2), & i>j,\\[2ex] \dfrac{r_i^2}{2}-\dfrac{S_j^2}{2}+S_j^2\log S_j-S_{j-1}^2\log r_i, & i=j.\end{cases}$$

Downloaded 03 May 2010 to 171.66.16.247. Redistribution subject to ASME license or copyright; see http://www.asme.org/terms/Terms_Use.cfm

Hisao Hasegawa
Professor,
Department of Mechanical Engineering,
Meiji University,
Tama-ku, Kawasaki, 214 Japan

Ven-Gen Lee
Graduate Student.

Toshio Mura
Professor,
Fellow ASME.

Department of Civil Engineering,
Northwestern University,
Evanston, IL 60208

The Stress Fields Caused by a Circular Cylindrical Inclusion

Exact solutions are presented in closed forms for the axisymmetric stress and displacement fields caused by a solid or hollow circular cylindrical inclusion (with uniform axial eigenstrain prescribed) in an infinite elastic solid. The same expressions are obtained for the elastic fields for interior and exterior points of the inclusion. Although Eshelby's solutions for ellipsoidal inclusions are uniform in the interior points, the present solutions do not show the uniformity. When the length of inclusion becomes infinite, the present solutions agree with Eshelby's results. The strain energy is also shown. The method of Green's function is used.

1 Introduction

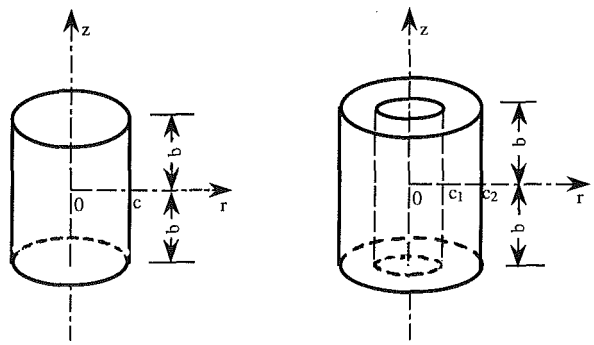
In the theory of micromechanics of materials (Mura, 1982), when an eigenstrain is prescribed in a finite region in a homogeneous material, the finite region is called an inclusion. The elastic moduli of the inclusion are assumed to be the same as the matrix. If the finite region has elastic moduli different from those of the matrix, the region is called an inhomogeneity. Defects raise stress concentrations. The theory of inclusions has been successfully applied to composite materials including fiber, precipitate, and martensite problems. A review of inclusion problems has been given by Mura (1982, 1988). However, many results are not expressed in explicit form but are in the form of numerical solutions.

A problem of an ellipsoidal inclusion with thermal expansion stress-free transformation strains in an isotropic infinite body was solved by Goodier (1937). For more general eigenstrains in an ellipsoidal inclusion, Eshelby (1957, 1959, 1961) derived analytically the uniform stress fields for the interior points, but the stress fields for the exterior points are not given in explicit forms. Although Chiu (1977) has shown the solution for a cuboidal inclusion by using Fourier transform, most of the works have been done for ellipsoidal inclusions. Takao et al. (1981) also investigated the problem of cylindrical inclusion due to uniform axial eigenstrain, but they obtained the closed-form solution for a stress and strain field only along the cylindrical axis ($x_1 = 0$). This paper establishes the closed-form solutions for the axisymmetric elastic fields due to a solid or hollow circular cylindrical inclusion with uniform eigenstrain prescribed in an isotropic infinite solid. The present results are compared with previous studies. The strain energy in the cylindrical inclusion is also shown.

It is well known (Mura, 1982) that the stress fields caused by an inclusion can be obtained by using Green's functions for body force problems. Therefore, in order to obtain the solution for a cylindrical inclusion mentioned above, we apply the stress functions (Hasegawa, 1975, 1976) for axisymmetric body force problems of elasticity. That is, we present a method of solution for axisymmetric inclusion problems by using Green's functions (Hasegawa et al., 1991) for axisymmetric body force problems.

2 Definition of the Problem

We consider a solid circular cylindrical inclusion with length $2b$ and radius, c, or a hollow circular cylindrical inclusion with inner and outer radii c_1 and c_2, in an isotropic infinite solid as shown in Fig. 1. Cylindrical coordinates (r, θ, z) or $(i =$



(a) Solid cylindrical inclusion (b) Hollow cylindrical inclusion

Fig. 1 Geometry of inclusions in cylindrical coordinates

Contributed by the Applied Mechanics Division of THE AMERICAN SOCIETY OF MECHANICAL ENGINEERS for presentation at the Winter Annual Meeting, Atlanta, Ga., Dec. 1-6, 1991.

Discussion on this paper should be addressed to the Technical Editor, Prof. Leon M. Keer, The Technological Institute, Northwestern University, Evanston, IL 60208, and will be accepted until two months after final publication of the paper itself in the JOURNAL OF APPLIED MECHANICS. Manuscript received by the ASME Applied Mechanics Division, Jan. 8, 1991; final revision, Mar. 27, 1991.
Paper No. 91-WA/APM-32.

Copyright © 1992 by ASME
Downloaded 03 May 2010 to 171.66.16.247. Redistribution subject to ASME license or copyright; see http://www.asme.org/terms/Terms_Use.cfm

1, 2, 3) are used, and the eigenstrain is assumed to be constant inside the inclusions as follows:

(i) for a solid cylindrical inclusion

$$\epsilon_z^* = \epsilon_0[S(z+b) - S(z-b)][1 - S(r-c)] \tag{1}$$

(ii) for a hollow cylindrical inclusion

$$\epsilon_z^* = \epsilon_0[S(z+b) - S(z-b)][S(r-c_1) - S(r-c_2)] \tag{2}$$

where $S(\ )$ is a Heaviside step function and ϵ_0 is the magnitude of the eigenstrain. It is well known that displacements $u_i(r, z)$, due to eigenstrains $\epsilon_{ij}^*(r, z)$, satisfy the fundamental equations

$$\mu\left(\nabla^2 - \frac{1}{r^2}\right)u_i + \mu\delta_{3i}\frac{u_i}{r^2} + (\lambda+\mu)\mathrm{grad}_i\mathrm{div}U + F_i = f_i \tag{3}$$

with

$$f_1 = \frac{2\mu}{r}\frac{\partial}{\partial r}[r(\epsilon_r^* - \epsilon_\theta^*)] + \lambda\frac{\partial}{\partial r}(\epsilon_r^* + \epsilon_z^*) + (\lambda+2\mu)\frac{\partial}{\partial r}\epsilon_\theta^* + \mu\frac{\partial}{\partial z}\gamma_{rz}^*,$$

$$f_2 = \mu\left(\frac{\partial}{\partial r}\gamma_{r\theta}^* + \frac{\partial}{\partial z}\gamma_{z\theta}^* + \frac{2}{r}\gamma_{r\theta}^*\right),$$

$$f_3 = \lambda\frac{\partial}{\partial z}(\epsilon_r^* + \epsilon_\theta^*) + (\lambda+2\mu)\frac{\partial}{\partial z}\epsilon_z^* + \frac{\mu}{r}\frac{\partial}{\partial r}(r\gamma_{rz}^*) \tag{4}$$

where $F_i(r, z)$ are body forces, U is a displacement vector with the components u_i, λ and μ are the Lame's constants, δ_{ij} is the Kronecker's delta, and $\gamma_{ij}^* = 2\epsilon_{ij}^*$, $(i \neq j)$.

3 Method of Solution

3.1 Green's Functions. For eigenstrain problems, the Kelvin's solutions for a point force have been widely used (Mura, 1982). However, for the present problem, it is convenient to use Green's functions (Hasegawa et al., 1991) for axisymmetric body force problems of elasticity. The Green's functions are defined as the solution for the problem of an infinite elastic solid subjected to the axisymmetric body force

$$F_i = \frac{1}{2\pi r}\delta(r-a)\delta(z-h) \tag{5}$$

distributed on the circle (r = a, z = h) as shown in Fig. 2 where $\delta(\ )$ is a Dirac delta function and F_1, F_2, and F_3 are a radial force, a torsional force and an axial force, respectively. We represent the Green's functions by $u_i^k(r, z, a, h)$ for displacements and $\sigma_{ij}^k(r, z, a, h)$ for stresses. Here u_i^k denotes the displacement component in i-direction at a point (r, z) when a unit ring force in the k-direction acts along a circle (a, h) of radius a.

It was shown in previous papers (Hasegawa, 1975, 1976) that the axisymmetric displacements caused by axisymmetric distribution of body force are expressed by

$$2\mu u_i = 2(1-\nu)\left(\nabla^2 - \frac{1}{r^2} + \delta_{3i}\frac{1}{r^2}\right)\phi_i - \mathrm{grad}_i\mathrm{div}\phi \tag{6}$$

where

$$\phi_i = \phi_{ic} + \phi_{is}, \quad (i = 1,2,3) \tag{7}$$

are stress functions for body force problems of elasticity and are expressed by

$$\begin{Bmatrix}\phi_{ic}\\ \phi_{is}\end{Bmatrix} = \frac{-1}{\pi(1-\nu)}\int_0^\infty\int_0^\infty \frac{\alpha J_n(\alpha r)}{(\alpha^2+\beta^2)^2}\begin{Bmatrix}\overline{F_{ic}}\cos(\beta z)\\ \overline{F_{is}}\sin(\beta z)\end{Bmatrix}d\alpha d\beta \tag{8}$$

where

$$\begin{Bmatrix}\overline{F_{ic}}\\ \overline{F_{is}}\end{Bmatrix} = \int_{-\infty}^{\infty}\int_0^\infty rF_i(r,z)J_n(\alpha r)\begin{Bmatrix}\cos(\beta z)\\ \sin(\beta z)\end{Bmatrix}drdz. \tag{9}$$

In these expressions, ν is the Poisson's ratio, ϕ is a vector with the components ϕ_i, and $J_n(\alpha r)$ is a Bessel function of the first kind of the order n. In this case we take $n = 1$ for $i = 1, 2$, and $n = 0$ for $i = 3$.

From (1), (2), and (4), we see that $F_2 = 0$ and $u_2 = 0$. By (5) and (9), we have

$$\begin{Bmatrix}\overline{F_{ic}}\\ \overline{F_{is}}\end{Bmatrix} = \frac{1}{2\pi}J_n(\alpha a)\begin{Bmatrix}\cos(\beta h)\\ \sin(\beta h)\end{Bmatrix}, \quad (i = 1.3). \tag{10}$$

Substituting (7) into (6) yields

$$2\mu u_i^k = u_{ic}^k + u_{is}^k, \quad (i,k = 1,3) \tag{11}$$

with

$$u_{1c}^1 = \frac{1}{\pi(1-\nu)}\int_0^\infty\int_0^\infty \overline{F_{1c}}\alpha J_1(\alpha r)\left\{\frac{2(1-\nu)}{\alpha^2+\beta^2} - \frac{\alpha^2}{(\alpha^2+\beta^2)^2}\right\}\cos(\beta z)d\alpha d\beta,$$

$$u_{3c}^1 = \frac{-1}{\pi(1-\nu)}\int_0^\infty\int_0^\infty \overline{F_{1c}}J_0(\alpha r)\frac{\alpha^2\beta}{(\alpha^2+\beta^2)^2}\sin(\beta z)d\alpha d\beta,$$

$$u_{1s}^1 = \frac{1}{\pi(1-\nu)}\int_0^\infty\int_0^\infty \overline{F_{1s}}\alpha J_1(\alpha r)\left\{\frac{2(1-\nu)}{\alpha^2+\beta^2} - \frac{\alpha^2}{(\alpha^2+\beta^2)^2}\right\}\sin(\beta z)d\alpha d\beta,$$

$$u_{3s}^1 = \frac{-1}{\pi(1-\nu)}\int_0^\infty\int_0^\infty \overline{F_{1s}}J_0(\alpha r)\frac{\alpha^2\beta}{(\alpha^2+\beta^2)^2}\cos(\beta z)d\alpha d\beta,$$

$$u_{1c}^3 = \frac{1}{\pi(1-\nu)}\int_0^\infty\int_0^\infty \overline{F_{3c}}J_1(\alpha r)\frac{\alpha^2\beta}{(\alpha^2+\beta^2)^2}\sin(\beta z)d\alpha d\beta,$$

$$u_{3c}^3 = \frac{1}{\pi(1-\nu)}\int_0^\infty\int_0^\infty \overline{F_{3c}}\alpha J_0(\alpha r)\left\{\frac{2(1-\nu)}{\alpha^2+\beta^2} - \frac{\beta^2}{(\alpha^2+\beta^2)^2}\right\}\cos(\beta z)d\alpha d\beta,$$

$$u_{1s}^3 = \frac{-1}{\pi(1-\nu)}\int_0^\infty\int_0^\infty \overline{F_{3s}}J_1(\alpha r)\frac{\alpha^2\beta}{(\alpha^2+\beta^2)^2}\cos(\beta z)d\alpha d\beta,$$

$$u_{3s}^3 = \frac{1}{\pi(1-\nu)}\int_0^\infty\int_0^\infty \overline{F_{3s}}\alpha J_0(\alpha r)\left\{\frac{2(1-\nu)}{\alpha^2+\beta^2} - \frac{\beta^2}{(\alpha^2+\beta^2)^2}\right\}\sin(\beta z)d\alpha d\beta, \tag{12}$$

where the superscript k implies that the body force is acting in k-direction. Expressions for the stresses σ_{ij}^k can be obtained from (10) and the Hooke's law.

3.2 Stresses and Displacements due to Eigenstrains. Using Green's functions $u_i^k(r, z, a, h)$ and $\sigma_{ij}^k(r, a, z, h)$, the displacement and stress fields caused by an inclusion can be expressed as

$$\begin{Bmatrix}u_i\\ \sigma_{ij}\end{Bmatrix} = -\int_\Omega \begin{Bmatrix}u_i^k(r, z, a, h)\\ \sigma_{ij}^k(r, z, a, h)\end{Bmatrix}f_k(a, h)d\Omega - \begin{Bmatrix}0\\ \sigma_{ij}^*\end{Bmatrix} \tag{13}$$

with

$$\begin{aligned}\sigma_{ij}^* &= 2\mu\epsilon_{ij}^* + \delta_{ij}\lambda\epsilon_{kk}^*, \quad (\text{in } \Omega),\\ &= 0, \quad (\text{outside of } \Omega)\end{aligned} \tag{14}$$

where Ω is the region of inclusion and $d\Omega$ is a volume element.

From (1), (2), and (4), (13) becomes

$$\begin{Bmatrix}u_i\\ \sigma_{ij}\end{Bmatrix} = -\int_\Omega\left[\lambda\begin{Bmatrix}u_i^1\\ \sigma_{ij}^1\end{Bmatrix}\frac{\partial\epsilon_z^*}{\partial a} + (\lambda+2\mu)\begin{Bmatrix}u_i^3\\ \sigma_{ij}^3\end{Bmatrix}\frac{\partial\epsilon_z^*}{\partial h}\right]d\Omega - \begin{Bmatrix}0\\ \sigma_{ij}^*\end{Bmatrix}. \tag{15}$$

Downloaded 03 May 2010 to 171.66.16.247. Redistribution subject to ASME license or copyright; see http://www.asme.org/terms/Terms_Use.cfm

Equation (15) indicates that there are no terms for u_i^2 and σ_{ij}^2 in the present problem.

4 A Solid Circular Cylindrical Inclusion

4.1 Displacements. Here we show the displacements u_i caused by a solid circular cylindrical inclusion. Substituting (1) into (15) yields

$$u_i = 2\pi c\lambda\epsilon_0 \int_{-b}^{b} u_i^1(r, z, c, h)dh + 2\pi(\lambda+2\mu)\epsilon_0 \int_0^c \{u_i^3(r, z, a, b) - u_i^3(r, z, a, -b)\}ada. \tag{16}$$

Integrating (16) with respect to h and a, we get

$$2\mu u_i = 2\pi c\lambda\epsilon_0 \overline{u}_i^1 + 2\pi c(\lambda+2\mu)\epsilon_0 \overline{u}_i^3 \tag{17}$$

with

$$\overline{u}_1^1 = \frac{1}{\pi^2(1-\nu)} \int_0^\infty \int_0^\infty \frac{\alpha}{\beta} \left\{\frac{2(1-\nu)}{\alpha^2+\beta^2} - \frac{\alpha^2}{(\alpha^2+\beta^2)^2}\right\} \times J_1(\alpha c)J_1(\alpha r)\sin(\beta b)\cos(\beta z)d\alpha d\beta$$

$$\overline{u}_3^1 = \frac{-1}{\pi^2(1-\nu)} \int_0^\infty \int_0^\infty \frac{\alpha^2}{(\alpha^2+\beta^2)^2} \times J_1(\alpha c)J_0(\alpha r)\sin(\beta b)\sin(\beta z)d\alpha d\beta$$

$$\overline{u}_1^3 = \frac{-1}{\pi^2(1-\nu)} \int_0^\infty \int_0^\infty \frac{\alpha\beta}{(\alpha^2+\beta^2)^2} \times J_1(\alpha c)J_1(\alpha r)\sin(\beta b)\cos(\beta z)d\alpha d\beta$$

$$\overline{u}_3^3 = \frac{1}{\pi^2(1-\nu)} \int_0^\infty \int_0^\infty \left\{\frac{1-2\nu}{\alpha^2+\beta^2} + \frac{\alpha^2}{\alpha^2+\beta^2}\right\} \times J_1(\alpha c)J_0(\alpha r)\sin(\beta b)\sin(\beta z)d\alpha d\beta. \tag{18}$$

Integrating (18), by using integral formulas (Erdelyi, 1954; Eason et al., 1955; Abramowitz and Stegun, 1972; Okuni, 1974), we obtain

$$\overline{u}_j^k = \frac{1}{D}\sum_{i=1}^{2} (-1)^i \overline{\overline{u}}_j^k \tag{19}$$

with

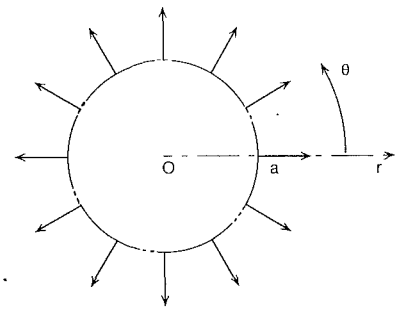
$$\overline{\overline{u}}_1^1 = z_i\left[2(1-\nu)Q_{1/2}(x_i) + \frac{1-2\nu}{2cr}\{(c^2+r^2)Q_{-1/2}(x_i) - (c-r)^2 k'\Pi(p,k')\}\right].$$

$$\overline{\overline{u}}_3^1 = cQ_{-1/2}(x_i) - rQ_{1/2}(x_i),$$

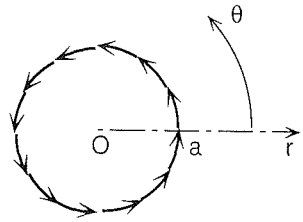
$$\overline{\overline{u}}_1^3 = -z_iQ_{1/2}(x_i),$$

$$\overline{\overline{u}}_3^3 = (3-4\nu)\{rQ_{1/2}(x_i) - cQ_{-1/2}(x_i)\} - \frac{(1-2\nu)z_i^2}{c}\left\{Q_{-1/2}(x_i) + \frac{c-r}{c+r}k'\Pi(p,k')\right\} + \frac{(1-2\nu)\pi\sqrt{cr}|z_i|}{c}\{1+SGN(c-r)\} \tag{20}$$

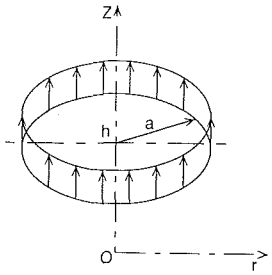
where $Q_n(x_i)$ is a Legendre function of the second kind of order n, and $SGN(c-r)$ is $+1$, 0, or -1 according to positive, zero, or negative value for $(c-r)$. Also, $\Pi(p, k')$ is a complete elliptic integral of the third kind and



(a) A radial force



(b) A torsional force



(c)An axial force

Fig. 2 The body force acting on a circle

$$z_1 = z-b,\ z_2 = z+b,$$
$$x_i = \frac{r^2+c^2+z_i^2}{2cr},$$
$$D = 8\pi^2\sqrt{cr}(1-\nu),$$
$$p = \frac{4cr}{(c+r)^2},\ k'^2 = \frac{4cr}{(c+r)^2+z_i^2}. \tag{21}$$

From the foregoing results, (17) becomes

$$2\mu u_j = \frac{\mu c\epsilon_0}{2\pi\sqrt{cr}(1-\nu)(1-2\nu)}\sum_{i=1}^{2}(-1)^i\{\nu\overline{\overline{u}}_j^1 + (1-\nu)\overline{\overline{u}}_j^3\}. \tag{22}$$

The detail of this technique is given in the Appendix.

4.2 Stresses. Here we show the stresses σ_{ij} caused by a solid circular cylindrical inclusion. Substituting (1) into (15), we get

$$\sigma_{ij} = 2\pi c\lambda\epsilon_0 \int_{-b}^{b} \sigma_{ij}^1(r, z, c, h)dh + 2\pi(\lambda+2\mu)\epsilon_0 \times \int_0^c \{\sigma_{ij}^3(r, z, a, b) - \sigma_{ij}^3(r, z, a, -b)\}ada - \sigma_{ij}^*. \tag{23}$$

Integrating (23) with respect to h and a yields

$$\sigma_{ij} = 2\pi c\lambda\epsilon_0\overline{\sigma}_{ij}^1 + 2\pi c(\lambda+2\mu)\epsilon_0\overline{\sigma}_{ij}^3 - \sigma_{ij}^* \tag{24}$$

with

Downloaded 03 May 2010 to 171.66.16.247. Redistribution subject to ASME license or copyright; see http://www.asme.org/terms/Terms_Use.cfm

$$\overline{\sigma_r}^1=\frac{1}{\pi^2(1-\nu)}\int_0^\infty\int_0^\infty\frac{\alpha}{\beta}J_1(\alpha c)\left[\alpha J_0(\alpha r)\left\{\frac{1-\nu}{\alpha^2+\beta^2}+\frac{\beta^2}{(\alpha^2+\beta^2)^2}\right\}-\frac{J_1(\alpha r)}{r}\left\{\frac{1-2\nu}{\alpha^2+\beta^2}+\frac{\beta^2}{(\alpha^2+\beta^2)^2}\right\}\right]\sin(\beta b)\cos(\beta z)\,d\alpha d\beta,$$

$$\overline{\sigma_\theta}^1=\frac{1}{\pi^2(1-\nu)}\int_0^\infty\int_0^\infty\frac{\alpha}{\beta}J_1(\alpha c)\left[\frac{J_1(\alpha r)}{r}\left\{\frac{1-2\nu}{\alpha^2+\beta^2}+\frac{\beta^2}{(\alpha^2+\beta^2)^2}\right\}+\nu J_0(\alpha r)\frac{\alpha}{\alpha^2+\beta^2}\right]\sin(\beta b)\cos(\beta z)\,d\alpha d\beta,$$

$$\overline{\sigma_z}^1=\frac{1}{\pi^2(1-\nu)}\int_0^\infty\int_0^\infty\frac{\alpha^2}{\beta}J_1(\alpha c)J_0(\alpha r)\left\{\frac{\alpha^2}{(\alpha^2+\beta^2)^2}-\frac{1-\nu}{\alpha^2+\beta^2}\right\}\sin(\beta b)\cos(\beta z)\,d\alpha d\beta,$$

$$\overline{\tau_{rz}}^1=\frac{1}{\pi^2(1-\nu)}\int_0^\infty\int_0^\infty\alpha J_1(\alpha c)J_1(\alpha r)\left\{\frac{\alpha^2}{(\alpha^2+\beta^2)^2}-\frac{1-\nu}{\alpha^2+\beta^2}\right\}\sin(\beta b)\sin(\beta z)\,d\alpha d\beta,$$

$$\overline{\sigma_r}^3=\frac{1}{\pi^2(1-\nu)}\int_0^\infty\int_0^\infty\beta J_1(\alpha c)\left[J_0(\alpha r)\left\{\frac{\nu}{\alpha^2+\beta^2}-\frac{\alpha^2}{(\alpha^2+\beta^2)^2}\right\}+\frac{J_1(\alpha r)}{r}\frac{\alpha}{(\alpha^2+\beta^2)^2}\right]\sin(\beta b)\cos(\beta z)\,d\alpha d\beta,$$

$$\overline{\sigma_\theta}^3=\frac{1}{\pi^2(1-\nu)}\int_0^\infty\int_0^\infty\beta J_1(\alpha c)\left\{\nu J_0(\alpha r)\frac{1}{\alpha^2+\beta^2}-\frac{J_1(\alpha r)}{r}\frac{\alpha}{(\alpha^2+\beta^2)^2}\right\}\sin(\beta b)\cos(\beta b)\,d\alpha d\beta,$$

$$\overline{\sigma_z}^3=\frac{1}{\pi^2(1-\nu)}\int_0^\infty\int_0^\infty\beta J_1(\alpha c)J_0(\alpha r)\left\{\frac{\alpha^2}{(\alpha^2+\beta^2)^2}+\frac{1-\nu}{\alpha^2+\beta^2}\right\}\sin(\beta b)\cos(\beta z)\,d\alpha d\beta,$$

$$\overline{\tau_{rz}}^3=\frac{1}{\pi^2(1-\nu)}\int_0^\infty\int_0^\infty\alpha J_1(\alpha c)J_1(\alpha r)\left\{\frac{\nu}{\alpha^2+\beta^2}-\frac{\alpha^2}{(\alpha^2+\beta^2)^2}\right\}\sin(\beta b)\sin(\beta z)\,d\alpha d\beta. \quad (25)$$

In the present problem, it holds always that $\tau_{r\theta}=\tau_{z\theta}=0$.

Integrals in (25) can be performed by using integral formulas (Erdelyi, 1954; Eason et al., 1955; Abramowitz and Stegun, 1972; Okuni, 1974) as follows:

$$\overline{\sigma}^k_{mn}=\frac{1}{2D}\sum_{i=1}^{2}(-1)^i\overline{\overline{\sigma}}^k_{mn}+\delta_{3k}\sigma^0_{mn} \quad (26)$$

with

$$\overline{\overline{\sigma_r}}^1=\frac{-z_i}{r}\left[(3-4\nu)Q_{1/2}(x_i)-\frac{r^2-(1-2\nu)c^2}{cr}Q_{-1/2}(x_i)+\frac{x_i-r/c}{x_i^2-1}G_1(x_i)-\left\{2(1-\nu)\frac{r}{c}\frac{c-r}{c+r}+(1-2\nu)\frac{(c-r)^2}{cr}\right\}k'\Pi(p,k')\right],$$

$$\overline{\overline{\sigma_\theta}}^1=\frac{z_i}{r}\left[4(1-\nu)Q_{1/2}(x_i)+\frac{r^2+(1-2\nu)c^2}{cr}Q_{-1/2}(x_i)+\left\{2\nu\frac{r}{c}\frac{c-r}{c+r}-(1-2\nu)\frac{(c-r)^2}{cr}\right\}k'\Pi(p,k')\right],$$

$$\overline{\overline{\sigma_z}}^1=\frac{z_i}{r}\left[2\nu\frac{r}{c}\left\{Q_{-1/2}(x_i)+\frac{c-r}{c+r}k'\Pi(p,k')\right\}-Q_{1/2}(x_i)+\frac{x_i-r/c}{x_i^2-1}G_1(x_i)\right],$$

$$\overline{\overline{\tau_{rz}}}^1=2(1-2\nu)Q_{1/2}(x_i)+\frac{z_i^2}{cr}\frac{1}{x_i^2-1}G_1(x_i),$$

$$\overline{\overline{\sigma_r}}^3=\frac{-z_i}{c}\left[2\nu\left\{Q_{-1/2}(x_i)+\frac{c-r}{c+r}k'\Pi(p,k')\right\}-\frac{c}{r}\left\{Q_{1/2}(x_i)+\frac{x_i-r/c}{x_i^2-1}G_1(x_i)\right\}\right],$$

$$\overline{\overline{\sigma_\theta}}^3=\frac{-2z_i}{c}\left[\frac{c}{r}Q_{1/2}(x_i)+\nu\left\{Q_{-1/2}(x_i)+\frac{c-r}{c+r}k'\Pi(p,k')\right\}\right],$$

$$\overline{\overline{\sigma_z}}^3=\frac{-z_i}{c}\left[2(1-\nu)\left\{Q_{-1/2}(x_i)+\frac{c-r}{c+r}k'\Pi(p,k')\right\}-\frac{c}{r}\left\{Q_{1/2}(x_i)-\frac{x_i-r/c}{x_i^2-1}G_1(x_i)\right\}\right],$$

$$\overline{\overline{\tau_{rz}}}^3=2(1-2\nu)Q_{1/2}(x_i)-\frac{z_i^2}{cr}\frac{1}{x_i^2-1}G_1(x_i) \quad (27)$$

and

$$\sigma^0_r=\sigma^0_\theta=\frac{\nu}{2\pi(1-\nu)},\ \sigma^0_z=\frac{1}{2\pi},\ \tau^0_{rz}=0,\ (\text{in }\Omega)$$
$$\sigma^0_{ij}=0,\qquad (\text{outside of }\Omega) \quad (27)'$$

where

$$G_1(x_i)=x_iQ_{1/2}(x_i)-Q_{-1/2}(x_i). \quad (28)$$

From the foregoing, (24) becomes

$$\sigma_{kl}=\frac{\mu c\epsilon_0}{4\pi\sqrt{cr}(1-\nu)(1-2\nu)}\sum_{i=1}^{2}(-1)^i\{\nu\overline{\overline{\sigma_{kl}}}^1+(1-\nu)\overline{\overline{\sigma_{kl}}}^3\}. \quad (29)$$

5 Hollow Cylindrical Inclusion

This chapter shows the expressions for stresses and displacements caused by a hollow circular cylindrical inclusion in an elastic solid. They are easily obtained by using the results shown above for a solid cylindrical inclusion.

Equation (2), for the eigenstrain distributed in a hollow cylindrical region, can be rearranged as

$$\epsilon^*_z=\sum_{n=1}^{2}(-1)^n\epsilon_0\{S(z+b)-S(z-b)\}\{(1-S(r-c_n)\}. \quad (30)$$

From (30) and (1), it is observed that the stress and displacement fields caused by the hollow cylindrical inclusion can be obtained by a simple superposition of the fields caused by two solid cylindrical inclusions with radius c_1 and c_2, respectively, and are expressed as follows:

$$2\mu u_j=\sum_{n=1}^{2}\left[\frac{\mu c_n\epsilon_0}{2\pi\sqrt{c_nr}(1-\nu)(1-2\nu)}\sum_{i=1}^{2}(-1)^i\{\nu\overline{\overline{u_j}}^1(r,z,c_n,b)-(1-\nu)\overline{\overline{u_j}}^3(r,z,c_n,b)\}\right],$$

Downloaded 03 May 2010 to 171.66.16.247. Redistribution subject to ASME license or copyright; see http://www.asme.org/terms/Terms_Use.cfm

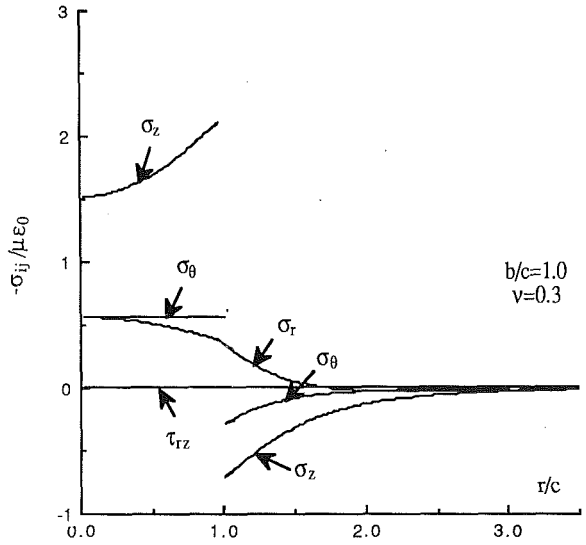


Fig. 3 Variation of normal stresses on the plane $z = 0$

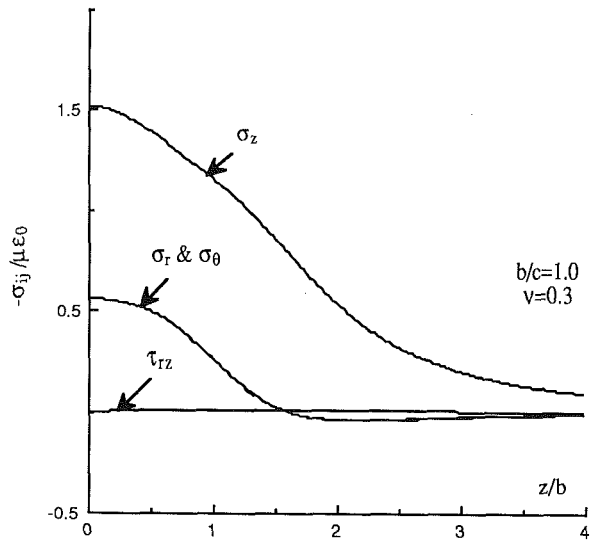


Fig. 4 Variation of normal stresses along the z-axis ($r = 0$)

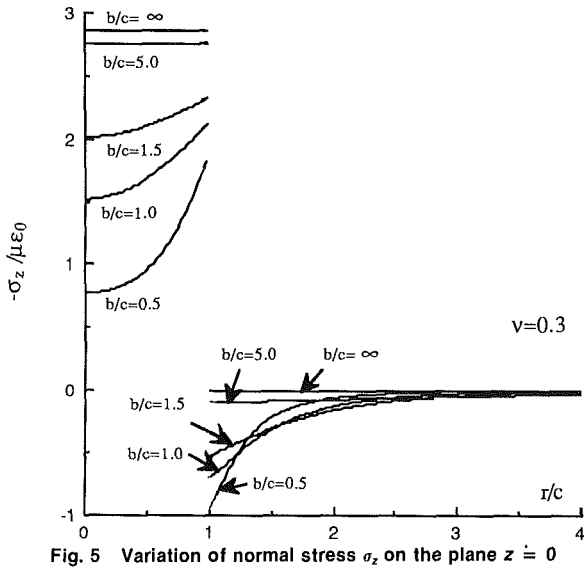


Fig. 5 Variation of normal stress σ_z on the plane $z = 0$

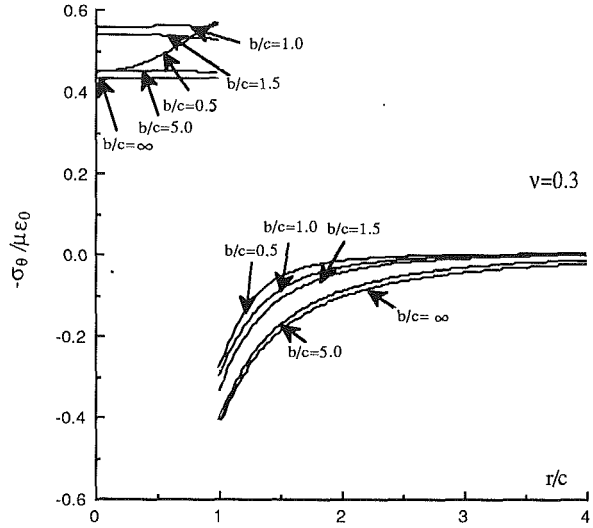


Fig. 6 Variation of normal stress σ_θ on the plane $z = 0$

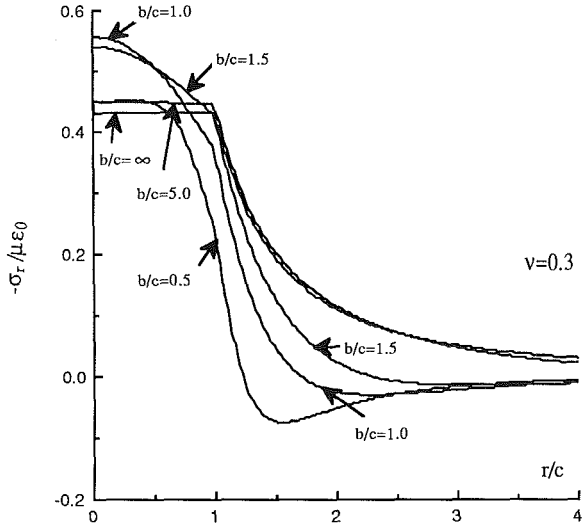


Fig. 7 Variation of normal stress σ_r on the plane $z = 0$

$$\sigma_{kl} = \sum_{n=1}^{2} (-1)^n \left[\frac{\mu c_n \epsilon_0}{4\pi\sqrt{c_n r}(1-\nu)(1-2\nu)} \sum_{i=1}^{2} (-1)^i \{ \nu \overline{\overline{\sigma_{kl}}}^1(r, z, c_n, b) + (1-\nu)\overline{\overline{\sigma_{kl}}}^3(r, z, c_n, b) \} \right]$$

where $\overline{\overline{u_j^k}}$ and $\overline{\overline{\sigma}}_{ij}^k$ are given by of (20) and (27).

6 An Infinite Cylindrical Inclusion

From the results shown above, we can obtain the solution for an infinite cylindrical inclusion ($b \to \infty$). When $b \to \infty$, we have the relation (Byrd and Friedman, 1971)

$$\lim_{b\to\infty} bQ_{1/2}(x) \to 0,$$

$$\lim_{b\to\infty} bQ_{-1/2}(x) \to \pi\sqrt{cr},$$

$$\lim_{b\to\infty} bk'\Pi(p,k')\frac{c-r}{c+r} \to \pi\sqrt{cr}SGN(c-r). \qquad (32)$$

Application of (32) to (22) and (29) yields
(i) for the interior points:

Downloaded 03 May 2010 to 171.66.16.247. Redistribution subject to ASME license or copyright; see http://www.asme.org/terms/Terms_Use.cfm

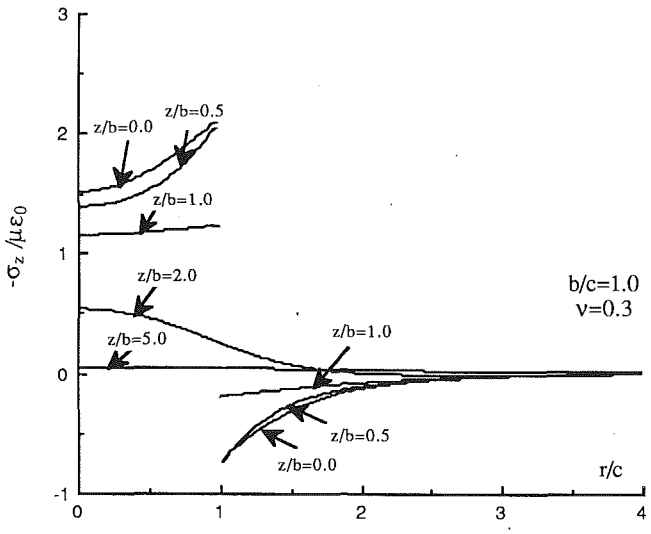


Fig. 8 Variation of normal stress σ_z along the r direction

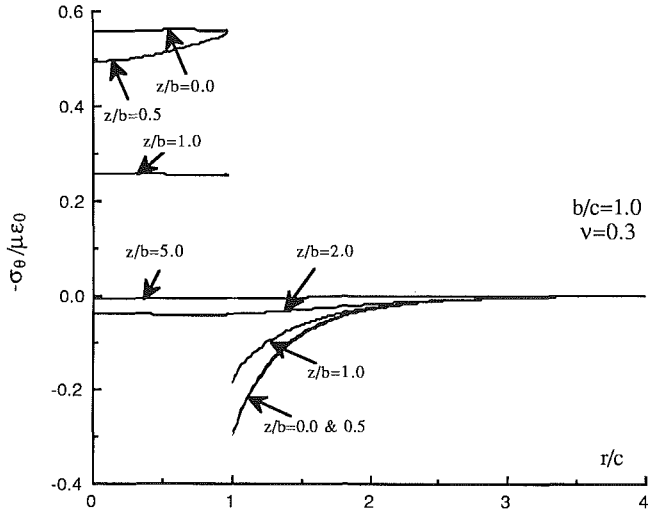


Fig. 9 Variation of normal stress σ_θ along the r direction

$$u_1=\frac{\nu\epsilon_0 cr}{2(1-\nu)},\quad u_2=u_3=0,$$

$$\sigma_r=\sigma_\theta=-\frac{\mu\nu\epsilon_0}{1-\nu},\quad \sigma_z=-\frac{2\mu\epsilon_0}{1-\nu},$$

$$\tau_{rz}=\tau_{r\theta}=\tau_{\theta z}=0. \tag{33}$$

(ii) for the exterior points:

$$u_1=\frac{\nu\epsilon_0 c^2}{2(1-\nu)r},\quad u_2=u_3=0,$$

$$\sigma_r=-\sigma_\theta=-\frac{\mu\nu\epsilon_0}{1-\nu}\frac{c^2}{r^2},$$

$$\sigma_z=\tau_{rz}=\tau_{r\theta}=\tau_{\theta z}=0. \tag{34}$$

Expression (33) for the interior points coincides with Eshelby's solutions.

7 Strain Energy

The stability of microstructures of materials with inclusions can be discussed in terms of the Gibbs free energy which is the elastic strain energy when the material is traction-free (Mura, 1982). Therefore, here we show the strain energy in the solid cylindrical inclusion. The strain energy W^* is expressed by

$$W^*=-\frac{1}{2}\int_\Omega \sigma_{ij}\epsilon_{ij}^* d\Omega \tag{35}$$

where σ_{ij} is the stress is caused by ϵ_{ij}^*.

From (1), (24), and (35), we have

$$W^*=-\pi c\epsilon_0^2\int_{-b}^{b}\int_0^c\{\lambda\bar{\sigma}_z^1+(\lambda+2\mu)\bar{\sigma}_z^3\}d\Omega-\pi bc^2(\lambda+2\mu)\epsilon_0^2. \tag{36}$$

Integrating (36) by using the integral formulae (Erdelyi, 1954; Eason et al., 1955; Byrd and Friedman, 1972), we can obtain

$$W^*=\frac{2\mu c\epsilon_0}{1-\nu}\{(c^2+2b^2)Q_{-1/2}(x)-c^2Q_{1/2}(x)-2c^2\} \tag{37}$$

where

$$x=1+2(b/c)^2. \tag{38}$$

The strain energy $\overline{W^*}$ per unit volume of inclusion is

$$\overline{W^*}=\frac{\mu\epsilon_0^2}{\pi(1-\nu)}\frac{1}{b/c}[\{1+2(b/c)^2\}Q_{-1/2}(x)-Q_{1/2}(x)-2]. \tag{39}$$

For the infinite cylindrical inclusion ($b\to\infty$), $\overline{W^*}$ becomes

$$\overline{W^*}=\frac{\mu\epsilon_0^2}{1-\nu}. \tag{40}$$

8 Discussions and Results

(1) It is seen from the results in Section 5 that the stress field caused by a circular cylindrical inclusion can be expressed by the same expressions for the interior points ($r<c$, $|z|<b$) and the exterior points ($r>c$ or $|z|>b$) of the inclusion, though the calculations were performed to the both cases separately.

(2) It is easily seen from (34) that the stresses and displacements for the exterior points in the infinite cylindrical inclusion are the same as those of an infinite solid with a circular cylindrical hole of radius c subjected to the uniform pressure $p=\mu\nu\epsilon_0/(1-\nu)$. The stress conditions are also the same as those of the uniform distribution of centers of dilatation on the z-axis from $z=-\infty$ to $z=\infty$ in an infinite solid (Hasegawa, 1978).

(3) When $r\to c$ and $|z|\to b$, we have the relations (Byrd and Friedman, 1971)

$$\lim_{r\to c,|z|\to b}\Pi(p,k')\to\text{const.}\frac{c+r}{c-r},$$

$$\lim_{r\to c,|z|\to b}Q_n(x_i)\to\text{const.}\log\{(r-c)^2+z_i^2\}. \tag{41}$$

Therefore, it is observed from (29) and (41) that there is a singularity of the order $\log\{(r-c)^2+z_i^2\}$ at the corners ($r\to c$, $|z|\to b$) of the inclusion for only the shear stress τ_{rz} as shown in Fig. 11. The result is the same as that of Chiu (1977) for a cuboidal inclusion.

(4) Figures 3–11 show the distributions of stresses caused by the inclusion. The figures are sketched in nondimensional form for a constant value of Poisson's ratio $\nu=0.3$. Figures 3 and 4 show the comparison of stress distributions on the symmetry plane ($z=0$) and the z-axis ($r=0$). All the normal stresses are continuous across the boundary ($z=b$) of inclusion and σ_z has the largest value among the stress components.

(5) Figures 5–7 show the influence of slender ratio b/c on the stress distributions. The stress σ_z increases as b/c becomes larger and approaches to the upper limit value (i.e., $b/c\to\infty$) when $b/c>5.0$. The stresses σ_r and σ_θ have the largest value when $b/c=1.0$ and approach to uniform distributions ac-

Downloaded 03 May 2010 to 171.66.16.247. Redistribution subject to ASME license or copyright; see http://www.asme.org/terms/Terms_Use.cfm

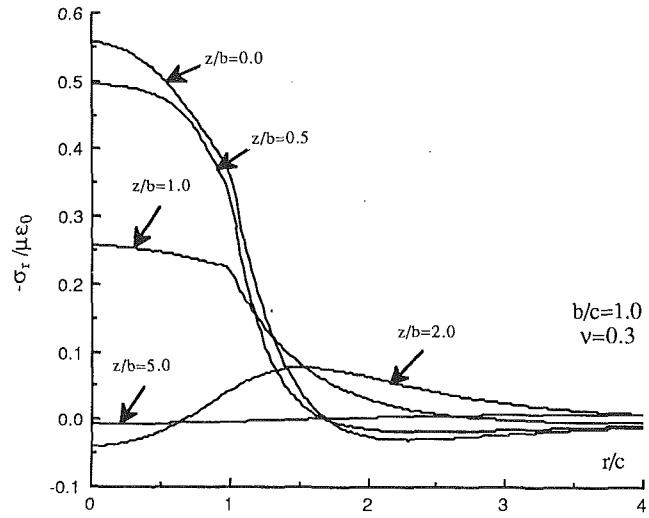


Fig. 10 Variation of normal stress σ_r along the r direction

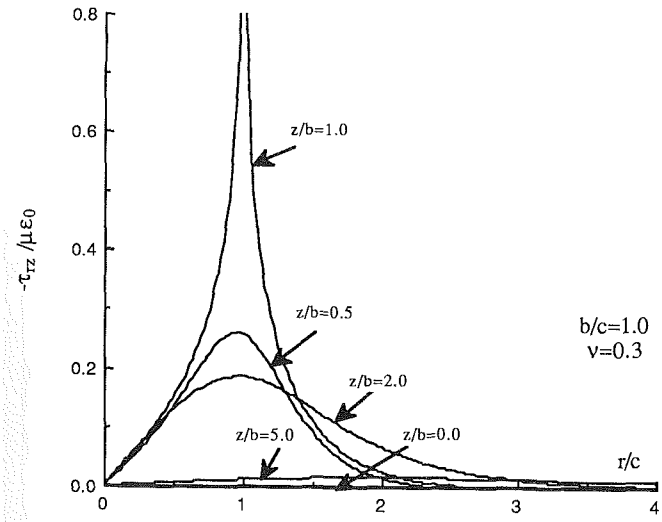


Fig. 11 Variation of shear stress τ_{rz} along the r direction

cording to the increase of b/c. The distributions of σ_z and σ_θ have discontinuity at the boundary $r = c$.

(6) Figures 8–11 illustrate the stress variations due to the relative positions z/b under the condition of $b/c = 1.0$. It is observed that all the normal stresses have the largest value at $z/b = 0$ and decrease as z/b becomes larger. However, the shear stress τ_{rz} is zero at $z/b = 0$ and has the largest value on the boundary $z = b$.

(7) It is well known that the stress fields in the interior points of an ellipsoidal inclusion become uniform. However, the stress fields in the circular cylindrical inclusion with finite length are not uniform as shown in Figs. 3–11.

(8) The strain energy $\overline{W}^*$ per unit volume in the inclusion depends on the slender ratio b/c, and it becomes constant for the infinite cylindrical inclusion ($b/c \to \infty$).

(9) It is easily seen from the results in Section 5 that the stress and displacement fields caused by cylindrical inclusions on the z-axis can be obtained by superposition of the results for a cylindrical inclusion shown in this paper.

Acknowledgment

This research was supported by the U.S. Army DAAL03-89-K-0019.

References

Abramowitz, M., and Stegun, I. A., 1972, *Handbook of Mathematical Functions*, 9th printing, Dover.

Byrd, P. F., and Friedman, M. D., 1971, *Handbook of Elliptic Integrals for Engineers and Scientists*, 2nd ed., Springer-Verlag; New York.

Chiu, Y. P., 1977, "On the Stress Field Due to Initial Strains in a Cuboid Surrounded by an Infinite Elastic Space," ASME JOURNAL OF APPLIED MECHANICS, Vol. 44, pp. 587–590.

Eason, G., Noble, B., and Sneddon, I. N., 1955, "On Certain Integrals of Lipschitz-Hankel Type Involving Products of Bessel Functions," *Philosophical Transaction of Royal Society of London*, Vol. A 247, pp. 529–551.

Erdelyi, A., 1954, *Tables of Integral Transforms*, Vol. 2, McGraw-Hill, New York.

Eshelby, J. D., 1957, "The Determination of the Elastic Field of an Ellipsoidal Inclusion and Related Problems," *Proceedings of the Royal Society, London*, Vol. A 241, pp. 376–396.

Eshelby, J. D., 1959, "The Elastic Field Outside an Elastic Inclusion," *Proceeding of the Royal Society, London*, Vol. A 252, pp. 561–569.

Eshelby, J. D., 1961, "Elastic Inclusions and Inhomogeneities," *Progress in Solid Mechanics*, Vol. 2, I. N. Sneddon and R. Hill, eds., North-Holland, Amsterdam, pp. 89–140.

Goodier, J. N., 1937, "On the Integration of the Thermo-Elastic Equations," *Philosophical Magazine and Journal of Science*, Vol. 23, pp. 1017–1032.

Hasegawa, H., 1975, "An Extension of Love's Solution for the Axisymmetric Problems of Elasticity," *Bulletin of the JSME*, Vol. 18, pp. 484–491.

Hasegawa, H., 1976, "Axisymmetric Body Force Problems of an Elastic Half Space," *Bulletin of the JSME*, Vol. 19, pp. 1262–1269.

Hasegawa, H., 1978, "An Investigation on Axisymmetric Concentrated Load Problems of Elasticity (Applications of Solution with Singularities)," *Bulletin of the JSME*, Vol. 21, pp. 1462–1468.

Hasegawa, H., Lee, V. G., and Mura, T., 1991, "Green's Functions for Axisymmetric Problems of Dissimilar Elastic Solids," ASME JOURNAL OF APPLIED MECHANICS, in press.

Mura, T., 1982, *Micromechanics of Defects in Solids*, Martinus-Nijhoff.

Mura, T., 1988, "Inclusion Problem," *Applied Mechanics Review*, Vol. 41, ASME, New York, pp. 15–20.

Okuni, S., 1974, "Complete Elliptic Integral Resulting from Infinite Integrals of Bessel Functions," *Journal of Research of the National Bureau of Standards*, Vol. 78B, pp. 113–135.

Takao, Y., Taya, M., and Chou, T. W., 1981, "Stress Field Due to a Cylindrical Inclusion with Constant Axial Eigenstrain in an Infinite Elastic Body," ASME JOURNAL OF APPLIED MECHANICS, Vol. 48, pp. 853–858.

APPENDIX

The following integral formulas are used to evaluate the integrals appearing in this paper.

$$\int_0^\infty J_1(\alpha a)J_0(\alpha r)e^{-\alpha z_i}d\alpha$$

$$=\frac{1}{2\sqrt{ar}}\left\{\sqrt{\frac{r}{a}}\,[1+\mathrm{sgn}(a-r)]-\frac{z_i}{\pi a}\,[Q_{-1/2}(x_i)+\frac{a-r}{a+r}\,k_i\Pi(p,k_i)]\right\} \quad \text{(A1)}$$

$$\int_0^\infty \alpha J_1(\alpha a)J_0(\alpha r)e^{-\alpha z_i}d\alpha$$

$$=\frac{1}{2\pi r\sqrt{ar}}\left\{Q_{1/2}(x_i)-\frac{x_i-\frac{r}{a}}{x_i^2-1}\,G_1(x_i)\right\} \quad \text{(A2)}$$

$$\int_0^\infty J_1(\alpha a)J_1(\alpha r)e^{-\alpha z_i}d\alpha=\frac{1}{\pi\sqrt{ar}}\,Q_{1/2}(x_i) \quad \text{(A3)}$$

$$\int_0^\infty \alpha J_1(\alpha a)J_1(\alpha r)e^{-\alpha z_i}d\alpha=$$

$$-\frac{1}{2\pi\sqrt{ar}}\,\frac{Z_i}{ar}\,\frac{1}{x_i^2-1}\,[x_iQ_{1/2}(x_i)-Q_{-1/2}(x_i)] \quad \text{(A4)}$$

Downloaded 03 May 2010 to 171.66.16.247. Redistribution subject to ASME license or copyright; see http://www.asme.org/terms/Terms_Use.cfm

$$\int_0^\infty J_1(\alpha a)J_0(\alpha r)d\alpha = \begin{Bmatrix} 0, & r>a \\ \frac{1}{2a}, & r=a \\ \frac{1}{a}, & r<a \end{Bmatrix} = q_1 \qquad \text{(A5)}$$

$$\int_0^\infty \frac{1}{\alpha} J_1(\alpha a)J_1(\alpha r)d\alpha = \begin{Bmatrix} \frac{r}{2a}, & a \geq r > 0 \\ \frac{a}{2r}, & r \geq a > 0 \end{Bmatrix} = q_2 \qquad \text{(A6)}$$

$$\int_0^\infty \frac{1}{\alpha} J_1(\alpha a)J_1(\alpha r)e^{-\alpha z_i}d\alpha = q_2 + \frac{1}{4\pi ar\sqrt{ar}}[z_i(a-r)^2 k_i \Pi(p, k_i) - 2arz_i Q_{1/2}(x_i) - z_i(a^2+r^2)Q_{-1/2}(x_i)] \qquad \text{(A7)}$$

$$\int_0^\infty \frac{1}{\alpha} J_1(\alpha a)J_0(\alpha r)e^{-\alpha z_i}d\alpha = -q_1 z_i + \frac{1}{\pi}\sqrt{\frac{r}{a}}\left[\frac{a-r}{a+r}\frac{z_i^2}{2ar} k_i \Pi(p,k_i) + G_2(x_i) + \frac{a^2-r^2}{2ar} Q_{-1/2}(x_i)\right] \qquad \text{(A8)}$$

Downloaded 03 May 2010 to 171.66.16.247. Redistribution subject to ASME license or copyright; see http://www.asme.org/terms/Terms_Use.cfm

Multiply Loaded Rigid Punch on a Stressed Orthotropic Half-Plane via a Thin Elastic Layer

Hans L. Bjarnehed
Research Associate,
Division of Solid Mechanics,
Chalmers University of Technology,
S-412 96 Göteborg, Sweden

A uniaxially stressed orthotropic half-plane indented on the free edge by a multiply loaded rigid punch via a thin elastic layer is considered. The layer is formulated as a generalized Winkler cushion including also shear stresses and strains. Governing singular integral equations are stated for the unknown interface stresses between the cushion and the half-plane. Two kinds of friction conditions between the cushion and half-plane are treated, viz. completely adhesive and frictionless contact. An analytical solution for contact with a rigid cushion and a numerical solution with an elastic cushion are presented. Also, a comparison with a corresponding FEM model is performed. For frictionless contact, some analytical results concerning optimum design of the elastic cushion are given.

1 Introduction

The background of the title problem is a steel clamping joint attached in the middle of a composite truck leaf spring which consists of a glass fiber-reinforced polymer. The clamping joint transmits a number of loads to the leaf spring. First, the joint is preloaded by a clamping force. Second, a vertical force, a horizontal force, and a tilting moment from the wheel axle are transmitted to the leaf spring. Cracks and delaminations have been observed in the clamped region, and wear has been detected in the contact area of such springs used under running conditions. The steel clamps and the composite beam form sharp corners at the ends of the interfaces of contact. It is a well-known theoretical result that the stresses reach infinite values at interface corners between elastic bodies in contact (Bogy and Wang 1971). It is of main interest, therefore, to reduce these very high local interface stresses. In order to protect the composite beam from wear, thin polymer layers have been glued on to the composite at the area of contact. However, these thin layers will also affect the distribution of the interface stresses in a favorable way.

In this study the contact is modeled as a rigid punch (steel clamp) indented into an orthotropic half-plane (composite leaf spring) via a thin generalized Winkler cushion (polymer layer) as shown in Fig. 1. The elastic cushion, which is made up of noninteracting springs, can transmit both normal and shear stresses. In addition to the loads mentioned above there is a load of uniform stress applied to the half-plane (representing bending stress at the surface of the leaf spring). Obviously, this model is applicable in a number of cases where a soft layer is used to diminish the stress concentration occurring in the contact between a stiff punch and an elastic foundation.

Plane contact problems for an elastic layer pressed into an elastic half-plane have been considered by a number of authors. The frictionless receding contact between an infinite layer and a half-space was studied by Keer, Dundurs, and Tsai (1972). The layer was loaded normally by a known distributed pressure over a finite part of the free edge. Among other results they presented the distribution of the interface pressure and the relations between the extent of contact, material parameters, and geometry (the extent of a receding contact is independent of the level of loading). The above contact problem, but with a layer loaded by a rigid stamp, was considered by Ratwani and Erdogan (1973) and they presented similar results as described above.

2 Problem Statement

Consider the orthotropic homogeneous elastic half-plane in

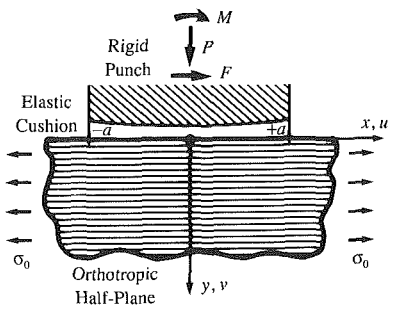


Fig. 1 Indentation of a stressed orthotropic half-plane by a multiply loaded rigid punch via a thin elastic cushion

Contributed by the ASME Applied Mechanics Division of THE AMERICAN SOCIETY OF MECHANICAL ENGINEERS for presentation at the Winter Annual Meeting, Atlanta, Ga., Dec. 1-6, 1991.

Discussion on this paper should be addressed to the Technical Editor, Prof. Leon M. Keer, The Technological Institute, Northwestern University, Evanston, IL 60208, and will be accepted until two months after final publication of the paper itself in the JOURNAL OF APPLIED MECHANICS. Manuscript received by the ASME Applied Mechanics Division, Nov. 28, 1990; final revision, May 14, 1991.

Paper No. 91-WA/APM-30.

Copyright © 1992 by ASME
Downloaded 03 May 2010 to 171.66.16.247. Redistribution subject to ASME license or copyright; see http://www.asme.org/terms/Terms_Use.cfm

Fig. 1. The principal directions of elasticity are parallel and perpendicular to the horizontal edge. The half-plane edge is subjected to indentation by a rigid punch via a thin elastic cushion. The punch is loaded vertically (P), horizontally (F), and by a tilting moment (M). In addition, there is a load of uniform stress (σ_0) in the half-plane, applied in the x-direction. The rigid punch has a symmetrically formed base, with respect to the y-axis, of width $2a$. The cushion has an upper surface shaped to conform with the base of the rigid punch and a flat lower surface which is in contact with the half-plane edge. It is assumed that the cushion is bonded to the punch. Two contact conditions in the cushion/half-plane interface will be treated, viz. completely adhesive and frictionless contact. We seek relations between interface stresses, material parameters, and geometry.

3 Governing Equations

Coupled singular integral equations for the unknown surface stresses in the half-plane region $|x| \le a$ can be derived either by means of Fourier transforms or by using complex analysis (Muskhelishvili, 1949). These equations, as they are expressed by Bjarnehed (1991), read (with $\oint$ denoting the principal value of the integral):

$$\oint_{-1}^{1} \frac{\tau(S)}{X-S}\,dS = -C_1\sigma(X) + C_2u'(X) - C_3\sigma_0, \quad |X| \le 1, \tag{1a}$$

$$\oint_{-1}^{1} \frac{\sigma(S)}{X-S}\,dS = C_4\tau(X) + C_5v'(X), \quad |X| \le 1. \tag{1b}$$

The components of surface shear (τ) and normal (σ) stresses are defined in the opposite directions of x and y while u and v, denoting surface displacements, are defined in the directions of x and y, respectively. The material parameters C_1, C_2, C_3, C_4, and C_5 are defined in the Appendix. Dimensionless variables have been used in (1), viz.

$$X = \frac{x}{a}, \quad S = \frac{s}{a}, \quad u'(X) = \frac{1}{a}\frac{du}{dX}, \quad v'(X) = \frac{1}{a}\frac{dv}{dX}. \tag{2a-d}$$

The thin cushion is formulated as a system of an infinite number of linearly elastic springs as shown in Fig. 2. It can be considered as an elastic continuum with both normal (E_c) and shear (G_c) stiffness but without any interaction between individual springs. Therefore, the following strain-stress relations are ascribed to the cushion

$$\gamma_c = \frac{u(X) - \Delta_x}{\delta(X)} = \frac{\tau(X)}{G_c}, \quad \epsilon_c = \frac{v(X) - \phi aX - \Delta_y}{\delta(X)} = \frac{\sigma(X)}{E_c}, \quad |X| \le 1, \tag{3a,b}$$

where Δ_x and Δ_y denote the displacements of the rigid punch in the directions of x and y, respectively. A clockwise angle of tilting is represented by ϕ, and δ denotes the cushion thickness.

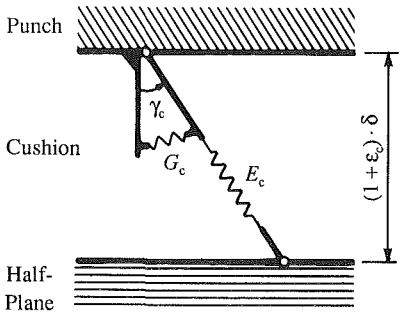


Fig. 2 The generalized Winkler model of the elastic cushion

The loads P and σ_0 give a symmetric and an antisymmetric distribution, with respect to the y-axis, of the interface normal (σ^s) and shear stress (τ^a), respectively. The conditions are the opposite for the loads F and M, and we denote the interface stresses in this case by σ^a and τ^s. Therefore, we will formulate and solve the stated problem separately for the two cases of loading as described above, and hence it is only necessary to define the Eqs. (1) and (3) in the region $0 \le X \le 1$.

By putting $\sigma(S) = \sigma(-S) = \sigma^s(S)$ and $\tau(S) = -\tau(-S) = \tau^a(S)$ and substituting u and v from the expressions (3a,b), with $\Delta_x = 0$ and $\phi = 0$, into (1) we get Eqs. (4a,c) below. In the same manner, but letting $\sigma(S) = -\sigma(-S) = \sigma^a(S)$ and $\tau(S) = \tau(-S) = \tau^s(S)$ and substituting u and v from the expressions (3a, b), with $\Delta_y = 0$, into (1) we obtain Eqs. (4b-d).

$$2\oint_0^1 \begin{Bmatrix} S \\ X \end{Bmatrix} \frac{1}{X^2-S^2} \begin{Bmatrix} \tau^a(S) \\ \tau^s(S) \end{Bmatrix} dS = -C_1 \begin{Bmatrix} \sigma^s(X) \\ \sigma^a(X) \end{Bmatrix} + \frac{C_2}{G_c a} \cdot \frac{d}{dX}\left(\delta(X) \begin{Bmatrix} \tau^a(X) \\ \tau^s(X) \end{Bmatrix}\right) - \begin{Bmatrix} C_3\sigma_0 \\ 0 \end{Bmatrix}, \tag{4a,b}$$

$$2\oint_0^1 \begin{Bmatrix} X \\ S \end{Bmatrix} \frac{1}{X^2-S^2} \begin{Bmatrix} \sigma^s(S) \\ \sigma^a(S) \end{Bmatrix} dS = C_4 \begin{Bmatrix} \tau^a(X) \\ \tau^s(X) \end{Bmatrix} + \frac{C_5}{E_c a} \cdot \frac{d}{dX}\left(\delta(X) \begin{Bmatrix} \sigma^s(X) \\ \sigma^a(X) \end{Bmatrix}\right) + \begin{Bmatrix} 0 \\ C_5\phi \end{Bmatrix}, \tag{4c,d}$$

When the two separate solutions of (4) are known, we obtain the total solution as

$$\sigma(X) = \sigma^s(X) + \sigma^a(X), \quad \tau(X) = \tau^a(X) + \tau^s(X). \tag{5a,b}$$

4 Completely Adhesive Contact

Here we assume fully bonded contact between the cushion and the half-plane, i.e., the two elastic bodies in contact can be considered as glued together. We seek the distribution of both normal (σ) and shear (τ) stresses within the contact region. The equations to solve are the coupled singular equations stated in (4). To get equations suitable for numerical solution we transform (4) into coupled nonsingular integrals equations of the Volterra type (Mikhlin, 1957). This is possible if we write T for X and apply the operators

$$\int_0^X \sqrt{X^2-T^2}\,dT \quad \text{and} \quad \int_0^X T\sqrt{X^2-T^2}\,dT$$

to (4a, d) and (4b, c), respectively. We then obtain

$$\gamma_1 \int_0^X \begin{Bmatrix} 1 \\ S \end{Bmatrix} \sqrt{X^2-S^2} \begin{Bmatrix} p^s(S) \\ p^a(S) \end{Bmatrix} dS - \gamma_2 \int_0^X \begin{Bmatrix} S \\ 2S^2-X^2 \end{Bmatrix} \frac{h(S)}{\sqrt{X^2-S^2}} \begin{Bmatrix} q^a(S) \\ q^s(S) \end{Bmatrix} dS + \int_X^1 \begin{Bmatrix} 1 \\ S \end{Bmatrix} \sqrt{S^2-X^2} \begin{Bmatrix} q^a(S) \\ q^s(S) \end{Bmatrix} dS - \int_0^1 \begin{Bmatrix} S \\ S^2 \end{Bmatrix} \begin{Bmatrix} q^a(S) \\ q^s(S) \end{Bmatrix} dS = \frac{X^2}{2} \begin{Bmatrix} \gamma_3\tilde{\sigma}_0 \\ -\tilde{F} \end{Bmatrix}, \tag{6a,b}$$

$$\gamma_4 \int_0^X \begin{Bmatrix} S \\ 1 \end{Bmatrix} \sqrt{X^2-S^2} \begin{Bmatrix} q^a(S) \\ q^s(S) \end{Bmatrix} dS + \gamma_5 \int_0^X \begin{Bmatrix} 2S^2-X^2 \\ S \end{Bmatrix} \frac{h(S)}{\sqrt{X^2-S^2}} \begin{Bmatrix} p^s(S) \\ p^a(S) \end{Bmatrix} dS$$

Downloaded 03 May 2010 to 171.66.16.247. Redistribution subject to ASME license or copyright; see http://www.asme.org/terms/Terms_Use.cfm

$$-\int_X^1 \begin{Bmatrix} S \\ 1 \end{Bmatrix} \sqrt{S^2-X^2} \begin{Bmatrix} p^s(S) \\ p^a(S) \end{Bmatrix} dS + \int_0^1 \begin{Bmatrix} S^2 \\ S \end{Bmatrix} \begin{Bmatrix} p^s(S) \\ p^a(S) \end{Bmatrix} dS = \frac{X^2}{2} \begin{Bmatrix} 1 \\ 1 \end{Bmatrix}, \quad (6c,d)$$

where

$$p^s(X), q^a(X) = -\frac{\sigma^s(X), \tau^a(X)}{P/2a}, \quad p^a(X), q^s(X) = -\frac{\sigma^a(X), \tau^s(X)}{C_5\phi/2}, \quad (7a\text{–}d)$$

$$\tilde{\sigma}_0 = \frac{\sigma_0}{P/2a}, \quad \tilde{F} = \frac{F/2a}{C_5\phi/2}, \quad h(X) = \frac{\delta(X)}{a}, \quad (8a\text{–}c)$$

$$\gamma_1 = \frac{C_1}{\pi}, \quad \gamma_2 = \frac{C_2}{\pi G_c}, \quad \gamma_3 = \frac{C_3}{2}, \quad \gamma_4 = \frac{C_4}{\pi}, \quad \gamma_5 = \frac{C_5}{\pi E_c}. \quad (9a\text{–}e)$$

Equations (6*a–d*) are solved numerically by the method described in the Appendix.

Assume that the cushion is rigid ($\gamma_2 = \gamma_5 = 0$). The system of singular integral equations (4*a–d*) then has the following analytical solutions

$$\begin{Bmatrix} p^s(X) \\ p^a(X) \end{Bmatrix} = \frac{2}{\pi} \cdot \frac{\cosh(\pi\eta)}{\sqrt{1-X^2}} \cdot \left[\begin{Bmatrix} 1 \\ -\rho\tilde{F} \end{Bmatrix} \begin{Bmatrix} \cos\Psi(X) \\ \sin\Psi(X) \end{Bmatrix} + \begin{Bmatrix} \kappa\rho\tilde{\sigma}_0 \\ 1 \end{Bmatrix} \left(X \begin{Bmatrix} \sin\Psi(X) \\ \cos\Psi(X) \end{Bmatrix} + 2\eta \begin{Bmatrix} -1 \\ 1 \end{Bmatrix} \begin{Bmatrix} \cos\Psi(X) \\ \sin\Psi(X) \end{Bmatrix} \right) \right] \quad (10a,b)$$

$$\begin{Bmatrix} q^a(X) \\ q^s(X) \end{Bmatrix} = \frac{2}{\pi} \cdot \frac{\cosh(\pi\eta)}{\sqrt{1-X^2}} \cdot \left[\begin{Bmatrix} 1/\rho \\ \tilde{F} \end{Bmatrix} \begin{Bmatrix} \sin\Psi(X) \\ \cos\Psi(X) \end{Bmatrix} + \begin{Bmatrix} -\kappa\tilde{\sigma}_0 \\ 1/\rho \end{Bmatrix} \left(X \begin{Bmatrix} \cos\Psi(X) \\ \sin\Psi(X) \end{Bmatrix} + 2\eta \begin{Bmatrix} 1 \\ -1 \end{Bmatrix} \begin{Bmatrix} \sin\Psi(X) \\ \cos\Psi(X) \end{Bmatrix} \right) \right] \quad (10c,d)$$

where

$$\Psi(X) = \eta \ln\left(\frac{1-X}{1-X}\right), \quad \eta = \frac{1}{2\pi} \ln\left(\frac{1+\sqrt{\gamma_1\gamma_4}}{1-\sqrt{\gamma_1\gamma_4}}\right), \quad \kappa = \gamma_3, \quad \rho = \sqrt{\frac{\gamma_4}{\gamma_1}}. \quad (11a\text{–}d)$$

Analytical solutions of coupled singular integrals equations as (10*a–d*) are given, among other authors, by Söhngen (1954). It appears from (10*a–d*) that the interface stresses have singular points at $|X| = 1$ and an oscillating behavior ($\sin\Psi$ and $\cos\Psi$) which grows stronger as $|X|$ approaches unity ($\Psi \to \infty$ when $|X| \to 1$).

5 Frictionless Contact

Here we consider perfectly smooth contact between the cushion and the half-plane, i.e., no tangential stress interaction is assumed at the interface. We seek the distribution of normal (σ) stress within the contact region. Obviously, neither the horizontal force F nor the uniform half-plane stress σ_0 are included. We also assume that the relation between the vertical force P and the tilting moment M is such that the total interface normal stress in (5*a*) is negative (i.e., a pressure) all over the area of contact $|X| \le 1$. This frictionless contact problem can be treated by ignoring (6*a*, *b*) and by putting $q^a(X) \equiv 0$ and $q^s(X) \equiv 0$ in 6(*c*) and (6*d*), respectively. We obtain

$$\gamma_5 \int_0^X \begin{Bmatrix} 2S^2-X^2 \\ S \end{Bmatrix} \frac{h(S)}{\sqrt{X^2-S^2}} \begin{Bmatrix} p^s(S) \\ p^a(S) \end{Bmatrix} dS - \int_X^1 \begin{Bmatrix} S \\ 1 \end{Bmatrix} \sqrt{S^2-X^2} \begin{Bmatrix} p^s(S) \\ p^a(S) \end{Bmatrix} dS + \int_0^1 \begin{Bmatrix} S^2 \\ S \end{Bmatrix} \begin{Bmatrix} p^s(S) \\ p^a(S) \end{Bmatrix} dS = \frac{X^2}{2} \begin{Bmatrix} 1 \\ 1 \end{Bmatrix}. \quad (12a,b)$$

Equations (12*a*, *b*) are solved numerically by the method described in the Appendix.

Assume that the cushion is rigid ($\gamma_5 = 0$). The singular integral equations (4*c*, *d*) then have the following analytical solutions:

$$\begin{Bmatrix} p^s(X) \\ p^a(X) \end{Bmatrix} = \frac{2/\pi}{\sqrt{1-X^2}} \begin{Bmatrix} 1 \\ X \end{Bmatrix}. \quad (13a,b)$$

Analytical solutions of singular integral equations as (13*a*, *b*) are given, among other authors, by Söhngen (1954). It appears from (13*a*, *b*) that the interface pressures have singular points at $|X| = 1$ and are independent of the half-plane material parameters. The total interface normal stress, expressed in terms of P and M, is found by substituting (13*a*, *b*), with aid of (7*a–c*) and the following condition of equilibrium

$$\tilde{M} = \int_0^1 p^a(X) \cdot X dX = \frac{M}{C_5\phi a^2}, \quad (14)$$

into (5*a*). Pressure is obtained all over the area of contact under the condition that $P > 2M/a$.

6 Design of the Cushion

Assume frictionless contact. Consider (4*c*, *d*) with $\tau^a(X) = \tau^s(X) \equiv 0$. For a given interface pressure distribution between the half-plane and the cushion, we now seek the corresponding shape of the cushion, i.e., $h(X)$. It is obvious, by studying (4*c*, *d*), that a given pressure distribution, which includes both P and M, gives a load dependence and an asymmetric $h(X)$. On the other hand, a given pressure distribution, which includes either P or M, gives a load independence and a symmetric $h(X)$. It is also obvious that all conceivable stress distributions will not give a physically meaningful $h(X)$. For instance, by substituting a steplike pressure distribution produced by a pure tilting moment M into (4*d*), we obtain an $h(X)$ which is not strictly positive. The thicknesses $h(X)$ derived here for frictionless contact are also useful for the case of complete adhesive contact. This is due to the fact that the interface normal stress is only slightly dependent of the condition of friction at the interface, as shown in Section 7. Let us assume, as an illustrative example, a constant and a linearly varying interface pressure for the case of a vertical force P and a tilting moment M, respectively, thus substituting

$$p^s(X) \equiv 1, \quad p^a(X) = p_1^a \cdot X, \quad (15a,b)$$

into Eqs. (4*c*) and 4(*d*), respectively. By integrating both sides of these equations and then evaluating the integrals we obtain

$$h(X) = h^P(X) = \frac{1}{\pi\gamma_5} \cdot [(1+X)\ln(1+X) + (1-X)\ln(1-X) - 2] - \frac{\lambda^s}{\pi\gamma_5}, \quad (16a)$$

$$h(X) = h^M(X) = \frac{1}{\pi\gamma_5} \cdot \left[\frac{2}{p_1^a} - 1 - \frac{1-X^2}{2X} \ln\left(\frac{1+X}{1-X}\right) \right], \quad (16b)$$

where λ^s is a constant of integration. The corresponding constant of integration for (4*d*) is zero because $p^a(X)$ is antisymmetric. With the condition

Downloaded 03 May 2010 to 171.66.16.247. Redistribution subject to ASME license or copyright; see http://www.asme.org/terms/Terms_Use.cfm

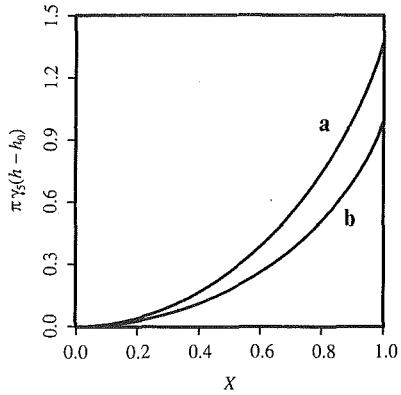


Fig. 3 Cushion thicknesses corresponding to (*a*) a constant interface pressure distribution due to pure vertical force P (*b*) a linearly varying interface pressure distribution due to pure tilting moment M in case of frictionless contact

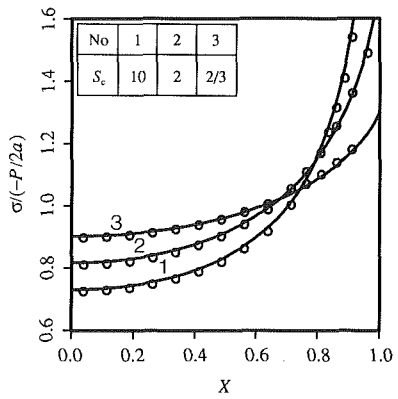


Fig. 4 Interface pressure distributions in the interval $0 \le X \le 1$ for frictionless contact with pure vertical loading (P). The markers indicate the FEM solution.

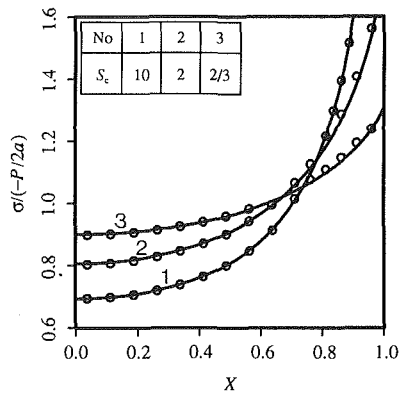


Fig. 5 Interface pressure distributions in the interval $0 \le X \le 1$ for complete adhesive contact with pure vertical loading (P). The markers indicate the FEM solution.

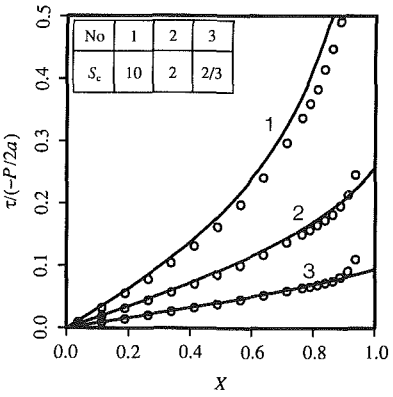


Fig. 6 Interface shear stress distributions in the interval $0 \le X \le 1$ for complete adhesive contact with pure vertical loading (P). The markers indicate the FEM solution.

$$h^P(0) = h_0^P, \quad h^M(0) = h_0^M, \tag{17a,b}$$

we find from (16*a*, *b*) that

$$\lambda^s = -\pi\gamma_5 h_0^P - 2, \quad p_1^a = \frac{2}{\pi\gamma_5 h_0^M + 2}. \tag{18a,b}$$

By substituting (15*b*) into (14) we find

$$p_1^a = \frac{3M}{C_5 \phi a^2}, \tag{19}$$

which relates the corner pressure $p_1^a = p^a(1)$ to the tilting moment M.

Finally, Eqs. (16*a*,*b*) give

$$h^P(X) = \frac{1}{\pi\gamma_5} \cdot [(1+X)\ln(1+X) + (1-X)\ln(1-X)] + h_0^P, \tag{20a}$$

$$h^M(X) = \frac{1}{\pi\gamma_5} \cdot \left[1 - \frac{1-X^2}{2X} \ln\left(\frac{1+X}{1-X}\right)\right] + h_0^M, \tag{20b}$$

which are the cushion thicknesses required in order to obtain the pressure distributions (15*a*) (pure vertical force P) and (15*b*) (pure tilting moment M), respectively. They are plotted in Fig. 3.

7 Numerical Results

Here we present numerical solutions for the interface stresses in the case of complete adhesive and frictionless contact. The equations solved are stated in (6*a–d*) and (12*a*, *b*), respectively. The assumed relation between the cushion stiffnesses is $G_c = E_c/2(1+\nu_c)$. In order to evaluate the generalized Winkler model of the cushion, the solutions for pure vertical loading (P) are compared with the corresponding solutions obtained with the FEM-code SOLVIA (see Figs. 4–6). In this FEM model both the cushion and the half-plane are modeled as linear elastic continua, and special contact elements are used at the interface. Only half of the cushion and the half-plane is modeled due to symmetry with respect to the y-axis. The size of the half-plane model is made $6a \times 6a$ where $2a$ is the extent of the cushion. The boundary conditions used are consistent nodal forces corresponding to a uniform interface pressure distribution with resulting double unit vertical force. The boundary conditions are also discussed in Section 8. All results are calculated with the assumption of plane stress and a uniform cushion thickness ($h(X) = \delta(X)/a \equiv$ constant). The FEM calculations are performed with $h(X) \equiv 1/20$. Furthermore, the following material parameters are kept constant during all calculations (using standard notation): $E_x/E_y = 5$, $E_y/G_{xy} = 2$, $\nu_{xy} = 0.3$, and $\nu_c = 0.3$. It is here convenient to introduce the following cushion stiffness: $S_c = (E_c/E_y) \cdot (a/\delta)$. The interface stress distributions shown in Figs. 4–12 below are plotted for three different values of S_c, viz. $S_c = 10$, 2, and 2/3.

8 Discussion

Due to the generalized Winkler model of the elastic cushion the interface stress distributions in Figs. 4–12 do not show the characteristic singular behavior at $X = 1$. However, these solutions show the leveling effect of a soft cushion on the

Downloaded 03 May 2010 to 171.66.16.247. Redistribution subject to ASME license or copyright; see http://www.asme.org/terms/Terms_Use.cfm

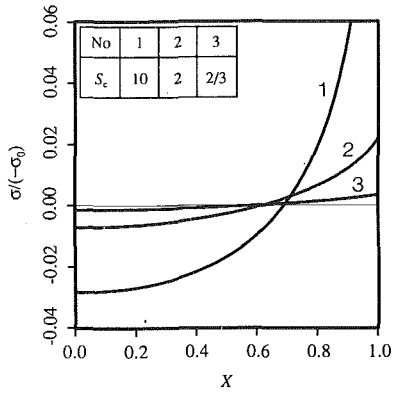


Fig. 7 Interface pressure distributions in the interval $0 \le X \le 1$ for complete adhesive contact with pure uniform half-plane loading (σ_0)

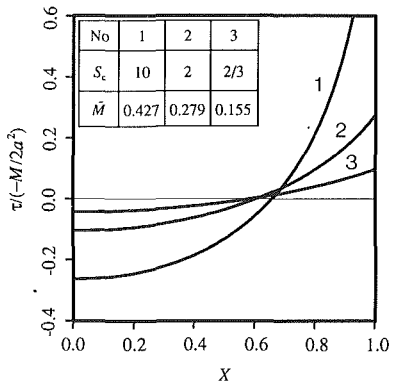


Fig. 10 Interface shear stress distributions in the interval $0 \le X \le 1$ for complete adhesive contact with pure moment loading (M)

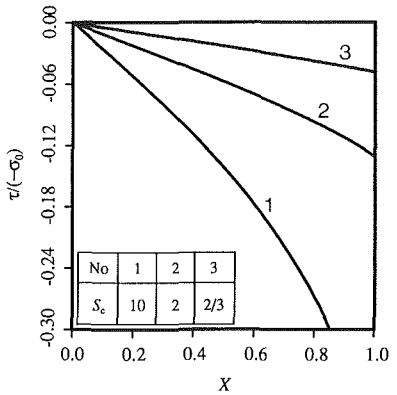


Fig. 8 Interface shear stress distributions in the interval $0 \le X \le 1$ for complete adhesive contact with pure uniform half-plane loading (σ_0)

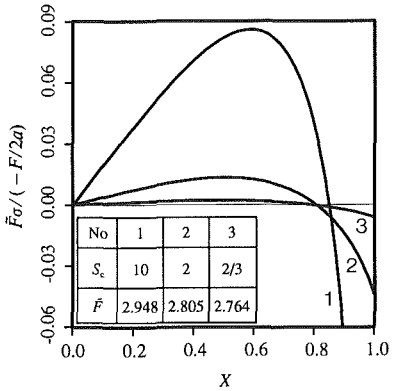


Fig. 11 Interface pressure distributions in the interval $0 \le X \le 1$ for complete adhesive contact with pure horizontal loading (F)

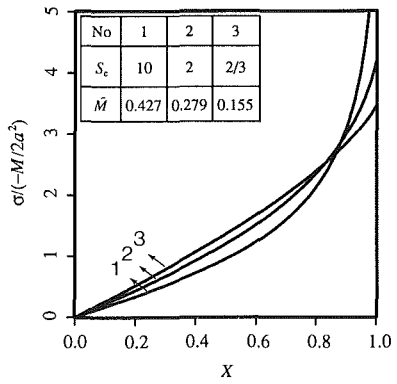


Fig. 9 Interface pressure distributions in the interval $0 \le X \le 1$ for complete adhesive contact with pure moment loading (M)

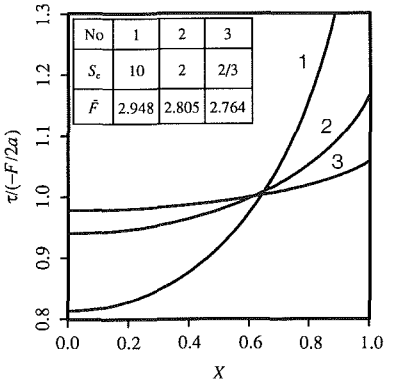


Fig. 12 Interface shear stress distributions in the interval $0 \le X \le 1$ for complete adhesive contact with pure horizontal loading (F)

interface stress distribution. A comparison between Figs. 4 and 5 for pure vertical loading shows only a slight difference between the interface pressure distribution for frictionless and complete adhesive contact, respectively. This difference grows smaller when the cushion is made softer. The same conclusion is found for a pure tilting loading and therefore only the pressure distribution for complete adhesive contact is plotted (Fig. 9). Consider the FEM solutions for pure vertical loading, i.e., the markers in Figs. 4–6. What kind of boundary condition to use in the FEM model is not completely obvious. Some conceivable boundary conditions are—different combinations of prescribed displacements or consistent nodal forces corresponding to different interface pressure distributions with resulting double unit vertical force. The interface pressure distributions, shown in Figs. 4 and 5, are relatively insensitive to the boundary conditions and also show a good agreement with the generalized Winkler solutions (solid lines). On the other hand, the interface shear stress distributions in Fig. 6 are very sensitive to different kinds of prescribed displacements as boundary conditions. This can be partly explained through a comparison between the Figs. 5–6 and 7–8, respectively. The conclusion is that a small amount of a uniform half-plane load has a relatively greater influence on the interface shear stress distribution than on the interface pressure distribution in case

Downloaded 03 May 2010 to 171.66.16.247. Redistribution subject to ASME license or copyright; see http://www.asme.org/terms/Terms_Use.cfm

of pure vertical loading. This small amount of uniform half-plane load can be considered here as a small disturbance in σ_x due to a modification of the boundary conditions. Therefore, consistent nodal forces corresponding to a uniform interface pressure distribution, with resulting double unit vertical force, are used as boundary condition in this FEM model. Consequently, the agreements with the generalized Winkler solutions are better for the more soft cushions as shown in Figs. 4–5 and especially in Fig. 6. Consistent nodal forces corresponding to a unit vertical point load at the origin can also be used; they only differ by a maximum of five percent from the nodal forces used in this model.

Acknowledgments

I want to thank my supervisor Prof. J. Hult and my colleague Dr. U. Stigh for helpful comments and discussions. This work is partially supported by the Product Development Division at Volvo Truck Corporation at Göteborg (Sweden), and by the Swedish National Board for Technical Development (STU) through the Project No. 722-88-02297.

References

Bjarnehed, H. L., 1991, "Rigid Punch on Stressed Orthotropic Half-Plane with Partial Slip," ASME JOURNAL OF APPLIED MECHANICS, Vol. 58, pp. 128–133.

Bogy, D. B., and Wang, K. C., 1971, "Stress Singularities at Interface Corners in Bounded Dissimilar Isotropic Elastic Materials," *International Journal of Solids and Structures*, Vol. 7, p. 993.

Keer, L. M., Dundurs, J., and Tsai, K. C., 1972, "Problems Involving a Receding Contact Between a Layer and a Half Space," ASME JOURNAL OF APPLIED MECHANICS, Vol. 39, p. 1115.

Lekhnitsky, S. G., 1937, "Plane Statical Problems of the Theory of Elasticity of an Anisotropic Body," *Prikladnaya matematika i mekhanica*, Vol. I., No. 1.

Mikhlin, S. G., 1957, *Integral Equations*, 2nd ed., Leningrad (English translation by A. H. Armstrong, Pergamon Press).

Muskhelishvili, N. I., 1949, *Some Basic Problems of the Mathematical Theory of Elasticity*, 3rd ed., Moscow (English translation by J. R. M. Radok, Nordhoff).

Ratwani, M., and Erdogan, F., 1973, "On the Plane Contact Problem for a Frictionless Elastic Layer," *International Journal of Solids and Structures*, Vol. 9, p. 921.

Söhngen, H., 1954, "Zur Theorie der endlichen Hilbert Transformation," *Math. Zeitschrift*, Vol. 60, p. 31.

APPENDIX

Numerical Method

Consider the equations (6*a–d*) and (12*a*, *b*). The interval of integration ($0 \le S \le 1$) is divided into N subintervals (l_i). Let X_i denote the midpoint of subinterval i. The continuous interface pressure and shear stress distributions are approximated by piecewise, i.e., within the subintervals, constant functions, thus

$$l_i = \{S : S_{i-1} < S < S_i\}, \quad 0 = S_0 < S_1 < \ldots < S_N = 1, \quad i = (1, N), \tag{A1a,b}$$

$$\begin{Bmatrix} p_i^s \\ p_i^a \end{Bmatrix} = \begin{Bmatrix} p^s(X_i) \\ p^a(X_i) \end{Bmatrix}, \quad \begin{Bmatrix} p_{i+N}^a \\ p_{i+N}^s \end{Bmatrix} = \begin{Bmatrix} q^a(X_i) \\ q^s(X_i) \end{Bmatrix},$$

$$X_i = \frac{1}{2}(S_i + S_{i-1}), \quad i = (1, N). \tag{A2a–c}$$

Now consider the complete adhesive contact problem stated in (6*a–d*). With the foregoing assumptions we rewrite (6*a*, *c*) and (6*b*, *d*) as $2N$ linear equations in the $2N$ unknowns p_i^s, p_{i+N}^a and p_i^a, p_{i+N}^s, respectively, thus

$$\sum_{j=1}^{N} \left[\gamma_1 \begin{Bmatrix} A_{ij} \\ D_{ij} \end{Bmatrix} \begin{Bmatrix} p_j^s \\ p_j^a \end{Bmatrix} - \left(\gamma_2 h_j \begin{Bmatrix} B_{ij} \\ E_{ij} \end{Bmatrix} + \begin{Bmatrix} C_{ij} \\ F_{ij} \end{Bmatrix} \right) \begin{Bmatrix} p_{j+N}^a \\ p_{j+N}^s \end{Bmatrix} \right] = \frac{X_i^2}{2} \begin{Bmatrix} \gamma_3 \tilde{\sigma}_0 \\ -\tilde{F} \end{Bmatrix}, \quad i = (1, N), \tag{A3a,b}$$

$$\sum_{j=1}^{N} \left[\gamma_4 \begin{Bmatrix} D_{ij} \\ A_{ij} \end{Bmatrix} \begin{Bmatrix} p_{j+N}^a \\ p_{j+N}^s \end{Bmatrix} + \left(\gamma_5 h_j \begin{Bmatrix} E_{ij} \\ B_{ij} \end{Bmatrix} + \begin{Bmatrix} F_{ij} \\ C_{ij} \end{Bmatrix} \right) \begin{Bmatrix} p_j^s \\ p_j^a \end{Bmatrix} \right] = \frac{X_i^2}{2} \begin{Bmatrix} 1 \\ 1 \end{Bmatrix}, \quad i = (1, N), \tag{A3c,d}$$

where

$$A_{ij} = \begin{cases} 0, & j > i, \\ \displaystyle\int_{S_{j-1}}^{X_i} \sqrt{X_i^2 - S^2}\, dS = \frac{X_i^2}{2}\left[\frac{\pi}{2} - \arcsin\left(\frac{S_{j-1}}{X_i} \right) \right] & \\ \quad - \dfrac{S_{j-1}}{2} \sqrt{X_i^2 - S_{j-1}^2}, & j = i, \\ \displaystyle\int_{S_{j-1}}^{S_j} \sqrt{X_i^2 - S^2}\, dS = \frac{X_i^2}{2}\left[\arcsin\left(\frac{S_j}{X_i} \right) - \arcsin\left(\frac{S_{j-1}}{X_i} \right) \right] & \\ \quad + \dfrac{S_j}{2} \sqrt{X_i^2 - S_j^2} - \dfrac{S_{j-1}}{2} \sqrt{X_i^2 - S_{j-1}^2}, & j < i, \end{cases} \tag{A4a}$$

$$B_{ij} = \begin{cases} 0, & j > i; \\ \displaystyle\int_{S_{j-1}}^{X_i} \frac{S\,dS}{\sqrt{X_i^2 - S^2}} = \sqrt{X_i^2 - S_{j-1}^2}, & j = i, \\ \displaystyle\int_{S_{j-1}}^{S_j} \frac{S\,dS}{\sqrt{X_i^2 - S^2}} = \sqrt{X_i^2 - S_{j-1}^2} - \sqrt{X_i^2 - S_j^2}, & j < i, \end{cases} \tag{A4b}$$

Downloaded 03 May 2010 to 171.66.16.247. Redistribution subject to ASME license or copyright; see http://www.asme.org/terms/Terms_Use.cfm

$$C_{ij}=\begin{cases}\displaystyle\int_{S_{j-1}}^{S_j}\left(S-\sqrt{S^2-X_i^2}\right)dS=\frac{X_i^2}{2}\ln\left(\frac{S_j+\sqrt{S_j^2-X_i^2}}{S_{j-1}+\sqrt{S_{j-1}^2-X_i^2}}\right)+\frac{1}{2}(S_j^2-S_{j-1}^2)\\ \quad+\dfrac{S_{j-1}}{2}\sqrt{S_{j-1}^2-X_i^2}-\dfrac{S_j}{2}\sqrt{S_j^2-X_i^2},\quad j>i,\\ \displaystyle\int_{S_{j-1}}^{S_j}SdS-\int_{X_i}^{S_j}\sqrt{S^2-X_i^2}dS=\frac{X_i^2}{2}\ln\left(\frac{S_j+\sqrt{S_j^2-X_i^2}}{X_i}\right)\\ \quad+\dfrac{1}{2}(S_j^2-S_{j-1}^2)-\dfrac{S_j}{2}\sqrt{S_j^2-X_i^2},\quad j=i,\\ \displaystyle\int_{S_{j-1}}^{S_j}SdS=\frac{1}{2}(S_j^2-S_{j-1}^2),\quad j<i,\end{cases}\tag{A4c}$$

$$D_{ij}=\begin{cases}0,\quad j>i,\\ \displaystyle\int_{S_{j-1}}^{X_i}S\sqrt{X_i^2-S^2}dS=\frac{1}{3}(X_i^2-S_{j-1}^2)^{3/2},\quad j=i,\\ \displaystyle\int_{S_{j-1}}^{S_j}S\sqrt{X_i^2-S^2}dS=\frac{1}{3}(X_i^2-S_{j-1}^2)^{3/2}-\frac{1}{3}(X_i^2-S_j^2)^{3/2},\quad j<i.\end{cases}\tag{A4d}$$

$$E_{ij}=\begin{cases}0,\quad j>i,\\ \displaystyle\int_{S_{j-1}}^{X_i}\frac{2S^2-X_i^2}{\sqrt{X_i^2-S^2}}dS=S_{j-1}\sqrt{X_i^2-S_{j-1}^2},\quad j=i,\\ \displaystyle\int_{S_{j-1}}^{S_j}\frac{2S^2-X_i^2}{\sqrt{X_i^2-S^2}}dS=S_{j-1}\sqrt{X_i^2-S_{j-1}^2}-S_j\sqrt{X_i^2-S_j^2},\quad j<i,\end{cases}\tag{A4e}$$

$$F_{ij}=\begin{cases}\displaystyle\int_{S_{j-1}}^{S_j}\left(S^2-S\sqrt{S^2-X_i^2}\right)dS=\frac{1}{3}(S_j^3-S_{j-1}^3)+\frac{1}{3}(S_{j-1}^2-X_i^2)^{3/2}\\ \quad-\dfrac{1}{3}(S_j^2-X_i^2)^{3/2},\quad j>i,\\ \displaystyle\int_{S_{j-1}}^{S_j}S^2dS-\int_{X_i}^{S_j}S\sqrt{S^2-X_i^2}dS=\frac{1}{3}(S_j^3-S_{j-1}^3)-\frac{1}{3}(S_j^2-X_i^2)^{3/2},\quad j=i,\\ \displaystyle\int_{S_{j-1}}^{S_j}S^2dS=\frac{1}{3}(S_j^3-S_{j-1}^3),\quad j<i,\end{cases}\tag{A4f}$$

$$h_j=h(X_j).\tag{A5}$$

Next, consider the frictionless contact problem stated in (12a,b). From the foregoing assumptions we rewrite (12a) and (12b) as N linear equations in the N unknowns p_i^s and p_i^a, respectively, thus

$$\sum_{j=1}^{N}\left(\gamma_5 h_j\begin{Bmatrix}E_{ij}\\ B_{ij}\end{Bmatrix}+\begin{Bmatrix}F_{ij}\\ C_{ij}\end{Bmatrix}\right)\begin{Bmatrix}p_j^s\\ p_j^a\end{Bmatrix}=\frac{X_i^2}{2}\begin{Bmatrix}1\\ 1\end{Bmatrix},\quad i=(1,N).\tag{A6a,b}$$

The solutions of (A3a–d) and (A6a,b) reported in Figs. 4–12 show that it is advisable to use different sizes of the subintervals l_i, especially for solutions with stiff cushions. A gradually refining division has been used when $i \to 1$ to N. Up to $N = 100$ subintervals have been used. Equations (A3a–d) and (A6a,b) are solved by using the numerical routine F04ATF (Mark 13) from the Fortran library NAG (Numerical Algorithms Group). These computations have been performed on a VAX-station.

Material Parameters

The material parameters C_1, C_2, C_3, C_4, and C_5, from the governing equations of the half-plane (1a,b), all depend on the orthotropic properties of the half-plane. However, Eqs. (1a,b) are applicable also for an isotropic half-plane. It is only a matter of difference in the material parameters. These parameters can, through their definition, be degenerated to material parameters valid for an isotropic half-plane. In the study by Bjarnehed (1991), the material parameters are formulated but not explicitly defined. They read

$$C_1=\pi\frac{\alpha\beta c_{11}+c_{12}}{(\alpha+\beta)c_{11}},\quad C_2=\frac{\pi}{(\alpha+\beta)c_{11}},$$

Downloaded 03 May 2010 to 171.66.16.247. Redistribution subject to ASME license or copyright; see http://www.asme.org/terms/Terms_Use.cfm

$$C_3 = \frac{\pi}{\alpha + \beta}, \quad \frac{C_1}{C_4} = \frac{C_2}{C_5} = \alpha\beta, \quad \text{(A7}a\text{–}e\text{)}$$

where

$$\alpha,\beta = \sqrt{\frac{c_{66} + 2c_{12}}{2c_{11}} \pm \sqrt{\left(\frac{c_{66} + 2c_{12}}{2c_{11}}\right)^2 - \frac{c_{22}}{c_{11}}}}, \quad \text{(A8}a,b\text{)}$$

and c_{11}, c_{12}, c_{22}, and c_{66}, are the elastic constants in the generalized Hooke's law for an orthotropic medium, i.e.,

$$\epsilon_x = c_{11}\sigma_x + c_{12}\sigma_y, \quad \epsilon_y = c_{12}\sigma_x + c_{22}\sigma_y, \quad \gamma_{xy} = c_{66}\tau_{xy}. \quad \text{(A9}a\text{–}c\text{)}$$

Lekhnitsky (1937) showed that the constants α and β must be either real or complex numbers, i.e., they cannot be purely imaginary. An isotropic half-plane under plane-stress or plane-strain conditions gives $\alpha = \beta = 1$.

Let us consider an orthotropic half-plane. It is obvious that both C_1 and C_4 are equal to zero if

$$\alpha\beta c_{11} + c_{12} = 0. \quad \text{(A10)}$$

Assume that the orthotropic half-plane has such properties that (A10) is satisfied. An incompressible isotropic material ($\nu = 0.5$) fulfills this condition. The problem with complete adhesive contact and elastic cushion stated in (4*a*–*d*) will then consist of four uncoupled equations similar to the equations considered in Section 5 (frictionless contact). The solutions of interface pressures produced by vertical force (P) and tilting moment (M) will in this respect be identical to the frictionless one. Furthermore, due to the fact that $\eta = 0$, the interface stresses for complete adhesive contact and rigid cushion expressed in (10*a*–*d*) will, for the same kind of loading, be identical to the corresponding frictionless solution expressed in (13*a*, *b*). It appears in (10*a*, *b*) that the horizontal force (F) and the uniform half-plane load (σ_0) will produce interface shear stresses but not any interface pressures.

Downloaded 03 May 2010 to 171.66.16.247. Redistribution subject to ASME license or copyright; see http://www.asme.org/terms/Terms_Use.cfm

M. T. Hanson

Department of Engineering Mechanics,
University of Kentucky,
Lexington, KY 40506-0046

The Elastic Field for Conical Indentation Including Sliding Friction for Transverse Isotropy

This paper gives closed-form expressions in terms of elementary functions for the title problem of conical indentation of elastic bodies possessing transverse isotropy. Traction in the contact region is also included in the form of Coulomb friction; thus, the shear stress is taken proportional to the contact pressure. The present expressions are derived here by integration of the point force Green's functions.

1 Introduction

Considerable attention has recently been given to the development of ceramic materials for tribological applications. As a result of this interest, methods of characterization of their mechanical properties and in service behavior, such as wear resistance, are needed. Microhardness testing (sharp indentation by a diamond pyramid indenter) has been developed as an effective technique to assess mechanical properties of brittle materials such as ceramics, and it allows the introduction of controlled flaws or cracks for strength and fracture toughness evaluation (see, for example, Lawn and Wilshaw, 1975; Lawn et al., 1980; Marshal et al., 1982; Marshal, 1983; Lawn, 1983). Furthermore, sharp indentation is also used as a model for abrasive wear of ceramic surfaces by sharp asperities or wear debri (Braza et al., 1989). Thus, it is important to understand the mechanics of sharp indentation and the resulting stress fields so models relating indentation test results to mechanical properties or models for mechanical damage can be developed. Sharp indentation involves contained plastic deformation under the indenter apex; however, the elastic field must be completely understood as a starting point for an elastic-plastic analysis.

Sharp frictionless indentation of a three-dimensional elastic isotropic half-space by a rigid cone was first analyzed by Love (1939). His solution procedure consisted of expanding the harmonic potential function into spheroidal harmonics in order to meet the boundary conditions, and he was able to sum the series in closed form for points on the axis of symmetry. Based on the form of the potential function on this axis, he ingeniously determined the closed-form solution for the complete potential function. Shortly after the paper by Love, Harding and Sneddon (1945) applied Hankel Transforms to frictionless indentation of an elastic isotropic half-space. This solution was for a general axially symmetric punch profile, and indentation by a cone was considered as a special case. In this investigation the stresses and displacements were only evaluated on the half-space surface. Other investigations of a similar nature are noted by Gladwell (1980). Sneddon (1948) subsequently evaluated the closed-form expressions for the subsurface elastic field resulting from frictionless conical indentation and gave numerical results illustrating the distribution of stress.

A potential function formulation for transversely isotropic materials was developed by Elliot (1948). Elliot (1949) then applied the Hankel transform technique of Harding and Sneddon (1945) to investigate frictionless indentation of a transversely isotropic half-space when the plane of isotropy was parallel to the half-space surface. Conical indentation was considered as one of the examples, and the surface stresses and displacements were evaluated. Although Elliot (1949) did not give explicit expressions for the elastic field, they are obtainable from the isotropic analysis of Sneddon (1948) which gives closed-form expressions for all of the required integrals.

The present paper considers conical indentation of a transversely isotropic half-space under both normal and tangential loading. The case of tangential loading has not been previously considered. The potential functions are found by integrating the Green's functions for point loading, and the integrals are evaluated in terms of closed-form expressions of elementary functions. The elastic field is obtained by differentiation of the potentials and thus is also given in terms of elementary functions. This method has been used previously by Fabrikant (1988) to evaluate the elastic field resulting from frictionless indentation of a transversely isotropic elastic half-space by a right circular cylinder under normal loading and a tilting moment. Hanson (1991a) recently used this method to re-evaluate the elastic field resulting from Hertzian contact of transversely isotropic elastic spheres including tangential traction in the form of Coulomb friction. This method allowed a much simpler form of the solution to be given over that of previous investigations. Similarly, the use of this method for the present problem allows simple expressions to be obtained for the elastic field and, furthermore, shear loading can be included with no additional difficulty.

It is assumed in this analysis that the indenter slides across

Contributed by the ASME Applied Mechanics Division of THE AMERICAN SOCIETY OF MECHANICAL ENGINEERS for presentation at the Winter Annual Meeting, Atlanta, Ga., Dec. 1-6, 1991.

Discussion on this paper should be addressed to the Technical Editor, Prof. Leon M. Keer, The Technological Institute, Northwestern University, Evanston, IL 60208, and will be accepted until two months after final publication of the paper itself in the JOURNAL OF APPLIED MECHANICS. Manuscript received by the ASME Applied Mechanics Division, Feb. 25, 1991; final revision, Apr. 28, 1991.
Paper No. 91-WA/APM-39.

Copyright © 1992 by ASME
Downloaded 03 May 2010 to 171.66.16.247. Redistribution subject to ASME license or copyright; see http://www.asme.org/terms/Terms_Use.cfm

the surface and a Coulomb friction law is used. The shear traction is thus taken as a coefficient of friction multiplied by the contact pressure. It is important to note two key factors which render this solution approximate. First, the effect of shear loading will alter the surface profile and hence the contact pressure will differ to some extent from the frictionless pressure distribution used here. In fact, the true contact area will not remain circular. Second, the shear stress will not align to oppose relative motion. This results, since points on the contact surface have tangential displacements in two directions, while the shear traction is assumed to be unidirectional. In the particular case of $\alpha = 0$ (α is a material constant defined in section 5), the solution derived here for shear loading becomes exact in that, for this value, shear loading produces no normally directed surface displacement, and hence the interaction vanishes (Fabrikant, 1989). The value $\alpha = 0$ corresponds to Poisson's ratio 1/2 for material isotropy. Although for nonzero values of α the above factors render the solution approximate, it is anticipated that the solution here will not differ to a substantial degree from the exact solution, which will require a numerical procedure. Furthermore, the solution here has the advantage that the elastic field can be evaluated in a simple manner without requiring extensive numerical calculations.

2 Potential Functions for Transverse Isotropy

Consider a transversely isotropic elastic half-space $z > 0$ where the surface $z = 0$ is parallel to the plane of isotropy. Using the notation of Fabrikant (1988, 1989), the stress strain relations in Cartesian components are

$$\sigma_{xx} = A_{11}\frac{\partial u}{\partial x} + (A_{11} - 2A_{66})\frac{\partial v}{\partial y} + A_{13}\frac{\partial w}{\partial z}, \tag{1}$$

$$\sigma_{yy} = (A_{11} - 2A_{66})\frac{\partial u}{\partial x} + A_{11}\frac{\partial v}{\partial y} + A_{13}\frac{\partial w}{\partial z}, \tag{2}$$

$$\sigma_{zz} = A_{13}\frac{\partial u}{\partial x} + A_{13}\frac{\partial v}{\partial y} + A_{33}\frac{\partial w}{\partial z}, \tag{3}$$

$$\tau_{xy} = A_{66}\left(\frac{\partial v}{\partial x} + \frac{\partial u}{\partial y}\right), \tag{4}$$

$$\tau_{xz} = A_{44}\left(\frac{\partial w}{\partial x} + \frac{\partial u}{\partial z}\right), \tag{5}$$

$$\tau_{yz} = A_{44}\left(\frac{\partial v}{\partial z} + \frac{\partial w}{\partial y}\right), \tag{6}$$

where u, v, and w are the displacements in the x, y, and z directions and A_{11}, A_{13}, A_{33}, A_{44}, and A_{66} are the five elastic constants.

The solution of the equilibrium equations in terms of three potential functions F_1, F_2, and F_3 may be given as (Fabrikant, 1989)

$$u^c = \Lambda(F_1 + F_2 + iF_3), \quad w = m_1\frac{\partial F_1}{\partial z} + m_2\frac{\partial F_2}{\partial z}, \tag{7}$$

where i is the complex number, $i = \sqrt{-1}$, m_1 and m_2 are constants defined below, and u^c is the complex displacement $u^c = u + iv$. The operator Λ above and the operator Δ used subsequently are defined as

$$\Lambda = \frac{\partial}{\partial x} + i\frac{\partial}{\partial y}, \quad \Delta = \frac{\partial^2}{\partial x^2} + \frac{\partial^2}{\partial y^2}. \tag{8}$$

The functions F_k satisfy the relations

$$\Delta F_k + \gamma_k^2\frac{\partial^2 F_k}{\partial z^2} = 0, \quad k = 1,2,3, \tag{9}$$

where γ_k are also constants. The constant γ_3 is given as $\gamma_3^2 = A_{44}/A_{66}$ while $\gamma_k^2 = n_k$, $k = 1, 2$ and n_k are the two (real or complex conjugate) roots of the quadratic equation

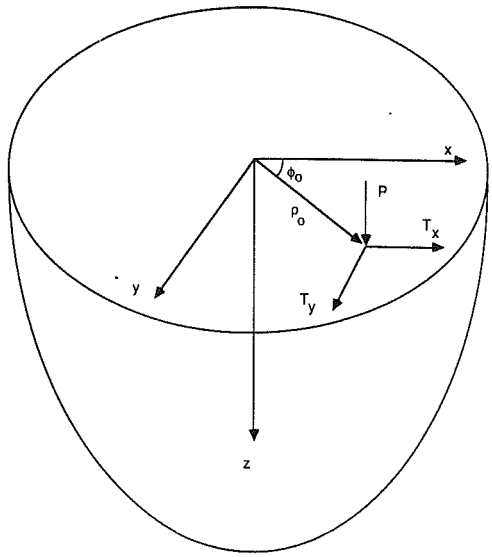


Fig. 1 Geometry and coordinate system for point loading

$$A_{11}A_{44}n^2 + [A_{13}(A_{13} + 2A_{44}) - A_{11}A_{33}]n + A_{33}A_{44} = 0. \tag{10}$$

The constants m_k are related to γ_k as

$$m_k = \frac{A_{11}\gamma_k^2 - A_{44}}{A_{13} + A_{44}} = \frac{(A_{13} + A_{44})\gamma_k^2}{A_{33} - \gamma_k^2 A_{44}}, \; k = 1,2. \tag{11}$$

Using the stress combinations $\sigma_1 = \sigma_{xx} + \sigma_{yy}$, $\sigma_2 = \sigma_{xx} - \sigma_{yy} + 2i\tau_{xy}$ and $\tau_z = \tau_{xz} + i\tau_{yz}$, the stress field is given as (Fabrikant, 1989)

$$\sigma_1 = 2A_{66}\frac{\partial^2}{\partial z^2}([\gamma_1^2 - (1 + m_1)\gamma_3^2]F_1 + [\gamma_2^2 - (1 + m_2)\gamma_3^2]F_2), \tag{12}$$

$$\sigma_2 = 2A_{66}\Lambda^2(F_1 + F_2 + iF_3), \tag{13}$$

$$\sigma_{zz} = A_{44}\frac{\partial^2}{\partial z^2}(\gamma_1^2(1 + m_1)F_1 + \gamma_2^2(1 + m_2)F_2), \tag{14}$$

$$\tau_z = A_{44}\Lambda\frac{\partial}{\partial z}((1 + m_1)F_1 + (1 + m_2)F_2 + iF_3). \tag{15}$$

3 Point Force Green's Functions

To obtain the solution for a distributed loading, integration of the point force solutions will be used. The geometry and coordinate system is shown in Fig. 1. Cylindrical coordinates ρ, ϕ, z are adopted. The point force is applied on the surface $z = 0$ at the point ρ_o, ϕ_o with components T_x, T_y and P in the x, y, and z-directions, respectively.

Considering the normal force P first, the elastic field is given in terms of the potential functions F_1, F_2, and F_3. These can be extracted from Fabrikant (1989) as

$$F_1(\rho,\phi,z;\, \rho_o,\phi_o) = \frac{H\gamma_1}{(m_1 - 1)}P\ln[R_1 + z_1], \tag{16}$$

$$F_2(\rho,\phi,z;\, \rho_o,\phi_o) = \frac{H\gamma_2}{(m_2 - 1)}P\ln[R_2 + z_2], \tag{17}$$

$$F_3(\rho,\phi,z;\, \rho_o,\phi_o) = 0 \tag{18}$$

with

$$R_k^2 = \rho^2 + \rho_o^2 - 2\rho\rho_o\cos(\phi - \phi_o) + z_k^2, \; z_k = \frac{z}{\gamma_k}, \; k = 1, 2, 3, \tag{19}$$

and the constant H is defined as

$$H = \frac{(\gamma_1 + \gamma_2)A_{11}}{2\pi(A_{11}A_{33} - A_{13}^2)}. \tag{20}$$

The potential functions for the point shear loading are given as

Downloaded 03 May 2010 to 171.66.16.247. Redistribution subject to ASME license or copyright; see http://www.asme.org/terms/Terms_Use.cfm

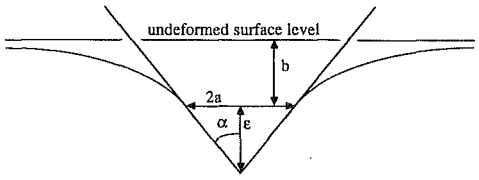


Fig. 2 Geometry of conical indentation

$$F_1(\rho,\phi,z;\ \rho_o,\phi_o)=\frac{H\gamma_1}{(m_1-1)}\frac{\gamma_2}{2}(T\bar{\Lambda}+\bar{T}\Lambda)\chi(z_1), \tag{21}$$

$$F_2(\rho,\phi,z;\ \rho_o,\phi_o)=\frac{H\gamma_2}{(m_2-1)}\frac{\gamma_1}{2}(T\bar{\Lambda}+\bar{T}\Lambda)\chi(z_2), \tag{22}$$

$$F_3(\rho,\phi,z;\ \rho_o,\phi_o)=i\frac{\gamma_3}{4\pi A_{44}}(T\bar{\Lambda}-\bar{T}\Lambda)\chi(z_3), \tag{23}$$

where $T = T_x + iT_y$, an overbar indicates complex conjugation, and the function $\chi(z_k)$ is

$$\chi(z_k)=(z_k\ \ln[R_k+z_k]-R_k),\ k=1,2,3. \tag{24}$$

4 Elastic Field for Frictionless Conical Indentation

The problem under consideration is shown in Fig. 2. A cone-shaped indenter with vertex angle α is pressed into an elastic half-space. The vertex undergoes a displacement of $(b+\epsilon)$ and the contact circle has a radius of a. The elastic field is obtained by first evaluating the potential functions and then differentiating. The potential functions can be obtained by integrating the point force solutions above. For the case of transverse isotropy considered here, the contact stress resulting from conical indentation has the same form as the isotropic case. This happens because the boundary values of the harmonic potential functions for isotropy and transverse isotropy have identical forms (Green and Zerna 1968, Kassir and Sih 1975, Hanson 1991b). The contact stress $\sigma_{zz}(\rho,\phi,0)$ for conical identation inside the circle $\rho = a$ can be extracted from the isotropic analysis of Sneddon (1948) or the transversely isotropic analysis of Elliot (1949) to be

$$\sigma_{zz}(\rho,\phi,0)=-\frac{P}{\pi a^2}\cosh^{-1}\left(\frac{a}{\rho}\right),\ 0<\rho<a.$$

The force P in Eqs. (16)—(18) is replaced with $P/\pi a^2 \cosh^{-1}(a/\rho_o)\ \rho_o d\rho_o d\phi_o$ (where now P is the total contact force) and the result is integrated over $0<\rho_o<a$, $0<\phi_o<2\pi$. The potential functions become

$$F_1(\rho,\phi,z)=\frac{H\gamma_1}{(m_1-1)}\frac{P}{\pi a^2}\psi(\rho,\phi,z_1), \tag{25}$$

$$F_2(\rho,\phi,z)=\frac{H\gamma_2}{(m_2-1)}\frac{P}{\pi a^2}\psi(\rho,\phi,z_2), \tag{26}$$

$$F_3(\rho,\phi,z)=0, \tag{27}$$

where

$$\psi(\rho,\phi,z)=\int_0^{2\pi}\int_0^a \cosh^{-1}\left(\frac{a}{\rho_o}\right)\ln\,[R+z]\rho_o d\rho_o d\phi_o, \tag{28}$$

and $R^2 = \rho^2+\rho_o^2-2\rho\rho_o\cos(\phi-\phi_o)+z^2$.

The integral is evaluated in Appendix A with the result

$$\psi(\rho,\phi,z)=2\pi\left[(az)\sin^{-1}\frac{l_1(a)}{\rho}+\frac{1}{4}(2a^2+\rho^2-2z^2)\ln[l_2(a)\right.$$
$$+\sqrt{l_2^2(a)-\rho^2}]+\frac{3zl_2(a)\ (\rho^2-2l_1^2(a))}{4\rho\sqrt{\rho^2-l_1^2(a)}}-\frac{3z\sqrt{\rho^2+z^2}}{4}$$
$$\left.-\frac{1}{4}(\rho^2-2z^2)\ln\,[z+\sqrt{z^2+\rho^2}]\right], \tag{29}$$

with

$$l_1(a)=\frac{1}{2}(\sqrt{(\rho+a)^2+z^2})-\sqrt{(\rho-a)^2+z^2}), \tag{30}$$

$$l_2(a)=\frac{1}{2}(\sqrt{(\rho+a)^2+z^2}+\sqrt{(\rho-a)^2+z^2}). \tag{31}$$

The elastic field can be evaluated by performing appropriate differentiations of the potential function. The differentiations of $\psi(\rho,\phi,z)$ are tabulated in Appendix A. The elastic field is

$$u^c=\frac{2HP}{a^2}e^{i\phi}\sum_{k=1}^{2}\frac{\gamma_k}{(m_k-1)}\left\{\frac{(\rho l_{2k}(a)-2al_{1k}(a))\sqrt{l_{2k}^2(a)-\rho^2}}{2\rho^2}\right.$$
$$+\frac{\rho}{2}\ln\,[l_{2k}(a)+\sqrt{l_{2k}^2(a)-\rho^2}]-\frac{z_k\sqrt{\rho^2+z_k^2}}{2\rho}$$
$$\left.-\frac{\rho}{2}\ln\,[z_k+\sqrt{\rho^2+z_k^2}]+\frac{a^2}{2\rho}\right\}, \tag{32}$$

$$w=\frac{2HP}{a^2}\sum_{k=1}^{2}\frac{m_k}{(m_k-1)}\left\{(a)\ \sin^{-1}\frac{l_{1k}(a)}{\rho}\right.$$
$$+\sqrt{l_{2k}^2(a)-a^2}-\sqrt{\rho^2+z_k^2}-z_k\ln\,[l_{2k}(a)$$
$$\left.+\sqrt{l_{2k}^2(a)-\rho^2}]+z_k\ln\,[z_k+\sqrt{\rho^2+z_k^2}]\right\}, \tag{33}$$

$$\sigma_1=-\frac{4HPA_{66}}{a^2}\sum_{k=1}^{2}\frac{[\gamma_k^2-(1+m_k)\gamma_3^2]}{\gamma_k(m_k-1)}(\ln\,[l_{2k}(a)$$
$$+\sqrt{l_{2k}^2(a)-\rho^2}]-\ln\,[z_k+\sqrt{\rho^2+z_k^2}]), \tag{34}$$

$$\sigma_2=\frac{4HPA_{66}}{a^2}e^{2i\phi}\sum_{k=1}^{2}\frac{\gamma_k}{(m_k-1)}$$
$$\times\left\{\frac{1}{a\rho^2}(2a^2-l_{2k}^2(a))\sqrt{a^2-l_{1k}^2(a)}+\frac{z_k\sqrt{\rho^2+z_k^2}}{\rho^2}-\frac{a^2}{\rho^2}\right\}, \tag{35}$$

$$\sigma_{zz}=\frac{P}{\pi a^2(\gamma_1-\gamma_2)}\sum_{k=1}^{2}(-1)^k\gamma_k(\ln\,[l_{2k}(a)$$
$$+\sqrt{l_{2k}^2(a)-\rho^2}]-\ln\,[z_k+\sqrt{\rho^2+z_k^2}]), \tag{36}$$

$$\tau_z=\frac{P}{\pi a^2(\gamma_1-\gamma_2)}e^{i\phi}$$
$$\times\sum_{k=1}^{2}(-1)^{k+1}\left(\frac{1}{\rho}\sqrt{l_{2k}^2(a)-a^2}-\frac{\sqrt{\rho^2+z_k^2}}{\rho}\right), \tag{37}$$

where the notation

$$l_{1k}(a)=\frac{1}{2}\left(\sqrt{(\rho+a)^2+z_k^2}-\sqrt{(\rho-a)^2+z_k^2}\right), \tag{38}$$

has been introduced along with a similar interpretation for $l_{2k}(a)$.

The relationship between contact force P and the indentation parameters shown in Fig. 2 are now obtained. From Fig. 2, the normal displacement in the contact region can be written as

$$w=b+\epsilon\left(1-\frac{\rho}{a}\right),\quad 0<\rho<a, \tag{39}$$

where ϵ and α are related by $\epsilon = a\cot(\alpha)$. From Eq. (33), the normal displacement in the contact region is

Downloaded 03 May 2010 to 171.66.16.247. Redistribution subject to ASME license or copyright; see http://www.asme.org/terms/Terms_Use.cfm

$$w=\frac{2HP}{a^2}\left(\frac{\pi}{2}a-\rho\right)$$
$$=\frac{2HP}{a}\left(\frac{\pi}{2}-1\right)+\frac{2HP}{a}\left(1-\frac{\rho}{a}\right),\ 0<\rho<a, \quad (40)$$

where H is a material constant given in Eq. (20). Comparison of these expressions yields

$$b=\epsilon\left(\frac{\pi}{2}-1\right),\ \epsilon=\frac{2HP}{a}. \quad (41)$$

If the contact force is specified, the contact parameters can be obtained as

$$a=\sqrt{2HP\tan(\alpha)},\quad \epsilon=\sqrt{2HP\cot(\alpha)},\quad b=\epsilon\left(\frac{\pi}{2}-1\right). \quad (42)$$

For isotropy, $H = (1-\nu^2/\pi E)$ where ν is Poisson's ratio and E is Young's modulus. The above relations agree with those given previously. If the penetration depth $d_p = b + \epsilon$ and cone angle α are given, then the contact radius and load P can be found as

$$a=\frac{2}{\pi}d_p\tan(\alpha),\quad P=\frac{2}{\pi^2 H}d_p^2\tan(\alpha). \quad (43)$$

5 Elastic Field for Shear Traction

The shear traction in the contact region is taken as a coefficient of friction multiplied by the contact pressure. Using f_x and f_y as the coefficients of friction in the x and y-directions, the complex shear force $T = T_x + iT_y$ in the potential functions of equations (21)–(23) is replaced by

$$T=\frac{fP}{\pi a^2}\cosh^{-1}\left(\frac{a}{\rho_o}\right)\rho_o d\rho_o d\phi_o,\quad f=f_x+if_y, \quad (44)$$

and the result is integrated on $0<\rho_o<a$, $0<\phi_o<2\pi$. The potentials become

$$F_1(\rho,\phi,z)=\frac{H\gamma_1\gamma_2}{(m_1-1)}\frac{P}{2\pi a^2}\{(f\bar{\Lambda}+\bar{f}\Lambda)\ (z_1\psi(\rho,\phi,z_1)-\Phi(\rho,\phi,z_1))\}, \quad (45)$$

$$F_2(\rho,\phi,z)=\frac{H\gamma_1\gamma_2}{(m_2-1)}\frac{P}{2\pi a^2}\{(f\bar{\Lambda}+\bar{f}\Lambda)\ (z_2\psi(\rho,\phi,z_2)-\Phi(\rho,\phi,z_2))\}, \quad (46)$$

$$F_3(\rho,\phi,z)=i\frac{P\gamma_3}{4\pi^2 a^2 A_{44}}\{(f\bar{\Lambda}-\bar{f}\Lambda)\ (z_3\psi(\rho,\phi,z_3)-\Phi(\rho,\phi,z_3))\}, \quad (47)$$

where $\psi(\rho,\phi,z)$ is given above and $\Phi(\rho,\phi,z)$ is

$$\Phi(\rho,\phi,z)=\int_0^{2\pi}\int_0^a \cosh^{-1}\left(\frac{a}{\rho_o}\right)R\rho_o d\rho_o d\phi_o, \quad (48)$$

and R is given after Eq. (28).

The integral is evaluated in Appendix B with the result

$$\Phi(\rho,\phi,z)=2\pi\left\{\frac{a}{12}(6z^2+3\rho^2+2a^2)\sin^{-1}\frac{l_1(a)}{\rho}\right.$$
$$+\frac{1}{3}z^3\ln\left[z+\sqrt{z^2+\rho^2}\right]-\frac{1}{3}z^3\ln\left[l_2(a)+\sqrt{l_2^2(a)-\rho^2}\right]$$
$$-\frac{1}{9}(4z^2+\rho^2)\sqrt{z^2+\rho^2}+\frac{1}{36}(21l_1^2(a)+16l_2^2(a)$$
$$\left.-12\rho^2-10a^2)\sqrt{l_2^2(a)-a^2}\right\}. \quad (49)$$

The elastic field can again be found by differentiation of the potential functions. The required differentiations of $\psi(\rho,\phi,z)$ are given in Appendix A and those for $\Phi(\rho,\phi,z)$ are given in Appendix B. The elastic field is given as

$$u^c=\frac{HP}{a^2}\gamma_1\gamma_2\sum_{k=1}^{2}\frac{1}{(m_k-1)}\left[f\left\{-(a)\sin^{-1}\frac{l_{1k}(a)}{\rho}\right.\right.$$
$$-\sqrt{l_{2k}^2(a)-a^2}+z_k\ln\left[l_{2k}(a)+\sqrt{l_{2k}^2(a)-\rho^2}\right]$$
$$\left.-z_k\ln\left[z_k+\sqrt{\rho^2+z_k^2}\right]+\sqrt{\rho^2+z_k^2}\right\}+\bar{f}e^{i2\phi}\left\{-\frac{a^2z_k}{\rho^2}\right.$$
$$\left.\left.+\frac{1}{3\rho^2}(\rho^2+z_k^2)^{3/2}+\frac{1}{3\rho^2}(4a^2-3l_{1k}^2(a)-l_{2k}^2(a))\sqrt{l_{2k}^2(a)-a^2}\right\}\right]$$
$$-\frac{P\gamma_3}{2\pi a^2 A_{44}}\left[f\left\{-(a)\sin^{-1}\frac{l_{13}(a)}{\rho}-\sqrt{l_{23}^2(a)-a^2}\right.\right.$$
$$+z_3\ln\left[l_{23}(a)+\sqrt{l_{23}^2(\mathrm{a})-\rho^2}\right]-z_3\ln\left[z_3+\sqrt{\rho^2+z_3^2}\right]$$
$$\left.+\sqrt{\rho^2+z_3^2}\right\}-\bar{f}e^{i2\phi}\left\{-\frac{a^2z_3}{\rho^2}+\frac{1}{3\rho^2}(\rho^2+z_3^2)^{3/2}\right.$$
$$\left.\left.+\frac{1}{3\rho^2}(4a^2-3l_{13}^2(a)-l_{23}^2(a))\sqrt{l_{23}^2(a)-a^2}\right\}\right], \quad (50)$$

$$w=\frac{HP\gamma_1\gamma_2}{a^2}(\bar{f}e^{i\phi}+fe^{-i\phi})\sum_{k=1}^{2}\frac{m_k}{(m_k-1)\gamma_k}\left\{\frac{\rho}{2}\ln\left[l_{2k}(a)\right.\right.$$
$$\left.+\sqrt{l_{2k}^2(a)-\rho^2}\right]-\frac{\rho}{2}\ln\left[z_k+\sqrt{\rho^2+z_k^2}\right]+\frac{a^2}{2\rho}-\frac{z_k\sqrt{\rho^2+z_k^2}}{2\rho}$$
$$\left.+\frac{(\rho l_{2k}(a)-2al_{1k}(a))\sqrt{l_{2k}^2(a)-\rho^2}}{2\rho^2}\right\}, \quad (51)$$

$$\sigma_1=\frac{2HPA_{66}\gamma_1\gamma_2}{a^2}(\bar{f}e^{i\phi}+fe^{-i\phi})\sum_{k=1}^{2}\frac{[\gamma_k^2-(1+m_k)\gamma_3^2]}{\gamma_k^2(m_k-1)}$$
$$\times\left\{\frac{\sqrt{l_{2k}^2(a)-a^2}}{\rho}-\frac{\sqrt{\rho^2+z_k^2}}{\rho}\right\}, \quad (52)$$

$$\sigma_2=\frac{2HPA_{66}\gamma_1\gamma_2}{a^2}\sum_{k=1}^{2}\frac{1}{(m_k-1)}\left[fe^{i\phi}\left\{\frac{\sqrt{\rho^2+z_k^2}}{\rho}\right.\right.$$
$$\left.-\frac{\sqrt{l_{2k}^2(a)-a^2}}{\rho}\right\}+\bar{f}e^{i3\phi}\left\{(12l_{1k}^2(a)+4l_{2k}^2(a)\right.$$
$$\left.\left.-3\rho^2-16a^2)\frac{\sqrt{l_{2k}^2(a)-a^2}}{3\rho^3}+\frac{4a^2z_k}{\rho^3}-\frac{4z_k^4+\rho^4+5\rho^2z_k^2}{3\rho^3\sqrt{\rho^2+z_k^2}}\right\}\right]$$
$$-\frac{P}{\pi a^2\gamma_3}\left[fe^{i\phi}\left\{\frac{\sqrt{\rho^2+z_3^2}}{\rho}-\frac{\sqrt{l_{23}^2(a)-a^2}}{\rho}\right\}\right.$$
$$-\bar{f}e^{i3\phi}\left\{(12l_{13}^2(a)+4l_{23}^2(a)-3\rho^2-16a^2)\frac{\sqrt{l_{23}^2(a)-a^2}}{3\rho^3}\right.$$
$$\left.\left.+\frac{4a^2z_3}{\rho^3}-\frac{4z_3^4+\rho^4+5\rho^2z_3^2}{3\rho^3\sqrt{\rho^2+z_3^2}}\right\}\right], \quad (53)$$

$$\sigma_{zz}=\frac{P\gamma_1\gamma_2}{2\pi a^2(\gamma_1-\gamma_2)}(\bar{f}e^{i\phi}+fe^{-i\phi})\sum_{k=1}^{2}(-1)^{k+1}$$
$$\times\left\{\frac{\sqrt{l_{2k}^2(a)-a^2}}{\rho}-\frac{\sqrt{\rho^2+z_k^2}}{\rho}\right\}, \quad (54)$$

$$\tau_z=\frac{P\gamma_1\gamma_2}{2\pi a^2(\gamma_1-\gamma_2)}\sum_{k=1}^{2}\frac{(-1)^{k+1}}{\gamma_k}\left[f\left\{\ln\left[l_{2k}(a)\right.\right.\right.$$
$$\left.\left.\left.+\sqrt{l_{2k}^2(a)-\rho^2}\right]-\ln\left[z_k+\sqrt{\rho^2+z_k^2}\right]\right\}\right.$$

Downloaded 03 May 2010 to 171.66.16.247. Redistribution subject to ASME license or copyright; see http://www.asme.org/terms/Terms_Use.cfm

$$+\bar{f}e^{i2\phi}\left\{\frac{(2a^2-l_{2k}^2(a))\sqrt{a^2-l_{1k}^2(a)}}{a\rho^2}+\frac{z_k\sqrt{\rho^2+z_k^2}}{\rho^2}-\frac{a^2}{\rho^2}\right\}\Bigg]$$

$$-\frac{P}{2\pi a^2}\left[f\left\{\ln\left[l_{23}(a)+\sqrt{l_{23}^2(a)-\rho^2}\right]-\ln\left[z_3+\sqrt{\rho^2+z_3^2}\right]\right\}\right.$$

$$\left.-\bar{f}e^{i2\phi}\left\{\frac{(2a^2-l_{23}^2(a))\sqrt{a^2-l_{13}^2(a)}}{a\rho^2}+\frac{z_3\sqrt{\rho^2+z_3^2}}{\rho^2}-\frac{a^2}{\rho^2}\right\}\right]. \quad (55)$$

It was noted previously that the present solution is approximate, since shear loading will generally produce a normal displacement in the contact region, thus altering the contact pressure. From Eq. (51) the normal displacement on the surface is given as (using the limits in Eq. (82))

$$w=\frac{HP\alpha}{2a^2}(\bar{f}e^{i\phi}+fe^{-i\phi})\left\{\rho\ln\left(\frac{a+\sqrt{a^2-\rho^2}}{\rho}\right)+\frac{a^2}{\rho}-\frac{a\sqrt{a^2-\rho^2}}{\rho}\right\},\ \rho<a, \quad (56)$$

$$w=HP\alpha(\bar{f}e^{i\phi}+fe^{-i\phi})\frac{1}{2\rho},\quad \rho>a, \quad (57)$$

where the relation

$$\alpha=\gamma_1\gamma_2\sum_{k=1}^{2}\frac{m_k}{(m_k-1)\gamma_k}=\frac{\sqrt{A_{11}A_{33}}-A_{13}}{A_{11}(\gamma_1+\gamma_2)}, \quad (58)$$

(Fabrikant, 1989) has been used. The normal displacement is maximum near the edge of contact at $\rho = 0.827a$ and vanishes at the center $\rho = 0$. In the special case $\alpha = 0$ the normal displacement vanishes everywhere, and there is no interaction between the normal and shear loading. In this case the above solution is exact (although the relative displacements still do not align with the direction of shear traction). In the isotropic limit $\alpha = (1-2\nu)/[2(1-\nu)]$, and thus $\alpha = 0$ corresponds to an incompressible material.

6 Discussion

At this stage it is interesting to compare the present results with those obtained previously. Sneddon (1948) has given closed-form expressions for the frictionless subsurface stress fields for isotropy. Using the present stress components, his results take the form

$$\sigma_1=-\frac{E\epsilon}{2a(1-\nu^2)}((1+2\nu)J_1^0-\xi J_2^0), \quad (59)$$

$$\sigma_2=\frac{E\epsilon}{2a(1-\nu^2)}e^{2i\phi}\left((1-2\nu)\left\{\frac{2}{\beta}J_0^1-J_1^0\right\}+\xi\left\{J_2^0-\frac{2}{\beta}J_1^1\right\}\right), \quad (60)$$

$$\sigma_{zz}=-\frac{E\epsilon}{2a(1-\nu^2)}(J_1^0+\xi J_2^0), \quad (61)$$

$$\tau_z=-\frac{E\epsilon}{2a(1-\nu^2)}e^{i\phi}\xi J_2^1, \quad (62)$$

where E is Young's modulus and ν is the Poisson's ratio. Here, $\beta = \rho/a$, $\xi = z/a$, and

$$J_1^0=\frac{1}{2}\ln[R^2+2rR\cos(\theta-\bar{\phi})+r^2]-\ln\left[\xi+\sqrt{\xi^2+\beta^2}\right], \quad (63)$$

$$J_2^0=\frac{1}{\sqrt{\beta^2+\xi^2}}-\frac{1}{R}\cos(\bar{\phi}), \quad (64)$$

$$J_1^1=\frac{1}{\beta}(\sqrt{\beta^2+\xi^2}-R\cos(\bar{\phi})), \quad (65)$$

$$J_2^1=\frac{1}{\beta}\left(\frac{r}{R}\cos(\theta-\bar{\phi})-\frac{\xi}{\sqrt{\beta^2+\xi^2}}\right), \quad (66)$$

$$J_0^1=\frac{1}{2}\left(\beta J_1^0+\frac{1}{\beta}(1-R\sin(\bar{\phi}))-\xi J_1^1\right). \quad (67)$$

The parameters r, R, θ, and $\bar{\phi}$ are given by

$$R^4=(\beta^2+\xi^2-1)^2+4\xi^2,\quad r^2=1+\xi^2, \quad (68)$$

$$\tan(\theta)=\frac{1}{\xi},\quad \tan(2\bar{\phi})=\frac{2\xi}{\beta^2+\xi^2-1}. \quad (69)$$

Sneddon (1948) uses the parameter ϕ which is replaced above with $\bar{\phi}$, since ϕ is used here for the polar angle. Since $\xi > 0$, θ can be computed using the principal value of the inverse tangent, while for $\bar{\phi}$,

$$2\bar{\phi}=\tan^{-1}\frac{2\xi}{\beta^2+\xi^2-1},\quad \beta^2+\xi^2-1>0,$$
$$2\bar{\phi}=\pi+\tan^{-1}\frac{2\xi}{\beta^2+\xi^2-1},\quad \beta^2+\xi^2-1<0, \quad (70)$$

and the principal value is used in each case. This was not noted by Sneddon (1948). Furthermore, the solution is also repeated in Sneddon (1951) where J has been replaced by K; however, the parameters R and ϕ (here $\bar{\phi}$) are incorrectly defined there.

The isotropic limit of the expressions derived here can be computed as follows: For isotropy γ_1, γ_2, γ_3, m_1 $m_2 \to 1$ (Fabrikant 1989), and the following results can be used

$$\sum_{k=1}^{2}\frac{\gamma_k}{m_k-1}f(z_k)=-\frac{(1-2\nu)f(z)+zf'(z)}{2(1-\nu)}, \quad (71)$$

$$\sum_{k=1}^{2}\frac{m_k}{m_k-1}f(z_k)=f(z)-\frac{z}{2(1-\nu)}f'(z), \quad (72)$$

$$\sum_{k=1}^{2}\frac{[\gamma_k^2-(1+m_k)\gamma_3^2]}{\gamma_k(m_k-1)}f(z_k)=\frac{(1+2\nu)f(z)+zf'(z)}{2(1-\nu)}, \quad (73)$$

$$\frac{1}{\gamma_1-\gamma_2}\sum_{k=1}^{2}(-1)^k\gamma_k f(z_k)=-f(z)+zf'(z), \quad (74)$$

$$\frac{1}{\gamma_1-\gamma_2}\sum_{k=1}^{2}(-1)^{k+1}f(z_k)=-zf'(z), \quad (75)$$

where $f'(z)$ denotes the derivative of $f(z)$. Using the aforementioned expressions, along with equation (41), and the isotropic limits $H = (1-\nu^2)/(\pi E)$, $A_{66} = E/[2(1+\nu)]$, the elastic field in equations (32)–(37) take the form

$$u^c=-\frac{\epsilon}{2a(1-\nu)}e^{i\phi}\left[(1-2\nu)\left(\frac{(\rho l_2(a)-2al_1(a))\sqrt{l_2^2(a)-\rho^2}}{2\rho^2}+\frac{\rho}{2}\ln\left[l_2(a)+\sqrt{l_2^2(a)-\rho^2}\right]-\frac{z\sqrt{\rho^2+z^2}}{2\rho}-\frac{\rho}{2}\ln\left[z+\sqrt{\rho^2+z^2}\right]+\frac{a^2}{2\rho}\right)+\frac{z}{\rho}\left(\sqrt{l_2^2(a)-a^2}-\sqrt{\rho^2+z^2}\right)\right], \quad (76)$$

$$w=\frac{\epsilon}{a}\left[(a)\sin^{-1}\frac{l_1(a)}{\rho}+\sqrt{l_2^2(a)-a^2}-\sqrt{\rho^2+z^2}-\frac{z(1-2\nu)}{2(1-\nu)}(\ln\left[l_2(a)+\sqrt{l_2^2(a)-\rho^2}\right]-\ln\left[z+\sqrt{\rho^2+z^2}\right])\right], \quad (77)$$

Downloaded 03 May 2010 to 171.66.16.247. Redistribution subject to ASME license or copyright; see http://www.asme.org/terms/Terms_Use.cfm

$$\sigma_1 = -\frac{E\epsilon}{2a(1-\nu^2)}\left[(1+2\nu)\,(\ln\,[l_2(a)+\sqrt{l_2^2(a)-\rho^2}]\right.$$

$$\left.-\ln\,[z+\sqrt{\rho^2+z^2}])+z\left(\frac{\sqrt{l_2^2(a)-a^2}}{(l_2^2(a)-l_1^2(a))}-\frac{1}{\sqrt{\rho^2+z^2}}\right)\right], \quad (78)$$

$$\sigma_2 = -\frac{E\epsilon}{2a(1-\nu^2)}\,e^{2i\phi}\left[(1-2\nu)\left(\frac{1}{a\rho^2}\,(2a^2-l_2^2(a))\sqrt{a^2-l_1^2(a)}\right.\right.$$

$$\left.+\frac{z\sqrt{\rho^2+z^2}}{\rho^2}-\frac{a^2}{\rho^2}\right)$$

$$\left.+\frac{z^2a[\rho^2+2l_1^2(a)-2l_2^2(a)]}{\rho^2\sqrt{a^2-l_1^2(a)}[l_2^2(a)-l_1^2(a)]}+\frac{z(\rho^2+2z^2)}{\rho^2\sqrt{\rho^2+z^2}}\right], \quad (79)$$

$$\sigma_{zz} = -\frac{E\epsilon}{2a(1-\nu^2)}\left[\ln\,[l_2(a)+\sqrt{l_2^2(a)-\rho^2}]-\ln[z+\sqrt{\rho^2+z^2}]\right.$$

$$\left.-\frac{z^2l_2(a)}{\sqrt{l_2^2(a)-\rho^2}\,[l_2^2(a)-l_1^2(a)]}+\frac{z}{\sqrt{\rho^2+z^2}}\right], \quad (80)$$

$$\tau_z = -\frac{E\epsilon}{2a(1-\nu^2)}\,e^{i\phi}\,\frac{1}{\rho}\left[\frac{zl_2(a)\sqrt{l_2^2(a)-\rho^2}}{[l_2^2(a)-l_1^2(a)]}-\frac{z^2}{\sqrt{\rho^2+z^2}}\right]. \quad (81)$$

Equations (78)–(81) for stresses agree with Sneddon's formulas in Eqs. (59)–(62) as long as $\bar{\phi}$ is taken as in Eq. (70). The above comparison illustrates the advantage of the present solution. Only two length parameters $l_1(a)$ and $l_2(a)$ need to be introduced, and the resulting expressions are given in simple forms of them. The present solution also allows the surface values to be simply obtained since

$$\lim_{z\to 0} l_1(a) = \min(a,\,\rho), \quad \lim_{z\to 0} l_2(a) = \max(a,\,\rho), \quad (82)$$

where $\min(a, \rho)$ implies the minimum of the two values and $\max(a, \rho)$ implies the maximum.

7 Conclusion

The present analysis has investigated the elastic field resulting from conical indentation. Sliding was included using a Coulomb friction model where the shear traction is equal to a coefficient of friction multiplied by the normal pressure. The interaction between the normal and shear stresses has been neglected. Using the Green's function method, it has been shown that the potential functions could be evaluated in terms of closed-form expressions of elementary functions. The elastic field was evaluated by differentiation, also resulting in closed-form expressions of elementary functions. The solution for frictionless indentation in the case of isotropy agrees with previous research. The solution for transverse isotropy, including sliding friction, appears to be new.

Acknowledgment

The author would like to thank one of the reviewers for pointing out the present solution for shear loading is exact for materials satisfying $\alpha = 0$.

References

Braza, J. F., Cheng, H. S., Fine, M. E., Gangopadhyay, A. K., Keer, L. M., and Worden, R. E., 1989, "Mechanical Failure Mechanisms in Ceramic Sliding and Rolling Contact," *Tribology Transactions*, Vol. 32, pp. 1–8.

Elliot, H. A., 1948, "Three-Dimensional Stress Distributions in Hexagonal Aeolotropic Crystals," *Proceedings of the Cambridge Philosophical Society*, Vol. 44, pp. 522–533.

Elliot, H. A., 1949, "Axial Symmetric Stress Distributions in Aeolotropic Hexagonal Crystals: The Problem of the Plane and Related Problems," *Proceedings of the Cambridge Philosophical Society*, Vol. 45, pp. 621–630.

Fabrikant, V. I., 1988, "Elastic Field Around a Circular Punch," ASME JOURNAL OF APPLIED MECHANICS, Vol. 55, pp. 604–610.

Fabrikant, V. I., 1989, *Applications of Potential Theory in Mechanics: A Selection of New Results*, Kluwer Academic Publishers, The Netherlands, pp. 71–79.

Gladwell, G. M. L., 1980, *Contact Problems in the Classical Theory of Elasticity*, Sijthoff and Noordhoff, The Netherlands, pp. 457–468.

Green, A. E., and Zerna, W., 1968, *Theoretical Elasticity*, Oxford University Press, London, U.K., pp. 177–181.

Hanson, M. T., 1991a, "The Elastic Field for Spherical Hertzian Contact Including Sliding Friction for Transverse Isotropy," *ASME Journal of Tribology*, submitted for publication.

Hanson, M. T., 1991b, "The Elastic Potentials for Coplanar Interaction Between an Infinitesimal Prismatic Dislocation Loop and a Circular Crack for Transverse Isotropy," *ASME Journal of Applied Mechanics*, in press.

Harding, J. W., and Sneddon, I. N., 1945, "The Elastic Stresses Produced by the Indentation of the Plane Surface of a Semi-Infinite Elastic Solid by a Rigid Cone," *Proceedings of the Cambridge Philosophical Society*, Vol. 41, pp. 16–26.

Kassir, M. K., and Sih, G. C., 1975, *Three-Dimensional Crack Problems*, Vol. 2, (Mechanics of Fracture) Noordhoff International Publishing, The Netherlands, pp. 339–342.

Lawn, B. R., and Wilshaw, T. R., 1975, "Review, Indentation Fracture: Principles and Applications," *Journal of Materials Science*, Vol. 10, pp. 1049–1081.

Lawn, B. R., Evans, A. G., and Marshal, D. B., 1980, "Elastic/Plastic Indentation Damage in Ceramics," *Journal of the American Ceramic Society*, Vol. 63, pp. 574–581.

Lawn, B. R., 1983, "The Indentation Crack as a Model Surface Flaw," *Fracture Mechanics of Ceramics*, Vol. 5, R. C. Bradt, A. G. Evans, D. P. H. Hasselman, and F. F. Lange, eds., Plenum, New York, pp. 1–25.

Love, A. E. H., 1939, "Boussinesq's Problem for a Rigid Cone," *Quarterly Journal of Mathematics*, Vol. 10, pp. 161–175.

Marshal, D. B., Lawn, B. R., and Evans, A. G., 1982, "Elastic/Plastic Indentation Damage in Ceramics: The Lateral Crack System," *Journal of the American Ceramic Society*, Vol. 65, pp. 561–566.

Marshal, D. B., 1983, "Controlled Flaws in Ceramics: A Comparison of Knoop and Vickers Indentation," *Journal of the American Ceramic Society*, Vol. 66, pp. 127–131.

Sneddon, I. N., 1948, "Boussinesq's Problem for a Rigid Cone," *Proceedings of the Cambridge Philosophical Society*, Vol. 44, pp. 492–507.

Sneddon, I. N., 1951, *Fourier Transforms*, McGraw-Hill, New York, pp. 462–468.

APPENDIX A

Here the function $\psi(\rho,\phi,z)$ defined in Eq. (28) is evaluated. First differentiation of Eq. (28), with respect to a, yields

$$\frac{\partial}{\partial a}\,\psi(\rho,\phi,z) = \int_0^{2\pi}\int_0^a \frac{1}{\sqrt{a^2-\rho_o^2}}\,\ln\,[R+z]\rho_o d\rho_o d\phi_o. \quad (A1)$$

This integral has been evaluated by Fabrikant (1988) with the result

$$\frac{\partial}{\partial a}\,\psi(\rho,\phi,z) = 2\pi\left\{(z)\,\sin^{-1}\frac{l_1(a)}{\rho}-\sqrt{a^2-l_1^2(a)}\right.$$

$$\left.+a\ln[l_2(a)+\sqrt{l_2^2(a)-\rho^2}]\right\}. \quad (A2)$$

Using the indefinite integrals

$$\int a\ln[l_2(a)+\sqrt{l_2^2(a)-\rho^2}]da$$

$$=\frac{1}{4}\,(2a^2+2z^2-\rho^2)\,\ln[l_2(a)+\sqrt{l_2^2(a)-\rho^2}]$$

$$+\frac{1}{4a}\,(2a^2-3l_2^2(a))\sqrt{a^2-l_1^2(a)}, \quad (A3)$$

$$\int \sin^{-1}\frac{l_1(a)}{\rho}\,da = (a)\sin^{-1}\frac{l_1(a)}{\rho}+\frac{1}{\rho}\,l_2(a)\sqrt{\rho^2-l_1^2(a)}$$

$$-z\ln[l_2(a)+\sqrt{l_2^2(a)-\rho^2}], \quad (A4)$$

$$\int \sqrt{a^2-l_1^2(a)}\,da = a\sqrt{a^2-l_1^2(a)}-\frac{1}{2}\,l_2(a)\sqrt{l_2^2(a)-\rho^2}$$

$$-\frac{\rho^2}{2}\ln[l_2(a)+\sqrt{l_2^2(a)-\rho^2}], \quad (A5)$$

the function $\psi(\rho,\phi,z)$ becomes

Downloaded 03 May 2010 to 171.66.16.247. Redistribution subject to ASME license or copyright; see http://www.asme.org/terms/Terms_Use.cfm

$$\psi(\rho,\phi,z)=2\pi\left\{(az)\sin^{-1}\frac{l_1(a)}{\rho}+\frac{1}{4\rho}\,3zl_2(a)\,(\rho^2-2l_1^2(a))\,\frac{1}{\sqrt{\rho^2-l_1^2(a)}}+\frac{1}{4}\,(2a^2-2z^2+\rho^2)\,\ln[l_2(a)+\sqrt{l_2^2(a)-\rho^2}]\right\}+f(\rho,\phi,z). \quad \text{(A6)}$$

Since the integral was evaluated as indefinite, an arbitrary function of the variables ρ, ϕ, and z may be added. This function can be found by the requirement that $\psi(\rho,\phi,z)\to 0$ for $a\to 0$ for any $\rho,z>0$.

This gives the result

$$f(\rho,\phi,z)=-2\pi\left\{\frac{3}{4}\,z\sqrt{\rho^2+z^2}-\frac{1}{4}\,(2z^2-\rho^2)\,\ln[z+\sqrt{z^2+\rho^2}]\right\}. \quad \text{(A7)}$$

The final form of the potential function can be given as

$$\psi(\rho,\phi,z)=2\pi\left\{(az)\sin^{-1}\frac{l_1(a)}{\rho}+\frac{1}{4\rho}\,3zl_2(a)(\rho^2-2l_1^2(a))\,\frac{1}{\sqrt{\rho^2-l_1^2(a)}}+\frac{1}{4}\,(2a^2-2z^2+\rho^2)\,\ln[l_2(a)+\sqrt{l_2^2(a)-\rho^2}]-\frac{3}{4}\,z\sqrt{\rho^2+z^2}+\frac{1}{4}\,(2z^2-\rho^2)\,\ln[z+\sqrt{z^2+\rho^2}]\right\}. \quad \text{(A8)}$$

The differentiations of $\psi(\rho,\phi,z)$ needed for the elastic field are

$$\frac{\partial}{\partial z}\,\psi(\rho,\phi,z)=2\pi\left\{(a)\sin^{-1}\frac{l_1(a)}{\rho}+\sqrt{l_2^2(a)-a^2}-z\,\ln[l_2(a)+\sqrt{l_2^2(a)-\rho^2}]-\sqrt{\rho^2+z^2}+z\,\ln[z+\sqrt{z^2+\rho^2}]\right\}, \quad \text{(A9)}$$

$$\Lambda\psi(\rho,\phi,z)=2\pi e^{i\phi}\left\{\frac{\rho}{2}\,\ln[l_2(a)+\sqrt{l_2^2(a)-\rho^2}]-\frac{\rho}{2}\,\ln[z+\sqrt{\rho^2+z^2}]+\frac{a^2}{2\rho}-\frac{z\sqrt{\rho^2+z^2}}{2\rho}+\frac{(\rho l_2(a)-2al_1(a))\sqrt{l_2^2(a)-\rho^2}}{2\rho^2}\right\}, \quad \text{(A10)}$$

$$\Lambda^2\psi(\rho,\phi,z)=2\pi e^{i2\phi}\left\{\frac{(2a^2-l_2^2(a))\sqrt{a^2-l_1^2(a)}}{a\rho^2}+\frac{z\sqrt{\rho^2+z^2}}{\rho^2}-\frac{a^2}{\rho^2}\right\}, \quad \text{(A11)}$$

$$\frac{\partial^2}{\partial z^2}\,\psi(\rho,\phi,z)=-2\pi\{\ln[l_2(a)+\sqrt{l_2^2(a)-\rho^2}]-\ln[z+\sqrt{\rho^2+z^2}]\}, \quad \text{(A12)}$$

$$\Delta\psi(\rho,\phi,z)=2\pi\{\ln[l_2(a)+\sqrt{l_2^2(a)-\rho^2}]-\ln[z+\sqrt{\rho^2+z^2}]\}, \quad \text{(A13)}$$

$$\frac{\partial}{\partial z}\,\Lambda\psi(\rho,\phi,z)=2\pi e^{i\phi}\,\frac{1}{\rho}\,(\sqrt{l_2^2(a)-a^2}-\sqrt{\rho^2+z^2}), \quad \text{(A14)}$$

$$\Lambda\Delta\psi(\rho,\phi,z)=-2\pi e^{i\phi}\left\{\frac{a\rho\sqrt{a^2-l_1^2(a)}}{l_1^2(a)[l_2^2(a)-l_1^2(a)]}-\frac{z}{\rho\sqrt{\rho^2+z^2}}\right\}, \quad \text{(A15)}$$

$$\Lambda^3\psi(\rho,\phi,z)=2\pi e^{i3\phi}\left\{\frac{4a^2}{\rho^3}-\frac{3z\rho^2+4z^3}{\rho^3\sqrt{\rho^2+z^2}}+\frac{\sqrt{a^2-l_1^2(a)}}{a\rho^3[l_2^2(a)-l_1^2(a)]}\,([2a^2-l_2^2(a)][4l_1^2(a)-4l_2^2(a)+\rho^2]-2a^2\rho^2)\right\}, \quad \text{(A16)}$$

where $l_1(a)$ and $l_2(a)$ are defined in Eqs. (30), (31).

APPENDIX B

Here the function $\Phi(\rho,\phi,z)$ defined in Eq. (48) is evaluated. First differentiation of Eq. (48), with respect to z, yields

$$\frac{\partial}{\partial z}\,\Phi(\rho,\phi,z)=z\int_0^{2\pi}\int_0^a\frac{\cosh^{-1}\left(\frac{a}{\rho_o}\right)\rho_o d\rho_o d\phi_o}{R}=z\,\frac{\partial}{\partial z}\,\psi(\rho,\phi,z). \quad \text{(B1)}$$

Using integration by parts, $\Phi(\rho,\phi,z)$ can be written as

$$\Phi(\rho,\phi,z)=z\psi(\rho,\phi,z)-\int\psi(\rho,\phi,z)dz, \quad \text{(B2)}$$

where $\psi(\rho,\phi,z)$ is given in Eq. (29) and (A8). Using the indefinite integrals (where $l_1(a)$ and $l_2(a)$ are defined in Eqs. (30), (31)).

$$\int(z)\sin^{-1}\frac{l_1(a)}{\rho}\,dz=\frac{1}{4}\,(2a^2+2z^2+\rho^2)\sin^{-1}\frac{l_1(a)}{\rho}+\frac{1}{4a}\,(2a^2+l_1^2(a))\sqrt{l_2^2(a)-a^2}, \quad \text{(B3)}$$

$$\int\frac{1}{4}\,(2a^2-2z^2+\rho^2)\,\ln[l_2(a)+\sqrt{l_2^2(a)-\rho^2}]dz=-\frac{a}{6}\,(4a^2+3\rho^2)\sin^{-1}\frac{l_1(a)}{\rho}+\frac{z}{12}\,(6a^2-2z^2+3\rho^2)\,\ln[l_2(a)+\sqrt{l_2^2(a)-\rho^2}]+\frac{1}{36}\,(-26a^2-15\rho^2-3l_1^2(a)+2l_2^2(a))\sqrt{l_2^2(a)-a^2}, \quad \text{(B4)}$$

$$\int\frac{1}{2}\,zl_2(a)(\rho^2-2l_1^2(a))\,\frac{1}{\sqrt{\rho^2-l_1^2(a)}}\,dz=-azl_1(a)\sqrt{l_2^2(a)-\rho^2}+\frac{1}{6}\,\rho\,(2a^2+l_2^2(a)-3l_1^2(a))\sqrt{l_2^2(a)-a^2}, \quad \text{(B5)}$$

$$\int\left\{\frac{3}{4}\,z\sqrt{\rho^2+z^2}-\frac{1}{4}\,(2z^2-\rho^2)\,\ln[z+\sqrt{z^2+\rho^2}]\right\}dz=\frac{1}{36}\,(11z^2-4\rho^2)\sqrt{\rho^2+z^2}+\frac{z}{12}\,(3\rho^2-2z^2)\,\ln[z+\sqrt{z^2+\rho^2}], \quad \text{(B6)}$$

the function $\Phi(\rho,\phi,z)$ can be given as

$$\Phi(\rho,\phi,z)=2\pi\left\{-\frac{1}{3}\,z^3\,\ln[l_2(a)+\sqrt{l_2^2(a)-\rho^2}]+\frac{1}{3}\,z^3\,\ln[z+\sqrt{z^2+\rho^2}]+\frac{a}{12}\,(2a^2+3\rho^2+6z^2)\sin^{-1}\frac{l_1(a)}{\rho}-\frac{1}{9}\,(4z^2+\rho^2)\sqrt{\rho^2+z^2}+\frac{1}{36}\,(-10a^2-12\rho^2+21l_1^2(a)+16l_2^2(a))\sqrt{l_2^2(a)-a^2}\right\}. \quad \text{(B7)}$$

Downloaded 03 May 2010 to 171.66.16.247. Redistribution subject to ASME license or copyright; see http://www.asme.org/terms/Terms_Use.cfm

Since the integral was evaluated as indefinite, an arbitrary function of the variables ρ, ϕ, and a must be added. However, it can be shown by considering the behavior at $z = \infty$ that this function is zero.

To evaluate the elastic field for shear loading, the following derivatives are needed

$$\Delta\Phi(\rho,\phi,z) = 2\pi \left\{(a)\sin^{-1}\frac{l_1(a)}{\rho} + \sqrt{l_2^2(a) - a^2} - \sqrt{\rho^2 + z^2}\right\}, \tag{B8}$$

$$\Lambda^2\Phi(\rho,\phi,z) = 2\pi e^{2i\phi}\left\{\frac{1}{3\rho^2}(l_2^2(a) - a^2 - 3z^2)\sqrt{l_2^2(a) - a^2} + \frac{1}{3\rho^2}(2z^2 - \rho^2)\sqrt{\rho^2 + z^2}\right\}, \tag{B9}$$

$$\Lambda\Delta\Phi(\rho,\phi,z) = 2\pi e^{i\phi}\left\{\frac{a(\rho^2 - l_1^2(a))^{3/2}}{\rho l_1(a)[l_2^2(a) - l_1^2(a)]} - \frac{\rho}{\sqrt{\rho^2 + z^2}}\right\}, \tag{B10}$$

$$\Lambda^3\Phi(\rho,\phi,z) = 2\pi e^{i3\phi}\left\{\frac{1}{3\rho^3\sqrt{\rho^2 + z^2}}(\rho^4 - 4\rho^2z^2 - 8z^4) + \frac{a\sqrt{\rho^2 - l_1^2(a)}}{3\rho^3 l_1(a)[l_2^2(a) - l_1^2(a)]}([\rho^2 - l_1^2(a)][4a^2 + 4z^2 - \rho^2] + 8z^2[a^2 + z^2 - 2l_1^2(a)])\right\}. \tag{B11}$$

Downloaded 03 May 2010 to 171.66.16.247. Redistribution subject to ASME license or copyright; see http://www.asme.org/terms/Terms_Use.cfm

A General Treatment of the Elastic Field of an Elliptical Inhomogeneity Under Antiplane Shear

S. X. Gong

S. A. Meguid

Engineering Mechanics and Design Laboratory, Department of Mechanical Engineering, University of Toronto, Toronto, Ontario M5S 1A4, Canada

A general solution to the antiplane problem of an elliptical inhomogeneity in an isotropic elastic medium is provided. The proposed analysis is based upon the use of conformal mapping and Laurent series expansion of the corresponding complex potentials. The general expressions of the complex potentials are derived explicitly in both the elliptical inhomogeneity and the surrounding matrix. Several specific solutions are provided in closed form which are verified by comparison with existing ones. The effect of material and geometrical parameters upon the change of the elastic energy, due to the presence of an elliptical inhomogeneity, has also been considered.

1 Introduction

It is known that most engineering materials contain some defects in the form of cracks, voids, inclusions, or second-phase particles. The presence of such inhomogeneities plays an important role in determining the mechanical behavior of these materials (Evans, 1974; Warren, 1984; Mura, 1987).

In view of its flexibility to cover a wide variety of particular cases, such as line and circular defects, the elliptical inhomogeneity has evoked most interest amongst researchers. Early work by Hardiman (1954) and Eshelby (1957) showed that a uniform stress applied at infinity induces a constant stress state within the elliptical inhomogeneity. Since then the inhomogeneity problem has received considerable interest, as evidenced by the extensive reviews of Mura (1987, 1988). In this respect, a number of techniques has been adopted in treating this class of problems, see, e.g., Eshelby (1961), Jaswon and Bhargara (1961), Theocaris and Ioakimidis (1977), Zhang and Zhe (1981), Stagni (1982), Hwu and Ting (1989), and Honein and Herrmann (1990).

Based upon the equivalent inclusion approach of Eshelby (1957) and the complex variable method of Muskhelishivili (1953), Wang et al. (1985) have considered the problem of a rigid line inhomogeneity in an isotropic elastic body under uniform remote loading. They obtained analytical expressions of the corresponding elastic field and examined the characteristics of the resulting stress singularity. The same problem has also been considered among others by Erdogan and Gupta (1972), Atkinson (1973), Ballarini (1987), and Dundurs and Markenscoff (1989).

All the aforementioned investigations have concentrated on the plane problem of an elastic inhomogeneity in an infinite medium. The corresponding antiplane problem has also been considered by a few authors; see, e.g., Smith (1968), Yang and Chou (1977), and Wang et al. (1986). Furthermore, most of the available solutions are confined to special geometries and/or material properties under particular loading conditions.

The objective of the present paper is to provide a general solution to the antiplane problem of an elliptical inhomogeneity in an isotropic elastic matrix. The analysis is based upon the use of conformal mapping and Laurent series expansion of the corresponding complex potentials. This work was partly motivated by the authors' interest in dealing with the problem of crack-tip shielding by microdefects in solids (Gong and Meguid, 1991). Indeed, the proposed series form of solution can be extended to treat this class of interaction problems. The general formulation of the present problem is provided in Section 2, while the general forms of the complex potentials are derived explicitly in Section 3. In Section 4 some particular cases of the problem are considered and discussed, and Section 5 concludes the article.

2 Problem Formulation

In antiplane strain state, the displacement w, the shear stresses τ_{xz} and τ_{yz}, and the resultant force T along any arc AB in the material can be expressed in terms of a single analytical function of the complex variable $z=x+iy$ (Muskhelishivili, 1953; Barenblatt and Cherepanov, 1961; Shi, 1963); as follows:

$$w=\frac{1}{2G}\left[\Phi\ (z)+\overline{\Phi(z)}\right] \tag{1}$$

$$\tau_{xz}-i\tau_{yz}=\Phi'(z) \tag{2}$$

$$T=\int_A^B(\tau_{xz}dy-\tau_{yz}dx)=\frac{i}{2}\left[\overline{\Phi(z)}-\Phi(z)\right]_A^B \tag{3}$$

Contributed by the Applied Mechanics Division of THE AMERICAN SOCIETY OF MECHANICAL ENGINEERS for presentation at the 1992 ASME Summer Mechanics and Materials Meeting, Tempe, AZ Apr. 28-May 1, 1992.

Discussion on this paper should be addressed to the Technical Editor, Prof. Leon M. Keer, The Technological Institute, Northwestern University, Evanston, IL 60208, and will be accepted until four months after final publication of the paper itself in the JOURNAL OF APPLIED MECHANICS. Manuscript received by the ASME Applied Mechanics Division, Mar. 19, 1991; final revision, Aug. 21, 1991.

Paper No. 92-APM-23.

Copyright © 1992 by ASME

Downloaded 03 May 2010 to 171.66.16.247. Redistribution subject to ASME license or copyright; see http://www.asme.org/terms/Terms_Use.cfm

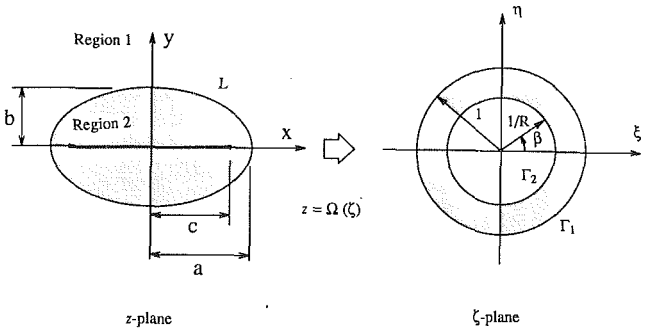


Fig. 1 An elliptical inhomogeneity and its mapped region

where G is the shear modulus of the material, the overbar represents the complex conjugate, the prime denotes the derivative with respect to the argument and $[\,]_A^B$ denotes the change in the bracketed function in going from point A to point B along the arc.

Consider now the present antiplane problem of an isotropic elastic material containing an elliptical inhomogeneity with different elastic properties, as shown in Fig. 1. The two materials are assumed to be perfectly bonded along the common boundary L. The regions occupied by the elastic matrix and the inhomogeneity will be referred to as regions 1 and 2, respectively, and the quantities associated with these regions will be denoted by the corresponding subscripts.

Let us now introduce the following mapping function

$$z=\Omega(\zeta)=\frac{c}{2}\left(R\zeta+\frac{1}{R\zeta}\right),\quad R\zeta=\frac{z}{c}\left\{1+\left[1-\left(\frac{c}{z}\right)^2\right]^{1/2}\right\} \tag{4}$$

where

$$\zeta=\xi+i\eta=\rho e^{i\beta},\quad c=(a^2-b^2)^{1/2}=a(1-\epsilon^2)^{1/2}$$
$$R=\left(\frac{a+b}{a-b}\right)^{1/2}=\left(\frac{1+\epsilon}{1-\epsilon}\right)^{1/2}\quad\text{with }\epsilon=b/a \tag{5}$$

which transforms region 1 of the z-plane into the exterior region of the unit circle Γ_1 ($\rho=1$) in the transformed ζ-plane and region 2 into the annular region between the unit circle Γ_1 and a circle Γ_2 of radius $\rho=1/R$ representing a cut from $-c$ to $+c$ in the z-plane; see Fig. 1.

With Eqs. (4), the basic equations (1)–(3) can be rewritten on the transformed ζ-plane as follows

$$w=\frac{1}{2G}\left[\Phi(\zeta)+\overline{\Phi(\zeta)}\right] \tag{6}$$

$$\tau_{xz}-i\tau_{yz}=\frac{\Phi'(\zeta)}{\Omega'(\zeta)} \tag{7}$$

$$T=\frac{i}{2}\left[\overline{\Phi(\zeta)}-\Phi(\zeta)\right]_A^B \tag{8}$$

where $\Phi(\zeta)$ implies $\Phi[\Omega(\zeta)]$ and the prime represents the derivative with respect to ζ.

The assumption of perfect bonding between regions 1 and 2 implies continuity of tractions and displacements across the elliptical interface. The traction continuity along the interface may also be integrated to become a resultant continuity condition. Formally, these conditions can be expressed as

$$T_1=T_2\text{ and }w_1=w_2\text{ on }\Gamma_1(\zeta=\zeta_0=e^{i\beta}) \tag{9}$$

Substituting equations (6) and (8) into (9), we have

$$\overline{\Phi_1(\zeta_0)}-\Phi_1(\zeta_0)=\overline{\Phi_2(\zeta_0)}-\Phi_2(\zeta_0) \tag{10}$$

$$\mu[\Phi_1(\zeta_0)+\overline{\Phi_1(\zeta_0)}]=\Phi_2(\zeta_0)+\overline{\Phi_2(\zeta_0)} \tag{11}$$

where $\mu=G_2/G_1$ is the shear modulus ratio. Furthermore, the following condition must be satisfied on Γ_2 since

$$\Phi_2(\zeta_0/R)=\Phi_2(\bar{\zeta}_0/R) \tag{12}$$

since points ζ_0/R and $\bar{\zeta}_0/R$ correspond to one and the same point of the cut from $-c$ to $+c$ in the z-plane.

The task now is to determine the complex potentials for regions 1 and 2, subject to the continuity conditions described by Eqs. (10)–(12). In the following section, we present a series solution to the problem and derive general forms of complex potentials for regions 1 and 2 in the physical z-plane.

3 General Forms of Complex Potentials

If we suppose that no singularities exist within both the inhomogeneity and the surrounding matrix in the immediate vicinity, then $\Phi_1(\zeta)$ and $\Phi_2(\zeta)$ must be holomorphic in the respective regions. Therefore, the complex potentials can be expanded into the following Laurent series:

$$\Phi_1(\zeta)=\sum_{k=0}^{\infty}\left(a_k\zeta^{k+1}+b_k\zeta^{-(k+1)}\right)\quad 1\le\rho\le\rho_0 \tag{13}$$

$$\Phi_2(\zeta)=\sum_{k=0}^{\infty}\left(c_k\zeta^{k+1}+d_k\zeta^{-(k+1)}\right)\quad 1/R\le\rho\le 1 \tag{14}$$

where $\rho_0(>1)$ signifies the radius of some circular contour enclosing the unit circle Γ_1 and the constant terms corresponding to rigid body motion have been ignored. Substituting Eqs. (13) and (14) into Eqs. (10)–(12) and comparing the coefficients of ζ_0^k, we obtain

$$d_k+\bar{a}_k=b_k+\bar{c}_k$$
$$\mu(\bar{a}_k+b_k)=d_k+\bar{c}_k\quad(k=0,\,1,\,2,\,\ldots)$$
$$d_k=\frac{c_k}{R^{2k+2}}. \tag{15}$$

For a given k, Eq. (15) provide a system of six linear equations (the other three equations being obtained by taking conjugate to Eq. (15)) with eight unknowns a_k, b_k, c_k, d_k, and $\bar{a}_k$, $\bar{b}_k$, $\bar{c}_k$, $\bar{d}_k$. Two additional equations relating the coefficients can be obtained from the conditions at the outer boundary of the matrix, which may be finite or infinite, and the problem is in principle solved.

At this stage, however, the outer boundary conditions of the matrix will not be specified as we are only interested in obtaining a general expression for the complex potentials, which are valid to both finite and infinite regions of matrix. For the present purpose, the coefficients b_k, c_k, d_k are solved in terms of a_k and $\bar{a}_k$ from (15). The results are obtained as

$$b_k=I_k a_k+J_k\bar{a}_k$$
$$c_k=L_k\bar{a}_k+N_k a_k$$
$$d_k=(L_k\bar{a}+N_k a_k)/R^{2k+2} \tag{16}$$

where

$$I_k=-\frac{4\mu R^{2k+2}}{(\mu-1)^2-(1+\mu)^2R^{4k+4}}$$
$$J_k=\frac{(1-\mu^2)(1-R^{4k+4})}{(\mu-1)^2-(1+\mu)^2R^{4k+4}}$$
$$L_k=-\frac{2\mu(\mu-1)R^{2k+2}}{(\mu-1)^2-(1+\mu)^2R^{4K+4}}$$
$$N_k=-\frac{2\mu(\mu+1)R^{4k+4}}{(\mu-1)^2-(1+\mu)^2R^{4k+4}}. \tag{17}$$

Equations (13) and (14), together with Eqs. (16) and (17), constitute the general expressions of complex potentials for the elastic matrix and the inhomogeneity in the transformed ζ-plane. These expressions can be transformed back to the physical z-plane via the use of Eq. (4).

To this end, it proves convenient to use the following series expansions as obtained from Eq. (4) (Isida, 1973):

Downloaded 03 May 2010 to 171.66.16.247. Redistribution subject to ASME license or copyright; see http://www.asme.org/terms/Terms_Use.cfm

$$z^{2p}=\left(\frac{c}{2}\right)^{2p}\left\{\binom{2p}{p}+\sum_{k=1}^{p}\binom{2p}{p-k}[(R\zeta)^{2k}+(R\zeta)^{-2k}]\right\}$$

$$z^{2p+1}=\left(\frac{c}{2}\right)^{2p+1}\sum_{k=0}^{p}\binom{2p+1}{p-k}\{(R\zeta)^{2k+1}+(R\zeta)^{-(2k+1)}\}$$

$$(R\zeta)^{-2k}=\sum_{n=k}^{\infty}A_{n-k,2k}\left(\frac{c}{z}\right)^{2n}$$

$$(R\zeta)^{-(2k+1)}=\sum_{n=k}^{\infty}A_{n-k,2k+1}\left(\frac{c}{z}\right)^{2n+1} \tag{18}$$

where

$$A_{n-k,2k}=\frac{2k}{2^{2n}2n}\binom{2n}{n-k}.$$

$$A_{n-k,2k+1}=\frac{2k+1}{2^{2n+1}(2n+1)}\binom{2n+1}{n-k}. \tag{19}$$

Furthermore, the coefficients a_k in Eq. (13) are expressed in terms of the newly introduced parameters M_{2p} and M_{2p+1} as:

$$a_{2k}=R^{2k+1}\sum_{p=k}^{\infty}\left(\frac{c}{2}\right)^{2p+1}\binom{2p+1}{p-k}M_{2p}$$

$$a_{2k+1}=R^{2k+2}\sum_{p=k}^{\infty}\left(\frac{c}{2}\right)^{2p+2}\binom{2p+2}{p-k}M_{2p+1}. \tag{20}$$

Substituting Eqs. (18)–(20) into Eqs. (13) and (14), and ignoring the constant terms corresponding to rigid body motion, the general form of the complex potentials in terms of z is derived explicitly as:

$$\Phi_1(z)=\sum_{n=0}^{\infty}\{(F_n^{\bullet}+iF_n^{*})z^{-(n+1)} + (M_n^{\bullet}+iM_n^{*})z^{n+1}\} \text{ in the matrix}$$

$$\Phi_2(z)=\sum_{n=0}^{\infty}(D_n^{\bullet}+iD_n^{*})z^{n+1} \quad \text{in the inhomogeneity} \tag{21}$$

where dots and asterisks denote real and imaginary parts, respectively, and the coefficients F_n and D_n can be expressed in terms of M_n as follows:

$$F_{2n}^{\bullet}=\sum_{p=0}^{\infty}a^{2n+2p+2}P_{2p}^{2n}M_{2p}^{\bullet}$$

$$F_{2n}^{*}=\sum_{p=0}^{\infty}a^{2n+2p+2}Q_{2p}^{2n}M_{2p}^{*}$$

$$F_{2n+1}^{\bullet}=\sum_{p=0}^{\infty}a^{2n+2p+4}P_{2p+1}^{2n+1}M_{2p+1}^{\bullet}$$

$$F_{2n+1}^{*}=\sum_{p=0}^{\infty}a^{2n+2p+4}Q_{2p+1}^{2n+1}M_{2p+1}^{*} \tag{22}$$

and

$$D_{2n}^{\bullet}=T_{2n}M_{2n}^{\bullet}$$
$$D_{2n}^{*}=V_{2n}M_{2n}^{*}$$
$$D_{2n+1}^{\bullet}=T_{2n+1}M_{2n+1}^{\bullet}$$
$$D_{2n+1}^{*}=V_{2n+1}M_{2n+1}^{*} \tag{23}$$

with

$$\begin{Bmatrix}P_{2p}^{2n}\\Q_{2p}^{2n}\end{Bmatrix}=\frac{(1-\epsilon^2)^{n+p+1}}{2^{2p+1}} \times\sum_{k=0}^{n,p}\binom{2p+1}{p-k}[(I_{2k}\pm J_{2k})R^{4k+2}-1]A_{n-k,2k+1}$$

$$\begin{Bmatrix}P_{2p+1}^{2n+1}z\\Q_{2p+1}^{2n+1}\end{Bmatrix}=\frac{(1-\epsilon^2)^{n+p+2}}{2^{2p+2}} \times\sum_{k=0}^{n,p}\binom{2p+2}{p-k}[(I_{2k+1}\pm J_{2k+1})R^{4k+4}-1]A_{n-k,2k+2}$$

$$\begin{Bmatrix}T_{2n}\\V_{2n}\end{Bmatrix}=\frac{1}{2^{2n}}\sum_{k=0}^{n}\binom{2n+1}{n-k}(N_{2k}\pm L_{2k})$$

$$\begin{Bmatrix}T_{2n+1}\\V_{2n+1}\end{Bmatrix}=\frac{1}{2^{2n+1}}\sum_{k=0}^{n}\binom{2n+2}{n-k}(N_{2k+1}\pm L_{2k+1}). \tag{24}$$

In Eq. (24), a smaller value of the summation upper limit (n or p) is implied.

It can be easily verified that Eq. (21) reduces to the general form of the complex potentials of Isida (1973) for an elliptical hole when $\mu=G_2/G_1=0$. In the following section some particular cases are provided to illustrate the validity and versatility of the present general solution.

4 Applications and Discussions

4.1 Circular Inhomogeneity in an Unbounded Matrix. Consider a circular inhomogeneity ($\epsilon=1$) embedded in an infinite isotropic elastic body under antiplane loading. In the absence of the inhomogeneity, the undisturbed stress function $\Phi_0(z)$ is holomorphic in the region of interest and can thus be expressed in terms of positive powers of z for an infinite matrix. Suppose that $\Phi_0(z)$ is represented by

$$\Phi_0(z)=\sum_{n=0}^{\infty}(K_n^{\bullet}+iK_n^{*})z^{n+1}. \tag{25}$$

The boundary conditions at infinity yield at once

$$M_n^{\bullet}=K_n^{\bullet},\ M_n^{*}=K_n^{*}. \tag{26}$$

Substituting $\epsilon=1$ into (17) leads to

$$I_k=0,\ J_k=\frac{1-\mu}{1+\mu}$$

$$L_k=0,\ N_k=\frac{2\mu}{1+\mu}. \tag{27}$$

Using the above relations, Eqs. (22) and (23) simplify to

$$F_n^{\bullet}=a^{2n+2}\frac{1-\mu}{1+\mu}K_n^{\bullet},\ F_n^{*}=-a^{2n+2}\frac{1-\mu}{1+\mu}K_n^{*}$$

$$D_n^{\bullet}=\frac{2\mu}{1+\mu}K_n^{\bullet},\qquad D_n^{*}=\frac{2\mu}{1+\mu}K_n^{*}. \tag{28}$$

Substituting Eqs. (25), (26), and (28) into (21), we obtain the following compact form for the stress functions

$$\Phi_1(z)=\Phi_0(z)+\frac{1-\mu}{1+\mu}\overline{\Phi_0(a^2/\bar{z})} \text{ in the matrix}$$

$$\Phi_2(z)=\frac{2\mu}{1+\mu}\Phi_0(z) \quad \text{in the inhomogeneity.} \tag{29}$$

Equation (29) coincides with Eqs. (9) and (10) of Smith (1968) who obtained the results by extending the circle theorem in hydrodynamics. The above relation provides a simple means of estimating the elastic fields inside and outside the circular inhomogeneity in an infinite matrix in terms of the undisturbed stress function.

As a simple example, let us consider an infinite body with a circular inhomogeneity subjected to shear stresses τ_{xz}^{∞} and τ_{yz}^{∞} at infinity. In this case, the undisturbed stress function is simply given by

$$\Phi_0(z)=(\tau_{xz}^{\infty}-i\tau_{yz}^{\infty})z. \tag{30}$$

Substituting (30) into (29), we obtain

Downloaded 03 May 2010 to 171.66.16.247. Redistribution subject to ASME license or copyright; see http://www.asme.org/terms/Terms_Use.cfm

$$\Phi_1(z) = (\tau_{xz}^{\infty} - i\tau_{yz}^{\infty})z + \frac{1-\mu}{1+\mu}(\tau_{xz}^{\infty} + i\tau_{yz})\ (a^2/z)$$

$$\Phi_2(z) = \frac{2\mu}{1+\mu}(\tau_{xz}^{\infty} - i\tau_{yz}^{\infty})z. \tag{31}$$

The displacement and stress fields can then be obtained by substituting Eq. (31) into Eqs. (1) and (2).

It is worth noting that a similar "circle theorem" to that of Eq. (29) has also been revealed for a circular inhomogeneity in plane elasticity; see, e.g., Aderogba (1973), Stagni (1982), and Honein and Herrmann (1990).

4.2 Elliptical Inhomogeneity Subject to Uniform Loading at Infinity. Consider now the problem of an elliptical inhomogeneity in an infinite matrix subject to the uniform stresses τ_{xz}^{∞} and τ_{yz}^{∞} at infinity, as shown in Fig. 2. The boundary conditions at infinity yield

$$M_0^{\bullet} = \tau_{xz}^{\infty},\ M_0^{*} = -\tau_{yz}^{\infty},$$
$$M_n^{\bullet} = M_n^{*} = 0\ (n \geq 1). \tag{32}$$

With the aid of Eq. (32), Eqs. (22) and (23) reduce to

$$F_{2n}^{\bullet} = \frac{c^{2n+2}}{2}[(I_0 + J_0)R^2 - 1]A_{n,1}\tau_{xz}^{\infty}$$
$$F_{2n}^{*} = -\frac{c^{2n+2}}{2}[(I_0 - J_0)R^2 - 1]A_{n,1}\tau_{yz}^{\infty}$$
$$F_{2n+1}^{\bullet} = F_{2n+1}^{*} = 0\ (n \geq 0) \tag{33}$$

and

$$D_0^{\bullet} = (N_0 + L_0)\tau_{xz}^{\infty}$$
$$D_0^{*} = (L_0 - N_0)\tau_{yz}^{\infty}$$
$$D_{2n}^{\bullet} = D_{2n}^{*} = 0 \quad (n \geq 1)$$
$$D_{2n+1}^{\bullet} = D_{2n+1}^{*} = 0 \quad (n \geq 0). \tag{34}$$

Substituting (33) and (34) into (21), the complex potential functions are obtained as

$$\Phi_1(z) = \frac{c}{2}[(I_0 + J_0)R^2 - 1]\tau_{xz}^{\infty}\sum_{n=0}^{\infty} A_{n,1}\left(\frac{c}{z}\right)^{2n+1}$$
$$- i\frac{c}{2}[(I_0 - J_0)R^2 - 1]\tau_{yz}^{\infty}\sum_{n=0}^{\infty} A_{n,1}\left(\frac{c}{z}\right)^{2n+1}$$
$$+ (\tau_{xz}^{\infty} - i\tau_{yz}^{\infty})z \tag{35}$$

$$\Phi_2(z) = (N_0 + L_0)\tau_{xz}^{\infty}z + i(L_0 - N_0)\tau_{yz}^{\infty}z. \tag{36}$$

The linear form of $\Phi_2(z)$ implies a constant stress distribution within the elliptical inhomogeneity, as is evident from Eq. (2). This result was first noticed by Hardiman (1954) for a two-dimensional problem and by Eshelby (1957) for the general three-dimensional case.

The infinite series terms in Eq. (35) can be summed up in a closed form by using Eqs. (18) and (4) and, after some reduction of constants, $\Phi_1(z)$ can be written in a compact form as follows:

$$\Phi_1(z) = \tau_{xz}^{\infty}\left\{z + \frac{\epsilon(1-\mu)(\epsilon+\mu)}{(1-\epsilon)[\mu(1+\epsilon^2)+\epsilon(1+\mu^2)]}[z - (z^2-c^2)^{1/2}]\right\}$$
$$- i\tau_{yz}^{\infty}\left\{z + \frac{\epsilon(\mu-1)(1+\epsilon\mu)}{(1-\epsilon)[\mu(1+\epsilon^2)+\epsilon(1+\mu^2)]}[z - (z^2-c^2)^{1/2}]\right\}. \tag{37}$$

As far as the authors are aware, the explicit expression (37) has not been given previously. Special cases of the problem have, however, been treated by some investigators. In the special case of an elliptical hole ($\mu = 0$), Eq. (37) reduces to

$$\Phi_1(z) = \tau_{xz}^{\infty}\left\{z + \frac{\epsilon}{1-\epsilon}[z - (z^2-c^2)^{1/2}]\right\}$$
$$- i\tau_{yz}^{\infty}\left\{z - \frac{1}{1-\epsilon}[z - (z^2-c^2)^{1/2}]\right\} \tag{38}$$

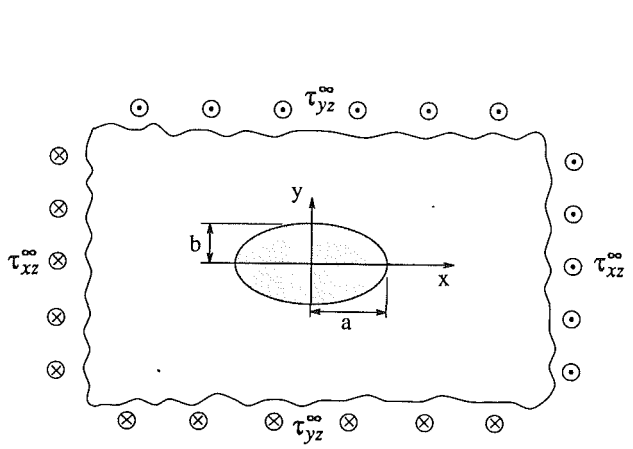


Fig. 2 An elliptical inhomogeneity under uniform antiplane loading at infinity

which can be shown to coincide with the previous solutions of Smith (1968) and Sih and Liebowitz (1968). In the case of a rigid elliptical inhomogeneity ($\mu \to \infty$), Eq. (37) reduces to

$$\Phi_1(z) = \tau_{xz}^{\infty}\left\{z - \frac{1}{1-\epsilon}[z - (z^2-c^2)^{1/2}]\right\}$$
$$- i\tau_{yz}^{\infty}\left\{z + \frac{\epsilon}{1-\epsilon}[z - (z^2-c^2)^{1/2}]\right\} \tag{39}$$

which agrees with the result of Smith (1968) who extended the circle theorem to the case of a rigid elliptical inhomogeneity.

Another interesting aspect of the present solution is the ability to determine the change of the elastic energy ΔW in the body due to the introduction of an elliptical inhomogeneity. Following the approach of Sih and Liebowitz (1968) and using the expanded form of $\Phi_1(z)$ (Eq. (35)), ΔW can be evaluated as

$$\Delta W = \frac{\pi a^2}{2G_1}\frac{(1-\mu)\epsilon(1+\epsilon)}{\mu(1+\epsilon^2)+\epsilon(1+\mu^2)}[(\epsilon+\mu)(\tau_{xz}^{\infty})^2 + (1+\mu\epsilon)(\tau_{yz}^{\infty})^2]. \tag{40}$$

In the special case of an elliptical hole ($\mu = 0$), ΔW reduces to

$$\Delta W = \frac{\pi a^2}{2G_1}(1+\epsilon)[\epsilon(\tau_{xz}^{\infty})^2 + (\tau_{yz}^{\infty})^2] \tag{41}$$

which is in agreement with the results of Sih and Liebowitz (1968) and Yang and Chou (1977). For $\epsilon = 0$, Eq. (41) reduces to the well-known result for a crack.

On the other hand, for a rigid elliptical inhomogeneity ($\mu \to \infty$), Eq. (40) simplifies to

$$\Delta W = \frac{-\pi a^2}{2G_1}(1+\epsilon)[(\tau_{xz}^{\infty})^2 + \epsilon(\tau_{yz}^{\infty})^2] \tag{42}$$

which coincides with the result of Yang and Chou (1977) for an isotropic material. In the case of a line rigid inhomogeneity ($\epsilon = 0$), Eq. (42) reduces to the previous result of Wang et al. (1986).

The above change of energy due to the presence of the elliptical inhomogeneity (Eq. 40) can be split into two parts $\Delta W = \Delta W_1 + \Delta W_2$, where ΔW_1 corresponds to the contribution due to the shear component τ_{xz}^{∞} and ΔW_2 due to the shear component τ_{yz}^{∞}. These expressions have been normalized by the factor $(\pi a^2/2G_1)$ and presented as $\Delta\overline{W}_1$, and $\Delta\overline{W}_2$ in Figs. 3(*a*) and 3(*b*), respectively.

Figures 3(*a*) and 3(*b*) clearly show the dependence of the change of the elastic energy upon the material parameters ($\mu = G_2/G_1$) and the geometry of the inhomogeneity ($\epsilon = b/a$). Some interesting features can be observed from these figures. In the case of a homogeneous material ($\mu = 1$), as expected, no change in energy is observed. However, the presence of an inhomogeneity with a lower modulus ($\mu < 1$), increases the elastic energy of the system. Conversely, the presence of an inhomogeneity with a higher modulus ($\mu > 1$) leads to a reduction in the elastic energy.

Downloaded 03 May 2010 to 171.66.16.247. Redistribution subject to ASME license or copyright; see http://www.asme.org/terms/Terms_Use.cfm

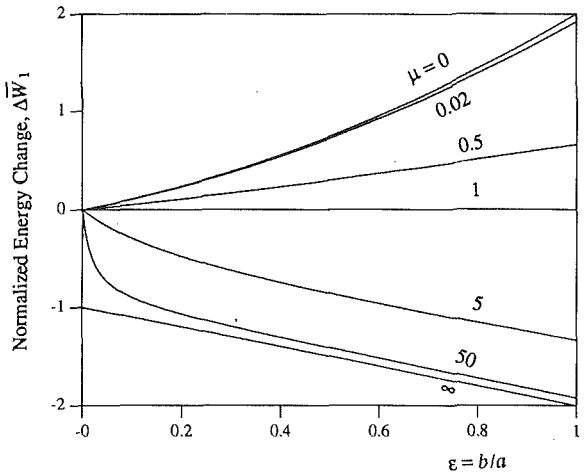


Fig. 3(a)

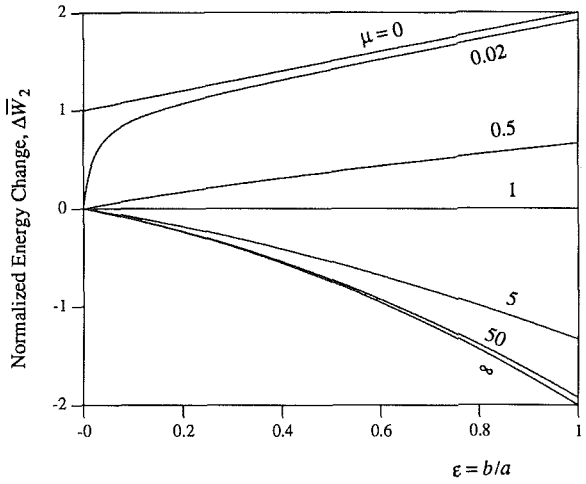


Fig. 3(b)

Fig. 3 The change of the elastic energy due to the presence of an elliptical inhomogeneity as a function of geometrical and material parameters: (*a*) the contribution due to the shear component τ_{xz}^{∞} and (*b*) the contribution due to the shear component τ_{yz}^{∞}

For a given aspect ratio, the amount of change in the elastic energy will depend upon the specific value of modulus ratio, $\mu = G_2/G_1$. The two extreme cases of an elliptical hole ($\mu = 0$) and a rigid elliptical inhomogeneity ($\mu = \infty$), provide the maximum increase and decrease in the elastic energy, respectively. The figures also show that the greatest change of energy occurs for a circular defect ($\epsilon = 1$).

Figure 3(*a*) also shows the reduction in the elastic energy associated with the presence of a rigid line inhomogeneity ($\mu = \infty$, $\epsilon = 0$) under remote shear loading, τ_{xz}^{∞}. In this case, no change in energy is observed for line cracks under the same loading. this trend has been reversed for the case where the shear loading τ_{yz}^{∞} is present, as depicted in Fig. 3(*b*). This is consistent with the results derived previously by Wang et al. (1986) for rigid line inhomogeneities.

5 Concluding Remarks

A general solution is obtained to the problem of an elliptical inhomogeneity under antiplane shear loading conditions. The analysis was based upon the use of conformal mapping and Laurent series expansion of the complex potentials. Explicit forms of the general stress functions in both the inhomogeneity and the matrix have been provided.

The validity and versatility of the present series solution have been demonstrated by application to some specific examples. Furthermore, the change of the elastic energy due to the presence of an elliptical inhomogeneity and its dependence upon the geometrical and material parameters as well as loading conditions have been discussed in detail.

Acknowledgments

This work has been supported by the Natural Sciences and Engineering Research Council, and Energy Mines and Resources of Canada.

References

Atkinson, C., 1973, "Some Ribbon-like Inclusion Problems," *Int. J. Eng. Sci.*, Vol. 11, pp. 243-265.

Ballarini, R., 1987, "An Integral Equation Approach for Rigid Line Inhomogeneity Problems," *Int. J. Fracture*, Vol. 33, pp. R23-R26.

Barenblatt, G. I., and Cherepanov, G. P., 1961, "On Brittle Cracks Under Longitudinal Shear," *Applied Mathematics and Mechanics*, Vol. 25, pp. 1654-1666.

Dundurs, J., and Markenscoff, X., 1989, "A Green's Function Formulation of Anticracks and Their Interaction with Load-Induced Singularities," ASME JOURNAL OF APPLIED MECHANICS, Vol. 56, pp. 550-555.

Erdogan, F., and Gupta, G. D., 1972, "Stress Near a Flat Inclusion in Bonded Dissimilar Materials," *Int. J. Solids Structures*, Vol. 8, pp. 533-547.

Eshelby, J. D., 1957, "The Determination of the Elastic Field of an Ellipsoidal Inclusion, and Related Problems," *Proc. Roy. Soc.*, Vol. A241, pp. 376-396.

Eshelby, J. D., 1961, "Elastic Inclusions and Inhomogeneities," *Progress in Solid Mechanics*, I. N. Sneddon and R. Hill, eds., North-Holland, Vol. 2, pp. 89-140.

Evans, A. G., 1974, "The Role of Inclusions in the Fracture of Ceramic Materials," *Journal of Materials Science*, Vol. 9, pp. 1145-1152.

Gong, S. X., and Meguid, S. A., 1991, "A General Solution to the Antiplane Problem of an Arbitrarily Located Elliptical Hole Near the Tip of a Main Crack," *Int. J. Solids Structures*, Vol. 28, pp. 249-263.

Hardiman, N. J., 1954, "Elliptical Elastic Inclusion in an Infinite Elastic Plane," *Q. J. Mech. Appl. Math.*, Vol. 7, pp. 226-230.

Honein, T., and Herrmann, G., 1990, "On Bonded Inclusions with Circular or Straight Boundaries in Plane Elastostatics," ASME JOURNAL OF APPLIED MECHANICS, Vol. 57, pp. 850-856.

Hwu, C., and Ting, T. C. T., 1989, "Two-Dimensional Problems of the Anisotropic Elastic Solid with an Elliptical Inclusion," *Q. J. Mech. Appl. Math.*, Vol. 42, pp. 553-572.

Isida, M., 1973, "Method of Laurent Series Expansion for Internal Crack Problems," *Methods of Analysis and Solutions of Crack Problems*, G. C. Sih, ed., Noordholf, Leyden, pp. 56-130.

Jawson, M. A., and Bhargava, R. D., 1961, "Two-Dimensional Elastic Inclusion Problems," *Proceedings of the Cambridge Philosophical Society*, Vol. 57, pp. 669-680.

Mura, T., 1987, *Micromechanics of Defects in Solids*, 2nd ed., Martinus Nijhoff, Boston, Mass.

Mura, T., 1988, "Inclusion Problems," *App. Mech. Rev.*, Vol. 41, ASME, New York, pp. 15-20.

Muskhelishvili, N. I., 1953, *Some Basic Problems of the Mathematical Theory of Elasticity*, Noorhoff Ltd., Groningen, Holland.

Sih, G. C., 1965, "Stress Distribution Near Internal Crack Tips for Longitudinal Shear Problems," ASME JOURNAL OF APPLIED MECHANICS, Vol. 32, pp. 51-58.

Sih, G. C., and Liebowitz, H., 1968, "Mathematical Theories of Brittle Fracture," *Fracture II*, Vol. 2, H. Liebowitz, ed., Academic Press, New York, pp. 67-190.

Smith, E., 1968, "The Interaction Between Dislocations and Inhomogeneities—I," *Int. J. Eng. Sci.*, Vol. 6, pp. 129-143.

Stagni, L., 1982, "On the Elastic Field Perturbation by Inhomogeneities in Plane Elasticity," *Journal of Applied Mathematics and Physics*, Vol. 33, pp. 315-325.

Theocaris, P. S., and Ioakimidis, N. I., 1977, "The Inclusion Problem in Plane Elasticity," *Q. J. Mech. Appl. Math.*, Vol. 30, pp. 437-448.

Wang, Z. Y., Zhang, H. T., and Chou, Y. T., 1985, "Characteristics of the Elastic Field of a Rigid Line Inhomogeneity," ASME JOURNAL OF APPLIED MECHANICS, Vol. 52, pp. 818-822.

Wang, Z. Y., Zhang, H. T., and Chou, Y. T., 1986, "Stress Singularity at the Tip of a Rigid Line Inhomogeneity under Antiplane Shear Loading," ASME JOURNAL OF APPLIED MECHANICS, Vol. 53, pp. 459-462.

Warren, W. E., 1984, "The Stress and Displacement Fields at the Tip of Crazes in Glassy Polymers," *Polymer*, Vol. 25, pp. 45-53.

Yang, H. C., and Chou, Y. T., 1977, "Antiplane Strain Problems of an Elliptical Inclusion in an Anisotropic Medium," ASME JOURNAL OF APPLIED MECHANICS, Vol. 44, pp. 437-441.

Zhang, H. T., and Zhe, X. L., 1981, "Theory of Inclusion and Applications in the Study of Fracture," *Acta Physica Sinica*, Vol. 30, pp. 761-774.

Downloaded 03 May 2010 to 171.66.16.247. Redistribution subject to ASME license or copyright; see http://www.asme.org/terms/Terms_Use.cfm

Analysis of Acoustic Pulses Reflected From Fiber-Reinforced Composite Laminates

A. K. Mal
Mem. ASME

C.-C. Yin

Mechanical, Aerospace, and Nuclear Engineering Department, University of California, Los Angeles, CA 90024

Y. Bar-Cohen

Douglas Aircraft Company, McDonnell Douglas Corporation, Long Beach, CA 90846

The time histories and spectral characteristics of acoustic pulses reflected from fiber-reinforced composite laminates immersed in water are recorded in the laboratory and analyzed through a generalized ray theory and an exact theory. Calculated results for an unidirectional laminate and two angle-ply laminates are compared with measured data. It is shown that for a unidirectional laminate a finite number of mode-converted waves contribute to the overall signal reflected from a thick specimen resulting in certain irregular behavior of the reflected pulses. A phenomenological model of wave attenuation is introduced in the theoretical simulation and the damping parameters are shown to have a strong influence on the amplitude of the reflected pulses. The phase velocity of the guided waves in the laminates are shown to be nearly independent of water loading and material dissipation in a broad frequency range. Agreement between measured and calculated results is found to be excellent to very good in all cases.

1 Introduction

The use of guided waves in the ultrasonic nondestructive evaluation of structural components, e.g., bonded plates and composite laminates, has received considerable attention in recent years. Highly accurate and efficient experimental techniques have been developed to generate, record, and analyze these waves in laboratory specimens, leading to an improved capability for flaw detection in and material characterization of a variety of samples (Tang and Henneke, 1989; Dayal and Kinra, 1989). A good understanding of the nature of the waves in both isotropic and anisotropic waveguides is being developed through modeling and analysis of the associated theoretical problems (Nayfeh and Chimenti, 1988; Mal and Bar-Cohen, 1989).

In this paper, we describe our efforts to theoretically simulate a relatively new technique based on an oblique insonification of the test specimen and to explain a number of hitherto unexplained phenomena observed in laboratory specimens. One such observation involves the behavior of the reflected signal from a relatively thick unidirectional graphite/epoxy laminate. The reflected signal from such specimens typically consists of a series of well-separated pulses, that may be unevenly spaced, and the amplitude of the successive reflections may have irregular variations. Although the theoretical results based on the solution of the associated elastodynamic boundary value problem are in excellent agreement with these observations (Mal and Bar-Cohen, 1988a, b), the source of the irregular behavior could not be identified from such calculations.

Another observation involves the spectral minima of the reflected signal. The amplitude spectrum of each reflected pulse is usually a simple curve similar to that of the incident pulse, exhibiting no special feature. However, if the first two reflected pulses are added, the resulting amplitude spectrum contains well defined minima which become deeper as more reflected pulses are added. The minima eventually coincide with the well-known nulls that are associated with the excitation of Lamb waves in the plate. In order to associate the nulls in the observed spectra with the dispersion curves of the leaky Lamb waves, it is necessary to include a sufficient number of reflected pulses in the recorded signal so that this coincidence may indeed occur. Since the time window of the experiment is limited in extent, it is important to know how many of the reflected pulses are needed to achieve this.

We present an analysis based on generalized ray theory to provide answers to these and other related questions. We develop the mathematical formulation of the ray theory for the composite plate to calculate the pulse shape associated with each reflected ray and determine the relative amplitudes of all the rays. The analysis not only identifies the source of the anomaly in the nature of the reflected pulses, but also gives a clear and relatively simple picture of the wave phenomena that are associated with the experiment. We also compare the results obtained from the ray theory with experimental data and with the exact solution of the corresponding elastodynamic boundary value problem.

Multilayered, multi-orientation composite laminates are

Contributed by the ASME Applied Mechanics Division of THE AMERICAN SOCIETY OF MECHANICAL ENGINEERS for presentation at the Winter Annual Meeting, Atlanta, Ga., Dec. 1-6, 1991.

Discussion on this paper should be addressed to the Technical Editor, Prof. Leon M. Keer, The Technological Institute, Northwestern University, Evanston, IL 60208, and will be accepted until two months after final publication of the paper itself in the JOURNAL OF APPLIED MECHANICS. Manuscript received by the ASME Applied Mechanics Division, Mar. 6, 1990; final revision, Jan. 8, 1991.
Paper No. 91-WA/APM-18.

Copyright © 1992 by ASME
Downloaded 03 May 2010 to 171.66.16.247. Redistribution subject to ASME license or copyright; see http://www.asme.org/terms/Terms_Use.cfm

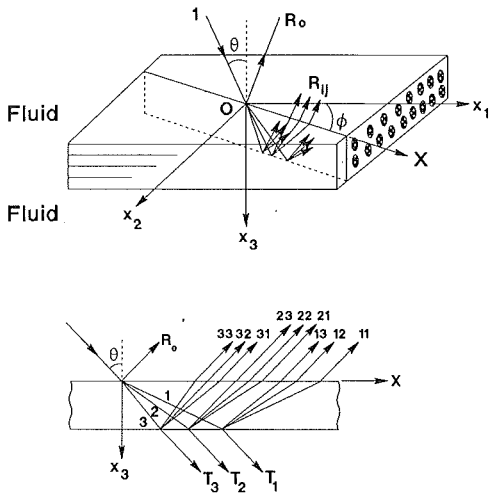


Fig. 1 A ray diagram of the leaky Lamb wave (LLW) experiment

often employed in engineered structures for a variety of practical reasons. The nature of waves propagating in these laminates is quite complex. We study the properties of the reflected wave field for two such laminates, namely, a cross-ply and a quasi-isotropic composite plate.

In what follows we use the following terminology for guided waves in laminates subject to different interface or boundary conditions. The phrase "leaky Lamb waves" is used to denote guided waves in a homogeneous plate immersed in water, and "free Lamb waves" or, simply Lamb waves is used when the plate surfaces are free of traction (i.e., in vacuum). The phrase "leaky guided waves" applies to a multilayered plate immersed in water and "free guided waves" or, simply "guided waves" applies to a multilayered plate with traction-free surfaces.

We first consider the ray analysis of a unidirectional fiber-reinforced composite plate of thickness H immersed in a fluid and insonified by a plane, time-harmonic acoustic wave of unit amplitude and frequency ω. Analysis of the multilayered angle-ply laminates is carried out by means of a global matrix approach presented in Mal (1988). The time dependence $e^{-i\omega t}$ in all field variables are suppressed throughout. The frequency domain calculations are used to obtain time histories of the reflected field for incident pulses through inversion by FFT.

2 Material Modeling

Within the frequency range normally used in ultrasonic NDE, the unidirectional graphite-epoxy composite can be assumed to be transversely isotropic with its symmetry axis parallel to the fibers. Referred to a Cartesian coordinate system with x_1-axis parallel to the symmetry axis shown in Fig. 1, the constitutive equation for the material can be written as

$$\begin{Bmatrix}\sigma_{11}\\ \sigma_{22}\\ \sigma_{33}\\ \sigma_{23}\\ \sigma_{31}\\ \sigma_{12}\end{Bmatrix} = \begin{bmatrix} C_{11} & C_{12} & C_{12} & 0 & 0 & 0\\ C_{12} & C_{22} & C_{23} & 0 & 0 & 0\\ C_{12} & C_{23} & C_{22} & 0 & 0 & 0\\ 0 & 0 & 0 & C_{44} & 0 & 0\\ 0 & 0 & 0 & 0 & C_{55} & 0\\ 0 & 0 & 0 & 0 & 0 & C_{55}\end{bmatrix} \begin{Bmatrix} u_{1,1}\\ u_{2,2}\\ u_{3,3}\\ u_{2,3}+u_{3,2}\\ u_{3,1}+u_{1,3}\\ u_{1,2}+u_{2,1}\end{Bmatrix} \tag{1}$$

where $C_{44} = (C_{22} - C_{23})/2$, σ_{ij} is the stress tensor, u_i is the displacement vector, C_{ij} is the stiffness matrix, and the comma notation for differentiation has been used. If the material is perfectly elastic, then the constants C_{ij} are real and frequency independent. However, it is well known that composite materials are, in general, highly dissipative and this needs to be incorporated in the constitutive relation especially at higher frequencies.

The dissipation of the waves is caused by the viscoelastic nature of the resin and by multiple scattering from the fibers and other inhomogeneities (e.g., prosity, uneven distribution of resin). Both these effects can be modeled in the frequency domain by assuming that the stiffness constants, C_{ij}, are complex and frequency dependent. In order to derive a suitable form of C_{ij} that can model the essential features of the dissipation caused by these factors, we first review the corresponding model for the isotropic solid.

We recall that in an isotropic solid, there are two possible bulk waves, namely, a longitudinal (or P) and a transverse (or S) wave. The propagation characteristics of each wave can be described by means of two real material constants, the phase velocity, and the quality factor. Let $\hat{\alpha}$, Q_α denote these quantities for the P-wave and $\hat{\beta}$, Q_β denote these for the S-waves. In general, $\hat{\alpha}$, $\hat{\beta}$, Q_α, and Q_β are frequency dependent, and Q_α and Q_β are inversely proportional to the degree of wave attenuation with propagation distance. The material constants $\hat{\alpha}$, $\hat{\beta}$, Q_α, and Q_β can be measured from relatively simple experiments. Laboratory measurements on a variety of materials have shown that (e.g., Knopoff, 1964),

(a) $\hat{\alpha}$, $\hat{\beta}$, Q_α, and Q_β are independent of frequency in a broad frequency range.

(b) Q_α and Q_β are proportional to the wave speeds $\hat{\alpha}$ and $\hat{\beta}$, respectively.

(c) The numerical values of Q_α and Q_β for many materials (e.g., aluminum, steel, etc.) are large (> 100).

Let λ, μ denote the complex Lamé constants for the material, α, β be the complex P and S wave speeds, and ρ be the density. Then the above results imply that α, β may be expressed in the forms,

$$\alpha^2 = \frac{\lambda+2\mu}{\rho} = \frac{\hat{\alpha}^2}{(1+ip\beta/\alpha)} \tag{2a}$$

$$\beta^2 = \frac{\mu}{\rho} = \frac{\hat{\beta}^2}{(1+ip)} \tag{2b}$$

where p is, in general, a frequency-dependent but dimensionless constant. Clearly, p is directly proportional to wave attenuation with propagation distance and is a small number.

In order to extend this concept to the fiber-reinforced composite, we introduce five additional constants, a_1, a_2, a_3, a_4, and a_5, related to C_{ij} and the density of the material, ρ, through

$$a_1 = C_{22}/\rho = \hat{a}_1/(1+ip\sqrt{\hat{a}_5/\hat{a}_1}) \tag{3a}$$

$$a_2 = C_{11}/\rho = \hat{a}_2/(1+ip\sqrt{\hat{a}_5/\hat{a}_2}) \tag{3b}$$

$$a_3 = (C_{12}+C_{55})/\rho = \hat{a}_3/(1+ip\sqrt{\hat{a}_5/\hat{a}_3}) \tag{3c}$$

$$a_4 = C_{44}/\rho = \hat{a}_4/(1+ip\sqrt{\hat{a}_5/\hat{a}_4}) \tag{3d}$$

$$a_5 = C_{55}/\rho = \hat{a}_5/(1+ip) \tag{3e}$$

where $\hat{a}_i$ is the real part of $a_i (i = 1, \ldots, 5)$. The quantities $\sqrt{\hat{a}_1}$, $\sqrt{\hat{a}_2}$, $\sqrt{\hat{a}_3}$, $\sqrt{\hat{a}_4}$, and $\sqrt{\hat{a}_5}$ represent the velocities of five independent bulk waves that can be transmitted along certain specific directions in the transversely isotropic solid (Buchwald, 1961).

As indicated earlier, for many isotropic solids, the damping factor p is independent of frequency in a broad frequency range. This is generally true if the wavelengths are long compared to the microstructural dimensions (e.g., grain size). In the case of the fiber-reinforced composite, the effect of wave scattering by the fibers is likely to be significant at higher frequencies. We assume that p is constant below a certain frequency ω_0, beyond which it becomes frequency dependent

Downloaded 03 May 2010 to 171.66.16.247. Redistribution subject to ASME license or copyright; see http://www.asme.org/terms/Terms_Use.cfm

(Bose and Mal, 1974; Datta and Ledbetter, 1983). In this study, the damping constant of the composite is selected as a simple function of ω

$$p = p_0\left[1 + a_0\left(\frac{f}{f_0} - 1\right)^2 H(f - f_0)\right] \tag{4}$$

where $f = \omega/2\pi$ is the frequency in cycles, $f_0 = \omega_0/2\pi$, $H(f)$ is the Heaviside step function, and p_0, a_0 are material constants which determine the degree of decay in the amplitude of the waves with propagation distance. Equation (4) implies that wave attenuation due to two-dimensional scattering effects are negligible below a frequency f_0 and becomes more and more significant as f increases from this value. The numerical values of f_0, a_0, and p_0 must be determined from laboratory or field experiments.

3 Formulation of the Boundary Value Problem

Let the displacement vector $\{u_1, u_2, u_3\}$ within the plate be expressed in terms of three scalar potentials Φ_j $(j = 1, 2, 3)$ through (Buchwald, 1961),

$$\begin{Bmatrix} u_1 \\ u_2 \\ u_3 \end{Bmatrix} = \begin{bmatrix} \partial/\partial x_1 & 0 & 0 \\ 0 & \partial/\partial x_2 & \partial/\partial x_3 \\ 0 & \partial/\partial x_3 & -\partial/\partial x_2 \end{bmatrix} \begin{Bmatrix} \Phi_1 \\ \Phi_2 \\ \Phi_3 \end{Bmatrix}. \tag{5}$$

Then, it can be shown that the potentials satisfy the following partially decoupled system of differential equations,

$$\begin{bmatrix} a_5\nabla_1^2 + a_2\dfrac{\partial^2}{\partial x_1^2} + \omega^2 & a_3\nabla_1^2 & 0 \\ a_3\dfrac{\partial^2}{\partial x_1^2} & a_1\nabla_1^2 + a_5\dfrac{\partial^2}{\partial x_1^2} + \omega^2 & 0 \\ 0 & 0 & a_5\dfrac{\partial^2}{\partial x_1^2} + a_4\nabla_1^2 + \omega^2 \end{bmatrix} \begin{Bmatrix} \Phi_1 \\ \Phi_2 \\ \Phi_3 \end{Bmatrix} = 0 \tag{6}$$

where

$$\nabla_1^2 = \partial^2/\partial x_2^2 + \partial^2/\partial x_3^2.$$

Plane acoustic waves in the fluid can be represented in terms of a scalar potential, Φ_0 and the displacement and stress components associated with plane time-harmonic waves in the fluid can be expressed in the form

$$u_i = \partial\Phi_0/\partial x_i, \quad i = 1, 2, 3$$
$$\sigma_{33} = -\rho_0\omega^2\Phi_0, \quad \sigma_{13} = \sigma_{23} = 0 \tag{7}$$

where

$$\Phi_0 = (e^{i\eta_0 x_3} + R_0 e^{-i\eta_0 x_3})e^{i\xi x}, \quad x_3 < 0$$
$$= T_0 e^{i\eta_0(x_3 - H) + i\xi x}, \quad x_3 > H \tag{8}$$

$\xi = k_0 \sin\theta$ is the horizontal component of the wave number, $\eta_0 = k_0 \cos\theta$ is the vertical wave number, $k_0 = \omega/\alpha_0$, $x = x_1 \cos\phi + x_2 \sin\phi$, α_0 is the acoustic wave speed in the fluid, R_0 is the as yet unknown reflection coefficient at the top interface, and T_0 is the unknown transmission coefficient at the bottom interface. For an ideal fluid the shear stress components vanish and the normal component of displacement is continuous at the fluid-solid interfaces, but tangential slip between the fluid and the solid is allowed. Thus, the boundary conditions at the top and bottom surfaces of the plate can be expressed in the form

$$e^{i\xi x}\{S(x_3)\} = [u_1\ u_2\ u_3\ \sigma_{13}\ \sigma_{23}\ \sigma_{33}]^T$$
$$= [U_0\ V_0\ i\eta_0\ \Phi_{0,3}\ 0\ 0\ -\rho_0\omega^2\Phi_0]^T, \quad x_3 = 0$$
$$= [U_1\ V_1\ i\eta_0\ \Phi_{0,3}\ 0\ 0\ -\rho_0\omega^2\Phi_0]^T, \quad x_3 = H \tag{9}$$

where $\{S(x_3)\}$ is the so-called stress-displacement vector, and (U_0, V_0) and (U_1, V_1) are the components of the slip on the tangential plane at $x_3 = 0$ and H, respectively.

3.1 The First Reflection at the Upper Interface. The potentials within the plate associated with the elastic bulk waves transmitted through the upper interface are given by

$$\begin{Bmatrix} \Phi_1 \\ \Phi_2 \\ \Phi_3 \end{Bmatrix} = \begin{bmatrix} q_{11} & q_{21} & 0 \\ q_{12} & q_{22} & 0 \\ 0 & 0 & 1 \end{bmatrix} \text{Diag}[e^{i\zeta_1 x_3}\ e^{i\zeta_2 x_3}\ e^{i\zeta_3 x_3}]\{A^+\}e^{i\xi x} \tag{10}$$

where the unknown vector $\{A^+\} = \{A_{11}^+ A_{12}^+ A_{13}^+\}$ corresponds to the three bulk waves refracted through the top interface and the superscript "+" indicates a "downgoing" wave. The wave numbers ζ_j $(j = 1, 2, 3)$ and the factors q_{ij} $(i, j = 1, 2)$ are given by

$$\zeta_1^2 = -\xi_2^2 + b_1, \quad \zeta_2^2 = -\xi_2^2 + b_2$$
$$\zeta_3^2 = -\xi_2^2 + (\omega^2 - a_5\xi_1^2)/a_4, \quad \text{Im}(\zeta_j) \geq 0, \quad j = 1, 2, 3$$
$$q_{11} = a_3 b_1, \quad q_{21} = \omega^2 - a_2\xi_1^2 - a_5 b_1$$
$$q_{12} = a_3 b_2, \quad q_{22} = \omega^2 - a_2\xi_1^2 - a_5 b_2$$

where

$$b_1 = -\beta/2\alpha - \sqrt{(\beta/2\alpha)^2 - \gamma/\alpha},$$
$$b_2 = -\beta/2\alpha + \sqrt{(\beta/2\alpha)^2 - \gamma/\alpha}$$
$$\alpha = a_1 a_5, \quad \beta = (a_1 a_2 + a_5^2 - a_3^2)\xi_1^2 - \omega^2(a_1 + a_5)$$
$$\gamma = (a_2\xi_1^2 - \omega^2)(a_5\xi_1^2 - \omega^2).$$

The boundary conditions at the top surface of the plate lead to a system of linear equations for the determination of the three unknown coefficients A_{ij}^+ and the surface reflection coefficient R_0. The equation can be written in the partitioned matrix form as

$$[Q_{21} \vdots B_1]\begin{Bmatrix} A^+ \\ \cdots \\ R_0 \end{Bmatrix} = \{B_2\} \tag{11a}$$

where

$$\{B_1\} = [i\eta_0\ 0\ 0\ \rho_0\omega^2]^T \tag{11b}$$

$$\{B_2\} = [i\eta_0\ 0\ 0 - \rho_0\omega^2]^T \tag{11c}$$

and the 4×3 matrix $[Q_{21}]$ is given in the Appendix. The system of Eqs. (11) can be solved in a straightforward manner to determine the amplitude and phase of the reflected acoustic wave and the refracted elastic waves at the upper fluid-solid interface.

3.2 The Second Reflection at the Bottom Interface. Each bulk wave that is refracted into the plate through the top surface generates three new bulk waves on reflection at the bottom surface and refracts one acoustic ray into the sur-

Downloaded 03 May 2010 to 171.66.16.247. Redistribution subject to ASME license or copyright; see http://www.asme.org/terms/Terms_Use.cfm

Table 1 Properties of the graphite/epoxy composite laminate

Mass density (g/cm^3)	C_{11} (Gpa)	C_{12} (Gpa)	C_{22} (Gpa)	C_{23} (Gpa)	C_{55} (Gpa)
1.578	160.73	6.44	13.92	6.92	7.07

rounding fluid. The potentials associated with these waves are given by

$$\begin{Bmatrix}\Phi_1\\ \Phi_2\\ \Phi_3\end{Bmatrix} = \begin{bmatrix} q_{11} & q_{12} & 0\\ q_{21} & q_{22} & 0\\ 0 & 0 & 1\end{bmatrix} [\mathrm{Diag}[\delta_{j1}e^{i\zeta_1 x_3}\ \delta_{j2}e^{i\zeta_2 x_3}\ \delta_{j3}e^{i\zeta_3 x_3}]\{A^+\} + \mathrm{Diag}[e^{i\zeta_1(H-x_3)}\ e^{i\zeta_2(H-x_3)}\ e^{i\zeta_3(H-x_3)}]\ \{A_j^-\}]e^{i\xi x} \quad (12)$$

where the unknown vector $\{A_j^-\} = \{A_{j1}^-\ A_{j2}^-\ A_{j3}^-\}$ is associated with the waves reflected from the bottom surface and the superscript "$-$" indicates an "upgoing" wave. The index j ($= 1, 2, 3$) corresponds to the order of a specific bulk wave, and δ_{ji} is the Kronecker delta. As in the previous case, the boundary conditions at the bottom surface yield a system of linear equations

$$[Q_{22} \vdots B_3]\begin{Bmatrix}A_j^-\\ \cdots\\ T_j\end{Bmatrix} = -[Q_{21}][E_0]\{A_j^+\} \quad (13a)$$

where

$$\{B_3\} = [-i\eta_0\ 0\ 0\ \rho_0\omega^2]^T$$

$$\{A_j^+\} = \{\delta_{j1}A_{11}^+\ \delta_{j2}A_{12}^+\ \delta_{j3}A_{13}^+\} \quad (13b)$$

$$[E_0] = \mathrm{Diag}[e^{i\zeta_1 H}\ e^{i\zeta_2 H}\ e^{i\zeta_3 H}] \quad (13c)$$

and T_j is the transmission coefficient for the associated rays refracted into the lower fluid. The matrix $[Q_{22}]$ is given in the Appendix. The amplitude and phase of the second set of waves can be determined by solving the system of Eqs. (13).

3.3 Higher Order Reflections. The waves generated by subsequent reflections and refractions can be handled in a similar manner. As an example, each "upgoing" bulk wave refracts a reflected acoustic wave into the overlying fluid above the plate. The reflection coefficients R_{ji} for the associated rays can be obtained by means of the above procedure. In this case the right-hand side of (11) is replaced by a vector—$[Q_{22}][E_0]\{A_{ji}^-\}$ and the reflection coefficient R_0 on the left-hand side is replaced by the components R_{ji}, where the vector $\{A_{ji}^-\}$ is given by $\{\delta_{i1}A_{j1}^-\ \delta_{i2}A_{j2}^-\ \delta_{i3}A_{j3}^-\}$. The coefficient R_{ji} for each ray in the recursive derivation (11)–(13) corresponds to a reflected acoustic wave generated by a bulk wave labeled "*ji*" after refraction at the top surface.

3.4 The Exact Reflection Coefficient and Dispersion Curves for Leaky Guided Waves. The above procedure can be used to calculate the complex reflection coefficients of the individual rays which emerge from the specimen after reflection and refraction at the two interfaces. In general, the total contribution from an infinite number of rays needs to be calculated to obtain the overall reflection coefficient. An alternative and more convenient procedure for the evaluation of the exact reflection coefficient for general, multilayered angle-ply laminates is through the solution of the associated boundary value problem. The details of this procedure can be found in a number of papers cited earlier and will be omitted. The dispersion curves for the leaky guided waves are obtained by locating the minima in the amplitude spectra of the reflection coefficients.

3.5 Dispersion Equation for Free Guided Waves. The dispersion equation for free Lamb waves in a general, multilayered angle-ply laminate can be obtained by replacing the "boundary conditions" at the fluid plate by the traction-free condition, and by treating the wave number ξ as the unknown wave number of the guided waves. If v denotes the phase velocity of the waves at angle ϕ to the fibers axis, then $\xi = \omega/v$. The details of these calculations can be found in the papers cited earlier and will be omitted. It should be noted that the dissipative properties of the composite or the influence of fluid loading on the boundary are not considered in the derivation of the dispersion equations. The real roots, ξ, of these equations give the wave numbers of the unattenuated free guided waves in the laminate.

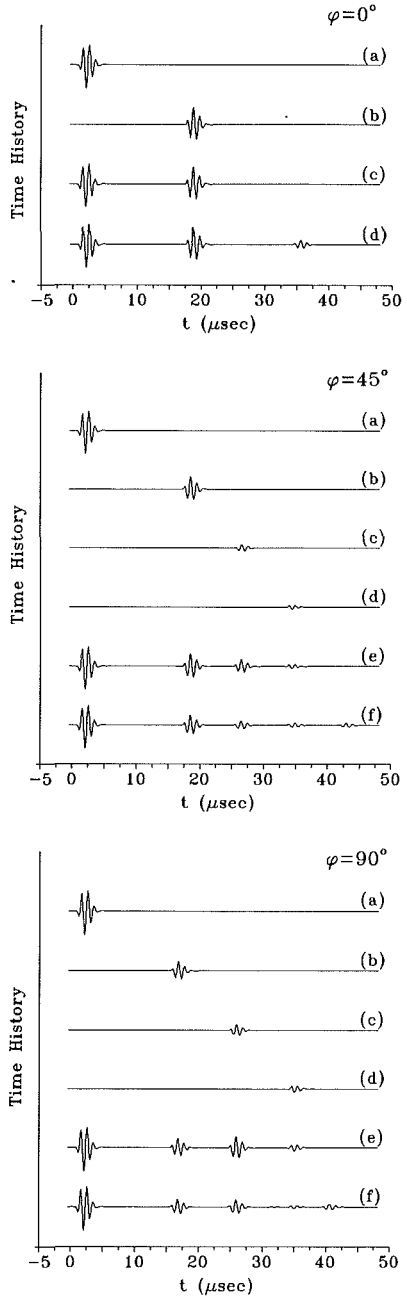


Fig. 2 Reflected time histories for a 24.5-mm thick unidirectional graphite/epoxy plate at 15-deg angle of incidence and three fiber orientations. Top panel for 0-deg orientation: (*a*) reflection from upper interface, (*b*) mode 2-2, (*c*) sum of first 5 rays, (*d*) exact reflected signal. Center panel for 45-deg orientation: (*a*) reflection from upper interface, (*b*) mode 2-2, (*c*) mode 2-3 or 3-2, (*d*) mode 3-3, (*e*) sum of first ten rays, (*f*) exact reflected signal. Bottom panel for 90-deg orientation: (*a*) reflection from upper interface, (*b*) mode 1-1, (*c*) mode 1-2 or 2-1, (*d*) mode 2-2, (*e*) combination of first five rays, (*f*) exact reflected signal.

4 Numerical Results and Discussion

The elastic properties of the graphite/epoxy AS4/3501-6

Downloaded 03 May 2010 to 171.66.16.247. Redistribution subject to ASME license or copyright; see http://www.asme.org/terms/Terms_Use.cfm

composite material used in the numerical calculation are given in Table 1. Results are obtained for both time-harmonic and transient waves. In the time-harmonic case, the incident wave is given by the first term in the right-hand side of (8) for $x_3 < 0$ unless noted otherwise. In the transient case, with a given incident pulse, the time-harmonic solution is multiplied by the Fourier transform of the incident pulse and the result is inverted by means of FFT.

In the experiments, the incident pulses were generated by transducers of two different center frequencies, namely, 5 MHz for the thin specimens and 1 MHz for the thick unidirectional specimen. The data were obtained at the NDE laboratory of Douglas Aircraft Company; the details of the experiment can be found in Mal and Bar-Cohen (1988a). It should be noted that attenuation has been included in calculating the reflected pulses from the specimens, but it is ignored in the generalized ray analysis.

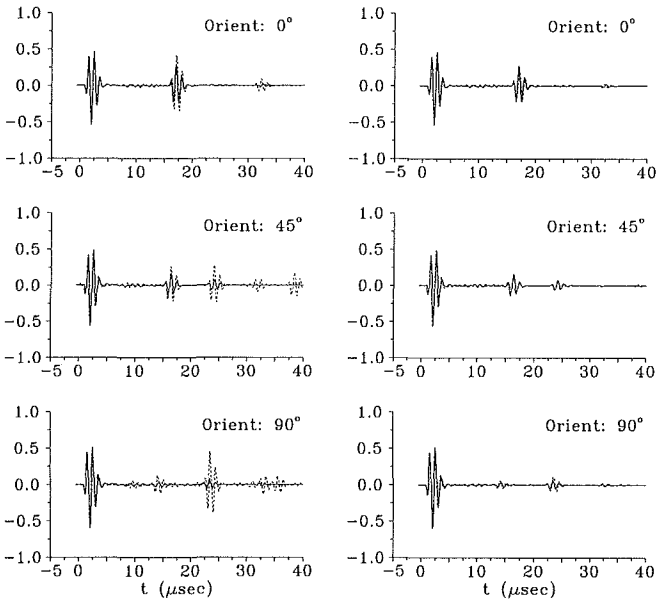


Fig. 3 Comparison between measured (solid lines) and calculated (dashed lines) LLW time histories for a 24.5-mm thick graphite/epoxy laminate at 20-deg incidence angle. The calculated results in the left panel assumes perfect elasticity while those at the right panel assumes a dissipative model with $f_0 = 0.3$, $p_0 = 0.005$, $a_0 = 0.3$.

The time histories of the reflected signals from a 24.5-mm thick composite plate at 15-deg angle of incidence and 0-deg, 45-deg, and 90-deg orientations are shown in Fig. 2. It can be seen that for 0-deg orientation, the reflected pulses emerge sequentially with equal times of flight. The quasi-shear-shear wave (mode 2-2) yields a series of significant reflected signals; the influence of the other bulk waves is negligible. This is similar to wave behavior in an isotropic plate.

However, for off-axis orientations, the time delays between the successively arrived signals are irregular. As an example, for waves travelling at 45-deg orientation, the reflected signal of mode 2-2 arrives after the signal reflected from the top surface, but they are followed by modes 2-3 (or 3-2), 3-3, etc., with different times of flight. The influence of other mode-converted waves is nearly negligible. The mode-converted bulk waves travel at different speeds resulting in irregular time delays between the arrived pulses. This is true even for motion on the quasi-isotropic plane ($\phi = 90$ deg), in sharp contrast to propagation along the fibers or in isotropic media, where all bulk waves generated at the same surface have equal influence on the reflected signals.

For propagation in the quasi-isotropic plane, the waves which appear in the plate are longitudinal or transverse, as in an isotropic plate. The reflected signal from the fastest longitudinal-longitudinal wave (mode 1-1) is followed by that from the longitudinal-transverse (mode 1-2), or the transverse-longitudinal (mode 2-1) wave. The latest arrived signal is from mode 2-2 (transverse-transverse wave). The reflected pulses due to the individual bulk waves and the top surface reflection clearly explain the anomalous behavior for off-axis propagation in a unidirectional composite plate.

The calculated reflected signals from two unidirectional graphite/epoxy laminates of 1-mm and 24.5-mm thicknesses, a cross-ply laminate and a quasi-isotropic laminate, each of 1-mm thickness are compared with measured data in Figs. 3 and 4. Transducer response and other unknown factors in the

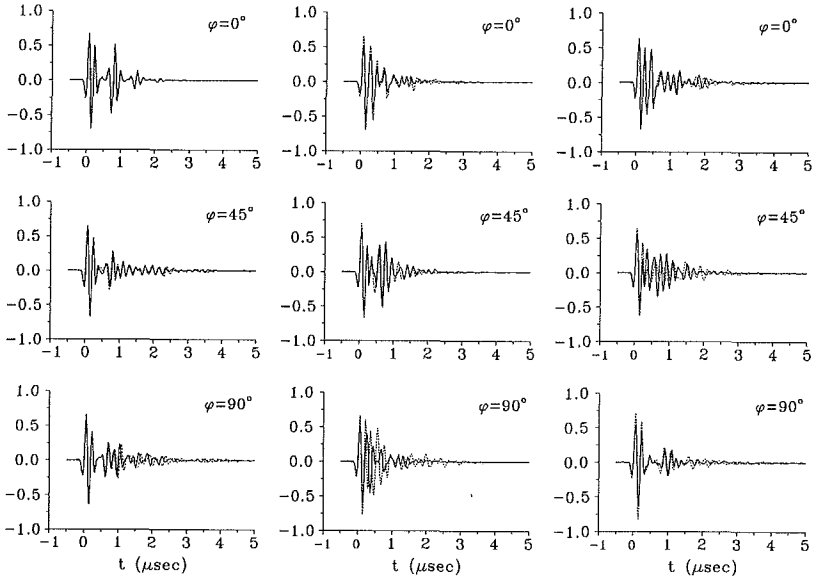


Fig. 4 Comparison between measured (solid lines) and calculated (dashed lines) LLW time histories for a unidirectional (left panel), a cross-ply $[0/90]_{2S}$ (center panel) and a quasi-isotropic $[0/45/90/-45]_s$ (right panel) graphite/epoxy laminate of 1-mm thickness. The angle of incidence is 15 deg and $f_0 = 0.3$, $p_0 = 0.005$, $a_0 = 0.06$. The orientation angle is measured relative to the fibers in top lamina.

Downloaded 03 May 2010 to 171.66.16.247. Redistribution subject to ASME license or copyright; see http://www.asme.org/terms/Terms_Use.cfm

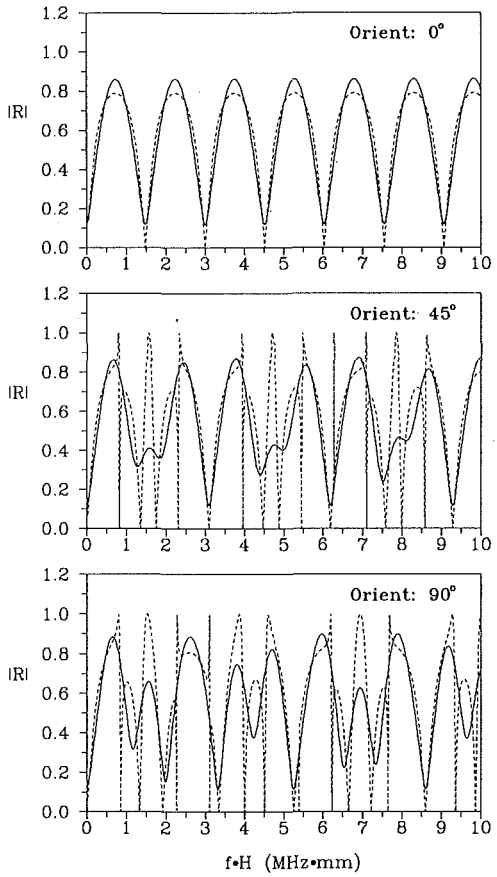


Fig. 5 Reflected amplitude spectra from a water-coupled homogeneous graphite/epoxy laminate. The angle of incidence is 15 deg. Solid lines represent $|R|$ for five rays for 0 deg, 90 deg and ten rays for 45 deg). Dashed lines represent the exact solution.

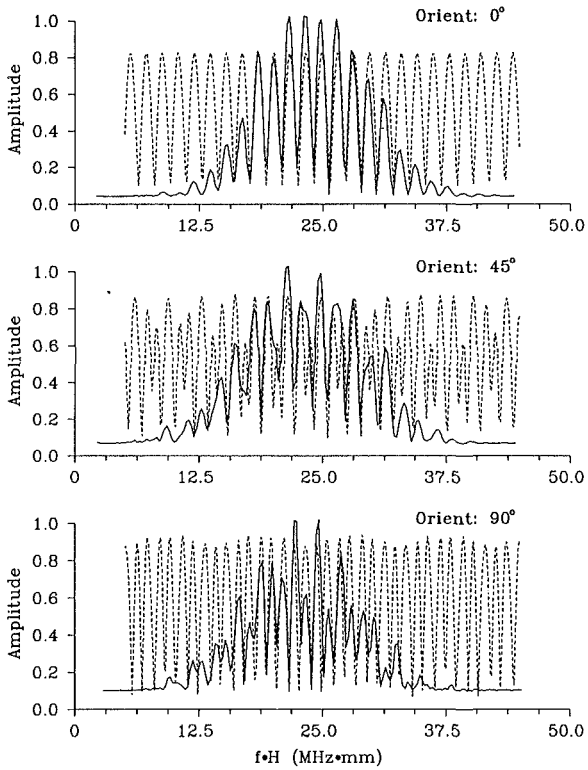


Fig. 6 Comparison between reflected spectra of LLW data (———) and approximate reflection coefficients by ray analysis (· · ·) for a 24.5-mm thick graphite/epoxy T650/1901 $[0]_{176}$ laminate. The angle of incidence is 20 deg.

experiments were eliminated by convolving the calculated impulse response with a reference reflected pulse obtained from a tungsten film placed over the specimen. The tungsten film is a total reflector, while the composite specimens are partial reflectors. To account for the transmitted energy, the theoretical reflected signals were multiplied by suitable constants. In general, the theoretical model without attenuation predicts a longer duration of motion than the data, and inclusion of dissipation in the model improves the agreement. The damping parameters were varied until a good visual fit between the measured and calculated results could be obtained. A satisfactory agreement was found to occur for $p_0 = 0.005$, $f_0 = 0.3$ MHz, and $a_0 = 0.06$ in the case of the thin plate and $a_0 = 0.3$ in the case of the thick plate. It should be noted that a higher value of a_0 for the thick plates indicates the presence of additional features (e.g., interface zones) in the laminate.

For the cross-ply laminate the later arrivals in the reflected signal appear to merge with the reflected signal from the top surface (Fig. 4). However, the major pulse shapes in the reflected signals are almost identical in both measured and calculated results. The calculated reflected pulses are in very good agreement with the measured data at 0-deg and 45-deg orientations, but the agreement is not as good for propagation at 90 deg to the fibers of top lamina.

For propagation in a quasi-isotropic laminate, good agreement was achieved at 0-deg and 90-deg orientations as can be seen from Fig. 4. The measurements appear to indicate that the quasi-isotropic specimen is a stronger reflector than what the theory predicts at 45-deg orientation. A number of later arrived, reflected pulses are present with relatively large amplitudes.

The calculated amplitude spectra of the approximate and exact reflection coefficients for a unidirectional composite plate are shown in Fig. 5, where the spectra calculated for the first few reflections by the ray theory for three fiber orientations are compared with the exact overall reflection coefficients. It can be seen that for propagation parallel to the fibers, the amplitude spectrum of the aggregate of five reflected rays, which includes the top reflection and the converted modes 11, 12, 21, 22, coincides with that of the exact reflection coefficient. Moreover, these minima are identical to the modal frequencies of free Lamb waves in the plate with phase velocity $v = 5.74$ mm/μsec (which corresponds to 15-deg angle of incidence). However, for propagation at 45-deg and 90-deg orientations, the minima of the amplitude spectra of a few pulses do not coincide with those of the exact reflection coefficient. Thus, unlike propagation along the fibers, the phase velocity of leaky guided waves can not be constructed from a small number of reflected rays.

Figure 5 further shows that the amplitudes of modes 11 and 12 for 0-deg orientation and of modes 11, 12, and 13 for 45-deg orientation are negligibly small. However, none of these can be neglected for propagation at 90 deg to the fibers. In general, there are three critical angles of refraction for the bulk waves generated at the fluid-solid interface. Once the angle of incidence is larger than a critical angle, the influence of the associated bulk wave becomes negligible. For 90-deg fiber orientation, the smallest critical angle is about 30 deg, so every mode-converted ray generated by the wave transmitted at 15-deg angle of incidence contributes to the reflected field.

The measured and calculated reflected spectra for the 24.5-mm thick graphite/epoxy laminate are shown in Fig. 6. The spectra of a finite number of reflected rays are in good agreement with measured LLW spectra in the number and location of the minima. As indicated earlier (Mal and Bar-Cohen, 1988b), a fewer number of minima were observed in the meas-

Downloaded 03 May 2010 to 171.66.16.247. Redistribution subject to ASME license or copyright; see http://www.asme.org/terms/Terms_Use.cfm

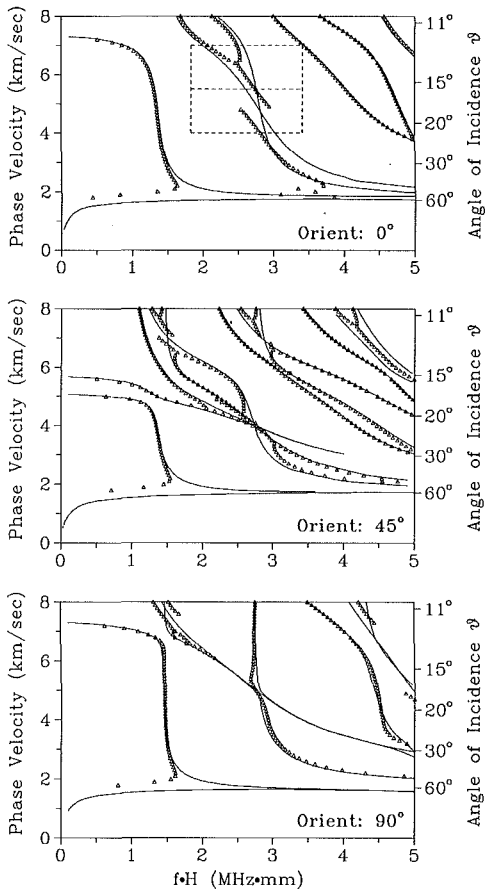


Fig. 7 Dispersion curves for leaky guided waves in a 1-mm thick $[0/90]_{2S}$ graphite/epoxy laminate immersed in water (Δ) and for free guided waves in the laminate (———)

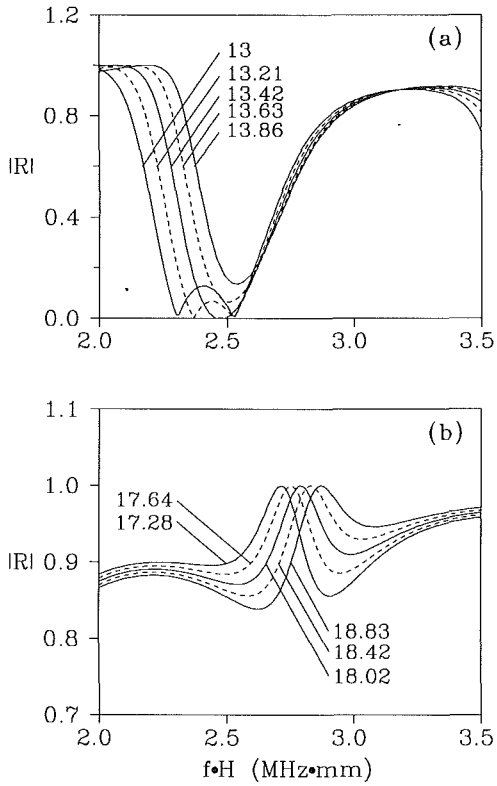


Fig. 8 Variations in the amplitude spectra of reflection coefficients for $\phi = 0$ deg at angles of incidence of (*a*) 13 deg–13.86 deg and (*b*) 17.28 deg–18.83 deg

ured spectra than that predicted by the exact theoretical calculation for the thick specimen. The present analysis shows that the minima in the measured LLW spectra are caused by the interference between a small number of mode-converted reflected body wave rays rather than guided waves in the plate.

The LLW experiment is a highly effective and accurate method to determine dispersion curves of leaky guided waves in a given specimen. In the theoretical approach, the dispersion curves can be obtained by means of two alternative procedures. One is through the calculation of the reflection coefficients, and the other through the solution of the dispersion equations. The main difference between the two procedures is that in the first method the effects of fluid loading and/or wave attenuation are included, while in the second method they are ignored. Thus, the first method is clearly a closer representation of the experiment. The main advantage of the second method is that only the real roots of the dispersion equations need to be calculated, making it computationally more efficient.

The dispersion curves for leaky Lamb waves in a unidirectional graphite/epoxy laminate with material dissipation immersed in water were compared with those for free Lamb waves in the laminate without material dissipation in Karim, Mal, and Bar-Cohen (1990). The two sets of dispersion curves were shown to be almost identical for phase velocities greater than about 2.5 mm/μsec, which corresponds to an angle of incidence of less than about 37 deg. The influence of material dissipation on the LLW dispersion curves was found to be negligible in a broad range of frequencies. A similar comparison for a cross-ply $[0/90]_{2S}$ laminate is presented in Fig. 7. As in the unidirectional case, the influence of water loading is found to be significant at lower phase velocities. However, there are other small but important differences even at higher phase velocities.

As an example, for propagation parallel to the fibers of the top lamina ($\phi = 0$ deg), and at angles of incidence and frequencies within the rectangular window shown in Fig. 7, two adjacent dispersion curves for leaky guided waves coalesce at $\theta \approx 13.42$ deg and $f \approx 2.45$ MHz, then split into two branches at $\theta \approx 18$ deg and $f \approx 2.75$ MHz. A detailed examination of this anomalous behavior and its implication in nondestructive material characterization are presented below.

The reflected amplitude spectra from the cross-ply laminate for propagation parallel to the fibers of the top lamina and for incident angle and frequency ranges within the rectangular window in Fig. 7 are shown in Fig. 8. It can be seen that at an incident angle of 13 deg, there are two distinct minima (nulls) in the spectra (Fig. 8(*a*)). As the incident angle is increased, the two minima come closer and eventually they merge at an incident angle of 13.42 deg, resulting in a single minimum at $f = 2.45$ MHz. At higher incident angles, the minimum point moves up and to the right.

The reflected amplitude spectra in the vicinity of the break point, at $\theta = 18$ deg, are shown in Fig. 8(*b*); they contain two local minima straddling a maximum. For $\theta < 18$ deg, the curve to the left of the peak becomes flat, while for $\theta > 18$ deg, the curve to the right of the peak becomes flat. In our computer codes for locating minima in both theoretical calculations and experimental data, a minimum is identified only if the value of the spectrum drops by 5 percent from its nearest peak, otherwise it is ignored. Thus, for angles of incidence below 18 deg, the minimum to the left of the peak is ignored and for angles of incidence larger than 18 deg the minimum to the right of the peak is ignored. The breaks in the leaky guided wave dispersion curves are the results of this numerical procedure and is consistent with the expected accuracy of our current experimental setup.

As an example, the calculated dispersion curves for free guided waves in the cross-ply laminate are compared with the measured dispersion curves for leaky guided waves in Fig. 9.

Downloaded 03 May 2010 to 171.66.16.247. Redistribution subject to ASME license or copyright; see http://www.asme.org/terms/Terms_Use.cfm

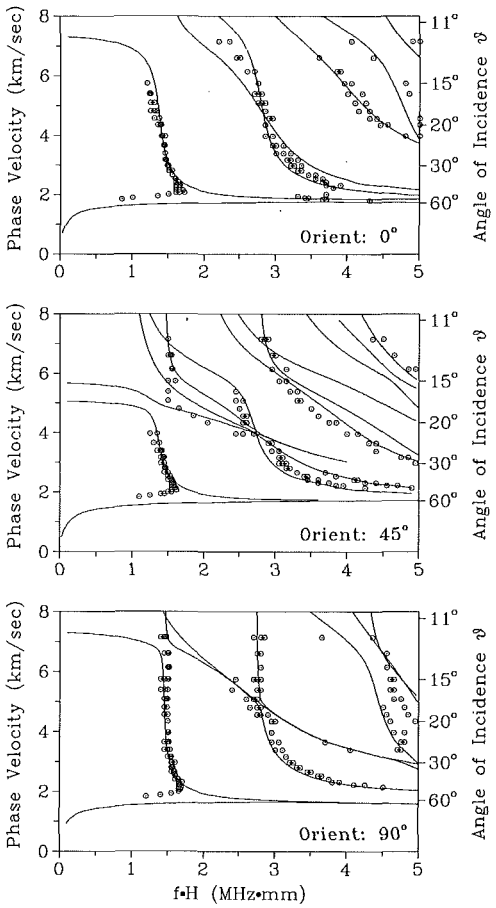


Fig. 9 Dispersion curves and LLW data for a 1-mm thick $[0/90]_{2S}$ laminate at 0-deg, 45-deg, and 90-deg orientations

The comparison was carried out in the lower frequency range of 0.1–5 MHz, since the data within this frequency range are more reliable. Although the agreement between measured and calculated dispersion curves is generally very good, there is not enough resolution in the data to identify their special features discussed above. Thus, although the differences in the dispersion curves of leaky guided waves and of free guided waves in the cross-ply laminate are interesting from a theoretical point of view, their significance in the determination of experimental dispersion curves is not clear.

5 Concluding Remarks

The most important features of the reflected signals in the LLW measurements for unidirectional fiber-reinforced composite specimens can be clearly explained through generalized ray theory. The analysis presented here shows that a small number of rays contribute to the overall reflected signal and that the irregular behavior of the reflected field is caused by mode-converted waves, many of which are extinguished during reflection. For waves propagating in the plane parallel or perpendicular to the fibers, the reflected acoustic field from the fiber-reinforced composite is similar to that of the isotropic case in many aspects. However, there are significant differences in certain properties of the field even for propagation perpendicular to the fibers.

Inclusion of material dissipation in the theoretical simulation of the LLW experiment is shown to be essential for accurate prediction of the wave amplitude, especially at higher fH values. The phenomenological model of wave attenuation presented here yields results that are in excellent agreement with laboratory measurements. Further studies are needed to evaluate the applicability of this model to other data and other types of composites.

When compared to LLW data for a relatively thick, unidirectional composite plate, the exact solution for the elastodynamic problem predicts a larger number of minima in reflected amplitude spectra. The present analysis shows that the minima in the LLW spectra are caused by the interference of bulk waves rather than the appearance of guided waves in the plate.

Water loading has significant influence on the dispersion curves for leaky Lamb waves in unidirectional laminates for phase velocities less than 2.5 mm/μsec. The influence of water loading results in other small but important differences between the dispersion curves for leaky guided waves and for free guided waves in a cross-ply laminate at higher phase velocities. We have shown that these differences would be difficult to measure in the current LLW experimental procedure. Material dissipation has negligible influence on the velocity of guided waves in all the laminates studied in a broad range of frequencies and velocities.

It is well known that the stiffness constants C_{22}, C_{23}, and C_{55} of the unidirectional composite have a strong influence on the dispersion curves of both leaky and free Lamb waves. Hence, these three material constants can be determined accurately through appropriate inversion schemes of the LLW data. Due to their weak influence on the dispersion curves, the other two material constants (C_{11} and C_{12}) must be determined through alternative ultrasonic techniques, e.g., those based on the time-of-flight of the individual rays.

Acknowledgment

This research was supported by the Office of Naval Research under contract N00014-90-J-1857. We are thankful to Dr. Y. Rajapakse of ONR for his encouragement and support during the course of this work.

References

Bose, S. K., and Mal, A. K., 1974, "Elastic Waves in a Fiber-Reinforced Composite," *J. Mech. Phys. Solids*, Vol. 22, pp. 217–229.

Buchwald, V. T., 1961, "Rayleigh Waves in Transversely Isotropic Media," *Quart. J. Mech. and Appl. Math.*, Vol. 14, pp. 293–317.

Datta, S. K., and Ledbetter, H. M., 1983, "Elastic Constants of Fiber-Reinforced Boron-Aluminum: Observation and Theory," *Int. J. Solids Structures*, Vol. 19, pp. 885–894.

Dayal, V., Iyer, V., and Kinra, V. K., 1989, "Ultrasonic Evaluation of Microcracks in Composites," *Advances in Fracture Research*, Vol. 5, K. Salama, K. Ravi-Chandar, D. M. R. Taplin, and P. Rama Rao eds., Pergamon Press, pp. 3291–3300.

Karim, M. R., Mal, A. K., and Bar-Cohen, Y., 1990, "Inversion of Leaky Lamb Wave Data by Simplex Algorithm," *J. Acoust. Soc. Am.*, Vol. 88, No. 1, pp. 482–491.

Knopoff, L., 1964, "Q," *Review of Geophysics*, Vol. 2, pp. 625–660.

Mal, A. K., 1988, "Wave Propagation in Layered Composite Laminates under Periodic Surface Loads," *Wave Motion*, Vol. 10, pp. 257–266.

Mal, A. K., and Bar-Cohen, Y., 1988a, "Ultrasonic Characterization of Composite Laminates," *Proceedings of the Joint ASME and SES Symposium on Wave Propagation in Structural Composites*, A. K. Mal and T. C. T. Ting, eds., ASME-AMD-Vol. 90, pp. 1–16.

Mal, A. K., and Bar-Cohen, Y., 1988b, "Ultrasonic NDE of Thick Composite Laminates," *Rev. of Progr. in QNDE*, D. Thompson and D. Chimenti, eds., Vol. 8B, pp. 1551–1558.

Mal, A. K., and Bar-Cohen, Y., 1989, "Stress Waves in Layered Composite Laminates," *Proc. 4th Japan-U.S. Conf. on Composite Materials*, June 27–29, pp. 361–370.

Nayfeh, A. H., and Chimenti, D. E., 1988, "Ultrasonic Wave Reflection From Liquid-Coupled Orthotropic Plates With Application to Fibrous Composites," ASME JOURNAL OF APPLIED MECHANICS, Vol. 55, pp. 863–870.

Tang, B., and Henneke, II, E. G., 1989, "Lamb-Wave Monitoring of Axial Stiffness Reduction of Laminated Composite Plates," *Material Evaluation*, Vol. 47, pp. 928–934.

APPENDIX

The expressions for some of the matrices used in Section 3 are given here.

Downloaded 03 May 2010 to 171.66.16.247. Redistribution subject to ASME license or copyright; see http://www.asme.org/terms/Terms_Use.cfm

$$[Q_{11}]=\begin{bmatrix} i\xi_1 q_{11} & i\xi_1 q_{12} & 0 \\ i\xi_2 q_{21} & i\xi_2 q_{22} & i\zeta_3 \end{bmatrix},\ [Q_{12}]=\begin{bmatrix} i\xi_1 q_{11} & i\xi_1 q_{12} & 0 \\ i\xi_2 q_{21} & i\xi_2 q_{22} & -i\zeta_3 \end{bmatrix}$$

$$[Q_{21}]=\begin{bmatrix} i\zeta_1 q_{21} & i\zeta_2 q_{22} & -i\xi_2 \\ -\rho a_5 \xi_1 \zeta_1 (q_{11}+q_{21}) & -\rho a_5 \xi_1 \zeta_2 (q_{12}+q_{22}) & \rho a_5 \xi_1 \xi_2 \\ -2\rho a_4 \xi_2 \zeta_1 q_{21} & -2\rho a_4 \xi_2 \zeta_2 q_{22} & \rho a_4 (\xi_2^2-\zeta_3^2) \\ \delta_1 & \delta_2 & 2\rho a_4 \xi_2 \zeta_3 \end{bmatrix}$$

$$[Q_{22}]=\begin{bmatrix} -i\zeta_1 q_{21} & -i\zeta_2 q_{22} & -i\xi_2 \\ \rho a_5 \xi_1 \zeta_1 (q_{11}+q_{21}) & \rho a_5 \xi_1 \zeta_2 (q_{12}+q_{22}) & \rho a_5 \xi_1 \xi_2 \\ 2\rho a_4 \xi_2 \zeta_1 q_{21} & 2\rho a_4 \xi_2 \zeta_2 q_{22} & \rho a_4 (\xi_2^2-\zeta_3^2) \\ \delta_1 & \delta_2 & -2\rho a_4 \xi_2 \zeta_3 \end{bmatrix}$$

$$\delta_1=\rho[(a_5-a_3)\xi_1^2 q_{11}-(a_1-2a_4)\xi_2^2 q_{21}-a_1\zeta_1^2 q_{21}]$$

$$\delta_2=\rho[(a_5-a_3)\xi_1^2 q_{12}-(a_1-2a_4)\xi_2^2 q_{22}-a_1\zeta_2^2 q_{22}]$$

Downloaded 03 May 2010 to 171.66.16.247. Redistribution subject to ASME license or copyright; see http://www.asme.org/terms/Terms_Use.cfm

Transient Wave Propagation in a Harmonically Heterogeneous Elastic Solid

Hyun-Sil Kim[1,2]
Postdoctoral Research Engineer,
Department of Mechanical Engineering,
Johns Hopkins University,
Baltimore, MD 21218

Jerry H. Ginsberg
George W. Woodruff Professor,
School of Mechanical Engineering,
Georgia Institute of Technology,
Atlanta, GA 30332
Fellow ASME

Transient propagation of a one-dimensional dilatational wave in a harmonically heterogeneous elastic solid is studied by several techniques. A regular perturbation analysis in terms of the characteristics of the differential equation shows that initiation of a temporally harmonic excitation that generates a signal whose wavelength is twice the periodicity of the heterogeneity leads to secularity in the first approximation. The frequency at which this situation occurs matches the frequency at which Floquet theory predicts that steady-state waves may be unstable. A finite difference algorithm based on integrating along the characteristics is developed and implemented to obtain a numerical solution. In the critical case, backscattering of the wave from the heterogeneity results in a mixture of propagating and standing wave features. However, rather than being unstable, the heterogeneity in this condition is shown to result in maximum interference with forward propagation. A comparable analysis for a step excitation on the boundary provides additional insight into the underlying propagation phenomena.

1 Introduction

Heterogeneity often leads to interesting wave propagation phenomena. For example, it has been generally accepted that in infinite elastic media whose material properties display a sinusoidal spatial fluctuation, steady-state harmonic waves might be unstable if the wavelength and periodicity of the heterogeneities satisfy certain relations. Nayfeh and Nemat-Nasser (1972) showed that instability is encountered in one-dimensional media when the wavelength is twice the periodicity of the heterogeneity. Watanabe (1984) considered oblique propagation of SH waves, such that the direction of wave propagation is oblique to the vertical coordinate along which the material properties vary. He obtained the instability frequency as a function of periodicity and angle. Schoenberg and Weitsman (1975) studied propagation of plane harmonic waves in an infinite fiber-reinforced medium whose fibers are assumed to wobble periodically about the dominant direction. They showed that responses are unstable in certain frequency bands. Zarembo and Prokhorov (1975) investigated generation of a second harmonic signal in a semi-infinite medium whose residual strain is a harmonic function of the spatial coordinate. Such residual strain plays a role equivalent to material heterogeneity. Finite amplitude wave propagation in periodically heterogeneous media were treated by Nair and Nemat-Nasser (1971), Nayfeh (1975), and Kluwick and Nayfeh (1979), although they did not consider the instability phenomenon.

Generally, the equations of motion governing steady-state harmonic waves in harmonically heterogeneous media are differential equations whose coefficients are periodic functions of the spatial coordinates. The most typical example is the Mathieu's equation, which has an infinite number of unstable regions that depend on the periodicity and magnitude of the heterogeneity and the frequency of the excitation (Ince, 1956). According to Floquet theory, unstable responses grow exponentially with distance in the steady-state condition.

The investigations that studied instability (Nayfeh and Nemat-Nasser, 1972; Watanabe, 1984; Schoenberg and Weitsman, 1975) are founded on the assumption of a steady-state condition. However, in real applications stress waves are excited in a transient manner. An *a priori* assumption of steady-state leaves one unable to ascertain the rate at which a transient wave evolves to a steady-state condition. Indeed, initial conditions are irrelevant to the derivation of Floquet theory. In a semi-infinite one-dimensional medium, one could argue that a steady-state condition never exists, because the wave front is always propagating into previously unexcited regions. Furthermore, the concept of instability in this situation leads to ambiguities regarding the balance between the work done by a boundary excitation and the mechanical energy contained in a wave that propagates as its amplitude increases.

In the present study, we consider transient propagation of a one-dimensional dilatational wave in a semi-infinite elastic

[1] A portion of this work appeared in H. S. Kim's Ph.D. Thesis, "Instability of Finite Amplitude Wave Propagation in Harmonically Heterogeneous Elastic Solids," Georgia Institute of Technology, Nov. 1989.

[2] Presently, Senior Research Engineer, Acoustic Laboratory, Korea Institute of Ships and Ocean Engineering, Deaduk Sciencetowon, Daejon, Korea.

Contributed by the ASME Applied Mechanics Division of THE AMERICAN SOCIETY OF MECHANICAL ENGINEERS for presentation at the Winter Annual Meeting, Atlanta, Ga., Dec. 1-6, 1991.

Discussion on this paper should be addressed to the Technical Editor, Prof. Leon M. Keer, The Technological Institute, Northwestern University, Evanston, IL 60208, and will be accepted until two months after final publication of the paper itself in the JOURNAL OF APPLIED MECHANICS. Manuscript received by the ASME Applied Mechanics Division, July 11, 1990; final revision, Feb. 25, 1991.

Paper No. 91-WA/APM-34.

Copyright © 1992 by ASME
Downloaded 03 May 2010 to 171.66.16.247. Redistribution subject to ASME license or copyright; see http://www.asme.org/terms/Terms_Use.cfm

solid. The density and elastic coefficients are assumed to deviate by small amounts from average values, where such variations are harmonic functions of the spatial coordinate. First, we develop a straightforward perturbation expansion in order to identify the manner in which the generated wave initially interacts with the medium. This solution breaks down as the wave evolves, due to the occurrence of secular terms. In the case of a transient harmonic excitation, this loss of validity is shown to arise at a lower perturbation order when the system parameters satisfy the instability condition which is summarized as the next step in the analysis.

In the last part of the investigation, we study the evolution of the wave for arbitrary time and position by implementing a numerical algorithm that solves the characteristic differential equations. Results obtained from that simulation for harmonic excitation suggest that no instability actually exists. In fact, they indicate that the system parameters corresponding to a Floquet instability actually produce backscattering which, in combination with the directly excited signal, generates standing wave features and maximum destructive interference. Application of the same numerical algorithm for the case of a step stress input at the boundary provides further evidence of backscattering. In a homogeneous medium, the wave would be a convected step, but the signal in the heterogeneous case is shown to display fluctuations along both forward and backward characteristics.

2 Perturbation Using the Method of Characteristics in a Special Case

We consider a planar dilatational wave of infinitesimal amplitude propagating through a linear elastic medium.[3] The basic equations are

$$\rho\frac{\partial v}{\partial t}=\frac{\partial \sigma}{\partial x},\ \sigma=\rho c^2 e,\ e=\frac{\partial u}{\partial x},\ v=\frac{\partial u}{\partial t}, \tag{1}$$

where u is the particle displacement and c is related to the Lamé coefficients and density by

$$c=[(\lambda+2\mu)/\rho]^{1/2}. \tag{2}$$

Equivalently, these relations are

$$\begin{Bmatrix}\partial v/\partial t\\ \partial e/\partial t\end{Bmatrix}-[A]\begin{Bmatrix}\partial v/\partial x\\ \partial e/\partial x\end{Bmatrix}=\begin{Bmatrix}\epsilon c^2 h(x)e\\ 0\end{Bmatrix},\ [A]=\begin{bmatrix}0 & c^2\\ 1 & 0\end{bmatrix}, \tag{3}$$

where $\epsilon h(x)$ represents the effect of heterogeneity, such that $\epsilon \ll 1$ and

$$\epsilon h(x)=\frac{1}{\rho c^2}\frac{\partial}{\partial x}(\rho c^2). \tag{4}$$

A stress is applied at the boundary at $t=0$, at which time the medium was rest in its undistributed state. With $H(t)$ denoting the Heaviside step operator, the corresponding boundary and initial conditions are

$$e(0,\ t)=F(t)\,H(t),\ v(x,\ 0)=e(x,\ 0)=0. \tag{5}$$

Let β_j and $\{\nu_j\}$ be the eigenvalues and left eigenvectors of $[A]$,

$$\{\nu\}^T[A]+\beta\{\nu\}^T=\{0\}^T, \tag{6}$$

whose nontrivial solution is

$$\beta_j=\pm c,\ \{\nu_j\}^T=\{1\ \mp c\}^T. \tag{7}$$

Premultiplication of Eq. (3) by $\{\nu_j\}^T$ leads to

$$\{\nu_j\}^T\begin{Bmatrix}\partial v/\partial t\\ \partial e/\partial t\end{Bmatrix}+\beta_j\{\nu_j\}^T\begin{Bmatrix}\partial v/\partial x\\ \partial e/\partial x\end{Bmatrix}=\{\nu_j\}^T\begin{Bmatrix}\epsilon c^2 h(x)e\\ 0\end{Bmatrix}. \tag{8}$$

The right-running and left-running characteristic variables, s_1 and s_2, respectively, are defined as a transformation from (x, t) such that

$$\left.\frac{dx}{dt}\right|_{sj}=\beta_j, \tag{9}$$

from which we obtain

$$\{\nu_j\}^T\begin{Bmatrix}dv\\ de\end{Bmatrix}=\{\nu_j\}^T\begin{Bmatrix}\epsilon c^2 h(x)e\\ 0\end{Bmatrix}\frac{dx}{\beta_j}\quad\text{along}\quad\left.\frac{dx}{dt}\right|_{sj}=\beta_j. \tag{10}$$

We shall solve these differential equations only for the special case where the heterogeneity is such that the spatial variation of the elasticity parameters matches that of the density, so that c is constant. This has the simplifying result that the characteristics are straight lines, so that Eq. (10) reduces to

$$dv-c\,de=\epsilon c h(x)e\,dx\ \text{along}\ t-x/c=s_1, \tag{11}$$

$$dv+c\,de=-\epsilon c h(x)e\,dx\ \text{along}\ t+x/c=s_2. \tag{12}$$

Equations (11) and (12) may be integrated to give a representation for the signal in the form of an integral equation. We draw the pair of characteristic lines L_1 and L_2 intersecting an arbitrary point (χ, τ), as shown in Fig. 1. The characteristic values for these lines are $s_1=\tau-\chi c$ and $s_2=\tau+\chi/c$, respectively. Both v and e vanish at the intersection S on the left-running characteristic and the characteristic $x=ct$, which represents the wave front. The value of e at the intersection Q of the right-running characteristic and the boundary $x=0$ is known from the boundary condition. In order to derive an expression for v at point Q, we consider the left-running characteristic L_3 through Q whose intersection with $x=ct$ is point R. The commonality of the intersection points enables us to determine that L_3 corresponds to the left-running characteristic value $s_2=s_1$, and that the coordinates of the intersection points are

$$Q\text{: }(0,\ s_1),\ S\text{: }(cs_2/2,\ s_2/2),\ R\text{: }(cs_1/2,\ s_1/2). \tag{13}$$

We use Eq. (11) to integrate from Q to (χ, τ) along L_1, and Eq. (12) to integrate from S to (χ, τ) along L_2 and from R to Q on L_3. This leads, respectively, to

$$v(\chi,\ \tau)-v(Q)-ce(\chi,\ \tau)+ce(Q)=\epsilon c\int_0^{\chi}h(x)\,e(x,\ x/c+s_1)\,dx, \tag{14}$$

$$v(\chi,\ \tau)+ce(\chi,\ \tau)=\epsilon c\int_{\chi}^{cs_2/2}h(x)\,e(x,\ -x/c+s_2)\,dx, \tag{15}$$

$$v(Q)++ce(Q)=\epsilon c\int_{\chi}^{cs_1/2}h(x)\,e(x,\ -x/c+s_1)\,dx. \tag{16}$$

Since $e(Q)$ is specified by the boundary condition, Eq. (5) with $t=s_1$, it is a simple matter to solve these equations for

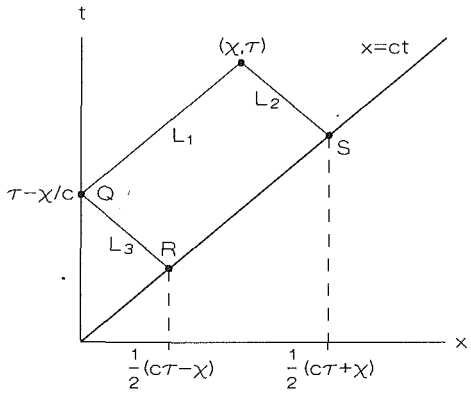


Fig. 1 Characteristic curves for the integral formulation when c is constant. Along L_1, $dx/dt=c$, while $dx/dt=-c$ along L_2 and L_3.

[3] The analysis if equally applicable to shear waves, provided that the dependent variables and parameters are redefined.

Downloaded 03 May 2010 to 171.66.16.247. Redistribution subject to ASME license or copyright; see http://www.asme.org/terms/Terms_Use.cfm

the strain. Also, because $e(x, t) \equiv 0$ for $x > ct$, we shall no longer explicitly indicate $H(s_1)$. The result for $x < ct$ may be written as

$$e(x, t) = F(s_1) + \epsilon \mathcal{L}[e], \tag{17}$$

where $\mathcal{L}$ is an integral operator defined by

$$\mathcal{L}[e] = -\frac{1}{2}\int_0^x h(x)\, e(x, x/c + s_1)\, dx - \frac{1}{2}\int_0^{cs_1/2} h(x)\, e(x, -x/c + s_1)\, dx + \frac{1}{2}\int_x^{cs_2/2} h(x)\, e(x, -x/c + s_2)\, dx. \tag{18}$$

Obviously, a similar expression may be obtained for $v(x, t)$.

Equation (17) could be employed as the basis of an iterative computational algorithm, but a more efficient and general computational procedure will be described later. Here we employ the integral representation to obtain a regular perturbation series for e. Let

$$e = e_0 + \epsilon e_1 + \epsilon^2 e_2 + \ldots . \tag{19}$$

Collecting like terms for each order of ϵ gives

$$e_0 = F(s_1),\ e_1 = \mathcal{L}[e_0],\ e_2 = \mathcal{L}[e_1] = \mathcal{L}^2[e_0]. \tag{20}$$

These relations are valid for arbitrary $h(x)$. Our interest in this paper is in situations where the heterogeneity is a sinusoidal fluctuation about a mean value, which we shall model by letting

$$h(x) = 2\gamma \cos(2\gamma x). \tag{21}$$

The present study is devoted to the case of a continuous harmonic excitation initiated when $t = 0$. Since the amplitude of stress is irrelevant in linear theory, we consider the excitation to be

$$F(t) = \sin(\omega t). \tag{22}$$

In that case, the first-order strain is

$$e_0 = \sin(\omega t - kx), \tag{23}$$

where $k = \omega/c$. We use e_0 to generate e_1 according to the second of Eqs. (20). For $k \neq \gamma$, we obtain

$$e_1 = \frac{1}{2(\gamma^2 - k^2)}[(k^2 - 2\gamma^2)\sin(\omega t - kx)\sin(2\gamma x) + \gamma k \cos(\omega t - kx)\cos(2\gamma x) + 2\gamma k \sin(\gamma x)\sin(\gamma c t) - \cos(\omega t - kx)], \tag{24}$$

while the case $k = \gamma$ corresponds to

$$e_1 = \frac{1}{4}[2\gamma(ct - x)\sin(\gamma x)\cos(\gamma c t) - 3\sin(2\gamma x)\sin(\gamma c t - \gamma x)]. \tag{25}$$

A noteworthy feature of Eq. (25) is the presence of the term $(ct - x)\sin(\gamma x)\cos(\gamma c t)$, which corresponds to a standing wave whose amplitude increases in proportion to the outward characteristic, and whose wavelength matches that of e_0 and is twice the periodicity of the heterogeneity. This term may be traced to the L_2 integrand in Eq. (20) which contains a square of like sinusoidal terms when e is estimated as e_0 and $k = \gamma$. In the context of a perturbation analysis such a term is secular, which means that the corresponding solution is not uniformly valid. Both the standing wave and growing aspects of the second-order solution will be seen to play a prominent role in the responses obtained later by numerical analysis.

It is possible to generate e_2 by using either expression for e_1 in conjunction with the last of Eqs. (20). Aside from the greater number of terms that occur in that result, the general harmonic features of e_1 are repeated in e_2, with one notable exception. Secular terms, whose magnitude is proportional to x and t, arise even when $k \neq \gamma$, while the secular terms in e_2 when $k = \gamma$ are proportional to quadratic, as well as linear, powers of x and t. Consequently, the straightforward perturbation series, Eq. (19), loses validity when $\epsilon^2 t$ or $\epsilon^2 x$ is 0(1) in the case $k \neq \gamma$, while the breakdown occurs sooner, at ϵt or $\epsilon x = 0(1)$, when $k = \gamma$. This is significant because $k = \gamma$ will be seen in the next section to be the first instability for steady-state waves in the limit of infinitesimal ϵ. It follows that the occurrence of secular terms is not a sufficient condition to identify the onset of instability in the propagation of transient waves.

In general, singular perturbation techniques are available to correct for secular terms and other types of irregularities that occur in regular perturbation series. However, the transient nature of the present problem, as well as the change in the nature of the secularity when $k = \gamma$, inhibit application of those methods here.

3 Instability of the Steady-State in the Special Case

When c is constant and $h(x)$ is as given by Eq. (21), we find from Eqs. (1) that the differential equation governing the displacement u is

$$\frac{\partial^2 u}{\partial x^2} + 2\epsilon\gamma \cos(2\gamma x)\frac{\partial u}{\partial x} - \frac{1}{c^2}\frac{\partial^2 u}{\partial t^2} = 0. \tag{26}$$

We assume here that, for sufficiently large t, the continuous harmonic excitation in Eq. (22) ultimately produces a steady-state wave having like time dependence. So we let

$$u = U(x)\exp(-i\omega t), \tag{27}$$

which leads to

$$U'' + 2\epsilon\gamma \cos(2\gamma x)U' + k^2 U = 0. \tag{28}$$

This is a Hill's equation, whose solutions are governed by Floquet theory. Rather than generating the appropriate solution, it is adequate for our purposes to identify the stability transitions, which are characterized by relations between k and γ for which periodic solutions exist. Such identification is assisted by introducing the transformation

$$W(x) = U\exp\left[\frac{1}{2}\epsilon \sin(2\gamma x)\right], \tag{29}$$

which converts Eq. (28) to

$$W'' + [k^2 - 2\epsilon\gamma^2 \sin(2\gamma x) - \epsilon^2\gamma^2 \cos(2\gamma x)^2]W = 0. \tag{30}$$

If the ϵ^2 term is ignored, this is Mathieu's equation (Ince, 1956). Instabilities occur in the region around $k = n\gamma$, where n is an integer. Treating Eq. (30) as a Mathieu equation leads to identification of the first instability region as

$$1 - \frac{1}{2}\epsilon + 0(\epsilon^2) < \frac{k}{\gamma} < 1 + \frac{1}{2}\epsilon + 0(\epsilon^2). \tag{31}$$

We note that it would be incorrect to employ the limits of the Mathieu equation to describe the higher order stability transitions, because the error introduced by ignoring the ϵ^2 term in Eq. (30) is at least as large as the dependence of those stability boundaries on ϵ. If it were necessary, we could derive such limits in the present case by seeking the relations between k and γ that must hold if W is to be a periodic function.

Knowledge of the stability properties of the steady-state leaves many questions unanswered. Most prominent of these is whether the phenomenon is physically meaningful in that an unstable response requires a finite time and a finite propagation distance to grow. It should be noted in this regard that Floquet theory merely states that if the system parameters lie in a zone of instability, then the response *may* be unstable. In the next section we present an efficient numerical algorithm by which the evolution of the wave may be studied.

4 Finite Differences Along Characteristics

The numerical solution of the characteristic differential we

Downloaded 03 May 2010 to 171.66.16.247. Redistribution subject to ASME license or copyright; see http://www.asme.org/terms/Terms_Use.cfm

develop here is not limited to a specific region in time or space, nor is c limited to being constant. The method is an extension to heterogeneous media of Whitham's (1974) suggestion for the method of characteristics. For the formulation we consider the particle velocity v and stress σ to be the dependent variables. The first-order equations now are

$$\begin{Bmatrix} \partial v/\partial t \\ \partial \sigma/\partial t \end{Bmatrix} = [B] \begin{Bmatrix} \partial v/\partial x \\ \partial \sigma/\partial x \end{Bmatrix}, \quad [B] = \begin{bmatrix} 0 & 1/\rho \\ \rho c^2 & 0 \end{bmatrix}. \tag{32}$$

In comparison to Eq. (3), this form has the advantage of only containing derivatives of the state variables.

The eigenvalues β_j and left eigenvectors $\{\nu_j\}^T$ of $[B]$ are

$$\beta_j = \pm c, \quad \{\nu_j\}^T = \{\mp \rho c \ 1\}^T. \tag{33}$$

We premultiply Eq. (32) by $\{\nu_j\}^T$, which leads to

$$\{\nu_j\}^T \begin{Bmatrix} \partial v/\partial t \\ \partial \sigma/\partial t \end{Bmatrix} + \beta_j \{\nu_j\}^T \begin{Bmatrix} \partial v/\partial x \\ \partial \sigma/\partial x \end{Bmatrix} = 0. \tag{34}$$

The right-running and left-running characteristic variables of Eq. (34), which are denoted as ξ_1 and ξ_2, respectively, are defined such that

$$\left.\frac{dx}{dt}\right|_{\xi_1} = \beta_1 = c, \quad \left.\frac{dx}{dt}\right|_{\xi_2} = \beta_2 = -c. \tag{35}$$

Note that these characteristics are the same as those defined by Eqs. (7) and (9). Using v and σ as the dependent variables merely alters the differential equations, which are obtained by substituting the definitions of the characteristics, Eq. (35), into Eq. (34). We thereby obtain

$$\{\nu_j\}^T \begin{Bmatrix} dv \\ d\sigma \end{Bmatrix} = 0 \text{ along constant } \xi_j. \tag{36}$$

Since $c(x)$ is a known function, we may integrate Eqs. (35) to obtain explicit expressions. When we combine those equations with the results of substituting Eq. (33) into Eq. (36), we find that

$$d\hat{\sigma} - r\, d\hat{v} = 0 \quad \text{on} \quad t - \int_0^x \frac{d\eta}{c(\eta)} = \xi_1, \tag{37}$$

$$d\hat{\sigma} + r\, d\hat{v} = 0 \quad \text{on} \quad t + \int_0^x \frac{d\eta}{c(\eta)} = \xi_2. \tag{38}$$

In the foregoing, $\hat{v}$ and $\hat{\sigma}$ are nondimensional quantities and $r(x)$ is the impedance ratio, defined such that

$$\hat{v} = v/c_0, \ \hat{\sigma} = \sigma/\rho_0 c_0^2, \ r = \rho c/\rho_0 c_0, \tag{39}$$

where ρ_0 and c_0 represent values at $x = 0$.

Our first step in the numerical solution of Eqs. (37) and (38) is to discretize the independent variables. We assign equal increments Δt to time, and divide x into the intervals at which characteristic curves intersect the constant t subdivisions. Hence,

$$t_n = n\Delta t, \quad \int_0^{x_m} \frac{d\eta}{c(\eta)} = m\,\Delta t. \tag{40}$$

The system has been assumed to be at rest at $t = 0$, so the acceleration front resulting from initiation at $x = 0$ of the transient excitation corresponds to the right-running characteristic $\xi_1 = 0$. If follows that, when $t = t_n$, the signal vanishes for $x_m \geq x_n$, which limits the domain of x requiring consideration at any instant.

It is a simple matter to approximate the evolutionary Eqs. (37) and (38) by first-order finite differences using the (x, t) mesh depicted in Fig. 2. The characteristic curves appearing there are incremented by $2\Delta t$; the present algorithm will yield values for $\hat{\sigma}$ and $\hat{v}$ at the intersection of these characteristics. We start with the presumption that the response for $t \leq t_{n-1}$ has already been determined. Let $(\,)_{m,n}$ denote a quantity evaluated at (x_m, t_n). For the integration along the right-running

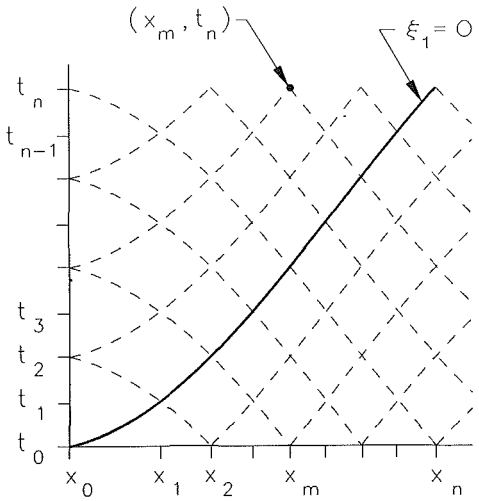


Fig. 2 Finite difference mesh for integrating along characteristic curves. The wave front corresponds to $\xi_1 = 0$.

characteristic through this point, the value of r is approximated by its value at the midpoint $x_{m-1/2} = (x_{m-1} + x_m)/2$, while the value for the left-running characteristic is approximated by the midpoint value at $x_{m+1/2} = (x_m + x_{m+1})/2$. Hence, an approximation to the characteristic equations is

$$\sigma_{m,n} - r_{m-1/2} v_{m,n} = \sigma_{m-1,n-1} - r_{m-1/2} v_{m-1,n-1}, \tag{41}$$

$$\sigma_{m,n} + r_{m+1/2} v_{m,n} = \sigma_{m+1,n+1} + r_{m+1/2} v_{m+1,n-1}, \tag{42}$$

where $m = 0, 2, \ldots, n$ if n is even, while $m = 1, 3, \ldots, n$ if n is odd. These difference equations may be solved for $v_{m,n}$ and $\sigma_{m,n}$ at all locations other than $x_0 = 0$ and x_n. The latter is the front of the acceleration wave, so

$$v_{n,n} = \sigma_{n,n} = 0. \tag{43}$$

The value of $\sigma_{0,n}$ is known from the boundary condition, Eq. (5). In order to determine $v_{0,n}$, we note that only left-running characteristics intersect the boundary $x = 0$ from below, so only Eq. (42) applies at this location. Solution of this equation with $m = 0$ yields $v_{0,n}$.

Higher-order integration schemes, as well as predictor-corrector formulations that employ the foregoing to generate initial estimates for the integrations, could be developed. However, we found that the results obtained by the present procedure rapidly converge with decreasing Δt, provided that the discretization is sufficiently fine to represent the temporal scale of the excitation and the spatial scale of the heterogeneity.

5 Results for Harmonic Excitation

Here we shall apply the foregoing numerical algorithm to the persistent excitation described by Eq. (22), so $\hat{\sigma}(0, t) = \sin(\omega t)$. The results we report were obtained with $\Delta t = \pi/200\omega$. We found this increment to be far smaller than necessary for convergence, since the results obtained with a time increment four times greater differed from the present values by less than 0.1 percent overall. Although the algorithm is suitable for arbitrary $h(x)$, we limit the present evaluations to the sinusoidal fluctuation in Eq. (21). Furthermore, in order to use the perturbation solution as an aid in understanding the numerical results, we shall consider c to be constant in the examples. Integration of Eq. (4) then leads to

$$\rho/\rho_0 = \exp[\epsilon \sin(2\gamma x)]. \tag{44}$$

Note that although this represents a periodic density variation, such variation reduces to a single sinusoidal term only when ϵ is very small. A simplification obtained by considering c to be constant is that the discretized spatial positions are uniformly spaced, $x_m = mc\Delta t$.

Downloaded 03 May 2010 to 171.66.16.247. Redistribution subject to ASME license or copyright; see http://www.asme.org/terms/Terms_Use.cfm

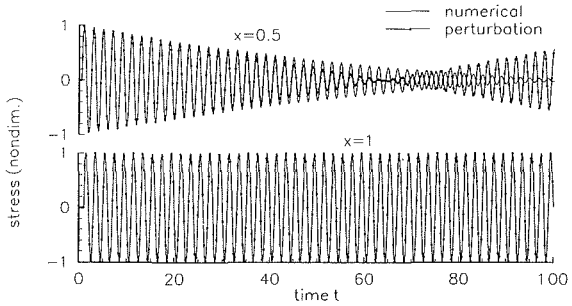


Fig. 3 Comparison of numerical and first-order regular perturbation predictions of wave forms when $\epsilon = 0.01$, $\gamma = k = \pi$, $c = 1$

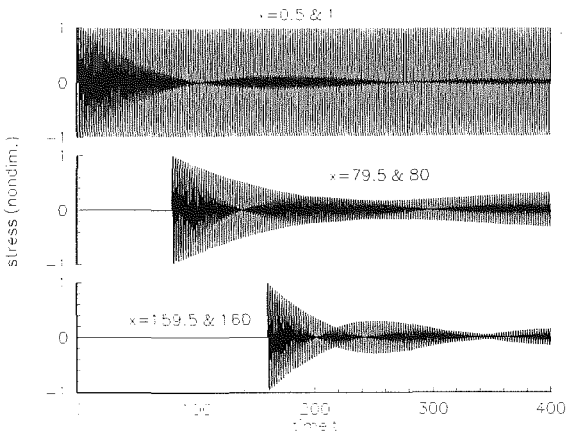


Fig. 4 Numerical results for wave forms when $\epsilon = 0.01$, $\gamma = k = \pi$, $c = 1$

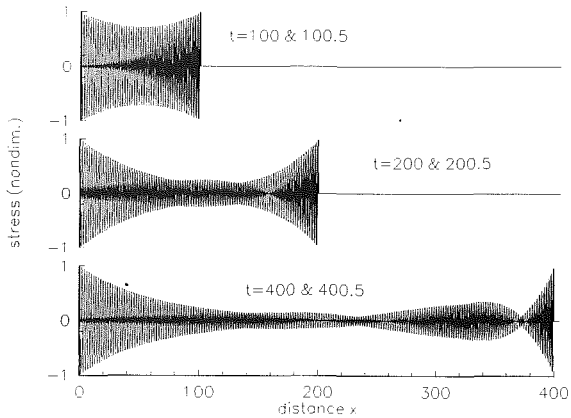


Fig. 5 Numerical results for spatial profiles when $\epsilon = 0.01$, $\gamma = k = \pi$, $c = 1$

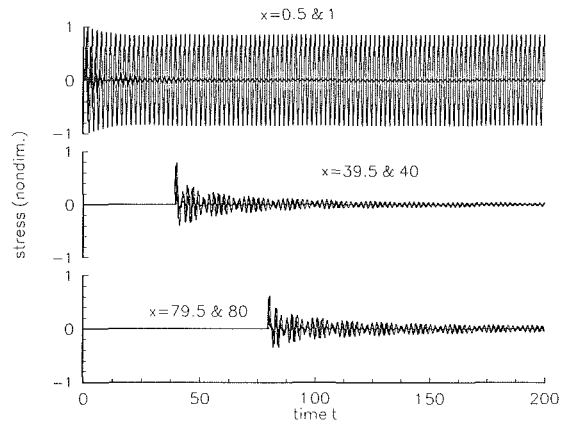


Fig. 6 Numerical results for wave forms when $\epsilon = 0.1$, $\gamma = k = \pi$, $c = 1$

The first results we present concern the case $k = \gamma$ and $\epsilon = 0.01$. (The actual values of c and γ merely define the temporal and spatial scales. The present results were obtained by setting $c = 1$, $\gamma = \pi$.) Figure 3 compares stress wave forms obtained from the numerical integration to those obtained from the two-term perturbation expansion, $\sigma_I = \sigma_0 + \epsilon\sigma_1$. According to Eq. (25), the secular term is a standing wave whose spatial periodicity is twice that of the heterogeniety. The locations $x = \pi/2\gamma$ and $x = \pi/\gamma$, which are adjacent zeros in the fluctuation of the density given in Eq. (44), should show the maximum and minimum effects. Such behavior is evident in Fig. 3, where the farther location displays a sinusoidal wave form, while the amplitude at the closer location decreases rapidly. For further insight into this behavior, let us consider the expressions for σ_I at the two locations when $k = \gamma = \pi$,

$$\sigma_I\Big|_{x=\pi/2\gamma} = -\cos(\pi t) + \frac{1}{2}\epsilon\pi\left(t - \frac{1}{2}\right)\cos(\pi t),$$

$$\sigma_I\Big|_{x=\pi/\gamma} = -\sin(\pi t). \tag{45}$$

We see that for the closer location the secular $0(\epsilon)$ term is 180 degrees out of phase from the first term. In contrast, the first perturbational correction vanishes at $x = \pi/\gamma$. A straightforward perturbation is only valid when the magnitude of each successive correction is smaller than that of the preceding correction. The first of Eqs. (45) suggests that this condition occurs prior to $t = 1/2 + 2/\epsilon\pi$, whose value is approximately twice as large as the time at which the difference between σ_I and the numerical result for $x = \pi/2\gamma$ in Fig. 3 begins to be noticeable. Note that the perturbation and numerical predictions for $x = \pi/\gamma$ are virtually identical, further confirming the standing wave behavior.

A longer view of the modification of wave forms is provided in Fig. 4, where the results in Fig. 3 are compared to those at adjacent zeroes of the density variation around $x = 80\pi/\gamma$ and $x = 160\pi/\gamma$. (In each pair, the envelope for the farther location appears in the figure as the one that is more lightly shaded in the vicinity of the arrival time, $t = x/c$.) These locations are sufficiently large to render the first-order perturbation correction completely invalid. The heterogeneity can be seen to result in substantial reduction of the amplitude at all locations, and the rate as well as the level of reduction increases with increasing distance.

For a different view of the evolution of the wave we display, in Fig. 5, spatial profiles at three pairs of instants where the separation within each pair is one quarter of a period. Close examination of the region very close to the wave front, $x = ct$, would show the profile for the later instant in each pair to have shifted by a quarter of a wavelength, as one would expect of a propagating wave. In contrast, near the boundary the amplitude is modulated in time, which is another feature of a standing wave. The profiles for the later instants indicate that in the midregion the signal displays both propagative and standing wave properties which seem to be associated with the occurrence of beating and the formation of wave packets. In addition, the amplitude in the midregion seems to undergo increasing reduction with time.

It is possible that although the results in Figs. 3–5 are contraindications of instability, such behavior would be observed if the computation were carried out for a much longer time interval. In other words, it might be that the elapsed time for those results is not adequate to attain steady-state conditions. The perturbation solution indicates that the rate at which the heterogeneous effects arise is scaled by ϵ. Considering larger values of ϵ enables us to reduce the number of integration steps required to make these effects noticeable. The temporal wave

Downloaded 03 May 2010 to 171.66.16.247. Redistribution subject to ASME license or copyright; see http://www.asme.org/terms/Terms_Use.cfm

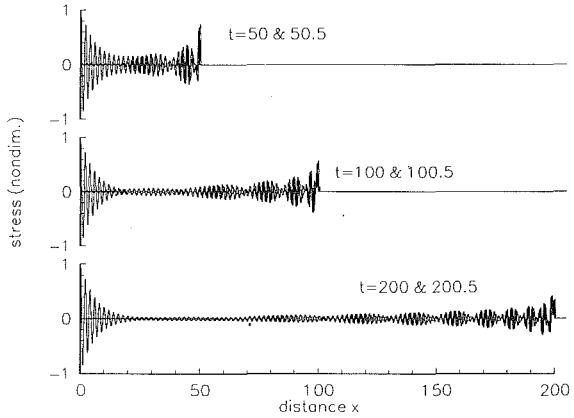


Fig. 7 Numerical results for spatial profiles when $\epsilon = 0.1, \gamma = k = \pi, c = 1$

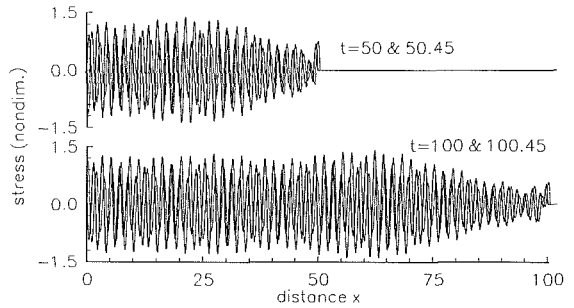


Fig. 8 Numerical results for spatial profiles when $\epsilon = 0.1, \gamma = \pi, k = 1.1\pi, c = 1$

forms in Fig. 6 and the spatial profiles in Fig. 7, for which $\epsilon = 0.10$, show that the trends indicated in the preceding figures continue. We confirmed this observation with additional computations for a $\epsilon = 0.5$, which are not shown for the sake of brevity. It can be seen that rather than creating an instability, increasing ϵ tends to lead to increasing interference with the wave.

The interference phenomenon is closely tied to the proximity of k and γ. Figure 8 depicts spatial profiles in the case $k = 1.1\gamma$ at two pairs of instants, where the separation within each pair is again one quarter of a period. The wave at the later instant of each pair has essentially advanced by one-quarter wavelength, as would a wave in a homogeneous medium. Also, the formation of wave packets, although noticeable, is substantially weaker than in the critical case. We found in a separate evaluation for $k = 1.5\gamma$ that deviations from a purely sinusoidal, forward-propagating wave are barely detectable in the time span for the present evaluations.

6 Response to a Step Input

Harmonic excitation at the boundary produces spatial and temporal fluctuations that are an interaction between the excitation and the heterogeneity. Such interaction makes it difficult to isolate the heterogeneity effect. We shall consider here a step jump in the normal stress applied at the boundary at $t = 0$, $\hat{\sigma}(0, t) = H(t)$ with the medium initially quiescent. This type of excitation is also of interest from a mathematical viewpoint, since the response to a step could be used to construct a convolution integral for the signal resulting from an arbitrary input, $\hat{\sigma}(0, t) = f(t)$. (It does not seem to us to be advisable to actually formulate such an integral, because the step response we obtain is only known in discrete form. Performing the associated quadratures would be less efficient than evaluating the response for each type of excitation directly by integrating along the characteristics.)

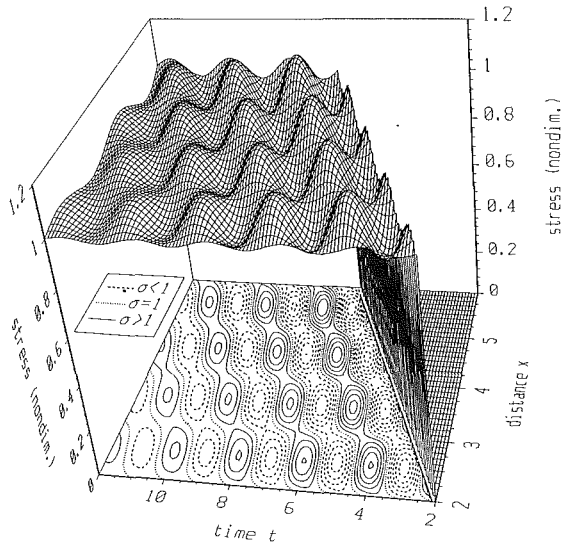


Fig. 9 Variation of stress in the characteristic plane resulting from a step excitation when $\epsilon = 0.1$, $c = 1$. Contours of equal stress are projected onto the x-t plane.

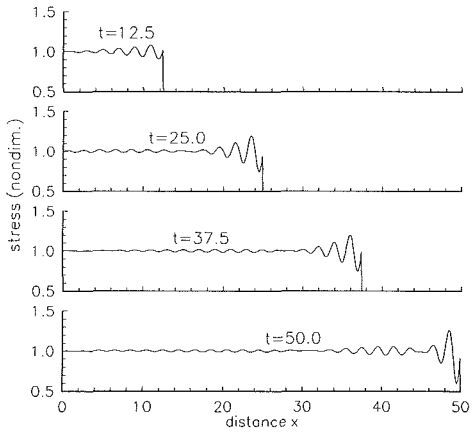


Fig. 10 Spatial profiles of stress resulting from a step excitation when $\epsilon = 0.1$, $c = 1$

The material properties for the example are taken to be the same as for Figs. 6–8. If the medium were homogeneous, the stress wave would be a shifted step, $\hat{\sigma}(x, t) = H(t - x/c)$, in which case the stress would be a constant unit value above the characteristic $s_1 = 0$ when viewed in the characteristic plane. Figure 9 shows the computed result for relatively early time and small distances, where contours of equal stress are plotted in the (horizontal) characteristic plane below a surface whose height is proportional to the stress. Propagation along the forward characteristics is evident in the contours, where regions in which the stress is greater than or less than unity are propagated essentially parallel to those characteristics. The spatial modulation of those regions seems to be a consequence of the heterogeneity.

The temporal fluctuations in Fig. 9, which occur even at the origin $x = 0$, are a consequence of backscattering corresponding to propagation along backward characteristics ξ_2 emanating from the shock front $\xi_1 = 0$. Although this feature is not evident in the contours, it can be seen in the darkened regions around the ridges of the surface plot. Projection of those regions onto the characteristic plane would show them to have slope $dt/dx = -1$.

As the wave propagates further, the magnitude of the ringing in the vicinity of the wave front increases. This feature is displayed in Fig. 10, which shows spatial profiles at four in-

Downloaded 03 May 2010 to 171.66.16.247. Redistribution subject to ASME license or copyright; see http://www.asme.org/terms/Terms_Use.cfm

stants. It is also interesting to note that a slight beating phenomenon seems to occur. For example, in the profile for $t = 50$ there are three regions behind the front where the deviation of the stress from unity is more pronounced, with this deviation being progressively smaller with increasing distance from the front.

7 Conclusions

We performed analytical and numerical analyses of transient wave propagation in harmonically heterogeneous media. A regular perturbation solution gave insight into the early-time phenomena, but it is not useful for exploration of steady-state instability because of the occurrence of secular terms. Such terms arose at the second perturbation order when the system parameters match the conditions for instability while they occur at the third order in all cases.

The correctness in a relatively small range of time of the regular perturbation solution was confirmed by a numerical analysis based on a finite difference integration along the characteristics. The first cases we considered corresponded to situations which steady-state analyses predict should be unstable. We found that with increasing time the perturbation solutions diverge rapidly from their numerical counterpart, which remained bounded. An interesting feature, which was encountered first in the perturbation solution, is the tendency of heterogeneity to backscatter the signal. This phenomenon is recognizable by the fact that the solution at any (x, t) depends on integrations along backward characteristics running from the wave front to (x, t) and to the boundary $x = 0$. This effect imparts standing wave features to the signal in the vicinity of the boundary while the signal in the vicinity of the wave front retains propagative wave properties. The significance of propagation along both forward and backward characteristics was confirmed by using the numerical method to determine the waves generated by a step rise in stress at the boundary.

The numerical solution for several levels of heterogeneity led us to the observation that a heterogeneity whose spatial periodicity is half the wavelength (i.e., $k = \gamma$) which steady-state analyses had indicated would lead to instability instead leads to maximum interference. This discrepancy with previous analyses of instability seems to stem from their assumption of a steady state which is never established in a transient wave propagating into a one-dimensional half-space. We also saw that the interference phenomenon decreases rapidly as the ratio k/γ deviates from unity.

An important question requiring further study is the significance of the observed phenomena for media whose heterogeneity is not spatially periodic. Small deviations from periodicity are known to lead in the steady-state case to localized enhancement of signals (Anderson, 1958). It seems plausible that the same phenomena would occur for transient excitation in such media. However, an important aspect of constructive and destructive interference in the present situation depends on the variation of material properties relative to the crossing sets of characteristic curves, as was shown by the rapidly decreasing heterogeneity effect as k/γ is changed from unity. It is quite possible that small deviations from periodicity only become significant after propagation over a very long distance or a long time interval. The main point to be gained from the present study is that steady-state analyses of waves in heterogeneous media might not be meaningful if one is interested in transient phenomena.

Another area worthy of investigation is the effects of multidimensionality. A simple case of this type would involve a material whose properties vary in only one dimension when a planar wave propagates obliquely to that direction. In this case, one could consider wave propagation qualitatively by employing linear superposition to resolve the wave into two components having nonuniform amplitude along their wave fronts where the directions of that resolution are parallel and perpendicular to the direction in which the material properties vary. From this viewpoint, it is reasonable to anticipate that comparable backscattering phenomena would be encountered in the wave component parallel to the heterogeneity direction. In principle, an accurate analysis of such a problem could be carried out by generalizing the present formulation to two dimensions through introduction of bicharacteristics.

Acknowledgment

This work was supported in part by the National Science Foundation, project MSM-8512818.

References

Anderson, P. W., 1958, "Absence of Diffusion in Certain Random Lattices," *Physical Review*, Vol. 109, pp.1492–1505.

Ince, E. L., 1956, *Ordinary Differential Equations*, Dover, pp. 175–177.

Kluwick, A., and Nayfeh, A. H., 1979, "Nonlinear Waves in Homogeneous and Heterogeneous Elastic Solids," *J. Physique*, Vol. 40, No. C-8, pp. 207–211.

Nair, S., and Nemat-Nasser, S., 1971, "On Finite Amplitude Waves in Heterogeneous Elastic Solids," *Int. J. Eng. Sci.*, Vol. 9, pp. 1087–1105.

Nayfeh, A. H., and Nemat-Nasser, S., 1972, "Elastic Waves in Inhomogeneous Elastic Media," ASME JOURNAL OF APPLIED MECHANICS, Vol. 39, pp. 696–702.

Nayfeh, A. H., 1975, "Finite-Amplitude Longitudinal Waves," *J. Sound and Vibration*, Vol. 42, pp. 357–361.

Schoenberg, M., and Weitsman, Y., 1975, "Wave Propagation and Parametric Instability in Materials Reinforced by Fibers with Periodically Varying Directions," ASME JOURNAL OF APPLIED MECHANICS, Vol. 42, pp. 825–831.

Watanabe, K., 1984, "Plane SH-Waves in Harmonically Inhomogeneous Elastic Media," *Wave Motion*, Vol. 6, pp. 477–488.

Whitham, G. B., 1974, *Linear and Nonlinear Waves*, John Wiley and Sons, New York, pp. 125–127.

Zarembo, L. K., and Prokhorov, V. M., 1975, "Generation of a Second Shear Harmonic in Media with Residual Internal Strains," *Sov. Phys. Acoust.*, Vol. 21, pp. 126–128.

Downloaded 03 May 2010 to 171.66.16.247. Redistribution subject to ASME license or copyright; see http://www.asme.org/terms/Terms_Use.cfm

Yasuhide Shindo
Professor.

Hiroaki Higaki

Department of Materials Processing,
Faculty of Engineering,
Tohoku University,
Sendai 980, Japan

Hideaki Nozaki
Lecturer,
Department of Mechanical Engineering,
Tokyo National College of Technology,
Hachioji, Tokyo 193, Japan

Impact Response of a Single Edge Crack in an Orthotropic Strip

The elastodynamic response of a single edge crack in an orthotropic strip under normal impact is considered in this study. The edge crack is oriented in a direction normal to the edge of the strip. Laplace and Fourier transforms are used to reduce the transient problem to the solution of a pair of dual integral equations in the Laplace transform plane. The solution to the dual integral equations is then expressed in terms of a Fredholm integral equation of the second kind. A numerical Laplace inversion routine is used to recover the time dependence of the solution. Numerical values on the dynamic stress intensity factor for several fiber-reinforced composite materials are obtained, and the results are graphed to display the influence of the material orthotropy.

Introduction

Recently, great interest has been shown in the dynamic crack problems of anisotropic elasticity. The study of these problems is motivated by the increased usage of macroscopically anistropic construction materials such as fiber-reinforced composites (Sih, 1981). Shindo et al. (1986) considered the elastodynamic response of an orthotropic strip containing a crack under the action of impact loading. The result for the limiting isotropic case coincides with the result for the isotropic material (Itou, 1980). The axisymmetric dynamic response of a penny-shaped crack in a transversely isotropic infinite cylinder under normal impact has been treated by Shindo et al. (1987).

In the structural members used in engineering applications, cracks are often initiated from free boundaries. The present paper deals with the problem of normal impact response of an orthotropic strip with a single edge crack. The plane of the edge crack is perpendicular to the edge of the strip and is assumed to coincide with one of the planes of elastic symmetry of the material. Laplace and Fourier transform techniques are used to reduce the elastodynamic problem to the solution of a pair of dual integral equations which is further reduced to a Fredholm integral equation of the second kind. The Fredholm integral equation is then treated by numerical techniques. A numerical Laplace inversion technique is used to recover the time dependence of the solution (Papoulis, 1957). The dynamic stress intensity factor is obtained numerically for several fiber-reinforced composite materials and the numerical values are shown in graphs for various geometrical parameters at designated time instances.

Statement of the Problem

The geometry of the considered problem is shown in Fig. 1. The strip is of width h. In the rectangular Cartesian coordinate system (x,y,z), a single edge crack of length a is situated on the x-axis so that it is normal to the edge of the strip. The strip is subjected to a time-dependent applied stress. Let E_i, μ_{ij}, and ν_{ij} $(i,j=1,2,3)$ denote the engineering elastic constants of the material where the subscripts 1, 2, 3 correspond to the

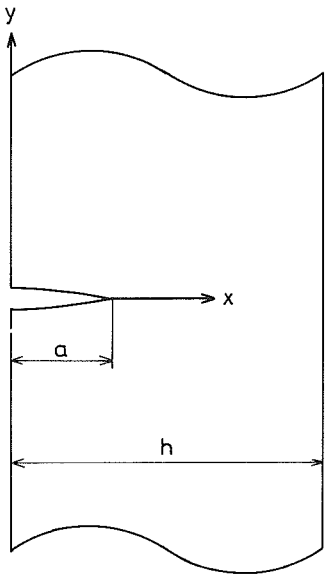


Fig. 1 Geometry of an orthotropic strip with a single-edge crack

Contributed by the Applied Mechanics Division of THE AMERICAN SOCIETY OF MECHANICAL ENGINEERS for presentation at the 1992 ASME Summer Mechanics and Materials Meeting, Tempe, AZ, Apr. 28–May 1, 1992.

Discussion on this paper should be addressed to the Technical Editor, Prof. Leon M. Keer, The Technological Institute, Northwestern University, Evanston, IL 60208, and will be accepted until four months after final publication of the paper itself in the JOURNAL OF APPLIED MECHANICS. Manuscript received by the ASME Applied Mechanics Division, Nov. 28, 1990; final revision, July 21, 1991.
Paper No. 92-APM-22.

Copyright © 1992 by ASME
Downloaded 03 May 2010 to 171.66.16.247. Redistribution subject to ASME license or copyright; see http://www.asme.org/terms/Terms_Use.cfm

x, y, z directions chosen to coincide with the axes of materials orthotropy. For generalized plane stress, the nonzero stress components are σ_{xx}, σ_{yy}, and σ_{xy}, the displacement components are u_x and u_y, and the nondimensional parameters c_{ij} $(i,j=1,2)$ are related to the elastic constants E_i, μ_{ij}, and ν_{ij} $(i,j=1,2)$ (Shindo et al., 1986).

Suppose that the edge crack is now loaded suddenly by a pair of normal stresses such that the upper and lower crack surfaces move in the opposite directions. The edges of the strip are assumed to be stress-free. The results can be used for a transient normal compression wave impinging on the edge crack and for the sudden appearance of the edge crack in a stressed strip under tension. Therefore, the boundary conditions may be written as

$$\sigma_{xy}(x,0,t)=0 \quad (0\leqq x\leqq h) \tag{1}$$

$$\sigma_{yy}(x,0,t)=-\sigma_0\sigma(x)H(t) \quad (0\leqq x<a)$$
$$u_y(x,0,t)=0 \quad (a\leqq x\leqq h) \tag{2}$$

$$\sigma_{xx}(0,y,t)=0$$
$$\sigma_{xy}(0,y,t)=0 \tag{3}$$

$$\sigma_{xx}(h,y,t)=0$$
$$\sigma_{xy}(h,y,t)=0 \tag{4}$$

where t is the time, $H(t)$ is the Heaviside unit step function in time, σ_0 is a constant with the dimension of stress, and $\sigma(x)$ is a function of x.

Solution Procedure

Define a Laplace transform pair by

$$f^*(p)=\int_0^\infty f(t)\exp(-pt)dt$$

$$f(t)=\frac{1}{2\pi i}\int_{B_r} f^*(p)\exp(pt)dp \tag{5}$$

where B_r denotes the Bromwich path of integration. A simple calculation leads to the expressions for the displacements in the Laplace transform plane (Shindo et al., 1986):

$$u_x^*(x,y,p)=\frac{2}{\pi}\int_0^\infty\{A_1(s,p)\exp(-\gamma_1 y)+A_2(s,p)\exp(-\gamma_2 y)\}\sin(sx)ds$$
$$+\frac{2}{\pi}\int_0^\infty\{B_1(s,p)\exp(\gamma_3 x)+B_2(s,p)\exp(-\gamma_3 x)+B_3(s,p)\exp(\gamma_4 x)+B_4(s,p)\exp(-\gamma_4 x)\}\cos(sy)ds$$
$$u_y^*(x,y,p)=\frac{2}{\pi}\int_0^\infty\{\alpha_1 A_1(s,p)\exp(-\gamma_1 y)+\alpha_2 A_2(s,p)\exp(-\gamma_2 y)\}\frac{1}{s}\cos(sx)ds$$
$$+\frac{2}{\pi}\int_0^\infty[\alpha_3\{B_1(s,p)\exp(\gamma_3 x)-B_2(s,p)\exp(-\gamma_3 x)\}+\alpha_4\{B_3(s,p)\exp(\gamma_4 x)-B_4(s,p)\exp(-\gamma_4 x)\}]\frac{1}{s}\sin(sy)ds \tag{6}$$

where $A_1(s,p)$, $A_2(s,p)$ and $B_i(s,p)$ $(i=1\sim4)$ are the unknowns to be solved, and γ_1^2, γ_2^2 and γ_3^2, γ_4^2 are the two roots of the quadratics

$$c_{22}\gamma^4+\{(c_{12}^2+2c_{12}-c_{11}c_{22})s^2-(1+c_{22})(p/c_s)^2\}\gamma^2+\{s^2+(p/c_s)^2\}\{c_{11}s^2+(p/c_s)^2\}=0 \quad (\gamma_1^2,\gamma_2^2) \tag{7}$$

$$c_{11}\gamma^4+\{(c_{12}^2+2c_{12}-c_{11}c_{22})s^2-(1+c_{11})(p/c_s)^2\}\gamma^2+\{s^2+(p/c_s)^2\}\{c_{22}s^2+(p/c_s)^2\}=0 \quad (\gamma_3^2,\gamma_4^2) \tag{8}$$

where $c_s=(\mu_{12}/\rho)^{1/2}$ with ρ being the mass density of the material. In the isotropic solid, c_s represents the velocity of the shear wave. Generally, the roots γ_1, γ_2, and γ_3, γ_4 are complex and α_i $(i=1\sim4)$ stand for the abbreviation

$$\alpha_i=\{c_{11}s^2+(p/c_s)^2-\gamma_i^2\}/(1+c_{12})\gamma_i \quad (i=1,2) \tag{9}$$

$$\alpha_i=\{s^2+(p/c_s)^2-c_{11}\gamma_i^2\}/(1+c_{12})\gamma_i \quad (i=3,4). \tag{10}$$

The stress field in the Laplace transform plane can also be obtained. Enforcing the boundary conditions (1) and (2) in the transform plane renders a pair of dual integral equations

$$\int_0^\infty sF(s,p)A(s,p)\cos(sx)ds$$
$$+\frac{1}{\theta_0}\int_o^\infty[(c_{12}\gamma_3+c_{22}\alpha_3)\{B_1(s,p)\exp(\gamma_3 x)-B_2(s,p)\exp(-\gamma_3 x)\}+[c_{12}\gamma_4+c_{22}\alpha_4)\{B_3(s,p)\exp(\gamma_4 x)-B_4(s,p)\exp(-\gamma_4 x)\}]ds$$
$$=-\frac{\pi\sigma_0}{2\mu_{12}\theta_0 p}\sigma(x) \quad (0\leqq x<a)$$
$$\int_0^\infty A(s,p)\cos(sx)ds=0 \quad (a\leqq x\leqq h) \tag{11}$$

where

$$A(s,p)=\frac{\alpha_1-\beta_1\alpha_2}{s}A_1(s,p)=\frac{\beta_1\alpha_2-\alpha_1}{s\beta_1}A_2(s,p) \tag{12}$$

$$F(s,p)=\frac{c_{12}s^2-c_{22}\alpha_1\gamma_1-\beta_1(c_{12}s^2-c_{22}\alpha_2\gamma_2)}{(\alpha_1-\beta_1\alpha_2)s\theta_0} \tag{13}$$

$$\beta_1=\frac{\alpha_1+\gamma_1}{\alpha_2+\gamma_2} \tag{14}$$

$$\theta_0=\frac{1}{c_{11}(1+c_{12})(N_1+N_2)}[(c_{12}^2+c_{12}-c_{11}c_{22})(c_{12}N_1N_2-c_{11})-c_{22}\{c_{12}N_1^2N_2^2+c_{11}(N_1^2+N_1N_2+N_2^2)\}]$$

$$N_1^2=\frac{1}{2c_{22}}[c_{11}c_{22}-c_{12}^2-2c_{12}+\{(c_{11}c_{22}-c_{12}^2-2c_{12})^2-4c_{11}c_{22}\}^{1/2}]$$

$$N_2^2=\frac{1}{2c_{22}}[c_{11}c_{22}-c_{12}^2-2c_{12}-\{(c_{11}c_{22}-c_{12}^2-2c_{12})^2-4c_{11}c_{22}\}^{1/2}]. \tag{15}$$

Through Eqs. (3) and (4), the unknowns $B_i(s,p)$ $(i=1\sim4)$ are related to the new parameter $A(\eta,p)$ by the following equations:

$$B_i(s,p)=\sum_{j=1}^{3}\delta_{ij}(s,p)\int_0^\infty g_j(s,\eta,p)A(\eta,p)d\eta \quad (i=1\sim4). \tag{16}$$

In Eqs. (16), the functions $\delta_{ij}(s,p)$ and $g_i(s,\eta,p)$ $(i=1\sim4,\ j=1\sim3)$ are given by Eqs. (A1) and (A7) in Appendix A.

The dual integral Eqs. (11) may be solved by using a procedure described in Shindo et al. (1986) and the result is

$$A(s,p)=-\frac{\pi\sigma_0 a^2}{2\mu_{12}\theta_0 p}\int_0^1\xi^{1/2}\Phi(\xi,p)J_0(sa\xi)d\xi \tag{17}$$

where $J_0(\ )$ is the zero-order Bessel function of the first kind. The function $\Phi(\xi,p)$ is governed by the following Fredholm integral equation of the second kind:

Downloaded 03 May 2010 to 171.66.16.247. Redistribution subject to ASME license or copyright; see http://www.asme.org/terms/Terms_Use.cfm

$$\Phi(\xi,p)+\int_0^1 \{K_1(\xi,\eta,p)+K_2(\xi,\eta,p)\}\Phi(\eta,p)d\eta = \frac{2}{\pi}\xi^{1/2}\int_0^{\xi}\frac{\sigma(x)}{(\xi^2-x^2)^{1/2}}dx \quad (18)$$

The Kernel functions $K_1(\xi,\eta,p)$ and $K_2(\xi,\eta,p)$ are given by

$$K_1(\xi,\eta,p)=(\xi\eta)^{1/2}\int_0^{\infty} s\{F(s/a,p)-1\}J_0(s\xi)J_0(s\eta)ds \quad (19)$$

$$\begin{aligned}K_2(\xi,\eta,p)=(\xi\eta)^{1/2}\int_0^{\infty}[&\{D_1(s/a,p)G_7(s/a,p,\eta)\\&+D_2(s/a,p)G_8(s/a,p,\eta)\\&+D_3(s/a,p)I_0(\gamma_7\eta)+D_4(s/a,p)I_0(\gamma_8\eta)\}Q_7(s/a,p,\xi)\\&+\{D_5(s/a,p)G_7(s/a,p,\eta)+D_6(s/a,p)G_8(s/a,p,\eta)\\&+D_7(s/a,p)I_0(\gamma_7\eta)+D_8(s/a,p)I_0(\gamma_8\eta)\}G_7(s/a,p,\xi)\\&+\{E_1(s/a,p)G_7(s/a,p,\eta)+E_2(s/a,p)G_8(s/a,p,\eta)\\&+E_3(s/a,p)I_0(\gamma_7\eta)+E_4(s/a,p)I_0(\gamma_8\eta)\}Q_8(s/a,p,\xi)\\&+\{E_5(s/a,p)G_7(s/a,p,\eta)+E_6(s/a,p)G_8(s/a,p,\eta)\\&+E_7(s/a,p)I_0(\gamma_7\eta)+E_8(s/a,p)I_0(\gamma_8\eta)\}G_8(s/a,p,\xi)]ds\end{aligned} \quad (20)$$

in which $I_0(\ )$ denotes the zero-order modified Bessel function of the first kind and γ_i^2 $(i=7,8)$ are the two roots of the following quadratic equation:

$$\begin{aligned}c_{11}\gamma^4+[(c_{12}^2+2c_{12}-c_{11}c_{22})s^2-(1+c_{11})(ap/c_s)^2]\gamma^2\\+\{s^2+(ap/c_s)^2\}\{c_{22}s^2+(ap/c_s)^2\}=0 \quad (\gamma_7,\gamma_8)\end{aligned} \quad (21)$$

The functions $G_i(s/a,p,\xi)$, $Q_i(s/a,p,\xi)$ $(i=7,8)$ and $D_i(s,p)$, $E_i(s,p)$ $(i=1\sim 8)$ are given by Eqs. (B1), (B2), and (B3) in Appendix B.

We note that the kernel function $K_1(\xi,\eta,p)$, Eq. (19), is an infinite integral which has a rather slow rate of convergence. Thus, for numerical calculation $K_1(\xi,\eta,p)$ is modified. By the use of the contour integration technique (van den Berg, 1981; Shindo et al., 1986), Eq. (19) can be written as

$$K_1(\xi,\eta,p)=-\frac{2}{\pi}(\xi\eta)^{1/2}P^2\left\{\int_0^{C_a}M_a(w)I_0(wP\xi)K_0(wP\eta)dw+\int_{C_a}^1 M_b(w)I_0(wP\xi)K_0(wP\eta)dw\right\} \quad (\xi<\eta) \quad (22)$$

under the conditions

$$\left\{\frac{1}{c_{22}^2}(c_{12}^2+2c_{12}-c_{11}c_{22})(1+c_{22})+\frac{2}{c_{22}}(1+c_{11})\right\}^2 - \left\{\frac{1}{c_{22}^2}(c_{12}^2+2c_{12}-c_{11}c_{22})^2-\frac{4}{c_{22}}c_{11}\right\}\times\left\{\frac{1}{c_{22}^2}(1+c_{22})^2+\frac{4}{c_{22}}\right\}^2<0 \quad (23)$$

$$c_{11}c_{22}-c_{12}^2-2c_{12}-1-c_{22}>0$$

$$c_{12}^2+2c_{12}+c_{11}>0 \quad (24)$$

which are satisfied for many orthotropic materials. In Eq. (22), $c_a=1/c_{11}^{1/2}$, $K_0(\ )$ is the zero-order modified Bessel function of the second kind and the functions $M_a(w)$, $M_b(w)$, the nondimensional transform parameter p are given in Appendix C. The kernel function $K_1(\xi,\eta,p)$ is symmetric in ξ and η. Thus, the value of $K_1(\xi,\eta,p)$ for $\xi>\eta$ is obtained by interchanging ξ and η in Eq. (22).

The asymptotic stress $\sigma_{yy}(x,0,t)$ near the crack tip may be obtained as

$$\sigma_{yy}(x,0,t)\sim\frac{1}{\{2\pi(x-a\}^{1/2}}K_I(t) \quad (25)$$

where $K_I(t)$ stands for the dynamic stress intensity factor and is defined by

$$K_I(t)=\frac{\sigma_0(\pi a)^{1/2}}{2\pi i}\int_{B_r}\frac{\Phi(1,p)}{p}\exp(pt)dp. \quad (26)$$

Upon application of the limiting value theorem, Eq. (26) becomes

$$\lim_{t\to\infty}K_I(t)=\sigma_0(\pi a)^{1/2}\lim_{p\to 0}\Phi(1,p). \quad (27)$$

Numerical Results and Discussions

The Fredholm integral equation of the second kind (18) can be solved on an electric computer by the standard techniques. In the calculated results, the use of Gaussian quadrature formulas gives practically adequate results at any desired transform parameter p. Once this is done, $K_I(t)$ can be found from Eq. (26) by using a numerical Laplace inversion scheme (Papoulis, 1957). As an example, the case of $\sigma(x)=1$ is considered. The engineering elastic constants for several orthotropic materials are listed in Table 1 (Sih and Chen, 1975). V_f denotes the fiber volume fraction and the fibers are perpendicular to the crack. The dynamic stress intensity factor is normalized by $\sigma_0(\pi a)^{1/2}$.

In the limit of $a/h=0.0$, we derive the results for the dynamic problem of a single-edge crack in a semi-infinite orthotropic medium. The results for $a/h=0$ have not been reported yet, either. First, we discuss the case of $a/h=0.0$. Figure 2 exhibits the variation of the nondimensional dynamic stress intensity

Table 1 Engineering elastic constants

	E_1(Pa)	E_2(Pa)	μ_{12}(Pa)	ν_{12}	ν_{23}	ν_{31}	V_f
Type I	Modulite II Graphite-Epoxi Composite						
	15.3×10^9	158.0×10^9	5.52×10^9	0.033	0.34	0.43	0.650
Type II	E-Type Glass-Epoxy Composite						
	9.79×10^9	42.3×10^9	3.66×10^9	0.063	0.27	0.34	0.565
Type III	Stainless Steel-Aluminum Composite						
	79.76×10^9	85.91×10^9	30.02×10^9	0.31	0.33	0.35	0.100

Downloaded 03 May 2010 to 171.66.16.247. Redistribution subject to ASME license or copyright; see http://www.asme.org/terms/Terms_Use.cfm

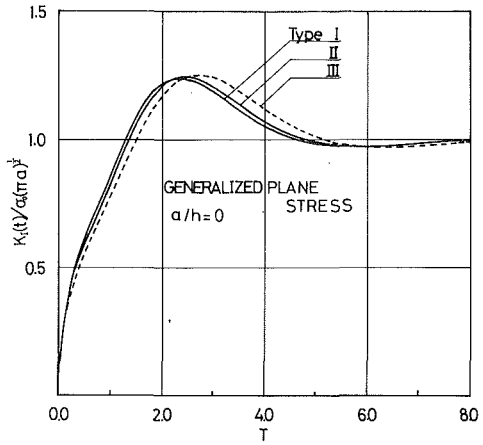


Fig. 2 Dynamic stress intensity factor versus time ($a/h = 0.0$)

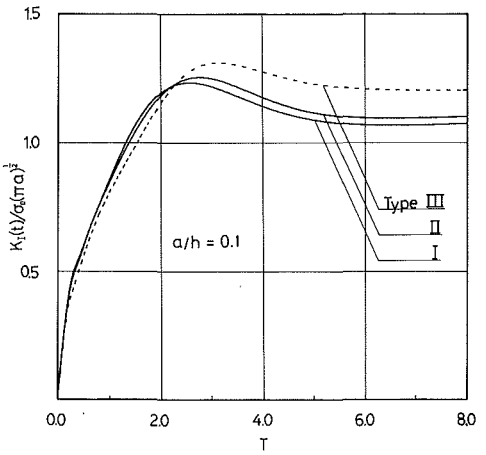


Fig. 3 Dynamic stress intensity factor versus time ($a/h = 0.1$)

factor $K_I(t)/\sigma_0(\pi a)^{1/2}$ with the nondimensional time $T = c_s t/a$ for the ratio $a/h = 0.0$. Theoretically the analysis cannot be applicable to isotropic material. But on taking the values of engineering elastic constants for the composite of type III (Stainless Steel-Aluminum Composite), which is nearly isotropic, we have calculated the limiting isotropic case. The result for the type III coincides with the result for the isotropic material (Tau and Lu, 1971). The effect of the material orthotropy can decrease the peak values of $K_I(t)/\sigma_0(\pi a)^{1/2}$ at an earlier time. Figures 3 and 4 show the same results for the ratios $a/h = 0.1$ and 0.2. The same gross effects are observed. The effect of the material orthotropy on the peak values of $K_I(t)/\sigma_0(\pi a)^{1/2}$ for $a/h = 0.2$ is more pronounced than that for $a/h = 0.1$. Figure 5 exhibits the variation of the normalized dynamic stress intensity factor $K_I(t)/\sigma_0(\pi a)^{1/2}$ with the normalized time T for type I (Modulite II Graphite Epoxy Composite). The values of the static stress intensity factor for $T \to \infty$ are found to be $K_I(\infty)/\sigma_0(\pi a)^{1/2} = 1.064$, 1.133, 1.289, 1.515, 2.199, 3.186 (Type I, $a/h = 0.0$, 0.1, 0.2, 0.3, 0.5, 0.7), 1.077, 1.143, 1.293 (Type II, $a/h = 0.0$, 0.1, 0.2), 1.121, 1.190, 1.371 (Type III, $a/h = 0.0$, 0.1, 0.2). The result for Type III, which is nearly isotropic, coincides with the result for the isotropic material (Keer and Freedman, 1973). The effect of the material orthotropy can decrease the static values of $K_I(\infty)/\sigma_0(\pi a)^{1/2}$. When a/h becomes large, it seems that the geometry effect dominates the dynamic stress intensity factor.

In conclusion, the dynamic response of an orthotropic strip with a single-edge crack under normal impact is determined in this study. The time dependence of the dynamic stress intensity factor is found to depend on the material orthotropy and the geometrical parameters.

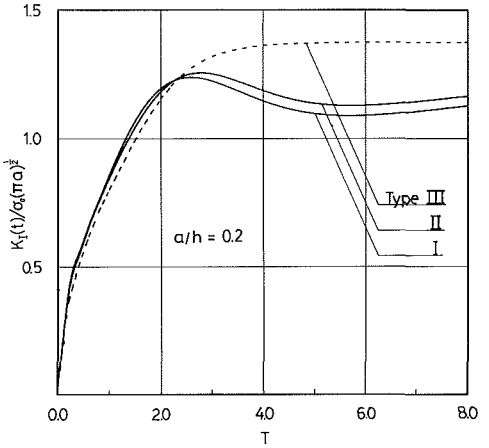


Fig. 4 Dynamic stress intensity factor versus time ($a/h = 0.2$)

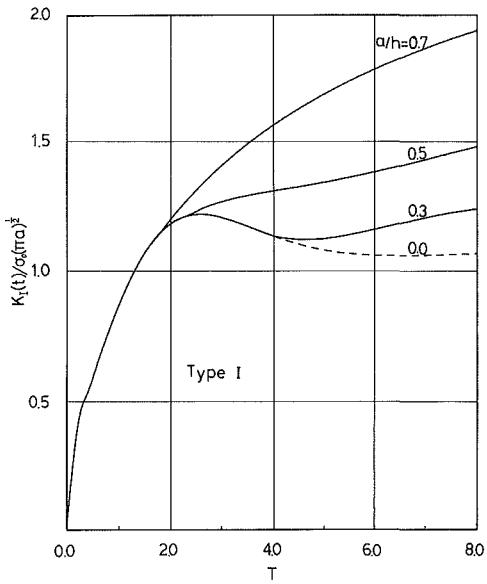


Fig. 5 Dynamic stress intensity factor versus time (Type I)

References

Itou, S., 1980, "Transient Response of a Finite Crack in a Strip with Stress-Free Edges," ASME Journal of Applied Mechanics, Vol. 47, pp. 801–805.

Keer, L. M., and Freedman, J. M., "Tensile Strip with Edge Cracks," *International Journal of Engineering Science*, Vol. 11, pp. 1265–1275.

Papoulis, A., 1957, "A New Method of Inversion of the Laplace Transform," *Quarterly of Applied Mathematics*, Vol. 14, pp. 405–414.

Shindo, Y., Nozaki, H., and Higaki, H., 1986, "Impact Response of a Finite Crack in an Orthotropic Strip," *Acta Mechanica*, Vol. 62, pp. 87–104.

Shindo, Y., and Nozaki, H., 1987, "Impact Response of a Transversely Isotropic Cylinder with a Penny-Shaped Crack," *International Journal of Solids and Structures*, Vol. 23, pp. 187–199.

Sih, G. C., and Chen, E. P., 1975, "Material Characterization on the Fracture of Filament Reinforced Composites," *Journal of the Composite Materials*, Vol. 9, pp. 167–186.

Sih, G. C., 1981, *Cracks in Composite Materials*, Martinus Nijhoff, The Netherlands, pp. 1–101.

Thau, S. A., and Lu, T.-H., 1971, "Transient Stress Intensity Factors for a Finite Crack in an Elastic Solid Caused by a Dilatational Wave," *International Journal of Solids and Structures*, Vol. 7, pp. 731–750.

van den Berg, Perter M., 1981, "Transition Matrix in Acoustic Scattering by a Strip," *Journal of the Acoustical Society of America*, Vol. 70, pp. 615–619.

APPENDIX A

$$\delta_{11}(s,p) = \frac{2}{\pi\Delta(s,p)} \{ T_d(s,p) L_a(s,p) + T_b(s,p) L_b(s,p) \}$$

Downloaded 03 May 2010 to 171.66.16.247. Redistribution subject to ASME license or copyright; see http://www.asme.org/terms/Terms_Use.cfm

$$\delta_{12}(s,p) = -\frac{2}{\pi\Delta(s,p)} Z_a(s,p) T_d(s,p)$$

$$\delta_{13}(s,p) = -\frac{2}{\pi\Delta(s,p)} Z_a(s,p) T_b(s,p)$$

$$\delta_{21}(s,p) = \frac{2}{\pi\Delta(s,p) Z_a(s,p)} [Z_a(s,p)\{T_d(s,p)L_a(s,p) + T_b(s,p)L_b(s,p)\} - Z_d(s,p)\{T_c(s,p)L_a(s,p) + T_b(s,p)L_b(s,p)\} + H_d(s,p)\Delta(s,p)]$$

$$\delta_{22}(s,p) = \frac{2}{\pi\Delta(s,p)} \{Z_d(s,p)T_c(s,p) - Z_b(s,p)T_d(s,p)\}$$

$$\delta_{23}(s,p) = \frac{2}{\pi\Delta(s,p)} \{Z_d(s,p)T_a(s,p) - Z_b(s,p)T_b(s,p)\}$$

$$\delta_{31}(s,p) = -\frac{2}{\pi\Delta(s,p)} \{T_c(s,p)L_a(s,p) + T_a(s,p)L_b(s,p)\}$$

$$\delta_{32}(s,p) = \frac{2}{\pi\Delta(s,p)} Z_a(s,p) T_c(s,p)$$

$$\delta_{33}(s,p) = \frac{2}{\pi\Delta(s,p)} Z_a(s,p) T_a(s,p)$$

$$\delta_{41}(s,p) = \frac{2}{\pi\Delta(s,p) Z_a(s,p)} [Z_b(s,p)\{T_c(s,p)L_a(s,p) + T_a(s,p)L_b(s,p)\} - Z_c(s,p)\{T_d(s,p)L_a(s,p) + T_b(s,p)L_b(s,p)\} - H_c(s,p)\Delta(s,p)]$$

$$\delta_{42}(s,p) = \frac{2}{\pi\Delta(s,p)} \{Z_c(s,p)T_d(s,p) - Z_b(s,p)T_c(s,p)\}$$

$$\delta_{43}(s,p) = \frac{2}{\pi\Delta(s,p)} \{Z_c(s,p)T_b(s,p) - Z_b(s,p)T_a(s,p)\} \tag{A1}$$

$$Z_a(s,p) = H_a(s,p)H_d(s,p) - H_b(s,p)H_c(s,p)$$
$$Z_b(s,p) = H_a(s,p)H_d(s,p) + H_b(s,p)H_c(s,p)$$
$$Z_c(s,p) = 2H_a(s,p)H_c(s,p)$$
$$Z_d(s,p) = 2H_b(s,p)H_d(s,p) \tag{A2}$$
$$H_a(s,p) = c_{11}\gamma_3 + c_{12}\alpha_3$$
$$H_b(s,p) = c_{11}\gamma_4 + c_{12}\alpha_4$$

$$H_c(s,p) = \frac{\alpha_3\gamma_3}{s} - s$$

$$H_d(s,p) = \frac{\alpha_4\gamma_4}{s} - s \tag{A3}$$

$$T_a(s,p) = \{Z_a(s,p)\exp(\gamma_3 h) - Z_b(s,p)\exp(-\gamma_3 h) + 2H_b(s,p)H_c(s,p)\exp(-\gamma_4 h)\}H_a(s,p)$$
$$T_b(s,p) = \{Z_a(s,p)\exp(\gamma_4 h) + Z_b(s,p)\exp(-\gamma_4 h) - 2H_a(s,p)H_d(s,p)\exp(-\gamma_3 h)\}H_b(s,p)$$
$$T_c(s,p) = \{Z_a(s,p)\exp(\gamma_3 h) + Z_b(s,p)\exp(-\gamma_3 h) - 2H_a(s,p)H_d(s,p)\exp(-\gamma_4 h)\}H_c(s,p)$$
$$T_d(s,p) = \{Z_a(s,p)\exp(\gamma_4 h) - Z_b(s,p)\exp(-\gamma_4 h) + 2H_b(s,p)H_c(s,p)\exp(-\gamma_3 h)\}H_d(s,p) \tag{A4}$$

$$L_a(s,p) = H_a(s,p)H_d(s,p)\exp(-\gamma_3 h) - H_b(s,p)H_c(s,p)\exp(-\gamma_4 h)$$

$$L_b(s,p) = H_c(s,p)H_d(s,p)\{\exp(-\gamma_3 h) - \exp(-\gamma_4 h)\} \tag{A5}$$

$$\Delta(s,p) = \{T_a(s,p)T_d(s,p) - T_b(s,p)T_c(s,p)\}\exp[(\gamma_3+\gamma_4)h] \tag{A6}$$

$$g_1(s,\eta,p) = \frac{1}{\alpha_5 - \beta_2\alpha_6}\left\{\frac{\gamma_5(c_{11}\eta^2 - c_{12}\alpha_5\gamma_5)}{s^2+\gamma_5^2} - \beta_2\frac{\gamma_6(c_{11}\eta^2 - c_{12}\alpha_6\gamma_6)}{s^2+\gamma_6^2}\right\}$$

$$g_2(s,\eta,p) = g_1(s,\eta,p)\cos(\eta h)$$

$$g_3(s,\eta,p) = \frac{s\eta(\alpha_5+\gamma_5)}{\alpha_5 - \beta_2\alpha_6}\left(\frac{1}{s^2+\gamma_5^2} - \frac{1}{s^2+\gamma_6^2}\right)\sin(\eta h) \tag{A7}$$

$$\alpha_i = \frac{c_{11}\eta^2 + (p/c_s)^2 - \gamma_i^2}{(1+c_{12})\gamma_i} \quad (i=5,6) \tag{A8}$$

$$\beta_2 = \frac{\alpha_5+\gamma_5}{\alpha_6+\gamma_6} \tag{A9}$$

In Eqs. (A7), (A8), and (A9), γ_5^2 and γ_6^2 are the two roots of the quadratic equation

$$c_{22}\gamma^4 + \{(c_{12}^2 + 2c_{12} - c_{11}c_{22})\eta^2 - (1+c_{22})(p/c_s)^2\}\gamma^2 + \{\eta^2 + (p/c_s)^2\}\{c_{11}\eta^2 + (p/c_s)^2\} = 0 \quad (\gamma_5^2, \gamma_6^2). \tag{A10}$$

The roots γ_5^2, γ_6^2 are subjected to the following relations:

$$\gamma_5^2 + \gamma_6^2 = -\frac{1}{c_{22}}\{(c_{12}^2 + 2c_{12} - c_{11}c_{22})\eta^2 - (1+c_{22})(p/c_s)^2\}$$

$$\gamma_5^2\gamma_6^2 = \frac{1}{c_{22}}\{c_{11}\eta^2 + (p/c_s)^2\}\{\eta^2 + (p/c_s)^2\}$$

$$(s^2+\gamma_5^2)(s^2+\gamma_6^2) = \frac{c_{11}}{c_{22}}(\eta^2+\gamma_3^2)(\eta^2+\gamma_4^2). \tag{A11}$$

Using the relations (A11), we see that Eqs. (A7) are reduced to

$$g_1(s,\eta,p) = \frac{1}{c_{11}}\left(-\frac{\gamma_3^2u_1 - u_2}{\eta^2+\gamma_3^2} + \frac{\gamma_4^2u_1 - u_2}{\eta^2+\gamma_4^2}\right)\frac{1}{\gamma_4^2 - \gamma_3^2}$$

$$g_2(s,\eta,p) = g_1(s,\eta,p)\cos(\eta h)$$

$$g_3(s,\eta,p) = \frac{s\eta}{c_{11}}\left(-\frac{\gamma_3^2u_3 - u_4}{\eta^2+\gamma_3^2} + \frac{\gamma_4^2u_3 - u_4}{\eta^2+\gamma_4^2}\right)\frac{\sin(\eta h)}{\gamma_4^2 - \gamma_3^2} \tag{A12}$$

where

$$u_1 = (c_{12}^2 - c_{11}c_{22})s^2 - c_{12}(p/c_s)^2$$
$$u_2 = -c_{12}\{s^2 + (p/c_s^2)\}(p/c_s)^2$$
$$u_3 = c_{11}c_{22} - c_{12}^2$$
$$u_4 = (c_{12}+c_{22})(p/c_s)^2. \tag{A13}$$

APPENDIX B

$$G_i(s/a,p,\xi) = I_0(\gamma_i\xi) - L_0(\gamma_i\xi) \quad (i=7,8)$$
$$Q_i(s/a,p,\xi) = I_0(\gamma_i\xi + L_0(\gamma_i\xi) \tag{B1}$$

$$D_1(s,p) = -D_0(s,p)\frac{R_1(s,p)}{\gamma_3}(\gamma_3^2u_1 - u_2)$$

$$D_2(s,p) = D_0(s,p)\frac{R_1(s,p)}{\gamma_3}(\gamma_4^2u_1 - u_2)$$

$$D_3(s,p) = -D_0(s,p)\left\{\frac{R_2(s,p)}{\gamma_3}(\gamma_3^2u_1 - u_2) + sR_3(s,p)(\gamma_3^2u_3 - u_4)\right\}\exp(-\gamma_3 h)$$

$$D_4(s,p) = D_0(s,p)\left\{\frac{R_2(s,p)}{\gamma_4}(\gamma_4^2u_1 - u_2) + sR_3(s,p)(\gamma_4^2u_3 - u_4)\right\}\exp(-\gamma_4 h)$$

Downloaded 03 May 2010 to 171.66.16.247. Redistribution subject to ASME license or copyright; see http://www.asme.org/terms/Terms_Use.cfm

$$D_5(s,p)=D_0(s,p)\,\frac{R_4(s,p)}{\gamma_3}\,(\gamma_3^2u_1-u_2)$$

$$D_6(s,p)=-D_0(s,p)\,\frac{R_6(s,p)}{\gamma_4}\,(\gamma_4^2u_1-u_2)$$

$$D_7(s,p)=D_0(s,p)\left\{\frac{R_5(s,p)}{\gamma_3}\,(\gamma_3^2u_1-u_2)+sR_6(s,p)\,(\gamma_3^2u_3-u_4)\right\}\exp(-\gamma_3h)$$

$$D_8(s,p)=-D_0(s,p)\left\{\frac{R_5(s,p)}{\gamma_4}\,(\gamma_4^2u_1-u_2)+sR_6(s,p)\,(\gamma_4^2u_3-u_4)\right\}\exp(-\gamma_4h) \quad \text{(B2)}$$

$$E_1(s,p)=-E_0(s,p)\,\frac{V_1(s,p)}{\gamma_3}\,(\gamma_3^2u_1-u_2)$$

$$E_2(s,p)=E_0(s,p)\,\frac{V_1(s,p)}{\gamma_4}\,(\gamma_4^2u_1-u_2)$$

$$E_3(s,p)=-E_0(s,p)\left\{\frac{V_2(s,p)}{\gamma_3}\,(\gamma_3^2u_1-u_2)+sV_3(s,p)\,(\gamma_3^2u_3-u_4)\right\}\exp(-\gamma_3h)$$

$$E_4(s,p)=E_0(s,p)\left\{\frac{V_2(s,p)}{\gamma_4}\,(\gamma_4^2u_1-u_2)+sV_3(s,p)\,(\gamma_4^2u_3-u_4)\right\}\exp(-\gamma_4h)$$

$$E_5(s,p)=E_0(s,p)\,\frac{V_4(s,p)}{\gamma_3}\,(\gamma_3^2u_1-u_2)$$

$$E_6(s,p)=-E_0(s,p)\,\frac{V_4(s,p)}{\gamma_4}\,(\gamma_4^2u_1-u_2)$$

$$E_7(s,p)=E_0(s,p)\left\{\frac{V_5(s,p)}{\gamma_3}\,(\gamma_3^2u_1-u_2)+sV_6(s,p)\,(\gamma_3^2u_3-u_4)\right\}\exp(-\gamma_3h)$$

$$E_8(s,p)=-E_0(s,p)\left\{\frac{V_5(s,p)}{\gamma_4}\,(\gamma_4^2u_1-u_2)+sV_6(s,p)\,(\gamma_4^2u_3-u_4)\right\}\exp(-\gamma_4h) \quad \text{(B3)}$$

where $L_0(\ )$ is the zero-order modified Struve function and

$$D_0(s,p)=\frac{c_{11}\gamma_3+c_{22}\alpha_3}{\theta_0c_{11}(\gamma_4^2-\gamma_3^2)} \quad \text{(B4)}$$

$$E_0(s,p)=\frac{c_{11}\gamma_4+c_{22}\alpha_4}{\theta_0c_{11}(\gamma_4^2-\gamma_3^2)} \quad \text{(B5)}$$

$$R_1(s,p)=\frac{1}{\Delta(s,p)}\,\{T_d(s,p)L_a(s,p)+T_b(s,p)L_b(s,p)\}\exp(-\gamma_3h)$$

$$R_2(s,p)=-\frac{1}{\Delta(s,p)}\,Z_a(s,p)T_d(s,p)\exp(-\gamma_3h)$$

$$R_3(s,p)=-\frac{1}{\Delta(s,p)}\,Z_a(s,p)T_b(s,p)\exp(-\gamma_3h)$$

$$R_4(s,p)=\frac{1}{\Delta(s,p)Z_a(s,p)}\,[Z_b(s,p)\{T_d(s,p)L_a(s,p)+T_b(s,p)L_b(s,p)\}\exp(-\gamma_3h)-Z_d(s,p)\{T_c(s,p)L_a(s,p)+T_a(s,p)L_b(s,p)\}\exp(-\gamma_4h)+H_d(s,p)\Delta(s,p)]$$

$$R_5(s,p)=\frac{1}{\Delta(s,p)}\,\{Z_d(s,p)T_c(s,p)\exp(-\gamma_4h)-Z_b(s,p)T_d(s,p)\}\exp(-\gamma_3h)\}$$

$$R_6(s,p)=\frac{1}{\Delta(s,p)}\,\{Z_d(s,p)T_a(s,p)\exp(-\gamma_4h)-Z_b(s,p)T_b(s,p)\}\exp(-\gamma_3h)\} \quad \text{(B6)}$$

$$V_1(s,p)=-\frac{1}{\Delta(s,p)}\,\{T_c(s,p)L_a(s,p)+T_a(s,p)L_b(s,p)\}\exp(-\gamma_4h)$$

$$V_2(s,p)=\frac{1}{\Delta(s,p)}\,Z_a(s,p)T_c(s,p)\exp(-\gamma_4h)$$

$$V_3(s,p)=\frac{1}{\Delta(s,p)}\,Z_a(s,p)T_a(s,p)\exp(-\gamma_4h)$$

$$V_4(s,p)=\frac{1}{\Delta(s,p)Z_a(s,p)}\,[Z_b(s,p)\{T_c(s,p)L_a(s,p)+T_a(s,p)L_b(s,p)\}\exp(-\gamma_4h)-Z_c(s,p)\{T_d(s,p)L_a(s,p)+T_b(s,p)L_b(s,p)\}\exp(-\gamma_3h)-H_c(s,p)\Delta(s,p)]$$

$$V_5(s,p)=\frac{1}{\Delta(s,p)}\,\{Z_c(s,p)T_d(s,p)\exp(-\gamma_3h)-Z_b(s,p)T_c(s,p)\}\exp(-\gamma_4h)\}$$

$$V_6(s,p)=\frac{1}{\Delta(s,p)}\,\{Z_c(s,p)T_b(s,p)\exp(-\gamma_3h)-Z_b(s,p)T_a(s,p)\}\exp(-\gamma_4h)\} \quad \text{(B7)}$$

APPENDIX C

$$M_a(w)=\frac{c_{12}w^2+c_{22}\alpha_a\gamma_a-\beta_a(c_{12}w^2+c_{22}\alpha_b\gamma_b)}{(\alpha_a-\beta_a\alpha_b)\theta_0}$$

$$M_b(w)=\frac{c_{12}w^2+c_{22}\alpha_a\gamma_a}{(\alpha_a-\beta_b\alpha_c)\theta_0} \quad \text{(C1)}$$

$$\gamma_a=\left[\frac{1}{2}\,\{-B_a+(B_a^2-4B_b)^{1/2}\}\right]^{1/2}$$

$$\gamma_b=\left[\frac{1}{2}\,\{-B_a-(B_a^2-4B_b)^{1/2}\}\right]^{1/2}$$

$$\gamma_c=\left[\frac{1}{2}\,\{B_a+(B_a^2-4B_b)^{1/2}\}\right]^{1/2} \quad \text{(C2)}$$

$$B_a=-\frac{1}{c_{22}}\,\{(c_{12}+2c_{12}-c_{11}c_{22})w^2+1+c_{22}\}$$

$$B_b=\frac{1}{c_{22}}\,(w^2-1)(c_{11}w^2-1) \quad \text{(C3)}$$

$$\alpha_a=\frac{-c_{11}w^2+1-\gamma_a^2}{(1+c_{12})\gamma_a}$$

$$\alpha_b=\frac{-c_{11}w^2+1-\gamma_b^2}{(1+c_{12})\gamma_b}$$

$$\alpha_c=\frac{c_{11}w^2-1-\gamma_c^2}{(1+c_{12})\gamma_c} \quad \text{(C4)}$$

$$\beta_a=\frac{\alpha_a+\gamma_a}{\alpha_b+\gamma_b}$$

$$\beta_b=\frac{\alpha_a+\gamma_a}{\alpha_c+\gamma_c} \quad \text{(C5)}$$

$$P=ap/c_s. \quad \text{(C6)}$$

Downloaded 03 May 2010 to 171.66.16.247. Redistribution subject to ASME license or copyright; see http://www.asme.org/terms/Terms_Use.cfm

Rafael Gallego[1]
Graduate Student.

José Dominguez
Professor.

Escuela Tecnica Superior de
Ingenieros Industriales,
Universidad de Sevilla,
41012 Sevilla, Spain

Dynamic Crack Propagation Analysis by Moving Singular Boundary Elements

An efficient boundary element procedure for the dynamic analysis of crack propagation in unbounded and arbitrary shape finite bodies is presented. The procedure is based on the direct time domain formulation of the boundary element method. A moving singular element and a remeshing technique have been developed to model the asymptotic solution of the stresses near the propagating crack tip. These ideas are easily implemented for a boundary discretization as opposed to similar procedures previously developed in a finite element context. The method is applied to problems of dynamic crack propagation in finite and infinite elastic domains. The obtained numerical results are compared with infinite domain analytical solutions and with available numerical solutions for finite domains.

Introduction

Dynamic crack propagation is devoted to the study of solid bodies containing cracks that propagate under conditions for which the inertia effects are important. A number of analytical solutions for crack propagation problems exists. However, these solutions are limited to simple loadings and infinite domains (Freund, 1972a, 1972b, 1973). Apart from experimental studies, numerical methods are the only alternative for the analysis of cracks propagating in finite bodies under general loading conditions.

In the past two decades, the application of the finite element method (FEM) to dynamic crack propagation has known an important advance. Interesting reviews of the FEM techniques for dynamic crack propagation can be found in the papers by Aoki et al. (1978), by Atluri and Nishioka (1985), and by Beskos (1987). The different approaches are based on one of the following two concepts: a stationary mesh, which includes a "node-release" mechanism, or a moving mesh which normally includes a singular element.

The boundary element method (BEM) has appeared recently as an alternative for elastic fracture mechanic problems. This method seems to be a better choice than the FEM for elastodynamic fracture mechanics because the discretization is restricted to the boundary surface and the concept of singular element is simplified. In particular, when dealing with dynamic crack propagation, the remeshing process is conceptually much simpler in the BEM than in any domain technique.

The direct formulation of the BEM was used in combination with singular quarter-point (SQP) elements for elastostatic crack problems by Blandford et al. (1981) and by Martinez and Dominguez (1984) who showed that very accurate results are obtained with simple BE meshes. Chirino and Dominguez (1989) used the same SQP element with the frequency domain formulation of the BEM to compute dynamic SIF of stationary cracks in finite and unbounded domains under the effects of time harmonic excitations. Dynamic SIFs for transient loads were computed using the Fourier transform. More recently, Dominguez and Gallego (1991) used the time domain formulation of the BEM in combination with space quadratic and SQP elements, to compute transient dynamic SIFs of stationary cracks in finite domains. The robustness of the approach for stationary crack problems, both simple and mixed mode, was shown in that paper.

In the present work, the direct time-domain formulation of the BEM is used in combination with a singular element to study dynamic crack propagation in finite and infinite elastic bodies. To the authors' knowledge, this is the first time that the general direct BEM is used to study dynamic crack propagation in arbitrary shape finite bodies. To do so, a moving singular element and a remeshing technique have been developed. These ideas are used in the general context of time domain BE with shape functions for space and time discretization. Integral equation formulations have been applied to problems of propagating cracks in elastic bodies by other authors. However, all these studies, directed towards the simulation of earthquake sources, are limited to infinite domains and use either the BEM in conjunction with a node release mechanism (Das, 1980; Das and Kostrov, 1987) or are restricted to particular formulations related to the BEM (Burridge, 1969; Bergkvist, 1978).

To start with, in the present paper, the direct time-domain

[1]Presently, Postdoctoral Research Fellow, Engineering Department, Brown University, Providence, RI 02912.

Contributed by the Applied Mechanics Division of THE AMERICAN SOCIETY OF MECHANICAL ENGINEERS for presentation at the 1992 ASME Summer Mechanics and Materials Meeting, Tempe, AZ, Apr. 28-May 1, 1992.

Discussion on this paper should be addressed to the Technical Editor, Prof. Leon M. Keer, The Technological Institute, Northwestern University, Evanston, IL 60208, and will be accepted until four months after final publication of the paper itself in the JOURNAL OF APPLIED MECHANICS. Manuscript received by the ASME Applied Mechanics Division, Dec. 10, 1990; final revision, Apr. 19, 1991.

Paper No. 92-APM-3.

Copyright © 1992 by ASME
Downloaded 03 May 2010 to 171.66.16.247. Redistribution subject to ASME license or copyright; see http://www.asme.org/terms/Terms_Use.cfm

formulation of the BEM is summarized and the SQP element presented. Next, the remeshing technique and the boundary element formulation for moving elements are studied. In doing this, numerical aspects of the process leading to the final system of equations are discussed. Finally, two numerical studies of propagating cracks are presented. One is dedicated to a semi-infinite crack that propagates at constant speed in an unbounded domain. The other includes a finite length central crack in a finite plane body subject to a uniformly distributed traction along opposite boundaries with a Heaviside-function time dependence. The crack remains stationary until a time t_o, where upon both tips start to propagate at constant speed. Results are compared with those obtained by other authors using analytical and numerical methods. The analysis is limited to cases where the crack motion is fully specified, but some generalizations are possible to deal with the determination of crack velocity history for a given fracture-toughness relation. The examples illustrate the accuracy of the present procedure.

Basic Formulation

The integral representation of the displacement of a point inside an elastic domain Ω or on its boundary Γ at time t is given by

$$c_{ij}u_j = \int_\Gamma (u^*_{ij} * p_j - p^*_{ij} * u_j)\, d\Gamma \tag{1}$$

where p^*_{ij} is the traction tensor obtained by differentiation of the fundamental solution displacement tensor u^*_{ij} corresponding to the impulse load, u_j and p_j represent displacement and traction components, respectively, $c_{ij} = \delta_{ij}$ for interior points, $c_{ij} = 1/2\ \delta_{ij}$ for smooth boundary points, and $*$ stands for time convolution. For the sake of brevity, zero initial conditions and zero body forces have been assumed. The above equation is valid for any general elastodynamic problem. However, hereafter only two-dimensional problems will be considered.

The singularities existing in p^*_{ij} are difficult to integrate. Because of that, the space derivatives are related to time derivatives and the integral representation becomes

$$c_{ij}u_j = \int_\Gamma \left[\int_0^{t^+} u^*_{ij} p_j d\tau \right] d\Gamma - \int_\Gamma \left[\int_0^{t^+} (z^*_{ij} u_j - w^*_{ij} \dot{u}_j) d\tau \right] d\Gamma \tag{2}$$

where the time convolution integral is written explicitly and the upper limit t^+ is used to avoid ending the integrals at the peak of a delta function. The expressions for the kernels z^*_{ij} and w^*_{ij} can be seen, for instance, in the paper by Antes (1985).

The numerical solution of Eq. (2) is done by discretization of the time into equal time steps Δt and of the boundary into line elements. Displacements and tractions are approximated using interpolation functions

$$u_j = \sum_q \sum_m \varphi^q(r)\eta^m(\tau)u_j^{mq}$$
$$p_j = \sum_q \sum_m \psi^q(r)\mu^m(\tau)p_j^{mq} \tag{3}$$

where u_j^{mq} and p_j^{mq} stand for the j displacement and traction, respectively, of the node q at the time $t_m = m\Delta t$. The functions $\varphi^q(r)$ and $\psi^q(r)$ are space interpolation functions and $\mu^m(\tau)$ and $\eta^m(\tau)$ time interpolation functions.

The approximation for the velocities is taken consistently with that of the displacements.

$$\dot{u}_j = \sum_q \sum_m \varphi^q(r)\dot{\eta}^m(\tau)u_j^{mq} \tag{4}$$

The time interpolation functions $\mu^m(\tau)$ and $\eta^m(\tau)$ are assumed to be piecewise constant and piecewise linear, respectively. This choice is made in accordance with accuracy and stability studies done by Mansur (1983) and Dominguez and Gallego (1990).

After the approximation, Eq. (2) for a boundary node p at the time step n takes the form:

$$c_{ij}u_j^{np} = \sum_{m=1}^{n} \sum_{q=1}^{Q} \left[\left\{ \int_{\Gamma_q} \left[\int_{\tau_{m-1}}^{\tau_m^+} u^*_{ij}\mu^m d\tau \right] \psi^q d\Gamma \right\} p_j^{mq} - \left\{ \int_{\Gamma_q} \left[\int_{\tau_{m-1}}^{\tau_m^+} (z^*_{ij}\eta^m - w^*_{ij}\dot{\eta}^m) d\tau \right] \varphi^q d\Gamma \right\} u_j^{mq} \right] \tag{5}$$

where Q is the total number of boundary nodes.

Equation (5) can be written in a more condensed form as a typical BE equation:

$$c_{ij}^p u_j^{np} + \sum_{m=1}^{n} \sum_{q=1}^{Q} H_{ij}^{nmpq} u_j^{mq} = \sum_{m=1}^{n} \sum_{q=1}^{Q} G_{ij}^{nmpq} p_j^{mq} \tag{6}$$

or, in matrix form:

$$\sum_{m=1}^{n} \mathbf{H}^{nm}\mathbf{u}^m = \sum_{m=1}^{n} \mathbf{G}^{nm}\mathbf{p}^m \tag{7}$$

where $\mathbf{u}^m$ and $\mathbf{p}^m$ include the two displacement and traction components of all the nodes at time step m. The coefficients of the matrices $\mathbf{H}^{nm}$ and $\mathbf{G}^{nm}$ depend on the difference $n - m$ and not on the actual values of n and m. In order to compute H_{ij}^{nmpq} and G_{ij}^{nmpq} an analytical integration along the time step Δt is done first. Explicit expressions for these integrals may be found in the work by Antes (1985). Then, the space integrals along the BE are done by numerical procedures except for the case when $n = m$ and the collocation point p belongs to the integration element q. In such a case there are singularities in the kernels and the integrals are done analytically. Closed-form expressions for those integrals are given by Gallego (1990).

The elements used in the present work are three-node space quadratic elements except for those in contact with the crack tips which are SQP elements. This kind of element represents the displacement components as:

$$u_i = a_i^1 + a_i^2\sqrt{\frac{r}{l}} + a_i^3\frac{r}{l} \tag{8}$$

where $a_i^1 = u_i^1$; $a_i^2 = -u_i^3 + 4u_i^2 - 3u_i^1$; $a_i^3 = 2u_i^3 - 4u_i^2 + 2u_i^1$; u_i^1, u_i^2, and u_i^3 are the nodal values at the nodes 1, 2, and 3, respectively; r is the distance to the tip and l the length of the element. The traction components are approximated as

$$p_i = \bar{a}_i^1\sqrt{\frac{l}{r}} + \bar{a}_i^2 + \bar{a}_i^3\sqrt{\frac{r}{l}} \tag{9}$$

where $\bar{a}_i^1 = \bar{p}_i^1$; $\bar{a}_i^2 = -\bar{p}_i^3 + 4\bar{p}_i^2 - 3\bar{p}_i^1$ and $\bar{a}_i^3 = 2\bar{p}_i^3 - 4\bar{p}_i^2 + 2\bar{p}_i^1$. The nodal values of the tractions representation, $\bar{p}_i^1$, $\bar{p}_i^2$, and $\bar{p}_i^3$, are related to the traction values at the nodes, p_i^1, p_i^2, and p_i^3 by

$$\bar{p}_i^3 = p_i^3;\ \bar{p}_i^2 = \frac{p_i^2}{2}$$
$$\bar{p}_i^1 = \lim_{r\to 0} p_i^1\sqrt{\frac{r}{l}}. \tag{10}$$

In the present technique, the domain is subdivided by a boundary running along the crack which leaves each side of the crack on the boundary of different subregions. This subdivision is done to avoid having the same BE equation for points on both sides of the crack. If the first element from the crack tip is a SQP element and follows the direction of the crack, the SIFs are given directly by the nodal values as:

$$K_I = \bar{p}_2^1(2\pi l)^{\frac{1}{2}}$$
$$K_{II} = \bar{p}_1^1(2\pi l)^{\frac{1}{2}}. \tag{11}$$

Downloaded 03 May 2010 to 171.66.16.247. Redistribution subject to ASME license or copyright; see http://www.asme.org/terms/Terms_Use.cfm

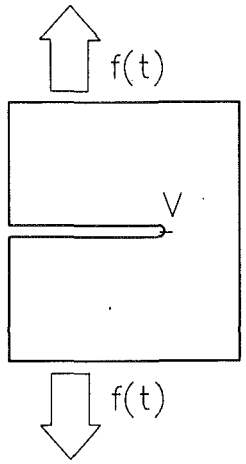


Fig. 1 Mode I dynamic crack propagation example

Details of the SQP boundary element formulation may be seen in the work by Martinez and Dominguez (1984).

Formulation for a Moving Singular Element

Consider a mode-I dynamic crack propagation problem as shown in Fig. 1. A boundary is introduced along the crack, following the known direction of propagation. Because of the symmetry, only one half of the domain is analyzed. Assume that the crack propagates at a certain speed C, and that at time t the position of the crack tip and the discretization of the part of the boundary that contains one side of the crack is as shown in Fig. 2(a). Two elements, one before and one after the tip, are SQP. After a time increment Δt, the crack tip has moved $C\Delta t$ (Fig. 2(b)). As the crack tip advanced from left to right, the size of the elements to the left is increased and that of the elements to the right is decreased.

The SQP elements are excluded from this adjustment and their size remains the same along the crack propagation process. The translation of the crack tip for each time step can take any value and is not related to the assumed discretization. After some time, the elements on the left-hand side would be much bigger than those on the right-hand side. To avoid this, when the ratio of the sizes is greater than 5/3 (Fig. 2(c)), the number of elements to the left is increased by one and the number of elements to the right is decreased by one. The element discretization of both sides is then redefined (Fig. 2(d)).

The BE matrix Eq. (7) for time step n can now be written in a subdivided form as

$$\sum_{m=1}^{n}\begin{bmatrix}\mathbf{H}_{ff}^{nm} & \mathbf{H}_{fc}^{nm}\\ \mathbf{H}_{cf}^{nm} & \mathbf{H}_{cc}^{nm}\end{bmatrix}\begin{Bmatrix}\mathbf{u}_f^m\\ \mathbf{u}_c^m\end{Bmatrix}=\sum_{m=1}^{n}\begin{bmatrix}\mathbf{G}_{ff}^{nm} & \mathbf{G}_{fc}^{nm}\\ \mathbf{G}_{cf}^{nm} & \mathbf{G}_{cc}^{nm}\end{bmatrix}\begin{Bmatrix}\mathbf{p}_f^m\\ \mathbf{p}_c^m\end{Bmatrix} \tag{12}$$

where the subindex "f" stands for the nodes which position remains fixed during the remeshing process and "c" for those that change position during that process. It is important to note that when Eq. (12) is written for a new time step n, the submatrices corresponding to changing collocation points and/or to changing integration elements have to be calculated anew for all the previous steps m. The translation property of the fundamental solution can not be used in those cases because the position of the nodes at time step n is not the same as before. Thus, H_{ij}^{nmpq} and G_{ij}^{nmpq} depend on the n and m values and not only on the difference $n - m$.

If the general time domain BE discretization given by Eq. (3) is used for moving elements, the results are poor because the space and time dependence of the variables are not uncoupled. The space interpolation functions of the variables move with the elements and therefore these functions are not only space dependent but also time dependent. Displacements and tractions are represented as follows:

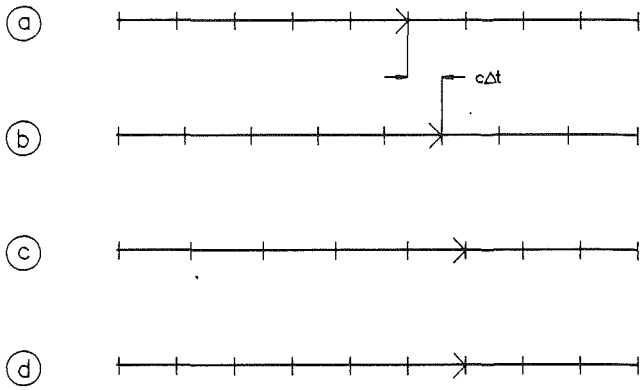


Fig. 2 Movement of the elements and remeshing process

$$u_j=\sum_q\sum_m \varphi^q(r,\tau)\eta^m(\tau)u_j^{mq}$$
$$p_j=\sum_q\sum_m \psi^q(r,\tau)\mu^m(\tau)u_j^{mq} \tag{13}$$

The velocities approximation is now

$$\dot{u}_j=\sum_q\sum_m [\varphi^q(r,\tau)\dot{\eta}^m(\tau)+\dot{\varphi}^q(r,\tau)\eta^m(\tau)]u_j^{mq} \tag{14}$$

and the integral representation, after substitution of the above approximations, can be written as

$$c_{ij}^p u_j^{np}=\sum_{m=1}^{n}\sum_{q=1}^{Q}\left\{\left[\int_{\Gamma_q}\int_{\tau_{m-1}}^{\tau_m^+} u_{ij}^{*m}\psi^q d\tau d\Gamma\right]p_j^{mq}-\left[\int_{\Gamma_q}\int_{\tau_{m-1}}^{\tau_m^+}(z_{ij}^{*}\eta^m\varphi^q-w_{ij}^{*}\dot{\eta}^m\varphi^q-w_{ij}^{*}\eta^m\dot{\varphi}^q)d\tau d\Gamma\right]u_j^{mq}\right\}. \tag{15}$$

In the regular formulation of the time domain BEM, the space shape functions are taken away from the time integrals which are done analytically. This is not possible when ψ^q and φ^q are time dependent. In order to do the time integration, an approximation of the space shape functions time dependence is done. Two terms of their series expansion are taken:

$$\psi^q(r,\tau)=\psi^q(r,\tau_{m-1})+(\tau-\tau_{m-1})\dot{\psi}^q(r,\tau_{m-1})$$
$$\phi^q(r,\tau)=\phi^q(r,\tau_{m-1})+(\tau-\tau_{m-1})\dot{\phi}^q(r,\tau_{m-1}). \tag{16}$$

By substitution of Eq. (16) into Eq. (15), the time integrals can be separated from the space integrals and Eq. (15) can be written as the typical BE Eq. (6), where now the coefficients of the system are

$$G_{ij}^{nmpq}=\int_{\Gamma_q}\left[\int_{\tau_{m-1}}^{\tau_m^+}u_{ij}^{*}\mu^m d\tau\right]\psi^q(r,\tau_{m-1})d\Gamma+\int_{\Gamma_q}\left[\int_{\tau_{m-1}}^{\tau_m^+}u_{ij}^{*}\mu^m(\tau-\tau_{m-1})d\tau\right]\dot{\psi}^q(r,\tau_{m-1})d\Gamma$$

$$H_{ij}^{nmpq}=\int_{\Gamma_q}\left\{\int_{\tau_{m-1}}^{\tau_m^+}(z_{ij}^{*}\eta^m-w_{ij}^{*}\dot{\eta}^m)d\tau\right\}\varphi^q(r,\tau_{m-1})d\Gamma+\int_{\Gamma_q}\left\{\int_{\tau_{m-1}}^{\tau_m^+}[(z_{ij}^{*}\eta^m-w_{ij}^{*}\dot{\eta}^m)(\tau-\tau_m)-w_{ij}^{*}\eta^m]d\tau\right\}\dot{\varphi}^q(r,\tau_{m-1})d\Gamma. \tag{17}$$

The first term of each coefficient is the same as in the stationary elements formulation. The computation of the second term requires a time integration followed by a space integra-

Downloaded 03 May 2010 to 171.66.16.247. Redistribution subject to ASME license or copyright; see http://www.asme.org/terms/Terms_Use.cfm

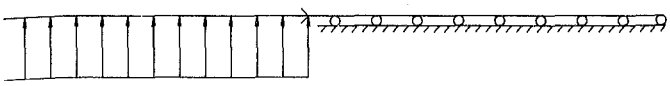


Fig. 3 Half-plane crack in unbounded domain

tion. The time integration is done analytically. Explicit expressions for those integrals may be found in the work by Gallego (1990). The space integration requires first the computation of the time derivatives of the shape functions φ^q and ψ^q.

Assuming that for each time step the elements move with a constant speed C, the shape functions can be written as

$$\varphi(r,t) = \varphi(y) \tag{18}$$

where $y = r - Ct$. Then,

$$\dot{\varphi}(r,\tau_{m-1}) = -C \left.\frac{d\varphi}{dy}\right|_{y=y_{m-1}} . \tag{19}$$

The expressions of the shape functions $\varphi(y)$ are those of the usual space-shape functions and their derivatives are easily obtained in terms of the natural coordinate ξ. In the present work at least one of the moving elements is singular of the kind $r^{-1/2}$. Its derivative is singular of the kind $r^{-3/2}$, which is too strong for a one-dimensional integration. Nevertheless, the singularity appears multiplied by the Heaviside function and the existence of the integral can be demonstrated in this case (Jones, 1966). Once the shape function has been differentiated, the resulting singular kernels of the second terms of Eq. (17) are integrated numerically. This integration can be done because the Heaviside function makes necessary only the computation of the finite part of the integrals (Kutt, 1975).

In the present work the numerical formulas given by Kutt (1975) for finite part computations have been used. A ten-point integration scheme produces accurate results for the finite parts of the integrals containing $r^{-3/2}$ singularities.

Half-Plane Crack Propagating in an Unbounded Domain

To check the accuracy of the present approach a problem with known analytical solution is solved first. The problem is that of a semi-infinite crack that extends at constant speed in an unbounded domain under the action of a uniform and time-independent normal pressure applied on the crack faces from $t = 0$. This problem was solved by Baker (1969) and its solution was extended by Freund (1972) to general loading and a time delay prior to crack growth. The properties of the elastic region are: Poisson's ratio, $\nu = 0.3$; shear modulus, $\mu = 2.24\ 10^{10}$ Pa and density, $\rho = 2450$ Kg/m^3. The resulting wave speeds are $c_1 = 5880$ m/s and $c_2 = 3143$ m/s. Because of the symmetry, only one half of the problem is studied (Fig. 3).

The boundary, which divides the domain into two equal half-planes, is modeled by a boundary element mesh containing 26 elements—13 to each side of the tip. The two elements ending at the crack tip are moving singular quarter-point elements 3.2 mm long. The rest of the elements are space quadratic elements which initial length increases uniformly with the distance to the tip until a maximum value of 5 mm. The time step $\Delta t = 0.27$ μs is such that the parameter $\beta = c_1 \Delta t/L$, L being the distance between two consecutive nodes, varies between 0.99 and 0.64. A study of the range of β values for which accurate and stable results can be expected may be found in the work by Dominguez and Gallego (1990). The problem is studied for two different values of the crack propagation velocity $C/c_1 = 0.2$ and 0.4.

In the present analysis the two SQP elements move with the tip and their size does not change with time. The rest of the elements change size in accordance with the remeshing technique described in the previous section. At each time step, the SIF is computed by Eq. (11) from the crack-tip nodal value of the traction p_2.

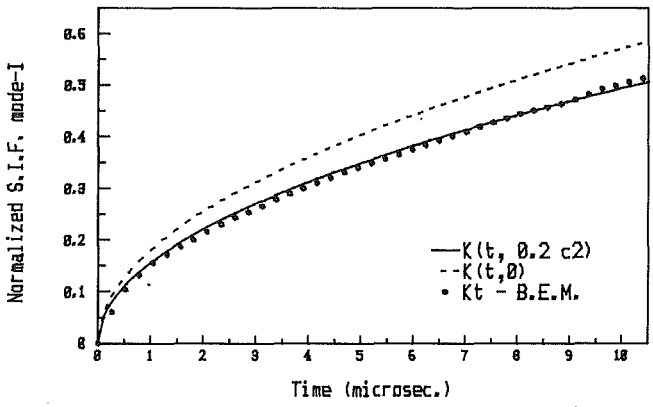


Fig. 4 Time dependence of dynamic SIF for a half-plane crack propagating with constant speed $C = 0.2\ c_2$

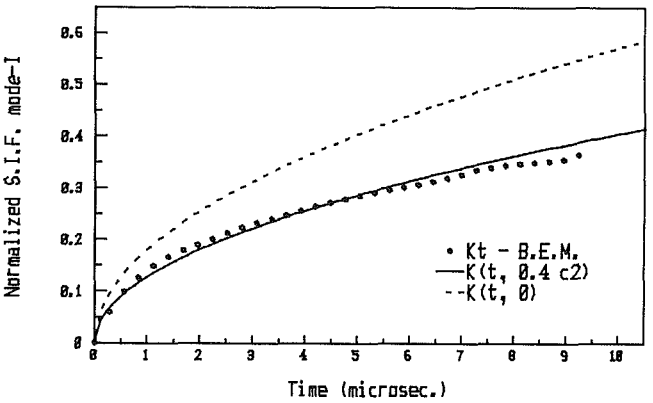


Fig. 5 Time dependence of dynamic SIF for half-plane crack propagating with constant speed $C = 0.4\ c_2$

Figures 4 and 5 show the computed values of the mode-I SIF normalized by $\sigma(0.06\ \pi)^{1/2}$ versus time for crack propagation velocities $C = 0.2\ c_2$ and $0.4\ c_2$, respectively. The BE results are compared with the analytical solutions for $0.2\ c_2$ and $0.4\ c_2$, denoted in the figures by $K(t, 0.2\ c_2)$ and $K(t, 0.4\ c_2)$, respectively. It can be seen in the figures that the agreement between the BE and the analytical solutions is very good. For the sake of completeness, the analytical solution for a stationary crack $-K(t, 0)-$ is also plotted in the figures.

Crack Propagation at Constant Speed in a Finite Body

In order to evaluate the application of the present approach to crack propagation in finite bodies under dynamic loading conditions, a problem of this kind (previously studied by Nishioka and Atluri (1980)) using a different numerical procedure is analysed. The problem is that of a rectangular plane domain with a central crack (Fig. 6). A uniformly distributed traction, with a Heaviside-function time dependence, is applied at the two sides parallel to the crack. The material properties are: shear modulus, $\mu = 2.94\ 10^{10}$ Pa; Poisson's ratio $\nu = 0.286$, and density $\rho = 2450$ Kg/m^3. The crack, with an initial length $2a = 24$ mm, remains stationary until a time $t_0 = 4.4$ μs and then propagates with a constant velocity $C = 1000$ m/s.

Due to symmetry, only one quarter of the plate is discretized by boundary elements. The discretization at the initial crack length is shown in Fig. 7. The two elements containing the crack tip are moving SQP elements and the rest are standard space quadratic elements. The boundary elements discretization is the same that results from Nishioka and Atluri's (1980) finite element discretization of the boundary. In modeling the crack propagation, the sizes of the two moving SQP do not change. The regular quadratic elements are readjusted in accordance with the aforementioned criterion. The time step Δt

Downloaded 03 May 2010 to 171.66.16.247. Redistribution subject to ASME license or copyright; see http://www.asme.org/terms/Terms_Use.cfm

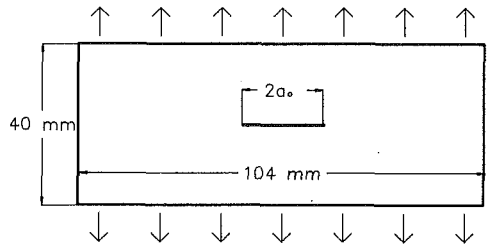


Fig. 6 Center-cracked rectangular plate subjected to a step-function normal stress

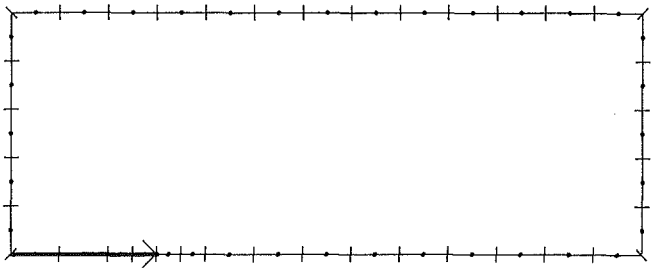


Fig. 7 Boundary element mesh for center-cracked rectangular plate

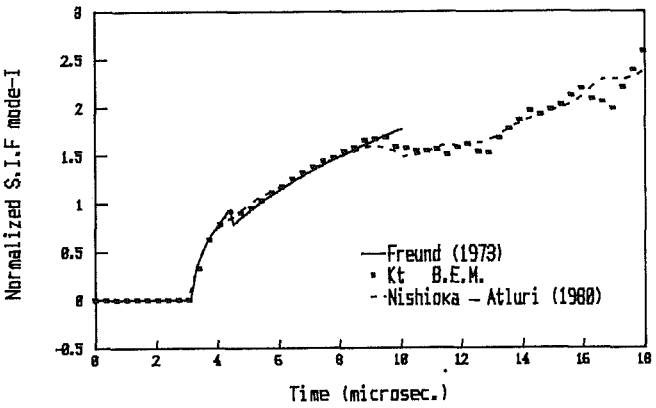


Fig. 8 Time dependence of dynamic SIF for a central crack propagating with c = 1000 m/s in a rectangular plate

$= 0.34\ \mu$s is such that the parameter β for the equal size regular elements that model most of the boundary is $\beta = c_1 \Delta t/L = 1.08$.

The computed values of the mode-I SIF normalized by $\sigma(\pi a)^{1/2}$ are shown versus time in Fig. 8, along with analytical results by Freund (1973) and the finite element results by Nishioka and Atluri (1980). The present boundary element results are in excellent agreement with the half-plane crack in infinite domain results by Freund (1973), until interaction of waves coming from one crack tip with the other crack tip takes place. The present results are also in good agreement with those computed by finite elements by Nishioka and Atluri (1980), for times after the time for which the infinite domain solution may be considered valid.

Concluding Remarks

A new translating singularity, boundary element procedure has been presented in this paper. For the first time the general direct boundary element method is used to study dynamic crack propagation in infinite and arbitrary shape finite two-dimensional bodies. A moving singular element has been developed and combined with a remeshing scheme. The procedure is applied to two dynamic crack propagation problems of different kind. One corresponds to a half-plane crack propagating in an unbounded domain and the other to a crack propagating in a finite body. The computed numerical results correlate well with the available analytical solution, for infinite domains, when this solution is valid; i.e., for the infinite domain problem and for the finite domain problem before wave interaction effects are noticeable. For the finite domain problem, the computed solution is in good agreement, for all times, with existing numerical results obtained by other authors using a different method.

The type of problems considered is limited to the case of determining the dynamic SIF of cracks that propagate with a prescribed velocity time history.

Since the present numerical procedure is based on a boundary element technique, the idea of a moving element and the subsequent remeshing process is simpler than in those procedures based on the finite element method.

Acknowledgment

The authors would like to express their gratitude to the Spanish "Comision Interministerial de Ciencia y Tecnologia" for supporting this work under a research grant. We would also like to thank Prof. L. B. Freund for his helpful review of the final copy of this paper.

References

Antes, H ., 1985, "A Boundary Element Procedure for Transient Wave Propagations in Two-dimensional Isotropic Elastic Media," *Finite Elem. Anal. Des.*, Vol. 1, pp. 313–322.

Aoki, S., Kishimoto, K., Kondo, H., and Sakata, M., 1978, "Elastodynamic Analysis of Crack by Finite Element Method Using Singular Elements," *Int. J. Fract.*, Vol. 14, pp. 59–68.

Atluri, S. N., and Nishioka, T., 1985, "Numerical Studies in Dynamic Fracture Mechanics," *Int. J. Fract.*, Vol. 27, pp. 245–261.

Baker, B. R., 1962, "Dynamic Stresses Created by a Moving Crack," ASME JOURNAL OF APPLIED MECHANICS, Vol. 29, pp. 449–454.

Bergkvist, H., 1978, "Brittle Crack Propagation at Non-uniform Velocity," *Proc. 1st Int. Conf. on Num. Meth. in Fracture Mechanics*, A. R. Luxmoore and D. R. J. Owen, eds., Quadrant, Swansea, pp. 685–695.

Beskos, D. E., 1987, "Numerical Methods in Dynamic Fracture Mechanics," Research report EUR 11300 EN, Ispra Establishment, European Joint Research Centre.

Blandford, G. E., Ingraffea, A. R., and Liggett, J. A., 1981, "Two-dimensional Stress Intensity Factor Computations Using the Boundary Element Method," *Int. J. Num. Meth. Eng.*, Vol. 17, pp. 387–404.

Burridge, R., 1969, "The Numerical Solution of Certain Integral Equations with Non-integrable Kernels Arising in the Theory of Crack Propagation and Elastic Wave Diffraction," *Proc. Roy. Soc., London*, Vol. A265, pp. 353–381.

Chirino, F., and Dominguez, J., 1989, "Dynamic Analysis of Crack Using Boundary Element Method," *Eng. Fract. Mech.*, Vol. 34, pp. 1051–1061.

Das, S., 1980, "A Numerical Method for Determination of Source Time Functions for General Three-Dimensional Rupture Propagation," *Geophys. J. Roy. Astr. Soc.*, Vol. 62, pp. 591–604.

Das, S. and Kostrov, B. V., 1987, "On the Numerical Boundary Integral Equation Method for Three-Dimensional Dynamic Shear Crack Problems," Vol. 54, pp. 99–104.

Dominguez, J., and Gallego, R., 1990, "On Time Domain Boundary Element Method for Elastodynamics," *Mathematical and Comp. Modelling*, in press.

Dominguez, J., and Gallego, R., 1991, "Time Domain Boundary Element Method for Dynamic Stress Intensity Factor Computations," *Int. J. Numer. Meth. Eng.*, in press.

Freund, L. B., 1972, "Crack Propagation in an Elastic Solid Subjected to General Loading-I: Constant Rate of Extension," *J. Mech. Phys. Solids*, Vol. 20, pp. 129–140.

Freund, L. B., 1972, "Crack Propagation in an Elastic Solid Subjected to General Loading-II: Non-uniform Rate of Extension," *J. Mech. Phys. Solids*, Vol. 20, pp. 141–152.

Freund, L. B., 1973, "Crack Propagation in an Elastic Solid Subjected to General Loading-III: Stress Wave Loading," *J. Mech. Phys. Solids*, Vol. 21, pp. 47–61.

Gallego, R., 1990, "Numerical Studies of Elastodynamic Fracture Mechanics Problems," Ph.D. Thesis, Universidad de Sevilla, in Spanish.

Jones, D. S., 1966, *Generalized Functions*; McGraw-Hill, London.

Kutt, H. R., 1975, "Quadrature Formulae for Finite-part Integrals," CSIR Special Report, WISK 178, National Research Institute for Mathematical Sciences, Pretoria, Republic of South Africa.

Mansur, W. J., 1983, "A Time-stepping Technique to Solve Wave Propagation Problems Using the Boundary Element Method," Ph.D. Thesis, University of Southampton, U.K.

Martinez, J., and Dominguez, J., 1984, "On the Use of Quarter-point Boundary Elements for Stress Intensity Factor Computations," *Int. J. Num. Mech. Eng.*, Vol. 20, pp. 1941–1950.

Nishioka, T., and Atluri, S. N., 1980, "Numerical Modelling of Dynamic Crack Propagation in Finite Bodies by Moving Singular Element, Part I: Formulation; Part II: Results," ASME JOURNAL OF APPLIED MECHANICS, Vol. 47, pp. 570–576; pp. 577–582.

Downloaded 03 May 2010 to 171.66.16.247. Redistribution subject to ASME license or copyright; see http://www.asme.org/terms/Terms_Use.cfm

Jin O. Kim
Assoc. Mem. ASME

Haim H. Bau[1]
Mem. ASME

Department of Mechanical Engineering
and Applied Mechanics,
University of Pennsylvania,
Philadelphia, PA 19104-6315

A Study of the Fiber-Matrix Interface in Composite Materials

A novel experimental technique for studying the characteristics of the interface between the fibers and the matrix in both undamaged and damaged fiber-reinforced composite materials is described. The experimental technique involves the transmission of stress waves in one or more fibers of the composite. The characteristics of the stress waves, such as speed, dispersion, and attenuation, are measured. These measured variables can be correlated with the characteristics of the bonding between the fiber and the matrix.

1 Introduction

The quality of the bond between the fiber and the matrix in fiber-reinforced composite materials may crucially affect the properties of the composite. Often the bond between the fiber and the matrix is not perfect (i.e., one cannot assume displacement continuity across the interface). This imperfect bond may occur because of a number of factors. The fibers may be coated with a thin layer, the interphase, to obtain desired bonding characteristics. An interphase may also be formed as a result of a physico-chemical interaction between the fiber and the matrix. Finally, degradation of the interface bonding due to fatigue, loading, or other service conditions such as temperature and moisture may lead to an imperfect bond. Knowledge of the bond's characteristics is essential for predicting the mechanical properties of undamaged and damaged composite materials (i.e., Benveniste, 1985; Achenbach and Zhu, 1989; and Hashin, 1990). Additionally, detection of bond deterioration may provide an early warning of an impending failure. In this paper, we describe an experimental technique which may allow us to determine the characteristics of the bond.

The technique consists of transmitting stress waves in the fiber itself and measuring their characteristics (i.e., speed and attenuation). These measurements can serve a number of purposes. By comparing the experimental results with predicted wave characteristics, one may be able to obtian the bond's characteristics, often expressed conveniently as "spring" constants (Mal and Bose, 1975), and their dependence on the stress field. By monitoring the waves' characteristics as a function of loading/service conditions, one can observe the initiation of debonding and the occurrence of permanent damage before such damage is visible. The measurements can be conducted continuously, in real time, while the composite is subjected to various loading conditions, thus allowing one to observe changes in the interface conditions as a function of factors such as loading, remote or adjacent crack propagation, and/or fatigue.

The idea of obtaining information on a medium adjacent to a solid wave guide by monitoring stress wave transmission in the waveguide is not new. For example, Bau (1986), Kim and Bau (1989a,b), and Kim et al. (1991) utilized submerged, solid wave guides to measure the rheological properties (such as density and viscosity) of adjacent liquids. The present paper is a spin-off of this prior work. Harrold and Sanjana (1986, 1987) embedded solid wave guides in thermosetting materials for evaluation of the curing process. They also suggested subsequent use of the same wave guides as a means of nondestructive testing of materials. In contrast, we propose here to utilize one or more of the naturally occurring fibers in the composite material as a wave guide sensor. This technique was developed as a part of Kim's Ph.D. dissertation (1989) where the interested reader may find additional details. In somewhat related works, Kim (1989) and Xu and Datta (1990b) demonstrated theoretically that the properties of stress waves transmitted in a clad cylinder can be correlated with the bond's characteristics. Recently, a similar technique, using leaky Lamb waves, has been advocated for the characterization of bonds or joints in layered composite plates (i.e., Mal et al., 1989; Xu and Datta, 1990a).

The objective of this paper is to describe the experimental technique and to demonstrate its utility rather than to present any specific results. We hope to provide sufficient information to allow others to continue from where we left off.

2 Experimental Feasibility Study

We have carried out a few preliminary, simple experiments to determine whether the proposed methodology is feasible. In this section, we describe our experimental procedure and point out various ways in which the procedure can be refined and improved to deal with more realistic composite materials than the ones considered here. The feasibility study was carried

[1]To whom correspondence should be addressed.

Contributed by the ASME Applied Mechanics Division of THE AMERICAN SOCIETY OF MECHANICAL ENGINEERS for presentation at the Winter Annual Meeting, Atlanta, Ga., Dec. 1–6, 1991.

Discussion on this paper should be addressed to the Technical Editor, Prof. Leon M. Keer, The Technological Institute, Northwestern University, Evanston, IL 60208, and will be accepted until two months after final publication of the paper itself in the JOURNAL OF APPLIED MECHANICS. Manuscript received by the ASME Applied Mechanics Division, June 13, 1990; final revision, May 24, 1991.

Paper No. 91-WA/APM-33.

Copyright © 1992 by ASME
Downloaded 03 May 2010 to 171.66.16.247. Redistribution subject to ASME license or copyright; see http://www.asme.org/terms/Terms_Use.cfm

out on crude, scaled-up models of composite materials. We manufactured the composites using a $1.22 \cdot 10^{-3}$ m-diameter fiber made from a magnetostrictive material (Remendur, Fe-Co-V alloy) embedded in a polycarbonate matrix whose thickness in the direction of the fiber varied between various samples. This particular fiber material was chosen, as a matter of convenience, to allow for easy introduction and detection of stress waves utilizing the magnetostrictive phenomenon. The technique can be used with fibers made of any material and of much smaller size (i.e., a few microns in diameter) than the ones used in our experiments. Magnetostrictive wires can be bonded to fibers made of other materials. Lynnworth et al. (1977, 1989), for example, successfully transmitted stress waves using the above techniques in glass fibers with diameters of 25 microns and smaller.

We manufactured our composite specimens by sandwiching a few fibers between two polycarbonate (Tuffak) plates inserted in a custom made die (specifically designed for this purpose) and subjecting the "sandwich" to elevated pressure and temperature in a press. In our samples, the "fiber" extruded from the matrix to facilitate convenient introduction of extensional and/or torsional stress waves. Such an extrusion can be avoided by selecting remote means (such as the use of lasers) for stress wave inducement and detection.

Our experimental set-up is schematically depicted in Fig. 1. The measurements were carried out in real time while the specimens were subjected to loading. Extensional and torsional stress waves were introduced into the fiber and detected by utilizing the magnetostrictive phenomenon (Tzannes, 1966).

To demonstrate the effect of debonding on the characteristics of the stress wave, we mounted our specimen on a testing machine (Instron 1125) and gradually loaded the specimen (see Fig. 1 for loading conditions) until failure occurred. The tensile loading was imposed in a direction perpendicular to the fiber's axis. In Fig. 2, we depict the amplitude of the torsional stress wave as a function of the load. The ordinate (M) in Fig. 2 is the detected amplitude normalized with the amplitude while the fiber is submerged in air. The abscissa (L) is the load normalized with the load at failure. In Fig. 3, we depict the corresponding relative displacement, ϵ (normalized with displacement at failure), as a function of the relative load (L). Figures 2 and 3 show results obtained when we tested four different specimens. Although the specimens were manufactured under similar conditions, there may have been some small differences in the manufacturing process which affected the characteristics of the bonds. Nevertheless, all the specimens demonstrated similar behavior.

Figure 2 shows the effect of tensile loading on the amplitude of the detected torsional stress wave. For small loads ($L < 0.1$), the amplitude is not affected by the load. As the load increases ($0.1 < L < 0.3$), we note a rapid increase in the amplitude. This increase may result from stress relaxation in the matrix. That is, the loading removes residual stresses around the fiber. This assertion is partially supported by experiment (e) in Fig. 2. In experiment e, we loaded the specimen up to a certain point ($L \sim 0.4$) and then we removed the load. Note that the amplitude curve is similar in both the directions of loading and unloading which suggests that the bond was not damaged. In the region $0.3 < L < 0.8$, the amplitude varies little as the load increases. For $L > 0.8$, we observe a rapid increase in the amplitude. The increase in amplitude is a result of a reduction in attenuation and/or a change in the dispersion characteristics which can be attributed to a deterioration of the bond. We found that the loading had no measurable effect on the wave speed. Examination of the matrix after failure suggests that an opening may occur between the fiber and the matrix at points located across the diameter aligned with the load direction (Fig. 4).

In Fig. 3, we show the strain-load relationships corresponding to the experiments depicted in Fig. 2. The strain-load figure

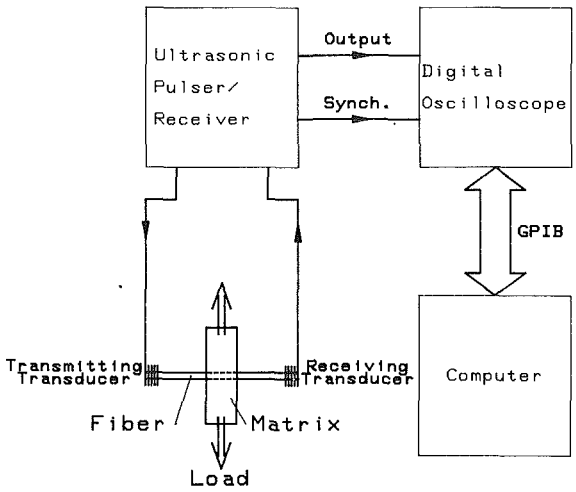


Fig. 1 Schematic description of the experimental set-up

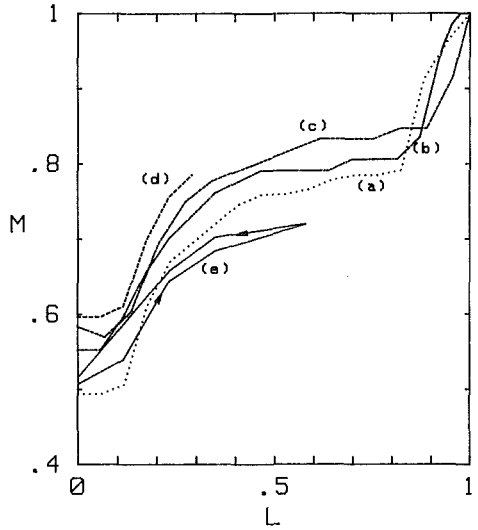


Fig. 2 The normalized amplitude of the detected torsional stress wave is depicted as a function of the normalized load

does not appear to convey any information on the characteristics of the bond in this case. This is not surprising, however, as in this experiment the fiber does not share meaningfully in the load bearing.

The experiments demonstrate that the characteristics of the stress wave transmitted in the fiber depend on the interface's condition. The experimental results may support some interesting conclusions. First, Fig. 2 shows that the attenuation varies as a function of the load. Thus, it appears that the interfacial condition is a function of the stress field. Second, the experiment shows insignificant variations in the wave speed. Given our theoretical calculations (Kim, 1989), this observation leads one to suspect that in the composite material tested here, the interface condition is either "visco-elastic" or frictional in nature. This speculation needs, of course, further verification.

3 Conclusions

In this paper, we demonstrated experimentally that by monitoring stress wave transmission in a fiber or fibers one can obtain information on the interfacial conditions between the fiber and the matrix. This technique can be used for a variety of fiber-reinforced composites such as carbon-polycarbonate and metal-ceramic composites. It can also be used as an empirical tool for monitoring the health of a composite material

Downloaded 03 May 2010 to 171.66.16.247. Redistribution subject to ASME license or copyright; see http://www.asme.org/terms/Terms_Use.cfm

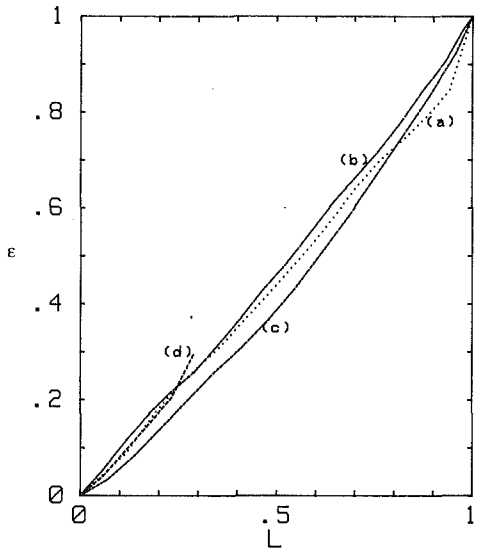


Fig. 3 The normalized displacement of the composite specimen is depicted as a function of the load

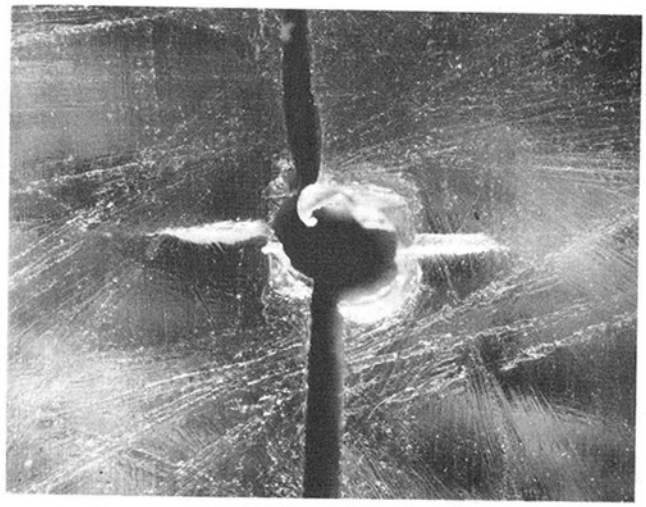


Fig. 4 Enlarged picture of the matrix after failure

and possibly as a sensor for a feedback control system during the manufacturing process. Additionally, the technique can be used to monitor the effect of service conditions such as loading, humidity, and temperature on the interface.

It is also hoped that measurements of the type described here can assist researchers in gaining a better understanding of the interfacial bonding between the fiber and the matrix. This knowledge should allow one to predict the global mechanical properties of the composite such as its elastic moduli (see, for example, Hashin, 1990 and Benveniste, 1985). By comparing the predictions with global measurements, one can verify indirectly the assumed interfacial relations.

Acknowledgment

We acknowledge useful discussions with Prof. Zvi Hashin and Mr. L. C. Lynnworth of Panametrics. We are grateful to Prof. C. Laird for allowing us the use of his laboratory facilities for manufacturing the specimens. This research is a spin-off of work supported by the National Science Foundation (Grant CBT83-51658) and Panametrics, Inc.

References

Achenbach, J. D., and Zhu, H., 1989, "Effect of Interfacial Zone on Mechanical Behavior and Failure of Fiber-Reinforced Composites," *J. Mech. Phys. Solids*, Vol. 37, pp. 381–393.

Bau, H. H., 1986, "Torsional Wave Sensor: A Theory," ASME JOURNAL OF APPLIED MECHANICS, Vol. 108, pp. 846–848. (See also Bau, H. H., Kim, J. O., Lynnworth, L. C., and Nguyen T. H., 1990, U.S. Patent 4,893,496.)

Benveniste, Y., 1985, "The Effective Mechanical Behavior of Composite Materials With Imperfect Contact Between the Constituents," *Mechanics of Materials*, Vol. 4, pp. 197–208.

Hashin, Z., 1990, "Thermoelastic Properties of Fiber Composites With Imperfect Interface," *Mechanics of Materials*, Vol. 8, pp. 333–348.

Harrold, R. T., and Sanjana, Z. N., 1986, "Acoustic Waveguide Monitoring of the Cure and Structural Integrity of Composite Materials," *Polymer Engineering and Science*, Vol. 26, pp. 367–372.

Harrold, R. T., and Sanjana, Z. N., 1987, "Non-Destructive Evaluation of the Curing of Resin and Prepreg using an Acoustic Waveguide Sensor," *Review of Progress in Quantitative Nondestructive Evaluation*, Vol. 6B (D. O. Thompson and D. E. Chimenti, eds., Plenum Publishing, pp. 1277–1285.

Kim, J. O., 1989, *The Interaction Between Stress Waves Transmitted in Solid Waveguides and Adjacent Media*, Ph.D. Thesis, University of Pennsylvania, Philadelphia, Pa.

Kim, J. O., and Bau, H. H., 1989a, "On Line, Real Time Densimeter—Theory and Optimization," *J. Acoustical Society of America*, Vol. 85, pp. 432–439.

Kim, J. O., and Bau, H. H., 1989b, "An Instrument for Simultaneous Measurement of Density and Viscosity," *Review of Scientific Instruments*, Vol. 60, pp. 1111–1115.

Kim, J. O., Wang, Y-Z., and Bau, H. H., 1991, "The Effect of Adjacent Viscous Fluid on the Transmission of Torsional Stress Waves in a Submerged Waveguide," *J. Acoustical Society of America*, Vol. 89, pp. 1414–1422.

Lynnworth, L. C., Papadakis, E. P., and Fowler, K. A., 1977, "Ultrasound Propagation Measurements and Applications," *International Advances in Nondestructive Testing*, Vol. 5, pp. 71–115.

Lynnworth, L. C., 1989, *Ultrasonic Methods for Process Control*, Academic Press.

Mal, A. K., and Bose, S. K., 1974, "Dynamic Elastic Moduli of Suspension of Imperfectly Bonded Spheres," *Proc. Cambridge Phil. Society*, Vol. 76, pp. 587–600.

Mal, A. K., Xu, P.-C., and Bar-Cohen, Y., 1989, "Analysis of Leaky Lamb Waves in Bonded Plates," *Int. J. Eng. Science*, Vol. 27, pp. 779–791.

Tzannes, N. S., 1966, "Joule and Wiedemann Effects—The Simultaneous Generation of Longitudinal and Torsional Stress Pulse in Magnetostrictive Materials," *IEEE Transactions, Sonics and Ultrasonics*, Vol. 13, pp. 33–41.

Xu, P.-C., and Datta, S. K., 1990a, "Guided Waves in a Bonded Plate: A Parametric Study," *J. Appl. Physics*, Vol. 67, pp. 6779–6786.

Xu, P.-C., and Datta, S. K., 1990b, "Characterization of Fiber-Matrix Interface by Guided Waves: Axisymmetric Case," Center for Space Structures and Controls, CU-CSSC-90-15, Univ. of Colorado.

Downloaded 03 May 2010 to 171.66.16.247. Redistribution subject to ASME license or copyright; see http://www.asme.org/terms/Terms_Use.cfm

A Variational Approach to Three-Dimensional Elasticity Solutions of Laminated Composite Plates

M. Savoia[1]

J. N. Reddy
Clifton C. Garvin Professor,
Fellow ASME.

Department of Engineering Science and Mechanics,
Virginia Polytechnic Institute and State University,
Blacksburg, VA 24061-0219

The displacements in a laminated composite are represented as products of two sets of unknown functions, one of which is only a function of the thickness coordinate and the other is a function of the in-plane coordinates (i.e., separation of variables approach), and the minimization of the total potential energy is reduced to a sequence of iterative linear problems. Analytical solutions are developed for cross-ply and angle-ply laminated composite rectangular plates. The solution for simply-supported cross-ply plates under sinusoidal transverse load reduces to that of Pagano. Numerical results for stresses and displacements for antisymmetric angle-ply laminates are presented. The three-dimensional elasticity solutions developed are important because they can be used to study the behavior of composite laminates, in addition to serving as reference for approximate solutions by numerical methods and two-dimensional theories.

1 Introduction

Laminated composite media are often represented as plate structures, and various theories are developed, depending on the kinematic assumptions used to represent thickness variations of displacements and/or stresses, to predict displacements and stresses. The laminate plate theories are typically two-dimensional theories obtained from three-dimensional elasticity theory by invoking assumptions on the variation of displacements through the laminate thickness.

The displacement-based two-dimensional laminate theories are of two kinds: (1) equivalent single-layer theories and (2) layer-wise theories. In equivalent single-layer theories, displacements are expanded in terms of various powers of the thickness coordinate x_3 and unknown functions $u_i^j(x_1, x_2)$:

$$u_i = \sum_{j=0}^{n_i} u_i^j(x_1, x_2) \cdot (x_3)^j \quad (i = 1,2,3) \tag{1}$$

where n_i denotes the number of terms in the ith displacement expansion. In most theories reported in the literature, it is assumed that $n_1 = n_2$ and $n_3 = 0$. In the first-order plate theory (Reddy, 1984a; Whitney and Pagano, 1970) it is assumed that $n_1 = n_2 = 1$ and $n_3 = 0$:

$$u_1 = u_1^0 + x_3 u_1^1,\ u_2 = u_2^0 + x_3 u_2^1,\ u_3 = u_3^0. \tag{2}$$

In the classical laminate theory, it is further assumed that u_1^1 and u_2^1 are equal to $-\partial u_3^0/\partial x_1$ and $-\partial u_3^0/\partial x_2$, respectively, to satisfy the normality condition (i.e., straight normal to mid-plane remain normal to the midsurface after deformation). The higher-order theories (often not exceeding third-order) are based on the displacement expansion (1) with $n_1 = n_2 = 2$ or $n_1 = n_2 = 3$ and $n_3 = 0$ or $n_3 = 1$ (Krishna Murty, 1977; Reddy 1984b, 1987a). A review of various single-layer theories can be found in recent papers by Reddy (1989a, 1990a, b). In all single-layer theories, the strains are continuous through the thickess, and stresses computed via stress-strain relations are discontinuous at interfaces of two dissimilar layers. In this context, an exception is provided by the model developed by Savoia et al. (1990) for laminated beams, where the through-the-thickness displacements are represented in terms of explicitly defined piecewise, C-deg polynomial functions to accommodate the continuity of equilibrated stresses. In the layer-wise theories (Srinivas, 1973; Hinrichsen and Palazotto, 1986; Reddy, 1987b, 1989b; Disciuva, 1987; Barbero et al., 1990) a layer-wise displacement or stress expansions are adopted, and therefore the theories yield more accurate stress fields even when computed using the constitutive relations.

The use of the three-dimensional elasticity theory to compute displacements and stresses in laminated composite plates was reported by Pagano (1970) and others (Srinivas and Rao, 1970, 1971). These results are usually restricted to exact solutions for simple configurations and lamination schemes. The most commonly referenced work of Pagano (1970) contains derivations for exact solutions of cross-ply laminates under sinusoidal transverse loads, where in a mixed formulation is used by Noor and Burton (1990) for antisymmetric angle-ply lam-

[1]Visiting Fellow, University of Bologna, Bologna, Italy.

Contributed by the ASME Applied Mechanics Division of THE AMERICAN SOCIETY OF MECHANICAL ENGINEERS for presentation at the Winter Annual Meeting, Atlanta, Ga, Dec. 1-6, 1991.

Discussion on this paper should be addressed to the Technical Editor, Prof. Leon M. Keer, The Technological Institute, Northwestern University, Evanston, IL 60208, and will be accepted until two months after final publication of the paper itself in the Journal of Applied Mechanics. Manuscript received by the ASME Applied Mechanics Division, Nov. 28, 1990; final revision, Mar. 15, 1991.

Paper No. 91-WA/APM-31.

Copyright © 1992 by ASME
Downloaded 03 May 2010 to 171.66.16.247. Redistribution subject to ASME license or copyright; see http://www.asme.org/terms/Terms_Use.cfm

inates. The present work was underway before the paper by Noor and Burton (1990) appeared in print, although the approach presented here is significantly different from and more general than that by Noor and Burton (1990). Exact analytical solutions of three-dimensional elasticity theory for arbitrarily laminated rectangular plates are not available.

In the present study, the Rayleigh-Ritz solutions of the three-dimensional elasticity theory are derived based on the assumption that the displacement field is separable into thickness variations and surface variations. The two sets of functions are assumed as unknown and the minimization of total potential energy is performed by reducing the problem to a sequence of linear problems involving the thickness and the surface variations, respectively. This procedure was used by Savoia et al. (1990) for multilayered, transversely rigid beams. It was shown that two or three terms are sufficient to yield almost continuous distributions of interlaminar stresses and an accurate representation of the stress distribution in the boundary layer as well as in the neighborhood of stress singularities (Choi and Horgan, 1978; Villaggio, 1977; Gregory and Gladwell, 1982). Moreover, the analytical exact solutions for bending of simply-supported cross-ply and antisymmetric angle-ply rectangular plates are obtained as particular cases of this approach and in these cases no iterative procedure is required.

2 Formulation

2.1 Assumed Displacement Field. Let the multilayered plate be composed of L individually homogeneous, linear elastic, anisotropic layers of uniform thickness. A right-handed orthogonal coordinate system (x_1, x_2, x_3) is adopted, where x_1 and x_2 lie on a reference plane Ω, parallel to the top and bottom surfaces of the plate. The plate is considered as a three-dimensional domain $\Omega \times [x_{3b}, x_{3t}]$, the interfaces between layers Ω_i as two-dimensional boundaries at $x_3 = x_{3i}$ and similarly, the top and bottom surfaces Ω_t, Ω_b as surfaces at $x_3 = x_{3t}$, x_{3b}, respectively. Unless mentioned otherwise, throughout this paper Greek indices assume the range 1,2 whereas Latin indices range from 1 to 3, and the Einstein summation convention on repeated indices will be used.

Following a displacement-based approach, we assume a kinematic field across the entire laminate thickness as follows:

$$u_\alpha(x_\beta, x_3) = \psi^m_\alpha(x_3)\chi^m_\alpha(x_\beta)$$
$$u_3(x_\beta, x_3) = \psi^p_3(x_3)\chi^p_3(x_\beta) \tag{3}$$

where the indices m (for u_1, u_2) and p (for u_3) are summed over the range of 1 to M and 1 to R, respectively. In the displacement field of Eq. (3) both the ψ's and the χ's are functions to be determined. The linear strain components associated with the displacement field in Eq. (3) are:

$$2\epsilon_{\alpha\beta} = u_{\alpha,\beta} + u_{\beta,\alpha} = \psi^m_\alpha\chi^m_{\alpha,\beta} + \psi^m_\beta\chi^m_{\beta,\alpha}$$
$$2\epsilon_{\alpha 3} = u_{\alpha,3} + u_{3,\alpha} = \psi^m_{\alpha,3}\chi^m_\alpha + \psi^p_3\chi^p_{3,\alpha}$$
$$2\epsilon_{33} = 2u_{3,3} = 2\psi^p_{3,3}\chi^p_3 \tag{4}$$

2.2 Constitutive Relations. We assume that each layer is made of an anisotropic material with elastic symmetry with respect to the x_1x_2-plane; then the generalized Hooke's law can be written as (Green and Naghdi, 1982; Librescu, 1975):

$$\sigma^{\alpha\beta} = C^{\alpha\beta\gamma\delta}\epsilon_{\gamma\delta} + C^{\alpha\beta 33}\epsilon_{33}$$
$$\sigma^{\alpha 3} = 2C^{\alpha 3\gamma 3}\epsilon_{\gamma 3}$$
$$\sigma^{33} = C^{33\gamma\delta}\epsilon_{\gamma\delta} + C^{3333}\epsilon_{33} \tag{5}$$

where C^{ijkl} denotes the anisotropic elastic tensor and varies with layers in the thickness direction.

2.3 Total Potential Energy Functional. We suppose that the plate is subjected to surface tractions $(\bar{q}_i, \hat{q}_i)$ on (Ω_t, Ω_b) and t_i on $\Gamma_f = \partial_f\Omega \times [x_{3b}, x_{3t}]$, and prescribed displacements $\bar{u}_i$ on $\Gamma_u = \partial_u\Omega \times [x_{3b}, x_{3t}]$, with $\partial_f\Omega + \partial_u\Omega = \partial\Omega$. The weak formulation of this problem can be derived, in a consistent way, by minimizing the total potential energy functional,

$$\pi(\psi^m_\alpha, \chi^m_\alpha, \psi^p_3, \chi^p_3) = \frac{1}{2}\int_\Omega\int_h (\sigma^{\alpha\beta}\epsilon_{\alpha\beta} + \sigma^{33}\epsilon_{33} + 2\sigma^{\alpha 3}\epsilon_{\alpha 3})dx_3 d\Omega$$
$$- \int_{\Omega_t} \bar{q}_i u_i d\Omega_t - \int_{\Omega_b} \hat{q}_i u_i d\Omega_b - \int_{\Gamma_f} t_i u_i d\Gamma_f$$
$$= \frac{1}{2}\int_\Omega\int_h [C^{\alpha\beta\gamma\delta}\psi^m_\alpha\chi^m_{\alpha,\beta}\psi^p_\gamma\chi^p_{\gamma,\delta} + C^{3333}\psi^p_{3,3}\chi^p_3\psi^s_{3,3}\chi^s_3$$
$$+ 2C^{\alpha\beta 33}\psi^m_\alpha\chi^m_{\alpha,\beta}\psi^r_{3,3}\chi^r_3 + C^{\alpha 3\gamma 3}(\psi^m_{\alpha,3}\chi^m_\alpha\psi^p_{\gamma,3}\chi^p_\gamma$$
$$+ 2\psi^m_{\alpha,3}\chi^m_\alpha\psi^r_3\chi^r_{3,\gamma} + \psi^r_3\chi^r_{3,\alpha}\psi^s_3\chi^s_{3,\gamma})]dx_3 d\Omega$$
$$- \int_{\Omega_t} (\bar{q}\psi^m_\alpha\chi^m_\alpha + \bar{q}_3\psi^p_3\chi^p_3)d\Omega_t - \int_{\Omega_b} (\hat{q}_\alpha\psi^m_\alpha\chi^m_\alpha$$
$$+ \hat{q}_3\psi^p_3\chi^p_3)d\Omega_b - \int_{\Gamma_f} (t_\alpha\psi^m_\alpha\chi^m_\alpha + t_3\chi^p_3\chi^p_3)d\Gamma_f. \tag{6}$$

Note that the functional in Eq. (6) is no longer quadratic in the unknown functions ψ's and χ's. In the next section a gradient technique will be adopted to minimize Π with respect to the two sets of functions of x_α and x_3 (i.e., the χ's and the ψ's, respectively). The resulting expressions are nonlinear in χ's and χ's. Hence, an iterative procedure is required to solve them. Thus, the problem is reduced to a sequence of linear problems, which are solved iteratively.

3 The Minimization Procedure.

3.1 Minimization with Respect to the Functions $\chi_i(x_\alpha)$. For this purpose, we define the following thickness constants:

$$I^{mp}_{\alpha\beta\gamma\delta} = \int_h C^{\alpha\beta\gamma\delta}\psi^m_\alpha\psi^p_\gamma dx_3;\ D^{mp}_{\alpha 3\gamma 3} = \int_h C^{\alpha 3\gamma 3}\psi^m_{\alpha,3}\psi^p_{\gamma,3}dx_3$$
$$F^{mr}_{\alpha\beta 33} = \int_h C^{\alpha\beta 33}\psi^m_\alpha\psi^r_{3,3}dx_3;\ D^{rs}_{3333} = \int_h C^{3333}\psi^r_{3,3}\psi^s_{3,3}dx_3$$
$$G^{mr}_{\alpha 3\gamma 3} = \int_h C^{\alpha 3\gamma 3}\psi^m_{\alpha,3}\psi^r_3 dx_3;\ H^{rs}_{\alpha 3\gamma 3} = \int_h C^{\alpha 3\gamma 3}\psi^r_3\psi^s_3 dx_3 \tag{7a}$$

and the higher-order thickness load resultants:

$$f^m_i = \bar{q}_i\psi^m_i|_{x_3=x_{3t}} + \hat{q}_i\psi^m_i|_{x_3=x_{3b}};\ t^m_i = \int_h t_i\psi^m_i dx_3. \tag{7b}$$

Then, the total potential energy in Eq. (6) takes the form:

$$\Pi = \frac{1}{2}\int_\Omega (I^{mp}_{\alpha\beta\gamma\delta}\chi^m_{\alpha,\beta}\chi^p_{\gamma,\delta} + D^{rs}_{3333}\chi^r_3\chi^s_3 + 2F^{mr}_{\alpha\beta 33}\chi^m_{\alpha,\beta}\chi^r_3 + D^{mp}_{\alpha 3\gamma 3}\chi^m_\alpha\chi^p_\gamma$$
$$+ 2G^{mr}_{\alpha 3\gamma 3}\chi^m_\alpha\chi^r_{3,\gamma} + H^{rs}_{\alpha 3\gamma 3}\chi^r_{3,\alpha}\chi^s_3)d\Omega - \int_\Omega (f^m_\alpha\chi^m_\alpha + f^r_3\chi^r_3)d\Omega$$
$$- \int_{\partial_f\Omega} (t^m_\alpha\chi^m_\alpha + t^r_3\chi^r_3)ds. \tag{8}$$

Taking the first variation of the functional Π in Eq. (8) and performing integration by parts, we obtain the following system of second-order partial differential equations:

$$\delta\chi^m_\alpha: \quad -I^{mp}_{\alpha\beta\gamma\delta}\chi^p_{\gamma,\delta\beta} - F^{mr}_{\alpha\beta 33}\chi^r_{3,\beta} + D^{mp}_{\alpha 3\gamma 3}\chi^p_\gamma + G^{mr}_{\alpha 3\gamma 3}\chi^r_{3,\gamma} = f^m_\alpha$$
$$\delta\chi^r_3: \quad D^{rs}_{3333}\chi^s_3 + F^{mr}_{\alpha\beta 33}\chi^m_{\alpha,\beta} - G^{mr}_{\alpha 3\gamma 3}\chi^m_{\alpha,\gamma} - H^{rs}_{\alpha 3\gamma 3}\chi^s_{3,\alpha\gamma} = f^r_3. \tag{9}$$

The boundary conditions for this problem turn out to be:

Downloaded 03 May 2010 to 171.66.16.247. Redistribution subject to ASME license or copyright; see http://www.asme.org/terms/Terms_Use.cfm

$$\chi_N^m = \bar{\chi}_N^m \quad \text{or} \quad M_N^m = t_N^m$$
$$\chi_T^m = \bar{\chi}_T^m \quad \text{or} \quad M_T^m = t_T^m \quad \text{on } \partial\Omega$$
$$\chi_3^r = \bar{\chi}_3^r \quad \text{or} \quad Q_N^r = t_3^r \tag{10}$$

where N and T mean normal and tangential components, respectively, of displacements or forces defined as follows:

$$\chi_N^m = \chi_1^m n_1 + \chi_2^m n_2$$
$$\chi_T^m = -\chi_1^m n_2 + \chi_2^m n_1$$
$$M_N^m = M_{11}^m n_1^2 + M_{22}^m n_2^2 + 2M_{12}^m n_1 n_2$$
$$M_T^m = (M_{22}^m - M_{d11}^m) n_1 n_2 + M_{12}^m (n_1^2 - n_2^2)$$
$$Q_N^r = Q_1^r n_1 + Q_2^r n_2 \tag{11}$$

and

$$M_{\alpha\beta}^m = I_{\alpha\beta\gamma\delta}^{mp} \chi_{\gamma,\delta}^p + F_{\alpha\beta 33}^{mr} \chi_3^r$$
$$Q_\gamma^r = G_{\alpha 3\gamma 3}^{mr} \chi_\alpha^m + H_{\alpha 3\gamma 3}^{rs} \chi_{3,\alpha}^s. \tag{12}$$

3.2 Minimization With Respect to the Functions $\psi_i^m(x_3)$. In order to make the total potential energy stationary with respect to an arbitrary variation of functions ψ_i^m, we first define the following plate constants:

$$P_{\alpha\beta\gamma\delta}^{mp} = \int_\Omega \chi_{\alpha,\beta}^m \chi_{\gamma,\delta}^p d\Omega;\ P_{3030}^{rs} = \int_\Omega \chi_3^r \chi_3^s d\Omega$$
$$P_{\alpha\beta 30}^{mr} = \int_\Omega \chi_{\alpha,\beta}^m \chi_3^r d\Omega;\ P_{\alpha 03\gamma}^{mr} = \int_\Omega \chi_\alpha^m \chi_{3,\gamma}^r d\Omega$$
$$P_{\alpha 0\gamma 0}^{mp} = \int_\Omega \chi_\alpha^m \chi_\gamma^p d\Omega;\ P_{3\alpha 3\gamma}^{rs} = \int_\Omega \chi_{3\chi}^r\ \chi_{3,\nu}^s\ d\Omega \tag{13}$$

and the higher-order plate load resultants:

$$\bar{q}_i^m = \int_\Omega \bar{q}_i \chi_i^m d\Omega;\ \hat{q}_i^m = \int_\Omega \hat{q}_i \chi_i^m d\Omega$$
$$p_i^m = \int_{\partial_f \Omega} t_i \chi_i^m ds \tag{14}$$

The total potential energy, for the ith layer, becomes

$$\Gamma(\psi_\alpha^m,\ \psi_3^r) = \frac{1}{2}\int_{x_{3i}}^{x_{3i+1}} (C^{\alpha\beta\gamma\delta} P_{\alpha\beta\gamma\delta}^{mp} \psi_\alpha^m \psi_\gamma^p + C^{3333} P_{3030}^{rs} \psi_{3,3}^r \psi_{3,3}^s + 2C^{\alpha\beta 33} P_{\alpha\beta 30}^{mr} \psi_\alpha^m \psi_{3,3}^r + C^{\alpha 3\gamma 3} P_{\alpha 0\gamma 0}^{mp} \psi_{\alpha,3}^m \psi_{\gamma,3}^p + 2C^{\alpha 3\gamma 3} P_{\alpha 03\gamma}^{mr} \psi_{\alpha,3}^m \psi_3^r + C^{\alpha 2\gamma 3} P_{3\alpha 3\gamma}^{rs} \psi_3^r \psi_3^s) dx_3 - \int_{x_{3i}}^{x_{3i+1}} (p_\alpha^m \psi_\alpha^m + p_3^r \psi_3^r) dx_3 - (\bar{q}_\alpha^m \psi_\alpha^m + \bar{q}_3^r \psi_3^r)\Big|_{x_3 = x_{3t}} - (\hat{q}_\alpha^m \psi_\alpha^m + \hat{q}_3^r \psi_3^r)\Big|_{x_3 = x_{3b}} \tag{15}$$

where the last two terms refer to the top and bottom layers only. By making the functional in Eq. (15) stationary with respect to the functions ψ's and performing an integration-by-parts we obtain, for the ith layer, the following differential equations:

$$\delta\psi_\alpha^m: \quad C^{\alpha\beta\gamma\delta} P_{\alpha\beta\gamma\delta}^{mp} \psi_\gamma^p + C^{\alpha\beta 33} P_{\alpha\beta 30}^{mr} \psi_{3,3}^r - C^{\alpha 3\gamma 3} P_{\alpha 0\gamma 0}^{mp} \psi_{\gamma,33}^p - C^{\alpha 3\gamma 3} P_{\alpha 03\gamma}^{mr} \psi_{3,3}^r = p_\alpha^m$$
$$\delta\psi_3^r: \quad C^{3333} P_{3030}^{rs} \psi_{3,33}^s - C^{\alpha\beta 33} P_{\alpha\beta 30}^{mr} \psi_{\alpha,3}^m + C^{\alpha 3\gamma 3} P_{\alpha 03\gamma}^{mr} \psi_{\alpha,3}^m + C^{\alpha 3\gamma 3} P_{3\alpha 3\gamma}^{rs} \psi_3^s = p_3^r \tag{16}$$

subjected to the boundary conditions:

$$\left[\delta\psi_\alpha^m (C^{\alpha 3\gamma 3} P_{\alpha 0\gamma 0}^{mp} \psi_{\gamma,3}^p + C^{\alpha 3\gamma 3} P_{\alpha 03}^{mr} \psi_3^r)\right]_{x_{3i}}^{x_{3i+1}}$$
$$x_{3i} \neq x_{3t},\ x_{3b}$$
$$\left[\delta\psi_3^r (C^{3333} P_{3030}^{rs} \psi_{3,3}^s + C^{\alpha\beta 33} P_{\alpha\beta 30}^{mr} \psi_\alpha^m)\right]_{x_{3i}}^{x_{3i+1}} = 0. \tag{17}$$

For $x_{3i} = x_{3b}$, the expressions in parentheses of Eq. (17) should be appended with the load terms in the last two boundary terms of Eq. (15).

The interface and boundary conditions for ψ's across the whole thickness are:

$$[\psi_\alpha^m]_{x_{3i}} = 0,\ [\psi_3^r]_{x_{3i}} = 0 \tag{18}$$
$$[C^{\alpha 3\gamma 3} (P_{\alpha 0\gamma 0}^{mp} \psi_{\gamma,3}^p + P_{\alpha 03}^{mr} \psi_3^r)]_{x_{3i}} = 0 \qquad x_{3i} \neq x_{3t},\ x_{3b}$$
$$[C^{3333} P_{3030}^{rs} \psi_{3,3}^s + C^{\alpha\beta 33} P_{\alpha\beta 30}^{mr} \psi_\alpha^m]_{x_{3i}} = 0 \tag{19}$$

and

$$C^{\alpha 3\gamma 3} (P_{\alpha 0\gamma 0}^{mp} \psi_{\gamma,3}^p + P_{\alpha 03\gamma}^{mr} \psi_3^r)\Big|_{x_{3t}} = \bar{q}_\alpha^m$$
$$C^{3333} P_{3030}^{rs} \psi_{3,3}^s + C^{\alpha\beta 33} P_{\alpha\beta 30}^{mr} \psi_\alpha^m\Big|_{x_{3t}} = \bar{q}_3^r. \tag{20}$$

Analogous expressions hold at the bottom of the plate. The symbol $[\cdot]$ denotes the jump in the enclosed quantity. It is interesting to note the physical meaning of conditions in Eqs. (19) and (20). For instance, by expanding Eq. (20) and making use of Eqs. (13) and (14), we obtain

$$\int_\Omega \chi_\alpha^m [C^{\alpha 3\gamma 3} (\chi_\gamma^p \psi_{\gamma,3}^p + \chi_{3,\gamma}^r \psi_3^r) \bar{q}_\alpha]_{x_{3t}} d\Omega = 0$$
$$\int_\Omega \chi_3^r [C^{3333} \chi_3^s \psi_{3,3}^s + C^{\alpha\beta 33} \chi_{\alpha,\beta}^m \psi_\alpha^m - \bar{q}_3]_{x_{3t}} d\Omega = 0. \tag{21}$$

Taking into account Eqs. (4) and (5), we obtain:

$$\int_\Omega \chi_\alpha^m (\sigma^{\alpha 3} - \bar{q}_\alpha) d\Omega = 0$$
$$\int_\Omega \chi_3^r (\sigma^{33} - \bar{q}_3) d\Omega = 0. \tag{22}$$

Analogously, Eq. (19) imposes the continuity of components of stress vector at the interface, weighted by functions χ_α^m and χ_3^r. Hence, by taking a large number of coordinate functions in the displacement field, the continuity of the stress vector at the interface can be satisfied more exactly; also a closer balance between stress vector and applied load at the top and bottom of the plate can be accomplished.

The solution of system (16) can be obtained by superposing a particular solution (if load is applied at the lateral boundary of the plate) to the homogeneous solution; the latter can be obtained by putting the solution in vectorial form:

$$\psi_\alpha = \mathbf{c}_\alpha e^{\lambda x_3};\quad \psi_3 = \mathbf{c}_3 e^{\lambda x_3} \tag{23}$$

and solving the following eigenvalue problem:

$$\left[\begin{array}{c|c} C^{\alpha\beta\gamma\delta}\mathbf{P}_{\alpha\beta\gamma\delta} - C^{\alpha 3\gamma 3}\mathbf{P}_{\alpha 0\gamma 0}\lambda^2 & (C^{\alpha\beta 33}\mathbf{P}^{\alpha\beta 30} - C^{\alpha 3\gamma 3}\mathbf{P}_{\alpha 03\gamma})\lambda \\ \hline -(C^{\alpha\beta 33}\mathbf{P}_{\alpha\beta 30} - C^{\alpha 3\gamma 3}\mathbf{P}_{\alpha 03\gamma})\lambda & C^{\alpha 3\gamma 3}\mathbf{P}_{3\alpha 3\gamma} - C^{3333}\mathbf{P}_{3030}\lambda^2 \end{array}\right] \left\{\begin{array}{c} \mathbf{c}_\alpha \\ \hline \mathbf{c}_3 \end{array}\right\} = \left\{\begin{array}{c} \mathbf{0} \\ \hline \mathbf{0} \end{array}\right\}. \tag{24}$$

In principle, the eigenvalues and the eigenvectors obtained by Eq. (24) can be real, purely imaginary or complex, depending on the material properties of each layer and the coefficients $\mathbf{P}$'s. However, by redefining Eq. (23) in terms of trigonometric or trigonometric times exponential terms, it is possible to ob-

Downloaded 03 May 2010 to 171.66.16.247. Redistribution subject to ASME license or copyright; see http://www.asme.org/terms/Terms_Use.cfm

tain real values for all the c's. Finally, the solution to system (16) is given by a linear combination of $2(2M + R)$ eigenvectors of Eq. (24) involving $L(2M + R)$ unknowns, which are determined by imposing the boundary and interface conditions (18)–(20).

functions are completely defined by Eqs. (28) except for its amplitudes. Hence, recalling Eq. (3), the solution can be found by assuming $a_1 = a_2 = a_3 = 1$ and solving problem (16) for the thickness displacements functions, ψ. Hence, the eigenvalue problem (24) is reduced to the following equation:

$$\begin{bmatrix} C_{11}\alpha^2 + C_{66}\beta^2 - C_{55}\lambda^2) & (C_{12}+C_{66})\alpha\beta & -(C_{13}+C_{55})\alpha\lambda \\ (C_{12}+C_{66})a\beta & C_{22}\beta^2 + C_{66}\alpha^2 - C_{44}\lambda^2 & -(C_{23}+C_{44})\beta\lambda \\ -(C_{13}+C_{55})\alpha\lambda & -(C_{23}+C_{44})\beta\lambda & -C_{55}\alpha^2 - C_{44}\beta^2 + C_{33}\lambda^2 \end{bmatrix} \cdot \begin{Bmatrix} c_1 \\ c_2 \\ c_3 \end{Bmatrix} = \begin{Bmatrix} 0 \\ 0 \\ 0 \end{Bmatrix}. \quad (30)$$

4 Application to Cross-Ply and Angle-Ply Laminates

In this section we specialize the equations developed in Section 3 to the cases of cross-ply (i.e., 0 and 90-deg orientations) and antisymmetric angle-ply laminated plates. It will be shown that in more simple cases of simply-supported (as will be described shortly) rectangular plates, this approach yields the exact three-dimensional elasticity solution for both types of lamination schemes. We employ the standard single subscript notation for the stress and strain components and the stress resultants.

4.1 Cross-Ply Rectangular Plates. Since for cross-ply lamination schemes the plate reference axes (x_1, x_2, x_3) can be made coincident with the orthotropic material axes, C_{16}, C_{26}, C_{36}, and C_{45} vanish and Eq. (9) reduces to:

$$\begin{aligned} -I_{11}^{mp}\chi_{1,11}^{p} - I_{66}^{mp}\chi_{1,22}^{p} - (I_{12}^{mp}+I_{66}^{mp})\chi_{2,12}^{p} \\ -F_{13}^{mr}\chi_{3,1}^{r} + D_{55}^{mp}\chi_{1}^{p} + G_{55}^{mr}\chi_{3,1}^{r} = f_1^m \\ -I_{22}^{mp}\chi_{2,22}^{p} - I_{66}^{mp}\chi_{2,11}^{p} - (I_{12}^{mp}+I_{66}^{mp})\chi_{1,12}^{p} \\ -F_{23}^{mr}\chi_{3,2}^{r} + D_{44}^{mp}\chi_{2}^{p} + G_{44}^{mr}\chi_{3,2}^{r} = f_2^m \\ D_{33}^{rs}\chi_{3}^{s} + F_{13}^{mr}\chi_{1,1}^{m} + F_{23}^{mr}\chi_{2,2}^{m} - G_{55}^{mr}\chi_{1,1}^{m} \\ -G_{44}^{mr}\chi_{2,2}^{m} - H_{55}^{rs}\chi_{3,11}^{s} - H_{44}^{rs}\chi_{3,22}^{s} = f_3^r \end{aligned} \quad (25)$$

for $m = 1,2, \ldots, M$ and $r = 1,2, \ldots, R$. The higher-order stress resultants, referred to the plate axes and expressed in terms of plate displacement functions χ's, take the form (see Eq. (12)):

$$\begin{aligned} M_1^m &= I_{11}^{mp}\chi_{1,1}^{p} + I_{12}^{mp}\chi_{2,2}^{p} + F_{13}^{mr}\chi_3^r \\ M_6^m &= I_{12}^{mp}(\chi_{1,2}^{p} + \chi_{2,1}^{p}) \qquad (m = 1, \ldots, M) \\ M_2^m &= I_{22}^{mp}\chi_{2,2}^{p} + I_{12}^{mp}\chi_{1,1}^{p} + F_{23}^{mr}\chi_3^r \\ Q_1^r &= G_{55}^{mr}\chi_1^m + H_{55}^{rs}\chi_{3,1}^{s} \qquad (r = 1, \ldots, R) \\ Q_2^r &= G_{44}^{mr}\chi_2^m + H_{44}^{rs}\chi_{3,2}^{s}. \end{aligned} \quad (26)$$

In the simplest case of simply-supported rectangular plate under transverse loading, the Navier approach can be used by expanding the applied loads $\bar{q}_3$ and $\hat{q}_3$ (applied at the top and bottom of the plate) in double Fourier series as:

$$q_t(x_1,x_2) = \tilde{q}_t \sin\alpha x_1 \sin\beta x_2;\ q_b(x_1,x_2) = \tilde{q}_b \sin\alpha x_1 \sin\beta x_2 \quad (27)$$

where $\alpha = i\pi/a$ and $\beta = j\pi/b$, a and b being the plane-form dimensions of the plate. Assuming $M = R = 1$ in the displacement field (3) and the following expressions for the unknown functions χ_1^1, χ_2^1, χ_3^1,

$$\begin{aligned} \chi_1^1 &= a_1 \cos\alpha x_1 \sin\beta x_2 \\ \chi_1^1 &= a_2 \sin\alpha x_1 \cos\beta x_2 \\ \chi_3^1 &= a_3 \sin\alpha x_1 \sin\beta x_2 \end{aligned} \quad (28)$$

we satisfy the boundary conditions (10):

$$\begin{aligned} &\text{At } x_1 = 0,a: \qquad M_1^1 = 0,\ \chi_2^1 = 0,\ \chi_3^1 = 0 \\ &\text{At } x_2 = 0,b: \qquad \chi_1^1 = 0,\ M_2^1 = 0, \chi_3^1 = 0. \end{aligned} \quad (29)$$

For this problem, no iterative procedure is necessary to find the solution associated with the minimum of the total potential energy, as described in the previous section. In fact, the χ's

Finally, the interface and boundary conditions (18)–(20) for the ψ's take the form:

$$[\psi_1]_{x_{3i}} = [\psi_2]_{x_{3i}} = [\psi_3]_{x_{3i}} = 0 \quad (31)$$

$$[C_{55}(\psi_{1,3} + \alpha\psi_3)]_{x_{3i}} = [C_{44}(\psi_{2,3} + \beta\psi_3)]_{x_{3i}} = 0$$

$$[-C_{13}\alpha\psi_1 - C_{23}\beta\psi_2 + C_{33}\psi_{3,3}]_{x_{3i}} = 0 \quad (32)$$

and

$$\begin{aligned} C_{55}(\psi_{1,3} + \alpha\psi_3)\Big|_{x_{3t},x_{3b}} &= C_{44}(\psi_{2,3} + \beta\psi_3)\Big|_{x_{3t},x_{3b}} = 0 \\ -C_{13}\alpha\psi_1 - C_{23}\beta\psi_2 + C_{33}\psi_{3,3}\Big|_{x_{3t}} &= \tilde{q}_t \\ -C_{13}\alpha\psi_1 - C_{23}\beta\psi_2 + C_{33}\psi_{3,3}\Big|_{x_{3b}} &= \tilde{q}_b. \end{aligned} \quad (33)$$

In view of Eqs. (4), (5), and (28), the conditions (32) and (33) imply pointwise continuity of the stress vector at the interface and at the top and bottom of the plate. It is easy to verify that the solution reported here coincides with Pagano's (1970) three-dimensional elasticity solution for cross-ply rectangular plates.

4.2 Angle-Ply Rectangular Plates. For general angle-ply laminates none of the elastic constants vanish, and Eqs. (9) can be rewritten as,

$$\begin{aligned} -I_{11}^{mp}\chi_{1,11}^{p} - I_{66}^{mp}\chi_{1,22}^{p} - (I_{12}^{mp}+I_{66}^{mp})\chi_{2,12}^{p} \\ -2I_{16}^{mp}\chi_{1,12} - I_{16}^{mp}\chi_{2,11}^{p} - I_{26}^{mp}\chi_{2,22}^{p} \\ -F_{13}^{mr}\chi_{3,1}^{r} - F_{36}^{mr}\chi_{3,2}^{r} + D_{55}^{mp}\chi_{1}^{p} + D_{45}^{mp}\chi_{2}^{p} + G_{55}^{mr}\chi_{3,1}^{r} + G_{45}^{mr}\chi_{3,2}^{r} = f_1^m \\ I_{22}^{mp}\chi_{2,22}^{p} - I_{66}^{mp}\chi_{2,11}^{p} - (I_{12}^{mp}+I_{66}^{mp})\chi_{1,12}^{p} - 2I_{26}^{mp}\chi_{2,12} - I_{26}^{mp}\chi_{1,22}^{p} - I_{16}^{mp}\chi_{1,11} \\ F_{23}^{mr}\chi_{3,2}^{r} - F_{36}^{mr}\chi_{3,1}^{r} + D_{44}^{mp}\chi_{2}^{p} + D_{45}^{mp}\chi_{1}^{p} + G_{44}^{mr}\chi_{3,2}^{r} + G_{45}^{mr}\chi_{3,1}^{r} = f_2^m \\ D_{33}^{rs}\chi_{3}^{s} + F_{13}^{mr}\chi_{1,1}^{m} + F_{23}^{mr}\chi_{2,2}^{m} + F_{36}^{mr}(\chi_{1,2}^{m} + \chi_{2,1}^{m}) - G_{55}^{mr}\chi_{1,1}^{m} - G_{44}^{mr}\chi_{2,2}^{m} \\ -G_{45}^{mr}(\chi_{1,2}^{m} + \chi_{2,1}^{m}) - H_{55}^{rs}\chi_{3,11}^{s} - H_{44}^{rs}\chi_{3,22}^{s} - 2H_{45}^{rs}\chi_{3,12}^{s} = f_3^r \end{aligned} \quad (34)$$

for $m = 1,2, \ldots, M$ and $r = 1,2, \ldots, R$. From Eq. (12) the higher-order stress resultants are:

$$\begin{aligned} M_1^m &= I_{11}^{mp}\chi_{1,1}^{p} + I_{12}^{mp}\chi_{2,2}^{p} + I_{16}^{mp}(\chi_{1,2}^{p} + \chi_{2,1}^{p}) + F_{13}^{mr}\chi_3^r \\ M_6^m &= I_{12}^{mp}(\chi_{1,2}^{p} + \chi_{2,1}^{p}) + I_{16}^{mp}\chi_{1,1}^{p} + I_{26}^{mp}\chi_{2,2}^{p} + F_{36}^{mr}\chi_3^r \\ M_2^m &= I_{22}^{mp}\chi_{2,2}^{p} + I_{12}^{mp}\chi_{1,1}^{p} + I_{26}^{mp}(\chi_{1,2}^{p} + \chi_{2,1}^{p}) + F_{23}^{mr}\chi_3^r \\ Q_1^r &= G_{55}^{mr}\chi_1^m + G_{45}^{mr}\chi_2^m + H_{55}^{rs}\chi_{3,1}^{s} + H_{45}^{rs}\chi_{3,2}^{s} \\ Q_2^r &= G_{44}^{mr}\chi_2^m + G_{45}^{mr}\chi_1^m + H_{44}^{rs}\chi_{3,2}^{s} + H_{45}^{rs}\chi_{3,1}^{s}. \end{aligned} \quad (35)$$

The Navier approach can be used to find the three-dimensional solution for antisymmetric angle-ply, simply-supported rectangular plates, subjected to transverse loadings equally applied at the top and bottom of the plate; that is, we assume $\tilde{q}_t = \tilde{q}_b = \tilde{q}/2$ in the Fourier expansion (27). Furthermore, we set $M = R = 2$ in the displacement field (3) and postulate ψ_1^1, ψ_2^1, ψ_3^1 and ψ_1^2, ψ_2^2, ψ_3^2 to be odd and even functions of x_3, respectively. Then, since C_{16}, C_{26}, C_{36}, C_{45} for antisymmetric angle-ply laminates are odd functions of x_3, the following expansions are assumed:

Downloaded 03 May 2010 to 171.66.16.247. Redistribution subject to ASME license or copyright; see http://www.asme.org/terms/Terms_Use.cfm

$$\chi_1^1 = a_1^1 \cos \alpha x_1 \sin \beta x_2 \; \chi_1^2 = a_1^2 \sin \alpha x_1 \cos \beta x_2$$
$$\chi_2^1 = a_2^1 \sin \alpha x_1 \cos \beta x_2; \; \chi_2^2 = a_2^2 \cos \alpha x_1 \sin \beta x_2$$
$$\chi_3^1 = a_3^1 \cos \alpha x_1 \cos \beta x_2; \; \chi_3^2 = a_3^2 \sin \alpha x_1 \sin \beta x_2. \quad (36)$$

The functions satisfy the governing equations (34) and the boundary conditions (10) in the following form:

$$\text{At } x_1 = 0, a\text{: } M_1^1 = 0, \; \chi_1^2 = 0, \; \chi_2^1 = 0, \; M_2^2 = 0, \; M_3^1 = 0, \; \chi_3^2 = 0$$
$$\text{At } x_2 = 0, b\text{: } x_1^1 = 0, \; M_1^2 = 0, \; M_2^1 = 0, \; \chi_2^2 = 0, \; M_3^1 = 0, \; \chi_3^2 = 0 \quad (37)$$

Hence, the tangential displacements of the midplane are admissible, but the normal are not. As in the previous case, no iterative solution is required and we can assume $a_i^j = 1$ and solve problem (16) in order to obtain the through-the-thickness displacement functions ψ. In this case the eigenvalue problem (24) takes the form:

$$(\mathbf{A} + \mathbf{B}\lambda - \mathbf{D}\lambda^2)\mathbf{c} = 0. \quad (38)$$

The nonvanishing components of symmetric 6 × 6 matrices **A**, **B**, **D** are:

$$A_{11} = A_{22} = C_{11}\alpha^2 + C_{66}\beta^2 \quad A_{33} = A_{44} = C_{22}\beta^2 + C_{66}\alpha^2$$
$$A_{55} = A_{66} = -C_{55}\alpha^2 - C_{44}\beta^2$$
$$A_{12} = 2C_{16}\alpha\beta \quad A_{13} = A_{24} = (C_{12} + C_{66})\alpha\beta$$
$$A_{34} = 2C_{26}\alpha\beta \quad A_{56} = 2C_{45}\alpha\beta$$
$$B_{15} = -B_{26} = (C_{36} + C_{45})\beta \quad B_{35} = -B_{46} = (C_{36} + C_{45})\alpha$$
$$B_{25} = -B_{16} = (C_{13} + C_{55})\alpha \quad B_{45} = -B_{36} = (C_{23} + C_{44})\beta$$
$$D_{11} = D_{22} = C_{55} \quad D_{33} = D_{44} = C_{44}$$
$$D_{55} = D_{66} = C_{33}. \quad (39)$$

The interface and boundary conditions (18)–(20) yield the following relations:

$$[\psi_1^1] = [\psi_1^2] = [\psi_2^1] = [\psi_2^2] = [\psi_3^1] = [\psi_3^2] = 0 \quad (40)$$

$$[C_{55}(\psi_{1,3}^1 + \alpha\psi_3^2) + C_{45}(\psi_{2,3}^2 - \beta\psi_3^1)]$$
$$= [C_{55}(\psi_{1,3}^2 - \alpha\psi_3^1) + C_{45}(\psi_{2,3}^1 + \beta\psi_3^2)] = 0$$
$$[C_{13}\alpha\psi_1^2 + C_{23}\beta\psi_2^2 + C_{33}\psi_{3,3}^1 + C_{36}(\beta\psi_1^1 + \alpha\psi_2^1)] = 0$$
$$[-C_{13}\alpha\psi_1^1 - C_{23}\beta\psi_2^1 + C_{33}\psi_{3,3}^2 - C_{36}(\beta\psi_1^2 + \alpha\psi_2^2)] = 0 \quad (41)$$

and

$$C_{55}(\psi_{1,3}^1 + \alpha\psi_3^2) + C_{45}(\psi_{2,3}^2 - \beta\psi_3^1)\Big|_{x_{3b}, x_{3t}}$$
$$= C_{55}(\psi_{1,3}^2 - \alpha\psi_3^1) + C_{45}(\psi_{2,3}^1 + \beta\psi_3^2)\Big|_{x_{3b}, x_{3t}} = 0$$

$$C_{44}(\psi_{2,3}^1 + \beta\psi_3) + C_{45}(\psi_{1,3}^2 - \psi_3^1)\Big|_{x_{3b}, x_{3t}}$$
$$= C_{44}(\psi_{2,3}^2 - \beta\psi_3^1) + C_{45}(\psi_{1,3}^1 + \alpha\psi_3^2)\Big|_{x_{3b}, x_{3t}} = 0$$

$$C_{13}\alpha\psi_1^2 + C_{23}\beta\psi_2^2 + C_{33}\psi_{3,3}^1 + C_{36}(\beta\psi_1^1 + \alpha\psi_2^1)\Big|_{x_{3b}, x_{3t}}$$
$$= -C_{13}\alpha\psi_1^1 - C_{23}\beta\psi_2^1 + C_{33}\psi_{3,3}^2 - C_{36}(\beta\psi_1^2 + \alpha\psi_2^2) \mp \tilde{q}/2\Big|_{x_{3b}, x_{3t}} = 0. \quad (42)$$

It is easy to verify that the relations reported above confirm the initial assumption of ψ_1^1, ψ_2^1, ψ_3^1 and ψ_1^2, ψ_2^2, ψ_3^2 are odd and even functions, respectively, and they assure pointwise continuity of the stress vector at the interface, and at the top and bottom over the whole plate. Finally, we point out that the eigenvalue problem (38) can be obtained in an alternative way by writing, for the ith layer, the three-dimensional equilibrium equations in terms of displacements functions (36), collecting the terms varying with $\cos \alpha x_1 \sin \beta x_2$ and $\sin \alpha x_1 \cos \beta x_2$, and then assuming the form (23) for the through-the-thickness displacements ψ's.

5 Numerical Results

Since three-dimensional elasticity solutions for cross-ply lamination schemes are available in the literature, we restrict our attention to antisymmetric angle-ply rectangular plates under sinusoidal loading (i.e., $n = 1$ in Eq. (27)). In all the examples, the layer elastic coefficients are those of a unidirectional fiber-reinforced composite:

$$E_L = 25\ 10^6 \text{ psi (174.6 GPa)} \quad E_T = 10^6 \text{ psi (7 GPa)}$$
$$G_{LT} = 0.5\ 10^6 \text{ psi (3.5 GPa)} \quad G_{TT} = 0.2 \times \text{psi (1.4 GPa)}$$
$$\nu_{LT} = \nu_{TT} = 0.25 \quad (43)$$

where subscripts L and T refers to the fiber direction and transverse direction, respectively. Two sets of laminates are considered here:

(1) two-layer angle-ply $(-\theta, +\theta)$ laminates with layers of equal thicknesses $(h/2)$.
(2) four-layer angle-ply $(-\theta, +\theta, -\theta, +\theta)$ laminates with layers of equal thickness $(h/4)$.

Here the angle θ is measured from the positive x_1-axis. Nondimensionalized deflections and stresses are presented according to the following definitions:

$$\{\bar{u}_1, \bar{u}_2\} = \frac{\{u_1, u_2\} E_T \times 10^2}{\tilde{q} h S^3}; \; \bar{u}_3 = \frac{10^2 E_T u_3}{\tilde{q} h S^4}$$
$$\{\bar{\sigma}_1, \bar{\sigma}_2, \bar{\sigma}_6\} = \frac{\{\sigma_1, \sigma_2, \sigma_6\}(a/2, b/2)}{\tilde{q} S^2}; \; \{\bar{\sigma}_4, \bar{\sigma}_5\} = \frac{\{\sigma_4, \sigma_5\}(a/2, 0)}{\tilde{q} S} \quad (44)$$

where $S = a/h$. Table 1 contains the maximum values of stress components and the transverse deflection $\bar{u}_3$ of the midplane for square and rectangular plates for different lamination

Table 1 Comparison of three-dimensional elasticity results with the first-order plate theory results (two layer plates)

θ	$\bar{u}_3(\frac{a}{2},\frac{b}{2})$	$\bar{\sigma}_1(\frac{a}{2},\frac{b}{2})$	$\bar{\sigma}_2(\frac{a}{2},\frac{b}{2})$	$\bar{\sigma}_6(\frac{a}{2},\frac{b}{2})$	$\bar{\sigma}_4(\frac{a}{2},0)$	$\bar{\sigma}_5(\frac{a}{2},0)$	$\bar{\sigma}_4(0,\frac{b}{2})$	$\bar{\sigma}_5(0,\frac{b}{2})$
				3D ELASTICITY				
				a = b; S = 4				
15°	1.7059	0.6645	0.1135	0.1489	0.0960	0.0841	0.0399	0.3145
30°	1.7297	0.4945	0.2089	0.2335	0.1546	0.13627	0.0868	0.2561
45°	1.6887	0.3092	0.3092	0.2327	0.2062	0.1239	0.1239	0.2062
				a = b ; S = 10				
15°	0.8027	0.5633	0.0806	0.1244	0.8138	0.9911	0.0412	0.3421
30°	0.8568	0.4204	0.1696	0.2018	0.1570	0.1639	0.1002	0.2699
45°	0.8250	0.2594	0.2594	0.2029	0.2154	0.1461	0.1461	0.2154
				3a = b ; S = 4				
15°	2.4903	0.9581	0.0911	0.2018	0.0365	0.0457	0.0591	0.3988
30°	3.4118	0.9282	0.3000	0.4260	0.0960	0.1029	0.1427	0.3885
45°	4.7596	0.7427	0.5943	0.5182	0.1956	0.1369	0.2009	0.3564
				FSDT				
				a = b ; S = 4				
15	1.7638	0.8441	0.1153	0.2322	0.1003	0.1195	0.0445	0.3322
30	1.7724	0.8837	0.3285	0.5006	0.1661	0.1821	0.1132	0.2763
45	1.7403	0.6086	0.6086	0.5793	0.2179	0.1526	0.1526	0.2179
				a = b ; S = 10				
15	0.8073	0.8933	0.1055	0.2450	0.0843	0.1102	0.0458	0.3477
30	0.8584	0.8941	0.3292	0.5058	0.1637	0.1814	0.1136	0.2785
45	0.8284	0.6086	0.6086	0.5793	0.2179	0.1526	0.1526	0.2179
				3a = b ; S = 4				
15	2.5974	1.5631	0.1331	0.4358	0.0412	0.0711	0.0691	0.4119
30	3.4998	1.9439	0.6428	1.0911	0.1097	0.1395	0.1750	0.3993
45	4.8540	1.5723	1.4334	1.4312	0.2045	0.1569	0.2192	0.3637

Downloaded 03 May 2010 to 171.66.16.247. Redistribution subject to ASME license or copyright; see http://www.asme.org/terms/Terms_Use.cfm

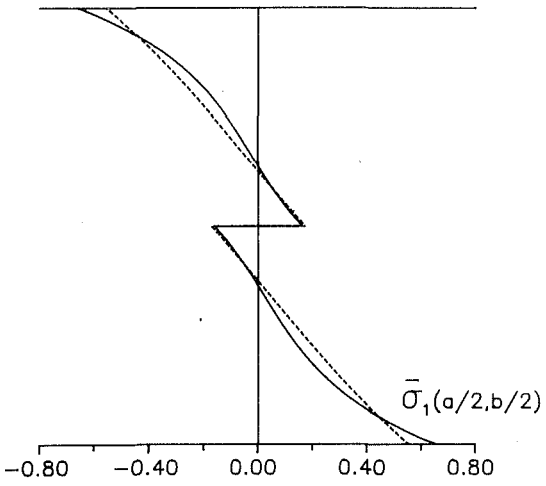


Fig 1(*a*)

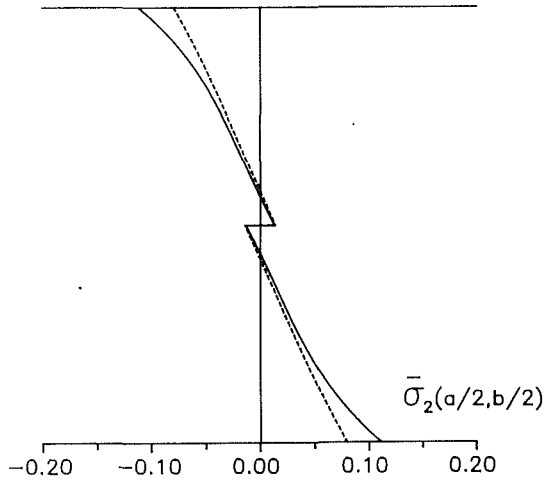


Fig 1(*b*)

Figs. 1(*a*) and 1(*b*) In-plane normal stresses through the thickness of two-layer (− 15/15) laminate for side-to-thickness ratios of $S = 4$ (solid line) and $S = 10$ (dashed line)

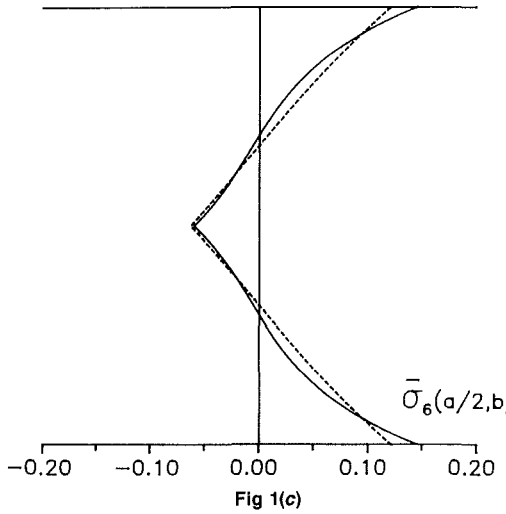


Fig 1(*c*)

Fig. 1(*c*) In-plane shear stress through the thickness of two-layer (− 15/15) laminates for side-to-thickness ratios of $S = 4$ (solid line) and $S = 10$ (dashed line)

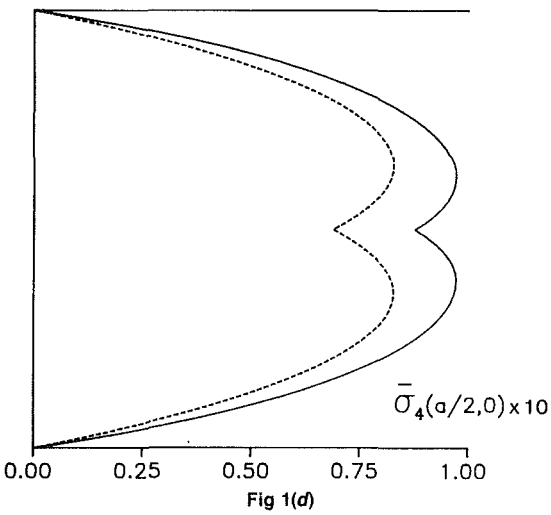


Fig 1(*d*)

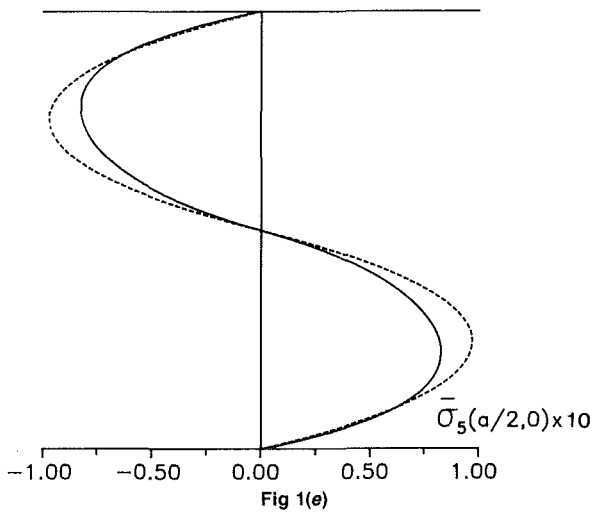


Fig 1(*e*)

Figs. 1(*d*) and 1(*e*) Transverse shear stresses through the thickness of two-layer (− 15/154) laminates for side-to-thickness ratios of $S = 4$ (solid line) and $S = 10$ (dashed line)

Downloaded 03 May 2010 to 171.66.16.247. Redistribution subject to ASME license or copyright; see http://www.asme.org/terms/Terms_Use.cfm

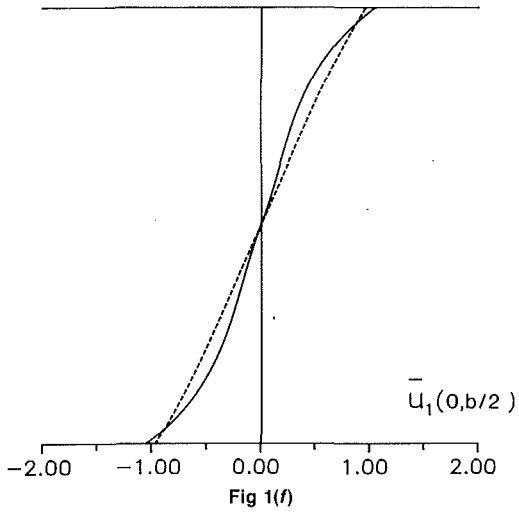


Fig 1(*f*)

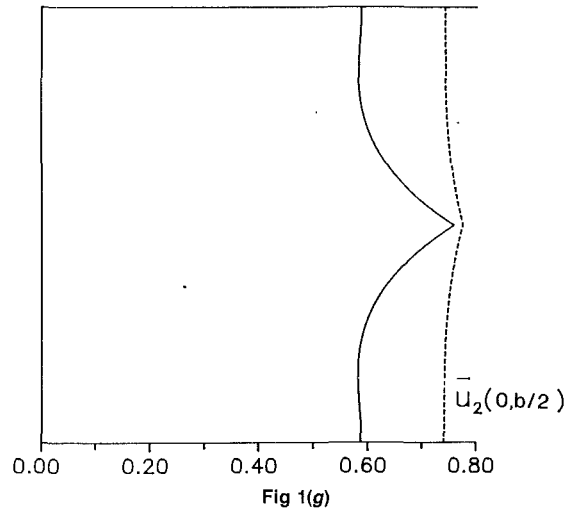


Fig 1(*g*)

Figs. 1(*f*) and 1(*g*) In-plane displacements through the thickness of two-layer (−15/15) laminates for side-to-thickness ratios of $S = 4$ (solid line) and $S = 10$ (dashed line)

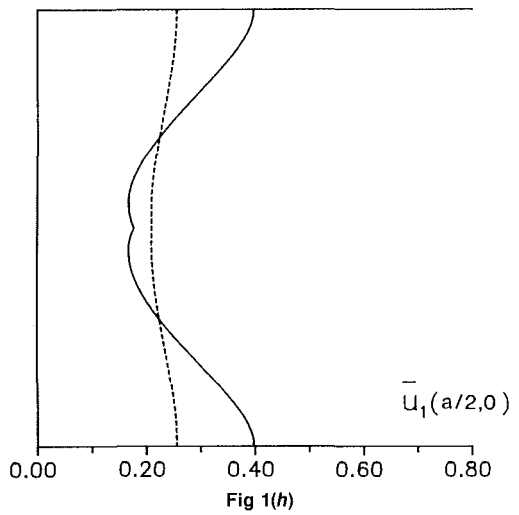


Fig 1(*h*)

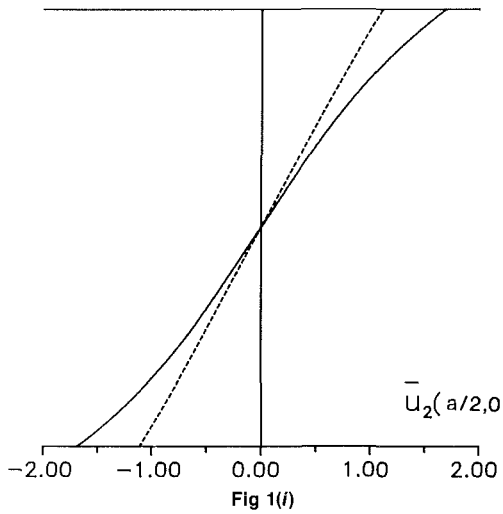


Fig 1(*i*)

Figs. 1(*h*) and 1(*i*) In-plane displacements through the thickness of two-layer (−15/15) laminates for side-to-thickness ratios of $S = 4$ (solid line) and $S = 10$ (dashed line)

schemes. The results are compared with the values obtained from the first-order shear deformation theory (FSDT). For FSDT, shear correction factors $K_1^2 = K_2^2 = 5/6$ are used and the shear stresses are computed from the equilibrium equations. It is interesting to note that the FSDT assumption of linear variation of the displacements through-the-thickness displacements is not valid for the four-layer one.

Stresses and displacements distributions through the thickness are shown in Figs. 1 and 2 for angle ply (−15 deg, +15 deg) and (−30 deg, +30 deg, −30 deg, +30 deg) square plates with span-to-depth ratios $S = 4$ (continuous line) and $S = 10$ (dashed line). For large values of S (side-to-thickness) ratio, i.e., for relatively thin plates, the displacement and stress variations through the thickness are very close to being linear. Thus, the first-order plate theory would be appropriate in those cases.

6 Conclusions

The expansion (3) allows us to obtain approximate solutions for a three-dimensional plate problem with general geometry, boundary conditions, and lamination schemes. The solution can be improved by increasing the number of parameters M and R in the expansion (3). However, in general, it is not possible to achieve the exact three-dimensional solution by employing a finite number of coordinate functions. A procedure to obtain approximate solutions is presented in Sections 2 and 3.

In Section 4 we studied the simplest case of cross-ply and antisymmetric angle-ply rectangular plates. If we expand the applied load in double Fourier series (27) and if the boundary condition of cross-ply (Eq. (29)) and angle-ply (Eq. (37)) are to be satisfied, no boundary layer phenomena occurs; hence, in this case the exact three-dimensional solution coincides with the interior domain solution and, consequently, can be obtained by making use of a finite number of coordinate functions. Moreover, the solution can be achieved without the iterative procedure. It can be proved that the expansion (3) with $M = R = 1$ for cross-ply rectangular plates with the χ's are defined by Eqs. (28), the ψ's defined by Eqs. (23), the λ's are the eigenvalues of problem (30), and the interface conditions (31)–(33) are imposed, yield the exact three-dimensional solution for this problem. In fact, this solution satisfies the three-dimensional equilibrium equations in terms of displace-

Downloaded 03 May 2010 to 171.66.16.247. Redistribution subject to ASME license or copyright; see http://www.asme.org/terms/Terms_Use.cfm

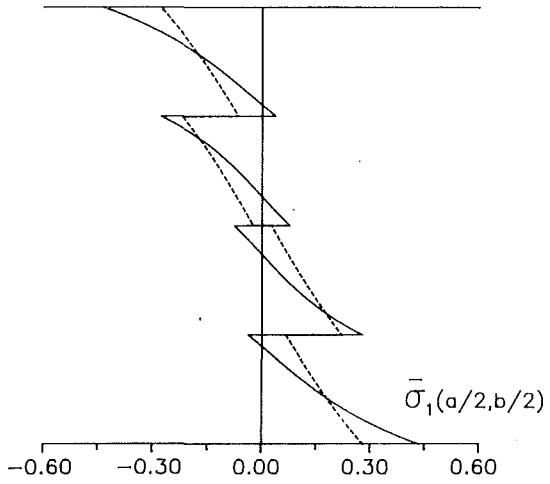


Fig 2(*a*)

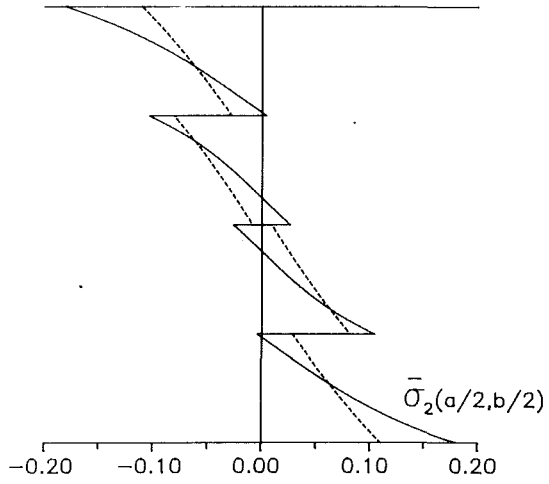


Fig 2(*b*)

Figs. 2(*a*) and 2(*b*) In-plane normal stresses through the thickness of four-layer (−30/30/−30/30) laminates for side-to-thickness ratios of $S = 4$ (solid line) and $S = 10$ (dashed line)

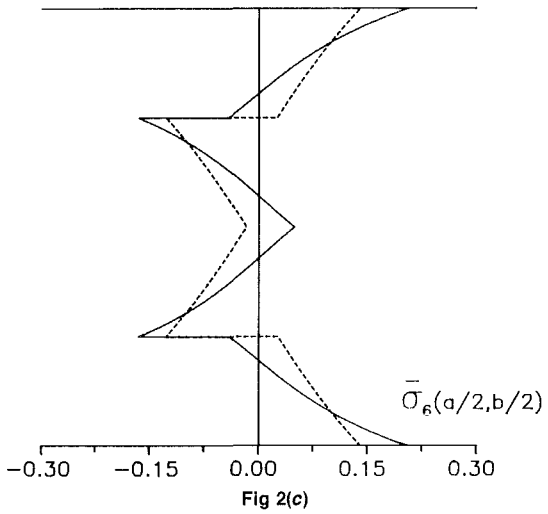


Fig 2(*c*)

Fig. 2(*c*) In-plane shear stress through the thickness of four-layer (−30/30/−30/30) laminates for side-to-thickness ratios of $S = 4$ (solid line) and $S = 10$ (dashed line)

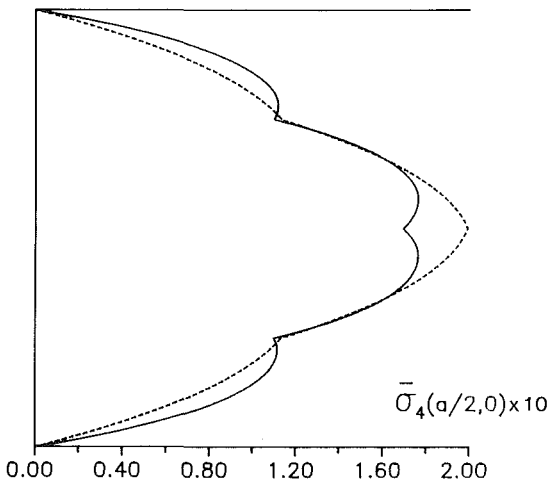


Fig 2(*d*)

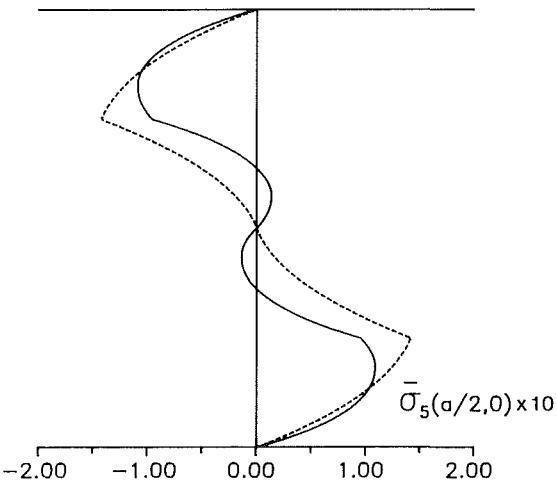


Fig 2(*e*)

Figs. 2(*d*) and 2(*e*) Transverse shear stresses through the thickness of four-layer (−30/30/−30/30) laminates for side-to-thickness ratios of $S = 4$ (solid line) and $S = 10$ (dashed line)

Downloaded 03 May 2010 to 171.66.16.247. Redistribution subject to ASME license or copyright; see http://www.asme.org/terms/Terms_Use.cfm

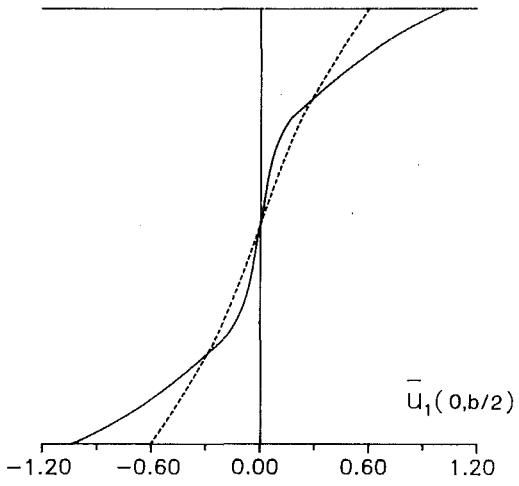


Fig 2(*f*)

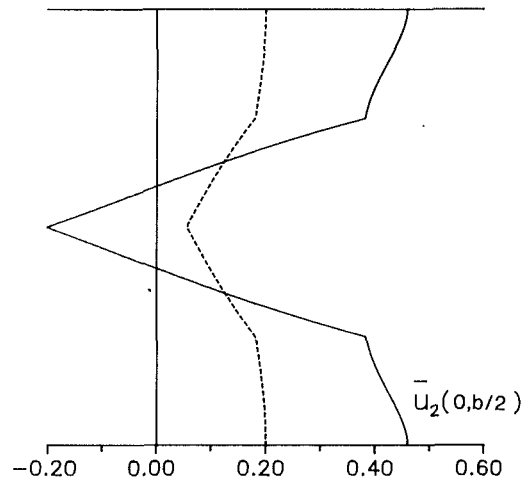


Fig 2(*g*)

Figs. 2(*f*) and 2(*g*) In-plane displacements through the thickness of four-layer (−30/30/−30/30) laminates for side-to-thickness ratios of $S = 4$ (solid line) and $S = 10$ (dashed line)

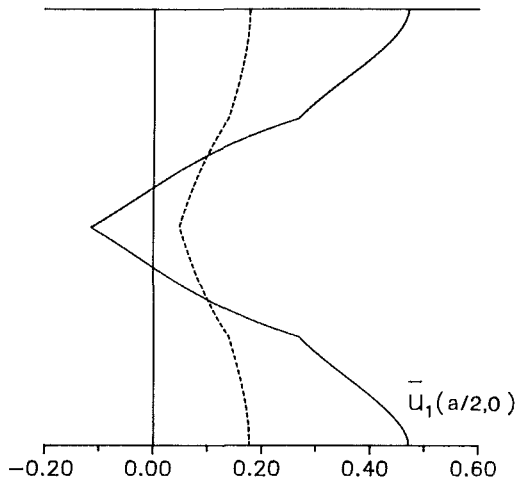


Fig 2(*h*)

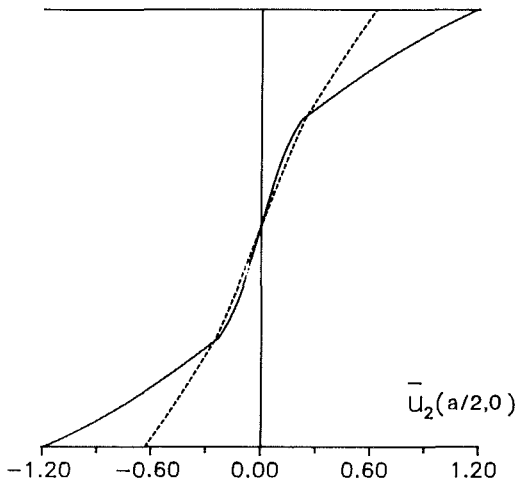


Fig 2(*i*)

Figs. 2(*h*) and 2(*i*) In-plane displacements through the thickness of four-layer (−30/30/−30/30) laminates for side-to-thickness ratios of $S = 4$ (solid line) and $S = 10$ (dashed line)

ments and satisfies the continuity of the stress vector at the interfaces.

Analogously, it can be proved that the solution presented for simply-supported antisymmetric angle-ply laminates with $M = R = 2$ represents the exact three-dimensional solution. For more general problems which don't admit exact closed-form solutions, the Pagano-like procedure cannot be used; on the contrary, our procedure yields variationally consistent approximate solutions that can be improved by increasing the number of coordinate functions.

In the simpler case of bending of transversely rigid beams, a similar procedure is used to obtain approximate solutions in the presence of clamped or free edges. By using a very low number of coordinate functions (2 or 3) in the expansion, very accurate stress fields were obtained even in the boundary layer, at a very small distance from the ends. The procedure presented here can be viewed as an "alternative" Kantorovich method; in fact, the problem of solving the partial differential equations (with discontinuous coefficients at the interfaces) which can be derived by imposing $\delta\Pi = 0$ (where Π is expressed in Eq. (6)) is reduced to a sequence of partial differential equations in terms of the χ's and of ordinary differential equations in the thickness coordinates ψ's. It is well known that the convergence of the Kantorovich method is very good and very few functions are usually required.

The three-dimensional elasticity solutions developed here for general anisotropic laminated plates, with specialization to simply-supported cross-ply and antisymmetric angle-ply rectangular plates, are important because they can be used to study the behavior of different types of laminated plates. The three-dimensional elasticity solutions presented here for angle-ply laminates can also serve as reference for approximate solutions developed by numerical methods.

Acknowledgments

The first author gratefully acknowledges the financial support of the Italian Ministry of University Scientific and Technological Research (MURST) and of the National Council of Research (CNR). The second author acknowledges the support of the research by NASA Langley Research Center through Grant NAG-1-1030.

References

Barbero, E. J., Reddy, J. N., and Teply, J. L., 1990, "An Accurate Deter-

Downloaded 03 May 2010 to 171.66.16.247. Redistribution subject to ASME license or copyright; see http://www.asme.org/terms/Terms_Use.cfm

mination of Stresses in Thick Laminates Using a Generalized Plate Theory," *Int. J. Num. Meth. Engng.*, Vol. 29, pp. 1–14.

Choi, I., and Horgan, C. O., 1978, "Saint-Venant End Effects for Plane Deformation of Sandwich Strips," *Int. J. Solids Struct.*, Vol. 14, pp. 187–195.

Disciuva, M., 1987, "An Improved Shear-Deformation Theory for Moderately Thick Multilayered Anisotropic Shells and Plates," ASME JOURNAL OF APPLIED MECHANICS, Vol. 54, pp. 589–596.

Gregory, R. D., and Gladwell, I., 1982, "The Cantilever Beam Under Tension, Bending or Flexure at Infinity," *J. Elasticity*, Vol. 12, pp. 317–343.

Green, A. E., and Naghdi, P. M., 1982, "A Theory of Laminated Composite Plates," *IMA J. Appl. Math.*, Vol. 29, pp. 1–23.

Hinrichsen, R. L., and Palazotto, A. N., 1986, "Nonlinear Finite Element Analysis of Thick Composite Plates using Cubic Spline Functions," *AIAA J.*, Vol. 24, pp. 1836–1842.

Krisna Murty, A. V., 1977,."Higher Order Theory for Vibration of Thick Plates," *AIAA J.*, Vol. 15, pp. 1823–24.

Librescu, L., 1975, *Elastostatics and Kinetics of Anisotropic and Heterogeneous Shell-Type Structures*, Noordhoff I. P., Leyden.

Noor, A. K., and Burton, W. S., 1990, "Three-Dimensional Solutions for Antisymmetrically Laminated Anisotropic Plates," ASME, JOURNAL OF APPLIED MECHANICS, Vol. 57, pp. 182–188.

Pagano, N. J., 1970, "Exact Solutions for Rectangular Bidirectional Composite and Sandwich Plates," *J. Comp. Mat.*, Vol. 4, pp. 20–34.

Pagano, N. J., and Hatfield, S. J., 1972, "Elastic Behavior of Multilayered Bidirectional Composites," *AIAA J.*, Vol. 10, pp. 931–933.

Reddy, J. N., 1984a, *Energy and Variational Methods in Applied Mechanics*, John Wiley and Sons, New York.

Reddy, J. N., 1984b, "A Simple Higher-Order Theory for Laminated Composite Plates," ASME JOURNAL OF APPLIED MECHANICS, Vol. 51, pp. 745–752.

Reddy, J. N., 1987a, "A Small Strain and Moderate Rotation Theory of Laminated Anisotropic Plates," ASME JOURNAL OF APPLIED MECHANICS, Vol. 54, pp. 623–626.

Reddy, J. N., 1987b, "A Generalization of Two-Dimensional Theories of Laminated Composite Plates," *Comm. Appl. Num. Meth.*, Vol. 3, pp. 173–180.

Reddy, J. N., 1989a, "On Refined Computational Models of Composite Laminates," *Int. J. Num. Meth. Engng.*, Vol. 27, pp. 361–382.

Reddy, J. N., 1989b, "On the Generalization of Displacement-Based Laminate Theories," *Applied Mechanics Reviews*, ASME, New York, Vol. 42, No. 11, pp. 5213–5222.

Reddy, J. N,. 1990a, "A General Third-Order Nonlinear Theory of Plates with Moderate Thickness," *Int. J. Nonlin. Mech.*, Vol. 25, pp. 677–686.

Reddy, J. N., 1990b, "On Redefined Theories of Composite Laminates," *Meccanica*, Vol. 25, No. 4, pp. 230–238.

Savoia, M., Laudiero, F., and Tralli, A., 1990, "A Refined Model for Laminated Composite Beams with Transversely Rigid Cross Sections," *Int. Congress on New Developments in Structural Mechanics*, July 4–6, Catania.

Savoia, M., Tralli, A., and Laudiero, F., 1990, "An Iterative Variational Technique for the Analysis of Multilayered Beams with Restrained End Sections," *Meccanica*, in review.

Srinivas, S., 1973, "A Refined Analysis of Composite Laminates," *J. Sound Vibr.* Vol. 30, pp. 495–507.

Srinivas, S., and Rao, A. K., 1970, "Bending, Vibration and Buckling of Simply Supported Thick Orthotropic Rectangular Plates and Laminates," *Int. J. Solids Struct.*, Vol. 6, pp. 1463–1481.

Srinivas, S., and Rao, A. K., 1971, "A Three-Dimensional Solution for Plates and Laminates," *J. Frank. Inst.*, Vol. 291, pp. 469–481.

Villaggio, P., 1977, *Qualitative Methods in Elasticity*, Noordhoff, I. P., Leyden.

Whitney, J. M., and Pagano, N. J., 1970, "Shear Deformation in Heterogeneous Anisotropic Plates," ASME JOURNAL OF APPLIED MECHANICS, Vol. 37, pp. 1031–1036.

Downloaded 03 May 2010 to 171.66.16.247. Redistribution subject to ASME license or copyright; see http://www.asme.org/terms/Terms_Use.cfm

Modification of the Shear Lag Analysis for Determination of Elastic Modulus of Short-Fiber (or Whisker) Reinforced Metal Matrix Composites

S. V. Nair
Assoc. Professor.

H. G. Kim[1]
Mem. ASME

Department of Mechanical Engineering,
University of Massachusetts,
Amherst, MA 01003

A major shortcoming of the original shear lag analysis is its inability to provide sufficiently accurate strengthening predictions when the fiber aspect ratio is small. This is due to its neglect of stress transfer across fiber ends and the stress concentrations that exist in the matrix regions near fiber ends. In this paper, a straightforward, yet rigorous, modification of the original shear lag analysis is presented by taking fiber end effects into account and to result in fully closed-form solutions. It is demonstrated that the modification not only results in a correct prediction of the modulus increases in the small aspect ratio regime when compared to finite element results, but is also able to correctly predict the values of interfacial shear stresses and local stress variations in the matrix and fiber.

1 Introduction

One of the earliest attempts to explain the reinforcing effect of fibers was described by Cox (1952), and is now referred to as the shear lag model which considers long, straight, discontinuous fibers completely embedded in a continuous matrix. The Cox model was elegant in its simplicity and provides accurate estimates of the elastic modulus increases due to the fibers when the fiber aspect ratio is sufficiently large. Furthermore, the model is also able to provide the variation of internal stresses in both the fiber and matrix and a description of the fiber/matrix interfacial shear stresses in the elastic deformation regime. However, a major shortcoming of the model is its inability to provide sufficiently accurate predictions when the fiber aspect ratio is small. The predicted modulus by the shear lag model is substantially smaller than the experimentally observed modulus increases in this regime. This is the regime applicable to major current short-fiber or whisker-reinforced composites. For example, in SiC whisker-reinforced aluminum alloys the average aspect ratio is only on the order of four (Arsenault, 1984; Nair et al., 1985; Nutt and Needleman, 1987) for which case the original shear lag model does not provide adequate descriptions of the stiffening effect of whiskers as discussed by Taya and Arsenault (1987). Recently, Kim and Nair (1990) presented results showing that the underestimation of composite modulus by the shear lag model is its neglect of normal stress transfer at fiber ends and the stress intensification in the matrix region between the fibers.

It is the purpose of this paper to provide a straightforward yet rigorous modification of the original shear lag analysis so as to retain its accuracy at small reinforcement aspect ratio values by taking fiber end effects into account. Starting from first principles and using equilibrium and continuity conditions, closed-form expressions are provided for the normal stresses at fiber ends and the enhanced local stresses in the matrix end regions. We will demonstrate that the modification not only results in a correct prediction of the modulus increases in the small aspect ratio regime when compared to finite element results, but is also able to correctly predict the values of interfacial shear stresses and local stress variations in the matrix and fiber. These local stress values are critical to the analysis of fracture micromechanisms in metal matrix composites (Murdeshwar, 1989).

Subsequent to the Cox model, rigorous elasticity models based on variational (Hashin and Shtrikman, 1962, Hashin and Shtrikman, 1963) and self-consistent methods (Hill, 1965a) were developed in order to predict the elastic moduli increases in the small aspect ratio regime. The variational method originally developed by Paul (1960) provides proper bounds to the elastic moduli increases but not the local stress values in the fiber and surrounding matrix. The self-consistent model was first developed by Hershey (1954) and Kröner (1958) as a means to model the behavior of polycrystalline materials and an extension of the self-consistent scheme to multiphase media was

[1]Presently, Post Doctoral Research Assoc., Penn State University, Department of Engineering Science and Mechanics, University Park, PA 16802.

Contributed by the ASME Applied Mechanics Division of THE AMERICAN SOCIETY OF MECHANICAL ENGINEERS for presentation at the Winter Annual Meeting, Atlanta, Ga., Dec. 1-6, 1991.

Discussion on this paper should be addressed to the Technical Editor, Prof. Leon M. Keer, The Technological Institute, Northwestern University, Evanston, IL 60208, and will be accepted until two months after final publication of the paper itself in the JOURNAL OF APPLIED MECHANICS. Manuscript received by the ASME Applied Mechanics Division, June 29, 1990; final revision, Nov. 21, 1990.

Paper No. 91-WA/APM-44.

Copyright © 1992 by ASME
Downloaded 03 May 2010 to 171.66.16.247. Redistribution subject to ASME license or copyright; see http://www.asme.org/terms/Terms_Use.cfm

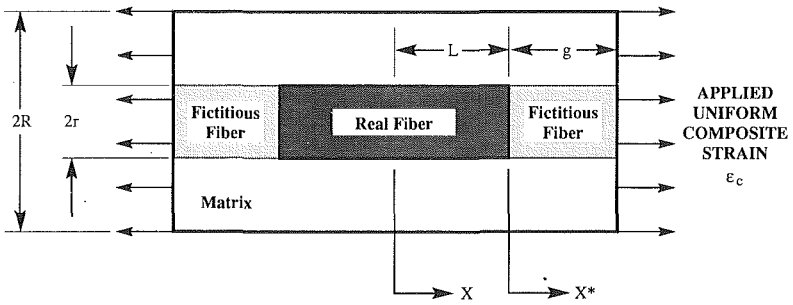


Fig. 1 Schematic of composite unit cell containing a single fiber in a cylindrical matrix volume

given by Hill (1965b) and Budiansky (1965). This method provides approximate predictions of composite elastic response that explicitly account for phase geometry. Eshelby's ellipsoidal inclusion method (Eshelby, 1957) is a basic solution of this type and has also been successfully applied to predict both the modulus and yield strength of short fiber composites (Taya and Arsenault, 1987). However, this model is restricted to an ellipsoidal reinforcement geometry for which case the internal reinforcement stress is predicted to be uniform. It is well known that for the case of rod-like fiber geometries, uniform reinforcement stresses are obtained only at sufficiently large aspect ratios. The uniform internal reinforcement stress results from the physical nature of the ellipsoidal geometry for which case both normal and shear load transfer to the reinforcement occurs along the entire inclusion/matrix boundary. For an axially cylindrical geometry, however, with the load applied in the axial direction, normal stress transfer occurs only at the fiber end and stress transfer is purely of a shear nature along the fiber length. This shear stress transfer gives rise to the known variation of the fiber axial stresses (Piggott, 1980). Accordingly, the shear lag approach is physically more realistic for fiber geometries provided fiber end effects can be rigorously accounted for.

There have been limited previous attempts to modify the shear lag approach. Muki and Sternberg (1969) and Sternberg and Muki (1970) used a shear lag approach in a more refined manner using integro-differential equations and have calculated the local stresses inside the fiber. However, this model assumed that the fiber center stress is given by the rule of mixture equation applicable strictly only to the long fiber case. Furthermore, Sternberg's results cannot be applied to obtain expressions for the matrix stress intensification in the fiber end region which provides a significant contribution to the stiffness. Recently, Nardone and Prewo (1986) and Nardone (1987) attempted to modify the shear lag model by assuming that the fiber end stress was equal to the matrix yield stress and further that the matrix average stress was also equal to the matrix yield stress. This made possible an approximate estimate of the macroscopic composite yield strength increase, but this approach is clearly not applicable to the purely elastic regime wherein the elastic modulus increase is to be calculated.

Taya and Arsenault (1989) attempted to modify the original shear lag approach by assuming that the fiber end stress was equal to the average matrix stress, i.e., the stress concentration at the fiber ends were ignored. The prediction of this limited modification is compared to that of the rigorous model presented below. More recently, Kim and Nair (1990) modified the shear lag analysis by using FEA (finite element analysis) to provide the fiber end normal stresses. Their results of the predicted modulus increases in short-fiber-reinforced alloys using the closed-form modified shear lag equations showed a good agreement with FEA results as well as experimental data. While this work clearly demonstrates that shear lag solutions have applicability to short-fiber composite provided fiber end effects are accounted for, the model does not calculate the fiber end stresses from first principles and relies instead on FEA.

Our approach in this paper involves replacing the matrix region between fiber ends with a fictitious fiber having the same elastic properties as the matrix and developing conventional shear lag solutions for both the real and "fictitious" fiber. Suitable interfacing of these solutions provides the needed results for the composite modulus and the local stress and strain values. The model is therefore entirely closed form in nature and does not rely on FEA for any parametric values. An axisymmetric finite element model is used to assess the predictions of the resulting analytical model derived in this paper.

2 Model Development

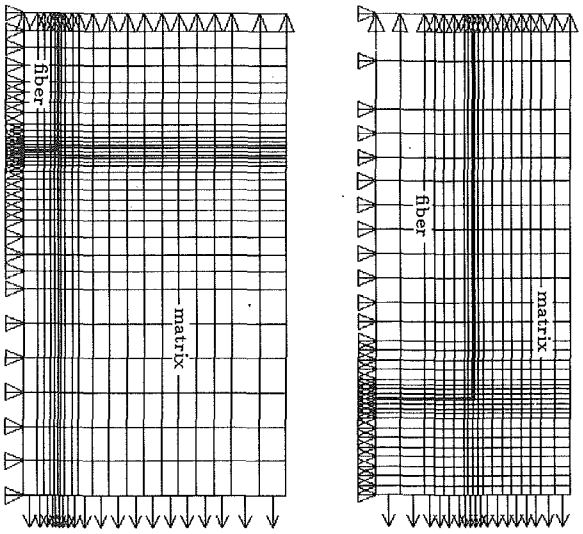
2.1 Closed-Form Solutions. In the following derivation of the MSL (modified shear lag) model, the short fibers are considered to be uniaxially aligned with the stress applied on the axial direction of the fibers. As in the SL (original shear lag) model (Cox, 1952), the fiber/matrix bond is assumed to be large and no debonding is allowed for in keeping with the actual situation in many metal matrix composites (Arsenault, 1983, Nutt and Needleman, 1987). Further, no plastic yielding is allowed, that is, both matrix and fiber deform in a purely elastic manner. Finally, in this treatment, residual stress effects are also neglected.

The composite unit cell showing the short fiber embedded in a continuous matrix is shown in Fig. 1. The actual, or real, fiber has a radius r, and length $2L$. On either end of the fiber is postulated a fictitious fiber also of diameter $2r$ but a length g = half the spacing between fiber ends in the composite. The outer surface of the unit cell can be said to have a hexagonal contour, however, the exact shape is not critical in this model. We treat the unit cell as an equivalent cylinder with radius, R. The spatial variable for the real fiber is x, with the coordinate origin at the fiber center, whereas the spatial variable for the fictitious fiber is x^* with the coordinate origin at the fiber end. The different origins are necessary because, as we shall show, the governing differential equations in the region of the real and fictitious fiber are different and consequently there can be no overlap of the x and x^* domains. The two domains are in contact at $x = L$, or $x^* = 0$, at which point proper boundary conditions need to be applied. Note, in the following, that all variables associated with the fictitious fiber will be denoted with a superscript $*$.

At the far end of the unit cell, that is at the surface $x^* = g$, is applied a uniform constant composite strain, ϵ_c. Under these conditions, as shown in detail in the SL model (Piggott, 1980), the governing equation for the fiber stress, σ_f, and the fiber/matrix interfacial shear stress, τ_s, can be given by

$$\frac{d^2\sigma_f}{dx^2} = \frac{n^2}{r^2}(\sigma_f - E_f\epsilon_c) \tag{1}$$

Downloaded 03 May 2010 to 171.66.16.247. Redistribution subject to ASME license or copyright; see http://www.asme.org/terms/Terms_Use.cfm



(a) (b)

Fig. 2 Axisymmetric finite element meshes of unit cell (RVE) at $s=4$ in case of (*a*) quasi-infinite matrix ($V_f=.005$) and (*b*) finite concentration ($V_f=.2$)

$$\tau_s = -\frac{r}{2}\frac{d\sigma_f}{dx} \tag{2}$$

where

$$n^2 = \frac{E_m}{E_f(1+\nu_m)\ln(R/r)}. \tag{3}$$

E_m and E_f are Young's moduli of the matrix and fiber, respectively, V_f is the volume fraction of fibers, and ν_m is the Poisson's ratio of the matrix. As mentioned, R is the unit cell radius. Equation (1) has the solution

$$\sigma_f = E_f\epsilon_c + A\sinh(nx/r) + B\cosh(nx/r). \tag{4}$$

Recognizing that σ_f must be symmetric about $x=0$, gives $A=0$, so that the expression for σ_f is

$$\sigma_f = E_f\epsilon_c + B\cosh(nx/r). \tag{5}$$

The interfacial shear stress is from Eq. (2)

$$\tau_s = -\frac{n}{2}B\sinh(nx/r). \tag{6}$$

Here, B is an unknown constant which needs to be determined in concert with the solution for the fictitious fiber.

By analogy with that for the real fiber, it follows that the governing equation for the fictitious fiber is

$$\frac{d^2\sigma_f^*}{dx^{*2}} = \frac{n^{*2}}{r^2}(\sigma_f^* - E_f^*\epsilon_c). \tag{7}$$

Here, since $E_f^* = E_m$, one obtains

$$n^{*2} = \frac{1}{(1+\nu_m)\ln(R/r)}, \tag{8}$$

and the solution for the fictitious fiber, or the matrix region between fiber ends, is

$$\sigma_f^* = E_m\epsilon_c + A^*\sinh(n^*x^*/r) + B^*\cosh(n^*x^*/r). \tag{9}$$

The interfacial shear stress in this region, τ_s^*, is given as before by

$$\tau_s^* = -\frac{n^*}{2}[A^*\cosh(n^*x^*/r) + B^*\sinh(n^*x^*/r)]. \tag{10}$$

Here, $A^* \neq 0$ since the end regions do not possess the symmetry of the fiber. The three unknown constants in Eq. (4) and Eq. (8) are B, A^*, and B^*, which can be simply determined using the following boundary conditions:

$$\sigma_f = \sigma_f^* \text{ at } x = L \text{ or } x^* = 0 \tag{11}$$

$$\frac{d\sigma_f}{dx} = \frac{d\sigma_f^*}{dx^*} \text{ at } x = L \text{ or } x^* = 0 \tag{12}$$

and

$$\tau_s^* = 0 \text{ at } x^* = g. \tag{13}$$

The first condition sets of fiber/matrix interfacial normal stress at the fiber end to be the same in both regions. The second requires that the shear stress at the fiber/matrix interface also be the same in the limit $x \to L$ and $x^* \to 0$. These are necessary continuity conditions. The final condition is based on the iso-strain conditions of the problem, namely, that the applied strain is uniform across the transverse boundary of the unit cell at $x^* = g$. This requires that the shear stress be also zero at $x^* = g$. It can then be shown that the unknown constants are given by

$$B = -\frac{(E_f - E_m)\epsilon_c}{\cosh(ns) + (n/n^*)\sinh(ns)\coth(n^*s^*)} \tag{14}$$

$$B^* = -B(n/n^*)\sinh(ns)\coth(n^*s^*) \tag{15}$$

$$A^* = -B\tanh(n^*s^*) \tag{16}$$

where $s(=L/r)$ is fiber aspect ratio and $s^*(=g/r)$ is the aspect ratio of fictitious fiber. The composite stress, σ_c, can be determined from the rule of averages as

$$\sigma_c = V_f\bar{\sigma}_f + V_m\bar{\sigma}_m = V_f\bar{\sigma}_f + V_f^*\overline{\sigma_f^*} + (V_m - V_f^*)\bar{\sigma}_m. \tag{17}$$

Here the dashed line above the variable indicates average values. These average values can be determined as follows:

$$\bar{\sigma}_f = \frac{1}{L}\int_0^L \sigma_f\,dx \tag{18}$$

$$\overline{\sigma_f^*} = \frac{1}{g}\int_L^{(L+g)} \sigma_f^*\,dx \tag{19}$$

$$\bar{\sigma}_m = E_m\epsilon_c. \tag{20}$$

σ_f and σ_f^* are given by Eqs. (4) and (9), respectively. The normalized longitudinal Young's modulus of the composite is $E_c = \sigma_c/\epsilon_c$. The final result for the modulus enhancement can then be given by

$$\frac{E_c}{E_m} = \frac{V_fE_f}{E_m} + \frac{V_fB}{E_m\epsilon_c p}\sinh(ns) + V_m + \frac{V_f^*}{E_m\epsilon_c n^*s^*}[A^*(\cosh(n^*s^*) - 1 + B^*\sinh(n^*s^*)]. \tag{21}$$

The maximum fiber stress, σ_{fm}, is at the fiber center, and is given by Eq. (4) with $x=0$: namely

$$\sigma_{fm} = E_f\epsilon_c + B. \tag{22}$$

The fiber end stress, σ_i, responsible for the normal stress transfer can be obtained by setting $x^* = 0$ in Eq. (8) from which the stress intensification at the fiber end, $\sigma_i/\bar{\sigma}_m$, is given by

$$\frac{\sigma_i}{\bar{\sigma}_m} = 1 + \frac{B^*}{E_m\epsilon_c}. \tag{23}$$

2.2 Finite Element Computations. The finite element computations were performed using four-noded axisymmetric isoparametric elements (Cook et al., 1989). Provided the fiber or whisker distribution is perfectly uniform, a representative volume element (RVE) or unit cell can be selected (Hashin, 1983) for finite element computations. The unit cells selected along with the corresponding mesh patterns are shown in Figs. 2(*a*) and 2(*b*). Two different unit cells were selected: (1) based on a single fiber in an quasi-infinite matrix using $V_f = 0.005$,

Downloaded 03 May 2010 to 171.66.16.247. Redistribution subject to ASME license or copyright; see http://www.asme.org/terms/Terms_Use.cfm

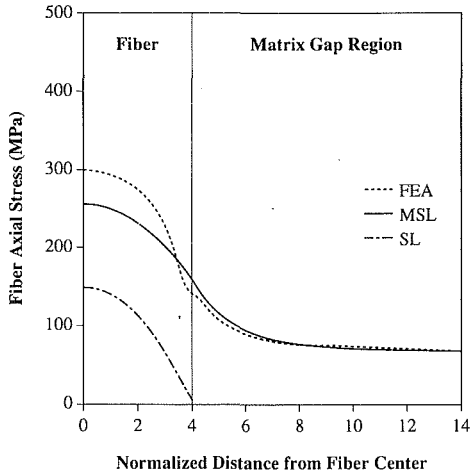


Fig. 3 Real and fictitious fiber axial stress distributions as predicted by SL, MSL, and FEA at $\epsilon_c = .001$ in case of ($V_f = .005$)

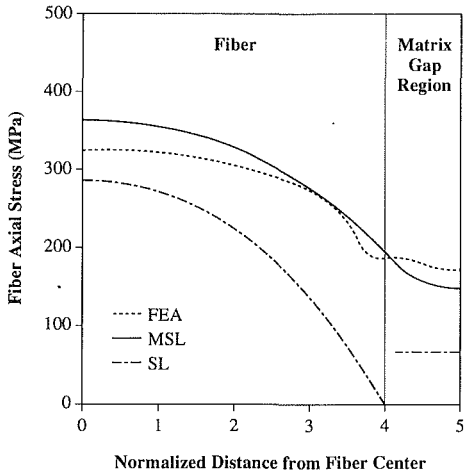


Fig. 4 Real and fictitious fiber axial stress distributions as predicted by SL, MSL, and FEA at $\epsilon_c = .001$ in case of ($V_f = .2$)

(Fig. 2(*a*)) and (2) that corresponding to a finite concentration of 20 vol. percent fibers (Fig. 2(*b*)). In the latter case, the unit cell configuration is similar to that used previously by Agarwal et al. (1974) for a uniform distribution of fibers with an end gap value equal to transverse spacing between fibers. In other words, $g = R - r$. This allows for comparison of volume fraction effects by both finite element analysis and the analytical model developed above. The fiber aspect ratio in the FEA is allowed to vary from 2–16, always maintaining the conditions $g = R - r$.

3 Results and Discussion

Material properties selected are for Al 2124 as matrix and SiC whisker as reinforcement. For this system, typical values (Nair et al., 1985) are $E_m = 67.2$ GPa, $\nu_m = 0.33$ for matrix and $E_f = 480$ GPa, $\nu_f = 0.17$ for reinforcement.

3.1 Fiber Stresses. The axial tensile stress in the fiber and matrix end region (fictitious fiber) at 0.1 percent composite strain is given in Fig. 3 for the case of a single fiber in a quasi-infinite matrix ($V_f = 0.005$). For this case, $r = 1$, $L = 4$, $g = 10$, $s = 4$, $s^* = 10$, $R/r = 7.56$, $n = 0.2281$, $n^* = 0.6097$. The analytical result of this model (MSL) is compared to the FEA result as well as to the prediction of the SL model. As shown in Fig. 3, the fiber stress in the SL model drops to zero as the fiber end region is approached. Further, the tensile stress in the matrix end region in the SL model is assumed constant throughout the gap region and equal to the average matrix stress ($= E_m \epsilon_c$). On the other hand, in the MSL model the fiber stresses are significantly higher than that in the SL model. These fiber stresses drop off to a finite interfacial value σ_i at the fiber end. The tensile stress in the matrix end region is not constant but decreases from the value σ_i at the fiber and approaches the SL model predictions at large distances from the fiber end. Further note that the shape of the fiber tensile stress curve in the MSL model is not the same as that in the SL model because of the different constant values in the shear lag equation solutions.

For finite fiber concentrations, $V_f = 0.2$, the results are shown in Fig. 4. Numerical values were set as $r = 1$, $L = 4$, $g = 1$, $s = 4$, $s^* = 1$, $R/r = 2$, $n = 0.3897$, $n^* = 1.0415$. Note from Fig. 4 that the matrix stresses in the end gap region are throughout larger than the average matrix stress, $\bar{\sigma}_m$, predicted by the SL model. σ_i is also larger than for the $V_f = 0.005$ case. Thus, fiber end gap stresses and σ_i are both increased as the fibers come close together along the axial direction.

The tensile results of the MSL model is in both qualitative and quantitative agreement with the FEA results, both for the single fiber (Fig. 3) and finite fiber concentration cases (Fig. 4). However, note that the maximum stress predicted at the fiber center by the MSL model in Fig. 3 is somewhat higher than the FEA result. This is due to the $\ln(R/r)$ term in Eq. (3). The MSL model is clearly invalid as $R \to \infty$ and, in this sense, is similar to the equation for the line tension of dislocations in metallic alloys (Hirth and Lothe, 1980). At more realistic fiber concentrations the FEA and MSL predictions are in better agreement as shown in Fig. 4. The MSL model is also not applicable in the limit as $R \to r$, for, in this case, as Eq. (4) and Eq. (9) will show, the fiber stresses show a singularity.

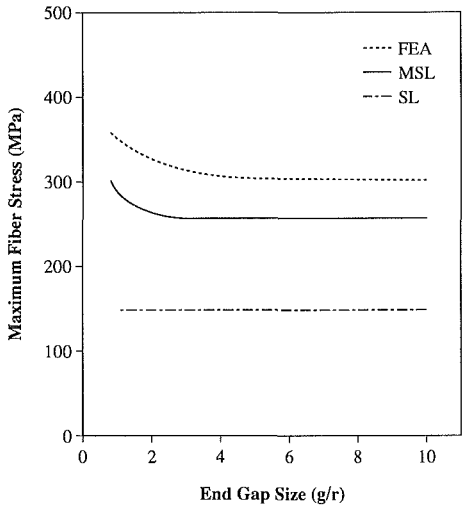


Fig. 5 Maximum fiber stresses as a function of end gap size at $\epsilon_c = .001$ in case of ($V_f = .005$)

The maximum fiber stress, see Eq. (22), is proportional to the macroscopic composite strain. Consequently, at composite strain close to the matrix yield strain (~0.5 percent) for SiC-reinforced Al 2124, the maximum fiber stress can be well over 1 GPa. The maximum fiber center stress is also dependent on the end gap size as shown in Fig. 5. The results are again comparable with FEA and show that the fiber stresses are enhanced when the end gap size is reduced. The high stress intensification at the fiber center compared to SL predictions is important from the standpoint of potential fiber fracture during deformation of the metal matrix composite. Preliminary results by Murdeshwar (1989) suggests that fibers may actually fracture during tensile straining of a SiC whisker-

Downloaded 03 May 2010 to 171.66.16.247. Redistribution subject to ASME license or copyright; see http://www.asme.org/terms/Terms_Use.cfm

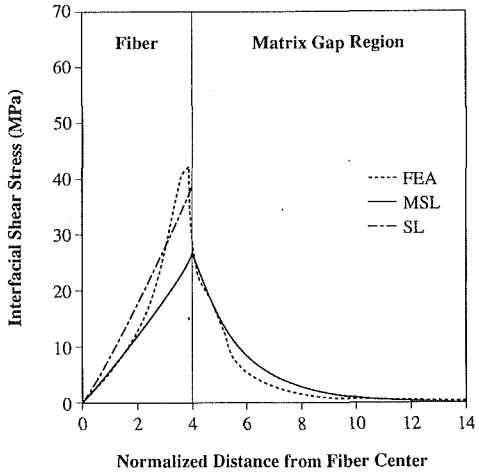


Fig. 6 Interfacial shear stress distributions at $\epsilon_c = .001$ in case of ($V_f = .005$)

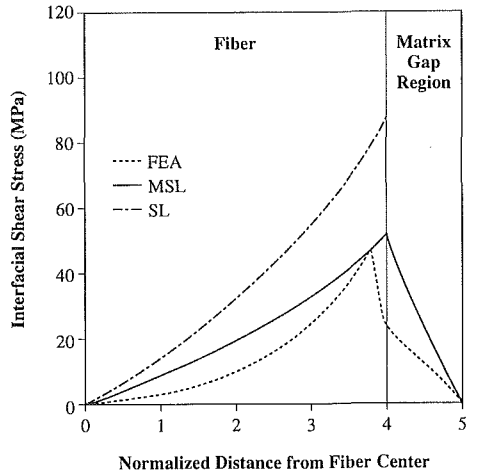


Fig. 7 Interfacial shear stress distributions at $\epsilon_c = .001$ in case of ($V_f = .2$)

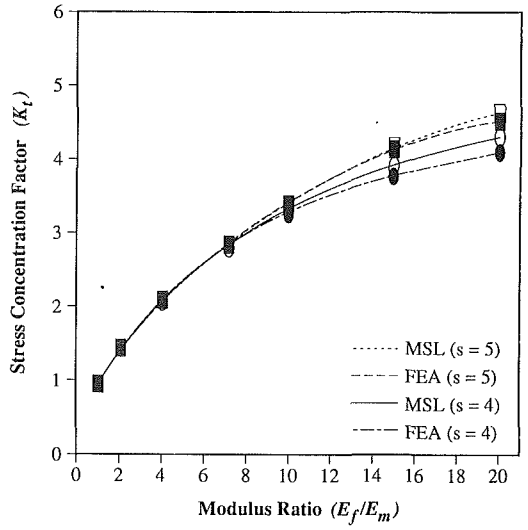


Fig. 8 Normalized fiber end stresses, $\sigma_i/\bar{\sigma}_m$ (stress concentration factors) in case of ($V_f = .2$)

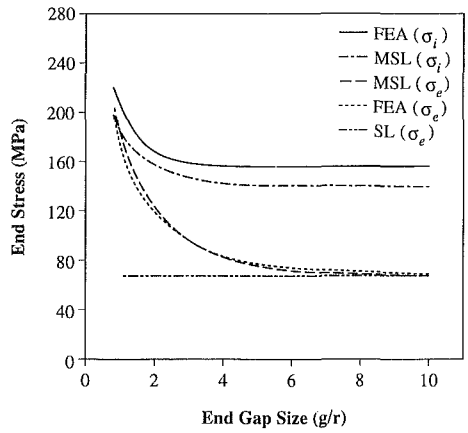


Fig. 9 Fiber end stresses as a function of end gap size at $\epsilon_c = .001$ in case of ($V_f = .2$)

reinforced aluminum alloy. The intensification of stresses in the matrix end region is also important from the standpoint of early plasticity confined to the end region during deformation of the composite. A fracture mechanism proposed by Nutt and Needleman (1987) involves the nucleation of voids in fiber end regions due to the stress intensification there resulting in lower ductility values for the short-fiber-reinforced metal matrix composite.

3.2 Interfacial Shear Stresses. Interfacial shear stresses at 0.1 percent composite strain are depicted in Fig. 6 and Fig. 7 for $V_f = 0.005$ and $V_f = 0.2$, respectively. For the case of the single fiber in an quasi-infinite matrix ($V_f = 0.005$), Fig. 6 indicates that the trends in shear stress show good agreement between the MSL model and FEA predictions. Note, however, that the SL model does not provide any shear stress values in the end gap region. The shear stresses at the fiber/matrix interface near the fiber end is somewhat underestimated in the MSL model, again due to the $\ln(R/r)$ term as explained earlier. The predicted shear stresses in the gap region by the MSL model agree excellently with calculated FEA results. For the more realistic case of $V_f = 0.2$, Fig. 7, there is even better agreement between the FEA shear stress results and that of the MSL model over both the fiber/matrix interface and the matrix gap regions. If local plastic yielding is driven by a Tresca flow criterion, Figs. 6 and 7 predict that plasticity would progress both into the gap region from the fiber end due to the high shear stresses there as well as towards the fiber center from the fiber corners because of the high shear stresses at the fiber/matrix interfaces near the fiber end. Consequently, plastic yielding of the composite would commence at stresses lower than the macroscopic matrix yield stress. These shear stress values can then be used to estimate the approximate sizes of the local yield zones around the short fiber ends. The elastic-plastic behavior is the subject of a subsequent paper (Kim and Nair, 1991).

3.3 Fiber End Stresses. The normalized axial stresses at the fiber end derived in the MSL model (Eq. (23)) are shown in Fig. 8 as a function of E_f/E_m for two fiber aspect ratio values in terms of the stress intensification $\sigma_i/\bar{\sigma}_m$ where $\bar{\sigma}_m$ is the average matrix stress ($=E_m\epsilon_c$). As shown in the Fig. 8, $\sigma_i/\bar{\sigma}_m$ increases with the fiber modulus and fiber aspect ratio. Also as shown in Fig. 8, the results show remarkable agreement with the predicted FEA results. The fiber end stress, σ_i, are also dependent on the end gap size (see Fig. 9). As the end gap size is reduced, the end stresses are significantly enhanced. These fiber end effects become more dominant for stiffer fibers, and for small fiber-to-fiber spacing in the end gap region. Also shown in Fig. 9, is σ_e, the normal matrix stress at $x = L + g$, or the outer boundary of the unit cell. Note that $\sigma_e \geqq \bar{\sigma}_m$ because of the constant strain boundary condition. σ_e also increases as the end gap size is reduced. In comparison, as mentioned, the SL model does not derive equations for the stresses in end gap

Downloaded 03 May 2010 to 171.66.16.247. Redistribution subject to ASME license or copyright; see http://www.asme.org/terms/Terms_Use.cfm

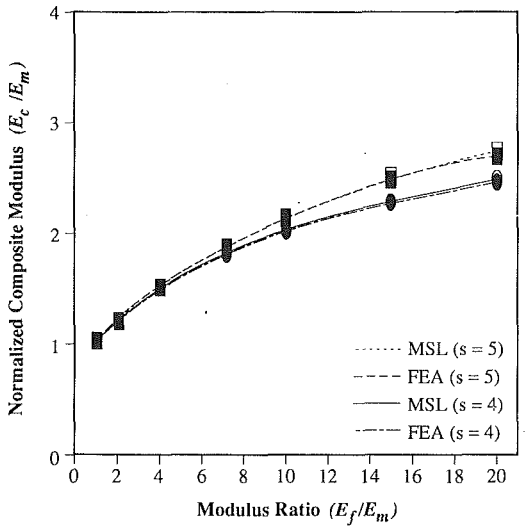


Fig. 10 Normalized composite longitudinal Young's modulus ratio, E_c/E_m, as predicted by MSL and FEA as a function of the modulus ratio, E_f/E_m, at different aspect ratios

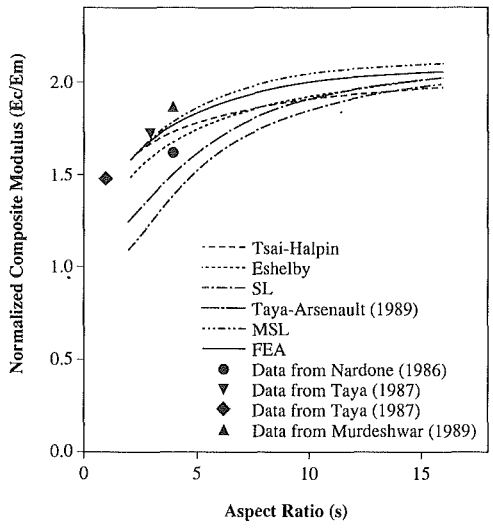


Fig. 11 Normalized composite longitudinal Young's modulus ratio as predicted by SL, MSL, and FEM as a function of aspect ratio compared with other strengthening models. Filled symbols represent experimental data whereas curves are theory predictions according to various models.

region. Consequently, $\sigma_e = \bar{\sigma}_m = E_m \epsilon_c$ for the SL case. When the end gap size is increased indefinitely, σ_e from the MSL model approaches $E_m \epsilon_c$ as expected.

3.4 Longitudinal Composite Young's Modulus Predictions and Comparison With Other Theories and Experimental Data. The overall increase in composite modulus E_c/E_m, Eq. (21) of the MSL model, is plotted in Fig. 10 for two aspect ratio values as a function of E_f/E_m, the ratio of fiber to matrix modulus. Also shown for comparison is the corresponding FEA results. Again, there is a remarkable coincidence between the MSL and FEA results. The result of Fig. 10 shows, without doubt, that the shear lag approach suitably modified by taking the fiber end region stresses into account provide correct modulus prediction when the aspect ratio is small.

The dependence of E_c/E_m to fiber aspect ratio for a fixed E_f/E_m is shown in Fig. 11. Figure 11 compares the prediction of MSL with FEA, SL as well as with the predictions of other elasticity theories, namely, the Tsai-Halpin model (Halpin and Kardos, 1976; Halpin, 1984) and the Eshelby model (Eshelby, 1957; Tandon and Weng, 1986). Also shown in Fig. 11 is the predictions of model of Taya and Arsenault who neglected stress intensification at fiber ends. Their equation for the modulus is (Taya and Arsenault, 1989)

$$E_c = V_m E_m + V_f E_f \left[1 + \left(\frac{E_m}{E_f} - 1 \right) \frac{\tanh(ns)}{ns} \right]. \qquad (24)$$

The modulus results from their model are slightly higher than the original shear lag model but still substantially underestimate the actual composite modulus. Superimposed on Fig. 11 are the available experimental data for SiC whisker-reinforced Al alloys. Note that it is the MSL predictions that agree most closely with FEA lending strong support to the contention that a shear lag approach taking end effects into account is physically most realistic. All methods, except the SL model and the Taya-Arsenault model, however, are reasonable comparable with available data. The SL model and Taya-Arsenault model is clearly an underestimation. However, as the aspect ratio is increased, the predictions of all models converge to the rule-of-mixture predictions as expected.

4 Conclusions

A rigorous modification of the original shear lag solutions by coupling the fibers to the associated end regions results in modulus predictions that most clearly match those obtained by finite element computations. The model provides closed-form solutions for the predicted modulus increases and also for the local tensile and shear stress values in the matrix and fiber. The local stress predictions also exactly match finite element results. We are therefore led to conclude that the shear lag approach is physically realistic for strengthening evaluations in short-fiber composites. The inaccurate predictions of the original shear lag analysis for small aspect ratios are due to its neglect of the influence of fiber end regions. When the fiber aspect ratio is sufficiently large, the modulus predictions of the modified shear lag model correctly approach those of the original shear lag analysis as it should.

Acknowledgments

This work supported by the National Science Foundation under grant No. MSM-8552720.

References

Agarwal, B. D., Lifsitz, J. M., and Broutman, L. J., 1974, "Elastic-Plastic Finite Element Analysis of Short Fiber Composites," *Fiber Science and Technology*, Vol. 7, pp. 45–62.

Arsenault, R. J., 1983, "Interfaces in Metal Matrix Composites," *Scripta Metallurgica*, Vol. 18, pp. 1131–1134.

Arsenault, R. J., 1984, "The Strengthening of Aluminum Alloy 6061 by Fiber and Platelet Silicon Carbide," *Materials Science and Engineering*, Vol. 64, pp. 171–181.

Budiansky, B., 1965, "On the Elastic Modulus of Some Heterogeneous Materials," *Journal of the Mechanics and Physics of Solids*, Vol. 13, pp. 223–227.

Cook, R. D., Malkua, D. S., and Plesha, M. E., 1989, *Concepts and Applications of Finite Element Analysis*, 3rd ed., John Wiley and Sons, pp. 163–295.

Cox, H. L., 1952, "The Elasticity and Strength of Paper and Other Fibrous Materials," *British Journal of Applied Physics*, Vol. 3, pp. 72–79.

Eshelby, J. D., 1957, "The Determination of the Elastic Field of an Ellipsoidal Inclusion, and Related Problems," *Proceedings of the Royal Society, London*, Vol. A241, pp. 376–396.

Halpin, J. C., 1984, *Primer on Composite Materials: Analysis*, Technomic Publishing Co., pp. 130–141.

Halpin, J. C., and Kardos, J. L., 1976, "The Halpin-Tsai Equations: A Review," *Polymer Engineering and Science*, Vol. 16, No. 5, pp. 344–352.

Hashin, Z., 1983, "Analysis of Composite Materials," ASME JOURNAL OF APPLIED MECHANICS, Vol. 50, pp. 481–505.

Hashin, Z., and Shtrikman, S., 1962, "On Some Variational Principles in Anisotropic and Nonhomogeneous Elasticity," *Journal of the Mechanics and Physics of Solids*, Vol. 10, pp. 335–332.

Hashin, Z., and Shtrikman, S., 1963, "A Variational Approach to the Theory of the Elastic Behavior of Multiphase Materials," *Journal of the Mechanics and Physics of Solids*, Vol. 11, pp. 127–140.

Hershey, A. V., 1954, "The Elasticity of an Isotropic Aggregate of an An-

Downloaded 03 May 2010 to 171.66.16.247. Redistribution subject to ASME license or copyright; see http://www.asme.org/terms/Terms_Use.cfm

isotropic Cubic Crystals," ASME JOURNAL OF APPLIED MECHANICS, Vol. 21, pp. 236–240.

Hill, R., 1965a, "Theory of Mechanical Properties of Fiber-Strengthened Materials—III. Self-Consistent Model," *Journal of the Mechanics and Physics of Solids*, Vol. 13, pp. 189–198.

Hill, R., 1965b, "A Self-Consistent Mechanics of Composite Materials," *Journal of the Mechanics and Physics of Solids*, Vol. 13, pp. 213–222.

Hirth, J. P., and Lothe, J., 1982, *Theory of Dislocations*, John Wiley and Sons, pp. 79–81.

Kim, H. G., and Nair, S. V., 1990, "Strengthening Analysis of SiC Whisker Reinforced Aluminum Alloys," *Proceedings of the 11th World Korean Scientist and Engineers Conference*, The Korean Federation of Science and Technology Societies, Seoul, Korea, Jun. 25–29, pp. 1737–1742.

Kim, H. G., and Nair, S. V., 1991, "Modification of the Shear Lag Analysis for Strengthening Predictions in Short Fiber or Whisker Reinforced Metal Matrix Composites," *Advanced Composite Materials*, Vol. 19, American Ceramic Society, pp. 535–541.

Kröner, E., 1958, "Berechnung der elastischen Konstanten des Vielkristalls aus den Konstanten des Einkristalls," *Zeitschrift für Physik*, Vol. 151, pp. 504–518.

Muki, R., and Sternberg, E., 1969, "On the Diffusion of an Axial Load from an Infinite Cylindrical Bar Embedded in an Elastic Medium," *International Journal of Solids and Structures*, Vol. 5, pp. 587–605.

Murdeshwar, N., 1989, "Fracture Development in a 20 Volume Percent Silicon Carbide Whisker Reinforced Al 2124 Metal Matrix Composite," M. S. Thesis, University of Massachusetts at Amherst.

Nair, S. V., Tien, J. K., and Bates, R. C., 1985, "SiC-Reinforced Aluminum Metal Matrix Composites," *International Metals Reviews*, Vol. 30, No. 6, pp. 275–290.

Nardone, V. C., 1987, "Assessment of Models Used to Predict the Strength of Discontinuous Silicon Carbide Reinforced Aluminum Alloys," *Scripta Metallurgica*, Vol. 21, pp. 1313–1318.

Nardone, V. C., and Prewo, K. M., "On the Strength of Discontinuous Silicon Carbide Reinforced Aluminum Composites," *Scripta Metallurgica*, Vol. 20, pp. 43–48.

Nutt, S. R., and Needleman, A., 1987, "Void Nucleation at Fiber Ends in Al-SiC Composites," *Scripta Metallurgica*, Vol. 21, pp. 705–710.

Paul, B., 1960, "Prediction of Elastic Constants of Multiphase Materials," *Transaction of Metallurgical Society of AIME*, Vol. 218, pp. 36–46.

Piggott, M. R., 1980, *Load Bearing Fiber Composites*, Pergamon Press, pp. 83–89.

Sternberg, E., and Muki, R., 1970, "Load Absorption by a Filament in a Fiber-Reinforced Material," *Journal of Applied Mathematics and Physics (ZAMP)*, Vol. 21, pp. 552–569.

Tandon, G. P., and Weng, G. J., 1986, "Stress Distribution In and Around Spheroidal Inclusions and Voids at Finite Concentration," ASME JOURNAL OF APPLIED MECHANICS, Vol. 53, pp. 511–518.

Taya, M., and Arsenault, R. J., 1987, "A Comparison Between a Shear Lag Type Model and an Eshelby Type Model in Predicting the Mechanical Properties of Short Fiber Composite," *Scripta Metallurgica*, Vol. 21, pp. 349–354.

Taya, M., and Arsenault, R. J., 1989, *Metal Matrix Composites: Thermomechanical Behavior*, Pergamon Press, pp. 25–28.

Downloaded 03 May 2010 to 171.66.16.247. Redistribution subject to ASME license or copyright; see http://www.asme.org/terms/Terms_Use.cfm

A. M. Waas

Department of Aerospace Engineering,
College of Engineering,
University of Michigan,
Ann Arbor, MI 48109-2140
Assoc. Mem. ASME

Effect of Interphase on Compressive Strength of Unidirectional Composites

1 Introduction

The mechanical behavior of the interface in fibrous composite materials has been a subject of intense research in the recent past (Piggot, 1990; Drzal, 1985, 1990; Lowden and More, 1990; Tredway and Prewo, 1990). Much insight has been gained in the past few years and it is widely acknowledged that the quality of the interface which influences the stress transfer between fiber and matrix is what finally determines the overall mechanical performance of the composite. Recent experimental investigations on fiber/polymer matrix composites (Piggot et al., 1986) have shown that the interfacial region of a composite is of a finite thickness and has different mechanical properties than the constituents, fiber, and matrix. This finding is contrary to the assumption usually adopted in mechanics models where the interface is conceptualized merely as a "line" of discontinuity in material properties between constituents. To distinguish between an interface, ideally of zero thickness and the experimental result of a finite thickness region between the constituents, the words interphase and mesophase (Theocaris, 1986) have been introduced to refer to the latter. Several researchers have contributed to an improved understanding of the different aspects of the interphase region as evident from the abundance of experimental and analytical work reported in the literature. A "good" bond between fiber and matrix is known to promote shear strength and off-axis strength and, consequently, a characterization of the interphase mechanical properties can serve as a measure of index for the quality of adhesion between fiber and matrix. Ideally, it has been postulated (Williams, Donellan, James, and Morris, 1990) that the elastic modulus of the interphase should lie between that of the fiber and the matrix to promote enhanced composite properties. However, in practice, it is revealed that the interphase may actually be weaker than both the fiber and the matrix in which case it influences the composite properties in a detrimental way. Several analytical studies exist in the literature aimed at assessing the compressive strength of fibrous composites as summarized in the literature review by Shuart (1985). When a unidirectional composite fails in compression, the fibers undergo undulations which lead to substantial shearing stresses across the fiber matrix interphase. Most analytical predictive models, however, do not explicitly model the interphase; instead they resort to using an interface. The present investigation is aimed at introducing a new model that characterizes the effect of the interphase on the compressive strength of unidirectional composites. To do so, a monofilament fiber composite is chosen as an example configuration. In what follows, the problem formulation is presented and typical results for a T300/BP907 composite are discussed.

2 Problem Formulation

The configuration to be studied is shown in Fig. 1. A single fiber of thickness H is embedded in a matrix of infinite extent. Interphases of thickness h are situated between the fiber and the matrix. The composite is subjected to undergo a plane strain deformation in the xy-plane. Sets of cartesian coordinates are placed as shown in the figure with subscripts 1, 2, and 3 to denote fiber, interphase, and matrix, respectively. u_i and v_i with i ranging from 1,3 denote fiber, interphase, and matrix displacements, respectively, in the x_i and y_i directions, respectively. This nomenclature will apply throughout this presentation. Perfect bonding is enforced at the fiber/interphase and interphase/matrix boundaries. The entire composite is compressed by smooth rigid end platens parallel to the y-axis in the x-direction. The analysis that follows is aimed at examining the existence of nontrivial equilibrium configurations of the composite other than the trivial uniform straining parallel to the x-axis.

In the transition from the uniformly strained state to the perturbed state, two deformation modes of the fiber are possible. The first, in which the fiber deforms antisymmetrically, is one in which the fiber displacements associated with the perturbation from the uniform straining are constrained to satisfy

$$u(x_1,y_1) = -u(x_1,-y_1)$$
$$v(x_1,y_1) = v(x_1,-y_1). \quad (1)$$

For fiber composite systems in which the fiber modulus greatly exceeds that of the matrix, this antisymmetric mode prevails as shown in previous studies by Steif (1990) and Waas et al.

Contributed by the Applied Mechanics Division of THE AMERICAN SOCIETY OF MECHANICAL ENGINEERS for presentation at the 1992 ASME Summer Mechanics and Materials Meeting, Tempe, AZ Apr. 28–May 1, 1992.

Discussion on this paper should be addressed to the Technical Editor, Prof. Leon M. Keer, The Technological Institute, Northwestern University, Evanston, IL 60208, and will be accepted until two months after final publication of the paper itself in the JOURNAL OF APPLIED MECHANICS. Manuscript received by the ASME Applied Mechanics Division, Feb. 14, 1991; final revision, Apr. 29, 1991.

Paper No. 92-APM-4.

Copyright © 1992 by ASME

Downloaded 03 May 2010 to 171.66.16.247. Redistribution subject to ASME license or copyright; see http://www.asme.org/terms/Terms_Use.cfm

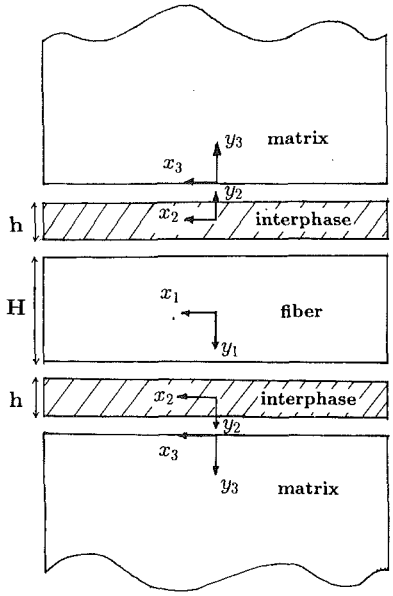


Fig. 1 Problem configuration

(1990). In view of this, symmetric fiber deformation modes for which the displacement constraints are

$$u(x_1,y_1)=u(x_1,-y_1)$$
$$v(x_1,y_1)=-v(x_1,-y_1) \tag{2}$$

are not considered in the present work.

Initially, when the composite is uniformly strained, the initial stresses corresponding to the uniform straining are given by $s_i(\equiv\sigma_i/2G_i)$ and $t_i(\equiv\zeta_i/2G_i)$ where σ_i are the stresses parallel to the x_i-direction, ζ_i are the stresses parallel to the z_i-direction, and G_i is the shear modulus. General equations of equillibrium for a solid slightly deformed from a state of initial stress have been derived in a form suitable for the present analysis by Biezeno and Hencky (1928), Biot (1939), and Novoshilov (1953). In a slightly disturbed state from the uniformly strained state, and with no body forces, the field equations governing the incremental stresses arising due to the perturbation from the uniformly strained state, following Novoshilov (1953) are three of the type

$$\frac{\partial}{\partial x}[\sigma_x'-\omega_z'\sigma_{xy}^0+\omega_y'\sigma_{xz}^0]+\frac{\partial}{\partial y}[\sigma_{xy}'-\omega_z'\sigma_y^0+\omega_y'\sigma_{yz}^0]$$
$$+\frac{\partial}{\partial z}[\sigma_{xz}'-\omega_z'\sigma_{yz}^0+\omega_y'\sigma_z^0]=0 \tag{3}$$

where ω_x', ω_y', ω_z' are the components of the rotation, 1/2 curl (u, v, w). A superscript "0" is used to identify quantities associated with the first (initial) position of equilibrium while a superscript "′" denotes those quantities arising due to the disturbance from the initial state of stress. For the sake of brevity, the perturbed displacement field is denoted simply by u, v, w without the prime.

In the present problem, the perturbed displacement field is restricted to one of plane strain and, consequently, $\omega_x'=\omega_y'=0$ and ω_z' is independent of z. Furthermore, the nonvanishing components of initial stress are $\sigma_x^0=\sigma$ and $\sigma_z^0=\zeta$. Thus, the three equations of the type (3) above when specialized to the present problem become

$$\frac{\partial\sigma_x'}{\partial x}+\frac{\partial\sigma_{xy}'}{\partial y}+\frac{\partial\sigma_{xz}'}{\partial z}=0$$
$$\frac{\partial}{\partial x}[\sigma_{xy}'+\omega_z'\sigma]+\frac{\partial\sigma_y'}{\partial y}+\frac{\partial\sigma_{zy}'}{\partial z}=0$$
$$\frac{\partial\sigma_{xz}'}{\partial x}+\frac{\partial\sigma_{yz}'}{\partial y}+\frac{\partial\sigma_z'}{\partial z}=0. \tag{4}$$

These field equations have to be satisfied in each of the fiber, interphase, and matrix. The fiber, interphase, and matrix are assumed to be homogeneous and linearly elastic solids. Thus, the stress components σ_{ij}' are related to the perturbed displacements by three equations of the type

$$\sigma_x'=\lambda(e_x'+e_y')+2Ge_x' \tag{5}$$

and three of the type

$$\sigma_{xy}'=2Ge_{xy}' \tag{6}$$

where $e_x'=\dfrac{\partial u}{\partial x}$, etc., $e_{xy}'=\dfrac{1}{2}\left(\dfrac{\partial v}{\partial x}+\dfrac{\partial u}{\partial y}\right)$, and λ, G are the Lamé constants. Using the above constitutive relations (5) and (6) to eliminate the stresses in favor of the strains in (4) yields

$$(\lambda_i+2G_i)\frac{\partial^2u_i}{\partial x_i^2}+G_i\frac{\partial^2u_i}{\partial y_i^2}+(\lambda_i+G_i)\frac{\partial^2v_i}{\partial x_i\partial y_i}=0$$
$$(\lambda_i+2G_i)\frac{\partial^2v_i}{\partial y_i^2}+(G_i-\frac{\sigma_i}{2})\frac{\partial^2v_i}{\partial x_i^2}+\left(\lambda_i+G_i+\frac{\sigma_i}{2}\right)\frac{\partial^2u_i}{\partial x_i\partial y_i}=0. \tag{7}$$

Here, the index i ranges from 1-3, with each number corresponding to fiber, interphase, and matrix, respectively. The last of the Eqs. (4) is satisfied identically on account of the restriction to plane strain.

The force boundary conditions associated with the equations of the type of (4) are three of the type

$$\Delta f_x=(\sigma_x'-\omega_z'\sigma_{xy}^0+\omega_y'\sigma_{xz}^0)\kappa+(\sigma_{xy}'-\omega_z'\sigma_{yy}^0+\omega_y'\sigma_{yz}^0)\theta$$
$$(\sigma_{xz}'-\omega_z'\sigma_{yz}^0+\omega_y'\sigma_{zz}^0)\mu \tag{8}$$

where Δf_x is the x-component of traction, accompanying the displacements u, v, w, per unit undeformed area and κ, θ, and μ are the direction cosines of the normal to the boundary element. Two other similar boundary conditions are obtainable by cyclic permutation of x, y, and z.

The field Eqs. (4) have to hold in each of the fiber, interphase, and matrix (denoted by a subscript 1, 2, and 3, respectively). The solution proceeds by seeking to examine the presence of periodic (in the x-direction) states of adjacent equilibrium of the uniformly strained composite with the restriction to antisymmetric modes in the fiber, $-H/2<y_1<H/2$. In view of the coordinate choices in Fig. 1, and since periodicity in the displacement field is favored over the boundary conditions in the x_i-direction, we can write the following solutions to the field Eqs. (7) in fiber, interphase, and matrix, respectively, subject to the requirement that the perturbed displacements vanish as $y_3\to+\infty$;

Fiber:

$$u_1(x_1,y_1)=[-B_1\sinh(\alpha y_1)+k_1D_1\sinh(\mu_1\alpha y_1)]\sin(\alpha x_1)$$
$$v_1(x_1,y_1)=[B_1\cosh(\alpha y_1)+D_1\cosh(\mu_1\alpha y_1)]\cos(\alpha x_1) \tag{9}$$

where

$$k_1=\frac{\mu_1\left(\beta_1+\dfrac{1}{2}\right)}{\dfrac{\mu_1^2}{2}-\beta_1-1} \tag{10}$$

and $\beta_1=\dfrac{\lambda_1}{2G_1}$, $\mu_1=\sqrt[2]{1-s_1^2}$, $\alpha=\dfrac{2\pi}{\lambda}$ and λ is the buckle wavelength.

Downloaded 03 May 2010 to 171.66.16.247. Redistribution subject to ASME license or copyright; see http://www.asme.org/terms/Terms_Use.cfm

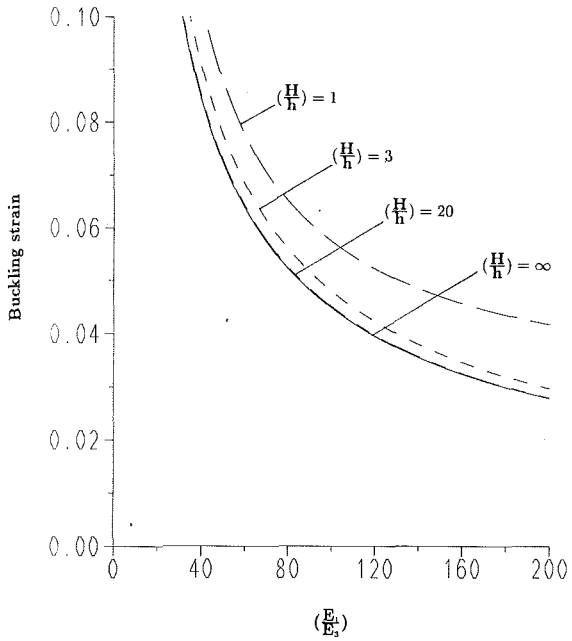


Fig. 2 Variation of buckling strain against the ratio fiber modulus to matrix modulus (E_1/E_3)

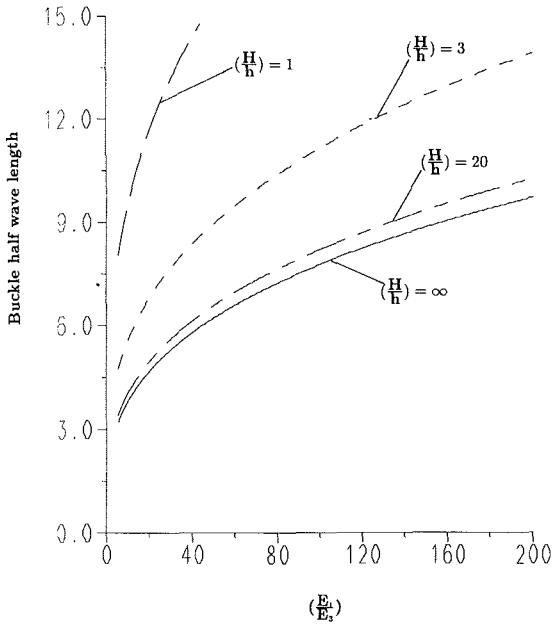


Fig. 3 Variation of buckle half wavelength $\left(\equiv \frac{1}{2}\frac{\lambda}{H}\right)$ against the ratio fiber modulus to matrix modulus (E_1/E_3)

Interphase:

$$u_2(x_2,y_2) = [-B_2\sinh(\alpha y_2) - A_2\cosh(\alpha y_2) + k_2D_2\sinh(\mu_2\alpha y_2) + k_2C_2\cosh(\mu_2\alpha y_2)]\sin(\alpha x_2)$$

$$v_2(x_2,y_2) = [A_2\sinh(\alpha y_2) + B_2\cosh(\alpha y_2) + C_2\sinh(\mu_2\alpha y_2) + D_2\cosh(\mu_2\alpha y_2)]\cos(\alpha x_2)$$

where

$$k_2 = \frac{\mu_2\left(\beta_2 + \frac{1}{2}\right)}{\frac{\mu_2^2}{2} - \beta_2 - 1} \tag{12}$$

and $\beta_2 = \dfrac{\lambda_2}{2G_2}$, $\mu_2 = \sqrt[2]{1 - s_2^2}$.

Matrix;

$$u_3(x_3,y_3) = [B_3e^{(-\alpha y_3)} - k_3D_3e^{(-\mu_3\alpha y_3)}]\sin(\alpha x_3)$$

$$v_3(x_3,y_3) = [B_3e^{(-\alpha y_3)} + D_3e^{(-\mu_3\alpha y_3)}]\cos(\alpha x_3) \tag{13}$$

where

$$k_3 = \frac{\mu_3\left(\beta_3 + \frac{1}{2}\right)}{\frac{\mu_3^2}{2} - \beta_3 - 1}. \tag{14}$$

and $\beta_3 = \lambda_3/2G_3$, $\mu_3 = \sqrt[2]{1 - s_3^2}$. B_1, D_1 ... etc. are eight arbitrary unknown constants associated with the above solutions.

The solutions given above, obtained in a similar manner as discussed in Waas et al. (1990), are subject to traction and displacement continuity conditions, two of each, at the fiber/interphase boundary and interphase/matrix boundary, respectively, for a total of eight equations. These equations are:

fiber/interphase boundary; $y_1 = \dfrac{H}{2}$, $y_2 = \dfrac{-h}{2}$

$$u_1 - u_2 = 0$$

$$v_1 - v_2 = 0$$

$$\Delta f_{x_1} - \Delta f_{x_2} = 0$$

$$\Delta f_{y_1} - \Delta f_{y_2} = 0 \tag{15}$$

Interphase/matrix boundary; $y_2 = \dfrac{h}{2}$, $y_3 = 0$

$$u_2 - u_3 = 0$$

$$v_2 - v_3 = 0$$

$$\Delta f_{x_2} - \Delta f_{x_3} = 0$$

$$\Delta f_{y_2} - \Delta f_{y_3} = 0 \tag{16}$$

Substitution of the solutions (9), (11), and (13) in (15) and (16) results in a system of eight linear algebraic homogeneous equations. Vanishing of the determinant associated with this system yields the value of critical strain associated with the transition to an adjacent state of equilibrium. Once this strain is found, the constants B_1, D_1 through B_3, D_3 can be determined up to an arbitrary constant. This enables us to characterize the buckle mode shapes associated with a given value of critical strain. In the section to follow, example results are presented to show the effect of a "soft" and "hard" interphase on the predicted buckling strain.

3 Results and Discussion

Numerical calculations for the composite critical strains (to cause buckling) using the above analysis were carried out to investigate the effect of a "soft" and "hard" interphase on the buckling strains. The symbolic manipulation programs, Reduce and Mathematica, were used in the computations. Figure 2 represents the variation of critical strain against the fiber/matrix modulus ratio (E_1/E_3) for different thicknesses of the interphase. The fiber Poissons ratio used was 0.2 and the matrix Poissons ratio, 0.38 (Palmer, 1981). These numbers are rep-

Downloaded 03 May 2010 to 171.66.16.247. Redistribution subject to ASME license or copyright; see http://www.asme.org/terms/Terms_Use.cfm

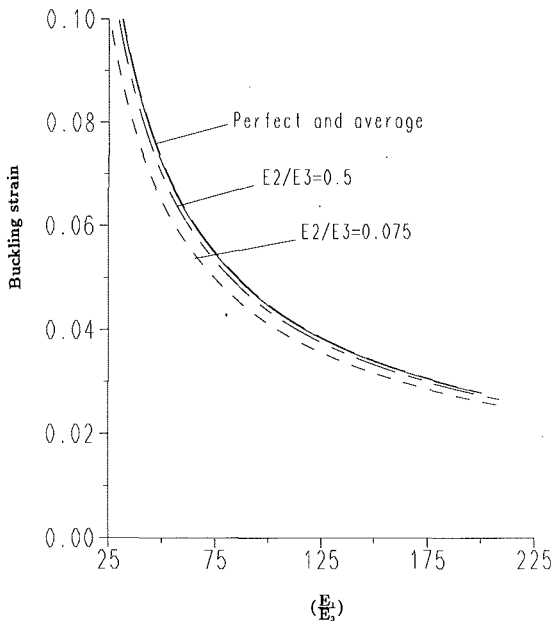


Fig. 4 Comparison of buckling strains for "average," "soft" and the ideal case of no interphase against the ratio fiber modulus to matrix modulus (E_1/E_3)

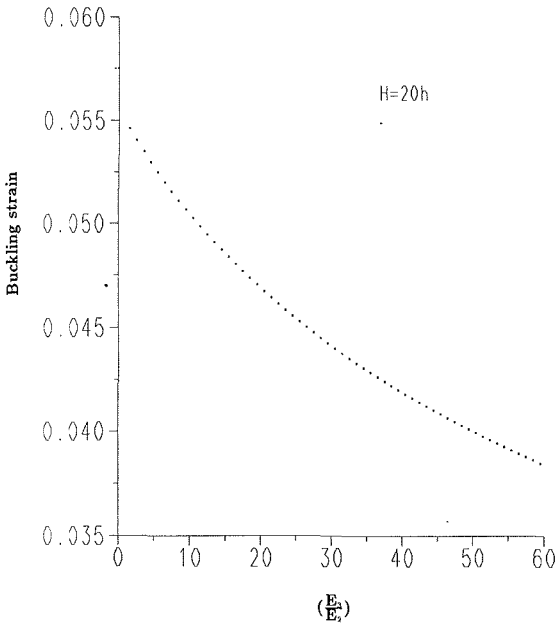


Fig. 6 Effect of varying interphase modulus on predicted buckling strain ($E_1/E_3 = 74.3$)

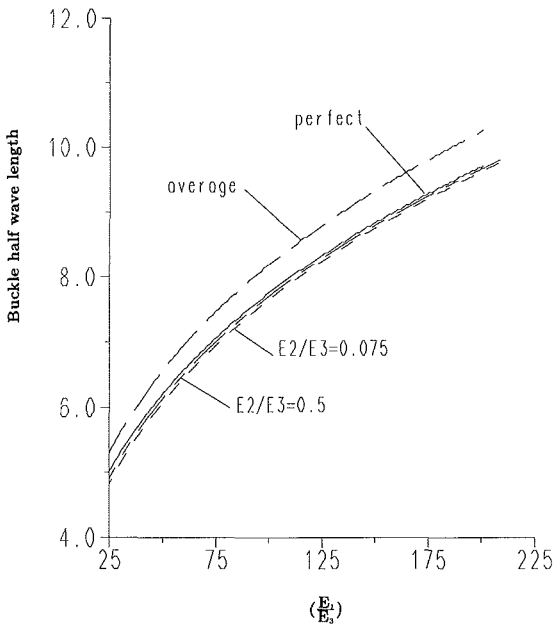


Fig. 5 Comparison of buckle half wavelength for "average," "soft" and the ideal case of no interphase against the ratio fiber modulus to matrix modulus (E_1/E_3)

resentative of typical graphite/epoxy composite systems. The interphase properties for this case were taken to be the arithmetic average of the fiber and matrix properties. Thus, this case is closest to the situation where a gradual transition in properties from matrix to fiber is anticipated. Such a situation was proposed in (Theocaris, 1986) (experimental evidence (Williams et al., 1990), however, suggest that the interphase region is much softer than both matrix and fiber). Indicated by a solid line in this figure is the case where the interphase has vanishing thickness, while the other curves are parametrized by the ratio (h/H) representing interphase thickness (h) to fiber thickness (H). Since the interphase modulus is higher than the matrix modulus for all curves in this figure and also since the matrix is of infinite extent, it is seen that a thicker interphase is desirable from a compressive stability standpoint. From this figure it seen that there is no appreciable differences in results for interphase thicknesses smaller than 1/20 H. The corresponding variation of critical half wavelength against (E_1/E_3) is shown in Fig. 3. Here it is seen that for fixed constituent properties, a thicker interphase induces a larger wavelength at buckling than a thinner interphase.

Experimental work reported in Williams et al. (1990) have indicated that a typical interphase thickness is approximately on the order $h = H/20$, and furthermore, it was shown that the interphase was a region much softer than both the fiber and matrix. Results for the buckling strain depicting such a situation (with $h = H/20$) are shown in Fig. 4. In this figure, the curves marked "soft" were generated for interphase properties (E_2/E_3) = 0.5 and (E_2/E_3) = 0.075. The results for these soft systems are contrasted against those for an average interphase and one without an interphase, marked "perfect." The softer interphases lower the buckling strain, and these differences tend to be larger for smaller ratios of (E_1/E_3) and diminishes with increasing (E_1/E_3). Thus, if the fiber modulus dominates the composite properties, then the presence of an interphase is seen to have very little effect on the buckling strain of the composite. The variation of buckle wavelength against the ratio (E_1/E_3) corresponding to the situation just discussed is shown in Fig. 5. Here it is seen that for a fixed interphase thickness, a "soft" interphase tends to induce smaller wavelengths at buckling than a "harder" interphase.

For a fixed interphase thickness and for fixed fiber/matrix modulus ratio (= 74.3), the effect of varying the interphase modulus compared to the matrix modulus is shown in Fig. 6. Notice here that the critical strain is seen to diminish as a function of the "softness" of the interphase. The rate at which this diminishing occurs is seen to decrease for increasing values of (E_3/E_2). However, the corresponding value of critical half wavelength is seen to initially decrease and then increase as (E_1/E_2) increases. This latter result is shown in Fig. 7. Finally, the contrasting behavior of "soft" and "hard" interphases of varying thickness is shown in Figs. 8 and 9. In Fig. 8, it is seen that for very thin interphases, the effect of varying interphase modulus has very little effect on the predicted buckling strain. However, as the interphase thickness becomes greater than

Downloaded 03 May 2010 to 171.66.16.247. Redistribution subject to ASME license or copyright; see http://www.asme.org/terms/Terms_Use.cfm

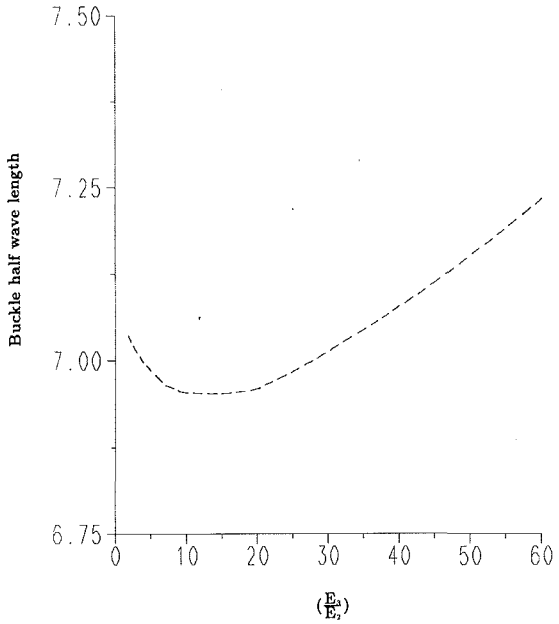


Fig. 7 Effect of varying interphase modulus on predicted buckle half wavelength ($E_1/E_3 = 74.3$)

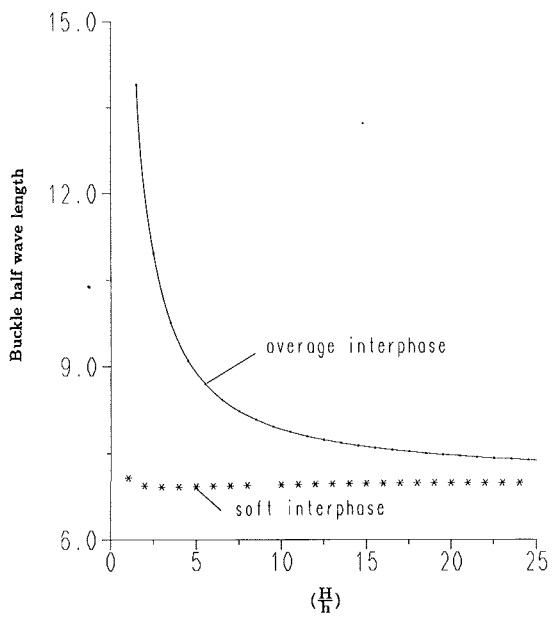


Fig. 9 Variation of buckle half wavelength against inverse normalized interphase thickness $\left[\frac{1}{h/H}\right]$ for two different interphase moduli

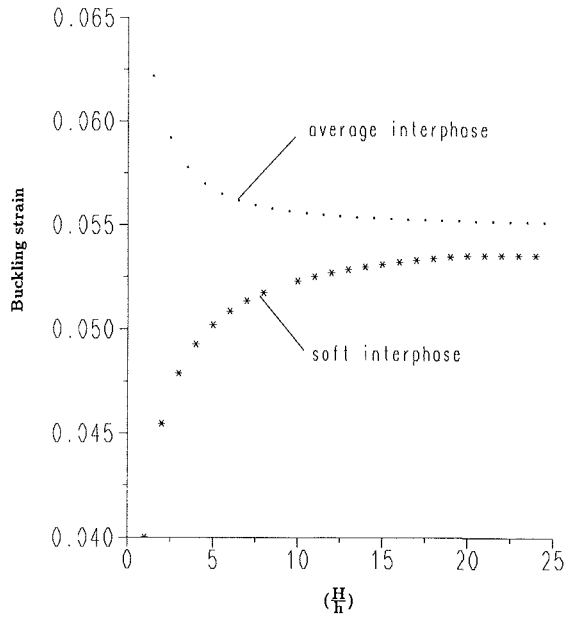


Fig. 8 Variation of buckling strain against inverse normalized interphase thickness $\left[\frac{1}{h/H}\right]$ for two different interphase moduli

(1/10)th of the fiber thickness, a rapid change in behavior is seen to occur. In this region, the softer interphase is seen to lower the buckling strain rather appreciably while a thicker and harder interphase is seen to promote desirable compressive properties. The corresponding variation of critical wavelength is shown in Fig. 9. In this figure, it is seen that over a wide range of (h/H) ratios, the critical buckle wavelength remains almost constant for a "soft" interphase, but shows a rapid decrease with increasing (h/H) for a harder interphase.

4 Concluding Remarks

The major focus of the present paper was to present an analytical method for predicting the compressive behavior of fiber composites in the presence of an interphase. A monofilament configuration was chosen to demonstrate the effect of interphase properties on the composites buckling strain. Each phase of the composite was modeled as a 2d-linear elastic continuum. Field equations representing a solid slightly deformed from a state of initial stress as presented in Novoshilov (1953) and under conditions of plane strain was adopted in the present analysis. Continuity of tractions and displacements at the straight and parallel interfaces between fiber/interphase and interphase/matrix was enforced in the analysis. The results obtained yielded the composite buckling strain and the associated critical wavelength. A drawback of the model presented is that it assumes the interphase to be of uniform thickness. In reality, the interphase region of a composite does not extend a uniform amount from the fiber surface into the matrix. The present analysis has to be modified to accomodate this geometrical change. This modification necessitates incorporating a spatial variation of the thickness of the interphase and thus would not lead to separable solutions for the perturbed displacements. In addition, inclusion of nonlinear viscoelastic effects in modeling the interphase constitutive behavior could also be effected.

The results that have been presented here have shown that a "soft" interphase, whose thickness is approximately (1/10) of the fiber thickness or greater, will have a detrimental effect on the compressive stability of unidirectional composites although this conclusion has been reached without consideration of fiber interaction effects. For a fixed interphase thickness and for a given fiber/matrix modulus ratio, the buckling strain shows little variation over a wide range of ratios of matrix to interphase modulus.

Acknowledgments

Financial support through the Horace Rackham Graduate School at the University of Michigan, Ann Arbor, is gratefully acknowledged. The author appreciates the constructive criticism of the reviewers.

References

Biezeno, C. B., and Hencky, H., 1928, "On the General Theory of Elastic

Downloaded 03 May 2010 to 171.66.16.247. Redistribution subject to ASME license or copyright; see http://www.asme.org/terms/Terms_Use.cfm

Stability," *Konknkiljki Akademie van Wetenschappen te Amsterdam*, Vol. 31.

Biot, M., 1939, "A Non-linear Theory of Elasticity and the Linearized Case for a Body Under Initial Stress," *Phil. Mag.*, Vol. 27, p. 468.

Drzal, L. T., 1985, "The Epoxy Interface in Composites," *Advances in Polymer Science II*, Vol. 75, K. Dusek, ed., Springer-Verlag.

Drzal, L. T., 1990; "Intrinsic Material Limitations in Using Interphase Modification to Alter Fiber-Matrix Adhesion in Composite Materials," *Mat. Res. Soc. Symp. Proc.*, Vol. 170, p. 275.

Lowden, R. A., and More, K. L., 1990, "The Effect of Fiber Coatings on Interfacial Shear Strength and the Mechanical Behavior of Ceramic Composites," *Mat. Res. Soc. Symp. Proc.*, Vol. 170, p. 205.

Novoshilov, V. V., 1953, *Foundations of the Nonlinear Theory of Elasticity*, Graylock, Rochester, N.Y., p. 153.

Palmer, R. J., 1981, "Investigation of the Effect of Resin Material on Impact Damage to Graphite/Epoxy Composites," NASA CR-165677, Mar.

Piggot, M. R., 1990; Tailored Interphases in Fibre Reinforced Polymers," Mat. Res. Soc. Symp. Proc., Vol. 170, p. 275.

Piggot, M. R., Sandai, A., Chua, P. S., and Andison, D., 1986, "Mechanical Interactions in the Interphasial Region of Fibre Reinforced Thermosets," *Composite Interfaces*, H. Ishida and J. L. Koenig, eds., North-Holland, Amsterdam.

Shuart, M. J., 1985, "Short Wavelength Buckling and Shear Failures of Compression-Loaded Composite Laminates," NASA TN87640, Nov.

Steif, P. S., 1990, "Interfacial Instabilities in an Unbonded Layered Solid," *Int. J. Solids Structures*, Vol. 26, No. 8, p. 915.

Theocaris, P. S., 1986, "The Concept and Properties of Mesophase in Composites," *Composite Interfaces*, H. Ishida and J. L. Loenig, eds., North-Holland, Amsterdam.

Tredway, W. K., and Prewo, K. M., 1990, "Improved Performance in Monofilament Fiber Reinforced Glass Matrix Composites Through the Use of Fiber Coatings," *Mat. Res. Soc. Symp. Proc.*, Vol. 170, p. 215.

Waas, A., Babcock, Jr., C. D., and Knauss, W. G., 1990, "A Mechanical Model for Elastic Fiber Microbuckling," ASME JOURNAL OF APPLIED MECHANICS, Vol. 57, p. 138.

Williams, J. L., Donellan, M. E., James, M. R., and Morris, W. L., 1990, "Elastic Modulus of the Interphase in Organic Matrix Composites," *Mat. Res. Soc. Symp. Proc.*, Vol. 170, p. 285.

Downloaded 03 May 2010 to 171.66.16.247. Redistribution subject to ASME license or copyright; see http://www.asme.org/terms/Terms_Use.cfm

Flexural Wave Propagation in an Elastic Beam With Periodic Structure

Sen Yung Lee
Professor,
Department of Mechanical Engineering,
National Cheng Kung University,
Tainan, Taiwan

Huei Yaw Ke
Assoc. Research Engineer,
Chung Shan Institute of Science and Technology,
Lung-Tan, Taiwan

The theory of flexural waves in an elastic beam with periodic structure is developed in terms of Floquet waves. Special relationships have been determined among the fundamental solutions of the governing equation. Two lemmas about the properties of the fundamental solutions are proved. With the help of these relations and lemmas, the analysis and classification of the dynamic nature of the problem is greatly simplified. We show that the flexural wave propagation in a periodic beam can be interpreted as the superposition of two pairs of waves propagating in opposite directions, of which one pair behaves as an attenuated wave. The dispersion spectrum of the second pair of waves shows the band structure, consisting of stopping bands and passing bands. Exploiting the symmetry of the structure, the dispersion equation at the end points of Brillouin zones is uncoupled into two simpler equations. These uncoupled equations represent the dispersion spectrum of waves which are either symmetric, or antisymmetric.

1 Introduction

Many structures are either designed in the form of periodic structures or almost periodic, in order to save time and reduce the cost of production. Aircraft fuselages, space and ship structures, pontoon bridges, apartment buildings, monorail tracks, parabolic antennas, etc., are all typical examples of periodic structures. A general characteristic of wave propagation in a periodic structure is typified by the existence of band structure in the dispersion spectrum, which consists of stopping and passing bands. This gives the periodic structure the characteristic of a filter, in which waves having frequency and wave number lying in the stopping bands are attenuated, while those lying outside these bands are transmitted. The diverse and wide applications of periodic structures in recent years have led to many research papers in this area. Examples are: (1) The development of various approximate continuum theories (Sun et al., 1968; Sve, 1971; Hegemier et al., 1974; Nayfeh, 1974), (2) the application of Floquet theory (Lee and Yang, 1973; Schoenberg, 1984) and (3) the experimental verification (Kinra et al., 1983; Touratier, 1986). An interesting review of the theory and applications of waves in periodic structures can be found in the review papers by Elachi (1976) and Noor (1988).

A study of this type of problem invariably leads to either a system of second order, or a system of fourth-order differential equations with periodic coefficients. Whereas problems governed by second-order differential equations have been extensively studied and the associated theory well developed (Magnus et al., 1979; Brillouin, 1953), the problems governed by fourth-order differential equation have not yet received sufficient attention. This is due to the fact that the governing theory of fourth-order ordinary differential equations with periodic coefficients have defied full exploration because of the complexity of the associated dispersion equation.

Recently, a preliminary study of flexural wave propagation in a periodic beam was studied by Lee, Ke and Kao (1990). In their study, the periodic beam is the union of an infinite number of identical cells. Each cell consists of two layers. The two-phase composite is made up of two differential materials. In this paper, we generalize the previous study and develop a general solution theory for flexural wave propagation in a periodic beam with continuously varied mechanical impedance. The governing eigenvalue equation is a fourth-order ordinary differential equation with periodic continuous coefficients. We first show that there exists several identities among the four fundamental solutions of the governing equation and then prove two lemmas about the properties of the solutions. Consequently, it is shown that the analysis and classification takes on an elegant and simple form. Making use of the inherent symmetry in periodic structure, we show how the dispersion equation at the end point of the Brillouin zone can be uncoupled. This then enables us to carry out a detailed investigation of the spectrum in its simpler form.

2 Governing Equation

Consider a periodic beam of infinite length as shown in Fig. 1. The one-dimensional domain along the length direction is

Contributed by the ASME Applied Mechanics Division of THE AMERICAN SOCIETY OF MECHANICAL ENGINEERS for presentation at the Winter Annual Meeting, Atlanta, Ga., Dec. 1-6, 1991.

Discussion on this paper should be addressed to the Technical Editor, Prof. Leon M. Keer, The Technological Institute, Northwestern University, Evanston, IL 60208, and will be accepted until two months after final publication of the paper itself in the JOURNAL OF APPLIED MECHANICS. Manuscript received by the ASME Applied Mechanics Division, Aug. 23, 1990; final revision, Mar. 14, 1991.

Paper No. 91-WA/APM-40.

Copyright © 1992 by ASME
Downloaded 03 May 2010 to 171.66.16.247. Redistribution subject to ASME license or copyright; see http://www.asme.org/terms/Terms_Use.cfm

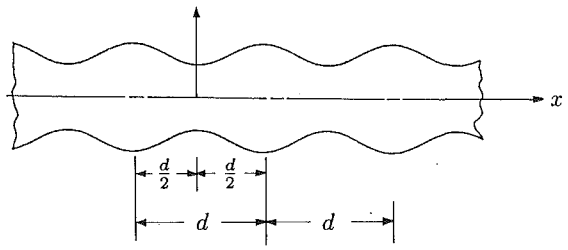


Fig. 1 Geometry of a periodic beam

the union of infinite number of cells with identical geometrical and material properties and has real minimal period d.

For time-harmonic flexural waves with angular frequency ω in radians/s., the governing Bernoulli-Euler differential equation for the flexural displacement $V(x) \in C^4$ is given by

$$\frac{d^2}{dx^2}\left[E(x)I(x)\frac{d^2V(x)}{dx^2}\right]-\rho(x)\omega^2V(x)=0, \quad x\in(-\infty,\infty) \tag{1}$$

where $E(x+d)I(x+d)=E(x)I(x)$ is the bending rigidity of the system, $\rho(x+d)=\rho(x)$ is mass density per unit length, and both are assumed periodic with minimal period d. For simplicity we divide this equation by a constant E_oI_o which has the meaning of bending rigidity at the origin of the coordinate system. Thus, Eq. (1) takes the form:

$$\frac{d^2}{dx^2}\left[G(x)\frac{d^2V(x)}{dx^2}\right]-Q(x)V(x)=0, \quad x\in(-\infty,\infty) \tag{2}$$

where $G(x)$ and $Q(x)$ are defined as

$$G(x)\equiv\frac{E(x)I(x)}{E_oI_o}, \quad Q(x)\equiv\frac{\rho(x)\omega^2}{E_oI_o}$$

with $G(x+d)=G(x)$, $Q(x+d)=Q(x)$, $G(0)=1$, $G(x)\in C^2$ and $G(x)\neq 0$ for $x\in(-\infty,\infty)$. Furthermore, with this choice of the origin of the coordinate system we further stipulate that $G'(0)=G'(d)=0$.

3 Displacement Field

Now, consider the general solution of the differential Eq. (2) in the form

$$V(x)=aV_1(x)+bV_2(x)+cV_3(x)+eV_4(x), \quad x\in(-\infty,\infty) \tag{3}$$

where a, b, c, and e are four arbitrary constants to be determined. In order that the four fundamental continuously differentiable solutions V_1, V_2, V_3, and V_4 are linearly independent and unique, they are chosen such that they satisfy the following normalization condition at the origin of the coordinate system:

$$\begin{bmatrix} V_1(0) & V_2(0) & V_3(0) & V_4(0) \\ V_1'(0) & V_2'(0) & V_3'(0) & V_4'(0) \\ V_1''(0) & V_2''(0) & V_3''(0) & V_4''(0) \\ V_1'''(0) & V_2'''(0) & V_3'''(0) & V_4'''(0) \end{bmatrix}=\begin{bmatrix} 1&0&0&0 \\ 0&1&0&0 \\ 0&0&1&0 \\ 0&0&0&1 \end{bmatrix}. \tag{4}$$

It is well known from Abel's theorem that the Wronskian $W[x]$ of the fundamental solutions satisfies the differential equation $G(x)W'[x]+2G'(x)W[x]=0$, $W[0]=1$ and therefore

$$W[x]\equiv W[V_1(x),\ V_2(x),\ V_3(x),\ V_4(x)]=\frac{1}{G^2(x)}, \quad x\in(-\infty,\infty). \tag{5}$$

With the fundamental solutions chosen in this manner, one can derive several important and useful identities among the four fundamental solutions. The algebraic details of the derivation of these identities are given in Appendix A. These identities are important and enable us to considerably simplify the analysis. In particular, if the structure is symmetric, useful formulas relating the four fundamental solutions and their first second, and third derivatives at period $x=d$ and at half period $x=\frac{d}{2}$ can be established through the use of these identities. As a result, a precise classification of the dynamic nature at the end point of Brillouin zones can be obtained.

Since the coefficients $G(x)$ and $Q(x)$ of the governing Eq. (1) are periodic, the solutions in the second cell can be written in terms of the fundamental solutions in the first cell, and therefore their linear combination satisfy relations of the form

$$\begin{bmatrix} V_1(x+d) \\ V_2(x+d) \\ V_3(x+d) \\ V_4(x+d) \end{bmatrix}=\begin{bmatrix} a_{11}&a_{12}&a_{13}&a_{14} \\ a_{21}&a_{22}&a_{23}&a_{24} \\ a_{31}&a_{32}&a_{33}&a_{34} \\ a_{41}&a_{42}&a_{43}&a_{44} \end{bmatrix}\begin{bmatrix} V_1(x) \\ V_2(x) \\ V_3(x) \\ V_4(x) \end{bmatrix} \tag{6}$$

where the coefficients a_{mn} need to be determined. Using the normalization condition Eq. (4), it can be shown that the coefficients a_{mn} are given by

$$\begin{bmatrix} a_{11}&a_{12}&a_{13}&a_{14} \\ a_{21}&a_{22}&a_{23}&a_{24} \\ a_{31}&a_{32}&a_{33}&a_{34} \\ a_{41}&a_{42}&a_{43}&a_{44} \end{bmatrix}=\begin{bmatrix} V_1(d) & V_1'(d) & V_1''(d) & V_1'''(d) \\ V_2(d) & V_2'(d) & V_2''(d) & V_2'''(d) \\ V_3(d) & V_3'(d) & V_3''(d) & V_3'''(d) \\ V_4(d) & V_4'(d) & V_4''(d) & V_4'''(d) \end{bmatrix}.$$

Hence, the solutions in the adjacent cell satisfy the relations

$$\begin{bmatrix} V_1(x+d) \\ V_2(x+d) \\ V_3(x+d) \\ V_4(x+d) \end{bmatrix}=\begin{bmatrix} V_1(d) & V_1'(d) & V_1''(d) & V_1'''(d) \\ V_2(d) & V_2'(d) & V_2''(d) & V_2'''(d) \\ V_3(d) & V_3'(d) & V_3''(d) & V_3'''(d) \\ V_4(d) & V_4'(d) & V_4''(d) & V_4'''(d) \end{bmatrix}\begin{bmatrix} V_1(x) \\ V_2(x) \\ V_3(x) \\ V_4(x) \end{bmatrix}. \tag{7}$$

This is the recurrence formula, with the help of which the solutions in the other cells can be easily generated once we know the solution in the fundamental cell.

4 Quasi-Periodic Condition

For a periodic beam, according to the Floquet's theorem, when $V(x)\neq 0$, the displacement, slope, bending moment, and shear force are at most quasi-periodic from cell to cell for some nonzero constant σ. It follows that at most

$$\begin{aligned} V(x+nd)&=\sigma V(x+(n-1)d), \\ V'(x+nd)&=\sigma V'(x+(n-1)d), \\ V''(x+nd)&=\sigma V''(x+(n-1)d), \\ V'''(x+nd)&=\sigma V'''(x+(n-1)d), \end{aligned} \tag{8}$$

where σ may be a real, imaginary, or complex number. From the fundamental property of the linear independence of the fundamental solutions it easily follows that for Eq. (8) to be true for all integers n and for all values of x, the coefficients a, b, c, and e must satisfy the system of homogeneous equations

$$\begin{bmatrix} V_1(d)-\sigma & V_2(d) & V_3(d) & V_4(d) \\ V_1'(d) & V_2'(d)-\sigma & V_3'(d) & V_4'(d) \\ V_1''(d) & V_2''(d) & V_3''(d)-\sigma & V_4''(d) \\ V_1'''(d) & V_2'''(d) & V_3'''(d) & V_4'''(d)-\sigma \end{bmatrix}\times\begin{bmatrix} a \\ b \\ c \\ e \end{bmatrix}=0. \tag{9}$$

Conversely, if Eq. (9) is satisfied, then $V(x+nd)$ satisfied Eq. (8).

A necessary and sufficient condition for the existence of

Downloaded 03 May 2010 to 171.66.16.247. Redistribution subject to ASME license or copyright; see http://www.asme.org/terms/Terms_Use.cfm

nontrivial solutions is that the determinant of the coefficients must vanish. This yields the characteristic σ equation

$$\sigma^4 + p\sigma^3 + q\sigma^2 + r\sigma + t = 0. \tag{10}$$

From Eqs. (5), (7), and (8), and the identities Eq. (A9), it can be shown that

$$p = r = -[V_1(d) + V_2'(d) + V_3''(d) + V_4'''(d)],$$

$$q = \begin{vmatrix} V_1(d) & V_2(d) \\ V_1'(d) & V_2'(d) \end{vmatrix} + \begin{vmatrix} V_1(d) & V_3(d) \\ V_1''(d) & V_3''(d) \end{vmatrix} + \begin{vmatrix} V_1(d) & V_4(d) \\ V_1'''(d) & V_4'''(d) \end{vmatrix} + \begin{vmatrix} V_2'(d) & V_3'(d) \\ V_2''(d) & V_3''(d) \end{vmatrix} + \begin{vmatrix} V_2'(d) & V_4'(d) \\ V_2'''(d) & V_4'''(d) \end{vmatrix} + \begin{vmatrix} V_3''(d) & V_4''(d) \\ V_3'''(d) & V_4'''(d) \end{vmatrix} \tag{11}$$

and $t = 1$. Obviously if $\sigma = \sigma_1$ is a root of Eq. (10), then there exists a nontrivial set of coefficients a, b, c, and e such that Eq. (3) holds for nontrivial $V(x)$ satisfying Eq. (8).

Because of the equivalence $p = r$, the characteristic σ equation can be factored into the product form

$$(\sigma^2 + H_1\sigma + 1)(\sigma^2 + H_2\sigma + 1) = 0, \tag{12}$$

where (H_1, H_2) has the representation

$$H_{1,2} = \frac{1}{2}\left[p \pm \sqrt{p^2 - 4(q-2)}\right]. \tag{13}$$

The factored form of the equation and its ensuing simplicity now enables us to explicity determine the roots of Eq. (10). If (σ_1, σ_2) and (σ_3, σ_4) are the roots of the equations $\sigma^2 + H_1\sigma + 1 = 0$ and $\sigma^2 + H_2\sigma + 1 = 0$, respectively, then

$$\sigma_{1,2} = \frac{1}{2}\left[-H_1 \pm \sqrt{H_1^2 - 4}\right], \tag{14}$$

and

$$\sigma_{3,4} = \frac{1}{2}\left[-H_2 \pm \sqrt{H_2^2 - 4}\right]. \tag{15}$$

If we define

$$Y_j(x) = e^{-i\lambda_j x} V(x)\,|_{\sigma=\sigma_j}, \quad j = 1,2,3,4 \tag{16}$$

where λ_j is a Floquet wave number, then $Y_j(x)$ is a periodic function with period d, provided σ_j is so chosen that

$$\sigma_j = e^{i\lambda_j d}. \tag{17}$$

Because $\sigma_1\sigma_2 = 1$ and $\sigma_3\sigma_4 = 1$, therefore $\lambda_2 = -\lambda_1 + \frac{m\pi}{d}$ and $\lambda_4 = -\lambda_3 + \frac{n\pi}{d}$, where m and n are integers. Without loss of generality, we can select $m = n = 0$ here. The general displacement field thus takes the following familiar form (Brillouin, 1953)

$$V(x) = C_1 Y_1(x) e^{i\lambda_1 x} + C_2 Y_2(x) e^{-i\lambda_1 x} + C_3 Y_3(x) e^{i\lambda_3 x} + C_4 Y_4(x) e^{-i\lambda_3 x}, \tag{18}$$

where C_1, C_2, C_3, and C_4 are four constants to be determined. This solution is a superposition of two pairs of waves propagated (or attenuated) in opposite directions. This is clearly seen if we retain the $e^{i\omega t}$ factor. If two pair of waves all attenuate, then the waves evanesce after propagating a finite number of cells. Hence, the frequency intervals in which both pairs of waves attenuate are known as stopping bands. On the other hand, the region of frequency in which any one pair of waves propagate are known as passing bands.

5 Characteristic of the Flexural Waves

In Appendix B, two lemmas are proved. In lemma I and lemma II it has been shown that, in the dynamic case ($\omega \neq 0$),

$$p > -4, \tag{19}$$

and

$$p^2 - 4(q-2) > 0, \tag{20}$$

respectively. Consequently,

$$H_2 < -2. \tag{21}$$

Hence, σ_3 and σ_4 are two distinct, positive real numbers. It follows from Eq. (17) that λ_3 is entirely imaginary. Therefore, there always exists one pair of standing waves attenuated in opposite directions. The characteristic of the other pair of waves will thus be determined by function H_1, which may be greater than, equal to or less than 2 in absolute value.

If $|H_1| < 2$, then it follows from Eqs. (14) and (17) that σ_1, σ_2 are complex conjugate with absolute value unity and λ_1, λ_2 are both real. Since $\lambda_2 = -\lambda_1$, therefore in this case the second pair of waves will propagate in opposite directions. Hence, the frequency intervals which correspond to $|H_1| < 2$ are passing bands.

If $H_1 > 2$ (or $H_1 < -2$), then from Eqs. (14) and (17) it follows that σ_1 and σ_2 are two distinct negative (or positive) real numbers and λ_1 has the form $(2n-1)\pi/d + ik/d$ (or $2n\pi/d + ik/d$), where k is a positive real number, n is an integer. In this case, the second pair of waves form a standing wave with amplitude attenuating in both directions and the adjacent cells vibrate in counter phase (or the same phase). Hence, the frequency intervals which correspond to $|H_1| > 2$ are stopping bands.

In case $H_1 = -2$ (or $H_1 = 2$), both σ_1 and σ_2 are equal to unity (or -1). If the group velocity $\partial\omega/\partial R_e\lambda$ is equal to zero, where $R_e\lambda$ represents the real part of Floquet wave number λ, then the waves will form a standing wave with period d (or double period $2d$). On the other hand, if the group velocity is not equal to zero, the waves will propagate in both directions. An interesting discussion on this specific problem can be found in Brillouin' book (1953).

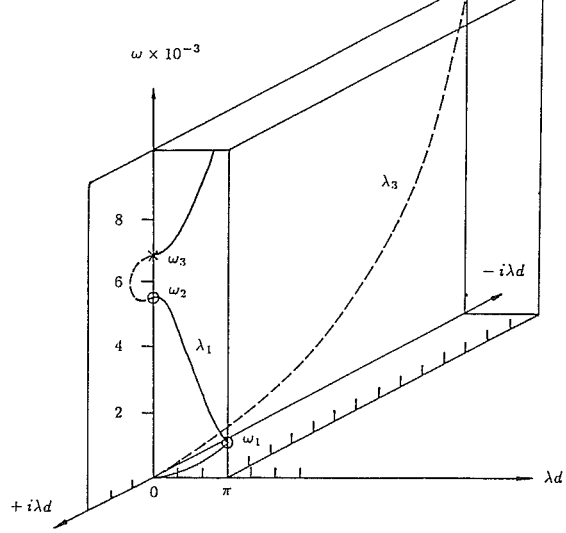


Fig. 2 Dispersion spectrum of a periodic beam in Brillouin reduced zone scheme; $\left(E(x) = 6.8947 \times 10^{10}\ \text{N/m}^2,\ \rho(x) = 2698.4\ \text{Kg/m}^3,\ A(x) = 4.0 \times 10^{-4}\left(2.0 - 1.2\cos\frac{2\pi x}{d}\right)\ \text{m}^2,\ I(x) = 1.333 \times 10^{-8}\left(2.0 - 1.2\cos\frac{2\pi x}{d}\right)\ \text{m}^2,\ d = 0.25\ \text{m}\right)$

Downloaded 03 May 2010 to 171.66.16.247. Redistribution subject to ASME license or copyright; see http://www.asme.org/terms/Terms_Use.cfm

6 Numerical Example

In the previous sections, the characteristic σ equation for the flexural wave propagation of a beam with periodic structure is derived in terms of four normalized fundamental solutions of the systems. However, in general, these fundamental solutions are not available in closed form. In this paper, the approximate fundamental solutions are obtained through the numerical algorithm developed by Lee and Ke (1990). The algorithm had been shown to be accurate and efficient.

Figure 2 shows the geometry, material parameters and dispersion spectrum in reduced Brillouin zone scheme for a periodic beam as shown in Fig. 1. Since $\lambda_1 = -\lambda_2$ and $\lambda_3 = -\lambda_4$, the figure shows only two curves corresponding to the branches λ_1 and λ_3. The dotted line and real line correspond to λ_3 and λ_1, respectively. From Eqs. (14), (15), and (17), we realize that λ_3 and λ_1 are dominated by H_2 and H_1, respectively. The branch λ_3 represents a pair of attenuated standing waves in the whole frequency domain. For the branch λ_1, the frequency interval between ω_{2n-1} and ω_{2n} are the stopping bands and correspond to the case $|H_1| > 2$. The remaining frequency intervals are passing bands. On the right and left-end points of Brillouin zones, H_1 is equal to -2 and 2, respectively. It can be observed that the dispersion spectrum for the branch λ_1 is similar to that of the dynamic systems governed by the second-order ordinary differential equation with periodic coefficients (Lee and Yang, 1973) and thus illustrates that the existence of passing bands and stopping bands is also a characteristic of flexural waves in periodic beams.

7 The Symmetric Case

If there exists a set of coordinate system which imparts symmetry to the structure, then with respect to this coordinate system the coefficients $G(x)$, $Q(x)$ of the governing Eq. (1) shall be even functions. It can then be shown that $V_1(x)$, $V_3(x)$, $V_2'(x)$, $V_4'(x)$, $V_1''(x)$, $V_3''(x)$, $V_2'''(x)$, $V_4'''(x)$ are even functions and $V_2(x)$, $V_4(x)$, $V_1'(x)$, $V_3'(x)$, $V_2''(x)$, $V_4''(x)$, $V_1'''(x)$, $V_3'''(x)$ are odd functions (Appendix C).

7.1 Double Angle Formulas. Differentiating Eq. (7) successively up to the third order, collecting terms together, setting $x = -\frac{d}{2}$ and making use of the even and odd properties of the fundamental solutions, we obtain

$$\begin{bmatrix} V_1\left(\frac{d}{2}\right) & V_1'\left(\frac{d}{2}\right) & V_1''\left(\frac{d}{2}\right) & V_1'''\left(\frac{d}{2}\right) \\ V_2\left(\frac{d}{2}\right) & V_2'\left(\frac{d}{2}\right) & V_2''\left(\frac{d}{2}\right) & V_2'''\left(\frac{d}{2}\right) \\ V_3\left(\frac{d}{2}\right) & V_3'\left(\frac{d}{2}\right) & V_3''\left(\frac{d}{2}\right) & V_3'''\left(\frac{d}{2}\right) \\ V_4\left(\frac{d}{2}\right) & V_4'\left(\frac{d}{2}\right) & V_4''\left(\frac{d}{2}\right) & V_4'''\left(\frac{d}{2}\right) \end{bmatrix}$$

$$= \begin{bmatrix} V_1(d) & V_1'(d) & V_1''(d) & V_1'''(d) \\ V_2(d) & V_2'(d) & V_2''(d) & V_2'''(d) \\ V_3(d) & V_3'(d) & V_3''(d) & V_3'''(d) \\ V_4(d) & V_4'(d) & V_4''(d) & V_4'''(d) \end{bmatrix}$$

$$\times \begin{bmatrix} V_1\left(\frac{d}{2}\right) & -V_1'\left(\frac{d}{2}\right) & V_1''\left(\frac{d}{2}\right) & -V_1'''\left(\frac{d}{2}\right) \\ -V_2\left(\frac{d}{2}\right) & V_2'\left(\frac{d}{2}\right) & -V_2''\left(\frac{d}{2}\right) & V_2'''\left(\frac{d}{2}\right) \\ V_3\left(\frac{d}{2}\right) & -V_3'\left(\frac{d}{2}\right) & V_3''\left(\frac{d}{2}\right) & -V_3'''\left(\frac{d}{2}\right) \\ -V_4\left(\frac{d}{2}\right) & V_4'\left(\frac{d}{2}\right) & -V_4''\left(\frac{d}{2}\right) & V_4'''\left(\frac{d}{2}\right) \end{bmatrix}. \quad (22)$$

The ith row of the left-hand side of this matrix equation is the product of the corresponding ith row of the first matrix and the 4×4 matrix on the right-hand side. Furthermore,

$$\begin{bmatrix} V_i\left(\frac{d}{2}\right) \\ V_i'\left(\frac{d}{2}\right) \\ V_i''\left(\frac{d}{2}\right) \\ V_i'''\left(\frac{d}{2}\right) \end{bmatrix}^T = \begin{bmatrix} V_i(d) \\ V_i'(d) \\ V_i''(d) \\ V_i'''(d) \end{bmatrix}^T$$

$$\times \begin{bmatrix} V_1\left(\frac{d}{2}\right) & -V_1'\left(\frac{d}{2}\right) & V_1''\left(\frac{d}{2}\right) & -V_1'''\left(\frac{d}{2}\right) \\ -V_2\left(\frac{d}{2}\right) & V_2'\left(\frac{d}{2}\right) & -V_2''\left(\frac{d}{2}\right) & V_2'''\left(\frac{d}{2}\right) \\ V_3\left(\frac{d}{2}\right) & -V_3'\left(\frac{d}{2}\right) & V_3''\left(\frac{d}{2}\right) & -V_3'''\left(\frac{d}{2}\right) \\ -V_4\left(\frac{d}{2}\right) & V_4'\left(\frac{d}{2}\right) & -V_4''\left(\frac{d}{2}\right) & V_4'''\left(\frac{d}{2}\right) \end{bmatrix}$$

$$i = 1,2,3,4. \quad (23)$$

From Cramer's rule and the special relationships Eqs. (A7) and (A8), we arrive at one set of equations which relate the value of V_1, V_2, V_3, V_4 and their first three derivates at full period $x = d$ and at half period $x = \frac{d}{2}$,

$$V_1(d) = 1 + 2\left[V_1'\left(\frac{d}{2}\right) V_4''\left(\frac{d}{2}\right) + V_1'''\left(\frac{d}{2}\right) V_4\left(\frac{d}{2}\right) \right]$$
$$= 2\left[V_1\left(\frac{d}{2}\right) V_4'''\left(\frac{d}{2}\right) + V_1''\left(\frac{d}{2}\right) V_4'\left(\frac{d}{2}\right) \right] - 1, \quad (24a)$$

$$V_1'(d) = 1 + 2\left[V_2\left(\frac{d}{2}\right) V_3'''\left(\frac{d}{2}\right) + V_2''\left(\frac{d}{2}\right) V_3'\left(\frac{d}{2}\right) \right]$$
$$= 2\left[V_2'\left(\frac{d}{2}\right) V_3''\left(\frac{d}{2}\right) + V_2'''\left(\frac{d}{2}\right) V_3\left(\frac{d}{2}\right) \right] - 1, \quad (24b)$$

$$V_1''(d) = 2\left[V_1\left(\frac{d}{2}\right) V_2'''\left(\frac{d}{2}\right) + V_1''\left(\frac{d}{2}\right) V_2'\left(\frac{d}{2}\right) \right]$$
$$= 2\left[V_1'\left(\frac{d}{2}\right) V_2''\left(\frac{d}{2}\right) + V_1'''\left(\frac{d}{2}\right) V_2\left(\frac{d}{2}\right) \right], \quad (24c)$$

Downloaded 03 May 2010 to 171.66.16.247. Redistribution subject to ASME license or copyright; see http://www.asme.org/terms/Terms_Use.cfm

$$V_1'''(d) = 2\left[V_1\left(\frac{d}{2}\right) V_1'''\left(\frac{d}{2}\right) + V_1''\left(\frac{d}{2}\right) V_1'\left(\frac{d}{2}\right)\right], \tag{24d}$$

$$V_2(d) = 2\left[V_2\left(\frac{d}{2}\right) V_4'''\left(\frac{d}{2}\right) + V_2''\left(\frac{d}{2}\right) V_4'\left(\frac{d}{2}\right)\right]$$
$$= 2\left[V_2'\left(\frac{d}{2}\right) V_4''\left(\frac{d}{2}\right) + V_2'''\left(\frac{d}{2}\right) V_4\left(\frac{d}{2}\right)\right], \tag{24e}$$

$$V_2'(d) = 1 + 2\left[V_2\left(\frac{d}{2}\right) V_3'''\left(\frac{d}{2}\right) + V_2''\left(\frac{d}{2}\right) V_3'\left(\frac{d}{2}\right)\right]$$
$$= 2\left[V_2'\left(\frac{d}{2}\right) V_3''\left(\frac{d}{2}\right) + V_2'''\left(\frac{d}{2}\right) V_3\left(\frac{d}{2}\right)\right] - 1, \tag{24f}$$

$$V_2''(d) = 2\left[V_2\left(\frac{d}{2}\right) V_2'''\left(\frac{d}{2}\right) + V_2''\left(\frac{d}{2}\right) V_2'\left(\frac{d}{2}\right)\right], \tag{24g}$$

$$V_2'''(d) = V_1''(d), \tag{24h}$$

$$V_3(d) = 2\left[V_3\left(\frac{d}{2}\right) V_4'''\left(\frac{d}{2}\right) + V_3''\left(\frac{d}{2}\right) V_4'\left(\frac{d}{2}\right)\right]$$
$$= 2\left[V_3'\left(\frac{d}{2}\right) V_4''\left(\frac{d}{2}\right) + V_3'''\left(\frac{d}{2}\right) V_4\left(\frac{d}{2}\right)\right], \tag{24i}$$

$$V_3'(d) = 2\left[V_3\left(\frac{d}{2}\right) V_3'''\left(\frac{d}{2}\right) + V_3''\left(\frac{d}{2}\right) V_3'\left(\frac{d}{2}\right)\right], \tag{24j}$$

$$V_3''(d) = V_2'(d), \tag{24k}$$

$$V_3'''(d) = V_1'(d), \tag{24l}$$

$$V_4(d) = 2\left[V_4\left(\frac{d}{2}\right) V_4'''\left(\frac{d}{2}\right) + V_4''\left(\frac{d}{2}\right) V_4'\left(\frac{d}{2}\right)\right], \tag{24m}$$

$$V_4'(d) = V_3(d), \tag{24n}$$

$$V_4''(d) = V_2(d), \tag{24o}$$

$$V_4'''(d) = V_1(d). \tag{24p}$$

These equations are called the double angle formulas. With the help of these formulas, the characteristic σ equation at the both ends of the Brillouin zone can be factored into a product form. The ensuing simplification allows a more detailed classification of the dynamic nature of the system.

7.2 Decomposition of the Dispersion Equation. If we set $\sigma = 1$ in Eq. (10) and make use of the identities Eq. (A8) and Eq. (24), then the dispersion equation corresponding to the left end points of the Brillouin zone (Fig. 2) uncouples into

$$V_1'\left(\frac{d}{2}\right) V_3'''\left(\frac{d}{2}\right) - V_1'''\left(\frac{d}{2}\right) V_3'\left(\frac{d}{2}\right) = 0, \tag{25}$$

$$V_2\left(\frac{d}{2}\right) V_4''\left(\frac{d}{2}\right) - V_2''\left(\frac{d}{2}\right) V_4\left(\frac{d}{2}\right) = 0. \tag{26}$$

Similarly, if we set $\sigma = -1$ in Eq. (10), then the dispersion equation corresponding to the right end point of the Brillouin zone (Fig. 2) uncouples into two simpler equations

$$V_1\left(\frac{d}{2}\right) V_3''\left(\frac{d}{2}\right) - V_1''\left(\frac{d}{2}\right) V_3\left(\frac{d}{2}\right) = 0, \tag{27}$$

$$V_2'\left(\frac{d}{2}\right) V_4'''\left(\frac{d}{2}\right) - V_2'''\left(\frac{d}{2}\right) V_4'\left(\frac{d}{2}\right) = 0. \tag{28}$$

The significance of this uncoupling can be explained as follows: For the symmetric motion, the displacement field, Eq. (3), is the combination of two even functions

$$V(x) = aV_1(x) + cV_3(x). \tag{29}$$

By setting $n = 1$, $\sigma = 1$ and $x = -\frac{d}{2}$ in Eq. (9) and realizing that $V_1(x)$, $V_3(x)$, $V_1''(x)$, $V_3''(x)$ are even functions and $V_1'(x)$, $V_3'(x)$, $V_1'''(x)$, $V_3'''(x)$ are odd functions, we can obtain two linear independent equations. For the existence of nontrivial solutions, the determinant of the coefficients vanishes. It yields Eq. (25). Hence, Eq. (25) is the dispersion equation for a symmetric standing wave with period d and adjacent cells vibrate in the same phase. Similarly, we can show that Eq. (26) is the dispersion equation for an antisymmetric standing wave with period d and adjacent cells vibrating in the same phase, while Eqs. (27) and (28) govern symmetric and antisymmetric standing wave with double period $2d$ and adjacent cells vibrating in opposite phase, respectively. In the special case that both Eqs. (25) and (26) are equal to zero, the stopping band vanishes and the group velocity is not equal to zero. A similar situation arises in the case when both Eqs. (27) and (28) are equal to zero. For instance, the flexural waves can propagate freely in a homogeneous beam at any frequency and it can be easily shown that Eq. (25) is equal to Eq. (26) and Eq. (27) is equal to Eq. (28).

On both ends of the Brillouin zone of Fig. 2, the marks "o" and "×" are used to indicate the symmetric and antisymmetric vibration modes, respectively. At frequency ω_1, Eq. (27) is equal to Eq. (28); the stopping band vanishes and the flexural waves can propagate freely.

8 Conclusions

In this paper, the theory of flexural waves propagation in an unbounded periodic beam is developed in terms of Floquet waves. As a preliminary study of the problem, the analytical model used is based on Bernoulli-Euler beam theory. With the help of the special relationships among the fundamental solutions of the system, two lemmas about the properties of the fundamental solutions and the double angle formulas developed in this paper, the analysis and classification of the dynamic nature of the system is shown to be possible and simple.

The flexural waves propagation in the periodic beam is considered as the superposition of two pairs of waves propagating in opposite directions. One pair of these waves form a standing wave with amplitude attenuating. The dispersion spectrum of the other pair of waves is shown to take the band structure, consisting of stopping bands and passing bands. This band structure of dispersion spectrum is similarly to that of the dynamic systems governed by the second-order ordinary differential equation with periodic coefficients. Hence, the justification of whether the flexural wave will propagate through the periodic beam or not is mainly determined by a simple function H_1, Eq. (14). Furthermore, it is shown that the dispersion relation which corresponds to the end points of Brillouin zone of the dispersion spectrum can be uncoupled into two simple equations. Each of them corresponds to a standing wave which is either symmetric or antisymmetric.

Acknowledgments

This work was supported by the National Science Council of Taiwan, R.O.C. (Grant No. NSC77-0401-E006-35).

The authors are very grateful to Prof. R. K. Kaul of the State University of New York at Buffalo who read the manuscript and made highly valuable comments.

References

Brillouin, L., 1953, *Wave Propagation in Periodic Structures*, Dover, New York.

Elachi, C., 1976, "Waves in Active and Passive Periodic Structures: A Review," *Proceedings of the IEEE*, Vol. 64, pp. 1666–1698.

Hegemier, G. A., and Bache, T. C., 1974, "A General Continuum Theory with Microstructure for Wave Propagation in Elastic Laminated Composite," ASME Journal of Applied Mechanics, Vol. 41, pp. 101–105.

Kinra, V. K., and Ker, E. L., 1983, "An Experimental Investigation of Pass Bands and Stop Bands in Two Periodic Particulate Composites," *International Journal of Solids and Structures*, Vol. 19, pp. 393–410.

Downloaded 03 May 2010 to 171.66.16.247. Redistribution subject to ASME license or copyright; see http://www.asme.org/terms/Terms_Use.cfm

Lee, E. H., and Yang, W. H., 1973, "On Waves in Composite Materials with Periodic Structures," *SIAM Journal on Applied Mathematics*, Vol. 25, pp. 492–499.

Lee, S. Y., Ke, H. Y., and Kao, M. J., 1990, "Flexural Waves in a Periodic Beam," ASME JOURNAL OF APPLIED MECHANICS, Vol. 57, pp. 779–783.

Lee, S. Y., and Ke, H. Y., 1990, "Free Vibrations of a Non-uniform Beam with General Elastically Restrained Boundary Conditions," *Journal of Sound and Vibration*, Vol. 136, pp. 425–437.

Magnus, W., and Winkler, S., 1979, *Hill's Equation*, Dover, New York.

Nayfeh, A. H., 1974, "Time-Harmonic Waves Propagating Normal to the Layers of Multilayered Periodic Media," ASME JOURNAL OF APPLIED MECHANICS, Vol. 41, pp. 92–96.

Noor, A. K., 1988, "Continuum Modeling for the Repetitive Lattice Structures," ASME *Applied Mechanics Reviews*, Vol. 41, pp. 285–296.

Schoenberg, M., 1984, "Wave Propagation in Alternating Solid and Fluid Layers," *Wave Motion*, Vol. 6, pp. 303–320.

Sun, C. T., Achenbach, J. D., and Herrmann, G., 1968, "Continuum Theory for a Laminated Medium," ASME JOURNAL OF APPLIED MECHANICS, Vol. 35, pp. 467–475.

Sve, C., 1971, "Time-Harmonic Waves Traveling Obliquely in a Periodically Laminated Medium," ASME JOURNAL OF APPLIED MECHANICS, Vol. 38, pp. 477–482.

Touratier, M., 1986, "Floquet Waves in a Body with Slender Periodic Structures," *Wave Motion*, Vol. 8, pp. 485–495.

APPENDIX A

Relations Among the Fundamental Solutions

If $V_i(x)$ and $V_j(x)$ are any two linearly independent fundamental solutions of Eq. (1), then

$$\int_0^x V_j(\xi)\cdot\left\{\frac{d^2}{d\xi^2}\left[G(\xi)\frac{d^2V_i(\xi)}{d\xi^2}\right]+Q(\xi)V_i(\xi)\right\}d\xi - \int_0^x V_i(\xi)\cdot\left\{\frac{d^2}{d\xi^2}\left[G(\xi)\frac{d^2V_j(\xi)}{d\xi^2}\right]+Q(\xi)V_j(\xi)\right\}d\xi$$
$$= \{G(\xi)[V_i(\xi)V_j'''(\xi)-V_i'(\xi)V_j''(\xi)+V_i''(\xi)V_j'(\xi) - V_i'''(\xi)V_j'(\xi)]+G'(\xi)[V_i(\xi)V_j''(\xi) - V_i''(\xi)V_j(\xi)]\}_{\xi=0}^{\xi=x}=0. \quad \text{(A1)}$$

This implies that the concomitant of the operator

$$G(x)[V_i(x)V_j'''(x)-V_i'(x)V_j''(x)+V_i''(x)V_j'(x) - V_i'''(x)V_j(x)]+G'(x)[V_i(x)V_j''(x)-V_i''(x)V_j(x)]=C_{ij}, \quad \text{(A2)}$$

is a constant, where the primes indicate differentiation with respect to variable x. The concomitant C_{ij} can be determined in terms of the fundamental solutions V_i and V_j and their first three derivatives, $G(x)$ and its first derivative, evaluated at the origin of the coordinates. Hence,

$$\begin{aligned}
&V_1V_2'''-V_1'V_2''+V_1''V_2'-V_1'''V_2+g[V_1V_2''-V_1''V_2]=0,\\
&V_1V_3'''-V_1'V_3''+V_1''V_3'-V_1'''V_3+g[V_1V_3''-V_1''V_3]=0,\\
&V_1V_4'''-V_1'V_4''+V_1''V_4'-V_1'''V_4+g[V_1V_4''-V_1''V_4]=f,\\
&V_2V_3'''-V_2'V_3''+V_2''V_3'-V_2'''V_3+g[V_2V_3''-V_2''V_3]=-f,\\
&V_2V_4'''-V_2'V_4''+V_2''V_4'-V_2'''V_4+g[V_2V_4''-V_2''V_4]=0,\\
&V_3V_4'''-V_3'V_4''+V_3''V_4'-V_3'''V_4+g[V_3V_4''-V_3''V_4]=0,
\end{aligned} \quad \text{(A3)}$$

where the symbols $g(x)$ and $f(x)$ are defined as

$$g(x)\equiv\frac{G'(x)}{G(x)} \text{ and } f(x)\equiv\frac{1}{G(x)}. \quad \text{(A4)}$$

We now define $V_{lmn}^{ijk}(x)$ as

$$V_{lmn}^{ijk}(x)=\begin{vmatrix} V_l^i(x) & V_m^i(x) & V_n^i(x)\\ V_l^j(x) & V_m^j(x) & V_n^j(x)\\ V_l^k(x) & V_m^k(x) & V_n^k(x)\end{vmatrix}, \quad \begin{matrix} i,j,k=0,1,2,3\\ l,m,n=1,2,3,4\end{matrix} \quad \text{(A5)}$$

where i, j, and k indicate the order of differentiation with respect to variable x. Using Eq. (A3), one can derive the following sixteen relations:

$$\begin{aligned}
&V_{123}^{012}=fV_1,\ V_{124}^{012}=fV_2,\ V_{134}^{012}=fV_3,\ V_{234}^{012}=fV_4,\\
&V_{123}^{013}=f(V_1'-gV_1),\ V_{124}^{013}=f(V_2'-gV_2),\\
&V_{134}^{013}=f(V_3'-gV_3),\ V_{234}^{013}=f(V_4'-gV_4),\\
&V_{123}^{023}=fV_1'',\ V_{124}^{023}=fV_2'',\ V_{134}^{023}=fV_3'',\ V_{234}^{023}=fV_4'',\\
&V_{123}^{123}=f(V_1'''-gV_1''),\ V_{124}^{123}=f(V_2'''-gV_2''),\\
&V_{134}^{123}=f(V_3'''-gV_3''),\ V_{234}^{123}=f(V_4'''-gV_4'').
\end{aligned} \quad \text{(A6)}$$

Combining Eq. (A6) with the Wronskian Eq. (5), it follows that

$$\begin{aligned}
&[V_1(x)V_4''(x)-V_1''(x)V_4(x)]+G'(0)[V_2(x)V_4''(x) - V_2''(x)V_4(x)]=[V_2(x)V_3''(x)-V_2''(x)V_3(x)],\\
&[V_1(x)V_4'(x)-V_1'(x)V_4(x)]+G'(0)[V_2(x)V_4'(x) - V_2'(x)V_4(x)]=[V_2(x)V_3'(x)-V_2'(x)V_3(x)].
\end{aligned} \quad \text{(A7)}$$

For a periodic beam, Eq. (A6) at half period $\left(x=\frac{d}{2}\right)$ and at the end of a period ($x=d$) can be simplified as

$$\begin{aligned}
&V_{123}^{012}\left(\frac{d}{2}\right)=V_1\left(\frac{d}{2}\right),\quad V_{123}^{013}\left(\frac{d}{2}\right)=V_1'\left(\frac{d}{2}\right),\\
&V_{123}^{023}\left(\frac{d}{2}\right)=V_1''\left(\frac{d}{2}\right),\quad V_{123}^{123}\left(\frac{d}{2}\right)=V_1'''\left(\frac{d}{2}\right),\\
&V_{124}^{012}\left(\frac{d}{2}\right)=V_2\left(\frac{d}{2}\right),\quad V_{124}^{013}\left(\frac{d}{2}\right)=V_2'\left(\frac{d}{2}\right),\\
&V_{124}^{023}\left(\frac{d}{2}\right)=V_2''\left(\frac{d}{2}\right),\quad V_{124}^{123}\left(\frac{d}{2}\right)=V_2'''\left(\frac{d}{2}\right),\\
&V_{134}^{012}\left(\frac{d}{2}\right)=V_3\left(\frac{d}{2}\right),\quad V_{134}^{013}\left(\frac{d}{2}\right)=V_3'\left(\frac{d}{2}\right),\\
&V_{134}^{023}\left(\frac{d}{2}\right)=V_3''\left(\frac{d}{2}\right),\quad V_{134}^{123}\left(\frac{d}{2}\right)=V_3'''\left(\frac{d}{2}\right),\\
&V_{234}^{012}\left(\frac{d}{2}\right)=V_4\left(\frac{d}{2}\right),\quad V_{234}^{013}\left(\frac{d}{2}\right)=V_4'\left(\frac{d}{2}\right),\\
&V_{234}^{023}\left(\frac{d}{2}\right)=V_4''\left(\frac{d}{2}\right),\quad V_{234}^{123}\left(\frac{d}{2}\right)=V_4'''\left(\frac{d}{2}\right),
\end{aligned} \quad \text{(A8)}$$

and

$$\begin{aligned}
&V_{123}^{012}(d)=V_1(d),\quad V_{123}^{013}(d)=V_1'(d),\\
&V_{123}^{023}(d)=V_1''(d),\quad V_{123}^{123}(d)=V_1'''(d),\\
&V_{124}^{012}(d)=V_2(d),\quad V_{124}^{013}(d)=V_2'(d),\\
&V_{124}^{023}(d)=V_2''(d),\quad V_{124}^{123}(d)=V_2'''(d),\\
&V_{134}^{012}(d)=V_3(d),\quad V_{134}^{013}(d)=V_3'(d),\\
&V_{134}^{023}(d)=V_3''(d),\quad V_{134}^{123}(d)=V_3'''(d),\\
&V_{234}^{012}(d)=V_4(d),\quad V_{234}^{013}(d)=V_4'(d),\\
&V_{234}^{023}(d)=V_4''(d),\quad V_{234}^{123}(d)=V_4'''(d),
\end{aligned} \quad \text{(A9)}$$

APPENDIX B

Proof of Two Lemmas

Consider the governing equation

$$\frac{d^2}{dx^2}\left[G(x)\frac{d^2V(x)}{dx^2}\right]-Q(x)V(x)=0,\quad x\in(-\infty,\infty) \quad \text{(B1)}$$

Downloaded 03 May 2010 to 171.66.16.247. Redistribution subject to ASME license or copyright; see http://www.asme.org/terms/Terms_Use.cfm

where

$$G(x)=\frac{E(x)I(x)}{E_oI_o},\quad G(x+d)=G(x),\quad G(0)=1,$$

$$Q(x)=\frac{\rho(x)\omega^2}{E_oI_o},\quad Q(x+d)=Q(x),$$

and $G(x)>0$, $Q(x)>0$ for all x. If the bending rigidity of the beam $E(x)I(x)$, is assumed to be in class C^2, then the origin of the coordinate system can always be chosen at the point where $G'(0)=G'(d)=0$.

Lemma I. If $V_1(x)$, $V_2(x)$, $V_3(x)$, and $V_4(x)$ are the four linearly independent fundamental solutions of Eq. (B1) and satisfy the normalization condition (4), then $p=-[V_1(d)-V_2'(d)+V_3''(d)+V_4'''(d)]<-4$.

Proof: Equation (B1) can be written in the form

$$\frac{d^2}{dx^2}\left[G(x)\frac{d^2V(x)}{dx^2}\right]=Q(x)V(x), \tag{B2}$$

and

$$V^{IV}(x)=-\frac{2G'(x)}{G(x)}V'''(x)-\frac{G''(x)}{G(x)}V''(x)+\frac{Q(x)}{G(x)}V(x). \tag{B3}$$

By successively integrating, the following equations are obtained:

$$G'(x)V''(x)+G(x)V'''(x)=\int_0^x Q(t)V(t)dt+C_1, \tag{B4}$$

$$V''(x)=\frac{1}{G(x)}\left[\int_0^x\int_0^\zeta Q(t)V(t)dtd\zeta+C_1x+C_2\right], \tag{B5}$$

and

$$[V'(x)]^2=2\int_0^x\frac{V'(\xi)}{G(\xi)}\left[\int_0^\xi\int_0^\xi Q(t)V(t)dtd\zeta+C_1\xi+C_2\right]d\xi+C_3, \tag{B6}$$

where C_1, C_2, and C_3 are constants.

(1) Since $V_1(0)=1$, $V_1'(0)=V_1''(0)=V_1'''(0)=0$, one has $C_1=C_2=C_3=0$ and $V_1^{IV}(0)>0$. It follows that $V_1'(x)>0$ in the neighborhood of $x=0$ and may has a greatest lower bound $\epsilon>0$. Since $V_1'(x)$ is continuous, this lower bound implies the point where $V_1'(\epsilon)=0$.

From Eq. (B6), one has

$$[V_1'(\epsilon)]^2=2\int_0^\epsilon\frac{V_1'(\xi)}{G(\xi)}\left[\int_0^\xi\int_0^\zeta Q(t)V_1(t)dtd\zeta\right]d\xi. \tag{B7}$$

Since $V_1(0)=1$ and $V_1'(x)\geq 0$ for $0\leq x\leq\epsilon$, one has $V_1(x)>0$ and $V_1'(x)>0$ for $0<x<\epsilon$. Also, $G(x)>0$ and $Q(x)>0$ for $0<x<\epsilon$. Therefore, the right-hand side of Eq. (B7) is positive whereas one had assumed that $V_1'=0$. This shows that $V_1'(x)>0$ if $x>0$. This means that $V_1(x)>1$ for $x>0$.

(2) Since $V_2(0)=0$, $V_2'(0)=1$ and $V_2''(0)=V_2'''(0)=0$, one has $C_1=C_2=0$ and $C_3=1$. It follows that $V_2'(x)>0$ in the neighborhood of $x=0$ and may has a greatest lower bound $\epsilon>0$. Since $V_2'(x)$ is continuous, this lower bound implies the point where $V_2'(\epsilon)=0$.

From Eg. (B6), one has

$$[V_2'(\epsilon)]^2=2\int_0^\epsilon\frac{V_2'(\xi)}{G(\xi)}\left[\int_0^\xi\int_0^\zeta Q(t)V_2(t)dtd\zeta]d\xi+1. \tag{B8}$$

Since $V_2(0)=0$ and $V_2'(x)\geq 0$ for $0\leq x\leq\epsilon$, one has $V_2(x)>0$ and $V_2'(x)>0$ for $0<x<\epsilon$. Also, $G(x)>0$ and $Q(x)>0$ for $0<x<\epsilon$. Therefore, the right-hand side of Eq. (B8) is positive whereas one had assumed that $V_2'(\epsilon)=0$. This shows that $V_2'(x)>0$ if $x>0$. This means that $V_2(x)>0$ for all $x>0$.

From Eq. (B6), one has

$$[V_2'(x)]^2=2\int_0^x\frac{V_2'(\xi)}{G(\xi)}\left[\int_0^\xi\int_0^\zeta Q(t)V_2(t)dtd\zeta\right]d\xi+1. \tag{B9}$$

Since $V_2(x)>0$, $V_2'(x)>0$ and $G(x)>0$ and $Q(x)>0$ for $x>0$, one has $[V_2'(x)]^2>1$ for $x>0$. This means that $V_2'(x)>1$ for $x>0$.

(3) Since $V_3(0)=V_3'=0$, $V_3''(0)=1$ and $V_3'''(0)=0$, one has $C_1=0$, $C_2=1$ and $C_3=0$. It follows that $V_3'(x)>0$ in the neighborhood of $x=0$ and may has a greatest lower bound $\epsilon>0$. Since $V_3'(x)$ is continuous, this lower bound implies the point where $V_3'(\epsilon)=0$.

From Eq. (B6), one has

$$[V_3'(\epsilon)]^2=2\int_0^\epsilon\frac{V_3'(\xi)}{G(\xi)}\left[\int_0^\xi\int_0^\zeta Q(t)V_3(t)dtd\zeta+1\right]d\xi. \tag{B10}$$

Since $V_3(0)=0$ and $V_3'(x)\geq 0$ for $0\leq x\leq\epsilon$, one has $V_3(x)>0$ and $V_3'(x)>0$ for $0<x<\epsilon$. Also, $G(x)>0$ and $Q(x)>0$ for $0<x<\epsilon$. Therefore, the right-hand side of Eq. (B10) is positive whereas one had assumed that $V_3'(\epsilon)=0$. This shows that $V_3'(x)>0$ if $x>0$. This means that $V_3(x)>0$ for $x>0$.

Consider the value of $V_3''(x)$ at $x=d$, since $G(d)=1$, one has

$$V_3''(d)=\int_0^d\int_0^\zeta Q(t)V_3(t)dtd\zeta+1. \tag{B11}$$

Since $V_3(x)>0$ and $Q(x)>0$ for $x>0$. Therefore, from Eq. (B11), one has $V_3''(d)>1$.

(4) Since $V_4(0)=V_4'=0$, $V_4''(0)=0$ and $V_4'''(0)=1$, one has $C_1=1$, and $C_2=C_3=0$. It follows that $V_4'(x)>0$ in the neighborhood of $x=0$ and may has a greatest lower bound $\epsilon>0$. Since $V_4'(x)$ is continuous, this lower bound implies the point where $V_4'(\epsilon)=0$.

From Eq. (B6), one has

$$[V_4'(\epsilon)]^2=2\int_0^\epsilon\frac{V_4'(\xi)}{G(\xi)}\left[\int_0^\xi\int_0^\zeta Q(t)V_4(t)dtd\zeta+\xi\right]d\xi. \tag{B12}$$

Since $V_4(0)=0$ and $V_4'(x)\geq 0$ for $0\leq x\leq\epsilon$, one has $V_4(x)>0$ and $V_4'(x)>0$ for $0<x<\epsilon$. Also, $G(x)>0$ and $Q(x)>0$ for $0<x<\epsilon$. Therefore, the right-hand side of Eq. (B12) is positive whereas one had assumed that $V_4'(\epsilon)=0$. This shows that $V_4'(x)>0$ if $x>0$. This means that $V_4(x)>0$ for $x>0$.

Consider the value of $V_4'''(x)$ at $x=d$, since $G(d)=1$ and $G'(d)=0$, one has

$$V_4'''(d)=\int_0^d Q(t)V_4(t)dtd\zeta+1 \tag{B13}$$

since $V_4(x)>0$ and $Q(x)>0$ for $x>0$. Therefore, from Eq. (B13), one has $V_4'''(d)>1$.

As a result, it is shown that $p=-[V_1(d)+V_2'(d)+V_3''(d)+V_4'''(d)]<-4$.

Lemma II. If $p<-4$ then $p^2-4(q-2)>0$.

Proof: If $p^2-4(q-2)<0$, then H_1 and H_2 in Eq. (14) are complex conjugate in the form such as $H_{1,2}=a\pm ib$ where a and b are real and $i^2=-1$. Therefore, the four roots of eq. (4) are

$$\sigma_1e^{\alpha+i\beta},\quad \sigma_2e^{-\alpha-i\beta},$$
$$\sigma_3e^{\alpha-i\beta},\quad \sigma_4e^{-\alpha+i\beta}, \tag{B14}$$

where α and β are obtained from the following equations

$$a=-(e^\alpha+e^{-\alpha})\cos\beta,$$
$$b=-(e^\alpha-e^{-\alpha})\sin\beta. \tag{B15}$$

Downloaded 03 May 2010 to 171.66.16.247. Redistribution subject to ASME license or copyright; see http://www.asme.org/terms/Terms_Use.cfm

Substituting these four roots back to Eq. (12), the coefficient p is

$$p = -2(e^{\alpha} + e^{-\alpha})\cos\beta$$
$$\leq -4\cos\beta. \tag{B16}$$

Since $|\cos\beta| \leq 1$, Eq. (B16) contradicts Lemma I. Therefore, $p^2 - 4(q-2)$ must always be greater than zero, i.e., $p^2 - 4(q-2) > 0$.

APPENDIX C

Properties of the Fundamental Solutions for Symmetric Case

If $V(x)$ is one of the solution of Eq. (1), then $V(-x)$ will be a solution too. However, every solution can be obtained as a linear combination of fundamental solutions $V_1(x)$, $V_2(x)$, $V_3(x)$, and $V_4(x)$, it follows that $V_1(-x)$, $V_2(-x)$, $V_3(-x)$, and $V_4(-x)$ satisfy linear relations of the form

$$\begin{bmatrix} V_1(-x) \\ V_2(-x) \\ V_3(-x) \\ V_4(-x) \end{bmatrix} = \begin{bmatrix} b_{11} & b_{12} & b_{13} & b_{14} \\ b_{21} & b_{22} & b_{23} & b_{24} \\ b_{31} & b_{32} & b_{33} & b_{34} \\ b_{41} & b_{42} & b_{43} & b_{44} \end{bmatrix} \begin{bmatrix} V_1(x) \\ V_2(x) \\ V_3(x) \\ V_4(x) \end{bmatrix}. \tag{C1}$$

By successively differentiating the above equation with respect to space variable x up to the third derivative, setting $x = 0$ and applying the normalization condition (4), it can be shown that

$$\begin{bmatrix} b_{11} & b_{12} & b_{13} & b_{14} \\ b_{21} & b_{22} & b_{23} & b_{24} \\ b_{31} & b_{32} & b_{33} & b_{34} \\ b_{41} & b_{42} & b_{43} & b_{44} \end{bmatrix} = \begin{bmatrix} 1 & 0 & 0 & 0 \\ 0 & -1 & 0 & 0 \\ 0 & 0 & 1 & 0 \\ 0 & 0 & 0 & -1 \end{bmatrix}. \tag{C2}$$

Therefore, $V_1(x)$, $V_3(x)$, $V_2'(x)$, $V_4'(x)$, $V_1''(x)$, $V_3''(x)$, $V_2'''(x)$, $V_4'''(x)$ are even functions and $V_2(x)$, $V_4(x)$, $V_1'(x)$, $V_3'(x)$, $V_2''(x)$, $V_4''(x)$, $V_1'''(x)$, $V_3'''(x)$ are odd functions.

Downloaded 03 May 2010 to 171.66.16.247. Redistribution subject to ASME license or copyright; see http://www.asme.org/terms/Terms_Use.cfm

Natural Frequencies and Normal Modes of a Spinning Timoshenko Beam With General Boundary Conditions

Jean Wu-Zheng Zu
Graduate Student.

Ray P. S. Han
Associate Professor,
Mem. ASME.

Department of Mechanical Engineering,
University of Manitoba,
Winnipeg, Manitoba R3T 2N2, Canada

A free flexural vibrations of a spinning, finite Timoshenko beam for the six classical boundary conditions are analytically solved and presented for the first time. Expressions for computing natural frequencies and mode shapes are given. Numerical simulation studies show that the simply-supported beam possesses very peculiar free vibration characteristics: There exist two sets of natural frequencies corresponding to each mode shape, and the forward and backward precession mode shapes of each set coincide identically. These phenomena are not observed in beams with the other five types of boundary conditions. In these cases, the forward and backward precessions are different, implying that each natural frequency corresponds to a single mode shape.

1 Introduction

Natural frequencies and mode shapes are important dynamic characteristics of a structure as they are required in the solution of resonant responses and for forced vibration analysis. Of particular interest here are those pertaining to a *spinning* Timoshenko beam of finite length. Practical applications of spinning structures can be found in rotating machinery systems such as turbines and engines, machining operations such as in lathe machining, space structures such as satellites, etc. The incorporation of the effects of rotary inertia and transverse shear deformations are often necessary as many of these structures are short and stubby, and also that the Euler-Bernoulli (EB) beam theory is known to be inadequate for vibrations of the higher modes. The free vibration response of a *stationary* Timoshenko beam with general boundary conditions is already well known, but for a spinning Timoshenko beam, only the simply-supported beam has been solved. For the beams with general boundary conditions, such work has not been previously investigated.

The study of free vibrations for a stationary Timoshenko beam can be traced back to the middle of this century when Kruszewski (1949) obtained the frequency equations for the fixed-free and the free-free beams. Anderson (1953) and Dolph (1954) presented general solutions for the simply-supported boundary condition. An almost complete theoretical treatment of the problem was published by Trail-Nash and Collar (1953), giving the frequency equations and mode shapes for all six types of boundary conditions, namely, simply-supported or hinged-hinged, hinged-free, free-free, fixed-fixed, fixed-free, and fixed-hinged. However, they only presented results for half the mode shapes as those associated with the bending angle were not derived. Using a more systematic approach, Huang (1961) independently resolved this problem, again for the six boundary conditions. His analysis was complete, both with regard to the frequency equations and the mode shapes. With the exception of the simply-supported beam, the solution of the frequency equations requires a fair amount of computational effort as they are transcendental in nature. This led to the popularity of approximate techniques, mainly based on energy methods, for analysis and solution. Huang (1958), and later Hurty and Rubenstein (1964), gave some results for the simply-supported beam. Carr (1970) presented solutions for all the six boundary conditions.

The study of spinning, finite beams was treated in a comprehensive manner by Bauer (1980) where he derived the relationship between natural frequencies of a spinning beam and a stationary one, based on the EB beam theory. His analysis is valid for any of the classical boundary conditions. Lee et al. (1988) obtained closed-form solutions for frequencies and mode shapes, using the Rayleigh beam model[1], for only two types of boundary conditions: simply supported and fixed free. An approximate solution via the Galerkin's method was also given by the paper. For the Timoshenko beam model, a thor-

Contributed by the Applied Mechanics Division of THE AMERICAN SOCIETY OF MECHANICAL ENGINEERS for presentation at the 1992 ASME Summer Mechanics and Materials Meeting, Tempe, AZ, Apr. 28–May 1, 1992.

Discussion on this paper should be addressed to the Technical Editor, Prof. Leon M. Keer, The Technological Institute, Northwestern University, Evanston, IL 60208, and will be accepted until four months after final publication of the paper itself in the JOURNAL OF APPLIED MECHANICS. Manuscript received by the ASME Applied Mechanics Division, Sept. 27, 1990; final revision, Apr. 30, 1991.

Paper No. 92-APM-6.

[1] Only rotary inertia effects are included in this model.

Copyright © 1992 by ASME
Downloaded 03 May 2010 to 171.66.16.247. Redistribution subject to ASME license or copyright; see http://www.asme.org/terms/Terms_Use.cfm

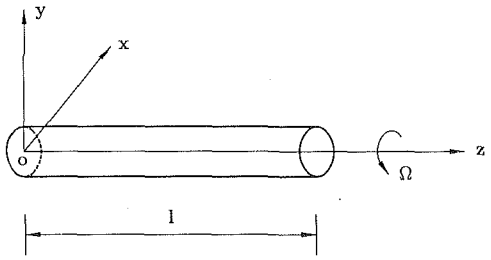


Fig. 1 A spinning shaft and its frame of reference

ough investigation, which is valid only for simply-supported beams, was carried out by Dimentberg (1961). Using an integral transform technique, Katz et al. (1988) developed the frequency equation, also for simply-supported beams. A different approach, one based on the physically more meaningful modal analysis, was presented by Han and Zu (1990) in their solution for the frequency response of a simply-supported Timoshenko beam. They gave exact results for the first two frequencies with respect to the spinning speed. For non-simply-supported boundary conditions some work was presented by Eshleman and Eubanks (1969) for fixed-fixed beams.

In this paper, a complete free vibration analysis of a spinning, finite Timoshenko beam with general boundary conditions is carried out. Analytical solutions of the frequency equations and mode shapes are given for the six types of boundary conditions. Numerical simulations show that the simply-supported beam possesses unusual free vibration characteristics which are not observed in the other five types of boundary conditions.

2 Equations of Motion and Boundary Conditions

The equations of motion based on an intertial frame *oxyz* as depicted in Fig. 1 for a spinning, uniform Timoshenko beam of a finite length l are given in Han and Zu (1990) as

$$\frac{\partial^2 u_x}{\partial t^2}+\frac{\kappa G}{\rho l^2}\left(l\frac{\partial \psi_x}{\partial \zeta}-\frac{\partial^2 u_x}{\partial \zeta^2}\right)=0 \tag{1}$$

$$\frac{\partial^2 u_y}{\partial t^2}+\frac{\kappa G}{\rho l^2}\left(l\frac{\partial \psi_y}{\partial \zeta}-\frac{\partial^2 u_y}{\partial \zeta^2}\right)=0 \tag{2}$$

$$\frac{\partial^2 \psi_x}{\partial t^2}+\frac{\Omega J_z}{\rho I}\frac{\partial \psi_y}{\partial t}-\frac{E}{\rho l^2}\frac{\partial^2 \psi_x}{\partial \zeta^2}+\frac{\kappa AG}{\rho I l}\left(l\psi_x-\frac{\partial u_x}{\partial \zeta}\right)=0 \tag{3}$$

$$\frac{\partial^2 \psi_y}{\partial t^2}-\frac{\Omega J_z}{\rho I}\frac{\partial \psi_x}{\partial t}-\frac{E}{\rho l^2}\frac{\partial^2 \psi_y}{\partial \zeta^2}+\frac{\kappa AG}{\rho I l}\left(l\psi_y-\frac{\partial u_y}{\partial \zeta}\right)=0 \tag{4}$$

where ρ is the mass density, A is the cross-sectional area, I is the transverse moment of inertia of an axisymmetric cross-section, J_z is the polar mass moment of inertia, and E, G, and κ are Young's modulus, shear modulus, and shear coefficient, respectively. For convenience, the parameter $\zeta=z/l$ has been introduced. The transverse deflections along *ox*, *oy* directions are represented by u_x, u_y, and their corresponding bending angles by ψ_x and ψ_y. Defining

$$\begin{aligned} u&=u_x+iu_y \\ \psi&=\psi_x+i\psi_y. \end{aligned} \tag{5}$$

Equations (1)–(4) become

$$\frac{\partial^2 u}{\partial t^2}+\frac{\kappa G}{\rho l^2}\left(l\frac{\partial \psi}{\partial \zeta}-\frac{\partial^2 u}{\partial \zeta^2}\right)=0 \tag{6}$$

$$\frac{\partial^2 \psi}{\partial t^2}-i\frac{\Omega J_z}{\rho I}\frac{\partial \psi}{\partial t}-\frac{E}{\rho l^2}\frac{\partial^2 \psi}{\partial \zeta^2}+\frac{\kappa AG}{\rho I l}\left(l\psi-\frac{\partial u}{\partial \zeta}\right)=0. \tag{7}$$

Uncoupling ψ and u yields the following equations for these variables

$$\frac{\rho^2 I}{\kappa G}\frac{\partial^4 u}{\partial t^4}-i\Omega\frac{\rho J_z}{\kappa G}\frac{\partial^3 u}{\partial t^3}+\rho A\frac{\partial^2 u}{\partial t^2}-\frac{\rho I}{l^2}\left(1+\frac{E}{\kappa G}\right)\frac{\partial^4 u}{\partial \zeta^2 \partial t^2}+i\Omega\frac{J_z}{l^2}\frac{\partial^3 u}{\partial \zeta^2 \partial t}+\frac{EI}{l^4}\frac{\partial^4 u}{\partial \zeta^4}=0 \tag{8}$$

$$\frac{\partial^2 I}{\kappa G}\frac{\partial^4 \psi}{\partial t^4}-i\Omega\frac{\rho J_z}{\kappa G}\frac{\partial^2 \psi}{\partial t^3}+\rho A\frac{\partial^2 \psi}{\partial t^2}-\frac{\rho I}{l^2}\left(1+\frac{E}{\kappa G}\right)\frac{\partial^4 \psi}{\partial \zeta^2 \partial t^2}+i\Omega\frac{J_z}{l^2}\frac{\partial^3 \psi}{\partial \zeta^2 \partial t}+\frac{EI}{l^4}\frac{\partial^4 \psi}{\partial \zeta^4}=0. \tag{9}$$

The necessary and sufficient boundary conditions at $\zeta=\zeta_0$, where $\zeta_0=0$, 1 are:

(a) Hinged End

$$u(\zeta_0, t)=0 \tag{10}$$

$$\psi'(\zeta_0, t)=0. \tag{11}$$

(b) Fixed End

$$u(\zeta_0, t)=0 \tag{12}$$

$$\psi(\zeta_0, t)=0. \tag{13}$$

(c) Free End

$$\psi'(\zeta_0, t)=0 \tag{14}$$

$$\frac{u'(\zeta_0, t)}{l}-\psi(0, t)=0. \tag{15}$$

3 Solutions

Assume that the solutions of Eqs. (8) and (9) are

$$u=U(\zeta)Q(t)=U_0 e^{ik_u\zeta}e^{i\omega t} \tag{16}$$

$$\psi=\Psi(\zeta)Q(t)=\Psi_0 e^{ik_\psi\psi}e^{i\omega t} \tag{17}$$

where U_0 and Ψ_0 are complex amplitudes, ω is the natural frequency and k_u and k_ψ are coefficients characterizing the normal modes. Noting that Eqs. (8) and (9) are identical in form, $k_u=k_\psi=k$. Substituting Eqs. (16) and (17) into Eqs. (8) and (9) yields

$$ak^4-bk^2+c=0 \tag{18}$$

where

$$\begin{aligned} a&=\frac{EI}{l^4\rho A} \\ b&=\frac{I}{l^2 A}\left(1+\frac{E}{\kappa G}\right)\omega^2-\frac{\Omega J_z}{l^2\rho A}\omega \\ c&=\frac{\rho I}{\kappa AG}\omega^4-\frac{\Omega J_z}{\kappa AG}\omega^3-\omega^2. \end{aligned} \tag{19}$$

Observe that k is dependent on the natural frequency ω. The quantity a is always positive, while b and c can take positive or negative values depending on the magnitude of ω. To solve Eq. (18), the following two cases are considered.

Case 1: $\sqrt{b^2-4ac}>b$. This is true for $c<0$. Physically, this case would correspond to lower frequency vibrations, as evident from Eq. (19*c*). The solutions for k are given by

$$k_{1,2}=\pm is_1,\ \pm s_2 \tag{20}$$

in which

$$s_1=\sqrt{\frac{-b+\sqrt{b^2-4ac}}{2a}} \tag{21}$$

$$s_2=\sqrt{\frac{b+\sqrt{b^2-4ac}}{2a}} \tag{22}$$

From the solutions of k, the normal modes for u and ψ, $U(\zeta)$, and $\Psi(\zeta)$ can be expressed as

Downloaded 03 May 2010 to 171.66.16.247. Redistribution subject to ASME license or copyright; see http://www.asme.org/terms/Terms_Use.cfm

$$U(\zeta)=A_1\cosh(s_1\zeta)+A_2\sinh(s_2\zeta)+A_3\cos(s_2\zeta)+A_4\sin(s_2\zeta) \quad (23)$$

$$\Psi(\zeta)=A_1'\sinh(s_1\zeta)+A_2'\cosh(s_1\zeta)+A_3'\sin(s_2\zeta)+A_4'\cos(s_2\zeta). \quad (24)$$

Note that only half the integration constants $A_1 \sim A_4$ and $A_1' \sim A_4'$ are independent. By substituting Eqs. (23) and (24) into Eqs. (6), their relations can be obtained as

$$A_1'=c_1A_1, \quad A_3'=c_2A_3$$
$$A_2'=c_1A_2, \quad A_4'=-c_2A_4 \quad (25)$$

where

$$c_1=\frac{1}{s_1}\left(\frac{\rho l}{\kappa G}\omega^2+\frac{1}{l}s_1^2\right)$$
$$c_2=\frac{1}{s_2}\left(\frac{\rho l}{\kappa G}\omega^2-\frac{1}{l}s_2^2\right). \quad (26)$$

Case 2: $\sqrt{b^2-4ac}<b$. This is true for b, $c>0$. Physically, this case would correspond to higher frequency vibrations, as is evident from Eq. (19*c*). Only the k_1 solution of k is modified to

$$k_1=\pm s_1' \quad (27)$$

in which

$$s_1'=is_2=\sqrt{\frac{b-\sqrt{b^2-4ac}}{2a}}. \quad (28)$$

The normal modes are

$$U(\zeta)=A_1\cos(s_1'\zeta)+A_2\sin(s_1'\zeta)+A_3\cos(s_2\zeta)+A_4\sin(s_2\zeta) \quad (29)$$

$$\Psi(\zeta)=A_1'\sin(s_1'\zeta)+A_2'\cos(s_1'\zeta)+A_3'\sin(s_2\zeta)+A_4'\cos(s_2\zeta). \quad (30)$$

As before, the coefficients, $A_1 \sim A_4$ and $A_1' \sim A_4'$ are related by

$$A_1'=c_1'A_1, \quad A_3'=c_2A_3$$
$$A_2'=-c_1'A_2, \quad A_4'=-c_2A_4 \quad (31)$$

in which

$$c_1'=\frac{1}{s_1'}\left(\frac{\rho l}{\kappa G}\omega^2-\frac{1}{l}s_1'^2\right). \quad (32)$$

4 Natural Frequencies and Normal Modes

Expressions for computing natural frequencies and normal modes for a spinning Timoshenko beam subjected to the six classical boundary conditions are listed here. These boundary conditions are, (a) simply-supported or hinged-hinged, (b) hinged-free, (c) free-free, (d) fixed-fixed, (e) fixed-free, and (f) fixed-hinged. Clearly, other types such as yielding supports can be derived without too much difficulty.

The application of appropriate boundary conditions (10)–(15) together with integration constants (25) (or (31)) and normal modes Eqs. (23) and (24) to Eqs. (16) and (17), yields for each type of beam a set of four homogeneous algebraic equations for the four constants, A_1 to A_4. The characteristic equations for each case are then obtained by setting the determinant of the coefficients of A_i to zero, and solutions of these equations yield the natural frequencies. Having computed the eigenvalue the corresponding eigenfunctions, normal modes $U(\zeta)$ and $\Psi(\zeta)$ can be evaluated accordingly.

(a) Simply-Supported Beam.

Boundary Conditions.

$$U(0)=0, \quad \Psi'(0)=0$$
$$U(1)=0, \quad \Psi'(1)=0 \quad (33)$$

Natural Frequencies.

$$\sin(s_2)=0 \quad (34)$$

Normal Modes.

$$U(\zeta)=U_0\sin(s_2\zeta) \quad (35)$$

$$\Psi(\zeta)=\Psi_0\cos(s_2\zeta) \quad (36)$$

(b) Hinged-Free Beam.

Boundary Conditions.

$$U(0)=0, \quad \Psi'(0)=0$$
$$\Psi'(1)=0, \quad \frac{1}{l}U'(1)-\Psi(1)=0 \quad (37)$$

Natural Frequencies.

$$c_1s_1\left(\frac{1}{l}s_2+c_2\right)\sinh(s_1)\cos(s_2)-c_2s_2\left(\frac{1}{l}s_1-c_1\right)\cosh(s_1)\sin(s_2)=0, \quad (\sqrt{b^2-4ac}>b) \quad (38)$$

$$c_1's_1'\left(\frac{1}{l}s_2+c_2\right)\sin(s_1')\cos(s_2)-c_2s_2\left(\frac{1}{l}s_1'+c_1'\right)\cos(s_1')\sin(s_2)=0, \quad (\sqrt{b^2-4ac}<b) \quad (39)$$

Normal Modes.

$$U(\zeta)=U_0\left[\sinh(s_1\zeta)-\frac{d}{c_2}\sin(s_1\zeta)\right],$$
$$\Psi(\zeta)=\Psi_0[c_1\cosh(s_1\zeta)+d\cos(s_2\zeta)], \quad (\sqrt{b^2-4ac}>b) \quad (40)$$

$$U(\zeta)=U_0\left[\sin(s_1'\zeta)-\frac{d'}{c_2}\sin(s_2\zeta)\right],$$
$$\Psi(\zeta)=\Psi_0[c_1'\cos(s_1'\zeta)+d'\cos(s_2\zeta)], \quad (\sqrt{b^2-4ac}<b) \quad (41)$$

where

$$d=\frac{c_1s_1\sinh(s_1)}{s_2\sin(s_2)}$$
$$d'=\frac{c_1's_1'\sin(s_1')}{s_2\sin(s_2)}. \quad (42)$$

(c) Free-Free Beam.

Boundary Conditions.

$$\Psi'(0)=0, \quad \frac{1}{l}U'(0)-\Psi(0)=0$$
$$\Psi'(1)=0, \quad \frac{1}{l}U'(1)-\Psi(1)=0 \quad (43)$$

Downloaded 03 May 2010 to 171.66.16.247. Redistribution subject to ASME license or copyright; see http://www.asme.org/terms/Terms_Use.cfm

Natural Frequencies.

$$c_1 s_1\left(\frac{1}{l}s_1 - c_1\right)[\cosh(s_1)-\cos(s_2)]^2 - \left(c_1 s_1 \sinh(s_1) - \frac{s_1/l - c_1}{s_2/l + c_2} c_2 s_2 \sin(s_2)\right) \times \left[\left(\frac{1}{l}s_1 - c_1\right)\sinh(s_1) + \frac{c_1 s_1}{c_2 s_2}\left(\frac{1}{l}s_2 + c_2\right)\sin(s_2)\right] = 0, \quad (\sqrt{b^2-4ac} > b) \quad (44)$$

$$c_1' s_1'\left(\frac{1}{l}s_1' + c_1'\right)[\cos(s_1') - \cos(s_2)]^2 + \left(c_1' s_1' \sin(s_1') - \frac{s_1'/l + c_1'}{s_2/l + c_2} c_2 s_2 \sin(s_2)\right) \times \left[\left(\frac{1}{l}s_1' + c_1'\right)\sin(s_1') - \frac{c_1' s_1'}{c_2 s_2}\left(\frac{1}{l}s_2 + c_2\right)\sin(s_2)\right] = 0, \quad (\sqrt{b^2-4ac} < b) \quad (45)$$

Normal Modes.

$$U(\zeta) = U_0\left[\cosh(s_1\zeta) - \frac{d}{s_1/l - c_1}\sinh(s_1\zeta) - \frac{c_1 s_1}{c_2 s_2}\cos(s_2\zeta) + \frac{d}{s_2/l + c_2}\sin(s_2\zeta)\right],$$

$$\Psi(\zeta) = \Psi_0\left[c_1\sinh(s_1\zeta) - \frac{dc_1}{s_1/l - c_1}\cosh(s_1\zeta) - \frac{c_1 s_1}{s_2}\sin(s_2\zeta) - \frac{dc_2}{s_2/l + c_2} d\cos(s_2\zeta)\right], \quad (\sqrt{b^2-4ac} > b) \quad (46)$$

$$U(\zeta) = U_0\left[\cos(s_1'\zeta) + \frac{d'}{s_1'/l + c_1'}\sin(s_1'\zeta) - \frac{c_1' s_1'}{c_2 s_2}\cos(s_2\zeta) - \frac{d'}{s_2/l + c_2}\sin(s_2\zeta)\right],$$

$$\Psi(\zeta) = \Psi_0\left[c_1'\sin(s_1'\zeta) - \frac{d' c_1'}{s_1'/l + c_1'}\cos(s_1'\zeta) - \frac{c_1' s_1'}{s_2}\sin(s_2\zeta) + \frac{d' c_2}{s_2/l + c_2} d'\cos(s_2\zeta)\right], \quad (\sqrt{b^2-4ac} < b) \quad (47)$$

where

$$d = \frac{\left(\frac{1}{l}s_1 - c_1\right)\sinh(s_1) + \frac{c_1 s_1}{c_2 s_2}\left(\frac{1}{l}s_2 + c_2\right)\sin(s_2)}{\cosh(s_1) - \cos(s_2)}$$

$$d' = \frac{\left(\frac{1}{l}s_1' + c_1'\right)\sin(s_1') - \frac{c_1' s_1'}{c_2 s_2}\left(\frac{1}{l}s_2 + c_2\right)\sin(s_2)}{\cos(s_1') - \cos(s_2)}. \quad (48)$$

(d) Fixed-Fixed Beam.

Boundary Conditions.

$$U(0) = 0, \quad \Psi(0) = 0$$
$$U(1) = 0, \quad \Psi(1) = 0 \quad (49)$$

Natural Frequencies.

$$c_1[\cosh(s_1) - \cos(s_2)]^2 - [c_1\sinh(s_1) - c_2\sin(s_2)]\left(\sinh(s_1) + \frac{c_1}{c_2}\sin(s_2)\right) = 0, \quad (\sqrt{b^2-4ac} > b) \quad (50)$$

$$c_1'[\cos(s_1') - \cos(s_2)]^2 + [c_1'\sin(s_1') - c_2\sin(s_2)]\left(\sin(s_1') - \frac{c_1'}{c_2}\sin(s_2)\right) = 0, \quad (\sqrt{b^2-4ac} < b) \quad (51)$$

Normal Modes.

$$U(\zeta) = U_0\left[\cosh(s_1\zeta) - \frac{d}{c_1}\sinh(s_1\zeta) - \cos(s_2\zeta) - \frac{d}{c_2}\sin(s_2\zeta)\right],$$

$$\Psi(\zeta) = \Psi_0[c_1\sinh(s_1\zeta) - d\cosh(s_1\zeta) - c_2\sin(s_2\zeta) + d\sin(s_2\zeta)], \quad (\sqrt{b^2-4ac} > b) \quad (52)$$

$$U(\zeta) = U_0\left[\cos(s_1'\zeta) + \frac{d'}{c_1'}\sin(s_1'\zeta) - \cos(s_2\zeta) - \frac{d'}{c_2}\sin(s_2\zeta)\right],$$

$$\Psi(\zeta) = \Psi_0[c_1'\sin(s_1'\zeta) - d'\cos(s_1'\zeta) - c_2\sin(s_2\zeta) + d'\cos(s_2\zeta)], \quad (\sqrt{b^2-4ac} < b) \quad (53)$$

where

$$d = \frac{c_1\sinh(s_1) - c_2\sin(s_2)}{\cosh(s_1) - \cos(s_2)}$$

$$d' = \frac{c_1'\sin(s_1') - c_2\sin(s_2)}{\cos(s_1') - \cos(s_2)}. \quad (54)$$

(e) Fixed-Free Beam.

Boundary Conditions.

$$U(0) = 0, \quad \Psi(0) = 0$$
$$\Psi'(1) = 0, \quad \frac{1}{l}U'(1) - \Psi(1) = 0 \quad (55)$$

Natural Frequencies.

$$[c_1 s_1\cosh(s_1) - c_2 s_2\cos(s_2)]\left[\left(\frac{1}{l}s_1 - c_1\right)\cosh(s_1) + \frac{c_1}{c_2}\left(\frac{1}{l}s_2 + c_2\right)\cos(s_2)\right] - c_1[s_1\sinh(s_1) + s_2\sin(s_2)]\left[\left(\frac{1}{l}s_1 - c_1\right)\sinh(s_1) + \left(\frac{1}{l}s_2 + c_2\right)\sin(s_2)\right] = 0, \quad (\sqrt{b^2-4ac} > b) \quad (56)$$

$$[c_1' s_1'\cos(s_1') - c_2 s_2\cos(s_2)]\left[\left(\frac{1}{l}s_1' + c_1'\right)\cos(s_1') - \frac{c_1'}{c_2}\left(\frac{1}{l}s_2 + c_2\right)\cos(s_2)\right] + c_1'[s_1'\sin(s_1') - s_2\sin(s_2)]\left[\left(\frac{1}{l}s_1' + c_1'\right)\sin(s_1') - \left(\frac{1}{l}s_2 + c_2\right)\sin(s_2)\right] = 0, \quad (\sqrt{b^2-4ac} < b) \quad (57)$$

Normal Modes.

$$U(\zeta) = U_0\left[\cosh(s_1\zeta) - \frac{d}{c_1}\sinh(s_1\zeta) - \cos(s_2\zeta) - \frac{d}{c_2}\sin(s_2\zeta)\right],$$

Downloaded 03 May 2010 to 171.66.16.247. Redistribution subject to ASME license or copyright; see http://www.asme.org/terms/Terms_Use.cfm

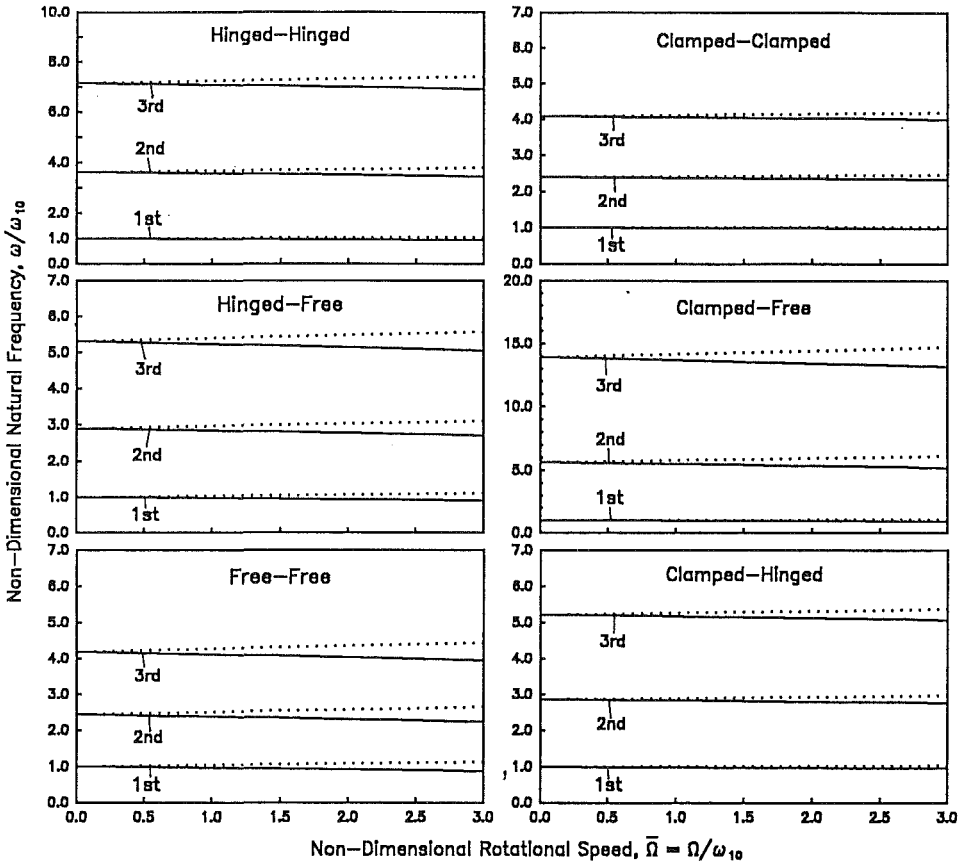


Fig. 2 Variation of frequency response with $\bar{\Omega}$ ($\beta = 0.15$, —— forward precession, ··· backward precession)

$$\Psi(\zeta) = \Psi_0[c_1\sinh(s_1\zeta) - d\cosh(s_1\zeta) - c_2\sin(s_2\zeta) + d\cos(s_2\zeta)], \quad (\sqrt{b^2-4ac} > b) \tag{58}$$

$$U(\zeta) = U_0\left[\cos(s_1'\zeta) - \frac{d'}{c_1'}\sin(s_1'\zeta) - \cos(s_2\zeta) + \frac{d'}{c_2}\sin(s_2\zeta)\right],$$
$$\Psi(\zeta) = \Psi_0[c_1'\sin(s_1'\zeta) + d'\cos(s_1'\zeta) - c_2\sin(s_2\zeta) - d'\cos(s_2\zeta)], \quad (\sqrt{b^2-4ac} < b) \tag{59}$$

where

$$d = \frac{c_1 s_1\cosh(s_1) - c_2 s_2\cos(s_2)}{s_1\sinh(s_1) + s_2\sin(s_2)}$$
$$d' = \frac{c_1' s_1'\cos(s_1') - c_2 s_2\cos(s_2)}{s_1'\sin(s_1') - s_2\sin(s_2)}. \tag{60}$$

(f) Fixed-Hinged Beam.

Boundary Conditions.

$$U(0) = 0, \quad \Psi(0) = 0$$
$$U(1) = 0, \quad \Psi'(1) = 0 \tag{61}$$

Natural Frequencies.

$$c_1[\cosh(s_1) - \cos(s_2)][s_1\sinh(s_1) + s_2\sin(s_2)] - \left(\sinh(s_1) + \frac{c_1}{c_2}\sin(s_2)\right)[c_1 s_1\cosh(s_1) - s_2 c_2\cos(s_2)] = 0, \quad (\sqrt{b^2-4ac} > b) \tag{62}$$

$$c_1'[\cos(s_1') - \cos(s_2)][s_1'\sin(s_1') - s_2\sin(s_2)] - \left(\sin(s_1') - \frac{c_1'}{c_2}\sin(s_2)\right)[c_1' s_1'\cos(s_1') - s_2 c_2\cos(s_2)] = 0, \quad (\sqrt{b^2-4ac} < b) \tag{63}$$

Normal Modes.

$$U(\zeta) = U_0\left[\cosh(s_1\zeta) - \frac{d}{c_1}\sinh(s_1\zeta) - \cos(s_2\zeta) - \frac{d}{c_2}\sin(s_2\zeta)\right],$$
$$\Psi(\zeta) = \Psi_0[c_1\sinh(s_1\zeta) - d\cosh(s_1\zeta) - c_2\sin(s_2\zeta) + d\cos(s_2\zeta)], \quad (\sqrt{b^2-4ac} > b) \tag{64}$$

$$U(\zeta) = U_0\left[\cos(s_1'\zeta) - \frac{d'}{c_1'}\sin(s_1'\zeta) - \cos(s_2\zeta) + \frac{d'}{c_2}\sin(s_2\zeta)\right],$$
$$\Psi(\zeta) = \Psi_0[c_1'\sin(s_1'\zeta) + d\cos(s_1'\zeta) - c_2\sin(s_2\zeta) - d'\cos(s_2\zeta)], \quad (\sqrt{b^2-4ac} < b) \tag{65}$$

where

$$d = \frac{c_1 s_1\cosh(s_1) - c_2 s_2\cos(s_2)}{s_1\sinh(s_1) + s_2\sin(s_2)}$$
$$d' = \frac{c_1' s_1'\cos(s_1') - c_2 s_2\cos(s_2)}{s_1'\sin(s_1') - s_2\sin(s_2)}. \tag{66}$$

5 Numerical Simulations

A numerical simulation of a spinning Timoshenko beam incorporating the six different boundary conditions is presented here. The free vibration characteristics of natural frequencies and mode shapes are given. The data used in this

Downloaded 03 May 2010 to 171.66.16.247. Redistribution subject to ASME license or copyright; see http://www.asme.org/terms/Terms_Use.cfm

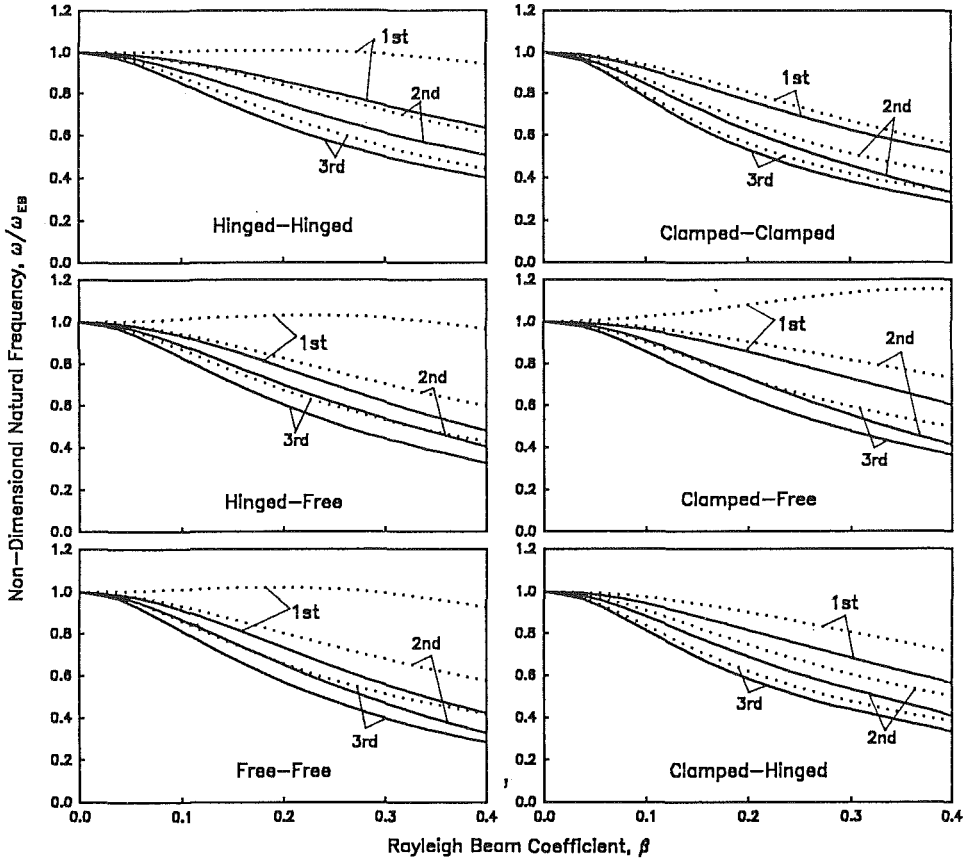


Fig. 3 Variation of frequency response with β ($\bar{\Omega}=2.5$, —— forward precession, ···· backward precession)

investigation pertains to a circular beam, taken from Katz et al. (1988) and is summarized as follows:

$$l=1.0\text{m}, \qquad G=77.6\text{GPa}$$
$$\rho=7700\text{kg/m}^3, \qquad \kappa=0.9.$$
$$E=207\text{GPa},$$

In addition, two nondimensional parameters $\bar{\Omega}$ and β are also employed in the study representing the rotational speed and slenderness ratio, respectively. They are defined as:

$\bar{\Omega}=\Omega/\omega_{10}$—nondimensional rotational speed

$\beta=\pi r_0/l$—Rayleigh beam coefficient

where ω_{10} is the at-rest fundamental natural frequency and r_0 is the radius of gyration. For a circular cross-section, the Rayleigh beam coefficient relates the diameter of the shaft to its length and thus, as $\beta\to 0$, and EB beam is realized. The two parameters are varied over a sufficiently wide range of values; $0\le\bar{\Omega}\le 3.0$, $0\le\beta\le 0.4$ which should reflect most of the cases of engineering interest. When a beam is put into a spinning motion, its at-rest natural frequency splits into two components: forward and backward precessions. In all the figures, the solid line indicates the forward precession while the dotted line denotes the backward precession. Only the first three pairs of natural frequencies and mode shapes are presented in the simulation results.

Figure 2 shows the variation of nondimensional natural frequencies with respect to the rotational speed parameter $\bar{\Omega}$. Note that the natural frequency ω has been normalized by the at-rest fundamental frequency ω_{10}. The distinction between the forward and backward precessions becomes more obvious at higher modes and at larger $\bar{\Omega}$. Another feature which is expected is that the more restrained a boundary condition represents, the closer are its forward and backward precession curves. It should also be pointed out that in the case of the simply-supported boundary condition, there are really four roots to Eq. (34), or two sets of natural frequencies corresponding to each normal mode (Han and Zu (1990)). However, the frequencies of the second set are of very large magnitude and thus not depicted in the plot.

The influence of effects due to shear deformation and rotary inertia on spinning structures is also an important consideration as many of the workpieces found in lathe machining operation are short and stubby. This is shown in Fig. 3. Unlike the previously used procedure for nondimensionalizing the natural frequencies, in this situation, it makes more sense to normalize these quantities by the corresponding frequencies[2] computed using the EB theory. In this way, the Timoshenko effects are more clearly displayed for varying β. Observe in Fig. 3 that at higher modes, the curves are lower which implies that the Timoshenko effects becomes more pronounced. Except for two cases, the clamped-clamped and clamped-hinged boundary conditions, for all other boundary conditions, the first backward precession frequency is larger than the corresponding EB frequency. This characteristic is thus related to the degree of restraint a boundary condition represents. This is not surprising as the linearized expression of natural frequencies given in Han and Zu (1990) clearly show this behavior for the case of a spinning, simply-supported Timoshenko beam.

The normal modes for both the transverse deflection U and the bending angle Ψ are given in Figs. 4 and 5 with $\bar{\Omega}=2.5$ and $\beta=0.15$. As depicted in these plots, the forward and backward precession normal modes coincide identically for the simply-supported boundary condition. This unusual phenomenon is not observed in beams with the other five remaining

[2] Note that in an inertial frame formulation, the natural frequencies of a *spinning* EB beam are identical to those of a *stationary* EB beam (Han and Zu, 1990). Hence, stationary EB frequencies are used here.

Downloaded 03 May 2010 to 171.66.16.247. Redistribution subject to ASME license or copyright; see http://www.asme.org/terms/Terms_Use.cfm

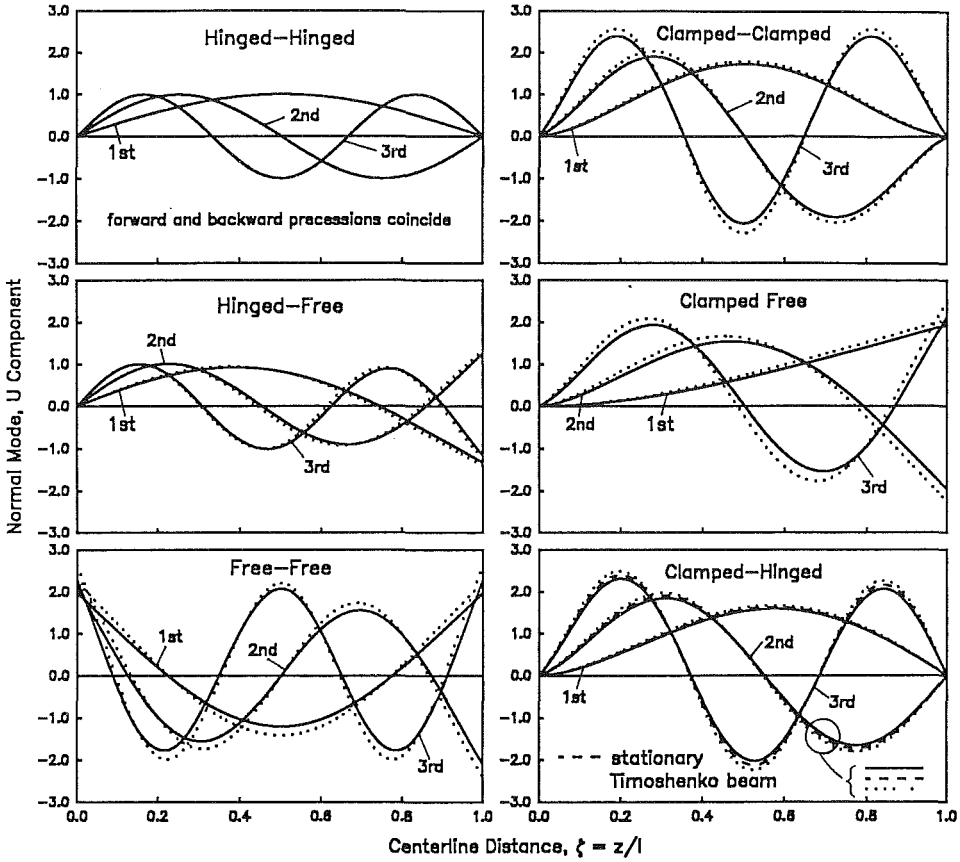


Fig. 4 The first three normal modes associated with bending deformations ($\beta = 0.15$, $\Omega = 2.5$, —— forward precession, ··· backward precession)

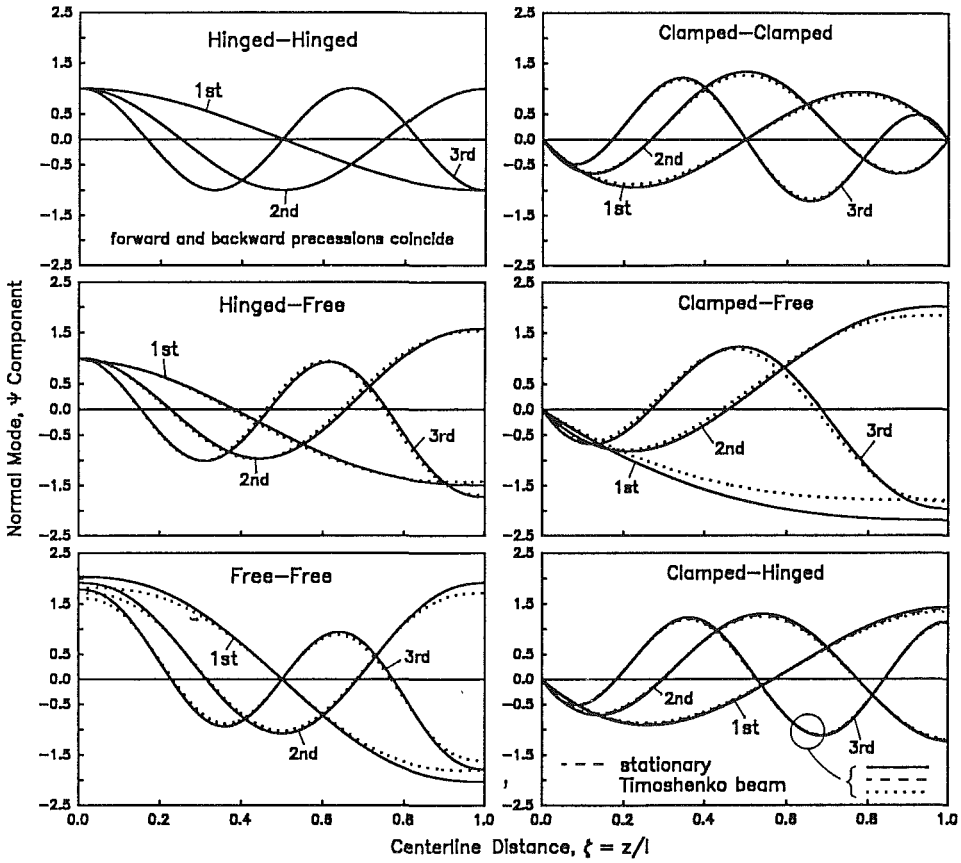


Fig. 5 The first three normal modes associated with shear deformations ($\beta = 0.15$, $\Omega = 2.5$, —— forward precession, ··· backward precession)

Downloaded 03 May 2010 to 171.66.16.247. Redistribution subject to ASME license or copyright; see http://www.asme.org/terms/Terms_Use.cfm

boundary conditions. In these cases, the forward and backward precession normal modes are different, implying that each natural frequencies correspond to a single normal mode. It would also be interesting to relate the at-rest normal modes with the spinning normal modes in the plot as this serves as a check of the formulation. This is done for one case—the clamped-hinged boundary condition. As expected, the at-rest normal modes lie exactly in between the forward and the backward precession normal modes.

6 Summary and Conclusions

A free vibration analysis of a spinning, finite Timoshenko beam is presented. Analytical solutions of natural frequencies and normal modes for the six classical boundary conditions are given. Based on the formulation and the results of the numerical simulations, the following conclusions can be made:

(*a*) The distinction between the forward and backward precessions becomes more obvious at higher modes and at larger $\bar{\Omega}$. For certain boundary conditions, the first backward precession frequency is larger than the corresponding EB frequency.

(*b*) The forward and backward precession normal modes become identical for the case of simply-supported boundary conditions. Also, there are two sets of natural frequencies corresponding to each normal mode.

(*c*) The above peculiar characteristics are not observed for the other five boundary conditions. In each of these cases, the forward and backward precessions are different, implying that each natural frequency correspond to a single normal mode.

Acknowledgments

This work was supported by an operating grant from the Natural Sciences and Engineering Research Council of Canada.

References

Anderson, R. A., 1953, "Flexural Vibrations in Uniform Beams According to the Timoshenko Theory," ASME JOURNAL OF APPLIED MECHANICS, Vol. 20, pp. 504–510.

Bauer, H. F., 1980, "Vibration of a Rotating Uniform Beam, Part I: Orientation in the Axis of Rotation," *Journal of Sound and Vibration*, Vol. 72, pp. 177–189.

Carr, J. B., 1970, "The Effect of Shear Flexibility and Rotatory Inertia on the Natural Frequencies of Uniform Beams," *The Aeronautical Quarterly*, Vol. 21, pp. 79–90.

Dimentberg, F. M., 1961, *Flexural Vibrations of Rotating Shafts*, Butterworths, London.

Dolph, C. L., 1954, "On the Timoshenko Beam Vibrations," *Quarterly of Applied Mathematics*, Vol. 12, pp. 175–187.

Eshleman, R. L., and Eubanks, R. A., 1969, "On the Critical Speeds of Continuous Motors," ASME *Journal of Engineering for Industry*, Vol. 91, pp. 1180–1188.

Han, Ray P. S., and Zu, Jean W. Z., 1990, "Analytical Dynamics of a Spinning Timoshenko Beam Subjected to a Moving Load," ASME JOURNAL OF APPLIED MECHANICS, submitted for publication.

Hurty, W. C., and Rubenstein, M. F., 1964, "On the Effect of Rotatory Inertia and Shear in Beam Vibration," *Journal of the Franklin Institute*, Vol. 278, pp. 341–350.

Huang, T. C., 1958, "Effect of Rotatory Inertia and Shear on the Vibration of Beams Treated by the Approximate Methods of Ritz and Galerkin," *ASME Proceedings of the Third U.S. National Congress of Applied Mechanics*, pp. 189–194.

Huang, T. C., 1961, "The Effect of Rotatory Inertia and of Shear Deformation on the Frequency and Normal Mode Equations of Uniform Beams With Simple End Conditions," ASME JOURNAL OF APPLIED MECHANICS, Vol. 28, pp. 579–584.

Katz, R., Lee, C. W., Ulsoy, A. G., and Scott, R. A., 1988, "The Dynamic Response of a Rotating Shaft Subject to a Moving Load," *Journal of Sound and Vibration*, Vol. 122, pp. 131–148.

Kruszewski, E. T., 1949, "Effect of Transverse Shear and Rotatory Inertia on the Natural Frequency of a Uniform Beam," NACA TN 1909.

Lee, C. W., Katz, R., Ulsoy, A. G., and Scott, R. A., 1988, "Modal Analysis of a Distributed Parameter Rotating Shaft," *Journal of Sound and Vibration*, Vol. 122, pp. 119–130.

Trail-Nash, R. W., and Collar, A. R., 1953, "The Effect of Shear Flexibility and Rotatory Inertial on the Bending Vibrations of Beams," *Quarterly Journal of Mechanics and Applied Mathematics*, Vol. 6, pp. 186–222.

Downloaded 03 May 2010 to 171.66.16.247. Redistribution subject to ASME license or copyright; see http://www.asme.org/terms/Terms_Use.cfm

Exact Solutions for the Analysis of General Elastically Restrained Nonuniform Beams

Sen Yung Lee
Professor,
Mechanical Engineering Department,
National Cheng Kung University,
Tainan, Taiwan 700

Yee Hsiung Kuo
Assistant Research Engineer,
Aeronautical Research Laboratory,
Taichung, Taiwan 400

The exact solutions for the problems governed by a general self-adjoint fourth-order nonhomogeneous ordinary differential equation with arbitrarily polynomial varying coefficients and general elastic boundary conditions are derived in Green's function form. To illustrate the analysis, the static deflection and dynamic analysis of a general elastically end restrained Bernoulli-Euler beam with polynomial varying bending rigidity, applied axial and force, and elastic foundation modulus along the beam, subjected to an arbitrary transverse force are presented. The Green's function is concisely expressed in terms of the four normalized fundamental solutions of the system and these fundamental solutions are given in power series forms. The characteristic equations for elastic stability and free vibrational analysis of the beam can be obtained by setting the denominator of the corresponding Green's function equal to zero. Finally, examples are given to illustrate the accuracy and efficiency of the analysis.

1 Introduction

In structural mechanics, there are many problems governed by a self-adjoint fourth-order ordinary differential equation with constant or variable coefficients. Typical examples are

(a) beam on Winkler elastic foundation with axial force (tensile or compressive) (Hetenyi, 1979; Sirosh et al., 1989).

(b) beam on two-parameter eleastic foundation with or without axial force (Eisenberger et al., 1987).

(c) rotating beam with or without end mass (Khulief 1989; Storti et al., 1987).

(d) warping torsion of a straight member, subjected to twisting action, with or without continuous elastic restraint (Timoshenko and Gere, 1961).

It is well known that if the coefficients of the differential equation are constants, then the closed-form solutions of the problems can be found (Timoshenko et al., 1961; Hetenyi 1979; Leissa, 1989). However, if those are variable, the closed-form solutions are available only for some particular cases such as the elastic stability of a beam with the bending rigidity and intensity of distributed axial force varying according to two arbitrary powers of the longitudinal coordinate (Timoshenko and Gere, 1961), the free vibration of a beam with thickness and width varying according to two arbitrary powers of the longitudinal coordinate (Wang, 1967), the free vibration of a double symmetric nonuniform beam with a vanishing thickness at the tip of the beam (Storti et al., 1987), the exact frequencies and mode shapes for rotating beams in which both the bending rigidity and the mass distribution varying linearly (Wright et al., 1982), and the exact static deflection of a rotating uniform beam (Carlson et al., 1978). From the existing literatures it reveals that no exact solutions were given for the problems governed by a general self-adjoint fourth-order nonhomogeneous ordinary differential equation with arbitrary polynomial varying coefficients. This is due to the fact that the solution theory for the fourth-order nonhomogeneous ordinary differential equation with variable coefficients was not well developed. Therefore, in the past, the problems were mainly studied approximately by analytical method such as the equivalent loading and the equivalent beam method (Chen, 1949), the comparison theorem of Collatz (Appl et al., 1959), the harmonic analysis (Sundara et al., 1963) and the Rayleigh-Ritz method (Bert, 1984) and numerical methods such as the Myklested method (Sutherland, 1949), the transfer matrix method (Djodjo, 1969; Stafford et al., 1975), the finite difference method (Iremonger, 1980), the transformed dynamic stiffness method (Beskos et al., 1983) and the finite element method (Hodges, 1979; Eisenberger et al., 1987; Khulief, 1989; Sirosh et al., 1989; Eisenberger, 1990). Recently, Lee et al. (1990) proposed a semi-exact solution method to study the vibration of a nonuniform beam with general elastic end restraints. The frequency equation and forced dynamic response of the beam were concisely expressed in terms of the fundamental solutions of the system. These fundamental solutions were obtained approximately by approximating the coefficients of the gov-

Contributed by the ASME Applied Mechanics Division of THE AMERICAN SOCIETY OF MECHANICAL ENGINEERS for presentation at the Winter Annual Meeting, Atlanta, Ga., Dec. 1-6, 1991.

Discussion on this paper should be addressed to the Technical Editor, Professor Leon M. Keer, The Technological Institute, Northwestern University, Evanston, IL 60208, and will be accepted until two months after final publication of the paper itself in the JOURNAL OF APPLIED MECHANICS. Manuscript received by the ASME Applied Mechanics Division, Sept. 9, 1990; final revision, Jan. 18, 1991.

Paper No. 91-WA/APM-26.

Copyright © 1992 by ASME
Downloaded 03 May 2010 to 171.66.16.247. Redistribution subject to ASME license or copyright; see http://www.asme.org/terms/Terms_Use.cfm

erning differential equation by piecewise constants. Even though the method is efficient and yields accurate solutions, it still is an approximate solution method. In addition, the second-order term resulting from axial forces or supporting force of a two-parameter elastic foundation was not considered.

In this paper, the exact solutions for the problems governed by a general self-adjoint fourth-order nonhomogeneous ordinary differential equation with arbitrarily polynomial varying coefficients are derived in Green's function form and concisely expressed in terms of the four normalized fundamental solutions of the system. The method of Frobenius is used to find the fundamental solutions. To illustrate the analysis, the static deflection and dynamic analysis of a general elastically end-restrained nonuniform Bernoulli-Euler beam with polynomial varying bending rigidity, applied axial force, and elastic foundation modulus along the beam subjected to an arbitrary transverse force are presented. The characteristic equation for the elastic stability and free vibrational analysis of the beam can be obtained by setting the denominator of the corresponding Green's function equal to zero. Finally, examples are given to verify the accuracy and efficiency of the analysis.

2 Analysis

2.1 Static Deflection and Stability Analysis. For a general elastically end-restrained nonuniform Bernoulli-Euler beam of finite length l, resting on nonhomogeneous elastic foundation subjected to axial tensile and transverse forces, as shown in Fig. 1, the static flexural deflection $\bar{V}(X)$ satisfies the ordinary differential equation

$$\frac{d^2}{dX^2}\left[E(X)I(X)\frac{d^2\bar{V}(X)}{dX^2}\right]-\frac{d}{dX}\left[N(X)\frac{d\bar{V}(X)}{dX}\right]+k^*(X)\bar{V}(X)=p(X),\qquad X\in(0,\,l),\quad(1)$$

where $E(X)$, $I(X)$, and $k^*(X)$ denote Young's modulus, moment of inertia, and Winkler's foundation modulus, respectively. $N(X)$ and $p(X)$ are arbitrarily axial tensile and transverse distributed forces, respectively. If the beam is subjected to an axial end force N_o, then $N(X)$ is a constant function $N(X) = N_o$. Instead, if the beam is subjected to distributed axial forces $\bar{g}(X)$, then $N(X) = \int_X^l \bar{g}(\eta)d\eta$. The associated boundary conditions are

$$\text{at } X=0:\ EI\frac{d^2\bar{V}}{dX^2}=K_{\theta L}\frac{d\bar{V}}{dX},\qquad \frac{d}{dX}\left[EI\frac{d^2\bar{V}}{dX^2}\right]-N\frac{d\bar{V}}{dX}=-K_{TL}\bar{V},\quad(2)$$

and

$$\text{at } X=l:\ EI\frac{d^2\bar{V}}{dX^2}=-K_{\theta R}\frac{d\bar{V}}{dX},\qquad \frac{d}{dX}\left[EI\frac{d^2\bar{V}}{dX^2}\right]-N\frac{d\bar{V}}{dX}=K_{TR}\bar{V},\quad(3)$$

where $K_{\theta L}$ and K_{TL} and $K_{\theta R}$ and K_{TR} are the rotational spring and translational spring constants at left end and right end of the beam, respectively.

Introduce the following nondimensional quantities

$$x=\frac{X}{l},\qquad V(x)=\frac{\bar{V}(X)}{l},\qquad G(x)=\frac{E(X)I(X)}{E_oI_o},$$

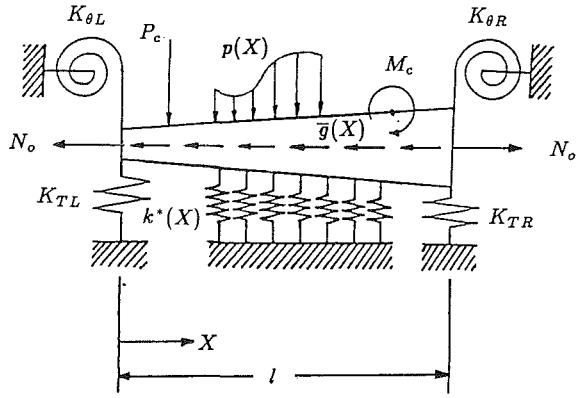


Fig. 1 Geometry and coordinate system of a general elastically end restrained nonuniform beam

$$R(x)=\frac{-N(X)l^2}{E_oI_o},\qquad Q(x)=\frac{k^*(X)l^4}{E_oI_o},\qquad P(x)=\frac{p(X)l^3}{E_oI_o},$$

$$\beta_{\theta L}=\frac{K_{\theta L}l}{E_oI_o},\qquad \beta_{\theta R}=\frac{K_{\theta R}l}{E_lI_l},\qquad \beta_{TL}=\frac{K_{TL}l^3}{E_oI_o},\qquad \beta_{TR}=\frac{K_{TR}l^3}{E_lI_l},$$

$$\gamma_R=\left.\frac{G'(x)}{G(x)}\right|_{x=1},\qquad \delta_R=\frac{N(l)l^2}{E_lI_l},\quad(4)$$

where $E_oI_o = E(0)I(0)$ and $E_lI_l = E(l)I(l)$ are the bending rigidities of beam at $X = 0$ and $X = l$, respectively. The governing differential equation can be rewritten in the following nondimensional form:

$$\frac{d^2}{dx^2}\left[G(x)\frac{d^2V}{dx^2}\right]+\frac{d}{dx}\left[R(x)\frac{dV}{dx}\right]+Q(x)V=P(x),\ x\in(0,\,1),\quad(5)$$

and the associated boundary conditions become

$$\text{at } x=0:\ V''-\beta_{\theta L}V'=0,\qquad V'''+G'(0)V''+R(0)V'+\beta_{TL}V=0,\quad(6)$$

and

$$\text{at } x=1:\ V''+\beta_{\theta R}V'=0,\ V'''+\gamma_RV''-\delta_RV'-\beta_{TR}V=0.\quad(7)$$

If the four linearly independent fundamental solutions $V_1(x)$, $V_2(x)$, $V_3(x)$, and $V_4(x)$ of Eq. (5) are chosen such that they satisfy the following normalization conditions at the origin of coordinate system

Downloaded 03 May 2010 to 171.66.16.247. Redistribution subject to ASME license or copyright; see http://www.asme.org/terms/Terms_Use.cfm

$$\begin{bmatrix} V_1(0) & V_2(0) & V_3(0) & V_4(0) \\ V_1'(0) & V_2'(0) & V_3'(0) & V_4'(0) \\ V_1''(0) & V_2''(0) & V_3''(0) & V_4''(0) \\ V_1'''(0) & V_2'''(0) & V_3'''(0) & V_4'''(0) \end{bmatrix} = \begin{bmatrix} 1 & 0 & 0 & 0 \\ 0 & 1 & 0 & 0 \\ 0 & 0 & 1 & 0 \\ 0 & 0 & 0 & 1 \end{bmatrix}, \quad (8)$$

where primes indicate differentiation with respect to variable x, then the general solution can be derived via the method of variation of parameters and shown to take the following concise form:

$$V(x) = C_1V_1(x) + C_2V_2(x) + C_3V_3(x) + C_4V_4(x) + \int_0^x \{[V_1(\xi)V_4(x) - V_1(x)V_4(\xi)] - [V_2(\xi)V_3(x) - V_2(x)V_3(\xi)] + G'(0)[V_2(\xi)V_4(x) - V_2(x)V_4(\xi)] - R(0)[V_3(\xi)V_4(x) - V_3(x)V_4(\xi)]\}P(\xi)d\xi, \quad (9)$$

where C_1, C_2, C_3, and C_4 are integration constants and will be determined from the specified boundary conditions. The algebraic details of the derivation of the general solution are similar to those given by Lee et al. (1990).

After substituting the general solution into the specified boundary conditions, the static deflection of the beam is shown to be

$$V(x) = \int_0^1 K(x, \xi)P(\xi)d\xi, = \int_0^x K_1(x, \xi)P(\xi)d\xi + \int_x^1 K_2(x, \xi)P(\xi)d\xi, \quad (10)$$

where $P(x)$ is the force function defined in Eq. (4) and $K(x, \xi)$ is the Green's function of the system. $K_1(x, \xi)$ and $K_2(x, \xi)$ are subfunctions of $K(x, \xi)$. They are symmetric, i.e., $K_1(x, \xi) = K_2(\xi, x)$. The Green's functions for the beam with general elastically end-restrained boundary conditions and four typical kinds of boundary conditions are given in Appendix A.

When the beam is subjected to axial compressive forces, then based on the linear elastic theory, the deflection of the beam is infinite when axial forces approach buckling loads. Hence, the characteristic equation for buckling loads can be obtained by setting the denominator of the Green's function equal to zero. The lowest root of the characteristic equation is the critical buckling load of the beam.

2.2 Dynamic Analysis. The governing equation for the dynamic response $\overline{U}(X, t)$ of a nonuniform beam, as specified in Section 2.1, is

$$\frac{\partial^2}{\partial X^2}\left[E(X)I(X)\frac{\partial^2\overline{U}(X, t)}{\partial X^2}\right] - \frac{\partial}{\partial X}\left[N(X)\frac{\partial\overline{U}(X, t)}{\partial X}\right] + k^*(X)\overline{U}(X, t) + m(X)\frac{\partial^2\overline{U}(X, t)}{\partial t^2} = p_o(X, t), \; X\in(0, l), \quad (11)$$

where $m(X)$ and $p_o(X, t)$ are the mass per unit length of the beam and an arbitrary transverse excitation force, respectively. The associated initial conditions are

$$\overline{U}(X, 0) = \overline{U}_o(X) \text{ and } \left.\frac{\partial\overline{U}(X, t)}{\partial t}\right|_{t=0} = \dot{\overline{U}}_o(X), \; X\in(0, l), \quad (12)$$

where $\overline{U}_o(X)$ and $\dot{\overline{U}}_o(X)$ are two prescribed initial functions.

After taking the Laplace transform with respect to time variable t, Eq. (11) yields to the following ordinary differential equation

$$\frac{d^2}{dX^2}\left[E(X)I(X)\frac{d^2u(X, s)}{dX^2}\right] - \frac{d}{dX}\left[N(X)\frac{du(X, s)}{dX}\right] + [k^*(X) + m(X)s^2]u(X, s) = p_1(X, s), \quad X\in(0, l), \quad (13)$$

where

$$u(X, s) = \int_0^\infty \overline{U}(X, t)e^{-st}dt,$$

$$p_1(X, s) = \int_0^\infty p_0(X, t)e^{-st}dt + m(X)[s\overline{U}_o(X) + \dot{\overline{U}}_o(X)], \quad (14)$$

and s is the Laplace transform parameter. In terms of the nondimensional quantities given in Eq. (4) and

$$U(x, s) = \frac{u(X, s)}{l},$$

$$Q_o(x, s) = \frac{[k^*(X) + m(X)s^2]l^4}{E_oI_o},$$

$$P_o(x, s) = \frac{p_1(X, s)l^3}{E_oI_o}, \quad (15)$$

Eq. (13) yields to:

$$\frac{d^2}{dx^2}\left[G(x)\frac{d^2U}{dx^2}\right] + \frac{d}{dx}\left[R(x)\frac{dU}{dx}\right] + Q_o(x, s)U = P_o(x, s), \quad x\in(0, 1). \quad (16)$$

Since Eqs. (16) and (5) are in the same form, the general solution and the Green's function associated to various boundary conditions will be the same as those given in Section 2.1. Consequently, the transformed solution is

$$U(x, s) = \int_0^1 K(x, \xi, s)P_o(\xi, s)d\xi, \quad x\in(0, 1). \quad (17)$$

By taking the inverse Laplace transform, one obtains the dynamic response of the system

$$\overline{U}(X, t) = \frac{l}{2\pi j}\int_{c-j\infty}^{c+j\infty} U(x, s)e^{st}ds, \quad x\in(0, 1), \quad (18)$$

where $j^2 = -1$.

For the free vibration problems, the frequency equation of the nonuniform beam can be obtained by first replacing the Laplace transform parameter s by $j\omega$, where ω is the angular natural frequency (Churchill, 1972), and then setting the denominator of the Green's function equal to zero.

Downloaded 03 May 2010 to 171.66.16.247. Redistribution subject to ASME license or copyright; see http://www.asme.org/terms/Terms_Use.cfm

3 Normalized Fundamental Solutions

In the previous sections, the static deflection, forced dynamic response, and the characteristic equations for the elastic stability and free vibrational analysis are derived in terms of the normalized fundamental solutions. However, in general, the exact closed-form fundamental solutions of Eq. (5) are not available. Nevertheless, if the coefficients of Eq. (5) are in arbitrarily polynomial variation form, then a power series representation of the fundamental solutions can be constructed by employing the method of Frobenius. The solutions are exact up to the accuracy of the computer or a preset value set by the analyst.

Now, consider the problems for which the coefficients $G(x)$, $R(x)$, and $Q(x)$ in Eq. (5) are given in the following polynomial variation form

$$G(x)=\sum_{i=0}^{e} g_i x^i,$$
$$R(x)=\sum_{i=0}^{f} r_i x^i,$$
$$Q(x)=\sum_{i=0}^{h} q_i x^i, \tag{19}$$

where e, f, and h are integers representing the number of terms in the series. Let the four normalized fundamental solutions be in the form of

$$V_n(x)=\sum_{i=0}^{\infty} b_{n,i} x^i, \quad n=1,2,3,4, \tag{20}$$

and

$$\begin{aligned}
&\text{for } V_1(x): b_{1,0}=1,\ b_{1,1}=b_{1,2}=b_{1,3}=0\\
&\text{for } V_2(x): b_{2,1}=1,\ b_{2,0}=b_{2,2}=b_{2,3}=0\\
&\text{for } V_3(x): b_{3,2}=\frac{1}{2},\ b_{3,0}=b_{3,1}=b_{3,3}=0\\
&\text{for } V_4(x): b_{4,3}=\frac{1}{6},\ b_{4,0}=b_{4,1}=b_{4,2}=0.
\end{aligned} \tag{21}$$

Substituting Eq. (20) into Eq. (5) and collecting the coefficients of like powers of x, the following recurrence formula can be obtained

$$\begin{aligned}
b_{n,i+4}=\frac{-1}{(i+1)(i+2)(i+3)(i+4)g_0}\Bigg\{&\sum_{k=1}^{i}\frac{(i-k+4)!}{(i-k)!}g_k b_{n,\,i-k+4}\\
&+\sum_{k=0}^{i}\frac{2(k+1)(i-k+3)!}{(i-k)!}g_{k+1}b_{n,i-k+3}\\
&+\sum_{k=0}^{i}\Bigg[\frac{(k+1)(k+2)(i-k+2)!}{(i-k)!}g_{k+2}\\
&\quad+(i-k+1)(i-k+2)r_k\Bigg]b_{n,i-k+2}\\
&+\sum_{k=0}^{i}(k+1)(i-k+1)r_{k+1}b_{n,i-k+1}+\sum_{k=0}^{i}q_k b_{n,i-k}\Bigg\}
\end{aligned}$$
$$n=1,2,3,4;\ i\geq 0. \tag{22}$$

With this recurrence formula, one can generate the four exact normalized fundamental solutions of differential Eq. (5). Consequently, after substituting these fundamental solutions into the corresponding Green's function and characteristic equation, the exact solutions for the static deflection and dynamic response of the nonuniform beam are obtained.

4 Verification and Example

To verify the previous analysis, the free and forced vibrations of a rotating cantilever beam with constant width and linearly varied depth are studied. The rotating beam is fixed at $X = 0$ and the material properties and the transverse distributed excitation forces are given as

$$E(X)I(X)=E_oI_o\left(1-0.5\frac{X}{l}\right)^3,$$
$$m(X)=m_o\left(1-0.5\frac{X}{l}\right),$$
$$p_o(X,t)=P_1\left[\left(\frac{X}{l}\right)^4-\left(\frac{X}{l}\right)^5\right]\sin\bar{\omega}t, \tag{23}$$

where m_o is mass per unit length of the beam at $X = 0$. Hence, the centrifugal force is

$$N(X)=\int_X^l m(\zeta)\Omega^2\zeta d\zeta \tag{24}$$

where Ω is the rotating speed. Since the transverse distributed excitation force $p_o(X, t)$ is sinusoidal in time, the forced response can therefore be assumed as

$$\bar{U}(X,t)=u(X)\sin\bar{\omega}t. \tag{25}$$

Substituting Eqs. (23)-(25) into Eq. (11) and using the nondimensional parameters given in Eq. (4) the governing differential equation becomes

$$\frac{d^2}{dx^2}\left[(1-0.5x)^3\frac{d^2U}{dx^2}\right]-\frac{d}{dx}\left[\left(\frac{1}{3}-\frac{x^2}{2}+\frac{x^3}{6}\right)\alpha^2\frac{dU}{dx}\right]$$
$$-\Lambda^2(1-0.5x)U=P^*(x^4-x^5),\quad x\in(0,1), \tag{26}$$

Table 1 The first three dimensionless bending frequencies of a rotating tapered beam.

$$\left[E(X)I(X)=E_oI_o\left(1-0.5\frac{X}{l}\right)^3 \text{ and } m(X)=m_o\left(1-0.5\frac{X}{l}\right)\right]$$

[★ : the results given by Hodges et al. (1981)].

α	J	Λ_1	Λ_2	Λ_3
0	10	4.2510	19.1949	67.8130
	20	3.8286	18.3758	47.4212
	30	3.8238	18.3172	47.2747
	40	3.8237	18.3172	47.2648
	60	3.8238	18.3172	47.2648
	★	3.8238	18.3173	47.2648
2	10	4.8614	20.2898	67.3980
	20	4.4360	18.9693	48.1265
	30	4.4368	18.9366	47.8789
	40	4.4368	18.9366	47.8717
	60	4.4368	18.9366	47.8717
	★	4.4368	18.9366	47.8716
5	10	7.0879	25.3252	65.7317
	20	6.7306	21.7700	51.1294
	30	6.7435	21.9046	50.9320
	40	6.7435	21.9053	50.9338
	60	6.7435	21.9053	50.9338
	★	6.7345	21.9053	50.9338
10	10	14.6172	34.6514	65.3191
	20	11.5034	30.0206	59.7326
	30	11.5010	30.1568	60.5557
	40	11.5016	30.1855	60.5681
	60	11.5016	30.1828	60.5639
	★	11.5015	30.1827	60.5639

Downloaded 03 May 2010 to 171.66.16.247. Redistribution subject to ASME license or copyright; see http://www.asme.org/terms/Terms_Use.cfm

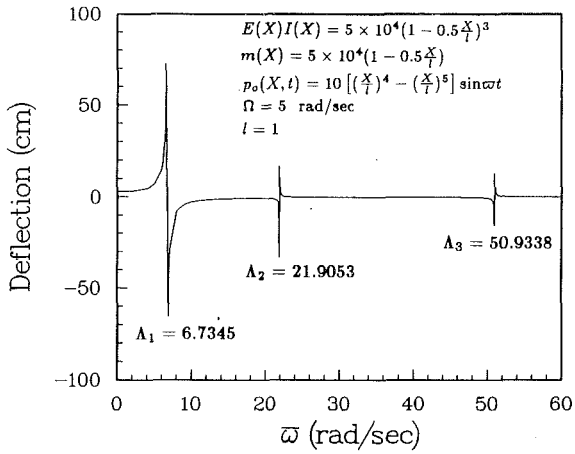


Fig. 2 Dynamic response curve at the tip of a rotating cantilever tapered beam subjected to transverse distributed excitation forces

where

$$U(x) = \frac{u(X)}{l},$$

$$\alpha^2 = \frac{m_o\Omega^2 l^4}{E_o I_o},$$

$$\Lambda^2 = \frac{m_o\bar{\omega}^2 l^4}{E_o I_o},$$

$$P^* = \frac{P_1 l^3}{E_o I_o}. \tag{27}$$

If the beam is in free vibration, the excitation frequency $\bar{\omega}$ given in Eq. (27) is replaced by ω representing the natural angular bending frequency.

Table 1 presents the first three dimensionless bending frequencies Λ at several dimensionless rotating speeds (α = 0, 2, 5, and 10). The results obtained by the present analysis are compared with those given by Hodges and Rutkowski (1981) who studied the problem by means of a variable order, finite element method. It can be observed that both results are almost the same when the number of terms (J) in each fundamental solution is equal to 60 and the difference between both results is within 0.55 percent when the number of terms employed is 20 only.

Figure 2 illustrates the vibrational response curve at the tip of the beam. It shows that when the excitation frequencies approach the natural bending frequencies of the beam, the response increases rapidly and becomes infinite as the excitation frequencies exactly coincide with the natural bending frequencies.

5 Conclusion

In this paper, the exact solutions for the problems governed by a general self-adjoint fourth-order nonhomogeneous ordinary differential equation with arbitrarily polynomial varying coefficients and general elastic boundary conditions are derived in Green's function form. The Green's function is concisely expressed in terms of the four normalized fundamental solutions of the system and these fundamental solutions are given in power series forms.

While comparing the proposed method to the other methods such as the finite element method, it takes advantage of: (1) less computer CPU time and memory storage are required, (2) no need for mesh refinements, and (3) the solutions are exact up to the accuracy of the computer or a preset value set by the analyst.

In the present analysis, the bending rigidity and axial tensile forces are assumed to be second and first-order differentiable, respectively. It is of interest to extend the present study to consider the problems for which these assumptions are invalid.

Acknowledgment

The support of the National Science Council of Taiwan, R.O.C., is gratefully acknowledged (Grant Number: NSC80-0401-E006-49).

References

Appl, F. C., and Zorowski, C. F., 1959, "Upper and Lower Bounds for Special Eigenvalues," ASME JOURNAL OF APPLIED MECHANICS, Vol. 26, pp. 246-250.

Bert, C. W., 1984, "Improved Technique for Estimating Buckling Loads," *ASCE Journal of Engineering Mechanics Division*, Vol. 110, pp. 1655-1665.

Beskos, D. E., and Narayanan, G. V., 1983, "Dynamic Response of Frameworks by Numerical Laplace Transform," *Computer Methods in Applied Mechanics and Engineering*, Vol. 37, pp. 289-307.

Carlson, R. M., and Wong, J. T., 1978, "An Exact Solution for the Static Bending of Uniform Rotating Beams," *Journal of the American Helicopter Society*, Vol. 23, No. 4, pp. 36-38.

Chen, P. P., 1949, "The Equivalent Loading Method and the Equivalent Beam Method," *Quarterly of Applied Mathematics*, Vol. 7, pp. 183-200.

Churchill, R. V., 1972, *Operational Mathematics*, 3rd ed., McGraw-Hill, New York.

Djodjo, B. A,. 1969, "Transfer Matrices for Beams Loaded Axially and Laid on an Elastic Foundation," *The Aeronautical Quarterly*, Vol. 20, pp. 281-306.

Eisenberger, M., and Clastornik, J., 1987, "Beams on Variable Two-Parameter Elastic Foundation," *ASCE Journal of the Engineering Mechanics*, Vol. 113, pp. 1454-1466.

Eisenberger, M., 1990, "Exact Static and Dynamic Stiffness Matrices for General Variable Cross Section Members," *AIAA Journal*, Vol. 28, pp. 1105-1109.

Hetenyi, M., 1979, *Beams on Elastic Foundation*, University of Michigan Press.

Hodges, D. H., 1979, "Vibration and Response on Nonuniform Rotating Beams with Discontinuities," *Journal of the American Helicopter Society*, Vol. 24, No. 10, pp. 43-50.

Hodges, D. H., and Rutkowski, M. J., 1981, "Free-Vibration Analysis of Rotating Beams by a Variable-Order Finite-Element Method," *AIAA Journal*, Vol. 19, pp. 1459-1466.

Iremonger, M J., 1980, "Finite Difference Buckling Analysis of Nonuniform Columns," *Computers & Structures*, Vol. 12, pp. 741-748.

Khulief, Y. A., 1989, "Vibration Frequencies of a Rotating Tapered Beam with End Mass," *Journal of Sound and Vibration*, Vol. 134, pp. 87-97.

Lee, S. Y., Ke, H. Y., and Kuo, Y. H., 1990, "Analysis of Non-uniform Beam Vibration," *Journal of Sound and Vibration*, Vol. 142, pp. 15-29.

Leissa, A. W., 1989, "Closed Form Exact Solutions for the Steady State Vibrations of Continuous Systems Subjected to Distributed Exciting Forces," *Journal of Sound and Vibration*, Vol. 134, pp. 435-453.

Sirosh, S. N., Ghali, A., and Razaqpur, A. G., 1989, "A General Finite Element for Beams or Beam-Columns with or without an Elastic Foundation," *International Journal for Numerical Methods in Engineering*, Vol. 28, pp. 1061-1076.

Stafford, R. D., and Giurgiutiu, V., 1975, "Semi-Analytic Methods for Rotating Timoshenko Beams," *International Journal of Mechanical Sciences*, Vol. 17, pp. 719-727.

Storti, D., and Aboelnaga, Y., 1987, "Bending Vibrations of a Class of Rotating Beams with Hypergeometric Solutions," ASME JOURNAL OF APPLIED MECHANICS, Vol. 54, pp. 311-314.

Sundara Raja Iyengar, K. T., and Anantharamu, S., 1963, "Finite Beam-Columns on Elastic Foundation," *ASCE Journal of Engineering Mechanics Division*, Vol. 89, No. 6, pp. 139-160.

Sutherland, R. L., 1949, "Bending Vibration of a Rotating Blade Vibrating in the Plane of Rotation," ASME JOURNAL OF APPLIED MECHANICS, Vol. 16, pp. 389-394.

Timoshenko, S. P., and Gere, J. M., 1961, *Theory of Elastic Stability*, 2nd ed., McGraw-Hill, New York.

Wang, H. C., 1967, "Generalized Hypergeometric Function Solutions on the Transverse Vibration of a Class of Nonuniform Beams," ASME JOURNAL OF APPLIED MECHANICS, Vol. 34, pp. 702-708.

Wright, A. D., Smith, C. E., Thresher, R. W., and Wang, J. C. L., 1982, "Vibration Modes of Centrifugally Stiffened Beams," ASME JOURNAL OF APPLIED MECHANICS, Vol. 49, pp. 197-202.

Downloaded 03 May 2010 to 171.66.16.247. Redistribution subject to ASME license or copyright; see http://www.asme.org/terms/Terms_Use.cfm

Downloaded 03 May 2010 to 171.66.16.247. Redistribution subject to ASME license or copyright; see http://www.asme.org/terms/Terms_Use.cfm

APPENDIX A
Green's Functions

Case	$K_{\theta L}$	K_{TL}	$K_{\theta R}$	K_{TR}	Green's function : $K(x,\xi) = \begin{cases} K_1(x,\xi), & \text{if} \quad \xi \le x \\ K_2(x,\xi), & \text{if} \quad \xi \ge x \end{cases}$
1	constant	constant	constant	constant	$K_1(x,\xi) = \Big\{ a_1 \Big[V_4(x)V_1(\xi) - V_3(x)V_2(\xi) + G'(0)V_4(x)V_2(\xi) + R(0)V_3(x)V_4(\xi) - R(0)G'(0)V_4(x)V_4(\xi) \Big]$ $+ a_1\beta_{\theta L} \Big[-V_3(x)V_3(\xi) + G'(0)V_3(x)V_4(\xi) + G'(0)V_4(x)V_3(\xi) - G'^2(0)V_4(x)V_4(\xi) \Big]$ $- a_1\beta_{TL} V_4(x)V_4(\xi) + a_2 V_1(x)V_1(\xi)$ $- a_2\beta_{TL} \Big[V_1(x)V_4(\xi) + V_3(x)V_2(\xi) - G'(0)V_4(x)V_2(\xi) - R(0)V_3(x)V_4(\xi) + R(0)G'(0)V_4(x)V_4(\xi) \Big]$ $+ a_2\beta_{\theta L}\beta_{TL} \Big[-V_3(x)V_3(\xi) + G'(0)V_3(x)V_4(\xi) + G'(0)V_4(x)V_3(\xi) - G'^2(0)V_4(x)V_4(\xi) \Big]$ $- a_3 \Big[V_1(x)V_2(\xi) + V_2(x)V_1(\xi) + G'(0)V_2(x)V_2(\xi) - R(0)V_3(x)V_2(\xi)$ $- R(0)V_1(x)V_4(\xi) - R(0)G'(0)V_2(x)V_4(\xi) + R^2(0)V_3(x)V_4(\xi) \Big]$ $+ a_3\beta_{\theta L} \Big[-V_1(x)V_3(\xi) - V_3(x)V_1(\xi) - G'(0)V_2(x)V_3(\xi) + R(0)V_3(x)V_3(\xi)$ $+ G'(0)V_1(x)V_4(\xi) + G'^2(0)V_2(x)V_4(\xi) - R(0)G'(0)V_3(x)V_4(\xi) \Big]$ $+ a_3\beta_{TL} \Big[V_4(x)V_2(\xi) + V_2(x)V_4(\xi) - R(0)V_4(x)V_4(\xi) \Big]$ $+ a_3\beta_{\theta L}\beta_{TL} \Big[V_4(x)V_3(\xi) + V_3(x)V_4(\xi) - G'(0)V_4(x)V_4(\xi) \Big]$ $+ a_4 \Big[V_2(x)V_2(\xi) - R(0)V_4(x)V_2(\xi) - R(0)V_2(x)V_4(\xi) + R^2(0)V_4(x)V_4(\xi) \Big]$ $+ a_4\beta_{\theta L} \Big[V_4(x)V_1(\xi) + V_2(x)V_3(\xi) - R(0)V_4(x)V_3(\xi) - G'(0)V_2(x)V_4(\xi) + R(0)G'(0)V_4(x)V_4(\xi) \Big]$ $- a_4\beta_{\theta L}\beta_{TL} V_4(x)V_4(\xi) + a_5\beta_{\theta L} V_1(x)V_1(\xi)$ $+ a_5\beta_{TL} \Big[V_2(x)V_2(\xi) - R(0)V_4(x)V_2(\xi) - R(0)V_2(x)V_4(\xi) + R^2(0)V_4(x)V_4(\xi) \Big]$ $+ a_5\beta_{\theta L}\beta_{TL} \Big[-V_1(x)V_4(\xi) + V_2(x)V_3(\xi) - R(0)V_4(x)V_3(\xi) - G'(0)V_2(x)V_4(\xi)$ $+ R(0)G'(0)V_4(x)V_4(\xi) \Big] \Big\} \Big/ \delta^*,$ $K_2(x,\xi) = K_1(\xi,x),$

Downloaded 03 May 2010 to 171.66.16.247. Redistribution subject to ASME license or copyright; see http://www.asme.org/terms/Terms_Use.cfm

					where $\delta^* = a_1 + a_2\beta_{TL} - (\beta_{\theta L}G'(0) + R(0))a_3 + a_4\beta_{\theta L} + a_5\beta_{\theta L}\beta_{TL},$ $a_1 = \left[V_1''(1)V_2'''(1) - V_1'''(1)V_2''(1)\right] + \beta_{\theta R}\left[V_1'(1)V_2'''(1) - V_1'''(1)V_2'(1)\right] + \beta_{TR}\left[V_1(1)V_2''(1) - V_1''(1)V_2(1)\right]$ $+ \beta_{\theta R}\beta_{TR}\left[V_1(1)V_2'(1) - V_1'(1)V_2(1)\right] + (\beta_{\theta R}\gamma_R + \delta_R)\left[V_1'(1)V_2''(1) - V_1''(1)V_2'(1)\right],$ $a_2 = \left[V_2''(1)V_4'''(1) - V_2'''(1)V_4''(1)\right] + \beta_{\theta R}\left[V_2'(1)V_4'''(1) - V_2'''(1)V_4'(1)\right] + \beta_{TR}\left[V_2(1)V_4''(1) - V_2''(1)V_4(1)\right]$ $+ \beta_{\theta R}\beta_{TR}\left[V_2(1)V_4'(1) - V_2'(1)V_4(1)\right] + (\beta_{\theta R}\gamma_R + \delta_R)\left[V_2'(1)V_4''(1) - V_2''(1)V_4'(1)\right],$ $a_3 = \left[V_1''(1)V_4'''(1) - V_1'''(1)V_4''(1)\right] + \beta_{\theta R}\left[V_1'(1)V_4'''(1) - V_1'''(1)V_4'(1)\right] + \beta_{TR}\left[V_1(1)V_4''(1) - V_1''(1)V_4(1)\right]$ $+ \beta_{\theta R}\beta_{TR}\left[V_1(1)V_4'(1) - V_1'(1)V_4(1)\right] + (\beta_{\theta R}\gamma_R + \delta_R)\left[V_1'(1)V_4''(1) - V_1''(1)V_4'(1)\right],$ $a_4 = \left[V_1''(1)V_3'''(1) - V_1'''(1)V_3''(1)\right] + \beta_{\theta R}\left[V_1'(1)V_3'''(1) - V_1'''(1)V_3'(1)\right] + \beta_{TR}\left[V_1(1)V_3''(1) - V_1''(1)V_3(1)\right]$ $+ \beta_{\theta R}\beta_{TR}\left[V_1(1)V_3'(1) - V_1'(1)V_3(1)\right] + (\beta_{\theta R}\gamma_R + \delta_R)\left[V_1'(1)V_3''(1) - V_1''(1)V_3'(1)\right],$ $a_5 = \left[V_3''(1)V_4'''(1) - V_3'''(1)V_4''(1)\right] + \beta_{\theta R}\left[V_3'(1)V_4'''(1) - V_3'''(1)V_4'(1)\right] + \beta_{TR}\left[V_3(1)V_4''(1) - V_3''(1)V_4(1)\right]$ $+ \beta_{\theta R}\beta_{TR}\left[V_3(1)V_4'(1) - V_3'(1)V_4(1)\right] + (\beta_{\theta R}\gamma_R + \delta_R)\left[V_3'(1)V_4''(1) - V_3''(1)V_4'(1)\right],$ $\beta_{\theta R} \equiv \frac{K_{\theta R}\, l}{E(l)I(l)}, \quad \beta_{\theta L} \equiv \frac{K_{\theta L}\, l}{E(0)I(0)}, \quad \beta_{TR} \equiv \frac{K_{TR}\, l^3}{E(l)I(l)}, \quad \beta_{TL} \equiv \frac{K_{TL}\, l^3}{E(0)I(0)}, \quad \delta_R \equiv \frac{N(l)\, l^2}{E(l)I(l)}, \quad R(0) = -\frac{N(0)\, l^2}{E(0)I(0)},$ $G'(0) = \frac{l}{E(X)I(X)} \frac{d}{dX}\left[E(X)I(X)\right]\Big|_{X=0}, \quad \gamma_R = \frac{l}{E(X)I(X)} \frac{d}{dX}\left[E(X)I(X)\right]\Big|_{X=l}.$
2	0	infinity	0	infinity	$\begin{cases} K_1(x,\xi) = \Big\{ -a_1\left[V_1(x)V_4(\xi) + V_3(x)V_2(\xi) - G'(0)V_4(x)V_2(\xi) - R(0)V_3(x)V_4(\xi) + R(0)G'(0)V_4(x)V_4(\xi)\right] \\ \qquad + a_2\left[V_2(x)V_2(\xi) - R(0)V_4(x)V_2(\xi) - R(0)V_2(x)V_4(\xi) + R^2(0)V_4(x)V_4(\xi)\right] \\ \qquad + a_3\left[V_2(x)V_4(\xi) + V_4(x)V_2(\xi) - R(0)V_4(x)V_4(\xi)\right] - a_4V_4(x)V_4(\xi) \Big\} \Big/ \delta^*, \\ K_2(x,\xi) = K_1(\xi,x), \end{cases}$ where $a_1 = V_2(1)V_4''(1) - V_2''(1)V_4(1),$ $a_2 = V_3(1)V_4''(1) - V_3''(1)V_4(1),$ $a_3 = V_1(1)V_4''(1) - V_1''(1)V_4(1),$ $a_4 = V_1(1)V_2''(1) - V_1''(1)V_2(1).$ $\delta^* = a_1.$

3	infinity	infinity	0	infinity	$\begin{cases} K_1(x,\xi) = \Big\{-a_1\big[V_1(x)V_4(\xi)-V_2(x)V_3(\xi)+G'(0)V_2(x)V_4(\xi)-R(0)V_3(x)V_4(\xi)\big]-a_2V_3(x)V_3(\xi) \\ \qquad +a_3\big[V_3(x)V_4(\xi)+V_4(x)V_3(\xi)-G'(0)V_4(x)V_4(\xi)\big]-a_4V_4(x)V_4(\xi)\Big\}\Big/\delta^*, \\ K_2(x,\xi) = K_1(\xi,x), \end{cases}$ where $a_1 = V_3(1)V_4''(1)-V_3''(1)V_4(1)$, $a_2 = V_2(1)V_4''(1)-V_2''(1)V_4(1)$, $a_3 = V_2(1)V_3''(1)-V_2''(1)V_3(1)$, $a_4 = V_1(1)V_3''(1)-V_1''(1)V_3(1)$, $\delta^* = a_1$.
4	infinity	infinity	0	0	$K(x,\xi)$ same as Case 3 where $a_1 = \big[V_3''(1)V_4'''(1)-V_3'''(1)V_4''(1)\big]+\delta_R\big[V_3'(1)V_4''(1)-V_3''(1)V_4'(1)\big]$, $a_2 = \big[V_2''(1)V_4'''(1)-V_2'''(1)V_4''(1)\big]+\delta_R\big[V_2'(1)V_4''(1)-V_2''(1)V_4'(1)\big]$, $a_3 = \big[V_2''(1)V_3'''(1)-V_2'''(1)V_3''(1)\big]+\delta_R\big[V_2'(1)V_3''(1)-V_2''(1)V_3'(1)\big]$, $a_4 = \big[V_1''(1)V_3'''(1)-V_1'''(1)V_3''(1)\big]+\delta_R\big[V_1'(1)V_3''(1)-V_1''(1)V_3'(1)\big]$, $\delta^* = a_1$, $\delta_R = \frac{N(l)\,l^2}{E(l)I(l)}$.
5	infinity	infinity	infinity	infinity	$K(x,\xi)$ same as Case 3 where $a_1 = V_3(1)V_4'(1)-V_3'(1)V_4(1)$, $a_2 = V_2(1)V_4'(1)-V_2'(1)V_4(1)$, $a_3 = V_2(1)V_3'(1)-V_2'(1)V_3(1)$, $a_4 = V_1(1)V_3'(1)-V_1'(1)V_3(1)$, $\delta^* = a_1$.

Downloaded 03 May 2010 to 171.66.16.247. Redistribution subject to ASME license or copyright; see http://www.asme.org/terms/Terms_Use.cfm

Amit Prakash
Associate Scientist,
Wire Science and Technology,
The Goodyear Tire and Rubber Company,
Technical Center,
Akron, OH 44316

Ted A. Conway
Assistant Professor,
Department of Mechanical Engineering,
University of Akron,
Akron, OH 44325-3903

George A. Costello
Professor,
Department of Theoretical
and Applied Mechanics,
University of Illinois at Urbana-Champaign,
Urbana, IL 61801
Fellow ASME

Compression of a Cord

Cord is a structural element that is generally used to resist relatively large axial loads in tension in comparison to bending and torsional loads. However, in certain cases, a cord may be called upon to resist a compressive load such as occurs when a cord is placed in a composite. When a cord is subjected to compression, the individual filaments lose contact with each other. This results in a considerable reduction in the axial stiffness of the cord. Generally, most cord composites are fabricated at elevated temperatures and cooled to room temperatures. Some remarks are made concerning the buckling of these cords since the coefficients of thermal expansion are different for the matrix and the cord.

Introduction

When a cord is subjected to an axial tensile load and an axial twisting moment, the axial strain and the axial rotation can be determined (Costello, 1983). There are many papers that deal with the behavior of wire rope, and a survey of the literature can be found in an article by Utting and Jones (1984). In a paper by Conway and Costello (1990), it is shown that, for certain values of axial and rotational strains, the wires or filaments separate from each other. This can occur in the dynamic case, even if the cord or rope is in tension.

The purpose of this paper is to investigate the response of a cord in compression. Some remarks will be made concerning the buckling of a cord contained in a matrix when the composite cools down to room temperature. A method is presented which will determine whether or not the cord will buckle.

Analysis

An analysis will be made of a cord which consists of three wires with the cross-section shown in Fig. 1. The method can be extended to other types of cross-sections (Phillips and Costello, 1985).

Contact Between Adjacent Wires. If the three wires are just contracting each other in the undeformed state, the following expression results (Costello and Phillips, 1974)

$$\frac{r}{R}=\sqrt{1+\frac{1}{3\sin^2\alpha}} \tag{1}$$

where R is the wire radius, r denotes the helical radius of a wire, and α is the helix angle; all in the unloaded state. When the cord is loaded, the following can be written

$$\frac{\bar{r}}{R(1-\nu\xi)}=\sqrt{1+\frac{1}{3\sin^2\bar{\alpha}}} \tag{2}$$

where $\bar{r}$ is the deformed helical radius, $\bar{\alpha}$ is the new helix angle,

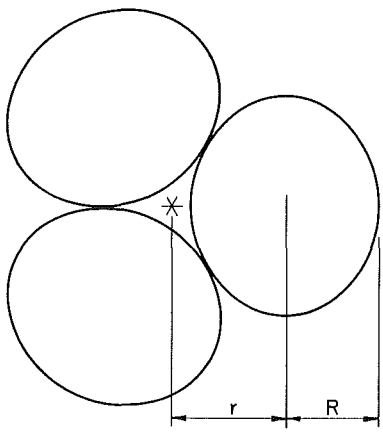


Fig. 1 Cross-section of a cord with three wires

Contributed by the ASME Applied Mechanics Division of THE AMERICAN SOCIETY OF MECHANICAL ENGINEERS for presentation at the Winter Annual Meeting, Atlanta, Ga., Dec. 1-6, 1991.

Discussion on this paper should be addressed to the Technical Editor, Professor Leon M. Keer, The Technological Institute, Northwestern University, Evanston, IL 60208, and will be accepted until two months after final publication of the paper itself in the JOURNAL OF APPLIED MECHANICS. Manuscript received by the ASME Applied Mechanics Division, Sept. 17, 1990; final revision, Feb. 25, 1991.

Paper No. 91-WA/APM-36.

Copyright © 1992 by ASME
Downloaded 03 May 2010 to 171.66.16.247. Redistribution subject to ASME license or copyright; see http://www.asme.org/terms/Terms_Use.cfm

ν is Poisson's ratio, and ξ is the axial wire strain. Since the change in the helix angle, $\Delta\alpha$, and the wire strain, ξ, are assumed small, Eq. (2) can be written as

$$\frac{\bar{r}}{R}=\frac{r}{R}\left[1-\nu\xi-\frac{\cos\alpha}{(1+3\sin^2\alpha)\sin\alpha}\Delta\alpha\right]. \tag{3}$$

The initial helix angle, α, is given by

$$\tan\alpha=\frac{p}{2\pi r} \tag{4}$$

where p is the original pitch of the wires.

An analysis of the deformed configuration of the cord shown in Fig. 1 yields

$$\epsilon=\frac{\bar{h}-h}{h}=\xi+\frac{\Delta\alpha}{\tan\alpha} \tag{5}$$

and

$$r\tau_c=r\frac{(\bar{\theta}-\theta)}{h}=\frac{(1+\nu)}{\tan\alpha}\xi+\left[\frac{1}{(1+3\sin^2\alpha)\tan^2\alpha}-1\right]\Delta\alpha, \tag{6}$$

where ϵ is the axial strain of the cord, h is the original length of the cord, $\bar{h}$ is the final length of the cord, τ_c is the angle of twist per unit length of the cord, θ is the original angle that a wire sweeps out in a plane perpendicular to the axis of the cord, and $\bar{\theta}$ is the final angle that a wire sweeps out in a plane perpendicular to the axis of the cord. The following equation can also be written as

$$\frac{r}{\bar{r}}=1+\nu\xi+\frac{1}{(1+3\sin^2\alpha)\tan\alpha}\Delta\alpha. \tag{7}$$

The loads and moments become

$$\frac{G'}{ER^3}=\frac{\pi}{4}R\Delta\kappa' \tag{8}$$

$$\frac{H}{ER^3}=\frac{\pi}{4(1+\nu)}R\Delta\tau \tag{9}$$

$$\frac{N}{ER^2}=\frac{H}{ER^3}\frac{\cos^2\alpha}{r/R}-\frac{G'}{ER^3}\frac{\sin\alpha\cos\alpha}{r/R} \tag{10}$$

$$\frac{T}{ER^2}=\pi\xi \tag{11}$$

$$\frac{X}{ER}=\frac{N}{ER^2}\frac{\sin\alpha\cos\alpha}{r/R}-\frac{T}{ER^2}\frac{\cos^2\alpha}{r/R} \tag{12}$$

$$\frac{F}{ER^2}=3\left[\frac{T}{ER^2}\sin\alpha+\frac{N}{ER^2}\cos\alpha\right] \tag{13}$$

and

$$\frac{M}{ER^3}=3\left[\frac{H}{ER^3}\sin\alpha+\frac{G'}{ER^3}\cos\alpha+\frac{r}{R}\left(\frac{T}{ER^2}\cos\alpha-\frac{N}{ER^2}\sin\alpha\right)\right] \tag{14}$$

where G is the bending moment in a wire, E is the modulus of elasticity, $\Delta\kappa$ is the change in curvature of a wire, $\Delta\tau$ is the twist per unit length of a wire, H is the twisting moment in a wire, N is the shearing force in a wire, T is the axial force in a wire, X is the resultant contact force per unit length acting on a wire, F is the total axial load acting on the cord, and M is the axial twisting moment acting on the strand.

The expressions for the change in curvature and twist of a wire are

$$R\Delta\kappa'=\frac{\cos^2\bar{\alpha}}{\bar{r}/R}-\frac{\cos^2\alpha}{r/R}=\frac{1}{r/R}\left\{(\nu\cos^2\alpha)\xi+\left[\frac{\cos^3\alpha}{(1+3\sin^2\alpha)\sin\alpha}-2\sin\alpha\cos\alpha\right]\Delta\alpha\right\} \tag{15}$$

and

$$R\Delta\tau=\frac{\nu\sin\alpha\cos\alpha}{r/R}\xi+\frac{1}{r/R}\left[1-2\sin^2\alpha+\frac{\cos^2\alpha}{(1+3\sin^2\alpha)}\right]\Delta\alpha. \tag{16}$$

In general, the total axial force, F, and the total axial twisting moment, M, can be expressed as

$$\frac{F}{AE}=C_1\epsilon+C_2\beta \tag{17}$$

and

$$\frac{M}{ER_c^3}=C_3\epsilon+C_4\beta \tag{18}$$

where $R_c=r+R$ is the cord radius, $A=\Sigma\pi R_f^2$ is the metallic cross-sectional area of the cord, C_1, C_2, C_3, and C_4 are constants, and β is the rotational strain defined by the equation

$$\beta=R_c\tau_c. \tag{19}$$

It should be noted that for a given value of α Eqs. (5)–(16) are functions of ξ and $\Delta\alpha$. Hence, the values of C_1, C_2, C_3, and C_4 can be determined. This is accomplished by choosing values of $\Delta\alpha$ and ξ. The values of F, M, ϵ, and β are then known. For example, for $\alpha=75$ deg, the following results

$$\frac{F}{AE}=0.8832\epsilon+0.1277\beta \tag{20}$$

and

$$\frac{M}{ER_c^3}=0.2130\epsilon+0.1227\beta. \tag{21}$$

It should be remembered that the above equations are valid if the contact force per unit length, X, is less than zero, since X is positive in tension.

No Contact Between Adjacent Wires. The above equations have to be modified if the wires do not touch each other. In this case Eq. (2) is no longer valid, and Eq. (12) becomes (since $X=0$)

$$\frac{N}{ER^2}\tan\alpha=\frac{T}{ER^2}=\pi\xi. \tag{22}$$

The following can be written down

$$R\Delta\kappa'=-\frac{\cos^2\alpha}{r/R}\frac{\Delta r}{r}-2\frac{\sin\alpha\cos\alpha}{r/R}\Delta\alpha \tag{23}$$

$$R\Delta\tau=-\frac{\sin\alpha\cos\alpha}{r/R}\frac{\Delta r}{r}+\frac{(1-2\sin^2\alpha)}{r/R}\Delta\alpha \tag{24}$$

where Δr is the change in r. Equations (8), (9), (10), and (22) yield the result that

$$\frac{N}{ER^2}=\frac{\pi\nu\sin\alpha\cos^3\alpha}{4(r/R)^2(1+\nu)}\frac{\Delta r}{r}+\frac{\pi\cos^2\alpha}{4(r/R)^2}\left[\frac{1-2\sin^2\alpha}{1+\nu}+2\sin^2\alpha\right]\Delta\alpha \tag{25}$$

and

$$\xi=\frac{\nu\sin^2\alpha\cos^2\alpha}{4(r/R)^2(1+\nu)}\frac{\Delta r}{r}+\frac{\sin\alpha\cos\alpha}{4(r/R)^2}\left[\frac{1-2\sin^2\alpha}{1+\nu}+2\sin^2\alpha\right]\Delta\alpha \tag{26}$$

ϵ and $r\tau_c$ become

$$\epsilon=\frac{\nu\sin^2\alpha\cos^2\alpha}{4(r/R)^2(1+\nu)}\frac{\Delta r}{r}+\left[\frac{\cos\alpha}{\sin\alpha}+\frac{\sin\alpha\cos\alpha}{4(r/R)^2}\left(\frac{1-2\sin^2\alpha}{1+\nu}+2\sin^2\alpha\right)\right]\Delta\alpha \tag{27}$$

Downloaded 03 May 2010 to 171.66.16.247. Redistribution subject to ASME license or copyright; see http://www.asme.org/terms/Terms_Use.cfm

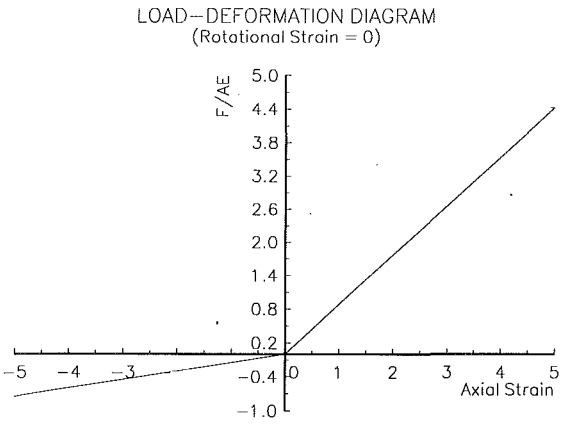


Fig. 2 Load deformation diagram

and

$$r\tau_c = \left(\frac{\nu \sin\alpha \cos^3\alpha}{4(r/R)^2(1+\nu)} - \frac{\cos\alpha}{\sin\alpha}\right)\frac{\Delta r}{r} + \left[\frac{\cos^2\alpha}{4(r/R)^2}\left(\frac{1-2\sin^2\alpha}{1+\nu}+2\sin^2\alpha\right)-1\right]\Delta\alpha. \quad (28)$$

In the above case, the various quantities are now functions of $\Delta r/r$ and $\Delta\alpha$. Again for $\alpha = 75$ deg, the following results:

$$\frac{F}{AE} = 0.1502\epsilon - 0.004735\beta \quad (29)$$

$$\frac{M}{ER_c^3} = -0.0154\epsilon + 0.08142\beta. \quad (30)$$

Equations (20) and (29) show that a considerable reduction in the effective modulus occurs when the cord is compressed. The effective modulus is defined by the equation

$$E_e = C_1 E \quad (31)$$

which is the axial modulus when $\beta = 0$. This is illustrated in Fig. 2, which depicts a kink at the origin of the load deformation diagram. This is a result of the loss in contact of the individual wires with each other.

Setting Eq. (20) equal to Eq. (29), or Eq. (21) equal to Eq. (30) yields ϵ as a linear function of β, which divides the ϵ, β plane into two regions. One region is the contact region and the other region is not. The result is (for the above example):

$$\epsilon = -0.1806\beta. \quad (32)$$

Compression of a Cord

Let a cord be subjected to an axial load in compression and let the twisting moment be zero. The wires will separate as can be shown by an examination of the ϵ, β plane. Again, for $\alpha = 75$ deg, Eq. (30) yields

$$\epsilon = 5.287\beta \quad (33)$$

and hence Eq. (29) becomes

$$\frac{F}{AE} = 0.1493\epsilon. \quad (34)$$

Costello (1977) has shown that the bending stiffness, B^*, of a helical spring is given by the equation

$$B^* = \frac{2\sin\alpha}{2+\nu\cos^2\alpha} EI \quad (35)$$

where

$$I = \frac{\pi R^4}{4}. \quad (36)$$

Hence, the buckling load, P^*, for a cord column with three wires, which are simply supported at the ends, would be given by

$$P^* = 3\pi^2 \frac{B^*}{L^2} \quad (37)$$

where L is the length of the cord.

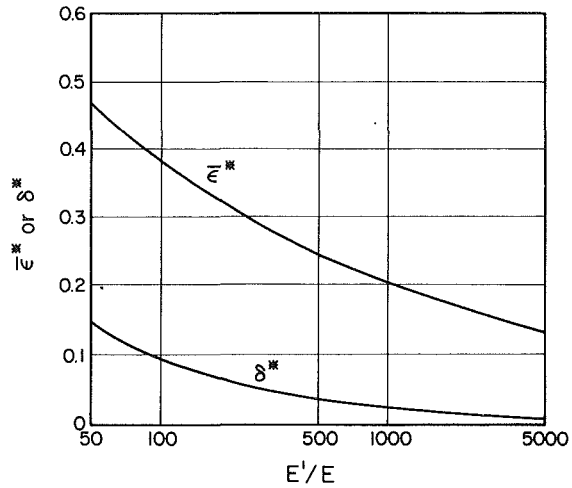


Fig. 3 Plot of $\bar{\delta}^*$ and $\bar{\epsilon}^*$ as functions of E'/E_m

Buckling of a Cord in a Composite

In a paper by Sadowsky et al. (1967), the buckling of microfibers is investigated. The fiber is surrounded by an infinitely large matrix. The results of this paper can be used to investigate the buckling of a cord surrounded by an infinitely large matrix.

In Sadowsky et al. (1967), the bending of a microfiber is treated as a flexible elastic rod with the relation

$$\frac{1}{\rho} = \frac{M}{E'\bar{I}} \quad (38)$$

where E' is the modulus of elasticity of the rod, $1/\rho$ is the curvature, and $\bar{I}$ is given by the relation

$$\bar{I} = \frac{\pi r_0^4}{4} \quad (39)$$

where r_0 is the rod radius. In the case of a cord with radius, R_c, r_0 will be set equal to R_c, and E' will be defined by the equation

$$E'\frac{\pi R_c^4}{4} = \frac{2\sin\alpha}{2+\nu\cos^2\alpha} 3E\frac{\pi R^4}{4}. \quad (40)$$

This determines E', the modulus of the fiber, so that the cord and the fiber, both of radius, R_c, will have the same bending stiffness.

Let the value δ^* be defined by the relation

$$\delta^* = \frac{P^*}{\pi R_c^2 E'} \quad (41)$$

where P^* is the longitudinal compressive force in the cord at the moment of buckling. Also, let L, the half wavelength of the buckled cord, be given by the equation

$$L = \frac{\pi R_c}{\bar{\epsilon}^*}. \quad (42)$$

A portion of the plot of δ^* and $\bar{\epsilon}^*$, as a function of E'/E_m (taken from Sadowsky et al., 1967), is shown in Fig. 3, where E_m is the modulus of the matrix. This, of course, determines the buckling load and the half wavelength for a given cord surrounded by an infinite matrix.

Downloaded 03 May 2010 to 171.66.16.247. Redistribution subject to ASME license or copyright; see http://www.asme.org/terms/Terms_Use.cfm

Consideration of Buckling Due to a Temperature Drop. Consideration is now given to a cord placed in a molten matrix. The mixture is allowed to cool down. The solidification temperature of the matrix is then reached and the mixture is then allowed to cool further. If the coefficients of thermal expansion are different where the matrix contracts faster than the cord, buckling of the cord may result.

Let T_1 be the solidification temperature of the matrix and T_2, the final cooling-off temperature of the composite ($T_1 > T_2$). Let α and α' be the coefficients of thermal expansion of the matrix and the cord, respectively, and let $\alpha > \alpha'$. The temperature drop $T_1 - T_2$ induces unequal stress-free contraction $\alpha(T_1 - T_2)$. Since the cord is bonded to the matrix, an additional contraction Δ' of the cord will have to take place under the action of the compressive force P applied by the matrix to the cord at its ends. The value of Δ' is

$$\Delta' = (\alpha - \alpha')(T_1 - T_2). \tag{43}$$

The value of δ', the axial strain at buckling, can be determined by Eqs. (17) and (18). Hence, since the axial moment is assumed zero,

$$\frac{P^*}{AE} = \left(C_1 - \frac{C_2 C_3}{C_4}\right)\delta'. \tag{44}$$

If $\Delta' < \delta'$, the cord will not buckle. If $\Delta' > \delta'$, the cord will buckle.

Example. Let $R = 0.0000925$ m, $\alpha = 75$ deg, $E = 200 \times 10^9$ Pa, $\nu = 0.3$, $\alpha = 0.0000691/°C$, $\alpha' = 0.0000117/°C$, $\Delta T = 125°C$, and $E_m = 8.3 \times 10^6$ Pa. Equation (43) yields $\Delta' = 0.007175$. The value of R_c is 0.0002003 m. Equation (40) determines E', and hence $E' = 26.1 \times 10^9$ Pa with $E'/E_m = 3.145 \times 10^3$. From Fig. 2, the values of δ^* and $\bar{\epsilon}^*$ are obtained with the result that $\delta^* = 0.015$ and $\bar{\epsilon}^* = 0.15$. The buckling load, given by Eq. (41), is $P^* = 49.345$ N. Equation (44) shows that $\delta' = 0.0205$. Since $0.007175 < 0.0205$, the cord will not buckle under this temperature change. Equation (42) yields the result that $L = 0.00420$ m, if the column were to buckle.

Summary and Conclusions

A theory is presented which will predict the axial response of a cord subjected to tensile and compressive loads. The results show that a kink in the load deformation diagram occurs at the origin. An equation is presented which will predict the buckling load of a cord where, under compression, the individual wires separate.

A method is also presented which will predict the buckling load of a cord in an infinite matrix. The cord is loaded by an axial load only, and the rotational strain is neglected. Also presented is a method which will determine or not a cord in an infinite matrix will buckle when the composite cools down.

The theory can be extended to complex cord cross-sections with a modification of the equations. The results show the existence of a buckled shape with a number of waves of a definite wavelength when the cord is surrounded by the matrix.

Acknowledgments

We would like to acknowledge the Wire Science and Technology group of the Goodyear Tire and Rubber Company for their support in this investigation.

References

Conway, T. A., and Costello, G. A., 1990, "Bird-Caging in Wire Rope," *Journal of the Engineering Mechanics Division*, ASCE, New York, Vol. 116, pp. 822–831.

Costello, G. A., 1977, "Large Deflections of Helical Spring Due to Bending," *Journal of the Engineering Mechanics Division*, ASCE, Vol. 103, No. EM3, Proc. Paper 1964, June, pp. 479–487.

Costello, G. A., 1983, "Stresses in Multilayered Cables," ASME *Journal of Energy Resources Technology*, Vol. 105, pp. 337–340.

Costello, G. A., and Phillips, J. W., 1974, "A More Exact Theory for Twisted Wire Cables," *Journal of Engineering Mechanics Division*, ASCE, Vol. 100, No. EM5, pp. 1096–1099.

Phillips, J. W., and Costello, G. A., 1985, "Analysis of Wire Ropes with Internal Wire Rope Cores," ASME JOURNAL OF APPLIED MECHANICS, Vol. 52, pp. 510–516.

Sadowsky, M. A., Pu, S. L., and Hussain, M. A., 1967, "Buckling of Microfibers," ASME JOURNAL OF APPLIED MECHANICS, Vol. 34, pp. 1011–1016.

Utting, W. S., and Jones, N., 1984, "A Survey of the Literature on the Behaviour of Wire Rope," Wire Industry, September.

Downloaded 03 May 2010 to 171.66.16.247. Redistribution subject to ASME license or copyright; see http://www.asme.org/terms/Terms_Use.cfm

V. Berdichevsky
School of Aerospace Engineering,
Georgia Institute of Technology,
Atlanta, GA 30332

V. Misyura
Leningrad Building Institute,
Leningrad, U.S.S.R

Effect of Accuracy Loss in Classical Shell Theory

It is shown that classical shell theory does not yield correct values of displacements in some shell problems. Underlying causes of this effect are discussed.

Introduction

Classical shell theory got its final form after recognizing that the Kirchhoff-Love hypotheses introduce in the shell theory relations errors of order h/R in comparison with 1 (h is the shell thickness, R is the characteristic curvature radius). Shell theory, neglecting terms of the order h/R, is called classical. The three versions of classical shell theory mostly used are: Love's theory (we shall refer to the theory from Love's monograph (Love, 1927) with some necessary improvements (Goldenweizer, 1976) as Love's theory), the Novozilov-Balabuch theory (Novozilov, 1962), and the Koiter-Sanders theory (Koiter, 1960; Sanders, 1959). They differ by small terms of order h/R. It was proved (Morgenstern, 1959, John, 1965; Koiter, 1971; Koiter and Simmonds, 1973; Vorovich, 1975; Ladeveze, 1986) that the classical shell theory predicts the stress state of shells correctly, i.e., with small errors of order h/R. It seems natural to assume that the same is true for displacements. The analogous statement for displacements is incorrect, however, and this paper aims to present some simple shell problems which illustrate this fact, consider the causes of accuracy loss, and discuss improved classical shell theories which are able to guarantee correct prediction of displacements.

1 A Simple Example Demonstrating the Effect of Accuracy Loss

Consider the well-known problem of deformation of an elastic isotropic cylindrical pipe under external pressure. Let the undeformed pipe occupy the region $V_0 = \{R - 1/2\ h \leqq r \leqq R + 1/2\ h,\ -\pi \leqq \theta \leqq \pi,\ 0 \leqq |x| \leqq L\}$ where r, θ, and x are cylindrical coordinates (Fig. 1). We assume that the pipe slides without friction between two rigid planes $x = L$ and $x = -L$. The stress distribution is (Love, 1927)

$$\sigma_{\theta\theta} = \frac{P}{2Rh}(R + 1/2\ h)^2\left(1 + \frac{(R - 1/2\ h)^2}{(R+\xi)^2}\right), \quad \xi \equiv r - R \qquad (1)$$
$$\sigma_{r\theta} = \sigma_{x\theta} = 0.$$

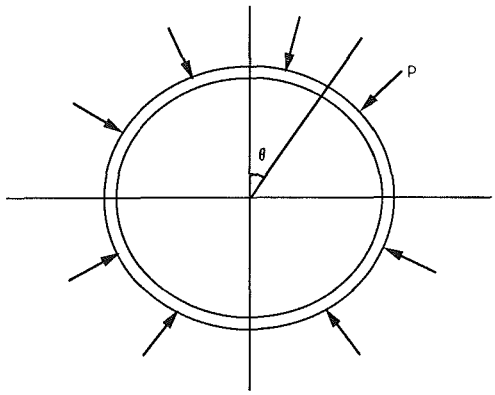


Fig. 1

We do not need to write out the component σ_{rr}. The displacement field is determined by the known stress state up to the rigid motion of the pipe cross-section. We fix this rigid motion by three constraints for displacements of the middle surface—the points $(-\pi/2, R)$ and $(\pi/2, R)$ have zero vertical displacements and the point $(0, R)$ has zero horizontal displacement[1]:

$$w_\theta\left(-\frac{\pi}{2}, R\right) = 0,\ w_\theta\left(\frac{\pi}{2}, R\right) = 0,\ w_\theta(0, R) = 0. \qquad (2)$$

The displacement field has only one nonzero component w_r under conditions (1)

$$w_r = \frac{P(1+\nu)}{2RhE}(R - 1/2\ h)^2\left[(1-2\nu)(R+\xi) + \frac{(R+1/2\ h)^2}{R+\xi}\right]. \qquad (3)$$

Denote, by u and v, the normal and tangent components of displacements of the middle surface

$$u = w_r,\ v = w_\theta \text{ at } r = R.$$

Contributed by the ASME Applied Mechanics Division of The American Society of Mechanical Engineers for presentation at the Winter Annual Meeting, Atlanta, Ga., Dec. 1-6, 1991.

Discussion on this paper should be addressed to the Technical Editor, Prof. Leon M. Keer, The Technological Institute, Northwestern University, Evanston, IL 60208, and will be accepted until two months after final publication of the paper itself in the Journal of Applied Mechanics. Manuscript received by the ASME Applied Mechanics Division, Dec. 21, 1990; final revision, Mar. 12, 1991.

Paper No. 91-WA/APM-38.

[1] It is easy to check that rigid motion is determined uniquely by conditions (2). Really, rigid motion, written in cylindrical coordinates, has the angle component w_θ of the form

$$w_\theta = a\cos\theta - b\sin\theta + \omega r$$

where a, b are horizontal and vertical translations of the body and ω is the rotation angle. Writing out the linear system of equations for a, b, and ω following from (2), one can find that the determinant of this system is not equal to zero.

Copyright © 1992 by ASME
Downloaded 03 May 2010 to 171.66.16.247. Redistribution subject to ASME license or copyright; see http://www.asme.org/terms/Terms_Use.cfm

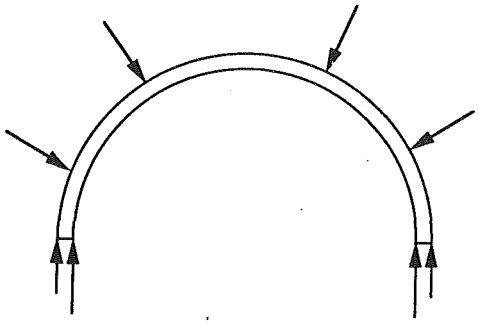


Fig. 2

When dropping small terms of order h/R, compared to unity, and in accordance with (3), we have

$$u=\frac{Pr^2(1-\nu^2)}{Eh}=\text{const.},\ v=0. \tag{4}$$

Note that in the relations (1), (3), and (4), positive and negative values of P relate, correspondingly, to uniform internal load and external pressure.

Consider now the following problem: Let us cut the pipe along the plane $\theta = \pm\pi/2$ and consider equilibrium of the upper half of the pipe. The upper semi-pipe is subjected to external pressure, and surface forces applied along the cut $\theta = \pm\pi/2$ (Fig. 2). We possess the exact three-dimensional solution of this problem in Eqs. (1) and (3).

Let us now solve this problem using the classical shell theory. Denote, by N and M, the stress resultants and stress moment along the angle coordinate

$$N=\int_{-h/2}^{h/2}\sigma_{\theta\theta}d\xi,\ M=\int_{-h/2}^{h/2}\sigma_{\theta\theta}\xi d\xi. \tag{5}$$

Then, the equilibrium equations of classical shell theory are

$$\frac{1}{R}\frac{dN}{d\theta}+\frac{1}{R^2}\frac{dM}{d\theta}=0,\ \frac{1}{R^2}\frac{d^2M}{d\theta^2}-\frac{N}{R}+P=0, \tag{6}$$

with boundary conditions

$$N=PR,\ M=-\frac{Ph^2}{12},\ \frac{dM}{d\theta}=0 \text{ at } \theta=\pm\frac{\pi}{2}. \tag{7}$$

The conditions (7) are obtained by substitution of the stress distribution (1) into (5) and neglecting terms of the order h/R in comparison with unity.

Equations (6) with boundary conditions (7) have the unique solution

$$N=PR,\ M=-\frac{Ph^2}{12} \tag{8}$$

which does not depend on material properties.

Now let us invoke the stress-strain relations of classical shell theory (Love, 1927; Novozilov, 1962; Koiter, 1960; Sanders, 1959)

$$N=2\ \mu h(1+\sigma)\gamma,\ M=-\frac{\mu h^3}{6}(1+\sigma)\rho,$$

where γ and ρ are measures of extension and change in curvature,

$$\gamma=\frac{1}{R}\left(u+\frac{dv}{d\theta}\right),\ \rho=\frac{1}{R^2}\left(\frac{d^2u}{d\theta^2}-\frac{dv}{d\theta}\right),$$

and μ is the shear modulus, $\sigma = \nu/(1-\nu)$.

To find displacements, one has to solve the system of ordinary differential equations with respect to functions $u(\theta)$ and $v(\theta)$

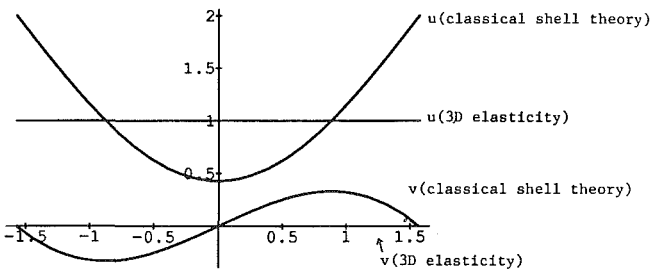


Fig. 3 Dependence of the displacement component u, v, divided by $Eh/PR^2(1-\nu^2)$, on the angle θ

$$\gamma=\frac{1}{R}\left(u+\frac{dv}{d\theta}\right)=\frac{N}{2\mu h(1+\sigma)}=\frac{PR}{2\mu h(1+\sigma)}$$
$$=\frac{Pr}{Eh}(1-\nu^2)=\text{const.}$$
$$\rho=\frac{1}{R^2}\left(\frac{d^2u}{d\theta^2}-\frac{dv}{d\theta}\right)=-\frac{6M}{\mu h^3(1+\sigma)}=\frac{P}{2\mu h(1+\sigma)}$$
$$=\frac{PR}{Eh}(1-\nu^2)=\text{const.} \tag{9}$$

with conditions

$$v=0 \text{ at } \theta=-\frac{\pi}{2},\ 0,\ \frac{\pi}{2}. \tag{10}$$

The only solution of (9), (10) is

$$u=-\frac{PR^2}{Eh}(1-\nu^2)\left(\frac{\pi}{2}\cos\theta-2\right)$$
$$v=\frac{Pr^2}{Eh}(1-\nu^2)\left(\frac{\pi}{2}\sin\theta-\theta\right). \tag{11}$$

It has differed drastically from the exact solution (4). The graphs of (11) and (4) are shown on Fig. 3. The maximum error is 100 percent. This example shows that the classical shell theory could give incorrect values of displacements, and the problems of predicting the correct displacement field deserves to be investigated.

2 Mechanism of Accuracy Loss

Here we explain the mechanism of the effect of accuracy loss following the monograph by V. L. Berdichevsky (1983).

Denote, by $\gamma_{\alpha\beta}$ and $\rho_{\alpha\beta}$, measures of extension and curvature changes, Greek indices running values 1, 2, and corresponding projections on the middle surface of shell Ω. (We use Koiter's notation (Koiter, 1960).) Let ϵ_γ and ϵ_ρ be amplitudes of $\gamma_{\alpha\beta}$ and $\rho_{\alpha\beta}$

$$\epsilon_\gamma=\max_\Omega(\gamma_{\alpha\beta}\gamma^{\alpha\beta})^{1/2}\qquad \epsilon_\rho=h\max_\Omega(\rho_{\alpha\beta}\rho^{\alpha\beta})^{1/2}.$$

Summation over repeated sub and super indices is implied.

The extensional strains in the shell body are given in the first approximation by the relation

$$\epsilon_{\alpha\beta}=\gamma_{\alpha\beta}+h\zeta\rho_{\alpha\beta}, \tag{12}$$

where ζ is the dimensionless coordinate in the normal direction ($\zeta = \xi/h$).

Classical theory allows one to calculate correct values of stresses in the first approximation, and, therefore, also strains $\epsilon_{\alpha\beta}$. However, this does not mean that each term on the right-hand side of (12) is determined correctly. Three cases are possible:

(1) The extension amplitude is of the same order as the bending amplitude

$$\epsilon_\gamma\sim\epsilon_\rho \tag{13}$$

Downloaded 03 May 2010 to 171.66.16.247. Redistribution subject to ASME license or copyright; see http://www.asme.org/terms/Terms_Use.cfm

(2) the extension amplitude is much greater than the bending amplitude

$$\epsilon_\gamma >> \epsilon_\rho, \text{ and} \tag{14}$$

(3) the opposite case is

$$\epsilon_\gamma << \epsilon_\rho. \tag{15}$$

If $\epsilon_\gamma \sim \epsilon_\rho$, classical theory predicts correct values for both $\gamma_{\alpha\beta}$ and $\rho_{\alpha\beta}$: On the right-hand side of (12) the two terms are independent (the first one does not depend on ζ, and the second one is linear in ζ) and of the same order. Therefore, the knowledge of $\epsilon_{\alpha\beta}$, guaranteed by classical theory, simultaneously implies knowledge of $\gamma_{\alpha\beta}$ and $\rho_{\alpha\beta}$. Hence, one knows the first and the second fundamental forms of the deformed middle surface, and displacements are determined up to rigid motion.

Quite a different situation appears in the second case (14). The second term on the right-hand side of (12) becomes a small correcting term. Classical theory guarantees only correct calculation of the leading terms, and the bending measure $\rho_{\alpha\beta}$, found from classical theory, could be wrong. Therefore, the displacement field could also be wrong. In fact, the example considered above pertains to this case: From (9) we see that,

$$\gamma = \frac{PR}{2\mu h(1+\sigma)} = \frac{R}{h}\, h\rho; \text{ i.e., } \epsilon_\gamma \sim \frac{R}{h}\, \epsilon_\rho >> \epsilon_\rho.$$

To obtain the correct displacement field one needs to construct a shell theory which guarantees correct calculation of all terms of order h/R in comparison with 1, i.e., the next approximation of the shell theory.

The analogous situation takes place in case (15): By the same reasoning, the bending measure $\rho_{\alpha\beta}$ is determined correctly, but the extension measure $\gamma_{\alpha\beta}$ can be incorrect. Nevertheless, the displacement field could be considered as asymptotically correct. In fact, suppose that we know $\gamma_{\alpha\beta}$ and $\rho_{\alpha\beta}$; the displacement field is then uniquely determined for given $\gamma_{\alpha\beta}$ and $\rho_{\alpha\beta}$ due to boundary conditions. Because of linearity, the displacement field could be regarded as the sum of displacement field $u_{(\gamma)}$, resulting from extensions $\gamma_{\alpha\beta}$ with zero bending, and displacement field $u_{(\rho)}$, resulting from bending $\rho_{\alpha\beta}$ with zero extensions:

$$u = u_{(\gamma)} + u_{(\rho)}$$

The orders of these displacement fields follow from the expressions for extension and bending measures in terms of displacements. For cylindrical shells, these orders are found from (9). For the general case, the displacement orders are obtained from (24), (25):

$$u_{(\gamma)} \sim \epsilon_\gamma l,\ u_{(\rho)} \sim \epsilon_\rho \frac{l^2}{h} \tag{16}$$

where l is the characteristic of the shell size. From (15) and (16) we have

$$u_{(\rho)} \sim \epsilon_\rho \frac{l^2}{h} >> \epsilon_\gamma \frac{l^2}{h} \sim u_{(\gamma)} \frac{l}{h}. \tag{17}$$

Because $l >> h$, we see from (17) that displacement field $u_{(\gamma)}$ is a correction of order h/l in comparison with 1, which can be neglected in classical theory. So, one can expect the accuracy loss only in case (14).

The condition (14) is necessary, but not sufficient for accuracy loss. There is one more essential constraint—existence of infinitesimally small bending. In fact, if the boundary conditions preclude infinitesimally small bending, i.e., the equations $\gamma_{\alpha\beta} = 0$, considered as equations for displacements have only zero solution, then the known values of $\gamma_{\alpha\beta}$ determine the unique displacement field, and therefore the unique values of $\rho_{\alpha\beta}$: bending measures $\rho_{\alpha\beta}$ are not kinematically independent of $\gamma_{\alpha\beta}$. In the example of a cylindrical shell considered above there are a lot of infinitesimal bendings, and the measures γ and ρ are kinematically independent.

To get correct values of the bending measure one has to use improved shell theories, taking into account corrections of order h/R. To explain how improved theory works, consider the energy density of elastic shell in symbolic form

$$\frac{1}{h}\,\Phi = A \bullet \gamma \bullet \gamma + B \bullet h\rho \bullet h\rho + \frac{h}{R}\, C \bullet \gamma \bullet h\rho. \tag{18}$$

The first term in the right-hand side of (18) is the extension energy, the second term is the bending energy, and the last one describes the interaction between bending and extension. The coefficients A, B, C are of the order of the shear modulus. The interaction energy is of the order h/R in comparison with extension and bending energies, and correct calculation of this energy is the essence of improved shell theories.

Let the shell be subject to infinitesimally small bending. Then γ and ρ are independent. To find ρ, one can fix γ and minimize energy with respect to additional degrees of freedom, contained in ρ. To do this, one has to keep, in the energy, all terms of the order of the bending energy. But for $h\rho \sim h/R\ \gamma$, as it is in the above example, the interaction energy is of the order of the bending energy

$$\frac{h}{R}\, C \bullet \gamma \bullet h\rho \sim C \bullet h\rho \bullet h\rho \sim B \bullet h\rho \bullet h\rho.$$

Therefore, to find the displacement field one needs to consider improved shell theories.

Displacement errors of classical shell theory were estimated by W. T. Koiter (1970) and J. G. Simmonds (1971). The Koiter estimation has the form

$$\|u - u^*\| \leqq g\epsilon^2 (\rho\omega^2)^{-1} P_2[u^*] \tag{19}$$

where $\|\bullet\|$ is the L_2-norm, $\epsilon < 1$, ρ-density (assumed constant), ω is the lowest natural frequency of a shell, and P_2 is the elastic energy. Since the extensional energy is large, and infinitesimal bending results in low frequency $\omega = 0(h)$, the right side of (19) is not small, and (19) is not in conflict with our considerations. The same pertains to the Simmonds estimate.

To the best of our knowledge, the first time the influence of correcting terms on displacement was mentioned by V. M. Darevskii (1961), who observed two different displacement fields for different correcting terms for deformation of a cylindrical shell. The difference was about 3 percent, but does not go to zero when h/R tends to zero. Berdichevsky and Misyura (1980) showed independently (the paper by Darevskii became known to the authors later), that there is a class of problems which require the retention of all terms of the order h/R compared to unity to find the correct displacement field. Later, Misyura (1982, 1985) constructed examples with 30 percent error of classical theory. Misyura (1985) proved that the refined shell theory, offered by Berdichevsky (1979), allows for the finding of the correct displacement field. Description of the mechanism of accuracy loss was completed by Berdichevsky (1983).

Examples constructed by Misyura (1982, 1985) are based on a comparison of displacement fields obtained by means of different two-dimensional shell theories. Here we provide some exact solutions of three-dimensional elasticity and compare them with the corresponding solutions of various two-dimensional shell theories. These test problems give us the opportunity to check the asymptotical accuracy of two-dimensional shell equations. For the convenience of the following references, we start from the list of some two-dimensional shell theories. This list might have independent interest, because we write out, in common notations, the relations offered by various authors.

3 Two-Dimensional Shell Theories

Equilibrium equations. Let x_i be cartesian coordinates in a three-dimensional space, $x_i = r_i\ (\xi^\alpha)$ are parametric equa-

Downloaded 03 May 2010 to 171.66.16.247. Redistribution subject to ASME license or copyright; see http://www.asme.org/terms/Terms_Use.cfm

tions of the middle surface, and ξ^α are some curvilinear coordinates on the middle surface. The stress resultants $T^{\alpha\beta}$ and stress couples $M^{\alpha\beta}$ are introduced by relations

$$T^{\alpha\beta} = \int_{-h/2}^{h/2} \tau^{\alpha\beta} d\xi,\ M^{\alpha\beta} = \int_{-h/2}^{h/2} \tau^{\alpha\beta} \xi d\xi \tag{20}$$

where ξ is the coordinate along a normal fiber in the undeformed state; $|\xi|$ is equal to the distance between the point of the fiber with coordinate ξ and the middle surface. $\tau^{\alpha\beta}$ are contravariant components of a nonsymmetric tensor

$$\tau^{\alpha\beta} = (1 - 2H\xi + K\xi^2)\,(\delta^\alpha_\gamma - \xi b^\alpha_\gamma) p^{\alpha\gamma}. \tag{21}$$

Here, $p^{\alpha\gamma}$ are the contravariant components of symmetric stress tensor in the curvilinear coordinate system (ξ^α, ξ); $b_{\alpha\beta}$ represents the second fundamental form of the middle surface; $H = 1/2\ b^\alpha_\alpha$, $K = \det \|b_{\alpha\beta}\| / \det \|a_{\alpha\beta}\|$; $\det \|b_{\alpha\beta}\|$ is the determinant of the matrix with components $b_{\alpha\beta}$; $a_{\alpha\beta}$ are the covariant components of the metric tensor of the middle surface; and δ^α_β is the Kroneker delta.

The tensors $T^{\alpha\beta}$ and $M^{\alpha\beta}$ are asymmetric. However, the antisymmetric part of the stress couple tensor $M^{\alpha\beta}$ is not essential in the sense that the equilibrium equations do not contain an antisymmetric part of $M^{\alpha\beta}$. Denote, by $M^{(\alpha\beta)}$, the symmetric part of $M^{\alpha\beta}$

$$M^{(\alpha\beta)} = \frac{1}{2}\,(M^{\alpha\beta} + M^{\beta\alpha}).$$

Then, equilibrium equations take the form

$$T^{\alpha\beta}{}_{;\beta} - b^\alpha_\lambda M^{(\lambda\beta)}{}_{;\beta} + \{P^\alpha\} = [P^\beta]\,\frac{h}{2}\,(b^\alpha_\beta + 2H\delta^\alpha_\beta)$$

$$M^{(\alpha\beta)}{}_{;\alpha\beta} + b_{\alpha\beta} T^{\alpha\beta} + \{P\} - \frac{h}{2}\,[P^\alpha]_{;\alpha} = hH[P]. \tag{22}$$

Here, the semi-colon denotes covariant differentiation along the middle surface Ω, $P_\alpha = P_i r^i_\alpha$, $P = P_i n^i$, P_i are components of external surface force, $r^i_\alpha = \partial r^i / \partial \xi^\alpha$ are components of tangent vectors to Ω, n^i are components of normal vector to Ω, and $\{\cdot\}$ and $[\cdot]$ denote the following operations: $\{A\} = A|_{\xi = h/2} + A|_{\xi = -h/2}$, $[A] = A|_{\xi = h/2} - A|_{\xi = -h/2}$. For example, $\{P\} = P|_{\xi = h/2} + P|_{\xi = -h/2}$; i.e., $\{P\}$ is the sum of normal forces acting on both faces of shell.

It is important to emphasize that Eqs. (22) are exact and do not contain simplifications (except the assumption on linearity).

The antisymmetric part of the stress couples $M^{[\alpha\beta]} = 1/2(M^{\alpha\beta} - M^{\beta\alpha})$ could be found, approximately, from the symmetry condition for the stress tensor. In the first approximation, from (20) and (21), one has

$$\left(M^{[\alpha\beta]} + \frac{h^2}{12}\, b^\alpha_\lambda T^{\lambda\beta}\right) e_{\alpha\beta} = 0. \tag{23}$$

Here, $e_{\alpha\beta}$ is the two-dimensional Levi-Cevita tensor (in local Cartesian coordinates $e_{12} = 1$, $e_{21} = -1$, $e_{11} = e_{22} = 0$).

Deformation Measures. Denote, by u_α and u, the projections of displacements of the middle surface u_i on tangent directions and normal: $u_\alpha = r^i_\alpha u_i$, $u = n^i u_i$. The extension measure is defined by the relation

$$\gamma_{\alpha\beta} = \frac{1}{2}\,(u_{\alpha;\beta} + u_{\beta;\alpha}) - u b_{\alpha\beta}. \tag{24}$$

Bending measures can be defined in different ways. For instance, the curvature changes $B_{\alpha\beta}$ are given by formulas

$$B_{\alpha\beta} = (u_{,\alpha} + b^\lambda_\alpha u_\lambda)_{;\beta} + b^\lambda_\alpha (u_{\lambda;\beta} - b_{\lambda\beta} u). \tag{25}$$

One can also use other measures such as (Koiter, 1960; Sanders, 1959)

$$\rho_{\alpha\beta} = B_{\alpha\beta} - \frac{1}{2}\,(b^\lambda_\alpha\, \gamma_{\lambda\beta} + b^\lambda_\beta \gamma_{\lambda\alpha})$$

or (Berdichevsky, 1982)

$$\kappa_{\alpha\beta} = -\rho_{\alpha\beta} - \frac{1}{2}\, H d_{\alpha\beta} d^{\mu\nu} \gamma_{\mu\nu}$$

where

$$d_{\alpha\beta} = \tilde{b}_{\alpha\beta} \Big/ \sqrt{\frac{1}{2}\,\tilde{b}_{\mu\nu}\tilde{b}^{\mu\nu}},\ \tilde{b}_{\alpha\beta} = \frac{1}{2}\,(e_{\alpha\mu} b^\mu_\beta + e_{\beta\mu} b^\mu_\alpha).$$

In the coordinate system that is directed along curvature lines, components of measure $\kappa_{\alpha\beta}$ are linked with other measures by relations:

$$\kappa_{11} = -\rho_{11},\ \kappa_{22} = -\rho_{22},\ \kappa_{12} = -B_{12}.$$

Classical Shell Theory. To complement the equilibrium equations one has to relate the stress resultants $T^{\alpha\beta}$ and stress couples $M^{(\alpha\beta)}$ with measures of extension and bending. These deformation measures are symmetric tensors, therefore one also needs to have symmetric measures of stresses. It is remarkable that there exists the symmetric object

$$N^{\alpha\beta} = T^{\alpha\beta} + \frac{1}{2}\,(b^\alpha_\sigma M^{\beta\sigma} - b^\beta_\sigma M^{\alpha\sigma}). \tag{26}$$

Symmetry of $N^{\alpha\beta}$ can be derived from symmetry of the stress tensor $p^{\alpha\beta}$ and (20), (21). To express $T^{\alpha\beta}$ in terms of symmetric stress measures $N^{\alpha\beta}$ and $M^{(\alpha\beta)}$, one can use Eq. (23): This equation shows that the antisymmetric part of stress couples $M^{[\alpha\beta]}$ is of order $h^2/R\,T$ where T is the order of stress resultants. Hence, the change of $M^{\alpha\beta}$ in (26) by $M^{(\alpha\beta)}$ introduces the error of order h^2/R^2 in comparison with 1—and in the framework of the accuracy level, either classical shell theory or refined shell theory, incorporating corrections of order h/R, one can write

$$T^{\alpha\beta} = N^{\alpha\beta} - \frac{1}{2}\,(b^\alpha_\sigma M^{(\beta\sigma)} - b^\beta_\sigma M^{(\alpha\sigma)}). \tag{27}$$

The stress-strain relations in a linear shell theory are relations between the stress measures $N^{\alpha\beta}$, $M^{(\alpha\beta)}$ and the deformation measures $\gamma_{\alpha\beta}$, $\rho_{\alpha\beta}$ (or $\gamma_{\alpha\beta}$, $B_{\alpha\beta}$ or $\gamma_{\alpha\beta}$, $\kappa_{\alpha\beta}$).

In the classical theory of isotropic shells these relations, for various representations of the theory, are as follows.

Love's theory (simplified version)

$$N^{\alpha\beta} = 2\mu h\,(\gamma^{\alpha\beta} + \sigma a^{\alpha\beta}\gamma^\lambda_\lambda),$$

$$M^{(\alpha\beta)} = \frac{\mu h^3}{6}\,(\kappa^{\alpha\beta} + \sigma a^{\alpha\beta}\kappa^\lambda_\lambda) \tag{28}$$

(μ is the shear modulus μ, $\sigma = \nu/(1 - \nu)$, ν is Poisson's ratio).

The Novozilov-Balabuch theory:

$$N^{\alpha\beta} = 2\mu h\,(\gamma^{\alpha\beta} + \sigma a^{\alpha\beta}\gamma^\lambda_\lambda) - \frac{\mu h^3}{12}\, H d^{\alpha\beta} d_{\mu\nu} \kappa^{\mu\nu}$$

$$M^{(\alpha\beta)} = \frac{\mu h^3}{6}\,(\kappa^{\alpha\beta} + \sigma a^{\alpha\beta}\kappa^\lambda_\lambda). \tag{29}$$

The Koiter-Sanders theory:

$$N^{\alpha\beta} = 2\mu h\,(\gamma^{\alpha\beta} + \sigma a^{\alpha\beta}\gamma^\lambda_\lambda),$$

$$M^{(\alpha\beta)} = -\frac{\mu h^3}{6}\,(\rho^{\alpha\beta} + \sigma a^{\alpha\beta}\rho^\lambda_\lambda). \tag{30}$$

Refined Shell Theories. Two-dimensional shell theories of the next accuracy level take into account the extention-bending interaction effect: appearance of bending moments under extention and, reciprocally, extension forces under bending. Many different equations have been suggested to describe this effect. The first approach was contained, in fact, in Love's paper of 1888. From the subsequent results, we mention here the theories suggested by Flugge (1932), Lurie (1940), Vlasov (1950), Goldenweizer (1976), Berdichevsky (1979), and Zhilin

Downloaded 03 May 2010 to 171.66.16.247. Redistribution subject to ASME license or copyright; see http://www.asme.org/terms/Terms_Use.cfm

(Zhilin and Skvortzov, 1983). In this section we write out the equations by Love, Lurie, Goldenweizer, Berdichevsky and Zhilin; equations by Flugge and Vlasov will be written out in the next section for cylindrical shells.

Love's theory (main version (Love, 1926)):

$$N^{\alpha\beta} = 2\mu h(\gamma^{\alpha\beta} + \sigma a^{\alpha\beta}\gamma^{\lambda}_{\lambda})$$

$$M^{(\alpha\beta)} = -\frac{\mu h^3}{6}(\rho^{\alpha\beta} + \sigma a^{\alpha\beta}\rho^{\lambda}_{\lambda}) - \frac{\mu h^3}{12}(\bar{b}^{\alpha}_{\lambda}\bar{\gamma}^{\lambda\beta} + \bar{b}^{\beta}_{\lambda}\bar{\gamma}^{\lambda\alpha} + Hd^{\alpha\beta}d_{\mu\nu}\bar{\gamma}^{\mu\nu}). \quad (31)$$

Here,

$$\bar{b}^{\alpha}_{\lambda} = b^{\alpha}_{\lambda} - 2H\delta^{\alpha}_{\lambda},\ \bar{\gamma}_{\alpha\beta} = \gamma_{\alpha\beta} + \sigma a_{\alpha\beta}\gamma^{\lambda}_{\lambda}.$$

Refined Love's theory (Love, 1926):

$$N^{\alpha\beta} = 2\mu h(\gamma^{\alpha\beta} + \sigma a^{\alpha\beta}\gamma^{\lambda}_{\lambda}) - \frac{\mu h^3}{3}\left[\frac{1}{2}(b'^{\beta}_{\lambda}\rho^{\lambda\alpha} + b'^{\alpha}_{\lambda}\rho^{\lambda\beta}) + \sigma a^{\alpha\beta}\left(b^{\mu\nu}\rho_{\mu\nu} + \left(\frac{3}{2}\sigma - 1\right)H\rho^{\mu}_{\mu}\right) + \frac{3}{4}\sigma b^{\alpha\beta}\rho^{\mu}_{\mu}\right]$$

$$M^{(\alpha\beta)} = -\frac{\mu h^3}{6}(\rho^{\alpha\beta} + \sigma a^{\alpha\beta}\rho^{\lambda}_{\lambda}) - \frac{\mu h^3}{12}(\bar{b}^{\alpha}_{\lambda}\bar{\gamma}^{\lambda\beta} + \bar{b}^{\beta}_{\lambda}\bar{\gamma}^{\lambda\alpha} + Hd^{\alpha\beta}d_{\mu\nu}\bar{\gamma}^{\mu\nu}). \quad (32)$$

Here, $b'_{\alpha\beta} = b_{\alpha\beta} - Ha_{\alpha\beta}$.

Lurie's theory (Lurie, 1940):

$$N^{\alpha\beta} = 2\mu h(\gamma^{\alpha\beta} + \sigma a^{\alpha\beta}\gamma^{\lambda}_{\lambda}) - \frac{\mu h^3}{6}[b'^{\alpha}_{\lambda}\bar{\rho}^{\lambda\beta} + b'^{\beta}_{\lambda}\bar{\rho}^{\lambda\alpha} + \sigma a^{\alpha\beta}(b^{\mu\nu}\bar{\rho}_{\mu\nu} - 2H\bar{\rho}^{\nu}_{\nu}) + \sigma b^{\alpha\beta}\bar{\rho}^{\mu}_{\mu}]$$

$$M^{(\alpha\beta)} = -\frac{\mu h^3}{6}(\rho^{\alpha\beta} + \sigma a^{\alpha\beta}\rho^{\lambda}_{\lambda}) + \frac{\mu h^3}{6}[b'^{\alpha}_{\lambda}\gamma^{\lambda\beta} + b'^{\beta}_{\lambda}\gamma^{\lambda\alpha} + \sigma a^{\alpha\beta}(b^{\mu\nu}\gamma_{\mu\nu} - 2H\gamma^{\nu}_{\nu}) + \sigma b^{\alpha\beta}\gamma^{\nu}_{\nu}]. \quad (33)$$

Here, $\bar{\rho}^{\alpha\beta} = B^{\alpha\beta} - 2\,b^{\alpha}_{\lambda}\,\gamma^{\lambda\beta}$.

Goldenweizer's iterational theory (Goldenweizer, 1976, equations (27.13.10))

$$N^{\alpha\beta} = 2\mu h(\gamma^{\alpha\beta} + \sigma a^{\alpha\beta}\gamma^{\lambda}_{\lambda}) - \frac{\mu h^3}{6}\left[b'^{\alpha}_{\lambda}\rho^{\lambda\beta} + b'^{\beta}_{\lambda}\rho^{\lambda\alpha} + 2\sigma a^{\alpha\beta}\left(b^{\mu\nu}\rho_{\mu\nu} + \left(\frac{3}{2}\sigma - 1\right)H\rho^{\mu}_{\mu}\right) + \frac{3}{2}\sigma b^{\alpha\beta}\rho^{\lambda}_{\lambda}\right] + \frac{1}{2}\sigma h[P]a^{\alpha\beta}$$

$$M^{(\alpha\beta)} = -\frac{\mu h^3}{6}(\rho^{\alpha\beta} + \sigma a^{\alpha\beta}\rho^{\lambda}_{\lambda}) + \frac{\mu h^3}{6}\left[b'^{\alpha}_{\lambda}\gamma^{\lambda\beta} + b'^{\beta}_{\lambda}\gamma^{\lambda\alpha} + 2\sigma a^{\alpha\beta}\left(\frac{1}{2}b^{\mu\nu}\gamma_{\mu\nu} + (\sigma - 1)H\gamma^{\lambda}_{\lambda}\right) + 2\sigma b^{\alpha\beta}\gamma^{\lambda}_{\lambda}\right] - \frac{\sigma h^2}{12}\{P\}a^{\alpha\beta}. \quad (34)$$

Goldenweizer's simplified theory (Goldenweizer, 1976):

$$N^{\alpha\beta} = 2\mu h(\gamma^{\alpha\beta} + \sigma a^{\alpha\beta}\gamma^{\lambda}_{\lambda}) + \frac{\sigma h}{2}a^{\alpha\beta}[P]$$

$$M^{(\alpha\beta)} = -\frac{\mu h^3}{6}(\rho^{\alpha\beta} + \sigma a^{\alpha\beta}\rho^{\lambda}_{\lambda}) + \frac{\mu h^3}{6}\left[b'^{\alpha}_{\lambda}\gamma^{\lambda\beta} + b'^{\beta}_{\lambda}\gamma^{\lambda\alpha} + 2\sigma a^{\alpha\beta}\left(\frac{1}{2}b^{\mu\nu}\gamma_{\mu\nu} + (\sigma - 1)H\gamma^{\lambda}_{\lambda}\right) + 2\sigma b^{\alpha\beta}\gamma^{\lambda}_{\lambda}\right] - \frac{\sigma h^2}{12}\{P\}a^{\alpha\beta}. \quad (35)$$

Theory incorporating geometrical corrections (Berdichevsky, 1979):

$$N^{\alpha\beta} = 2\mu h(\gamma^{\alpha\beta} + \sigma a^{\alpha\beta}\gamma^{\lambda}_{\lambda}) - \frac{\mu h^3}{6}\left[b'^{\alpha}_{\lambda}\rho^{\lambda\beta} + b'^{\beta}_{\lambda}\rho^{\lambda\alpha} + 2\sigma a^{\alpha\beta}\left(b^{\mu\nu}\rho_{\mu\nu} + \left(\frac{6}{5}\sigma - 1\right)H\rho^{\lambda}_{\lambda}\right) + \frac{6}{5}\sigma b^{\alpha\beta}\rho^{\lambda}_{\lambda}\right] + \frac{1}{2}\sigma h\, a^{\alpha\beta}[P]$$

$$M^{(\alpha\beta)} = -\frac{\mu h^3}{6}(\rho^{\alpha\beta} + \sigma a^{\alpha\beta}\rho^{\lambda}_{\lambda}) + \frac{\mu h^3}{6}\left[b'^{\alpha}_{\lambda}\gamma^{\lambda\beta} + b'^{\beta}_{\lambda}\gamma^{\lambda\alpha} + 2\sigma a^{\alpha\beta}\left(\frac{3}{5}b^{\mu\nu}\gamma_{\mu\nu} + \left(\frac{6}{5}\sigma - 1\right)H\gamma^{\lambda}_{\lambda}\right) + 2\sigma b^{\alpha\beta}\gamma^{\lambda}_{\lambda}\right] - \frac{\sigma h^2}{10}\{P\}a^{\alpha\beta}. \quad (36)$$

Zhilin's theory (Zhilin and Skvortzov, 1983):

$$N^{\alpha\beta} = 2\mu h(\gamma^{\alpha\beta} + \sigma a^{\alpha\beta}\gamma^{\lambda}_{\lambda}) - \frac{\mu h^3}{6}[b'^{\alpha}_{\lambda}\rho^{\lambda\beta} + b'^{\beta}_{\lambda}\rho^{\lambda\alpha} + 2\sigma a^{\alpha\beta}(b^{\mu\nu}\rho_{\mu\nu} + (\sigma - 1)H\rho^{\lambda}_{\lambda}) + \sigma b^{\alpha\beta}\rho^{\lambda}_{\lambda}] + \frac{\sigma h}{2}[P]a^{\alpha\beta}$$

$$M^{\alpha\beta} = -\frac{\mu h^3}{6}(\rho^{\alpha\beta} + \sigma a^{\alpha\beta}\rho^{\lambda}_{\lambda}) + \frac{\mu h^3}{6}[b'^{\alpha}_{\lambda}\gamma^{\lambda\beta} + b'^{\beta}_{\lambda}\gamma^{\lambda\alpha} + \sigma a^{\alpha\beta}(b^{\mu\nu}\gamma_{\mu\nu} + 2(\sigma - 1)H\gamma^{\lambda}_{\lambda}) + 2\sigma b^{\alpha\beta}\gamma^{\lambda}_{\lambda}] + \frac{\sigma h^2}{12}\{P\}a^{\alpha\beta}. \quad (37)$$

Comments:

1 The main version of Love's theory (31) was obtained from the Kirchhoff-Love hypothesis. The simplified Love's theory (28) follows from (31) after neglecting the small terms.

2 Lurie's theory was also derived from the Kirchhoff-Love hypothesis, keeping all terms of the order h/R in comparison with 1. As was mentioned by A. I. Lurie, this theory is not self-consistent because h/R is the error of the Kirchhoff-Love's hypothesis.

3 The appearance and structure of Eqs. (34) and (36) are different. For instance, the coefficient near the term $h^2\{P\}$ is equat to $\sigma/12$ in (34), while in (36), it is equal $\sigma/10$. However, these equations are asymptotically equivalent; i.e., the differences between solutions should be negligibly small (Berdichevsky, 1983).

4 Originally, the equations of Goldenweizer's iterational theory were written in the terms of measures $\gamma_{\alpha\beta}$ and $\kappa_{\alpha\beta}$. After neglecting correcting terms, they are reduced to Love's equations (28). Equations of the theory, incorporating geometrical correction (36) become, after neglecting correcting terms, the Koiter-Sanders Eq. (30).

5 Displacements have the sense of displacements of the middle surface in all equations except (36). In (36), only the tangent components of displacements have this sense, while the normal component u is related to the normal component of the middle surface (denoted for the moment by $u_{(m)}$) by

$$u = u_{(m)} + \frac{\sigma h^2}{40}\rho^{\lambda}_{\lambda}. \quad (38)$$

Although this difference is not essential for calculation of displacements, it does affect the stress-strain relations.

The displacement (38) has the sense of the normal displacement of a shell body, averaged along the norm with the weight $\xi^2 - h^2/12$.

6 Using the displacement u (38) instead of $u_{(m)}$ has the following advantage: Equations (36) are variationally consistent in contrast to (34).

Downloaded 03 May 2010 to 171.66.16.247. Redistribution subject to ASME license or copyright; see http://www.asme.org/terms/Terms_Use.cfm

7 Equations (28), (31), (32), (34), and (35) are not variationally consistent, while Eqs. (29), (30), (33), (36), and (37) are.
8 Zhilin's Eqs. (37) could be considered as a modification of Goldenweizer's simplified theory, and they are variationally consistent.
9 The refined Love's theory (32) was derived for pure bending states and differs from Goldenweizer's iterational theory (34) for bending deformations by the term $1/2\ \sigma h a^{\alpha\beta}[P]$, because for $\epsilon_\gamma \sim h\epsilon_\rho/R$, correcting terms in the equations for $M^{\alpha\beta}$ have the order $(h/R)^2$ in comparison with 1.

4 Test Problem

Consider the test problem, discussed in Section 1, in the framework of refined shell theories. Let axis 1 and axis 2 be directed along the shell axis and angle axis. Correspondingly, we use notations: $N_{22} \equiv N$, $M_{22} \equiv M$, $\gamma_{22} \equiv \gamma$, $\rho_{22} \equiv \rho$.

For a cylindrical shell, the stress-strain relations take the form:

Lurie's theory, Flugge's theory, Vlasov's theory:

$$N = 2\mu h(1+\sigma)\gamma + \frac{\mu h^3}{6R}(1+\sigma)\left(\rho + \frac{\gamma}{R}\right)$$

$$M = -\frac{\mu h^3}{6}(1+\sigma)\left(\rho + \frac{\gamma}{R}\right).$$

Goldenweizer's iterational theory:

$$N = 2\mu h(1+\sigma)\gamma + \frac{\mu h^3}{6R}\left(1+\frac{3}{2}\sigma\right)\rho + \frac{\sigma h}{2}P$$

$$M = -\frac{\mu h^3}{6}(1+\sigma)\rho - \frac{\mu h^3}{6R}(1+\sigma)^2\gamma + \frac{\sigma h^2}{12}P.$$

Goldenweizer's simplified theory:

$$N = 2\mu h(1+\sigma)\gamma + \frac{\sigma h}{2}P$$

$$M = -\frac{\mu h^3}{6}(1+\sigma)\rho - \frac{\mu h^3}{6R}(1+\sigma)^2\gamma + \frac{\sigma h^2}{12}P.$$

Theory incorporating geometrical corrections:

$$N = 2\mu h(1+\sigma)\gamma + \frac{\mu h^3}{6R}(1+\sigma)\left(1+\frac{6}{5}\sigma\right)\rho + \frac{\sigma h}{2}P$$

$$M = -\frac{\mu h^3}{6}(1+\sigma)\rho - \frac{\mu h^3}{6R}(1+\sigma)\left(1+\frac{6}{5}\sigma\right)\gamma + \frac{\sigma h^2}{10}P.$$

Zhilin's theory:

$$N = 2\mu h(1+\sigma)\gamma + \frac{\mu h^3}{6R}(1+\sigma)^2\rho + \frac{\sigma h}{2}P$$

$$M = -\frac{\mu h^3}{6}(1+\sigma)\rho - \frac{\mu h^3}{6R}(1+\sigma)^2\gamma + \frac{\sigma h^2}{12}P.$$

We do not consider here the main version of Love's theory, because it coincides with the simplified Love's theory discussed in Sect. 1. Also, the refined Love's theory is omitted because it was derived only for pure bending states. From the written stress-strain relations and values N, M (8), we find the strain measures γ, ρ.

For the theories by Lurie, Flugge, Vlasov, Goldenweizer, Zhilin, and the theory incorporating geometrical corrections, we have

$$\gamma = \frac{PR(1-\nu^2)}{Eh},\ \rho = 0. \tag{39}$$

In the expression for γ, we write out only the leading term and neglect all corrections of order h/R in comparison with 1,—because we use (39) to find the first-order approximation for displacements. Recalling the expressions of γ and ρ in terms of u and v, along with conditions (10), we find

$$u = \frac{PR^2(1-\nu^2)}{Eh},\ v = 0 \tag{40}$$

to be in full agreement with the exact value (4).

One should expect this result for the theory incorporating geometrical corrections, asymptotically self-consistent, as it was proved by Misyura (1985). The same could be expected with respect to Goldenweizer's iterational theory, because it is asymptoticaly equivalent to the theory, incorporating geometrical corrections (Berdichevsky, 1983). Theories by Lurie, Flugge, and Vlasov are not asymptotically self-consistent, and the fact that correct results are predicted by these theories requires an explanation. To give this explanation, let us rewrite the equation for M in the theory incorporating geometrical corrections in the form

$$M = \underline{-\frac{\mu h^3}{6}(1+\sigma)\left(\rho + \frac{\gamma}{R}\right)} - \frac{\mu h^3}{5R}\sigma(1+\sigma)\gamma + \frac{\sigma h^2}{10}P. \tag{41}$$

The underlined terms in (41) are the terms which are in the theories by Lurie, Flugge, and Vlasov. It turns out that for the strain state (39) the terms in (41), which are not underlined, vanish. This is why the theories by Lurie, Flugge, and Vlasov give the correct answer in spite of their asymptotical inconsistency.

Goldenweizer's simplified theory and Zhilin's theory give the correct answer by the following reason. The difference of these theories from the theory, incorporating geometrical corrections, is due to additional terms in the constitutive equation for N. For extensional strain states $\epsilon_\rho \sim h/R\ \epsilon_\gamma$, these additional terms have the order h^2/R^2 and are not essential for the extension-bending interaction effect.

5 Second Test Problem

Let us consider a problem for which the theories by Lurie, Flugge, and Vlasov give the incorrect value of displacement. Consider a cylindrical semi-pipe

$$\left\{R - \frac{h}{2} \leqq r \leqq R + \frac{h}{2},\ -\frac{\pi}{2} \leqq \theta \leqq \frac{\pi}{2},\ 0 \leqq x \leqq L\right\}$$

by loaded homogeneously distributed surface forces on the edges $x = 0$, $x = L$, directed along the pipe axis x. The three-dimensional solution to this problem is elementary (see, for example, Sedov, 1980): The only nonzero components of the stress tensor and strain tensor are:

$$\sigma_{xx} = P = \text{const.},\ \epsilon_{xx} = C = \frac{P}{E} = \frac{P(\lambda+\mu)}{\mu(3\lambda+2\mu)} = \text{const.}$$

$$\epsilon_{rr} = \epsilon_{\theta\theta} = -\nu\frac{P}{E} = \text{const.} \tag{41}$$

All remaining rigid motion is suppressed by conditions (2). Assuming $w_x = cx$, we have

$$w_\theta = 0,\ w_r = -\nu cr. \tag{43}$$

Hence,

$$v = 0,\ u = -\nu cR. \tag{44}$$

Let us solve this problem using the theories of Lurie and Vlasov.

It follows from (20), (21) and the fact that (42) is the exact solution that equilibrium equations and boundary conditions are satisfied for $T_{11} = Ph$; all other components of $T^{\alpha\beta}$ and $M^{\alpha\beta}$ are equal to zero. The two-dimensional equilibrium equations and two-dimensional force boundary conditions are consequences of three-dimensional ones. To find the first approximation of displacement, one has to find the first approximation of deformation measures. It is obvious that for any two-dimensional shell theory, $\gamma_{11} = c$ and $u_1 = cx$ is in

Downloaded 03 May 2010 to 171.66.16.247. Redistribution subject to ASME license or copyright; see http://www.asme.org/terms/Terms_Use.cfm

full agreement with the three-dimensional solution. Now let us find other nonzero components of deformation measures $\gamma = \gamma_{22}$ and $\rho = \rho_{22}$. Denoting $T = T_{22}$, $N = N_{22}$, $M = M_{22}$, we have the following constitutive equations:

Theories by Lurie, Flugge, and Vlasov:

$$T = N = 2\mu h[(1+\sigma)\gamma + \sigma\gamma_{11}] + \frac{\mu h^3}{6R}(1+\sigma)\left(\rho + \frac{\gamma}{R}\right)$$

$$M = -\frac{\mu h^3}{6}(1+\sigma)\left(\rho + \frac{\gamma}{R}\right). \tag{45}$$

Theory incorporating geometrical corrections:

$$N = 2\mu h[(1+\sigma)\gamma + \sigma\gamma_{11}] + \frac{\mu h^3}{6R}(1+\sigma)\left(1 + \frac{6}{5}\sigma\right)\rho$$

$$M = -\frac{\mu h^3}{6}(1+\sigma)\rho - \frac{\mu h^3}{6R}(1+\sigma) \times \left(1 + \frac{6}{5}\sigma\right)\gamma - \frac{\mu h^3}{6R}\sigma\left(1 + \frac{6}{5}\sigma\right)\gamma_{11}. \tag{46}$$

Here we take into account that $\rho_{11} = 0$.

Equating N and M to zero, we obtain algebraical equations for γ, u, and ρ. From (45) we have, in the first approximation,

$$\gamma = -\nu c, \ \rho = \frac{\nu c}{R}. \tag{47}$$

Then, using expressions γ and ρ through displacements (9) and kinematical conditions (10), we obtain

$$u = -\frac{\nu c R \pi}{2}\cos\phi$$

$$v = \nu c R\left(\frac{\pi}{2}\sin\theta - \theta\right). \tag{48}$$

Comparing (48) with the exact result of (44), we see that the theories by Lurie, Flugge, and Vlasov lead to 100 percent errors in the displacement field.

Constitutive equations (46) give

$$\gamma = -\nu c, \ \rho = 0$$

which is in full agreement with the exact result. Theories by Goldenweizer and Zhilin also give the correct answer for this problem.

6 On the Accuracy Loss for Spherical Shells

Here we show that classical theory predicts the displacements of an isotropic spherical shell, even if this shell experiences infinitesimally small bending. Applying the general expression (Berdichevsky, 1979) for the interaction energy Φ_{int} between extension and bending to the case of isotropic spherical shell, we have

$$\Phi_{\text{int}} = \frac{1}{5R}\mu h^3\sigma(1+2\sigma)\gamma_\alpha^\alpha\rho_\beta^\beta. \tag{49}$$

Here, R is the shell radius.

For any spherical shell, the following remarkable identity is true: The first invariant of bending measure ρ_β^β could be expressed in terms of extension measure $\gamma_{\alpha\beta}$:

$$\rho_\beta^\beta = \text{Re}^{\mu\nu}e^{\sigma\alpha}\gamma_{\sigma\mu;\nu\alpha}. \tag{50}$$

The proof is obtained by substituting in (50) the expressions

$$\rho_\beta^\beta = \theta_{;\beta}^\beta, \ \theta^\beta = \text{Re}^{\beta\sigma}e^{\mu\nu}\gamma_{\sigma\mu;\nu} - \text{Re}^{\beta\nu}\omega_{,\nu}$$

$$\omega \equiv e^{\alpha\beta}u_{\alpha;\beta}.$$

In accordance with (49) and (50), the interaction energy does not depend on degrees-of-freedom of infinitesimally small bending. Therefore, the interaction energy can be ignored while displacements are calculated.

We emphasize that these conclusions are true only for isotropic materials. For anisotropic spherical shells the interaction energy contains all components of the bending measure and influences on the displacement field.

Conclusions

We showed that the accuracy level of classical shell theory is not enough to obtain the first approximation of the displacement field in some problems of shell theory. These problems were characterized by three conditions:

(i) The shell is not shallow (otherwise the extension-bending interaction is small).

(ii) The shell extension is strong (in other words, $\epsilon_\gamma \gg \epsilon_\rho$).

(iii) Boundary conditions admit infinitesimally small bending.

The last condition explains why the effect of accuracy loss is rarely encountered in engineering practice.

Acknowledgments

The first author cordially thanks Dr. D. Hodges for fruitful discussions and also Dr. J. G. Simmonds for useful comments on this paper.

References

Berdichevsky, V. L., 1979, "Variational-Asymptotic Method of Construction of Shell Theory," *J. Appl. Math. Mech.*, Vol. 43, pp. 711–736.

Berdichevsky, V. L., and Misyura, V. A., 1980, "On Interaction Effect Between Extension and Bending for Cylindrical Shells," *Proc. 13 All Union Conf. on Plate and Shell Theory*, Erevan, pp. 165–171 (in Russian).

Berdichevsky, V. L., 1982, "Tensor Form of Novozilov-Balabuch Equations," *Mechanics of Solids*, No. 4, pp. 167–170.

Berdichevsky, V. L., 1983, *Variational Principles of Continuum Mechanics*, Nauka, Moscow (in Russian).

Darevskii, V. M., 1961, "On Basic Relations in the Theory of Thin Shells," *J. Appl. Math. Mech. (PMM)*, Vol. 25, No. 3, pp. 768–784.

Flugge, V., 1932, "Die Stabilitat der Kreiszylindershale," *Ing.-Arch.*, Vol. 3, p. 463.

Goldenweizer, A. L., 1976, *Theory of Thin Elastic Shells*, Nauka, Moscow (in Russian).

John, F., 1965, "Estimate for the Derivative of the Stresses in a Thin Shell and Interior Shell Equations," *Comm. Pure and Appl. Math.*, Vol. 18, pp. 235–267.

Koiter, W. T., 1960, "A Consistent First Approximation in the General Theory of Thin Elastic Shells," *Proc. IVTAM, Symp. Theory of Thin Elastic Shells*, W. T. Koiter ed., North-Holland Publ. Co., Amsterdam.

Koiter, W. T., 1970, "Error Estimates for Certain Approximate Solutions of Problems in the Linear Theory of Elasticity," *ZAMP*, Vol. 21, pp. 534–538.

Koiter, W. T., 1971, "On the Mathematical Foundation of Shell Theory," *Proc. Int. Congr. Math.*, Nice, 1970, Paris, Gautheier-Villars, Vol.3, pp. 123–130.

Koiter, W. T., and Simmonds, J. G., 1973, "Foundation of Shell Theory," *Theoretical and Applied Mechanics, Proceedings 13 Int. Congr. Theor. Appl. Mech.*, Moscow, 1972, Springer, Berlin.

Ladeveze, P., 1986, "Justification de la Theorie Lineaire des Coques Elastiques," *J. de Mechanique*, Vol. 15, No. 5, pp. 813–856.

Love, A. E. H., 1927, *Mathematical Theory of Elasticity*, 4th ed., Cambridge University Press, Cambridge, U.K.

Lurie, A. I., 1940, "General Theory of Thin Elastic Shells," *J. Appl. Math. Mech. (PMM)*, Vol. 4, No. 2.

Misyura, V. A., 1982, "Loss of Accuracy of the Classical Theory of Shells," *Soviet Physics-Doklady*, Vol. 264, No. 3, pp. 423–425.

Misyura, V. A., 1985, "Proof of the Accuracy-Loss Effect in Classical Shell Theory," *Soviet Physics-Doklady*, Vol. 285, No. 1, pp. 986–988.

Morgenstern, D., 1959, "Mathematiche Begruudung des Sheibentheorie," *Arch. Rat. Mech. and Analysis*, Vol. 5, No. 1.

Novozilov, V. V., 1962, *Theory of Thin Shells*, Moscow, (in Russian).

Sanders, J. L., 1959, "An Improved First-Approximation Theory of Thin Shells," NASA Report, No. 24.

Sedov, L. I., 1971, *A Course in Continuum Mechanics*, Groningen, Wolters-Noordhoff.

Simmonds, J. G., 1971, "Extension of Koiter's L_2-Error Estimate to Approximate Shell Solutions with No Strain Energy Functional," *ZAMP*, Vol. 22, pp. 339–345.

Vlasov, V. Z., 1950, *General Theory of Thin Elastic Shells and Its Applications*, Nauka, Moscow (in Russian).

Vorovich, I. I., 1975, "Some Results and Problems of Asymptotical Theory of Plates and Shells," *Proc. I. Allunion Meeting on Shell Theory*, Tbilisi, pp. 51–150 (in Russian).

Zhilin, P. A., and Skvortzov, V. R., 1983, "Description of Shell Edge Effect by 3D Elasticity," *Mechanics of Solids*, No. 5, pp. 137–147.

Downloaded 03 May 2010 to 171.66.16.247. Redistribution subject to ASME license or copyright; see http://www.asme.org/terms/Terms_Use.cfm

Warren N. White
Assoc. Professor,
Assoc. Mem. ASME.

Srinivasan Venkatasubramanian
Graduate Student.

Mechanical Engineering Department,
Kansas State University,
Manhattan, KS 66506-5106

P. Michael Lynch
Professor,
Mechanical Engineering Department,
Tulane University,
New Orleans, LA 70118
Mem. ASME.

Chi-Lung D. Huang
Professor,
Mechanical Engineering Department,
Kansas State University,
Manhattan, KS 66506-5106
Mem. ASME.

The Equations of Motion for the Torsional and Bending Vibrations of a Stranded Cable

Equations of motion of a thin, stranded elastic cable with an eccentric, attached mass and subject to aerodynamic loading are derived using Hamilton's principle. Coupling between the translational and rotational degrees of freedom owing to inertia, elasticity, and stranded geometry are considered. By invoking simplifying assumptions, the equations of motion are reduced to those obtained previously by other researchers.

Introduction

A cable in the form of a catenary is found in many engineering structures such as suspension bridges, aerial transmission lines, and underwater anchors for deep sea drilling platforms to name just a few. One underlying similarity among these mechanical structures is that the cable is intended to remain static. Motion of the cable is then of concern since this represents a departure from the intended state in which the structure would be employed. By understanding the cable dynamics, engineers are able to either accommodate the cable motion or seek suitable ways to quench or limit its oscillation.

A significant problem concerning the oscillation of the cable is that of the galloping of aerial transmission lines. Galloping, which is a low-frequency, high-amplitude oscillation, has been a concern for many decades for overhead electric power transmission line designers. Transmission line galloping occurs when ice or freezing precipitation adheres to a power line conductor. Owing to the ice build up, the cross-section of the conductor becomes noncircular. A noncircular profile gives the conductor both aerodynamic lift and drag characteristics. Aerodynamic lift force can give rise to dynamic instability even at low wind speeds. When conditions are suitable for dynamic instability, spectacularly large-amplitude, low-frequency mechanical vibration of the line occurs. Since galloping can cause various kinds of structural damage and power outages, each having its own associated cost and problems, many attempts have been made to stop galloping or at least minimize its amplitude. In order to design a better preventative or damping mechanism, a knowledge of the mechanics of galloping is required.

A history of the means by which cable motion has been described begins with the wave equation which applies to any thin cable of symmetric cross-section in which both the tension and axial strain are constant. Routh (1905) presented the equations of motion of an inelastic chain having symmetric cross-section (cable cross-sectional mass center coincides with the cable center). However, the mass per unit length in the example in Routh's text was sufficient so that the constant tension assumption was invalid. Also, only the in-plane motions were considered in Routh's analysis. The solution of the static inelastic chain equations is the familiar catenary shape. Cheers (1950) used a small perturbation analysis for the cable motion which resulted in wave equation analysis. Equations of motion for an elastic cable of symmetric cross-section were presented by Shea (1955) and by Simpson (1963). The equations of motion, presented by Shea and Simpson, assume an absence of torsional motion. In both of these investigations, motion of

Contributed by the ASME Applied Mechanics Division of THE AMERICAN SOCIETY OF MECHANICAL ENGINEERS for presentation at the Winter Annual Meeting, Atlanta, Ga., Dec. 1-6, 1991.

Discussion on this paper should be addressed to the Technical Editor, Prof. Leon M. Keer, The Technological Institute, Northwestern University, Evanston, IL 60208, and will be accepted until two months after final publication of the paper itself in the JOURNAL OF APPLIED MECHANICS. Manuscript received by the ASME Applied Mechanics Division, Nov. 15, 1990; final revision, Apr. 25, 1991.

Paper No. 91-WA/APM-19.

Copyright © 1992 by ASME
Downloaded 03 May 2010 to 171.66.16.247. Redistribution subject to ASME license or copyright; see http://www.asme.org/terms/Terms_Use.cfm

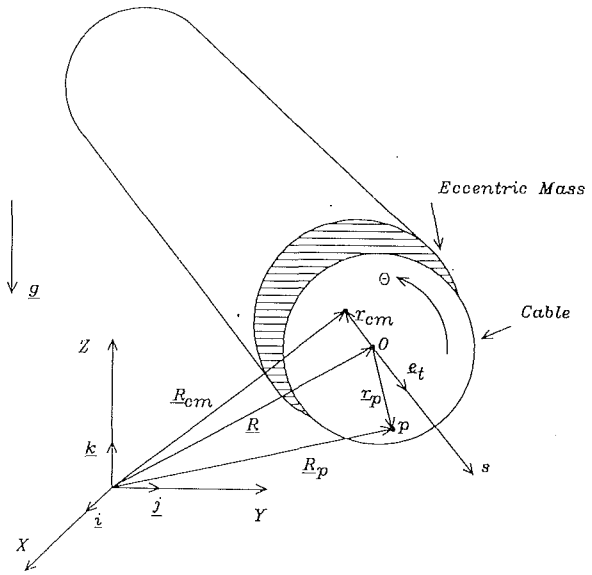


Fig. 1 Conductor geometry

the cable in all three Cartesian coordinates was considered.

In what appears to be the first work regarding the torsional motion of the conductor, Simpson (1972) presented equations of motion for a bundled conductor. These equations of Simpson governed the three Cartesian directions of motion as well as the axial twist. Thompson (1975) also considered the torsional motion of a single conductor with the added assumption that no motion takes place in the cable axial direction.

The bundled conductor work of Simpson (1972) included bending stresses. In most work involving single conductor motion, bending stresses have been excluded from consideration owing to the small cable radius and the large radius of the curvature of the line. An exception to this is Cheers (1950). Since the radius of the conductor bundle is much larger than the radius of a single conductor, bending stresses now become significant. Gawronski (1977) also treated bundled conductors; however, the axis of bending was assumed to pass through both conductors of his two conductor bundle which indicates that the bending stresses would not be greater than that found on a single conductor span. Gawronski was first to consider an axial-torsional coupling which linked the axial tension to the determination of torsional stiffness of the bundle.

In this paper, the equations of motion of a single conductor span having an eccentric mass attached to the cable which provides no additional strength to the line are derived through Hamilton's principle. Validity of the equations will be checked through a virtual work argument. By invoking additional assumptions such as the absence of ice, shallow catenary, and the lack of torsional motion, it is possible to compare the work presented here to the results produced by others. It will be seen that a term will appear in the equations of motion which is new to the galloping mechanics literature. This new term demonstrates that the torsional motion and the Cartesian motion are coupled together even if there is no ice on the line. This new term stems from a constraint upon conductor orientation which reduces the number of degrees-of-freedom for motion of a differential portion of the cable from six to four, namely three Cartesian directions and axial twist.

Mechanical Analysis

The analysis of a galloping line begins with the presentation of the assumptions made in the derivation of the dynamic equations. The equations of motion will be determined by setting the first variation of the Lagrangian of the translating and rotating cable equal to the applied excitations. In order to facilitate the calculation of the kinetic and potential energies

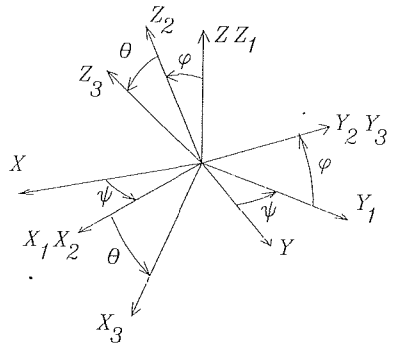


Fig. 2 Euler angle definitions

necessary to construct the Lagrangian, two coordinate systems will be used. These coordinate systems and the transformations between these frames will be presented. While the calculation of the Lagrangian component energies is an application of familiar procedures, determination of the first variation involves considerable effort. At this point of the analysis, detailed steps of the computation of the first variation will be given. The analysis section will then conclude with the dynamic equations.

Assumptions. Governing equations of motion for a galloping cable are derived in accordance with several assumptions. All of these assumptions pertain either to mechanics of conductor motion or the materials and shapes peculiar to galloping cables. These assumptions are as follows:

1 The cable is an elastic string with constant mass per unit length and circular cross-section.

2 The material used in the cable construction is isotropic with constant material properties.

3 Bending stresses in a single conductor span are small owing to the large radius of curvature of the cable.

4 Mass per unit length, cross-sectional area, shape, and angle of deposit of the eccentric mass is constant along the length of the cable.

5 The only source of damping present in the mechanical system comes from wind drag. No damping forces arise from elastic hysteresis or relative conductor strand movement.

6 The eccentric mass provides no additional axial, torsional, or bending stiffness to the cable.

Coordinate Systems. The analysis will make use of two separate coordinate systems. Motion of the conductor center is described with respect to a frame fixed in space. Attached to the conductor center is a local frame which translates and rotates with respect to the fixed or global frame. The local, conductor centered frame is used to describe both the orientation of the conductor cross-section and the angle of twist of the cable. The transformation between the fixed frame and the local frame is described in terms of Euler angles.

Figure 1 illustrates the global coordinate system and a cross-section of the aerial conductor. Vectors $\mathbf{R}$ and $\mathbf{R}_{cm}$ denote the position, with respect to the global frame, of the conductor center and the cross-sectional mass center, respectively. Vector $\mathbf{r}_{cm}$ denotes the mass center with respect to the conductor center, O. Vector $\mathbf{e}_t$ is a unit vector tangent to the cable. Each of the vectors $\mathbf{R}$, $\mathbf{R}_{cm}$, $\mathbf{r}_{cm}$, and $\mathbf{e}_t$ are functions of the scalar parameter s which measures unstressed distance along the conductor. The angle of twist of the cable is the angle θ. The point p is an arbitrary point on the cable cross-section.

The three Euler angles ψ, ϕ, and θ describing the rotational transformation between the global frame and the local frame are illustrated in Fig. 2. The transformation is accomplished by first rotating about the global Z axis by ψ to produce the X_1, Y_1, Z_1 frame. A rotation about the X_1-axis by ϕ produces the frame X_2, Y_2, Z_2. The coordinate frame determined by X_2,

Downloaded 03 May 2010 to 171.66.16.247. Redistribution subject to ASME license or copyright; see http://www.asme.org/terms/Terms_Use.cfm

Y_2, Z_2 is important to the analysis since the X_2-Z_2 plane constitutes the conductor cross-section. The angle θ (which is the final Euler angle) measures conductor twist about the Y_2 axis, and the Y_2 (and Y_3) axis is parallel to the conductor unit tangent vector $\mathbf{e}_t$. Details of the transformations will be included in the analysis as needed.

The Lagrangian. Coordinate systems previously presented will now be used to develop expressions for the kinetic, gravitational potential, and elastic strain energies necessary to form the Lagrangian.

Kinetic Energy. We will now determine the kinetic energy of a translating and rotating cable with an eccentric additional mass. Referring to Fig. 1, consider an arbitrary particle p on the conductor cross-section. The position vector to that particle with respect to the global coordinate system is

$$\mathbf{R}_p = \mathbf{R} + \mathbf{r}_p \tag{1}$$

where $\mathbf{r}_p$ is the position of the particle with respect to the conductor center. The velocity of the particle in the fixed frame is given by

$$\mathbf{V}_p = \dot{\mathbf{R}} + \omega \times \mathbf{r}_p = \mathbf{V} + \omega \times \mathbf{r}_p \tag{2}$$

where $\mathbf{V}$ is the velocity of the cable center in the global frame and the dot represents differentiation with respect to time. The vector ω is the angular velocity of the conductor as seen by an observer in the fixed frame. The kinetic energy, KE_p, of this particle which has mass m_p, is

$$KE_p = \frac{1}{2} m_p |\mathbf{V}_p|^2. \tag{3}$$

The kinetic energy, KE, of a unit length of line is

$$KE = \sum_p \frac{1}{2} m_p |\mathbf{V}_p|^2 \tag{4}$$

where the sum is computed over all particles composing a unit length of the cable. Carrying out the operation of Eq.(4) produces

$$KE = \frac{1}{2}\sum_p m_p |\mathbf{V}|^2 + \mathbf{V}\cdot(\omega \times \sum_p m_p \mathbf{r}_p) + \frac{1}{2}\sum_p m_p (\omega \times \mathbf{r}_p)^2$$

$$= \frac{1}{2} m |\mathbf{V}|^2 + m\,\mathbf{V}\cdot(\omega \times \mathbf{r}_{cm}) + \frac{1}{2}\sum_{i,j} I_{ij}\,\omega_i\,\omega_j \tag{5}$$

where m is the total cable mass per unit unstressed length determined by

$$m = \sum_p m_p \tag{6}$$

and where I_{ij} are inertia tensor components computed as

$$I_{ij} = \sum_p m_p [\delta_{ij} |\mathbf{r}_p|^2 - r_{p_i} r_{p_j}]. \tag{7}$$

Note that δ_{ij} is the Kronecker delta and that r_{p_i} and r_{p_j} are components of the vector $\mathbf{r}_p$. Likewise, ω_i and ω_j are components of the angular velocity ω. Futhermore, it should be noted that all vector quantities in (5) are expressed in the fixed frame.

The total kinetic energy of the line, KE_T, is determined by integrating (5) over the length of the line to yield

$$KE_T = \frac{m}{2}\int_0^{FL} |\dot{\mathbf{R}}|^2\,ds + m\int_0^{FL} \dot{\mathbf{R}}\cdot(\omega \times \mathbf{r}_{cm})\,ds$$

$$+ \frac{1}{2}\int_0^{FL}\int_{A_T} \rho(\omega \times \mathbf{r}_p)\cdot(\omega \times \mathbf{r}_p)\,dA\,ds \tag{8}$$

where FL is the free, unstressed length of the line, A_T is the total cross-sectional region of the line including eccentric mass, and ρ is the mass density which varies over the cross-section.

Potential Energy. The potential energy is divided into two parts which consist of the gravitational potential energy and the elastic strain energy. We will treat each part separately.

Gravitational Potential Energy. The gravitational potential energy is

$$PE_g = -m\,\mathbf{g}\cdot\int_0^{FL} (\mathbf{R} + \mathbf{r}_{cm})\,ds \tag{9}$$

where $\mathbf{g}$ is the gravitational acceleration vector.

Elastic Strain Energy. The total elastic strain energy of the line is determined by integrating the strain energy density over the entire region of the conductor. Before this can be accomplished, both the axial and torsional strains and the accompanying stresses must be expressed in terms of the conductor displacements. To this end we adopt the constitutive relation presented by McConnell and Zemke (1976) which, for the purposes of this work, is

$$P = AE\,\epsilon + B\frac{\partial\theta}{\partial s} \tag{10}$$

for the axial tension P and

$$T = B\,\epsilon + JG\frac{\partial\theta}{\partial s} \tag{11}$$

for the torsion T. In (10) and (11), AE and JG are the axial and torsional stiffness of the cable, respectively. A is the cross-sectional area of the bare, unstressed cable. B represents the coupling between axial and torsional displacements owing to the stranded, wound nature of the cable construction. The axial strain ϵ is

$$\epsilon = \left|\frac{\partial \mathbf{R}}{\partial s}\right| - 1. \tag{12}$$

The constitutive model gives the strain energy as

$$SE = \frac{1}{2}\int_0^{FL} P\epsilon\,ds + \frac{1}{2}\int_0^{FL} T\frac{\partial\theta}{\partial s}\,ds$$

$$= \frac{1}{2}\int_0^{FL} \begin{bmatrix} \epsilon & \dfrac{\partial\theta}{\partial s} \end{bmatrix} \begin{bmatrix} AE & B \\ B & JG \end{bmatrix} \begin{bmatrix} \epsilon \\ \dfrac{\partial\theta}{\partial s} \end{bmatrix} ds. \tag{13}$$

By combining the results of (8), (9), and (13), we can write the Lagrangian, L, of the line as

$$L(\mathbf{R}, \dot{\mathbf{R}}, \mathbf{R}_s, \dot{\mathbf{R}}_s, \theta, \dot{\theta}, \theta_s) = KE_T - PE_g - SE \tag{14}$$

where the subscript s denotes partial differentiation with respect to s.

The First Variation. Equations of motion for the cable originate from the determination of the first variation of (14). This process will produce a coupled system of one vector equation and one scalar equation for determination of cable displacement $\mathbf{R}$ and twist θ. We will consider each of the component energies in turn beginning with the potential energies and concluding with the kinetic energy.

Gravitational Potential Energy. The variation of the gravitational potential energy arises because of cable displacement and rotation. The first variation of PE_g is

$$\delta PE_g = -m\mathbf{g}\cdot\int_0^{FL}\left[\frac{\partial}{\partial \mathbf{R}}(\mathbf{R} + \mathbf{r}_{cm})\delta\mathbf{R} + \frac{\partial}{\partial\theta}(\mathbf{R} + \mathbf{r}_{cm})\delta\theta\right] ds$$

$$= -m\mathbf{g}\cdot\int_0^{FL} [\delta\mathbf{R} + (\delta\beta \times \mathbf{r}_{cm})]\,ds$$

$$= -m\mathbf{g}\cdot\int_0^{FL} \delta\mathbf{R}\,ds - \int_0^{FL} (\mathbf{r}_{cm} \times m\mathbf{g})\cdot\delta\beta\,ds. \tag{15}$$

where $\delta\beta$ is a rotational or pseudo vector formed by variations in the three Euler angles. The terms on the right side of (15)

Downloaded 03 May 2010 to 171.66.16.247. Redistribution subject to ASME license or copyright; see http://www.asme.org/terms/Terms_Use.cfm

will eventually contribute a gravitational force and a gravitational moment about the conductor center.

The vector $\delta\beta$ is readily obtained from the Euler transformation itself. Let $\mathbf{r}_p'$ be an arbitrary vector in the local frame. The corresponding representation in the global frame is the vector $\mathbf{r}_p$ given by

$$\begin{aligned}\mathbf{r}_p &= [\Gamma]\mathbf{r}_p' \\ &= [Rot(Z,\ \psi)][Rot(X_1,\ \phi)][Rot(Y_2,\ \theta)]\mathbf{r}_p' \end{aligned} \tag{16}$$

where $[Rot(w,\ v)]$ represents a rotation matrix formed by a rotation of angle v in the right-handed sense about axis w and $[\Gamma]$ is the Euler angle transformation which converts vectors from representation in the local frame to their representation in the fixed frame. The variation of $\mathbf{r}_p$ with respect to the Euler angles is given by

$$\begin{aligned}\delta\mathbf{r}_p &= \left\{\frac{\partial}{\partial\psi}[\Gamma]\delta\psi + \frac{\partial}{\partial\phi}[\Gamma]\delta\phi + \frac{\partial}{\partial\theta}[\Gamma]\delta\theta\right\}[\Gamma]^T\mathbf{r}_p \\ &= \delta\beta\times\mathbf{r}_p \end{aligned} \tag{17}$$

where the superscript T denotes matrix transpose. The result of the differentiation and matrix multiplication in (17) produces the pseudo vector $\delta\beta$ which is given by

$$\delta\beta = \delta\psi\mathbf{k} + \delta\phi\hat{\mathbf{X}}_1 + \delta\theta\mathbf{e}_t = [D]\delta\Lambda \tag{18}$$

where $\hat{\mathbf{X}}_1$ is a unit vector which points along the X_1-axis of Fig. 2. Note that by employing the same algebraic steps we could consider the time derivative of $\mathbf{r}_p$, a process which leads to the angular velocity pseudo-vector ω given by

$$\omega = \dot{\beta} = \dot{\psi}\mathbf{k} + \dot{\phi}\hat{\mathbf{X}}_1 + \dot{\theta}\mathbf{e}_t = [D]\dot{\Lambda}. \tag{19}$$

Here, $[D]$ is the matrix

$$[D] = [\mathbf{k}\ \hat{\mathbf{X}}_1\ \mathbf{e}_t] \tag{20}$$

and Λ is the column vector

$$\Lambda = [\psi\ \phi\ \theta]^T. \tag{21}$$

Strain Energy. By determining the first variation of the strain energy, we will recover expressions which contain the axial and torsional stiffness terms. The variation of the strain energy is found, after setting the first variation of $\mathbf{R}$ and θ at the ends of the line to zero, as

$$\delta SE = \int_0^{FL}\left[\frac{\partial}{\partial s}\left(\frac{P}{1+\epsilon}\frac{\partial\mathbf{R}}{\partial s}\right)\cdot\delta\mathbf{R} + \frac{\partial}{\partial s}(T)\delta\theta\right]ds. \tag{22}$$

Kinetic Energy. The task remaining in finding the first variation is the consideration of the kinetic energy. Its variation is

$$\begin{aligned}\delta\int_{t_1}^{t_2} KE_T dt = \delta\int_{t_1}^{t_2}\int_0^{FL}\frac{1}{2}m\dot{\mathbf{R}}\cdot\dot{\mathbf{R}}dsdt \\ + \delta\int_{t_1}^{t_2}\int_0^{FL}\int_{A_T}\rho\dot{\mathbf{R}}\cdot(\omega\times\mathbf{r}_p)dAdsdt \\ + \delta\int_{t_1}^{t_2}\int_0^{FL}\int_{A_T}\frac{\rho}{2}(\omega\times\mathbf{r}_p)\cdot(\omega\times\mathbf{r}_p)dAdsdt. \end{aligned} \tag{23}$$

After computing the variation, integrating by parts, and finally setting the variations of $\mathbf{R}$ at either end point in time to zero, the first term on the right of (23) becomes

$$\delta\int_{t_1}^{t_2}\int_0^{FL}\frac{1}{2}m\dot{\mathbf{R}}\cdot\dot{\mathbf{R}}\ dsdt = -\int_{t_1}^{t_2}\int_0^{FL} m\ddot{\mathbf{R}}\cdot\delta\mathbf{R}\ dsdt. \tag{24}$$

The next two terms can be manipulated into the intermediate form of

$$\begin{aligned}\delta\int_{t_1}^{t_2}\int_0^{FL}\int_{A_T}\rho\left[\dot{\mathbf{R}}\cdot(\omega\times\mathbf{r}_p) + \frac{1}{2}(\omega\times\mathbf{r}_p)\cdot(\omega\times\mathbf{r}_p)\right]dAdsdt \\ = -\int_{t_1}^{t_2}\int_0^{FL} m(\alpha\times\mathbf{r}_{cm} + \omega\times(\omega\times\mathbf{r}_{cm}))\cdot\delta\mathbf{R}\ dsdt \\ + \int_{t_1}^{t_2}\int_0^{FL}\int_{A_T}\rho(\mathbf{r}_p\times(\ddot{\mathbf{R}} + (\omega\times\mathbf{r}_p)))\cdot\delta\omega\ dAdsdt \\ + \int_{t_1}^{t_2}\int_0^{FL}\int_{A_T}\rho(\mathbf{r}_p\times((\ddot{\mathbf{R}} + \omega\times\mathbf{r}_p)\times\omega))\cdot\delta\beta\ dAdsdt. \end{aligned} \tag{25}$$

The first term on the right of (25) is in the desired form; the last two terms require further attention.

At this point of the derivation there are two directions which we can follow. The first is to write the variation of ω as

$$\delta\omega = \frac{\partial\omega}{\partial\dot{\Lambda}}\delta\dot{\Lambda} + \frac{\partial\omega}{\partial\Lambda}\delta\Lambda \tag{26}$$

which is the most direct way. The other path requires that we realize that

$$\frac{d}{dt}(\delta\beta) = \delta\dot{\beta} + \omega\times\delta\beta. \tag{27}$$

Now, (27) can be most easily verified by directly substituting the various quantities. The form of (27) arises since the last two Euler angles represent rotations around unit vectors which are themselves rotating. From (27) we now recognize that

$$\delta\dot{\beta} = \delta\omega = \frac{d}{dt}(\delta\beta) - \omega\times\delta\beta. \tag{28}$$

In completing the determination of the variations in (25) we can use either (26) or (28) to arrive at the same result; however, the algebraic complexity of using (28) is considerably less than the alternative.

After substituting (28) into (25), integrating by parts, substituting the definitions of the inertia tensor and the center of mass, simplifying, and combining the end result with (24), the variation of the kinetic energy with respect to $\mathbf{R}$ and the Euler angles becomes

$$\begin{aligned}\delta\int_{t_1}^{t_2} KE_T dt = -\int_{t_1}^{t_2}\int_0^{FL}[m(\ddot{\mathbf{R}} + \alpha\times\mathbf{r}_{cm} + \omega\times(\omega\times\mathbf{r}_{cm}))\cdot\delta\mathbf{R} \\ + (\mathbf{r}_{cm}\times m\ddot{\mathbf{R}} + I\alpha + \omega\times I\omega)\cdot\delta\beta]dsdt. \end{aligned} \tag{29}$$

In order to finish this step we must expand $\delta\beta$ in terms of line displacement and twist.

Determining the variation $\delta\beta$ as a function of the variations $\delta\theta$ and $\delta\mathbf{R}_s$ is facilitated by using (18). This process produces

$$\delta\beta = [D]\delta\Lambda = [D]\frac{\partial\Lambda}{\partial\mathbf{R}_s}\delta\mathbf{R}_s + \mathbf{e}_t\delta\theta. \tag{30}$$

In order to evaluate the derivative $\partial\Lambda/\partial\mathbf{R}_s$ we note that the unit tangent to the line can be written as

$$\mathbf{e}_t = -\sin\psi\cos\phi\,\mathbf{i} + \cos\psi\cos\phi\,\mathbf{j} + \sin\phi\,\mathbf{k} = \frac{1}{1+\epsilon}\frac{\partial\mathbf{R}}{\partial s}. \tag{31}$$

By equating components and computing differentials then it is possible, after considerable algebra, to demonstrate that

$$\frac{\partial\psi}{\partial\mathbf{R}_s} = -\frac{\hat{\mathbf{X}}_1^T}{(X_s^2 + Y_s^2)^{1/2}} \tag{32}$$

and

$$\frac{\partial\phi}{\partial\mathbf{R}_s} = \hat{\mathbf{Z}}_2^T\frac{1}{1+\epsilon} \tag{33}$$

where $\hat{\mathbf{Z}}_2$ is a unit vector along the Z_2-axis of Fig. 2. Substituting (32) and (33) into (30) finally produces

Downloaded 03 May 2010 to 171.66.16.247. Redistribution subject to ASME license or copyright; see http://www.asme.org/terms/Terms_Use.cfm

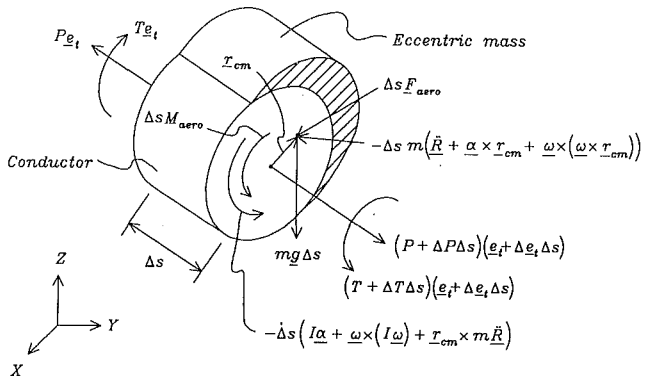


Fig. 3 Cable loading with elastic, external, and inertial forces

$$\delta\beta = \frac{1}{1+\epsilon}\left[\hat{\mathbf{X}}_1\,\hat{\mathbf{Z}}_2^T - \mathbf{k}\,\hat{\mathbf{X}}_1^T\frac{(1+\epsilon)}{(X_s^2+Y_s^2)^{1/2}}\right]\delta\mathbf{R}_s + \mathbf{e}_t\delta\theta. \quad (34)$$

We can now complete the first variation of the kinetic energy by substituting (34) into (29), integrating by parts, and setting the first variation of $\mathbf{R}$ at the ends of the line to zero. Doing this gives

$$\delta\int_{t_1}^{t_2} KE_T\,dt = \int_{t_1}^{t_2}\int_0^{FL}\left\{\left[-m(\ddot{\mathbf{R}} + \boldsymbol{\alpha}\times\mathbf{r}_{cm} + \boldsymbol{\omega}\times(\boldsymbol{\omega}\times\mathbf{r}_{cm})) + \frac{\partial}{\partial s}\left(\frac{1}{1+\epsilon}\left(-\mathbf{r}_{cm}\times m\ddot{\mathbf{R}} - I\boldsymbol{\alpha} - \boldsymbol{\omega}\times(I\boldsymbol{\omega})\right)^T \cdot\left[\mathbf{k}\,\hat{\mathbf{X}}_1^T\frac{1+\epsilon}{(X_s^2+Y_s^2)^{1/2}} - \hat{\mathbf{X}}_1\,\hat{\mathbf{Z}}_2^T\right]\right)\right]\cdot\delta\mathbf{R} + [(-\mathbf{r}_{cm}\times m\ddot{\mathbf{R}} - I\boldsymbol{\alpha} - \boldsymbol{\omega}\times(I\boldsymbol{\omega}))\cdot\mathbf{e}_t]\delta\theta\right\} ds\,dt. \quad (35)$$

The Equations of Motion. By equating the variations of the Lagrangian with respect to $\mathbf{R}$ and θ to the virtual work done by these external excitations, which are not represented through a potential, we produce the equations of motion. These are given by

$$m(\ddot{\mathbf{R}} + \boldsymbol{\alpha}\times\mathbf{r}_{cm} + \boldsymbol{\omega}\times(\boldsymbol{\omega}\times\mathbf{r}_{cm})) = \mathbf{F}_{\text{aero}} + m\mathbf{g} + \frac{\partial}{\partial s}\left\{\frac{1}{1+\epsilon}\left[P\frac{\partial\mathbf{R}}{\partial s} + \left(\hat{\mathbf{X}}_1\mathbf{k}^T\frac{(1+\epsilon)}{(X_s^2+Y_s^2)^{1/2}} - \hat{\mathbf{Z}}_2\,\hat{\mathbf{X}}_1^T\right)\cdot(\mathbf{r}_{cm}\times m\mathbf{g} - \mathbf{r}_{cm}\times m\ddot{\mathbf{R}} - I\boldsymbol{\alpha} - \boldsymbol{\omega}\times(I\boldsymbol{\omega}))\right]\right\} \quad (36)$$

and

$$(\mathbf{r}_{cm}\times m\mathbf{g} - \mathbf{r}_{cm}\times m\ddot{\mathbf{R}} - I\boldsymbol{\alpha} - \boldsymbol{\omega}\times(I\boldsymbol{\omega}))\cdot\mathbf{e}_t + \frac{\partial T}{\partial s} = -M_{\text{aero}} \quad (37)$$

where $\mathbf{F}_{\text{aero}}$ and M_{aero} are the external aerodynamic force and pitching moment, respectively.

Verification. As an independent means of verifying the equations of motion, we use the principle of virtual work. The procedure to be followed is to consider the sum of the elastic, inertial, and gravitational forces and moments acting on a section of cable. The work done by the net force and moment in moving the entire cable through a virtual displacement $\delta\mathbf{R}$ and $\delta\beta$, a displacement consistent with the constraints, is then set to zero. By factoring the various components of the virtual displacement, namely, δX, δY, δZ, and $\delta\theta$ and by noting that these displacements are independent, the equations of motion are obtained.

Figure 3 shows a small portion of cable with internal, external, and inertial loadings. The net force and moment will now be considered. Summing forces and ignoring the products of small terms provides

$$\sum\mathbf{F} = \Delta s[\Delta(P\mathbf{e}_t) + m\mathbf{g} + \mathbf{F}_{\text{aero}} - m(\ddot{\mathbf{R}} + \boldsymbol{\alpha}\times\mathbf{r}_{cm} + \boldsymbol{\omega}\times(\boldsymbol{\omega}\times\mathbf{r}_{cm}))]. \quad (38)$$

The moment sum is

$$\sum\mathbf{M} = \Delta s[\Delta(T\mathbf{e}_t) + \mathbf{M}_{\text{aero}} + \mathbf{r}_{cm}\times m\mathbf{g} - (I\boldsymbol{\alpha} + \boldsymbol{\omega}\times(I\boldsymbol{\omega}) + \mathbf{r}_{cm}\times m\ddot{\mathbf{R}})]. \quad (39)$$

By letting Δs shrink to differential proportions, we can then compute the work, δW, done through a virtual displacement as

$$\delta W = \int_0^{FL}\left(\sum\mathbf{F}\cdot\delta\mathbf{R} + \sum\mathbf{M}^T\delta\boldsymbol{\beta}\right)ds. \quad (40)$$

The constraint on the motion given by

$$\delta\boldsymbol{\beta} = \frac{\partial\boldsymbol{\beta}}{\partial\mathbf{R}_s}\delta\mathbf{R}_s + \delta\theta\mathbf{e}_t \quad (41)$$

is now included. By substituting (41) into (40), integrating by parts, and finally setting the virtual displacement $\delta\mathbf{R}$ at the end points to zero, produces

$$\delta W = \int_0^{FL}\left[\left(\sum\mathbf{F} - \frac{\partial}{\partial s}\left(\sum\mathbf{M}^T\frac{\partial\boldsymbol{\beta}}{\partial\mathbf{R}_s}\right)\right)\cdot\delta\mathbf{R} + \sum\mathbf{M}\cdot\mathbf{e}_t\delta\theta\right]ds. \quad (42)$$

Since the displacements are consistent with the constraints, the virtual work vanishes. The displacements $\delta\mathbf{R}$ and $\delta\theta$ are independent and arbitrary. The independence of the virtual displacements leads to the conclusion

$$\sum\mathbf{F}^T - \frac{\partial}{\partial s}\left(\sum\mathbf{M}^T\frac{\partial\boldsymbol{\beta}}{\partial\mathbf{R}_s}\right) = 0 \quad (43)$$

and

$$\sum\mathbf{M}\cdot\mathbf{e}_t = 0 \quad (44)$$

which produces the original Eqs. (36) and (37).

Comparisons With Previous Work

Comparisons of the equations of motion given in (36) and (37) with results of other investigators are possible provided additional assumptions are made. It is instructive to see what additional assumptions are necessary in order to match the results of others since this provides an understanding of the assumption influence upon the equations of motion.

Shallow Catenary Assumption. The first assumption to be invoked is that the sag-to-span ratio is small. The implication of this assumption is that the unit tangent to the line is everywhere horizontal and can be made to coincide with one of the fixed frame axes. Making the Y-axis coincide with the line means that the vector $\mathbf{r}_{cm}$ is contained in the X-Z plane. Another influence of this assumption is that all torsional motion is about the Y-axis exclusively.

Under this assumption the equations of motion simplify significantly. The translational part of the motion is governed by

$$m(\ddot{\mathbf{R}} + \ddot{\theta}\mathbf{j}\times\mathbf{r}_{cm} - \dot{\theta}^2\mathbf{r}_{cm}) = \mathbf{F}_{\text{aero}} + m\mathbf{g} + \frac{\partial}{\partial s}\left(\frac{1}{1+\epsilon}\left[P\frac{\partial\mathbf{R}}{\partial s} - \left(\mathbf{i}\,\mathbf{k}^T\frac{(1+\epsilon)}{|Y_s|} - \mathbf{k}\,\mathbf{i}^T\right)\cdot(\mathbf{r}_{cm}\times m\ddot{\mathbf{R}})\right]\right) \quad (45)$$

while the torsional equation becomes

$$(\mathbf{r}_{cm}\times m\mathbf{g} - \mathbf{r}_{cm}\times m\ddot{\mathbf{R}} - I\ddot{\theta}\mathbf{e}_t)\cdot\mathbf{e}_t + \frac{\partial T}{\partial s} = -M_{\text{aero}}. \quad (46)$$

If we make the additional assumption of no axial motion

Downloaded 03 May 2010 to 171.66.16.247. Redistribution subject to ASME license or copyright; see http://www.asme.org/terms/Terms_Use.cfm

of the cable, then $\ddot{Y}$ vanishes. Under this circumstance, the rightmost term of (45) also vanishes. The equations now govern the torsional, vertical, and transverse (wind direction) motions of the cable. This particular set of circumstances was treated by Thompson (1975). The simplification of (36) and (37) agrees with his analysis. In Thompson's constitutive model, the parameter B is zero.

Absence of Ice. If there is no ice attached to the cable, then the center of the conductor and the center of mass of the cable cross-section coincide. The vector $\mathbf{r}_{cm}$ vanishes, and under this condition the equations of motion become

$$m\ddot{\mathbf{R}} = \mathbf{F}_{\text{aero}} + m\mathbf{g} + \frac{\partial}{\partial s}\left(\frac{1}{1+\epsilon}\left[P\frac{\partial \mathbf{R}}{\partial s} - \left(\hat{\mathbf{X}}_1\mathbf{k}^T\frac{1+\epsilon}{(X_s^2+Y_s^2)^{1/2}} - \hat{\mathbf{Z}}_2\hat{\mathbf{X}}_1^T\right)\cdot(I\alpha+\omega\times(I\omega))\right]\right) \quad (47)$$

and

$$(I\alpha+\omega\times(I\omega))\cdot\mathbf{e}_t = M_{\text{aero}} + \frac{\partial T}{\partial s}. \quad (48)$$

The remarkable aspect of (47) and (48) is that the torsional motion and the vertical motion are coupled together. It was previously believed that in the absence of ice, the torsional motion would uncouple from the translational motion, since in the work of Nigol and Havard (1978), it was noticed that the torsional frequency of vibration aligned with the translational frequency after ice had accumulated on the cable.

An important simplification occurs in the absence of both ice and torsional motion. Under this additional condition (47) becomes

$$m\ddot{\mathbf{R}} = \mathbf{F}_{\text{aero}} + m\mathbf{g} + \frac{\partial}{\partial s}\left(\frac{P}{1+\epsilon}\frac{\partial \mathbf{R}}{\partial s}\right) \quad (49)$$

which was originally presented by Shea (1955) and by Simpson (1963).

Ice-Free, Shallow Catenary Torsional Motion. Under these conditions, the moment balance expressed in (48) becomes

$$I\ddot{\theta} = M_{\text{aero}} + \frac{\partial T}{\partial s}. \quad (50)$$

Simpson (1972) presented the torsional equation for a bundled conductor. According to Simpson, the torsional moment attributed to stiffness is

$$M_T = \frac{\partial}{\partial s}\left(\frac{JG}{1+\epsilon}\frac{\partial \theta}{\partial s}\right) \quad (51)$$

where no elastic axial-torsional coupling is assumed. Equation (51) is true for Simpson's analysis regardless of the number (even one) of conductors making up the bundle. In comparing (51) with the work presented here, namely,

$$M_T = \frac{\partial}{\partial s}\left(JG\frac{\partial \theta}{\partial s}\right) \quad (52)$$

we see that the difference is a factor of $1/(1+\epsilon)$. By including the $1/(1+\epsilon)$ factor in the constitutive Eqs. of (10) and (11), rederiving the equations of motion, and invoking the same assumptions which lead to (50), the equations of motion as presented by Simpson are not recovered. There were additional terms not included in Simpson's analysis. It was found that only by using the constitutive model of (10) and (11) were we able to determine a result which was consistent with the virtual work analysis.

Conclusions

Equations of motion on a thin cable consisting of several wound strands subject to aerodynamic and eccentric mass loading have been derived. The equations of motion have been verified through a virtual work argument. By invoking suitable assumptions, simplifications of the presented work were shown to be in agreement with the work of previous investigators.

The equations of motion for the case where no ice is attached to the conductor demonstrated that the translational and torsional modes remained coupled. The presence of the coupling has not been known until now. In the galloping literature there is disagreement as to the initiating mode for galloping; i.e., does the instability stem from the torsional or vertical mode? The level of this disagreement is clearly seen in the two papers delivered by Nigol and Buchan (1981) and the following discussion. Nigol and his co-workers have demonstrated that given a conductor-ice geometry which is Den Hartog stable, an unstable system can be created by introducing a torsional oscillation. A significant contribution of the present work is that it provides a new direction for studying the various sources of mechanical instability which may be present in an iced conductor geometry.

Acknowledgments

The work presented here grew out of a study which was supported by Louisiana Power and Light Company. The authors wish to recognize LP&L and the Mechanical Engineering Departments of Kansas State University and Tulane University for their generous support of this work.

References

Cheers, F., 1950, "A Note on Galloping Conductors," Report No. MT-14, National Research Council of Canada, Ottawa, Canada.

Den Hartog, J. P., 1932, "Transmission Line Vibration due to Sleet," *Transactions of the American Institute of Electrical Engineers*, Vol. 51, pp. 1074–1076.

Gawronski, K. E., 1977, "Non-linear Galloping of Bundle-Conductor Transmission Lines," Ph.D. Dissertation, Clarkson College of Technology.

McConnell, K. G., and Zemke, W. P., 1976, "The Measurement of Flexural Stiffness of Multistranded Electrical Conductors While Under Tension," ERI Rep. No. 79194, Eng. Res. Inst., Iowa State University, Ames, Iowa.

Nigol, O., and Havard, D. G., 1978, "Control of Torsionally-Induced Conductor Galloping with Detuning Pendulums," IEEE Power Engineering Society Paper No. A78 125-7.

Nigol, O., and Buchan, P. G., 1981, "Conductor Galloping: Part I, Den Hartog Mechanism," *IEEE Transactions on Power Apparatus and Systems*, PAS-100, pp. 699–707.

Nigol, O., and Buchan, P. G., 1981, "Conductor Galloping: Part II, Torsional Mechanism," *IEEE Transactions on Power Apparatus and Systems*, PAS-100, pp. 708–720.

Routh, E. J., 1905, *A Treatise on the Dynamics of a System of Rigid Bodies, Part II*, 6th ed., Macmillan and Co., London, U.K., pp. 407–408.

Shea, J. F., 1955, "A Study of Wind Forces on Suspended Cables and Related Structures," Ph.D. Thesis, University of Michigan, Ann Arbor, Mich.

Simpson, A., 1963, "Oscillations of Catenaries and Systems of Overhead Transmission Lines," Ph.D. Thesis, University of Bristol, Bristol, U.K.

Simpson, A., 1972, "Determination of the Natural Frequencies of Multiconductor Overhead Transmission Lines," *Journal of Sound and Vibration*, Vol. 20, No. 4, pp. 417–449.

Thompson, H. A., 1975, "Galloping Vibration of Transmission Line Conductors Under Icing Conditions—Final Report," prepared for Louisiana Power and Light Co., Tulane University, New Orleans, La.

Downloaded 03 May 2010 to 171.66.16.247. Redistribution subject to ASME license or copyright; see http://www.asme.org/terms/Terms_Use.cfm

Effects of Load Parameters on the Natural Frequencies and Stability of a Flexible Spinning Disk With a Stationary Load System

Jen-San Chen

D. B. Bogy
Mem. ASME.

Computer Mechanics Laboratory,
Department of Mechanical Engineering,
University of California,
Berkeley, CA 94720

The orthogonality properties among the eigenfunctions for a gyroscopic system are derived for a stiffness operator that is not positive definite. The derivatives of the eigenvalues with respect to certain parameters in the system are then obtained. The results are applied to a spinning disk in contact with a stationary load system, which contains such parameters as friction force, transverse mass, damping, stiffness, and the analogous pitching elements, to predict the effects of these parameters and the stiffening of the disk due to the centrifugal force on the natural frequencies and stability of the spinning disk. The results obtained provide a theoretical understanding for previously reported observations based on numerical solutions.

Introduction

The dynamics of spinning disks in contact with stationary load systems has been a research topic of interest because of its important applications in such fields as computer disk memory units and circular saws. Early investigations dealt with the determination of the natural frequencies of vibration and the effects of various parameters in the load system on the stability of the spinning disk. Iwan and Moeller (1976) used an eigenfunction expansion to calculate the eigenvalues of the system, and they discussed the instabilities caused by transverse mass, damping and stiffness in the load system. Ono et al. (1991) extended Iwan and Moeller's work to include the pitching parameters in the load system as well as the friction force between the spinning disk and the stationary load system. Hutton et al. (1987) analyzed the response of a rotating disk subjected to excitation produced by stationary point loads and restrained by a number of stationary point springs. Most of these efforts were concerned with calculating the natural frequencies and identifying the characteristic instabilities induced by the load system. There is still no theoretical analysis to explain the phenomena discovered in these extensive calculations.

There is another class of problems in which a stationary disk is subjected to a rotating load system. The work of Iwan and Stahl (1973) showed similar instability characteristics as those in a spinning disk. In an attempt to explain the mechanisms of these instabilities, Shen and Mote (1991) examined the nonconservative character of the stationary disk-moving load system through the energy required to rotate the load system.

In this paper we present a theoretical study of a general gyroscopic system to predict the effects of parameter changes on the eigenvalues of the system. The results are applied to a spinning disk in contact with a stationary load system to predict the effects of the stiffening due to centrifugal force and various parameters in the load system on the natural frequencies and stability of the spinning disk. Some of these effects have been reported in previous calculations, but some of them have not been pointed out explicitly before. For instance, the mass in the load system tends to decrease the natural frequencies of the forward and backward travelling waves, but tends to increase the natural frequency of the supercritical "reflected" wave.

Gyroscopic System

Since a spinning disk observed by a stationary observer is a standard gyroscopic system, we start with a treatment of the general gyroelastic continuum. The equation for free vibration of a gyroelastic continuum S and the associated boundary conditions on ∂S can be written as

$$\begin{aligned} &\mathbf{M}\ddot{u}+\mathbf{G}\dot{u}+\mathbf{K}u=0 \qquad \text{in } S \\ &\Lambda_j u=0 \qquad j=1,\ \ldots,\ p \quad \text{on } \partial S \end{aligned} \tag{1}$$

where $\mathbf{M}$, $\mathbf{G}$, and $\mathbf{K}$ are the mass, gyral, and stiffness operators, respectively. In general, $\mathbf{M}$ is real, symmetric, and positive definite, $\mathbf{G}$ is real and skew, and $\mathbf{K}$ is real and symmetric. The boundary conditions are assumed to be independent of the eigenvalues. Equation (1) can also be cast in the first-order operator form,

$$\mathbf{A}\dot{\mathbf{x}}-\mathbf{B}\mathbf{x}=\mathbf{0} \tag{2}$$

by defining the state vector

Contributed by the Applied Mechanics Division of THE AMERICAN SOCIETY OF MECHANICAL ENGINEERS for presentation at the 1992 ASME Summer Mechanics and Materials Meeting, Tempe, AZ, Apr. 28–May 1, 1992.

Discussion on this paper should be addressed to the Technical Editor, Prof. Leon M. Keer, The Technological Institute, Northwestern University, Evanston, IL 60208, and will be accepted until four months after final publication of the paper itself in the JOURNAL OF APPLIED MECHANICS. Manuscript received by the ASME Applied Mechanics Division, Oct. 5, 1990; final revision, Apr. 10, 1991.
Paper No. 92-APM-2.

Copyright © 1992 by ASME
Downloaded 03 May 2010 to 171.66.16.247. Redistribution subject to ASME license or copyright; see http://www.asme.org/terms/Terms_Use.cfm

$$\mathbf{x} = \begin{Bmatrix} \dot{u} \\ u \end{Bmatrix}$$

and the matrix differential operators

$$\mathbf{A} = \begin{bmatrix} \mathbf{M} & \mathbf{0} \\ \mathbf{0} & \mathbf{K} \end{bmatrix}, \quad \mathbf{B} = \begin{bmatrix} -\mathbf{G} & -\mathbf{K} \\ \mathbf{K} & \mathbf{0} \end{bmatrix} \tag{3}$$

where $\mathbf{0}$ is a null operator. It can be shown that $\mathbf{A}$ is symmetric and positive definite if $\mathbf{K}$ is positive definite, and $\mathbf{B}$ is skew.

The inner product between two vectors $\mathbf{x}_1$ and $\mathbf{x}_2$ in the domain S is defined as

$$<\mathbf{x}_1, \mathbf{x}_2> = \int_S \bar{\mathbf{x}}_1^T \mathbf{x}_2 \, dV$$

where $\mathbf{x}_1^T$ is the transpose of the state vector $\mathbf{x}_1$ and overbar means complex conjugate. It is noted that $<\mathbf{x}_1, \mathbf{x}_2> = \overline{<\mathbf{x}_2, \mathbf{x}_1>}$. Accordingly, operators $\mathbf{A}$ and $\mathbf{B}$ have the following properties:

$$<\mathbf{A}\,\mathbf{x}_1, \mathbf{x}_2> = <\mathbf{x}_1, \mathbf{A}\,\mathbf{x}_2>, \quad <\mathbf{B}\,\mathbf{x}_1, \mathbf{x}_2> = -<\mathbf{x}_1, \mathbf{B}\,\mathbf{x}_2>. \tag{4}$$

Substituting the separable solution

$$\mathbf{x} = \mathbf{x}_n e^{\lambda_n t}$$

into the homogeneous equation (2), we obtain the eigenvalue problem

$$\lambda_n \mathbf{A}\,\mathbf{x}_n = \mathbf{B}\,\mathbf{x}_n \tag{5}$$

where λ_n and $\mathbf{x}_n$ may be complex. If an eigenvalue λ_n is complex, it must occur in complex conjugate pairs. For a special class of gyroscopic systems in which the stiffness operator is positive definite, it can be proved that all the eigenvalues are purely imaginary (Lancaster, 1966), and the real parts as well as the imaginary parts of the state eigenfunctions are orthogonal with respect to $\mathbf{A}$ and $\mathbf{B}$ (Meirovitch, 1974; D'Eleuterio et al., 1984). However, in practice we often encounter the situation in which the stiffness operator is not positive definite—for instance, the vibration of a disk rotating faster than the critical speed. In the following, we will establish the orthogonality properties among the eigenfunctions even when the definiteness of the stiffness operator is lost. Based on this orthogonality property, we then obtain the expressions for the derivatives of the eigenvalues with respect to certain parameters in the system. Since the real parts and the imaginary parts of the eigenvalues represent the stability properties and the natural frequencies of the system, respectively, the derivatives of the eigenvalues are then used to predict the effects of various parameter changes on these dynamic characteristics of the system.

Orthogonality Properties Among the Eigenfunctions

Suppose λ_1 and λ_2 are two different eigenvalues of Eq. (5) and $\mathbf{x}_1$ and $\mathbf{x}_2$ are the eigenfunctions corresponding to λ_1 and λ_2, i.e.,

$$\lambda_1 \mathbf{A}\,\mathbf{x}_1 = \mathbf{B}\,\mathbf{x}_1 \tag{6}$$

$$\lambda_2 \mathbf{A}\,\mathbf{x}_2 = \mathbf{B}\,\mathbf{x}_2 \tag{7}$$

Take the inner product between $\mathbf{x}_2$ and both sides of Eq. (6) to obtain

$$<\lambda_1 \mathbf{A}\,\mathbf{x}_1, \mathbf{x}_2> = <\mathbf{B}\,\mathbf{x}_1, \mathbf{x}_2>. \tag{8}$$

Similarly, take the inner product between $\mathbf{x}_1$ and both sides of Eq. (7),

$$<\mathbf{x}_1, \lambda_2 \mathbf{A}\,\mathbf{x}_2> = <\mathbf{x}_1, \mathbf{B}\,\mathbf{x}_2>. \tag{9}$$

By comparing Eqs. (8) and (9) and referring back to Eq. (4), we obtain

$$(\bar{\lambda}_1 + \lambda_2)<\mathbf{x}_1, \mathbf{A}\,\mathbf{x}_2> = 0. \tag{10}$$

If all the eigenvalues are purely imaginary, then $(\bar{\lambda}_1 + \lambda_2) \neq 0$ and from Eq. (10) we can conclude that

$$<\mathbf{x}_1, \mathbf{A}\,\mathbf{x}_2> = 0 \text{ if } \lambda_1 \neq \lambda_2. \tag{11}$$

Furthermore, since

$$<\mathbf{x}_1, \mathbf{A}\,\mathbf{x}_1> = <\mathbf{A}\,\mathbf{x}_1, \mathbf{x}_1> = \overline{<\mathbf{x}_1, \mathbf{A}\,\mathbf{x}_1>},$$

we can conclude that $<\mathbf{x}_1, \mathbf{A}\,\mathbf{x}_1>$ is real. Similarly, we can also obtain

$$<\mathbf{x}_1, \mathbf{B}\,\mathbf{x}_2> = 0 \text{ if } \lambda_1 \neq \lambda_2 \tag{12}$$

and since

$$<\mathbf{x}_1, \mathbf{B}\,\mathbf{x}_1> = -<\mathbf{B}\,\mathbf{x}_1, \mathbf{x}_1> = -\overline{<\mathbf{x}_1, \mathbf{B}\,\mathbf{x}_1>},$$

we can conclude that $<\mathbf{x}_1, \mathbf{B}\,\mathbf{x}_1>$ is purely imaginary.

On the other hand, if some of the eigenvalues are not purely imaginary, then the condition $\lambda_1 \neq \lambda_2$ does not necessarily lead to $\bar{\lambda}_1 + \lambda_2 \neq 0$ (for instance, $\lambda_1 = 1 + i$, $\lambda_2 = -1 + i$, where $i = \sqrt{-1}$), and there is no guarantee that $<\mathbf{x}_1, \mathbf{A}\,\mathbf{x}_2>$ will vanish. Therefore, orthogonality properties such as Eqs. (11) and (12) do not necessarily exist when some of the eigenvalues are not purely imaginary. It is noted that in deriving Eqs. (11) and (12), no requirement for a positive definite $\mathbf{K}$ is needed.

It can also be shown that the orthogonality properties reported in previous papers (Meirovitch, 1974; D'Eleuterio et al., 1984) in which $\mathbf{K}$ is positive definite are special cases of Eq. (11) in this paper. Since the eigenvalues occur in complex conjugate, purely imaginary pairs, we use the following notation

$$\lambda_n = i\omega_n, \quad \bar{\lambda}_n = -i\omega_n, \quad n = 1, 2, \cdots$$

where ω_n are positive real numbers. The corresponding complex eigenfunctions are

$$\mathbf{x}_n = \mathbf{y}_n + i\mathbf{z}_n, \quad \bar{\mathbf{x}}_n = \mathbf{y}_n - i\mathbf{z}_n \tag{13}$$

where $\mathbf{y}_n$ and $\mathbf{z}_n$ are real-valued functions. The orthogonality properties reported in D'Eleuterio et al., (1984) are

$$<\mathbf{y}_m, \mathbf{A}\,\mathbf{y}_n> = <\mathbf{z}_m, \mathbf{A}\,\mathbf{z}_n> = 0 \quad \text{if } m \neq n \tag{14a}$$

$$<\mathbf{y}_m, \mathbf{A}\,\mathbf{z}_n> = <\mathbf{z}_m, \mathbf{A}\,\mathbf{y}_n> = 0 \quad \text{for any } m \text{ and } n. \tag{14b}$$

With this convention, Eq. (11) can be rewritten as

$$<\mathbf{x}_m, \mathbf{A}\,\mathbf{x}_n> = 0 \quad \text{if } m \neq n \tag{15a}$$

$$<\mathbf{x}_m, \mathbf{A}\,\bar{\mathbf{x}}_n> = 0 \quad \text{for any } m \text{ and } n. \tag{15b}$$

After substituting Eqs. (13) into (15*a*,*b*) and using the fact that $<\mathbf{x}_n, \mathbf{A}\,\mathbf{x}_n>$ is real, we can prove that Eqs. (15*a*,*b*) are the necessary and sufficient conditions for Eqs. (14*a*,*b*).

While the gyroelastic continuum is stable (all the eigenvalues are purely imaginary) in the case that $\mathbf{K}$ is positive definite, the system may be stable or unstable, depending on $\mathbf{G}$, when $\mathbf{K}$ is not positive definite, and determining the stability criteria is itself a topic for research. In the following we will be interested in a system which is gyroscopic and stable at a certain value in the parameter space but may not be gyroscopic or stable in the neighborhood of these parameter values.

Derivative of Eigenvalues

The equation of free vibration for a general continuous system can be written as

$$\hat{\mathbf{M}}\,\ddot{u} + \hat{\mathbf{G}}\,\dot{u} + \hat{\mathbf{K}}\,u = 0 \tag{16}$$

where $\hat{\mathbf{M}}$, $\hat{\mathbf{G}}$, and $\hat{\mathbf{K}}$ are not necessarily symmetric or skew. Similar to Eqs. (3) and (5), we can define the matrix differential operators $\hat{\mathbf{A}}$ and $\hat{\mathbf{B}}$, and the associated eigenvalue problem as

$$\hat{\mathbf{A}} \equiv \begin{bmatrix} \hat{\mathbf{M}} & \mathbf{0} \\ \mathbf{0} & \hat{\mathbf{K}} \end{bmatrix}, \quad \hat{\mathbf{B}} \equiv \begin{bmatrix} -\hat{\mathbf{G}} & -\hat{\mathbf{K}} \\ \hat{\mathbf{K}} & \mathbf{0} \end{bmatrix} \tag{17}$$

$$\lambda_n \hat{\mathbf{A}}\,\mathbf{x}_n = \hat{\mathbf{B}}\,\mathbf{x}_n. \tag{18}$$

We assume that the differential operators $\hat{\mathbf{M}}$, $\hat{\mathbf{G}}$, and $\hat{\mathbf{K}}$ in Eq. (16) are functions of certain parameters ρ_k ($k = 1, \ldots, l$) in the neighborhood of a point ρ_k^0 ($k = 1, \ldots, l$) in the l-dimensional

Downloaded 03 May 2010 to 171.66.16.247. Redistribution subject to ASME license or copyright; see http://www.asme.org/terms/Terms_Use.cfm

parameter space. The eigenvalues λ_n and eigenfunctions $\mathbf{x}_n$ in Eq. (18) are continuous functions of ρ_k in that neighborhood. We further assume that Eq. (16) represents the motion of a gyroscopic system and that all the eigenvalues are purely imaginary at $\rho_k = \rho_k^0$ $(k = 1, \ldots, l)$, but the system is not necessarily gyroscopic or stable for $\rho_k \neq \rho_k^0$. At the point ρ_k^0, the operators $\hat{\mathbf{M}}$, $\hat{\mathbf{G}}$, $\hat{\mathbf{K}}$, $\hat{\mathbf{A}}$, and $\hat{\mathbf{B}}$ become $\mathbf{M}$, $\mathbf{G}$, $\mathbf{K}$, $\mathbf{A}$, and $\mathbf{B}$, respectively, and Eqs. (16), (17), and (18) reduce to Eqs. (1), (3), and (5), respectively. Assume λ_n is a distinct eigenvalue of Eq. (18) and take the inner product between $\mathbf{x}_n$ and both sides of Eq. (18) to obtain

$$<\mathbf{x}_n,\ (\lambda_n \hat{\mathbf{A}} - \hat{\mathbf{B}})\mathbf{x}_n> = 0. \tag{19}$$

Taking the partial derivative of Eq. (19) with respect to the parameter ρ_k, we get

$$<\mathbf{x}_{n,k},\ (\lambda_n \hat{\mathbf{A}} - \hat{\mathbf{B}})\mathbf{x}_n> + <\mathbf{x}_n,\ \lambda_{n,k} \hat{\mathbf{A}}\ \mathbf{x}_n>$$
$$+ <\mathbf{x}_n,\ (\lambda_n \hat{\mathbf{A}}_{,k} - \hat{\mathbf{B}}_{,k})\mathbf{x}_n> + <\mathbf{x}_n,\ (\lambda_n \hat{\mathbf{A}} - \hat{\mathbf{B}})\mathbf{x}_{n,k}> = 0 \tag{20}$$

where the standard subscript notation for partial derivative is used. Referring to Eqs. (4), which are valid when $\rho_k = \rho_k^0$ and using the fact that $\lambda_n = \lambda_n^0$ is purely imaginary when $\rho_k = \rho_k^0$, we obtain for the last term in Eq. (20)

$$<\mathbf{x}_n^0,\ (\lambda_n^0 \mathbf{A} - \mathbf{B})\mathbf{x}_{n,k}^0> = <(\overline{\lambda}_n^0 \mathbf{A} + \mathbf{B})\mathbf{x}_n^0,\ \mathbf{x}_{n,k}^0>$$
$$= <(-\lambda_n^0 \mathbf{A} + \mathbf{B})\mathbf{x}_n^0,\ \mathbf{x}_{n,k}^0> \quad \text{when } \rho_k = \rho_k^0 \tag{21}$$

where $\mathbf{x}_n^0$ is the eigenfunction corresponding to λ_n^0. So, at $\rho_k = \rho_k^0$, the first and the last terms of Eq. (20) vanish, because of Eqs. (5) and (21), and the derivative $\lambda_{n,k}$ evaluated at the point ρ_k^0, $\lambda_{n,k}^0$, can be simplified to

$$\lambda_{n,k}^0 = -\frac{<\mathbf{x}_n^0,\ (\lambda_n^0 \mathbf{A}_{,k} - \mathbf{B}_{,k})\mathbf{x}_n^0>}{<\mathbf{x}_n^0,\ \mathbf{A}\ \mathbf{x}_n^0>} \tag{22}$$

Equation (22) is the desired expression for the partial derivatives of the eigenvalues at $\rho_k = \rho_k^0$. It is important to note that Eq. (22) is not necessary true if the derivative is evaluated at some point other than ρ_k^0. It is also found that in calculating the derivative $\lambda_{n,k}^0$, only the eigenvalue and eigenfunction of the system at ρ_k^0 are needed.

The change of the eigenvalue $\Delta\lambda_n^0$ corresponding to a set of parametric increments $\Delta\rho_k$ can be approximated as

$$\Delta\lambda_n^0 = \sum_{k=1}^{l} \lambda_{n,k}^0 \Delta\rho_k. \tag{23}$$

The imaginary part of $\Delta\lambda_n^0$ determines the change of the natural frequency, and the real part determines the stability property of the system.

Spinning Disk in Contact With a Stationary Load System

Consider a circular, elastic disk rotating in contact with a stationary load system containing transverse mass m_z, spring k_z, dashpot c_z, and the analogous pitching elements I_ϕ, k_ϕ, c_ϕ, as shown in Fig. 1. In addition, the load system applies a constant friction force F_θ to the disk in the circumferential direction at the coupling point between the load system and the spinning disk. The equation of motion of this coupled system in terms of transverse displacement w and with respect to the stationary coordinate system (r, θ) can be written as (Ono et al., 1991)

$$\rho h(w_{,tt} + 2\Omega w_{,t\theta} + \Omega^2 w_{,\theta\theta}) + D\nabla^4 w - \frac{h}{r}(\sigma_r r w_{,r})_{,r} - \frac{h\sigma_\theta}{r^2} w_{,\theta\theta}$$
$$= \frac{1}{r}\delta(r-\xi)\delta(\theta)\left(F_z - \frac{F_\theta}{r} w_{,\theta}\right) - \frac{1}{r^2}\delta(r-\xi)[M_\phi \delta(\theta)]_{,\theta} \tag{24}$$

where

$$D = \frac{E h^3}{12(1-\nu^2)},\quad \nabla^4 = \left(\frac{\partial^2}{\partial r^2} + \frac{1}{r}\frac{\partial}{\partial r} + \frac{1}{r^2}\frac{\partial^2}{\partial\theta^2}\right)^2$$

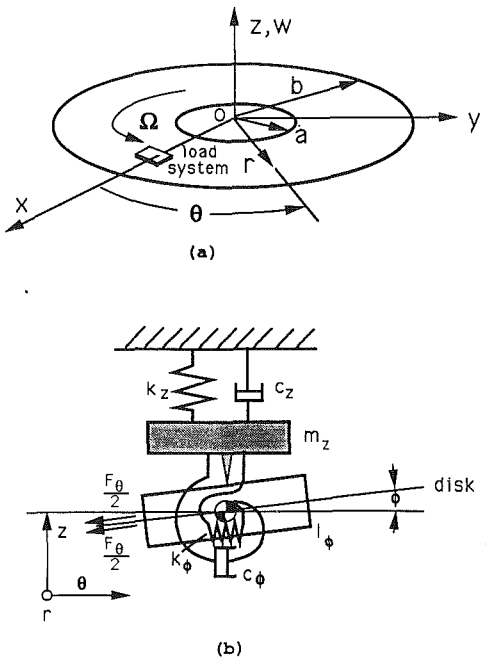


Fig. 1 *(a)* Global picture of the spinning disk and the stationary load system; *(b)* parameters in the load system

and

$$F_z = -m_z w_{,tt} - c_z w_{,t} - k_z w$$
$$M_\phi = -\frac{1}{r}(I_\phi w_{,t\theta} + c_\phi w_{,t\theta} + k_\phi w_{,\theta}).$$

The parameters Ω, ρ, h, E, and ν are the rotation speed, density, thickness, Young's modulus, and Poisson's ratio of the disk. $\delta(:)$ is the Dirac delta function. The coupling position between the load system and disk is assumed to be $r = \xi$ and $\theta = 0$. The spinning disk is clamped at the inner radius $r = a$ and free at the outer radius $r = b$. The generalized plane stresses σ_r and σ_θ due to the centrifugal effect are given by

$$\sigma_r = \Omega^2\left(C_1 + \frac{C_2}{r^2} + C_3 r^2\right),\quad \sigma_\theta = \Omega^2\left(C_1 - \frac{C_2}{r^2} + C_4 r^2\right)$$

$$C_1 = \frac{1+\nu}{8}\rho\frac{(\nu-1)a^4 - (3+\nu)b^4}{(\nu-1)a^2 - (1+\nu)b^2}$$

$$C_2 = \frac{1-\nu}{8}\rho a^2 b^2 \frac{(1+\nu)a^2 - (3+\nu)b^2}{(\nu-1)a^2 - (1+\nu)b^2}$$

$$C_3 = -\frac{3+\nu}{8}\rho,\quad C_4 = -\frac{1+3\nu}{8}\rho.$$

We neglect the effect of the friction force on these in-plane stresses because the coefficients of friction in the systems of interest are usually relatively low. By comparing with Eq. (16), we can identify the differential operators for Eq. (24) as

$$\hat{\mathbf{M}} = \mathbf{I} + \delta(r-\xi)\delta(\theta)\left(m_z^* - I_\phi^*\frac{\partial^2}{\partial\theta^2}\right) - I_\phi^*\delta(r-\xi)\delta'(\theta)\frac{\partial}{\partial\theta}$$

$$\hat{\mathbf{G}} = 2\Omega\frac{\partial}{\partial\theta} + \delta(r-\xi)\delta(\theta)\left(c_z^* - c_\phi^*\frac{\partial^2}{\partial\theta^2}\right) - c_\phi^*\delta(r-\xi)\delta'(\theta)\frac{\partial}{\partial\theta}$$

$$\hat{\mathbf{K}} = D^*\nabla^4 + \Omega^2\frac{\partial^2}{\partial\theta^2} + \mathbf{L} + \delta(r-\xi)\delta(\theta)\left(k_z^* - k_\phi^*\frac{\partial^2}{\partial\theta^2} + F_\theta^*\frac{\partial}{\partial\theta}\right)$$
$$- k_\phi^*\delta(r-\xi)\delta'(\theta)\frac{\partial}{\partial\theta}$$

where the starred quantities are defined by

Downloaded 03 May 2010 to 171.66.16.247. Redistribution subject to ASME license or copyright; see http://www.asme.org/terms/Terms_Use.cfm

$$m_z^* = \frac{m_z}{\xi\rho h} \quad c_z^* = \frac{c_z}{\xi\rho h} \quad k_z^* = \frac{k_z}{\xi\rho h} \quad F_\theta^* = \frac{F_\theta}{\xi^2\rho h}$$

$$D^* = \frac{D}{\rho h} \quad I_\phi^* = \frac{I_\phi}{\xi^3\rho h} \quad c_\phi^* = \frac{c_\phi}{\xi^3\rho h} \quad k_\phi^* = \frac{k_\phi}{\xi^3\rho h}$$

and

$$\mathbf{L} = -\frac{1}{\rho r}\frac{\partial}{\partial r}\left(\sigma_r r \frac{\partial}{\partial r}\right) - \frac{\sigma_\theta}{\rho r^2}\frac{\partial^2}{\partial \theta^2}$$

$\delta'(:)$ is the derivative of the Dirac delta function. $\mathbf{I}$ is the identity operator. $\mathbf{L}$ is called the membrane operator, and it is readily shown to be symmetric and positive definite. While Eq. (24) is not a gyroscopic equation because it involves the dissipative elements c_z and c_ϕ, as well as the friction force, F_θ, it is a standard gyroscopic equation in the special case when the right hand side vanishes, i.e., the freely spinning disk. This special case is identified as the parameter set ρ_k^0 in the above analysis. For the freely spinning disk, the eigenvalues $\lambda_{mn} = \lambda_{mn}^0$ are all purely imaginary, i.e., $\lambda_{mn}^0 = i\omega_{mn}$, where ω_{mn} is real. The corresponding eigenfunctions are in general complex, and assume the form

$$w_{mn}^0 = R_{mn}(r)\, e^{\pm in\theta}. \tag{25}$$

R_{mn} is a real-valued function of r. If we consider only the positive ω_{mn}, then w_{mn}^0 in Eq. (25) with $+in\theta$ is a backward travelling wave with n nodal diameters and m nodal circles. Similarly, w_{mn}^0 with $-in\theta$ is a forward travelling wave. The critical speed Ω_{mn}^c for the mode w_{mn}^0 is defined as the rotation speed at which ω_{mn} of the backward travelling wave vanishes. As Ω continues to increase beyond Ω_{mn}^c, this mode becomes a forward travelling wave, and is called a "reflected wave." This is illustrated in Fig. 2, which will be explained more later.

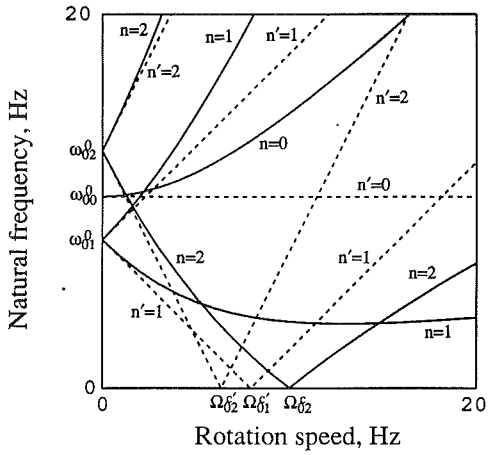


Fig. 2 Comparison of the spinning disk and the stationary disk

The Membrane Effect

In order to study the membrane effect due to the centrifugal force on the natural frequencies of the spinning disk, we compare the frequency-speed relations of a spinning disk with those of a stationary disk viewed from a reference frame rotating at speed Ω (Iwan et al., 1973). For simplicity, in the following, a "stationary disk" is understood as a stationary disk viewed from a rotating reference frame. The equation of motion for the stationary disk is the same as that of the spinning disk viewed from a stationary reference frame, except that the membrane operator disappears in the former. It follows that if the membrane terms are neglected in a spinning disk, the two equations are identical. Furthermore, the eigenfunctions for the stationary disk assume the same form as Eq. (25). Before applying Eq. (22) to investigate the membrane effect on the eigenvalues λ_{mn}, we first evaluate the denominator on the right-hand side

$$<\mathbf{x}_{mn}^0,\ \mathbf{A}\,\mathbf{x}_{mn}^0> = \int_{-\pi}^{\pi}\int_a^b (\omega_{mn}^2 \overline{w}_{mn}^0 w_{mn}^0 + \overline{w}_{mn}^0 \mathbf{K} w_{mn}^0) r\, dr\, d\theta \tag{26}$$

where

$$\mathbf{x}_{mn}^0 \equiv \begin{Bmatrix} i\omega_{mn} \\ 1 \end{Bmatrix} w_{mn}^0.$$

By using Eq. (24) with the right-hand side equal to zero, we can obtain

$$\mathbf{K}\, w_{mn}^0 = \omega_{mn}(\omega_{mn} \pm 2n\Omega) R_{mn}(r) e^{\pm in\theta} \quad \begin{cases} + & \text{for backward wave} \\ - & \text{for forward and reflected waves.} \end{cases} \tag{27}$$

It is noted that this expression is true for both the spinning disk and the stationary disk, although R_{mn} is different for each case. Substituting Eqs. (25) and (27) into (26), we get

$$<\mathbf{x}_{mn}^0,\ \mathbf{A}\,\mathbf{x}_{mn}^0> = 4\pi\omega_{mn}(\omega_{mn} \pm n\Omega)\int_a^b R_{mn}^2(r) r\, dr \quad \begin{cases} + & \text{for backward wave} \\ - & \text{for forward and reflected waves.} \end{cases} \tag{28}$$

For the case of a stationary disk, after evaluating $\mathbf{A}_{,\Omega}$ and $\mathbf{B}_{,\Omega}$, and substituting eigenfunction w_{mn}^0 in Eq. (25) into (22), we obtain

$$\frac{\partial \lambda_{mn}^0}{\partial \Omega} = \pm in \quad \begin{cases} + & \text{for forward and reflected waves} \\ - & \text{for backward wave.} \end{cases}$$

Since this derivative is purely imaginary, the change of rotation speed of the reference frame will affect the natural frequencies of the stationary disk. In addition, the slope of the frequency-speed curve is constant and proportional to the number of nodal diameters. Therefore, the relations between the natural frequencies and the rotation speed are as follows:

$$\omega_{mn} = \omega_{mn}^0 - n\Omega \quad \text{for backward wave}$$
$$\omega_{mn} = \omega_{mn}^0 + n\Omega \quad \text{for forward wave}$$
$$\omega_{mn} = -\omega_{mn}^0 + n\Omega \quad \text{for reflected wave}$$

where ω_{mn}^0 is the natural frequency of mode w_{mn}^0 at $\Omega = 0$. From these results we can conclude that $<\mathbf{x}_{mn}^0,\ \mathbf{A}\,\mathbf{x}_{mn}^0>$ in (28) is positive for forward and backward travelling waves, but negative for the reflected wave. So $\mathbf{A}$ is no longer positive definite as Ω exceeds the critical speed.

In the case of a spinning disk, for which the membrane operator $\mathbf{L}$ is present, we follow the same procedure as above to obtain

$$\frac{\partial \lambda_{mn}^0}{\partial \Omega} = in + i\frac{<w_{mn}^0, \mathbf{L} w_{mn}^0>}{2\pi\Omega(\omega_{mn} - n\Omega)\int_a^b R_{mn}^2(r) r dr} \quad \text{for forward and reflected waves} \tag{29a}$$

$$= -in + i\frac{<w_{mn}^0, \mathbf{L} w_{mn}^0>}{2\pi\Omega(\omega_{mn} + n\Omega)\int_a^b R_{mn}^2(r) r dr} \quad \text{for backward wave.} \tag{29b}$$

Downloaded 03 May 2010 to 171.66.16.247. Redistribution subject to ASME license or copyright; see http://www.asme.org/terms/Terms_Use.cfm

Since $\mathbf{L}$ is positive definite and $\omega_{mn}+n\Omega$ is always positive for a backward travelling wave, we can conclude from (29*b*) that the slope of the frequency-speed curve corresponding to a backward travelling wave in a spinning disk is always larger than that of the corresponding mode in a stationary disk, i.e., $-n$. As a result, the critical speed Ω^c_{mn} for a spinning disk is always larger than that of a stationary disk. For the forward travelling wave, $\omega_{mn}-n\Omega$ is positive for sufficiently small Ω, and because of the positive definiteness of $\mathbf{L}$, we can conclude that the slope of the frequency-speed curve is always larger than that of a stationary disk, i.e., $+n$. And consequently, $\omega_{mn}-n\Omega$ for a forward travelling wave is always positive and greater than ω^0_{mn}. On the other hand, for a reflected wave, since $\omega_{mn}-n\Omega$ is negative for sufficiently small ω_{mn}, we can conclude from Eq. (29*a*) that the slope of the frequency-speed curve is smaller than $+n$. And in turn, $\omega_{mn}-n\Omega$ is always negative and less than $-\omega^0_{mn}$. The above discussions lead to the conclusion that for a spinning disk $<\mathbf{x}^0_{mn}, \mathbf{A}\,\mathbf{x}^0_{mn}>$ in (28) is positive for forward and backward travelling waves, but negative for a reflected wave, which is exactly the same property as that of a stationary disk. Figure 2 demonstrates a comparison of the frequency-speed relations between a spinning disk and a stationary disk. The solid lines represent the frequency-speed curves for the spinning disk, and the dashed lines are those for the stationary disk. Ω^c_{mn} and n represent the critical speed and the number of nodal diameters for the mode w^0_{mn} of a spinning disk, and $\Omega^{c\prime}_{mn}$ and n' are those for the stationary disk.

Effects of the Parameters in the Load System

We investigate next how the eigenvalues of the freely spinning disk change when small load system parameters are included. As a result of the previous conclusions on the membrane effect of the spinning disk, the following discussions on the effects of various parameters in the load system will apply equally well to both the spinning disk and the stationary disk.

Transverse Mass Effect. In order to calculate the derivative of the eigenvalue λ^0_{mn} with respect to m^*_z, we first observe that

$$\frac{\partial \mathbf{A}}{\partial m^*_z}=\begin{bmatrix}\delta(r-\xi)\delta(\theta) & \mathbf{0}\\ \mathbf{0} & \mathbf{0}\end{bmatrix},\quad \frac{\partial \mathbf{B}}{\partial m^*_z}=\mathbf{0}. \tag{30}$$

After substituting Eq. (30) into (22), we get

$$\frac{\partial \lambda^0_{mn}}{\partial m^*_z}=-\frac{i\omega^3_{mn}R^2_{mn}(\xi)\xi}{<\mathbf{x}^0_{mn}, \mathbf{A}\,\mathbf{x}^0_{mn}>}. \tag{31}$$

According to Eq. (31), the effect on λ^0_{mn} of the freely spinning disk of adding a small load system mass m^*_z can be stated as follows: For the forward and backward travelling waves, adding the mass tends to decrease the natural frequency of the disk. But after a backward travelling wave becomes a reflected wave by increasing Ω beyond the critical speed, adding the mass will have the opposite effect i.e., it will increase the natural frequency of the reflected wave. In addition, by referring back to Eq. (28) it is found that the magnitude of the derivative is roughly (exactly for a stationary disk) proportional to the square of the natural frequency, so the higher natural frequency modes are more susceptible to change by the addition of a small mass.

Transverse Stiffness Effect. By a similar procedure as above, we can get

$$\frac{\partial \lambda^0_{mn}}{\partial k^*_z}=\frac{i\omega_{mn}R^2_{mn}(\xi)\xi}{<\mathbf{x}^0_{mn}, \mathbf{A}\,\mathbf{x}^0_{mn}>}. \tag{32}$$

Clearly, addition of a weak spring tends to increase the natural frequencies of the forward and backward travelling waves, but decrease the natural frequency of the reflected wave.

Suppose the load system contains both m_z and k_z with natural frequency $\omega_z=\sqrt{\dfrac{k^*_z}{m^*_z}}$. By applying Eq. (23) we obtain

$$\Delta\lambda^0_{mn}=\frac{i\omega_{mn}(\omega^2_z-\omega^2_{mn})R^2_{mn}(\xi)\xi m^*_z}{<\mathbf{x}^0_{mn}, \mathbf{A}\,\mathbf{x}^0_{mn}>}.$$

For the modes with $\omega_{mn}<\omega_z$, the load system tends to increase the natural frequencies of all the forward and backward travelling waves, but it decreases the natural frequency of the reflected wave. In other words, the stiffness effect is dominant for $\omega_{mn}<\omega_z$. For the modes with $\omega_{mn}>\omega_z$, the load system will have exactly the opposite effect on the natural frequencies and the mass effect is dominant. The natural frequencies of all the modes with $\omega_{mn}=\omega_z$ will not be affected by this load system.

Transverse Damping Effect. For the case of damping

$$\frac{\partial \lambda^0_{mn}}{\partial c^*_z}=-\frac{\omega^2_{mn}R^2_{mn}(\xi)\xi}{<\mathbf{x}^0_{mn}, \mathbf{A}\,\mathbf{x}^0_{mn}>}. \tag{33}$$

Note that this derivative is real and so the dashpot will affect the stability of the system instead of the natural frequency. For the forward and backward travelling waves, adding the damper tends to stabilize the system. On the contrary, damping increase will destabilize the reflected wave as reported in the previous studies (Iwan et al., 1976; Ono et al., 1991).

Effects of Pitching Parameters. The derivatives of λ^0_{mn} with respect to I^*_ϕ, k^*_ϕ, and c^*_ϕ are the same as the right-hand sides of Eqs. (31), (32), and (33), respectively, except that there is a multiplicative factor n^2 on the right-hand side of each equation, where n is the number of nodal diameters of mode w^0_{mn}. Therefore, the effects of the pitching parameters are the same as those of the corresponding transverse parameters, except that pitching parameters have no effect on the zero nodal diameter modes, for which $n=0$, and the effects are more pronounced for the modes with more nodal diameters.

Friction Effect. In this case,

$$\frac{\partial \lambda^0_{mn}}{\partial F^*_\theta}=\pm\frac{n\omega_{mn}R^2_{mn}(\xi)\xi}{<\mathbf{x}^0_{mn}, \mathbf{A}\,\mathbf{x}^0_{mn}>}\begin{cases}+ & \text{for forward and reflected waves}\\ - & \text{for backward wave.}\end{cases}$$

It is obvious that friction force tends to destabilize the forward travelling wave, but stabilizes both the backward travelling and the reflected waves. It is also noted that the magnitude of the derivative is proportional to the number of nodal diameters of the mode shape.

Summary and Discussions

The partial derivatives of the eigenvalues of a system are evaluated at a certain point ρ^0_k in the parameter space, at which the system is gyroscopic and stable. The results are applied to a spinning disk in contact with a stationary load system to predict the effects of the centrifugal force and various parameters in the load system on the natural frequencies and stability of the spinning disk, which can be summarized as follows:

(1) The slopes of the frequency-speed curves are greater than $+n$ and $-n$ for forward and backward travelling waves, respectively, where n is the number of nodal diameters of mode w^0_{mn}. For the reflected wave, the slope is less than $+n$.

(2) Adding a small (weak) transverse mass (spring) in the load system tends to decrease (increase) the natural frequencies of the forward and backward travelling waves, but tends to increase (decrease) the natural frequency of the reflected wave.

(3) Adding a small damper in the load system tends to stabilize the forward and backward travelling waves, but tends to destabilize the reflected wave.

(4) Effects of the pitching parameters are the same as those of the corresponding transverse parameters, except that pitch-

Downloaded 03 May 2010 to 171.66.16.247. Redistribution subject to ASME license or copyright; see http://www.asme.org/terms/Terms_Use.cfm

ing parameters have no effect on the zero nodal diameter modes.

(5) The friction force between the load system and the spinning disk tends to destabilize the forward travelling wave, but tends to stabilize the reflected and the backward travelling waves.

While the technique presented in this paper is applied to the case of a spinning disk, it is certainly applicable to other kinds of gyroscopic systems, for instance, axially moving structures. The orthogonality properties among the eigenfunctions for a gyroscopic system, in which the stiffness operator is not positive definite, will facilitate the technique of modal analysis and Green's function method for a gyroscopic system moving beyond the critical speed.

It is noted that the natural frequencies considered in this paper are restricted to be distinct. For the case of repeated eigenvalues, there are infinitely many ways of choosing orthogonal eigenfunctions corresponding to these eigenvalues. Among them there is only one set of eigenfunctions which can be substituted into Eq. (22) to evaluate the derivatives of the corresponding eigenvalues. The details of this special case will be described in a future paper by the authors.

References

D'Eleuterio, G. M. T., and Hughes, P. C., 1984, "Dynamics of Gyroelastic Continua," ASME JOURNAL OF APPLIED MECHANICS, Vol. 51, pp. 415–422.

Hutton, S. G., Chonan, S., and Lehmann, B. F., 1987, "Dynamic Response of a Guided Circular Saw," *Journal of Sound and Vibration*, Vol. 112, pp. 527–539.

Iwan, W. D., and Stahl, K. L., 1973, "The Response of an Elastic Disk With a Moving Mass System," ASME JOURNAL OF APPLIED MECHANICS, Vol. 40, pp. 445–451.

Iwan, W. D., and Moeller, T. L., 1976, "The Stability of a Spinning Elastic Disk With a Transverse Load System," ASME JOURNAL OF APPLIED MECHANICS, Vol. 43, pp. 485–490.

Lancaster, P., 1966, *Lambda-Matrices and Vibrating Systems*, Pergamon Press, Oxford, U.K.

Meirovitch, L., 1974, "A New Method of Solution of the Eigenvalue Problem for Gyroscopic Systems," *AIAA Journal*, Vol. 12, pp. 1337–1342.

Ono, K., Chen, J.-S., and Bogy, D. B., 1991, "Stability Analysis for the Head-Disk Interface in a Flexible Disk Drive," ASME JOURNAL OF APPLIED MECHANICS, Vol. 58, pp. 1005–1014.

Shen, I. Y., and Mote, C. D., 1991, "On the Mechanisms of Instability of a Circular Disk Under a Rotating Mass-Spring-Damper System," *Journal of Sound and Vibration*, Vol. 148, pp. 307–318.

Downloaded 03 May 2010 to 171.66.16.247. Redistribution subject to ASME license or copyright; see http://www.asme.org/terms/Terms_Use.cfm

Frequency Window Method for Strongly Coupled and Multiply Connected Structural Systems: One-Mode Windows

Kyung-Won Min

Takeru Igusa

Jan D. Achenbach
Fellow ASME

Robert R. McCormick School of Engineering and Applied Science, Department of Civil Engineering, Northwestern University, Evanston, IL 60208

A method is presented to analyze the dynamic behavior of a structural system consisting of a main structure and strongly coupled, multiply connected substructures. Lagrange's equations are used to develop a characteristic equation for connected substructures in terms of substructure impedances and mobilities. Then, a frequency window method is used to reduce the complexity of the problem by a decomposition of the impedance and mobility functions into dominant and high-order rational expressions. From the reduced problem, simple expressions for the modal properties are developed using matrix algebraic methods, which provide insight into the resonance characteristics of the connected substructures. Higher-order terms, which become significant for strongly coupled substructures, are included in the eigenvalue analysis by using an iterative procedure. It is shown that the frequency window method developed in this paper, used as a numerical scheme, produces results which converge to exact results after only a few iterations.

1 Introduction

The dynamic characteristics of a main structure with connected substructures have complex and interesting features. Many theoretical approaches have been developed for the dynamic analysis of such systems. Mode synthesis (Hurty and Rubinstein, 1964) and statistical energy analysis (Lyon, 1975) are standard methods for investigating the low and high-frequency response characteristics, respectively.

Recently, demands on light weight, high strength, and low noise or vibration have led to the design of complicated structural systems. Although finite elements, mode synthesis, and statistical energy analysis can be used to compute the dynamic response of such systems, the structural complexity has made the interpretation of the results of such analyses difficult. Many researchers in dynamic analysis have sought to further develop existing theories or develop alternate methods to obtain greater insight in the behavior of connected substructures. Gladwell and Bishop (1960), Nicholson and Bergman (1986), and Kelkel (1987) used Green's functions of vibrating continuous structures; Jacquot and Soedel (1970) used modal expansions and substructure impedances to formulate the equations of motion; Hallquist and Snyder (1973) used "tie-vectors" to develop equations for combined substructures; Leissa (1974) investigated curve-veering phenomena in coupled modes; Dowell (1979) used Lagrange multipliers for the constraints at the interface of connected structures; Sackman and Kelly (1979), Sackman et al. (1983), and Igusa and Der Kiureghian (1985) have combined mode synthesis concepts, matrix algebraic theory, and perturbation methods for characterizing weakly coupled substructures; and Keane and Price (1987) and Pinnington and White (1981) have extended statistical energy analysis and power flow techniques.

Recently, Igusa, Achenbach, and Min (1990a,b) have developed a new technique to analyze the dynamic characteristics of coupled, continuous substructures. Their analysis begins with the eigenvalue problem for the combined system which is derived from Lagrange's equations and is recast in terms of modal expansions of the substructure impedances and the main structure mobility. The central concept of the technique is a frequency window method wherein detail, in both the mathematical and the computational sense, is maintained for frequency terms which lie within a range of interest. Terms outside the window are also retained, but with less detail. The authors take advantage of the complexity reduction by developing simple expressions for the system modal properties which provide new insight into the dynamic characteristics of connected, continuous substructures.

The theory developed by Igusa et al. (1990a,b) has two significant limitations: First, the substructure supports were restricted to rigid, single-point connections. Second, for simplicity, some higher-order terms in the substructure impedances and mobilities were neglected, which led to inaccuracies in the

Contributed by the ASME Applied Mechanics Division of THE AMERICAN SOCIETY OF MECHANICAL ENGINEERS for presentation at the Winter Annual Meeting, Atlanta, Ga., Dec. 1-6, 1991.

Discussion on this paper should be addressed to the Technical Editor, Prof. Leon M. Keer, The Technological Institute, Northwestern University, Evanston, IL 60208, and will be accepted until two months after final publication of the paper itself in the JOURNAL OF APPLIED MECHANICS. Manuscript received by the ASME Applied Mechanics Division, June 19, 1990; final revision, Feb. 26, 1991.

Paper No. 91-WA/APM-23.

Copyright © 1992 by ASME

Downloaded 03 May 2010 to 171.66.16.247. Redistribution subject to ASME license or copyright; see http://www.asme.org/terms/Terms_Use.cfm

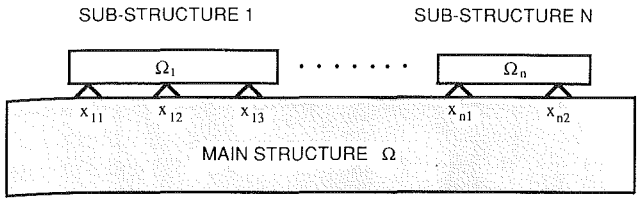


Fig. 1 Structural system

analysis of strongly coupled substructures. In this paper, these limitations have been removed.

First, continuous substructures with multiple-point connections are considered, which, unlike substructures with single-point connections, contain static and dynamic force effects arising from differential support motions. Second, higher-order terms in the substructure impedances and mobilities are included in the eigenvalue analysis through the introduction of dynamic coupling matrices. It is found that the approach, used with an iterative procedure, enhances numerical accuracy of the solutions for the combined system modal properties, particularly for strongly coupled substructures.

The basic configuration examined herein is a "main" structure which supports a number of substructures (see Fig. 1). The plan of analysis is as follows: The partial differential equations for the motion of the continuous system is reformulated in terms of the modal coordinates of each individual substructure using Lagrange's equations, where Lagrange multipliers are used for the constraints at the connections. The resulting set of equations, which are similar to those developed by Jacquot and Soedel (1970) and Dowell (1979), can be solved numerically to obtain the modal properties of the combined structure. In this paper, the equations are developed further to gain insight into the characteristics and complexity of the problem.

First, the equations are reduced by including only the motion of the connection points as independent variables. The resulting equations, which are in matrix polynomial form, are in terms of mobilities of the main structure and impedances of the substructures. Next, the relationship between the complexity of the problem, measured by the degree of the polynomials in the characteristic equation, and the substructure coupling, measured by the modal masses and cross-mobility terms of the main structure and substructures, is established using perturbation methods. By separating the higher-order terms in the expressions, the complexity of the problem is reduced. Insight of the dominant system characteristics is obtained by the formulation of simple analytical expressions for several fundamental cases. These expressions contain physically meaningful parameters which quantify the dynamic coupling effects and which are in terms of the modal properties of the main structure and substructures.

The mathematics is developed for one dimensional structures to avoid complications in notation. The theory, however, can be generalized to three-dimensional elastic bodies by making appropriate changes in the notation.

The entire procedure of analysis is illustrated by examples of multiply connected beams.

2 Formulation

Consider the structural system illustrated in Fig. 1 consisting of a main structure with domain Ω, and n substructures with domains Ω_k, $k=1, \ldots, n$. Substructure k is simply connected to the main structure at $l(k) \geq 1$ support locations defined by the vector $\mathbf{x}_k = \{x_{k1}, \ldots, x_{kl(k)}\}$. Throughout the paper, vectors and matrices are denoted by bold lower case letters and bold upper case letters, respectively. The total number of support points on the main structure is denoted

$$l(0) = \sum_{k=1}^{n} l(k).$$

The dynamic properties of the main structure are described by mode shapes, $\phi_i(x)$, natural frequencies, ω_i, and mass density $\rho(x)$, where $x \in \Omega$ is the coordinate vector and the mode shapes are normalized with respect to the mass density. Similarly, the dynamic properties of each substructure k are described by normalized mode shapes, $\psi_{kj}(x)$, for fixed support points, natural frequencies, ω_{kj}, and mass densities $\rho_k(x)$.

It is necessary to introduce functions describing the static response characteristics of each substructure k. Let the $l(k)$-component vector $\mathbf{p}_k(x)$ be the static displacement function in which the ith element of $\mathbf{p}_k(x)$ corresponds to the continuous displacement of substructure k resulting from a unit displacement applied at support i with all other supports fixed. Let the $l(k) \times l(k)$ matrix $\mathbf{S}_k$ be the static stiffness matrix for substructure k in the which the (i,j)th element of $\mathbf{S}_k$ corresponds to the reaction force at support i resulting from unit force applied at support j with all other supports fixed.

In the following, Lagrange's equations are used to develop a characteristic equation for the combined system using the impedances and mobilities of the substructures which are expressed in terms of $\varphi_i(x)$, $\psi_{kj}(x)$, $\mathbf{p}_k(x)$, and $\mathbf{S}_k$. This characteristic equation will be treated by the frequency window method (Igusa et al., 1990a,b) to determine the modal properties of the combined system.

For harmonic response, the free vibration displacement fields are given by

$$w(x,t) = \sum_{i=1}^{\infty} a_i \varphi_i(x) e^{-i\omega t} \tag{1}$$

for the main structure, where $x \in \Omega$ and

$$w_k(x,t) = \left[\sum_{j=1}^{\infty} b_{kj} \psi_{kj}(x) + \mathbf{f}_k^T \mathbf{p}_k(x) \right] e^{-i\omega t}, \tag{2}$$

for substructure k, where $x \in \Omega_k$. The coefficients a_i and b_{kj} are modal coordinates and $\mathbf{f}_k$ is the $l(k)$vector which defines the displacements of the support points of the kth substructure. In the following, the omnipresent harmonic term $e^{-i\omega t}$ will not be explicitly included in the equations with the understanding that all response expressions are multiplied by this term.

Following standard modal procedures for the Lagrange's equations formulation (Dowell, 1979), the kinetic energy, K, and potential energy, U, are given by

$$K = \frac{1}{2}\omega^2 \left\{ \sum_{i=1}^{\infty} a_i^2 + \sum_{k=1}^{\infty} \left[\sum_{j=1}^{\infty} b_{kj}^2 + 2 \sum_{j=1}^{\infty} b_{kj} \mathbf{f}_k^T \mathbf{m}_{kj} + \mathbf{f}_k^T \mathbf{M}_{kpp} \mathbf{f}_k \right] \right\}, \tag{3}$$

$$U = \frac{1}{2} \left\{ \sum_{i=1}^{\infty} a_i^2 \omega_i^2 + \sum_{k=1}^{\infty} \sum_{j=1}^{\infty} b_{kj}^2 \omega_{kj}^2 + \sum_{k=1}^{\infty} \mathbf{f}_k^T \mathbf{S}_k \mathbf{f}_k \right\}. \tag{4}$$

For each substructure k,

$$\mathbf{M}_{kpp} \equiv \int_{\Omega_k} \mathbf{p}_k(x) \mathbf{p}_k^T(x) \rho_k(x) dx \tag{5}$$

is an $l(k) \times l(k)$ modal mass matrix in which the (i,j)th element of $\mathbf{M}_{kpp}$ represents the coupling between the ith and jth elements of $\mathbf{p}_k(x)$. (The product in the integrand is an outer product between a column vector and a row vector.)

Also, for each substructure k,

$$\mathbf{m}_{kj} \equiv \int_{\Omega_k} \mathbf{p}_k(x) \psi_{kj}(x) \rho_k(x) dx \tag{6}$$

is an $l(k)$-component modal mass vector in which the ith element of $\mathbf{m}_{kj}$ represents the coupling between the ith element

Downloaded 03 May 2010 to 171.66.16.247. Redistribution subject to ASME license or copyright; see http://www.asme.org/terms/Terms_Use.cfm

of $\mathbf{p}_k(x)$ and the jth mode shape of the main structure. The physical dimensions of $\mathbf{M}_{kpp}$ and $\mathbf{m}_{kj}$ are mass and $(\text{mass})^{1/2}$, respectively, due to the mass normalization of the mode shape $\psi_{kj}(x)$.

The constraints of the system are specified by the displacements at the support locations $\mathbf{x}_k$. Equating the displacements of substructure k with those of the main structure yields

$$\mathbf{f}_k = \sum_{i=1}^{\infty} a_i \boldsymbol{\phi}_{ik}, \tag{7}$$

where $\boldsymbol{\phi}_{ik} = \{\phi_i(x_{k1}), \ldots, \phi_i(x_{kl(k)})\}^T$ is the $l(k)$vector of displacements corresponding to mode i of the main structure at support points $\mathbf{x}_k$. Using an $l(k)$vector of Lagrange multipliers, $\boldsymbol{\lambda}_k$, for the displacements constraints of each substructure k in Eq. (7), the Lagrange's equations of motion are

$$(\omega_i^2 - \omega^2)a_i + \boldsymbol{\lambda}_k^T \boldsymbol{\phi}_{ik} = 0, \tag{8}$$

$$(\omega_{kj}^2 - \omega^2)b_{kj} - \omega^2 \mathbf{f}_k^T \mathbf{m}_{kj} = 0, \tag{9}$$

$$\omega^2 \left\{ \mathbf{M}_{kpp}\mathbf{f}_k + \sum_{j=1}^{\infty} b_{kj}\mathbf{m}_{kj} \right\} - \mathbf{S}_k \mathbf{f}_k + \boldsymbol{\lambda}_k = 0. \tag{10}$$

The modal properties of the entire assemblage of connected substructures are determined by solving the above equations. This can be performed numerically for any particular example. However, in this paper analytical results are sought in order to gain insight into the general problem, therefore further mathematical analysis is performed.

The Lagrange's Eqs. (8)–(10) are condensed by using the support motions $\mathbf{f}_k$ as the unknown variables. First, Eq. (9) is used to express b_{kj} in terms of $\mathbf{f}_k$

$$b_{kj} = \frac{\omega^2}{\omega_{kj}^2 - \omega^2} \mathbf{m}_{kj}^T \mathbf{f}_k. \tag{11}$$

Substituting b_{kj} in Eq. (10) and solving for the Lagrange multipliers results in expressions in terms of $\mathbf{f}_k$. Combining the result with Eq. (8) yields expressions for a_i in terms of $\mathbf{f}_k$ as

$$a_i = \frac{\omega^2}{\omega_i^2 - \omega^2} \sum_{k=1}^{n} \boldsymbol{\phi}_{ik}^T \left\{ \mathbf{M}_{kpp} - \frac{\mathbf{S}_k}{\omega^2} + \sum_j \frac{\omega^2}{\omega_{kj}^2 - \omega^2} \mathbf{m}_{kj}\mathbf{m}_{kj}^T \right\} \mathbf{f}_k. \tag{12}$$

It can be shown that the terms in the braces are proportional to the $l(k) \times l(k)$ impedance matrix $\mathbf{Z}_k(\omega)$ of substructure k in which the (i,j)th element of $\mathbf{Z}_k(\omega)$ corresponds to the reaction force divided by $e^{-i\omega t}$ at support i resulting from a velocity $e^{-i\omega t}$ applied at support j with all other supports fixed. The modal expression for $\mathbf{Z}_k(\omega)$ is

$$\mathbf{Z}_k(\omega) = -i\omega \left\{ \mathbf{M}_{kpp} - \frac{\mathbf{S}_k}{\omega^2} + \sum_{j=1}^{\infty} \frac{\omega^2}{\omega_{kj}^2 - \omega^2} \mathbf{m}_{kj}\mathbf{m}_{kj}^T \right\}, \tag{13}$$

which, when substituted into Eq. (12) yields the modal coefficients a_i as

$$a_i = \frac{i\omega}{\omega_i^2 - \omega^2} \sum_{k=1}^{n} \boldsymbol{\phi}_{ik}^T \mathbf{Z}_k \mathbf{f}_k \tag{14}$$

where $i = \sqrt{-1}$ (which is not italic, to distinguish it from the subscript i).

Equations (11) and (14) give the motion of the substructures and the main structure, respectively, in terms of the motions $\mathbf{f}_k$ at the supports. The support motion is obtained by substituting Eq. (7) into Eq. (14) and switching the order of summation. The result is

$$\mathbf{f}_k = \sum_{l=1}^{\infty} \left\{ \sum_{i=1}^{\infty} \frac{i\omega}{\omega_i^2 - \omega^2} \boldsymbol{\phi}_{ik}\boldsymbol{\phi}_{il}^T \right\} \mathbf{Z}_l \mathbf{f}_l. \tag{15}$$

It is well known (Lin, 1976) that the summation in the brackets is the $l(k) \times l(k)$ mobility matrix $\mathbf{N}_{kl}(\omega)$ of the main structure. The (i,j)th element of $\mathbf{N}_{kl}(\omega)$ is the response velocity divided by $e^{-i\omega t}$ at support i of substructure k resulting from a force $e^{-i\omega t}$ applied at support j of substructure l with all other supports free. We have

$$\mathbf{N}_{kl}(\omega) \equiv \sum_{i=1}^{\infty} \frac{-i\omega}{\omega_i^2 - \omega^2} \boldsymbol{\phi}_{ik}\boldsymbol{\phi}_{il}^T. \tag{16}$$

Substituting the mobility function into Eq. (12) and recasting the results in matrix form yields

$$[\mathbf{I}_{l(0)} + \mathbf{N}(\omega)\text{diag}\{\mathbf{Z}_1(\omega), \ldots, \mathbf{Z}_n(\omega)\}]\mathbf{f} = 0, \tag{17}$$

where $\mathbf{I}_l$ denotes the $l \times l$ identity matrix, $\mathbf{N}(\omega)$ is the $l(0) \times l(0)$ mobility matrix of all support points of the main structure given by

$$\mathbf{N}(\omega) \equiv \begin{bmatrix} \mathbf{N}_{11}(\omega) & \ldots & \mathbf{N}_{1n}(\omega) \\ \vdots & \ddots & \vdots \\ \mathbf{N}_{n1}(\omega) & \ldots & \mathbf{N}_{nn}(\omega) \end{bmatrix} = \sum_{i=1}^{\infty} \frac{-i\omega}{\omega_i^2 - \omega^2} \boldsymbol{\phi}_i \boldsymbol{\phi}_i^T \tag{18}$$

and diag $\{.\}$ represents a block diagonal matrix with diagonally aligned submatrices listed in the braces. Here, $\boldsymbol{\phi}_i$ is the $l(0)$ vector of displacements corresponding to mode i of the main structure at all support points

$$\boldsymbol{\phi}_i \equiv [\boldsymbol{\phi}_{i1}^T \ \ldots \ \boldsymbol{\phi}_{in}^T]^T, \tag{19}$$

and $\mathbf{f}$ is the $l(0)$ vector of all support displacements

$$\mathbf{f} = [\mathbf{f}_1^T \ \ldots \ \mathbf{f}_n^T]^T. \tag{20}$$

In summary, the eigenvalue problem obtained through Lagrange's equations has been reformulated in analytical form in terms of the mobilities of the main structure and impedances of the substructures. The result, given by Eq. (17), is an eigenvalue problem for the system in rational matrix polynomial form which is similar to the results by Jacquot and Soedel (1970) and Dowell (1979). This form of the eigenvalue problem is not commonly used in structural dynamics, and extensive computer algorithms do not exist for its solution. However, it has certain mathematical properties which facilitate further analytical treatment. In the following sections, Eq. (17) will be used to examine system complexity and the characteristics of substructure resonances and coupling using a frequency window method developed by Igusa et al. (1990a,b).

3 Frequency Windows

The complexity of the eigenvalue problem is reduced by using a frequency window centered about the frequencies of interest. The rational polynomials in Eqs. (13) and (16) are decomposed into sums of two rational polynomials:

$$\mathbf{Z}_k(\omega) \approx \mathbf{Z}_{k0}(\omega, \omega_0, \delta) + \mathbf{Z}_{k1}(\omega_0, \delta), \tag{23}$$

$$\mathbf{N}(\omega) \approx \mathbf{N}_0(\omega, \omega_0, \delta) + \mathbf{N}_1(\omega_0, \delta), \tag{24}$$

where the poles of the first function in the sums are within the frequency window, the poles of the second function lie outside the window, ω_0 is the central frequency value, and δ is the width of the window.

It is convenient to define the following index sets to indicate the modes within a frequency window:

$$I(\omega_0, \delta) \equiv \{\text{all } i \text{ such that } |\omega_i - \omega_0| < \delta\}, \tag{25}$$

$$I(\omega_0, \delta, k) \equiv \{\text{all } kj \text{ such that } |\omega_{kj} - \omega_0| < \delta\}, \tag{26}$$

where it is understood that single indices i refer to mode i of the main structure and double indices kj refer to mode j of substructure k. According to the index sets, $\mathbf{Z}_{k0}(\omega, \omega_0, \delta)$ and $\mathbf{N}_0(\omega, \omega_0, \delta)$ are the dominant terms of the impedance and mobility, respectively, defined by

$$\mathbf{Z}_{k0}(\omega, \omega_0, \delta) = \sum_{j \in I(\omega_0, \delta, k)} \frac{-i\omega_0^3}{\omega_{kj}^2 - \omega^2} \mathbf{m}_{kj}\mathbf{m}_{kj}^T, \tag{27}$$

$$\mathbf{N}_0(\omega, \omega_0, \delta) = \sum_{i \in I(\omega_0, \delta)} \frac{-i\omega_0}{\omega_i^2 - \omega^2} \boldsymbol{\phi}_i \boldsymbol{\phi}_i^T, \tag{28}$$

Downloaded 03 May 2010 to 171.66.16.247. Redistribution subject to ASME license or copyright; see http://www.asme.org/terms/Terms_Use.cfm

and $\mathbf{Z}_{k1}(\omega_0,\delta)$ and $\mathbf{N}_1(\omega_0,\delta)$ are the higher-order terms of the impedance and mobility, respectively, defined by

$$\mathbf{Z}_{k1}(\omega_0,\delta) = -i\omega_0\left\{\mathbf{M}_{kpp} - \frac{\mathbf{S}_k}{\omega_0^2} + \sum_{j\notin I(\omega_0,\delta,k)} \frac{\omega_0^2}{\omega_{kj}^2-\omega_0^2}\mathbf{m}_{kj}\mathbf{m}_{kj}^T\right\}, \quad (29)$$

$$\mathbf{N}_1(\omega_0,\delta) = \sum_{i\notin I(\omega_0,\delta)} \frac{-i\omega_0}{\omega_i^2-\omega_0^2}\boldsymbol{\phi}_i\boldsymbol{\phi}_i^T. \quad (30)$$

Substituting Eqs. (23) and (24) into the characteristic Eq. (17) yields an approximate formulation of the eigenvalue problem which has rational polynomials with lower order than the original equations, and hence reduced complexity. The problem reduction described above and its subsequent analytical treatment was developed by Igusa et al. (1990a,b) and is called the frequency window method. It was shown that the approximate results are in good agreement with exact ones for weakly coupled substructures. However, inaccuracies were observed in the approximate results for strongly coupled substructures. These arise from the effects of higher-order terms in the substructure impedances and mobilities which were neglected in the analysis.

In the present paper, the frequency window method is extended in two ways: First, multiple-point connections for each substructure are considered. These give rise to the additional support stiffness term, $\mathbf{S}_k$, in Eq. (13) and in the development of generalized masses, $\mathbf{M}_{kpp}$ and $\mathbf{m}_{kj}$ in the impedance and mobility functions. Second, higher-order terms in the substructure impedances and mobilities are included in the eigenvalue analysis. This increases the numerical accuracy of the approximate results for strongly coupled substructures.

The general form of the results is still too complicated to provide insight into the dynamic characteristics of the system. However, for several fundamental cases, it is possible to reduce the complexity of the problem into an analytically tractable form. In the next sections, one and two-mode windows are examined and simple expressions for the modal properties of the combined system are derived. Next, more general windows are examined based on the approach developed for one and two-mode cases.

4 One-Mode Windows

For the simplest and most fundamental cases, the frequency window contains only one mode, and $I(\delta,\omega_0)$ has only a single element. For these cases a main structure or a substructure natural frequency is not in a neighborhood of all remaining natural frequencies of the complete structure. There are two possible types of one-mode windows given, defined by the following representations of $I(\delta,\omega_0)$:

$$\{kj\} \text{ and } \{i\}$$

which correspond to a single mode of the substructure k and the main structure, respectively. Each type is examined in detail in the next sections.

4.1 Mode $\{kj\}$. First, the case of mode $\{kj\}$ is studied, where, without any loss of generality, it is assumed that the index for substructure k is 1. The jth frequency of substructure one, ω_{1j}, is the only frequency within the frequency window. The index sets used in Eqs. (25) and (26) are simply $I(\omega_0,\delta) = \{\ \}$, $I(\omega_0,\delta,1) = \{1j\}$, and $I(\omega_0,\delta,l) = \{\ \}$ for $l \neq 1$ and it is natural to let $\omega_0 = \omega_{1j}$ be the central frequency in the analysis. The index sets are applied to the decomposition of the mobilities and impedances in Eqs. (23)–(30) and the approximate results are subsequently introduced in Eq. (17) to yield the following eigenvalue problem

$$[\mathbf{I}_{l(0)} + \mathbf{N}(\omega_0)\text{diag}\{\mathbf{Z}_{10}(\omega,\omega_0,\delta) + \mathbf{Z}_{11}(\omega_0,\delta),\ \mathbf{Z}_2(\omega_0),\ \ldots,\ \mathbf{Z}_n(\omega_0)\}]\mathbf{f} = 0, \quad (31)$$

where

$$\mathbf{Z}_{10}(\omega,\omega_0,\delta) = \frac{-i\omega_0^3}{\omega_{1j}^2-\omega^2}\mathbf{m}_{1j}m_{1j}^T \quad (32)$$

and the $l(1)\times l(1)$ matrix $\mathbf{Z}_{11}(\omega_0,\delta)$ is given by Eq. (29).

There are three steps to solving this problem: finding the natural frequency, ω; finding the component, $\mathbf{f}_1$, of the mode shape; and finding the remaining components, $\mathbf{f}_2, \ldots, \mathbf{f}_n$, of the mode shape. The first two steps are performed by expanding the second term in brackets in Eq. (31) as a sum of matrix products, considering only the first $l(1)$ components of the problem, and premultiplying Eq. (31) by the $l(0)\times l(0)$ matrix

$$\mathbf{J} = [\mathbf{I}_{l(0)} + \mathbf{N}(\omega_0)\text{diag}\{\mathbf{Z}_{11}(\omega_0,\delta),\ \mathbf{Z}_2(\omega_0),\ \ldots,\ \mathbf{Z}_n(\omega_0)\}]^{-1}$$

The result is

$$\left[\mathbf{I}_{l(1)} + \sum_{m=1}^{n}\mathbf{J}_{1m}\mathbf{N}_{m1}(\omega_0)\mathbf{Z}_{10}(\omega,\omega_0,\delta)\right]\mathbf{f}_1 = \left[\mathbf{I}_{l(1)} + \frac{-i\omega_0^3}{\omega_{1j}^2-\omega^2}\sum_{m=1}^{n}\mathbf{J}_{1m}\mathbf{N}_{m1}(\omega_0)\mathbf{m}_{1j}\mathbf{m}_{1j}^T\right]\mathbf{f}_1 = 0 \quad (33)$$

where $\mathbf{J}_{km}$ denotes the $l(k)\times l(m)$ submatrix of $\mathbf{J}$ with rows corresponding to the support displacements of substructure k and columns corresponding to the support displacements of substructure m. The matrix $\mathbf{J}_{km}$ includes the higher-order terms of the impedance and mobility matrices, and is an additional term which was not included in the original development of the frequency window method developed by Igusa et al. (1990a,b).

It might seem that the eigenvalue problem in Eqs. (33) is of order $l(1)\times l(1)$. However, the outer product $\mathbf{m}_{1j}\mathbf{m}_{1j}^T$ is an $l(1)\times l(1)$ matrix which is composed of column vectors which are all scalar multiples of $\mathbf{m}_{1j}$, which, by definition, means that the matrix is rank one (Bishop et al., 1965). It is shown in the following how this property can be used to reduce the eigenvalue problem in Eq. (33) to 1×1 (i.e., scalar) form. This scalar eigenvalue problem is obtained from Eq. (33) by premultiplying by $\mathbf{m}_{1j}^T$ and defining

$$q_1 \equiv \frac{\omega_0^2}{\omega_{1j}^2-\omega^2}\mathbf{m}_{1j}^T\mathbf{f}_1, \quad (34)$$

to yield the scalar equation

$$\left[\omega_{1j}^2 - \omega^2 - i\omega_0^3\mathbf{m}_{1j}^T\sum_{m=1}^{n}\mathbf{J}_{1m}\mathbf{N}_{m1}(\omega_0)\mathbf{m}_{1j}\right]q_1\omega_0^{-2} = 0. \quad (35)$$

The frequency is obtained immediately as

$$\omega = \omega_{1j}\left(1 - \frac{\omega_0^2}{\omega_{1j}^2}\gamma_1\right)^{1/2}, \quad (36)$$

where

$$\gamma_1 = i\omega_0\mathbf{m}_{1j}^T\sum_{m=1}^{n}\mathbf{J}_{1m}\mathbf{N}_{m1}(\omega_0)\mathbf{m}_{1j}. \quad (37)$$

The scalar constant γ_1 is dimensionless. It measures the effect of the main structure flexibility at the support points of substructure one on the natural frequency of the combined system. If $\gamma_1 = 0$, then the main structure acts as a rigid support and the natural frequency of the combined system is identical to that of the fixed-base substructure, as expected. Positive real values for γ_1 correspond to a flexible support and result in a reduction of the natural frequency.

It can be shown, by examination of the mass terms in Eq. (37), that γ_1 is proportional to the ratio of the mass of substructure one and the mass of the main structure, i.e., if the mass density $\rho_1(x)$ of substructure one is multiplied by a scalar c and all other dynamic properties of the problem are fixed, then γ_1 is also multiplied by c. The implication is that as the

Downloaded 03 May 2010 to 171.66.16.247. Redistribution subject to ASME license or copyright; see http://www.asme.org/terms/Terms_Use.cfm

mass of a substructure becomes small relative to the mass of the main structure, the parameter γ_1 approaches zero, and the main structure behaves as a rigid support, as explained earlier. These mathematical conclusions agree with the physical interpretation of the dynamics problem. The term *support flexibility parameter* is applied to γ_1, and the parameter reappears in more general form for other mode cases.

At this point in the analysis, it is possible to give a mathematical definition of coupling. In the context of the frequency window method, the dynamic coupling that is of interest is between groups of modes. For the case of mode $\{kj\}$, there are two groups of modes which can be considered as modes within and outside the frequency window, respectively. Coupling between modes within the outside group is quantified by the second term in $\mathbf{J}$, i.e., $\mathbf{N}(\omega_0)\text{diag}\{\mathbf{Z}_{11}(\omega_0,\delta), \mathbf{Z}_2(\omega_0), \ldots, \mathbf{Z}_n(\omega_0)\}$. Coupling between the two groups of modes is quantified by the parameter γ_1. When both of these terms are small in relation to unity, the coupling is defined to be weak; otherwise, the coupling is strong.

This coupling definition is used to make some observations on the natural frequency given by Eq. (36). For weakly coupled substructures, $\mathbf{J}_{11} \approx \mathbf{I}_{l(1)}$ and $\mathbf{J}_{m1} \approx 0$ for $m \neq 1$, and Eqs. (36) and (37) become nearly identical to the corresponding expressions developed for substructures with single-point supports in Igusa et al. (1990a,b). These simplified expressions contain information of mode $1j$ of substructure one and the modes of the main structure, only. For strongly coupled substructures, the expressions for the natural frequency contain characteristics of all substructure modes.

The central frequency ω_0 used in Eqs. (31)–(37) is an estimate of the combined-system natural frequency corresponding to mode $1j$. For weakly coupled substructures, γ_1 is small in relation to unity and the combined-system natural frequency ω is nearly equal to the jth frequency of substructure one, ω_{1j}. Thus, in such cases it is natural to assign the central frequency ω_0 to ω_{1j}. However, for strongly coupled substructures, where γ_1 is not small in relation to unity, updating of ω_0 is necessary to improve the accuracy of the results. This is performed by the following iterative procedure: The substructure natural frequency ω_{1j} is used for the first value ω_0 and Eq. (36) is evaluated to obtain an initial estimate for the combined system natural frequency ω. This estimate, in turn, is used as the second value for ω_0 to obtain a second estimate for ω. This process is continued until convergence is achieved. It can be shown, by substitution, that the limit of the sequence of estimates for ω is the exact value of the natural frequency. This numerical procedure can be enhanced by using more sophisticated nonlinear solver schemes; however, this is beyond the scope of this paper.

The $l(1)$ components of the mode shape, $\mathbf{f}_1$, is determined by substituting the result for the natural frequency in Eq. (36) into the original $l(1) \times l(1)$ eigenvalue Eq. (33); expressing the result in terms of q_1 using Eq. (34); and setting the undetermined scalar q_1 equal to 1. The result is

$$\mathbf{f}_1 = \mathrm{i}\omega_0 \sum_{m=1}^{n} \mathbf{J}_{1m}\mathbf{N}_{m1}(\omega_0)\mathbf{m}_{1j}. \tag{38}$$

The remaining components of the mode shape are determined by premultiplying Eq. (31) by $\mathbf{J}$, substituting Eq. (38) for the first $l(1)$ components of $\mathbf{f}$, and solving for the remaining components of $\mathbf{f}$. The result is

$$\mathbf{f}_k = \mathrm{i}\omega_0 \sum_{m=1}^{n} \mathbf{J}_{km}\mathbf{N}_{m1}(\omega_0)\mathbf{m}_{1j}, \tag{39}$$

for $k = 2, \ldots, n$, which is similar to Eq. (38).

For weakly coupled substructures, the mode shape $\mathbf{f}$ has a simple physical interpretation: The components of $\mathbf{f}$ correspond to the response of the main structure, without attached substructures, resulting from an array of input harmonic forces of magnitude $\omega_0^2\mathbf{m}_{1j}$ applied at the support locations of substructure one.

As explained in Section 2, the $l(0)$ vector $\mathbf{f}$, which consists of the components of the mode shape at the support points, is used to determine the mode shapes for the remainder of the structure. The mode shapes are given by Eqs. (1) and (2) where the modal coordinates a_i and b_{kj} are determined by Eqs. (11) and (12). Substituting Eqs. (38) and (39) into Eqs. (11) and (12) yields

$$b_{kh} = \frac{\mathrm{i}\omega^3}{\omega_{kh}^2 - \omega^2}\mathbf{m}_{kh}^T \sum_{m=1}^{\infty} \mathbf{J}_{km}\mathbf{N}_{m1}(\omega_0)\mathbf{m}_{1j}, \quad \text{for } kh \neq 1j, \tag{40}$$

$$b_{1j} = \frac{\omega_{1j}^2}{\omega_0^2} - \gamma_1, \tag{41}$$

$$a_i = \frac{-\omega^2}{\omega_i^2 - \omega^2} \sum_{k=1}^{n} \boldsymbol{\phi}_{ik}^T\mathbf{Z}_k \sum_{m=1}^{n} \mathbf{J}_{km}\mathbf{N}_{m1}(\omega_0)\mathbf{m}_{1j}. \tag{42}$$

The modal coordinates b_{kh} and a_i become larger as the corresponding substructure natural frequencies ω_{kh} and ω_i approach the combined system natural frequency ω. The largest modal coordinate is b_{1j}, which corresponds to the mode $1j$ under study.

4.2 Mode $\{i\}$. In mode case $\{i\}$, the ith frequency of the main structure, ω_i, is the only substructure frequency within the frequency window. The index sets are $I(\omega_0,\delta) = \{i\}$ and $I(\omega_0,\delta,k) = \{\ \}$ and it is natural to let $\omega_0 = \omega_i$ be the central frequency in the analysis. The index sets are used in the decomposition of the mobilities and impedances in Eqs. (23)–(30) and the approximate results are subsequently introduced in Eq. (17) to yield the following eigenvalue problem

$$[\mathbf{I}_{l(0)} + \{\mathbf{N}_0(\omega,\omega_0,\delta) + \mathbf{N}_1(\omega_0,\delta)\}\text{diag}\{\mathbf{Z}_1(\omega_0), \ldots, \mathbf{Z}_n(\omega_0)\}]\mathbf{f} = 0, \tag{43}$$

where $\mathbf{N}_0(\omega,\omega_0,\delta)$ is an $l(0) \times l(0)$ matrix of dominant mobility terms

$$\mathbf{N}_0(\omega,\omega_0,\delta) = \frac{-\mathrm{i}\omega_0}{\omega_i^2 - \omega^2}\boldsymbol{\phi}_i\boldsymbol{\phi}_i^T. \tag{44}$$

Since $\mathbf{N}_0(\omega,\omega_0,\delta)$ is an outer product of vectors, it is a matrix of rank one. Premultiplying Eq. (43) by the $l(0) \times l(0)$ matrix

$$\hat{\mathbf{K}} = [\mathbf{I}_{l(0)} + \mathbf{N}_1(\omega_0,\delta)\text{diag}\{\mathbf{Z}_1(\omega_0), \ldots, \mathbf{Z}_n(\omega_0)\}]^{-1}$$

yields

$$[\mathbf{I}_{l(0)} + \mathbf{K}\mathbf{N}_0(\omega,\omega_0,\delta)\text{diag}\{\mathbf{Z}_1(\omega_0), \ldots, \mathbf{Z}_n(\omega_0)\}]\mathbf{f} = 0. \tag{45}$$

The matrix $\mathbf{K}$ includes higher-order terms of the impedance and mobility matrices and corresponds to the matrix $\mathbf{J}$ of the preceding section.

This eigenvalue problem is nominally of order $l(0) \times l(0)$. However, since $\mathbf{N}_0(\omega,\omega_0,\delta)$ is of rank one, the eigenvalue problem is actually of order 1×1. This reduced eigenvalue problem is obtained from Eq. (45) by premultiplying by $\mathrm{i}\omega_0^{-1}\boldsymbol{\phi}_i^T\text{diag}\{\mathbf{Z}_1(\omega_0), \ldots, \mathbf{Z}_n(\omega_0)\}$ and defining

$$p_i \equiv \frac{\mathrm{i}\omega_0}{\omega_0^2 - \omega^2}\boldsymbol{\phi}_i^T\text{diag}\{\mathbf{Z}_1(\omega_0), \ldots, \mathbf{Z}_n(\omega_0)\}\mathbf{f} \tag{46}$$

to yield the scalar equation

$$[\omega_i^2 - \omega^2 - \mathrm{i}\omega_0\boldsymbol{\phi}_i^T\text{diag}\{\mathbf{Z}_1(\omega_0), \ldots, \mathbf{Z}_n(\omega_0)\}\mathbf{K}\boldsymbol{\phi}_i]p_i\omega_0^{-2} = 0. \tag{47}$$

The solution for the frequency is

$$\omega = \omega_i\left(1 - \frac{\omega_0^2}{\omega_i^2}\mu_i\right)^{1/2} \tag{48}$$

where

$$\mu_i = \mathrm{i}\omega_0^{-1}\boldsymbol{\phi}_i^T\text{diag}\{\mathbf{Z}_1(\omega_0), \ldots, \mathbf{Z}_n(\omega_0)\}\mathbf{K}\boldsymbol{\phi}_i. \tag{49}$$

The constant μ_i is dimensionless and is a physical measure of the effect of the impedance of all the substructures on the

Downloaded 03 May 2010 to 171.66.16.247. Redistribution subject to ASME license or copyright; see http://www.asme.org/terms/Terms_Use.cfm

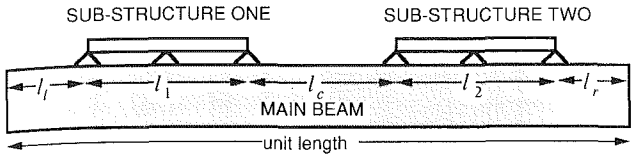


Fig. 2 Multiply connected beams

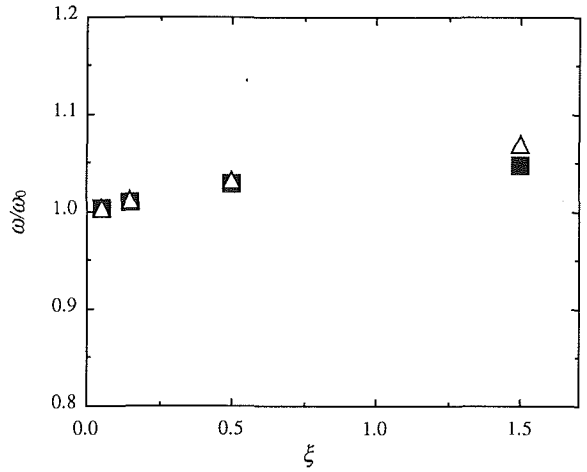


Fig. 3 Frequency ratios, ω/ω_o, versus rib mass density ratios, ξ, for mode $\{kj\}$ by both exact (■) and approximate (△) analysis

natural frequency of the combined system. If $\mu_i = 0$, then the substructures act as massless entities and the natural frequency of the combined system is identical to that of the main structure, as expected. Positive real values for μ_i correspond to a mass effect and result in a reduction of the natural frequency, and negative real values correspond to a stiffness effect and result in an increase of the natural frequency.

It can be shown that μ_i is proportional to the ratio of the substructure masses divided by the main-structure mass. Thus, as this ratio of masses becomes small, μ_i becomes zero and the dynamic behavior of the main structure, as expected, approaches the free, decoupled state. The term *substructure mass parameter* is applied to μ_i, and the parameter reappears in more general form for other cases.

There are two groups of modes in mode case $\{i\}$: mode i of the main structure and all remaining modes. Coupling between modes within the second group is quantified by the second term in $\mathbf{K}$, i.e., $\mathbf{N}_1(\omega_0)\text{diag}\{\mathbf{Z}_1(\omega_0), \ldots, \mathbf{Z}_n(\omega_0)\}$. Coupling between the two groups of modes is quantified by the parameter μ_i. When these terms are small in relation to unity, the coupling is defined to be weak; otherwise, the coupling is strong.

The central frequency ω_0 used in Eqs. (43)–(39) is an estimate of the combined system natural frequency corresponding to mode i. For weakly coupled substructures, μ_i is small in relation to unity and the combined-system natural frequency ω is nearly equal to the ith frequency of the main structure ω_i. Thus, in such cases it is natural to assign the central frequency ω_0 to ω_i. However, for strongly coupled substructures, where μ_i is not small in relation to unity, updating of ω_0 is necessary to obtain accurate results. This is performed by the iterative procedure described for mode case $\{kj\}$.

The $l(0)$ components of the mode shape, $\mathbf{f}$, are determined by substituting the result for the natural frequency given by Eq. (48) into the original $l(0) \times l(0)$ eigenvalue Eq. (45); expressing the results in terms of p_i using Eq. (46); and setting the undetermined scalar p_i equal to 1. The result is

$$\mathbf{f} = \mathbf{K}\phi_i. \tag{50}$$

For weakly coupled substructures, $\mathbf{K}$ is approximately equal to the identity matrix and the mode shape components at the support points are equal to those of the ith mode shape of the main structure.

Table 1 Components of nondimensional length of main beam

Configuration	$\{kj\}$	$\{i\}$
l_1	0.283	0.283
l_2	0.083	0.283
l_l	0.092	0.092
l_c	0.333	0.333
l_r	0.208	0.092

The mode shape for the remainder of the system is obtained by substituting Eqs. (48) and (50) into Eqs. (11) and (14) to solve for the modal coordinates a_i and b_{kj}, and substituting these quantities into Eqs. (1) and (2). The results for the modal coordinates are

$$b_{kh} = \frac{\omega^2}{\omega_{kh}^2 - \omega^2} \mathbf{m}_{kh}^T \sum_{m=1}^{n} \mathbf{K}_{km}\phi_{im}, \tag{51}$$

$$a_j = \frac{i\omega}{\omega_j^2 - \omega^2} \sum_{k=1}^{n} \phi_{jk}^T \mathbf{Z}_k \phi_{ik}. \tag{52}$$

The modal coordinates b_{kh} and a_j become larger as the corresponding substructure natural frequencies ω_{kh} and ω_j approach the combined system natural frequency ω. The largest modal coordinate is a_i which corresponds to the mode i under study.

5 Example Studies

To illustrate the results of this paper, the structural system shown in Fig. 2 is studied in detail. The main structure is a free Euler-Bernoulli beam and the substructures are two smaller beams, each connected to the main structure by three simple supports. The modulus of elasticity, E, is the same for all beams, and the moments of inertia and masses per unit length are denoted I and m for the main beam and I_s and m_s for the two substructures. It is useful to define nondimensional parameters

$$\xi \equiv \frac{m_s}{m} \text{ and } \chi\xi \equiv \frac{EI_s}{EI}, \tag{53}$$

where ξ is a mass density ratio and $\chi\xi$ is a rigidity ratio. For simplicity, vibrations corresponding to axial deformations are not considered and damping is neglected. The parameter l_k denotes the length of substructure k normalized by the length of the main beam. The nondimensional lengths l_l, l_c, and l_r shown in Fig. 2 specify the attachment locations of the substructure on the main beam. The middle attachment of each substructure is located at the midpoint of the substructure beams.

Two frequency windows are studied in this section corresponding to mode cases $\{kj\}$ and $\{i\}$. The nondimensional beam lengths for each case are shown in Table 1. For each mode case, four mass density ratios, $\xi = 0.05$, 0.15, 0.5, and 1.5, are considered and the parameter χ is held constant at 0.25. In this way, the degree of coupling between the main beam and the substructures is varied, while the fixed-base modal properties of each substructure are held constant.

For each example, the natural frequencies and mode shapes corresponding to each window are obtained using the exact and two approximate analyses. The exact results are determined by numerically solving the original eigenvalue problem of Eqs. (13) and (16)–(18) using a sufficiently large number of substructure modes to produce convergent values. The first set of approximate results are obtained by using the closed-

Downloaded 03 May 2010 to 171.66.16.247. Redistribution subject to ASME license or copyright; see http://www.asme.org/terms/Terms_Use.cfm

Table 2 Exact and approximate frequency ratios and mode shape components for mode $\{kj\}$

	$\xi = 0.05$		$\xi = 0.15$		$\xi = 0.5$		$\xi = 1.5$	
	Ex.	Ap.	Ex.	Ap.	Ex.	Ap.	Ex.	Ap.
Freq. ratio	1.004	1.004	1.011	1.012	1.028	1.033	1.047	1.069
Mode								
x1	-0.06	-0.06	-0.10	-0.10	-0.10	-0.13	-0.01	-0.12
x2	-0.08	-0.08	-0.11	-0.11	-0.14	-0.15	-0.14	-0.15
x3	0.15	0.15	0.23	0.24	0.32	0.36	0.31	0.43
x4	-0.12	-0.12	-0.21	-0.20	-0.36	-0.31	-0.55	-0.42
x5	-0.00	-0.00	-0.01	-0.00	-0.04	-0.01	-0.09	-0.03
x6	0.12	0.12	0.19	0.20	0.30	0.29	0.43	0.37

Table 3 Exact and approximate frequency ratios and mode shape components for mode $\{i\}$ (***: results outside of frequency window)

	$\xi = 0.05$		$\xi = 0.15$		$\xi = 0.5$		$\xi = 1.5$	
	Ex.	Ap.	Ex.	Ap.	Ex.	Ap.	Ex.	Ap.
Freq. ratio	1.002	1.003	1.007	1.008	1.022	1.041	1.057	***
Mode								
x1	-0.57	-0.57	-0.58	-0.58	-0.59	-0.61	-0.58	
x2	0.11	0.11	0.09	0.09	0.07	0.07	0.05	
x3	0.55	0.55	0.54	0.55	0.52	0.54	0.48	
x4	0.55	0.55	0.54	0.55	0.52	0.54	0.48	
x5	0.11	0.11	0.09	0.09	0.07	0.07	0.05	
x6	-0.57	-0.57	-0.58	-0.58	-0.59	-0.61	-0.58	

form expressions derived in this paper for each window. The second set of approximate results are obtained by using the same expressions as in the first approximation, but iterating until convergence is achieved. In all cases, it was found that iteration converges to the exact results. In the following, the results of the numerical studies are discussed for each case.

For the example study of mode case $\{kj\}$, the modal properties corresponding to the first mode of substructure one is examined, i.e., $kj = 1,1$. The approximate results are computed using Eqs. (36) and (39). The natural frequencies, normalized with respect to $\omega_0 = \omega_{11}$, are plotted in Fig. 3 with respect to the substructure mass density parameter ξ. The exact results and the first set of approximate results are represented by squares and triangles, respectively. As mentioned earlier, the second set of approximate results, obtained by iteration, coincides with the exact results; therefore, these results are not represented by separate symbols. The components of the mode shapes at the support points, normalized with respect to modal mass, are shown in Table 2.

To gain insight into the numerical results, the support flexibility parameter γ_1 is plotted versus ξ in Fig. 4. For low values of ξ, the parameter γ_1 is nearly zero, which, as described after Eq. (37), is equivalent to a nearly rigid support condition. This result agrees with physical intuition since small values of ξ correspond to a light substructure vibrating on a massive main structure: The reaction forces of the substructure at the main structure support points are small, resulting in low-amplitude support motions. These observations are confirmed by the values for the modal properties. The normalized natural frequency for small ξ is nearly unity, indicating that the natural frequency of the combined system is nearly equal to that of the fixed-base substructure. The corresponding mode-shape components in Table 2 are small relative to unity, indicating low-amplitude support motions.

A physical interpretation of the problem is obtained by considering the relative motion of various parts of the substructure when the structure is freely vibrating in the mode shape of interest. Figure 4 shows that for larger values of ξ, the parameter γ_1 becomes increasingly negative. The reason is that the substructure becomes sufficiently massive to produce substantial reaction forces at the supports, which cause non-negligible motion of the main structure. The negative values for γ_1 indicate that the motion of the supports are, in a modal

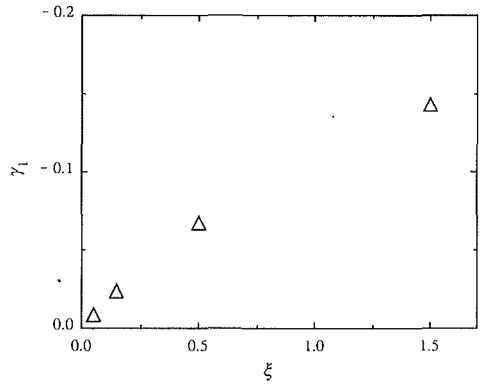


Fig. 4 Support flexibility parameters, γ_1, versus rib mass density ratios, ξ, for mode $\{kj\}$

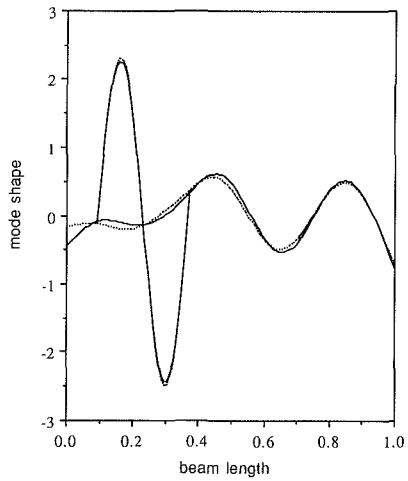


Fig. 5 Mode shape for $\xi = 0.5$ of mode $\{kj\}$ by exact (——) and approximate (- - -) analysis

sense, moving 180 degrees out of phase with the substructure motion. This causes an increase in the combined system natural frequency and an increase in the support motion for the corresponding mode shapes. This is observed in Fig. 3 and Table 2.

For $\xi = 0.5$, the mode shape of the entire beam system is shown in Fig. 5 for the exact (solid line) and the approximate (dotted line) analysis. The predominant motion is that of the left substructure beam, which has a vibration shape that closely resembles its first fixed-base mode shape. The mode shapes for smaller values of ξ, which are not shown here, are characterized by increased motion of the left substructure beam relative to the main beam motion. This is in agreement with the preceding discussion because for smaller ξ, the parameter γ_1 approaches zero and the main structure behaves closer to a rigid beam.

For the example study of mode case $\{i\}$, the modal properties of the combined systems corresponding to the fifth mode of the free-free beam is examined, i.e., $i = 5$. The approximate results are computed using Eqs. (48) and (50). The natural frequencies, normalized with respect to $\omega_0 = \omega_i$ are plotted in Fig. 6 using the same axes and symbols as in Fig. 3. The components of the mode shapes at their support points are shown in Table 3.

For low values of ξ, the parameter μ_i is nearly zero, which, as described after Eq. (47), is equivalent to a massless substructure. The normalized natural frequency for small ξ is nearly unity, indicating that the natural frequency of the combined system is nearly equal to that of the main structure. For larger values of ξ, the parameter μ_i becomes increasingly neg-

Downloaded 03 May 2010 to 171.66.16.247. Redistribution subject to ASME license or copyright; see http://www.asme.org/terms/Terms_Use.cfm

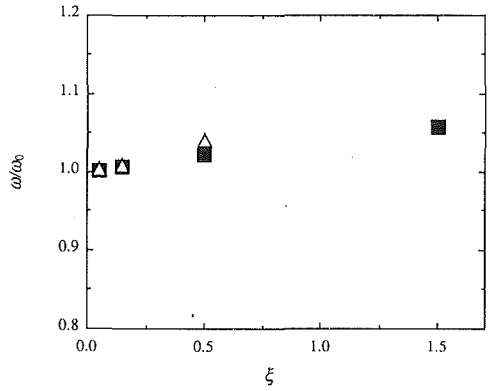


Fig. 6 Frequency ratios, ω/ω_o, versus rib mass density ratios, ξ, for mode $\{i\}$ by both exact (■) and approximate (△) analysis

ative, which, in a manner similar to that described for mode case $\{kj\}$, causes an increase in the combined-system natural frequency. However, there is no significant change in the mode shape components, simply because the values of ξ are too small to influence the motion of the main structure. This is observed in Fig. 6 and Table 3. For $\xi = 1.5$, the largest value in this study, it was found that coupling between mode i of the main structure and a mode outside the frequency window becomes large. As noted earlier, the single iteration approximation is inappropriate for such strong coupling problems and the results are not shown in Fig. 6 and Table 3. The approximate analysis is improved by widening the frequency window to include the mode that is strongly coupled to mode i.

6 Conclusions

The frequency window method, which has been proposed by Igusa, Achenbach, and Min (1990a,b) has been extended to include strong coupling and multiple connections between the main structure and the substructure. The rational polynomial expansion of the eigenvalue problem and the analytical methods for its solution are novel and distinguish this work from other eigenvalue analysis methods. The key results are: the identification of parameters which quantify the substructure resonance and coupling characteristics; the derivation of analytical closed-form expressions describing the fundamental modal properties in the frequency windows; and the development of an iterative procedure which yields accurate convergent results for strongly coupled substructures. The example study shows that the parameter definitions and analytical expressions in this paper can provide considerable insight into the dynamic properties of complex structures. This is an important feature which further distinguishes this work from numerical techniques.

Acknowledgments

This research was supported by the Office of Naval Research under Contract No. 88K-0514, Dr. P. B. Abraham, Scientific Officer. This support is gratefully acknowledged.

References

Bishop, R. E. D., Gladwell, G. M. L., and Michaelson, S., 1965, *Matrix Analysis of Vibration*, Cambridge University Press, Cambridge, U.K.

Dowell, E. H., 1979, "On Some General Properties of Combined Dynamical Systems," ASME JOURNAL OF APPLIED MECHANICS, Vol. 46, pp. 206–209.

Gladwell, G. M. L., and Bishop, R. E. D., 1960, "Interior Receptances of Beams," *Journal of Mechanical Engineering Science*, Vol. 2, pp. 1–15.

Hallquist, J., and Snyder, V. W., 1973, "Linear Damped Vibratory Structures with Arbitrary Support Conditions," ASME JOURNAL OF APPLIED MECHANICS, Vol. 40, pp. 312–313.

Hurty, W. C., and Rubinstein, M. F., 1964, *Dynamics of Structures*, Prentice-Hall, Englewood Cliffs, N.J.

Igusa, T., Achenbach, J. D., and Min, K.-W., 1990, "Resonance Characteristics of Connected Subsystems: Theory and Simple Configurations," *Journal of Sound and Vibration*, Vol. 146, No. 3, pp. 407–421.

Igusa, T., Achenbach, J. D., and Min, K.-W., 1990, "Resonance Characteristics of Connected Subsystems: General Configurations," *Journal of Sound and Vibration*, Vol. 146, No. 3, pp. 423–437.

Igusa, T., and Der Kiureghian, A., 1985, "Dynamic Characterization of Two-Degree-of-Freedom Equipment-Structure Systems," *Journal of Engineering Mechanics*, Vol. 111, No. 1, pp. 1–19.

Igusa, T., and Der Kiureghian, A., 1985, "Dynamic Response of Multiply Supported Secondary Systems," *Journal of Engineering Mechanics*, Vol. 111, No. 1, pp. 20–41.

Jacquot, R. G., and Soedel, W., 1970, "Vibrations of Elastic Surface Systems Carrying Dynamic Elements," *Journal of the Acoustical Society of America*, Vol. 47, pp. 1354–1358.

Keane, A. J., and Price, W. G., 1987, "Statistical Energy Analysis of Strongly Coupled Systems," *Journal of Sound and Vibration*, Vol. 117, No. 2, pp. 363–386.

Kelkel, K., 1987, "Green's Function and Receptance for Structures Consisting of Beams and Plates," *AIAA Journal*, Vol. 25, No. 11, pp. 1482–1489.

Leissa, A. W., 1974, "On a Curve Veering Aberration," *Journal of Applied Mathematics and Physics*, Vol. 25, pp. 99–111.

Lin, Y. K., 1976, *Probabilistic Theory of Structural Dynamics*, Krieger Publishing, Huntington, New York.

Lyon, R. H., 1975, *Statistical Energy Analysis of Dynamical Systems: Theory and Applications*, MIT Press, Cambridge, Mass.

Mead, D. J., 1975, "Wave Propagational and Natural Modes in Periodic Systems: I. Mono-Coupled Systems," *Journal of Sound and Vibration*, Vol. 40, No. 1, pp. 1–18.

Nicholson, J. W., and Bergman, L. A., 1986, "Free Vibration of Combined Dynamical Systems," *Journal of Engineering Mechanics*, Vol. 112, No. 1, pp. 1–13.

Pinnington, R. J., and White, R. G., 1981, "Power Flow Through Machine Isolations to Resonant and Non-Resonant Beams," *Journal of Sound and Vibration*, Vol. 75, No. 2, pp. 179–197.

Sackman, J. L., Der Kiureghian, A., and, Nour-Omid, B., 1983, "Dynamic Analysis of Light Equipment in Structures: Modal Properties of the Combined System," *Journal of the Engineering Mechanics Division*, ASCE, Vol. 109, No. 1, pp. 73–89.

Sackman, J. L., and Kelly, J. M., 1979, "Seismic Analysis of Internal Equipment and Components in Structures," *Engineering Structures*, Vol. 1, pp. 179–190.

Downloaded 03 May 2010 to 171.66.16.247. Redistribution subject to ASME license or copyright; see http://www.asme.org/terms/Terms_Use.cfm

Frequency Window Method for Strongly Coupled and Multiply Connected Structural Systems: Multiple-Mode Windows

K.-W. Min

T. Igusa

J. D. Achenbach
Fellow ASME

Robert R. McCormick School of Engineering and Applied Science, Department of Civil Engineering, Northwestern University, Evanston, IL 60208

In a companion paper, a method is presented to analyze the dynamic behavior of a structural system consisting of a main structure and strongly coupled, multiply connected substructures. Lagrange's equations are used to develop a characteristic equation for connected substructures in terms of substructure impedances and mobilities. A frequency window method is used to reduce the complexity of the problem by a decomposition of the impedance and mobility functions into dominant and higher-order rational expressions. From the reduced problem, simple expressions for the modal properties are developed using matrix algebraic methods, which provide insight into the resonance characteristics of the connected substructures. One-mode windows were discussed in detail and examples were presented. In the present paper the theory is extended to multiple-mode windows.

1 Introduction

In the companion paper (Min et al., 1991), Lagrange's equations were used to develop the eigenvalue problem for a system of n substructures connected to a main structure, and modal analysis was used to formulate the problem in terms of substructure impedances and the main structure mobility. The eigenvalue equation was derived in the form

$$[\mathbf{I}_{l(0)} + \mathbf{N}(\omega)\,\mathrm{diag}\{\mathbf{Z}_1(\omega), \cdots, \mathbf{Z}_n(\omega)\}]\mathbf{f} = 0 \tag{1}$$

where $\mathbf{N}(\omega)$ is the $l(0) \times l(0)$ mobility matrix of the main structure, $\mathbf{Z}_k(\omega)$ is the $l(k) \times l(k)$ impedance matrix of substructure k, and $\mathbf{f}$ is the $l(0)$ vector of support displacements. This result is similar to those developed by Jacquot and Soedel (1970) and Dowell (1979).

Next, the complexity of the problem was reduced by choosing modes with natural frequencies in a frequency window defined around a central frequency ω_0. These modes were denoted by index sets

$$I(\omega_0, \delta) \equiv \{\text{all } i \text{ such that } |\omega_i - \omega_0| < \delta\} \tag{2}$$

$$I(\omega_0, \delta, k) \equiv \{\text{all } kj \text{ such that } |\omega_{kj} - \omega_0| < \delta\} \tag{3}$$

where it is understood that single indices i refer to the main structure and double indices kj refer to substructure k. This classification of modes was subsequently used to decompose the substructure impedances and mobilities into two parts

$$\mathbf{Z}_k(\omega) \approx \mathbf{Z}_{k0}(\omega, \omega_0, \delta) + \mathbf{Z}_{k1}(\omega_0, \delta) \tag{4}$$

$$\mathbf{N}(\omega) \approx \mathbf{N}_0(\omega, \omega_0, \delta) + \mathbf{N}_1(\omega_0, \delta) \tag{5}$$

where $\mathbf{Z}_{k0}(\omega, \omega_0, \delta)$ and $\mathbf{N}_0(\omega, \omega_0, \delta)$ are the dominant terms for the impedances and mobility, respectively, defined by

$$\mathbf{Z}_{k0}(\omega, \omega_0, \delta) = \sum_{j \in I(\omega_0, \delta, k)} \frac{-i\omega_0^3}{\omega_{kj}^2 - \omega^2} \mathbf{m}_{kj}\mathbf{m}_{kj}^T, \tag{6}$$

$$\mathbf{N}_0(\omega, \omega_0, \delta) = \sum_{i \in I(\omega_0, \delta)} \frac{-i\omega_0}{\omega_i^2 - \omega^2} \boldsymbol{\phi}_i\boldsymbol{\phi}_i^T, \tag{7}$$

and $\mathbf{Z}_{k1}(\omega_0, \delta)$ and $\mathbf{N}_1(\omega_0, \delta)$ are the secondary terms for the impedances and mobility, respectively, defined by

$$\mathbf{Z}_{k1}(\omega_0, \delta) = -i\omega_0 \left\{ \mathbf{M}_{kpp} \frac{-\mathbf{S}_k}{\omega^2} + \sum_{j \notin I(\omega_0, \delta, k)} \frac{\omega_0^2}{\omega_{kj}^2 - \omega_0^2} \mathbf{m}_{kj}\mathbf{m}_{kj}^T \right\} \tag{8}$$

$$\mathbf{N}_1(\omega_0, \delta) = \sum_{i \notin I(\omega_0, \delta)} \frac{-i\omega_0}{\omega_i^2 - \omega_0^2} \boldsymbol{\phi}_i\boldsymbol{\phi}_i^T. \tag{9}$$

The relationship between the parameter δ used to define the index sets, the complexity of the problem, and the accuracy of the solutions for the modal properties was discussed in the companion paper (Min et al., 1991).

Frequency windows with only one mode, where one of the index sets defined in Eqs. (2) and (3) has one element and the other index set is null, were examined in detail. Using the fact that the approximate eigenvalue problem contains matrices of rank one, matrix algebra techniques were applied to reduce

Contributed by the ASME Applied Mechanics Division of THE AMERICAN SOCIETY OF MECHANICAL ENGINEERS for presentation at the Winter Annual Meeting, Atlanta, Ga., Dec. 1-6, 1991.

Discussion on this paper should be addressed to the Technical Editor, Prof. Leon M. Keer, The Technological Institute, Northwestern University, Evanston, IL 60208, and will be accepted until two months after final publication of the paper itself in the JOURNAL OF APPLIED MECHANICS. Manuscript received by the ASME Applied Mechanics Division, June 19, 1990; final revision, Feb. 26, 1991.

Paper No. 91-WA/APM-24.

Copyright © 1992 by ASME

Downloaded 03 May 2010 to 171.66.16.247. Redistribution subject to ASME license or copyright; see http://www.asme.org/terms/Terms_Use.cfm

the problem to size 1 × 1. The closed-form solutions provided interesting and insightful information about the effect of connection flexibilities and substructure masses on the modal properties of the combined system. In the next sections, these analysis techniques and modal results are generalized to frequency windows with two modes and many modes.

2 Two-Mode Frequency Windows

In two-mode combinations, these modes have frequencies close to a given frequency ω_0, i.e., $I(\delta, \omega_0)$ has two elements. There are four possible cases of two-mode combinations given by the following representations of $I(\delta, \omega_0)$:

$$\{i_1, i_2\},\ \{kj, kh\},\ \{kj, lh\},\ \{i, kj\} \text{ where } i_1 \neq i_2,\ k \neq l,\ j \neq h.$$

The first two cases are for two closely spaced modes of the main structure and of substructure k, respectively. The third case involves a mode of substructure k and a mode of a different substructure l. The last case concerns a mode of the main structure and a mode of substructure k. The last two cases involve the effects of resonances and interaction between two different substructures, and since there are fundamental differences in their mathematical treatment, both are studied in depth in the next sections.

2.1 Mode Combination $\{kj, lh\}$. First, combination $\{kj, lh\}$ is examined where, without loss of generality, it is assumed that the indices for the substructures are $k = 1$ and $l = 2$. It is natural to assign the central frequency of the frequency window to the average of frequencies, defined by $\omega_0^2 = (\omega_{1j}^2 + \omega_{2h}^2)/2$. The index sets used in Eqs. (2) and (3) are $I(\omega_0, \delta) = \{\ \}$, $I(\omega_0, \delta, 1) = \{1j\}$, $I(\omega_0, \delta, 2) = \{2h\}$, and $I(\omega_0, \delta, k) = \{\ \}$ for $k \neq 1, 2$. These index sets are applied to the decomposition of the mobilities and impedances in Eqs. (4)–(9) and the results are subsequently applied to Eq. (1) to yield the following $l(0) \times l(0)$ eigenvalue problem

$$[\mathbf{I}_{l(0)} + \mathbf{N}(\omega_0)\text{diag}\{\mathbf{Z}_{10}(\omega, \omega_0, \delta) + \mathbf{Z}_{11}(\omega_0, \delta), \mathbf{Z}_{20}(\omega, \omega_0, \delta) + \mathbf{Z}_{21}(\omega_0, \delta), \mathbf{Z}_3(\omega_0), \cdots, \mathbf{Z}_n(\omega_0)\}]\mathbf{f} = 0, \quad (10)$$

where

$$\mathbf{Z}_{k0}(\omega, \omega_0, \delta) = \frac{-i\omega_0^3}{\omega_{k1}^2 - \omega^2}\,\mathbf{m}_{k1}\mathbf{m}_{k1}^T. \quad (11)$$

There are three steps to solving this problem: finding the natural frequency, ω; finding the components of the mode shape, $\mathbf{f}_1$ and $\mathbf{f}_2$, corresponding to the first two substructures; and finding the components of the mode shape for the remaining substructures, $\mathbf{f}_3, \ldots, \mathbf{f}_n$. The first two steps are performed by considering only the first $l(1) + l(2)$ components of the problem and premultiplying Eq. (10) by the $l(0) \times l(0)$ matrix

$$\mathbf{L} = [\mathbf{I}_{l(0)} + \mathbf{N}(\omega_0)\text{diag}\{\mathbf{Z}_{11}(\omega_0, \delta), \mathbf{Z}_{21}(\omega_0, \delta), \mathbf{Z}_3(\omega_0), \cdots, \mathbf{Z}_n(\omega_0)\}]^{-1}.$$

The result is

$$\left\{\begin{bmatrix}\mathbf{I}_{l(1)} & 0\\ 0 & \mathbf{I}_{l(1)}\end{bmatrix} + \begin{bmatrix}\sum_{m=1}^{n}\mathbf{L}_{1m}\mathbf{N}_{m1}(\omega_0) & \sum_{m=1}^{n}\mathbf{L}_{1m}\mathbf{N}_{m2}(\omega_0)\\ \sum_{m=1}^{n}\mathbf{L}_{2m}\mathbf{N}_{m1}(\omega_0) & \sum_{m=1}^{n}\mathbf{L}_{2m}\mathbf{N}_{m2}(\omega_0)\end{bmatrix} \times \begin{bmatrix}\frac{-i\omega_0^3}{\omega_{1j}^2-\omega^2}\mathbf{m}_{1j}\mathbf{m}_{1j}^T & 0\\ 0 & \frac{-i\omega_0^3}{\omega_{2h}^2-\omega^2}\mathbf{m}_{2h}\mathbf{m}_{2h}^T\end{bmatrix}\right\}\begin{bmatrix}\mathbf{f}_1\\ \mathbf{f}_2\end{bmatrix} = 0 \quad (12)$$

where $\mathbf{L}_{km}$ denotes the $l(k) \times l(m)$ submatrix of $\mathbf{L}$ with rows corresponding to support displacements of substructure k and columns corresponding to the support displacements of substructure m.

The eigenvalue problem is nominally of order $(l(1) + l(2)) \times (l(1) + l(2))$. However, the outer products indicate that the second matrix term in brackets is of rank two, which implies that the eigenvalue problem is actually of order 2 × 2. This reduced eigenvalue problem is obtained from Eq. (12) by premultiplying by

$$\begin{bmatrix}\mathbf{m}_{1j} & 0\\ 0 & \mathbf{m}_{2h}\end{bmatrix}^T$$

and defining

$$q_k \equiv \frac{\omega_0^2}{\omega_{k1}^2 - \omega^2}\,\mathbf{m}_{k1}^T\mathbf{f}_k. \quad (13)$$

This gives the 2 × 2 equation

$$\left\{\begin{bmatrix}\omega_{1j}^2 - \omega^2 & 0\\ 0 & \omega_{2h}^2 - \omega^2\end{bmatrix} - \omega_0^2\boldsymbol{\Gamma}\right\}\begin{bmatrix}q_1\\ q_2\end{bmatrix}\omega_0^{-2} = 0, \quad (14)$$

where $\boldsymbol{\Gamma}$ is a non-dimensional 2 × 2 matrix

$$\boldsymbol{\Gamma} \equiv i\omega_0\begin{bmatrix}\mathbf{m}_{1j}^T & 0\\ 0 & \mathbf{m}_{2h}^T\end{bmatrix}\begin{bmatrix}\sum_{m=1}^{n}\mathbf{L}_{1m}\mathbf{N}_{m1}(\omega_0) & \sum_{m=1}^{n}\mathbf{L}_{1m}\mathbf{N}_{m2}(\omega_0)\\ \sum_{m=1}^{n}\mathbf{L}_{2m}\mathbf{N}_{m1}(\omega_0) & \sum_{m=1}^{n}\mathbf{L}_{2m}\mathbf{N}_{m2}(\omega_0)\end{bmatrix} \times \begin{bmatrix}\mathbf{m}_{1j} & 0\\ 0 & \mathbf{m}_{2h}\end{bmatrix}. \quad (15)$$

It is useful to define a *tuning parameter*

$$\beta \equiv \frac{\omega_{1j}^2 - \omega_0^2}{\omega_0^2} = \frac{\omega_0^2 - \omega_{2h}^2}{\omega_0^2}, \quad (16)$$

and to give parameter definitions for each element of $\boldsymbol{\Gamma}$ as

$$\begin{bmatrix}\gamma_1 & \kappa\\ \kappa & \gamma_2\end{bmatrix} \equiv \boldsymbol{\Gamma}, \quad (17)$$

where

$$\gamma_k = i\omega_0\mathbf{m}_{kj}^T\sum_{m=1}^{n}\mathbf{L}_{km}\mathbf{N}_{mk}(\omega_0)\mathbf{m}_{kj}, \quad (18)$$

$$\kappa = i\omega_0\mathbf{m}_{1j}^T\sum_{m=1}^{n}\mathbf{L}_{1m}\mathbf{N}_{m2}(\omega_0)\mathbf{m}_{2h}. \quad (19)$$

It can be seen that γ_k is a generalized form of the support flexibility parameter defined in Eq. (37) of the companion paper. The new parameter κ is defined to be the *support coupling parameter*.

The solution for the combined system natural frequencies are obtained by finding the roots of the quadratic characteristic polynomial of Eq. (14)

$$\omega = \omega_0\left[1 - \frac{\gamma_1 + \gamma_2}{2} \pm \sqrt{\left(\beta - \frac{\gamma_1 - \gamma_2}{2}\right)^2 + \kappa^2}\right]^{1/2}. \quad (20)$$

Results with similar form, but quite different parameters, have been derived for lumped-mass substructures (Sackman and Kelly, 1979; Sackman, et al., 1983; Igusa and Der Kiureghian, 1985). There is a coupling term in these references which corresponds to the parameter κ and is defined in terms of a ratio of substructure to main structure masses. The parameter κ is also proportional to essentially the same mass ratio, but is defined in terms of more complicated dynamic terms given in Eq. (15) which arise from the continuous formulation in this paper.

The simple formula given by Eq. (20) has considerable information about the dynamic effects of the main structure on

Downloaded 03 May 2010 to 171.66.16.247. Redistribution subject to ASME license or copyright; see http://www.asme.org/terms/Terms_Use.cfm

the vibration of the two substructures. Consider the case where $\kappa = 0$. Then, the combined system natural frequencies become

$$\omega = \omega_0\left[1 - \frac{\gamma_1+\gamma_2}{2} \pm \left(\beta - \frac{\gamma_1-\gamma_2}{2}\right)\right]^{1/2} = \omega_{1j}\left(1 - \frac{\omega_0^2}{\omega_{1j}^2}\gamma_1\right)^{1/2} \text{ and } \omega_{2h}\left(1 - \frac{\omega_0^2}{\omega_{2h}^2}\gamma_2\right)^{1/2}, \quad (21)$$

which are identical to the solution for the one mode case in Eq. (36) of the companion paper. The physical interpretation is that for $\kappa = 0$ there is no effect of the vibration at the supports of substructure one on the motion at the supports of substructure two. Consequently, the motion of the two substructures becomes decoupled, and can be solved separately using the simpler one mode solutions.

The preceding discussion suggests the definition of a set of *equivalent substructure natural frequencies* defined by

$$\tilde{\omega}_{1j} \equiv \omega_{1j}\left(1 - \frac{\omega_0^2}{\omega_{1j}^2}\gamma_1\right)^{1/2} \text{ and } \tilde{\omega}_{2h} \equiv \omega_{2h}\left(1 - \frac{\omega_0^2}{\omega_{2h}^2}\gamma_2\right)^{1/2}, \quad (22)$$

which account for the support flexibilities. Substituting into Eq. (21) leads to a simplified expression

$$\omega = \tilde{\omega}_0\left[1 \pm \sqrt{\tilde{\beta}^2 + \kappa^2}\right]^{1/2}, \quad (23)$$

where $\tilde{\omega}_0^2 \equiv (\tilde{\omega}_{1j}^2 + \tilde{\omega}_{2h}^2)/2$ and $\tilde{\beta} \equiv (\tilde{\omega}_{1j}^2 - \tilde{\omega}_0^2)/\tilde{\omega}_0^2 = (\tilde{\omega}_0^2 - \tilde{\omega}_{2h}^2)/\tilde{\omega}_0^2$. Equation (23) shows that the natural frequencies are symmetrically spaced about the average equivalent frequency $\tilde{\omega}_0$, with spacing governed by both the equivalent tuning $\tilde{\beta}$ and the coupling κ. The spacing between the two natural frequencies is minimized when $\tilde{\beta} = 0$, when the natural frequencies are given by

$$\omega = \tilde{\omega}_0(1 \pm \kappa)^{1/2}. \quad (24)$$

This result shows that the coupling of substructure motions, quantified by κ, has the additional effect of maintaining a lower bound on the separation of natural frequencies for combination $\{kj, lh\}$.

There are two groups of modes in combination $\{kj, lh\}$: One group consists of modes $1j$ and $2h$ which lie within the frequency window; the second group consists of all remaining modes which lie outside the frequency window. Coupling between modes within the outside group is quantified by the second term in $\mathbf{L}$, i.e., $\mathbf{N}(\omega_0)\text{diag}\{\mathbf{Z}_{11}(\omega_0, \delta)\, \mathbf{Z}_{21}(\omega_0, \delta)\, \mathbf{Z}_3(\omega_0) \cdots \mathbf{Z}_n(\omega_0)\}$. Coupling between the two groups of modes is quantified by the parameters γ_1, γ_2, and κ. When these terms are small as compared to unity, the coupling is defined to be weak; otherwise, the coupling is strong.

The central frequency ω_0 used in Eqs. (10)–(24) is an estimate of the combined-system natural frequencies corresponding to modes $1j$ and $2h$. For weakly coupled substructures, the parameters of the problem, given by matrix $\mathbf{\Gamma}$ in Eq. (17), are small compared to unity and accurate results can be obtained by using the initial estimate, $\omega_0^2 = (\omega_{1j}^2 + \omega_{2h}^2)/2$. However, for strongly coupled substructures, iteration is necessary for each of the two modes of the combined system. The process begins with $\omega_0^2 = (\omega_{1j}^2 + \omega_{2h}^2)/2$, and the succeeding estimates for ω_0 use the first root of Eq. (23) to obtain a sequence converging to the lower of the two natural frequencies. The process is repeated using the second root of Eq. (23) to obtain the upper natural frequency. More efficient procedures may exist, but such numerical analysis is not the primary goal of this paper.

The first $l(1) + l(2)$ components of the mode shape, $\mathbf{f}_1$ and $\mathbf{f}_2$, are determined by substituting the natural frequency given by Eq. (20) into the reduced 2×2 eigenvalue Eq. (14) to obtain q_1 and q_2, and by subsequently substituting all results into the original $(l(1) + l(2)) \times (l(1) + l(2))$ eigenvalue Eq. (12). The result, in terms of previously defined properties, is

$$\mathbf{f}_k = -i\tilde{\omega}_0\left[-\kappa\sum_{m=1}^{n}\mathbf{L}_{km}\mathbf{N}_{m1}(\omega_0)\mathbf{m}_{1j} + \left(\tilde{\beta} \mp \sqrt{\tilde{\beta}^2+\kappa^2}\right)\sum_{m=1}^{n}\mathbf{L}_{km}\mathbf{N}_{m2}(\omega_0)\mathbf{m}_{2h}\right] \quad (25)$$

for $k = 1$ and 2. The remaining components of the mode shape are determined by premultiplying Eq. (10) by $\mathbf{L}$, substituting Eq. (23) for the first $l(1) + l(2)$ components of $\mathbf{f}$, and solving for the remaining components of $\mathbf{f}$. The final results are also given by Eq. (25) for $k > 2$.

The mode shape for the remainder of the system is obtained by substituting Eq. (25) into Eqs. (11) and (14) of the companion paper. The results are

$$b_{ki} = \frac{-i\omega^3}{\omega_{ki}^2 - \omega^2}\left[-\kappa\mathbf{m}_{ki}^T\sum_{m=1}^{n}\mathbf{L}_{km}\mathbf{N}_{m1}(\omega_0)\mathbf{m}_{1j} + \left(\tilde{\beta} \mp \sqrt{\tilde{\beta}^2+\kappa^2}\right)\mathbf{m}_{ki}^T\sum_{m=1}^{n}\mathbf{L}_{km}\mathbf{N}_{m2}(\omega_0)\mathbf{m}_{2h}\right], \quad \text{for } kh \neq 1j, 2h, \quad (26)$$

$$b_{1j} = \frac{\kappa\left[\gamma_1 - \tilde{\beta} \mp \sqrt{\tilde{\beta}^2+\kappa^2}\right]}{\gamma_1 + \tilde{\beta} \mp \sqrt{\tilde{\beta}^2+\kappa^2}}, \quad (27)$$

$$b_{2h} = \frac{\left[-\tilde{\beta} \pm \sqrt{\tilde{\beta}^2+\kappa^2}\right]\left[-\gamma_2 - \tilde{\beta} \mp \sqrt{\tilde{\beta}^2+\kappa^2}\right]}{\gamma_2 - \tilde{\beta} \mp \sqrt{\tilde{\beta}^2+\kappa^2}}, \quad (28)$$

$$a_i = \frac{\omega^2}{\omega_i^2 - \omega^2}\left[-\kappa\boldsymbol{\phi}_{i1}^T\mathbf{m}_{1j} + \left(\tilde{\beta} \mp \sqrt{\tilde{\beta}^2+\kappa^2}\right)\boldsymbol{\phi}_{i2}^T\mathbf{m}_{2h}\right] + \frac{i\omega}{\omega_i^2 - \omega^2}\left(\sum_{k\neq 1,2}\boldsymbol{\phi}_{ik}^T\mathbf{Z}_k\mathbf{f}_k + \boldsymbol{\phi}_{i1}^T\mathbf{Z}_{11}\mathbf{f}_1 + \boldsymbol{\phi}_{i2}^T\mathbf{Z}_{21}\mathbf{f}_2\right). \quad (29)$$

The modal coordinates b_{ki} and a_i become larger as the corresponding substructure natural frequencies ω_{ki} and ω_i approach ω. The largest modal coordinates are b_{1j} and b_{2h} which correspond to the modes $1j$ and $2h$ under study.

2.2 Mode Combination $\{i, kj\}$. In the analysis of combination $\{i, kj\}$, it is assumed, without any loss of generality, that $k = 1$. It is natural to assign the central frequency of the frequency window to the average of frequencies, $\omega_0^2 = (\omega_i^2 + \omega_{1j}^2)/2$. The index sets are $I(\omega_0, \delta) = \{i\}$, $I(\omega_0, \delta, 1) = \{1j\}$, and $I(\omega_0, \delta, k) = \{\ \}$ for $k \neq 1$. These index sets are applied to the decomposition of the mobilities and impedances in Eqs. (4)–(9) and the approximate results are subsequently introduced in Eq. (1) to yield the following $l(0) \times l(0)$ eigenvalue problem

$$[\mathbf{I}_{l(0)} + \{\mathbf{N}_0(\omega, \omega_0, \delta) + \mathbf{N}_1(\omega_0, \delta)\}\text{diag}\{\mathbf{Z}_{10}(\omega, \omega_0, \delta) + \mathbf{Z}_{11}(\omega_0, \delta), \mathbf{Z}_2(\omega_0), \cdots, \mathbf{Z}_n(\omega_0)\}]\mathbf{f} = 0. \quad (30)$$

Premultiplying this result by the $l(0) \times l(0)$ matrix

$$\mathbf{H} = [\mathbf{I}_{l(0)} + \mathbf{N}_1(\omega_0, \delta)\text{diag}\{\mathbf{Z}_{11}(\omega_0, \delta), \mathbf{Z}_2(\omega_0), \cdots, \mathbf{Z}_n(\omega_0)\}]^{-1}$$

yields

$$[\mathbf{I}_{l(0)} + \mathbf{H}\{\mathbf{N}_0(\omega, \omega_0, \delta)\text{diag}\{\mathbf{Z}_{10}(\omega, \omega_0, \delta) + \mathbf{Z}_{11}(\omega_0, \delta), \mathbf{Z}_2(\omega_0), \cdots, \mathbf{Z}_n(\omega_0)\}]\mathbf{f} = 0. \quad (31)$$

The problem is further reduced by using essentially a combination of the methods developed for the analysis of the two types of one-mode windows. Equation (31) is premultiplied by the $2 \times l(0)$ matrix

$$\mathbf{S} = \begin{bmatrix} -i\omega_0^{-1}\boldsymbol{\phi}_{i1}^T\mathbf{Z}_{11} & -i\omega_0^{-1}\boldsymbol{\phi}_{i2}^T\mathbf{Z}_2 \cdots -i\omega_0^{-1}\boldsymbol{\phi}_{in}^T\mathbf{Z}_n \\ \mathbf{m}_{1j}^T & 0 \quad \cdots \quad 0 \end{bmatrix}.$$

Downloaded 03 May 2010 to 171.66.16.247. Redistribution subject to ASME license or copyright; see http://www.asme.org/terms/Terms_Use.cfm

The result can be expressed as two scalar equations

$$\begin{bmatrix} \omega_i^2-\omega^2 & 0 \\ 0 & \omega_{1j}^2-\omega^2 \end{bmatrix}\begin{bmatrix} p_i \\ q_1 \end{bmatrix} - \omega_0^2\tilde{\mathbf{\Gamma}} = 0, \tag{32}$$

where

$$p_i \equiv \frac{i\omega_0}{\omega_i^2-\omega^2}\,\boldsymbol{\phi}_i^T \text{diag}\{\mathbf{Z}_{11}(\omega_0)\ \cdots\ \mathbf{Z}_n(\omega_0)\}\mathbf{f} \tag{33}$$

is similar to Eq. (46) of the companion paper, $q_1 = \omega_0^2/(\omega_{1j}^2 - \omega^2)\mathbf{m}_{1j}^T\mathbf{f}_1$ is identical to Eq. (34) of the companion paper, and $\tilde{\mathbf{\Gamma}}$ is the 2×2 matrix

$$\tilde{\mathbf{\Gamma}} \equiv -\mathbf{SH}\left[\frac{-i\omega_0}{\omega_i^2-\omega^2}\,\boldsymbol{\phi}_i\boldsymbol{\phi}_i^T + \mathbf{N}_1\right] \times [\text{diag}\{\mathbf{Z}_{11}, \mathbf{Z}_2, \cdots, \mathbf{Z}_n\}\mathbf{f} - i\omega_0\mathbf{m}_{1j}q_1]. \tag{34}$$

The matrix $\tilde{\mathbf{\Gamma}}$ reduces to the product

$$\tilde{\mathbf{\Gamma}} = \mathbf{\Gamma}\begin{bmatrix} p_i \\ q_1 \end{bmatrix} = \begin{bmatrix} \mu_i\,\dfrac{\omega_0^2}{\omega_i^2-\omega^2}\,\mu_i\alpha_{i1} \\ \alpha_{i1}\,\dfrac{\omega_0^2}{\omega_i^2-\omega^2}\,\alpha_{i1}^2+\gamma_1 \end{bmatrix}\begin{bmatrix} p_i \\ q_1 \end{bmatrix}, \tag{35}$$

where $\mathbf{\Gamma}$ is a nondimensional 2×2 matrix which contains the support flexibility parameter

$$\gamma_1 = i\omega_0\mathbf{m}_{1j}^T\sum_{m=1}^{n}\mathbf{H}_{1m}\mathbf{N}_{m1}(\omega_0)\mathbf{m}_{1j}, \tag{36}$$

and the substructure mass parameter

$$\mu_i = i\omega_0^{-1}\boldsymbol{\phi}_i^T\text{diag}\{\mathbf{Z}_1(\omega_0), \cdots, \mathbf{Z}_n(\omega_0)\}\mathbf{H}\boldsymbol{\phi}_i, \tag{37}$$

which were introduced in the study of one-mode windows. The third parameter α_{i1} which appears in matrix $\mathbf{\Gamma}$ is given by

$$\alpha_{i1} \equiv \boldsymbol{\phi}_{i1}^T\mathbf{m}_{1j}. \tag{38}$$

The new parameter α_{i1} is termed the *substructure coupling parameter*, and is a measure of the coupling between the ith mode of the main structure and the jth mode of substructure one.

Substituting Eq. (35) into Eq. (32) yields an asymmetric eigenvalue problem. To make the problem symmetric, a transformation matrix $\mathbf{T}$ defined by

$$\mathbf{T} \equiv \begin{bmatrix} 1 & \dfrac{-\omega_0^2}{\omega_i^2-\omega^2}\,\alpha_{i1} \\ 0 & 1 \end{bmatrix}, \tag{39}$$

is used to transform Eq. (32) to

$$\left\{\begin{bmatrix} \omega_i^2-\omega^2 & 0 \\ 0 & \omega_{1j}^2-\omega^2 \end{bmatrix} - \omega_0^2\mathbf{\Gamma}\right\}\mathbf{T}\mathbf{T}^{-1}\begin{bmatrix} p_i \\ q_1 \end{bmatrix} = \left\{\begin{bmatrix} \omega_i^2-\omega^2 & 0 \\ 0 & \omega_{1j}^2-\omega^2 \end{bmatrix} - \omega_0^2\hat{\mathbf{\Gamma}}\right\}\begin{bmatrix} \hat{p}_i \\ q_1 \end{bmatrix} = 0, \tag{40}$$

where

$$\hat{p}_i \equiv \frac{\omega_0^2}{\omega_i^2-\omega^2}\,\alpha_{i1}q_1 + p_i, \quad \hat{\mathbf{\Gamma}} \equiv \begin{bmatrix} \mu_i & \alpha_{i1} \\ \alpha_{i1} & \gamma_1 \end{bmatrix}. \tag{41}$$

The solution for the combined-system natural frequencies can be written as

$$\omega = \tilde{\omega}_0\left[1 \pm \sqrt{\tilde{\beta}^2+\alpha_{i1}^2}\right]^{1/2}, \tag{42}$$

where

$$\tilde{\beta} \equiv \frac{\tilde{\omega}_i^2-\tilde{\omega}_0^2}{\tilde{\omega}_0^2} = \frac{\tilde{\omega}_0^2-\tilde{\omega}_{1j}^2}{\tilde{\omega}_0^2} \text{ and } \tilde{\omega}_0^2 \equiv \frac{\tilde{\omega}_i^2+\tilde{\omega}_{1j}^2}{2} \tag{43}$$

are the equivalent tuning parameter and central frequency, respectively, and

$$\tilde{\omega}_i \equiv \omega_i\sqrt{1-\frac{\omega_0^2}{\omega_i^2}\,\mu_i} \text{ and } \tilde{\omega}_{1j} \equiv \omega_{1j}\sqrt{1-\frac{\omega_0^2}{\omega_{1j}^2}\,\gamma_1} \tag{44}$$

are the equivalent substructure natural frequencies.

The result of Eq. (41) has nearly the same form as that obtained for the $\{kj, lh\}$ mode combination in Eq. (23). This is remarkable since the mathematical treatment leading to the final results has fundamental differences. The main difference in the final expressions is that the parameter κ, which appears in Eq. (23), is replaced by α_{i1} in Eq. (42). This is intuitively clear since κ measures coupling between substructures k and l, and α_{i1} measures coupling between substructure one and the main structure. Due to the similarity of the results with those of mode combination $\{kj, lh\}$, the discussion in the previous section from Eqs. (20) to (24) is also applicable here.

There are two groups of modes in mode combination $\{i, kj\}$: One group consists of modes i and $1j$ which lie within the frequency window; the second group consists of all remaining modes which lie outside the frequency window. Coupling between modes within the second group is quantified by the second term in $\mathbf{H}$, i.e., $\mathbf{N}_1(\omega_0, \delta)\text{diag}\{\mathbf{Z}_{11}(\omega_0, \delta)\ \mathbf{Z}_2(\omega_0)\ \cdots\ \mathbf{Z}_n(\omega_0)\}$. Coupling between the two groups of modes is quantified by the parameters γ_1, μ_i, and α_{i1}. When these terms are small in relation to unity, the coupling is defined to be weak; otherwise, the coupling is strong.

The central frequency β_0 used in Eqs. (30)–(44) is an estimate of the combined system natural frequencies corresponding to modes i and $1j$. For weakly coupled substructures, the parameters of the problem, given by matrix $\tilde{\mathbf{\Gamma}}$ in Eq. (41), are small compared to unity and accurate results can be obtained by using the approximate initial estimate, $\omega_0^2 = (\omega_i^2 + \omega_{1j}^2)/2$. However, for strongly coupled substructures, iteration is necessary for each of the two modes of the combined system. The procedure is essentially the same as that described for mode combination $\{kj, lh\}$.

The mode shape $\mathbf{f}$ is determined by substituting the natural frequency given by Eq. (42) into the reduced 2×2 eigenvalue Eq. (40) to obtain $\tilde{p}_i$ and q_1. These results are substituted into the original $l(0) \times l(0)$ eigenvalue Eq. (31). The final expression for the mode shape $\mathbf{f}$ is

$$\mathbf{f}_k = -\alpha_{i1}\mathbf{H}_{kk}\boldsymbol{\phi}_{ik} + i\tilde{\omega}_0\left(\tilde{\beta} \mp \sqrt{\tilde{\beta}^2+\alpha_{i1}^2}\right)\sum_{m=1}^{n}\mathbf{H}_{km}\mathbf{N}_{m1}(\omega_0)\mathbf{m}_{1j} \tag{45}$$

for $k = 1, 2, \ldots, n$.

The mode shape for the remainder of the system is obtained by substituting Eq. (45) into Eqs. (11) and (14) of the companion paper. The results are

$$b_{kh} = \frac{\omega^2}{\omega_{kh}^2-\omega^2}\left[-\alpha_{i1}\mathbf{m}_{kh}^T\mathbf{H}_{kk}\boldsymbol{\phi}_{ik} + i\tilde{\omega}_0\left(\tilde{\beta} \mp \sqrt{\tilde{\beta}^2+\alpha_{i1}^2}\right)\mathbf{m}_{kh}^T\sum_{m=1}^{n}\mathbf{H}_{km}\mathbf{N}_{m1}(\omega_0)\mathbf{m}_{1j}\right], \quad \text{for } kh \neq 1j, \tag{46}$$

$$b_{1j} = \frac{\alpha_{i1}^2 - \left(\tilde{\beta} \mp \sqrt{\tilde{\beta}^2+\alpha_{i1}^2}\right)\gamma_1}{\gamma_1 + \tilde{\beta} \mp \sqrt{\tilde{\beta}^2+\kappa^2}}, \tag{47}$$

$$a_l = \frac{\omega^2}{\omega_l^2-\omega^2}\,\frac{-\alpha_{i1}^2 + \left(\tilde{\beta} \mp \sqrt{\tilde{\beta}^2+\alpha_{i1}^2}\right)\gamma_1}{\gamma_1 + \tilde{\beta} \mp \sqrt{\tilde{\beta}^2+\alpha_{i1}^2}}\,\boldsymbol{\phi}_{i1}^T\mathbf{m}_{1j} + \frac{i\omega}{\omega_l^2-\omega^2}\left(\sum_{k\neq 1}\boldsymbol{\phi}_{lk}^T\mathbf{Z}_k\mathbf{f}_k + \boldsymbol{\phi}_{i1}^T\mathbf{Z}_{11}\mathbf{f}_1\right), \quad \text{for } l \neq i, \tag{48}$$

Downloaded 03 May 2010 to 171.66.16.247. Redistribution subject to ASME license or copyright; see http://www.asme.org/terms/Terms_Use.cfm

$$a_i = \frac{\alpha_{i1}}{\mu_{i1} + \tilde{\beta} \mp \sqrt{\tilde{\beta}^2 + \alpha_{i1}^2}} \frac{-\alpha_{i1}^2 + \left(\tilde{\beta} \mp \sqrt{\tilde{\beta}^2 + \alpha_{i1}^2}\right)\gamma_1}{\gamma_1 + \tilde{\beta} \mp \sqrt{\tilde{\beta}^2 + \alpha_{i1}^2}} + \frac{i\omega}{\omega_i^2 - \omega^2}\left(\sum_{k \neq 1} \boldsymbol{\phi}_{ik}^T \mathbf{Z}_k \mathbf{f}_k + \boldsymbol{\phi}_{i1}^T \mathbf{Z}_{11} \mathbf{f}_1\right). \quad (49)$$

The modal coordinates b_{kh} and a_l become larger as the corresponding substructure natural frequencies ω_{kh} and ω_l approach ω. The largest modal coordinates are a_i and b_{1j} which corresponds to the modes i and $1j$ under study.

3 Multi-Mode Combination

In this section, multi-mode windows, for systems with more than two modes, are examined. The analysis is basically a multi-mode generalization of the $\{i, kj\}$ combination, and the derivations closely follow the methodology of Section 2.1. Due to the similarity of the derivations and the length of some of the intermediate expressions, only a few essential steps of the mathematics are explicitly given below.

It is assumed that the main structure has n_1 modes, the first n_2 substructures have one mode, and the remaining $n - n_2$ substructures have no modes in the frequency window. This combination is represented by the index sets

$$I(\omega_0, \delta) = \{1, 2, \ldots, n_1\}, \quad (50)$$

$$I(\omega_0, \delta, k) = \{1\} \text{ for } k \leq n_2, \; I(\omega_0, \delta, k) = \{\ \} \text{ for } k > n_2, \quad (51)$$

where the mode numbers, which are chosen for notational convenience, can represent any mode of the respective substructure.

As in the previous combinations, it is natural to assign the central frequency of the frequency window to the average of the frequencies

$$\omega_0^2 = \frac{1}{n_1 + n_2}\left(\sum_i \omega_i^2 + \sum_k \omega_{k1}^2\right). \quad (52)$$

Substituting Eqs. (4)–(9) for the mobilities and impedances into Eq. (1) yields the following $l(0) \times l(0)$ eigenvalue problem

$$[\mathbf{I}_{l(0)} + \{\mathbf{N}_0(\omega, \omega_0, \delta) + \mathbf{N}_1(\omega_0, \delta)\}\text{diag}\{\mathbf{Z}_{10}(\omega, \omega_0, \delta) + \mathbf{Z}_{11}(\omega_0, \delta), \ldots, \mathbf{Z}_{n_20}(\omega, \omega_0, \delta) + \mathbf{Z}_{n_21}(\omega_0, \delta), \mathbf{Z}_{n_2+1}(\omega_0), \cdots, \mathbf{Z}_n(\omega_0)\}]\mathbf{f} = 0. \quad (53)$$

Pre-multiplying Eq. (53) by the $l(0) \times l(0)$ matrix

$$\mathbf{F} = [\mathbf{I}_{l(0)} + \mathbf{N}_1(\omega_0, \delta)\text{diag}\{\mathbf{Z}_{11}(\omega_0, \delta), \cdots, \mathbf{Z}_{n_21}(\omega_0, \delta), \mathbf{Z}_{n_2+1}(\omega_0), \cdots, \mathbf{Z}_n(\omega_0)\}]^{-1}$$

leads to

$$[\mathbf{I}_{l(0)} + \mathbf{F}\{\mathbf{N}_0(\omega, \omega_0, \delta)\text{diag}\{\mathbf{Z}_{11}(\omega_0, \delta), \cdots, \mathbf{Z}_{n_21}(\omega_0, \delta), \mathbf{Z}_{n_2+1}(\omega_0), \cdots, \mathbf{Z}_n(\omega_0)\} + \{\mathbf{N}_0(\omega, \omega_0, \delta) + \mathbf{N}_1(\omega_0, \delta)\}\text{diag}\{\mathbf{Z}_{10}(\omega, \omega_0, \delta), \cdots, \mathbf{Z}_{n_20}(\omega, \omega_0, \delta), 0, \cdots, 0\}\}]\mathbf{f} = 0. \quad (54)$$

To reduce the size of this equation, it is premultiplied by the $2n_1 \times l(0)$ matrix

$$\begin{bmatrix} i\omega_0^{-1}\boldsymbol{\phi}_1^T \text{diag}\{\mathbf{Z}_{11}, \cdots, \mathbf{Z}_{n_21}, \mathbf{Z}_{n_2+1}, \cdots, \mathbf{Z}_n\} \\ \vdots \\ i\omega_0^{-1}\boldsymbol{\phi}_{n_1}^T \text{diag}\{\mathbf{Z}_{11}, \cdots, \mathbf{Z}_{n_21}, \mathbf{Z}_{n_2+1}, \cdots, \mathbf{Z}_n\} \\ \hline \mathbf{m}_{11}^T \quad 0 \quad \cdots \quad 0 \\ 0 \quad \mathbf{m}_{12}^T \quad \cdots \quad 0 \\ \vdots \quad \vdots \quad \ddots \quad \vdots \\ 0 \quad 0 \quad \cdots \quad \mathbf{m}_{1n_1}^T \end{bmatrix} \quad (55)$$

where horizontal partition divides the first n_1 rows from the remaining n_1 rows. Then $q_k = \omega_0^2/(\omega_{k1}^2 - \omega^2)\mathbf{m}_{k1}^T\mathbf{f}_k$ and p_i, defined in Eq. (32), are used to yield the $(n_1 + n_2) \times (n_1 + n_2)$ equation

$$[\text{diag}\{\omega_1^2 - \omega^2, \ldots, \omega_{n_1}^2 - \omega^2, \omega_{11}^2 - \omega^2, \ldots, \omega_{n_21}^2 - \omega^2\} - \omega_0^2\boldsymbol{\Gamma}]\begin{bmatrix}\mathbf{p} \\ \mathbf{q}\end{bmatrix}\omega_0^{-2} = 0, \quad (56)$$

where

$$\mathbf{p} \equiv \begin{bmatrix} p_1 \\ \vdots \\ p_{n_1} \end{bmatrix} \text{ and } \mathbf{q} = \begin{bmatrix} q_1 \\ \vdots \\ q_{n_2} \end{bmatrix}, \quad (57)$$

and $\boldsymbol{\Gamma}$ is a generalization of Eq. (35).

The problem is transformed into a symmetric form by using a transformation matrix $\boldsymbol{\Gamma}$ that is a generalization of Eq. (39)

$$\mathbf{T} \equiv \begin{bmatrix} \mathbf{I}_{n_1} & \mathbf{W} \\ \mathbf{0} & \mathbf{I}_{n_2} \end{bmatrix}, \quad (58)$$

where the (i, k) element of the $n_1 \times n_2$ matrix $\mathbf{W}$ is given by $-\omega_0^2/(\omega_i^2 - \omega^2)\alpha_{ik}$ in which α_{ik} is defined by Eq. (38). Following the procedure shown in Eq. (40), the eigenvalue problem reduces to

$$-\omega_0^2/(\omega_i^2 - \omega^2)\left\{\text{diag}\{\omega_1^2, \ldots, \omega_{n_1}^2, \omega_{11}^2, \ldots, \omega_{n_21}^2\} - \omega_0^2\begin{bmatrix}\mathbf{U} & \mathbf{A} \\ \mathbf{A}^T & \mathbf{G}\end{bmatrix} - \omega^2\mathbf{I}_{n_1+n_2}\right\}\begin{bmatrix}\hat{\mathbf{p}} \\ \mathbf{q}\end{bmatrix} = 0, \quad (59)$$

where $\hat{\mathbf{p}}$ is the n_1 vector

$$\hat{\mathbf{p}} \equiv \mathbf{p} - \mathbf{W}\mathbf{q}, \quad (60)$$

and $\mathbf{U}$, $\mathbf{A}$, and $\mathbf{G}$ are $(n_1 \times n_1)$, $(n_1 \times n_2)$ and $(n_2 \times n_2)$ matrices, respectively, with elements given by

$$U_{il} \equiv i\omega_0^{-1}\boldsymbol{\phi}_i^T \text{diag}\{\mathbf{Z}_{11}, \ldots, \mathbf{Z}_{n_21}, \mathbf{Z}_{n_2+1}, \ldots, \mathbf{Z}_n\}\mathbf{F}\boldsymbol{\phi}_l, \quad (61)$$

$$G_{kh} \equiv i\omega_0\mathbf{m}_{k1}^T \sum_{n=1}^{n_2} \mathbf{F}_{km}\mathbf{N}_{mh}(\omega_0)\mathbf{m}_{h1}, \quad (62)$$

$$A_{ik} \equiv \mathbf{m}_{i1}^T\boldsymbol{\phi}_{ki}. \quad (63)$$

Equations (61)–(63) contain coupling and resonance parameters which are generalizations of those discussed previously in detail for one and two-mode combinations. In particular, the diagonal elements of $\mathbf{U}$ are the substructure mass parameters measuring the impedance effects of the substructure on

Downloaded 03 May 2010 to 171.66.16.247. Redistribution subject to ASME license or copyright; see http://www.asme.org/terms/Terms_Use.cfm

each mode of the main structure (see Eq. (49) of the companion paper). The off-diagonal elements of **U** measure coupling between pairs of main structure modes arising from the presence of the substructure. The diagonal elements of **G** are the support flexibility parameters for each substructure, and they measure the effect of the flexibility of the main structure at the support point on the vibration of the supported substructure (see Eq. (37) of the companion paper). The off-diagonal elements of **G** are the support coupling parameters which measure the degree of coupling between pairs of support points of the main structure (see Eq. (19)). Finally, the elements of **A** are the substructure coupling parameters which measure the coupling between modes of the main structure and the substructure (see Eq. (38)).

The combined system natural frequencies are the roots of the characteristic polynomial of Eq. (59), which is of order $n_1 + n_2$. Although closed-form results cannot be obtained, the order of the problem is, in general, much reduced from the original problem.

There are two groups of modes in the multi-mode combination: One group consists of modes $\{1, 2, \cdots, n_1\}$ and $\{11, 21, \cdots, n_21\}$ which lie within the frequency window; the second group consists of all remaining modes which lie outside the frequency window. Coupling between modes within the outside group is quantified by the second term in **F**, i.e.,

$$\mathbf{N}_1(\omega_0, \delta)\text{diag}\{\mathbf{Z}_{11}(\omega_0, \delta), \cdots, \mathbf{Z}_{n_21}(\omega_0, \delta), \mathbf{Z}_{n_2+1}(\omega_0), \cdots, \mathbf{Z}_n(\omega_0)\}.$$

Coupling between the two groups of modes is quantified by the parameters in Eqs. (61)–(63). When these terms are small in relation to unity, the coupling is defined to be weak; otherwise, the coupling is strong.

The central frequency used in the expressions in Eqs. (52)–(63) is an estimate of the combined-system natural frequencies corresponding to the modes within the frequency window. For weakly coupled substructures, the parameters of the problem in Eqs. (61)–(63) are small compared to unity and accurate results can be obtained by using the approximate initial estimate,

$$\omega_0^2 = \frac{1}{n_1 + n_2}\left(\sum_i \omega_i^2 + \sum_k \omega_{k1}^2\right).$$

However, for strongly coupled substructures, iteration is necessary for each of the $n_1 + n_2$ modes of the combined system. The procedure is essentially the same as that described for mode combination $\{kj, lh\}$.

The $l(k)$ components of the mode shape, $\mathbf{f}_k$, are determined by substituting the result for the eigenvector of Eq. (59) into the original $l(0) \times l(0)$ eigenvalue Eq. (54). The results are

$$\mathbf{f}_k = \mathbf{F}_{kk}\sum_{i=1}^{n_1}\hat{p}_i\boldsymbol{\phi}_{ik} + \mathrm{i}\tilde{\omega}_0\sum_{l=1}^{n_2} q_l \sum_{m=1}^{n}\mathbf{F}_{km}\mathbf{N}_{ml}(\omega_0)\mathbf{m}_{l1}. \quad (64)$$

where $\hat{p}_i$ is the ith component of $\hat{\mathbf{p}}$.

The mode shapes for the remainder of the system are obtained by substituting Eq. (64) into Eqs. (11) and (14) of the companion paper. The results are

$$b_{kj} = \frac{\omega^2}{\omega_{kj}^2 - \omega^2}\left[-\sum_{i=1}^{n_1}\hat{p}_i\mathbf{m}_{kj}^T\mathbf{F}_{kk}\boldsymbol{\phi}_{ik} + \mathrm{i}\tilde{\omega}_0\sum_{l=1}^{n_2} q_l\mathbf{m}_{kj}^T\sum_{m=1}^{n}\mathbf{F}_{km}\mathbf{N}_{ml}(\omega_0)\mathbf{m}_{l1}\right], \quad (65)$$

$$a_i = \frac{\mathrm{i}\omega}{\omega_i^2 - \omega^2}\sum_{k=1}^{n}\boldsymbol{\phi}_{ik}^T\mathbf{Z}_k\mathbf{f}_k. \quad (66)$$

Table 1 Components of nondimensional length of main beam

Configuration	$\{kj,lh\}$	$\{i,kj\}$
l_1	0.283	0.255
l_2	0.283	0.083
l_l	0.092	0.120
l_c	0.333	0.333
l_r	0.092	0.208

As in the previous mode combinations, the modal coordinates becomes large as their corresponding sub-structure natural frequencies approach ω. The largest coordinates correspond to the modes in the window.

This concludes the in-depth analysis of the fundamental windows. The analysis has shown that there are precise mathematical parameters to define four types of substructure coupling effects; the problem complexity can be considerably reduced by frequency window analysis; and numerical accuracy of the solutions for the combined system modal properties are enhanced by an iterative procedure.

4 Example Studies

To illustrate the results of this paper, two example systems are studied. The systems are similar to the multiply connected beams examined in the companion paper (see Fig. 2 in the companion paper). The modulus of elasticity, E, is the same for all beams, and the moments of inertia and masses per unit length are denoted I and m for the main beam and I_s and m_s for the two substructures, respectively. It is useful to define nondimensional parameters

$$\xi \equiv \frac{m_s}{m} \text{ and } \chi\xi \equiv \frac{EI_s}{EI}, \quad (67)$$

where ξ is a mass density ratio and $\chi\xi$ is a rigidity ratio. For simplicity, vibrations corresponding to axial deformations are not considered and damping is neglected. The parameter l_k denotes the length of substructure k normalized by the length of the main beam. The nondimensional lengths l_l, l_c, and l_r shown in Fig. 2 of the companion paper specify the attachment locations of the substructure on the main beam. The middle attachment of each substructure is located at the midpoint of the substructure beams.

Two frequency windows are studied in this section corresponding to cases $\{kj, lh\}$ and $\{i, kj\}$. The nondimensional beam lengths for each case are shown in Table 1. For each mode case, four mass density ratios, $\xi = 0.05$, 0.15, 0.5, and 1.5, are considered and the parameter χ is held constant at 0.25. In this way, the degree of coupling between the main beam and the substructures is varied, while the fixed-base modal properties of each substructure are held constant.

For each example, the natural frequencies and mode shapes corresponding to each case are obtained using the exact and two approximate analyses. The exact results are determined by numerically solving the original eigenvalue problem of Eqs. (13) and (16)–(18) of the companion paper using a sufficiently large number of substructure modes to produce convergent values. The first set of approximate results are obtained by using the closed-form expressions derived in this paper for each mode combination. The second set of approximate results are obtained by using the same expressions as in the first approximation, but iterating until convergence is achieved. In all cases, it was found that iteration converges to the exact results. In the following, the results of the numerical studies are discussed for each case.

Downloaded 03 May 2010 to 171.66.16.247. Redistribution subject to ASME license or copyright; see http://www.asme.org/terms/Terms_Use.cfm

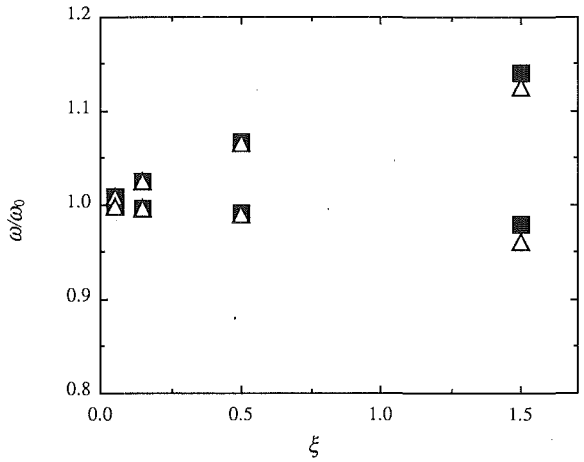


Fig. 1 Frequency ratios, ω/ω_o, versus rib mass density ratios, ξ, for mode combination {*kj, lh*} by both exact (■) and approximate (△) analysis

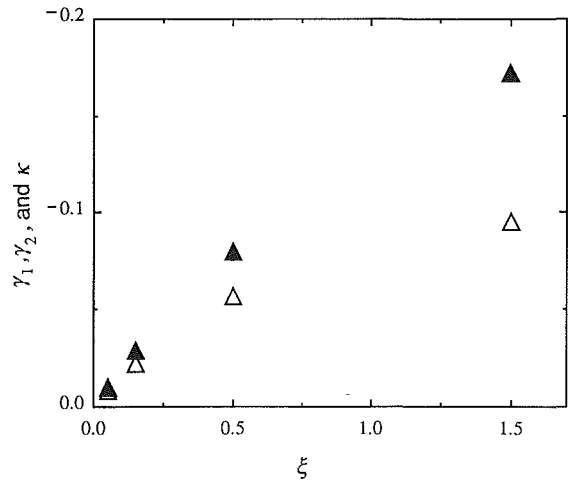


Fig. 2 Support flexibility parameters, γ_1 and γ_2, (△) and support coupling parameter, κ, (▲) versus rib mass density ratios, ξ, for mode combination {*kj, lh*}

For the example study of mode combination {*kj, lh*}, the modal properties of the combined system corresponding to the first mode of each of the two substructures are examined, i.e., $kj = 1,1$ and $lh = 2,1$. The approximate results are computed using Eqs. (20) and (25). The natural frequencies, normalized with respect to $\omega_0 = \{(\omega_{1j}^2 + \omega_{2h}^2)/2\}^{1/2}$ are plotted in Fig. 1. The components of mode shapes at the support points are shown in Table 2.

The support flexibility parameters γ_1 and γ_2 and the substructure coupling parameter κ are plotted in Fig. 2. The behavior of the parameters γ_1 and γ_2 closely follows that observed for mode case {*kj*} of the companion paper. For low values of ξ, the parameter κ is nearly zero, which implies that the two substructures become decoupled and the two natural frequencies corresponding to modes *kj* and *lh* can be treated as two separate one mode cases. For larger values of ξ, the modulus of κ increases, which signifies an increased modal coupling, and results in a separation of the two natural frequencies as shown mathematically in Eq. (23). In summary, increasing ξ results in increasingly negative values for γ_1, γ_2, and κ, which has the compound effect of increasing the average values of the natural frequencies as well as separating the natural frequencies on the frequency axis. Furthermore, the support mo-

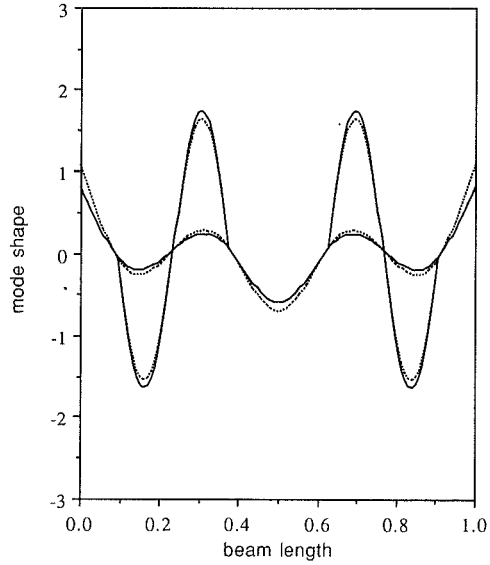


Fig. 3 Lower mode shape for $\xi = 0.5$ of mode combination {*kj, lh*} by exact (—) and approximate (· · ·) analysis

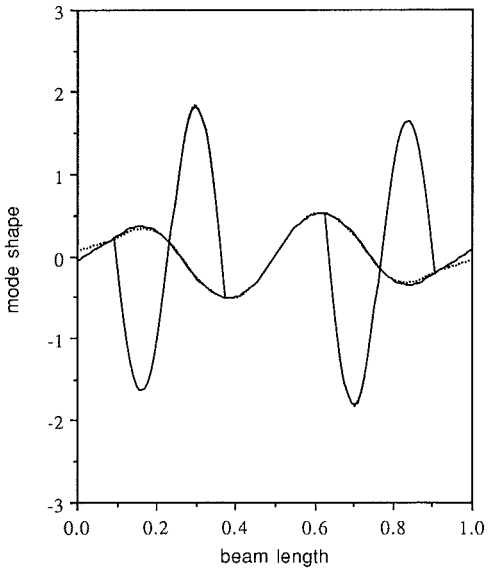


Fig. 4 Higher mode shape for $\xi = 0.5$ of mode combination {*kj, lh*} by exact (—) and approximate (· · ·) analysis

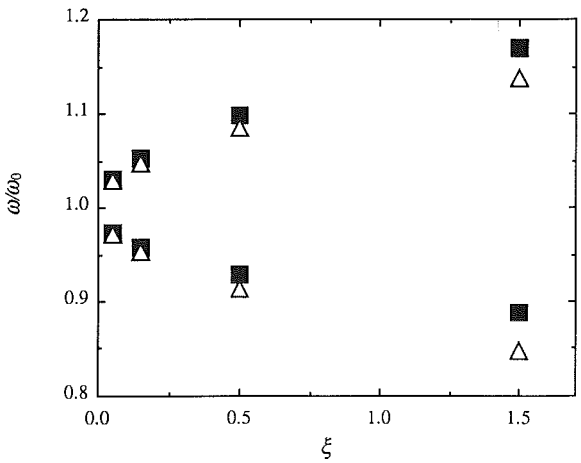


Fig. 5 Frequency ratios, ω/ω_o, versus rib mass density ratios, ξ, for mode combination {*i, kj*} by both exact (■) and approximate (△) analysis

Downloaded 03 May 2010 to 171.66.16.247. Redistribution subject to ASME license or copyright; see http://www.asme.org/terms/Terms_Use.cfm

Table 2 Exact and approximate frequency ratios and mode shape components for mode combination $\{kj, lh\}$

	ξ = 0.05				ξ = 0.15			
	mode 1		mode 2		mode 1		mode 2	
	Ex.	Ap.	Ex.	Ap.	Ex.	Ap.	Ex.	Ap.
Freq. ratio	0.999	0.999	1.009	1.009	0.997	0.997	1.025	1.025
Mode								
x1	-0.01	-0.01	0.10	0.10	-0.03	-0.03	0.16	0.16
x2	0.02	0.02	0.09	0.09	0.03	0.03	0.12	0.12
x3	0.02	0.02	-0.23	-0.23	0.04	0.04	-0.36	-0.36
x4	0.02	0.02	0.23	0.23	0.04	0.04	0.36	0.36
x5	0.02	0.02	-0.09	-0.09	0.03	0.03	-0.12	-0.12
x6	-0.01	-0.01	-0.10	-0.10	-0.03	-0.03	-0.16	-0.16

	ξ = 0.5				ξ =1.5			
	mode 1		mode 2		mode 1		mode 2	
	Ex.	Ap.	Ex.	Ap.	Ex.	Ap.	Ex.	Ap.
Freq. ratio	0.991	0.989	1.067	1.066	0.980	0.961	1.141	1.126
Mode								
x1	-0.04	-0.06	0.21	0.20	-0.06	-0.05	0.21	0.21
x2	0.04	0.04	0.15	0.15	0.03	0.02	0.15	0.14
x3	0.05	0.06	-0.52	-0.51	0.05	0.04	-0.63	-0.57
x4	0.05	0.06	0.52	0.51	0.05	0.04	0.63	0.57
x5	0.04	0.04	-0.15	-0.15	0.03	0.02	-0.15	-0.14
x6	-0.04	-0.06	-0.21	-0.20	-0.06	-0.05	-0.21	-0.21

Table 3 Exact and approximate frequency ratios and mode shape components for mode combination $\{i, kj\}$

	ξ = 0.05				ξ = 0.15			
	mode 1		mode 2		mode 1		mode 2	
	Ex.	Ap.	Ex.	Ap.	Ex.	Ap.	Ex.	Ap.
Freq. ratio	0.973	0.972	1.030	1.028	0.957	0.953	1.052	1.048
Mode								
x1	0.67	0.67	-0.57	-0.57	0.61	0.64	-0.63	-0.60
x2	-0.31	-0.31	0.14	0.14	-0.32	-0.33	0.12	0.11
x3	-0.37	-0.37	0.42	0.42	-0.27	-0.28	0.50	0.48
x4	-0.76	-0.76	0.47	0.47	-0.75	-0.76	0.47	0.43
x5	-0.30	-0.30	0.23	0.23	-0.27	-0.28	0.25	0.23
x6	0.29	0.29	-0.14	-0.14	0.33	0.33	-0.12	-0.09

	ξ = 0.5				ξ = 1.5			
	mode 1		mode 2		mode 1		mode 2	
	Ex.	Ap.	Ex.	Ap.	Ex.	Ap.	Ex.	Ap.
Freq. ratio	0.928	0.914	1.099	1.085	0.888	0.847	1.169	1.137
Mode								
x1	0.57	0.61	-0.68	-0.62	0.53	0.61	-0.38	-0.56
x2	-0.31	-0.32	0.04	0.05	-0.28	-0.32	-0.17	-0.02
x3	-0.12	-0.12	0.62	0.56	0.05	0.07	0.84	0.61
x4	-0.74	-0.76	0.43	0.34	-0.72	-0.69	0.48	0.23
x5	-0.23	-0.24	0.25	0.20	-0.16	-0.14	0.33	0.15
x6	0.40	0.41	-0.08	-0.06	0.49	0.47	-0.09	-0.03

tion for the corresponding mode shapes are increased. This is observed in Fig. 1 and Table 2.

The two mode shapes for combination $\{kj, lh\}$ are shown for $\xi = 0.5$ in Figs. 3 and 4 for the exact (solid line) and the approximate (dotted line) analysis. As was observed for mode case $\{kj\}$ of the companion paper, the motions of the substructure closely resemble their first fixed-base mode shapes. The difference between the two modes is that in Fig. 3, the substructure motions are out of phase, whereas in Fig. 4, they are in phase.

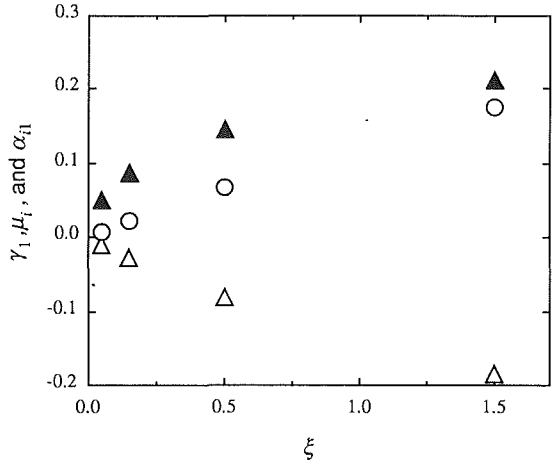


Fig. 6 Support flexibility parameter, γ_1, ($\triangle$), substructure mass parameter, μ_i, ($\circ$), and support coupling parameter, α_{i1}, ($\blacktriangle$), versus rib mass density ratios, ξ, for mode combination $\{i, kj\}$

For the example study of combination $\{i, kj\}$, the modal properties of the combined system corresponding to the first mode of substructure one and the fifth mode of the main beam is examined, i.e., $i = 5$ and $kj = 1,1$. The approximate results are computed using Eqs. (42) and (45). The natural frequencies, normalized with respect to $\omega_0 = \{(\omega_i^2 + \omega_{1j}^2)/2\}^{1/2}$ are plotted in Fig. 11. The components of the mode shapes at the support points are shown in Table 3.

The support flexibility parameter γ_1, the substructure mass parameter μ_i and the substructure coupling parameter a_{i1} are plotted in Fig. 6. For larger values of ξ, the parameters μ_i and a_{i1} become increasingly positive and the parameter γ_1 becomes increasingly negative. These parameter variations have the compound effect of increasing the natural frequency associated with the first mode of substructure one, decreasing the natural frequency associated with the fifth mode of the main structure, and separating the values of the two natural frequencies. This is observed in Fig. 5.

5 Conclusions

The method of analysis and the expressions for the parameters and modal properties not only are useful by themselves, but form a framework for further theoretical work. The spacing between resonant substructure frequencies discussed herein are directly applicable to the curve veering phenomena first studied by Leissa (1974). The results are also applicable to a wide class of continuous periodic structures composed of a main structure with equally spaced substructures (Mead, 1975). The modal coupling terms for the various mode combinations may provide further insight into the governing equations of statistical energy analysis (Lyon, 1975; Keane and Price, 1987) and power-flow methods (Pinnington and White, 1981). The frequency window method with an iterative procedure can be used for the Green's function analysis of combined systems (Nicholson and Bergman, 1986; Kelkel, 1987). Finally, the methods of this paper are applicable to acoustics problems involving submerged structural systems with internal substructure components.

Acknowledgments

This research was supported by the Office of Naval Research under Contract No. 88K-0514, Dr. P. B. Abraham, Scientific Officer. This support is gratefully acknowledged.

Downloaded 03 May 2010 to 171.66.16.247. Redistribution subject to ASME license or copyright; see http://www.asme.org/terms/Terms_Use.cfm

References

Dowell, E. H., 1979, "On Some General Properties of Combined Dynamical Systems," ASME JOURNAL OF APPLIED MECHANICS, Vol. 46, pp. 206–209.

Igusa, T., and Der Kiureghian, A., 1985, "Dynamic Characterization of Two-Degree-of-Freedom Equipment-Structure Systems," *Journal of Engineering Mechanics*, Vol. 111, No. 1, pp. 1–19.

Jacquot, R. G., and Soedel, W., 1970, "Vibrations of Elastic Surface Systems Carrying Dynamic Elements," *Journal of the Acoustical Society of America*, Vol. 47, pp. 1354–1358.

Keane, A. J., and Price, W. G., 1987, "Statistical Energy Analysis of Strongly Coupled Systems," *Journal of Sound and Vibration*, Vol. 117, No. 2, pp. 363–386.

Kelkel, K., 1987, "Green's Function and Receptance for Structures Consisting of Beams and Plates," *AIAA Journal*, Vol. 25, No. 11, pp. 1482–1489.

Leissa, A. W., 1974, "On a Curve Veering Aberration," *Journal of Applied Mathematics and Physics*, Vol. 25, pp. 99–111.

Lyon, R. H., 1975, *Statistical Energy Analysis of Dynamical Systems: Theory and Applications*, MIT Press, Cambridge, Mass.

Mead, D. J., 1975, "Wave Propagation and Natural Modes in Periodic Systems: I. Mono-Coupled Systems," *Journal of Sound and Vibration*, Vol. 40, No. 1, pp. 1–18.

Min, K.-W., Igusa, T., and Achenbach, J. D., 1991, "Frequency Window Method for Strongly-Coupled and Multiply-Connected Structural Systems: One Mode Windows," ASME JOURNAL OF APPLIED MECHANICS, Vol. 59, pp. S236-S243.

Nicholson, J. W., and Bergman, L. A., 1986, "Free Vibration of Combined Dynamical Systems," *Journal of Engineering Mechanics*, Vol. 112, No. 1, pp. 1–13.

Pinnington, R. J., and White, R. G, 1981, "Power Flow Through Machine Isolations to Resonant and Non-Resonant Beams," *Journal of Sound and Vibration*, Vol. 75, No. 2, pp. 179–197.

Sackman, J. L., Der Kiureghian, A., and Nour-Omid, B., 1983, "Dynamic Analysis of Light Equipment in Structures: Modal Properties of the Combined System," *Journal of the Engineering Mechanics Division*, ASCE, Vol. 109, No. 1, pp. 73–89.

Sackman, J. L., and Kelly, J. M., 1979, "Seismic Analysis of Internal Equipment and Components in Structures," *Engineering Structures*, Vol. 1, pp. 179–190.

Downloaded 03 May 2010 to 171.66.16.247. Redistribution subject to ASME license or copyright; see http://www.asme.org/terms/Terms_Use.cfm

Response of a Flexible Printed Circuit Board to Periodic Shock Loads Applied to its Support Contour

E. Suhir

AT&T Bell Laboratories,
Murray Hill, NJ 07974
Mem. ASME

Treating a printed circuit board (PCB) as a thin flexible rectangular plate, we evaluate its dynamic response to periodic shock loads applied to the support contour. The effect of the load periodicity on the amplitudes, accelerations, and stresses is analyzed for transient and steady-state damped linear vibrations, as well as for steady-state undamped nonlinear vibrations. It is shown that the transient nonresonant linear response can exceed the steady-state response by up to two times, and that the linear approach can be misleading in the case of a nondeformable support contour and intense loading. The obtained results can be of help when evaluating the accelerations, experienced by surface mounted electronic components and devices, and the dynamic stresses in a PCB of the given type, dimensions, and support conditions.

Introduction

Dynamic loading often plays a crucial role in the performance and reliability of electronic equipment (Steinberg, 1973; Carg and Smolik, 1989; Suhir and Lee, 1990). Such loading can occur during mechanical handling or accidental misuse of the equipment, during shipment (transportation), or, in military applications, even during normal operation of the equipment (see, for instance, Military Handbook, 1987). In the analysis below we evaluate the dynamic response of a flexible printed circuit board (PCB) to periodic shock loads applied to its support contour. This type of loading can be due, for example, to repeated impacts by typing, machine gun or rapid shooting artillery fire, vortex separation because of the unfavorable shape of aircraft or ship structures, etc. The purpose of the study is to determine the maximum accelerations experienced by the electronic components and devices surface mounted (SM) on the PCB, as well as the dynamic stresses in the board. While the elevated accelerations can affect the mechanical integrity and normal functioning of the SM components, the stresses in the board itself must be kept low enough to ensure is sufficient ultimate and fatigue strength.

Limiting our analysis to the first mode of PCB vibrations and treating the repetitive impact loads as instantaneous impulses, we proceed from the following differential equation for the principal coordinate $z(t)$:

$$\ddot{z}+2r\dot{z}+\lambda_0^2 z+\alpha z^3=\frac{P}{M}\sum_{k=0}^{n}\delta(t-kT_s),\ n=0,1,2,\ldots . \quad (1)$$

In this equation, which describes the PCB vibrations after the nth impact, z, $\dot{z}$, and $\ddot{z}$ are the maximum displacement, velocity, and acceleration, respectively; λ_0 is the frequency of undamped linear vibrations; r is the coefficient of damping; α is the parameter of nonlinearity; P is the magnitude of the impulses; M is the mass of the system; T_s is the time between impacts; t is time; and $\delta(t)$ is Dirac's delta function.

The fundamental result in the theory in question has been obtained by G. Duffing (see Duffing, 1918, or Loytsyansky and Lurie, 1960) who derived the following formula for the dimensionless amplitude (periodicity factor) of steady-state linear vibrations:

$$A_\infty=\frac{1}{2}\left|\operatorname{cosec}\frac{\lambda_0 T_s}{2}\right| . \quad (2)$$

Here, A_∞ is the ratio of the amplitude of vibrations caused by periodic impulses to the amplitude

$$A_1=\frac{P}{M\lambda_0} \quad (3)$$

of vibrations due to a single impulse. Duffing's derivation was based on the conditions of periodicity

$$z(0)=z(T_s),\ \dot{z}(0)=\dot{z}(T_s)+\frac{P}{M}, \quad (4)$$

and uses an obvious assumption that vibration damping is small

Contributed by the Applied Mechanics Division of THE AMERICAN SOCIETY OF MECHANICAL ENGINEERS for presentation at the 1992 ASME Summer Mechanics and Materials Meeting, Tempe, AZ, Apr. 28–May 1, 1992.

Discussion on this paper should be addressed to the Technical Editor, Prof. Leon M. Keer, The Technological Institute, Northwestern University, Evanston, IL 60208, and will be accepted until four months after final publication of the paper itself in the JOURNAL OF APPLIED MECHANICS. Manuscript received by the ASME Applied Mechanics Division, Apr. 17, 1990; final revision, May 24, 1991.

Paper No. 92-APM-9.

Copyright © 1992 by ASME
Downloaded 03 May 2010 to 171.66.16.247. Redistribution subject to ASME license or copyright; see http://www.asme.org/terms/Terms_Use.cfm

and has an effect only on the final steady-state nature of the vibrations but not on the vibration amplitude. Linear and nonlinear vibrations caused by repetitive instantaneous impulses were later examined, using different approaches and in application to various engineering problems, by Burton (1958), Panovko and Gubanova (1967), Krajcinovic (1968), Suhir (1970, 1975, 1982, 1985), Veluswami (1973), Paz and O'Charoen (1973), Halbauer (1974), Hsu, Chen, and Lee (1977), and others.

In this study we evaluate the effect of the periodicity of impacts on transient and steady-state linear vibrations ($\alpha = 0$) and on steady-state nonlinear undamped vibrations ($r = 0$). In the latter case the nonlinearity of the PCB vibrations is due to the nondeformability of the support contour. This results in reactive in-plane (membrane) stresses which are proportional to the lateral deflections squared (see, for instance, Timoshenko and Woinowski-Krieger (1940) or Timoshenko and Young (1965)) and can be significant, if the deflections are large. From the viewpoint of structural analysis, a PCB can be treated as a thin flexible plate. Although an actual PCB has somewhat different mechanical properties in different directions, in this study we assume that it is homogeneous and isotropic.

Note that various linear and nonlinear problems of structural dynamics, including plate structures, were analyzed and discussed in numerous monographs, manuals, and reference books. Examples are: Timoshenko and Young (1955, 1956, 1965), Den Hartog (1956), Jacobsen and Ayre (1958), Skudrzyk (1968), and Harris and Crede (1976). Approximate analyses of nonlinear oscillators with stiff cubic characteristics (so-called "Duffing oscillators") can be found in the books by Kauderer (1958) and Hayashi (1964). The emphasis in these books and monographs is, however, on weak, rather than strong, nonlinearities, and on continuous, rather than shock, excitations. Solutions to static problems of nonlinear bending of plates with nondeformable contours were presented by Bubnov (1902) for elongated plates, by Prescott (1924), for finite aspect ratio, simply-supported plates, and by Levy (1942) for finite aspect ratio clamped plates. Linear static and dynamic analyses of the mechanical behavior of printed circuit boards and cards have been performed recently by Engel (1990), Wong, Stevens, and Wang (1990), Kim and Gupta (1990), and Crovetto, Gupta, and Kim (1990). Nonlinear dynamic response of a flexible thin plate to constant acceleration of its support contour, with application to PCBs used in avionic packaging, was analyzed by Suhir (1991).

Analysis

Equation of Motion. Limiting our analysis to the first mode of vibrations, we present the deflection function ω and the stress function ϕ in the form:

$$w = w_c(t) - w_1(x,y)z(t),\ \phi = \phi_1(x,y)z^2(t), \tag{5}$$

where w_c is the displacement of the PCB contour, $w_1(x,y)$ is the coordinate function, z is the principal coordinate, and $\phi_1(x,y)$ is the static stress function. In the case of a finite aspect ratio ($1 \le b/a \le 2$), simply-supported board (Prescott, 1924)

$$w_1 = \cos\frac{\pi x}{a}\cos\frac{\pi y}{b}, \tag{6}$$

$$\phi_1 = \frac{E}{32}\left\{\frac{2\pi^2}{1-\nu^2}\left[\left(\frac{\nu}{a^2}+\frac{1}{b^2}\right)x^2+\left(\frac{1}{a^2}+\frac{\nu}{b^2}\right)y^2\right] - \frac{a^2}{b^2}\cos\frac{\pi x}{a} - \frac{b^2}{a^2}\cos\frac{\pi y}{b}\right\}. \tag{7}$$

In the case of a finite aspect ratio ($1 \le b/a \le 1.5$) clamped board (Levy, 1942),

$$w_1 = \cos^2\frac{\pi x}{a}\cos^2\frac{\pi y}{b}, \tag{8}$$

$$\phi_1 = \frac{E}{32}\left\{\frac{3\pi^2}{2(1-\nu^2)}\left[\left(\frac{\nu}{a^2}+\frac{1}{b^2}\right)x^2+\left(\frac{1}{a^2}+\frac{\nu}{b^2}\right)y^2\right] - \frac{a^2}{b^2}\cos\frac{\pi x}{a} - \frac{b^2}{a^2}\cos\frac{\pi y}{b} - \left(\frac{a}{4b}\right)^2\cos\frac{4\pi x}{a} - \left(\frac{b}{4a}\right)^2\cos\frac{4\pi y}{b} - \frac{2a^2b^2}{(a^2+b^2)^2}\cos\frac{2\pi x}{a}\cos\frac{2\pi y}{b} - \frac{a^2b^2}{(4a^2+b^2)^2}\cos\frac{2\pi x}{a}\cos\frac{4\pi y}{b} - \frac{a^2b^2}{(a^2+4b^2)^2}\cos\frac{4\pi x}{a}\cos\frac{2\pi y}{b}\right\}. \tag{9}$$

The kinetic energy T and the strain energy V of a thin flexible plate (PCB) subjected to nonlinear vibrations are expressed as follows (see, for instance, Timoshenko and Young, 1955):

$$T = \frac{1}{2}m\int_A\left(\frac{\partial w}{\partial t}\right)^2 dA, \tag{10}$$

$$V = \frac{1}{2}D\int_A[(\Delta w)^2 - 2(1-\nu)L(w)]dA + \frac{1}{2}\frac{h}{E}\int_A[(\Delta\phi)^2 - 2(1+\nu)L(\phi)]dA, \tag{11}$$

where $A = ab$ is the PCB area, m is its mass (per unit area) with consideration of the masses of the SM components (these are assumed small in size, so that they affect only the PCB mass, but not its flexural rigidity), $D = Eh^3/12(1-\nu^2)$ is the board's flexural rigidity, h is its thickness, t is time, and the operators Δ and L are

$$\Delta = \frac{\partial^2}{\partial x^2}+\frac{\partial^2}{\partial y^2}, \qquad L = \frac{\partial^2}{\partial x^2}\frac{\partial^2}{\partial y^2} - \left(\frac{\partial^2}{\partial x\partial y}\right)^2.$$

Substituting (5) into (10) and (11), we obtain

$$T = \frac{1}{2}(m\,\dot{w}_c^2 A - 2M_0\dot{w}_c\dot{z} + M\dot{z}^2)$$

$$V = \frac{1}{2}M\left(\lambda_0^2 z^2 + \frac{1}{2}\alpha z^4\right), \tag{12}$$

where the following notation is used:

$$M_0 = m\int_A w_1 dA, \qquad M = m\int_A w_1^2 dA,$$

$$\lambda_0 = \sqrt{\frac{D}{M}\int_A[(\Delta w_1)^2 - 2(1-\nu)L(w_1)]dA}$$

$$\alpha = \frac{2h}{EM}\int_A[(\Delta\phi_1)^2 - 2(1+\nu)L(\phi_1)]dA \tag{13}$$

Here, M_0 and M are generalized masses, associated with the excitation force and the vibration system, respectively, λ_0 is the linear frequency of free undamped vibrations, and α is the parameter of nonlinearity.

Introducing (12) into the Lagrange equation (see, for instance, Pars, 1965)

$$\frac{d}{dt}\frac{\partial T}{\partial\dot{z}}+\frac{\partial V}{\partial z}=0,$$

we obtain the following nonlinear differential equation for the principal coordinate $z(t)$

Downloaded 03 May 2010 to 171.66.16.247. Redistribution subject to ASME license or copyright; see http://www.asme.org/terms/Terms_Use.cfm

$$\ddot{z} + + \lambda_0^2 z + \alpha z^3 = \frac{Q(t)}{M}, \tag{14}$$

where $Q(t) = M_0 \ddot{w}_c(t)$ is the excitation force. If this force is due to periodic instantaneous impulses, causing the change in the contour's velocity by the magnitude $\dot{w}_c$, then it can be presented as follows:

$$Q(t) = M_0 \dot{w}_c \sum_{k=0}^{n} \delta\ (t - kT_s),\ n = 0,1,2,\ldots\ . \tag{15}$$

Supplementing the left part of Eq. (14) with a dissipation term and assuming linear viscous damping, we obtain the equation of motion in the form (1), where the generalized impulse is $P = M_0 w_c$.

The relationships (6), (7), and (13) result in the following formulas for the vibration parameters of a finite aspect ratio, simply-supported board

$$\left.\begin{aligned} M_0 &= \frac{4}{\pi^2} mA,\ M = \frac{1}{4} mA,\ \lambda_0 = \pi^2 \frac{a^2 + b^2}{a^2 b^2} \sqrt{\frac{D}{m}}, \\ \alpha &= \frac{3\pi^4 D}{4mh^2} \frac{(3 - \nu^2)(a^4 + b^4) + 4\nu a^2 b^2}{a^2 b^4} \end{aligned}\right\}. \tag{16}$$

Similarly, the relationships (8) and (9) lead to the following parameters of vibration of a clamped board

$$\left.\begin{aligned} M_0 &= \frac{1}{4} mA, M = \frac{9}{64} mA,\ \lambda_0 = \frac{4\pi^2}{3a^2 b^2} \sqrt{[3(a^4 + b^4) + 2a^2 b^2]\, \frac{D}{m}}, \\ \alpha &= \frac{\pi^4 Eh}{18ma^4 b^4} \left[\frac{9(a^4 + b^4 + 2\nu a^2 b^2)}{4(1 - \nu^2)} + \frac{17}{8}(a^4 + b^4) + \frac{12a^4 b^4}{(a^2 + b^2)^2} \right. \\ &\quad \left. + \frac{5a^4 b^4}{(4a^2 + b^2)^2} + \frac{5a^4 b^4}{(a^2 + 4b^2)^2} \right] \end{aligned}\right\}. \tag{17}$$

Linear Vibrations. In the linear case ($\alpha = 0$), the solution to Eq. (1) can be obtained on the basis of the Duhamel integral (see, for instance, Harris and Crede, 1976)

$$z(t) = \int_0^t Q(\xi) h(t - \xi) d\xi, \tag{19}$$

where, in the case in question, the excitation force $Q(\xi)$ and the impulse response function $h(t - \xi)$ are expressed as

$$Q(t) = P \sum_{k=0}^{n} \delta(t - kT_s),$$

$$h(t - \xi) = \frac{1}{M\lambda} e^{-r(t-\xi)} \sin \lambda (t - \xi). \tag{20}$$

Here, $\lambda = \sqrt{\lambda_0^2 - r^2}$ is the frequency of free damped vibrations. Substituting (20) into (19), and considering that

$$\int_0^t f(\xi) \delta(\xi - a) d\xi = f(a)$$

(see, for instance, Bateman and Erdelyi, 1955), we obtain

$$z(t) = \frac{P}{M\lambda} \sum_{k=0}^{n} e^{-r(t - kT_s)} \sin \lambda\ (t - kT_s). \tag{21}$$

This solution, obtained in "global" time, counted from the moment of the application of the first ($n = 0$) impulse, can be rewritten, by replacing t with $t + nT_s$, in "local" time, counted from the moment of the application of the sequential nth impulse. Then we have

$$z(t) = \frac{P}{M\lambda} e^{-rt} A_n \cos(\lambda t + \epsilon_n), \tag{22}$$

where the dimensionless amplitude A_n (factor reflecting the effect of the periodicity of the impulses on the vibration amplitudes) and the initial phase angle ϵ_n are as follows:

$$\left.\begin{aligned} A_n &= \sqrt{\frac{1 + e^{-2(n+1)rT_s} - 2e^{-(n+1)rT_s} \cos(n+1)\lambda T_s}{1 + e^{-2rT_s} - 2e^{-rT_s} \cos \lambda\ T_s}} \\ \epsilon_n &= -\arctan \frac{e^{rT_s} - \cos \lambda\ T_s - e^{-nrT_s} \cos(n+1)\lambda T_s + e^{-(n+1)rT_s} \cos n\ \lambda T_s}{\sin \lambda\ T_s - e^{-nrT_s} \sin(n+1)\ \lambda T_s + e^{-(n+1)rT_s} \cos n\ \lambda\ T_s} \end{aligned}\right\}. \tag{23}$$

In the case of an elongated board ($b \to \infty$), the coordinate function is (see, for instance, Timoshenko and Woinowski-Krieger (1940)):

$$w_1 = C \cosh \beta \frac{x}{a} + \cos \beta \frac{x}{a}, \tag{18}$$

where $C = 0$, $\beta = \pi$ for a simply-supported board, and $C = 0.1329$, $\beta = 4.73$ for a clamped board. Then we obtain

$$M_0 = \frac{2}{\pi} ma,\ M = \frac{1}{2} ma,\ \lambda_0 = \frac{\pi^2}{a^2} \sqrt{\frac{D}{m}},\ \alpha = 3 \frac{\lambda_0^2}{h^2}$$

in the case of a simply-supported board, and

$$M_0 = 0.5928\ ma,\ M = 0.5088\ ma,\ \lambda_0 = \frac{10}{a^2} \sqrt{\frac{5D}{m}},\ \alpha \cong 0.282 \frac{\lambda_0^2}{h^2}$$

in the case of a clamped board.

Putting in these equations $n \to \infty$, we find that the dimensionless steady-state amplitude A_∞ and phase angle ϵ_∞ are expressed by the formulas

$$A_\infty = (1 + e^{-2rT_s} - 2e^{-rT_s} \cos \lambda\ T_s)^{-1/2},$$

$$\epsilon_\infty = -\arctan \frac{e^{rT_s} - \cos \lambda\ T_s}{\sin \lambda\ T_s}. \tag{24}$$

When damping is small, assuming $r = 0$, we have

$$A_\infty = \frac{1}{2} \left| \operatorname{cosec} \frac{\lambda_0 T_s}{2} \right|,\ \epsilon_\infty = -\frac{\lambda_0 T_s}{2}. \tag{25}$$

This coincides with Duffing's formula (2) obtained on the basis of the periodicity conditions. When $T_s = 2m\pi/\lambda$, $m = 1, 2, 3, \ldots$ (impulse resonance), the Eqs. (23) yield $A_n = [1 - e^{-(n+1)rT_s}]/[1 - e^{-rT_s}]$, $\epsilon_n = -\pi/2$. For steady-state ($n \to \infty$) resonance vibrations we obtain $A_\infty = 1/[1 - e^{-rT_s}]$. Thus, the ratio $A_n/A_\infty = 1 - e^{-(n+1)rT_s}$ of the current amplitude to the steady-state amplitude is always smaller than unity, especially at the beginning of the vibrations (small n), as well as in the case of small damping (small r) and frequent impulses (small T_s). At nonresonant conditions, the current-to-steady-state amplitude ratio can be obtained from (23) and (24) and is as follows:

Downloaded 03 May 2010 to 171.66.16.247. Redistribution subject to ASME license or copyright; see http://www.asme.org/terms/Terms_Use.cfm

$$\frac{A_n}{A_\infty}=\sqrt{1+e^{-2(n+1)rT_s}-2e^{-(n+1)rT_s}\cos(n+1)\lambda\ T_s}. \quad (26)$$

In the case of small damping and/or frequent impulses (small rT_s value), this formula yields

$$\frac{A_n}{A_\infty}=2\left|\sin\left[(n+1)\frac{\lambda T_s}{2}\right]\right|. \quad (27)$$

As evident from this formula, the transient nonresonant response can exceed the steady-state response by up to two times. Note, that in reality, this ratio can never reach two exactly, because of the discrete nature of Eq. (27).

Nonlinear Vibrations. In order to assess the effect of the nonlinearity on the steady-state shock-excited vibrations with low damping, we seek the solution to Eq. (1), assuming $r = 0$, in the form:

$$z(t)=A\frac{P}{M\lambda_0}\,cn(\sigma t+\epsilon,k)=A\frac{P}{M\lambda_0}\,cn\ u, \quad (28)$$

where $cn\ u$ is an elliptic cosine (see, for instance, Bateman and Erdelyi, 1955), k is the modulus of the elliptic function, ϵ is the initial phase angle, and σ is the frequency parameter. From (28) we obtain, by differentiation:

$$\dot{z}(t)=-A\frac{P}{M\lambda_0}\,\sigma\ sn\ \ u\ dn\ \ u,$$

$$\ddot{z}(t)=-A\frac{P}{M\lambda_0}\,\sigma^2\ cn\ u\ (1-2k^2sn^2u), \quad (29)$$

where $sn\ u$ is an elliptic sine, and $dn\ u = \sqrt{1 - k^2sn^2u}$ is the function of delta amplitude. After substituting (28) and the second formula in (29) into Eq. (1), and putting in this equation $r = 0$, we obtain:

$$\sigma=\lambda_0\sqrt{1+\bar{\alpha}A^2},\ k=\sqrt{\frac{\bar{\alpha}A^2}{2(1+\bar{\alpha}A^2)}}, \quad (30)$$

where

$$\bar{\alpha}=\alpha\left(\frac{P}{M\lambda_0^2}\right)^2=\alpha\left(\frac{M_0}{M}\frac{\dot{w}_c}{\lambda_0^2}\right)^2 \quad (31)$$

is the dimensionless parameter of nonlinearity.

Using Duffing's approach and introducing (28) and the first formula in (29) into the periodicity conditions (4), we obtain the following two equations for the amplitude A and the initial phase angle ϵ:

$$\left.\begin{aligned} &cn\ (\epsilon,k)=cn(\sigma T_s+\epsilon,k)\\ &-sn\ (\epsilon,k)\ dn(\epsilon,k)=sn(\sigma T_s+\epsilon,k)dn(\sigma T_s+\epsilon,k)+\frac{\lambda_0}{A\sigma}\end{aligned}\right\}. \quad (32)$$

The first of these equations yields:

$$sn(\sigma T_s+2\epsilon,k)=0,\ cn(\sigma T_s+2\epsilon,k)=1,$$

so that the amplitude of the elliptic function is

$$\phi=am(\sigma T_s+2\epsilon,k)=2\pi i, i=0,\pm1,\pm2,\ldots,$$

and therefore

$$\sigma T_s+2\epsilon=\int_0^{2\pi i}\frac{d\xi}{\sqrt{1-k^2\sin^2\xi}}=4i\,K(k), \quad (33)$$

where $K(k) = \int_0^{\pi/2} d\xi/\sqrt{1-k^2\sin^2\xi}$ is the complete elliptic integral of the first kind. From (33) we obtain the following formula for the initial phase angle ϵ:

$$\epsilon=2iK(k)-\frac{1}{2}\sigma T_s,\ i=0,\ \pm1,\pm2,\ldots. \quad (34)$$

The second equation in (32) can be written, considering the first equation, as follows:

$$A=\frac{\lambda_0}{2\sigma F}, \quad (35)$$

where the function F is

$$F=|sn(\epsilon,k)dn(\epsilon,k)|=|sn(\epsilon,k)\sqrt{1-k^2sn^2(\epsilon,k)}|. \quad (36)$$

After introducing the first formula in (30) into (35) and solving the obtained equation for the dimensionless amplitude A, we obtain:

$$A=\sqrt{\frac{\sqrt{1+\bar{\alpha}/F^2}-1}{2\bar{\alpha}}}. \quad (37)$$

Since the period of the elliptic cosine $cn(t,k)$ is $4K(k)$, the period of the function $cn(\sigma t+\epsilon,\ k)$, which is the vibration period, is $4K(k)/\sigma$. Then the vibration frequency is $\omega = \pi\sigma/2K(k)$. In the case of linear vibrations ($\alpha = 0$), we have: $k = 0$, $K(k) = \pi/2$, $\omega = \sigma = \lambda_0$, $\epsilon = i\pi - 1/2\ \lambda_0\ T_s$, $sn(\epsilon,\ 0) = \sin\epsilon = -\sin\lambda_0T_s/2$, $dn(\epsilon,\ 0) = 1$, and therefore $F = |\sin\lambda_0T_s/2|$. Then the formula (37) yields:

$$A=\lim_{\alpha\to0}\sqrt{\frac{\sqrt{1+\bar{\alpha}/F^2}-1}{2\bar{\alpha}}}=\frac{1}{2F}=\frac{1}{2}\left|\operatorname{cosec}\frac{\lambda_0T_s}{2}\right|$$

and coincides with (25).

In the case of a single impulse, the conditions of periodicity (4) should be replaced by the initial conditions $z(0) = 0$, $\dot{z}(0) = P/M$, while the initial phase angle ϵ should be put equal to zero. This leads to the following formula for the dimensionless amplitude:

$$A_1=\sqrt{\frac{\sqrt{1+2\bar{\alpha}}-1}{\bar{\alpha}}}. \quad (38)$$

Clearly, the amplitude of periodically excited vibrations, expressed by (37), is minimum when $F = F_{max}$. From (36) one can find

$$F_{max}^2=\frac{1+\sqrt{1+\bar{\alpha}/2}}{2\sqrt{1+\bar{\alpha}/2}}. \quad (39)$$

Hence,

$$A_{min}=\sqrt{\frac{\sqrt{1+\bar{\alpha}/2}-1}{\bar{\alpha}}}. \quad (40)$$

The amplitude of the shock-excited vibrations, due to periodic impacts, can be computed as a function of the excitation frequency $\lambda_s = 2\pi/T_s$ using the following procedure:

(1) For the given board and the given step $\dot{w}_c$ in the contour velocity, determine the generalized masses M_0 and M, the linear frequency λ_0, the parameter of nonlinearity α, the dimensionless parameter of nonlinearity $\bar{\alpha}$, and the F_{max}^2 value.

(2) For the F^2 values within the range $0 \le F^2 \le F_{max}^2$, compute the dimensionless amplitudes A by (37) and the corresponding k^2 values by the second formula in (30).

(3) In accordance with Lance's (1960) recommendations for calculating elliptic functions and integrals, for each k^2, starting with

$$a_0 = 1,\ b_0 = \sqrt{1-k^2},\ \phi_0 = \arcsin\sqrt{\frac{1-\sqrt{1-4k^2F^2}}{2k^2}},$$

compute $a_{r+1} = a_r + b_r/2$, $b_{r+1} = \sqrt{a_rb_r}$, $c_r = \sqrt{a_r^2 - b_r^2}$, $r = 0, 1, 2, \ldots$

Downloaded 03 May 2010 to 171.66.16.247. Redistribution subject to ASME license or copyright; see http://www.asme.org/terms/Terms_Use.cfm

$$\phi_r = \arcsin\left[\sin 2\,\phi_{r-1}/\sqrt{1+\frac{c_r^2}{a_r^2}+2\,\frac{c_r}{a_r}\cos 2\,\phi_{r-1}}\right],\ r = 1, 2, \ldots,$$

stop the iterations at $r = N$, when $c_r \approx 0$, and then determine $\ell = a_N = b_N$, and $n = \phi_{N-1}$.

(4) For each amplitude A, calculate the frequency

$$\omega = \lambda_0 \ell \sqrt{1+\bar{\alpha}A^2}$$

of nonlinear vibrations and the frequency ratios

$$\left(\frac{\lambda_0}{\lambda_s}\right)_i = \frac{\lambda_0}{\omega}\left|i+\frac{n}{\pi}\,2^{1-N}\right|,\ i=0,\pm,\pm 2,\ldots .$$

Note that for sufficiently large λ_0/λ_s ratios (i.e., for large i values), the latter formula can be simplified:

$$\left(\frac{\lambda_0}{\lambda_s}\right)_i = i\,\frac{\lambda_0}{\omega},\ i=0,\pm 1,\pm 2,\ldots .$$

The maximum acceleration, in accordance with the second formula in (29), is

$$\ddot{z}_{\max} = A\,\frac{P}{M\lambda_0}\,\sigma^2 = \eta_{\ddot{z}}\,\frac{P\lambda_0}{M}, \tag{41}$$

where the factor $\eta_{\ddot{z}} = A\,(1 + \bar{\alpha}A^2)$ reflects the effects of the nonlinearity of vibrations and the periodicity of the impacts. Note that nonlinear shock-excited vibrations can turn out stochastically unstable, especially when the ratios λ_0/λ_s are small (Suhir, 1975, 1985).

Stresses. The dynamic stresses in the PCB can be computed on the basis of the well-known formulas for thin flexible plates (see, for instance, Timoshenko and Woinowski-Krieger, 1940). These, with Eqs. (6) and (7) for the coordinate function w and the static stress function ϕ, result in the following equations for the maximum normal stresses at the center of a simply-supported board:

$$\left.\begin{aligned}\sigma_x &= \frac{\pi^2 E h^2}{2a^2b^2}\,\frac{\nu a^2+b^2}{1-\nu^2}\,\zeta\left[1+\frac{\nu a^2+(2-\nu^2)b^2}{4(\nu a^2+b^2)}\,\zeta\right]\\ \sigma_y &= \frac{\pi^2 E h^2}{2a^2b^2}\,\frac{a^2+\nu b^2}{1-\nu^2}\,\zeta\left[1+\frac{(2-\nu^2)a^2+\nu b^2}{4(a^2+\nu b^2)}\,\zeta\right]\end{aligned}\right\}. \tag{42}$$

Here, $\zeta = A = P/M\lambda_0 h$ is the dimensionless maximum displacement (the ratio of the vibration amplitude to the PCB thickness). The maximum shearing stress takes place along the rectangle $x = \pm a/2$, $y = \pm b/2$, and is

$$\tau_{xy} = \frac{\pi^2 G h^2}{ab}\,\zeta,$$

where $G = E/2\,(1 + \nu)$ is the shear modulus of the material. In the case of an elongated board ($b \to \infty$), the shearing stress is zero, and the maximum normal stress is

$$\sigma_x = \frac{\pi^2 E}{2(1-\nu^2)}\left(\frac{h}{a}\right)^2\zeta\left(1+\frac{\zeta}{2}\right). \tag{43}$$

Equations (8) and (9) result in the following formulas for the normal stresses at the center of a clamped board:

$$\left.\begin{aligned}\sigma_x &= \frac{\pi^2 E h^2}{a^2b^2}\,\frac{\nu a^2+b^2}{1-\nu^2}\,\zeta\left\{1+\frac{1-\nu^2}{32}\,\frac{b^2}{\nu a^2+b^2}\right.\\ &\qquad\times\zeta\left[5+\frac{3}{1-\nu^2}\left(1+\nu\,\frac{a^2}{b^2}\right)\right.\\ &\qquad\left.\left.+\frac{8a^2b^2}{(a^2+b^2)^2}+\frac{16a^2b^2}{(4a^2+b^2)^2}+\frac{4a^2b^2}{(a^2+4b^2)^2}\right]\right\}\\ \sigma_y &= \frac{\pi E h^2}{a^2b^2}\,\frac{a^2+\nu b^2}{1-\nu^2}\,\zeta\left\{1+\frac{1-\nu^2}{32}\,\frac{a^2}{a^2+\nu b^2}\right.\\ &\qquad\times\zeta\left[5+\frac{3}{1-\nu^2}\left(1+\nu\,\frac{b^2}{a^2}\right)\right.\\ &\qquad\left.\left.+\frac{8a^2b^2}{(a^2+b^2)^2}+\frac{4a^2b^2}{(4a^2+b^2)^2}+\frac{16a^2b^2}{(a^2+4b^2)^2}\right]\right\}\end{aligned}\right\}. \tag{44}$$

The maximum shearing stress in such a board occurs along the perimeter of a rectangle $x = \pm a/4$, $y = \pm b/4$ and is

$$\tau_{xy} = \frac{\pi^2 G h^2}{ab}\,\zeta\left[1+\frac{1+\nu}{2}\,\frac{a^2b^2}{(a^2+b^2)^2}\,\zeta\right].$$

The maximum normal stress in an elongated clamped board is

$$\sigma_x \cong 16\,\frac{E}{1-\nu^2}\left(\frac{h}{a}\right)^2\zeta(1+0.193\,\zeta). \tag{45}$$

Table 1

$\bar{\alpha} = 4.664$, $\lambda_0 = 320.9\ \text{sec}^{-1}$

F^2	0	0.1	0.2	0.4	0.6	0.7	0.75	0.7739
A^2	∞	0.6327	0.4215	0.2742	0.2103	0.1896	0.1808	0.1770
A	∞	0.7954	0.6492	0.5237	0.4586	0.4354	0.4252	0.4207
k^2	0.5	0.3734	0.3314	0.2806	0.2476	0.2346	0.2287	0.2261
k	0.7071	0.6111	0.5757	0.5297	0.4976	0.4844	0.4783	0.4755
a_0	1	1	1	1	1	1	1	1
b_0	0.7071	0.7916	0.8177	0.8482	0.8674	0.8749	0.8782	0.8797
a_1	0.8535	0.8958	0.9088	0.9241	0.9337	0.9374	0.9391	0.9398
b_1	0.8409	0.8897	0.9043	0.9210	0.9313	0.9354	0.9371	0.9379
c_1	0.1461	0.1042	0.09065	0.07590	0.0663	0.0618	0.0609	0.0594
a_2	0.8472	0.8927	0.9065	0.9225	0.9325	0.9364	0.9381	0.9388
b_2	0.8472	0.8927	0.9065	0.9225	0.9325	0.9364	0.9381	0.9388
c_2	0	0	0	0	0	0	0	0
ℓ	0.8472	0.8927	0.9065	0.9225	0.9325	0.9364	0.9381	0.9388
N	2	2	2	2	2	2	2	2
ϕ_0	0	0.3284	0.4826	0.7445	1.0278	1.2215	1.3730	1.5708
ϕ_1	0	0.5918	0.8878	1.4078	1.1508	0.7432	0.4222	0
n	0	0.5918	0.8878	1.4078	1.1508	0.7432	0.4222	0
$\frac{n}{\pi}2^{1-N}$	0	0.09419	0.14130	0.22406	0.18316	0.11828	0.06719	0
ω/λ_0	∞	1.7744	1.5611	1.3926	1.3124	1.2854	1.2736	1.2684
$\eta_{\ddot{z}}$	∞	3.1426	1.9254	1.1934	0.9084	0.8204	0.7837	0.7680
σ_x, $\frac{\text{kgf}}{\text{cm}^2}$	∞	85.0	65.1	49.6	42.1	39.5	38.4	37.9
i	$\frac{\lambda_s}{\lambda_0}=\frac{\omega}{\lambda_0}\left\vert i+\frac{n}{\pi}2^{1-N}\right\vert^{-1}$, i = 0, ± 1, ± 2, ...							
0	∞	18.8385	11.0481	6.2153	7.1653	10.8674	18.9552	∞
−1	∞	1.9589	1.8180	1.7947	1.6067	1.4578	1.3653	1.2684
1	∞	1.6217	1.3678	1.1377	1.1092	1.1494	1.1934	1.2684
−2	∞	0.9310	0.8399	0.7841	0.7223	0.6831	0.6589	0.6342
2	∞	0.8473	0.7290	0.6261	0.6011	0.6068	0.6161	0.6342
−3	∞	0.6106	0.5461	0.5017	0.4659	0.4460	0.4343	0.4228
3	∞	0.5735	0.4970	0.4319	0.4123	0.4122	0.4152	0.4228
−4	∞	0.4543	0.4046	0.3688	0.3438	0.3311	0.3238	0.3171
4	∞	0.4334	0.3770	0.3297	0.3137	0.3121	0.3131	0.3171

Numerical Example

The numerical example is carried out for an elongated, simply-supported 0.159-cm thick and 20.3-cm wide ASTM/NEMA Class G-10 fiber-glass PCB ($\rho = 1.8\ \text{g/cm}^3$, $E = 17.20 \times 10^4\ \text{kgf/cm}^2$, $\nu = 0.3$). Let the weight of all the SM devices be, say, 20 percent of the board's own weight. Our purpose is to determine the PCB accelerations and the maximum stresses for the velocity step of $\dot{w}_c = 0.5$ m/sec.

The mass of the board per unit area is $m = 1.2\,\rho h = 0.3456\ \text{g/cm}^2$, and its flexural rigidity is $D = Eh^3/12(1 - \nu^2) = 64.5$ kgf cm. Then the formulas (16) yield: $M_0 = 4.467$ g/cm, $M = 3.508$ g/cm, $\lambda_0 = 320.9$ 1/sec, $\alpha = 12.2 \times 10^6\ \text{cm}^{-2}\text{sec}^{-2}$. The dimensionless parameter of nonlinearity, defined by (31), is $\bar{\alpha} = 4.664$. Then the formula (38) yields: $A_1 = 0.689$. Hence,

Downloaded 03 May 2010 to 171.66.16.247. Redistribution subject to ASME license or copyright; see http://www.asme.org/terms/Terms_Use.cfm

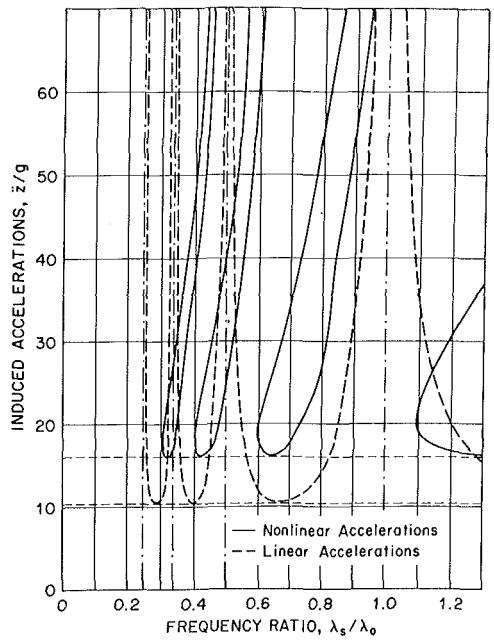


Fig. 1

the amplitude of the nonlinear vibrations caused by a single impact is by a factor of 0.689 smaller than the amplitude $A_1 = M_0\dot{w}_c/M\lambda_0 = 0.198$ cm of linear vibrations, and is only 0.136 cm. The parameter $F^2_{\max}$, defined by (39), is $F^2_{\max} = 0.7739$, and the minimum dimensionless amplitude of the vibrations caused by periodic impacts is, in accordance with (40), $A_{\min} = 0.4207$. Hence, for the most favorable ratio of the natural and excitation frequencies, the amplitude of the nonlinear vibrations, due to repetitive impulses, is by a factor of 0.4207 smaller than the amplitude of linear vibrations due to a single impulse of the same magnitude.

The calculations of the induced displacements, accelerations, and dynamic stresses are carried out in the Table 1. As evident from this table, the induced stresses are very low, while the accelerations can exceed significantly the accelerations due to a single impact. The calculated response functions for the maximum accelerations $\ddot{z}_{\max}$ are plotted in Fig. 1, where the ratios of the induced accelerations $\ddot{z}_{\max}$ to the acceleration g due to gravity are presented versus the ratios λ_s/λ_0 of the frequency of the impacts to the linear natural frequency of the undamped vibrations. Figure 1 shows that the linear and nonlinear responses are quite different and that the nonlinear accelerations can exceed substantially the linear ones. If, for instance, the frequency ratio of the impacts is $\lambda_s/\lambda_0 = 0.85$, then the nonlinear accelerations are by a factor of 2.2 larger than the linear accelerations. On the other hand, since nonlinearity "destroys resonances," the maximum accelerations in a nonlinear system can never be as high as in a linear system at resonant or close to resonant conditions. Let, for instance, the frequency ratio in the example in question be close to 0.5 and let the given electronic component be unable to withstand accelerations higher than, say, 50 g. As follows from Fig. 1, mounting of such a component can be permitted, since the actual (nonlinear) accelerations never exceed 40 g. A linear approach, however, would lead to an erroneous conclusion that mounting of this component should not be allowed. In this connection it may be pointed out that if the actual support conditions of the PCB are such that the supports can draw closer during the board's vibrations (i.e., if the system is linear indeed), then at resonant conditions such a PCB can impose substantially higher accelerations on the SM components, than a board with a nondeformable contour. Therefore, if the resonant frequencies cannot be avoided and/or predicted with sufficient accuracy, fixing of the PCB support contour can be regarded as a feasible design measure aimed at the "destruction" of would-be resonance conditions. Clearly, this may not be necessary in the case of strong damping, which would keep even resonance amplitudes at a sufficiently low level.

Conclusions

- Simple and easy to apply analytical models have been developed for the prediction of the linear and nonlinear dynamic responses of a flexible PCB to periodic impact loads applied to its support contour.
- Analysis of the transient amplitudes, accelerations, and stresses, carried out on the basis of a linear approach, indicated that transient nonresonant responses can exceed the steady-state responses by up two times. The resonant amplitudes, however, are always greater in the steady-state conditions.
- In the case of large deflections of a board with a nondeformable contour, it is important to account for the nonlinear effects. Application of a linear approach can be misleading in this case. Such an approach can, depending on the frequency ratio, either underestimate or overestimate substanially the actual response substantially.
- The obtained data can be of help when evaluating the accelerations experienced by surface-mounted electronic components, as well as when computing the dynamic stresses in a PCB of the given type, dimensions, and support conditions.

References

Abulesz, E.-M., and Lyberatos, G., 1988, "Periodic Impulse-Forcing of Non-Linear Systems: A New Method," *Int. J. of Control*, Vol. 48, No. 2.

Bateman, H., and Erdelyi, A., 1955, *Higher Transcendental Functions*, McGraw-Hill, New York.

Bubnov, I. G., 1902, *On the Stresses in Ship Plating Due to Water Pressure*, Polytechnic Institute, Saint Petersburg (in Russian).

Burton, R., 1958, *Vibration Impact*, Addison-Wesley, Mass.

Carg, V. K., and Smolik, F., 1989, "Vibration Fatigue Life Evaluation of Electronic Equipment," ASME-WAM, San Francisco, Calif.

Crovetto, J., Gupta, A., and Kim, M. J., 1990, "Vibration and Damping Analysis of Boards Used for Printed Circuits," *Proc. 8th Int. Modal Analysis Conf.*, Kissimmee, Fla.

Duffing, G., 1918, "Erzwungene Schwingungen bei veränderlicher Eigenfrequenz und ihre technische Bedeutung," Sammlung Vieweg, Braunschweig, (in German).

Engel, P. A., 1990, "Structural Analysis of Circuit Card Systems Subjected to Bending," ASME *Journal of Electronic Packaging*, Vol. 112.

Halbauer, K., 1974, "Die Anwendung der periodischen Stosserregung zur Messung von Übertragungsfunctionen mechanisch steifer Systeme," Dissertation, Technische Universität, Hannover (in German).

Harris, C. M., and Crede, C. E., ed., 1976, *Shock and Vibration Handbook*, 2nd. ed., McGraw-Hill, New York.

Den Hartog, J. P., 1956, *Mechanical Vibrations*, 4th ed., McGraw-Hill, New York.

Hayashi, C., 1964, *Nonlinear Oscillators in Physical Systems*, McGraw-Hill, New York.

Hsu, C. S., Cheng, W. H., and Lee, H. C., 1977, "Steady-State Response of a Non-Linear System Under Impulsive Periodic Parametric Excitation," *J. of Sound and Vibration*, Vol. 50, No. 1.

Jacobsen, L. S., and Ayre, R. S., 1958, *Engineering Vibrations*, New York.

Kauderer, H., 1958, *Nichtlineare Mechanik*, Springer-Verlag, Berlin (in German).

Kim, M. J., and Gupta, A., 1990, "Finite Element Analysis of Free Vibrations of Laminated Composite Plates," *Proc. 8th Int. Modal Analysis Conf.*, Kissimmee, Fla.

Krajcinovic, D., 1968, "Dynamic Stability of Elastic Systems Subjected to Periodic Impulsive Loading," Ph.D. Dissertation, Northwestern University, Evanston, Ill.

Lance, G. N., 1960, *Numerical Methods for High-Speed Computers*, Hiffe and Sons, Ltd., London.

Loytsyansky, L. G., and Lurie, A. I., 1960, *Theoretical Mechanics*, McGraw-Hill, New York.

Military Handbook, 1987, MIL-HDBK-SE, June.

Panovko, Ya, G., and Gubanova, I. I., 1967, *Stability and Vibration of Elastic Systems*, Nauka, Moscow (in Russian).

Pars, L. A., 1970, *A Treatise on Analytical Dynamics*, Heinemann, London.

Paz, M., and O'Charoen, P., 1973, "Structural Response to Periodic Impulses," ASME-WAM, Detroit, Mich.

Skudrzyk, E., 1968, *Simple and Complex Vibratory Systems, The Penn. State Press*, University Park, Penn.

Downloaded 03 May 2010 to 171.66.16.247. Redistribution subject to ASME license or copyright; see http://www.asme.org/terms/Terms_Use.cfm

Steinberg, D. S., 1973, *Vibration Analysis of Electronic Equipment*, Wiley and Sons, New York.

Suhir, E., 1970, "Exact Solution to the Problem of Steady-State Vibrations of a Nonlinear Shock-Excited Oscillator with a Cubic Characteristic," *Transactions, Institute of Marine Engineers*, No. 4, Odessa (in Russian).

Suhir, E., 1975, "Stochastically Unstable Vibrations of Rectangular Plates Subjected to Periodic Shock Loads," USSR National Conference on the Theory of Shells and Plates, Tbilisi, Georgia (in Russian).

Suhir, E., 1982, "Shock-Excited Vibrations with Application to the Slamming Response of a Flexible Ship to a Regular Wave Packet," *Journal of Ship Research*, Vol. 26, No. 4.

Suhir, E., 1985, "Linear and Nonlinear Vibrations Caused by Periodic Impulses," AIAA/ASME/ASCE/AHS 26th Structures, Structural Dynamics, and Materials Conference, Orlando, Fla.

Suhir, E., and Lee, Y.-C., 1990, "Thermal, Mechanical, and Environmental Durability Design Methodologies," *Electronic Materials Handbook*, Vol. 1, Packaging, ASME International.

Suhir, E., 1991, "Nonlinear Dynamic Response of a Flexible Thin Plate to Constant Acceleration of Its Support Contour, With Application to Printed Circuit Boards, Used in Avionic Packaging," *Int. J. of Solids and Structures*, Vol. 29, No. 1.

Timoshenko, S. P., and Woinowski-Krieger, S., 1940, *Theory of Plates and Shells*, McGraw-Hill, New York.

Timoshenko, S. P., and Young, D. H., 1955, *Vibration Problems in Engineering*, 3d ed., Van Nostrand, Princeton, N.J.

Timoshenko, S. P., and Young, D. H., 1956, *Advanced Dynamics*, McGraw-Hill, New York.

Timoshenko, S. P., and Young, D. H., 1965, *Theory of Structures*, McGraw-Hill, New York.

Veluswami, M. A., 1973, "Vibroimpacts of a Ball Between Restraints," Ph.D. issertation, University of Massachusetts, Amherst, Mass.

Wong, T.-L., Stevens, K. K., and Wang, G., 1990, "Experimental Modal Analysis and Dynamic Response Prediction of PC Boards with Surface Mount Electronic Components," ASME-WAM, Dallas, Texas.

Downloaded 03 May 2010 to 171.66.16.247. Redistribution subject to ASME license or copyright; see http://www.asme.org/terms/Terms_Use.cfm

Marc P. Mignolet
Asst. Professor,
Department of Mechanical
and Aerospace Engineering,
Arizona State University,
Tempe, AZ 85287-6106
Assoc. Mem. ASME

Pol D. Spanos
L. B. Ryon Chair in Engineering,
Rice University,
Houston, TX 77251
Fellow ASME

Simulation of Homogeneous Two-Dimensional Random Fields: Part I—AR and ARMA Models

The determination of autoregressive (AR) and autoregressive moving average (ARMA) algorithms for simulating realizations of two-dimensional random fields with a specified (target) power spectrum is examined. The form of both of these models is justified first by considering infinite-variate vector processes of appropriate spectral matrix. Next, the AR parameters are selected to achieve the minimum of a positive integral. Then, a technique is formulated to derive an ARMA simulation algorithm from the prior AR approximation by relying on the minimization of frequency domain errors. Finally, these procedures are critically assessed and an example of application is presented.

Introduction

In recent years, it has become widely accepted within the engineering community that records of structural excitations associated with natural phenomena such as earthquakes, ocean waves, and wind gusts are best modeled as realizations of random processes. As long as the structure can be idealized as a single degree-of-freedom system, an appropriate representation of the load is a scalar stochastic process. In the case of a multi-degree-of-freedom system, however, it is often required to employ a vector process which can account for the temporal and spatial correlations between forces associated with different degrees-of-freedom. When the structural system involves elements such as beams, plates, or shells, the time and space-dependent excitation is represented as an n-dimensional random field with $n = 2$, 3 or 4, respectively. A probabilistic model of wind gust as a multidimensional random field can be found in Madsen et al. (1986). Similarly, a random field representation of ocean waves elevations can be produced in terms of directional spectra (Chakrabarti, 1987). Finally, random field models accounting for the spatial variations of seismic waves are given by Harichandran and Vanmarcke (1986).

In parallel to the increased sophistication in representation of the forces associated with natural phenomena, structural models have been refined to include in particular both material and geometrical nonlinearities. Unfortunately, these improvements lead to random vibration problems which are in general exceedingly difficult to solve exactly even in the case of a few degrees-of-freedom. In this context, the Monte Carlo simulation technique has become quite useful and versatile; it involves recasting the random structural dynamics analysis in a series of deterministic ones. The problem of simulating multivariate but one-dimensional random processes has been addressed extensively by several researchers; see Spanos and Mignolet (1989) for a review and a rather comprehensive list of references.

The purpose of the present two-part series is to derive simulation algorithms of random fields which are similar in nature to the ones already available for generating realizations of vector processes. Comparatively, the problem of simulating multidimensional random fields has received much less attention (Naganuma et al., 1985 and 1987). However, with the advent of computer hardware and the evolution of numerical analysis, this problem is becoming quite important. For clarity, the discussion will be restricted to the case of a scalar two-dimensional field. Nevertheless, most of the results obtained can readily be extended to apply to a greater number of dimensions and to the multivariate (or vector) case. For similar reasons, it will be assumed that the first of the two coordinates is a spatial location while the second one represents time. This convention has no bearing on the validity of the results derived which are also applicable when both dimensions are spatial ones.

Discrete Two-Dimensional Random Fields

One-Dimensional Vector Process Representation. From a purely mathematical point of view, a discrete homogeneous two-dimensional random field $y_{k,r}$ is a doubly indexed sequence of random variables which is characterized by its probabilistic properties such as the autocorrelation function

$$R_{yy}(l,s) = E[y_{k,r}y_{k+l,r+s}], \tag{1}$$

and the power spectrum

Contributed by the ASME Applied Mechanics Division of THE AMERICAN SOCIETY OF MECHANICAL ENGINEERS for presentation at the Winter Annual Meeting, Atlanta, Ga., Dec. 1-6, 1991.

Discussion on this paper should be addressed to the Technical Editor, Prof. Leon M. Keer, The Technological Institute, Northwestern University, Evanston, IL 60208, and will be accepted until two months after final publication of the paper itself in the JOURNAL OF APPLIED MECHANICS. Manuscript received by the ASME Applied Mechanics Division, Oct. 25, 1990; final revision, May 14, 1991.

Paper No. 91-WA/APM-28.

Copyright © 1992 by ASME
Downloaded 03 May 2010 to 171.66.16.247. Redistribution subject to ASME license or copyright; see http://www.asme.org/terms/Terms_Use.cfm

$$S_{yy}(\phi,\omega)=\frac{1}{4\omega_b\phi_b}\sum_{l=-\infty}^{\infty}\sum_{s=-\infty}^{\infty}R_{yy}(l,s)e^{-jl\phi\Delta}e^{-js\omega T}. \quad (2)$$

In these equations the symbol E [.] denotes the operation of mathematical expectation. Further, the variables Δ and T represent the spatial and temporal sampling intervals, respectively. The corresponding two cutoff frequencies ϕ_b and ω_b satisfy the Nyquist relations

$$\Delta=\frac{\pi}{\phi_b} \quad (3)$$

and

$$T=\frac{\pi}{\omega_b}. \quad (4)$$

In engineering problems, the mathematical entity $y_{k,r}$ is used to represent a physical variable defined over a spatial or mixed spatial-temporal grid of points $(k, r) \in [k_1, k_2] \times [r_1, r_2]$. In this context, note that another description of the variable of interest could be obtained by stacking the values $y_{k,r}$ for a fixed number $r \in [r_1, r_2]$ and for integers $k \in [k_1, k_2]$ in a vector $\mathbf{Y}_r$. In this manner, the two-dimensional random field $y_{k,r}$ can be viewed as a one-dimensional vector process $\mathbf{Y}_r$ whose components are

$$[\mathbf{Y}_r]_k=y_{k,r}. \quad (5)$$

The elements of the corresponding autocorrelation and spectral matrices are readily found to be

$$[R_{\mathbf{YY}}(l)]_{ui}=[E[\mathbf{Y}_r\mathbf{Y}_{r+l}^{\dagger}]]_{ui}=E[[\mathbf{Y}_r]_u[\mathbf{Y}_{r+l}]_i]$$
$$=E[y_{u,r}y_{i,r+l}]=R_{yy}(i-u,l) \quad (6)$$

and

$$[S_{\mathbf{YY}}(\omega)]_{ui}=\frac{1}{2\omega_b}\sum_{l=-\infty}^{\infty}[R_{\mathbf{YY}}(l)]_{ui}e^{-jl\omega T}$$
$$=\frac{1}{2\omega_b}\sum_{l=-\infty}^{\infty}R_{yy}(i-u,l)e^{-jl\omega T} \quad (7)$$

where the symbol † denotes the operation of matrix transposition.

This equivalence between two-dimensional random fields and one-dimensional vector processes suggests the following simulation technique. Given an arbitrary power spectrum $S_{yy}(\phi, \omega)$ (target), zero or negligible outside the domain $(\phi, \omega) \in [-\phi_b, \phi_b]$ X $[-\omega_b, \omega_b]$, compute its autocorrelation function $R_{yy}(l, s)$ using the equation

$$R_{yy}(l,s)=\int_{-\phi_b}^{\phi_b}\int_{-\omega_b}^{\omega_b}S_{yy}(\phi,\omega)e^{jl\phi\Delta}e^{js\omega T}d\omega d\phi \quad (8)$$

and the corresponding autocorrelation and spectral matrices, $R_{\mathbf{YY}}(l)$ and $S_{\mathbf{YY}}(\omega)$ using Eq. (6) and (7). Then, relying on the methods devised for multivariate but one-dimensional processes (see Spanos and Mignolet (1989) for a review), time histories of the vector process $\mathbf{Y}_r$ can be generated from which realizations of the random field $y_{k,r}$ are readily extracted according to Eq. (5). Clearly, the computational effort associated with the determination of the parameters of the AR and ARMA vector models is prohibitive when the number of variates, or equivalently the size of the domain $k \in [k_1, k_2]$, is large. Thus, an accurate AR or ARMA modeling of the entire field $y_{k,r}$, $(k, r) \in (-\infty, \infty) \times (-\infty, \infty)$ corresponding to an infinitely long vector process $\mathbf{Y}_r$, cannot be achieved in practical situations by relying directly on the above equivalence. Nevertheless, the theoretical analysis of this limiting case can be used to derive reliable two-dimensional AR and ARMA modeling methods.

Properties of the Finite-Variate AR and ARMA Models. The autocorrelation and spectral matrices, $R_{\mathbf{YY}}(l)$ and $S_{\mathbf{YY}}(\omega)$, defined by Eq. (6) and (7) exhibit a property which is independent of the two-dimensional field considered. Specifically, the dependency of the element $[R_{\mathbf{YY}}(l)]_{ui}$ on the difference $u - i$ implies that $R_{\mathbf{YY}}(l)$ and $S_{\mathbf{YY}}(\omega)$ are both Toeplitz matrices for all values of l and ω, respectively. The corresponding AR(m) model can be written in the form

$$\hat{\mathbf{Y}}_r=-\sum_{k=1}^{m}\hat{A}_k\hat{\mathbf{Y}}_{r-k}+\hat{B}_0\mathbf{W}_r \quad (9)$$

where the symbol $\mathbf{W}_r$ denotes a n-variate bandlimited, in the interval $[-\omega_b, \omega_b]$, white noise vector process. The autocorrelation matrices of $\mathbf{W}_r$ are

$$E[\mathbf{W}_i\mathbf{W}_u^{\dagger}]=2\omega_bI_n\delta_{iu} \quad (10)$$

where the integer n equals the number of variates involved in the simulation. Further, the symbols I_n and δ_{iu} denote the $n \times n$ identity matrix and the Kronecker symbol, respectively. Introducing the convention

$$\hat{A}_0=I_n \quad (11)$$

it can be shown (Mignolet and Spanos, 1987) that the optimum values of the AR parameters $\hat{A}_k$ and $\hat{B}_0$ satisfy the Yule-Walker equations

$$R_{\mathbf{YY}}^{\dagger}(l)+\sum_{k=1}^{m}\hat{A}_kR_{\mathbf{YY}}(k-l)=0 \quad l=1, \ldots, m \quad (12)$$

and

$$\sum_{k=0}^{m}\hat{A}_kR_{\mathbf{YY}}(k)=2\omega_b\hat{B}_0\hat{B}_0^{\dagger}. \quad (13)$$

The Toeplitz structure of the autocorrelation matrices implies that the AR parameters $\hat{A}_k$ and $\hat{B}_0$ computed from the above equations accordingly have a specific form. For simplicity, it is assumed that the autocorrelation function $R_{yy}(l, s)$ is symmetric. That is,

$$R_{yy}(l,s)=R_{yy}(-l,s)=R_{yy}(l,-s)=R_{yy}(-l,-s). \quad (14)$$

An arbitrary $n \times n$ matrix U is said to be centrosymmetric if and only if

$$U=P_nUP_n \quad (15)$$

where P_n is the $n \times n$ reflection matrix defined as

$$P_n=\begin{bmatrix}0 & & & 1\\ & & \cdot & \\ & \cdot & & \\ 1 & & & 0\end{bmatrix}. \quad (16)$$

In terms of the elements $[U]_{kl}$ of the matrix U, Eq. (15) is equivalent to the conditions

$$[U]_{kl}=[U]_{n+1-k,n+1-l} \quad \text{for } k,l=1, \ldots, n. \quad (17)$$

Using the identity

$$P_n^2=I_n \quad (18)$$

it is readily shown that the sums, products, and inverses of centrosymmetric matrices are also centrosymmetric.

Under the assumption of symmetry, Eq. (14), the elements of the spectral matrix $S_{\mathbf{YY}}(\omega)$ satisfy the relations

$$[S_{\mathbf{YY}}(\omega)]_{n+1-k,n+1-l}=\frac{1}{2\omega_b}\sum_{u=-\infty}^{\infty}R_{yy}[(n+1-l)$$
$$-(n+1-k),u]e^{-ju\omega T}=[S_{\mathbf{YY}}(\omega)]_{lk}=[S_{\mathbf{YY}}(\omega)]_{kl}$$
$$k,l=1, \ldots, n. \quad (19)$$

Consequently, the spectral matrix $S_{\mathbf{YY}}(\omega)$ is both symmetric and centrosymmetric. Then, using the inverse Fourier transform of Eq. (7), that is,

Downloaded 03 May 2010 to 171.66.16.247. Redistribution subject to ASME license or copyright; see http://www.asme.org/terms/Terms_Use.cfm

$$R_{\mathbf{YY}}(l)=\int_{-\omega_b}^{\omega_b} S_{\mathbf{YY}}(\omega)e^{jl\omega T}d\omega, \tag{20}$$

it is readily shown that all the autocorrelations $R_{\mathbf{YY}}(l)$ are symmetric and centrosymmetric matrices.

Premultiplying and postmultiplying Eq. (12) and (13) by P_n and taking into account the identity given by Eq. (18), it can be shown that

$$P_nR^{\dagger}_{\mathbf{YY}}(l)P_n+\sum_{k=1}^{m}[P_n\hat{A}_kP_n][P_nR_{\mathbf{YY}}(k-l)P_n]=0$$

$$\text{for } l=1,\ldots,m \tag{21}$$

and

$$P_n(\hat{B}_0\hat{B}_0^{\dagger})P_n=\frac{1}{2\omega_b}\left\{\sum_{k=0}^{m}[P_n\hat{A}_kP_n][P_nR_{\mathbf{YY}}(k)P_n]\right\}. \tag{22}$$

Relying on the centrosymmetry of the autocorrelation function and on the uniqueness of the solution to the Yule-Walker equations (Spanos and Mignolet, 1987), it is readily seen that

$$P_n\hat{A}_kP_n=\hat{A}_k \quad k=0,\ldots,m \tag{23}$$

and

$$P_n\hat{B}_0\hat{B}_0^{\dagger}P_n=\hat{B}_0\hat{B}_0^{\dagger}. \tag{24}$$

Consequently, the AR matrices $\hat{A}_k$, $k=0,\ldots,m$ and $\hat{B}_0\hat{B}_0^{\dagger}$ are also centrosymmetric. A decomposition $\hat{B}_0$ possessing the same property can be obtained by requiring the symmetry of this matrix so that (Mignolet, 1987)

$$(P_n\hat{B}_0P_n)^2=\hat{B}_0^2=\frac{1}{2\omega_b}\sum_{k=0}^{m}\hat{A}_kR_{\mathbf{YY}}(k). \tag{25}$$

The arguments presented in context with the Yule-Walker relations, Eq. (12) and (13), can be repeated in connection with any of the two-stage AR to ARMA modeling techniques (Gersch and Yonemoto, 1977; Samaras et al., 1985; Mignolet and Spanos, 1987) to show that the corresponding ARMA matrix coefficients are also centrosymmetric.

Finally, these results can be combined to prove that the AR and ARMA spectral matrices share with the target expression the centrosymmetry property. This fact implies in particular that any of these matrices satisfies the relations

$$[S(\omega)]_{i,n+1-i}=[P_nS(\omega)P_n]_{i,n+1-i}$$
$$=[S(\omega)]_{n+1-i,i}=[S(\omega)]^*_{i,n+1-i} \tag{26}$$

where the last of the above equalities results from the Hermitian character of the spectral matrix of any vector process. Thus, the elements $[S_{\hat{\mathbf{Y}}\hat{\mathbf{Y}}}(\omega)]_{i,n+1-i}$ and $[S_{\tilde{\mathbf{Y}}\tilde{\mathbf{Y}}}(\omega)]_{i,n+1-i}$, $i=1,\ldots,n$ of the AR and ARMA spectral matrices are real.

The Infinite-Variate AR and ARMA Models. As n tends to infinity, the previous simulation procedure involves the entire space domain and the vector process $\mathbf{Y}_r$ becomes a complete description of the two-dimensional scalar random field $y_{k,r}$. The corresponding AR coefficients have a doubly infinite number of elements $[\hat{A}_k]_{iu}$ and $[\hat{B}_0]_{iu}$, $i,u\in(-\infty,\infty)$, which can be computed from the Yule-Walker relations, Eq. (12) and (13). In particular, it is found that

$$\sum_{u=-\infty}^{\infty}\sum_{k=0}^{m}[\hat{A}_k]_{iu}[R_{\mathbf{YY}}(k-l)]_{uv}=0$$

$$\text{for } l=1,\ldots,m \text{ and } i,v\in(-\infty,\infty). \tag{27}$$

Relying on these equations and the definition of the autocorrelation matrices $R_{\mathbf{YY}}(l)$, Eq. (6), it can be shown that

$$\sum_{u=-\infty}^{\infty}\sum_{k=0}^{m}[\hat{A}_k]_{i,v-u}R_{yy}(u,k-l)=0$$

$$\text{for } l=1,\ldots,m \text{ and } i,v\in(-\infty,\infty). \tag{28}$$

Note that the two indices i and v appear only in the first term so that there exist infinite Toeplitz matrices $\hat{A}_k$ satisfying Eq. (28).

To prove this property, introduce the following description of an arbitrary infinite Toeplitz matrix U in terms of its diagonals $[u]_\alpha$

$$U=\sum_{\alpha=-\infty}^{\infty}[u]_\alpha J_\alpha \tag{29}$$

where J_α is the matrix whose iu element is defined by the equation

$$[J_\alpha]_{iu}=\delta_{u(i+\alpha)} \quad \text{for } i,u\in(-\infty,\infty). \tag{30}$$

With this notation, a Toeplitz solution $\hat{A}_k$ of Eq. (28) exists if it is possible to find an infinite set of coefficients $[\hat{a}_k]_\alpha$, $\alpha=0,\pm1,\pm2,\ldots$ satisfying the infinite system of equations

$$\sum_{u=-\infty}^{\infty}\sum_{k=0}^{m}[\hat{a}_k]_{\alpha-u}R_{yy}(u,k-l)=0$$

$$\text{for } l=1,\ldots,m \text{ and } \alpha=0,\pm1,\pm2,\ldots. \tag{31}$$

The elements of the corresponding matrix coefficient $\hat{B}_0$ can be computed from Eq. (13). Specifically, it is found that

$$[\hat{B}_0\hat{B}_0^{\dagger}]_{iu}=\frac{1}{2\omega_b}\sum_{l=-\infty}^{\infty}\sum_{k=0}^{m}[\hat{a}_k]_{(u-i)-l}R_{yy}(l,k). \tag{32}$$

From this relation, it is seen that the infinite matrix $\hat{B}_0\hat{B}_0^{\dagger}$ is symmetric, Toeplitz, and positive definite. Thus, as shown by Youla and Kazanjian (1978) and Mignolet (1987), there exists a lower triangular Toeplitz matrix $\hat{B}_0$ that satisfies Eq. (32). Denoting by $[\hat{b}_0]_\alpha$ the terms in its diagonals, in accordance with the convention of Eq. (29), the two-dimensional AR simulation scheme becomes

$$[\hat{\mathbf{Y}}_r]_i=-\sum_{k=1}^{m}\sum_{u=-\infty}^{\infty}[\hat{A}_k]_{iu}[\hat{\mathbf{Y}}_{r-k}]_u+\sum_{u=-\infty}^{\infty}[\hat{B}_0]_{iu}[\mathbf{W}_r]_u \tag{33}$$

or

$$\hat{y}_{i,r}=-\sum_{k=1}^{m}\sum_{u=-\infty}^{\infty}[\hat{a}_k]_u\hat{y}_{i+u,r-k}+\sum_{u=-\infty}^{0}[\hat{b}_0]_u[\mathbf{W}_r]_{i+u}. \tag{34}$$

An equivalent form of this equation can be obtained by premultiplying Eq. (33) by the infinite lower triangular Toeplitz matrix $[\hat{b}_0]_0\hat{B}_0^{-1}$ of diagonals $[\hat{b}_0]_0[\hat{b}_0^{-1}]_\alpha$. Then, it is found that the AR model can be written as

$$\sum_{k=0}^{m}\sum_{u=-\infty}^{\infty}[\bar{a}_k]_u\hat{y}_{i+u,r-k}=[\hat{b}_0]_0[\mathbf{W}_r]_i \tag{35}$$

where the parameters $[\bar{a}_k]_u$ are defined by the equation

$$[\bar{a}_k]_u=\sum_{l=-\infty}^{0}[\hat{b}_0]_0[\hat{b}_0^{-1}]_l[\hat{a}_k]_{u-l}. \tag{36}$$

The last form, Eq. (35), of the simulation scheme is analogous to the one discussed by Marzetta (1980) and Delsarte et al. (1980). A similar, yet different model has often been proposed (Naganuma et al., 1985, 1987; Dudgeon and Mersereau, 1984; for example) in which the summation over the u index in Eq. (35) is limited to the nonpositive values only. It was first proved by Chang and Aggarwal (1978) that this one-sided model cannot accurately represent any arbitrary two-dimensional field; for this purpose, both the positive and negative values of the index u are required. The present investigation confirms this result and shows that the requirement $u\in(-\infty,\infty)$ corresponds to the use of full matrices $\hat{A}_k$ and $\hat{B}_0$ in Eq. (12)–(13) versus lower triangular ones when $u\leq 0$.

In view of the present analysis, the AR simulation scheme defined by Eq. (34) appears as the most logical extension of the AR multivariate one-dimensional model. Thus, it will be

Downloaded 03 May 2010 to 171.66.16.247. Redistribution subject to ASME license or copyright; see http://www.asme.org/terms/Terms_Use.cfm

preferred in the sequel over the equivalent description given by Eq. (35).

Note that the second term in the right-hand side of Eq. (34) can be considered as the rth-independent realization of the one-dimensional scalar stationary random process x_i whose one-sided MA representation is

$$x_i = \sqrt{\frac{2\omega_b}{2\phi_b}} \sum_{u=0}^{\infty} [\hat{b}_0]_{-u} w_{i-u}, \tag{37}$$

where w_i is a $[-\phi_b, \phi_b]$ bandlimited one-dimensional white noise process. Relying on Eq. (32), it is readily shown that the autocorrelation function $R_{xx}(l)$ of the process x_i is

$$R_{xx}(l) = E[x_i x_{i+l}] = \sum_{k=0}^{m} \sum_{u=-\infty}^{\infty} [\hat{a}_k]_u R_{yy}(l-u,k). \tag{38}$$

The values x_i can be generated from Eq. (38) by applying any known simulation technique of one-dimensional processes.

Introducing the notation x_i^r for the ith sample of the rth realization of the process x_i, it is seen that the AR simulation scheme finally becomes

$$\hat{y}_{i,r} = -\sum_{k=1}^{m} \sum_{u=-\infty}^{\infty} [\hat{a}_k]_u \hat{y}_{i+u,r-k} + x_i^r. \tag{39}$$

A similar analysis conducted with any two-stage matching method (Gersch and Yonemoto, 1977; Samaras et al., 1985; Mignolet and Spanos, 1987) leads to the infinite-variate ARMA model (Mignolet, 1987)

$$\tilde{y}_{i,r} = -\sum_{k=1}^{p} \sum_{u=-\infty}^{\infty} [a_k]_u \tilde{y}_{i+u,r-k} + \sum_{l=0}^{q} \sum_{u=-\infty}^{\infty} [b_l \hat{b}_0^{-1}]_u x_{i+u}^{r-l} \tag{40}$$

where x_i^r denotes as before the rth realization of the process x_i defined by Eq. (37).

Two-Dimensional AR Modeling

The AR Random Field. Practical considerations dictate the use of simulation algorithms such that the computation of a sample is achieved in a finite number of arithmetic operations. This requirement eliminates the direct use of the infinite-variate AR process, Eq. (39), and motivates the analysis of the truncated model

$$\hat{y}_{i,r} = -\sum_{k=1}^{m} \sum_{u=-\delta_2}^{\delta_1} \hat{a}_{u,k} \hat{y}_{i+u,r-k} + x_i^r. \tag{41}$$

The random field $\hat{y}_{k,r}$ defined by Eq. (41) can be considered as the response of a linear two-dimensional digital system whose transfer function in terms of multidimensional z-transform notations is

$$h(z_1,z_2) = \frac{1}{1 + \sum_{k=1}^{m} \sum_{u=-\delta_2}^{\delta_1} \hat{a}_{u,k} z_1^u z_2^{-k}} \tag{42}$$

when the excitation is the process x_i. The corresponding impulse response sequence $h_{u,k}$ is implicitly defined by the relation

$$h(z_1,z_2) = \sum_{k=-\infty}^{\infty} \sum_{u=-\infty}^{\infty} h_{u,k} z_1^{-u} z_2^{-k}. \tag{43}$$

The computation of the AR samples implied by Eq. (41) and recursive on the second index corresponds to an impulse response $h_{u,k}$ which is zero for negative values of k. Moreover, the recurrence relation

$$\sum_{k=0}^{m} \sum_{u=-\delta_2}^{\delta_1} \hat{a}_{u,k} h_{i+u,r-k} = \delta_{i0}\delta_{r0} \quad \text{for all } i \text{ and } r \geq 0 \tag{44}$$

where

$$\hat{a}_{u,0} = \delta_{u0} \tag{45}$$

implies that $h_{u,k}$ is nonzero only in the domain $k \geq 0$ and $u \in [-k\delta_1, k\delta_2]$, termed the region of support.

Some relations between the input-output crosscorrelation function, $R_{\hat{y}x}(u, v)$, and the output autocorrelation function, $R_{\hat{y}\hat{y}}(u, v)$, can be obtained by postmultiplying Eq. (41) by x_{i+u}^{r-v} and $\hat{y}_{i+u,r+v}$ and taking expected values. Specifically, it is found that

$$R_{\hat{y}x}(u,-v) = E[\hat{y}_{i,r} x_{i+u}^{r-v}] = 0 \quad \text{for } v<0 \tag{46a}$$

$$R_{\hat{y}x}(u,-v) = R_{xx}(u) \quad \text{for } v=0 \tag{46b}$$

and

$$R_{\hat{y}x}(u,-v) = -\sum_{k=1}^{m} \sum_{l=-\delta_2}^{\delta_1} \hat{a}_{l,k} R_{\hat{y}x}(u-l,k-v) \quad \text{for } v>0 \tag{46c}$$

as well as

$$R_{\hat{y}\hat{y}}(u,v) = -\sum_{k=1}^{m} \sum_{l=-\delta_2}^{\delta_1} \hat{a}_{l,k} R_{\hat{y}\hat{y}}(u-l,v+k) + R_{\hat{y}x}(-u,-v). \tag{47}$$

Additional properties of the two-dimensional AR process, Eq. (41), including in particular the boundary and/or initial conditions required by the recursion, are presented in Mignolet (1987).

The Optimum AR Model. For the purpose of simulation, the AR spectrum defined as

$$S_{\hat{y}\hat{y}}(\phi,\omega) = |h(e^{j\phi\Delta}, e^{j\omega T})|^2 \frac{S_{xx}(\phi)}{2\omega_b} \tag{48}$$

where

$$S_{xx}(\phi) = \frac{1}{2\phi_b} \sum_{k=-\infty}^{\infty} R_{xx}(k) e^{-jk\phi\Delta} \tag{49}$$

should represent a close approximation of the target expression $S_{yy}(\phi, \omega)$. Further, for consistency of the approximation technique, the values of the AR parameters corresponding to the above model should converge to their infinite-variate one-dimensional counterparts as the orders δ_1 and δ_2 tend to infinity.

The determination of the optimum one-dimensional AR system through Eq. (12) and (13) was shown (Makhoul, 1975) to represent an optimum "flattening" of the spectrum $S_{yy}(\phi, \omega)$ by the inverse of the AR transfer function. On the basis of this interpretation, the optimum two-dimensional AR model will be selected to minimize the frequency domain error

$$\epsilon_{AR}^{(2)} = \frac{1}{4\omega_b\phi_b} \int_{-\phi_b}^{\phi_b} \int_{-\omega_b}^{\omega_b} |\hat{d}(e^{j\phi\Delta}, e^{j\omega T})|^2 S_{yy}(\phi,\omega) d\omega d\phi \tag{50}$$

where

$$\hat{d}(z_1,z_2) = \sum_{k=0}^{m} \sum_{u=-\delta_2}^{\delta_1} \hat{a}_{u,k} z_1^u z_2^{-k}. \tag{51}$$

Further, the spectrum $S_{xx}(\phi)$, of the one-dimensional process x_i will be chosen to represent at best the approximately cylindrical surface $|\hat{d}(e^{j\phi\Delta}, e^{j\omega T})|^2 S_{yy}(\phi, \omega)$. Specifically, the choice

$$S_{xx}(\phi) = \int_{-\omega_b}^{\omega_b} |\hat{d}(e^{j\phi\Delta}, e^{j\omega T})|^2 S_{yy}(\phi,\omega) d\omega \tag{52}$$

minimizes the error

$$\epsilon_x = \frac{1}{4\omega_b\phi_b} \int_{-\phi_b}^{\phi_b} \int_{-\omega_b}^{\omega_b} [S_{xx}(\phi) - 2\omega_b |\hat{d}(e^{j\phi\Delta}, e^{j\omega T})|^2 S_{yy}(\phi,\omega)]^2 d\omega d\phi. \tag{53}$$

Downloaded 03 May 2010 to 171.66.16.247. Redistribution subject to ASME license or copyright; see http://www.asme.org/terms/Terms_Use.cfm

It is readily shown that $\epsilon_{AR}^{(2)}$ can be written in the form

$$\epsilon_{AR}^{(2)}=\frac{1}{4\omega_b\phi_b}\sum_{k=0}^{m}\sum_{l=0}^{m}\sum_{i=-\delta_2}^{\delta_1}\sum_{u=-\delta_2}^{\delta_1}\hat{a}_{i,k}\hat{a}_{u,l}R_{yy}(u-i,k-l). \quad (54)$$

Setting to zero the derivatives of this error with respect to the AR parameters yields the following system of linear equations

$$\sum_{k=0}^{m}\sum_{i=-\delta_2}^{\delta_1}\hat{a}_{i,k}R_{yy}(u-i,k-l)=0$$

$$\text{for } l=1,\ \ldots,\ m \text{ and } u=-\delta_2,\ \ldots,\ \delta_1 \quad (55)$$

together with the constraint, Eq. (45). The corresponding values of the autocorrelations $R_{xx}(k)$ can be computed from Eq. (52) as

$$R_{xx}(k)=\sum_{u=0}^{m}\sum_{l=0}^{m}\sum_{i=-\delta_2}^{\delta_1}\sum_{v=-\delta_2}^{\delta_1}\hat{a}_{i,u}\hat{a}_{v,l}R_{yy}(k+v-i,u-l). \quad (56)$$

As required, the AR parameters $\hat{a}_{i,k}$ correspond to the coefficients $[\hat{a}_k]_i$ satisfying Eq. (31) as δ_1 and δ_2 tend to infinity. The same convergence result holds also for the autocorrelation functions $R_{xx}(k)$, Eqs. (38) and (56) (Mignolet, 1987).

Stability. The stability of the simulation scheme Eq. (41) is a fundamental requirement for the homogeneity of the generated time series $\hat{y}_{k,r}$. Many of the available methods to check this property, in particular Huang's and DeCarlo-Strintzis' tests (see Dudgeon and Mersereau, 1984, and Jury, 1988), are valid only for impulse response sequence $h_{u,k}$ with quarter plane region of support, $u,\ k \geq 0$. To account for this fact, note that the transfer function $h(z_1, z_2)$, Eq. (43), can be written in the form

$$h(z_1,z_2)=\sum_{k=0}^{\infty}\sum_{u=-k\delta_1}^{k\delta_2}h_{u,k}z_1^{-u}z_2^{-k}=\sum_{k=0}^{\infty}\sum_{u=0}^{k(\delta_1+\delta_2)}$$

$$h_{u-k\delta_1,k}z_1^{-u}\left[\frac{z_2}{z_1^{\delta_1}}\right]^{-k}=h'\left[z_1,\frac{z_2}{z_1^{\delta_1}}\right] \quad (57)$$

where the expansion of $h'(z_1, z_3)$ includes only the terms z_1^{-u} z_3^{-k}, $u,\ k \geq 0$, as required. Proceeding with the corresponding change of index in $\hat{d}(z_1, z_2)$ yields

$$h'\left[z_1,\frac{z_2}{z_1^{\delta_1}}\right]=\frac{1}{\hat{d}'\left[z_1,\frac{z_2}{z_1^{\delta_1}}\right]} \quad (58)$$

where

$$\hat{d}'\left[z_1,\frac{z_2}{z_1^{\delta_1}}\right]=1+\sum_{k=1}^{m}\sum_{u=(k-1)\delta_1}^{\delta_2+k\delta_1}\hat{a}_{k\delta_1-u,k}z_1^{-u}\left[\frac{z_2}{z_1^{\delta_1}}\right]^{-k}$$

$$=\hat{d}(z_1,z_2). \quad (59)$$

The application of the aforementioned methods to $\hat{d}(z_1, z_3)$ with $z_3 = z_2/z_1^{\delta_1}$ yields the following stability conditions

$$\hat{d}(z_1,z_2)\neq 0 \quad \text{for } |z_1|=1 \text{ and } |z_2|\geq 1 \quad (60)$$

or

$$\hat{d}(z_1,z_2)\neq 0 \quad \text{for } |z_2|=|z_1|^{\delta_1} \text{ and } |z_1|\geq 1 \quad (61a)$$

together with

$$|\hat{a}_{\delta_1,1}|\leq 1 \quad (61b)$$

when Huang's test is selected. Equivalently, using DeCarlo-Strintzis' conditions yields

$$\hat{d}(z_1,z_2)\neq 0 \quad \text{for } |z_1|=1 \text{ and } |z_2|=1 \quad (62a)$$

$$\hat{d}(1,z_2)\neq 0 \quad \text{for } |z_2|\geq 1 \quad (62b)$$

and

$$\hat{d}(z_1,z_2)\neq 0 \quad \text{for } z_2=z_1^{\delta_1} \text{ and } |z_1|\geq 1. \quad (62c)$$

Quality of Matching. The minimum value of the error $\epsilon_{AR}^{(2)}$ which corresponds to the AR parameters satisfying Eq. (55) is equal to

$$\epsilon_{AR}^{(2)}=\frac{1}{4\omega_b\phi_b}\sum_{k=0}^{m}\sum_{i=-\delta_2}^{\delta_1}\hat{a}_{i,k}R_{yy}(-i,k)=\frac{R_{xx}(0)}{4\omega_b\phi_b}. \quad (63)$$

As in the one-dimensional case (Mignolet and Spanos, 1987), the above minimum error does not provide a readily discernible measure of the quality of the matching of the AR and target spectra. The infinite-variate interpretation of the two-dimensional optimum AR modeling allows for the introduction of a meaningful AR matching error by relying on the results derived in Mignolet and Spanos (1987). Specifically, consider the asymptotic, $n \to \infty$, expression of the following error

$$\epsilon_M'=[\det(\hat{B}_0\hat{B}_0^{\dagger})]^{\frac{1}{n}}-\exp\left\{\frac{1}{2\omega_b}\int_{-\omega_b}^{\omega_b}\log[\det S_{\mathbf{YY}}(\omega)]^{\frac{1}{n}}d\omega\right\}. \quad (64)$$

Clearly, the limiting process involves the computation of both $\lim_{n\to\infty}[\det S_{\mathbf{YY}}(\omega)]^{1/n}$ and $\lim_{n\to\infty}[\det(\hat{B}_0\hat{B}_0^{\dagger})]^{1/n}$. Noting that the matrix $\hat{B}_0\hat{B}_0^{\dagger}$ becomes Toeplitz as the number of variates tends to infinity, the two previous limits appear as special cases of $\lim_{n\to\infty}[\det D_n]^{1/n}$ where D_n is an arbitrary $n\times n$ Toeplitz matrix.

Introduce the decomposition

$$D_n=\sum_{i=-(n-1)}^{(n-1)}d_iJ_i^{(n)} \quad (65)$$

where $J_i^{(n)}$ denotes, similarly to J_i Eq. (30), the $n\times n$ Toeplitz matrix whose elements are all zero except the ones located on the ith diagonal. Then, it can be shown (Grenander and Szego, 1958) that

$$\lim_{n\to\infty}[\det D_n]^{\frac{1}{n}}=\exp\left\{\frac{1}{2\phi_b}\int_{-\phi_b}^{\phi_b}\log f(\phi)d\phi\right\} \quad (66)$$

where

$$d_i=\frac{1}{2\phi_b}\int_{-\phi_b}^{\phi_b}f(\phi)e^{-ji\phi\Delta}d\phi. \quad (67)$$

Applying this result to both matrices $S_{\mathbf{YY}}(\omega)$ and $\hat{B}_0\hat{B}_0^{\dagger}$ yields

$$\epsilon_M^{(2)}=\lim_{n\to\infty}\epsilon_M'=2\phi_b\left\{\exp\left\{\frac{1}{2\phi_b}\int_{-\phi_b}^{\phi_b}\log\left[\frac{S_{xx}(\phi)}{2\omega_b}\right]d\phi\right\}\right.$$

$$\left.-\exp\left\{\frac{1}{4\phi_b\omega_b}\int_{-\omega_b}^{\omega_b}\int_{-\phi_b}^{\phi_b}\log[S_{yy}(\phi,\omega)]d\phi d\omega\right\}\right\} \quad (68)$$

which will be termed the two-dimensional AR matching error. On the basis of the properties of ϵ_M' (Mignolet and Spanos, 1987) it is readily seen that $\epsilon_M^{(2)}$ is non-negative and converges monotonically to zero as the system orders m, δ_1 and δ_2 tend to infinity.

Note that the above definition of $\epsilon_M^{(2)}$ is in complete agreement with the minimum prediction formula derived by Helson and Lowdenslager (1958) provided that the input process x_i is expressed as the infinite autoregression

$$\sum_{k=0}^{\infty}\hat{\alpha}_k x_{i-k}=\hat{\beta}_0 w_i \quad (69)$$

where w_i is a $[-\phi_b,\ \phi_b]$ bandlimited one-dimensional white noise process and

$$\hat{\beta}_0^2=\exp\left\{\frac{1}{2\phi_b}\int_{-\phi_b}^{\phi_b}\log[S_{xx}(\phi)]d\phi\right\}. \quad (70)$$

Downloaded 03 May 2010 to 171.66.16.247. Redistribution subject to ASME license or copyright; see http://www.asme.org/terms/Terms_Use.cfm

As in the one-dimensional case (Mignolet and Spanos, 1987), Eq. (68) can be used to detect some pathological target spectra. Specifically, if the condition

$$\int_{-\omega_b}^{\omega_b}\int_{-\phi_b}^{\phi_b} \log[S_{yy}(\phi,\omega)]d\phi d\omega = -\infty \tag{71}$$

is satisfied, then the convergence of $\epsilon_M^{(2)}$ to zero as m, δ_1, and δ_2 tend to infinity implies that

$$\int_{-\phi_b}^{\phi_b} \log[S_{xx}(\phi)]d\phi \rightarrow -\infty. \tag{72}$$

The two previous equations can only be satisfied if the asymptotic spectrum $S_{xx}^{(\infty)}(\phi)$ corresponding to $m = \delta_1 = \delta_2 = \infty$ and the target expression $S_{yy}(\phi, \omega)$ vanish at one point each at least. Denote by $\phi_i(\omega)$, $i = 1, \ldots, \eta$ and ϕ_l', $l = 1, \ldots, \eta'$ the location of the zeros of $S_{yy}(\phi, \omega)$ and $S_{xx}^{(\infty)}(\phi)$, respectively, and assume first that ϕ_l' is not a zero of the two-dimensional spectrum $S_{yy}(\phi, \omega)$ for all frequencies ω, that is

$$S_{yy}(\phi_l',\omega) \neq 0 \quad \text{on } \omega \in \Omega_l \subseteq [-\omega_b,\omega_b]. \tag{73}$$

Then the equality

$$S_{xx}^{(\infty)}(\phi_l') = 0 = \int_{-\omega_b}^{\omega_b} |\hat{d}(e^{j\phi_l'\Delta}, e^{j\omega T})|^2 S_{yy}(\phi_l',\omega)d\omega \tag{74}$$

can only be achieved if the infinite AR polynomial $\hat{d}(e^{j\phi_l'\Delta}, e^{j\omega T})$ vanishes almost everywhere on the domain $\omega \in \Omega_l$. Thus, almost all the points of this region of the (ϕ, ω) plane are poles of the infinite AR transfer function. This situation is entirely analogous to the modeling of the Pierson-Moskowitz wave spectrum (see Mignolet and Spanos, 1987) and the AR spectrum $S_{\hat{y}\hat{y}}(\phi, \omega)$ corresponding to large, but finite, values of m, δ_1, δ_2 is expected to display sharp peaks. The condition Eq. (73) is satisfied in particular if there is no value of ϕ such that

$$S_{yy}(\phi,\omega) = 0 \quad \text{for all } \omega \in [-\omega_b,\omega_b]. \tag{75}$$

Assume now on the contrary that this relation is satisfied for some frequency $\phi = \phi_l$. Then Eq. (52) implies that the one-dimensional spectrum $S_{xx}^{(\infty)}(\phi)$ must also vanish at this frequency. That is,

$$S_{xx}^{(\infty)}(\phi_l) = 0 \tag{76}$$

and Eq. (74) is identically satisfied independently of the denominator $\hat{d}(e^{j\phi_l\Delta}, e^{j\omega T})$ of the infinite AR model. In particular, it is possible that this function does not vanish on the unit circle so that the problem of approximating the zero of the spectrum $S_{yy}(\phi, \omega)$ has been "transferred" to the one-dimensional process x_i. In view of the good results eventually obtained in connection with the Pierson-Moskowitz spectrum (Spanos and Mignolet, 1987), this transfer property represents an interesting feature of the present AR modeling approach.

Two-Dimensional ARMA Modeling

The ARMA Random Field. It is readily seen that the two-dimensional ARMA model corresponding to the AR field described in the previous section is

$$\tilde{y}_{i,r} = -\sum_{k=1}^{p}\sum_{u=-\mu_2}^{\mu_1} a_{u,k}\tilde{y}_{i+u,r-k} + \sum_{l=0}^{q}\sum_{u=-\nu_2}^{\nu_1} b_{u,l}x_{i+u}^{r-l}. \tag{77}$$

The symbol x_i^r denotes as before the ith sample of the rth realization of the one-dimensional stochastic process x whose spectrum $S_{xx}(\phi)$ and autocorrelation function $R_{xx}(l)$ are defined by Eq. (52) and (56), respectively.

The random field $\tilde{y}_{i,r}$ can be seen as the response to the excitation x_i^r of the linear system whose transfer function is

$$h(z_1,z_2) = \frac{n(z_1,z_2)}{d(z_1,z_2)} \tag{78}$$

where

$$n(z_1,z_2) = \sum_{l=0}^{q}\sum_{k=-\nu_2}^{\nu_1} b_{k,l}z_1^k z_2^{-l} \tag{79}$$

and

$$d(z_1,z_2) = \sum_{k=0}^{p}\sum_{i=-\mu_2}^{\mu_1} a_{i,k}z_1^i z_2^{-k} \tag{80}$$

together with

$$a_{k,0} = \delta_{k0} \quad k = -\mu_2, \ldots, \mu_1. \tag{81}$$

For the purpose of simulation, the coefficients $a_{i,k}$ and $b_{k,l}$ should be selected so that the spectrum of the ARMA field

$$S_{\tilde{y}\tilde{y}}(\phi,\omega) = |h(e^{j\phi\Delta}, e^{j\omega T})|^2 \frac{S_{xx}(\phi)}{2\omega_b} \tag{82}$$

represents a close approximation of the target expression, $S_{yy}(\phi, \omega)$. The excellent results presented in Spanos and Mignolet (1987) in connection with some two-stage AR to ARMA approximation procedures motivate the investigation of similar techniques for two-dimensional fields.

The Generalized Original Spectrum Procedure. This procedure involves the minimization, with respect to the ARMA parameters $a_{i,k}$ and $b_{k,l}$, of the frequency domain error

$$\epsilon = \frac{1}{4\omega_b\phi_b}\int_{-\phi_b}^{\phi_b}\int_{-\omega_b}^{\omega_b} |d(e^{j\phi\Delta}, e^{j\omega T})h_{AR}(e^{j\phi\Delta}, e^{j\omega T}) - n(e^{j\phi\Delta}, e^{j\omega T})|^2 S_{xx}(\phi)d\omega d\phi \tag{83}$$

where $h_{AR}(e^{j\phi\Delta}, e^{j\omega T})$ is defined by Eq. (42). Further, assume that the ARMA coefficients are restricted to satisfy the relations

$$\sum_{k=0}^{p}\sum_{i=-\mu_2}^{\mu_1} a_{i,k}R_{\hat{y}x}(u-i,k-l) = 0$$

$$\text{for } l = q+1, \ldots, q+r \text{ and } u = -\rho_2, \ldots \rho_1. \tag{84}$$

The minimization of ϵ under these constraints can be achieved by considering the modified error

$$\tilde{\epsilon} = \epsilon + \frac{1}{\phi_b}\sum_{l=q+1}^{q+r}\sum_{u=-\rho_2}^{\rho_1}\lambda_{u,l}\left[\sum_{k=0}^{p}\sum_{i=-\mu_2}^{\mu_1} a_{i,k}R_{\hat{y}x}(u-i,k-l)\right] \tag{85}$$

where $\lambda_{u,l}$ are the Lagrange multipliers corresponding to the conditions, Eq. (84).

Setting to zero the derivative of the above error with respect to the coefficients $a_{i,k}$ and $b_{u,l}$, it is readily shown that the minimum of $\tilde{\epsilon}$ is achieved when the ARMA parameters satisfy the following system of equations

$$\sum_{k=0}^{p}\sum_{i=-\mu_2}^{\mu_1} a_{i,k}R_{\hat{y}\hat{y}}(v-i,k-u) - \sum_{l=0}^{q}\sum_{k=-\nu_2}^{\nu_1} b_{k,l}R_{\hat{y}x}(k-v,u-l) + \sum_{l=q+1}^{q+r}\sum_{k=-\rho_2}^{\rho_1}\lambda_{k,l}R_{\hat{y}x}(k-v,u-l) = 0 \tag{86}$$

for $u = 1, \ldots, p$ and $v = -\mu_2, \ldots, \mu_1$ and

$$\sum_{k=0}^{p}\sum_{i=-\mu_2}^{\mu_1} a_{i,k}R_{\hat{y}x}(v-i,k-u) = \sum_{l=-\nu_2}^{\nu_1} b_{l,u}R_{xx}(v-l)$$

$$\text{for } u = 0, \ldots, q \text{ and } v = -\nu_2, \ldots, \nu_1 \tag{87}$$

together with the constraints, Eq. (81) and (84). The AR input-output crosscorrelations $R_{\hat{y}x}(u, v)$ are readily computed from the recurrence relations (46*a*)-(46*c*).

Combining Eq. (83)-(87), the corresponding minimum value of ϵ is readily computed as

Downloaded 03 May 2010 to 171.66.16.247. Redistribution subject to ASME license or copyright; see http://www.asme.org/terms/Terms_Use.cfm

$$\epsilon_{\min}=\tilde{\epsilon}_{\min}=\frac{1}{2\phi_b}\left[\sum_{k=0}^{p}\sum_{i=-\mu_2}^{\mu_1}a_{i,k}R_{\hat{y}\hat{y}}(-i,k)\right.$$

$$-\sum_{l=0}^{q}\sum_{u=-\nu_2}^{\nu_1}b_{u,l}R_{\hat{y}x}(u,-l)$$

$$\left.+\sum_{l=q+1}^{q+r}\sum_{u=-\rho_2}^{\rho_1}\lambda_{u,l}R_{\hat{y}x}(u,-l)\right]. \quad (88)$$

Note that the value of $b_{u,0}$ can be computed directly from Eq. (87) for $u = 0$. Indeed, using Eq. (46*a*) and (46*b*), this relation can be written in the form

$$\sum_{l=-\nu_2}^{\nu_1}b_{l,0}R_{xx}(v-l)=R_{xx}(v) \quad \text{for } v=-\nu_2,\ \ldots,\ \nu_1 \quad (89)$$

which admits the solution

$$b_{l,0}=\delta_{l0} \quad l=-\nu_2,\ \ldots,\ \nu_1. \quad (90)$$

It has been shown (Mignolet, 1987) that the system of Eqs. (81), (84), and (86)–(87) for the parameters $a_{i,k}$ and $b_{u,l}$ becomes identical as μ_1, μ_2, ν_1, and ν_2 tend to infinity to the set of relations for the diagonal elements of the matrices A_k and B_l corresponding to the infinite variate one-dimensional generalized original spectral matrix method. Thus, the present approximation technique is consistent with the vector representation, Eq. (5).

The Generalized Inverse Spectrum Approach. An alternative ARMA modeling procedure can be developed that relies on a rational approximation of the inverse of the AR transfer function. Specifically, select the ARMA parameters $a_{i,k}$ and $b_{u,l}$ in order to minimize the frequency domain error

$$\delta=\frac{1}{4\omega_b\phi_b}\int_{-\phi_b}^{\phi_b}\int_{-\omega_b}^{\omega_b}|n(e^{j\phi\Delta},e^{j\omega T})\hat{d}(e^{j\phi\Delta},e^{j\omega T})$$

$$-d(e^{j\phi\Delta},e^{j\omega T})|^2 d\omega d\phi \quad (91)$$

where $\hat{d}(e^{j\phi\Delta}, e^{j\omega T})$ is defined by Eq. (51). Further, assume that the ARMA coefficients are restricted to satisfy the equations

$$\sum_{l=\max(0,k-m)}^{\min(q,k)}\sum_{u=\max(-\nu_2,i-\delta_1)}^{\min(\nu_1,i+\delta_2)}b_{u,l}\hat{a}_{i-u,k-l}=0$$

$$\text{for } k=p+1,\ \ldots,\ p+r \text{ and } i=-\rho_2,\ \ldots,\ \rho_1. \quad (92)$$

These constraints can be combined with the definition of δ to yield the modified error

$$\tilde{\delta}=\delta$$

$$+2\sum_{k=p+1}^{p+r}\sum_{i=-\rho_2}^{\rho_1}\lambda_{i,k}\left[\sum_{l=\max(0,k-m)}^{\min(q,k)}\sum_{u=\max(-\nu_2,i-\delta_1)}^{\min(\nu_1,i+\delta_2)}b_{u,l}\hat{a}_{i-u,k-l}\right] \quad (93)$$

where $\lambda_{i,k}$ are the Lagrange multipliers corresponding to the conditions, Eq. (92). Finally, the nonhomogeneous constraints

$$b_{l,0}=\delta_{l0} \quad l=-\nu_2,\ \ldots,\ \nu_1 \quad (94)$$

are enforced. Setting equal to zero the derivatives of $\tilde{\delta}$ with respect to the unknown parameters $a_{i,k}$ and $b_{u,l}$ yields the following system of linear equations

$$\sum_{l=0}^{q}\sum_{s=-\nu_2}^{\nu_1}b_{s,l}\left[\sum_{k=\max(l,u)}^{m+\min(l,u)}\sum_{i=\max(s,v)-\delta_2}^{\delta_1+\min(s,v)}\hat{a}_{i-s,k-l}\hat{a}_{i-v,k-u}\right]$$

$$-\sum_{k=u}^{\min(p,m+u)}\sum_{i=\max(-\mu_2,v-\delta_2)}^{\min(\mu_1,v+\delta_1)}a_{i,k}\hat{a}_{i-v,k-u}$$

$$+\sum_{k=\max(p+1,u)}^{\min(p+r,m+u)}\sum_{i=\max(-\rho_2,v-\delta_2)}^{\min(\rho_1,v+\delta_1)}\lambda_{i,k}\hat{a}_{i-v,k-u}=0$$

$$\text{for } u=1,\ \ldots,\ q \text{ and } v=-\nu_2,\ \ldots,\ \nu_1 \quad (95)$$

and

$$a_{i,k}=\sum_{l=\max(0,k-m)}^{\min(q,k)}\sum_{u=\max(-\nu_2,i-\delta_1)}^{\min(\nu_1,i+\delta_2)}b_{u,l}\hat{a}_{i-u,k-l}$$

$$\text{for } k=0,\ \ldots,\ p \text{ and } i=-\mu_2,\ \ldots,\ \mu_1 \quad (96)$$

which must be solved together with the constraints, Eq. (92) and (94).

The corresponding minimum value of the design error is readily computed as

$$\delta_{\min}=\tilde{\delta}_{\min}=\sum_{l=0}^{q}\sum_{u=-\nu_2}^{\nu_1}b_{u,l}\left[\sum_{k=l}^{m}\sum_{i=\max(u,0)-\delta_2}^{\delta_1+\min(u,0)}\hat{a}_{i-u,k-l}\hat{a}_{i,k}\right]$$

$$-\sum_{k=0}^{\min(p,m)}\sum_{i=\max(-\mu_2,-\delta_2)}^{\min(\mu_1,\delta_1)}a_{i,k}\hat{a}_{i,k}$$

$$+\sum_{k=p+1}^{\min(p+r,m)}\sum_{i=\max(-\rho_2,-\delta_2)}^{\min(\rho_1,\delta_1)}\lambda_{i,k}\hat{a}_{i,k} \quad (97)$$

Note that Eq. (96) expressed for $k = 0$ directly yields

$$a_{i,0}=\delta_{i0} \quad i=-\mu_2,\ \ldots,\ \mu_1 \quad (98)$$

so that the ARMA system derived by the present procedure is indeed characterized by the recurrence relation, Eq. (77).

It has been shown (Mignolet, 1987) that the system of Eqs. (92), (94)–(96) for the parameters $a_{i,k}$ and $b_{u,l}$ becomes identical as μ_1, μ_2, ν_1 and ν_2 tend to infinity to the set of relations for the diagonal elements of the matrices A_k and B_l corresponding to the infinite variate one-dimensional generalized inverse spectral matrix method. Thus, the present approximation technique is consistent with the vector representation, Eq. (5).

Special Cases

Separable Spectrum. One of the simplest possible form that can be used to model a two-dimensional power spectrum consists of the product of two functions each of one variable, that is

$$S_{yy}(\phi,\omega)=S_1(\phi)S_2(\omega)$$

$$\text{for } (\phi,\omega)\in[-\phi_b,\phi_b]\times[-\omega_b,\omega_b]. \quad (99)$$

Such functions and the corresponding processes $y_{k,r}$ are traditionally termed separable. It can be shown (Mignolet, 1987) that the approximation techniques presented in this paper lead to AR and ARMA models of separable processes whose parameters are

$$\hat{a}_{i,k}=\hat{\alpha}_k\delta_{i0} \quad \text{for } k=0,\ \ldots,\ m \text{ and } i=-\delta_2,\ \ldots,\ \delta_1 \quad (100)$$

$$a_{i,k}=\alpha_k\delta_{i0} \quad \text{for } k=0,\ \ldots,\ p \text{ and } i=-\mu_2,\ \ldots,\ \mu_1 \quad (101)$$

and

$$b_{u,l}=\beta_l\delta_{u0} \quad \text{for } l=0,\ \ldots,\ q \text{ and } u=-\nu_2,\ \ldots,\ \nu_1. \quad (102)$$

The spectrum of the corresponding one-dimensional process x_i is

$$S_{xx}(\phi)=\chi S_1(\phi) \quad \phi\in[-\phi_b,\phi_b] \quad (103)$$

where the constant χ is defined as

$$\chi=\sum_{k=0}^{m}\sum_{l=0}^{m}\hat{\alpha}_k\hat{\alpha}_l R_2(k-l). \quad (104)$$

In the above equation, the symbol $R_2(k)$ denotes the one-

Downloaded 03 May 2010 to 171.66.16.247. Redistribution subject to ASME license or copyright; see http://www.asme.org/terms/Terms_Use.cfm

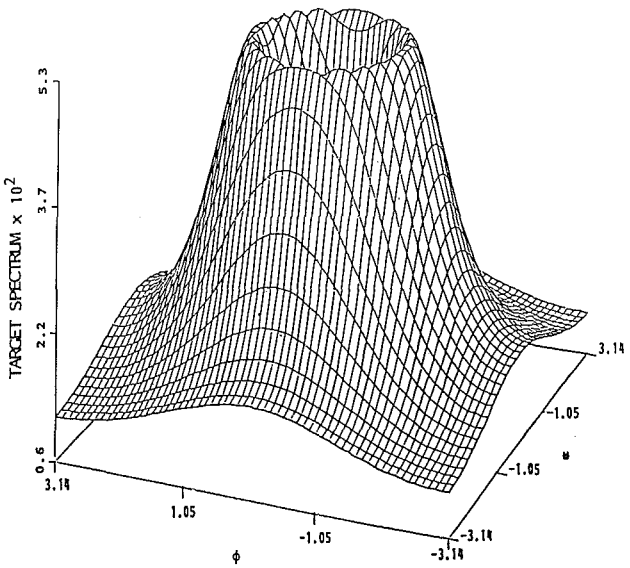


Fig. 1 The two-dimensional target spectrum corresponding to Eq. (108); $T = \Delta x = 1.00$

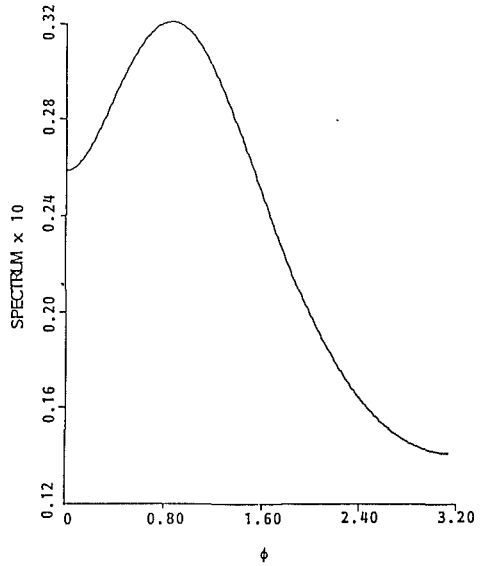


Fig. 3 The spectrum of the one-dimensional process corresponding to the autocorrelation sequence, Eq. (108)

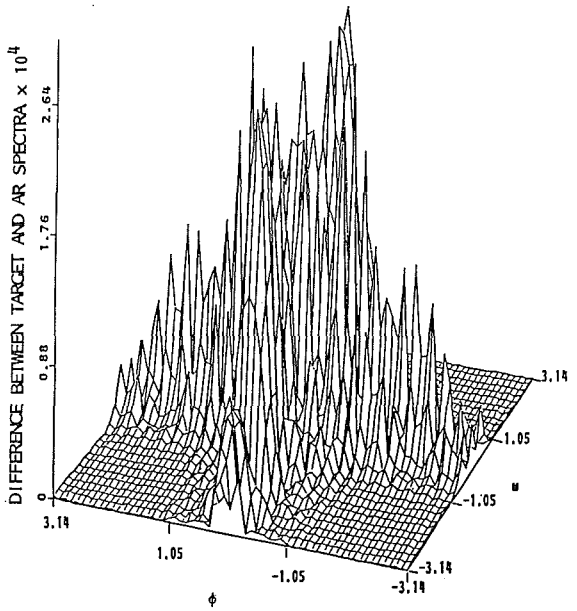


Fig. 2 The modulus of the difference between the two-dimensional target and AR spectra, $m = \delta_1 = \delta_2 = 12$, $T = \Delta x = 1.00$

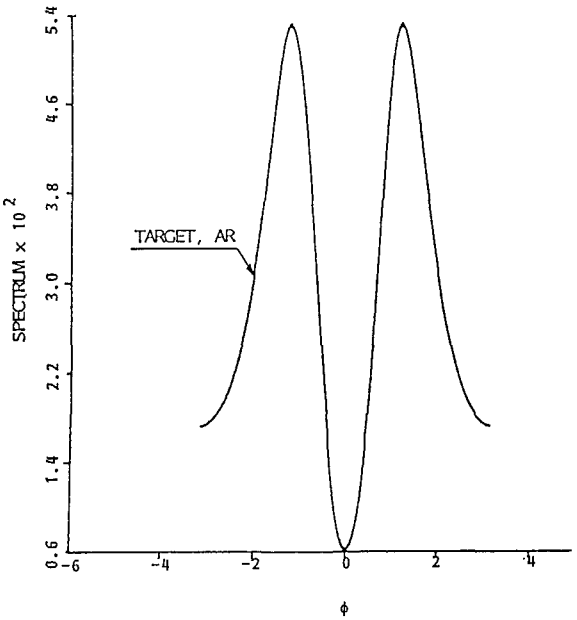


Fig. 4 Cut through the target and AR spectral surfaces by the plane $\omega = 0$

dimensional autocorrelation function associated with the spectrum $S_2(\omega)$.

Thus, as it is readily seen from Eq. (100)–(103), the AR and ARMA spectra $S_{\bar{y}\bar{y}}(\phi, \omega)$ and $S_{\bar{y}\bar{y}}(\phi, \omega)$ corresponding to separable target expressions are also separable.

Symmetric Spectrum. Another model often used in practical applications assumes that the autocorrelation function $R_{yy}(k, l)$ is symmetric. That is, it satisfies Eq. (14). Then, it is readily shown (Mignolet, 1987) that the parameters of the corresponding two-dimensional AR and ARMA systems are also symmetric when the positive and negative system orders are equal. That is, the selection $\delta_1 = \delta_2$, $\mu_1 = \mu_2$, $\nu_1 = \nu_2$ and $\rho_1 = \rho_2$ leads to the equalities

$$\hat{a}_{i,k} = \hat{a}_{-i,k} \quad \text{for } k = 0, \ldots, m \text{ and } i = -\delta_1, \ldots, \delta_1 \tag{105}$$

$$a_{i,k} = a_{-i,k} \quad \text{for } k = 0, \ldots, p \text{ and } i = -\mu_1, \ldots, \mu_1 \tag{106}$$

and

$$b_{u,l} = b_{-u,l} \quad \text{for } l = 0, \ldots, q \text{ and } u = -\nu_1, \ldots, \nu_1. \tag{107}$$

Thus, it is readily proved that the AR and ARMA approximations of the symmetric spectrum $S_{yy}(\phi, \omega)$ are also symmetric. Note finally that the relations (105)–(107) can be used to effectively reduce the size of the systems of equations to solve for the AR and ARMA parameters.

Numerical Example

Following Naganuma et al. (1985, 1987), the two-dimensional autocorrelation sequence $R_{yy}(k, l)$ given by the equation

$$R_{yy}(k,l) = \exp\left[-\sqrt{k^2+l^2}\right] \cos\sqrt{k^2+l^2} \tag{108}$$

was selected to assess the usefulness of the present AR and ARMA modeling techniques. The corresponding spectrum $S_{yy}(\phi, \omega)$ is shown in Fig. 1 when the sampling intervals are chosen to be $\Delta = T = 1$.

Downloaded 03 May 2010 to 171.66.16.247. Redistribution subject to ASME license or copyright; see http://www.asme.org/terms/Terms_Use.cfm

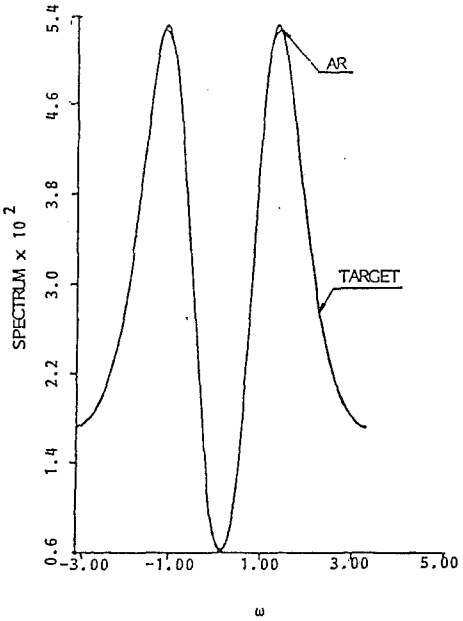


Fig. 5 Cut through the target and AR spectral surfaces by the plane $\varphi = 0$

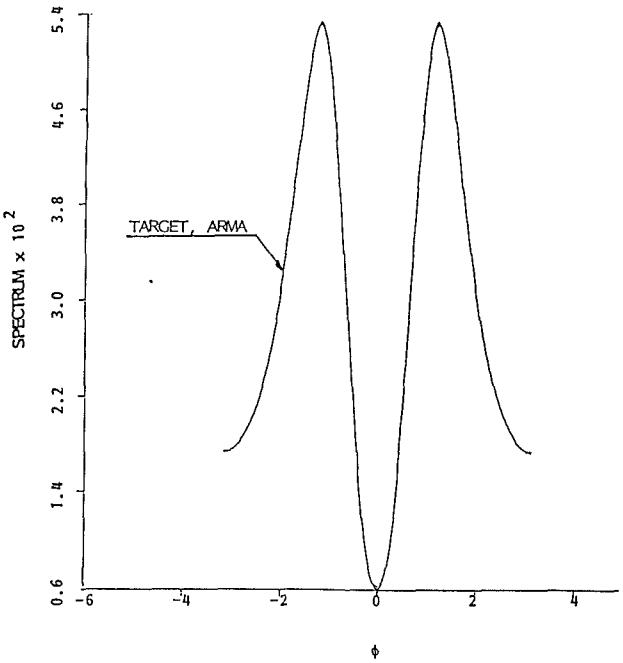


Fig. 7 Cut through the target and ARMA spectral surfaces by the plane $\omega = 0$

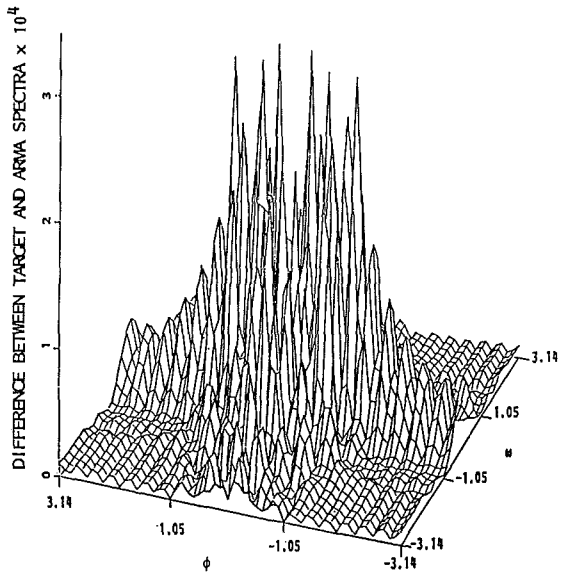


Fig. 6 The modulus of the difference between the two-dimensional target and ARMA spectra, $p = 5$, $\mu_1 = \mu_2 = 9$, $q = 2$, $\nu_1 = \nu_2 = 1$, $T = \Delta x = 1.00$

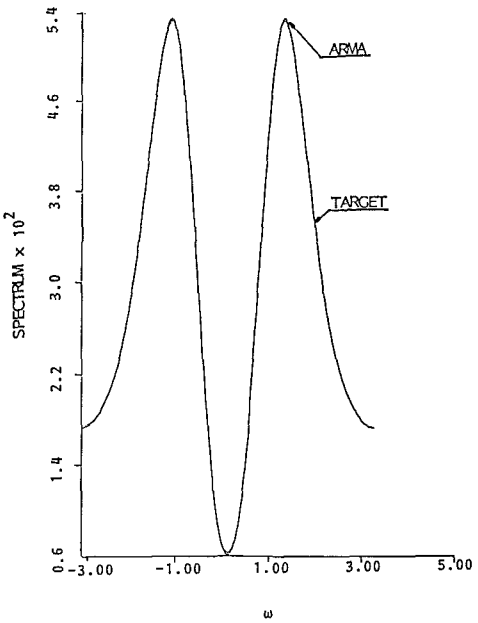


Fig. 8 Cut through the target and ARMA spectral surfaces by the plane $\varphi = 0$

An AR approximation of this expression is sought first. Displayed in Figs. 2 and 3 are the modulus of the difference between the target and AR spectra and the spectrum of the one-dimensional process x_i, respectively, corresponding to the choice $m = \delta_1 = \delta_2 = 12$. Further, shown in Figs. 4 and 5 are the intersections of the spectral surfaces by the planes $\omega = 0$ and $\phi = 0$, respectively, where the maxima of the difference between spectra occur. The matching between the target and AR expressions is excellent, the two curves are almost indistinguishable from one another. Thus, the AR simulation scheme can be used for a reliable generation of records of values of the two-dimensional random field described by Eq. (108).

Next, the generalized original spectral matrix approach, with $r = 0$, was selected to obtain an ARMA approximation of the target spectrum on the basis of the previous AR model. Shown in Fig. 6 is the modulus of the difference between the target and ARMA spectra corresponding to the choice $p = 5$, $q = 2$, $\mu_1 = \mu_2 = 9$ and $\nu_1 = \nu_2 = 1$. The intersections of the spectral surfaces and the planes $\omega = 0$ and $\phi = 0$, where the maxima of the difference still occur, are shown in Figs. 7 and 8, respectively. Clearly, the ARMA model can be used as an accurate representation of the target random field. Further, note that this approximation involves only 102 parameters as opposed to 300 as required by the AR modeling technique.

Finally, note that the AR and ARMA systems have been found stable in the Lyapunov sense.

Concluding Remarks

The determination of AR and ARMA systems for the simulation of two-dimensional random fields with a specified (tar-

Downloaded 03 May 2010 to 171.66.16.247. Redistribution subject to ASME license or copyright; see http://www.asme.org/terms/Terms_Use.cfm

get) spectrum has been studied. The contribution of this part of the series may be summarized as follows.

On the basis of the equivalence between discrete scalar two-dimensional fields and one-dimensional vector processes, Eq. (5), a new autoregressive (AR) algorithm has been introduced, Eq. (41). According to this model, a sample of the random field to be generated can be expressed as the sum of a linear combination of previous ones and of a colored one-dimensional process.

An optimum strategy to determine the parameters of the AR model has been introduced that relies on a frequency domain error, Eq. (50). The minimization of this quantity has been shown to lead to a set of linear equations for the AR coefficients that can readily be solved. Further, the power spectrum of the colored noise has been selected, Eq. (52), to minimize a second frequency domain error, Eq. (53), involving the target spectrum and the optimum AR parameters.

Relying on the asymptotic behavior of the AR approximation, a matching error has been defined that can be used to detect pathological target spectra. In particular, it has been found that target expressions satisfying the nonintegrability condition, Eq. (71) can lead, as in the one-dimensional case, to AR spectra that exhibit sharp peaks.

A novel ARMA random field has been introduced as the response to the one-dimensional colored noise of a two-dimensional linear system possessing a rational transfer function. Two simple procedures have been presented to approximate the AR transfer function by an ARMA one. Both of these techniques have been derived from the standpoint of minimizing frequency domain errors, Eq. (85) and Eq. (93), and have been shown to lead to linear equations for the unknown ARMA parameters.

The two special cases of a separable and a symmetric target autocorrelation function have been investigated. It has been found that the corresponding AR and ARMA approximations posssess the same properties as their target counterparts. Finally, a numerical example has been presented that shows the usefulness of the present techniques for an accurate simulation of two-dimensional random fields.

References

Chakrabarti, S. K., 1987, *Hydrodynamics of Offshore Structures*, Springer, New York.

Chang, H., and Aggarwal, J. K., 1978, "Design of Two-Dimensional Semi-Causal Recursive Filters," *IEEE Transactions on Circuits and Systems*, Vol. CAS-25, pp. 1051–1059.

Delsarte, P., Genin, Y., and Kamp, Y., 1980, "Half-Plane Toeplitz Systems," *IEEE Transactions on Information Theory*, Vol. IT-26, No. 4, pp. 465–474.

Dudgeon, D. E., and Mersereau, R. M., 1984, *Multidimensional Digital Signal Processing*, Prentice-Hall, Englewood Cliffs, N.J.

Gersch, W., and Yonemoto, J., 1977, "Synthesis of Multivariate Random Vibration Systems: A Two-Stage Least Squares AR-MA Model Approach," *Journal of Sound and Vibration*, Vol. 52, No. 4, pp. 553–565.

Grenander, U., and Szego, G., 1958, *Toeplitz Forms and their Applications*, University of California Press, Berkeley, Calif.

Harichandran, R. S., and Vanmarcke, E. H., 1986, "Stochastic Variation of Earthquake Ground Motion in Space and Time," *Journal of Engineering Mechanics*, Vol. 112, No. 2, pp. 154–174.

Helson, H., and Lowdenslager, D., 1958, "Prediction Theory and Fourier Series in Several Variables," *Acta Mathematica*, Vol. 99, pp. 165–202.

Jury, E. I., 1988, "Modified Stability Table for 2-D Digital Filters," *IEEE Transactions on Circuits and Systems*, Vol. CAS-35, No. 1, pp. 116–119.

Makhoul, J., 1975, "Linear Prediction: A Tutorial Review," *Proceedings of the IEEE*, Vol. 63, pp. 561–580.

Madsen, H. O., Krenk, S., and Lind, N. C., 1986, *Methods of Structural Safety*, Prentice-Hall, Englewood Cliffs, N.J.

Marzetta, T. L., 1980, "Two-Dimensional Linear Prediction: Autocorrelation Arrays, Minimum-Phase Prediction Error Filters, and Reflection Coefficient Arrays," *IEEE Transactions on Acoustics, Speech and Signal Processing*, Vol. ASSP-28, No. 6, pp. 725–733.

Mignolet, M. P., 1987, ARMA Simulation of Multivariate and Multidimensional Random Processes, Ph.D. Dissertation, Rice University, Houston, Texas.

Mignolet, M. P., and Spanos, P. D., 1987, "Recursive Simulation of Stationary Multivariate Random Processes: Part I," ASME JOURNAL OF APPLIED MECHANICS, Vol. 109, pp. 674–680.

Naganuma, T., Deodatis, G., Shinozuka, M., and Samaras, E., 1985, "Digital Generation of Multidimensional Random Fields," *Proceedings of the Fourth International Conference on Structural Safety and Reliability*, ICOSSAR, Vol. 1, pp. 251–260.

Naganuma, T., Deodatis, G., and Shinozuka, M., 1987, "ARMA Model for Two-Dimensional Processes," *Journal of Engineering Mechanics*, Vol. 113, No. 2, pp. 234–251.

Samaras, E., Shinozuka, M., and Tsurui, A., 1985, "ARMA Representation of Random Processes," *Journal of Engineering Mechanics*, Vol. 111, No. 3, pp. 449–461.

Spanos, P. D., and Mignolet, M. P., 1987, "Recursive Simulation of Stationary Multivariate Random Processes: Part II," ASME JOURNAL OF APPLIED MECHANICS, Vol. 109, pp. 681–687.

Spanos, P. D., and Mignolet, 1989, "ARMA Monte Carlo Simulation in Probabilistic Structural Analysis," *The Shock and Vibration Digest*, Vol. 21, No. 11, pp. 3–14.

Youla, D. C., and Kazanjian, N. N., 1978, "Bauer-Type Factorization of Positive Matrices and the Theory of Matrix Polynomials Orthogonal on the Unit Circle," *IEEE Transactions on Circuits and Systems*, Vol. CAS-25, No. 2, pp. 57–69.

Downloaded 03 May 2010 to 171.66.16.247. Redistribution subject to ASME license or copyright; see http://www.asme.org/terms/Terms_Use.cfm

Simulation of Homogeneous Two-Dimensional Random Fields: Part II—MA and ARMA Models

Pol D. Spanos
L. B. Ryon Chair in Engineering,
Rice University,
Houston, TX 77251
Fellow ASME

Marc P. Mignolet
Asst. Professor,
Department of Mechanical and
Aerospace Engineering,
Arizona State University,
Tempe, AZ 85287-6106
Assoc. Mem. ASME

Alternatively to the autoregressive (AR) models examined in Part I, the determination of moving average (MA) algorithms for simulating realizations of two-dimensional random fields with a specified (target) power spectrum is presented. First, the mathematical form of these models is addressed by considering infinite-variate vector processes of an appropriate spectral matrix. Next, the MA parameters are determined by relying on the maximization of an energy-like quantity. Then, a technique is formulated to derive an autoregressive moving average (ARMA) simulation algorithm from a prior MA approximation by relying on the minimization of frequency domain errors. Finally, these procedures are critically assessed and an example of application is presented.

Introduction

In the first part of this series, an autoregressive (AR) linear system is introduced for the accurate representation of random fields with a given (target) power spectrum. It is demonstrated in that part that this first approximation can be used in a two-stage format to derive efficiently reliable autoregressive moving average (ARMA) algorithms for the simulation of a target random field.

The purpose of this part of the series is to investigate the applicability of moving average (MA) models for the simulation of random fields. Furthermore, the feasibility of a two-step determination of ARMA simulation algorithms from this prior MA approximation is addressed. For clarity, the present discussion will be restricted to the case of scalar two-dimensional fields. However, the techniques and results can readily be extended to the multidimensional case. Further, as in Part I, it is assumed that the first of the two coordinates is a spatial location while the second one represents time. This convention has no bearing, indeed, on the validity of the results and techniques derived which are also applicable when both dimensions represent space.

Discrete Two-Dimensional Random Fields

One-Dimensional Vector Process Representation. It is shown in Part I that a discrete two-dimensional field $y_{k,r}$, $(k, r) \in [k_1, k_2] \times [r_1, r_2]$, can be viewed as a one-dimensional vector process $\mathbf{Y}_r$ whose components are

$$[\mathbf{Y}_r]_k = y_{k,r} \quad k = 1, \ldots, n. \tag{1}$$

Using this equivalence, the simulation of two-dimensional fields with specified autocorrelation function

$$R_{yy}(l,s) = E[y_{k,r} y_{k+l,r+s}] \tag{2}$$

is recast as the better known problem of the generation of realizations of the one-dimensional vector process $\mathbf{Y}_r$. The elements of its autocorrelation matrices are readily computed from Eqs. (1) and (2) as

$$[R_{\mathbf{YY}}(l)]_{ui} = [E[\mathbf{Y}_r \mathbf{Y}_{r+l}^{\dagger}]]_{ui} = E[[\mathbf{Y}_r]_u [\mathbf{Y}_{r+l}]_i] = E[y_{u,r} y_{i,r+l}] = R_{yy}(i-u,l)\, u,i = 1, \ldots, n. \tag{3}$$

In the above equations, the symbols $E[\bullet]$ and † denote the operations of mathematical expectation and matrix transposition, respectively.

The connections between the random field $y_{k,r}$ and the vector process $\mathbf{Y}_r$ can also be investigated in the frequency domain. Specifically, it is readily shown that the power spectrum $S_{yy}(\phi, \omega)$ and the spectral matrix $S_{\mathbf{YY}}(\omega)$ which satisfy the Fourier transform relations

$$S_{yy}(\phi,\omega) = \frac{1}{4\omega_b \phi_b} \sum_{l=-\infty}^{\infty} \sum_{s=-\infty}^{\infty} R_{yy}(l,s) e^{-jl\phi\Delta} e^{-js\omega T} \tag{4}$$

and

$$S_{\mathbf{YY}}(\omega) = \frac{1}{2\omega_b} \sum_{k=-\infty}^{\infty} R_{\mathbf{YY}}(k) e^{-jk\omega T} \tag{5}$$

are related through the equation

$$[S_{\mathbf{YY}}(\omega)]_{ui} = \int_{-\phi_b}^{\phi_b} S_{yy}(\phi,\omega) e^{j(i-u)\phi\Delta} d\phi \quad u,i = 1, \ldots, n. \tag{6}$$

Contributed by the ASME Applied Mechanics Division of THE AMER. SOCIETY OF MECHANICAL ENGINEERS for presentation at the Winter Annual Meeting, Atlanta, Ga., Dec. 1-6, 1991.

Discussion on this paper should be addressed to the Technical Editor, Prof. Leon M. Keer, The Technological Institute, Northwestern University, Evanston, IL 60208, and will be accepted until two months after final publication of the paper itself in the JOURNAL OF APPLIED MECHANICS. Manuscript received by the ASME Applied Mechanics Division, Oct. 25, 1990; final revision, May 14, 1991. Paper No. 91-WA/APM-29.

Copyright © 1992 by ASME
Downloaded 03 May 2010 to 171.66.16.247. Redistribution subject to ASME license or copyright; see http://www.asme.org/terms/Terms_Use.cfm

The variables Δ, T, ϕ_b, and ω_b designate, respectively, the two sampling intervals, spatial and temporal, and the corresponding two cutoff frequencies satisfying the Nyquist relations

$$\Delta = \frac{\pi}{\phi_b} \tag{7}$$

and

$$T = \frac{\pi}{\omega_b}. \tag{8}$$

Properties of the Finite-Variate MA and ARMA Models. In Part I, one-dimensional autoregressive (AR) based simulation algorithms of vector processes are used in conjunction with the equivalence relation, Eq. (1), to generate realizations of two-dimensional random fields. In this part, the applicability of the moving average (MA) based approximation techniques devised by Spanos and Mignolet (1990) will be investigated.

Specifically, given the two-dimensional power spectrum $S_{yy}(\phi, \omega)$, vanishing outside the domain $(\phi, \omega) \in [-\phi_b, \phi_b] \times [-\omega_b, \omega_b]$, the elements of the $n \times n$ spectral matrix $S_{\mathbf{YY}}(\omega)$ are readily computed from Eq. (6). Then, following Spanos and Mignolet (1990), a decomposition $Q(\omega)$ can be computed satisfying the relation

$$S_{\mathbf{YY}}(\omega) = Q^*(\omega) Q^{\dagger}(\omega) \tag{9}$$

where * denotes the operation of complex conjugation. Finally, a MA(m) approximation of the target vector process can be derived in the form

$$\mathbf{Y}'_r = \sum_{k=-m}^{m} B'_k \mathbf{W}_{r-k} \tag{10}$$

where the MA matrix parameters B'_k are the Fourier coefficients of $Q(\omega)$. That is

$$B'_k = \frac{1}{2\omega_b} \int_{-\omega_b}^{\omega_b} Q(\omega) e^{jk\omega T} d\omega. \tag{11}$$

The symbol $\mathbf{W}_r$ designates an n-variate bandlimited in the interval $[-\omega_b, \omega_b]$ white noise vector process. Its autocorrelation matrices are defined to be

$$E[\mathbf{W}_i \mathbf{W}_k^{\dagger}] = 2\omega_b I_n \delta_{ik} \tag{12}$$

where δ_{ik} and I_n represent the Kronecker symbol and the $n \times n$ identity matrix, respectively.

The MA model, Eq. (10), can be used as a basis to determine the matrix parameters A_k and B_l of fast and reliable autoregressive moving average (ARMA) algorithms

$$\tilde{\mathbf{Y}}_r = -\sum_{k=1}^{p} A_k \tilde{\mathbf{Y}}_{r-k} + \sum_{l=0}^{q} B_l \mathbf{W}_{r-l} \tag{13}$$

following the procedures devised by Spanos and Mignolet (1990).

Both MA and ARMA approximation techniques are applicable, in general, in connection with any target spectral matrix $S_{\mathbf{YY}}(\omega)$ and in particular with the one corresponding to a two-dimensional random field and whose ui element is defined by Eq. (6). Note, in this respect, that the dependence of the elements $[S_{\mathbf{YY}}(\omega)]_{ui}$ on the difference $i - u$ indicates that the corresponding spectral matrix $S_{\mathbf{YY}}(\omega)$ is Toeplitz for all frequencies $\omega \in [-\omega_b, \omega_b]$. This property implies a special structure of the decomposition $Q(\omega)$ and of both the MA and ARMA coefficients. Specifically, it can be shown (Mignolet, 1987) that under the additional assumption of symmetry of the autocorrelation function

$$R_{yy}(l,s) = R_{yy}(-l,s) = R_{yy}(l,-s) = R_{yy}(-l,-s), \tag{14}$$

there exist decompositions $Q(\omega)$ satisfying the relations

$$[Q(\omega)]_{iu} = [Q(\omega)]_{n+1-i,n+1-u} \text{ for all } \omega \text{ and } i, u = 1, \ldots, n. \tag{15}$$

These centrosymmetric decompositions can be obtained in particular by requiring $Q(\omega)$ to be either a Hermitian matrix or a matrix-valued function whose Fourier coefficients B'_k vanish for negative values of k (one-sidedness). It can readily be shown from Eq. (11) that the corresponding MA coefficients are also centrosymmetric matrices and consequently that the ARMA parameters A_k and B_l also possess this property. This fact can be used to induce a computational savings in the determination of these coefficients.

The Infinite-Variate MA and ARMA Models. Proceeding as in Part I, reliable MA and ARMA models of the target two-dimensional random field $y_{i,r}$ can be obtained by letting n, the number of variates involved in the simulation, tend to infinity. The corresponding MA and ARMA coefficients are matrices of infinite dimensions without, in general, any specific property or form. Thus, unless the decomposition $Q(\omega)$ is carefully chosen, a doubly infinite number of values will be necessary to describe any of the MA or ARMA parameters B'_k, A_k, or B_l. Note in this context that the centrosymmetry property, proved for an arbitrary number of variates in the preceding section, reduces the number of unknown coefficients by a factor of two.

It has been observed that some decompositions, among which are the Hermitian and one-sided ones, become Toeplitz matrices as the number of variates tends to infinity. Further, in this limiting case it has been proved (Mignolet, 1987) that the Hermitian decomposition becomes optimum in the sense defined by Spanos and Mignolet (1990). To investigate the MA and ARMA models corresponding to Toeplitz decompositions, introduce first the following description of an arbitrary infinite Toeplitz matrix U in terms of its diagonals $[u]_\alpha$

$$U = \sum_{\alpha=-\infty}^{\infty} [u]_\alpha J_\alpha \tag{16}$$

where J_α is the matrix whose iu element is defined by the equation

$$[J_\alpha]_{iu} = \delta_{u(i+\alpha)} \quad \text{for } i, u \in (-\infty, \infty). \tag{17}$$

Then, it is readily shown that the infinite-variate MA model can be written in the form

$$y'_{i,r} = [\mathbf{Y}'_r]_i = \sum_{k=-m}^{m} \sum_{u=-\infty}^{\infty} [b'_k]_u [\mathbf{W}_{r-k}]_{i+u} = \frac{1}{\sqrt{2\phi_b}} \sum_{k=-m}^{m} \sum_{u=-\infty}^{\infty} [b'_k]_u w_{i+u,r-k} \tag{18}$$

where, following the convention of Eq. (16), $[b'_k]_u$ denotes the diagonals of the matrix parameters B'_k related to the corresponding elements $[q(\omega)]_u$ of the decomposition $Q(\omega)$ through the Fourier transform relation

$$[b'_k]_u = \frac{1}{2\omega_b} \int_{-\omega_b}^{\omega_b} [q(\omega)]_u e^{jk\omega T} d\omega \quad |k| \le m. \tag{19}$$

Further,

$$w_{i,r} = \sqrt{2\phi_b} [\mathbf{W}_r]_i \tag{20}$$

denotes a two-dimensional white noise process whose autocorrelation function and spectrum are readily computed as

$$R_{ww}(k,l) = E[w_{i,r} w_{i+k,r+l}] = E[\sqrt{2\phi_b}[\mathbf{W}_r]_i \sqrt{2\phi_b}[\mathbf{W}_{r+l}]_{i+k}] = 4\omega_b \phi_b \delta_{k0} \delta_{l0} \tag{21}$$

and

$$S_{ww}(\phi,\omega) = 1 \quad \text{for } (\phi,\omega) \in [-\phi_b,\phi_b] X [-\omega_b,\omega_b]. \tag{22}$$

Following Spanos and Mignolet (1990), the infinite Toeplitz MA matrix parameters B'_k can be used in a two-stage format to determine reliable ARMA algorithms, Eq. (13), for the simulation of the infinite-variate process $\mathbf{Y}_r$. Specifically, it can be shown (Mignolet, 1987) that the Toeplitz character of

Downloaded 03 May 2010 to 171.66.16.247. Redistribution subject to ASME license or copyright; see http://www.asme.org/terms/Terms_Use.cfm

the coefficients B'_k implies the existence of ARMA parameters A_k and B_l also possessing this property and the corresponding infinite-variate ARMA model can be written in the form

$$\tilde{y}_{i,r}+\sum_{k=1}^{p_0+p_1}\sum_{u=-\infty}^{\infty}[a_k]_u\tilde{y}_{i+u,r-k}=\frac{1}{\sqrt{2\phi_b}}\sum_{l=-\max(p_1,q_1)}^{\max(p_0,q_0)}\sum_{u=-\infty}^{\infty}[b_l]_u w_{i+u,r-l}. \quad (23)$$

Two-Dimensional MA Modeling

The MA Random Field. The infinite-variate MA model, Eq. (18), cannot be used directly for the simulation of random fields because of the infinite number of parameters it contains; it can serve, however, as a basis to formulate an appropriate MA algorithm. Specifically, consider the truncated model

$$y'_{i,r}=\sum_{k=-m}^{m}\sum_{u=-\delta}^{\delta}b'_{u,k}w_{i+u,r-k} \quad (24)$$

where $w_{i,r}$ is the Gaussian two-dimensional white noise process defined by Eqs. (21) and (22). The random field $y'_{i,r}$ can be considered as the response of a linear discrete system whose transfer function, in terms of two-dimensional z-transform, is

$$h(z_1,z_2)=\sum_{k=-m}^{m}\sum_{u=-\delta}^{\delta}b'_{u,k}z_1^u z_2^{-k} \quad (25)$$

when the input is the white noise process $w_{i,r}$. For the purpose of simulation, the corresponding spectrum

$$S_{y'y'}(\phi,\omega)=|h(e^{j\phi\Delta},e^{j\omega T})|^2 \quad (26)$$

must represent a close approximation of a target expression $S_{yy}(\phi, \omega)$.

The Optimum MA Model. Adapting the one-dimensional approach of Spanos and Mignolet (1990) to the present two-dimensional random field, a MA model can be derived on the basis of a decomposition $q(\phi, \omega)$ of the target spectrum satisfying the equation

$$|q(\phi,\omega)|^2=S_{yy}(\phi,\omega). \quad (27)$$

Specifically, select the MA parameters so that $h(e^{j\phi\Delta}, e^{j\omega T})$ is an optimum approximation of $q(\phi, \omega)$ in the sense that the frequency domain error

$$\epsilon^{(2)}_{MA}=\frac{1}{4\omega_b\phi_b}\int_{-\omega_b}^{\omega_b}\int_{-\phi_b}^{\phi_b}|q(\phi,\omega)-h(e^{j\phi\Delta},e^{j\omega T})|^2 d\phi d\omega \quad (28)$$

is minimized. Upon differentiating $\epsilon^{(2)}_{MA}$ with respect to the coefficients $b'_{u,k}$, it is readily shown that the optimum value of these parameters are the Fourier coefficients of $q(\phi, \omega)$. That is,

$$b'_{u,k}=\frac{1}{4\omega_b\phi_b}\int_{-\omega_b}^{\omega_b}\int_{-\phi_b}^{\phi_b}q(\phi,\omega)e^{-ju\phi\Delta}e^{jk\omega T}d\phi d\omega \quad |k|\le m \text{ and } |u|\le\delta. \quad (29)$$

It can be shown (Mignolet, 1987) that the MA model characterized by Eqs. (24), (27), and (29) is consistent with the infinite-variate approximation technique provided that the following correspondence relations hold for $\delta = \infty$

$$b'_{u,k}=\frac{1}{\sqrt{2\phi_b}}[b'_k]_u \quad \text{for } |k|\le m \quad (30)$$

and

$$[q(\omega)]_u=\frac{1}{\sqrt{2\phi_b}}\int_{-\phi_b}^{\phi_b}q(\phi,\omega)e^{-ju\phi\Delta}d\phi \quad \text{for } \omega\in[-\omega_b,\omega_b]. \quad (31)$$

The above equation provides an interesting connection between decompositions of one-dimensional spectral matrices and two-dimensional power spectra. Note in particular that the selection of a lower triangular matrix $Q(\omega)$ satisfying the equation

$$[q(\omega)]_u=0 \text{ for } u>0 \text{ and for all } \omega \quad (32)$$

corresponds to a one-sided function $q(\phi, \omega)$. Similarly, the Hermitian decomposition $Q(\omega)$ characterized by the symmetry relations

$$[q(\omega)]^*_u=[q(\omega)]_{-u} \quad (33)$$

can be associated on the basis of Eq. (31) with the real function

$$q(\phi,\omega)=\sqrt{S_{yy}(\phi,\omega)}. \quad (34)$$

The Optimum Two-Dimensional MA Decomposition. For a meaningful simulation of a real two-dimensional field $y_{i,r}$, the samples $y'_{i,r}$ generated according to Eq. (24) should all be real. Thus, in addition to satisfying Eq. (27), the decomposition $q(\phi, \omega)$ is required to yield real MA coefficients $b'_{u,k}$, Eq. (29). Even with this additional requirement, it can be shown that the computation of the function $q(\phi, \omega)$ cannot be achieved in a unique manner from Eq. (27). Indeed, this equation determines only the magnitude of the decomposition $q(\phi, \omega)$ without providing any information on the corresponding phase.

To address this issue, it is decided to select the decomposition $q(\phi, \omega)$ that leads to a MA spectrum $S_{y'y'}(\phi, \omega)$, Eq. (26), which is an optimum approximation of the target expression $S_{yy}(\phi, \omega)$. To this end, note that the difference between these two functions is associated with the nonzero values of some Fourier coefficients of $q(\phi, \omega)$, Eq. (29), outside the domain $(k, u) \in [-m, m] \times [-\delta, \delta]$. Following this argument, the decomposition $q(\phi, \omega)$ should be selected to maximize the energy $E^{(2)}_n$ defined as

$$E^{(2)}_n=\sum_{k=-m}^{m}\sum_{u=-\delta}^{\delta}|b'_{u,k}|^2=\frac{1}{4\omega_b^2\phi_b^2}\int_{-\omega_b}^{\omega_b}\int_{-\omega_b}^{\omega_b}\int_{-\phi_b}^{\phi_b}\int_{-\phi_b}^{\phi_b}q^*(\phi_1,\omega_1)q(\phi_2,\omega_2)D_m(\omega_1-\omega_2)\times D_\delta(\phi_1-\phi_2)d\phi_1 d\phi_2 d\omega_1 d\omega_2 \quad (35)$$

where $D_m(\omega)$ and $D_\delta(\phi)$ are the Dirichlet's kernels of orders m and δ, respectively. These functions can be expressed in the form

$$D_m(\omega)=\frac{1}{2}\sum_{k=-m}^{m}e^{jk\omega T} \quad (36)$$

and

$$D_\delta(\phi)=\frac{1}{2}\sum_{k=-\delta}^{\delta}e^{jk\phi\Delta}. \quad (37)$$

To be a bonafide decomposition, $q(\phi, \omega)$ must also satisfy Eq. (27) and lead to real MA coefficients $b'_{u,k}$. That is, it must satisfy the constraints

$$\int_{-\omega_b}^{\omega_b}\int_{-\phi_b}^{\phi_b}[q(\phi,\omega)e^{-ju\phi\Delta}e^{jk\omega T}-q^*(\phi,\omega)e^{ju\phi\Delta}e^{-jk\omega T}]d\phi d\omega=0 \quad \text{for } |k|\le m \text{ and } |u|\le\delta. \quad (38)$$

The maximization of $E^{(2)}_n$ under the above conditions can be accomplished by maximizing the modified energy $\tilde{E}^{(2)}_n$ defined as

$$\tilde{E}^{(2)}_n=E^{(2)}_n+\int_{-\omega_b}^{\omega_b}\int_{-\phi_b}^{\phi_b}\lambda(\phi,\omega)[|q(\phi,\omega)|^2-S_{yy}(\phi,\omega)]d\phi d\omega+\sum_{k=-m}^{m}\sum_{u=-\delta}^{\delta}\frac{\gamma_{u,k}}{4j\omega_b\phi_b}\int_{-\omega_b}^{\omega_b}\int_{-\phi_b}^{\phi_b}[q(\phi,\omega)e^{-ju\phi\Delta}e^{jk\omega T}-q^*(\phi,\omega)e^{ju\phi\Delta}e^{-jk\omega T}]d\phi d\omega \quad (39)$$

Downloaded 03 May 2010 to 171.66.16.247. Redistribution subject to ASME license or copyright; see http://www.asme.org/terms/Terms_Use.cfm

where $\lambda(\phi, \omega)$ and $\gamma_{u,k}$ denote the real Lagrange multipliers associated with the constraints Eqs. (27) and (38), respectively.

Further, it can readily be shown that the first variation of $\tilde{E}_n^{(2)}$ vanishes for all functions $\delta q(\phi, \omega)$ if the decomposition $q(\phi, \omega)$ satisfies the integral equation

$$\frac{1}{4\omega_b^2\phi_b^2}\int_{-\omega_b}^{\omega_b}\int_{-\phi_b}^{\phi_b} q^*(\phi_1,\omega_1)D_m(\omega-\omega_1)D_\delta(\phi-\phi_1)d\phi_1 d\omega_1 + \lambda(\phi,\omega)q^*(\phi,\omega)+\sum_{k=-m}^{m}\sum_{u=-\delta}^{\delta}\frac{\gamma_{u,k}}{4j\omega_b\phi_b}e^{-ju\phi\Delta}e^{jk\omega T}=0 \quad (40)$$

or, equivalently,

$$\frac{1}{4\omega_b\phi_b}\int_{-\omega_b}^{\omega_b}\int_{-\phi_b}^{\phi_b} q(\phi_1,\omega_1)D_m(\omega-\omega_1)D_\delta(\phi-\phi_1)d\phi_1 d\omega_1 + \omega_b\phi_b\lambda(\phi,\omega)q(\phi,\omega)+\frac{j}{4}\sum_{k=-m}^{m}\sum_{u=-\delta}^{\delta}\gamma_{u,k}e^{ju\phi\Delta}e^{-jk\omega T}=0 \quad (41)$$

where $(\phi, \omega) \in [-\phi_b, \phi_b] \times [-\omega_b, \omega_b]$. Combining Eqs. (29) and (41), it is found that

$$\lambda(\phi,\omega)q(\phi,\omega)= -\frac{1}{4\omega_b\phi_b}\sum_{k=-m}^{m}\sum_{u=-\delta}^{\delta}(b'_{u,k}+j\gamma_{u,k})e^{ju\phi\Delta}e^{-jk\omega T}. \quad (42)$$

Finally, taking the modulus of both sides of the above equation and relying on the real character of the Lagrange multipliers, it can be shown that

$$\lambda^{-1}(\phi,\omega)=\frac{\pm 4\omega_b\phi_b\sqrt{S_{yy}(\phi,\omega)}}{\left|\sum_{k=-m}^{m}\sum_{u=-\delta}^{\delta}(b'_{u,k}+j\gamma_{u,k})e^{ju\phi\Delta}e^{-jk\omega T}\right|} \quad (43)$$

and

$$q(\phi,\omega) = \mp\sqrt{S_{yy}(\phi,\omega)}\left[\frac{\sum_{k=-m}^{m}\sum_{u=-\delta}^{\delta}(b'_{u,k}+j\gamma_{u,k})e^{ju\phi\Delta}e^{-jk\omega T}}{\left|\sum_{k=-m}^{m}\sum_{u=-\delta}^{\delta}(b'_{u,k}+j\gamma_{u,k})e^{ju\phi\Delta}e^{-jk\omega T}\right|}\right]. \quad (44)$$

In particular, note that the term in brackets has modulus 1. Thus, it can be rewritten as $e^{j\psi(\phi,\omega)}$ where $\psi(\phi, \omega)$ denotes the argument of $q(\phi, \omega)$.

It can be proved (Mignolet, 1987) that the function $q(\phi, \omega)$ satisfying Eqs. (27), (38), and (41) for $\delta = \infty$ corresponds through the equivalence relation Eq. (31) to the optimum Toeplitz decomposition $Q(\omega)$ defined by Spanos and Mignolet (1990). Thus, the present optimum MA modeling technique is consistent with the vector representation, Eq. (1).

Further, it can be shown, as in the one-dimensional case (Spanos and Mignolet, 1990), that the real decomposition Eq. (34) is optimum for all values of the system orders m and δ and that the corresponding Lagrange multipliers are

$$\gamma_{u,k}=0 \quad |u|\le\delta \text{ and } |k|\le m \quad (45)$$

and

$$\lambda(\phi,\omega)=\frac{\left|\sum_{k=-m}^{m}\sum_{u=-\delta}^{\delta}b'_{u,k}e^{ju\phi\Delta}e^{-jk\omega T}\right|}{-4\omega_b\phi_b\sqrt{S_{yy}(\phi,\omega)}}. \quad (46)$$

Finally, it should be noted that the nature of the optimum achieved, maximum, minimum, or saddle point, cannot be determined directly from Eq. (41). However, proceeding as in the one-dimensional case (Spanos and Mignolet, 1990), a sufficient condition can be derived to test that the optimum attained is indeed a maximum (Mignolet, 1987).

Two-Dimensional ARMA Modeling

The ARMA Random Field. The infinite-variate ARMA model, Eq. (23), exhibits, from the point of view of simulation, the same defects as its MA counterparts, Eq. (18). That is, it involves an infinite number of parameters. To remedy this situation, consider the truncated ARMA model

$$\tilde{y}_{i,r}=-\sum_{k=1}^{p}\sum_{u=-\mu_2}^{\mu_1}a_{u,k}\tilde{y}_{i+u,r-k}+\sum_{l=-Q}^{q}\sum_{u=-\nu_2}^{\nu_1}b_{u,l}w_{i+u,r-l} \quad (47)$$

where $w_{i,r}$ denotes the two-dimensional white noise defined by Eqs. (21) and (22). Note that the above recurrence relation reduces to Eq. (23) as the system orders μ_1, μ_2, ν_1, and ν_2 tend to infinity.

The ARMA random field $\tilde{y}_{i,r}$ can be seen as the response to the excitation $w_{i,r}$ of the linear system whose transfer function is

$$h(z_1,z_2)=\frac{n(z_1,z_2)}{d(z_1,z_2)} \quad (48)$$

where

$$d(z_1,z_2)=\sum_{k=0}^{p}\sum_{u=-\mu_2}^{\mu_1}a_{u,k}z_1^u z_2^{-k} \quad (49)$$

and

$$n(z_1,z_2)=\sum_{l=-Q}^{q}\sum_{u=-\nu_2}^{\nu_1}b_{u,l}z_1^u z_2^{-l} \quad (50)$$

together with

$$(a_{u,0})=\delta_{u0} \quad u=-\mu_2,\ \ldots,\ \mu_1. \quad (51)$$

It should be noted that the stability of the recurrence relation, Eq. (47), is a necessary condition for the homogeneity of the corresponding field $\tilde{y}_{i,r}$. This property, which is associated with the location of the zeros of the polynomial $d(z_1, z_2)$, can be tested using standard techniques as explained in Part I.

For simulation, the spectrum of the ARMA field

$$S_{\tilde{y}\tilde{y}}(\phi,\omega)=|h(e^{j\phi\Delta},e^{j\omega T})|^2 \quad (52)$$

must represent a close approximation of the target expression, $S_{yy}(\phi, \omega)$. Proceeding as in the one-dimensional case (Spanos and Mignolet, 1990), a two-stage determination procedure of the parameters $a_{u,k}$ and $b_{u,l}$ will be sought by relying on the separation of the MA transfer function $h_{MA}(e^{j\phi\Delta}, e^{j\omega T})$, Eq. (25), into its causal and anticausal parts,

$$h_{MA}(e^{j\phi\Delta},e^{j\omega T})=h^C_{MA}(e^{j\phi\Delta},e^{j\omega T})+h^A_{MA}(e^{j\phi\Delta},e^{j\omega T}). \quad (53)$$

Relying on a definition of causality similar to the one introduced by Marzetta (1980), it is found that the functions $h^C_{MA}(e^{j\phi\Delta}, e^{j\omega T})$ and $h^A_{MA}(e^{j\phi\Delta}, e^{j\omega T})$ are, respectively,

$$h^C_{MA}(e^{j\phi\Delta},e^{j\omega T})=\frac{1}{2}\sum_{u=-\delta}^{\delta}b'_{u,0}e^{ju\phi\Delta}+\sum_{k=1}^{m}\sum_{u=-\delta}^{\delta}b'_{u,k}e^{-jk\omega T}e^{ju\phi\Delta} \quad (54)$$

and

$$h^A_{MA}(e^{j\phi\Delta},e^{j\omega T})=\frac{1}{2}\sum_{u=-\delta}^{\delta}b'_{u,0}e^{ju\phi\Delta}+\sum_{k=1}^{m}\sum_{u=-\delta}^{\delta}b'_{u,-k}e^{jk\omega T}e^{ju\phi\Delta}. \quad (55)$$

The Optimum ARMA Model. Given the functions $h^C_{MA}(e^{j\phi\Delta}, e^{j\omega T})$ and $h^A_{MA}(e^{j\phi\Delta}, e^{j\omega T})$, an ARMA model will now be constructed by relying on the following approximations

$$h^C_{MA}(e^{j\phi\Delta},e^{j\omega T})\approx\frac{n_0(e^{j\phi\Delta},e^{j\omega T})}{d_0(e^{j\phi\Delta},e^{j\omega T})} \quad (56)$$

Downloaded 03 May 2010 to 171.66.16.247. Redistribution subject to ASME license or copyright; see http://www.asme.org/terms/Terms_Use.cfm

or

$$h^A_{MA}(e^{j\phi\Delta},e^{j\omega T}) \approx \frac{n^*_1(e^{j\phi\Delta},e^{j\omega T})}{d^*_1(e^{j\phi\Delta},e^{j\omega T})} \tag{57}$$

where the polynomials $d_s(z_1, z_2)$ and $n_s(z_1, z_2)$ are defined by the relations

$$d_s(z_1,z_2) = \sum_{k=0}^{p_s} \sum_{i=-\mu_{s2}}^{\mu_{s1}} a^s_{i,k} z_1^i z_2^{-k} \tag{58}$$

and

$$n_s(z_1,z_2) = \sum_{l=0}^{q_s} \sum_{i=-\nu_{s2}}^{\nu_{s1}} b^s_{i,l} z_1^i z_2^{-l} \tag{59}$$

for $s = 0$ and 1. The determination of the rational approximations of the causal and anticausal parts of the MA transfer function will be approached, as in the one-dimensional case (Spanos and Mignolet, 1990), from the standpoint of minimization of frequency domain errors. Specifically, select the unknown coefficients of the polynomials $d_0(z_1, z_2)$ and $n_0(z_1, z_2)$ to minimize the error

$$\epsilon_c = \frac{1}{4\omega_b\phi_b} \int_{-\omega_b}^{\omega_b} \int_{-\phi_b}^{\phi_b} | d_0(e^{j\phi\Delta},e^{j\omega T}) h^C_{MA}(e^{j\phi\Delta},e^{j\omega T}) - n_0(e^{j\phi\Delta},e^{j\omega T})|^2 d\phi d\omega \tag{60}$$

and to satisfy the constraints

$$a^0_{i,0} = \delta_{i0} \quad \text{for } i = -\mu_{02}, \ldots, \mu_{01} \tag{61}$$

and

$$\sum_{k=\max(0,i-m)}^{\min(i,p_0)} \sum_{u=\max(-\mu_{02},l-\delta)}^{\min(\mu_{01},l+\delta)} a^0_{u,k} b''_{l-u,i-k} = 0 \quad \text{for } i = q_0+1, \ldots, q_0+r_0 \text{ and } l = -\rho_{02}, \ldots, \rho_{01}. \tag{62}$$

Note that in the above equation the parameters $b''_{u,k}$ are defined as

$$b''_{u,k} = b'_{u,k} \; 0 < k \le m, \; u = -\delta, \ldots, \delta \tag{63a}$$

$$b''_{u,k} = \frac{1}{2} b'_{u,k} \; k = 0, \; u = -\delta, \ldots, \delta. \tag{63b}$$

The minimization of ϵ_C, Eq. (60), under the conditions Eq. (62) can equivalently be accomplished by minimizing the modified error $\tilde{\epsilon}_C$ defined as

$$\tilde{\epsilon}_C = \epsilon_C + 2 \sum_{l=q_0+1}^{q_0+r_0} \sum_{i=-\rho_{02}}^{\rho_{01}} \sum_{k=\max(0,l-m)}^{\min(l,p_0)} \sum_{u=\max(-\mu_{02},i-\delta)}^{\min(\mu_{01},i+\delta)} \lambda^0_{i,l} a^0_{u,k} b''_{i-u,l-k} \tag{64}$$

where $\lambda^0_{i,l}$ denotes the Lagrange multipliers associated with the constraints, Eq. (62).

Upon differentiating the error $\tilde{\epsilon}_C$ with respect to the ARMA coefficients $a^0_{i,k}$, $b^0_{j,l}$, it is found that the optimum values of these parameters satisfy the following relations

$$\sum_{k=0}^{p_0} \sum_{u=-\mu_{02}}^{\mu_{01}} a^0_{u,k} \left[\sum_{s=\max(k,i)}^{m+\min(k,i)} \sum_{\alpha=-\delta+\max(u,l)}^{\delta+\min(u,l)} b''_{\alpha-u,s-k} b''_{\alpha-l,s-i} \right] - \sum_{k=i}^{\min(q_0,m+i)} \sum_{u=\max(-\nu_{02},l-\delta)}^{\min(\nu_{01},l+\delta)} b^0_{u,k} b''_{u-l,k-i} + \sum_{k=\max(q_0+1,i)}^{\min(q_0+r_0,m+i)} \sum_{u=\max(-\rho_{02},l-\delta)}^{\min(\rho_{01},l+\delta)} \lambda^0_{u,k} b''_{u-l,k-i} = 0$$

$$\text{for } i = 1, \ldots, p_0 \text{ and } l = -\mu_{02}, \ldots, \mu_{01} \tag{65}$$

and

$$b^0_{l,i} = \sum_{k=\max(0,i-m)}^{\min(i,p_0)} \sum_{u=\max(-\mu_{02},l-\delta)}^{\min(\mu_{01},l+\delta)} a^0_{u,k} b''_{l-u,i-k}$$

$$\text{for } i = 0, \ldots, q_0 \text{ and } l = -\nu_{02}, \ldots, \nu_{01} \tag{66}$$

which must be solved together with the constraints, Eqs. (61) and (62). The corresponding minimum value of $\tilde{\epsilon}_C$ is readily shown to be

$$(\tilde{\epsilon}_C)_{\min} = \sum_{k=0}^{p_0} \sum_{u=-\mu_{02}}^{\mu_{01}} a^0_{u,k} \left[\sum_{s=k}^{m} \sum_{\alpha=-\delta+\max(u,0)}^{\delta+\min(u,0)} b''_{\alpha-u,s-k} b''_{\alpha,s} \right] - \sum_{l=0}^{\min(q_0,m)} \sum_{u=\max(-\nu_{02},-\delta)}^{\min(\nu_{01},\delta)} b^0_{u,l} b''_{u,l} + \sum_{l=q_0+1}^{\min(q_0+r_0,m)} \sum_{u=\max(-\rho_{02},-\delta)}^{\min(\rho_{01},\delta)} \lambda^0_{u,l} b''_{u,l}. \tag{67}$$

The anticausal approximation problem can be approached in an analogous manner on the basis of the frequency domain error

$$\epsilon_A = \frac{1}{4\omega_b\phi_b} \int_{-\omega_b}^{\omega_b} \int_{-\phi_b}^{\phi_b} | d^*_1(e^{j\phi\Delta},e^{j\omega T}) h^A_{MA}(e^{j\phi\Delta},e^{j\omega T}) - n^*_1(e^{j\phi\Delta},e^{j\omega T})|^2 d\phi d\omega \tag{68}$$

and of constraints similar to Eqs. (61) and (62).

Combining the causal and anticausal approximations, it is readily shown that the ARMA power spectrum can be written in the form

$$S_{\bar{y}\bar{y}}(\phi,\omega) = \left| \frac{n_0(e^{j\phi\Delta},e^{j\omega T}) d^*_1(e^{j\phi\Delta},e^{j\omega T}) + n^*_1(e^{j\phi\Delta},e^{j\omega T}) d_0(e^{j\phi\Delta},e^{j\omega T})}{d_0(e^{j\phi\Delta},e^{j\omega T}) d^*_1(e^{j\phi\Delta},e^{j\omega T})} \right|^2 \tag{69}$$

or, noting that a complex number and its conjugate have the same magnitude,

$$S_{\bar{y}\bar{y}}(\phi,\omega) = \left| \frac{n_0(e^{j\phi\Delta},e^{j\omega T}) d^*_1(e^{j\phi\Delta},e^{j\omega T}) + n^*_1(e^{j\phi\Delta},e^{j\omega T}) d_0(e^{j\phi\Delta},e^{j\omega T})}{d_0(e^{j\phi\Delta},e^{j\omega T}) d_1(e^{j\phi\Delta},e^{j\omega T})} \right|^2. \tag{70}$$

The term inside the vertical bars in the previous equation can be written as an ARMA transfer function, Eq. (48), by selecting the numerator and denominator to be, respectively,

$$n(z_1,z_2) = n_0(z_1,z_2) d_1\left(\frac{1}{z_1},\frac{1}{z_2}\right) + d_0(z_1,z_2) n_1\left(\frac{1}{z_1},\frac{1}{z_2}\right) = \sum_{l=-\max(p_1,q_1)}^{\max(p_0,q_0)} \sum_{u=-\max(\nu_{02}+\mu_{11},\mu_{02}+\nu_{11})}^{\max(\nu_{01}+\mu_{12},\nu_{12}+\mu_{01})} b_{u,l} z_1^u z_2^{-l} \tag{71}$$

and

$$d(z_1,z_2) = d_1(z_1,z_2) d_0(z_1,z_2) = \sum_{k=0}^{p_0+p_1} \sum_{u=-(\mu_{12}+\mu_{02})}^{\mu_{11}+\mu_{01}} a_{u,k} z_1^u z_2^{-k}. \tag{72}$$

In the above equations, the ARMA parameters $a_{u,k}$ and $b_{u,l}$ are related to the causal and anticausal coefficients $a^s_{u,k}$ and $b^s_{u,l}$, $s = 0$, 1, according to

$$a_{u,k} = \sum_{t=\max(0,k-p_0)}^{\min(p_1,k)} \sum_{v=\max(-\mu_{12},-\mu_{01}+u)}^{\min(\mu_{11},\mu_{02}+u)} a^1_{v,t} a^0_{u-v,k-t} \tag{73}$$

and

Downloaded 03 May 2010 to 171.66.16.247. Redistribution subject to ASME license or copyright; see http://www.asme.org/terms/Terms_Use.cfm

$$b_{u,l}=\sum_{t=\max(0,l)}^{\min(q_0,p_1+l)}\ \sum_{v=\max(-\nu_{02},u-\mu_{12})}^{\min(\nu_{01},u+\mu_{11})} b^0_{v,t}a^1_{v-u,t-l}$$
$$+\sum_{t=\max(0,l)}^{\min(p_0,q_1+l)}\ \sum_{v=\max(-\mu_{02},u-\nu_{12})}^{\min(\mu_{01},u+\nu_{11})} a^0_{v,t}b^1_{v-u,t-l}. \quad (74)$$

The determination of the ARMA algorithm is then completed by noting that the model corresponding to Eqs. (71)–(74) is

$$\tilde{y}_{i,r}+\sum_{k=1}^{p_0+p_1}\ \sum_{u=-(\mu_{12}+\mu_{02})}^{\mu_{11}+\mu_{01}} a_{u,k}\tilde{y}_{i+u,r-k}$$
$$=\sum_{l=-\max(p_1,q_1)}^{\max(p_0,q_0)}\ \sum_{u=-\max(\nu_{02}+\mu_{11},\mu_{02}+\nu_{11})}^{\max(\nu_{01}+\mu_{12},\nu_{12}+\mu_{01})} b_{u,l}w_{i+u,r-l}. \quad (75)$$

It can be shown (Mignolet, 1987) that the present ARMA approximation technique reduces to its infinite-variate counterpart as the orders μ_{kl} and ν_{kl}, $k = 0$, 1 and $l = 1$, 2, tend to infinity provided that the following equivalence relations

$$a_{i,k}=[a_k]_i \quad k=0,\ \ldots,\ p_0+p_1 \quad (76)$$

and

$$b_{i,l}=\frac{1}{\sqrt{2\phi_b}}\,[b_l]_i \quad l=-\max(p_1,\,q_1),\ \ldots,\ \max(p_0,\,q_0) \quad (77)$$

are enforced. Thus, the present two-dimensional MA to ARMA modeling technique is consistent with the vector process representation, Eq. (1).

Special Cases

Separable Decomposition. The particular case of a separable spectrum represents one of the simplest possible models of a two-dimensional random field. Such a spectrum can be written as the product of two functions of one variable each, that is

$$S_{yy}(\phi,\omega)=S_1(\phi)S_2(\omega) \quad (\phi,\omega)\in[-\phi_b,\phi_b]\times[-\omega_b,\omega_b]. \quad (78)$$

Upon selecting a separable decomposition $q(\phi,\omega)$ satisfying the relation

$$q(\phi,\omega)=q_1(\phi)q_2(\omega) \quad (\phi,\omega)\in[-\phi_b,\phi_b]\times[-\omega_b,\omega_b], \quad (79)$$

it is readily found that the MA coefficients $b'_{u,k}$ are separable in the sense that

$$b'_{u,k}=b'^{(1)}_u b'^{(2)}_k \quad |k|\le m,\ |u|\le\delta. \quad (80)$$

Next, it can be shown (Mignolet, 1987) that the corresponding ARMA parameters $a_{i,k}$ also possess this property. That is,

$$a_{i,k}=a^{(1)}_i a^{(2)}_k \quad k=0,\ \ldots,\ p_0+p_1,$$
$$i=-(\mu_{12}+\mu_{02}),\ \ldots,\ (\mu_{11}+\mu_{01}). \quad (81)$$

Further, under the additional assumption that the causal and anticausal orders are equal, $\mu_{01}=\mu_{12}$, $\mu_{02}=\mu_{11}$, $\nu_{01}=\nu_{12}$ and $\nu_{02}=\nu_{11}$, it can be proved that the coefficients $b_{u,l}$ are also separable, that is

$$b_{u,l}=b^{(1)}_u b^{(2)}_l \quad l=-\max(p_1,q_1),\ \ldots,\ \max(p_0,q_0),$$
$$u=-(\nu_{02}+\mu_{11}),\ \ldots,\ \nu_{01}+\mu_{12}. \quad (82)$$

Finally, combining Eqs. (80)–(82), it is readily seen that both the MA and ARMA spectra corresponding to a separable target expression also possess that property.

Real Decomposition. The special case of the real decomposition $q(\phi,\omega)$, Eq. (34), is of particular interest as it is optimum for all values of the system orders m and δ. The corresponding MA parameters $b'_{u,k}$ are readily seen to possess the property of symmetry

$$b'_{u,k}=b'_{-u,-k} \quad \text{for } |u|\le\delta \text{ and } |k|\le m \quad (83)$$

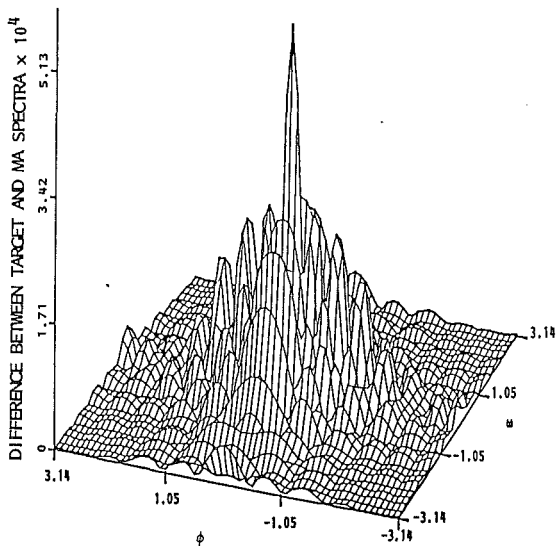


Fig. 1 The modulus of the difference between the two-dimensional target and MA spectra, $m = \delta = 5$, $T = \Delta x = 1.00$

so that the corresponding MA transfer function is also real. Note that the above relation also implies that the causal and anticausal functions $h^C_{MA}(e^{j\phi\Delta}, e^{j\omega T})$ and $h^A_{MA}(e^{j\phi\Delta}, e^{j\omega T})$ are complex conjugates of one another. Thus, selecting $p_0 = p_1$, $q_0 = q_1$, $r_0 = r_1$ and $\mu_{0i} = \mu_{1i}$, $\nu_{0i} = \nu_{1i}$, $\rho_{0i} = \rho_{1i}$ for $i = 1$ and 2, it can be shown that

$$d_0(e^{j\phi\Delta},\,e^{j\omega T})=d_1(e^{j\phi\Delta},\,e^{j\omega T}) \quad (84a)$$

and

$$n_0(e^{j\phi\Delta},e^{j\omega T})=n_1(e^{j\phi\Delta},e^{j\omega T}) \quad (84b)$$

and thus, that

$$b_{j,-l}=b_{-j,l} \quad l=-\max(p_1,q_1),\ \ldots,\ \max(p_0,q_0),$$
$$j=-\max(\nu_{02}+\mu_{11},\mu_{02}+\nu_{11}),\ \ldots,\ \max(\nu_{01}+\mu_{12},\nu_{12}+\mu_{01}). \quad (85)$$

and

$$S_{\tilde{y}\tilde{y}}(\phi,\omega)=4\left\{\mathrm{Re}\left[\frac{n_0(e^{j\phi\Delta},e^{j\omega T})}{d_0(e^{j\phi\Delta},e^{j\omega T})}\right]\right\}^2. \quad (86)$$

If the target autocorrelation function is symmetric, Eq. (14), the spectrum $S_{yy}(\phi,\,\omega)$ is an even function of the frequencies ϕ and ω

$$S_{yy}(\phi,\omega)=S_{yy}(\phi,-\omega)=S_{yy}(-\phi,\omega)=S_{yy}(-\phi,-\omega) \quad (87)$$

and the corresponding real decomposition $q(\phi,\,\omega)$ also possess this property. Then, it is readily shown that the MA parameters satisfy the symmetry relations

$$b'_{u,k}=b'_{-u,k}=b'_{u,-k}=b'_{-u,-k} \text{ for } |u|\le\delta \text{ and } |k|\le m \quad (88)$$

which include Eq. (83). Finally, under the assumption that the positive and negative orders are equal, $\mu_{s1}=\mu_{s2}$, $\nu_{s1}=\nu_{s2}$ and $\rho_{s1}=\rho_{s2}$ for $s = 0$ and 1, it can be proved that the ARMA coefficients exhibit, in addition to Eqs. (84)–(86), the following properties

$$a_{i,k}=a_{-i,k} \quad k=0,\ \ldots,\ p_0+p_1,$$
$$i=-(\mu_{12}+\mu_{02}),\ \ldots,\ (\mu_{11}+\mu_{01}) \quad (89a)$$

and

$$b_{j,l}=b_{-j,l} \quad l=-\max(p_1,q_1),\ \ldots,\ \max(p_0,q_0),$$
$$j=-\max(\nu_{02}+\mu_{11},\mu_{02}+\nu_{11}),\ \ldots,\ \max(\nu_{01}+\mu_{12},\nu_{12}+\mu_{01}). \quad (89b)$$

The symmetry relations, Eqs. (88) and (89), imply that both

Downloaded 03 May 2010 to 171.66.16.247. Redistribution subject to ASME license or copyright; see http://www.asme.org/terms/Terms_Use.cfm

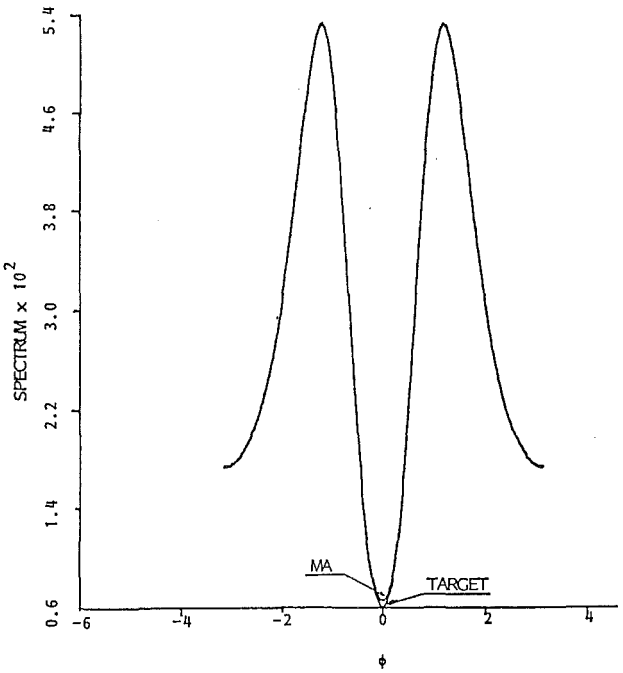


Fig. 2 Cut through the target and MA spectral matrices by the plane $\omega = 0$

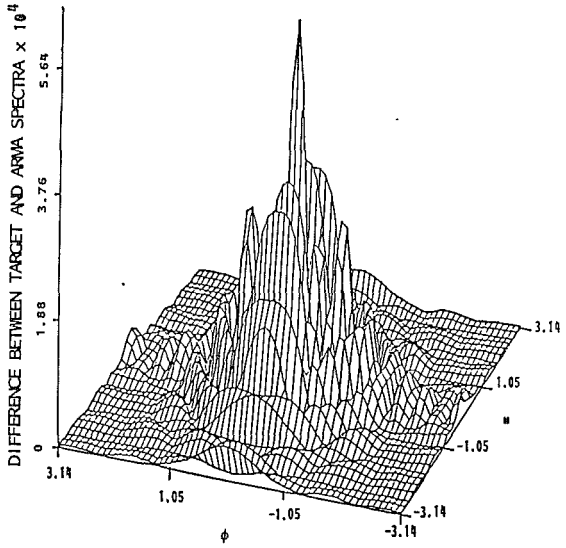


Fig. 3 The modulus of the difference between the two-dimensional target and ARMA spectra, $p = 3$, $\mu_1 = \mu_2 = 0$, $q = 3$, $\nu_1 = \nu_2 = 5$, $T = \Delta x = 1.00$

the MA and ARMA autocorrelations corresponding to a symmetric target autocorrelation function also possess this property. These equations can also be used to provide a computational savings in the determination of the MA and ARMA simulation algorithms, Eqs. (24) and (75).

Numerical Example

Use again, as in Part I, the example by Naganuma et al. (1985, 1987) with two-dimensional autocorrelation function $R_{yy}(k, l)$ given by the equation

$$R_{yy}(k,l) = \exp\left[-\sqrt{k^2+l^2}\right]\cos\sqrt{k^2+l^2} \qquad (90)$$

to demonstrate the usefulness of the present MA and ARMA modeling techniques. The corresponding spectrum $S_{yy}(\phi, \omega)$ is shown in Fig. 1 of Part I with the sampling intervals chosen to be $\Delta = T = 1$.

In this part of the series, MA based algorithms will be investigated by relying on the real decomposition, Eq. (34), chosen because of its optimum character for all values of the system order m and δ. Displayed in Fig. 1 is the modulus of the difference between the target expression and its MA approximation corresponding to the choice $m = \delta = 5$. Further, the intersections of these surfaces with the plane $\omega = 0$, Fig. 2, shows that the maximum error, which is seen from Fig. 1 to occur for $\omega = \phi = 0$, is quite small in comparison with the values of the target spectrum. Thus, the MA simulation scheme can be used for a reliable generation of realizations of the process defined by Eq. (90).

Next, the MA to ARMA modeling technique described in this part of the series was used with $r = 0$ to obtain a rational approximation of the target spectrum. Shown in Fig. 3 is the modulus of the difference between this expression and its ARMA approximation corresponding to the choice $p = 3$, $\mu_1 = \mu_2 = 0$, $q = 3$ and $\nu_1 = \nu_2 = 5$. Further, the intersections of the spectral surfaces with the plane $\omega = 0$ in which the maximum of the difference occurs, are displayed in Fig. 4. Clearly, the 83-parameter ARMA model can be used to accurately represent the target random field described by Eq. (90). Finally, note that the ARMA system was found to be stable in the Lyapunov sense.

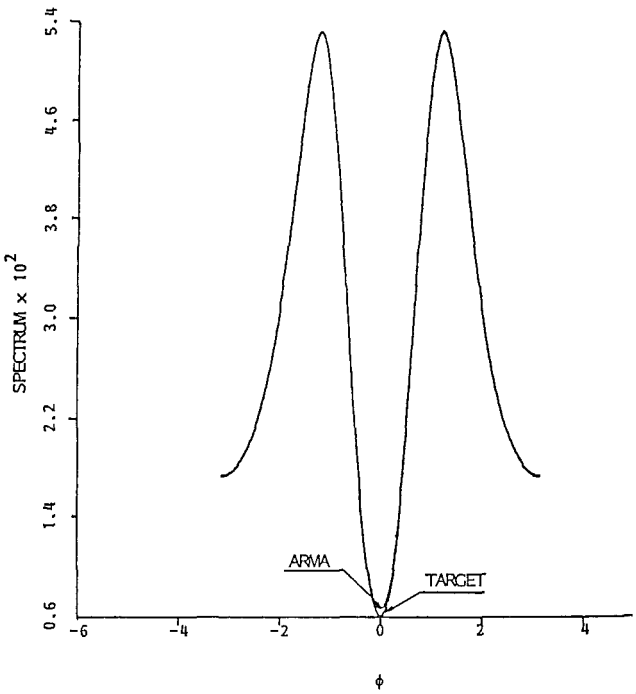


Fig. 4 Cut through the target and ARMA spectral surfaces by the plane $\omega = 0$

Concluding Remarks

The determination of MA and ARMA systems for the simulation of two-dimensional random fields with a specified (target) spectrum has been studied. The contribution of this part of the series may be summarized as follows:

On the basis of the equivalence between discrete scalar two-dimensional fields and one-dimensional vector processes, Eq. (1), a moving average (MA) algorithm has been introduced,

Downloaded 03 May 2010 to 171.66.16.247. Redistribution subject to ASME license or copyright; see http://www.asme.org/terms/Terms_Use.cfm

Eq. (24). According to this model, a sample of the random field to be generated can be expressed as a linear combination of previous, current, and future values of a two-dimensional white noise.

Relying on the existence of decompositions $q(\phi, \omega)$ satisfying Eq. (27), an optimum strategy to determine the coefficients of the MA model has been introduced through the minimization of a frequency domain error, Eq. (28). Specifically, it has been found that the optimum value of these parameters corresponds to the Fourier coefficients of the function $q(\phi, \omega)$.

The existence of multiple solutions $q(\phi, \omega)$ to Eq. (27) has been recognized and justified by noting that this equation involves only the magnitude of the decomposition $q(\phi, \omega)$. The ambiguity in the selection of this function has been resolved by introducing a measure of energy, Eq. (35), whose maximization leads to an integral equation for the optimum function $q(\phi, \omega)$, Eq. (41). Interestingly, it has been shown that the real decomposition, Eq. (34), obtained as the square root of the spectrum is optimum for all values of the system orders.

A two-stage MA to ARMA modeling technique has been presented that relies on separate rational approximations of the causal and anticausal parts of the MA transfer function, Eqs. (53)–(57). Specifically, a frequency domain error has been introduced, Eq. (60), whose minimization is sought under a set of constraints, Eqs. (61) and (62). Upon solving the corresponding linear system of equations in both the causal and anticausal cases and summing the respective rational approximations, an ARMA model of the target spectrum has been obtained, Eq. (69). Finally, a numerator and a denominator have readily been identified and the parameters of the corresponding ARMA simulation algorithm have been determined, Eq. (75).

The special case of a separable power spectrum, expressible as the product of two functions of one variable each, Eq. (78), has been investigated. It has been proved that the selection of a separable decomposition leads to MA and ARMA models also possessing this property. The special case of the real decomposition, Eq. (34), has been studied next because of its optimum character for all values of the system orders. It has first been shown that the corresponding MA transfer function is also real. Then, under the additional assumption of symmetry of the target autocorrelations, Eq. (14), it has been shown that the autocorrelation function of the corresponding MA and ARMA random fields is also symmetric. Finally, a numerical example has been presented that demonstrates the usefulness of the derived MA and ARMA modeling technique in general and of the real decomposition, Eq. (34), in particular.

It should be recognized from the preceding mathematical developments that a reliable ARMA model of a given two-dimensional spectrum can be obtained from an accurate representation in terms of either an AR or a MA system. For most target spectra, the selection of an AR(m) or MA(m) prior approximation does not lead to a significant difference in the quality of matching. However, the availability of a reliable AR model cannot be guaranteed especially when the target spectrum satisfies the non-integrability condition presented in Part I. The MA modeling technique, which does not exhibit such difficulties and does not require the solution of a linear system of equations, appears then as the most trouble-free method to derive a prior approximation to be used in connection with a two-stage ARMA system determination.

It should be noted that the algorithms investigated in Parts I and II of this series are readily extended to simulate n-dimensional random fields with $n > 2$.

References

Marzetta, T. L., 1980, "Two-Dimensional Linear Prediction: Autocorrelation Arrays, Minimum-Phase Prediction Error Filters, and Reflection Coefficient Arrays," *IEEE Transactions on Acoustics, Speech and Signal Processing*, Vol. ASSP-28, No. 6, pp. 725–733.

Mignolet, M. P., 1987, "ARMA Simulation of Multivariate and Multidimensional Random Processes," Ph.D. Dissertation, Rice University, Houston, Texas.

Naganuma, T., Deodatis, G., Shinozuka, M., and Samaras, E., 1985, "Digital Generation of Multidimensional Random Fields," *Proceedings of the Fourth International Conference on Structural Safety and Reliability*, ICOSSAR, Vol. 1, pp. 251–260.

Naganuma, T., Deodatis, G., and Shinozuka, M., 1987, "ARMA Model for Two-Dimensional Processes," *Journal of Engineering Mechanics*, Vol. 113, No. 2, pp. 234–251.

Spanos, P. D., and Mignolet, M. P., 1990, "Simulation of Stationary Random Processes: A Two-Stage MA to ARMA Approach," *Journal of Engineering Mechanics*, Vol. 116, No. 3, pp. 620–641.

Downloaded 03 May 2010 to 171.66.16.247. Redistribution subject to ASME license or copyright; see http://www.asme.org/terms/Terms_Use.cfm

Eigenvalue Inclusion Principles for Discrete Gyroscopic Systems

B. Yang
Asst. Professor,
Department of Mechanical Engineering,
University of Southern California,
Los Angeles, CA 90089-1453
Assoc. Mem. ASME

In his famous treatise The Theory of Sound, *Rayleigh enunciated an eigenvalue inclusion principle for modified discrete nongyroscopic systems. According to this principle, the natural frequencies of a nongyroscopic system without and with modification are alternatively located along the positive real axis. Although vibration and dynamics of discrete gyroscopic systems have been extensively studied, the problem of inclusion principles for discrete gyroscopic systems has not been addressed. This paper presents several eigenvalue inclusion principles for a class of discrete gyroscopic systems. A transfer function formulation is proposed to describe modified gyroscopic systems. Six types of modifications and their effects on the system natural frequencies are studied. It is shown that the transfer function formulation provides a systematic and convenient way to handle modification problems for discrete gyroscopic systems.*

1 Introduction

In his famous treatise *The Theory of Sound*, Rayleigh (1945) enunciated a theorem about the eigenvalues of modified nongyroscopic systems, which may be stated as follows:

Theorem 1. Consider the linear, discrete nongyroscopic system

$$M\dot{x}(t)+Kx(t)=f(t), \quad M^T=M>0,\ K^T=K>0$$

whose natural frequencies are ω_k, arranged in ascending order of magnitude. If a spring is attached to the system or if one point of the system is fixed, the natural frequencies Ω_k of the modified system are such that

$$\omega_k \le \Omega_k \le \omega_{k+1}, \quad k=1,2,\ldots.$$

This theorem, now called the inclusion principle, was proven based on Rayleigh's quotient. The inclusion principle has been used to develop algorithms for computing eigenvalues of modified vibrating systems, and to estimate the bounds of natural frequencies of structures.

Vibration and dynamics of discrete gyroscopic systems have been extensively studied by Meirovitch (1974 and 1980), Hagedorn (1975), Huseyin (1976 and 1978), Inman (1988), and many others. The problem of inclusion principles for discrete gyroscopic systems, however, has not been addressed. In Meirovitch (1980), a state space formulation with a generalized Rayleigh's quotient is proposed to estimate the eigenvalues of discretized models of distributed gyroscopic systems. This method, while useful in discretization and numerical analysis, is not convenient in handling modification[1] of gyroscopic systems. Because the state space vector and the displacement vector have different dimensions and because the modal coordinates are complex, description of system modification in the state space is difficult. No inclusion principles for physically modified discrete gyroscopic systems are given in Meirovitch (1980).

This paper presents several inclusion principles for a class of discrete gyroscopic systems. In the development, instead of Rayleigh's quotient, a transfer function formulation is proposed. In Section 2 a Green's function is obtained to predict the response of the unmodified system. The modification problem is formulated in the Laplace transform domain in Section 3. The unmodified system is an open-loop system; the modified system is a closed-loop system with the modification as a feedback controller. The closed-loop transfer function is derived in terms of the Green's function of the unmodified system. In Section 4 several types of modifications and their effects on the system natural frequencies are studied through investigation of the close-loop transfer function.

2 System Description

Consider the linear, n-dimensional, discrete gyroscopic system described by

$$M\ddot{x}(t)+G\dot{x}(t)+Kx(t)=f(t), \quad x(0)=a_0,\ \dot{x}(0)=b_0$$
$$x, f\in R^n,\ M,\ G,\ K\in R^{n\times n},\ M^T=M>0,\ G^T=-G,\ K^T=K>0 \tag{1}$$

Contributed by the Applied Mechanics Division of THE AMERICAN SOCIETY OF MECHANICAL ENGINEERS for presentation at the Winter Annual Meeting, Atlanta, Ga., Dec. 1-6, 1991.

Discussion on this paper should be addressed to the Technical Editor, Prof. Leon M. Keer, The Technological Institute, Northwestern University, Evanston, IL 60208, and will be accepted until two months after final publication of the paper itself in the JOURNAL OF APPLIED MECHANICS. Manuscript received by the ASME Applied Mechanics Division, July 11, 1990; final revision, Dec. 20, 1990.

Paper No. 91-WA/APM-14.

[1]The term "modification" means removal of one degree-of-freedom from the original system, or addition of a spring (a lumped mass, a spring-mass system, etc.) to the original system.

Copyright © 1992 by ASME
Downloaded 03 May 2010 to 171.66.16.247. Redistribution subject to ASME license or copyright; see http://www.asme.org/terms/Terms_Use.cfm

where $x(t)$ is the displacement vector, $f(t)$ is the external force vector, M is the mass matrix, G is the gyroscopic matrix, and K is the stiffness matrix. The skew symmetric matrix G is associated with the Coriolis acceleration or mass transport.

The eigenvalue problem associated with (1)

$$(\lambda_k^2 M+\lambda_k G+K)\nu_k=0 \tag{2}$$

has the eigensolutions of the form

$$\lambda_{\pm k}=\pm i\omega_k \quad \nu_{\pm k}=\nu_k^R \pm i\nu_k^I, \quad k=1,2,\ldots,n$$
$$\omega_k>0, \quad \nu_k^R,\ \nu_k^I \in R^n, \quad i=\sqrt{-1}. \tag{2}$$

The ω_k is the kth natural frequency and ν_k is the corresponding mode shape distribution. For zero G, ν_k are real and orthogonal. For nonzero G, ν_k are complex and nonorthogonal.

For the nonorthogonal eigenfunctions ν_k, the system response $x(t)$ can not be evaluated by the classical modal analysis. In this work, bi-orthogonal eigenvectors are investigated. Equation (1) is transformed into an equivalent first-order form

$$\dot z(t)=Az(t)+Q(t), \quad z(0)=z_0$$
$$z,\ Q\in R^{2n},\ A\in R^{2n\times 2n} \tag{4a}$$

where

$$z(t)=\begin{pmatrix}\dot x(t)\\ x(t)\end{pmatrix},\ A=\begin{bmatrix}-M^{-1}G & -M^{-1}K\\ I & 0\end{bmatrix},$$
$$Q(t)=\begin{pmatrix}M^{-1}f(t)\\ 0\end{pmatrix},\ z_0=\begin{pmatrix}b_0\\ a_0\end{pmatrix}. \tag{4b}$$

The eigenvalue problem associated with (4a)

$$A\phi_k=\lambda_k\phi_k \tag{5}$$

has the eigensolutions

$$\lambda_k=i\omega_k,\ \phi_k=\begin{pmatrix}\lambda_k\nu_k\\ \nu_k\end{pmatrix};\ \lambda_{-k}=\bar\lambda_k,\ \phi_{-k}=\bar\phi_k \tag{6}$$

where λ_k are ν_k are from (2), and the super bar denotes complex conjugation. The adjoint eigenvalue problem to (5) is

$$A^T\psi_k=\bar\lambda_k\psi_k. \tag{7}$$

The adjoint eigenvectors are

$$\psi_k=\begin{pmatrix}\lambda_k M\nu_k\\ K\nu_k\end{pmatrix}\ \psi_{-k}=\bar\psi_k \tag{8}$$

where M and K are from (1), and λ_k and ν_k are from (2). The ϕ_k and ψ_k satisfy the bi-orthogonality conditions

$$\langle\psi_j,\phi_k\rangle=2\delta_{jk} \qquad \langle\psi_j,A\phi_k\rangle=2\lambda_j\delta_{jk} \tag{9}$$

where the inner product $\langle a,b\rangle \triangleq \bar a^T b$, $a,\ b\in C^{2n}$.

With the complete sets $\{\phi_k\}$ and $\{\psi_k\}$, the state vector $z(t)$ can be represented as

$$z(t)=\sum_{k=\pm 1}^{\pm n}\alpha_k(t)\phi_k \tag{10}$$

where $\alpha_k(t)$ are complex modal coordinates. Substitution of the expansion (10) into (4a) and use of the bi-orthogonality conditions (9) yields a set of independent first-order equations

$$\dot\alpha_k(t)=\lambda_k\alpha_k(t)+q_k(t) \quad k=\pm 1,\pm 2,\ldots,\pm n$$
$$\alpha_k(0)=\frac{1}{2}\langle\psi_k,z_0\rangle \quad q_k(t)=\frac{1}{2}\langle\psi_k,Q(t)\rangle. \tag{11}$$

Because $z(t)$ and $Q(t)$ are real, α_k and $\alpha_{-k}q_k$ and q_{-k} are complex conjugates. Solution of (11) and substitution of $\alpha_k(t)$ into (10) gives

$$z(t)=S(t)z_0+\int_0^t S(t-\tau)Q(\tau)d\tau \tag{12a}$$

where the $2n\times 2n$ real matrix

$$S(t)\equiv\begin{bmatrix}s_{11}(t) & s_{12}(t)\\ s_{21}(t) & s_{22}(t)\end{bmatrix}$$
$$=\frac{1}{2}\sum_{k=\pm 1}^{\pm n}e^{\lambda_k t}\begin{bmatrix}\omega_k^2\nu_k\bar\nu_k^T M & \lambda_k\nu_k\bar\nu_k^T K\\ \bar\lambda_k\nu_k\bar\nu_k^T M & \nu_k\bar\nu_k^T K\end{bmatrix}. \tag{12b}$$

By (4) and (12)

$$x(t)=s_{21}(t)b_0+s_{22}(t)a_0+\int_0^t s_{21}(t-\tau)M^{-1}f(\tau)d\tau. \tag{13}$$

Using (2) and (12b), it can be shown that

$$s_{22}(t)=\dot s_{21}(t)+s_{21}(t)M^{-1}G. \tag{14}$$

Thus, the response of the gyroscopic system under external and initial disturbances is expressed by

$$x(t)=g(t)(Ga_0+Mb_0)+\dot g(t)Ma_0+\int_0^t g(t-\tau)f(\tau)d\tau \tag{15}$$

where the Green's function $g(t)$, an n by n real matrix, is given by

$$g(t)=s_{21}(t)M^{-1}=\frac{1}{2}\sum_{k=\pm 1}^{\pm n}e^{\lambda_k t}\bar\lambda_k\nu_k\bar\nu_k^T. \tag{16}$$

The presence of the skew symmetric matrix G makes the system (1) non-self-adjoint; the system response $x(t)$ can not be evaluated by the classical modal analysis. The explicit representation of the bi-orthogonal eigenvectors ϕ_k and ψ_k by the modes of vibration (ω_k, ν_k), however, makes it possible to express $x(t)$ in a modal expansion form.

3 Problem Formulation

The discrete gyroscopic system (1) under a modification is considered as a feedback control system. The system (1) without the modification is an open-loop system. The system (1) with the modification is a closed-loop system; the modification is a feedback controller. Both the open-loop and closed-loop transfer functions are obtained, from which the eigenvalues of unmodified and modified systems can be evaluated.

Open Loop: The Unmodified System. Laplace transform of (15) with respect to t gives

$$X(s)=W_o(s)\{F(s)+F_I(s)\} \tag{17}$$

where $X(s)$ and $F(s)$ are the Laplace transforms of $x(t)$ and $f(t)$, respectively, s is a complex parameter, and $F_I(s)=(G+sM)a_0+Mb_0$ representing the initial conditions. The open-loop transfer function, $W_o(s)$, is the Laplace transform of the Green's function $g(t)$, and is given by

$$W_o(s)=\frac{1}{2}\sum_{k=\pm 1}^{\pm n}\frac{-\lambda_k}{s-\lambda_k}\nu_k\bar\nu_k^T. \tag{18}$$

It is seen that (17) is the solution of the Laplace transform of (1)

$$(s^2M+sG+K)X(s)=F(s)+F_I(s).$$

Note that the poles of $W_o(s)$ are the eigenvalues of the system (1), $\lambda_k=i\omega_k$.

Closed Loop: The Modified System. Assume that a modification is imposed on the unmodified system (1) at the jth point. The modification will generate a force, which is applied at the jth point and depends on the jth displacement $x_j(t)$ of $x(t)$. This force can be considered as the control force from a feedback controller that has a sensor and an actuator both located at the jth point of the system (1); i.e.,

$$F_c(s)=H(s)e_j e_j^T X(s). \tag{19}$$

Here, $F_c(s)$ is the Laplace transform of the force due to the modification

Downloaded 03 May 2010 to 171.66.16.247. Redistribution subject to ASME license or copyright; see http://www.asme.org/terms/Terms_Use.cfm

$$e_j \equiv (0 \cdots 0 \quad 1 \quad 0 \cdots 0)^T \in R^n$$

with 1 in the jth position and 0 elsewhere, and $H(s)$, the transfer function of the modification (the controller), has the form

$$H(s) = \mu \frac{N(s)}{D(s)} \tag{20}$$

where $N(s)$ and $D(s)$ are polynomials in s, and $\mu > 0$ is a gain parameter. Two examples of modifications are given as follows:

(a) A spring of coefficient μ attached to the system (1)

$$H(s) = -\mu \quad N(s) = -1 \quad D(s) = 1. \tag{21}$$

(b) A mass μ added to the system (1)

$$H(s) = -\mu s^2 \quad N(s) = -s^2 \quad D(s) = 1. \tag{22}$$

With the above description, the total external force is given by

$$F(s) = F_c(s) + F_e(s) = \mu \frac{N(s)}{D(s)} e_j e_j^T X(s) + F_e(s)$$

where $F_e(s)$ is the Laplace transform of other external disturbance. Substituting the foregoing expression into (17) gives

$$X(s) = \left[I - \mu \frac{N(s)}{D(s)} W_o(s) e_j e_j^T \right]^{-1} W_o(s) \{F_e(s) + F_l(s)\}$$
$$= W_{cl}(s) \{F_e(s) + F_l(s)\} \tag{23}$$

where the closed-loop transfer function

$$W_{cl}(s) = \frac{1}{\Delta(s)} N_{cl}(s) \tag{24a}$$

$$N_{cl}(s) = D(s) W_o(s) + \mu N(s) [W_o(s) e_j e_j^T W_o(s) - e_j^T W_o(s) e_j W_o(s)] \in C^{n \times n} \tag{24b}$$

$$\Delta(s) = D(s) - \mu N(s) \sum_{k=1}^{n} \frac{\omega_k^2}{s^2 + \omega_k^2} |\nu_{kj}|^2 \in C \tag{24c}$$

and ν_{kj} is the jth element of the eigenvector ν_k. The eigenvalues of the modified gyroscopic system are the poles of the closed-loop transfer function $W_{cl}(s)$.

Theorem 2. The eigenvalues of the modified system (23) are the roots of

$$\Delta(s) = 0$$

and λ_l for some l if $\nu_{lj} = 0$ or $N(\lambda_l) = 0$.

Proof: See Appendix A.

Theorem 2 relates to controllability of the gyroscopic system (Yang and Mote, 1990). If the modification is away from all nodes of the n modes of vibration, and has no pole-zero cancellation, the modified system is controllable for all modes; the modification will change all the system eigenvalues. If the modification is at a node of the kth mode or has a zero canceling the kth eigenvalue λ_k, the modified system is not controllable for the kth mode; the modification will not influence λ_k.

4 Inclusion Principles

With the closed-loop transfer function $W_{cl}(s)$, eigenvalue inclusion principles are developed for six types of nondissipative modifications. Without loss of generality, assume that the natural frequencies ω_k of the unmodified system are distinct. For the gyroscopic system (1) under a nondissipative modification, the system eigenvalues have the form $i\Omega_k$, where Ω_k are the natural frequencies of the modified system. In the following analyses, the ω_k and Ω_k are arranged in ascending order of magnitude.

Modification 1: A Spring Attached to the Gyroscopic System. A spring of coefficient μ is attached to the system (1) at the jth point. The modification is described in (21). If the jth point is not a node of any mode of the unmodified system, i.e.,

$$\nu_{kj} \neq 0 \quad \text{for } k = 1, 2, \ldots, n,$$

according to Theorem 2, the natural frequencies, Ω_k, are the roots of

$$h_1(\Omega) \equiv \Delta(i\Omega) = 1 + \mu \sum_{k=1}^{n} \frac{\omega_k^2}{-\Omega^2 + \omega_k^2} |\nu_{kj}|^2 = 0 \tag{25}$$

where (21) and (24c) have been used. The function $h_1(\Omega)$ has the following properties:

$$h_1(0) > 0, \quad \lim_{\Omega \to +\infty} h_1(\Omega) > 0$$

$$\lim_{\Omega \to \omega_k - 0} h_1(\Omega) = +\infty, \quad \lim_{\Omega \to \omega_k + 0} h_1(\Omega) = -\infty \quad \text{for all } k$$

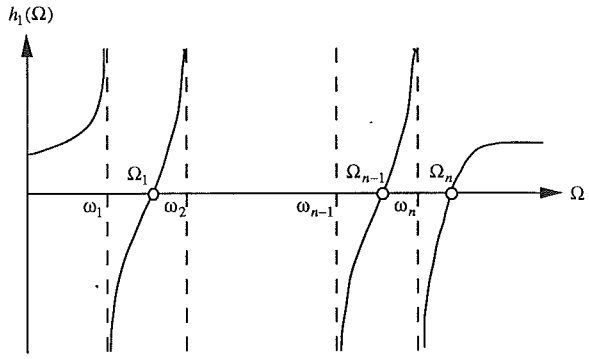


Fig. 1 Natural frequencies of the gyroscopic system (1) under Modification 1, $\nu_{kj} \neq 0$ for $k = 1, 2, \ldots n$

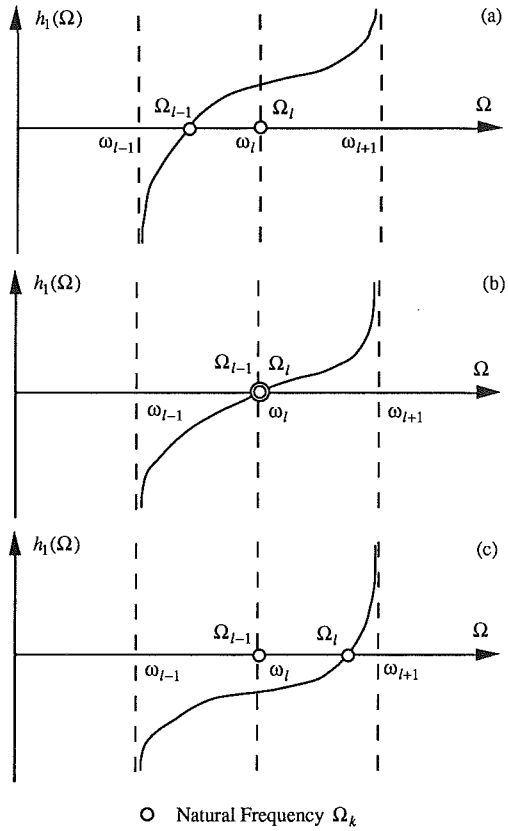


Fig. 2 Natural frequencies of the gyroscopic system (1) under Modification 1, $\nu_{lj} = 0$: (a) $h_1(\omega_l) > 0$; (b) $h_1(\omega_l) = 0$; (c) $h_1(\omega_l) < 0$

Downloaded 03 May 2010 to 171.66.16.247. Redistribution subject to ASME license or copyright; see http://www.asme.org/terms/Terms_Use.cfm

$$\frac{d}{d\Omega} h_1(\Omega) > 0 \text{ for } \Omega \in (0, +\infty) \text{ and } \Omega \neq \omega_k,\ k = 1,2, \ldots, n.$$

Because $h_1(\Omega)$ is continuous and monotonically increasing on (ω_k, ω_{k+1}) and because $h_1(\omega_k + 0)$ and $h_1(\omega_{k+1} - 0)$ have different signs, there is at least and at most one root Ω_k of (25) in each interval (ω_k, ω_{k+1}), $k = 1, 2, \ldots, n-1$; see Fig. 1. Also, there is a root $\Omega_n > \omega_n$. No root falls in the interval $(0, \omega_1)$. All these indicate that

$$0 < \omega_1 < \Omega_1 < \omega_2 < \Omega_2 < \cdots < \omega_n < \Omega_n.$$

Addition of the spring increases all the system natural frequencies.

If the jth point is a node of the lth mode of the unmodified system, $\nu_{l,j} = 0$ and $h_1(\omega_l)$ is finite. According to Theorem 2, ω_l is a natural frequency of the modified system. Because $h_1(\Omega)$ is continuous and monotonically increasing on $(\omega_{l-1}, \omega_{l+1})$ and because $h_1(\omega_{l-1} + 0)$ and $h_1(\omega_{l+1} - 0)$ have different signs, (25) has a root in $(\omega_{l-1}, \omega_{l+1})$. This means that the modified system has two natural frequencies, Ω_{l-1} and Ω_l, in $(\omega_{l-1}, \omega_{l+1})$. The locations of these two natural frequencies depend on the value of $h_1(\omega_l)$ (see Fig. 2):

(a) $\omega_{l-1} < \Omega_{l-1} < \omega_l = \Omega_l < \omega_{l+1}$ for $h_1(\omega_l) > 0$;
(b) $\omega_{l-1} < \Omega_{l-1} = \omega_l = \Omega_l < \omega_{l+1}$ for $h_1(\omega_l) = 0$;
(c) $\omega_{l-1} < \Omega_{l-1} = \omega_l < \Omega_l < \omega_{l+1}$ for $h_1(\omega_l) < 0$.

Note that the modified system may have repeated eigenvalues even if the unmodified system has distinct eigenvalues.

The above discussion is summarized as follows:

Claim 1. If a spring is attached to the discrete gyroscopic system (1) whose natural frequencies are ω_k, the natural frequencies Ω_k of the modified system are such that

$$0 < \omega_1 \le \Omega_1 \le \omega_2 \le \Omega_2 \le \cdots \le \omega_n \le \Omega_n. \tag{26}$$

Modification 2: A Mass Added to the Gyroscopic System. A mass μ is added to the system (1) at the jth point. The modification is described in (22). If the jth point is away from any node of all modes of the unmodified system, by Theorem 2, the natural frequencies Ω_k of the modified system are the roots of

$$h_2(\Omega) \equiv \Delta(i\Omega) = 1 - \mu\Omega^2 \sum_{k=1}^{n} \frac{\omega_k^2}{-\Omega^2 + \omega_k^2} |\nu_{k,j}|^2 = 0 \tag{27}$$

where (22) and (24c) have been used. The function $h_2(\Omega)$ has the following properties:

$$h_2(0) > 0, \quad \lim_{\Omega \to +\infty} h_2(\Omega) > 0$$

$$\lim_{\Omega \to \omega_k - 0} h_2(\Omega) = -\infty, \quad \lim_{\Omega \to \omega_k + 0} h_2(\Omega) = +\infty \quad \text{for all } k$$

$$\frac{d}{d\Omega} h_2(\Omega) < 0 \text{ for } \Omega \in (0, +\infty) \text{ and } \Omega \neq \omega_k,\ k = 1,2, \ldots, n.$$

With these properties it can be shown that

$$0 < \Omega_1 < \omega_1 < \Omega_2 < \omega_2 \ldots < \Omega_n < \omega_n.$$

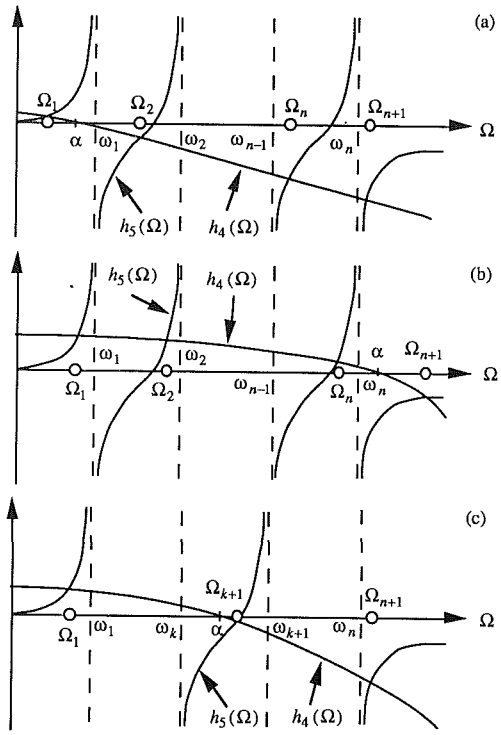
Addition of the mass decreases the system natural frequencies.

If the jth point is a node of the lth mode of the unmodified system, based on a similar argument to that in Modification 1, the modified system has two natural frequencies, Ω_l and Ω_{l+1}, in $(\omega_{l-1}, \omega_{l+1})$:

(a) $\omega_{l-1} < \Omega_l = \omega_l < \Omega_{l+1} < \omega_{l+1}$ for $h_2(\omega_l) > 0$;
(b) $\omega_{l-1} < \Omega_l = \omega_l = \Omega_{l+1} < \omega_{l+1}$ for $h_2(\omega_l) = 0$;
(c) $\omega_{l-1} < \Omega_l < \omega_l = \Omega_{l+1} < \omega_{l+1}$ for $h_2(\omega_l) < 0$.

The results are summarized as follows:

Claim 2. If a mass is added to the discrete gyroscopic system (1) whose natural frequencies are ω_k, the natural frequencies Ω_k of the modified system are such that



○ Natural Frequency Ω_k

Fig. 3 Natural frequencies of the gyroscopic system (1) under Modification 4, (*a*) $\alpha \in (0, \omega_1)$; (*b*) $\alpha > \omega_n$; (*c*) $\alpha \in (\omega_k, \omega_{k+1})$ and $h_5(\alpha) < 0$

$$0 < \Omega_1 \le \omega_1 \le \Omega_2 \le \omega_2 \le \ldots \le \Omega_n \le \omega_n. \tag{28}$$

Modification 3: One Point of the Gyroscopic System Fixed. Let the jth point of the gyroscopic system (1) be fixed, i.e.,

$$x_j(t) \equiv 0 \quad \forall t > 0 \tag{29}$$

where $x_j(t)$ is the jth component of $x(t)$. As a result one degree-of-freedom of the gyroscopic system is removed. The modification can be considered as the limiting case of Modification 1 as the spring coefficient μ approaches infinity. According to Appendix B, the natural frequencies Ω_k of the modified system are the roots of

$$h_3(\Omega) \equiv \sum_{k=1}^{n} \frac{\omega_k^2}{-\Omega^2 + \omega_k^2} |\nu_{k,j}|^2 = 0 \tag{30}$$

and ω_l for some l if $\nu_{l,j} = 0$.

Claim 3. If the modification (29) is imposed on the discrete gyroscopic system (1) whose natural frequencies are ω_k, the natural frequencies Ω_k of the modified system are such that

$$0 < \omega_1 \le \Omega_1 \le \omega_2 \le \Omega_2 \le \cdots \omega_{n-1} \le \Omega_{n-1} \le \omega_n \tag{31}$$

where one degree-of-freedom of the system (1) is removed due to the modification.

Modification 4: A Mass-Spring System Connected to the Gyroscopic System. A mass m is connected to the system (1) at the jth point by a spring of coefficient μ. The displacement $\xi(t)$ of m is in the direction of the jth displacement $x_j(t)$. The motion of the modified system is described by

$$M\ddot{x}(t) + G\dot{x}(t) + Kx(t) = \mu(\xi(t) - x_j(t))e_j$$
$$m\ddot{\xi}(t) + \mu(\xi(t) - x_j(t)) = 0 \tag{32}$$

where e_j is defined in (19). Note that the one degree-of-freedom of the mass m is added to the modified system. Laplace transform of (32) and elimination of ξ lead to

Downloaded 03 May 2010 to 171.66.16.247. Redistribution subject to ASME license or copyright; see http://www.asme.org/terms/Terms_Use.cfm

$$(s^2M+sG+K)X(s) = -\mu \frac{ms^2}{ms^2+\mu} e_j e_j^T X(s) + F_e(s) + F_I(s) + F_{I\xi}(s)$$

where $F_{I\xi}(s)$ contains the initial conditions of $\xi(t)$. By (19) the transfer function of the modification is

$$H(s) = -\mu \frac{s^2}{s^2+\alpha^2}, \quad \alpha^2 = \frac{\mu}{m}. \tag{33}$$

According to Theorem 2, the natural frequencies Ω_k of the modified system are the roots of

$$\Delta(i\Omega) = -\Omega^2 + \alpha^2 - \mu\Omega^2 \sum_{k=1}^{n} \frac{\omega_k^2}{-\Omega^2+\omega_k^2} |\nu_{k,j}|^2 = 0 \tag{34}$$

and ω_l for some l if $\nu_{l,j} = 0$. Rewrite (34) as

$$h_4(\Omega) = h_5(\Omega) \tag{35}$$

where

$$h_4(\Omega) \equiv -\Omega^2 + \alpha^2 \quad h_5(\Omega) \equiv \mu\Omega^2 \sum_{k=1}^{n} \frac{\omega_k^2}{-\Omega^2+\omega_k^2} |\nu_{k,j}|^2 = 0. \tag{36}$$

The roots of (34) are determined by the intersections of $h_4(\Omega)$ and $h_5(\Omega)$. With the properties

$$h_4(\Omega) > 0 \text{ for } \Omega \in [0,\alpha),\ h_4(\alpha) = 0,\ h_4(\Omega) < 0 \text{ for } \Omega \in (\alpha, +\infty)$$

$$h_5(0) = 0,\ \lim_{\Omega \to +\infty} h_5(\Omega) < 0$$

$$\lim_{\Omega \to \omega_k - 0} h_5(\Omega) = +\infty,\ \lim_{\Omega \to \omega_k + 0} h_5(\Omega) = -\infty \text{ for all } k$$

$$\frac{d}{d\Omega} h_5(\Omega) > 0 \text{ for } \Omega \in (0, +\infty) \text{ and } \Omega \neq \omega_k,\ k = 1, 2, \ldots, n$$

it can be shown that (see Fig. 3):

(a) for $\alpha \in (0, \omega_1)$, $0 < \Omega_1 < \alpha < \omega_1 \le \Omega_2 \le \cdots \le \omega_{n-1} \le \Omega_n \le \omega_n \le \Omega_{n+1}$;

(b) for $\alpha > \omega_n$, $0 < \Omega_1 \le \omega_1 \le \cdots \le \Omega_n \le \omega_n < \alpha < \Omega_{n+1}$;

(c) for $\alpha \in (\omega_k, \omega_{n+1})$, $0 < \Omega_1 \le \omega_1 \le \cdots \le \Omega_k \le \omega_k$, $\omega_{k+1} \le \Omega_{k+2} \cdots \le \omega_n \le \Omega_{n+1}$ with

$$\omega_k \le \Omega_{k+1} < \alpha \le \omega_{k+1} \quad \text{if } h_5(\alpha) > 0$$

$$\omega_k < \alpha = \Omega_{k+1} \le \omega_{k+1} \quad \text{if } h_5(\alpha) = 0$$

$$\omega_k < \alpha < \Omega_{k+1} \le \omega_{k+1} \quad \text{if } h_5(\alpha) < 0;$$

(d) for $\alpha = \omega_k$, $0 < \Omega_1 \le \omega_1 \le \cdots \le \Omega_k \le \alpha = \omega_k \le \Omega_{k+1} \le \cdots \le \omega_n \le \Omega_{n+1}$.

Thus, a statement is given as follows:

Claim 4. If a mass-spring system is connected to the discrete gyroscopic system (1) whose natural frequencies are ω_k, the natural frequencies Ω_k of the modified system are such that

$$0 < \Omega_1 \le \omega_1 \le \Omega_2 \le \omega_2 \le \cdots \le \Omega_n \le \omega_n \le \Omega_{n+1} \tag{37}$$

where one degree-of-freedom is gained for the modified systems

There are two extreme cases. First, when the spring coefficient μ goes to infinity, (33) becomes $H(s) = -ms^2$, which is Modification 2. This is expected. As μ goes to infinity, the mass m is rigidly connected to the system (1). Second, when the mass m approaches infinity, (33) reduces to (21), Modification 1. This is also expected. As m approaches infinity, its displacement $\xi(t)$ vanishes rendering the spring attached to the system (1).

Modification 5: A Linear Constraint on the Displacements. The system (1) is constrained by

$$\sum_{k=1}^{n} d_k x_k(t) \equiv 0,\ d_k \in R, \forall t > 0 \tag{38}$$

where $x_k(t)$ is the kth component of $x(t)$, and at least one of the coefficients d_k is nonzero. One example of (38) is that the jth and lth points of the system (1) are rigidly connected, i.e., $x_j = x_l$.

Assume that d_l is nonzero for a specific l. Under the coordinate transformation

$$y(t) = Tx(t),$$

$$T = \begin{bmatrix} 1 & & & & & & \\ & \ddots & & & & & \\ & & 1 & & & & \\ d_1 & \cdots & d_{l-1} & d_l & d_{l+1} & \cdots & d_n \\ & & & & 1 & & \\ & & & & & \ddots & \\ & & & & & & 1 \end{bmatrix}, \quad \det T = d_l \neq 0 \tag{39}$$

the system (1) with the modification (38) is transformed into

$$\tilde{M}\ddot{y}(t) + \tilde{G}\dot{y}(t) + \tilde{K}y(t) = q(t) \tag{40}$$

with the modification

$$y_l(t) \equiv 0 \quad \forall t > 0 \tag{41}$$

where $y_l(t)$ is the lth component of the vector $y(t)$, and

$$\tilde{M} = T^{-T}MT^{-1} = \tilde{M}^T,\ \tilde{G} = T^{-T}GT^{-1} = -\tilde{G}^T,$$
$$\tilde{K} = T^{-T}KT^{-1} = \tilde{K}^T,\ q = T^{-T}f. \tag{42}$$

In the new coordinates the system (40) is under Modification 3; i.e., the lth point is fixed. Because the transformation T does not change the system eigenvalues, the following result is obtained by applying Claim 3 to (40) and (41).

Claim 5. If the modification (38) is imposed on the discrete gyroscope system (1) whose natural frequencies are ω_k, the natural frequencies Ω_k of the modified system are such that

$$0 < \omega_1 \le \Omega_1 \le \omega_2 \le \Omega_2 \le \cdots \omega_{n-1} \le \Omega_{n-1} \le \omega_n \tag{43}$$

where one degree-of-freedom of the system (1) is removed due to the modification.

Modification 6: A Spring Connecting Two Points of the Gyroscopic System. Without loss of generality, consider that a spring of coefficient μ is added to connect the first and second points of the system (1). The equation of motion for the modified system is

$$M\ddot{x}(t) + G\dot{x}(t) + Kx(t) = -\mu \begin{bmatrix} 1 & -1 & & & \\ -1 & 1 & & & \\ & & 0 & & \\ & & & \ddots & \\ & & & & 0 \end{bmatrix} x(t) + f(t). \tag{44}$$

Under the coordinate transformation

$$y(t) = Tx(t),\ T = \begin{bmatrix} 1 & -1 & & & \\ & 1 & & & \\ & & \ddots & & \\ & & & \ddots & \\ & & & & 1 \end{bmatrix}, \quad \det T = 1 \neq 0, \tag{45}$$

(44) is transformed into

$$\tilde{M}\ddot{y}(t) + \tilde{G}\dot{y}(t) + \tilde{K}y(t) = -\mu e_1 e_1^T y(t) + q(t) \tag{46}$$

where $e_1 = (1\ 0 \cdots 0)^T \in R^n$, and

$$\tilde{M} = T^{-T}MT^{-1} = \tilde{M}^T,\ \tilde{G} = T^{-T}GT^{-1} = -\tilde{G}^T,$$
$$\tilde{K} = T^{-T}KT^{-1} = \tilde{K}^T,\ q = T^{-T}f. \tag{47}$$

In the new coordinates, (46) is a gyroscopic system under Modification 1; i.e., a spring is attached to the gyroscopic system at the first point. Because the transformation T does

Downloaded 03 May 2010 to 171.66.16.247. Redistribution subject to ASME license or copyright; see http://www.asme.org/terms/Terms_Use.cfm

not change the system eigenvalues, the following conclusion is drawn by applying Claim 1 to (46).

Claim 6. If a spring is added to connect any two points of the discrete gyroscopic system (1) whose natural frequencies are ω_k, the natural frequencies Ω_k of the modified system are such that

$$0<\omega_1\le\Omega_1\le\omega_2\le\Omega_2\le\cdots\le\omega_n\le\Omega_n. \tag{48}$$

As an extreme case, when the spring coefficient μ goes to infinity, the two points of the system (1) are rigidly connected; one degree-of-freedom is removed. Claim 6 is still valid if the Ω_n is removed from (48). On the other hand, this limiting case is an example of Modification 5. Claim 5 can be directly used here.

5 Conclusions

Six types of nondissipative modifications and their effects on the system natural frequencies have been studied through investigation of the close loop transfer function $W_{cl}(s)$. Many other modifications can be treated in the same manner. This paper provides a systematic and convenient way to handle modification problems for discrete gyroscopic systems. The transfer function formulation is also useful in study of eigenvalue problems for discrete gyroscopic systems with dissipative modifications such as dashpots.

This work can be easily extended to discrete gyroscopic systems with repeated eigenvalues. Analyses follow the same steps as in Sections 3 and 4. Results similar to Claims 1 to 6 are expected.

The inclusion principle for the classical nongyroscopic system (Theorem 1) has been proven using Rayleigh's quotient and the maximum-minimum characteristic of the system eigenvalues. Because the nongyroscopic system is a special case of the gyroscopic system (1) with $G = 0$, Claims 1 and 3 in fact give a different proof of Theorem 1.

The methodology presented in this paper has been extended to develop eigenvalue inclusion principles for distributed gyroscopic systems (Yang, 1992).

Acknowledgment

This research is sponsored by the Charles Lee Powell Foundation. The author wishes to thank the reviewers for the helpful suggestions with the presentation.

References

Hagedorn, P., 1975, "Uber Die Instabilitat Konservativer System Mit Gyroskopischen Kraften," *Arch. Rat. Mech. Anal.*, Vol. 58, pp. 1-9.

Huseyin, K., 1976, "Standard Forms of the Eigenvalue Problems Associated with Gyroscopic Systems," *Journal of Sound and Vibration*, Vol. 45, No. 1, pp. 29-37.

Huseyin, K., 1978, *Vibration and Stability of Multiple Parameter Systems*, Noordholl International Publishing.

Inman, D. J., 1988, "A Sufficient Condition for the Stability of Conservative Gyroscopic Systems," ASME JOURNAL OF APPLIED MECHANICS, Vol. 55, No. 4, pp. 895-898.

Meirovitch, L., 1974, "A New Method of Solution of the Eigenvalue Problem for Gyroscopic Systems," *AIAA Journal*, Vol. 12, No. 10, pp. 1337-1342.

Meirovitch, L., 1980, *Computational Methods in Structural Dynamics*, Sijthoff and Noordhoff.

Rayleigh, J. W. S., 1945, *The Theory of Sound*, Dover, New York, Vol. 1, p. 119.

Yang, B., 1992, "Eigenvalue Inclusion Principles for Distributed Gyroscopic Systems," to appear in ASME JOURNAL OF APPLIED MECHANICS.

Yang, B., and Mote, C. D., Jr., 1991, "Controllability and Observability of Distributed Gyroscopic Systems," *ASME Journal of Dynamic Systems, Measurement, and Control*, Vol. 113, pp. 11-17.

APPENDIX A

Proof of Theorem 2

Consider the limit of $W_{cl}(s)$ as $s \to \lambda_k$. Write $s - \lambda_k = \epsilon e^{i\theta}$, $\epsilon > 0$. Given a j (the location of the modification), if $\nu_{k,j} = 0$ for some k, by (18) and (24), as $s \to \lambda_k$, $\epsilon \to 0$ and

$$W_{cl}(s)\to\frac{e^{-i\theta}}{\epsilon}B_1$$

$$B_1\in C^{n\times n},\ 0<\eta_1\le\|B_1\| \tag{A1}$$

where η_1 is a constant. The limit in (A1) is unbounded, implying that λ_k is a pole of $W_{cl}(s)$. If $\nu_{k,j} \neq 0$, by (18) and (24), as $s \to \lambda_k$, $\epsilon \to 0$, and

$$W_{cl}(s)\to\frac{1}{\mu\lambda_k N(\lambda_k+\epsilon e^{i\theta})\,|\nu_{k,j}|^2}B_2$$

$$B_2\in C^{n\times n},\ 0<\eta_2\le\|B_2\|\le\eta_3<+\infty \tag{A2}$$

where η_2 and η_3 are constants. Recall that $\mu > 0$ and $\omega_k > 0$. The limit in (A2) has two possibilities:

(i) $N(\lambda_k) = 0$, the limit in (A2) is unbounded; λ_k is a pole of $W_{cl}(s)$.

(ii) $N(\lambda_k) \neq 0$, the limit in (A2) is determinate and finite; λ_k is not a pole of $W_{cl}(s)$.

Note that $N_{cl}(s)$ in (24) has no singular points in the complex plane other than λ_k. Besides those λ_k which are the poles of $W_{cl}(s)$, all other poles of the modified system can only be the roots of $\Delta(s) = 0$.

APPENDIX B

Eigenvalues of the System (1) Under Modification 3

Modification 3 can be considered as the limiting case of Modification 1 as the spring coefficient μ goes to infinity. By (21) and (24), as $\mu \to +\infty$, the closed-loop transfer function

$$W_{cl}(s)\to\frac{-1}{\sum_{k=1}^{n}\frac{\omega_k^2}{s^2+\omega_k^2}|\nu_{k,j}|^2}\,[W_o(s)e_je_j^TW_o(s) - e_j^TW_o(s)e_jW_o(s)]. \tag{B1}$$

With a similar argument to that in Appendix A, it can be shown that the poles of $W_{cl}(s)$ in (B1) are the roots of

$$\sum_{k=1}^{n}\frac{\omega_k^2}{s^2+\omega_k^2}\,|\nu_{k,j}|^2=0 \tag{B2}$$

and λ_l for some l if $\nu_{l,j} = 0$.

Downloaded 03 May 2010 to 171.66.16.247. Redistribution subject to ASME license or copyright; see http://www.asme.org/terms/Terms_Use.cfm

Vibration of Harmonically Excited Oscillators With Asymmetric Constraints

S. Natsiavas
Asst. Professor,
Assoc. Mem. ASME.

H. Gonzalez
Graduate Student.

Department of Mechanical and Aerospace Engineering,
Arizona State University,
Tempe, AZ 85287

An investigation is carried out for a class of piecewise linear oscillators with asymmetric characteristics. The damping and restoring forces are general trilinear functions of the system velocity and displacement, respectively, while the excitation is harmonic in time. First, an analysis is presented which determines harmonic and subharmonic steady-state response. Then, a special formulation is employed in examining the stability of located periodic motions. Finally, numerical results are presented for several representative sets of the system parameters. Effects of asymmetries in the response due to unequal gaps as well as unequal stiffness and damping coefficients are analyzed in detail. Asymmetric response of a system with symmetric technical characteristics is also investigated. The behavior of the systems examined resembles response of similar nonlinear systems with continuous characteristics, like the response of the Duffing and van der Pol oscillators. Complicated nonperiodic response is also encountered and analyzed.

Introduction

There are many cases in practice for which various aspects of the behavior of dynamical systems cannot be modeled and explained adequately by employing linear formulations. One special class of systems with nonlinear technical characteristics is represented by oscillators with motion limiting constraints. The practical significance of these oscillators led to a large number of analytical, numerical, and experimental studies on their dynamics. Due to the complexity involved, most of these studies concentrated on harmonically excited single degree-of-freedom systems. Depending on the form of the damping and restoring forces, these investigations can be classified in three general categories. The first category involves oscillators with trilinear restoring forces (e.g., Den Hartog and Heiles, 1936; Klotter, 1953; Nguyen et al., 1986; Natsiavas, 1989). Another category includes oscillators with bilinear stiffness and damping characteristics (e.g., Masri, 1978; Shaw and Holmes, 1983). Finally, a large portion of these studies is devoted to impact oscillators (e.g., Masri and Caughey, 1966; Heiman et al., 1988; Moon and Shaw, 1983; Shaw, 1985; Tung and Shaw, 1988; Karyeaclis and Caughey, 1989).

The objective of the present investigation is to extend the study on piecewise linear oscillators presented by Natsiavas (1989). Oscillators with general asymmetric trilinear restoring and damping forces are examined here. This study is also useful in analyzing asymmetric motions of symmetric systems. A special approach is adopted in determining periodic steady-state solutions and examining their stability characteristics, due to the discontinuities present in the equations of motion. The basic steps of the analysis applied are presented in the next two sections. Then numerical results are presented for several representative cases. These results reveal that for some sets of the parameters the system response is characterized by regular behavior encountered in other classical nonlinear oscillators, like the Duffing and the van der Pol oscillators. Also, for some sets of parameters the system exhibits characteristics of chaotic behavior.

Periodic Steady-State Response

The system examined is a strongly nonlinear single degree-of-freedom oscillator. Figure 1 presents a mechanical model of this system. The dynamic behavior of this oscillator under harmonic forcing is governed by the following equation of motion:

$$m\ddot{x} + g(\dot{x}, x) = f\sin(\omega t + \phi), \tag{1}$$

where ϕ is a phase angle. The damping and restoring forces are expressed by g, which is a general trilinear function of the form:

$$g(\dot{x}, x) = \begin{cases} c_1\dot{x} + k_1x + (k_2 - k_1)x_r, & x > x_r \\ c_2\dot{x} + k_2x, & -x_l \le x \le x_r \\ c_3\dot{x} + k_3x + (k_3 - k_2)x_l, & x < -x_l. \end{cases} \tag{2}$$

The first objective of the present study is to determine periodic steady-state solutions of the above system. The form of

Contributed by the ASME Applied Mechanics Division of THE AMERICAN SOCIETY OF MECHANICAL ENGINEERS for presentation at the Winter Annual Meeting, Atlanta, Ga., Dec. 1-6, 1991.

Discussion on this paper should be addressed to the Technical Editor, Prof. Leon M. Keer, The Technological Institute, Northwestern University, Evanston, IL 60208, and will be accepted until two months after final publication of the paper itself in the JOURNAL OF APPLIED MECHANICS. Manuscript received by the ASME Applied Mechanics Division, Jan. 15, 1990; final revision, Sept. 19, 1990.
Paper No. 91-WA/APM-21.

Copyright © 1992 by ASME
Downloaded 03 May 2010 to 171.66.16.247. Redistribution subject to ASME license or copyright; see http://www.asme.org/terms/Terms_Use.cfm

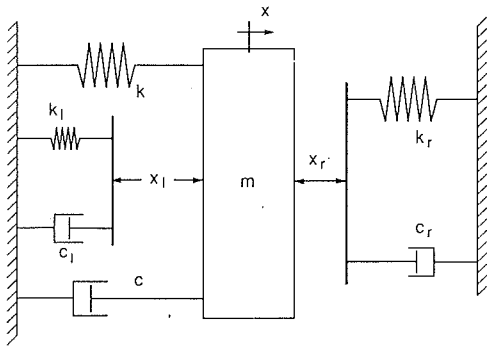


Fig. 1 Mechanical model of system examined

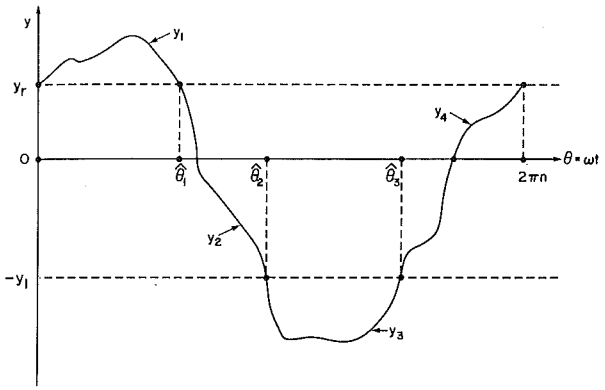


Fig. 2 First response period of solutions sought

the solutions sought is depicted in Fig. 2. The lengths appearing in that figure are normalized by a characteristic length x_c, i.e., $y_l = x_l/x_c$ and $y_r = x_r/x_c$, while the time is normalized by $\theta \equiv \omega t$. Then, $\hat{\theta}_i = \omega t_i$, represents the normalized ith contact time—i.e., when the stiffness and/or damping coefficients change—within the response period of a steady-state solution, with $\hat{\theta}_o = 0$ and $\hat{\theta}_4 = 2\pi n$, for subharmonic response of order n. Consequently, using $\theta_i = \theta - \hat{\theta}_{i-1}$ as the independent variable, the normalized form of the equation of motion in the time interval $0 \le \theta_i \le \theta_{ic} \equiv \hat{\theta}_i - \hat{\theta}_{i-1}$, looks like:

$$\ddot{y}_i + 2\delta_i \dot{y}_i + \omega_i^2 y_i = P \sin(\theta_i + \hat{\phi}_i) + \omega_i^2 f_i,$$

where: $y_i(\theta_i) = x(t - t_{i-1})x_c$, $f_1 = (1 - \omega_2^2/\omega_1^2)y_r$, $f_2 = 0 = f_4$, $f_3 = (\omega_2^2/\omega_3^2 - 1)y_l$, $P = f/(m\omega^2 x_c)$, $\hat{\phi}_i = \phi + \hat{\theta}_{i-1}$, $\overline{\omega}_i = \sqrt{k_i/m}$, $\omega_i = \overline{\omega}_i/\omega$, $\zeta_i = c_i/(2\sqrt{k_i m})$ and $\delta_i = \zeta_i \omega_i$, $(i = 1,2,3,4)$.

Then, the corresponding solution for underdamped oscillators (i.e., $|\zeta_i| < 1$) with non-negative stiffness has the form:

$$y_i(\theta_i) = e^{-\delta_i \theta_i}[A_i \sin(\eta_i \theta_i) + B_i \cos(\eta_i \theta_i)] + P_i \sin(\theta_i + \alpha_i) + f_i, \quad (3)$$

where: $P_i = P/\sqrt{(\omega_i^2 - 1)^2 + 4\delta_i^2}$, $\eta_i = \omega_i^2\sqrt{1 - \zeta_i^2}$, $\alpha_i = \hat{\phi}_i - \phi_i$ and $\tan\phi_i = 2\delta_i/(\omega_i^2 - 1)$.

The unknown constants A_i and B_i $(i = 1,2,3,4)$, ϕ, $\hat{\theta}_1$, $\hat{\theta}_2$ and $\hat{\theta}_3$ can be determined systematically, by imposing the following set of periodicity and matching conditions:

$$y_1(0) = y_1(\theta_{1c}) = y_2(0) = y_4(\theta_{4c}) = y_r \quad (4)\text{–}(7)$$

$$y_2(\theta_{2c}) = y_3(0) = y_3(\theta_{3c}) = y_4(0) = -y_l \quad (8)\text{–}(11)$$

$$\dot{y}_1(0) = \dot{y}_4(\theta_{4c}) \equiv \nu_o,\ \dot{y}_1(\theta_{1c}) = \dot{y}_2(0) \equiv \nu_1 \quad (12), (13)$$

$$\dot{y}_2(\theta_{2c}) = \dot{y}_3(0) \equiv \nu_2,\ \dot{y}_3(\theta_{3c}) = \dot{y}_4(0) \equiv \nu_3. \quad (14), (15)$$

These conditions represent a set of 12 coupled transcendental equations. However, following a procedure similar to that employed by Natsiavas (1989), this set can be reduced to only three equations. Namely, application of (4)–(11) yields the A_i's and B_i's in the following form:

$$A_i = A_{io} + A_{is}\sin\phi + A_{ic}\cos\phi,\ B_i = B_{io} + B_{is}\sin\phi + B_{ic}\cos\phi,$$

while use of the above and application of (12)–(15) results in four equations of the form:

$$E_{io} + E_{is}\sin\phi + E_{ic}\cos\phi = 0.$$

The A_{ij}'s, B_{ij}'s, and E_{ij}'s appearing in the foregoing equations are functions of the system parameters and the contact times only. Then, combining the last four equations with the trigonometric identity $\cos^2\phi + \sin^2\phi = 1$ leads to three equations involving $\hat{\theta}_1$, $\hat{\theta}_2$ and $\hat{\theta}_3$ only. Numerical solution of these equations determines the contact times, while the other variables are determined by simple back substitution.

Stability of Steady-State Solutions

The stability analysis of located periodic solutions is performed according to the method employed by Natsiavas (1989). This method examines the time propagation of an error introduced in the initial conditions of a located steady-state solution. For example, in order to illustrate the basic steps of the procedure, let $y_1(\theta_1)$ be the first branch of a periodic solution in $0 \le \theta_1 \le \theta_{1c}$ (Fig. 2), satisfying the initial conditions:

$$y_1(0) = y_r \text{ and } \dot{y}_1(0) = \nu_o.$$

Next, arbitrary perturbations are introduced in these initial conditions by letting $\bar{\theta}_1 = \theta_1 - \Delta\theta_o$ and $\bar{y}_1(\bar{\theta}_1)$ be another solution with:

$$\bar{y}_1(0) = y_r \text{ and } \dot{\bar{y}}_1(0) = \nu_o + \Delta\nu_o,$$

where Δ indicates a perturbation of the variable it is applied on. The propagation of the error introduced in the initial conditions is examined by using the equations describing the time response of the system. For example, the solution resulting from the perturbed initial conditions will be:

$$\bar{y}_1(\bar{\theta}_1) = e^{-\delta_1\bar{\theta}_1}[G_1 \sin(\eta_1\bar{\theta}_1) + H_1 \cos(\eta_1\,\bar{\theta}_1)] + P_1 \sin(\bar{\theta}_1 + \Delta\theta_o + \alpha_1) + f_1, \quad (16)$$

where the coefficients G_1 and H_1 are obtained by Taylor expanding A_1 and B_1, respectively, with respect to the error quantities $\Delta\theta_o$ and $\Delta\nu_o$. Next, assume that the perturbed solution $\bar{y}_1$ will take the value y_r at a time equal to $\theta_{1c} + \Delta\theta_1$, i.e.,

$$\bar{y}_1(\theta_{1c} + \Delta\theta_1 - \Delta\theta_o) = y_r. \quad (17)$$

At the same time instance, the corresponding velocity will be:

$$\dot{\bar{y}}_1(\theta_{1c} + \Delta\theta_1 - \Delta\theta_o) = \nu_1 + \Delta\nu_1. \quad (18)$$

Using (16) in applying (17) and (18), expanding the resulting equations in Taylor series and setting the first-order terms in matrix form gives:

$$\epsilon_1 \equiv [\Delta\theta_1\ \Delta\nu_1]^T = R_1\epsilon_o.$$

The zero-order terms of the above equation cancel out because they satisfy the periodicity conditions (5) and (13), while the elements of the matrix R_1 are determined as functions of the system parameters (Gonzalez, 1989).

The above steps can be applied in exactly the same manner for the following three branches of the solution (Fig. 2). Then the error at the end of the first response period will be related to the original perturbation ϵ_p to first order by:

$$\epsilon_4 = \Pi\epsilon_o \equiv (R_4 \cdots R_1)\epsilon_o. \quad (19)$$

Similarly, the perturbations of the initial conditions after $m \times n$ forcing cycles will be related to the initial perturbations to first order by:

$$\epsilon_{4m} = \Pi^m\epsilon_o.$$

Therefore, if λ is the eigenvalue of Π with the largest modulus, the original error will vanish eventually and the solution examined will be asymptotically stable provided that $|\lambda| < 1$. For the cases with $|\lambda| > 1$, the original error will grow in time rendering the corresponding solution unstable.

Downloaded 03 May 2010 to 171.66.16.247. Redistribution subject to ASME license or copyright; see http://www.asme.org/terms/Terms_Use.cfm

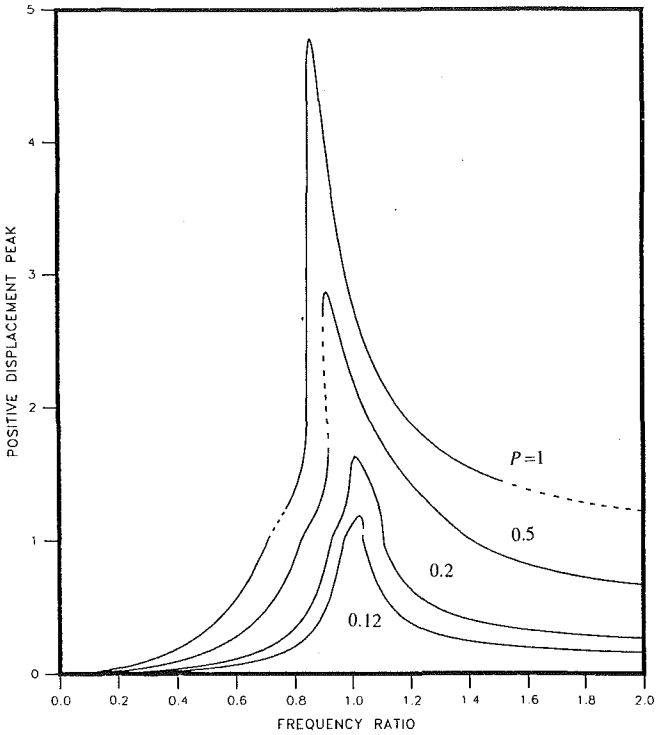


Fig. 3 Response diagram of systems with mixed hardening/softening characteristics ($\zeta_1 = \zeta_2 = \zeta_3 = 0.05$)

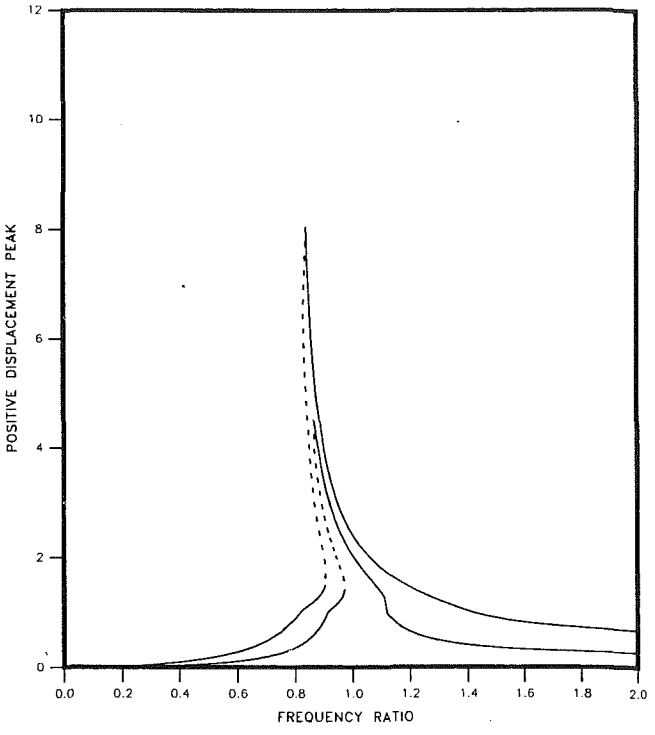


Fig. 4 Response diagram of system with mixed hardening/softening characteristics ($\zeta_1 = \zeta_2 = \zeta_3 = 0.01$, $P = 0.02$ and 0.05)

Some combinations of the system parameters lead to $|\lambda| = 1$, which results in bifurcations, indicating qualitative changes in the system response (Guckenheimer and Holmes, 1983). In these cases, the foregoing analysis is not sufficient to determine the stability of the resulting motions. Higher-order terms need to be kept when Taylor expanding equations like (17) and (18), in deriving (19). It is briefly mentioned here that cases with $\lambda = -1$ result in flip or period doubling bifurcations, while $\lambda = +1$ give rise to three different types of saddle-node bifurcations. Finally, bifurcations with complex λ are known as Hopf bifurcations. Changes in the response associated with these bifurcations are explained in the next section.

It is worth pointing out that calculation of the determinant of the matrix R_i (Natsiavas, 1990) leads to:

$$|R_i| = \frac{\nu_{i-1}}{\nu_i} e^{-2\delta_i \hat{\theta}_i},$$

while straightforward calculation of the determinant of Π yields:

$$|\Pi| = e^{-2\sum_{i=1}^{4} \delta_i \hat{\theta}_i}.$$

Since the $\hat{\theta}_i$'s are positive scalars, the last relation shows that if all the damping coefficients are positive, then $|\Pi| < 1$, excluding the Hopf bifurcations.

Numerical Examples

This section presents results obtained by applying the above analysis for several representative cases. The solutions obtained are acceptable if they are of the form depicted in Fig. 2. When the amplitude of oscillation is less than the minimum value of y_l and y_r, the system behaves as a linear oscillator.

Oscillators With Asymmetric Stiffness and Damping Coefficients. Figure 3 shows the response diagram for a trilinear oscillator with stiffness parameters $k_1/k_2 = 4$, $k_3/k_2 = 0.25$, damping ratios $\zeta_1 = \zeta_2 = \zeta_3 = 0.05$, gap sizes $y_r = y_l = 1$ and four different levels of forcing, i.e., $P = 0.12$, 0.2, 0.5, and 1. These parameters are chosen so that the right constraint causes a hardening, while the left constraint causes a softening of the original stiffness of the oscillating mass. As a result, the case with $P = 0.12$ is found to exhibit behavior characterizing the response of classical hardening systems, with a small branch of unstable solutions for forcing frequency values $\bar{\omega} \equiv \omega/\bar{\omega}_2 > 1$. The system with $P = 0.5$ presents characteristics of softening oscillators while $P = 0.2$ results in mixed behavior. All the bifurcations occurring for the last three forcing values are of saddle-node type ($\lambda = 1$), resulting in jump phenomena.

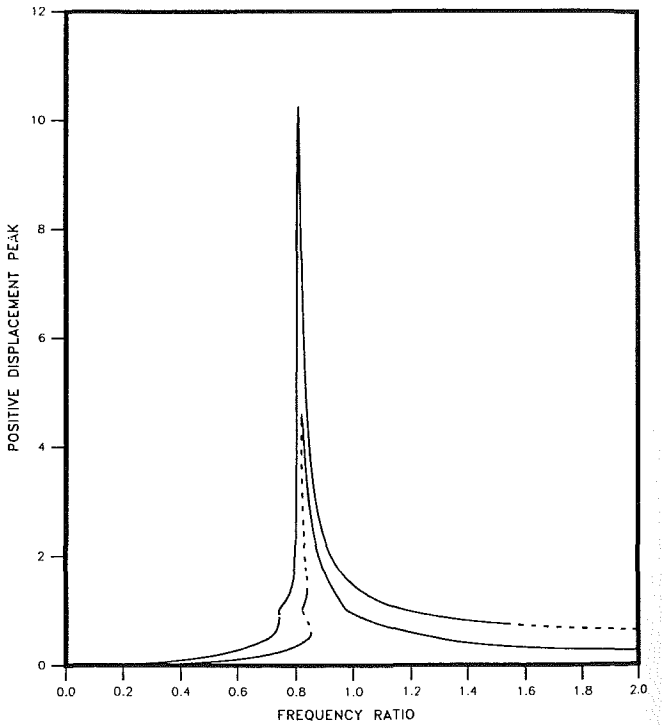


Fig. 5 Response diagram of systems with asymmetric gaps ($y_l = 0.5$, $y_r = 1$, $P = 0.2$ and 0.5)

Downloaded 03 May 2010 to 171.66.16.247. Redistribution subject to ASME license or copyright; see http://www.asme.org/terms/Terms_Use.cfm

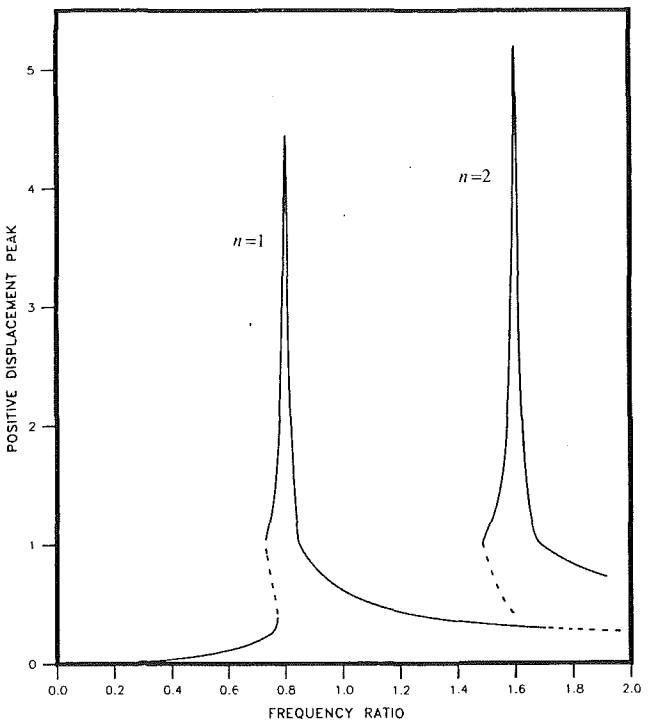


Fig. 6 Response diagram of harmonic and subharmonic solutions ($P = 0.2$)

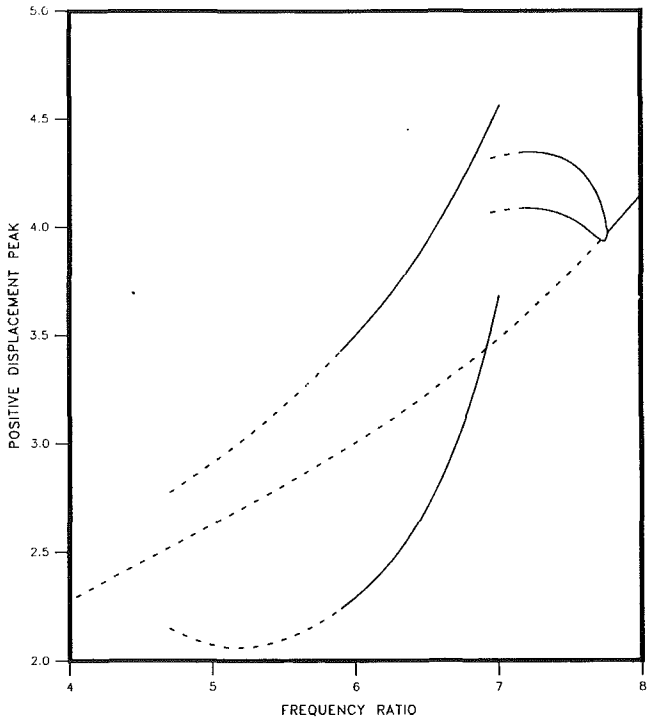


Fig. 7 Response diagram of a symmetric oscillator ($\omega_1/\omega_2 = \omega_3/\omega_4 = 16.25$) in $4 \leq \bar{\omega} \leq 8$

For $P = 1$, the maximum amplitude is about five times larger than the gap sizes. As a consequence, the system tends to behave like a bilinear oscillator with no gap. This is indicated here by the fact that, as the forcing is increased, the system resonance shifts gradually to $\bar{\omega} = 0.8$, which is the "natural" frequency for the oscillators examined. For $P = 1$, the two unstable branches present are generated through period doubling ($\lambda = -1$) bifurcations. It is noted that the unstable solution branch on the right recovers stability at $\bar{\omega} = 2.75$, with $\lambda = -1$.

In order to illustrate effects of the damping parameters, Fig. 4 presents the response diagram of the same system, for $P = 0.2$ and 0.5, but with damping coefficients reduced to 0.01.

Oscillators With Asymmetric Gaps. In the next example, the system examined has the same stiffness and damping parameters as the last example, but the left gap is now reduced to $y_l = 0.5$. Figure 5 shows the response diagram for forcing levels $P = 0.2$ and 0.5. Once again, mixed hardening/softening characteristics are present in the dynamic behavior of the same oscillator. For $P = 0.2$, this behavior results in forcing frequency values where five solutions are possible, three of which are stable. Finally, comparison with Fig. 4 reveals that the displacement amplitudes are higher for the cases with smaller gap size.

Figure 6 illustrates the effects of reducing the left gap size to $y_l = 0.25$, for the case where $P = 0.2$. This further reduction affects the response amplitude of the $n = 1$ solutions slightly, but changes the stability of one unstable solution branch. The bifurcations near primary resonance happen with $\lambda = 1$, while the bifurcation at $\bar{\omega} = 1.71$ occurs with $\lambda = -1$. However, the $n = 2$ branch shown in Fig. 6, which has the same form as the $n = 1$ solution branch, seems to arise independently of the $n = 1$ branch.

Asymmetric Response of a Symmetric Oscillator. The objective of the following example is to present information for a symmetric oscillator examined before. Namely, numerical integration of an oscillator with parameters $\omega_1/\omega_2 = \omega_3/\omega_2 = 16.25$, $\zeta_1 = \zeta_3 = 0.04$, $\zeta_2 = 0.75$, and $P = 7.036$ resulted in

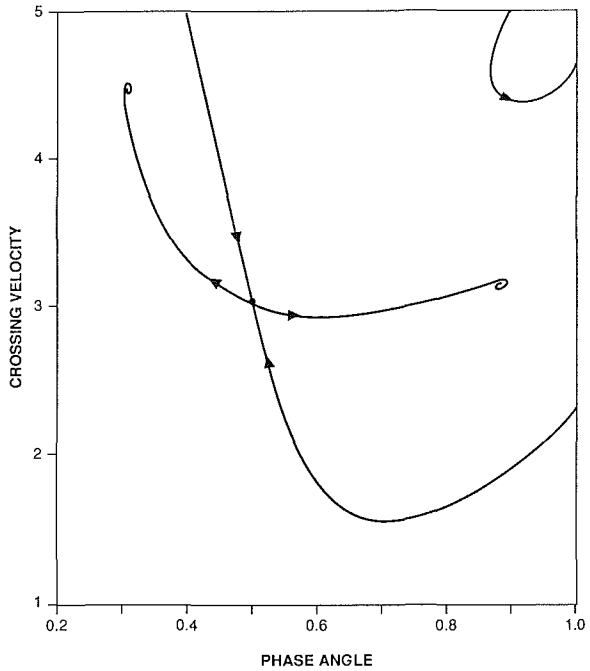


Fig. 8 Phase portrait at $\bar{\omega} = 7.6$

irregular behavior (Natsiavas and Babcock, 1988) for forcing frequencies around $\bar{\omega} = 5$.

Figure 7 shows the response diagram obtained for this system, in the range $4 \leq \bar{\omega} \leq 8$. The symmetric motions become unstable for $\bar{\omega} < 7.7$. At that frequency point, a pitchfork bifurcation ($\lambda = 1$) occurs and results in the appearance of pairs of antisymmetric stable solutions, represented by the two solution branches emanating from the bifurcation frequency $\bar{\omega} = 7.7$. Figure 8 shows the phase portrait of the fixed points corresponding to the periodic solutions at $\bar{\omega} = 7.6$. At this frequency, the eigenvalues of Π corresponding to the two stable

Downloaded 03 May 2010 to 171.66.16.247. Redistribution subject to ASME license or copyright; see http://www.asme.org/terms/Terms_Use.cfm

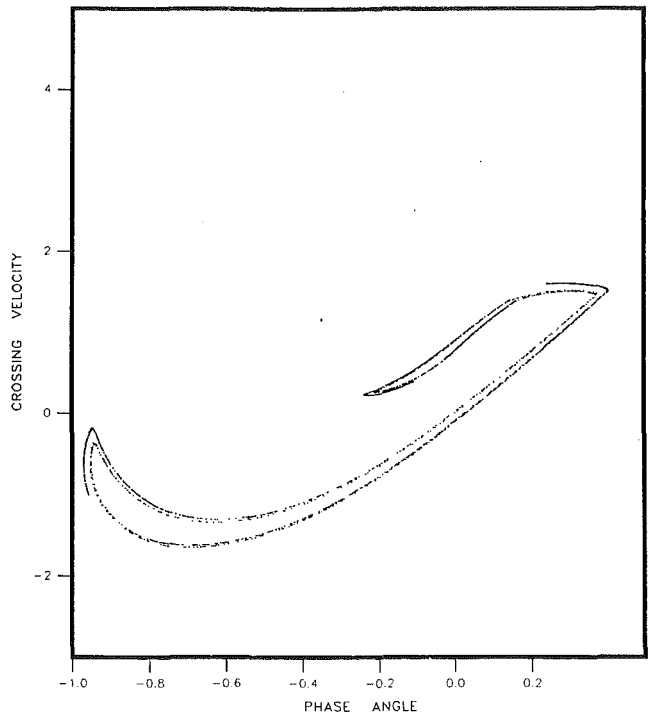


Fig. 9 Poincaré plot at $\bar{\omega}=5$

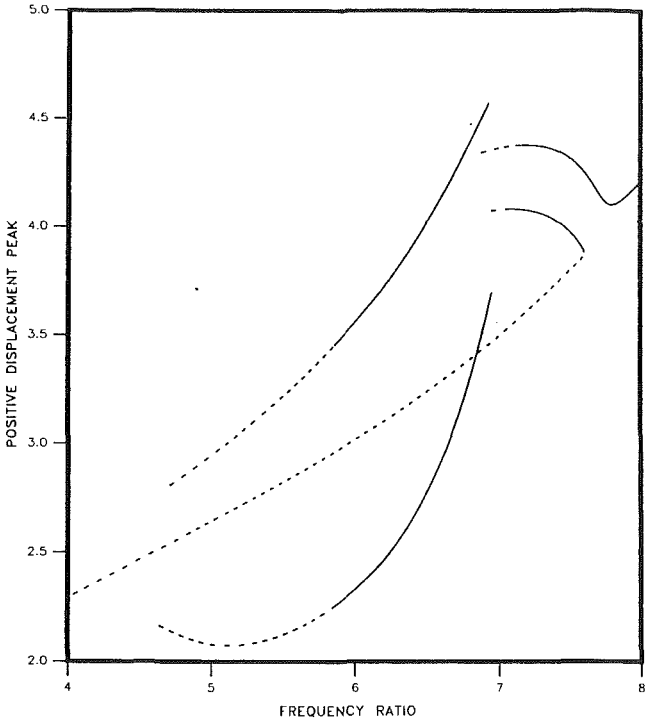


Fig. 11 Response diagram of a slightly asymmetric system ($\omega_1/\omega_2=16$)

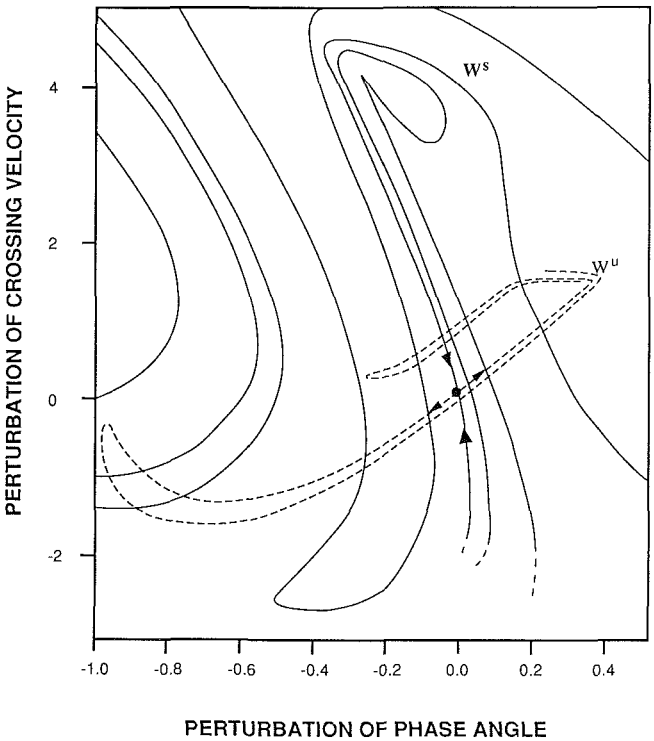


Fig. 10 Manifolds of symmetric solution at $\bar{\omega}=5$

antisymmetric solutions are already complex and the nodes appearing originally have become focii. Eventually these antisymmetric solutions loose stability at $\bar{\omega}=7.14$ through a flip bifurcation.

Similar behavior is exhibited by the other pair of asymmetric solutions, shown in Fig. 7. In this case, the original $\lambda=-1$ bifurcation at $\bar{\omega}=5.89$ is actually found to be followed by a sequence of such bifurcations. For example, $n=1$, 2, 4, and 8 solutions were obtained at $\bar{\omega}=5.90$, 5.85, 5.75, and 5.71, respectively. Eventually, this sequence leads to chaotic response. Figure 9 shows a Poincaré section at $\bar{\omega}=5$. This plot is constructed by sampling every time where $y=1$ and the velocity is positive, between 8000 and 10,000 forcing cycles. Figure 10 shows the stable (W^s) and unstable (W^u) invariant manifolds of the saddle corresponding to the symmetric solution at $\bar{\omega}=5$. Comparison with Fig. 9 shows that the Poincaré plot is similar to the unstable manifold (e.g., Guckenheimer and Holmes, 1983). The stable and unstable manifolds intersect transversely resulting in homoclinic oscillations which is a necessary condition for the appearance of chaotic response.

Finally, it is noted that the "isolated" asymmetric branches of Fig. 7 continue to exist for $\bar{\omega}>7.01$. This was verified by direct integration which showed that those solutions are characterized by multiple (more than three) contacts.

A "Slightly" Asymmetric Oscillator. In the next example, a slight asymmetry is introduced in the form of the restoring force of the previous oscillator by changing the value of ω_1/ω_2 to 16. This results in virtually no change of the response diagram, except near the frequency where the pitchfork bifurcation took place in the previous example. In this case, the two extra solutions below $\bar{\omega}=7.7$ are generated through a saddle-node bifurcation instead, as shown in Fig. 11.

Oscillators With Asymmetric van der Pol-Type Damping. Oscillators with linear restoring force ($k_1/k_2=k_3/k_2=1$) and negative damping ratio ζ_2 are examined next. Figure 12 shows the response diagram for a system with equal gaps $y_r=y_l=1$, forcing parameter $\beta=f/(k_2x_c)=0.0201$, $\zeta_2=-0.01$, $\zeta_3=0.01$, and three different values of ζ_1, i.e., 0.01 (symmetric case), 0.02, and 0.20. The detuning parameter is defined by $\sigma\equiv(\bar{\omega}-1)(2|\zeta_2|)$. The response of these systems resembles behavior similar to that exhibited by the classical van der Pol oscillator (e.g., Nayfeh and Mook, 1979). The response diagrams are symmetric with respect to $\sigma=0$, except for a slight asymmetry for $\zeta_1=0.2$, while all the bifurcations happen with $\lambda=1$.

An Oscillator with Mixed Duffing/van der Pol-Type Characteristics. In the last example, the oscillator examined is characterized by $k_1/k_2=4$, $k_3/k_2=0.25$, $\zeta_1=-\zeta_2=\zeta_3=0.05$,

Downloaded 03 May 2010 to 171.66.16.247. Redistribution subject to ASME license or copyright; see http://www.asme.org/terms/Terms_Use.cfm

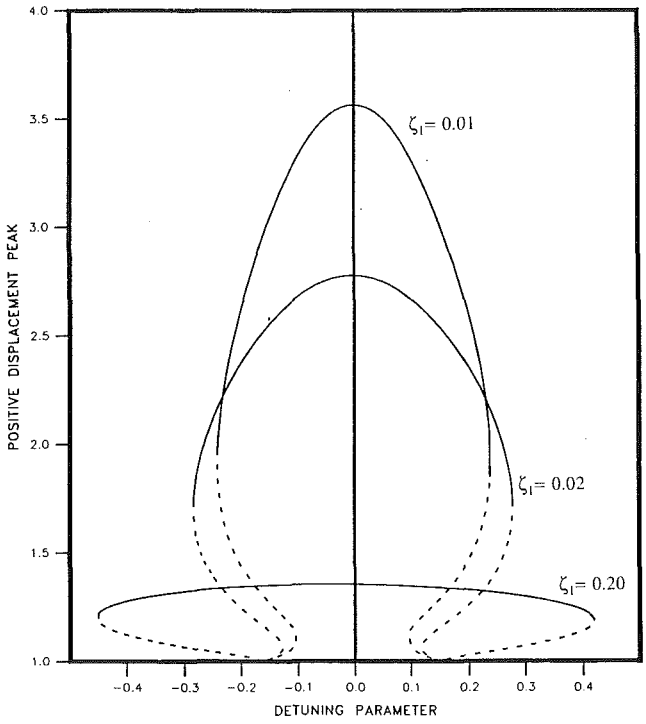


Fig. 12 Response diagram of oscillators with $\zeta_2 = -0.01$ ($\beta = 0.0201$)

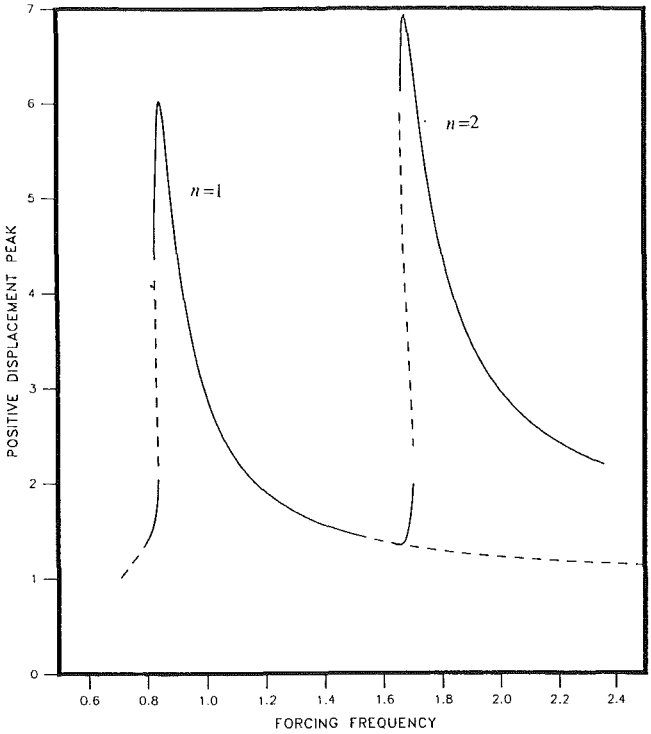


Fig. 13 Response diagram of an oscillator with mixed duffing/van der Pol-type characteristics ($P = 1$)

and $y_l = y_r = 1$. These parameters are the same as those of the first example, but here $\zeta_2 < 0$. Figure 13 presents the response diagram of the $n = 1$ and 2 solutions obtained for $P = 1$. The subharmonic branch has again the same form as the $n = 1$ branch. Comparison with Fig. 3 reveals that the harmonic solutions in the present case have larger amplitudes than the corresponding solutions for $\zeta_2 > 0$. Another difference lies in the types of the bifurcations that take place. Here, the left $n = 1$ unstable branch gains stability at $\bar{\omega} = 0.805$, through a Hopf bifurcation. The middle unstable branch appears and disappears through a saddle-node bifurcation, while the right unstable branch appears after a period-doubling bifurcation.

The behavior of the above system for frequency values below the one that gives rise to Hopf bifurcation (i.e., for $\bar{\omega} < 0.805$) was investigated further by performing direct numerical integration. Figure 14 shows the Poincaré plot at $\bar{\omega} = 0.804$. The points between 9000 and 10,000 forcing cycles are plotted and the resulting invariant circle indicates that the response is quasi-periodic. Reducing $\bar{\omega}$ below 0.804 results in intervals with apparently chaotic response while further reduction of $\bar{\omega}$ results in a gradual smoothening of the Poincaré plots and the reappearance of quasi-periodic response. These changes in the response, as $\bar{\omega}$ is varied away from the Hopf bifurcation value, are in agreement with results presented by Aronson et al. (1982).

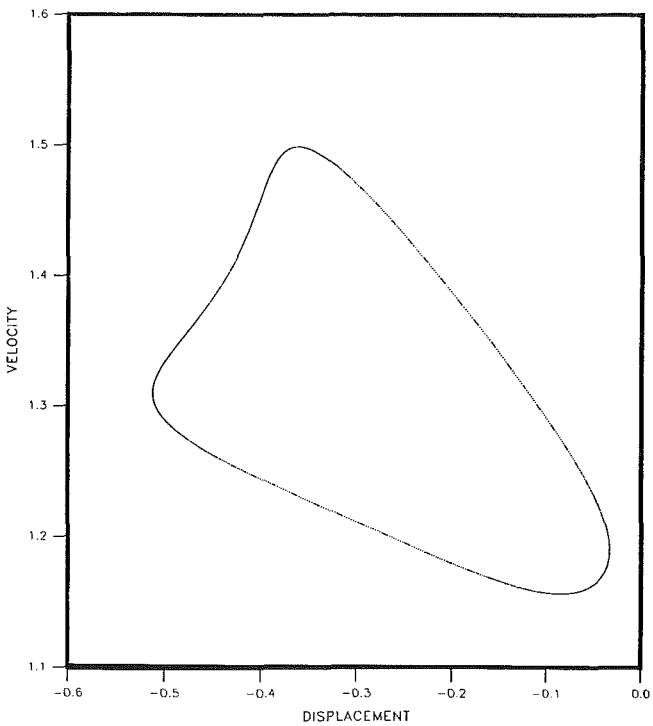


Fig. 14 Poincaré plot at $\bar{\omega} = 0.804$

Summary and Conclusions

The first part of this investigation presents an analysis for determining exact, periodic, steady-state response of harmonically excited trilinear oscillators with general asymmetric characteristics. The asymmetry appears in the damping and stiffness coefficients, as well as in the distance of the left and right constraint from the equilibrium position of the oscillating mass of the system. Harmonic and subharmonic motions are analyzed. These motions are characterized by three sudden changes of the stiffness and/or damping parameters within the duration of a response cycle. The stability and bifurcation characteristics of the located periodic solutions are also investigated by employing a formulation which is suitable for piecewise linear oscillators.

The second part of the present work presents numerical results for six different categories of asymmetric oscillators. Effects from asymmetries in the restoring an damping forces, including the gap sizes are first analyzed. The oscillators examined are shown to exhibit behavior with characteristics similar to those observed in hardening and/or stiffening Duffing-type systems. Then, symmetric and asymmetric response of an oscillator with symmetric technical characteristics is examined.

Downloaded 03 May 2010 to 171.66.16.247. Redistribution subject to ASME license or copyright; see http://www.asme.org/terms/Terms_Use.cfm

For some combinations of parameters, this system is shown to undergo a cascade of flip bifurcations leading to chaotic response. The effect of introducing a slight asymmetry in the stiffness parameters of that system is also analyzed. Finally, systems with combinations of positive and negative damping coefficients are analyzed. These systems are shown to exhibit characteristics similar to the classical van der Pol oscillator. In this last case, Hopf bifurcations are possible, leading to loss of stability of periodic solutions and the appearance of beating and chaotic response.

References

Aronson, D. G., Chory, M. A., Hall, G. R., and McGehee, R. P., 1982, "Bifurcations from an Invariant Circle for Two-Parameter Families of Maps of the Plane: A Computer Assisted Study," *Commun. Math. Physics*, Vol. 83, pp. 303–354.

Den Hartog, J. P., and Heiles, R. M., 1936, "Forced Vibration in Nonlinear Systems with Various Combinations of Linear Springs," ASME JOURNAL OF APPLIED MECHANICS, Vol. 58, pp. 127–130.

Gonzalez, H., 1989, "Steady-State Response of Asymmetric Trilinear Oscillators," M. S. Thesis, Arizona State University, Tempe, Ariz.

Guckenheimer, J., and Holmes, P., 1983, *Nonlinear Oscillations, Dynamical Systems and Bifurcations of Vector Fields*, Springer-Verlag, New York.

Heiman, M. S., Bajaj, A. K., and Sherman, P. J., 1988, "Periodic Motions and Bifurcations in Dynamics of an Inclined Impact Pair," *J. of Sound and Vibration*, Vol. 124, pp. 55–78.

Karyeaclis, M., and Caughey, T. K., 1989, "Stability of a Semi-Active Impact Damper," Parts 1 and 2, ASME JOURNAL OF APPLIED MECHANICS, Vol. 56, pp. 453–464.

Klotter, K., 1953, "Steady-State Vibrations in Systems Having Arbitrary Restoring and Damping Forces," *Symposium on Nonlinear Circuit Analysis*, New York, pp. 234–257.

Masri, S. F., and Caughey, T. K., 1966, "On the Stability of the Impact Damper," ASME JOURNAL OF APPLIED MECHANICS, Vol. 33, pp. 586–592.

Masri, S. F., 1978, "Analytical and Experimental Studies of a Dynamic System with a Gap," *J. of Mechanical Design*, Vol. 100, pp. 480–486.

Moon, F. C., and Shaw, S. W., 1983, "Chaotic Vibrations of a Beam with Non-Linear Boundary Conditions," *Intl. J. of Non-Linear Mechanics*, Vol. 18, pp. 465–477.

Natsiavas, S., and Babcock, C. D., 1988, "Behavior of Unanchored Fluid-Filled Tanks Subjected to Ground Excitation," ASME JOURNAL OF APPLIED MECHANICS, Vol. 55, pp. 654–659.

Natsiavas, S., 1989, "Periodic Response and Stability of Oscillators with Symmetric Trilinear Restoring Force," *J. of Sound and Vibration*, Vol. 134, pp. 315–331.

Natsiavas, S., 1990, "Stability and Bifurcation Analysis for Oscillators with Motion Limiting Constraints," *J. of Sound and Vibration*, Vol. 141, pp. 907–1002.

Nayfeh, A. H., and Mook, D. T., 1979, *Nonlinear Oscillations*, John Wiley and Sons, New York.

Nguyen, D. T., Noah, S. T., and Kettleborough, C. F., 1986, "Impact Behavior of an Oscillator With Limiting Stops," Parts I and II, *J. of Sound and Vibration*, Vol. 109, pp. 293–307.

Shaw, S. W., and Holmes, P. J., 1983, "A Periodically Forced Piecewise Linear Oscillator," *J. of Sound and Vibration*, Vol. 90, pp. 129–155.

Shaw, S. W., 1985, "The Dynamics of a Harmonically Excited System Having Rigid Amplitude Constraints," Parts 1 and 2, ASME JOURNAL OF APPLIED MECHANICS, Vol. 52, pp. 453–464.

Tung, P. C., and Shaw, S. W., 1988, "The Dynamics of an Impact Print Hammer," *J. of Vibration, Acoustics, Stress and Reliability in Design*, Vol. 110, pp. 193–200.

Downloaded 03 May 2010 to 171.66.16.247. Redistribution subject to ASME license or copyright; see http://www.asme.org/terms/Terms_Use.cfm

Weakly Nonlinear Instability of a Liquid Jet in a Viscous Gas

E. A. Ibrahim
Mechanical Engineering Department,
Tuskegee University,
Tuskegee, AL
Mem. ASME

S. P. Lin
Department of Mechanical and
Aeronautical Engineering,
Clarkson University,
Potsdam, NY
Mem. ASME

The weakly nonlinear instability of a viscous liquid jet emanated into a viscous gas contained in a coaxial vertical circular pipe is investigated as an initial-value problem. The linear stability theory predicted that the jet may become unstable either due to capillary pinching or due to interfacial stress fluctuation. The results of nonlinear stability analysis shows no tendency of supercritical stability for both of the linearly unstable modes. In fact, the nonlinear growth rate of the disturbance is faster than the exponential growth rate of the linear normal mode disturbance for the same flow parameters. Moreover, the most amplified linear normal mode disturbance evolves nonlinearly into a nonsinusoidal wave of shorter wavelength. No nonlinear instability is found for the linearly stable disturbances. Thus, while the linear theory is adequate for the prediction of the onset of jet breakup, nonlinear theory is required to describe the outcome of the jet breakup.

Introduction

A computational investigation of the stability of cylinderical jets is undertaken as an attempt to understand the atomization phenomena of liquid jets. These phenomena occur in many applications such as the liquid fuel injection in internal combustion engines, spray coatings of surfaces, forming submicron solid particles, and in various printing devices.

For many purposes, the linear theory adequately describes the salient features of the jet instability; for example, it accurately predicts the small amplitude growth rate of a sinusoidal disturbance. However, it is a common observation that the wave form of an initially sinusoidal perturbation becomes nonsinusoidal close to the point of drop formation, i.e., the point at which the surface wave amplitude equals the radius of the jet (in capillary instability). In order to explain this phenomena, much work has been done on the nonlinear capillary instability of liquid jets. Wang (1968) investigated the effect of a finite amplitude on a circular column of inviscid liquid with a third-order perturbation approach but points out that this solution is not uniformly valid for all wave numbers. Yuen (1968) also used the perturbation approach to third order, but his choice for the third-order term gives rise to a secular term whose elimination leads to a small amplitude-dependent shift in the cutoff wave number. Yuen (1968) concluded that the asymmetrical development of an initially sinusoidal wave is a nonlinear effect with generation of higher harmonics as well as feedback into the fundamental. Nayfeh (1970) pointed out that Yuen's analysis is valid to second order, but that his third-order term is incorrect for wave numbers close to the cutoff wave number. A comparison between an experimental wave profile and one calculated using Yuen's formulation was made by Rutland and Jameson (1970); however, it was for relatively large displacements and showed only qualitative agreement. Lafrance (1975) used a drop spectrometer to measure the size of the main and satellite drops as a function of the perturbation frequency. He compared these to sizes calculated from a modified version of Yuen's analysis and found good agreement which is surprising since, in principle, the theory is invalid in the region where drops are being formed. Chaudhary (1977) indicated that Lafrance's analysis couldn't satisfy its own initial conditions, and Lafrance's multiple-time scale failed in the third-order problem. Consequently, Chaudhary and Redekopp (1980a) and Chaudhary and Maxworthy (1980b) used a comparable model and performed experiments on the jet behaviors and satellite drop formation. With a third-order component in the disturbance, Chaudhary et al. (1977, 1980a, 1980b) were able to control experimentally the satellite behaviors, but his theory didn't agree with his experiment. Lee (1974) derived a pair of nonlinear one-dimensional equations for the jet radius and its axial velocity. He further solved his one-dimensional equations numerically for the infinite jet problem and obtained main drops and satellite drops. Bogy (1978a, 1978b, 1979) expanded the Cosserat theory of Green (1976) to develop a new analytical model for higher harmonics based on spatial and temporal instability. The theory is capable of describing the satellite drop behavior. The numerical investigation of Shokoohi and Elrod (1987) by using the vorticity-stream function method shows that the nonlinear terms are responsible for the nonuniformity of the size of drops produced in jet disintegration. The computations were limited to a low Reynolds number by numerical stability considerations and a computational time requirement. Phinney (1972) carried out experiments that lead him to support the conjecture that the

Contributed by the Applied Mechanics Division of THE AMERICAN SOCIETY OF MECHANICAL ENGINEERS for presentation at the Winter Annual Meeting, Atlanta, Ga., Dec. 1-6, 1991.

Discussion on this paper should be addressed to the Technical Editor, Prof. Leon M. Keer, The Technological Institute, Northwestern University, Evanston, IL 60208, and will be accepted until two months after final publication of the paper itself in the JOURNAL OF APPLIED MECHANICS. Manuscript received by the ASME Applied Mechanics Division, July 26, 1990; final revision, Mar. 15, 1991.

Paper No. 91-WA/APM-15.

Copyright © 1992 by ASME
Downloaded 03 May 2010 to 171.66.16.247. Redistribution subject to ASME license or copyright; see http://www.asme.org/terms/Terms_Use.cfm

theory and understanding that were developed in connection with the breakup of laminar jets can be used as a guide for turbulent jets as well.

The nonlinear studies cited in the previous paragraph are relevant to the ink jet breakup. By use of linear theory of convective instability Lin and Lian (1990) showed that there are two physically distinctive modes of jet breakup. The first is the Rayleigh mode which produces drops of diameters comparable with the jet diameter. The second is the Taylor mode which atomizes the jet into droplets of diameters much smaller than the jet diameter. Lin and Creighton (1990) showed that the former mode is caused by capillary pinching, but the latter mode is caused by the interfacial pressure fluctuation.

To the best knowledge of the present authors, this investigation is the first nonlinear analysis of the jet breakup in the atomization regime taking into account the viscosities of the liquid jet and the ambient gas as well as the gravitational force.

Analysis

We shall resort to the application of the nonlinear theory of hydrodynamic stability in which disturbances are superimposed upon a stationary flow field. These disturbances are time dependent, and it is the aim of the theory to look for disturbances whose amplitude increases, decreases, or does not vary with time. Disturbances of the first type we shall call unstable, whereas those of the second or third type will be called stable. We shall focus our attention on disturbances of wave form that repeats itself every wavelength. Such an analysis is called a temporal stability analysis, as opposed to a spatial stability analysis where wave forms repeat themselves periodically in time. Temporal stability analysis is adequate for an infinitely long jet compared to the jet radius, while a spatial stability analysis is adequate for a finite jet. Keller et al. (1973) have shown, in a linear analysis, that the growth rate for these two cases coincide when the jet velocity is much greater than the characteristic velocity $\sigma/(\rho_1 R)$. The approach we follow is similar to that of Lin and Ibrahim (1990).

Consider the circular liquid jet of radius R that is issued into a viscous gas bounded by a cylinderical wall at a distance S from the jet axis as shown in Fig. 1. Both the liquid and gas are assumed to be incompressible and Newtonian. The onset of ligament formation and its subsequent breakup into droplets are governed by the continuity and Navier-Stokes equations of the two-dimensional disturbed flow which can be written in dimensionless form as

$$(U+u)_{ir}+(U+u)_i/r+(W+w)_{iz}=0 \quad (i=1,2) \tag{1}$$

$$(U+u)_{it}+(U+u)_i(U+u)_{ir}+(W+w)_i(U+u)_{iz} = -(\rho_1/\rho_i)(P+p)_{ir}+\nu_i/(\nu_1 \mathrm{Re})[(U+u)_{irr} +(U+u)_{ir}/r+(U+u)_{izz}-(U+u)_i/r^2] \tag{2}$$

$$(W+w)_{it}+(U+u)_i(W+w)_{ir}+(W+w)_i(W+w)_{iz} = -(\rho_1/\rho_i)(P+p)_{iz}-Fr^{-1}+(\nu_i/\nu_1 \mathrm{Re})[(W+w)_{irr} +(W+w)_{ir}/r+(W+w)_{izz}] \tag{3}$$

where U and W are, respectively, the radial and axial velocities of the undisturbed flow, u and w are, respectively, the radial and axial velocities of the disturbance, and P and p are, respectively, the undisturbed flow and the disturbance pressures. Subscript 1 is for liquid and 2 is for gas. Subscripts t, r, and z stand for partial differentiations with respect to time, radial distance, and axial distance, respectively. Re is the Reynolds number based on the liquid properties, $\mathrm{Re} = W_0 R/\nu_1$, where W_0 is the axial velocity along the jet axis, R is the jet radius, and ν_1 is the liquid kinematic viscosity. Fr is the Froude number, $\mathrm{Fr} = W_1^2/(gR)$, where g is the gravitational acceleration. All lengths are made nondimensional by the jet radius R. Velocities are made dimensionless by dividing by W_0. Time is made dimensionless by R/W_0. The pressure is made dimensionless by dividing by $\rho_1 W_0^2$, where ρ_1 is the liquid density.

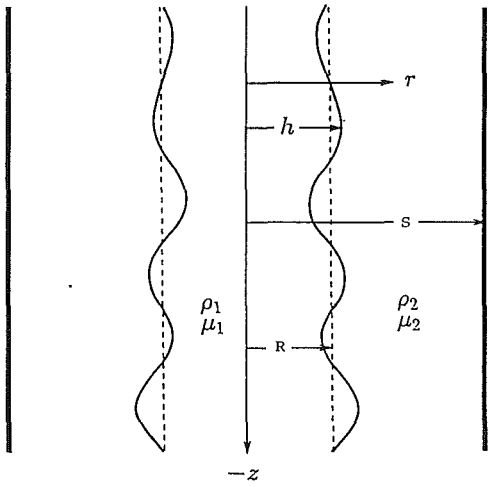


Fig. 1 Definition sketch

The continuity and Navier-Stokes equations of the undisturbed (basic) flow are given by

$$W_{iz}=0 \tag{4}$$

$$U_i=0, \quad P_{ir}=0 \tag{5}$$

$$0=-(\rho_1/\rho_i)P_{iz}-\mathrm{Fr}^{-1}+\nu_i/(\nu_1 \mathrm{Re})(W_{irr}+W_{ir}/r). \tag{6}$$

Note that $W_{it}=0$ because the basic flow is steady. W_{iz} and W_{izz} both vanish by virtue of the continuity equation which also leads to the conclusion that W_i is a function of radial distance alone.

Substitution from the governing equations of the basic flow into the equations, which govern the disturbed flow, and eliminating the pressure by cross differentiation yield;

$$[\partial_t-\nu_i/(\nu_1 \mathrm{Re})E^2]E^2\psi_i+W_iE^2\psi_{iz}-r\psi_{iz}(W_i/r)_r = r[\psi_{ir}r^{-2}E^2\psi_{iz}-\psi_{iz}(r^{-2}E^2\psi_i)_r] \tag{7}$$

where ψ is the dimensionless disturbance stream function defined as,

$$u_i=\psi_{iz}/r, \; w_i=-\psi_{ir}/r \text{ and } E^2=\partial_{rr}-(1/r)\partial_r+\partial_{zz}.$$

The solution of the basic state equations subject to the boundary conditions,

$W_1(0)=-1$	(finite velocity along the jet axis)
$W_2(\beta)=0$	(no-slip velocity at the wall)
$W_1(1)=W_2(1)$	(velocity continuity at the interface)
$W_{1r}(1)=NW_{2r}(1)$	(tangential force balance at the interface)
$(P_1-P_2)=\mathrm{We}$	(normal force balance at the interface)

is given by Ibrahim (1989) as

$$W_1=-1+Nr^2/[N-(1-\beta^2)]\{1-[(1-Q)/(4N)] \times(\mathrm{Re/Fr})[2\ln\beta+(1-\beta^2)]\} \tag{8}$$

$$W_2=-(\beta^2-r^2)/[N-(1-\beta^2)]\{1 -[(1-Q)/(4N)](\mathrm{Re/Fr})[2\ln\beta+(1-\beta^2)]\} +[(1-Q)/(4N)](\mathrm{Re/Fr})[\beta^2-r^2-2\ln(\beta/r)] \tag{9}$$

where β is the aspect ratio, $\beta = S/R$, with S being the distance from the jet axis to the wall and We is the Weber number, $\mathrm{We} = \sigma/(\rho_1 W_0^2 R)$, σ is the surface tension. N is the gas to liquid dynamic viscosity ratio and Q is the gas to liquid density ratio.

The solution to Eq. (7) is sought in the form of the Fourier-Bessel series;

Downloaded 03 May 2010 to 171.66.16.247. Redistribution subject to ASME license or copyright; see http://www.asme.org/terms/Terms_Use.cfm

Table 1 Demonstration of convergence of the eigenvectors, Re = 400, Re/Fr = 0., We = 0.0025, Q = 0.0013, N = 0.018, β = 10., k = 0.3

L	N_1	N_2	$\eta(-1, 1)$
1	3	15	0.001704
2	3	15	0.001818
3	3	15	0.001834
2	2	8	0.001797

$$\psi_1(r,z,t) = r\sum_{n=1}^{N_i} F(\lambda_{in}r)\sum_{l=0}^{L}[a_{inl}(t)\cos(lkz) + b_{inl}(t)\sin(lkz)] \quad (10)$$

where, following Lin and Ibrahim (1990),

$$F(\lambda_{1n}r) = J_1(\lambda_{1n}r) \quad (11)$$

$$F(\lambda_{2n}r) = J_1(\lambda_{2n}r)\,Y_1(\lambda_{2n}\beta) - J_1(\lambda_{2n}\beta)\,Y_1(\lambda_{2n}r) \quad (12)$$

where J_1 and Y_1 are the first-order Bessel functions of the first and second kind, respectively, k is the wave number, and λ_{in} are obtainable from the orthogonality conditions of $F(\lambda_{in}r)$ given by

$$\lambda_{1n}J_0(\lambda_{1n}) - J_1(\lambda_{1n}) = 0 \quad (13)$$

$$\lambda_{2n}F^*(\lambda_{2n}) - F(\lambda_{2n}) = 0 \quad (14)$$

where J_1 is the Bessel function of the zero order of the first kind, and

$$F^*(\lambda_{2n}) = J_0(\lambda_{2n})\,Y_1(\lambda_{2n}\beta) - J_1(\lambda_{2n}\beta)\,Y_0(\lambda_{2n}) \quad (15)$$

where Y_0 is the Bessel function of the zero order of the second kind.

To obtain the even mode of the governing equations we multiply Eq. (7) by $F(\lambda_{im}r)\cos(jkz)$ and integrate with respect to r between the limits e_1 and q_1 for the liquid and the limits e_2 and q_2 for the gas where, $e_1 = 0$, $q_1 = e_2 = (1 + \eta)$, $q_2 = \beta$, and integrate with respect to z between the limits 0 and $2\pi/k$, where

$$\eta(z,t) = [h(z,t) - 1]$$

is the dimensionless free surface displacement with h being the distance from jet free surface to jet axis. Using a Taylor series expansion about $r = 1$ we can express integrations between the limits 1 and $(1 + \eta)$ as,

$$\int \Lambda_{im}dr = \sum_{\kappa=0}^{K}[\eta^{\kappa+1}/(\kappa+1)!](d^{\kappa}\Lambda_{im}/dr^{\kappa})_{r=1}$$

where Λ_{im} is any function of r, and K is the number of terms in the Taylor series expansion required for convergence of the series within a specific tolerence. The solution of $\eta(z, t)$ is sought in a Fourier series of the form

$$\eta(z,t) = \sum_{l=0}^{L}[c_l(t)\cos(lkz) + d_l(t)\sin(lkz)]. \quad (16)$$

The odd mode of the governing equations is obtained by multiplying Eq. (7) by $F(\lambda_{im}r)\sin(jkz)$ and integrating with respect to r between the limits e_1 and q_1 for the liquid and the limits e_2 and q_2 for the gas and integrating with respect to z between the limits 0 and $2\pi/k$. Here, $j = 0, 1, 2, \ldots, L$ and $m = 1, 2, \ldots, N_1$ for liquid and $m = 1, 2, \ldots, N_2$ for gas, where N_1, N_2, and L are the number of terms in Eq. (10) required to yield a sufficiently accurate representation of $\psi_i(r,z,t)$. The reason behind including only $(N_2 - 5)$ equations of the governing equations of the gas is that only five of the eight boundary conditions are not readily satisfied by the series representation in Eq. (10) and that we are adopting the Lanczos (1956) tau method in our solution by the Spectral method. The three boundary conditions that are readily satisfied by Eq. (10) are those which require finite radial and axial components of disturbance velocity along the jet axis and the vanishing of the radial component of velocity at the wall. The remaining five boundary conditions are those which require zero axial velocity at the wall, continuous radial and axial velocity, tangential stresses and normal stresses at the liquid-gas interface, which can be written in equation form as,

$$w_2(\beta,z) = 0 \quad (17)$$

$$u_1(h,z) = u_2(h,z) \quad (18)$$

$$W_1(h) + w_1(h) = W_2(h) + w_2(h) \quad (19)$$

$$[u_{1z}(h,z) + W_{1\ell}(h) + w_{1r}(h,z)] = N[u_{2z}(h,z) + W_{2r}(h) + w_{2r}(h,z)] \quad (20)$$

$$-\{-[P_1(h) + p_1(h,z)] + (2/\mathrm{Re})u_{1r}(h,z)\} + \{-[P_2(h) + p_2(h,z)] + (2N/\mathrm{Re})u_{2r}(h,z)\} - \mathrm{We}(1 - \eta + \eta^2 - \eta_{zz} - \eta_z^2/2) = 0, \quad (21)$$

respectively. Note that the last term in Eq. (21), which represents the surface tension stresses, is simplified to its second-order form in disturbance components (Ibrahim, 1989). We are going to adopt only second-order analysis in the present work due to the complexity of the equations. The boundary conditions in Eq. (18) through Eq. (21) apply at the liquid-gas interface which is not known *a priori*. These boundary conditions are expanded in the Taylor series of second order. Carrying out this expansion and using the basic state boundary conditions, Eq. (17) through Eq. (21) become, in terms of the disturbance stream function,

$$\psi_{2r}(\beta,z) = 0 \quad (22)$$

$$\psi_{2z}(1,z) - \psi_{1z}(1,z) = \eta\{[\psi_{1rz}(1,z) - \psi_{1z}(1,z)] - [\psi_{2rz}(1,z) - \psi_{2z}(1,z)]\} \quad (23)$$

$$\eta[W_{2r}(1) - W_{1r}(1)] + (\eta^2/2)[W_{2rr}(1) - W_{1rr}(1)] = [-\psi_r(1,z) - \eta(\psi_{rr}(1,z) - \psi_r(1,z))]_2^1 \quad (24)$$

$$[(\mu_i/\mu_1)\{\psi_{zz} + (\psi_r - \psi_{rr}) + \eta(\psi_{rzz} - \psi_{zz}) + \eta([-(D^2\psi)_r]_{r=1} + (\psi_{rr} - \psi_r))\}]_2^1 = (1 - Q)(\mathrm{Re}/\mathrm{Fr})(\eta^2 - \eta) \quad (25)$$

$$[(\rho_i/\rho_1)\mathrm{Re}\{(\psi_{rt} - \eta\psi_{zzt} - \eta_s\psi_{zt}) - W_r(1)\psi_z - \psi_z(\psi_r - \psi_{rr}) + (W(1) - \psi_r)\psi_{rz} - W(1)\eta\psi_{zzz} - W(1)\eta_z\psi_{zz}\} + (\mu_i/\mu_1)\{[-(D^2\psi)_r]_{r=1} - (3\psi_{rzz} - 2\psi_{zz}) + \eta[(3\psi_{rzz} - \psi_{rrzz} - 4\psi_{zz}) + \psi_{zzzz}] + \eta_z[(3\psi_{rz} - \psi_{rrz} - 4\psi_z) + \psi_{zzz}]\}]_2^1 + \mathrm{Re}\ \mathrm{We}(\eta_z + \eta_{zzz} - 2\eta\eta_z + \eta_z^2) = 0, \quad (26)$$

where μ is the dynamic viscosity. An additional equation is needed to account for the unknown η. This equation is obtained from the relation between the radial component of velocity of the liquid at the liquid-gas interface $u_1(h,z)$ and η;

$$u_1(h,z) = D\eta/Dt. \quad (27)$$

The boundary conditions corresponding to the even and odd modes are obtained by multiplying Eq. (22) through Eq. (27) by $\cos(jkz)$ and $\sin(jkz)$, respectively, and integrating with respect to z between the limits 0 and $2\pi/k$.

The number of unknowns is equal to the number of equations is equal to $2(L + 1)(N_1 + N_2) + 2(L + 1)$. The problem is solved as an initial-value problem with the initial conditions given by the solution of the corresponding linear problem as obtained by Lin and Ibrahim (1990). A fourth-order multistep predictor corrector scheme described in Burden and Faires (1985) is used. The values of N_1, N_2, and L are chosen to be 3, 15, and 2, respectively, as justified by the results of the convergence test shown in Table 1. More details on the solution procedure can be found in Ibrahim (1989).

Results and Discussion

Figure 2 depicts a comparison between the linear and nonlinear predictions of temporal evolution of the free surface displacement in the atomization mode. The linear solution is

Downloaded 03 May 2010 to 171.66.16.247. Redistribution subject to ASME license or copyright; see http://www.asme.org/terms/Terms_Use.cfm

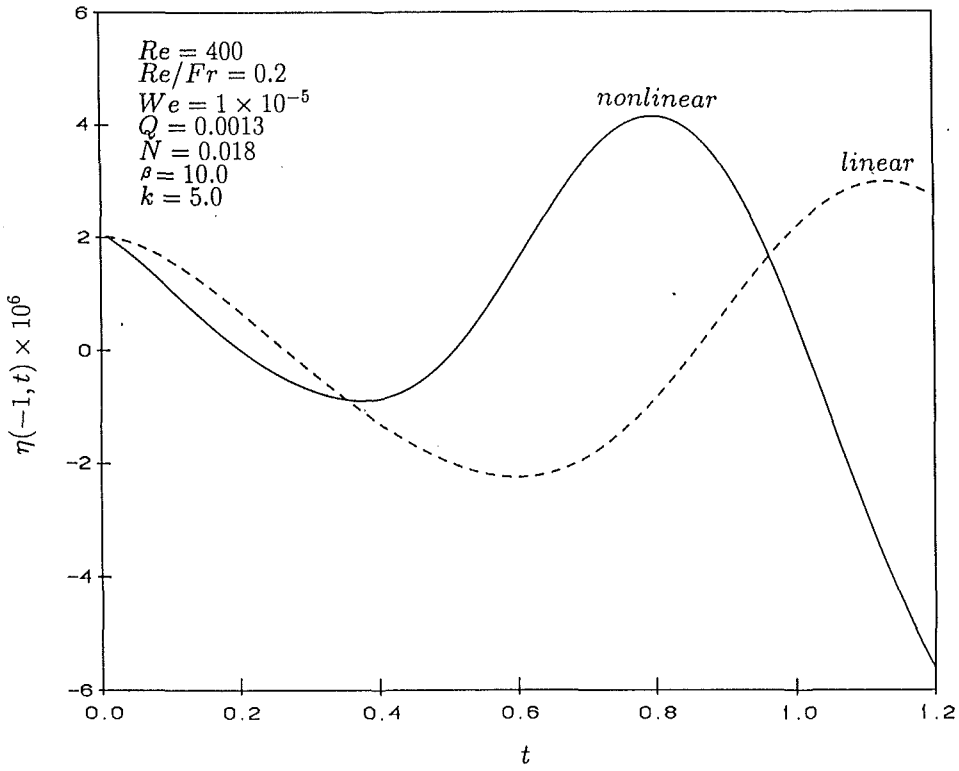


Fig. 2 Comparison of the linear and nonlinear predictions of the temporal evolution of the interface displacement in the atomization mode

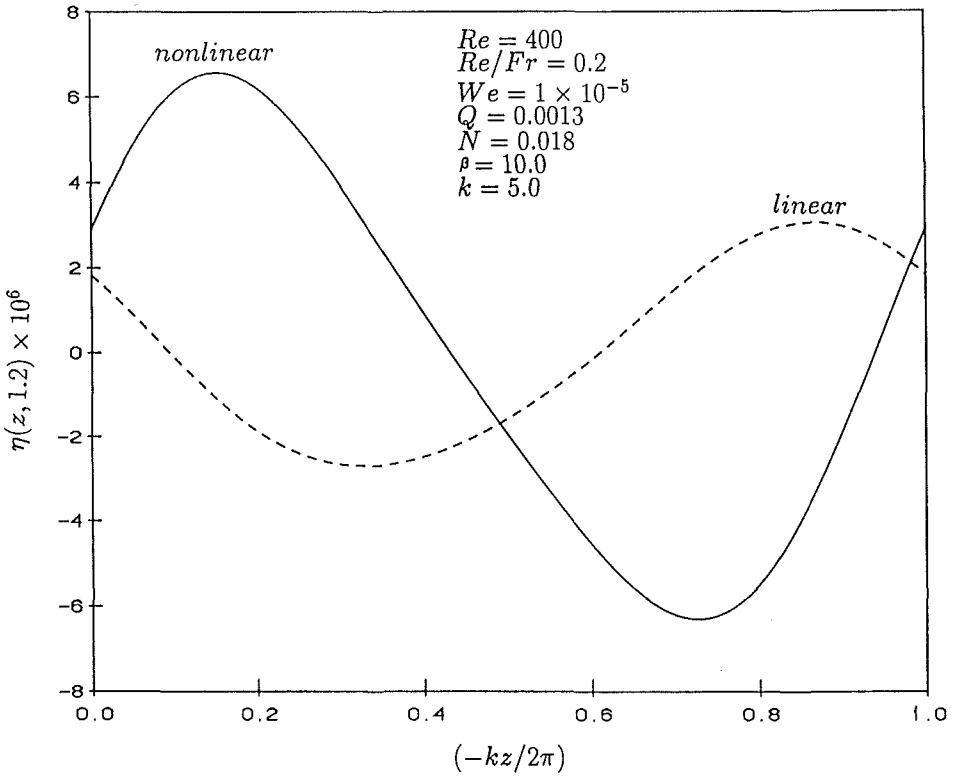


Fig. 3 Comparison of the linear and nonlinear predictions of the interfacial profile in the atomization mode

being that of Lin and Ibrahim (1990). It is seen that the nonlinear analysis predicts a peak that occurs sooner and reaches a higher magnitude than that of the linear analysis. In other words, the initial temporal evolution of finite disturbances occurs at a higher growth rate and frequency than those associated with infinitesimal disturbances. This means that finite disturbances are more unstable than infinitesimal disturbances which leads to the conclusion that if linear theory predicts that a jet is unstable to infinitesimally small disturbances, then nonlinear theory further predicts that the disturbances will

Downloaded 03 May 2010 to 171.66.16.247. Redistribution subject to ASME license or copyright; see http://www.asme.org/terms/Terms_Use.cfm

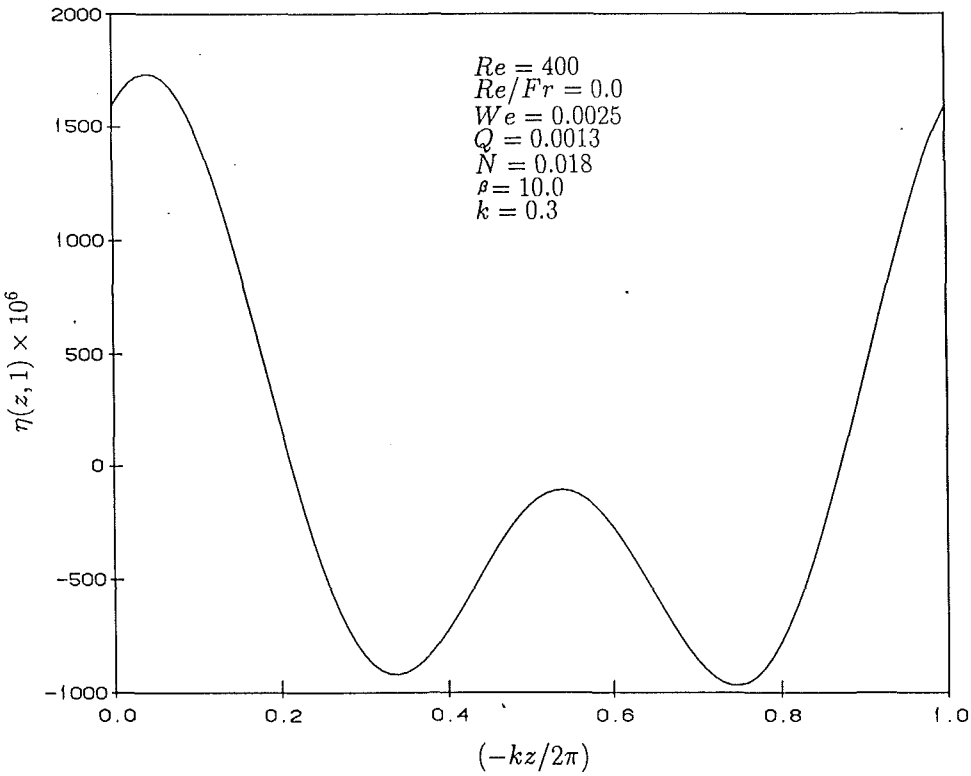


Fig. 4 Nonlinear interfacial profile in the capillary mode, $\eta(-1, 0) = 0.00148$

continue to grow after they become finite and ultimately the jet will be atomized.

Figure 3 describes the interfacial profile of the jet surface in the atomization mode as predicted by both the linear and nonlinear analyses. The horizontal axis is normalized with $(-k/2\pi)$ so that the interfacial profile is depicted for one wavelength $2\pi/k$. Since the present analysis is temporal, this profile repeats itself every wavelength $2\pi/k$. The negative sign in the normalization $(-k/2\pi)$ is to make the horizontal coordinate increase in the flow direction since the axial coordinate z is chosen to be negative downward as shown in Fig. 1. Figure 3 shows that the nonlinear analysis produces larger deformation of the jet surface than the linear instability analysis. This would eventually result in larger droplet size, after disintegration of the jet, than those that would be predicted by the linear analysis.

Figure 4 shows the configuration of the liquid-gas interface in the capillary mode of instability as predicted by the nonlinear analysis. It is seen that the initially sinusoidal wave develops into an asymmetric wave with a higher harmonic. This higher harmonic was discovered in the analysis of Yuen (1968) and the experiments conducted by Rutland and Jameson (1970), Lafrance (1975), and Taub (1976) among others. The asymmetry is due to the higher harmonics as well as feedback into the fundamental. Since the present analysis is only of second order, we don't expect to see more than one swelling between the crests of the primary disturbance waves. As a matter of fact, this is exactly what Rutland and Jameson (1970) and Lafrance (1975) observed up to the point of jet breakup. After breakup, of course, the ligaments between large drops can often disintegrate further, in which case many undulations per primary wavelength could be observed as reported by Rutland and Jameson (1970). However, Taub (1976) reported up to three undulations before jet breakup. It should be noted that, our results are obtained at a much smaller time than those of other authors and hence the amplitude of the interface displacement in Fig. 4 is much smaller. Unfortunately, the CPU time required to advance the solution one dimensionless time unit was too large to attempt to obtain results at a larger time.

The occurence of higher harmonics explains the common observation that once the jet breakup it disintegrates into droplets of various sizes. This is in contrast to the predictions of the linear theory of jet disintegration into droplets of uniform size.

Referring back to Fig. 3, it is obvious that, unlike Rayleigh mode, the results don't indicate any higher harmonics for the atomization mode. This could be explained by observing that the amplitude of the interface displacement in the capillary mode is two order of magnitudes larger than in the atomization mode so it is easier for internodal undulation of finite amplitude to take place in the capillary mode. Also, the higher growth rates and frequencies associated with the atomization mode could be the reason why it is improbable for asymmetry to set in. However, it is possible that if the nonlinear solution is carried out for a larger time, we will see higher harmonics for the atomization mode. Such an investigation was not carried out because of the enormous CPU time required.

Conclusions

While no nonlinear stability was found for unstable linear disturbances, stable linear disturbances were found to be also stable with respect to weakly nonlinear disturbances in a wide range of flow parameters. The nonlinear instability of the atomization mode indicated that finite disturbances are more unstable than infinitesimally small disturbances. No higher harmonics are observed for the atomization mode for the time range investigated.

Asymmetry of the interfacial profile is revealed in the nonlinear analysis of capillary instability. This explains the observed satellite formation in ink jets. The amplitude of the interfacial disturbances are two order of magnitude larger than those associated with the atomization mode of instability. Lin-

Downloaded 03 May 2010 to 171.66.16.247. Redistribution subject to ASME license or copyright; see http://www.asme.org/terms/Terms_Use.cfm

ear theories are adequate for predicting the onset of either the Rayleigh or the Taylor mode instability. The outcome of atomization process requires fully nonlinear treatment.

Acknowledgments

This work was funded in part by Grant No. DAAL 03-89-K-0179 of ARO, Grant No. MSM-8817372 of NSF and a New York State Science and Technology Foundation Grant. The computations were carried out with the computer facility at Clarkson University and with the Cornell National Supercomputer Facility, which is founded by the NSF, the State of New York, and IBM Corporation.

References

Bogy, D. B., 1978a, "Use of One-Dimensional Cosserat Theory to Study Instability in a Viscous Liquid Jet," *Physics Fluids*, Vol. 21, pp. 190–197.

Bogy, D. B., 1978b, "Wave Propagation and Instability in a Circular Semi-Infinite Liquid Jet Harmonically Forced at the Nozzle," ASME JOURNAL OF APPLIED MECHANICS, Vol. 45, pp. 469–474.

Bogy, D. B., 1979, "Breakup of a Liquid Jet: Third Perturbation Cosserat Solution," *Physics Fluids*, Vol. 22, pp. 224–230.

Burden, R. L., and Faires, J. D., 1985, *Numerical Analysis*, 3rd ed., Prindle, Weber and Schmidt.

Chaudhary, K. C., 1977, "The Nonlinear Capillary Instability of a Jet," Ph.D. Thesis, University of Southern California, Los Angeles, Calif.

Chaudhary, K. C., and Redekopp, L. C., 1980a, "The Nonlinear Capillary Instability of a Liquid Jet, Part 1 Theory," *J. Fluid Mech.*, Vol. 96, pp. 257–274.

Chaudhary, K. C., and Maxworthy, T., 1980b, "The Nonlinear Capillary Instability of a Liquid Jet, Part 2, Experiments on the Jet Behaviors before Droplet Formation," *J. Fluid Mech.*, Vol. 96, pp. 275–286.

Green, A. E., 1976, "On the Nonlinear Behavior of Fluid Jets," *Int. J. Engng. Sci.*, Vol. 14, pp. 49–63.

Ibrahim, E. A., 1989, "Linear and Nonlinear Instability of a Liquid Jet in a Viscous Gas," Ph.D. Dissertation, Clarkson University, Potsdam, N.Y.

Keller, J. B., Rubinow, S. I., and Tu, Y. O., 1973, "Spatial Instability of a Jet," *Physics Fluids*, Vol. 16, pp. 2052–2055.

Lafrance, P., 1975, "Nonlinear Break-up of a Liquid Jet," *Physics Fluids*, Vol. 18, pp. 428–432.

Lanczos, C., 1956, *Applied Analysis*, Prentice-Hall, Englewood Cliffs, N.J.

Lee, H. C., 1974, "Drop Formation in a Liquid Jet," *IBM J. Res. Dev.*, Vol. 18, pp. 364–369.

Lin, S. P., and Creighton, B., 1990, "Energy Budjet in Atomization," *Aerosol. Sci. Tech.*, Vol. 12, No. 3, pp. 630–636.

Lin, S. P., and Ibrahim, E. A., 1990, "Instability of a Viscous Liquid Jet Surrounded by a Viscous Gas in a Vertical Pipe," *J. Fluid Mech.*, Vol. 218, pp. 641–658.

Lin, S. P., and Lian, Z. W., 1990, "Mechanisms of the Breakup of Liquid Jets," *AIAA J.*, Vol. 28, pp. 120–126.

Neyfeh, A. H., 1970, "Nonlinear Stability of a Liquid Jet," *Physics Fluids*, Vol. 13, pp. 841–847.

Phinney, R. E., 1972, "The Breakup of a Turbulent Liquid Jet in a Gaseous Atmosphere," *J. Fluid Mech.*, Vol. 60, pp. 689–701.

Rutland, D. F., and Jameson, G. J., 1970, "A Nonlinear Effect in the Capillary Instability of Liquid Jets," *J. Fluid Mech.*, Vol. 46, pp. 267–271.

Shokoohi, F., and Elrod, H. G., 1987, "Numerical Investigation of the Disintegration of Liquid Jets," *J. Comp. Physics*, Vol. 71, pp. 324–342.

Taub, H. H., 1976, "Investigation of Nonlinear Waves on Liquid Jets," *Physics Fluids*, Vol. 19, pp. 1124–1129.

Wang, D. P., 1968, "Finite Amplitude Effect on the Stability of a Jet of Circular Cross-Section," *J. Fluid Mech.*, Vol. 34, pp. 299–313.

Yuen, M. C., 1968, "Nonlinear Capillary Instability of a Liquid Jet," *J. Fluid Mech.*, Vol. 33, pp. 151–163.

Downloaded 03 May 2010 to 171.66.16.247. Redistribution subject to ASME license or copyright; see http://www.asme.org/terms/Terms_Use.cfm